9-Borafluoren:
Strukturelle Vielfalt durch Reduktion

Dissertation

zur Erlangung des Doktorgrades

der Naturwissenschaften

vorgelegt dem Fachbereich Biochemie, Chemie und Pharmazie

der Johann Wolfgang Goethe-Universität

in Frankfurt am Main

von

Thomas Kaese

aus Offenbach am Main

Frankfurt am Main 2018

D30

vom Fachbereich Biochemie, Chemie und Pharmazie der

Johann Wolfgang Goethe-Universität als Dissertation angenommen

Dekan:	Prof. Dr. Clemens Glaubitz	
Gutachter:	Prof. Dr. Matthias Wagner	(1)
	Prof. Dr. Max C. Holthausen	(2)
	Prof. Dr. Maik Finze	(3)
Datum der Disputation:	03. Dezember 2018	

Meiner Familie

Die vorliegende Arbeit wurde im Zeitraum von Januar 2015 bis August 2018 unter der Anleitung von Herrn Prof. Dr. Matthias Wagner am Institut für Anorganische und Analytische Chemie der Johann Wolfgang Goethe-Universität in Frankfurt am Main angefertigt.

Danksagung

Die Danksagung wurde aus der digitalen Version entfernt.

Inhaltsverzeichnis

1 Einleitung 1

1.1 Aromatizität und Antiaromatizität am Beispiel der Cyclopentadienyl-Ionen 1

1.2 Borole 2

1.3 9-Borafluorene 3

1.4 Reduzierte 9-Borafluorene 5

1.5 Nucleophile Borverbindungen 12

1.5.1 Boran-Anionen und -Dianionen 12

1.5.2 Boryl-Anionen 15

1.5.3 Borylene 16

1.6 Elektronenpräzise B–B-Bindungen 20

1.6.1 Reduktion von Halogenboranen 20

1.6.2 Reduktion von Diboranen(6) 21

1.6.3 Kupplung redoxaktiver Organoborverbindungen 22

1.6.4 Dehydrokupplung von Boranen 22

1.6.5 Reaktionen von Metallborylenen und Metallborylen 23

1.6.6 Hydroborierung von Diborenen 24

1.6.7 Deprotonierung von B–H-Verbindungen 25

1.7 Moleküle mit B=B-Bindungen 26

1.8 Zwischenfazit 28

1.9 Zielsetzung 29

2 Übersicht der Ergebnisse 31

2.1 Reduktionschemie des Diboran(6)-Derivats **12** 31

2.1.1 Gerüstumlagerungen im Zuge der Reduktion von **12** 32

2.1.2 Hydridtransfers im Zuge der Reduktion von **12** 36

2.1.3 Reaktivität der Triade **12**/[**116**]$^{-}$/[**37**]$^{2-}$ 38

2.2 Reduktionschemie des Bis(9-borafluorenyl)methans **7** 53

2.3 Reduktionschemie des 9-Borafluorens **6**·THF 55

2.3.1 Reduktion von **6**·THF mit Lithium 56

2.3.2 Erstmalige Isolierung und Charakterisierung von Li_2[**6**] und Li_4[**146**] 56

2.3.3 Gezielte Darstellung von M_2[**6**] 58

2.3.4 Entstehung von [**34**]$^{-}$, [**35**]$^{-}$, [**36**]$^{-}$ und [**37**]$^{2-}$ durch Reduktion von **6**·THF 59

2.3.5 Reaktionen zwischen M_2[**6**] und 1,2-Dibromethan, M_2[**6**] und Ethen sowie M[**116**] und Ethen 63

2.3.6 Gezielte Darstellung von Li_4[**146**] 66

3 Zusammenfassung 69

4 Experimentelle Daten nicht publizierter Verbindungen 74
4.1 Allgemeine Arbeitstechniken 74
4.1.1 NMR-Spektroskopie 74
4.1.2 Einkristall-Röntgendiffraktometrie 74
4.2 Synthese und NMR-Daten unpublizierter Verbindungen 75
4.2.1 Li_2[**6**] 75
4.2.2 Li_4[**7**] 75
4.2.3 Li_4[**146**] 76
4.2.4 Li[**147**] 77
4.2.5 Li[**149**] und Li[**150**] 78
4.3 Kristallographische Daten unpublizierter Verbindungen 79
5 Referenzen 81
6 Anhang 91
6.1 Publikationsliste mit Angabe des eigenen Anteils 91
6.2 Eigene Publikationen in Fachjournalen 93
6.2.1 A Redox-Active Diborane Platform Performs C(sp^3)–H Activation and Nucleophilic Substitution Reactions 93
6.2.2 Doping Polycyclic Aromatics with Boron for Superior Performance in Materials Science and Catalysis 174
6.2.3 Deprotonation of a Seemingly Hydridic Diborane(6) to Build a B–B Bond 191
6.2.4 Hydroboration as an Efficient Tool for the Preparation of Electronically and Structurally Diverse N→B-Heterocycles 227
6.2.5 Forming B–B Bonds by the Controlled Reduction of a Tetraaryldiborane(6) 353
6.2.6 A Preorganized Ditopic Borane as Highly Efficient One- or Two-Electron Trap 393
6.3 Lebenslauf 474
6.4 Erklärung über frühere Promotionsverfahren und Versicherung 476

Abkürzungsverzeichnis

9-BBN-H	9-Borabicyclo[3.3.1]nonan
1E2Z	Einelektron-Zweizentrenbindung
2E2Z	Zweielektronen-Zweizentrenbindung
2E3Z	Zweielektronen-Dreizentrenbindung
Ad	1-Adamantyl
B_2pin_2	Bis(pinakolato)diboran
Bn	Benzyl ($CH_2C_6H_5$)
cAAC	cyclisches Alkylaminocarben (engl. cyclic alkyl amino carbene)
COD	1,5-Cyclooctadien
$[Cp]^-$	Cyclopentadienyl-Anion ($[\eta^5\text{-}C_5H_5]^-$)
$[Cp^*]^-$	$[\eta^5\text{-}C_5Me_5]^-$
Dipp	2,6-Di(*i*Pr)phenyl
DMAP	4-(Dimethylamino)pyridin
DME	1,2-Dimethoxyethan
Dur	2,3,5,6-Tetramethylphenyl
Eind	1,1,3,3,5,5,7,7-Octaethyl-*s*-hydrindacen-4-yl
ESR	Elektronenspinresonanz
Et	Ethyl
et al.	und andere
h	Stunde(n)
HBCat	Catecholboran
HBpin	Pinakolboran
HOMO	höchstes besetztes Molekülorbital (engl. highest occupied molecular orbital)
IDip	1,3-Bis(2,6-di(*i*Pr)phenyl)imidazol-2-yliden
I*i*Pr	1,3-Di(*i*Pr)imidazol-2-yliden
IMe	1,3-Dimethylimidazol-2-yliden
IMes	1,3-Bis(2,4,6-trimethylphenyl)imidazol-2-yliden
in situ	ohne Aufreinigung (Ausnahme: Entfernen flüchtiger Bestandteile im Vakuum)
*i*Pr	*iso*-Propyl
LDA	Lithiumdi(*i*Pr)amid
LDBB	Lithium-4,4‘-di(*t*Bu)biphenylid
LiNaph	Lithiumnaphthalenid
LUMO	niedrigstes unbesetztes Molekülorbital (engl. lowest unoccupied molecular orbital)
Me	Methyl
Mes	1,3,5-Trimethylphenyl
Mes*	1,3,5-Tri(*t*Bu)phenyl
min	Minute(n)
MO	Molekülorbital

MPind	1,1,7,7-Tetramethyl-3,3,5,5-tetrapropyl-*s*-hydrindacen-4-yl
n. b.	nicht beobachtet
NHC	*N*-heterocyclisches Carben
NMR	kernmagnetische Resonanz (engl. nuclear magnetic resonance)
OFET	organischer Feldeffekttransistor
OLED	organische Leuchtdiode (engl. organic light emitting diode)
Ph	Phenyl
R	beliebiger Rest
RT	Raumtemperatur
SIDep	1,3-Bis(2,6-diethylphenyl)-4,5-dihydroimidazol-2-yliden
SMD	implizites Lösungsmittelmodell, das die Elektronendichte des Solvats nutzt (engl. solvation model based on density)
*t*Bu	*tert*-Butyl
TEMPO	2,2,6,6-Tetramethylpiperidinyloxyl
Tf	Triflyl (SO_2CF_3)
THF	Tetrahydrofuran
tht	Tetrahydrothiophen
Tipp	2,4,6-Tri(*i*Pr)phenyl
TMEDA	*N*,*N*,*N*',*N*'-Tetramethylethylendiamin
TMS	Trimethylsilyl
Tp	2,6-Di(2,4,6-tri(*i*Pr)phenyl)phenyl

1 Einleitung

Chemie ist die Wissenschaft, die sich mit dem Knüpfen, Brechen und der Analyse von Atom-Atom-Bindungen beschäftigt. Allein an der empirischen Unterscheidung von Bindungen, unter anderem in kovalent, ionisch oder metallisch, lässt sich leicht erkennen, dass die Wechselwirkung positiv geladener Atomkerne und negativ geladener Elektronen schwer zu definieren und quantifizieren ist. Ein genaues Verständnis von Bindungen ist aber entscheidend, um neue relevante Substanzen herzustellen und deren Eigenschaften im Detail zu erschließen und zu nutzen. Quantenchemische Modelle haben das Feld massiv bereichert. Die Genauigkeit semi-empirischer Vorhersagen, die bei komplexen Systemen verwendet werden, ist jedoch in der Regel von der exakten Kenntnis von Vergleichssystemen abhängig, die als Standard zur Kalibrierung dienen. Theorie und Experiment sind daher heutzutage eng verwoben. Beide Bereiche müssen die Grenzen der chemischen Bindung ausloten, um eine möglichst perfekte Beschreibung zu erzielen. Ein historisch gewachsenes und seit jeher prägendes Konzept ist die Aromatizität von Verbindungen, die zur Vorhersage von Reaktivitäten und Eigenschaften vieler Substanzen genutzt wird.

1.1 Aromatizität und Antiaromatizität am Beispiel der Cyclopentadienyl-Ionen

Im Jahr 1931 führte Hückel theoretische Betrachtungen zur Elektronenkonfiguration des Benzols und verwandter Verbindungen durch.[1] Nach der daraus entstandenen Theorie können konjugierte ungesättigte monocyclische Kohlenwasserstoffe in zwei Klassen eingeteilt werden: Aromaten mit $(4n + 2)$ π-Elektronen zeichnen sich durch höchste besetzte Molekülorbitale (HOMOs) mit bindendem Charakter aus und sind thermodynamisch besonders stabil. Antiaromaten mit $4n$ π-Elektronen weisen dagegen halbbesetzte nichtbindende oder besetzte schwach bindende Grenzorbitale auf und sind in der Regel deutlich instabiler.[2] Die energetischen Lagen der Orbitale und daraus resultierende Verzerrungen der Moleküle lassen sich qualitativ durch Frost-Musulin-[3] und Walsh-Diagramme[4] ableiten. Zur Bestimmung des aromatischen oder antiaromatischen Charakters einer Verbindung werden neben der Anzahl an π-Elektronen auch Eigenschaften wie Bindungslängen und magnetische Suszeptibilitäten sowie allgemeine Reaktivität und thermodynamische Stabilisierung gegenüber geeigneten Referenzsystemen herangezogen, wodurch dem Begriff Aromatizität in der Literatur unterschiedliche Bedeutungen beigemessen werden. Aromaten und Antiaromaten finden in der organischen Synthese breite Anwendung, sodass das Verständnis ihrer Eigenschaften von fundamentaler Bedeutung ist. Cyclopentadien ist ein prototypisches Molekül, an dem Aromatizität und Antiaromatizität diskutiert werden können:[5, 6] Bereits seit dem Jahr 1900 ist bekannt, dass Cyclopentadien leicht zu deprotonieren ist.[7] Das resultierende Cyclopentadienyl-Anion mit $(4n + 2)$ π-Elektronen ($n = 1$) und D_{5h}-Symmetrie erfährt durch seine Aromatizität ausreichende Stabilisierung, um als einer der vielseitigsten Liganden in der metallorganischen Chemie

zu dienen (Abbildung 1).[8] Das antiaromatische Cyclopentadienyl-Kation hingegen ist nur unter harschen experimentellen Bedingungen spektroskopisch charakterisiert worden,[9-11] obwohl umfassende theoretische Studien existieren (Abbildung 1).[5, 12, 13] Das Kation liegt als D_{5h}-symmetrische, planare Verbindung mit Triplett-Grundzustand und kleiner Singulett-Triplett-Energielücke vor.[5, 13] Im energetisch höher liegenden Singulett-Zustand besitzt das Cyclopentadienyl-Kation C_{2v}-Symmetrie.[5, 13]

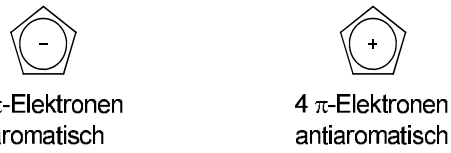

Abbildung 1. Cyclopentadienyl-Anion (links) und -Kation (rechts).

1.2 Borole

Analog zur Delokalisierung von π-Elektronen über das positiv geladene Kohlenstoffatom eines Carbeniumions hinweg, kann ein isoelektronisches, trigonal-planar koordiniertes Boratom ebenfalls die Delokalisierung von Elektronendichte ermöglichen. Der formale Austausch einer CH^+-Einheit in einem Cyclopentadienyl-Kation durch ein BH-Fragment erzeugt ein antiaromatisches Borol.[12, 14] Im Singulett-Grundstand mit C_{2v}-Symmetrie besitzt es stark alternierende C–C-Bindungslängen.[12] Die Reaktivität des Borols ist vielfältig, da ein stark Lewis-saures Borzentrum in Kombination mit einem aktivierten Dien und labilen B–C-Bindungen vorliegt (Abbildung 2).

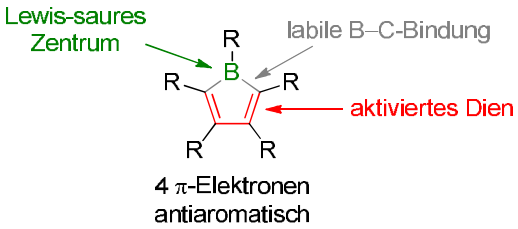

Abbildung 2. Generelle Eigenschaften und Bindungsanalyse des Borols.

Entsprechend sind die Stammverbindung H_4C_4BH sowie allein am Boratom substituierte Derivate ausgesprochen instabil und konnten bisher nur in der Koordinationssphäre von Übergangsmetallen erzeugt werden, wie beispielsweise im Bis(η^5-borol)nickel-Komplex $(H_4C_4BH)_2Ni$ (**1**; Abbildung 3).[15-17] Bei dem Versuch, 1-Phenyl-2,3,4,5-tetramethylborol (Me_4C_4BPh) herzustellen, wurde nicht das Monomer, sondern das Dimer **2** gefunden, das aus einer Diels-Alder-Reaktion hervorgeht (Abbildung 3).[18] Das Dimer **2** kann als Quelle für Borol-Monomere in Reaktionen mit nicht-aktivierten Alkenen und Alkinen dienen.[18] Die Isolation eines monomeren Borols ohne anellierte aromatische Gruppen gelang erstmalig 1969 anhand der Synthese von Pentaphenylborol (**3**; Ph_4C_4BPh; Abbildung 3).[19] Im Jahr 2008 folgte mithilfe der Röntgendiffraktometrie der strukturelle Beleg.[20] Seit der Entdeckung des Pentaphenylborols wurden dessen physikalische Eigenschaften[20, 21] und

Reaktivität ausgiebig untersucht. Das Reaktionsspektrum erstreckt sich von Lewis-Säure-Base-Adduktbildungen[21] über Protodeborierungen,[21] Oxidationen,[19, 21] Reduktionen,[22-24] Diels-Alder-Reaktionen,[19, 21] Ringerweiterungen[25-31] und Aktivierungen von Element-Element-Bindungen.[32-36]

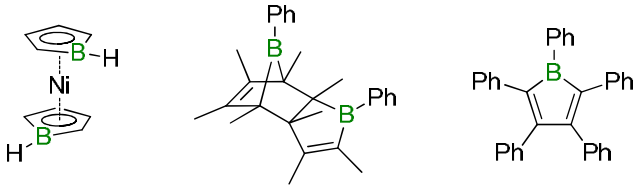

1 **2** **3**

Abbildung 3. Bis(η^5-borol)nickel-Komplex ($H_4C_4BH)_2Ni$ (**1**; links), Me_4C_4BPh-Dimer (**2**; Mitte) und monomeres Ph_4C_4BPh (**3**; rechts).

1.3 9-Borafluorene

Ein bewährtes Konzept zur Stabilisierung cyclischer Systeme basiert auf deren Benzanellierung.[37] In der Literatur wird allerdings kontrovers diskutiert, inwiefern Benzanellierung die Antiaromatizität eines zentralen Cyclopentadienyl-Kations herabsetzt.[38] Erst im Jahr 2015 gelang die Isolierung des Fluorenyl-Kations [**4**]$^+$ in einer Matrix aus niederdichtem amorphem Eis (Abbildung 4).[39] Analog zur formalen Erzeugung des Fluorenyl-Kations [**4**]$^+$ durch zweifache Anellierung des Cyclopentadienyl-Kations mit Benzolringen, ist das neutrale 9-Borafluoren das formale Produkt einer zweifachen Benzanellierung des Borols. 9-Borafluorene sind unter Inertbedingungen in der Regel recht stabil, sodass eine Vielzahl borgebundener Substituenten unter Erhalt des monomeren 9-Borafluoren-Grundgerüsts **A** eingeführt werden konnte (R = Alkyl, Aryl, Ferrocenyl, NR_2, PR_2, OR, Halogen; Abbildung 4).[40-57] Die Stabilität der 9-Borafluorene ermöglicht eine Untersuchung der Eigenschaften und Reaktivitäten dieser Verbindungsklasse und erlaubt in gewissem Umfang auch Rückschlüsse auf verwandte Moleküle wie das Fluorenyl-Kation.

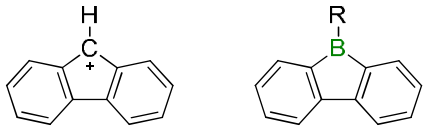

[**4**]$^+$ **A**

Abbildung 4. Fluorenyl-Kation ([**4**]$^+$; links) und substituierte 9-Borafluorene (**A**; R = Organyl; rechts).

Theoretische und experimentelle Studien deuten auf einen antiaromatischen Charakter des zentralen Borolrings hin, der durch Derivatisierung des 9-Borafluorenkörpers weiter beeinflusst werden kann.[44, 51, 52, 56-62] Das native 9-Borafluoren mit B–H-Bindung stellt eine Besonderheit dar, da es nur in Gegenwart von Lewis-Basen wie SMe_2,[63] Pyridin[64] oder THF[65] monomer vorliegt (**5**·Base; Schema 1).

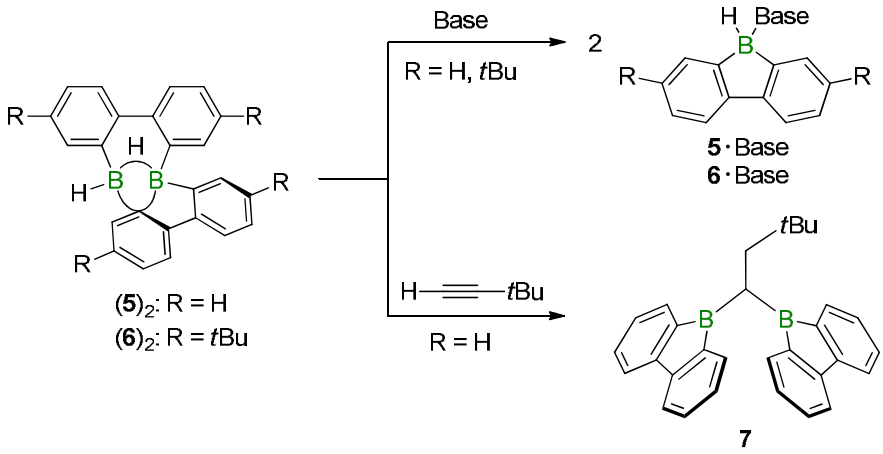

Schema 1. Die partielle Ringöffnung der C_1-symmetrischen Dimere $(\mathbf{5})_2$ und $(\mathbf{6})_2$ ist durch Zugabe von Lewis-Basen (z. B. SMe_2, Pyridin oder THF) oder ungesättigten Kohlenwasserstoffen (z. B. *t*BuC≡CH) umkehrbar.

In Abwesenheit entsprechender Elektronenpaardonoren bildet sich ein partiell ringgeöffnetes, C_1-symmetrisches Dimer $(\mathbf{5})_2$, bei dem die Boratome über ein Wasserstoffatom und einen Arylring durch Zweielektronen-Dreizentrenbindungen (2E3Z-Bindungen) verbrückt werden (Schema 1).[66] Für das *t*Bu-substituierte 9-Borafluoren $(\mathbf{6})_2$ wurde die C_1-symmetrische Molekülgeometrie mittels Röntgenstrukturanalyse bewiesen.[66] Die partielle Ringöffnung ist umkehrbar durch Adduktbildung mittels Lewis-Basen (z. B. SMe_2, Pyridin oder THF) oder im Zuge von Hydroborierungsreaktionen an ungesättigten Kohlenwasserstoffen (z. B. mit *t*BuC≡CH zur Synthese von **7**; Schema 1).[64, 65, 67, 68] *t*Bu-Gruppen (R) in der Molekülperipherie tragen maßgeblich zur kinetischen Stabilisierung des Dimers $(\mathbf{6})_2$ bei. Fehlen sie, so schreitet eine ringöffnende Oligomerisation bei Raumtemperatur fort und erzeugt bordotierte Oligophenylenstränge wie **8**, die durch intramolekulare B–H–B-Bindungen stabilisiert sind (Schema 2).[64]

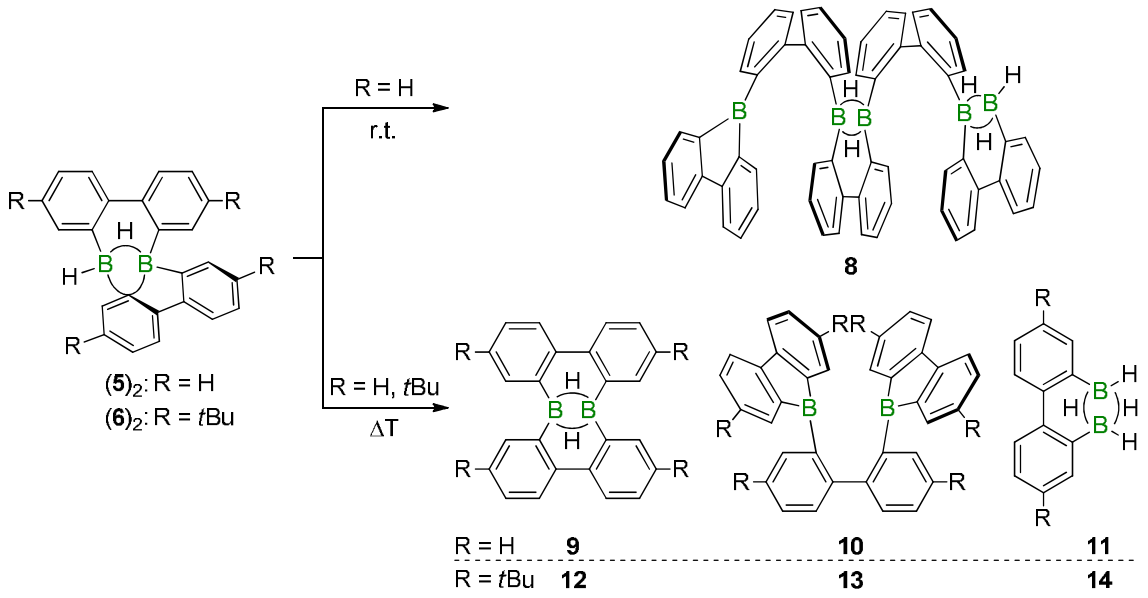

Schema 2. Ringöffnende Oligomerisation von $(\mathbf{5})_2$ (oben) und Thermolyse von $(\mathbf{5})_2$ und $(\mathbf{6})_2$ (unten).

Bei erhöhter Temperatur bilden (**5**)$_2$ und (**6**)$_2$ keine Oligomere, sondern entropisch begünstigte niedermolekulare Verbindungen (für R = H: **9**-**11**, für R = *t*Bu: **12**-**14**; Schema 2). Die Reaktivität von 9-Borafluorenen ist maßgeblich durch energetisch niedrig liegende LUMOs geprägt, die die Mitglieder der Substanzklasse zu guten Elektronenakzeptoren und starken Lewis-Säuren machen.[52, 59, 69-71] Zahlreiche Lewis-Säure-Base-Addukte[41, 45, 46, 55, 63, 72-77] und frustrierte Lewis-Paare (FLPs)[78, 79] sind publiziert. Nach Adduktbildung mit ausgewählten Lewis-Basen können 9-Borafluorene unter Ringerweiterung reagieren.[80-82] Beispielsweise beschrieben Bettinger et al. im Jahr 2012, dass die Umsetzung von 9-Cl-9-Borafluoren **15** mit $Me_3SiON(H)SiMe_3$ bereits unterhalb von Raumtemperatur über das 9-Amino-9-borafluoren **16** zum benzanellierten 1,2-Dihydro-1,2-azaborin **17** führt (Schema 3).[80] Fukushima et al. berichteten im Jahr 2016, dass **15** durch 1,2-Carboborierung von Alkinen in vicinal substituierte, zweifach benzanellierte Borepine wie **18** überführt werden kann (Schema 3). Die Borepine können mittels anschließender Einelektronoxidation (z. B. mit $FeCl_3$) zu 9,10-disubstituierten Phenanthrenen wie **19** reagieren (via Deborylierungsreaktion mit C–C-Bindungsknüpfung).[82]

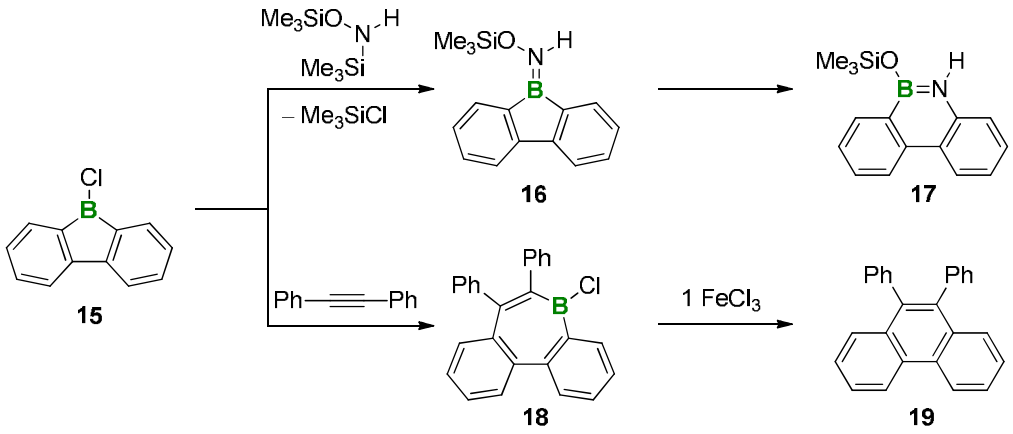

Schema 3. Das Azaborin **17** und das Borepin **18** können durch Ringerweiterungsreaktionen von 9-Cl-9-Borafluoren **15** mit einem Hydroxylamin bzw. Alkin synthetisiert werden. Mit $FeCl_3$ reagiert **18** unter Einelektronoxidation zu Phenanthren **19**.

1.4 Reduzierte 9-Borafluorene

9-Borafluorene sind die Boranaloga von Fluoren und Carbazol. Letztere sind wichtige Bausteine für organische Lochleiter und stark fluoreszierende Materialien.[83-85] Aufgrund ihrer niedrig liegenden LUMO-Energien sind 9-Borafluorene dazu prädestiniert, Elektronen aufzunehmen. Die entstehenden 9-Borafluoren-Anionen/-Dianionen sind vielversprechende Kandidaten als Elektronenleiter in Bauelementen für organische Leuchtdioden (OLEDs) oder organische Feldeffekttransistoren (OFETs) sowie als borzentrierte Nucleophile für die Synthese. Ein dianionisches Borol ist isoelektronisch mit dem Cyclopentadienyl-Anion, das eine hohe aromatische Stabilisierung erfährt. Entsprechend wurden in der Literatur bereits erste elektrochemische sowie präparative Reduktionen durchgeführt, um organisch substituierte 9-Borafluoren-Dianionen zu erhalten: Power et al. publizierten im Jahr 1996 die Reduktion sterisch beladener Arylborandihalogenide,

2,6-$Mes_2C_6H_3BX_2$, bei der dianionische 9-Borafluorene wie $[Li(Et_2O)]_2$[**20**] entstanden (Abbildung 5; Mes = 1,3,5-Trimethylphenyl).[86] 2001 berichteten Wehmschulte et al. von der gezielten Reduktion des 9-Borafluorens **21** mit Lithium zum Dianion [**21**]$^{2-}$, das in mäßiger Ausbeute isoliert wurde (Abbildung 5).[45] Bei dem Versuch, das Lithiumsalz Li_2[**21**] durch Metathesereaktionen in Übergangsmetallkomplexe umzuwandeln, entstand wieder das neutrale 9-Borafluoren **21**. Piers et al. versetzten im Jahr 2003 fluorierte 9-Borafluorene und 9-Phenyl-9-borafluoren (**22**) mit ¼ $[Cp^*Al]_4$ ($[Cp^*]^- = [\eta^5\text{-}C_5Me_5]^-$).[48] In beiden Fällen wurden die entsprechenden 9-Borafluoren-Addukte mit jeweils einer η^1-gebundenen Cp*Al(I) Lewis-Base gebildet (vgl. **22**·AlCp*; Abbildung 5). Die Autoren folgerten, dass die Adduktbildung mit Cp*Al(I) gegenüber einer Redoxreaktion bevorzugt sei, da trotz der Neigung von Al(I), zu Al(III) oxidiert zu werden, die Aufhebung der Aromatizität der Phenylringe im zweifach reduzierten 9-Borafluoren energetisch zu ungünstig wäre. Mit dem starken Reduktionsmittel Lithium wird hingegen die Bildung von η^5-koordinierten Borol-Komplexen beobachtet, was der Reduktion zu den Borol-Dianionen entspricht (vgl. Li_2[**20**] und Li_2[**21**]). Eine Transmetallierung von Li_2[**22**] mit Cp^*AlCl_2·THF war nicht erfolgreich, sondern lieferte die neutrale Verbindung **22**. Yamaguchi et al. bestimmten in den Jahren 2008 und 2011 für die Tipp- und Mes*-substituierten 9-Borafluorene **23**-**26** Reduktionspotentiale mittels cyclovoltammetrischer Messungen (Abbildung 5; Tabelle 1; Tipp = 2,4,6-Tri(*i*Pr)phenyl, Mes* = 1,3,5-Tri(*t*Bu)phenyl).[51, 60] Die einfach bordotierten Derivate weisen eine reversible 1. Reduktionswelle bei kathodischen Potentialen auf (–2.04 V bis –2.28 V). Die 2. Reduktionswelle ist nur im Fall der Dithienyl-Substitution reversibel (**24**; –2.70 V), bei den anderen Molekülen sind die 2. Reduktionswellen irreversibel oder wurden nicht beobachtet.

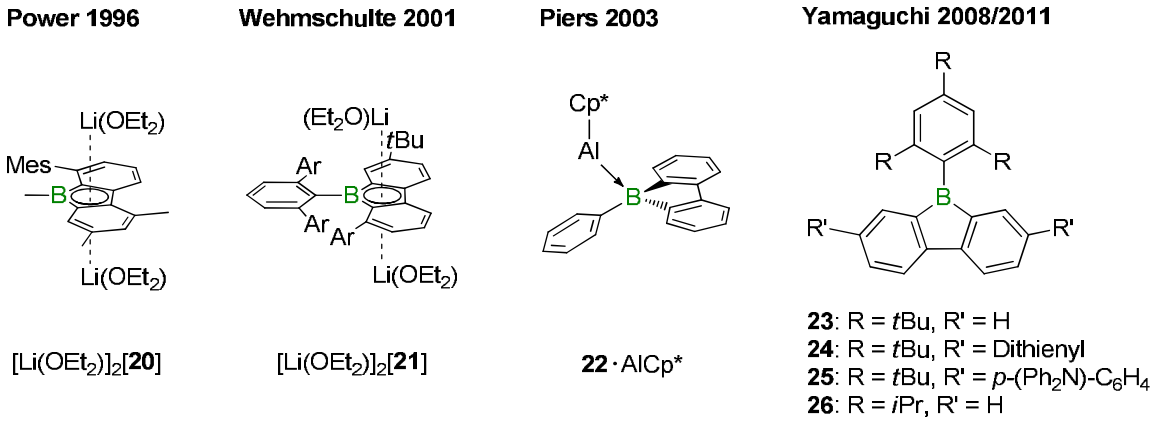

Abbildung 5. Die zweifach reduzierten 9-Borafluorene Li_2[**20**] und Li_2[**21**], das Cp*Al-Addukt an 9-Phenyl-9-borafluoren **22**·AlCp* sowie 9-Aryl-9-borafluorene **23**-**26**, die elektrochemisch auf ihre Reduzierbarkeit untersucht wurden. Ar = 4-*t*BuC_6H_4; $[Cp^*]^- = [\eta^5\text{-}C_5Me_5]^-$.

Werden zwei Boratome in räumliche Nähe zueinander gebracht, so ist eine kooperative Wechselwirkung der beiden leeren p_z-Orbitale mit Elektronendichte denkbar. Ein Vergleich mit isoelektronischen Carbeniumionen verrät, dass es hier Systeme gibt, bei denen durch Reduktion zweier benachbarter C^+-Zentren eine elektronenpräzise C–C-Bindung aufgebaut und durch Oxidation wieder gebrochen werden kann.[87, 88]

Tabelle 1. Reduktionspotentiale ausgewählter 9-Borafluorene.

Verbindung	1. Reduktionspotential	2. Reduktionspotential
23	–2.28 V ($E_{1/2}$)[a]	nicht beobachtet
24	–2.04 V ($E_{1/2}$)[a]	–2.70 V ($E_{1/2}$)[a]
25	–2.19 V ($E_{1/2}$)[a]	–3.00 V (E_{pc})[a]
26	–2.11 V ($E_{1/2}$)[b]	–3.05 V (E_{pc})[b]
33	–2.14 V ($E_{1/2}$)[b]	–2.56 V ($E_{1/2}$)[b]
10	–1.49 V ($E_{1/2}$)[c]	–1.75 V ($E_{1/2}$)[c]
7	–1.76 V ($E_{1/2}$)[b]	–2.17 V ($E_{1/2}$)[b]

[a] vs FcH/FcH$^+$, THF, [*n*Bu$_4$N][ClO$_4$] (0.1 M), 0.10 V s^{-1}; [b] vs FcH/FcH$^+$, THF, [*n*Bu$_4$N][PF$_6$] (0.1 M), 0.10 V s^{-1}; [c] vs FcH/FcH$^+$, THF, [*n*Bu$_4$N][PF$_6$] (0.1 M), 0.20 V s^{-1}.

Redoxreaktionen, bei denen während des Elektronentransfers drastische strukturelle Änderungen und/oder reversible σ-Bindungsbildungen/-spaltungen auftreten, werden auch als dynamische Redoxprozesse (Abkürzung: „Dyrex“) bezeichnet.[88-92] Derivate des Hexaphenylethans sind gut zur Untersuchung dynamischer Redoxprozesse geeignet: Im Jahr 1900 beschrieb Gomberg, dass Hexaphenylethan **27** aus der Dimerisierung zweier Triphenylmethyl-Radikale **28•** (Gomberg-Radikale) hervorgeht.[93, 94] Erst im Jahr 1968 konnten McLean et al. aufklären, dass **27** nicht stabil ist und dass zwei Triphenylmethyl-Radikale **28•** stattdessen zu der chinoiden Struktur **29** dimerisieren (Schema 4).[95] Durch Einführen von *t*Bu-Substituenten in allen *meta*-Positionen der Phenylringe von **27** entsteht das Hexaphenylethan **30**, dessen erhöhte Stabilität eine Kristallisation im Jahr 1986 durch Mislow et al. ermöglichte (Schema 4).[96] Als Grund für die höhere Stabilität des scheinbar überfrachteten Hexaphenylethans **30** gegenüber **27** wird in der Literatur eine Überkompensation der repulsiven Wechselwirkungen zwischen den sterisch anspruchsvollen *t*Bu-Resten durch attraktive London‘sche Dispersionswechselwirkungen diskutiert.[97] Die C–C-Bindungslänge der Ethan-Einheit in **30** beträgt 1.67(3) Å.[96]

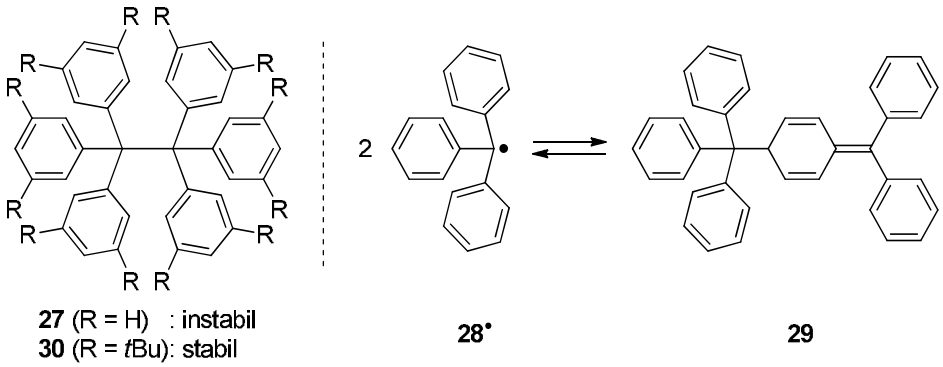

Schema 4. Das Hexaphenylethan **27** ist ein formales Dimer von **28•**, aber instabil. **28•** liegt stattdessen in einem Gleichgewicht mit der chinoiden Verbindung **29** vor. Durch *t*Bu-Gruppen in den *meta*-Positionen der Phenylringe (**30**) lässt sich die Hexaphenylethan-Struktur stabilisieren.

Noch effektiver als mit *t*Bu-Substituenten kann die homolytische Spaltung des Hexaphenylethans durch Verknüpfung von mindestens zwei vicinalen Phenylringen unterdrückt werden. Im Gegensatz zur homolytischen Bindungsspaltung in zwei Triphenylmethyl-Radikale ist eine mesolytische Spaltung nach Einelektronoxidation in ein

kationisches C^+- und ein radikalisches $C^\bullet$-Fragment mit einer deutlich geringeren Energiebarriere versehen und bleibt damit möglich.[98, 99] 9,9,10,10-Tetraaryl-9,10-dihydrophenanthrene wie **31** sind sterisch gehinderte Hexaphenylethane mit zwei vicinal verknüpften Phenylringen und einer langen C9-C10 Bindung (**31**: d(C9-C10) = 1.635(2) Å; Schema 5).[100] Das Di(spiroacridan) **31** reagiert bei zweifacher Elektronenabgabe reversibel zu Biphenyl-2,2'-ylenbis(10-methylacridinium) [**32**]$^{2+}$ (Schema 5).[88, 90, 101-103]

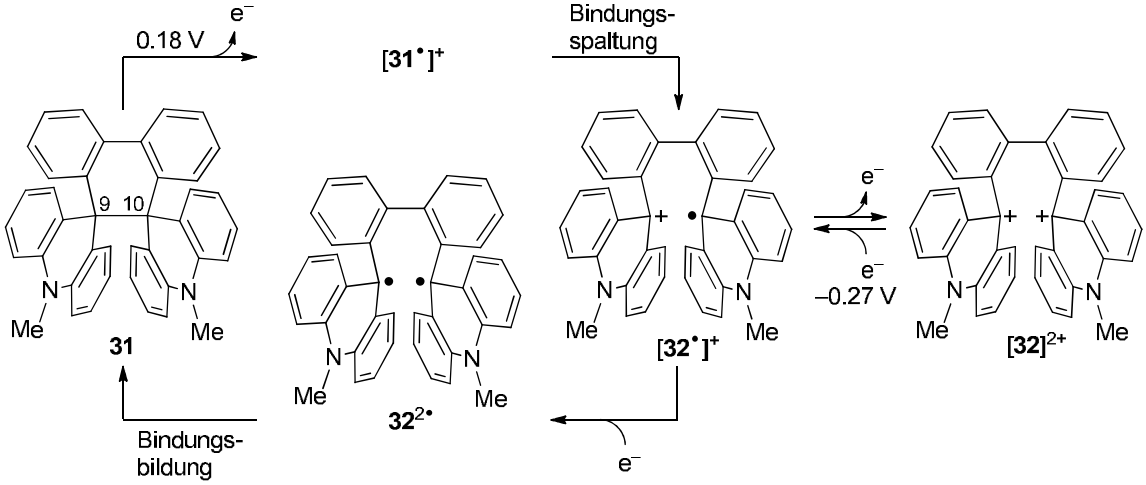

Schema 5. Mechanismus der reversiblen Redoxprozesse zwischen Di(spiroacridan) **31** und Biphenyl-2,2'-ylenbis(10-methylacridinium) [**32**]$^{2+}$.

Für die Oxidation und Reduktion beobachteten die Experimentatoren jeweils eine irreversible Welle im Cyclovoltammogramm, passend zu Zweielektronen-Transferprozessen.[88, 102] **31** ist ein ungeladenes Molekül, das zwei nicht-aromatische Dihydropyridine enthält. [**32**]$^{2+}$ hingegen ist zweifach positiv geladen, besitzt aber in einer mesomeren Grenzstruktur zwei stabile aromatische Pyridinium-Ionen. Bemerkbar macht sich der strukturelle Unterschied des Paars **31**/[**32**]$^{2+}$ in einer ausgeprägten Bistabilität bzw. den sehr unterschiedlichen Potentialen von Oxidation (+0.18 V vs Kalomelelektrode in MeCN) und Reduktion (–0.27 V).[88, 102] Anhand unsymmetrisch substituierter Hexaphenylethane (z. B. 9,9-Bis(*p*-Me_2N-C_6H_4)-10,10-bis(*p*-MeO-C_6H_4)-9,10-dihydrophenanthren) konnten die Reduktionsschritte Dikation→Radikal-Kation und Radikal-Kation→Neutralform im Cyclovoltammogramm als Einelektronprozesse aufgelöst werden.[90] Daraus leiteten die Autoren einen Mechanismus ab,[88] den Sie auch auf **31**/[**32**]$^{2+}$ übertrugen (Schema 5): Die Oxidation von **31** führt zur Bildung des instabilen Radikal-Kations [**31**$^\bullet$]$^+$, das unter C–C-Bindungsspaltung zu [**32**$^\bullet$]$^+$ reagiert. Unter den anodischen Bedingungen, bei denen [**31**$^\bullet$]$^+$ entsteht, wird [**32**$^\bullet$]$^+$ spontan zu [**32**]$^{2+}$ weiteroxidiert. Durch den Strukturunterschied zwischen **31** und [**32**]$^{2+}$ erfolgt die Reduktion von [**32**]$^{2+}$ zu [**32**$^\bullet$]$^+$ bei einem kathodischeren Potential als die Oxidation von **31** zu [**31**$^\bullet$]$^+$. Bei gleichem kathodischem Potential bildet sich im anschließenden Reduktionsschritt **32**$^{2\bullet}$, das schnell unter C–C-Bindungsbildung zu **31** reagiert. Der beschriebene Mechanismus basiert auf klassischen Zweielektronen-Zweizentrenbindungen (2E2Z-Bindungen) und schließt keine Einelektron-Zweizentrenbindungen (1E2Z-Bindungen) ein.

Für analoge ditope Borane beschrieben Gabbaï et al. im Jahr 2004 die elektrochemische Reduktion des 8-(Mes_2B)-naphth-1-yl substituierten 9-Borafluorens **33** und postulierten die Erzeugung des entsprechenden Radikals $[\mathbf{33}^{\bullet}]^{-}$ ($E_{1/2}$ = –2.14 V vs FcH/FcH^{+}; Tabelle 1; Abbildung 6).[49, 104] Die Bis(9-borafluorene) **7** und **10** sind bereits bei deutlich anodischeren Potentialen von $E_{1/2}$ = –1.76, –2.17 V für **7** und $E_{1/2}$ = –1.49, –1.75 V für **10** reversibel reduzierbar (Tabelle 1; Abbildung 6).[105, 106]

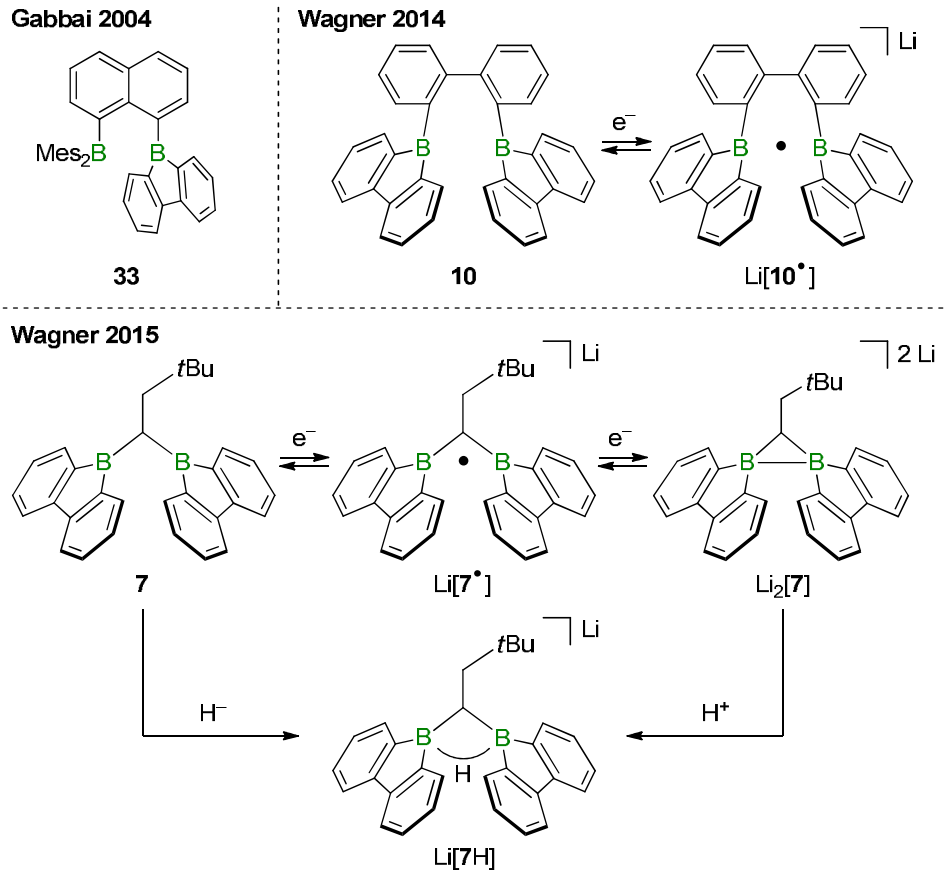

Abbildung 6. Redoxaktive ditope Borane **7**, **10** und **33**. Für **7** und **10** wurde gezeigt, dass Einelektronreduktionen unter B•B-1E2Z-Bindungsbildung verlaufen. **7** kann darüber hinaus zum Dianion $[\mathbf{7}]^{2-}$ reduziert werden, das eine protonierbare B–B-Bindung enthält.

10 besitzt wie $[\mathbf{32}]^{2+}$ eine Biphenyl-2,2'-ylenbrücke zwischen den elektrophilen Positionen, sodass sich die Moleküle, abgesehen von den verschiedenen aber isoelektronischen C^{+}/B-Zentren, nur in den eingeschobenen NMe-Gruppen (statt direkter C–C-Bindungen) unterscheiden. Entsprechend lassen sich beide Verbindungen zum Radikal reduzieren. Während das ungepaarte Elektron in $[\mathbf{32}^{\bullet}]^{+}$ an einem Kohlenstoffatom lokalisiert sein soll, wechselwirkt es in $[\mathbf{10}^{\bullet}]^{-}$ mit beiden Borzentren. Die resultierende B•B-1E2Z-Bindung wurde im Jahr 2014 erstmalig von Wagner et al. kristallographisch bestätigt (Abbildung 6).[105] Nur ein Jahr später wurde unter meiner Beteiligung die Isolierung und Charakterisierung von $Li[\mathbf{7}^{\bullet}]$ und $Li_2[\mathbf{7}]$ publiziert (Abbildung 6).[106] Verbindung **7** ist das erste Boran, an dem nach Reduktion sowohl eine B•B-1E2Z-Bindung als auch eine B–B-2E2Z-Bindung für dasselbe Rückgrat kristallographisch und mittels quantenchemischen Rechnungen nachgewiesen wurden. Im Einklang mit der zunehmenden Bindungsordnung verringert sich der B···B-Abstand kontinuierlich entlang der Sequenz **7** (2.534(2) Å) →

$[\mathbf{7}^{\bullet}]^{-}$ (2.166(4) Å) → $[\mathbf{7}]^{2-}$ (1.906(3) Å). Im Unterschied zu Verbindung **31**, bei der eine einfache Oxidation bereits zum C–C-Bindungsbruch führt, verbleibt in $[\mathbf{7}]^{2-}$ nach Einelektronoxidation eine B•B-1E2Z-Bindung. Des Weiteren konnte gezeigt werden, dass die B–B-2E2Z-Bindung in $Li_2[\mathbf{7}]$ protonierbar ist (Abbildung 6). Das resultierende Produkt Li[**7**H] enthält ein μ-H Atom in einer 2E3Z-Bindung. Dabei entspricht die Sequenz aus Reduktion und Protonierung der Einführung eines Hydridions im neutralen Boran **7**, was experimentell durch Umsetzung von **7** mit $LiHBEt_3$ bestätigt wurde.
Die reversible Reduktion der Bis(9-borafluorene) **7** und **10** bei niedrigen kathodischen Potentialen unter B•B- und B–B-Bindungsbildung verdeutlicht die kooperative Wechselwirkung der Lewis-aciden Zentren (Tabelle 1). Der Nachweis ungewöhnlicher Bindungsverhältnisse ist von Bedeutung für interdisziplinäre Bereiche der Chemie und Physik; beispielsweise wird für den interstellaren und zirkumstellaren Raum die Photoionisierung und Photodissoziation von Cyclohexan diskutiert, mit $[C_6H_{12}^{\bullet}]^{-}$, das eine C•C-1E2Z-Bindung aufweisen sollte, als mögliche Zwischenstufe.[107]
Entgegen der Reduktion der borsubstituierten 9-Borafluorene **7** und **10** unter Erhalt des ursprünglichen Molekülgerüsts (ggf. begleitet von B•B-/B–B-Bindungsbildung) verläuft die Reduktion des 9-Borafluorendimers $(\mathbf{6})_2$ mit Lithium in Gegenwart eines Halogensilans unter weitgehenden strukturellen Umlagerungen (Schema 6).[108]

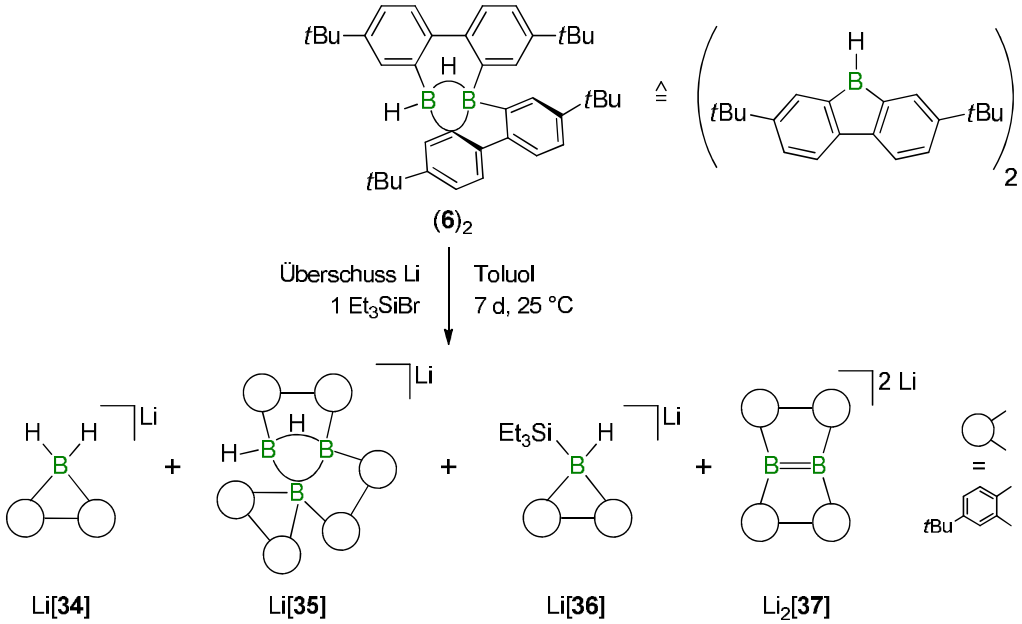

Schema 6. Die Reduktion des 9-Borafluorendimers $(\mathbf{6})_2$ in Toluol mit Lithium in Gegenwart des Bromsilans Et_3SiBr liefert die vier Hauptprodukte Li[**34**], Li[**35**], Li[**36**] und Li_2[**37**].

Wagner et al. berichteten im Jahr 2014 von den vier Hauptprodukten Li[**34**]–Li[**36**] und Li_2[**37**]: Das Boratafluoren $[\mathbf{34}]^{-}$ ist das *t*Bu-substituierte Derivat des literaturbekannten 9,9-Dihydroboratafluorens, das von Nöth et al.[75] beschrieben wurde, und kann als organisches Derivat von $[BH_4]^{-}$ angesehen werden.[108] Wenn alle organischen Reste in $[\mathbf{35}]^{-}$ formal durch Wasserstoffatome ersetzt werden, gelangt man zum Octahydrotriborat-Cluster $[B_3H_8]^{-}$, der neben $[BH_4]^{-}$ durch Reduktion von B_2H_6 zugänglich ist (vgl. Schema 17). Die Bildung der organischen Analoga $[\mathbf{34}]^{-}$ und $[\mathbf{35}]^{-}$ durch Reduktion von

(**6**)$_2$ verknüpft damit in gewisser Weise die klassische Organoboran-Chemie mit der Cluster-Chemie.[108] Chen et al. postulierten, gestützt von Rechnungen, in einem im Jahr 2018 erschienenen Artikel, dass die Entstehung von $[B_3H_8]^-$ durch Berücksichtigung des nucleophilen Charakters der B–H-Bindung verstanden werden kann (Schema 7): Bei der Reaktion von Li[BH_4] mit einem Äquivalent BH_3·THF entsteht in kleinen Mengen Li[B_2H_7]. Mit einem zweiten Äquivalent BH_3·THF reagiert Li[B_2H_7] in der Siedehitze zu Li[B_3H_{10}], das sich weiter zu Li[BH_4] und B_2H_6 umwandeln kann. Ausgehend von Li[BH_4]/B_2H_6 sind in THF zwei Reaktionen energetisch günstig, die beide die Edukte zurückliefern (Umkehr der beschriebenen Schritte oder Spaltung des gebildeten B_2H_6 mit dem Lösungsmittel THF in zwei BH_3·THF). Ein alternativer Pfad mit hoher kinetischer Barriere, bei dem die intermediär gebildeten B_2H_6 und Li[BH_4] miteinander reagieren, führt zu Li[B_2H_5] und einem H_2-Addukt an BH_3 ($H_3B{\cdot}H_2$). Die anschließende Eliminierung des Wasserstoffs aus dem $H_3B{\cdot}H_2$-Addukt macht diesen Pfad irreversibel und stellt die benötigte thermodynamische Triebkraft. Da alle anderen Reaktionsschritte reversibel verlaufen (wenn kein BH_3/B_2H_6 entweicht), entsteht Li[B_3H_8] als Hauptprodukt.[109]

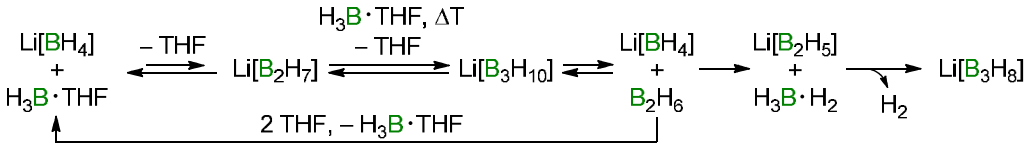

Schema 7. Mechanismus zur Bildung des Octahydrotriborat-Anions $[B_3H_8]^-$ durch Reaktion von $[BH_4]^-$ mit $H_3B{\cdot}THF$ in der Siedehitze.

Die Bindungssituation in [**35**]$^-$ lässt sich des Weiteren durch formale Insertion eines zum Singulett-Carben analogen 9-Borafluorenyl-Anions [**38**]$^-$ in die B–C–B-Brücke des Edukts (**6**)$_2$ beschreiben (Schema 8).[108]

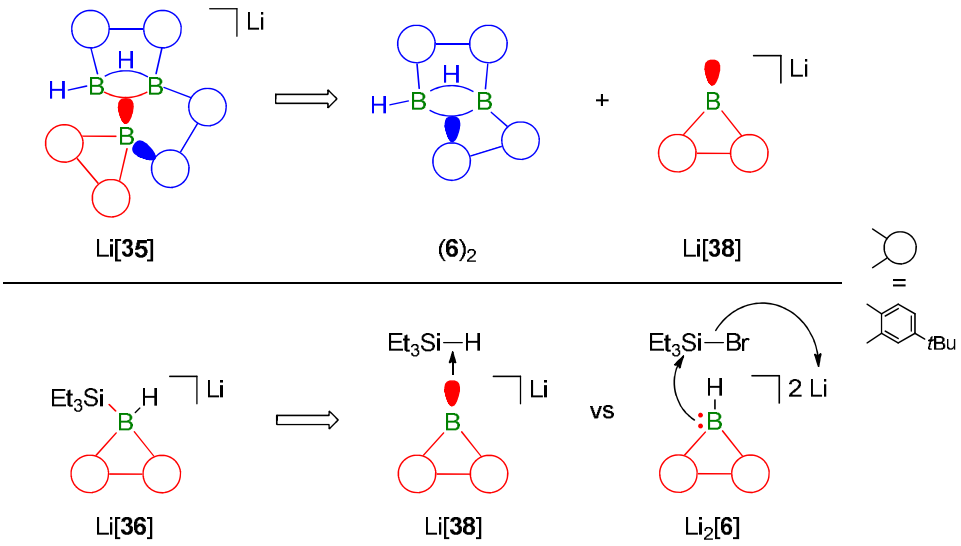

Schema 8. Li[**35**] kann als formales Insertionsprodukt des 9-Borafluorenyl-Anions Li[**38**] in (**6**)$_2$ beschrieben werden (oben). Plausible Mechanismen zur Bildung von Li[**36**] sind die Insertion von Li[**38**] in die Et_3Si–H-Bindung oder der nucleophile (bzw. radikalische) Angriff von Li_2[**6**] an Et_3Si–Br unter LiBr-Eliminierung (unten).

Auch die Bildung des Silylborats [**36**]$^-$ kann plausibel über den Einschub eines 9-Borafluorenyl-Anions in eine Et_3Si–H-Bindung erklärt werden (Schema 8). Alternativ ist ein nucleophiler (bzw. radikalischer) Angriff eines 9-Borafluoren-Dianions an Et_3Si–Br unter LiBr-Eliminierung denkbar. Von besonderem Interesse ist die Entstehung des Dibenzo[*g*,*p*]chrysen-Derivats [**37**]$^{2-}$ mit zentraler B=B-Doppelbindung, da diese hochreaktiv sein sollte und damit großes Anwendungspotential besitzt.
Die geschilderten Reaktionen aus unserem Arbeitskreis leisten einen wichtigen Beitrag zur Darstellung von Boranen mit ungewöhnlichen Bindungssituationen. Im Zuge der Reduktionen von (**6**)$_2$, **7** und **10** werden B–B-, B=B- und B-B-B-Bindungen gebildet. Der zugrundeliegende Mechanismus könnte im ersten Fall auf der Entstehung nucleophiler Borverbindungen beruhen. Daher wird im Folgenden ein Überblick über diese Thematik gegeben.

1.5 Nucleophile Borverbindungen

Carbene, die einen elektrophilen und nucleophilen Charakter vereinen, wurden lange Zeit als reine Intermediate betrachtet, die hochgradig reaktiv sind, aber für viele Reaktionen eine wichtige Rolle spielen. Spätestens mit der Synthese und Charakterisierung des ersten kristallinen Carbens durch Arduengo et al. im Jahr 1991 begann eine neue Ära dieser Chemie (Abbildung 7).[110] Seither wurden viele stabile, leicht zugängliche Carbene entwickelt, deren Eigenschaften gut untersucht sind und die zahlreiche Anwendungen besitzen, z. B. als Katalysatoren oder stabilisierende Liganden.[111-113] Eine ähnliche Entwicklung hat in den vergangenen Jahren auch mit den Synthesen elektronenreicher Boran-Anionen ([$BR_3^{\bullet}$]$^-$), Boran-Dianionen ([BR_3]$^{2-}$), Boryl-Anionen ([BR_2]$^-$) und Borylenen (:BR) begonnen, sodass umgepolte Borverbindungen in Zukunft eine große Rolle spielen dürften (Abbildung 7).

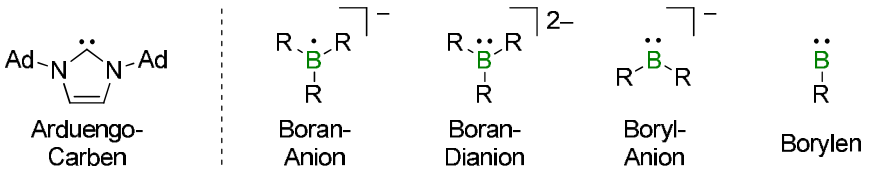

Abbildung 7. Gegenüberstellung des Arduengo-Carbens mit einem Boran-Anion, Boran-Dianion, Boryl-Anion und einem neutralen Borylen. Ad = 1-Adamantyl.

1.5.1 Boran-Anionen und -Dianionen

In den Jahren 1924 und 1926 berichteten Krause et al., dass bei der Reaktion von Natrium mit Triphenylboran (Ph_3B; **39**) das Salz Na[$BPh_3^{\bullet}$] (Na[**39**$^{\bullet}$]) gebildet wird.[114, 115] Eisch et al. konnten im Jahr 1993 zeigen, dass **39** unter diesen Bedingungen nur intermediär als Radikal-Anion [**39**$^{\bullet}$]$^-$ vorliegt, da eine anschließende Dimerisierung zu [**40**]$^{2-}$ als Hauptprodukt stattfindet (Schema 9).[116] Die Bildung des Diborat-Dianions [**40**]$^{2-}$, anstatt des B–B-gebundenen Dianions [**41**]$^{2-}$, offenbart eine bemerkenswerte Parallele der

Reaktivitäten des Radikal-Anions [**39**•]$^-$ und des isoelektronischen Triphenylmethyl-Radikals **28**• (vgl. Schema 4). Die Bildung von [**39**•]$^-$ konnte durch ESR-Messungen nachgewiesen werden.[117, 118] Mit sterisch anspruchsvollen Mesitylgruppen am Boratom (Mes_3B) wird eine Dimerisierung nach Reduktion zum Anion [$Mes_3B^•$]$^-$ kinetisch gehemmt, sodass Power et al. im Jahr 1986 eine Röntgenstrukturanalyse von [Li(12-Krone-4)$_2$][$Mes_3B^•$] durchführen konnten.[119]

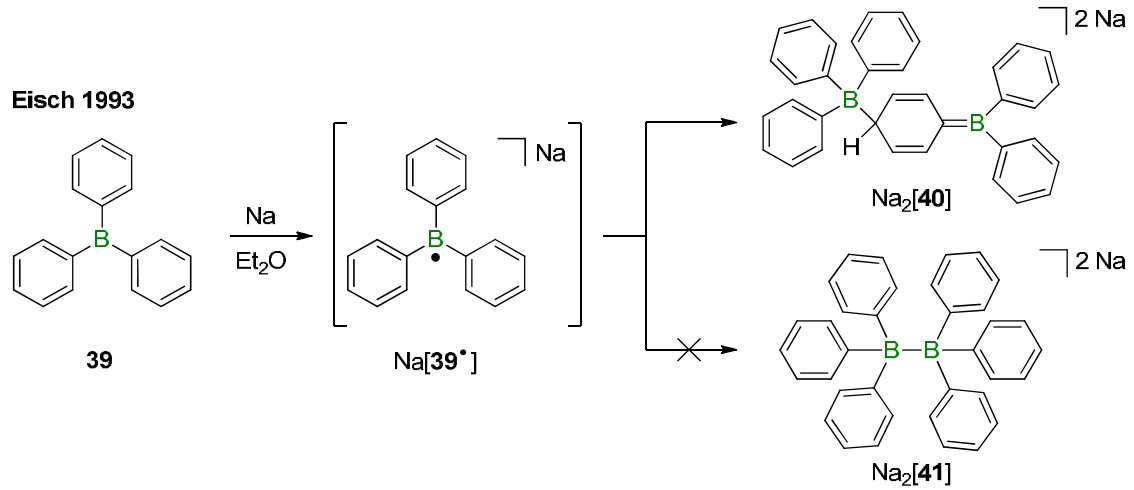

Schema 9. Die Reduktion des Triphenylborans **39** mit Natrium in Et_2O liefert das Dimer Na_2[**40**] anstatt Na_2[**41**] als Hauptprodukt.

Der Ersatz eines Alkyl- oder Arylsubstituenten in R_3B durch einen Rest, der über ein Pnictogenatom an das Borzentrum koordiniert, ermöglicht es, Anionen mit diamagnetischem Charakter zu erzeugen: Die Gruppen um Schmidbaur und Imamoto beschrieben in den Jahren 1993/1994, dass das Tricyclohexylphosphan-koordinierte Monoiodboran **42** mit Lithium-4,4‘-di(*t*Bu)biphenylid (LDBB) intermediär Li[(*c*-$C_6H_{11})_3PBH_2$] (Li[**43**]) erzeugt (Schema 10). Letzteres greift zahlreiche Elektrophile wie Trimethylchlorsilan, Benzaldehyd oder Kohlenstoffdioxid nucleophil an.[120, 121]

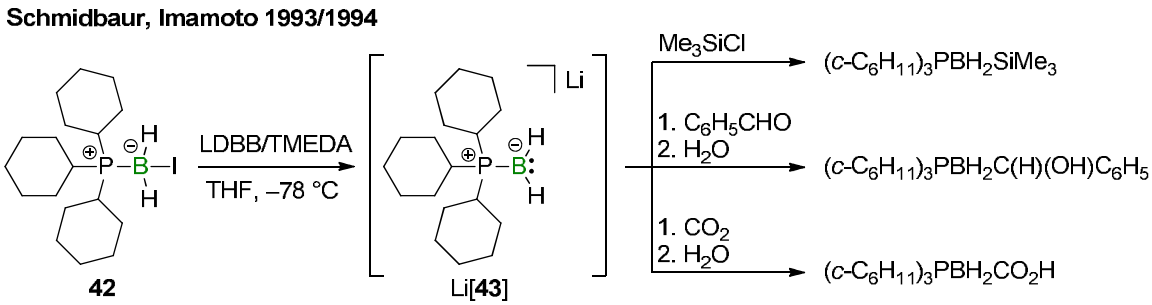

Schema 10. Das Tricyclohexylphosphan-koordinierte Monoiodboran **42** reagiert nach Reduktion zu Li[**43**] (*in situ*) mit unterschiedlichen Elektrophilen. LDBB = Lithium-4,4‘-di(*t*Bu)biphenylid, TMEDA = *N*,*N*,*N*‘,*N*‘-Tetramethylethylendiamin.

Es sei angemerkt, dass Li[**43**] auch als Phosphan-koordiniertes Boryl-Anion aufgefasst werden kann, insbesondere beim Vergleich mit dem NHC-koordinierten Boryl-Anion [**44**]$^-$ von Curran, Fensterbank, Malacria und Lacôte et al. aus dem Jahr 2010, dessen Existenz

anhand von Abfangexperimenten mit zahlreichen Elektrophilen nachgewiesen wurde (Abbildung 8).[122]

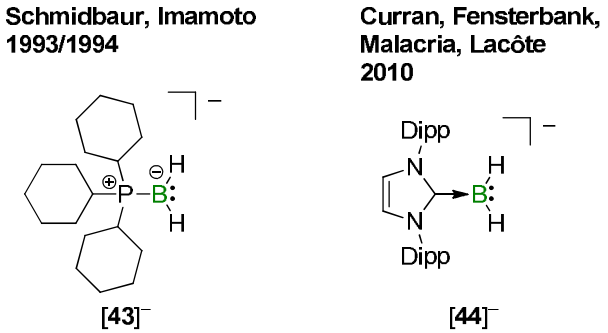

Abbildung 8. Gegenüberstellung des Boran-Anions [**43**]⁻ mit dem Boryl-Anion [**44**]⁻. Beide Intermediate wurden durch Abfangreaktionen nachgewiesen.

Piers und Gendy et al. publizierten im Jahr 2018 das 1-Bora-7a-azaindenid [**45**]⁻, das in einer Grenzform auch als Pyridyl-koordiniertes Boryl-Anion betrachtet werden kann (Schema 11). Das Anion [**45**]⁻ reagiert mit Alkylhalogeniden R–X (CH_2Cl_2, CH_3I und BrCH(D)CH(D)*t*Bu) nach einem klassischen S_N2-Mechanismus als borzentriertes Nucleophil (Schema 11).[123] Dabei trägt die Rearomatisierung des Pyridyl-Rings entscheidend zur Triebkraft der Reaktion bei. Im Gegensatz dazu kommt es bei Umsetzung von [**45**]⁻ mit CO_2 zu einer (reversiblen) Carboxylierung des Kohlenstoffatoms in α-Position zum Borzentrum (Schema 11). Der Energiegewinn durch Ausbildung sowohl einer C–C- als auch einer B–O-Bindung überwiegt den energetischen Betrag der Rearomatisierung beim hypothetischen elektrophilen Angriff des CO_2 am Boratom.

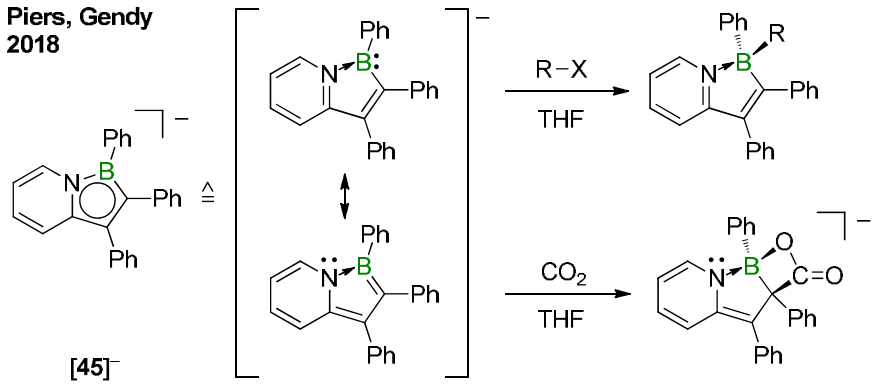

Schema 11. Das 1-Bora-7a-azaindenid [**45**]⁻ reagiert in Abhängigkeit des Substrats als borzentriertes oder kohlenstoffzentriertes Nucleophil. R = -CH_2Cl, -CH_3, -CH(D)CH(D)*t*Bu.

Die hohen negativen Ladungen von Boran-Dianionen $[BR_3]^{2-}$ machen Verbindungen dieser Substanzklasse leicht oxidierbar. Nucleophiles Verhalten wurde bisher nur für das Tricyanoboran-Dianion [**46**]$^{2-}$ aufgezeigt, beispielsweise gegenüber Ethyliodid unter Bildung von $[EtB(CN)_3]^-$ (Schema 12).[124, 125] Entscheidend für die Stabilität und Reaktivität von [**46**]$^{2-}$ sind die Cyanosubstituenten, die als starke π-Akzeptoren die negative Ladung effektiv über das gesamte Molekülgerüst delokalisieren (vgl. Cyanoboryl-Anionen in Kapitel 1.5.2 und Abbildung 10).

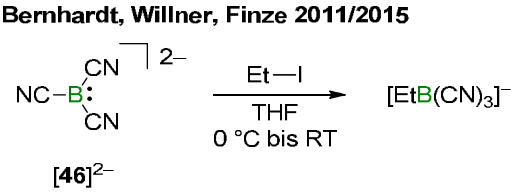

Schema 12. Das Tricyanoboran-Dianion [**46**]$^{2-}$ reagiert nucleophil gegenüber Elektrophilien wie Ethyliodid.

1.5.2 Boryl-Anionen

Im Jahr 2006 leisteten Yamashita, Nozaki et al. Pionierarbeit auf dem Gebiet der nucleophilen Borverbindungen, indem sie die Isolierung und Charakterisierung des Boryllithiums Li[**47**] publizierten, das isoelektronisch zu stabilen NHCs ist (Abbildung 9; vgl. Arduengo-Carben in Abbildung 7).[126-131] Durch die starke Polarisation der Li–B-Bindung weisen Li[**47**] sowie vergleichbare 1,3,2-Diazaborolyl-Anionen nucleophilen Charakter auf und reagieren mit organischen Elektrophilen[129, 132, 133] (z. B. halogenierten Alkanen/Aromaten, Carbonylen), Hauptgruppenelementverbindungen[132, 134-141] (z. B. $MgBr_2{\cdot}OEt_2$, $AlMe_3$) sowie Übergangsmetallverbindungen[134, 142-145] (z. B. Ti(O*i*Pr)$_4$, Ph_3PAuCl, CuBr).[146]
Durch heterolytische Spaltung eines Tetraalkoxy-Diborans(4) nach Adduktbildung mit Alkoxiden lassen sich *in situ* Boryl-Nucleophile erzeugen, die präparativ nutzbar sind (vgl. K[**48**] in Abbildung 9):[147-149] Unter anderem die Gruppen von Lin, Kleeberg und Marder verwenden seit 2009 Alkoxid-induzierte Spaltungsreaktionen von Bis(pinakolato)diboran (B_2pin_2) zur Beschleunigung des Transmetallierungsschritts in übergangsmetallkatalysierten Borylierungsreaktionen.[147-151] Weitere Anwendungen sind Diborierungen ungesättigter organischer Reagenzien sowie konjugierte Additionen, wie beispielsweise die kupferkatalysierte β-Borylierung α,β-ungesättigter Verbindungen.[152, 153] Die *in situ* erzeugten Boryl-Anionen können aber auch als Nucleophile in metallfreien Borylierungsprozessen zum Einsatz kommen.[154-157]

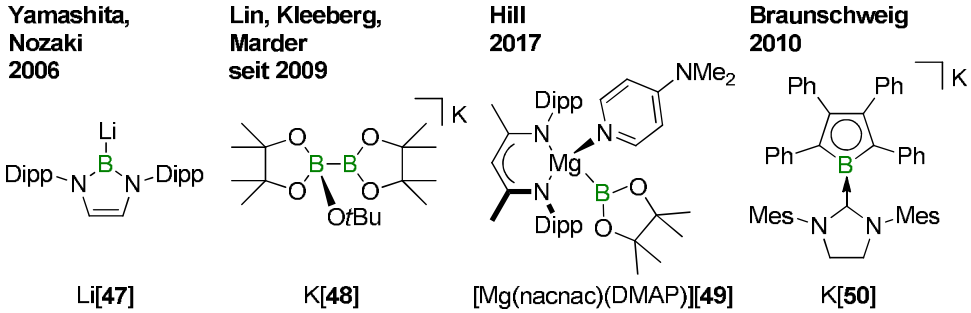

Abbildung 9. Ausgewählte Boryl-Anionen bzw. deren unmittelbare Präkursoren. Dipp = 2,6-Di(*i*Pr)phenyl, DMAP = 4-(Dimethylamino)pyridin, [nacnac]$^-$ = [{N(Dipp)C(CH$_3$)}$_2$CH]$^-$.

Hill et al. erweiterten 2017 das Spektrum an Boryl-Anionen, indem sie den isolierbaren β-Diketiminato-Magnesium-Pinacolatoboryl-Komplex [Mg(nacnac)(DMAP)][**49**] synthetisierten und mit ausgewählten Elektrophilen umsetzten (Abbildung 9; DMAP = 4-(Dimethylamino)pyridin, [nacnac]$^-$ = [{N(Dipp)C(CH$_3$)}$_2$CH]$^-$; siehe auch Kapitel 1.6.5).[158, 159]

Braunschweig et al. publizierten im Jahr 2010 das NHC-stabilisierte Boryl-Anion K[**50**], dessen Boratom im Festkörper eine trigonal-planare Konfiguration besitzt.[160] Im Gegensatz zu den bisher beschriebenen Derivaten ist das freie Elektronenpaar nicht in der R_2B-Ebene lokalisiert. Stattdessen lässt sich das HOMO von K[**50**] als ein zur R_2B-Ebene orthogonales, π-artiges Bindungsorbital zwischen dem Boratom und dem Carben-Kohlenstoffatom beschreiben.[160] Die signifikante Beteiligung des Borzentrums deuten die Autoren als Hinweis auf ein π-nucleophiles Boratom. Der NHC-Ligand übernimmt sowohl die Rolle eines starken σ-Donors als auch die eines π-Akzeptors, über den die Elektronen des Boratoms delokalisiert werden. Der C_4B-Ring in K[**50**] besitzt vergleichbare geometrische Parameter wie Borol-Dianionen, was auf einen aromatischen Charakter hindeutet. Eine Umsetzung mit MeI lieferte das neutrale, am Boratom methylierte Produkt einer formalen Substitutionsreaktion. In einer späteren Studie wurde jedoch beschrieben, dass der Reaktionsverlauf von K[**50**] mit MeI wahrscheinlich auf einen radikalischen Mechanismus zurückzuführen ist.[161] Diese Vermutung steht im Einklang mit der oben ausgeführten bereitwilligen Oxidierbarkeit organisch-substituierter dianionischer 9-Borafluorene.
Eine gewisse Sonderrolle nehmen cyanosubstituierte Boryl-Anionen ein, da deren CN-Gruppen nicht nur als organische Reste, sondern auch als stabilisierende Lewis-basische Liganden aufgefasst werden können: Willner, Finze et al. befassen sich seit 2011 mit der Synthese und Reaktivität des $[B(CN)_3]^{2-}$ ([**46**]$^{2-}$), eines dianionischen Borans mit nucleophilen Eigenschaften (Abbildung 10; vgl. Kapitel 1.5.1).[124, 125, 162] Die Gruppen von Bertrand (2013)[163] und Hörner, Frank (2017)[164] konnten zeigen, dass statt des dritten CN-Liganden auch ein cAAC- oder NHC-Ligand einsetzbar ist ([**51**]$^-$ und [**52**]$^-$; Abbildung 10). Die entsprechenden Boryl-Anionen [**51**]$^-$ und [**52**]$^-$ reagieren ebenfalls als Nucleophile, z. B. gegenüber Alkylhalogeniden.[163, 164] Vor diesem Hintergrund schlagen die CN-Gruppen eine Brücke zwischen den Boran-Dianionen und den Boryl-Anionen.

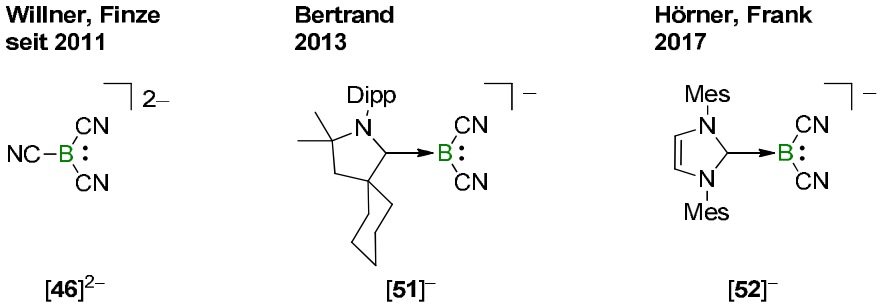

Abbildung 10. Das Tricyanoboran-Dianon [**46**]$^{2-}$ sowie die carbenstabilisierten Dicyanoboryl-Anionen [**51**]$^-$ und [**52**]$^-$.

1.5.3 Borylene

Wie ein Boryl-Anion besitzt ein neutrales Borylen ein freies Elektronenpaar. In beiden Fällen ist diese Elektronendichte dem HOMO zuzuordnen, das im letzteren Fall auf ein nicht-bindendes n_σ-Typ-Orbital mit sp-Charakter projiziert werden kann.[165, 166] Im Gegensatz zu den Carbenen, die in Abhängigkeit ihrer beiden Substituenten im Singulett-

oder Triplett-Grundzustand vorliegen können, aber im Einklang mit nahezu allen Silylenen,[167, 168] weisen alle bislang (theoretisch) untersuchten Borylene Singulett-Grundzustände auf.[165, 169] Auf Basis von Abfangexperimenten wurde das kurzzeitige Auftreten von Borylenen zur Erklärung von Reaktionsverläufen bereits mehrfach postuliert,[86, 170-174] so beispielsweise von West et al. im Jahr 1984 im Rahmen der Photolyse von $(Ph_3Si)_3B$ in Gegenwart eines Acetylids, die ein Boriren erzeugt.[171] Mit nur einem Substituenten, aber zwei freien Orbitalen sind Borylene noch elektronenziehender und instabiler als Boryl-Anionen oder Carbene. Deswegen gibt es neben der mikrowellenspektroskopischen Untersuchung zweiatomiger Borylene (BH, BF, BCl, BBr und BI) nur wenige spektroskopische Messungen an anderen freien Borylenen, die zudem unter harschen Bedingungen und/oder in Tieftemperatur-Matrizes hergestellt wurden.[165, 166]
Durch Adduktbildung mit zwei Lewis-Basen können Borylene der formalen Oxidationsstufe +I effektiv stabilisiert werden, sodass sie präparativ zugänglich und unter inerter Atmosphäre über Monate lagerbar sind. Isoelektronisch zu Aminen und Phosphanen zeichnen sich diese Borylen-Diaddukte zumeist als elektronenreiche Verbindungen aus: Im Jahr 2011 fingen Kinjo, Bertrand et al. erstmalig ein *in situ* erzeugtes, cAAC-substituiertes Borylen mithilfe eines weiteren cAAC-Liganden ab und konnten auf diese Weise das zweifach cAAC-stabilisierte B–H-Borylen **53** in 33% Ausbeute isolieren (Schema 13).[175]

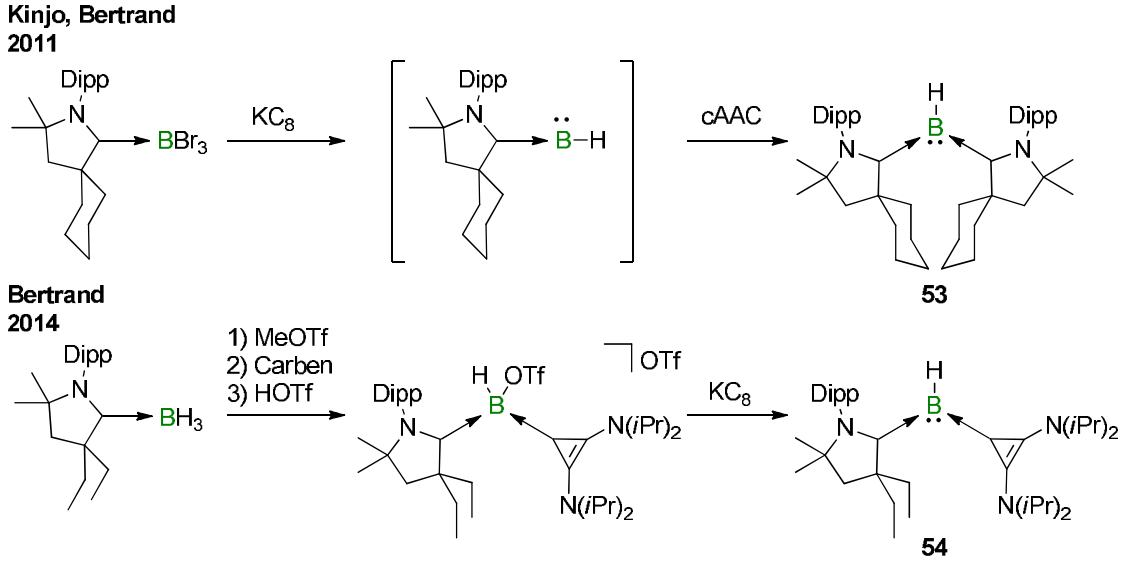

Schema 13. Synthesen der Borylene **53** und **54**, die durch Liganden stabilisiert sind.

53 erwies sich als protonierbar mit HOTf und einfach oxidierbar mit $GaCl_3$. Auf ähnliche Weise wie Kinjo et al. isolierten die Gruppen von Braunschweig und Xie B–R-Borylene, die sie mit unterschiedlichen Liganden stabilisierten.[176-178] Einen effizienten Syntheseweg zu B–H-Borylenen mit zwei verschiedenen Carbenliganden präsentierten Bertrand et al. im Jahr 2014, was am Beispiel der Synthese von **54** in Schema 13 gezeigt ist.[179] Im Schlüsselschritt nutzten sie eine Hydrideliminierung in Gegenwart eines Carbenliganden aus. Ein Vergleich mehrerer koordinierter Borylene zeigt, dass die B–Ligand-Bindungsstärken

den π-Akzeptor-Eigenschaften der Liganden weitestgehend folgen: cAAC > NHC > CO > PPh_3.[166]

Um den kritischen Schritt der Erzeugung freier, reaktiver Carbene zu umgehen, generierten Kinjo et al. im Jahr 2014 Carbene in der Koordinationssphäre eines Boratoms, indem sie gebundene Oxazolinylgruppen an deren Stickstoffatomen methylierten.[180] Das gewünschte Borylen-Produkt **55** wurde durch anschließende Reduktion erhalten (Schema 14). **55** diente als borzentrierter Ligand bei Umsetzungen mit unterschiedlichen Metallsalzen und Hauptgruppenverbindungen.[181, 182] Zudem besitzt **55** die Besonderheit, dass es bei Oxidation mit AgOTf unter B–B-Bindungsbildung dimerisiert und das dikationische Kupplungsprodukt durch Reduktion wieder zu **55** gespalten werden kann (vgl. [**68**]$^{2+}$ in Kapitel 1.6.3).[183] Kinjo et al. beschrieben ab 2015 eine bemerkenswerte Variante ihres Systems (Schema 14): Über den Austausch der beiden N-gebundenen Methylgruppen in **55** gegen einen verbrückenden BPh-Rest entsteht **56**, mit der neuen NBN-Einheit als elektrophiles Zentrum. Nach Adduktbildung an der NBN-Einheit mit Lewis-Basen (und Entstehung eines Janovsky-Komplexes) tritt die Borylen-Chemie der CBC-Einheit in den Vordergrund.[184] Auf diese Weise sind schrittweise Additionen[184] oder kooperative Aktivierungen kleiner Moleküle möglich.[185-187]

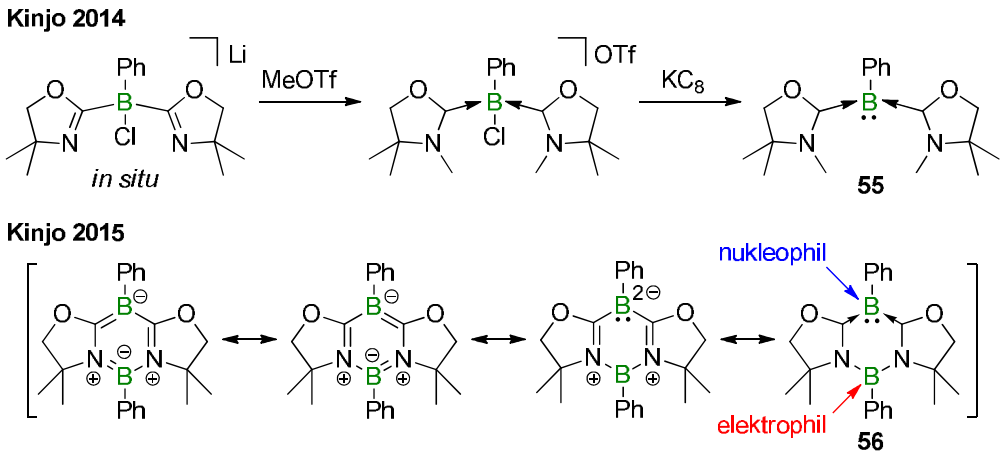

Schema 14. Die Erzeugung von Carbenen in der Koordinationssphäre eines Boratoms durch Methylierung von Oxazolinylliganden ermöglichte nach Reduktion die Isolierung des Borylens **55**. Verbindung **56**, die sowohl ein elektrophiles Zentrum als auch ein nucleophiles Borylen enthält, ist strukturell verwandt mit **55**.

Braunschweig et al. nutzen seit über 10 Jahren Übergangsmetalle zur Stabilisierung von Borylenen, wie im Falle des Dimanganborylen-Komplexes Li[**57**] (Schema 15).[188-191] Zudem veröffentlichten sie in den Jahren 2015 und 2016, dass übergangsmetallgebundene Borylene auch als Edukte dienen können, um ligandenstabilisierte Alkyl-/Aryl-Borylene zu synthetisieren.[192, 193] Als Beispiel ist in Schema 15 die Umsetzung des Molybdän-Borylen-Komplexes **58** mit CO zu Borylen **59** abgebildet. Auf diese Weise konnte unter anderem gezeigt werden, dass bereits CO-Liganden ausreichen, um Borylene zu stabilisieren.

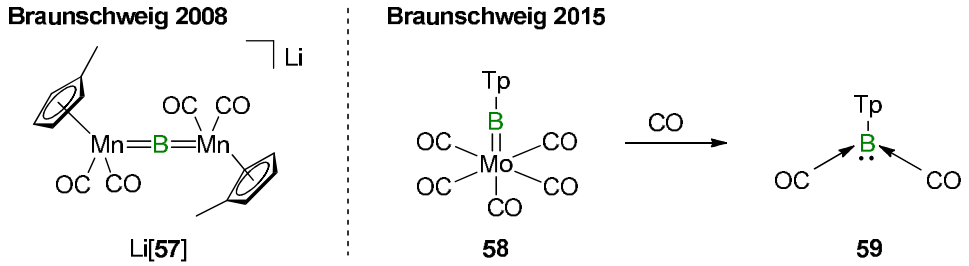

Schema 15. Übergangsmetallstabilisierte Borylene Li[**57**] und **58**. Letzteres eignet sich als Edukt für die Synthese des Borylens **59**. Tp = 2,6-Di(2,4,6-tri(*i*Pr)phenyl)phenyl.

Borylene mit nur einem einzigen Lewis-basischen Liganden zu stabilisieren, gelang bisher in sehr wenigen Fällen. Im Jahr 2007 berichteten Robinson et al. von Verbindung **60**, die als Dimer eines Monoaddukts des Stammborylens „BH“ aufgefasst werden kann (Abbildung 11, Kasten). Bertrand et al. gelang 2014 die Isolierung des Borylens **61**, das im Festkörper eine nahezu lineare Struktur besitzt.[194] Als Ligand kam ein Vertreter der cAACs zum Einsatz, die noch stärkere π-Akzeptoren sind als NHCs und damit eine ausreichende Delokalisierung des borständigen freien Elektronenpaars ermöglichen.

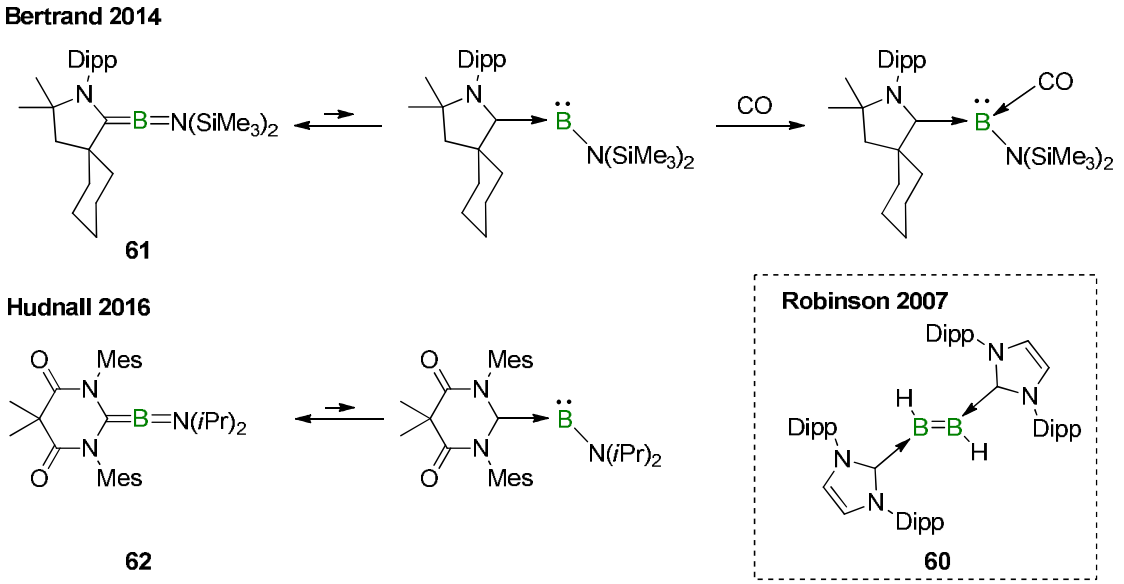

Abbildung 11. Verbindung **60** kann als dimeres Monocarbenaddukt des Stammborylens „BH“ angesehen werden. Die Borylene **61** und **62** werden durch nur einen Carbenliganden stabilisiert und sind strukturell flexibel, was die Reaktivität von **61** gegenüber CO erklärt.

Im Gegensatz zu Aminoboraalkenen ($R_2C{=}B{=}NR'_2$)[195-198] ist **61** gemäß quantenchemischer Rechnungen[194] strukturell flexibel (Abbildung 11): In der linearen Struktur von **61** ist das Boratom sp-hybridisiert. Die hohe Energie des ersten borzentrierten unbesetzten Molekülorbitals (LUMO+2) macht eine elektrophile Reaktivität des Boratoms in der linearen C-B-N-Struktur von **61** unwahrscheinlich. Durch das Abknicken des C-B-N-Winkels von ca. 175° auf 155° ändert sich die Hybridisierung des Boratoms zu sp^2. Das HOMO der gewinkelten Struktur ist gegenüber dem HOMO der linearen energetisch nur geringfügig angehoben. Das LUMO der gewinkelten Struktur ist nun borzentriert und energetisch deutlich niedriger gelegen als das der linearen Struktur, wodurch ein elektrophiler

Charakter des Boratoms wahrscheinlicher wird. Daher besitzt **61** in der gewinkelten Struktur sowohl elektrophiles als auch nucleophiles Verhalten, das vergleichbar ist mit der Reaktivität eines Singulett-Carbens. Als Beispiel ist in Abbildung 11 die Reaktivität von **61** gegenüber CO dargestellt.[194] Von dem zu **61** strukturell vergleichbaren Borylen **62**, das durch einen Diamidocarbenliganden stabilisiert ist, berichteten Hudnall et al. im Jahr 2016 (Abbildung 11).[199]

1.6 Elektronenpräzise B–B-Bindungen

Während seit Jahrzehnten eine Vielzahl universeller Protokolle zu C–C-Bindungsknüpfungen existieren, sind die Vorgehensweisen zur Bildung von B–B-Bindungen oftmals nur auf spezifische Fälle anwendbar.[200, 201] Wichtige Methoden zur Knüpfung von B–B-Bindungen sind im Folgenden kurz beschrieben und Reaktivitäten an ausgewählten Beispielen erläutert.

1.6.1 Reduktion von Halogenboranen

Die Mehrheit aller elektronenpräzisen B–B-Bindungen wurde durch Reduktion von Halogenboranen geknüpft.[201-204] Die erste Synthese eines elektronenpräzisen Diborans(4) erfolgte durch Stock et al. im Jahr 1925 über die Reduktion von BCl_3 zu B_2Cl_4 in einem elektrischen Zinklichtbogen (Schema 16).[205] Ein weiterer Meilenstein war die Reduktion von $(Me_2N)_2BX$ mit Natrium zum luftstabilen $B_2(NMe_2)_4$ durch Brotherton et al. im Jahr 1960 (X = Cl, Br; Schema 16). Auf diesem Protokoll beruht letztlich auch die Synthese des kommerziell erhältlichen und vielseitig eingesetzten Bis(pinakolato)diborans (B_2pin_2).[206] Insbesondere Nöth et al. nutzten in den folgenden 20 Jahren π-Donorsubstituenten zur thermodynamischen Stabilisierung höherer Oligoborane wie $B_n(NMe_2)_{n+2}$ und cyclo-$B_6[NMe_2]_6$ (Schema 16).[207, 208] Eine kinetische Stabilisierung von B–B-Bindungen kann durch Einführen sterisch anspruchsvoller Gruppen erfolgen, wie im Falle des *closo*-$B_4(t\text{Bu})_4$-Clusters **63**, den Paetzold, Boese et al. im Jahr 1991 publizierten.[209] Power et al. erzeugten 1996 ausgehend von 2,6-$Tipp_2$-$C_6H_3BBr_2$ über die Reduktion mit KC_8 das dianionische Bis(9-boratafluoren) [**64**]$^{2-}$ (Schema 16).[86] Bisher ist mechanistisch nicht geklärt, ob bei der reduktiven Kupplung zweier Halogenborane zunächst ein Boryl-Anion erzeugt wird, das an dem zweiten Halogenboran nucleophil angreift, oder ob zwei Boryl-Radikale gebildet werden, die anschließend dimerisieren.[200]

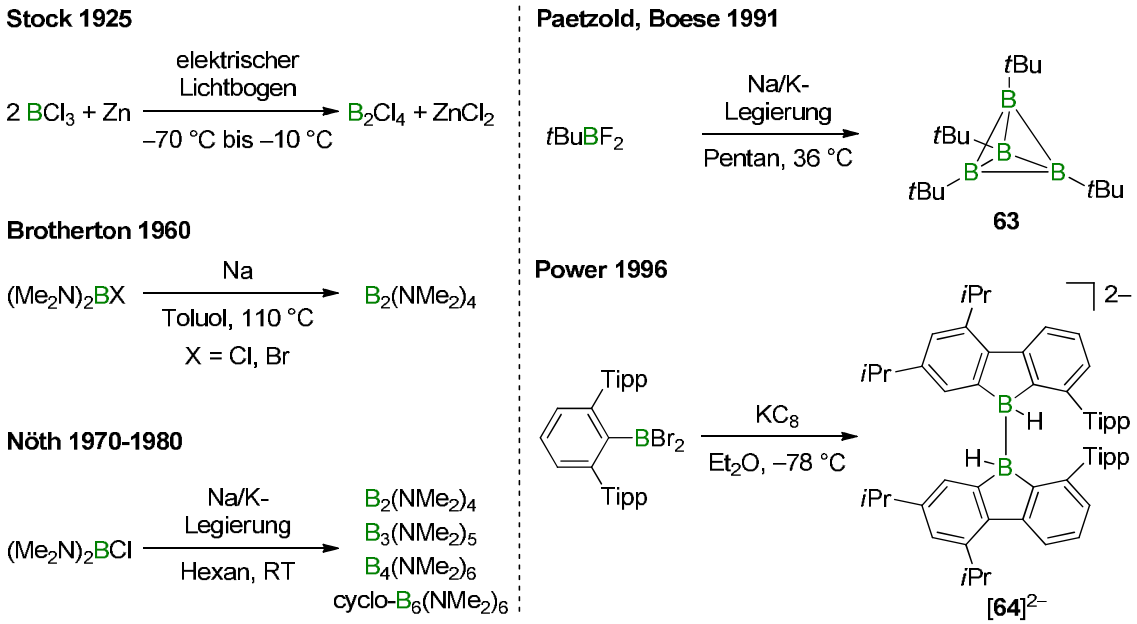

Schema 16. Aufbau von B–B-Bindungen durch Reduktion von Halogenboranen. Tipp = 2,4,6-Tri(*i*Pr)phenyl.

1.6.2 Reduktion von Diboranen(6)

Bereits in den 1930er Jahren versuchten Stock et al. durch Reduktion von Diboran(6) das Dianion $[H_3B–BH_3]^{2–}$ zu synthetisieren und dadurch eine elektronenpräzise B–B-Bindung aufzubauen.[210] Die Reaktion erweckte großes Interesse und wurde mehrfach reproduziert.[211-216] Shore et al. konnten im Jahr 1994 zeigen, dass $[H_3B–BH_3]^{2–}$ nur intermediär auftritt, da es sich rasch zu den Endprodukten $[BH_4]^–$ und $[B_3H_8]^–$ zersetzt (Schema 17).[217]

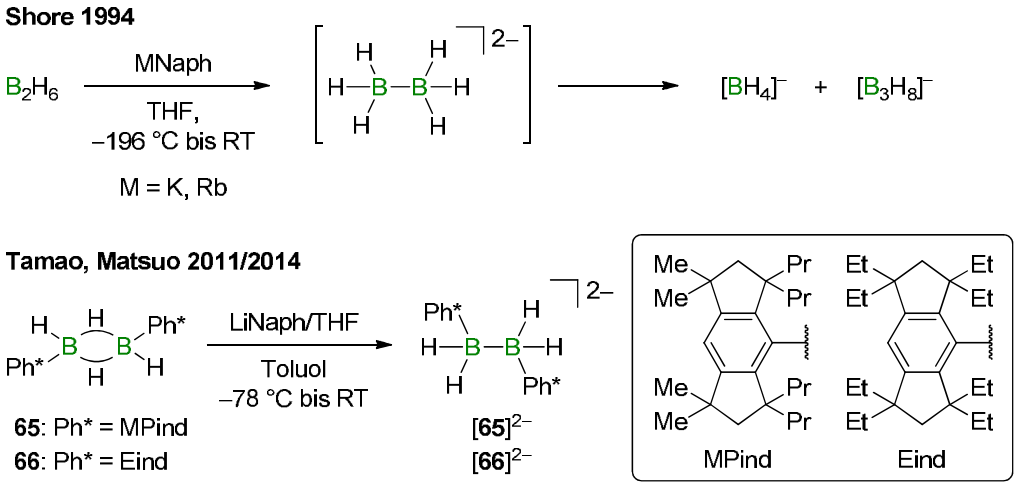

Schema 17. Aufbau von B–B-Bindungen durch Reduktion von Diboranen(6).

Erst in den Jahren 2011 und 2014 gelang es Matsuo und Tamao et al., durch das Einführen sterisch ausgesprochen anspruchsvoller Phenylreste (Ph*), die Dianionen $[\mathbf{65}]^{2–}$ und $[\mathbf{66}]^{2–}$ der Form $[(Ph^*)H_2B–BH_2(Ph^*)]^{2–}$ zu isolieren (Ph* = MPind, Eind; Schema 17).[218, 219]

1.6.3 Kupplung redoxaktiver Organoborverbindungen

Das Hexacyanodiboran(6)-Dianion $[B_2(CN)_6]^{2-}$ ([**67**]$^{2-}$) von Bernhardt, Finze et al. aus dem Jahr 2015 ist außergewöhnlich unreaktiv gegenüber Luft, siedendem Wasser und wasserfreiem HF (Abbildung 12). Es ist über mehrere Wege darstellbar, z. B. über die Oxidation von $[B(CN)_3]^{2-}$ ([**46**]$^{2-}$) oder die Reduktion von $[BF(CN)_3]^-$.[220] Kinjo et al. publizierten im Jahr 2016 die Synthese des Diboran(6)-Dikations [**68**]$^{2+}$ durch Einelektronoxidation des Borylens L_2PhB: (**55**; L = Oxazol-2-yliden; Abbildung 12; vgl. Schema 14). Die B–B-Bindung des Dikations [**68**]$^{2+}$ reagiert mit AuCl oder Isonitrilen (*n*BuNC, *t*BuNC) unter Bildung der chlorid- bzw. cyanogebundenen Boronium-Kationen $[L_2PhBCl]^+$ oder $[L_2PhBCN]^+$.[183] Stephan et al. stellten im Jahr 2017 durch Einelektronreduktion des korrespondierenden Borenium-Vorläufers mit Cp^*_2Co das neutrale, doppelt basenstabilisierte Diboran(4) **69** her (Abbildung 12; $[Cp^*]^-$ = $[\eta^5\text{-}C_5Me_5]^-$). Die B–B-Bindung in **69** reagiert mit TEMPO, $(PhC(O)O)_2$, PhNO, (tht)AuCl und S_8 unter homolytischer Bindungsspaltung (TEMPO = 2,2,6,6-Tetramethylpiperidinyloxyl, tht = Tetrahydrothiophen).[221]

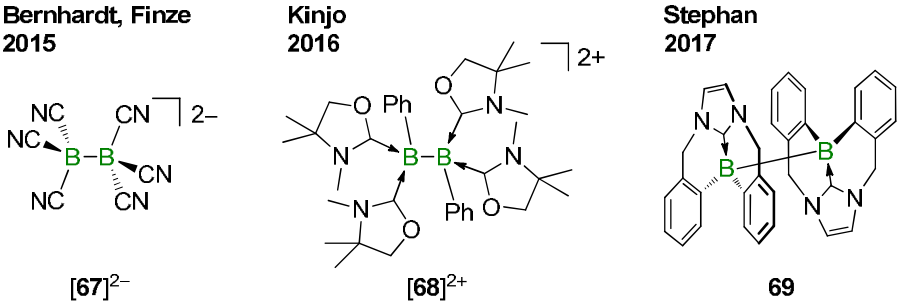

Abbildung 12. Moleküle mit B–B-Bindungen, die durch Kupplung redoxaktiver Organoborverbindungen synthetisiert wurden.

1.6.4 Dehydrokupplung von Boranen

Im Jahr 1983 präsentierten Sneddon et al. die erste übergangsmetallvermittelte Dehydrodimerisierung von zwei B_5H_9-Clustern zu einem 1:2'-$[B_5H_8]_2$-Cluster durch Zugabe von $PtBr_2$ (Schema 18).[222] Bei der Rhodium-katalysierten Synthese von Boronsäureestern, ausgehend von Pinakolboran (HBpin), stießen Marder et al. 2001 auf kleine Mengen an B_2pin_2.[223] Darauf aufbauend konnten Braunschweig et al. 2011 mithilfe von homogenen und heterogenen Übergangsmetallkatalysatoren (u. a. Pt/Al) die Dehydrokupplung von HBpin oder Catecholboran (HBCat) zu den entsprechenden Diboranen(4), B_2pin_2 oder B_2Cat_2, in guten Ausbeuten durchführen (Schema 18).[224] Ab 2007 untersuchten Himmel et al. die thermische und katalytische Dehydrogenierung des Guanidin-Boran-Adduktes **70** zu **71** (Schema 18; Präkatalysatoren: $[Rh(1,5\text{-}COD)Cl]_2$ oder Cp_2TiCl_2/*n*BuLi; COD = 1,5-Cyclooctadien).[225-228] Mit S_8 erfolgt die oxidative Insertion eines Schwefelatoms in die B–B-Bindung von **71**.[228] Die Substitution der borständigen Wasserstoffatome durch unterschiedliche Reste lieferte Rückschlüsse auf daraus resultierende Änderungen der Nucleophilie der B–B-Bindung in **71**. Das Hauptaugenmerk galt der Protonenaffinität der

verschiedenen Addukte (quantenchemische Rechnungen).[229] Die erste übergangsmetallfreie intramolekulare Dehydrokupplung beschrieben Fontaine et al. im Jahr 2016 anhand der Reaktion des frustrierten Lewis-Paars (FLP) **72** zu **73** (Schema 18; vgl. Kapitel 1.6.7).[230]

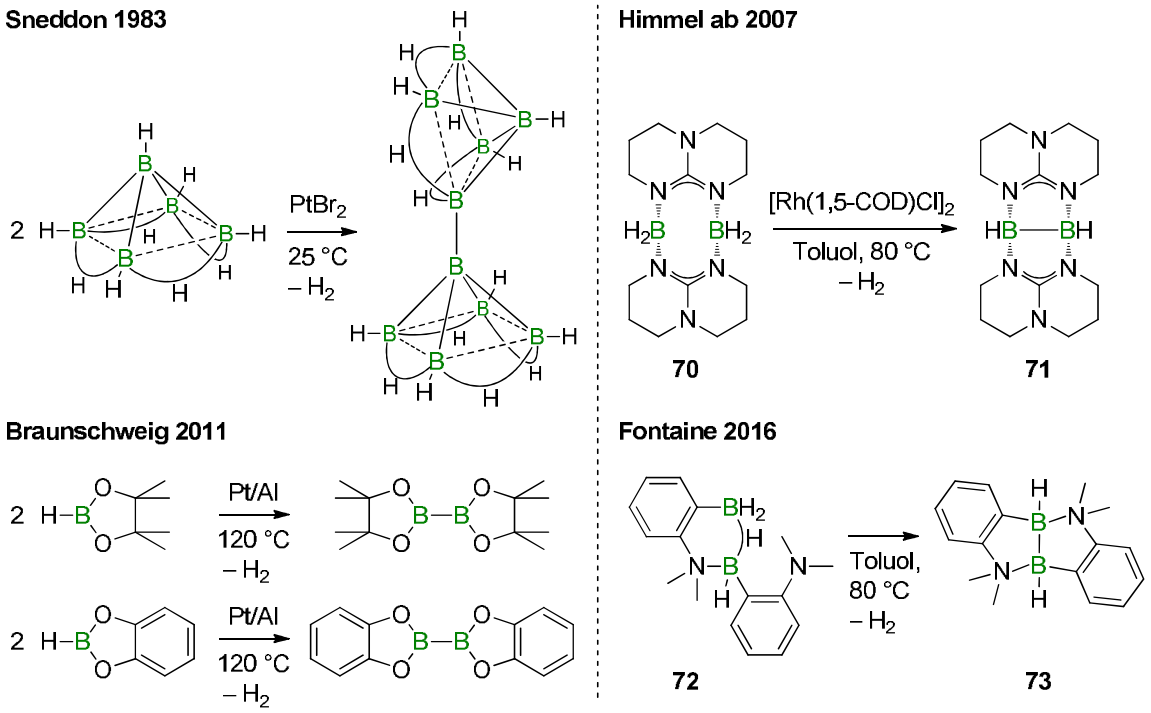

Schema 18. Aufbau von B–B-Bindungen durch Dehydrokupplung von Boranen.

1.6.5 Reaktionen von Metallborylenen und Metallborylen

Es existieren nur wenige Beispiele übergangsmetallgebundener Borylene, die unter B–B-Bindungsbildung reagieren. Repräsentative Produkte sind die Verbindung **74** und **75** von Braunschweig et al. aus den Jahren 2011 und 2012 (Abbildung 13).[231, 232] Ein großer Nachteil der Verwendung übergangsmetallgebundener Borylene besteht darin, dass es bis heute nicht gelungen ist, die Oligoborane anschließend von den Metallzentren zu lösen.

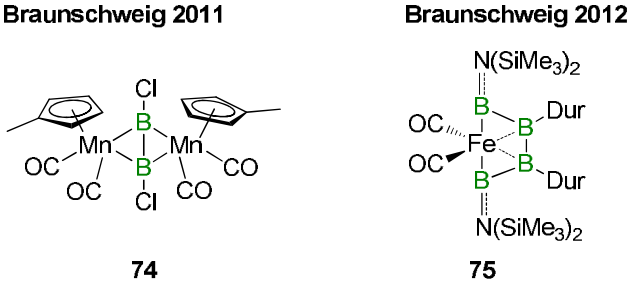

Abbildung 13. Moleküle mit übergangsmetallstabilisierten B–B-Bindungen.

Auch Metallboryle werden zum Aufbau von B–B-Bindungen genutzt. Nozaki et al. isolierten 2011 das Triboran **76** durch sequenzielle Reaktion des Boryllithiums Li[**47**] mit $BF_3{\cdot}Et_2O$ und $ClSiMe_3$ (Schema 19).[233]

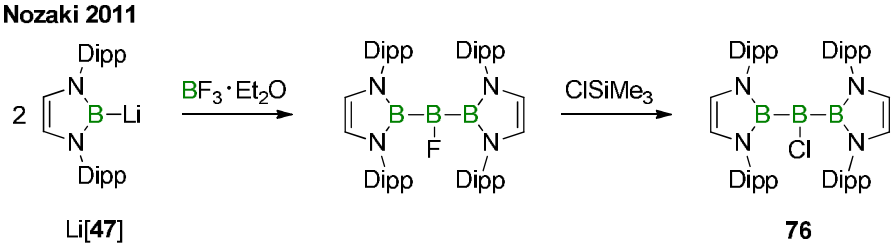

Schema 19. Synthese des Triborans **76** durch Reaktion des Boryllithiums Li[**47**] mit $BF_3{\cdot}Et_2O$ und $ClSiMe_3$.

Ein weiteres Triboran, [Mg(nacnac)][**78**], stellten Hill et al. im Jahr 2017 durch Umsetzung von [Mg(nacnac)][**77**] mit B_2pin_2 dar (Schema 20).[158, 159] In der Reaktion von [Mg(nacnac)][**77**] mit 9-Borabicyclo[3.3.1]nonan (9-BBN-H) entsteht das B–B-Kupplungsprodukt [Mg(nacnac)][**79**] (Schema 20).[158, 159]

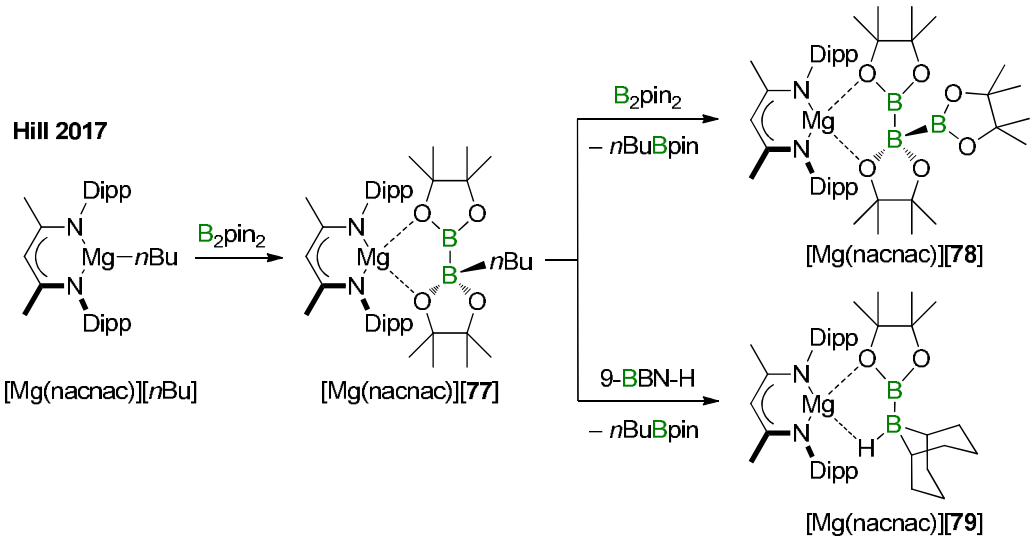

Schema 20. Synthese des Triboran-Salzes [Mg(nacnac)][**78**] und des Diboran-Salzes [Mg(nacnac)][**79**] ausgehend von [Mg(nacnac)][nBu] ($[nacnac]^-$ = $[\{N(Dipp)C(CH_3)\}_2CH]^-$).

Als Elektrophil eignet sich anstatt 9-BBN-H auch BPh_3. [Mg(nacnac)][**77**] entsteht durch Reaktion des β-Diketiminatomagnesium-*n*Bu-Komplexes [Mg(nacnac)][*n*Bu] mit B_2pin_2 (Schema 20). Mit 4-(Dimethylamino)pyridin (DMAP) bildet [Mg(nacnac)][**77**] den Boryl-Komplex [Mg(nacnac)(DMAP)][**49**], der in Abbildung 9 gezeigt ist ($[nacnac]^-$ = $[\{N(Dipp)C(CH_3)\}_2CH]^-$).

1.6.6 Hydroborierung von Diborenen

Im Jahr 1979 erhielt Brown den Nobelpreis für die Hydroborierung von C=C-Bindungen.[234-236] Diese Reaktion konnte durch Übergangsmetallkatalyse zu einem

milden und selektiven Werkzeug zur Erzeugung unterschiedlicher Alkylborane erweitert werden, bei denen die Option einer nachträglichen Derivatisierung am borgebundenen Kohlenstoffatom besteht.[237-239] Im Jahr 2014 konnten Braunschweig et al. zeigen, dass neben C=C-Bindungen von organischen Molekülen auch B=B-Bindungen von Diborenen prinzipiell für Hydroborierungsreaktionen geeignet sind. Beispielsweise führt die Reaktion von **80** mit Catecholboran (HBCat) zum Triboran **81** (Schema 21; IMe = 1,3-Dimethylimidazol-2-yliden).[240, 241]

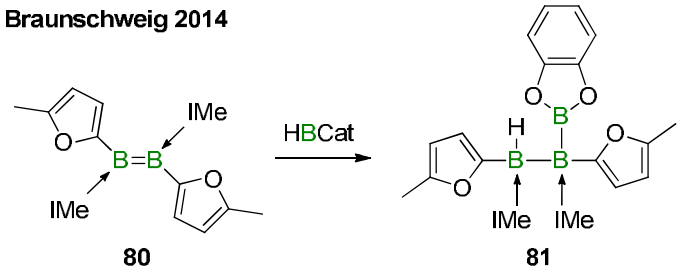

Schema 21. Aufbau einer B–B-Bindung in **81** durch Hydroborierung eines Diborens **80**. IMe = 1,3-Dimethylimidazol-2-yliden.

1.6.7 Deprotonierung von B–H-Verbindungen

B–B-Kupplungsreaktionen durch Deprotonierung von Molekülen mit borgebundenen Wasserstoffatomen sind sehr rar, da diese Wasserstoffatome in der Regel negativ polarisiert sind und damit eher hydridischen statt protischen Charakter besitzen (vgl. die Allred-Rochow-Elektronegativität von H (2.2) und B (2.0)). Die Deprotonierung terminaler B–H Bindungen beschränkt sich auf Systeme, in denen ausgeprägt elektronenziehende Cyanogruppen und/oder cyclische Alkylaminocarbene als Substituenten verwendet werden. Entsprechende Umsetzungen wurden im Jahr 2013 von Bertrand et al. (vgl. **82**) und 2017 von Finze et al. (vgl. [**83**]$^-$) publiziert (Abbildung 14).

Vor dem Jahr 2016 war die Deprotonierung neutraler Verbindungen mit B(μ-H)B-Einheiten auf B_nH_m-Cluster höherer Ordnung beschränkt ($n \geq 4$), wie z. B. im Falle der Deprotonierung von **84** mit *n*BuLi zu [**85**]$^-$ (Abbildung 14).[242, 243] Fontaine et al. gelang im Jahr 2016 bei erhöhter Temperatur (> 80 °C) die thermodynamisch begünstigte Eliminierung von H_2 aus dem dimeren Lewis-Paar **72** (vgl. Schema 18).[230] Gemäß quantenchemischer Rechnungen verläuft die Eliminierung über eine intramolekulare Deprotonierung des B(μ-H)B-Fragments. Es ist wichtig anzumerken, dass es sich bei dem neutralen Produkt **73** nicht um die konjugierte Base des Edukts **72** handelt. Zwei Jahre zuvor konnten Himmel et al. bereits zeigen, dass das positiv geladene Diboranaddukt $[H_3B_2(hpp)_2]^+$ ([**86**]$^+$) mit verbrückenden Guanidinateinheiten in einer (wenig selektiven) Reaktion mit KO*t*Bu unter B–B-Bindungsbildung zu **87** deprotoniert werden kann (Abbildung 14).[244]

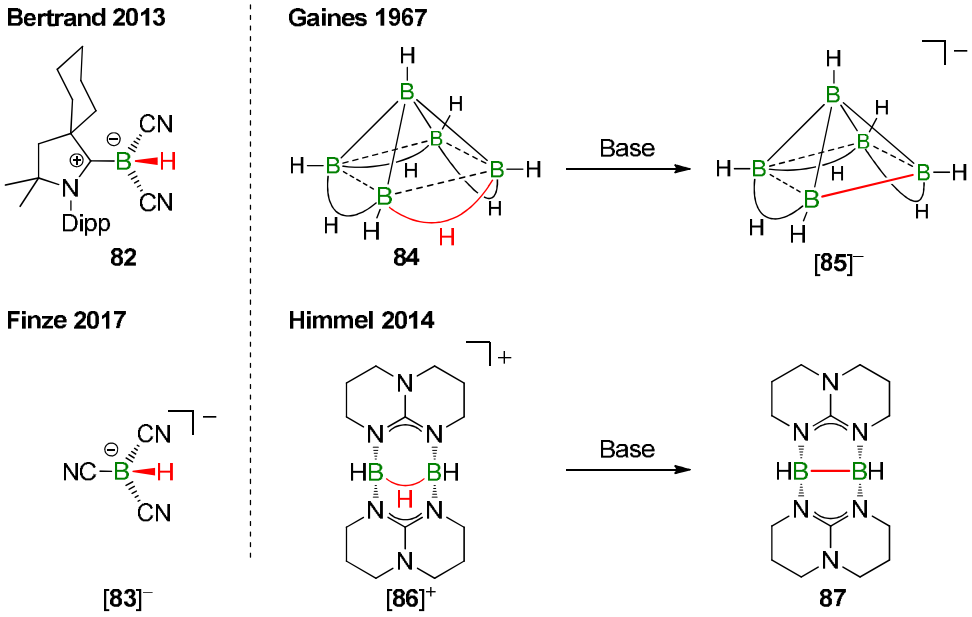

Abbildung 14. Deprotonierbare terminale B–H-Bindungen (links) und Aufbau von B–B-Bindungen durch Deprotonierung von BHB-Zweielektronen-Dreizentrenbindungen (rechts).

1.7 Moleküle mit B=B-Bindungen

Dianionische Diborane(4) der allgemeinen Strukturformel $[R_2B{=}BR_2]^{2-}$ sind isoelektronisch zu neutralen Alkenen der Gruppe 14. Die zweifach negative Ladung der B=B-Spezies erzeugt eine Coulomb-Repulsion, wodurch die Doppelbindung destabilisiert wird. Im Gegensatz zum bereits beschriebenen Li_2[**37**] (Stabilisierung durch zwei Biphenyl-2,2'-ylenbrücken; vgl. Schema 6), sind allen anderen dianionischen Diboranen sterisch anspruchsvolle Substituenten und/oder geeignete π-Akzeptorliganden[201, 245] zur Stabilisierung gemeinsam: Power et al. publizierten in den Jahren 1992 und 1996 die Einkristall-Röntgenstrukturen der Dianionen $[Mes_2B{=}B(Mes)Ph]^{2-}$ ([**88**]$^{2-}$), $[Ph(Me_2N)B{=}B(NMe_2)Ph]^{2-}$ ([**89**]$^{2-}$) und $[Mes(MeO)B{=}B(OMe)Mes]^{2-}$ ([**90**]$^{2-}$), die durch Zweielektronenreduktion der neutralen Diboran(4)-Vorläufer synthetisiert wurden.[246-248] Im Jahr 1999 konnten Nöth et al. die Kristallstrukturen von $[(Me_2N)(R_2N)B{=}B(NR_2)(NMe_2)]^{2-}$ (NR_2 = Pyrrolyl ([**91**]$^{2-}$), Indolyl ([**92**]$^{2-}$), Carbazolyl ([**93**]$^{2-}$)) bestimmen.[249] Der Ersatz von NR_2-Gruppen durch *N*-heterocyclische Carbene (NHCs) ermöglichte es Robinson et al. in den Jahren 2007 und 2008, neutrale Diborene der Form NHC(H)B=B(H)NHC zu isolieren (NHC: IDip = 1,3-Bis(2,6-di(*i*Pr)phenyl)imidazol-2-yliden (**94**), IMes = 1,3-Bis(2,4,6-trimethylphenyl)imidazol-2-yliden (**95**)).[250, 251] Im Jahr 2016 ergänzten Braunschweig et al. die Liste der L(H)B=B(H)L-Diborene um ein weiteres NHC- (SIDep = 1,3-Bis(diethylphenyl)-4,5-dihydroimidazol-2-yliden (**96**)) und ein cAAC-Derivat (cAAC: 1-(2,6-Di(*i*Pr)phenyl)-3,3,5,5-tetramethyl-pyrrolidin-2-yliden (**97**)).[252] Zuvor bedienten sie sich ebenfalls der NHCs, um Diborene der Strukturformel NHC(R)B=B(R)NHC mit Alkyl- (NHC: I*i*Pr = 1,3-Di(*i*Pr)imidazol-2-yliden; R = *i*Pr (**98**)),[24] Aryl- (NHC: IMe = 1,3-Dimethylimidazol-2-yliden; R = Mes (**99**), Dur = 2,3,5,6-Tetramethylphenyl (**100**))[253] und Heteroaryl- (NHC = IMe; R =

2-Thienyl (**101**), 5-(SiMe$_3$)-2-thienyl (**102**), 5-(Me)-2-furanyl (**103**))[240] Substituenten herzustellen. Während die Heteroarylsubstituenten der NHC-koordinierten Diborene in der >B=B<-Ebene liegen und eine π-Konjugation ermöglichen, sind die Arylsubstituenten aus der Ebene herausgedreht. Zur Stabilisierung von Diborenen eignen sich ebenfalls Phosphanliganden. Braunschweig et al. beschrieben in den Jahren 2014 und 2015 Diborene der Form R$_3$P(Mes)B=B(Mes)PR$_3$ mit *trans*- (R = Me (**104**), Et (**105**))[254, 255] und *cis*-Konfiguration (PR$_3$ = ½ Me$_2$PC$_2$H$_4$PMe$_2$ (**106**), ½ Ph$_2$PCH$_2$PPh$_2$ (**107**))[255]. Letztere werden durch Zugabe der chelatisierenden Diphosphane während der Reduktion erzeugt. Rechnungen ergaben, dass die Phosphan-Addukte einen größeren HOMO-LUMO-Abstand besitzen als analoge NHC-Addukte, da die Phosphanliganden schlechtere π-Akzeptoren (geringere Stabilisierung des LUMOs) und schwächere σ-Donoren (geringere Destabilisierung des HOMOs) sind.[254, 255]

Die bekannten B=B-Bindungslängen der oben genannten Verbindungen sind in Tabelle 2 aufgeführt. Theoretische Studien zu Diborenen legen nahe, dass das HOMO hauptsächlich entlang der jeweiligen B=B-Bindung lokalisiert ist.[201] Durch Verringerung der Coulomb-Repulsion bei gleichzeitigem Erhalt der lokalen Ladungsdichte im Bereich der B=B-Doppelbindung, kann der Abstand der Boratome zueinander minimiert werden (z. B. mit NHC-Liganden; cAACs erhöhen die Bindungslänge gegenüber NHCs; Tabelle 2).

Braunschweig et al. fanden in den Jahren 2012 und 2015 heraus, dass die B=B-Einheit von IMe(Dur)B=B(Dur)IMe (**100**) an Münzmetallsalze MCl koordinieren kann und die entstehenden Metallkomplexe **108** (M = Cu) und **109** (M = Ag) eine starke Lumineszenz mit nahezu 100% Quantenausbeute zeigen (Schema 22).[253, 256]

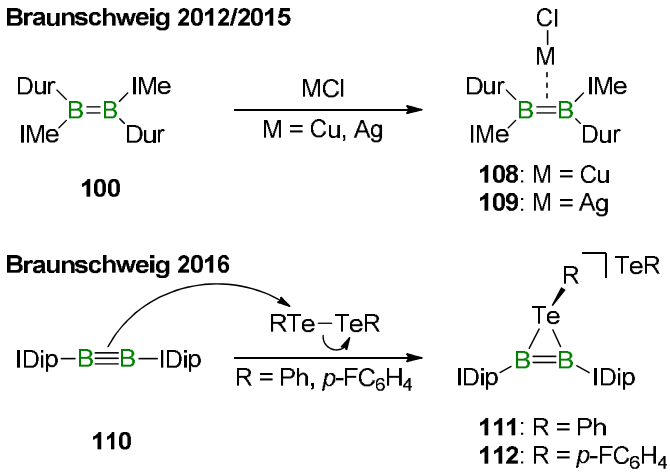

Schema 22. Synthese der Übergangsmetallkomplexe **108**/**109** und **111**/**112**. Dur = 2,3,5,6-Tetramethylphenyl; IMe = 1,3-Dimethylimidazol-2-yliden; IDip = 1,3-Bis(2,6-di(*i*Pr)phenyl)imidazol-2-yliden).

In Erweiterung dieser Arbeiten publizierten sie im Jahr 2016, dass durch Umsetzung von IDip-B≡B-IDip (**110**) mit RTeTeR die Synthese der Te-koordinierten Diborene **111** (R = Ph) und **112** (R = *p*-FC$_6$H$_4$) möglich ist (Schema 22).[257] Aktuell ist die Koordinationschemie von B–B-Mehrfachbindungen allerdings auf Derivate mit sterisch anspruchsvollen Liganden beschränkt, was die Palette der Metallkomplexe stark einschränkt. Ausgewählte

Heteroaryl-substituierte, NHC-stabilisierte Diborene reagieren unter Hydroborierung der B=B-Doppelbindung (vgl. Schema 21).[240, 241] Das energetisch vergleichsweise hoch liegende HOMO der NHC-stabilisierten Diborene macht einige Vertreter der Verbindungsklasse (z. B. **100** und **102**) trotz der fehlenden Ladung zu Reduktionsmitteln gegenüber ausgewählten Oxidationsmitteln wie $[C_7H_7][BAr^F_4]$, Ph_4C_4BMes oder Chalkogenen (Se, Te).[24, 257]

Tabelle 2. Durch Röntgenkristallographie an Einkristallen bestimmte B=B-Bindungslängen literaturbekannter Verbindungen.

Verbindung		**B=B-Länge (Å)**
[**37**]$^{2-}$	[R(R‘)B=B(R‘)R]$^{2-}$ (2 R = 2 R‘ = 4,4‘-Di-*t*Bu-biphenyl-2,2‘-ylen)	1.608(4)
[**88**]$^{2-}$	$[Mes_2B=B(Mes)Ph]^{2-}$	1.636(11)
[**89**]$^{2-}$	$[Ph(Me_2N)B=B(NMe_2)Ph]^{2-}$	1.631(9), 1.623(8)
[**90**]$^{2-}$	$[Mes(MeO)B=B(OMe)Mes]^{2-}$	1.636(7)
[**91**]$^{2-}$	$[(Me_2N)(R_2N)B=B(NR_2)(NMe_2)]^{2-}$ (NR_2 = Pyrrolyl)	1.59(1)
[**92**]$^{2-}$	$[(Me_2N)(R_2N)B=B(NR_2)(NMe_2)]^{2-}$ (NR_2 = Indolyl)	1.584(4), 1.578(3)
[**93**]$^{2-}$	$[(Me_2N)(R_2N)B=B(NR_2)(NMe_2)]^{2-}$ (NR_2 = Carbazolyl)	1.566(9), 1.571(8)
94	NHC(H)B=B(H)NHC (NHC = IDip)	1.561(18)
95	NHC(H)B=B(H)NHC (NHC = IMes)	planar: 1.602(5), verdreht: 1.582(4), trans-gebogen: 1.679(9)
96	SIDep(H)B=B(H)SIDep	1.589(4)
97	cAAC(H)B=B(H)cAAC	1.624(2)
98	NHC(R)B=B(R)NHC (NHC = I*i*Pr; R = *i*Pr)	1.578(3)
99	NHC(R)B=B(R)NHC (NHC = IMe; R = Mes)	1.593(5)
100	NHC(R)B=B(R)NHC (NHC = IMe; R = Dur)	1.590(5)
103	NHC(R)B=B(R)NHC (NHC = IMe; R = 5-(Me)-2-furanyl)	1.585(4)
104	$R_3P(Mes)B=B(Mes)PR_3$ (R = Me)	1.573(6)
105	$R_3P(Mes)B=B(Mes)PR_3$ (R = Et)	1.579(3)
106	$R_3P(Mes)B=B(Mes)PR_3$ (PR_3 = ½ $Me_2PC_2H_4PMe_2$)	1.583(2)
107	$R_3P(Mes)B=B(Mes)PR_3$ (PR_3 = ½ $Ph_2PCH_2PPh_2$)	1.593(2)

1.8 Zwischenfazit

Die Themenfelder „nucleophile Borverbindungen“ und „elektronenpräzise B–B-/B=B-Bindungen“ wachsen rasant. Den meisten dieser Verbindungen ist gemeinsam, dass sie zur Stabilisierung sterisch anspruchsvolle Reste oder Substituenten mit starkem π-Akzeptorcharakter tragen. Die Anforderung an zukünftige Systeme besteht darin, die Reaktivität passgenau zu justieren, um ein breiteres Anwendungsspektrum zu eröffnen. Zudem sind die unter reduzierenden Bedingungen ablaufenden Prozesse, die zur Entstehung von B–B-/B=B-Bindungen oder nucleophilen Borverbindungen führen, bislang nicht detailliert verstanden und bedürfen weiterer Forschung.

1.9 Zielsetzung

Basierend auf den Vorarbeiten im Arbeitskreis zur dynamisch kovalenten Chemie von neutralem 9-Borafluoren (**6**)$_2$ sollte dessen Reduktionschemie eingehend untersucht werden. Insbesondere die Abläufe, die bei Reduktion von 9-Borafluorenderivaten zu B–B-, B=B- sowie B-B-B-Bindungen führen, waren zu Beginn der vorliegenden Promotion mechanistisch ebenso wenig aufgeklärt, wie die begleitenden Gerüstumlagerungen. Über die Reaktivität entsprechender reduzierter Borane war ebenfalls sehr wenig bekannt. Experimentelle und theoretische Arbeiten zu 9-Borafluoren und verwandten Verbindungen sollten die Reaktionspfade aufzeigen, die durch Reduktion betreten werden.

Hieraus ergaben sich zwei Themenschwerpunkte:

(1) In Analogie zur Entwicklung der Organometallverbindungen, die durch Umpolung eine fundamentale Erweiterung der Kohlenstoffchemie bewirkt haben (z. B. Grignardreagenzien), galt es die Chemie reduzierter 9-Borafluorene zu untersuchen, um eine mögliche Nucleophilie des Borzentrums synthetisch nutzen zu können.

(2) Die Produktgemische der Reduktionsexperimente an dimerem 9-Borafluoren (**6**)$_2$ und dessen Isomer **12** ließen auf komplizierte Reaktionspfade schließen. Im Rahmen dieser Promotion sollten Schlüsselintermediate charakterisiert und mechanistische Studien angestellt werden.

Konkret waren folgende Projekte zu bearbeiten:

- Untersuchungen im Rahmen meiner Masterarbeit und der Promotion von Dr. Alexander Hübner zur Reduktion des Diborans(6) **12** unter variierten Bedingungen hatten neue Moleküle mit ungewöhnlichen Bindungssituationen hervorgebracht ([**37**]$^{2-}$, [**113**]$^{2-}$, [**114**]$^{2-}$, [**115**]$^{2-}$ und [**116**]$^{-}$), deren Bildungsmechanismen im Detail aufzuklären war.

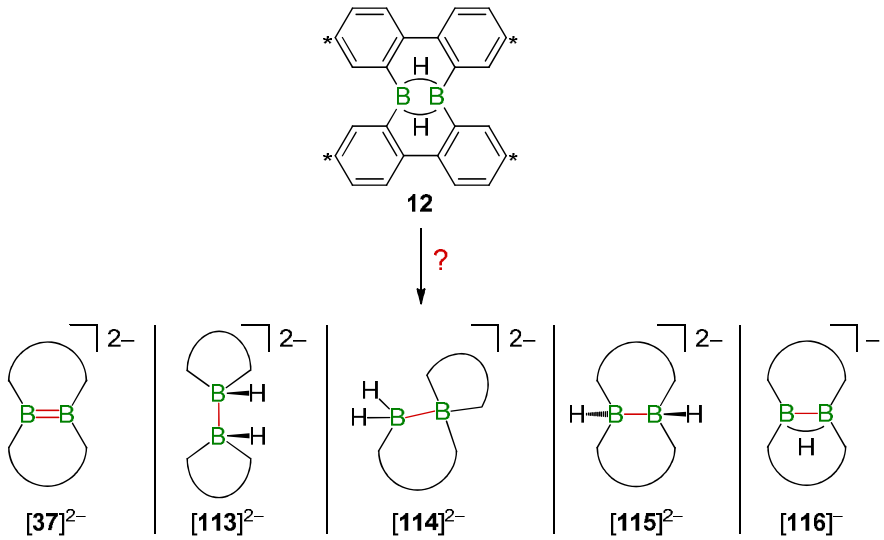

Schema 23. Was sind die mechanistischen Pfade, die bei unterschiedlichen Reduktionsbedingungen zu den Produkten [**37**]$^{2-}$, [**113**]$^{2-}$, [**114**]$^{2-}$, [**115**]$^{2-}$ und [**116**]$^{-}$ führen? Kohlenstoffatome, die mit * gekennzeichnet sind, tragen *t*Bu-Gruppen.

- Die Moleküle **12**, [**116**]$^-$ und [**37**]$^{2-}$ besitzen das gleiche Grundgerüst, aber unterscheiden sich hinsichtlich der Verknüpfung ihrer Boratome. Die drei verschiedenen Bindungsmodi sollten auf ihre Reaktivitäten hin untersucht und neue oder optimierte Synthesen für die drei Verbindungen entwickelt werden.

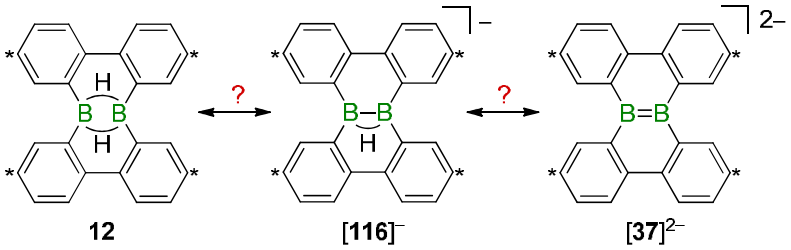

Schema 24. Lässt sich ein präparativer Zusammenhang zwischen **12**, [**116**]$^-$ und [**37**]$^{2-}$ finden? Welche Reaktivitäten zeigen diese Verbindungen? Kohlenstoffatome, die mit * gekennzeichnet sind, tragen *t*Bu-Gruppen.

- Das Reaktionsverhalten des reduzierten Bis(9-borafluorenyl)methans [**7**]$^{2-}$ mit gespanntem dreigliedrigem Ring war zu analysieren.

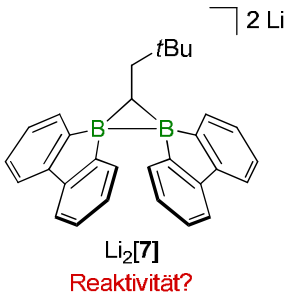

Abbildung 15. Wie ist die Reaktivität des reduzierten Bis(9-borafluorenyl)methans [**7**]$^{2-}$?

- Die literaturbekannte Reduktion von (**6**)$_2$ in Toluol mit Lithium in Gegenwart von Et_3SiBr lieferte vier Produkte, deren Entstehungsmechanismen ungeklärt waren. In THF wurde [**37**]$^{2-}$ mit einer höheren Ausbeute von 43% isoliert, aber entstehende Nebenprodukte wurden nicht identifiziert. Im Zuge der vorliegenden Arbeit waren Studien an (**6**)$_2$ in THF geplant, um dessen chemische Eigenschaften besser zu verstehen und Erkenntnisse für die Reaktivität in Toluol ableiten zu können.

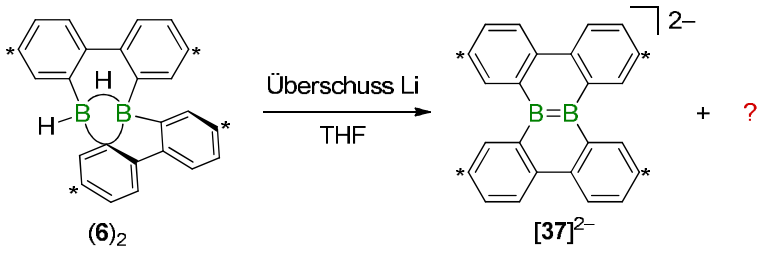

Schema 25. Was sind Nebenprodukte der Reduktion von (**6**)$_2$ in THF und warum werden diese Verbindungen gebildet? Kohlenstoffatome, die mit * gekennzeichnet sind, tragen *t*Bu-Gruppen.

2 Übersicht der Ergebnisse

2.1 Reduktionschemie des Diboran(6)-Derivats **12**

Die literaturbekannte Reduktion des C_1-symmetrischen Dimers (**6**)$_2$ mit Lithium in THF liefert das zweifach bordotierte Dibenzo[*g*,*p*]chrysen-Dianion [**37**]$^{2-}$ in einer Ausbeute von 43% (Schema 26).[108] Für [**37**]$^{2-}$ lassen sich vier aromatische π-Sextette nach Clar[258] zeichnen, sodass ein weitgehend lokalisiertes B=B-Fragment verbleibt (Schema 26). Um Moleküle mit B=B-Doppelbindungen kinetisch und/oder thermodynamisch zu stabilisieren, werden in vergleichbaren Systemen sterisch anspruchsvolle Gruppen und/oder Liganden mit ausgeprägten π-Akzeptor- und σ-Donoreigenschaften genutzt (vgl. Kapitel 1.7). Das Dianion [**37**]$^{2-}$ ist einzigartig in der Hinsicht, dass die Stabilisierung der B=B-Bindung allein durch zwei Biphenyl-2,2'-ylenbrücken erfolgt, die eine Dissoziation der Boratome über strukturellen Zwang erschweren. Die B=B-Doppelbindung in [**37**]$^{2-}$ sollte eine besonders hohe Reaktivität besitzen, weshalb ein verbesserter präparativer Zugang für anschließende Reaktivitätsstudien angestrebt war. Im Rahmen meiner Masterarbeit[259] und der Dissertation von Dr. Alexander Hübner[260] wurden Untersuchungen zur Reaktivität des Diborans(6) **12** unter reduzierenden Bedingungen begonnen. Die mechanistischen Zusammenhänge wurden im Zuge meiner Promotion herausgearbeitet und werden in den folgenden Unterkapiteln beschrieben. Wie in Kapitel 6.1 aufgeführt, sind dabei auch Ergebnisse der Masterarbeit von Timo Trageser[261] sowie der Bachelorarbeit von Hendrik Budy[262] eingearbeitet, die von mir eng betreut wurden.

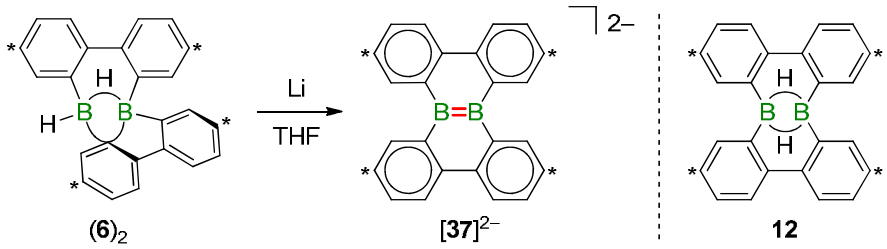

Schema 26. Die Reduktion von (**6**)$_2$ mit Lithium in THF liefert das bordotierte Dibenzo[*g*,*p*]chrysen-Dianion [**37**]$^{2-}$, das nach Clar mit vier aromatischen π-Sextetten und einer lokalisierten B=B-Bindung beschrieben werden kann. Das rechts abgebildete Diboran(6) **12**, das durch Thermolyse von (**6**)$_2$ zugänglich ist, sollte sich für die Synthese von [**37**]$^{2-}$ aufgrund der strukturellen Ähnlichkeit gut eignen. Kohlenstoffatome, die mit * gekennzeichnet sind, tragen *t*Bu-Gruppen.

12 ist ein Isomer des C_1-symmetrischen Dimers (**6**)$_2$ und durch dessen Thermolyse zugänglich (Schema 26).[66, 263] Aufgrund der Präorganisation war zu erhoffen, dass durch Reduktion von **12** das Dianion [**37**]$^{2-}$ in höherer Ausbeute erhalten wird als ausgehend von (**6**)$_2$ (43%).[108] Obwohl unter reduzierenden Bedingungen auch ausgehend von **12** eine B–B-Bindungsknüpfung eintritt, konnte [**37**]$^{2-}$ nur in vergleichbarer Ausbeute (41%) synthetisiert werden. Wie in Schema 27 dargestellt, ist das Hauptprodukt, das durch Reduktion von **12** entsteht, signifikant von der Art und Menge des Reduktionsmittels abhängig: Mit 2 Äquivalenten Lithiumnaphthalenid (LiNaph) bildet sich das Bis(9-boratafluoren) Li_2[**113**] als Hauptprodukt, begleitet von der spirocyclischen Verbindung Li_2[**114**] als Nebenprodukt. Das Isomer Li_2[**114**] kann mit 4 Äquivalenten LiNaph als Hauptprodukt in Lösung erzeugt werden, lagert aber bei erhöhter Temperatur und begünstigt von

apolaren Lösungsmitteln zu Li_2[**113**] um. Der Einsatz eines größeren Überschusses an einem lithiumbasierten Reduktionsmittel (11 Äquivalente LiNaph oder 60 Äquivalente Lithiummetall) unterdrückt Gerüstumlagerungen weitgehend und liefert Li_2[**37**] als Hauptkomponente. Die Umsetzung von **12** mit einem Überschuss an KC_8 (20 Äquivalente) ergab kein K_2[**37**], sondern nahezu quantitativ K_2[**115**]. Das Anion [**115**]$^{2-}$ ist isomer zu [**113**]$^{2-}$ und [**114**]$^{2-}$. Wie ein Überschuss an Lithium unterdruckt ein Überschuss an KC_8 strukturelle Umlagerungen, jedoch bleibt bei KC_8 die Anzahl an Wasserstoffatomen in Edukt und Produkt unverändert. Bei der Reduktion von **12** mit nur 1 Äquivalent an KC_8 wurde das diamagnetische Salz K[**116**] als Hauptprodukt isoliert.

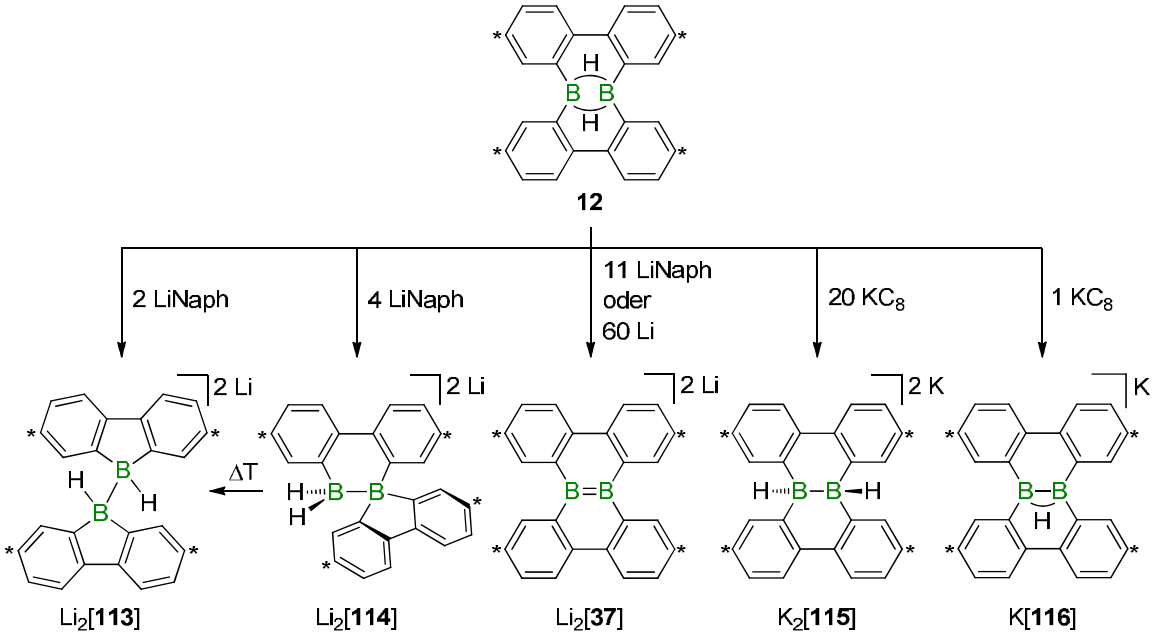

Schema 27. B–B-Bindungsbildung durch Reduktion von **12** (abgebildet ist jeweils das Hauptprodukt). Der Grad an Gerüstumlagerung und Hydridtransfer ist von der Art und Menge des Reduktionsmittels abhängig. Kohlenstoffatome, die mit * gekennzeichnet sind, tragen *t*Bu-Gruppen.

Die in den Reduktionsreaktionen von **12** entstandenen Hauptprodukte, die alle eine B–B- oder B=B-Bindung aufweisen, unterscheiden sich lediglich im Ausmaß an Gerüstumlagerungen und in der Anzahl der H-Atome. In den folgenden zwei Kapiteln werden diese Aspekte separat betrachtet, die in Summe das Gesamtbild beschreiben.

2.1.1 Gerüstumlagerungen im Zuge der Reduktion von **12**

1,2-Phenylverschiebungen, die zu umgelagerten Gerüsten führen, sind aus der Chemie der polycyclischen aromatischen Kohlenwasserstoffe bekannt und auf borhaltige Moleküle übertragbar: Die Clemmensen-Reduktion von 9*H*-Fluoren-9-on zur Synthese von Dibenzo[*g*,*p*]chrysen verläuft nach der Reaktion zum 9-Hydroxy-9,9‘-bifluorenyl über Wagner-Meerwein-artige Umlagerungen von Tetraphenylethyliumionen wie [**117**]$^+$ (Schema 28).[264-266] In Analogie ($C^+ \triangleq B$) wären die Umlagerungen von **12** zu Li_2[**113**] und Li_2[**114**] durch Reduktion auf intermediäre Boran-Borate zurückzuführen, die durch Transferprozesse von Hydridionen gebildet würden. Solche Umlagerungen müssten über

[**116**]$^-$ und das zugehörige Boran-Borat [**118**]$^-$ verlaufen (Schema 28). Das isolierte Anion [**116**]$^-$ lagert in THF-Lösung bei Raumtemperatur nicht zu [**113**]$^{2-}$ und [**114**]$^{2-}$ um, was diesen Mechanismus unwahrscheinlich macht. Da sich [**116**]$^-$ in einer Reaktionsmischung anders verhalten könnte als in isolierter Form, kann dieser Mechanismus jedoch nicht mit letzter Sicherheit ausgeschlossen werden.

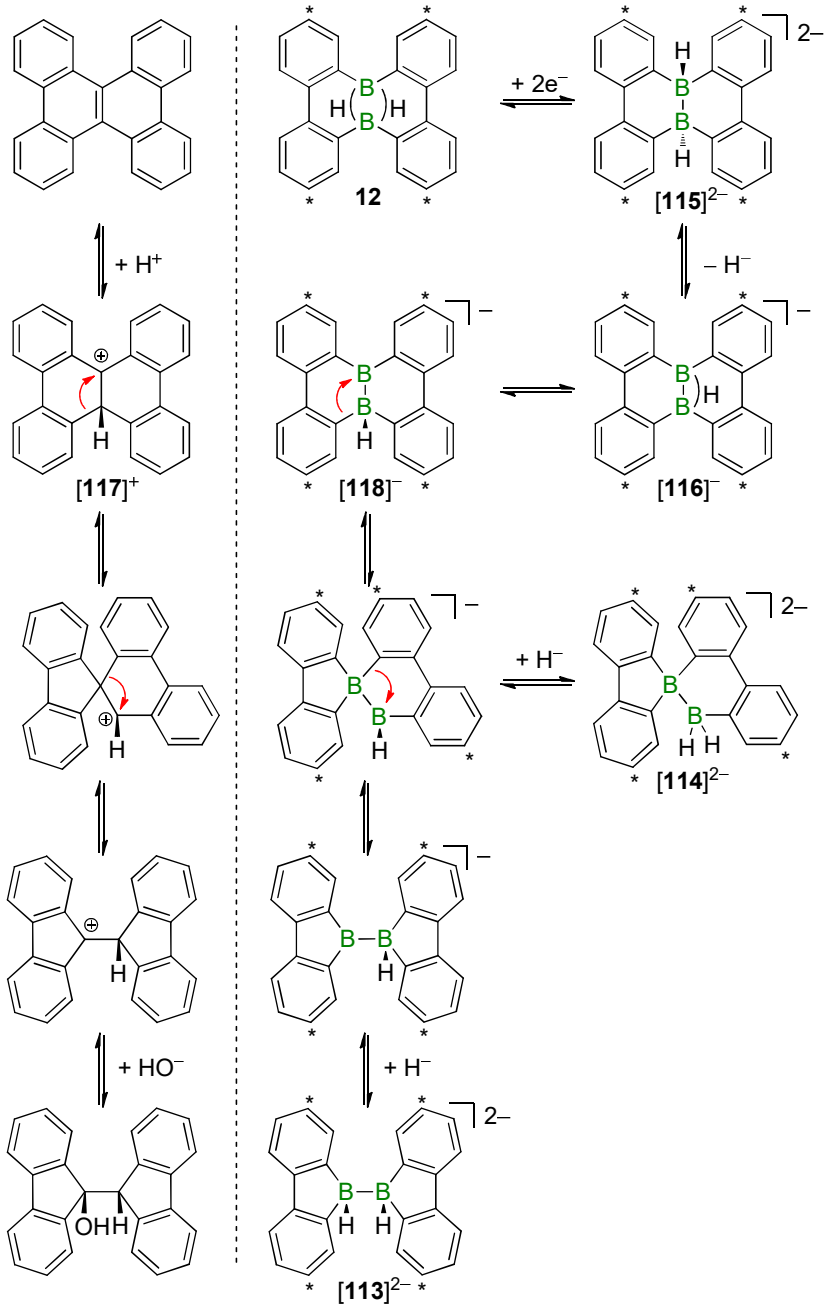

Schema 28. Die literaturbekannte Umlagerung von 9-Hydroxy-9,9‘-bifluorenyl zu Dibenzo[*g*,*p*]-chrysen unter Clemmensen-Bedingungen verläuft über Wagner-Meerwein-artige Umlagerungen von Tetraphenylethyliumionen wie [**117**]$^+$ (links). Über die Bildung und Umlagerung von Boran-Boraten lässt sich analog die Entstehung von [**113**]$^{2-}$–[**115**]$^{2-}$ und [**116**]$^-$ durch Reduktion von **12** formulieren (rechts). Da das isolierte Anion [**116**]$^-$ bei Raumtemperatur in THF-Lösung nicht zu einem anderen Produkt umlagert, ist dieser Mechanismus jedoch unwahrscheinlich. Kohlenstoffatome, die mit * gekennzeichnet sind, tragen *t*Bu-Gruppen.

Alternativ zum Auftreten von Boran-Boraten könnten die Umlagerungen zu Li_2[**113**] und Li_2[**114**] durch Einelektronüberträge hervorgerufen werden, die reaktive radikalische Intermediate erzeugen. Auch für dieses Szenario findet sich eine vergleichbare radikalisch induzierte Reaktion in der Chemie der polycyclischen aromatischen Kohlenwasserstoffe, nämlich die Umlagerung von Dibenzo[*g*,*p*]chrysen zu Bifluorenyliden, die von Harvey et al. detailliert mithilfe von quantenchemischen Rechnungen untersucht wurde.[267]
In Schema 29 sind die berechneten Strukturen der Kohlenwasserstoffe links abgebildet. Indem ausgewählte C–C-Bindungen durch BHB-2E3Z-Bindungen ersetzt werden, lässt sich die links abgebildete Sequenz auf die Reduktion von **12** übertragen (Schema 29, rechts): Die Reaktionspfade zur Bildung von [**113**]$^{2-}$, [**114**]$^{2-}$ und [**115**]$^{2-}$, beruhen auf drei prinzipiellen Reaktionstypen: (i) Redoxreaktionen zur Änderung der Molekülladung zwischen neutral, monoanionisch und dianionisch. Damit verbunden ist der Wechsel zwischen offenschaligen und geschlossenschaligen Konfigurationen. (ii) Homolytische Spaltung der π-Bindung einer C=C-Einheit unter gleichzeitiger Ausbildung einer B–C-σ-Bindung (und umgekehrt). (iii) Verschiebung eines Wasserstoffatoms aus einer B···B-verbrückenden Position in eine terminale Position (und umgekehrt), begleitet von einer Ladungsumverteilung im Molekül.
Die Anwendung der drei Grundreaktionen soll am Beispiel der Bildung von [**114**]$^{2-}$ verdeutlicht werden: Die Injektion eines Elektrons in **12** gemäß Reaktionstyp (i) erzeugt ein radikalisches Intermediat [**12**$^{\bullet}$]$^{-}$, das durch eine Reaktion des Typs (iii) zu Intermediat [**118**$^{\bullet}$]$^{-}$ reagiert. Durch Reaktionen des Typs (ii) lagert [**118**$^{\bullet}$]$^{-}$ zu [**119**$^{\bullet}$]$^{-}$ und anschließend zu [**120**$^{\bullet}$]$^{-}$ um. Nach Anwendung des Reaktionstyps (iii) befinden sich die Wasserstoffatome in [**114**$^{\bullet}$]$^{-}$ in terminaler Position. Aus der finalen Injektion eines weiteren Elektrons gemäß Typ (i) resultiert [**114**]$^{2-}$.
Entlang der Reduktionssequenzen werden die Intermediate [**113**$^{\bullet}$]$^{-}$, [**114**$^{\bullet}$]$^{-}$ und [**115**$^{\bullet}$]$^{-}$ mit ungewöhnlichen B•B-1E2Z-Bindungen postuliert. Um deren Entstehung auf Plausibilität zu überprüfen, ist ein Vergleich mit bereits isolierten Verbindungen hilfreich. Die in der Einleitung geschilderten Spezies Li[**7**$^{\bullet}$] und Li[**10**$^{\bullet}$] weisen B•B-1E2Z-Bindungen auf und sind strukturell vergleichbar mit [**113**$^{\bullet}$]$^{-}$ und [**114**$^{\bullet}$]$^{-}$ (Abbildung 16a).[105, 106] Für das Intermediat [**115**$^{\bullet}$]$^{-}$ ist bekannt, dass das Grundgerüst sowohl mit der Neutralform **115** ohne B–B-Bindung (berechnete Struktur mit terminalen B–H-Bindungen)[64] als auch mit der dianionischen Form [**115**]$^{2-}$ (Kristallstruktur) ohne große strukturelle Veränderungen kompatibel ist (Abbildung 16b). Daher sollte das Rückgrat mit zwei Biphenyl-2,2‘-ylenbrücken auch eine B•B-1E2Z-Bindungen in [**115**$^{\bullet}$]$^{-}$ tolerieren. Ferner besitzt das C_1-symmetrische Dimer (**6**)$_2$ eine hohe strukturelle Ähnlichkeit mit dem Intermediat [**119**$^{\bullet}$]$^{-}$ (Abbildung 16c). Aus den ausgeführten Vergleichen kann geschlussfolgert werden, dass die intermediäre Entstehung von Anionen mit B•B-1E2Z-Bindungen durch Reduktion von **12** möglich sein sollte.
Mit dem dargelegten Mechanismus über radikalische Intermediate sind nicht nur die Pfade zur Bildung der dianionischen Produkte [**113**]$^{2-}$, [**114**]$^{2-}$ und [**115**]$^{2-}$ plausibel erklärt, sondern auch der Bezug zwischen der Menge an Reduktionsäquivalenten und dem Ausmaß an Gerüstumlagerung aufgezeigt: Durch einfache Reduktion entstehen radikalische Spezies, die Umlagerungen unterliegen. Die zweite Reduktion verwandelt diese dynamischen Monoanionen in statische Dianionen, sodass das zum Zeitpunkt des

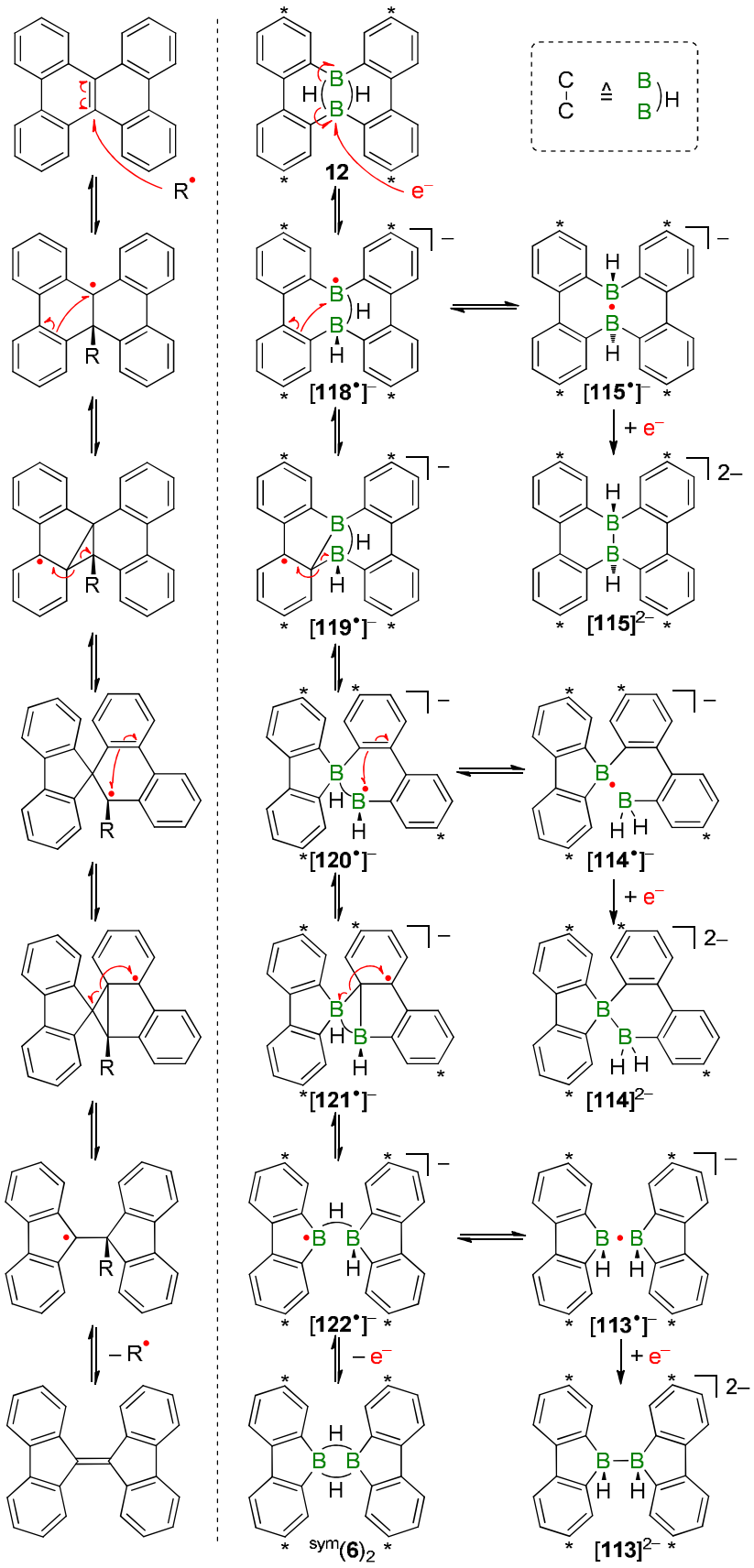

Schema 29. Quantenchemisch berechnete Strukturen der Umlagerungskaskade von Dibenzo[*g*,*p*]chrysen zu Bifluorenyliden (links) und die analog formulierte Sequenz zur Erzeugung von [**113**]$^{2-}$, [**114**]$^{2-}$ und [**115**]$^{2-}$ durch Reduktion von **12** (rechts). Kohlenstoffatome, die mit * gekennzeichnet sind, tragen *t*Bu-Gruppen.

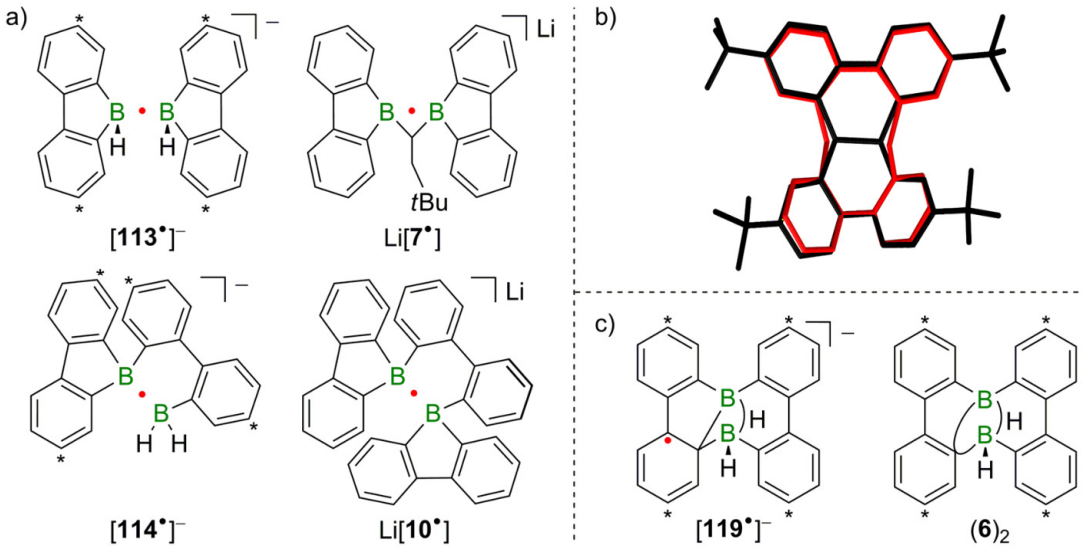

Abbildung 16. (a) Gegenüberstellung der postulierten B•B-1E2Z-gebundenen Intermediate [**113**•]⁻ und [**114**•]⁻ mit den isolierten Verbindungen Li[**7**•] und Li[**10**•], (b) Überlagerung der Kristallstruktur von [**115**]$^{2-}$ (schwarz) mit der berechneten Struktur des neutralen Moleküls **115** ohne B–B-Bindung und ohne *t*Bu-Gruppen (rot), (c) Gegenüberstellung des postulierten B–C–B-gebundenen Radikals [**119**•]⁻ mit röntgenkristallographisch charakterisiertem (**6**)$_2$. Kohlenstoffatome, die mit * gekennzeichnet sind, tragen *t*Bu-Gruppen.

zweiten Reduktionsschritts bestehende Produktgemisch unverändert bleibt. Daraus folgt, dass ein großes Angebot an Elektronen die Lebensdauer der dynamischen Radikale verkürzt. Gerüstumlagerungen werden unterdrückt und die Dianionen [**115**]$^{2-}$ bzw. [**37**]$^{2-}$ sind die beobachteten Hauptprodukte. Im Umkehrschluss führen wenige Äquivalente an Reduktionsmittel zu längeren Lebenszeiten der dynamischen, radikalischen Intermediate. In diesem Fall können sich Gleichgewichte einstellen, in denen nach zweiter Reduktion [**113**]$^{2-}$ und [**114**]$^{2-}$ als Hauptprodukte vorliegen. 4 Äquivalente an Reduktionsmittel stellen einen Grenzfall dar: Umlagerungen finden bereits statt, aber es kann sich noch kein vollständiges Gleichgewicht einstellen, sodass die Bildung von [**114**]$^{2-}$ als Hauptprodukt beobachtet wird.

2.1.2 Hydridtransfers im Zuge der Reduktion von **12**

Um die Bildung von Li_2[**37**] durch Reduktion von **12** zu erklären, muss in Betracht gezogen werden, dass neben der intramolekularen Verschiebung von Hydriden, im Zuge von Gerüstumlagerungen, auch intermolekulare Hydridtransfers eine Rolle spielen können. Während die Reduktion von **12** mit einem Überschuss an KC_8 das Kaliumsalz K_2[**115**] mit unveränderter Anzahl an Wasserstoffatomen gegenüber **12** liefert, führt ein Überschuss an LiNaph oder Lithiummetall zur Entstehung von Li_2[**37**], einer Verbindung die zwei Wasserstoffatome weniger trägt als das Edukt. Die B=B-gebundene Graphenflocke [**37**]$^{2-}$ kann plausibel aus der H–B–B–H-Spezies [**115**]$^{2-}$ hervorgehen, wenn eine Triebkraft zur Hydrideliminierung besteht (z. B. durch einen Hydridfänger) und das resultierende Elektronendefizit durch ausreichend Reduktionsmittel ausgeglichen werden kann (Schema 30). Letztere Bedingung ist durch den verwendeten Überschuss an Reduktionsmittel erfüllt. Als

Hydridfänger könnte bei Reduktion mit LiNaph oder Lithiummetall das Alkalikation dienen: Das kleine, harte Li^+-Kation ist eine stärkere Lewis-Säure als das große, weiche K^+-Kation und der Betrag der Bildungsenthalpie von LiH ($\Delta_B H^0$ = –91 kJ mol^{-1}) ist um 35 kJ mol^{-1} höher als der von KH ($\Delta_B H^0$ = –56 kJ mol^{-1}).[268] Der strukturelle Unterschied der Interkalationsverbindung KC_8 gegenüber LiNaph oder Lithiummetall kann ebenfalls entscheidende Auswirkungen auf die Verfügbarkeit der Kationen und deren Interaktion mit den in Lösung befindlichen Anionen haben. Dementsprechend wurde mit den lithiumbasierten Reduktionsmitteln LiNaph und Lithiummetall die Bildung von Li_2[**37**] beobachtet, wohingegen bei Verwendung von KC_8 kein K_2[**37**] entstand.

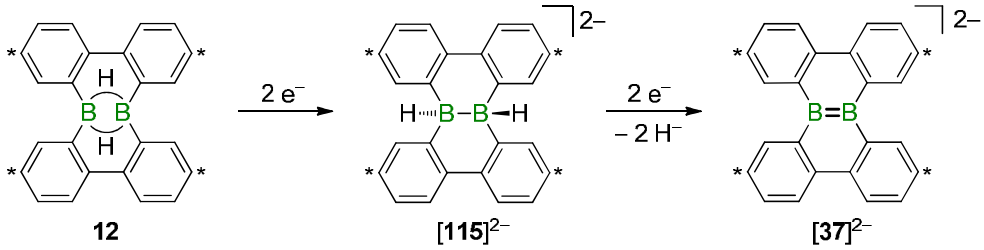

Schema 30. Ein plausibler Reaktionspfad zur Entstehung von [**37**]$^{2-}$ durch Reduktion von **12** läuft über [**115**]$^{2-}$ als Zwischenprodukt. Kohlenstoffatome, die mit * gekennzeichnet sind, tragen *t*Bu-Gruppen.

Zu einem Hydridtransfer kann es auch kommen, wenn nur 1 Äquivalent an Reduktionsmittel verwendet wird, wie bei der Reduktion von **12** mit 1 Äquivalent KC_8, bei der das diamagnetische Salz K[**116**] als ein Hauptprodukt entsteht (Schema 27). Das Anion [**116**]$^-$ trägt ein Wasserstoffatom weniger als das Edukt **12** und als [**115**]$^{2-}$. Der Farbverlauf der Reduktionsreaktion von farblos (**12**) über orange-rot zu gelb ([**116**]$^-$) deutet auf ein intermediäres Auftreten von [**115**]$^{2-}$ hin. Da K^+-Kationen selbst bei einem Überschuss an KC_8 nicht in der Lage sind, Hydride von [**115**]$^{2-}$ zu entfernen, sollte ein anderer Mechanismus in Betracht gezogen werden: Unter der Annahme, dass bei Reduktion mit 1 Äquivalent KC_8 zunächst selektiv [**115**]$^{2-}$ erzeugt wird, muss noch 50% unverbrauchtes Edukt (**12**) zurückbleiben. Das Diboran **12** ist eine Lewis-Säure und könnte an einem intermolekularen Hydridaustausch mit [**115**]$^{2-}$ beteiligt sein.

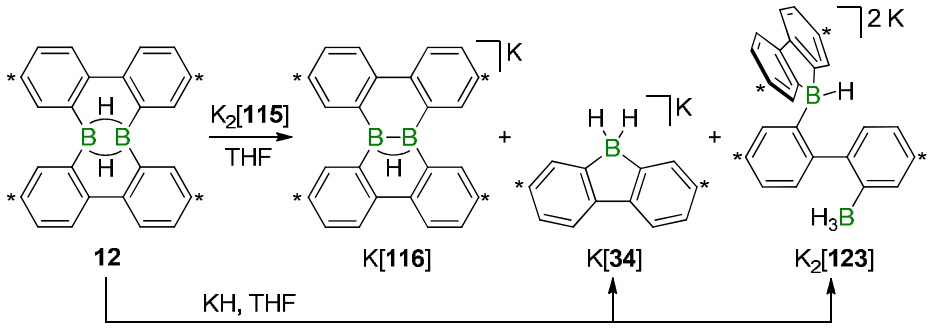

Schema 31. Die Reaktion von **12** mit der H–B–B–H-gebundenen Verbindung K_2[**115**] liefert K[**116**], K[**34**] und K_2[**123**] als Hauptprodukte. K[**34**] und K_2[**123**] entstehen ebenfalls bei der Reaktion von **12** mit KH. Kohlenstoffatome, die mit * gekennzeichnet sind, tragen *t*Bu-Gruppen.

Um diese Hypothese zu prüfen, wurden äquimolare Mengen an **12** und [**115**]$^{2-}$ zur Reaktion gebracht (Schema 31). Sowohl der Farbverlauf, als auch die anschließende Produktverteilung waren identisch zum Fall der Reduktion von **12** mit 1 Äquivalent KC_8. Als Nebenprodukte entstanden in beiden Fällen K[**34**] und K_2[**123**]. Diese Anionen bilden sich durch Hydridübertragung auf **12**, wie durch Reaktion von **12** mit KH unabhängig bestätigt wurde (Schema 31).

2.1.3 Reaktivität der Triade **12**/[**116**]$^-$/[**37**]$^{2-}$

Die Anionen [**116**]$^-$ und [**37**]$^{2-}$ können durch Reduktion von **12** synthetisiert werden. Strukturell handelt es sich bei [**116**]$^-$ sowohl um die konjugierte Brønsted-Säure von [**37**]$^{2-}$, als auch um die konjugierte Base von **12**. Experimentell galt es herauszufinden, inwiefern die Triade **12**/[**116**]$^-$/[**37**]$^{2-}$ tatsächlich über eine Protonierungs-/Deprotonierungssequenz verknüpft ist oder ob den borständigen Wasserstoffatomen ein rein hydridischer Charakter zukommt. Für die Stammverbindung B_2H_6 ist seit Jahrzehnten bekannt, dass die Reaktion mit Donormolekülen (Do) zur symmetrischen (2 $DoBH_3$) oder unsymmetrischen Spaltung ($[Do_2BH_2][BH_4]$) des Dimers führt.[269] Eine Deprotonierung wurde nie beschrieben, obwohl Pitzer bereits im Jahr 1945 die elektronische Struktur von B_2H_6 als $[H_2B{=}BH_2]^{2-}$ mit zwei zusätzlichen Protonen beschrieb.[270] Quantenchemische Rechnungen aus dem Jahr 2005 von Wenthold et al. unterstützen dieses Strukturmodell (Abbildung 17): Zwar besitzen die zwei mesomeren Formen, die der symmetrischen (31%) und unsymmetrischen (25%) Spaltung des Diborans entsprechen, einen großen Beitrag, die Hauptresonanzstruktur (36%) ist aber jene, in der ein Proton und ein borsubstituiertes Borhydrid vorliegen. Eine kanonische Form mit B=B-Bindung hat ebenfalls einen nicht vernachlässigbaren Anteil (6%). Insgesamt tragen die μ-H-Atome in B_2H_6 eine positive Partialladung von 0.10 und die μ-H–B-Bindungen sind zu 50% kovalent und 50% ionisch. Die berechnete B–B-Bindungsordnung in B_2H_6 beträgt 0.5.[271]

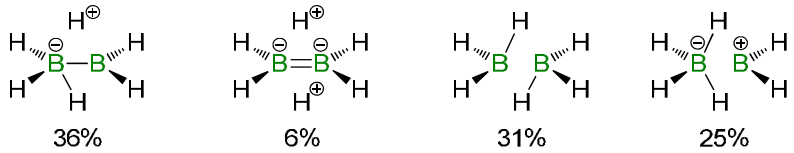

Abbildung 17. Die vier relevantesten kanonischen Strukturen von B_2H_6.

Um die Basizität von [**37**]$^{2-}$ zu überprüfen, wurde Li_2[**37**] mit etherischer HCl titriert und die Reaktion NMR-spektroskopisch verfolgt (Abbildung 18). Die schrittweise Zugabe der Säure führte zu einer selektiven Reaktion, in der zunächst Li_2[**37**] zu Li[**116**] protoniert wurde (≤ 1 Äquivalent HCl) und dieses bei weiterer Zugabe der Säure zu **12** (> 1 Äquivalent HCl). Der Farbverlauf von dunkelrot (Li_2[**37**]) zu gelb (Li[**116**]) zu farblos (**12**) steht mit den NMR-Daten im Einklang. **12** zerfiel in THF selbst in Gegenwart eines leichten Überschusses an etherischer HCl nur sehr langsam in das 9-Borafluoren-THF-Addukt (ca. 1% nach 4 Tagen).
Um die Acidität von **12** zu untersuchen, wurde als erstes die Basizität von Li_2[**37**] genutzt: In einer Komproportionierungsreaktion äquimolarer Mengen an **12** und Li_2[**37**] bildete

sich quantitativ Li[**116**] (Schema 32). Auch wenn der zugrundeliegende Mechanismus nicht unbedingt auf einem unmittelbaren H^+-Transfer beruhen muss, war dieses Testexperiment vielversprechend hinsichtlich der Verwendung klassischer Basen zur Deprotonierung von **12**. Während Lithiumdi(*i*Pr)amid (LDA) zu keiner selektiven Reaktion führte, gelang es mit der sterisch anspruchsvollen Base $(Me_3Si)_2NK$ das Kaliumsalz K[**116**] in nahezu quantitativer Reaktion darzustellen (Schema 32). Dieser Reaktionspfad ist deutlich effizienter als die Erzeugung mittels Reduktion von **12**, bei der K[**116**] in einem Produktgemisch anfällt. Die Synthese von Li[**116**] erfolgte ebenfalls mit sehr guten Ausbeuten im präparativen Maßstab mit den Basen $(Me_3Si)_3CLi$ und $(Me_3Si)_2NLi$ (Schema 32).[272]

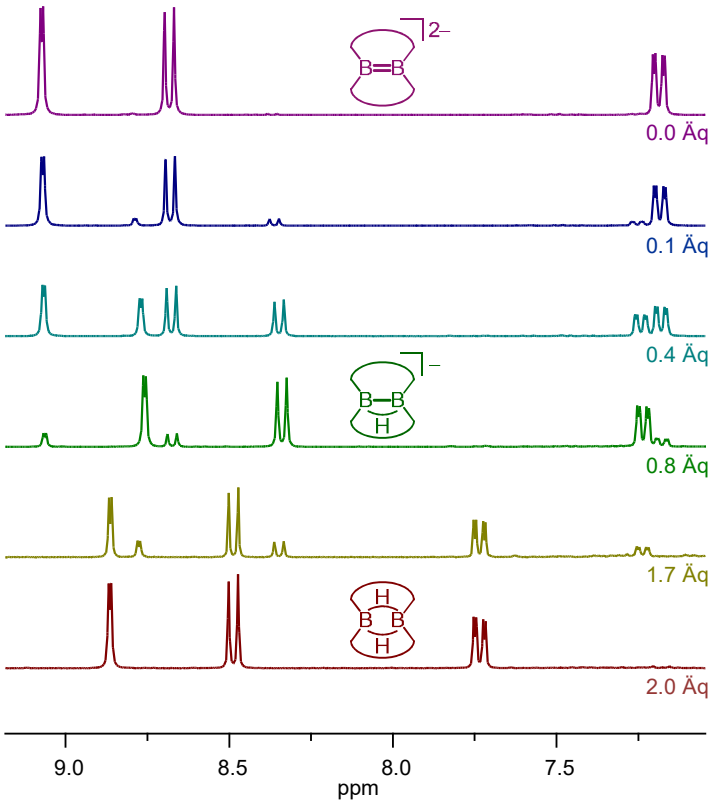

Abbildung 18. ^{1}H-NMR-spektroskopische Kontrolle der Reaktion von Li_2[**37**] (oben) zu Li[**116**] (Mitte) und **12** (unten) durch Titration mit etherischer HCl in THF-d_8.

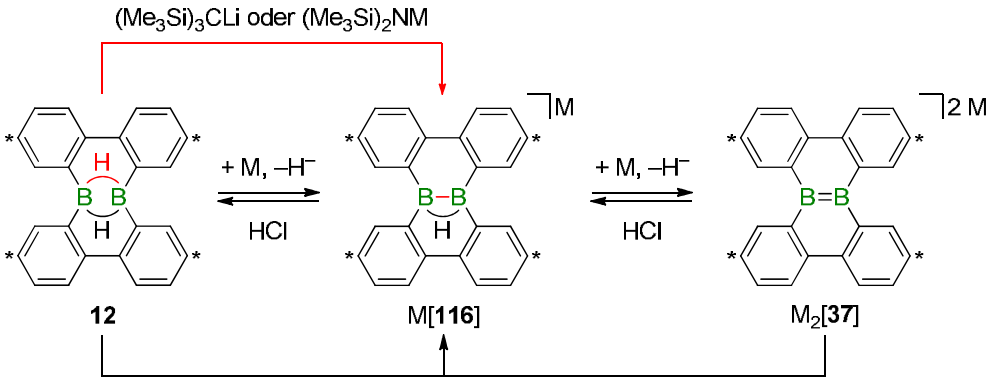

Schema 32. Deprotonierung von **12** zu M[**116**] (oben); sequenzielle Reduktion von **12** zu M[**116**] und M_2[**37**] sowie Umkehrreaktion durch Titration von M_2[**37**] mit etherischer HCl (Mitte; M = Li oder K); Komproportionierung von **12** und Li_2[**37**] zu Li[**116**] (unten). Kohlenstoffatome, die mit * gekennzeichnet sind, tragen *t*Bu-Gruppen.

Die über Röntgenkristallographie ermittelte Festkörperstruktur von [Li(Et$_2$O)$_2$][**116**] bestätigt nicht nur die Bildung von Li[**116**], sondern ist darüber hinaus bemerkenswert, weil vier symmetrieunabhängige [**116**]$^-$-Anionen vorliegen, die sich signifikant in ihrer Konformation unterscheiden: Die Torsionswinkel zwischen den zentralen C–C-Bindungen der beiden Biphenyl-2,2‘-ylenbrücken variieren zwischen 4.2(2)° und 32.1(3)° (Abbildung 19).

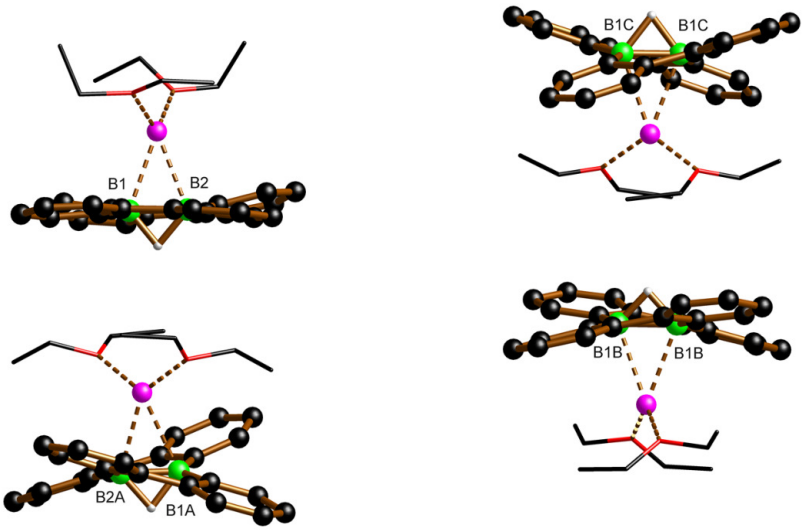

Abbildung 19. Festkörperstruktur von [Li(Et$_2$O)$_2$][**116**]. *t*Bu-Gruppen und C*H*-Atome wurden aus Gründen der Übersichtlichkeit nicht abgebildet.

Prinzipiell könnten die Anionen [(Me$_3$Si)$_3$C]$^-$ und [(Me$_3$Si)$_2$N]$^-$ auch als Reduktionsmittel mit anschließender radikalischer H-Abstraktion reagieren.[273] Da weder eine Deuteriumabstraktion vom omnipräsenten Lösungsmittel THF-d_8 unter Bildung von (Me$_3$Si)$_3$CD beobachtet wurde, noch die Zugabe des bekannten Radikalfängers *n*Bu$_3$SnH[274] den Verlauf der Reaktion änderte, ist ein radikalischer Mechanismus weniger wahrscheinlich als eine direkte Deprotonierung. Mit einem Überschuss an Base wurde im Falle von (Me$_3$Si)$_3$CLi und (Me$_3$Si)$_2$NLi keine Bildung der B=B-gebundenen Spezies [**37**]$^{2-}$ beobachtet, mit (Me$_3$Si)$_2$NK entsteht diese in Spuren. Die Einwirkung eines Überschusses an Amid-Base führt über längere Zeit zu einer Zersetzungsreaktion.
Der Verknüpfung der Boratome in **12** über zwei Biphenyl-2,2‘-ylenbrücken kommt möglicherweise eine entscheidende Rolle für eine erfolgreiche Deprotonierung zu, da sie eine Dissoziation der Borzentren und eine Adduktbildung mit sterisch anspruchsvollen Lewis-Basen erschwert. Im Falle des Borans (Mes$_2$BH)$_2$, das in Lösung im Gleichgewicht mit der monomeren Form Mes$_2$BH vorliegt,[275] wurde bei Zugabe von (Me$_3$Si)$_2$NK die Bildung des Addukts K[Mes$_2$(H)BN(SiMe$_3$)$_2$] mittels NMR-Spektroskopie und Röntgenkristallstrukturanalyse nachgewiesen. Die Bedeutung des sterischen Anspruchs der Base wird beim Wechsel zu den kommerziell erhältlichen Basen *t*BuLi, *n*BuLi und MeLi deutlich. Während bei Verwendung von *t*BuLi noch ca. 45% Li[**116**] entstanden, lagen die Ausbeuten mit *n*BuLi und MeLi lediglich bei ca. 25% Li[**116**]. Als bedeutendes Nebenprodukt wurde in den Reaktionen mit *n*BuLi das anionische Bis(9-borafluorenyl)methan [**124**]$^-$ und in der Reaktion mit MeLi das entsprechende Anion [**125**]$^-$ identifiziert und strukturell charakterisiert (beide ca. 25%; Abbildung 20). In beiden Verbindungen befinden sich jeweils zwei 9-Borafluorenylsubstituenten am selben (terminalen) Kohlenstoffatom, das aus dem

Lithiierungsreagenz stammen muss (Abbildung 20). Eine negative Ladung wird von dem formal hydridischen Wasserstoffatom eingebracht, das die Boratome verbrückt. Als Ladungsausgleich dienen lösungsmittelseparierte Li^+-Kationen. Durch dynamisches Verhalten in Lösung sollten die 9-Borafluorenyleinheiten in [**125**]$^-$ mittels Drehung oder Spiegelung ineinander überführt werden können. Der C_4H_8-Rest im Anion [**124**]$^-$ erzeugt jedoch ein prochirales Zentrum, das die mittlere Symmetrie von [**124**]$^-$ (C_s) gegenüber der von [**125**]$^-$ (C_{2v}) verringert. Dementsprechend enthält das ^{1}H-NMR-Spektrum von [**125**]$^-$ nur einen Satz an Resonanzen für alle vier *t*Bu-C_6H_3-Ringe, während [**124**]$^-$ zwei Signalsätze erzeugt. Einer der zwei Signalsätze von [**124**]$^-$ stimmt weitgehend mit dem Signalsatz von [**125**]$^-$ überein, sodass er mit großer Wahrscheinlichkeit den Hälften der 9-Borafluorenyleinheiten zugeordnet werden kann, in die das Proton der Methylenbrücke zeigt.

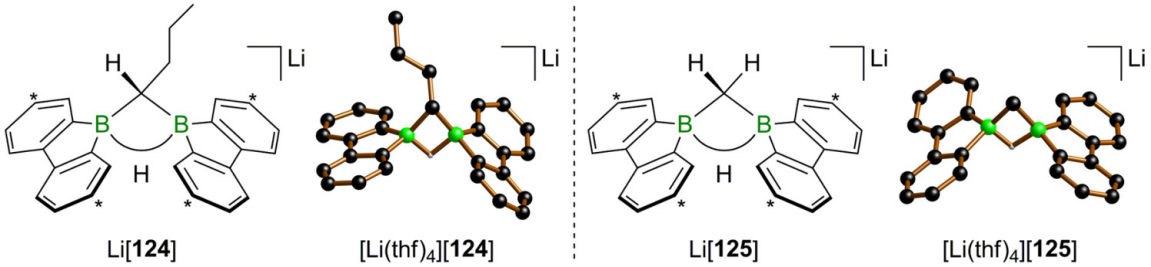

Abbildung 20. Schematische Darstellungen von Li[**124**] (links) und Li[**125**] (rechts) mit den dazugehörigen Festkörperstrukturen [Li(thf)$_4$][**124**] bzw. [Li(thf)$_4$][**125**] (vereinfachte Darstellungen ohne lösungsmittelseparierte Kationen, C*H*-Atome und *t*Bu-Gruppen). Kohlenstoffatome, die mit * gekennzeichnet sind, tragen *t*Bu-Gruppen.

Zusammenfassend wurde die Deprotonierungsstudie an dem Diboran(6)-Derivat **12** erfolgreich durchgeführt. Hinsichtlich einer Übertragung der B–B-Bindungsbildung durch Deprotonierung auf andere Systeme sind folgende Schlussfolgerungen zu beachten: 1) Die gewählte Base sollte einen großen sterischen Anspruch besitzen, um eine konkurrierende Adduktbildung zu vermeiden. 2) Sterisch anspruchsvolle Substituenten an der B(μ-H)B-Brücke führen zu einer Verschiebung des Monomer-Dimer-Gleichgewichts auf die Seite des Monomers und sollten vermieden werden. Die Monomere bilden selbst mit sterisch beladenen Basen Addukte, sodass eine Deprotonierung des Dimers verhindert wird. 3) Verbrückende Liganden wie die Biphenyl-2,2‘-yleneinheit sind hilfreich, da sie eine Dissoziation des B(μ-H)B-Fragments erschweren und einer Tetrakoordination der Boratome durch Adduktbildung entgegenwirken. 4) Um eine große Coulomb-Repulsion zu vermeiden, sollten die zu deprotonierenden Verbindungen möglichst neutral oder kationisch geladen sein.

Die Isolierung der anionischen Bis(9-borafluorenyl)methane [**124**]$^-$ und [**125**]$^-$ als Nebenprodukte bei der Deprotonierung von **12** warf die Frage auf, wie der verbrückende Methylen- bzw. Butylen-Rest in das Produkt eingebaut wurde. Da die Reaktionsverläufe zur Bildung von [**124**]$^-$ und [**125**]$^-$ sehr vergleichbar waren, aber [**125**]$^-$ ein vereinfachtes System darstellt, wurden mechanistische Untersuchungen an [**125**]$^-$ durchgeführt: Ein Vergleich der Edukte **12** (zwei μ-H-Atome) und H_3CLi (drei C*H*-Atome) mit dem Produkt [**125**]$^-$ (ein μ-H-Atom und zwei C*H*-Atome) offenbart, dass aus der Summe von fünf entscheidenden Wasserstoffatomen der beiden Edukte nur drei im Produkt verblieben sind.

Obwohl sich diese Bilanz durch die Annahme einer Eliminierung von H_2 ausgleichen ließe, gab es keinen Hinweis auf die Entwicklung des Gases bei Reaktionen in abgeschmolzenen NMR-Rohren. Anhand von Markierungsexperimenten mit Deuterium konnte abgeleitet werden, dass sowohl die H-Atome der Methylenbrücke als auch das borverbrückende H-Atom in [**125**]$^-$ aus dem Methyllithiumreagenz stammten (Schema 33). Keines der verbrückenden H-Atome in **12** fand sich im Produkt [**125**-d_3] wieder.

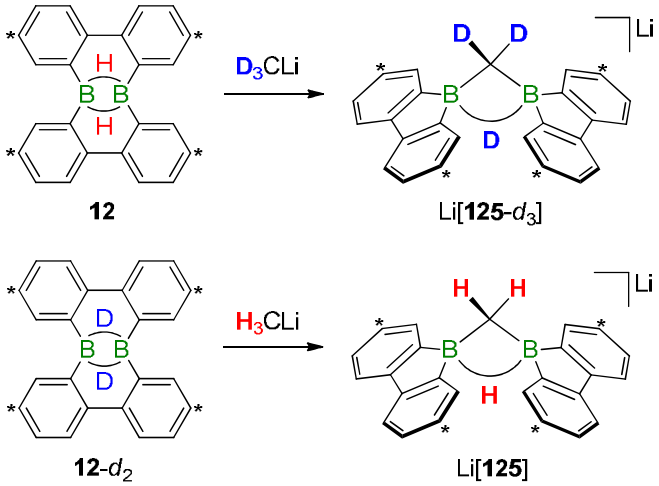

Schema 33. Reaktion von **12** mit D_3CLi zum C–D-Aktivierungsprodukt [**125**-d_3]$^-$ (oben) und von **12**-d_2 mit H_3CLi zum C–H-Aktivierungsprodukt [**125**]$^-$ (unten). Kohlenstoffatome, die mit * gekennzeichnet sind, tragen *t*Bu-Gruppen.

Das Isotopenmarkierungsexperiment legte nahe, dass an der Umsetzung der Organolithiumverbindungen mit **12** C–H-Aktivierungsreaktionen beteiligt sind. C–H-Aktivierungen sind wichtige Reaktionen, mit deren Hilfe unreaktive Startmaterialien in funktionalisierte Produkte umgewandelt werden können. Diese Art der Aktivierung ist für gewöhnlich eine Domäne der Übergangsmetallchemie, doch Derivatisierungen von C(sp^3)–H-Bindungen sind selbst in Gegenwart von d-Block-Elementen anspruchsvoll und selten.[276-279] Noch weniger Beispiele gibt es für entsprechende borvermittelte C(sp^3)–H-Aktivierungen, die sich in drei Klassen einteilen lassen, für die Beispiele in Schema 34 zusammengestellt sind: 1) Eine *in situ* Erzeugung von Borylenen unter reduktiven Bedingungen und Insertion dieser Borylene in benachbarte C–H-Bindungen.[86, 280-285] Beispielsweise publizierten Braunschweig et al. im Jahr 2011, dass bei Reduktion von **126** mit KC_8 eine Insertion des Boratoms in die H_3C-Gruppe des räumlich nahen Mesitylrests stattfindet.[282] 2) Die Erzeugung von Diradikalen führt zu H-Abstraktion und B–C-Bindungsbildung. Wang et al. beschrieben 2017 einen entsprechenden Fall, als sie das 2,6-Bis($BMes_2$)mesitylen **127** zum Diradikal reduzierten.[286] 3) FLP-artige Aktivierung.[287-289] Fontaine et al. untersuchten 2017 die intramolekulare Deprotonierung des FLP-Systems **128**, bei der unter thermodynamisch begünstigter H_2-Eliminierung eine NCH_2–B-Bindung ausgebildet wird.[289]

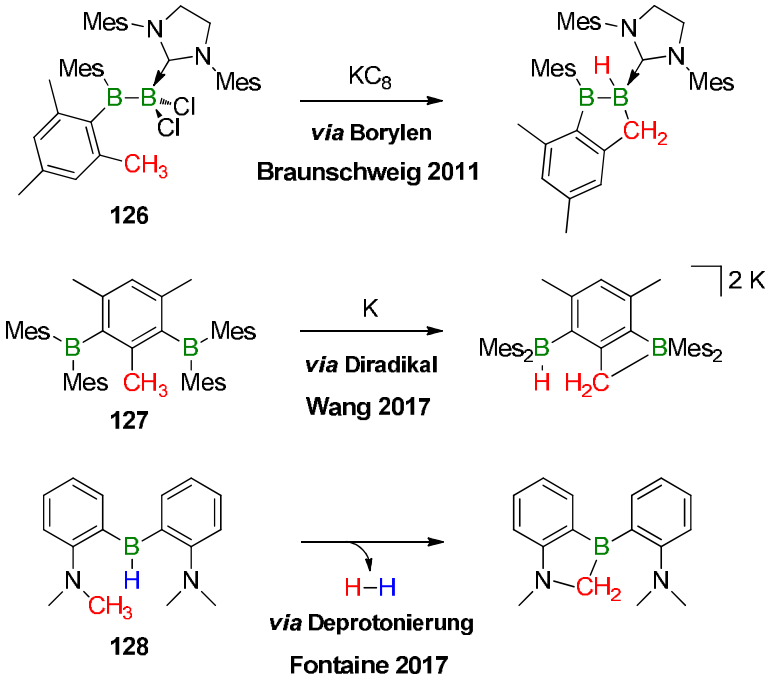

Schema 34. Ausgewählte Beispiele übergangsmetallfreier C(sp^3)–H-Aktivierungen über ein Borylen-Intermediat (oben), ein Diradikal-Intermediat (Mitte) und eine Deprotonierungsreaktion (unten).

Um die ungewöhnliche C–H-Aktivierungsreaktion an **12** bei Zugabe von Organolithiumverbindungen zu verstehen und gezielt nutzen zu können, wurden weitere Experimente durchgeführt und die Ergebnisse zu einem mechanistischen Bild zusammengefügt (Schema 35). Dieses erklärt neben der C–H-Aktivierung auch den Verbleib der beiden μ-H-Atome des Edukts **12** und die kombinierte Ausbeute von ca. 50% an [**116**]$^-$ und [**125**]$^-$. Im Folgenden wird der Mechanismus aus Schema 35 erläutert und anschließend mit den gesammelten experimentellen Befunden untermauert: In Analogie zu der Synthese von Li[**116**] mit der sterisch anspruchsvollen Base $(Me_3Si)_3CLi$ besteht der erste Schritt in der Deprotonierung von **12** mit H_3CLi zu Li[**116**]. Das Nebenprodukt der Deprotonierung, CH_4, wurde mittels NMR-Spektroskopie nachgewiesen. Im Gegensatz zu $(Me_3Si)_3CLi$ ist die kleine Lewis-Base H_3CLi in der Lage, im Folgeschritt Li[**116**] nucleophil anzugreifen. Dieser Angriff erfolgt an einem der Boratome, führt zur Ausbildung einer B–CH_3-Bindung und verschiebt das verbrückende H-Atom in eine terminale Position. Das resultierende Strukturmotiv von [**129**]$^{2-}$ ist bereits vom Dianion [**115**]$^{2-}$ bekannt, das anstelle der borständigen Methylgruppe ein weiteres H-Atom trägt (vgl. $[K_2(thf)_4]$[**115**]; Schema 35, oben und unten). Beim nächsten Schritt entlang des Reaktionspfades lagert Li_2[**129**] durch eine 1,2-Phenyl- und eine 1,2-H-Verschiebung zu Li_2[**130**] um. Für Li_2[**130**] wurde ebenfalls eine Festkörperstruktur mit vergleichbarem Molekülgerüst publiziert (vgl. $[Li(thf)_3][Li(thf)_2]$[**114**]; Schema 35, unten). Nach LiH-Eliminierung geht aus Li_2[**130**] das Salz Li[**131**] hervor. Die bisher beschriebene Sequenz aus Deprotonierung (1. Schritt) und Hydrideliminierung (4. Schritt) entspricht somit einer formalen Abspaltung von H_2, ohne dass gasförmiges H_2 freigesetzt wird. Li[**131**], das ein tetrakoordiniertes Boratom neben einem trigonal-planar koordinierten Boratom mit freiem p_z-Orbital besitzt, lagert zu Li[**132**] um.

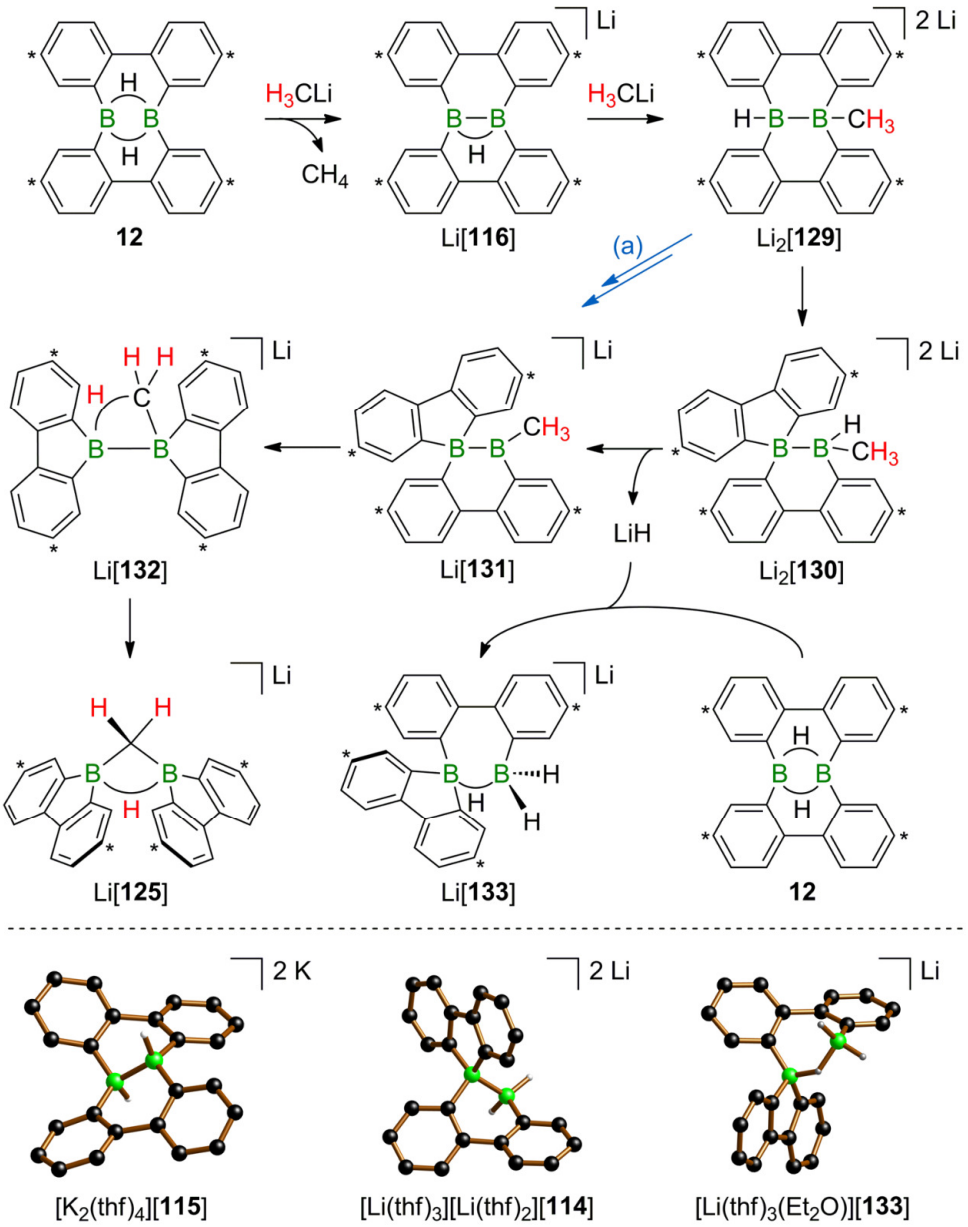

Schema 35. Mechanismus zur Entstehung von [**116**]$^-$, [**125**]$^-$ und [**133**]$^-$ bei Reaktion von **12** mit 1 Äquivalent H_3CLi (oben; Kohlenstoffatome, die mit * gekennzeichnet sind, tragen *t*Bu-Gruppen). Die blauen Pfeile (a) kennzeichnen einen alternativen Pfad von [**129**]$^{2-}$ nach [**131**]$^-$, bei dem zuerst eine Hydrideliminierung und anschließend eine 1,2-Phenylverschiebung stattfinden (Mitte). Festkörperstrukturen von $[K_2(thf)_4]$[**115**], $[Li(thf)_3][Li(thf)_2]$[**114**] und $[Li(thf)_3(Et_2O)]$[**133**]. Alle lösungsmittelseparierten Kationen, *t*Bu-Gruppen und C*H*-Atome wurden aus Gründen der Übersichtlichkeit nicht abgebildet (unten).

Das Anion [**132**]$^-$ kann als Addukt von $[H_3C]^-$ an ein Diboran(4) beschrieben werden. Das Diboran(4) besteht aus zwei 9-Borafluorenyleinheiten, die über eine B–B-Bindung verknüpft sind. Nur das sp^3-hybridisierte Boratom mit der B–CH_3-Bindung besitzt ein Elektronenoktett, aber auch das B(sp^2)-Zentrum kann seine starke Lewis-Acidität durch eine agostische Wechselwirkung mit der CH_3-Gruppe herabsetzen.[290] Diese Interaktion endet in der C–H-Aktivierung, die bei gleichzeitigem B–B-Bindungsbruch zu Li[**125**] führt.
Der formale Ersatz der zwei Biphenyl-2,2'-ylenbrücken in Li[**132**] durch je zwei H-Atome erzeugt das Anion $[B_2CH_7]^-$, das isoelektronisch zu protoniertem Cyclopropan ($[C_3H_7]^+$) ist.

Für dieses Kation wurde experimentell und theoretisch bestätigt, dass es eine fluktuierende Struktur besitzt, sodass für das Anion $[B_2CH_7]^-$ ebenfalls ein gewisses dynamisches Verhalten plausibel ist.[291-294] Im Gegensatz zu $[C_3H_7]^+$ sind die Ecken in $[B_2CH_7]^-$ nicht äquivalent und die BHB-Brücke sollte gegenüber der BHC-Brücke energetisch bevorzugt sein. Entsprechend stoppt die Umlagerung von Li[**132**] auf der Stufe von Li[**125**], das eine thermodynamische Senke darstellt.

Neben dieser qualitativen Betrachtung wurde die C–H-Aktivierung auch mit quantenchemischen Methoden berechnet (Abbildung 21). Die kalkulierten Strukturen, bei denen die *t*Bu-Gruppen und die lösungsmittelseparierten Kationen vernachlässigt wurden, sind mit einem hochgestellten „k“ versehen (z. B. ist [**125**^{k}]$^-$ die Modellverbindung für [**125**]$^-$). Beginnend mit [**131**^{k}]$^-$ führt eine endergonische 1,2-Phenylverschiebung über den Übergangszustand **ÜZ1** zu offenkettigem [**132**^{k}-offen]$^-$ ($\Delta G^‡$ = 9.9 kcal mol^{-1}, ΔG_R = 5.9 kcal mol^{-1}). Das Anion [**132**^{k}-offen]$^-$ besitzt einen großen B–B–CH_3-Bindungswinkel von 121° und das leere p_z-Orbital des B(sp^2)-Atoms steht nahezu orthogonal zum B–CH_3-Bindungsvektor, was eine agostische Wechselwirkung in diesem Konformer verhindert. Durch Drehen des 9-Borafluorenylfragments, das ein dreifach-koordiniertes Boratom besitzt, um ca. 70° um die B–B-Achse und Verkleinern des B–B–CH_3-Bindungswinkels auf 68° gelangt man über **ÜZ2** ($\Delta G^‡$ = 7.0 kcal mol^{-1}) zu [**132**^{k}]$^-$. Die Struktur des Anions [**132**^{k}]$^-$ repräsentiert ein lokales Minimum, in dem eine agostische Wechselwirkung in Form einer BHC-Brücke vorliegt. Gegenüber dem offenkettigen Isomer [**132**^{k}-offen]$^-$ ist [**132**^{k}]$^-$ um ΔG_R = 4.6 kcal mol^{-1} destabilisiert. Der eigentliche C–H-Aktivierungsschritt verläuft über **ÜZ3**, bei dem gleichzeitig die B–B-Bindung und eine C–H-Bindung gebrochen werden und eine neue B–C-Bindung entsteht ($\Delta G^‡$ = 4.4 kcal mol^{-1}). Das dabei gebildete offenkettige [**125**^{k}-offen]$^-$ ist stabiler als die Vorstufe [**132**^{k}]$^-$ (ΔG_R = –14.1 kcal mol^{-1}) und die Eingangsverbindung [**131**^{k}]$^-$ (ΔG_R = –3.6 kcal mol^{-1}).

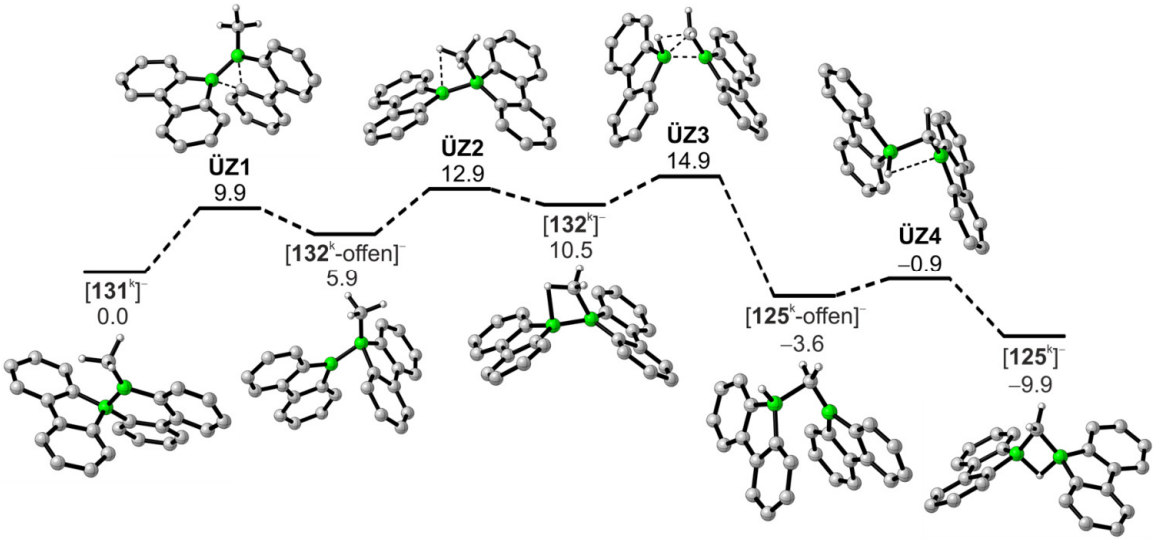

Abbildung 21. Reaktionspfad der Umwandlung von [**131**^{k}]$^-$ zu [**125**^{k}]$^-$ (berechnet auf PBE0D/TZVP-Niveau und mit dem SMD Modell zur Solvatation in THF). Freie Gibbs-Energien bei 298 K (ΔG) sind in kcal mol^{-1} angegeben und beziehen sich auf [**131**^{k}]$^-$.

Durch Rotation um die B–C-Bindung und Ausbildung einer B(μ-H)B-Brücke entsteht über **ÜZ4** ($\Delta G^{\ddagger}$ = 2.7 kcal mol^{-1}) das Produkt [**125**^{k}]$^{-}$, das gegenüber [**125**^{k}-offen]$^{-}$ eine weitere Stabilisierung um ΔG_R = –6.3 kcal mol^{-1} erfährt. Insgesamt besitzt die exergonische Umwandlung von [**131**^{k}]$^{-}$ zu [**125**^{k}]$^{-}$ eine Energiebarriere, die bei Raumtemperatur leicht zu überwinden ist ($\Delta G^{\ddagger}$ = 14.9 kcal mol^{-1}, ΔG_R = –9.9 kcal mol^{-1}).
Dass Li[**116**] tatsächlich das erste Intermediat auf dem Reaktionspfad von **12** nach Li[**125**] ist, wurde durch die Zugabe eines Äquivalents H_3CLi zu Li[**116**] überprüft (Schema 36). Das NMR-Spektrum der Reaktion enthielt keine Signale des Edukts, sondern einen neuen Signalsatz, der Li_2[**130**] zuzuordnen war. Die LiH-Eliminierung aus Li_2[**130**] ist demnach kein spontaner Vorgang, sondern benötigt einen Hydridfänger, sodass sich Li[**125**] erst bei Zugabe der Lewis-Säure **12** bildete (Schema 36). Dieser Befund steht im Einklang mit der üblicherweise eingesetzten 1:1 Stöchiometrie von **12** zu H_3CLi: Wenn **12** schnell und quantitativ mit H_3CLi zu Li_2[**130**] umgesetzt würde, wofür 2 Äquivalente H_3CLi nötig sind, müsste eine äquimolare Menge an **12** in Lösung verbleiben. Infolge könnten **12** und Li_2[**130**] miteinander reagieren, um Li[**125**] zu bilden. Passend dazu wurden sowohl bei der Reaktionsabfolge ausgehend von Li[**116**] als auch bei der Mischung H_3CLi/**12** zwei ^{1}H-NMR-Signalsätze gefunden, die zu den isomeren Hydridabfangprodukten Li[**133**] und Li[**134**] gehören (Schema 36). Da die Reaktionen H_3CLi/**12** und H_3CLi/Li[**116**] miteinander in Konkurrenz stehen, verbleibt am Ende auch Li[**116**] in Lösung, sodass ein Produktgemisch aus Li[**116**], Li[**125**], Li[**133**] und Li[**134**] vorliegt.

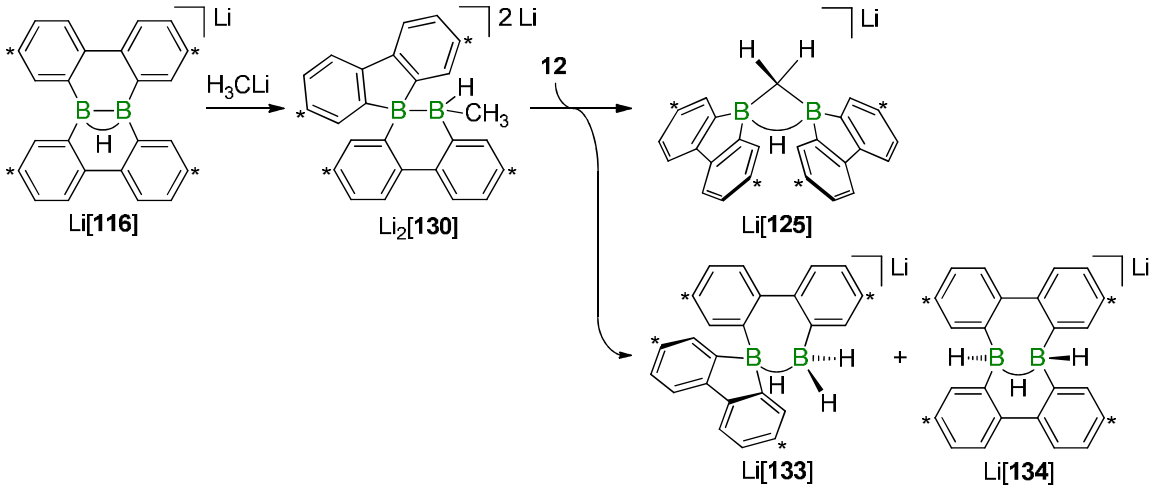

Schema 36. Li[**116**] reagiert mit H_3CLi zu Li_2[**130**]. Erst bei Zugabe des Diborans(6) **12** als Hydridfänger setzt eine Folgereaktion ein, bei der Li[**125**], Li[**133**] und Li[**134**] entstehen. Bezogen auf Li[**116**] wird Li[**125**] nahezu quantitativ gebildet.

Als mechanistische Alternative muss das Intermediat Li_2[**130**] bei der Reaktion von **12** nach Li[**125**] nicht unbedingt durchlaufen werden, wenn ein Hydridtransfer von Li_2[**129**] zu **12** schneller ist als die Umlagerung von Li_2[**129**] zu Li_2[**130**] (blauer Pfad (a) in Schema 35). Für diese Alternative spricht, dass eine Umlagerung bei einem B(sp^2)–B(sp^3)-Grundgerüst schneller ablaufen sollte als bei einem B(sp^3)–B(sp^3)-Rückgrat und dass Li_2[**130**] nur ausgehend von Li[**116**] beobachtet wurde, also in Abwesenheit des Hydridfängers **12**.

Die Hydridabfangprodukte Li[**133**] und Li[**134**], die bei der Reaktion von **12** mit H_3CLi in guter Näherung 50% der Komponenten in Lösung ausmachen, wurden unabhängig durch Reaktion von **12** mit 1 Äquivalent an „Superhydrid“, $Li[HBEt_3]$, dargestellt (Schema 37): Bei tiefen Temperaturen bildet sich selektiv Li[**134**], das NMR-spektroskopisch bei –30 °C charakterisiert wurde. Bei Raumtemperatur lagert Li[**134**] innerhalb von Stunden zu seinem Isomer Li[**133**] um. Die Struktur von Li[**133**] wurde NMR-spektroskopisch und mittels Röntgenbeugung am Einkristall bestätigt (Schema 35, unten). Während Li[**134**] zwei Signalsätze im ^{1}H-NMR-Spektrum zeigt (die beiden Phenylringe derselben Biphenyl-2,2‘-yleneinheit sind chemisch nicht äquivalent), erzeugt Li[**133**] drei Signalsätze, von denen zwei gut aufgelöst sind (H-a, H-b) und einer verbreitert ist (H-c; Schema 37). Die Integrale der gut aufgelösten Signale sind halb so groß wie die der verbeiterten Resonanzen. Das Signalmuster des ^{1}H-NMR-Spektrums von Li[**133**] ist im Einklang mit dem der strukturell verwandten Verbindung Li_2[**114**] (Schema 35), die anstelle der BHB-Brücke eine elektronenpräzise B–B-Bindung aufweist. Die verbreiterten Signale von Li_2[**114**] und Li[**133**] in Lösung deuten auf ein dynamisches Verhalten auf der NMR-Zeitskala hin, vermutlich hervorgerufen durch konformationelle Änderungen des B_2-Heterocyclus. Gleiches gilt für das Intermediat Li_2[**130**], dessen NMR-Daten ähnlich zu Li_2[**114**] und Li[**133**] sind, aber aufgrund der großen Linienbreiten nicht eindeutig zugeordnet werden können.

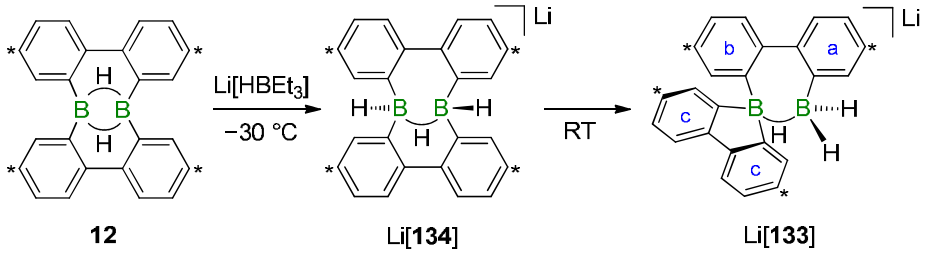

Schema 37. Bei der Reaktion von **12** mit $Li[HBEt_3]$ entsteht bei –30 °C selektiv Li[**134**], das bei Raumtemperatur zu Li[**133**] isomerisiert. Kohlenstoffatome, die mit * gekennzeichnet sind, tragen *t*Bu-Gruppen.

Da Li_2[**130**] nicht in einkristalliner Form erhalten werden konnte, wurde durch Reaktion von *t*BuC≡CLi mit Li[**116**] das Derivat Li_2[**135**] synthetisiert, in dem die Me-Gruppe von Li_2[**130**] durch einen sterisch wenig anspruchsvollen *t*BuC≡C-Substituenten ersetzt ist (Schema 38). Die Analyse der Einkristalle von $[Li(12\text{-Krone-4})(thf)][Li(thf)_2]$[**135**] bestätigte die vorgeschlagene Struktur von Li_2[**135**], dessen NMR-Daten mit denen des Intermediates Li_2[**130**] im Einklang stehen. Bemerkenswerterweise ist Li_2[**135**] nicht nur über das Reaktionsgemisch *t*BuC≡CLi/Li[**116**] zugänglich, sondern auch durch Reaktion der konjugierten Säure *t*BuC≡CH des Acetylids mit Li_2[**37**], der konjugierten Base von Li[**116**] (Schema 38).

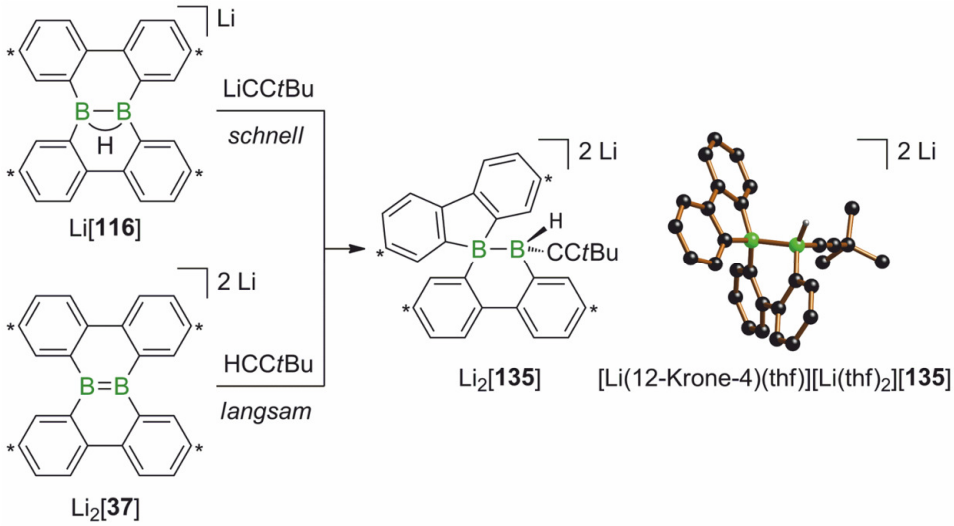

Schema 38. Das Salz Li$_2$[**135**] entsteht sowohl in der schnellen Reaktion zwischen Li[**116**] und LiCC*t*Bu als auch in der langsamen Reaktion zwischen Li$_2$[**37**] und HCC*t*Bu. Das Ergebnis der Röntgenstrukturanalyse von [Li(12-Krone-4)(thf)][Li(thf)$_2$][**135**] ist aus Gründen der Übersicht ohne solvatisierte Kationen, phenylgebundene *t*Bu-Gruppen und kohlenstoffgebundene H-Atome abgebildet. Kohlenstoffatome, die mit * gekennzeichnet sind, tragen *t*Bu-Gruppen.

Die B=B-Doppelbindung im Dianion [**37**]$^{2-}$ wird weder durch Carben- oder Heteroatomliganden noch durch sterisch anspruchsvolle Gruppen stabilisiert. Aufgrund der vier aromatischen π-Sextette nach Clar[258] sollte zudem eine vergleichsweise isolierte B=B-Bindung vorliegen. In der Literatur sind Reaktivitäten von B=B-Bindungen wenig untersucht (vgl. Kapitel 1.7). Die Reaktionen von Li$_2$[**37**] gegenüber *t*BuC≡CH und etherischer HCl warfen die Frage auf, ob die Elektronendichte zwischen den Boratomen auch genutzt werden kann, um durch Zugabe eines geeigneten Elektrophils über Li[**132**] zu Li[**125**] zu gelangen: Eine Betrachtung der Bindungssituation in [**132**]$^-$ offenbart, dass dieses Intermediat nicht nur (a) als ein Addukt zwischen [H$_3$C]$^-$ und einem Diboran(4), sondern auch (b) als ein Addukt zwischen [H$_3$C]$^+$ und dem Dianion [**37**]$^{2-}$ angesehen werden kann (Abbildung 22). Die beiden Grenzfälle (a) und (b) sind durch eine formale Elektronenübertragung zwischen der Methyleinheit und der Borverbindung ineinander überführbar.

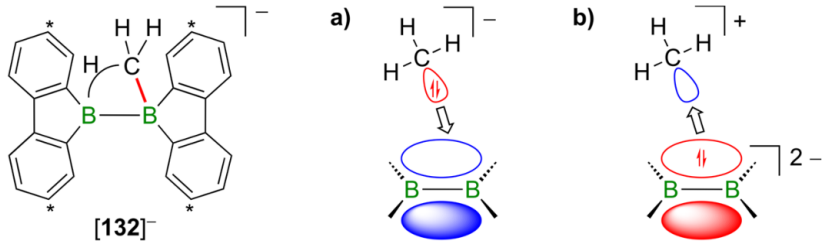

Abbildung 22. Das Anion [**132**]$^-$ kann in zwei Grenzdarstellungen (a) als Addukt von [H$_3$C]$^-$ an ein Diboran(4) oder (b) als Addukt von [H$_3$C]$^+$ an [**37**]$^{2-}$ beschrieben werden. Kohlenstoffatome, die mit * gekennzeichnet sind, tragen *t*Bu-Gruppen.

Dass die Grenzbetrachtung in Abbildung 22 nicht nur ein Gedankenexperiment ist, sondern zu einer effektiven Syntheseoptimierung genutzt werden kann, wurde durch die Umsetzung einer THF-Lösung von Li$_2$[**37**] mit H$_3$CCl-Gas gezeigt, bei der Li[**125**] quantitativ entstand (Schema 39). Der Umpolungsansatz ist weitaus atom- und zeitökonomischer, da

kein Startmaterial als Hydridfänger verbraucht wird und keine Abtrennung der Nebenprodukte Li[**116**], Li[**133**] und Li[**134**] erfolgen muss.
Mechanistisch ist für die Bildung von Li[**125**] ausgehend von Li_2[**37**] plausibel, dass zunächst ein nucleophiler Angriff von Li_2[**37**] an H_3CCl stattfindet, der das methylierte Boran-Borat Li[**136**] mit zentraler B–B-Bindung erzeugt (Schema 39). Eine anschließende 1,2-Phenylverschiebung liefert das Salz Li[**131**], das auch entlang des Reaktionspfads der Umsetzung von **12** mit CH_3Li gebildet wird. Gemäß der Vereinigung beider Reaktionswege ausgehend von **12** oder Li_2[**37**], verläuft die weitere Sequenz über Li[**132**] zum Produkt Li[**125**] (Schema 39).

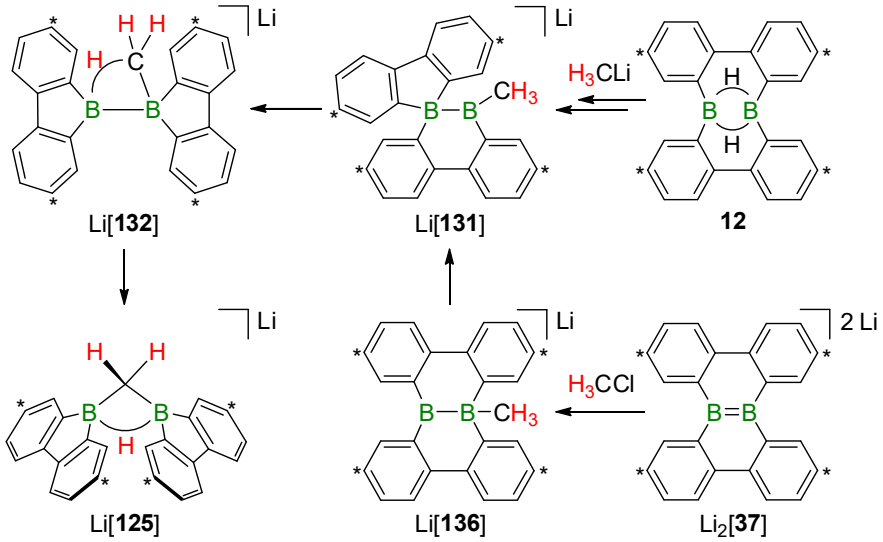

Schema 39. Die Reaktion von Li_2[**37**] mit H_3CCl in THF liefert Li[**125**] in quantitativer Umsetzung. Die Reaktionswege zu Li[**125**], sowohl ausgehend von **12** als auch von Li_2[**37**], vereinigen sich auf der Stufe von Li[**131**]. Kohlenstoffatome, die mit * gekennzeichnet sind, tragen *t*Bu-Gruppen.

Die Abgangsgruppe des elektrophilen Methylierungsreagenzes hat einen entscheidenden Einfluss auf den Reaktionsausgang: Während die Reaktion von Li_2[**37**] mit H_3CCl quantitativ Li[**125**] erzeugte, wurde mit 1 Äquivalent Iodmethan (H_3C–I) eine Mischung aus Li[**125**], 9-Methyl-9-borafluoren **137** und verbliebenem Li_2[**37**] erhalten (Schema 40). Die Zugabe von 3 Äquivalenten H_3C–I zu Li_2[**37**] führte selektiv zu **137** (Schema 40).

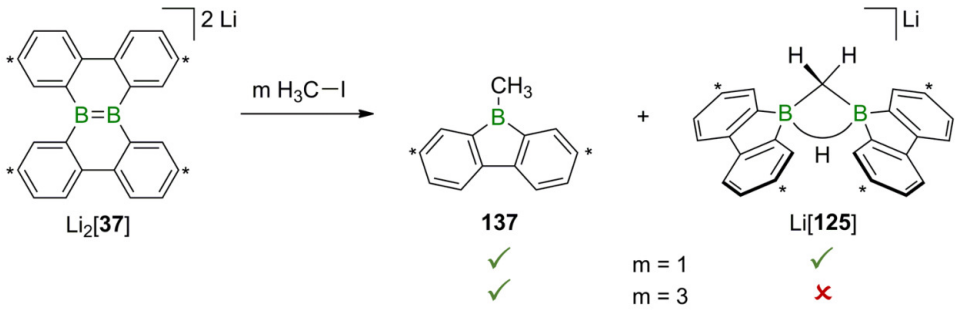

Schema 40. Die Zugabe von 1 Äquivalent an H_3C–I zu Li_2[**37**] führt zu einer Mischung aus **137** und Li[**125**] (sowie unverbrauchtem Li_2[**37**]). Wird der Anteil an H_3C–I auf 3 Äquivalente erhöht, entsteht selektiv 9-Methyl-9-borafluoren **137**. Kohlenstoffatome, die mit * gekennzeichnet sind, tragen *t*Bu-Gruppen.

Das unterschiedliche Verhalten der Halogenmethane lässt sich folgendermaßen qualitativ erklären: Das Intermediat [**132**]$^-$ kann als Addukt des 9-Borafluorenyl-Anions [**38**]$^-$ an 9-Methyl-9-borafluoren **137** beschrieben werden (Schema 41). [**38**]$^-$ ist isoelektronisch zu Carbenen, die sich in ihrer Reaktivität durch C–H-Insertionen auszeichnen. Dementsprechend vermag das Fragment [**38**]$^-$ eine intramolekulare Insertion in eine C–H-Bindung der borständigen Methylgruppe des Fragments **137** zu vollziehen, um Li[**125**] zu bilden. Ein alternativer, intermolekularer Reaktionspfad wird zugänglich, wenn das stärkere Elektrophil H_3C–I vorhanden ist. Die hervorragende Abgangsgruppe I$^-$ ermöglicht eine Übertragung des nucleophilen Fragments [**38**]$^-$ auf ein Molekül H_3C–I, sodass 2 Äquivalente **137** entstehen. Je größer die Konzentration an H_3C–I in der Reaktionsmischung ist, desto stärker tritt die intermolekulare Reaktion in den Vordergrund.

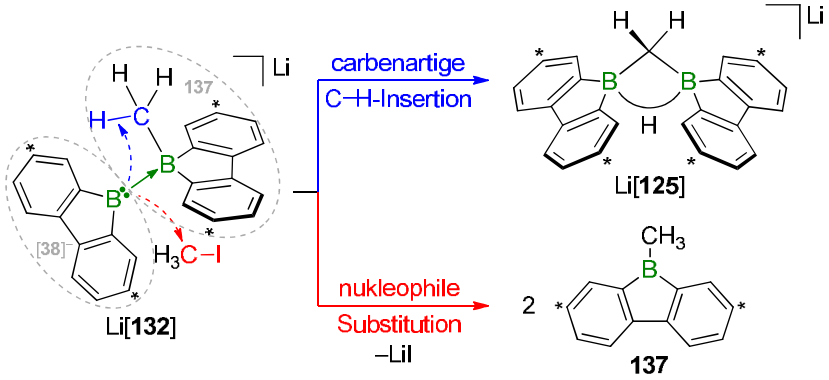

Schema 41. Das Intermediat Li[**132**] kann als Addukt zwischen 9-Borafluorenyl-Anion [**38**]$^-$ und 9-Methyl-9-borafluoren **137** beschrieben werden. Eine intramolekulare C–H-Insertion von [**38**]$^-$ in **137** erzeugt Li[**125**], wohingegen eine intermolekulare nucleophile Substitution an H_3C–I 2 Äquivalente **137** liefert. Kohlenstoffatome, die mit * gekennzeichnet sind, tragen *t*Bu-Gruppen.

Für die Aktivierung der Methylhalogenide ausgehend von Li_2[**37**] sind beide Borzentren wichtig, da zunächst ein Boratom methyliert wird und anschließend das andere Boratom intra- oder intermolekular abreagiert. Um ein detaillierteres Verständnis über die Kooperativität der Boratome und die Konkurrenz zwischen C–H-Insertion und nucleophiler Substitution zu erhalten, wurde eine systematische Studie mit α,ω-Dihalogenalkanen $X(CH_2)_nX$ durchgeführt (n = 2–6; X = Cl, Br). Hierbei war intendiert, dass kürzere Kettenlängen n im Sinne einer hohen lokalen Konzentration des Elektrophils wirken und dass die bromsubstituierten Ketten eine höhere Reaktivität besitzen als die chlorsubstituierten. Die Produkte der Reaktionen mit den unterschiedlichen α,ω-Dihalogenalkanen wurden NMR-spektroskopisch charakterisiert und die Strukturen in ausgewählten Fällen zusätzlich röntgenkristallographisch belegt. Eine Übersicht der Ergebnisse der Reaktionen von Li_2[**37**] mit $X(CH_2)_nX$ ist in Schema 42 dargestellt: Mit den kurzkettigen Substraten $X(CH_2)_2X$ und $X(CH_2)_3X$ wurde selektiv die zweifache nucleophile C–X-Substitution unter Entstehung von **138**^{C2} bzw. **138**^{C3} beobachtet (Ausnahme: 1,3-Dichlorpropan führte zu einer komplexen Mischung an Produkten). Quantitative C–H-Insertionen unter Bildung von Li[**139**^{C5,Cl}]/Li[**139**^{C5,Br}] bzw. Li[**139**^{C6,Cl}]/Li[**139**^{C6,Br}] wurden mit den langkettigen Substraten $X(CH_2)_5X$ und $X(CH_2)_6X$ beobachtet. Den Umschlagspunkt markierten die Substrate der Kettenlänge n = 4. 1,4-Dichlorbutan reagiert schon bevorzugt unter C–H-Aktivierung (Li[**139**^{C4,Cl}]), wohingegen 1,4-Dibrombutan aufgrund der besseren Bromidabgangs-

gruppe hauptsächlich eine zweifache nucleophile Substitution durchläuft (**138**^{C4}). Aus dieser Studie ergibt sich, dass (i) sowohl die C–H-Aktivierung als auch die zweite nucleophile Substitution bei den α,ω-Dihalogenalkanen auf intramolekulare Prozesse mit zwei kooperierenden Boratomen zurückzuführen sein sollten und (ii) die Rate der zweiten nucleophilen Substitution mit wachsender Kettenlänge abnimmt, wohingegen die Rate der C–H-Insertion näherungsweise unverändert bleibt. Letzteres hat zur Folge, dass die C–H-Aktivierung bei wachsender Kettenlänge immer relevanter wird, um schließlich die zweifache nucleophile Substitution vollständig zu verdrängen.

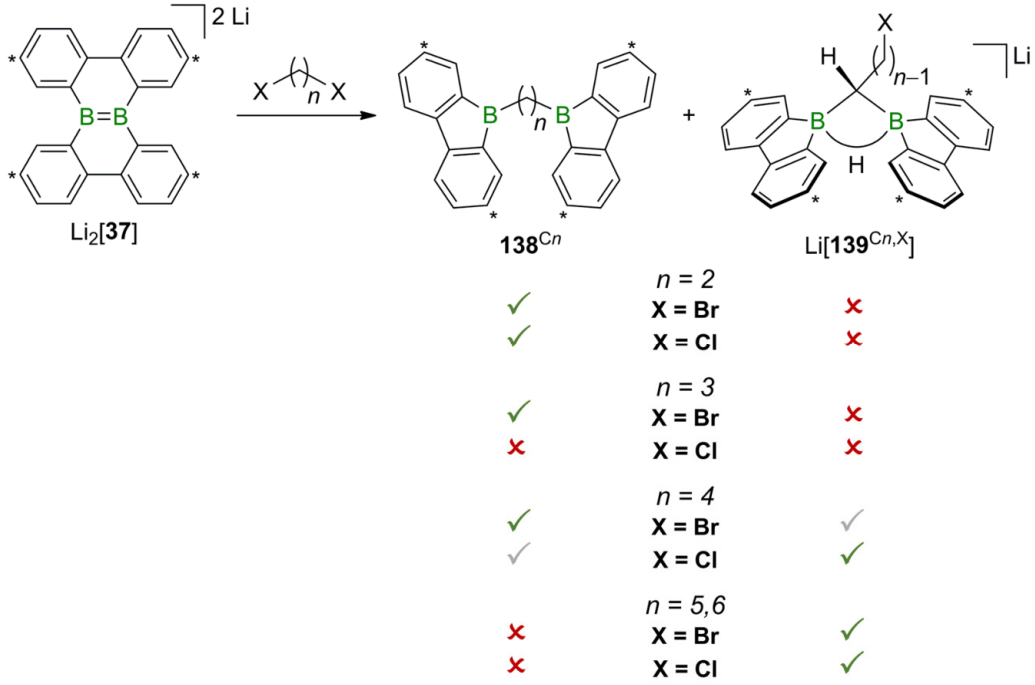

Schema 42. Die Zugabe der α,ω-Dihalogenalkane X(CH$_2$)$_n$X zu Li$_2$[**37**] führt zur Bildung ditoper Borane **138**^{Cn} (*n* = 2–4) und/oder Li[**139**^{Cn,X}] (*n* = 4–6; X = Cl, Br). Kohlenstoffatome, die mit * gekennzeichnet sind, tragen *t*Bu-Gruppen.

Neben den oben beschriebenen Reaktionspfaden, die auf geschlossenschaligen Systemen beruhen, sind prinzipiell auch radikalische Wege denkbar, aber wenig wahrscheinlich, da die Reaktion von Li$_2$[**37**] mit 1,2-Dibromethan nicht unter reduktiver Dehalogenierung zu Ethen verlief, sondern zu **138**^{C2} führte. Yamashita, Nozaki et al. berichteten von der Reaktion ihres Boryllithiums Li[**47**] sowohl mit H$_3$COTf, bei der das methylierte Boran **140** erhalten wurde, als auch mit BnBr, bei der selektiv das Bromboran **141** entstand (Schema 43, oben; Tf = SO$_2$CF$_3$, Bn = CH$_2$C$_6$H$_5$).[129] Zur Erklärung der unterschiedlichen Reaktionsverläufe nahmen sie im Falle von BnBr einen halogenophilen Angriff des Anions [**47**]$^-$ oder Einelektronübertragung auf das Benzylhalogenid an. Im Zuge der vorliegenden Arbeit wurde auch Li$_2$[**37**] mit beiden Reagenzien umgesetzt (Schema 43, Mitte): Mit H$_3$COTf ergab sich der gleiche Reaktionsverlauf wie mit H$_3$C–I, nämlich die Bildung von Li[**125**] und **137**. Mit BnBr wurden hingegen keine Halogenborane beobachtet, sondern allein das C–H-Insertionsprodukt Li[**142**], sodass auch hier keine Anzeichen für einen radikalischen Mechanismus vorliegen.

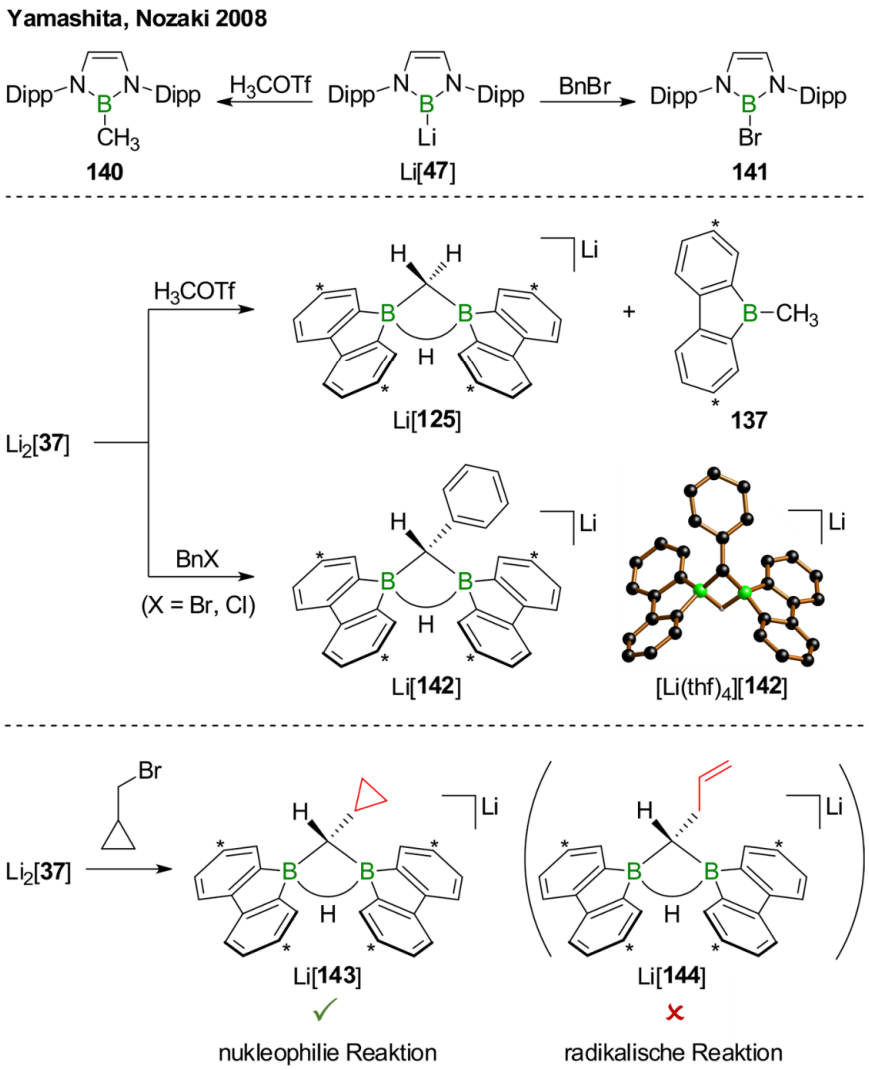

Schema 43. Die Zugabe von H_3COTf oder BnBr zu Li[**47**] ergibt das entsprechende Methylboran **140** oder das Bromboran **141** (oben). Bei den analogen Reaktionen mit Li_2[**37**] werden ausschließlich die Kohlenwasserstoffreste auf die Boratome übertragen wobei Li[**125**], **137** bzw. Li[**142**] entstehen. In der abgebildeten Kristallstruktur von [Li(thf)$_4$][**142**] wurden das [Li(thf)$_4$]$^+$-Kation, *t*Bu-Gruppen und kohlenstoffgebundene H-Atome zur besseren Übersicht nicht abgebildet (Mitte). Die Reaktion der Radikaluhr (Brommethyl)cyclopropan mit Li_2[**37**] liefert Li[**143**] in quantitativer Umsetzung (unten). Kohlenstoffatome, die mit * gekennzeichnet sind, tragen *t*Bu-Gruppen. Dipp = 2,6-Di(*i*Pr)phenyl, Bn = $CH_2C_6H_5$, Tf = SO_2CF_3.

Als ultimativer Test wurde die Reaktion von Li_2[**37**] mit 1 Äquivalent der Radikaluhr (Brommethyl)cyclopropan durchgeführt, bei der sich quantitativ das C–H-Aktivierungsprodukt Li[**143**] bildete (Schema 43, unten). Li[**143**] besitzt einen intakten Cyclopropylrest. Die Abwesenheit des Anions [**144**]$^-$, mit Allylgruppe statt Cyclopropylrest, macht einen radikalischen Mechanismus unwahrscheinlich und stützt die oben postulierten geschlossenschaligen Reaktionspfade.[295-297]

Die dargestellten ditopen Borane sind für potentielle Anwendungen von Bedeutung, z. B. als Organokatalysatoren oder als Elektronenspeichermaterialien.[37, 105, 106, 298, 299] Die Verbindungen der Klasse **138**^{Cn} stellen aktive, freie Säuren dar, die unmittelbar eingesetzt werden können. Sie verfügen jedoch über keine funktionellen Gruppen für weitere Derivatisierungen. Die Salze Li[**139**^{Cn,X}] besitzen hingegen jeweils ein terminales Halogen-

atom, das weitere Funktionalisierungen erlaubt, müssen jedoch zunächst durch LiH-Eliminierung aktiviert werden. Es konnte gezeigt werden, dass H_3C–I, im Gegensatz zum sterisch anspruchsvollen $(H_3C)_3SiCl$, effizient in der Lage ist, die Modellverbindung Li[**125**] in **138**^{C1} zu überführen (Schema 44). Entsprechend der Fähigkeit von H_3C–I, eine LiH-Eliminierung aus Li[**125**] hervorzurufen, sind die halogenalkylsubstituierten Derivate Li[**139**^{Cn,X}], vor allem für kurze Kettenlängen *n*, nicht langzeitstabil in THF-Lösung. Über die Zeit hinweg entstehen Moleküle mit terminalen CH_3-Gruppen. Die Zersetzungsprozesse sind bei den meisten Derivaten langsam genug, um bei Raumtemperatur eine gezielte Derivatisierung der terminalen Halogenfunktion zu ermöglichen. Durch tiefe Temperaturen lässt sich die Zersetzung zudem verlangsamen oder sogar vollständig unterdrücken.

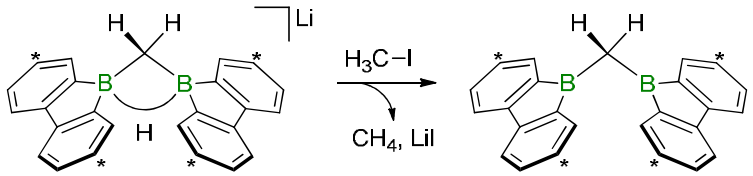

Schema 44. Die Reaktion von Li[**125**] mit H_3C–I erzeugt das Bis(9-borafluorenyl)methan **138**^{C1}. Kohlenstoffatome, die mit * gekennzeichnet sind, tragen *t*Bu-Gruppen.

2.2 Reduktionschemie des Bis(9-borafluorenyl)methans **7**

In der Literatur ist beschrieben, dass Diborane im neutralen oder reduzierten Zustand vielversprechende Katalysatoren sein können, jedoch sind nur wenige Systeme umfassend untersucht.[37, 298, 300] In diesem Kontext deutete die Protonierbarkeit von Li_2[**7**] zu Li[**7**H] auf eine ausgeprägte Nucleophilie der B–B-Bindung in [**7**]$^{2-}$ hin, die zur Aktivierung von Molekülen nützlich sein könnte (vgl. Abbildung 6 in Kapitel 1.4).[106] Um die Reaktivität der B–B-Bindung von Li_2[**7**] näher zu untersuchen, galt es zunächst, die Verbindung in hoher Reinheit zu synthetisieren. Die folgenden Ergebnisse wurden unter meiner Betreuung zusammen mit Hendrik Budy (Tätigkeit als Hilfswissenschaftler) und Jannik Gilmer (Vertiefungspraktikum im Bachlorstudiengang) erzielt. Bei der Reproduktion der literaturbekannten Reduktion von **7** mit Lithium in Toluol entstand wie erwartet eine rote Suspension.[106] Gemäß ^{1}H-NMR-Spektroskopie bestand das Präzipitat nach Filtration zu ca. 95% aus Li_2[**7**], aber enthielt zusätzlich noch ca. 5% einer unbekannten Verbindung. Monomere 9-Borafluorene können bei Reduktion mit Lithium bis zu zwei Elektronen aufnehmen (vgl. Li_2[**20**] und Li_2[**21**]). Da **7** zwei 9-Borafluorenyleinheiten enthält, sollte theoretisch die Reduktion zum Tetraanion Li_4[**7**] möglich sein (Schema 45). Andererseits präzipitiert bereits das Salz Li_2[**7**] aus einer Toluollösung, was die vierfache Reduktion wiederum erschweren sollte. Basierend auf diesen Überlegungen wurde die Reduktion in THF durchgeführt, damit das Diboran **7** auch nach Überführung in das Dianion gelöst bleibt: Die selektive Entstehung des oben genannten Nebenprodukts und die Abwesenheit von Li_2[**7**] waren ein erstes Indiz dafür, dass es sich bei der neuen Verbindung tatsächlich um Li_4[**7**] handeln könnte (für NMR-Daten siehe Kapitel 4.2.2).

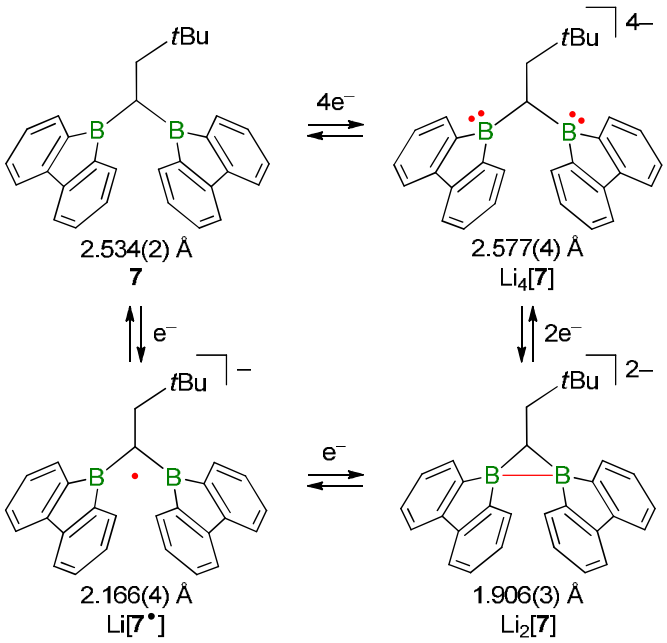

Schema 45. Das Diboran **7** ist durch Redoxprozesse in die Salze Li[**7**•], Li_2[**7**] und Li_4[**7**] überführbar. Zugehörige B···B-Abstände aus Kristallstrukturen sind unter den Molekülformeln aufgeführt.

Mittels Röntgendiffraktometrie an Einkristallen von [Li(thf)]$_2$[Li(Et_2O)][Li(Et_2O)(thf)][**7**], die durch Diffusion von Et_2O in ein Aliquot der Reaktionslösung erhalten wurden, erfolgte der Strukturbeleg (Abbildung 23): In der Festkörperstruktur bildet das Tetraanion [**7**]$^{4-}$ Kontaktionenpaare mit vier Li^+-Kationen, wobei zwei Kationen außerhalb der von beiden 9-Borafluorenylfragmenten ausgebildeten Kavität zentral über den Borolringen sitzen. Die beiden anderen Kationen liegen innerhalb dieser Kavität und sind so angeordnet, dass sie zusammen mit den zwei Boratomen die Ecken eines verzerrten Tetraeders besetzen (die Kantenlänge d(Li1···Li2) = 2.952(7) Å ist länger als die übrigen Kantenlängen, die im Bereich von 2.497(5) Å – 2.591(5) Å liegen). Der Abstand der beiden Boratome d(B1···B2) = 2.577(4) Å ist um 0.67 Å größer als in [**7**]$^{2-}$, um 0.41 Å größer als in [**7**•]$^-$ und immer noch 0.04 Å größer als in **7**. Daraus folgt, dass in [**7**]$^{4-}$ keine B–B-Bindung besteht, sondern sich die 9-Borafluorenyleinheiten aufgrund der repulsiven Coulomb-Wechselwirkungen abstoßen. Passend zur fehlenden B–B-Bindung sind die Boratome nicht tetrakoordiniert sondern trigonal-planar konfiguriert ($\Sigma(\sphericalangle^{B1}) = \Sigma(\sphericalangle^{B2}) = 359.9°$). Die strukturellen Parameter der 9-Borafluorenyleinheiten von [**7**]$^{4-}$ sind vergleichbar mit denen der Dianionen [**20**]$^{2-}$ und [**21**]$^{2-}$:[45, 86] Während im neutralen 9-Br-9-Borafluoren **145** keine ausgeprägte Bindungslängenalternanz in den Phenylringen vorliegt, weisen die entsprechenden Bindungen der 9-Borafluoren-Dianionen eine ausgeprägte Alternanz auf, was anhand der grün/rot hervorgehobenen Differenzen in Tabelle 3 (Kapitel 2.3.2) ersichtlich ist. Die C–C-Bindungslängen in den Borolringen der Dianionen sind im Gegenzug weniger stark alternierend. Die systematischen Veränderungen der Bindungslängen deuten auf einen weniger antiaromatischen/stärker aromatischen Borolring und weniger aromatische Phenylringe in den Dianionen hin.

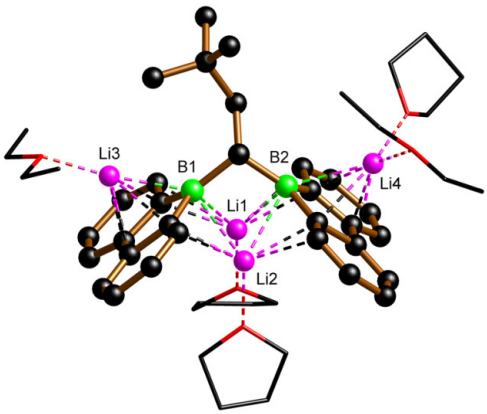

Abbildung 23. Festkörperstruktur von $[Li(thf)]_2[Li(Et_2O)][Li(Et_2O)(thf)]$[**7**]. Der B···B-Abstand beträgt 2.577(4) Å. C*H*-Atome wurden aus Gründen der Übersichtlichkeit nicht abgebildet.

Das Tetraanion [**7**]$^{4-}$ lässt sich in THF bei Raumtemperatur selektiv durch 1:1-Komproportionierung mit **7** in das Dianion [**7**]$^{2-}$ und durch 1:3-Komproportionierung in das Radikal-Anion [**7**$^{\bullet}$]$^{-}$ umwandeln. Die Zugabe von Elektrophilen wie 1,2-Dibromethan, Me_2SiCl_2, BH_3·THF, $TiCl_4$ oder $GeCl_2$·Dioxan zu [**7**]$^{4-}$ führte nicht zur Ausbildung von Bor-Element-Bindungen oder Sandwichkomplexen, sondern zur Oxidation von [**7**]$^{4-}$. Diese Beobachtungen stehen im Einklang mit Berichten zu versuchten Transmetallierungen der 9-Borafluorensalze Li_2[**21**] und Li_2[**22**], die in Oxidationen zu den neutralen Boranen **21** und **22** endeten (vgl. Kapitel 1.4).[45, 48] Auch wenn Li_4[**7**] keine Anwendung als Synthesebaustein finden sollte, da keine ausgeprägte Nucleophilie vorliegt, ist es eine vielversprechende Verbindung im Hinblick auf Elektronenspeicheranwendungen, weil eine verhältnismäßig hohe Ladungsdichte erzielt wird ($4e^-$ / **7** [410.2 g mol^{-1}]).[105, 106] Andere organische Materialien, wie beispielsweise P(O)R-überbrückte Bipyridylkationen, die nur zweifach reversibel reduzierbar sind (z. B. $2e^-$ / $C_{18}H_{17}N_2OP$ [308.3 g mol^{-1}]), werden aktuell auf ihre Einsetzbarkeit in Batterien hin untersucht.[301] Eine innovative Anwendung des Redoxsystems **7** könnte im Bereich der molekularen Maschinen liegen, da **7** durch Kontraktion und Expansion des B···B-Abstands während der Reduktion zum Tetraanion einen Flügelschlag imitiert. Gezielte Bewegungen auf molekularer Ebene sind ein zukunftsträchtiges Feld, v.a. vor dem Hintergrund, dass die meisten biologischen Prozesse auf gerichteten Transportreaktionen innerhalb von Zellen beruhen.[302-304]

2.3 Reduktionschemie des 9-Borafluorens **6**·THF

Das Bis-9-borafluoren **7**, in dem beide 9-Borafluorenyleinheiten über eine Methylenbrücke verbunden sind, reagiert bei Reduktion reversibel unter B·B- und B–B-Bindungsbildung/-bruch ohne sonstige strukturelle Veränderungen (vgl. Schema 45). Im Gegensatz dazu bilden sich bei Reduktion des borständig wasserstoffsubstituerten 9-Borafluorendimers $(\mathbf{6})_2$ in Toluol die vier unterschiedlichen Produkte Li[**34**], Li[**35**], Li[**36**] und Li_2[**37**] (vgl. Schema 6).[108] Zu Beginn meiner Promotion war ungeklärt, welche mechanistischen Prozesse jeweils zu diesen vier Produkten führen, inwiefern die unsymmetrische Struktur von $(\mathbf{6})_2$ eine Rolle spielt oder ob einzig das borgebundene Wasserstoffatom für den Reaktionsverlauf entscheidend ist. Die folgenden Ergebnisse wurden unter meiner Anleitung mit Unterstützung von Hendrik Budy (Praktikum im Masterstudiengang), Jannik

Gilmer (Bachelorarbeit[305] und Tätigkeit als Hilfswissenschaftler) und Timo Trageser (Promotion[311]) erzielt.

2.3.1 Reduktion von **6**·THF mit Lithium

Es ist literaturbekannt, dass nach Reduktion von (**6**)$_2$ in THF in Gegenwart eines Äquivalents Et_3SiBr das B=B-gebundene Diboran Li_2[**37**] in einer Ausbeute von 43% isoliert werden kann.[108] Nebenprodukte wurden nicht publiziert. Im Rahmen meiner Arbeiten wurde durch NMR-spektroskopische Untersuchungen gezeigt, dass (**6**)$_2$ in THF schnell unter Adduktbildung zu **6**·THF monomerisiert (Schema 46).[65] Die NMR-spektroskopische Analyse der Reduktion von **6**·THF in THF ergab, dass die in Schema 46 gezeigten vier Produkte in Lösung vorliegen: Li_2[**37**] (30-45%), Li_2[**6**] (25-40%), Li[**34**] (15-30%) und Li_4[**146**] (5-10%). Die prozentualen Anteile variierten zwischen einzelnen Versuchen und scheinen von mehreren Kriterien wie Durchmischung, Konzentration, Temperatur und Oberfläche des Lithiummetalls abhängig zu sein. Li_2[**37**] und Li[**34**] sind bereits aus der Reduktion von (**6**)$_2$ in Toluol bekannt.[108] Die Verbindungen Li_2[**6**] und Li_4[**146**] werden im Folgenden näher beleuchtet.

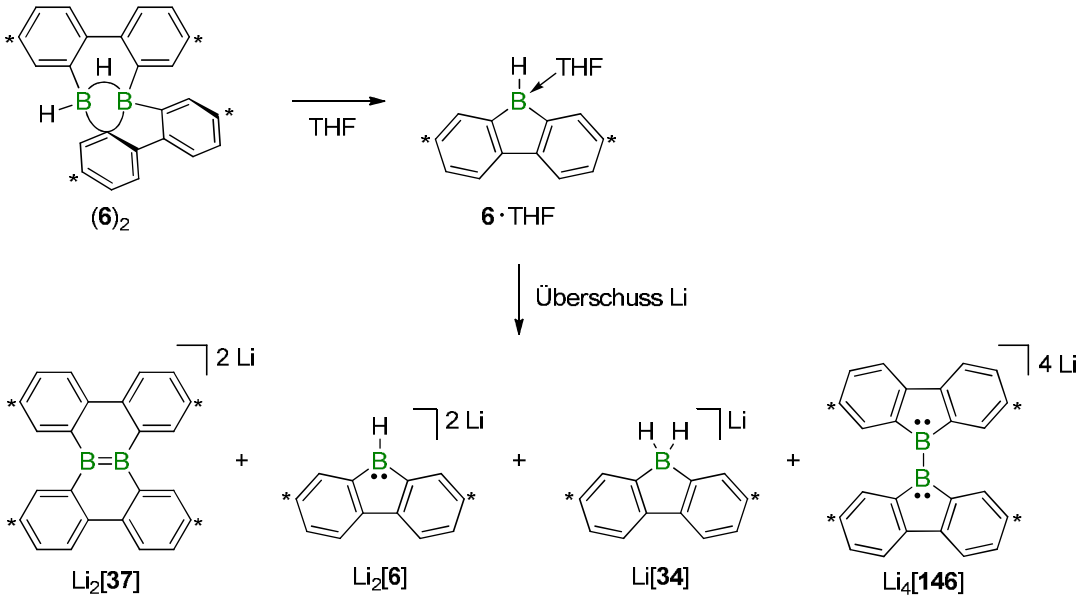

Schema 46. Durch Reduktion von **6**·THF mit Lithium in THF entstehen Li_2[**37**], Li_2[**6**], Li[**34**] und Li_4[**146**]. Kohlenstoffatome, die mit * gekennzeichnet sind, tragen *t*Bu-Gruppen.

2.3.2 Erstmalige Isolierung und Charakterisierung von Li_2[**6**] und Li_4[**146**]

Li_2[**37**] kristallisiert in der Regel zügig aus einer THF-Lösung bei –30 °C, sodass dieses Salz von den anderen drei Produkten aus Schema 46 durch kurze Kristallisationszeiten abgetrennt werden kann (z. B. aus der Reduktion von 200 mg (**6**)$_2$ in 3 mL THF innerhalb von 1-3 Tagen). Li_2[**6**] und Li_4[**146**] wurden aus einer entsprechenden, an Li_2[**37**] verarmten und aufkonzentrieren, Lösung ebenfalls bei –30 °C kristallisiert und manuell für die Charakterisierung selektiert: [$Li_2(thf)_3$][**6**] bildet schwarz-grüne Nadeln und

$[Li(thf)_2]_2[Li_2(thf)_3]$[**146**] schwarze Blöcke (ca. 100 mg/0.4-0.6 mL; 2 Wochen; Abbildung 24).

In der Festkörperstruktur von $[Li_2(thf)_3]$[**6**] koordiniert das 9-Borafluoren-Dianion [**6**]$^{2-}$ je ein Li^+-Kation oberhalb und unterhalb der Molekülebene (Abbildung 24, links). Das Kation $Li1^+$, das über eine B–C-Bindung an das Dianion bindet, sättigt seine Koordinationssphäre mit drei THF-Liganden ab. Zwei dieser THF-Liganden sind zusätzlich verbrückend an $Li2^+$ gebunden, das darüber hinaus im η^5-Modus mit dem Borolring eines weiteren Dianions [**6**]$^{2-}$ wechselwirkt. Hierdurch entsteht ein Koordinationspolymer im Festkörper. Die Bindungslängen in [**6**]$^{2-}$ sprechen für eine ausgeprägte Delokalisierung der Elektronendichte über das gesamte Molekülgerüst, wodurch der Borolring aromatischer und die Phenylringe weniger aromatisch werden als in vergleichbaren neutralen 9-Borafluorenen (vgl. Tabelle 3).

Im ^{1}H-NMR-Spektrum von [**6**]$^{2-}$ (THF-d_8) zeigt sich ein verbreitertes Signal bei 4.37 ppm, das durch ^{11}B-Entkopplung aufgeschärft wird. Das Integral dieses B*H*-Signals, ist halb so groß wie die drei Integrale der aromatischen Protonen (ein Signalsatz für beide Phenylringe) und beträgt 1/18 des Integrals der *t*Bu-Gruppen. Das Boratom erzeugt durch die Kopplung zum borständigen Wasserstoffatom im ^{11}B-NMR-Spektrum ein verbreitertes Dublett bei 3.6 ppm (^1J(B,H) ≈ 80 Hz, $h_{1/2}$ ≈ 240 Hz). Das ^{11}B-Signal ist, wie zu erwarten, etwa 10 ppm weiter ins Hochfeld verschoben als die Resonanzen vergleichbarer alkylsubstituierter 9-Borafluoren-Dianionen, die ebenfalls ausgeprägt verbreitert sind {vgl. δ([Li(OEt$_2$)]$_2$[**20**], C_6D_6) = 14.3 ($h_{1/2}$ ≈ 380 Hz); δ([Li(OEt$_2$)]$_2$[**21**], C_6D_6) = 13.6 ($h_{1/2}$ ≈ 430 Hz); Anmerkung: C_6D_6 sollte keine signifikanten Abweichungen der chemischen Verschiebungen im Vergleich zu THF-d_8 induzieren, da bei 9-Borafluoren-Dianionen in THF-d_8 keine Adduktbildung mit dem Borzentrum zu erwarten ist}.[45, 86, 306]

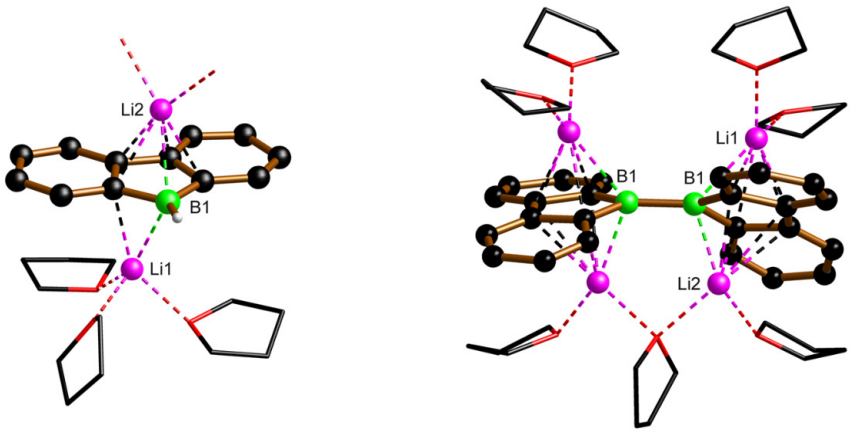

Abbildung 24. Festkörperstrukturen von $[Li_2(thf)_3]$[**6**] (links) und $[Li(thf)_2]_2[Li_2(thf)_3]$[**146**] (rechts). *t*Bu-Gruppen und C*H*-Atome wurden zur besseren Übersicht nicht abgebildet.

In der Festkörperstruktur von $[Li(thf)_2]_2[Li_2(thf)_3]$[**146**] sind zwei 9-Borafluorenyl-Dianionen über eine direkte B–B-Bindung verknüpft, durch die orthogonal eine C_2-Achse läuft (Abbildung 24, rechts). Die B–B-Bindungslänge liegt mit 1.704(5) Å im Bereich einer Einfachbindung (vgl. B_2pin_2: d(B–B) = 1.704(2) Å).[307] Die Boratome sind trigonal-planar koordiniert ($\Sigma(\sphericalangle^{B1})$ = 358.9°) und die 9-Borafluorenylfragmente entlang der B–B-Bindung um ca. 37° gegeneinander verdreht. Oberhalb und unterhalb jedes Borolrings sitzt je ein

η^5-koordiniertes Li^+-Kation. Die Absättigung der Koordinationssphären der Li^+-Kationen erfolgt über zusätzliche THF-Liganden.
Die vier Phenylringe von Li_4[**146**] erzeugen sowohl im ^{1}H- als auch im ^{13}C-NMR-Spektrum nur einen Signalsatz (THF-d_8). Die Resonanz des ^{11}B-Kerns liegt bei 12.3 ppm ($h_{1/2}$ ≈ 450 Hz) und damit im Bereich alkylsubstituierter 9-Borafluoren-Dianionen (vgl. δ([Li(OEt$_2$)]$_2$[**20**], C_6D_6) = 14.3 ($h_{1/2}$ ≈ 380 Hz); δ([Li(OEt$_2$)]$_2$[**21**], C_6D_6) = 13.6 ($h_{1/2}$ ≈ 430 Hz).[45, 86]

Tabelle 3. Ausgewählte Bindungslängen (Å) im Festkörper der tetraanionischen Bis-9-borafluorene [**7**]$^{4-}$ und [**146**]$^{4-}$ (DME-Solvat[308]) sowie der dianionischen 9-Borafluorene [**6**]$^{2-}$, [**20**]$^{2-}$ und [**21**]$^{2-}$.[45, 86, 106] Zur Abschätzung der Veränderung der Aromatizität der Borol- und Phenylfragmente im Vergleich zu neutralen 9-Borafluorenen sind Bindungslängen des 9-Br-9-borafluorens (**145**)[54] aufgeführt. Unter den Bindungslängen der reduzierten Spezies sind die entsprechenden Differenzen gegenüber den Bindungslängen von **145** gelistet. Die Nummerierungen wurden zur besseren Vergleichbarkeit gemäß **145** vereinheitlicht.

	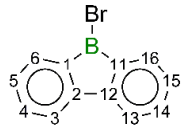 **145**	[**7**]$^{4-}$	[**146**]$^{4-}$	[**6**]$^{2-}$	[**20**]$^{2-}$	[**21**]$^{2-}$
B–C1	1.557(12)	1.549(4)	1.557(5)	1.512(16)	1.538(14)	1.544(6)
		-0.01	0.00	-0.04	-0.02	-0.01
B–C11	1.554(12)	1.553(4)	1.541(5)	1.564(15)	1.524(14)	1.536(6)
		0.00	-0.01	0.01	-0.03	-0.02
C1–C2	1.422(11)	1.473(3)	1.466(5)	1.465(14)	1.478(13)	1.479(6)
		0.05	0.04	0.04	0.06	0.06
C11–C12	1.408(11)	1.490(3)	1.471(5)	1.442(14)	1.472(13)	1.472(5)
		0.08	0.06	0.03	0.06	0.06
C2–C12	1.482(10)	1.427(4)	1.441(5)	1.428(12)	1.435(13)	1.423(6)
		-0.06	-0.04	-0.05	-0.05	-0.06
C2–C3	1.420(11)	1.414(4)	1.425(5)	1.406(13)	1.431(13)	1.420(6)
		-0.01	0.01	-0.01	0.01	0.00
C3–C4	1.387(11)	1.374(4)	1.368(5)	1.370(12)	1.373(14)	1.364(6)
		-0.01	-0.02	-0.02	-0.01	-0.02
C4–C5	1.394(12)	1.422(4)	1.451(5)	1.431(13)	1.428(14)	1.419(6)
		0.03	0.06	0.04	0.03	0.03
C5–C6	1.387(12)	1.376(4)	1.381(5)	1.359(13)	1.380(13)	1.371(6)
		-0.01	-0.01	-0.03	-0.01	-0.02
C1–C6	1.386(10)	1.439(4)	1.444(5)	1.444(12)	1.441(14)	1.454(6)
		0.05	0.06	0.06	0.06	0.07

2.3.3 Gezielte Darstellung von M_2[**6**]

Gerüstumlagerungen und Hydridübertragungen im Zuge der Reduktion von **6**·THF in THF mit Alkalimetallen lassen sich durch tiefe Temperaturen (–78 °C) vollständig unterdrücken. Hierdurch sind die Salze Li_2[**6**] und Na_2[**6**] in guten Ausbeuten darstellbar (Schema 47). Für die Synthese von K_2[**6**] kann dieser Weg ebenfalls genutzt werden, einfacher ist aber die Reduktion von **6**·THF in THF mit KC_8 bei Raumtemperatur (Schema 47). Offensichtlich verläuft die Reduktion mit KC_8 schneller oder nach einem gänzlich

unterschiedlichen Mechanismus (z. B. bezüglich der Beteiligung der Kationen), sodass auch bei höheren Temperaturen wenig Umlagerungen eintreten. Insgesamt verliefen die Synthesen von Li_2[**6**] und Na_2[**6**] jedoch selektiver (Reinheit nach Filtration > 90%) als die von K_2[**6**] (Reinheit nach Filtration > 60%).

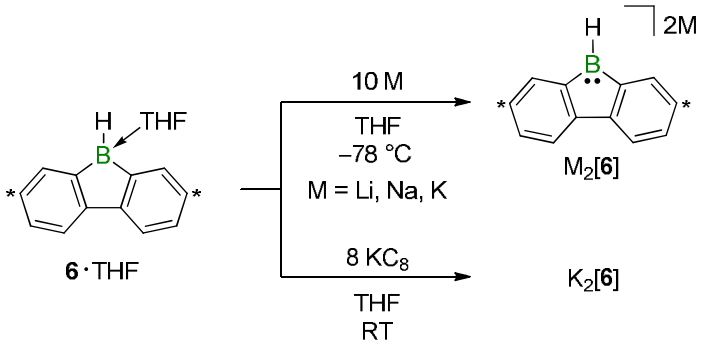

Schema 47. Synthesen der Salze M_2[**6**] ausgehend von **6**·THF in THF (M = Li, Na, K). Kohlenstoffatome, die mit * gekennzeichnet sind, tragen *t*Bu-Gruppen.

2.3.4 Entstehung von [**34**]$^-$, [**35**]$^-$, [**36**]$^-$ und [**37**]$^{2-}$ durch Reduktion von **6**·THF

Für alkylsubstituierte 9-Borafluoren-Dianionen ist bekannt, dass sie leicht zu den Neutralverbindungen oxidierbar sind (vgl. Kapitel 1.4). Im Rahmen meiner Promotion wurde gezeigt, dass das wasserstoffsubstituierte 9-Borafluoren-Dianion [**6**]$^{2-}$ mit ausgewählten Elektrophilen formal nucleophil reagieren kann (die Produkte könnten allerdings auch über radikalische Pfade gebildet worden sein). Im Folgenden werden die in Schema 48 zusammengefassten Reaktivitäten von Li_2[**6**] in THF gegenüber Et_3SiBr und **6**·THF mit bedeutsamen Folgereaktionen näher erläutert: Das 9-Borafluoren-Dianion [**6**]$^{2-}$ reagiert mit Et_3SiBr nahezu quantitativ unter formaler Substitution der Bromidgruppe zum Silylborat [**36**]$^-$. In analoger Weise reagiert [**6**]$^{2-}$ auch mit Bromethan zum entsprechenden Ethylborat. Mit der Radikaluhr (Brommethyl)cyclopropan[295-297] tritt eine weniger selektive Reaktion ein. Dabei deutet das Auftreten von Signalen im Allylbereich des ^{1}H-NMR-Spektrums möglicherweise auf radikalische Intermediate hin. Durch Zugabe des 9-Borafluorens **6**·THF zu [**6**]$^{2-}$ entsteht das dimere 9-Borafluoren-Dianion [**113**]$^{2-}$, das durch Reduktion wieder quantitativ zu [**6**]$^{2-}$ gespalten werden kann. Dieser Befund ist vergleichbar mit dem eintretenden B–B-Bindungsbruch bei der Reaktion von Li_2[**7**] zu Li_4[**7**] (Kapitel 2.2). Das Dianion [**113**]$^{2-}$ besitzt eine potenziell nucleophile B–B-Bindung und zwei borständige hydridische Wasserstoffatome. Ein heterolytischer B–B-Bindungsbruch in [**113**]$^{2-}$ zu **6**·THF und [**6**]$^{2-}$ sowie die anschließende Ausbildung einer neuen B–B-Bindung zwischen dem gebildeten Dianion [**6**]$^{2-}$ und einem neuen Molekül **6**·THF sollte wieder zu den Ausgangsstoffen führen (Schema 49a). Ein Hydridtransfer müsste hingegen eine stoffliche Veränderung hervorrufen, was experimentell bestätigt wurde (Schema 48): Im Zuge der Übertragung eines Hydridions von [**113**]$^{2-}$ auf **6**·THF kommt es zu einer Gerüstumlagerung der Bis-9-borafluorenstruktur, sodass [**116**]$^-$ und [**34**]$^-$ entstehen. Dass [**113**]$^{2-}$ prinzipiell neben einer Hydridübertragung auch unter B–B-Bindungsbruch reagiert, wird durch die Reaktion mit Et_3SiBr deutlich, bei der die Produkte Et_3SiH, [**36**]$^-$ und [**147**]$^-$ gebildet werden (Schema 49b).

Auf der Stufe des Anions [**116**]$^-$ trennt sich der Mechanismus aus Schema 48 in zwei Pfade auf. Durch Reduktion kann [**116**]$^-$ in das B=B-gebundene Dianion [**37**]$^{2-}$ überführt werden.[309] Mit einem Äquivalent **6**·THF hingegen reagiert [**116**]$^-$ quantitativ unter Bildung der Verbindung [**147**]$^-$, die im ^{1}H-NMR-Spektrum zwei Signalsätze erzeugt (Integralverhältnis 2:1; für NMR-Daten siehe Kapitel 4.2.4) und die beim Abdampfen der THF-Lösung zu [**35**]$^-$ umlagert. Auf dieser Kenntnis basiert der abgebildete Strukturvorschlag für [**147**]$^-$, einem Derivat von $[B_3H_8]^-$, dass formal durch das Ersetzen eines verbrückenden Wasserstoffatoms im Diboran(6) **12** durch ein 9-Borafluorenmolekül entsteht. Das Anion [**35**]$^-$ ist über die Zugabe von **6**·THF zu [**116**]$^-$ nun selektiv darstellbar.
Über die Reaktivität von [**35**]$^-$ war zu Beginn meiner Promotion nichts bekannt, zumal es sich in Toluol so schlecht löst, dass es auch innerhalb von Wochen nicht weiter mit Lithium reagiert. Löst man Kristalle von [**35**]$^-$ in THF-d_8, so dominieren zunächst dessen Signale im ^{1}H-NMR-Spektrum, aber über lange Zeit steigt der Anteil an [**147**]$^-$ ([**35**]$^-$: [**147**]$^-$ ≈ 3:4 nach 2 Jahren). Das Rühren dieser gealterten Lösung über 90 Minuten mit einem Überschuss an Lithium führte zur Bildung höher reduzierter Spezies (u. a. [**37**]$^{2-}$, [**6**]$^{2-}$ und [**34**]$^-$).

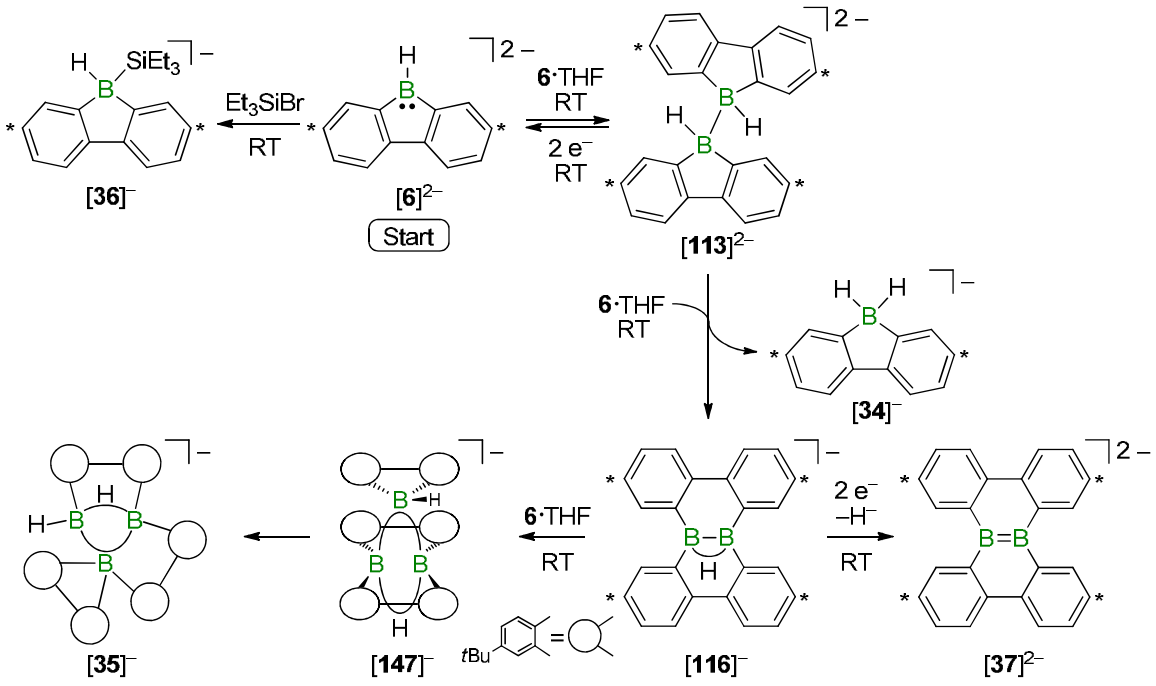

Schema 48. Reaktionspfade von [**6**]$^{2-}$ in THF mit Et_3SiBr oder **6**·THF, die die Bildung von [**36**]$^-$, [**113**]$^{2-}$, [**116**]$^-$, [**35**]$^-$ und [**37**]$^{2-}$ vor dem Hintergrund der Reduktionsreaktionen von **6**·THF erklären. Bei der abgebildete Struktur für [**147**]$^-$ handelt es sich um einen vorläufigen Vorschlag, der auf NMR-Daten basiert. Kohlenstoffatome, die mit * gekennzeichnet sind, tragen *t*Bu-Gruppen.

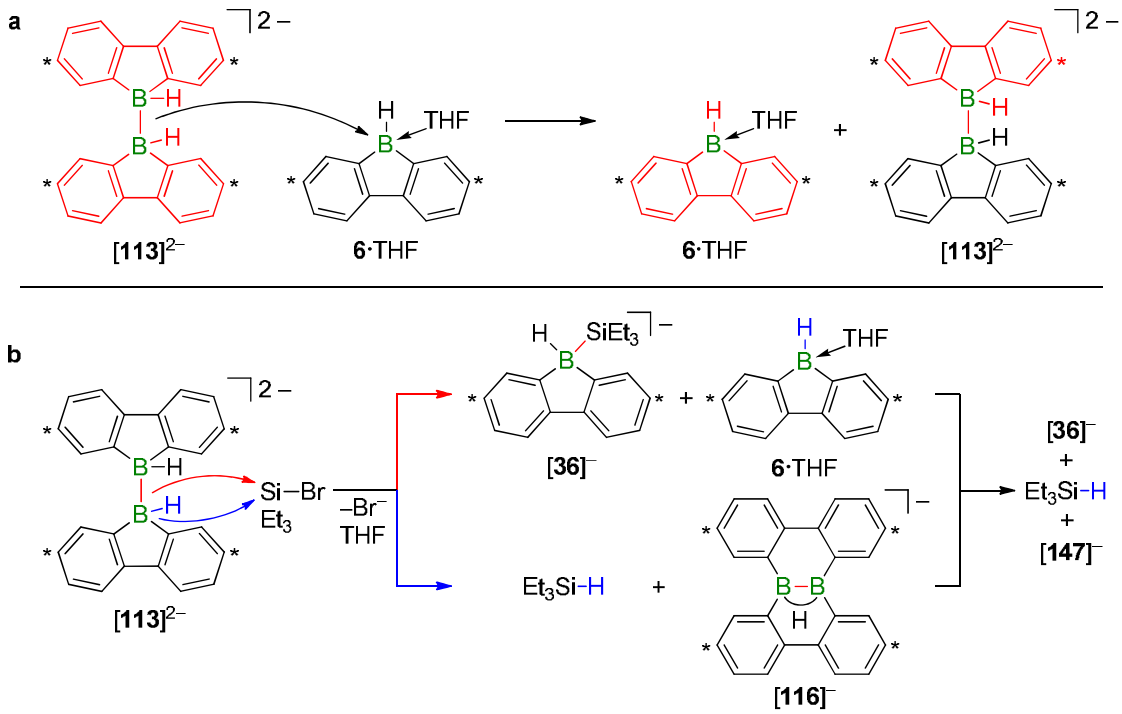

Schema 49. (a) Ein nucleophiler Angriff der B–B-Bindung von [**113**]$^{2-}$ an **6**·THF sollte keine stoffliche Veränderung hervorrufen. (b) Bei der Umsetzung von [**113**]$^{2-}$ mit Et_3SiBr treten B–B-Bindungsbruch/B–Si-Bindungsbildung (roter Pfad) und Hydridübertragung (blauer Pfad) ein, sodass Et_3SiH, [**36**]$^-$ und [**147**]$^-$ gebildet werden (vgl. Schema 48). Kohlenstoffatome, die mit * gekennzeichnet sind, tragen *t*Bu-Gruppen.

Die aufgezeigten Reaktionspfade aus Schema 48 erklären das Produktspektrum, das durch Reaktion von (**6**)$_2$ mit Lithium in Toluol in Gegenwart von Et_3SiBr beschrieben wurde ([**34**]$^-$, [**35**]$^-$, [**36**]$^-$ und [**37**]$^{2-}$; vgl. Schema 6):[108] Die Reduktion von (**6**)$_2$ verläuft in Toluol langsamer als in THF, sodass entstehendes 9-Borafluoren-Dianion [**6**]$^{2-}$ ausreichend Zeit hat, mit weiterem Edukt (**6**)$_2$ unter Bildung von [**34**]$^-$ und [**35**]$^-$ oder mit Et_3SiBr zu [**36**]$^-$ zu reagieren. Die vereinzelte Reduktion intermediär gebildeter Anionen [**116**]$^-$ führt zur Bildung von [**37**]$^{2-}$ als Minderkomponente. Wechselt man das Lösungsmittel zu THF (in Abwesenheit von Et_3SiBr), dann werden die Reaktionen von [**113**]$^{2-}$ zu [**6**]$^{2-}$ und von [**116**]$^-$ zu [**37**]$^{2-}$ dominant. Zusätzlich kann das Anion [**147**]$^-$, falls gebildet, in THF zum Teil zu [**6**]$^{2-}$ und [**37**]$^{2-}$ umgesetzt werden. Als Folge wird bei der Reduktion in THF im Vergleich zu der in Toluol ein deutlich höherer Anteil an [**6**]$^{2-}$ und [**37**]$^{2-}$ beobachtet.
Die beschriebenen experimentellen Ergebnisse lassen sich mit der Analyse von Wagner et al. (2014) vergleichen, die darlegt, dass [**35**]$^-$ formal als ein Insertionsprodukt des 9-Borafluorenyl-Anions [**38**]$^-$ in (**6**)$_2$ angesehen werden kann (vgl. Schema 8 in Kapitel 1.4 und Schema 50b).[108] Das Anion [**38**]$^-$ ließ sich bisher nicht in freier Form nachweisen, sodass selbst eine formale Beteiligung von [**38**]$^-$ anfechtbar ist. Als weiteres Beispiel sei die analoge Analyse für Molekül [**36**]$^-$ angeführt (Schema 50a; vgl. Schema 8): Die Bildung von [**36**]$^-$ kann über die Insertion des 9-Borafluorenyl-Anions [**38**]$^-$ in die Et_3Si–H Bindung oder durch einen nucleophilen Angriff von [**6**]$^{2-}$ an Et_3SiBr plausibel erklärt werden. Die Beobachtung, dass das isolierte 9-Borafluoren-Dianion [**6**]$^{2-}$ mit Et_3SiBr unter Entstehung von [**36**]$^-$ reagiert, schließt den Pfad über [**38**]$^-$ zwar nicht aus, macht ihn aber ohne experimentelle Hinweise auf das freie Boryl-Anion wenig wahrscheinlich (Schema 50a,

rechts). Dennoch hilft die Beschreibung reduzierter 9-Borafluorenderivate als maskierte Boryl-Anionen [**38**]$^-$, deren Reaktivität besser zu verstehen. Dies soll ebenfalls an Beispielen erläutert werden (Schema 50b): [**37**]$^{2-}$ lässt sich als umgelagertes Dimer des Boryl-Anions [**38**]$^-$ beschreiben. Wie in Kapitel 2.1.3 detailliert dargelegt, reagiert [**37**]$^{2-}$ nach Zugabe des Elektrophils Chlormethan zum Intermediat [**132**]$^-$, das [**38**]$^-$ als Fragment enthält. Dieses ermöglicht eine C–H-Aktivierung, bei der [**125**]$^-$ generiert wird (Schema 50b, links).[310] Mit etherischer HCl anstelle des Chlormethans entsteht [**116**]$^-$, das formal durch Insertion von [**38**]$^-$ in **6** beschrieben werden kann (Schema 50b, rechts).[309] Für [**116**]$^-$ zeigt sich die nucleophile Reaktivität des maskierten Anions [**38**]$^-$, wenn durch Zugabe von **6**·THF das Anion [**35**]$^-$ quantitativ gebildet wird.

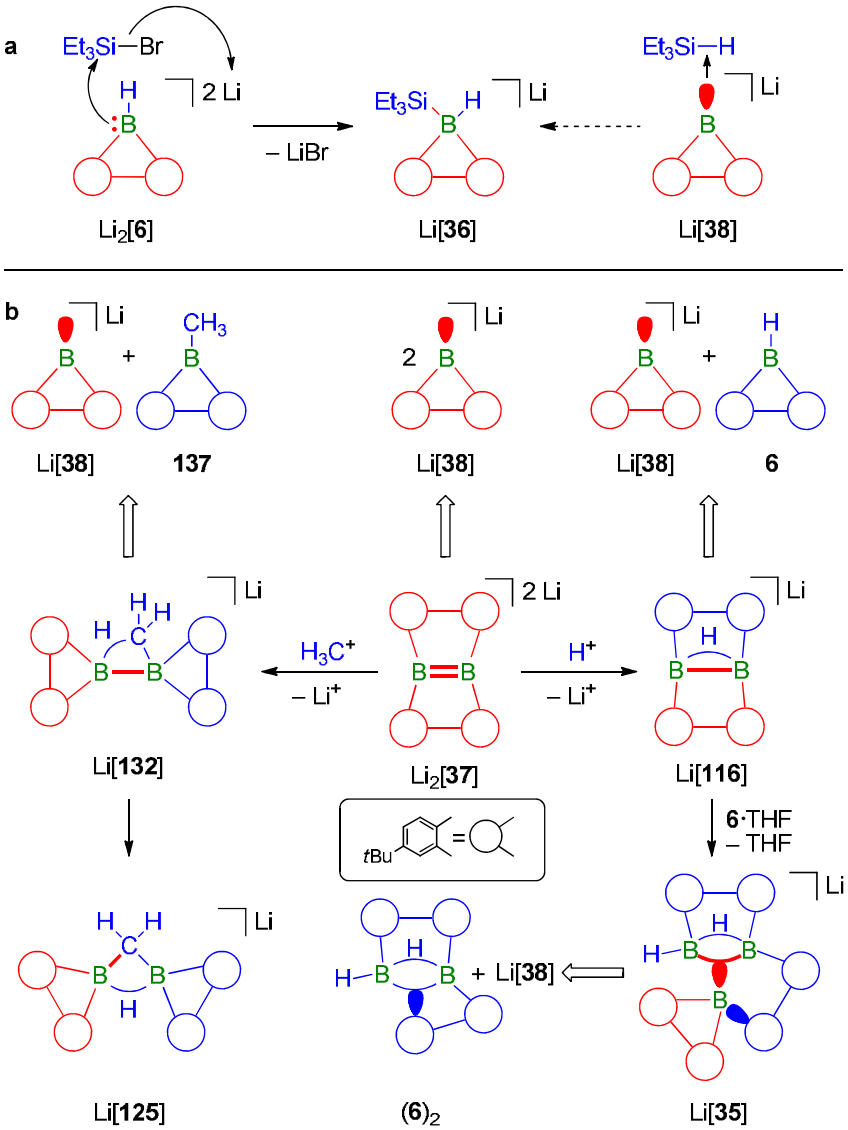

Schema 50. (a) Der experimentelle Beleg, dass Li[**36**] durch Reaktion von Li_2[**6**] mit Et_3SiBr gebildet wird, macht eine Entstehung von Li[**36**] durch Insertion von Li[**38**] in die Et_3Si–H-Bindung unwahrscheinlich. (b) Erweiterte formale Bindungsanalyse von Li[**35**], Li_2[**37**] und Li[**125**] auf Grundlage der Addition des 9-Borafluorenyl-Anions [**38**]$^-$ an geeigneten Partner (vgl. Schema 8).

2.3.5 Reaktionen zwischen M_2[**6**] und 1,2-Dibromethan, M_2[**6**] und Ethen sowie M[**116**] und Ethen

Das Dianion [**6**]$^{2-}$ hat zwei plausible Möglichkeiten, mit 0.5 Äquivalenten an 1,2-Dibromethan zu reagieren (Schema 51): (i) Oxidation zu [**113**]$^{2-}$ unter Eliminierung von Br^- und 0.5 Ethen oder (ii) Substitution beider Bromidgruppen unter Bildung des ethylenverbrückten Bis-9-borafluorens [**148**]$^{2-}$ (0.5 Äquivalente).

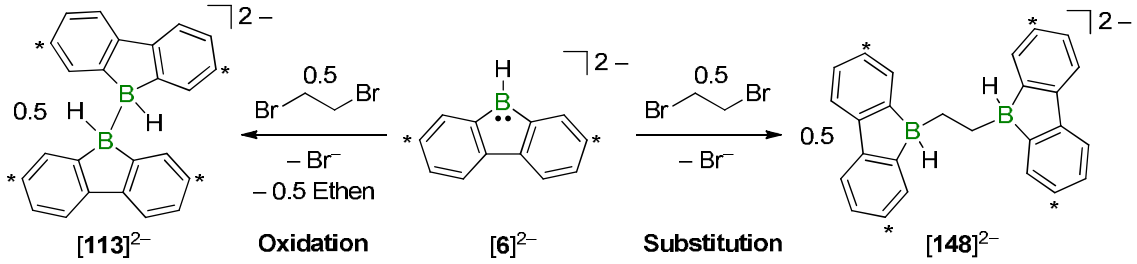

Schema 51. Plausible Reaktivitäten des Dianions [**6**]$^{2-}$ mit 1,2-Dibromethan (0.5 Äquivalente): Oxidationsreaktion zu [**113**]$^{2-}$ oder Substitutionsreaktion zu [**148**]$^{2-}$. Kohlenstoffatome, die mit * gekennzeichnet sind, tragen *t*Bu-Gruppen.

Das experimentell beobachtete Hauptprodukt der Reaktion von [**6**]$^{2-}$ mit 1,2-Dibromethan ist stark von der eingesetzten Stöchiometrie abhängig, wie in Abbildung 25 skizziert ist: Bei Zugabe von ≤ 0.5 Äquivalenten an 1,2-Dibromethan wird der zu erwartende Anteil des Startmaterials [**6**]$^{2-}$ selektiv in das Oxidationsprodukt [**113**]$^{2-}$ umgewandelt (unter Bildung von Ethen). Selbst wenn die Menge von 0.5 Äquivalenten nur geringfügig überschritten wird, verschwindet [**113**]$^{2-}$ ebenso wie der Großteil an Ethen aus dem Produktgemisch (geschlossenes Gefäß). Stattdessen bildet sich [**148**]$^{2-}$ als Hauptprodukt und [**116**]$^-$ sowie [**34**]$^-$ als geringe Nebenprodukte. Das Dianion [**148**]$^{2-}$ ist in Form des Natriumsalzes nur begrenzt in THF löslich. Grund hierfür könnte sein, dass [Na(thf)$_2$]$_2$[**148**] ein Koordinationspolymer bildet, wie mithilfe einer Kristallstruktur gezeigt wurde (Abbildung 26). Zwischen 0.5 Äquivalenten und 1 Äquivalent an 1,2-Dibromethan rücken zwei neue Verbindungen in den Vordergrund, [**149**]$^-$ (Hauptprodukt) und [**150**]$^-$ (Nebenprodukt), deren Anteil bei 0.75 Äquivalenten des Halogenalkans ein Maximum erreicht (Strukturvorschläge siehe Schema 53; für NMR-Daten siehe Kapitel 4.1). Bei Zugabe von > 0.75 Äquivalenten 1,2-Dibromethan bildet sich innerhalb weniger Tage das 1,2-Bis(9-borafluorenyl)ethan **138**^{C2} (Nebenprodukt: 2,7-Di-*t*Bu-9-ethyl-9-borafluoren).

Die abrupte Veränderung des Produktspektrums bei 0.5 Äquivalenten an 1,2-Dibromethan spricht für eine autokatalytische Reaktion, die entweder nach vollständiger Umsetzung von [**6**]$^{2-}$ endet oder einsetzt. Solch eine autokatalytische Reaktion bei Anwesenheit von [**6**]$^{2-}$ könnte beispielsweise auf Einelektronübertragung zurückzuführen sein, falls das Dianion [**148**]$^{2-}$ unter reduzierenden Bedingungen schnell zu Ethen und [**113**]$^{2-}$ zerfällt. In einem diesbezüglichen Versuch induzierte das Dianion [**6**]$^{2-}$ jedoch keine Zersetzung einer isolierten Probe von [**148**]$^{2-}$ (THF), sodass eine ab 0.5 Äquivalenten 1,2-Dibromethan einsetzende Autokatalyse wahrscheinlicher ist. Dabei deutet die Abnahme des in Lösung befindlichen Ethens auf dessen Reaktion mit einer der anderen Spezies hin. Es konnte gezeigt werden, dass [**113**]$^{2-}$ (Reinheit ~ 85%) durch Zugabe von Ethen (1 atm) innerhalb von 2 Wochen bei 50 °C verbraucht wird und [**148**]$^{2-}$ entsteht (Schema 52). Da

[**148**]$^{2-}$ bei Zugabe von 1,2-Dibromethan zu [**6**]$^{2-}$ innerhalb von Minuten gebildet wird, kann die unkatalysierte Reaktion von [**113**]$^{2-}$ mit Ethen mechanistisch für die schnelle Reaktion keine unmittelbare Relevanz besitzen.

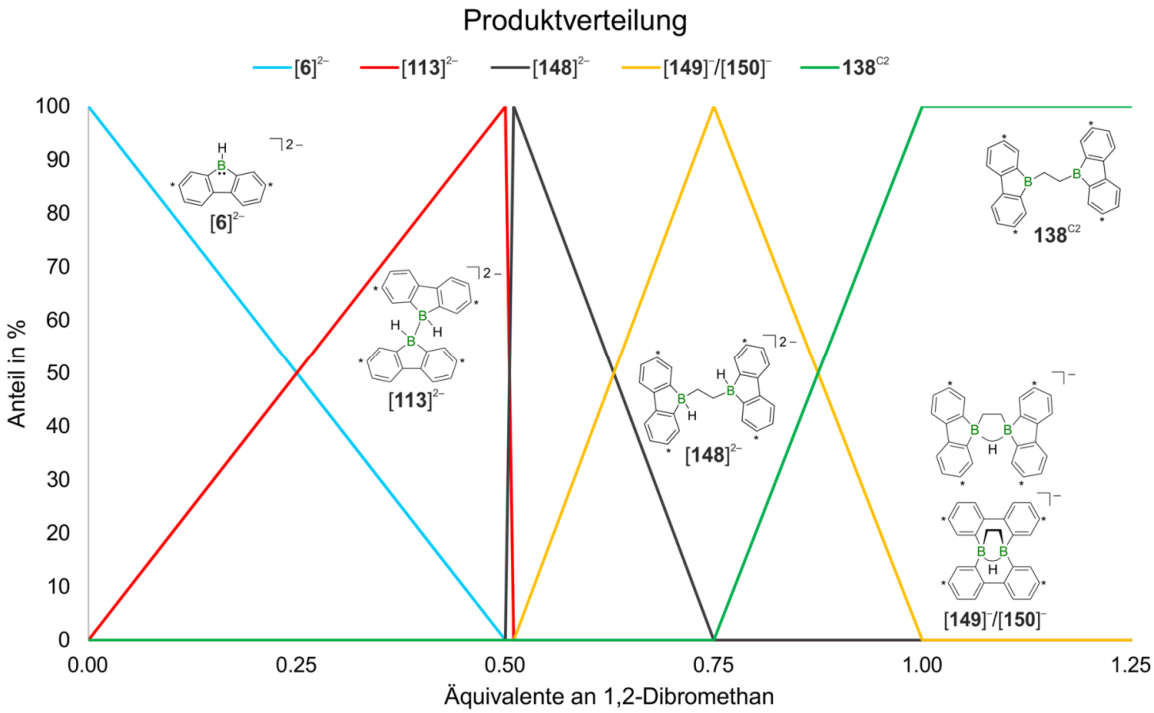

Abbildung 25. Produktverteilung der Reaktion von [**6**]$^{2-}$ mit unterschiedlichen Äquivalenten an 1,2-Dibromethan. Kohlenstoffatome, die mit * gekennzeichnet sind, tragen *t*Bu-Gruppen.

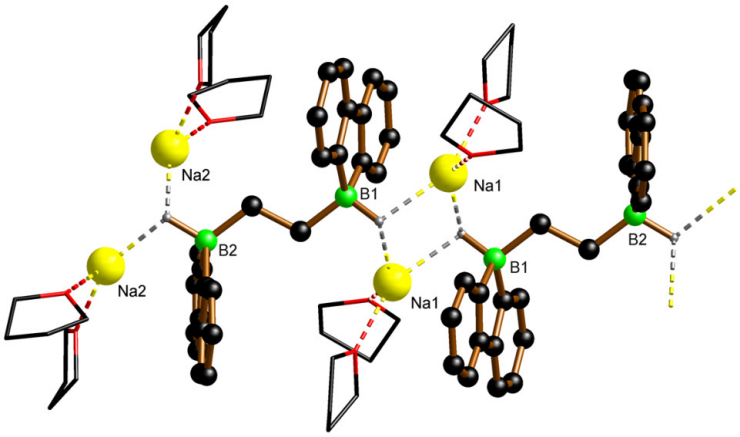

Abbildung 26. Ausschnitt eines Koordinationspolymers von [Na(thf)$_2$]$_2$[**148**] im Festkörper. Die *t*Bu-Gruppen sind zur besseren Übersicht nicht abgebildet.

Im Kontrast zu [**113**]$^{2-}$ reagiert [**116**]$^-$, das aus [**113**]$^{2-}$ mit 1,2-Dibromethan als Hydridfänger unter Entstehung von Bromethan bzw. Ethan gebildet werden kann, schnell mit Ethen zu [**149**]$^-$ (Hauptprodukt) und [**150**]$^-$ (Nebenprodukt), wie in Schema 53 gezeigt. Anhand der NMR-Daten ist davon auszugehen, dass es sich bei [**149**]$^-$ und [**150**]$^-$ um isomere Produkte einer formalen [2+2]-Addition der B–B-Bindung von [**116**]$^-$ an die C=C-Bindung des Ethens handelt (Schema 53). Da eine derartige [2+2]-Addition nach Woodward-Hoffmann thermisch verboten ist, reagiert [**116**]$^-$ vermutlich mit Ethen, weil das darin enthaltene maskierte Boryl-Anion [**38**]$^-$ eine carbenartige [2+1]-Addition

ermöglicht (vgl. Schema 50b, rechts). Die Strukturvorschläge für [**149**]$^-$ und [**150**]$^-$ sind noch nicht vollständig gesichert und in ihrer Zuordnung vertauschbar.

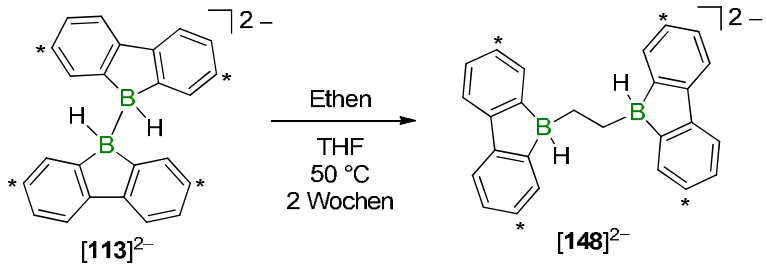

Schema 52. Das Dianion [**113**]$^{2-}$ reagiert mit Ethen in THF bei 50 °C über zwei Wochen selektiv zu [**148**]$^{2-}$. Kohlenstoffatome, die mit * gekennzeichnet sind, tragen *t*Bu-Gruppen.

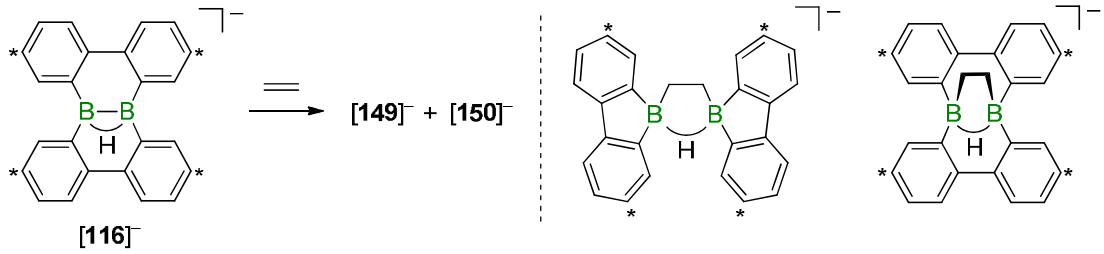

Schema 53. Das Anion [**116**]$^-$ reagiert schnell mit Ethen zu zwei Produkten, [**149**]$^-$ (Hauptprodukt) und [**150**]$^-$ (Nebenprodukt), für die rechts Strukturvorschläge abgebildet sind (nicht vollständig gesichert). Kohlenstoffatome, die mit * gekennzeichnet sind, tragen *t*Bu-Gruppen.

Mit diesen Erkenntnissen kann der in Abbildung 25 gezeigte Reaktionsverlauf unter der Annahme einer autokatalytischen Übertragung von Hydridionen erklärt werden (Schema 54): Bei Zugabe von ≤ 0.5 Äquivalenten an 1,2-Dibromethan (DBE) zu [**6**]$^{2-}$ entsteht das Oxidationsprodukt [**113**]$^{2-}$ sowie Ethen. Erst bei einer geringen Überschreitung (ε) der 0.5 Äquivalente an 1,2-Dibromethan wird zusätzlich ein Hydridakzeptor (unbekannte Struktur) gebildet. Dieser abstrahiert ein Hydridion von [**113**]$^{2-}$, sodass [**116**]$^-$ und ein Hydriddonor (unbekannte Struktur) hervorgehen. Das Anion [**116**]$^-$ reagiert schnell mit Ethen zu [**149**]$^-$/[**150**]$^-$, die ein Hydridion des Hydriddonors übernehmen, wodurch [**148**]$^{2-}$ und der ursprüngliche Hydridakzeptor freigesetzt werden. Die Regeneration des Hydridakzeptors ermöglicht über die geschilderte Reaktionskaskade eine katalysierte Umwandlung von [**113**]$^{2-}$ mit Ethen zu [**148**]$^{2-}$. Eine größere Menge an 1,2-Dibromethan wirkt als stöchiometrischer Hydridfänger, weshalb aus [**148**]$^{2-}$ die Anionen [**149**]$^-$/[**150**]$^-$ und schließlich das Bis-9-borafluoren **138**^{C2} hervorgehen. Timo Trageser konnte zeigen, dass [**116**]$^-$ und [**149**]$^-$/[**150**]$^-$ kein Hydridion von [**113**]$^{2-}$ entfernen.[311] Das Boran **6**·THF eignet sich hingegen als Hydridakzeptor (vgl. Kapitel 2.3.4) und in dessen Gegenwart wurde eine signifikante Beschleunigung der Reaktion von [**113**]$^{2-}$ mit Ethen zu [**148**]$^{2-}$ beobachtet.[311] Die Geschwindigkeitserhöhung ist richtungsweisend, jedoch noch nicht ausreichend, um den in Schema 54 postulierten Mechanismus zu belegen.

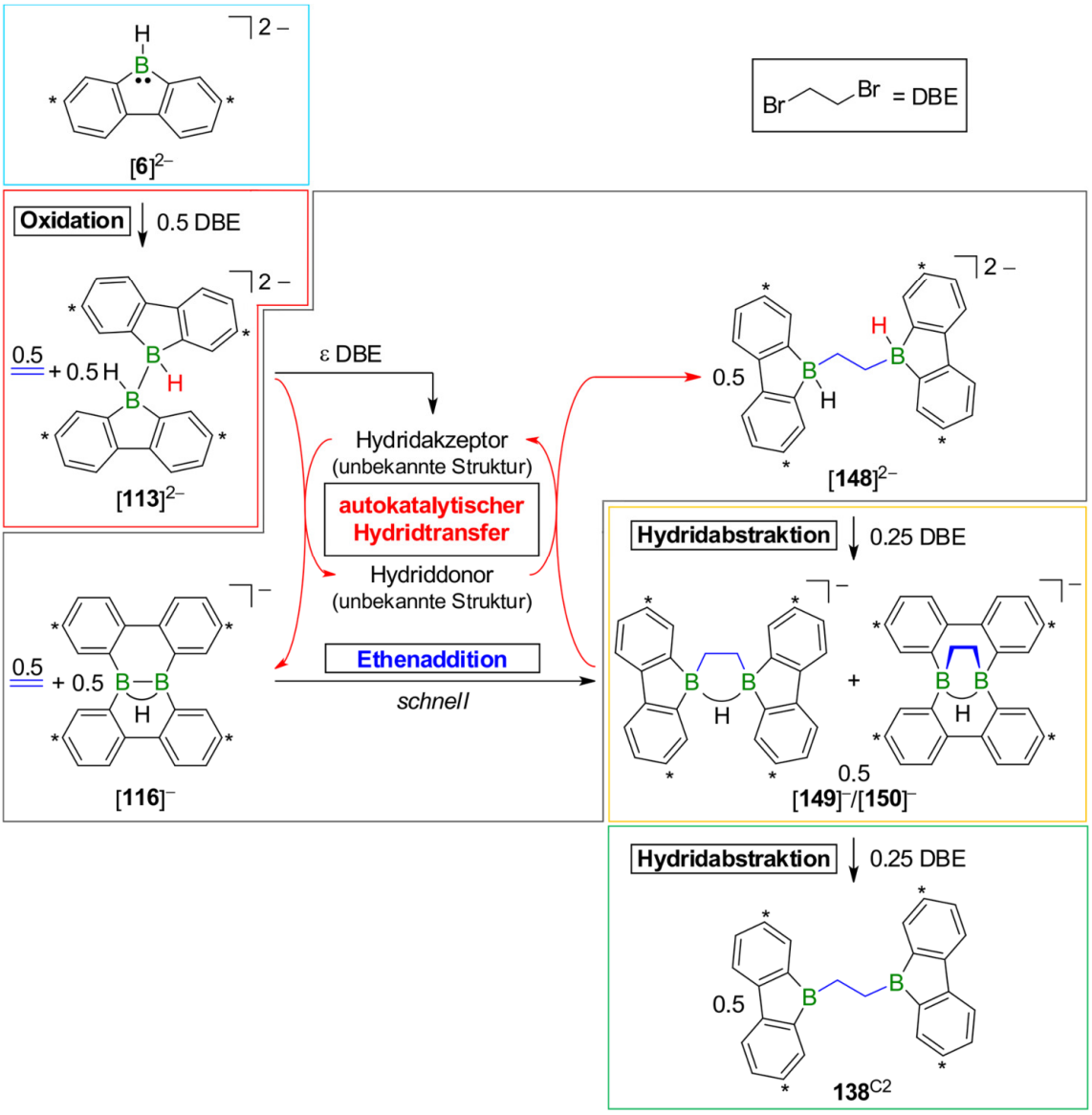

Schema 54. Auf Grundlage einer autokatalytischen Übertragung von Hydridionen, einer Oxidationsreaktion, einer Ethenaddition und Hydridabstraktionen lässt sich die Entstehung von [**113**]$^{2-}$, [**148**]$^{2-}$, [**149**]$^{-}$/[**150**]$^{-}$ oder **138**^{C2} als Hauptprodukte bei Zugabe unterschiedlicher Äquivalente an 1,2-Dibromethan zu [**6**]$^{2-}$ plausibel erklären ($\varepsilon \leq 0.05$). Die Rahmenfarben repräsentieren die Farben der Funktionen aus Abbildung 25. Kohlenstoffatome, die mit * gekennzeichnet sind, tragen *t*Bu-Gruppen.

2.3.6 Gezielte Darstellung von Li_4[**146**]

Ausgehend von kristallinem 9-Borafluorendimer (**6**)$_2$ entsteht Li_4[**146**] in kleinen Mengen durch Reduktion mit Lithium in THF. Zwei naheliegende Szenarien für die Bildung von [**146**]$^{4-}$ sind in Schema 55 gezeigt: (A) Überreduktion von [**37**]$^{2-}$ mit Gerüstumlagerung, (B) Überreduktion von [**113**]$^{2-}$ mit zweifacher Hydrideliminierung.

Die experimentelle Überprüfung widerlegt beide Wege: (A) Rühren der B=B-gebundenen Verbindung [**37**]$^{2-}$ in THF in Gegenwart eines Überschusses an Lithiummetall bei Raumtemperatur oder 60 °C führte zu keiner Reaktion. (B) Die Umsetzung des Bis-9-borafluoren-Dianions [**113**]$^{2-}$ mit einem Überschuss an Lithium führt nicht zu einer Hydrid-

eliminierung, sondern zur Bildung des monomeren Dianions [**6**]$^{2-}$. Durch Zugabe von Et_3SiBr oder (**6**)$_2$ als Hydridfänger während der Reduktion von [**113**]$^{2-}$ wurde zwar [**146**]$^{4-}$ in kleinen Mengen erzeugt, jedoch lässt sich dieser Anteil auf die Reaktion des intermediär vorliegenden **6**·THF mit Lithium zurückführen.

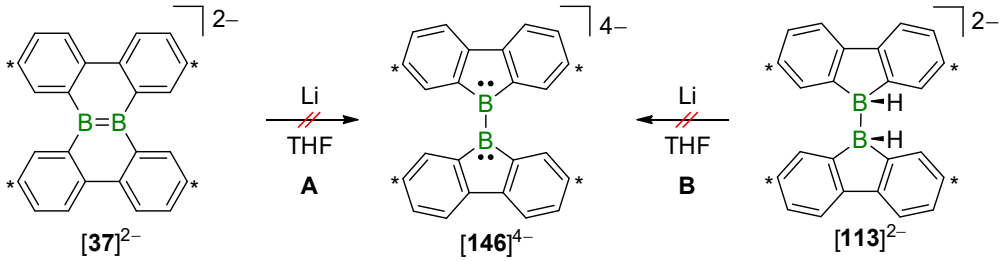

Schema 55. Weder die Zugabe von Lithium zu [**37**]$^{2-}$ (A) noch zu [**113**]$^{2-}$ (B) führten zur Bildung von [**146**]$^{4-}$ in THF. Kohlenstoffatome, die mit * gekennzeichnet sind, tragen *t*Bu-Gruppen.

Um den Zugang zu Li_4[**146**] durch Reduktion von (**6**)$_2$ zu verbessern, wurde das Lösungsmittel variiert. Während Et_2O, Pyridin und SMe_2 keine Verbesserung erbrachten, konnte die Ausbeute an Li_4[**146**] durch Arbeiten in DME signifikant verbessert werden (Schema 56; DME = 1,2-Dimethoxyethan). Da Li_2[**37**] aus DME zum Großteil präzipitiert, liegt Li_4[**146**] nach Filtration im Filtrat in einer höheren Reinheit vor als in THF-Reaktionslösungen. Bei –30 °C kristallisiert [Li(dme)]$_4$[**146**] aus DME innerhalb weniger Tage (Schema 56; Tabelle 3 in Kapitel 2.3.2). Die B–B-Bindungslänge in [Li(dme)]$_4$[**146**] beträgt 1.705(8) Å. Die Parameter der Festkörperstruktur von [Li(dme)]$_4$[**146**] sind gut vergleichbar mit denen von [Li(thf)$_2$]$_2$[Li_2(thf)$_3$][**146**] (vgl. Kapitel 2.3.2). Die Verdrehung der beiden 9-Borafluorenyleinheiten entlang der B–B-Bindung ist in [Li(dme)]$_4$[**146**] (ca. 48°) jedoch stärker ausgeprägt als in [Li(thf)$_2$]$_2$[Li_2(thf)$_3$][**146**] (ca. 37°).

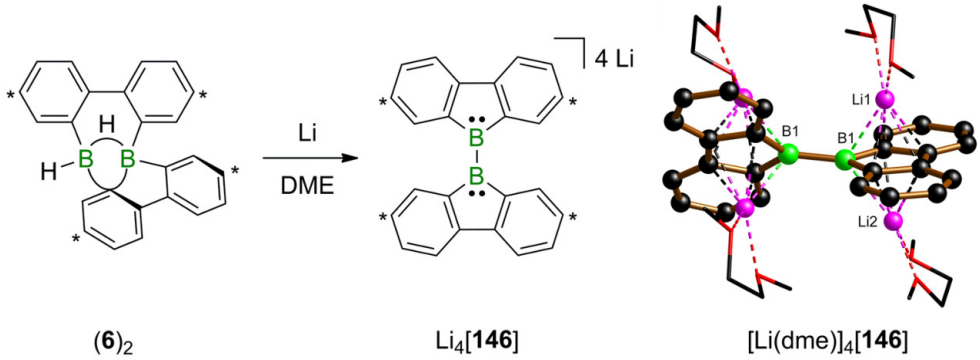

Schema 56. Optimierte Synthese von Li_4[**146**] durch Reduktion von (**6**)$_2$ mit Lithium in DME. Kohlenstoffatome, die mit * gekennzeichnet sind, tragen *t*Bu-Gruppen. Festkörperstruktur von [Li(dme)]$_4$[**146**], bei der *t*Bu-Gruppen zur besseren Übersicht nicht abgebildet wurden.

Mit der gezielteren Synthese von Li_4[**146**] durch Reduktion von (**6**)$_2$ in DME sollte der Weg zur Untersuchung der Reaktivität des Tetraanions [**146**]$^{4-}$ geebnet sein. Es stellt sich die Frage, ob Li_4[**146**] bei Zugabe eines Elektrophils (E^+) nucleophil reagiert und/oder oxidiert wird (Schema 57). Im Falle der nucleophilen Reaktion sollte [**B**]$^{3-}$ entstehen, falls die B–B-Bindung erhalten bleibt. Bei Bruch der B–B-Bindung sollten sich die Anionen [**38**]$^-$ und [**C**]$^{2-}$ bilden. Im Falle einer Oxidation von [**146**]$^{4-}$ könnte das Rückgrat unter

Ausbildung einer B=B-Doppelbindung erhalten bleiben oder umlagern, sodass [**151**]$^{2-}$ oder [**37**]$^{2-}$ hervorgehen.

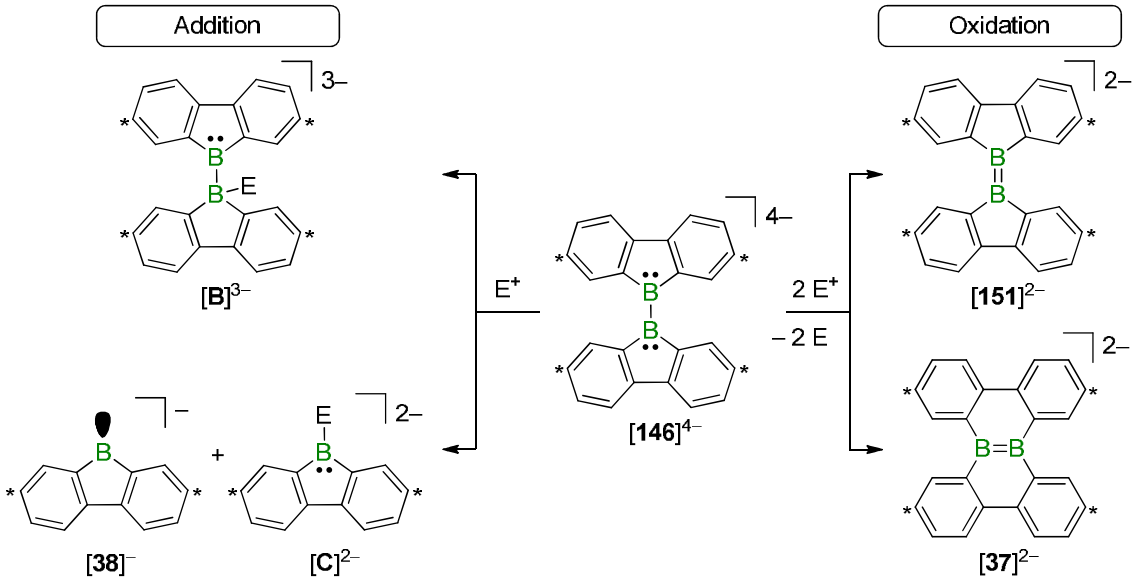

Schema 57. Die Zugabe eines Elektrophils (E^+) zu [**146**]$^{4-}$ könnte zur Addition des Elektrophils und/oder zur Oxidation von [**146**]$^{4-}$ führen, sodass die hier abgebildeten (intermediären) Produkte plausibel sind. Kohlenstoffatome, die mit * gekennzeichnet sind, tragen *t*Bu-Gruppen.

3 Zusammenfassung

Ausgangspunkt für die vorliegende Arbeit war die Fragestellung, warum bei Reduktion des borständig wasserstoffsubstituierten 9-Borafluorendimers (**6**)$_2$ mit Lithium in Toluol in Gegenwart von Et_3SiBr umfassende Änderungen der Gerüststruktur eintreten (Produkte: Li[**34**], Li[**35**], Li[**36**] und Li_2[**37**]; Schema 58).[108] Allein die ausgeprägten strukturellen Unterschiede der einzelnen Salze offenbaren, dass deren Entstehung ein komplexes mechanistisches Szenario zugrunde liegt. Um diese fundamentalen Reaktionsmuster unter reduzierenden Bedingungen zu verstehen, wurden zunächst zwei Modellverbindungen untersucht. Anschließend erfolgte eine erneute Betrachtung des Ursprungssystems unter Berücksichtigung der gewonnenen Erkenntnisse, die weitere wesentliche mechanistische Prinzipien aufdeckte.

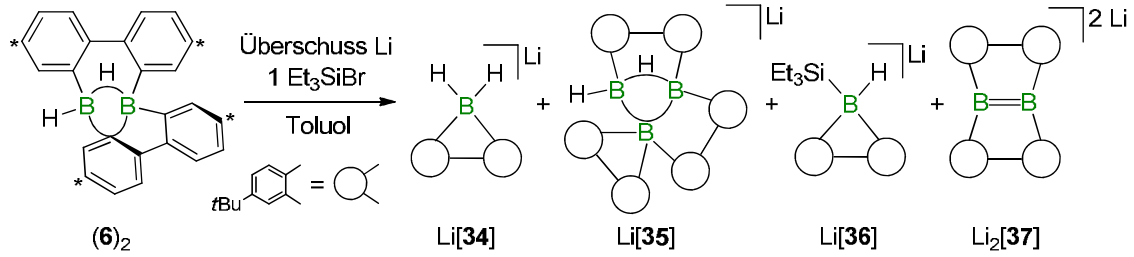

Schema 58. Die publizierte Reduktion des 9-Borafluorendimers (**6**)$_2$ mit Lithium in Toluol in Gegenwart von Et_3SiBr, bei der die vier unterschiedlichen Produkte Li[**34**]–Li[**36**] und Li_2[**37**] entstehen, war Ausgangspunkt für die vorliegende Arbeit.[108] Kohlenstoffatome, die mit * gekennzeichnet sind, tragen *t*Bu-Gruppen.

Die erste Modellverbindung war das Bis(9-borafluorenyl)methan **7**, das wie (**6**)$_2$ zwei Boratome in unmittelbarer Nachbarschaft enthält (Schema 59).[106] Im Gegensatz zu (**6**)$_2$ besitzt **7** jedoch keine borständigen Wasserstoffatome, sondern eine Methyleneinheit, die beide 9-Borafluorenylreste verbindet. Durch sequentielle Reduktion von **7** wird zunächst eine B·B-Einelektron-Zweizentrenbindung ([**7**$^{\bullet}$]$^-$)[106] gebildet, dann eine B–B-Zweielektronen-Zweizentrenbindung ([**7**]$^{2-}$)[106] und schließlich tritt ein B–B-Bindungsbruch ein ([**7**]$^{4-}$; Schema 59). Das Grundgerüst von **7** bleibt während der Reduktionen intakt, was darauf hindeutet, dass das borständige Wasserstoffatom in (**6**)$_2$ Umlagerungen begünstigt. Unterschiedliche Elektrophile oxidierten [**7**]$^{4-}$ je nach Stöchiometrie zu [**7**]$^{2-}$/[**7**$^{\bullet}$]$^-$/**7**.

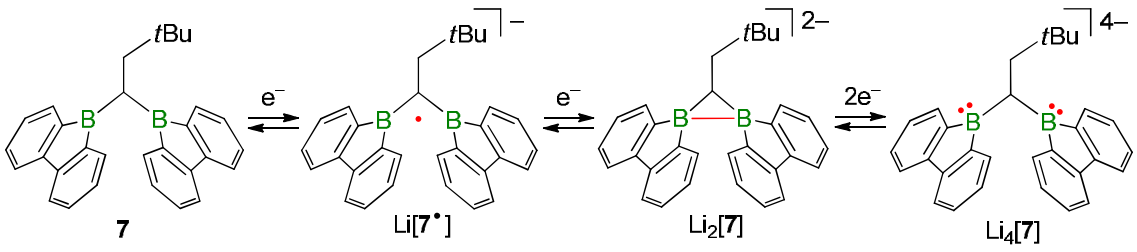

Schema 59. Bei der Reduktion des Bis(9-borafluorenyl)methans **7** treten B·B- und B–B-Bindungsbildung/-bruch ein, wobei die übrigen Bindungen erhalten bleiben (im Gegensatz zur Reduktion von (**6**)$_2$).

Die zweite Modellverbindung war das Diboran(6) **12**, das durch Erhitzen seines Isomers (**6**)$_2$ zugänglich ist (Schema 60).[66] Die Reduktion von **12** führt in Abhängigkeit von der

Natur und der Stöchiometrie des eingesetzten Reduktionsmittels zu unterschiedlichen Hauptprodukten, in denen die Boratome kovalent miteinander verknüpft sind (Schema 60).[65, 259, 260]

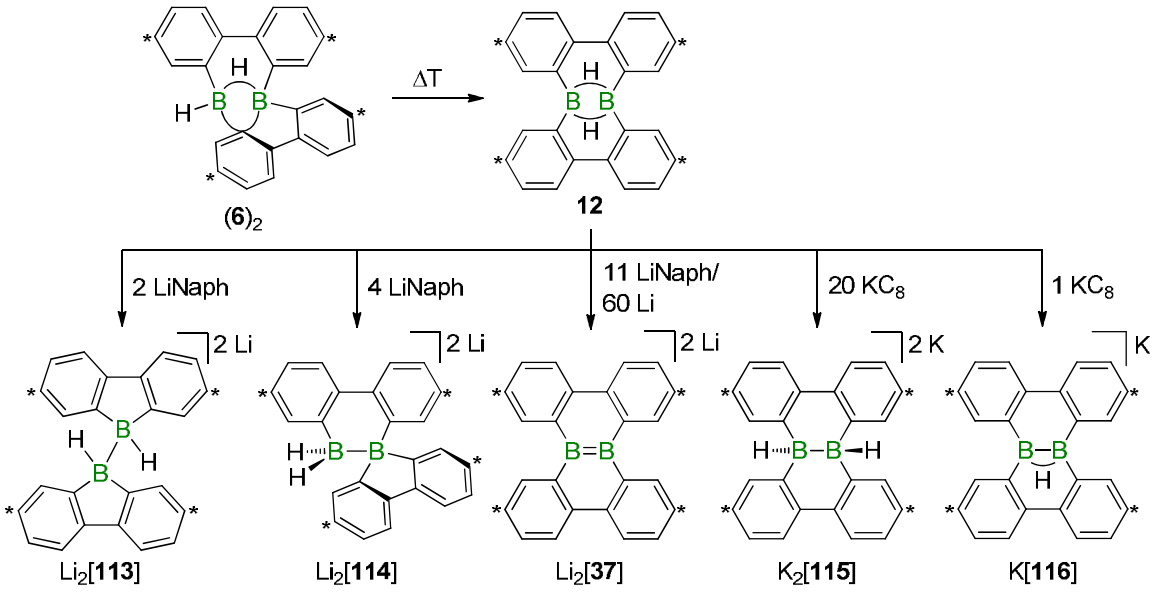

Schema 60. Das Diboran **12**, das durch thermisch induzierte Isomerisierung des Dimers (**6**)$_2$ darstellbar ist, reagiert bei Reduktion je nach Stöchiometrie und Art des Reduktionsmittels zu unterschiedlichen Hauptprodukten, deren beide Boratome kovalent verknüpft sind. Kohlenstoffatome, die mit * gekennzeichnet sind, tragen *t*Bu-Gruppen.

Für die Gerüstumlagerungen wurde ein mechanistisches Bild erarbeitet: Durch Einelektronreduktion werden offenschalige Spezies erzeugt, die schnell 1,2-Phenylverschiebungen durchlaufen.[65] Die Injektion eines zweiten Elektrons stoppt die Dynamik der Verbindungen. Daher hemmt ein Überschuss eines starken Reduktionsmittels Umlagerungen, wohingegen geringe Mengen eines Reduktionsmittels Umlagerungen begünstigen. Während der Reduktion von **12** kann es auch zur Übertragung von Hydridionen kommen, z. B. von [**115**]$^{2-}$ auf **12**, wodurch [**116**]$^-$ generiert wird (Schema 61).[65]

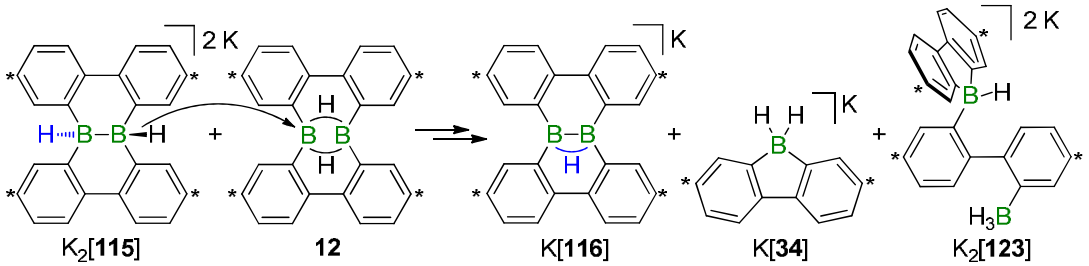

Schema 61. Durch Hydridübertragung von K$_2$[**115**] auf **12** entstehen K[**116**], K[**34**] und K$_2$[**123**]. Kohlenstoffatome, die mit * gekennzeichnet sind, tragen *t*Bu-Gruppen.

Untersuchungen zur Reaktivität der Verbindungen **12**, [**116**]$^-$ und [**37**]$^{2-}$ haben gezeigt, dass diese über Protonierungs-/Deprotonierungsreaktionen miteinander verknüpft sind (Schema 62): Durch Zugabe von etherischer HCl kann [**37**]$^{2-}$ zunächst quantitativ zu [**116**]$^-$ und anschließend zu **12** protoniert werden.[309] Umgekehrt lässt sich **12** durch sterisch anspruchsvolle Basen selektiv zu [**116**]$^-$ deprotonieren.[309] Dieser Sachverhalt ist

bemerkenswert, da die Wasserstoffatome von Boranen allgemein als hydridisch betrachtet werden. Das Anion [**116**]$^-$ besitzt eine einzigartige Reaktivität. Beispielsweise ist es in der Lage, Ethen zu aktivieren. Eine Deprotonierung von **12** zu [**37**]$^{2-}$ mit sterisch anspruchsvollen Basen wurde nur in Spuren beobachtet.

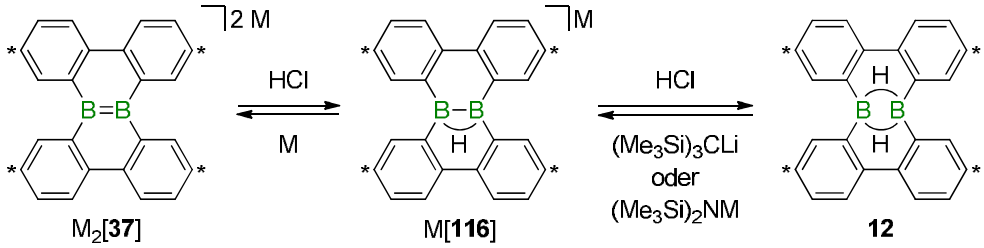

Schema 62. Die sequentielle Protonierung von M_2[**37**] mit etherischer HCl liefert selektiv M[**116**] bzw. **12**. Das Diboran **12** kann mit sterisch anspruchsvollen Basen quantitativ zu M[**116**] deprotoniert werden. Zur Darstellung von M_2[**37**] aus M[**116**] wird hingegen elementares Metall benötigt (M = Li, K). Kohlenstoffatome, die mit * gekennzeichnet sind, tragen *t*Bu-Gruppen.

Der Einsatz der sterisch wenig anspruchsvollen Base H_3CLi führt neben der Deprotonierung von **12** zur Bildung des Bis(9-borafluorenyl)methans [**125**]$^-$ sowie der Anionen Li[**133**] und Li[**134**] (Schema 63).[310] Über die Isolierung von Zwischenstufen, Markierungsexperimente mit Deuterium und quantenchemische Rechnungen ließ sich ein Mechanismus entwickeln, der unter anderem postuliert, dass im Zuge der Bildung von [**125**]$^-$ eine C–H-Aktivierung im Intermediat [**132**]$^-$ stattfindet. Die mechanistischen Erkenntnisse halfen einen Pfad zu [**125**]$^-$ zu etablieren, der deutlich atomökonomischer ist, als ausgehend von **12**: Das Dianion [**37**]$^{2-}$ reagiert mit H_3CCl in nahezu quantitativer Ausbeute zu [**125**]$^-$ (Schema 63).

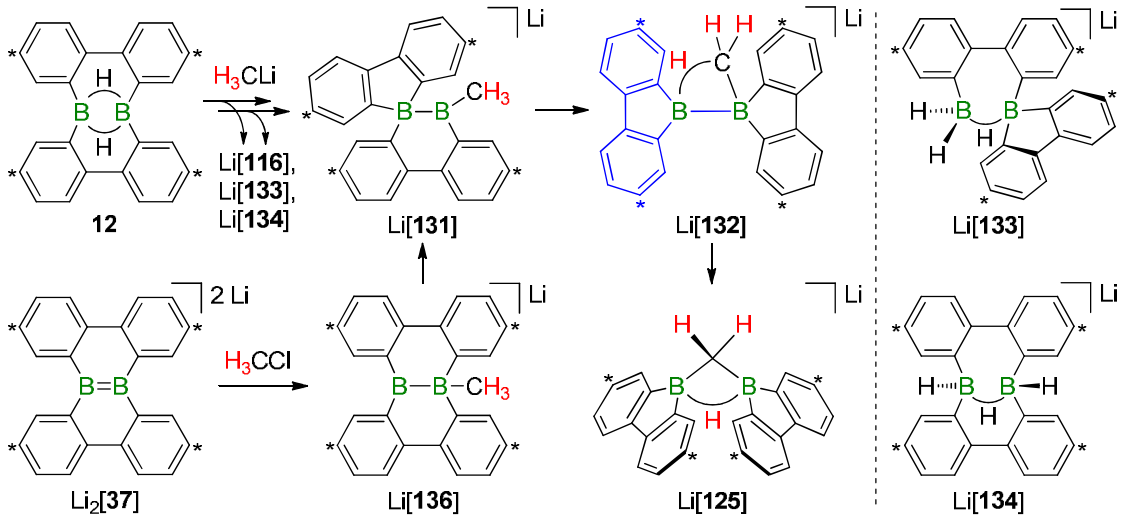

Schema 63. Die Pfade zur Bildung von Li[**125**] ausgehend von **12** oder Li_2[**37**] vereinigen sich auf der Stufe von Li[**131**]. Li[**132**] enthält ein maskiertes Boryl-Anion (blau). Kohlenstoffatome, die mit * gekennzeichnet sind, tragen *t*Bu-Gruppen.

Das Schlüsselintermediat für die C–H-Aktivierung, [**132**]$^-$, enthält formal ein Boryl-Anion (blau in Schema 63), das analog zu einem Singulett-Carben reagiert. Deshalb können, abhängig von der borständigen Alkylkette, folgende Reaktionen auftreten (Schema 64): (i)

intramolekulare C–H-Aktivierung, (ii) intramolekulare Substitutionen einer Halogenfunktion (Zugabe eines kurzkettigen α,ω-Dihalogenalkans zu [**37**]$^{2-}$) oder (iii) intermolekulare Substitution (Zugabe eines Überschusses an H_3C–I).[310] Mit diesen drei Reaktionstypen ließen sich in effizienter Weise neue Borane herstellen, die z. B. für katalytische Anwendungen relevant sein könnten.

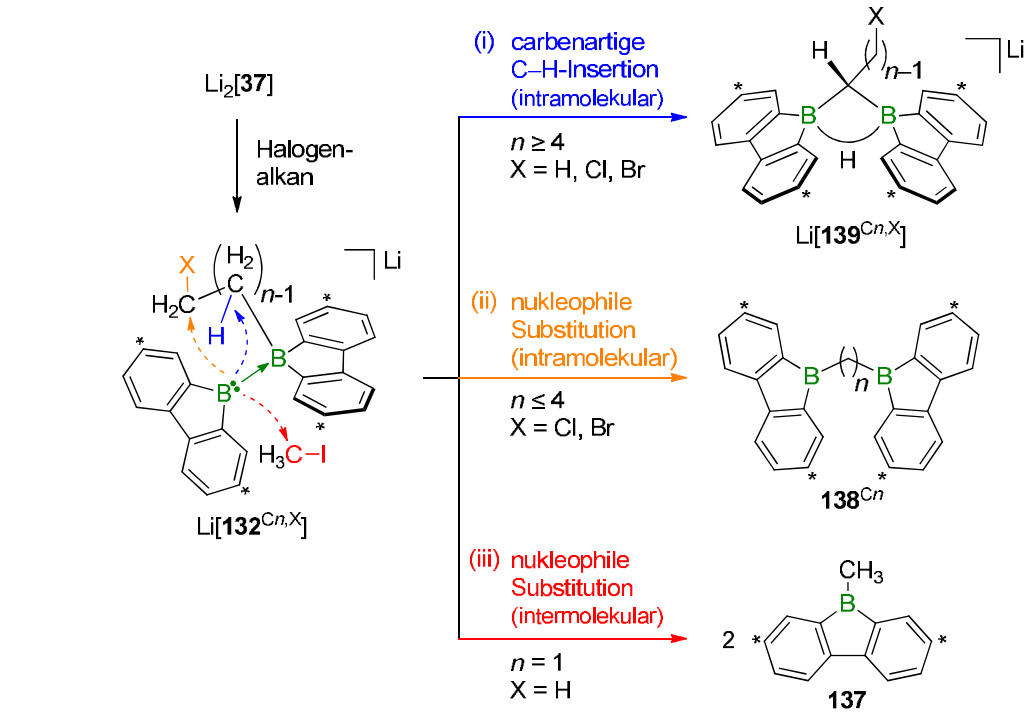

Schema 64. Durch Zugabe unterschiedlicher Halogenalkane bzw. α,ω-Dihalogenalkane zu Li_2[**37**] entstehen die Intermediate Li[**132**^{Cn,X}], die in Abhängigkeit der Alkylkette unter (i) intramolekularer C–H-Aktivierung zu Li[**139**^{Cn,X}], (ii) intramolekularer Substitutionen einer Halogenfunktion zu **138**^{Cn} oder (iii) intermolekularer Substitution einer Halogenfunktion zu **137** reagieren. Kohlenstoffatome, die mit * gekennzeichnet sind, tragen *t*Bu-Gruppen.

Mit den an den Modellverbindungen **7** und **12** gewonnenen Erkenntnissen zu B–B-Bindungsbildungen, 1,2-Phenylverschiebungen und Hydridtransfers wurde anschließend die Reduktion von (**6**)$_2$ in THF näher untersucht. In diesem Lösungsmittel dissoziiert die Startverbindung zum Addukt **6**·THF. Bei Zugabe von Lithium entstehen Li_2[**37**] und Li_2[**6**] als Hauptprodukte sowie Li[**34**] und Li_4[**146**] als Nebenprodukte (Schema 65). Die neuen Verbindungen Li_2[**6**] und Li_4[**146**] wurden mittels Röntgenstrukturanalyse charakterisiert. Die Synthese von Li_4[**146**] konnte durch einen Wechsel des Lösungsmittels von THF zu Dimethoxyethan (DME) optimiert werden.

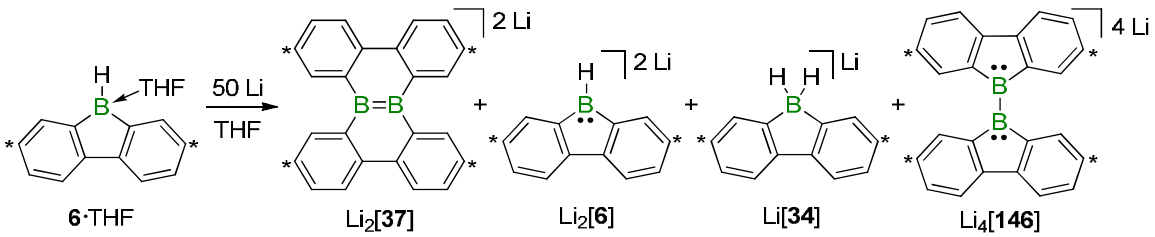

Schema 65. Durch Reduktion von **6**·THF mit Lithium in THF entstehen Li_2[**37**], Li_2[**6**], Li[**34**] und Li_4[**146**]. Kohlenstoffatome, die mit * gekennzeichnet sind, tragen *t*Bu-Gruppen.

Ausgehend vom 9-Borafluoren-Dianion [**6**]$^{2-}$, das bei tiefen Temperaturen quantitativ zugänglich gemacht wurde, konnte eine Reaktionsfolge etabliert werden, über die die Produkte [**34**]$^{-}$, [**35**]$^{-}$, [**36**]$^{-}$, [**113**]$^{2-}$, [**116**]$^{-}$, [**147**]$^{-}$ und [**37**]$^{2-}$ zugänglich sind (Schema 66). Dabei wird [**6**]$^{2-}$ als Nucleophil mit **6**·THF oder Et_3SiBr zur Reaktion gebracht, um eine B–B- ([**113**]$^{2-}$) oder B–Si-Bindung ([**36**]$^{-}$) zu bilden (radikalischer Mechanismus nicht ausgeschlossen). Die Verbindungen [**34**]$^{-}$, [**116**]$^{-}$ und [**35**]$^{-}$/[**147**]$^{-}$ entstehen anschließend durch Reaktion von [**113**]$^{2-}$ mit **6**·THF, wobei Hydridübertragungen und Umlagerungen stattfinden. [**37**]$^{2-}$ geht aus [**116**]$^{-}$ durch Reduktion hervor.

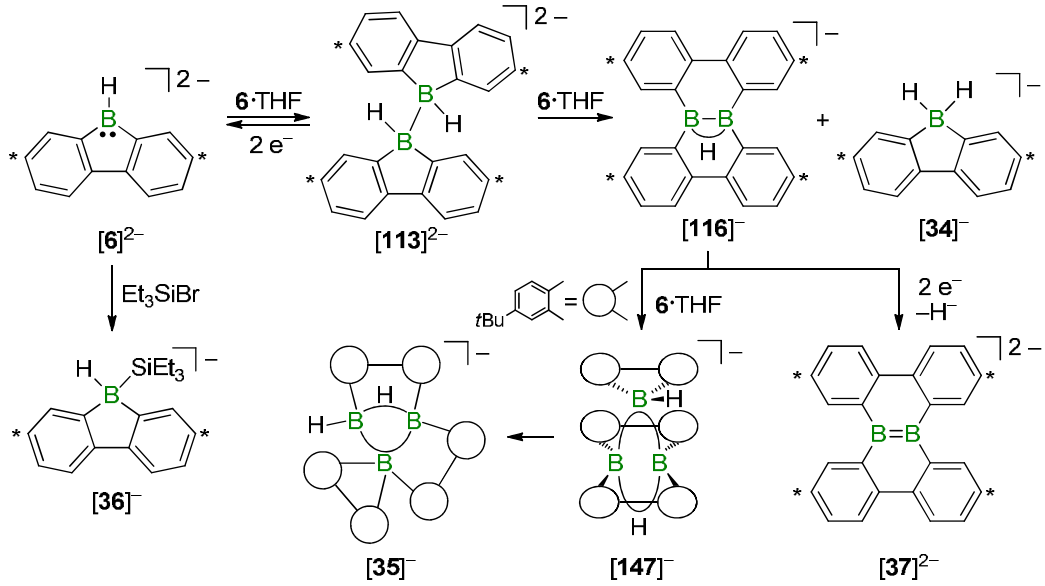

Schema 66. Reaktionspfade zur Darstellung von [**34**]$^{-}$, [**35**]$^{-}$, [**36**]$^{-}$, [**113**]$^{2-}$, [**116**]$^{-}$, [**147**]$^{-}$ und [**37**]$^{2-}$ ausgehend von [**6**]$^{2-}$. Kohlenstoffatome, die mit * gekennzeichnet sind, tragen *t*Bu-Gruppen.

Die Ergebnisse dieser Arbeit liefern fundamentale Erkenntnisse zur Chemie nucleophiler Borzentren, die unter B·B-, B–B- und B=B-Bindungsbildungen reagieren. Zusammen mit den aufgedeckten Prinzipien zu e^{-}-induzierten Umlagerungen des 9-Borafluorengrundgerüsts und Übertragungen von Hydridionen liegt nun ein umfassendes mechanistisches Wissen vor, dass die effiziente Synthese neuartiger Moleküle ermöglicht.

4 Experimentelle Daten nicht publizierter Verbindungen

4.1 Allgemeine Arbeitstechniken

Die Handhabung luftempfindlicher Verbindungen erfolgte in einer mit Argon (5.0) gefüllten Glovebox oder unter Verwendung von gängigen Schlenk-Arbeitstechniken in einer Inertgasatmosphäre (Argon oder Stickstoff). THF und THF-d_8 wurden mithilfe von Na/K-Legierungen getrocknet, durch vier Einfrieren-Pumpen-Auftauen-Cyclen entgast und anschließend über aktiviertem Molekularsieb (3.0 Å) gelagert. Die Synthese von (**6**)$_2$ in Benzol ist literaturbekannt.[66] Zur Aufreinigung wurden alle flüchtigen Bestandteile der Reaktionslösung im dynamischen Vakuum entfernt und der hochviskose Rückstand in wenig Pentan (≈ 1 mL / 750 mg (**6**)$_2$ [theoretische Ausbeute]) aufgenommen. (**6**)$_2$ kristallisiert aus dieser Lösung bei Raumtemperatur innerhalb weniger Minuten bis Stunden. Durch Lösen von (**6**)$_2$ in THF bildet sich **6**·THF.[65] Die Darstellung von **7** erfolgte nach der Literaturvorschrift (Anmerkung: Es wurden 90 µL *t*BuCCH verwendet).[64]

4.1.1 NMR-Spektroskopie

Alle NMR-spektroskopischen Messungen erfolgten bei 298 K an NMR-Spektrometern der Firma *Bruker* mit den hier angegebenen Messfrequenzen:
Avance-300 (^{1}H: 300.0 MHz, ^{11}B: 96.3 MHz, ^{13}C: 75.4 MHz),
Avance-500 (^{1}H: 500.2 MHz, ^{11}B: 160.5 MHz, ^{13}C: 125.8 MHz).
Die Angabe der chemischen Verschiebungen δ erfolgt in ppm (tiefes Feld: positives Vorzeichen) und die der Kopplungskonstanten *J* in Hz. Als interner Standard diente das Signal des (unvollständig) deuterierten Lösungsmittels (THF-d_8: $\delta(^1\text{H})$ = 3.58, $\delta(^{13}\text{C}\{^1\text{H}\})$ = 67.21).[312]
Mit den Abkürzungen s (Singulett), d (Dublett), t (Triplett), br (verbreitert), vbr (stark verbreitert), m (Multiplett), dd (Dublett von Dubletts) und n. b. (nicht beobachtet) werden die Multiplizitäten der Signale angegeben. Zur Strukturaufklärung und Signalzuordnung wurden neben homonuclearen, eindimensionalen NMR-Experimenten auch die Korrelationsexperimente ^{1}H-^{1}H-COSY, ^{1}H-^{13}C-HSQC, ^{1}H-^{11}B-HSQC, ^{1}H-^{13}C-HMBC und ^{1}H-^{11}B-HMBC eingesetzt.

4.1.2 Einkristall-Röntgendiffraktometrie

Sämtliche Daten der Röntgenbeugungsexperimente an Einkristallen wurden an einem *STOE IPDS II* Zweikreisdiffraktometer mit einer Genix Mikrofokusröhre, Spiegeloptiken und MoK_α-Strahlung (λ = 0.71073 Å) aufgenommen. Die Skalierung der Daten erfolgte mit der *frame-scaling Prozedur* des *X-AREA* Programms.[313] Die Strukturen wurden über direkte Methoden unter Verwendung des Programms *SHELXS* gelöst und gegen F^2 mit *full-matrix least-square* Techniken mithilfe des Programms *SHELXL* verfeinert.[314]

4.2 Synthese und NMR-Daten unpublizierter Verbindungen

4.2.1 Li_2[**6**]

Zu einer gerührten und auf –78 °C gekühlten Suspension von Lithium (28 mg, 4.0 mmol) in THF (1 mL) wurde über 10 min eine Lösung von (**6**)$_2$ (103 mg, 0.189 mmol) in THF (1.5 mL) getropft. Nach 2 h bei –78 °C und 22 h bei RT wurde die dunkelgrüne Reaktionslösung für NMR-spektroskopische Untersuchungen mithilfe einer Spritze von verbliebenem Lithium separiert, alle flüchtigen Bestandteile im Vakuum entfernt und der Rückstand in THF-d_8 (0.5 mL) gelöst. Li_2[**6**] kristallisiert aus einer konzentrierten THF-Lösung bei –78 °C (≈ 100 mg/0.4 mL).

^{1}H-NMR (500.2 MHz, THF-d_8): δ = 7.88 (dd, ^3J(H,H) = 8.6 Hz, ^5J(H,H) = 0.7 Hz, 2H; H-4), 7.71 (dd, ^4J(H,H) = 2.0 Hz, ^5J(H,H) = 0.7 Hz, 2H; H-1), 6.34 (dd, ^3J(H,H) = 8.6 Hz, ^4J(H,H) = 2.0 Hz, 2H; H-3), 4.37 (br, 1H; BH), 1.34 (s, 18H; CH_3).
^{11}B-NMR (160.5 MHz, THF-d_8): δ = 3.6 (br d, ^1J(B,H) ≈ 80 Hz, $h_{1/2}$ ≈ 240 Hz).
^{13}C{^{1}H}-NMR (125.8 MHz, THF-d_8): δ = 133.6 (C-2), 131.3 (br, C-6), 125.3 (C-1), 120.6 (C-4), 114.8 (C-5), 108.4 (C-3), 34.9 (CCH$_3$), 32.4 (CH$_3$).
Anmerkung: δ(^{1}H) variiert in Abhängigkeit der Konzentration um ±0.05 ppm.

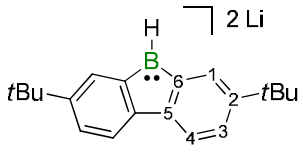

Li_2[**6**]

4.2.2 Li_4[**7**]

Zu einer Lösung von **7** (21 mg, 0.051 mmol) in THF-d_8 (0.8 mL) erfolgte die Zugabe von Lithium (21 mg, 3.0 mmol). Nach 5 h Rühren wurde die dunkelrote Reaktionslösung mithilfe einer Spritze von verbliebenem Lithium abgetrennt und in ein NMR-Rohr überführt. Für die Kristallisation wurde die Probe zum Verdampfen des Lösungsmittels offen gelagert und der Rückstand in Et_2O (0.3 mL) aufgenommen. Dunkelrote Plättchen von [Li(thf)]$_2$[Li(Et_2O)][Li(Et_2O)(thf)][**7**] wuchsen durch langsames Verdampfen des Lösungsmittels bei –30°C.

^{1}H-NMR (500.2 MHz, THF-d_8): δ = 8.19 (d, ^3J(H,H) = 8.2 Hz, 4H), 7.84 (d, ^3J(H,H) = 8.2 Hz, 4H), 6.37–6.34 (m, 4H), 6.11–6.08 (m, 4H), 2.89 (d, ^3J(H,H) = 5.8 Hz, 2H; CHCH_2), 2.83 (t, ^3J(H,H) = 5.8 Hz, 1H; CHCH$_2$), 1.13 (s, 9H; CH$_3$).
^{11}B-NMR (160.5 MHz, THF-d_8): δ = 18.4 (br, $h_{1/2}$ ≈ 750 Hz).
^{13}C{^{1}H}-NMR (125.8 MHz, THF-d_8): δ = 128.7, 121.5, 121.3 (br), 115.0, 114.8, 108.5, 53.6 (CHCH$_2$), 34.1 (CCH$_3$), 30.9 (CH$_3$), 10.7 (CHCH$_2$).
Anmerkung: δ(^{1}H) variiert in Abhängigkeit der Konzentration um ±0.06 ppm.

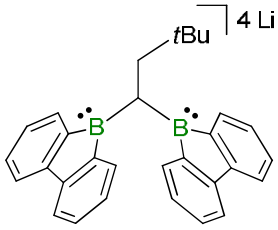

Li_4[**7**]

4.2.3 Li_4[**146**]

Synthese in THF:
Die Zugabe von THF (3 mL) zu einer Feststoffmischung aus (**6**)$_2$ (200 mg, 0.36 mmol) und Lithium (126 mg, 18.1 mmol) erzeugte eine tief dunkelrote Lösung. Nicht reagiertes Lithium wurde nach 6 h durch Filtration über eine Glasfritte abgetrennt (Anteile der Produkte im Filtrat gemäß ^{1}H-NMR-Spektrum (THF-d_8): Li_4[**146**] ≈ 6%, Li_2[**37**] ≈ 38%, Li_2[**6**] ≈ 35%). Bei –30 °C kristallisierte ein Großteil von Li_2[**37**] aus der Reaktionslösung (24 h). Die überstehende Lösung wurde mit einer Spritze separiert und im dynamischen Vakuum auf etwas weniger als 1 mL eingeengt. Die erneute Lagerung bei –30 °C ließ $[Li(thf)_2]_2[Li_2(thf)_3]$[**146**] innerhalb von 20 Tagen in Form schwarzer Blöcke wachsen, die manuell von schwarzen Nadeln ($[Li_2(thf)_3]$[**6**]) separiert wurden.

Synthese in DME:
Verbindung (**6**)$_2$ (100 mg, 0.18 mmol) wurde in DME (1.5 mL) gelöst. Die Zugabe von Lithium (60 mg, 8.6 mmol) erzeugte innerhalb von 5 min eine tief dunkelrote Reaktionslösung. Nach 20 h wurde die Mischung über eine Glasfritte filtriert. Gemäß ^{1}H-NMR-spektroskopischer Untersuchung bestand der in THF-d_8 lösliche Teil des Filterkuchens aus Li_2[**37**]. Das Filtrat wies mehr als sieben Komponenten auf, mit Li_4[**146**] als Hauptverbindung (≈ 25%). Durch Kristallisation bei –30 °C wurde ein schwarzer Feststoff erhalten (≈ 80 mg), der laut ^{1}H-NMR-Spektrum ca. 50% Li_4[**146**] enthielt. Zwei rautenförmige Blöcke wurden röntgenkristallographisch vermessen: beide Kristalle bestanden aus $[Li(dme)]_4$[**146**].

^{1}H-NMR (500.2 MHz, THF-d_8): δ = 8.10 (d, ^4J(H,H) = 2.0 Hz, 4H; H-1), 7.96 (d, ^3J(H,H) = 8.5 Hz, 4H; H-4), 6.38 (dd, ^3J(H,H) = 8.5 Hz, ^4J(H,H) = 2.0 Hz, 4H; H-3), 1.35 (s, 36H; CH_3).
^{11}B-NMR (160.5 MHz, THF-d_8): δ = 12.3 (br, $h_{1/2}$ ≈ 450 Hz).
^{13}C{^{1}H}-NMR (125.8 MHz, THF-d_8): δ = 136.3 (C-6), 132.6 (C-2), 127.1 (C-1), 120.7 (C-4), 118.4 (C-5), 108.2 (C-3), 35.1 (*C*CH_3), 32.7 (CH_3).

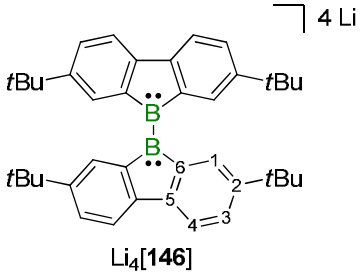

Li_4[**146**]

4.2.4 Li[**147**]

THF-d_8 (0.5 mL) wurde zu einer Mischung aus (**6**)$_2$ (8 mg, 14 µmol) und [Li(thf)$_3$][**116**] (22 mg, 28 µmol) gegeben. Die ^{1}H-NMR-spektroskopische Kontrolle zeigte die Umsetzung beider Edukte zu Li[**147**] (Strukturvorschlag). Langsames Abdampfen des Lösungsmittels ließ kleine Plättchen kristallisieren, von denen drei mittels Röntgenbeugungsexperimenten untersucht wurden. In allen Fällen waren die Zellparameter identisch mit den literaturbekannten Daten von [Li(thf)$_4$][**35**].[108] Die ^{1}H-NMR-spektroskopische Analyse (THF-d_8) des Feststoffs bestätigte die Umlagerung von [**147**]$^-$ zu [**35**]$^-$ im Zuge der Kristallisation.

^{1}H-NMR (500.2 MHz, THF-d_8): δ = 7.84 (d, ^4J(H,H) = 2.3 Hz, 4H; H-1a), 7.76 (d, ^3J(H,H) = 8.4 Hz, 4H; H-4a), 7.22 (d, ^3J(H,H) = 7.8 Hz, 2H; H-4b), 7.02 (dd, ^3J(H,H) = 8.4 Hz, ^4J(H,H) = 2.3 Hz, 4H; H-3a), 6.86 (dd, ^3J(H,H) = 7.8 Hz, ^4J(H,H) = 1.9 Hz, 2H; H-3b), 6.13 (d, ^4J(H,H) = 1.9 Hz, 2H; H-1b), 3.28 (br, 2H), 1.21 (s, 36H, CH_3-a), 0.96 (s, 18H, CH_3-b)
^{11}B-NMR (160.5 MHz, THF-d_8): δ = 4 (vbr), –17.7 (br).
^{13}C{^{1}H}-NMR (125.8 MHz, THF-d_8): δ = 151.1 (br, C-6b), 146.7 (C-2b), 146.5 (C-5b), 145.9 (br, C-6a), 145.7 (C-2a), 140.8 (C-5a), 137.1 (C-1a), 130.7 (C-1b), 123.3 (C-4a), 122.7 (C-3b), 122.0 (C-3a), 117.0 (C-4b), 34.8 (*C*CH_3-b), 34.6 (*C*CH_3-a), 32.2 (CH_3-b), 32.0 (CH_3-a).

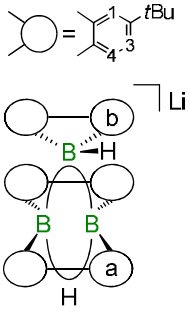

Li[**147**]

4.2.5 Li[**149**] und Li[**150**]

Methode I:
Im Rahmen der Studie aus Kapitel 2.3.5 wurde Li_2[**6**] (ca. 70 µmol) in THF-d_8 (0.5 mL) in mehreren Experimenten mit unterschiedlichen Mengen an 1,2-Dibromethan (DBE) versetzt. Gemäß ^{1}H-NMR-spektroskopischer Untersuchungen lag bei 0.75 Äquivalenten an DBE ein hoher Anteil an Li[**149**]/Li[**150**] in Lösung vor.

Methode II:
In einem NMR-Rohr wurde eine Lösung von [Li(thf)$_3$][**116**] (5 mg, 6 µmol) in THF-d_8 (0.5 mL) bei –196 °C gefroren. Das Rohr wurde evakuiert und anschließend eine Atmosphäre Ethen eingeleitet. Die gefrorene Lösung wurde aufgetaut und das NMR-Rohr mehrfach geschwenkt. Nach dem erneuten Einfrieren der Reaktionslösung erfolgte das Abschmelzen des NMR-Rohrs im dynamischen Vakuum und das erneute Auftauen des Reaktionsgemischs.

Li[**149**]:
^{1}H-NMR (500.2 MHz, THF-d_8): δ = 8.13 (d, ^4J(H,H) = 1.8 Hz, 4H; H-1), 7.25 (d, ^3J(H,H) = 7.8 Hz, 4H; H-4), 7.00 (dd, ^3J(H,H) = 7.8 Hz, ^4J(H,H) = 1.8 Hz, 4H; H-3), 1.44 (s, 4H; CH_2), 1.37 (s, 36H, CH_3), n. b. (BH).
^{11}B-NMR (160.5 MHz, THF-d_8): δ = 8.3 (br).
^{13}C{^{1}H}-NMR (125.8 MHz, THF-d_8): δ = 158.4 (C-6), 146.9 (C-5), 146.9 (C-2), 128.5 (C-1), 122.7 (C-3), 117.4 (C-4), 35.1 (CCH_3), 32.5 (CH_3), 15.3 (CH_2).

Li[**150**]:
^{1}H-NMR (300.0 MHz, THF-d_8): δ = 7.99 (d, ^4J(H,H) = 2.1 Hz, 4H; H-1), 7.29 (d, ^3J(H,H) = 7.8 Hz, 4H; H-4), 6.99 (dd, ^3J(H,H) = 7.8 Hz, ^4J(H,H) = 2.1 Hz, 4H; H-3), 1.38 (s, 36H, CH_3), n. b. (BH, CH_2).
Die ^{1}H-NMR-Daten für Li[**150**] sind mit Werten von Timo Trageser abgeglichen und vervollständigt, da er die Verbindung bei mehrfacher Reproduktion der Reaktion von Li[**116**] mit Ethen zum Teil in einem höheren Anteil erhalten hat.[311]

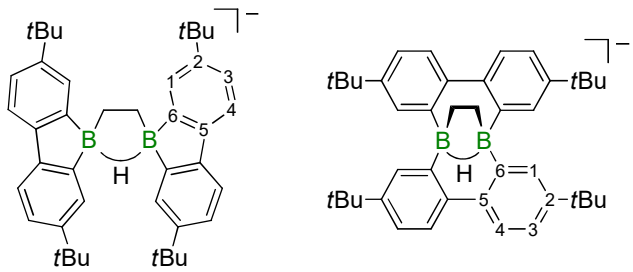

[**149**]$^-$ / [**150**]$^-$

4.3 Kristallographische Daten unpublizierter Verbindungen

Tabelle 4. Kristallographische Daten von $[Li_2(thf)_3]$[**6**] und $[Li(thf)]_2[Li(Et_2O)][Li(Et_2O)(thf)]$[**7**].

	$[Li_2(thf)_3]$[**6**]	$[Li(thf)]_2[Li(Et_2O)][Li(Et_2O)(thf)]$[**7**]
Interner Code	wa2221	wa2448
Summenformel	$C_{32}H_{49}BLi_2O_3$	$C_{50}H_{72}B_2Li_4O_5$
M_r [g mol^{-1}]	506.40	802.45
Farbe, Morphologie	schwarz, Nadel	dunkelrot, Plättchen
T [K]	173(2)	173(2)
Strahlung, λ [Å]	MoK_α, 0.71073	MoK_α, 0.71073
Kristallsystem	monoklin	monoklin
Raumgruppe	$P2_1/c$	$P2_1/n$
a [Å]	7.051(3)	16.5414(8)
b [Å]	13.694(3)	16.7794(8)
c [Å]	30.783(15)	18.6982(9)
α [°]	90	90
β [°]	91.81(4)	112.175(4)
γ [°]	90	90
V [Å^3]	2971(2)	4805.9(4)
Z	4	4
$D_{berechnet}$ [g cm^{-3}]	1.132	1.109
μ [mm^{-1}]	0.068	0.067
F(000)	1104	1736
Kristallgröße [mm^3]	0.19 x 0.09 x 0.08	0.22 x 0.19 x 0.11
Gesammelte Reflexe	20350	47279
Unabhängige Reflexe (R_{int})	20350	8466 (0.0633)
Daten/Restraints/ Parameter	20350 / 615 / 348	8466 / 118 / 615
GOF on F^2	0.865	1.171
R_1, wR_2 [$I > 2\sigma(I)$]	0.1138, 0.1559	0.0727, 0.1535
R_1, wR_2 (alle Daten)	0.3129, 0.2489	0.1035, 0.1649
Restelektronendichte (peak and hole) [e Å^{-3}]	0.392, –0.414	0.431, –0.298

Tabelle 5. Kristallographische Daten von $[Li(thf)_2]_2[Li_2(thf)_3]$[**146**], $[Li(dme)]_4$[**146**] und $[Na(thf)_2]_2$[**148**].

	$[Li(thf)_2]_2[Li_2(thf)_3]$[**146**]	$[Li(dme)]_4$[**146**]	$[Na(thf)_2]_2$[**148**]
Interner Code	wa2220	wa2198	wa2515
Summenformel	$C_{68}H_{104}B_2Li_4O_7$	$C_{56}H_{88}B_2Li_4O_8$	$C_{58}H_{86}B_2Na_2O_4$
M_r [g mol^{-1}]	1082.89	938.64	914.86
Farbe, Morphologie	schwarz, Block	schwarz, Block	farblos, Block
T [K]	173(2)	173(2)	173(2)
Strahlung, λ [Å]	MoK_α, 0.71073	MoK_α, 0.71073	MoK_α, 0.71073
Kristallsystem	orthorhombisch	monoklin	monoklin
Raumgruppe	*Pbcn*	*C*2/*c*	$P2_1/n$
a [Å]	14.5844(4)	22.502(3)	14.1783(10)
b [Å]	20.0136(7)	13.8076(16)	24.524(3)
c [Å]	22.2645(7)	22.056(4)	15.9758(12)
α [°]	90	90	90
β [°]	90	119.826(11)	99.598(6)
γ [°]	90	90	90
V [Å^3]	6498.7(4)	5945.0(16)	5477.2(9)
Z	4	4	4
$D_{berechnet}$ [g cm^{-3}]	1.107	1.049	1.109
μ [mm^{-1}]	0.068	0.066	0.080
F(000)	2360	2040	1992
Kristallgröße [mm^3]	0.29 x 0.28 x 0.26	0.19 x 0.11 x 0.10	0.18 x 0.14 x 0.12
Gesammelte Reflexe	61578	19966	33617
Unabhängige Reflexe (R_{int})	5755 (0.0705)	5242 (0.1242)	9657 (0.1525)
Daten/Restraints/ Parameter	5755 / 24 / 376	5242 / 0 / 316	9657 / 84 / 669
GOF on F^2	1.126	0.949	0.835
R_1, wR_2 [$I > 2\sigma(I)$]	0.0806, 0.1836	0.0825, 0.1344	0.0702, 0.1043
R_1, wR_2 (alle Daten)	0.1015, 0.1950	0.1842, 0.1674	0.1919, 0.1367
Restelektronendichte (peak and hole) [e Å^{-3}]	0.400, –0.371	0.250, –0.188	0.224, –0.228

5 Referenzen

[1] E. Hückel, *Z. Phys.* **1931**, *70*, 204-286.

[2] K. B. Wiberg, *Chem. Rev.* **2001**, *101*, 1317-1331.

[3] A. A. Frost und B. Musulin, *J. Chem. Phys.* **1953**, *21*, 572-573.

[4] A. D. Walsh, *J. Chem. Soc.* **1953**, 2260-2266.

[5] E. P. F. Lee und T. G. Wright, *Phys. Chem. Chem. Phys.* **1999**, *1*, 219-225.

[6] A. D. Allen und T. T. Tidwell, *Chem. Rev.* **2001**, *101*, 1333-1348.

[7] J. Thiele, *Ber. Dtsch. Chem. Ges.* **1900**, *33*, 666-673.

[8] P. Jutzi und N. Burford, *Chem. Rev.* **1999**, *99*, 969-990.

[9] E. Wasserman und R. S. Hutton, *Acc. Chem. Res.* **1977**, *10*, 27-32.

[10] M. Saunders, R. Berger, A. Jaffe, J. M. McBride, J. O'Neill, R. Breslow, J. M. Hoffman (Jr.), C. Perchonock, E. Wasserman, R. S. Hutton und V. J. Kuck, *J. Am. Chem. Soc.* **1973**, *95*, 3017-3018.

[11] H. Vančik, I. Novak und D. Kiđemet, *J. Phys. Chem. A* **1998**, *102*, 8437-8438.

[12] P. von Ragué Schleyer, P. K. Freeman, H. Jiao und B. Goldfuss, *Angew. Chem. Int. Ed.* **1995**, *34*, 337-340.

[13] H. Jiao, P. von Ragué Schleyer, Y. Mo, M. A. McAllister und T. T. Tidwell, *J. Am. Chem. Soc.* **1997**, *119*, 7075-7083.

[14] M. K. Cyrañski, T. M. Krygowski, A. R. Katritzky und P. von Ragué Schleyer, *J. Org. Chem.* **2002**, *67*, 1333-1338.

[15] G. E. Herberich, B. Hessner und R. Saive, *J. Organomet. Chem.* **1987**, *319*, 9-27.

[16] G. E. Herberich und M. Negele, *J. Organomet. Chem.* **1988**, *350*, 81-89.

[17] G. E. Herberich, U. Englert, M. Hostalek und R. Laven, *Chem. Ber.* **1991**, *124*, 17-23.

[18] P. J. Fagan, E. G. Burns und J. C. Calabrese, *J. Am. Chem. Soc.* **1988**, *110*, 2979-2981.

[19] J. J. Eisch, N. K. Hota und S. Kozima, *J. Am. Chem. Soc.* **1969**, *91*, 4575-4577.

[20] H. Braunschweig, I. Fernández, G. Frenking und T. Kupfer, *Angew. Chem. Int. Ed.* **2008**, *47*, 1951-1954.

[21] J. J. Eisch, J. E. Galle und S. Kozima, *J. Am. Chem. Soc.* **1986**, *108*, 379-385.

[22] C.-W. So, D. Watanabe, A. Wakamiya und S. Yamaguchi, *Organometallics* **2008**, *27*, 3496-3501.

[23] H. Braunschweig, V. Dyakonov, J. O. C. Jimenez-Halla, K. Kraft, I. Krummenacher, K. Radacki, A. Sperlich und J. Wahler, *Angew. Chem. Int. Ed.* **2012**, *51*, 2977-2980.

[24] P. Bissinger, H. Braunschweig, A. Damme, C. Hörl, I. Krummenacher und T. Kupfer, *Angew. Chem. Int. Ed.* **2015**, *54*, 359-362.

[25] J. J. Eisch und J. E. Galle, *J. Am. Chem. Soc.* **1975**, *97*, 4436-4437.

[26] S. A. Couchman, T. K. Thompson, D. J. D. Wilson, J. L. Dutton und C. D. Martin, *Chem. Commun.* **2014**, *50*, 11724-11726.

[27] H. Braunschweig, C. Hörl, L. Mailänder, K. Radacki und J. Wahler, *Chem. - Eur. J.* **2014**, *20*, 9858-9861.

[28] H. Braunschweig, M. A. Celik, F. Hupp, I. Krummenacher und L. Mailänder, *Angew. Chem. Int. Ed.* **2015**, *54*, 6347-6351.

[29] K. Huang und C. D. Martin, *Inorg. Chem.* **2015**, *54*, 1869-1875.

[30] K. Huang, S. A. Couchman, D. J. D. Wilson, J. L. Dutton und C. D. Martin, *Inorg. Chem.* **2015**, *54*, 8957-8968.

[31] J. H. Barnard, S. Yruegas, K. Huang und C. D. Martin, *Chem. Commun.* **2016**, *52*, 9985-9991.

[32] C. Fan, L. G. Mercier, W. E. Piers, H. M. Tuononen und M. Parvez, *J. Am. Chem. Soc.* **2010**, *132*, 9604-9606.

[33] A. Y. Houghton, V. A. Karttunen, C. Fan, W. E. Piers und H. M. Tuononen, *J. Am. Chem. Soc.* **2013**, *135*, 941-947.

[34] Z.-W. Qu und H. Zhu, *J. Phys. Chem. C* **2013**, *117*, 11989-11993.

[35] H. Braunschweig, A. Damme, C. Hörl, T. Kupfer und J. Wahler, *Organometallics* **2013**, *32*, 6800-6803.
[36] B. C. Caputo, Z. J. Manning, J. H. Barnard und C. D. Martin, *Polyhedron* **2016**, *114*, 273-277.
[37] E. von Grotthuss, A. John, T. Kaese und M. Wagner, *Asian J. Org. Chem.* **2018**, *7*, 37-53.
[38] S. Pogodin und I. Agranat, *J. Org. Chem.* **2007**, *72*, 10096-10107.
[39] P. Costa, I. Trosien, M. Fernandez-Oliva, E. Sanchez-Garcia und W. Sander, *Angew. Chem. Int. Ed.* **2015**, *54*, 2656-2660.
[40] R. Köster und G. Benedikt, *Angew. Chem.* **1963**, *75*, 419.
[41] C. K. Narula und H. Nöth, *Inorg. Chem.* **1985**, *24*, 2532-2539.
[42] C. K. Narula und H. Nöth, *J. Organomet. Chem.* **1985**, *281*, 131-134.
[43] U. Gross und D. Kaufmann, *Chem. Ber.* **1987**, *120*, 991-994.
[44] P. A. Chase, W. E. Piers und B. O. Patrick, *J. Am. Chem. Soc.* **2000**, *122*, 12911-12912.
[45] R. J. Wehmschulte, M. A. Khan, B. Twamley und B. Schiemenz, *Organometallics* **2001**, *20*, 844-849.
[46] S. Yamaguchi, T. Shirasaka, S. Akiyama und K. Tamao, *J. Am. Chem. Soc.* **2002**, *124*, 8816-8817.
[47] R. J. Wehmschulte, A. A. Diaz und M. A. Khan, *Organometallics* **2003**, *22*, 83-92.
[48] P. E. Romero, W. E. Piers, S. A. Decker, D. Chau, T. K. Woo und M. Parvez, *Organometallics* **2003**, *22*, 1266-1274.
[49] J. D. Hoefelmeyer, S. Solé und F. P. Gabbaï, *Dalton Trans.* **2004**, 1254-1258.
[50] P. A. Chase, L. D. Henderson, W. E. Piers, M. Parvez, W. Clegg und M. R. J. Elsegood, *Organometallics* **2006**, *25*, 349-357.
[51] A. Wakamiya, K. Mishima, K. Ekawa und S. Yamaguchi, *Chem. Commun.* **2008**, 579-581.
[52] L. Kaufmann, H. Vitze, M. Bolte, H.-W. Lerner und M. Wagner, *Organometallics* **2008**, *27*, 6215-6221.
[53] S. P. Lewis, J. Chai, S. Collins, T. J. J. Sciarone, L. D. Henderson, C. Fan, M. Parvez und W. E. Piers, *Organometallics* **2009**, *28*, 249-263.
[54] A. Hübner, H.-W. Lerner, M. Wagner und M. Bolte, *Acta Cryst.* **2010**, *E66*, o444.
[55] S. Biswas, I. M. Oppel und H. F. Bettinger, *Inorg. Chem.* **2010**, *49*, 4499-4506.
[56] A. Iida, A. Sekioka und S. Yamaguchi, *Chem. Sci.* **2012**, *3*, 1461-1466.
[57] M. F. Smith, S. J. Cassidy, I. A. Adams, M. Vasiliu, D. L. Gerlach, D. A. Dixon und P. A. Rupar, *Organometallics* **2016**, *35*, 3182-3191.
[58] D. R. Armstrong und P. G. Perkins, *J. Chem. Soc. A* **1966**, 1026-1031.
[59] R.-F. Chen, C. Zheng, Q.-L. Fan und W. Huang, *J. Comput. Chem.* **2007**, *28*, 2091-2101.
[60] A. Iida und S. Yamaguchi, *J. Am. Chem. Soc.* **2011**, *133*, 6952-6955.
[61] J. F. Araneda, B. Neue, W. E. Piers und M. Parvez, *Angew. Chem. Int. Ed.* **2012**, *51*, 8546-8550.
[62] J. F. Araneda, W. E. Piers, M. J. Sgro und M. Parvez, *Chem. Sci.* **2014**, *5*, 3189-3196.
[63] A. Das, A. Hübner, M. Weber, M. Bolte, H.-W. Lerner und M. Wagner, *Chem. Commun.* **2011**, *47*, 11339-11341.
[64] A. Hübner, Z.-W. Qu, U. Englert, M. Bolte, H.-W. Lerner, M. C. Holthausen und M. Wagner, *J. Am. Chem. Soc.* **2011**, *133*, 4596-4609.
[65] T. Kaese, A. Hübner, M. Bolte, H.-W. Lerner und M. Wagner, *J. Am. Chem. Soc.* **2016**, *138*, 6224-6233.
[66] A. Hübner, M. Diefenbach, M. Bolte, H.-W. Lerner, M. C. Holthausen und M. Wagner, *Angew. Chem. Int. Ed.* **2012**, *51*, 12514-12518.
[67] I. Gorokhovik, S. Rieder, G. Povie und P. Renaud, *Arkivoc* **2014**, *2014*, 274-286.
[68] M. Grandl, T. Kaese, A. Krautsieder, Y. Sun und F. Pammer, *Chem. - Eur. J.* **2016**, *22*, 14373-14382.
[69] U. Salzner, J. B. Lagowski, P. G. Pickup und R. A. Poirier, *Synth. Met.* **1998**, *96*, 177-189.
[70] S. Yamaguchi und K. Tamao, *Chem. Lett.* **2005**, *34*, 2-7.

[71] A. Wakamiya und S. Yamaguchi, *Bull. Chem. Soc. Jpn.* **2015**, *88*, 1357-1377.

[72] C. Summerford und K. Wade, *J. Chem. Soc. A* **1970**, 2010-2016.

[73] L. Komorowski, W. Maringgele, A. Meller, K. Niedenzu und J. Serwatowski, *Inorg. Chem.* **1990**, *29*, 3845-3849.

[74] D. Männig, H. Nöth, H. Prigge, A.-R. Rotsch, S. Gopinathan und J. W. Wilson, *J. Organomet. Chem.* **1986**, *310*, 1-20.

[75] J. Knizek und H. Nöth, *J. Organomet. Chem.* **2000**, *614-615*, 168-187.

[76] J.-H. Son und J. D. Hoefelmeyer, *Org. Biomol. Chem.* **2012**, *10*, 6656-6664.

[77] C. J. Berger, G. He, C. Merten, R. McDonald, M. J. Ferguson und E. Rivard, *Inorg. Chem.* **2014**, *53*, 1475-1486.

[78] S. Bontemps, M. Devillard, S. Mallet-Ladeira, G. Bouhadir, K. Miqueu und D. Bourissou, *Inorg. Chem.* **2013**, *52*, 4714-4720.

[79] J. M. Breunig, A. Hübner, M. Bolte, M. Wagner und H.-W. Lerner, *Organometallics* **2013**, *32*, 6792-6799.

[80] S. Biswas, C. Maichle-Mössmer und H. F. Bettinger, *Chem. Commun.* **2012**, *48*, 4564-4566.

[81] M. Müller, C. Maichle-Mössmer und H. F. Bettinger, *Angew. Chem. Int. Ed.* **2014**, *53*, 9380-9383.

[82] Y. Shoji, N. Tanaka, S. Muranaka, N. Shigeno, H. Sugiyama, K. Takenouchi, F. Hajjaj und T. Fukushima, *Nat. Commun.* **2016**, *7*, 12704.

[83] K. R. J. Thomas, J. T. Lin, Y.-T. Tao und C.-W. Ko, *J. Am. Chem. Soc.* **2001**, *123*, 9404-9411.

[84] J.-F. Morin und M. Leclerc, *Macromolecules* **2001**, *34*, 4680-4682.

[85] M. R. Craig, M. M. de Kok, J. W. Hofstraat, A. P. H. J. Schenning und E. W. Meijer, *J. Mater. Chem.* **2003**, *13*, 2861-2862.

[86] W. J. Grigsby und P. P. Power, *J. Am. Chem. Soc.* **1996**, *118*, 7981-7988.

[87] T. Muramatsu, A. Toyota, M. Kudou, Y. Ikegami und M. Watanabe, *J. Org. Chem.* **1999**, *64*, 7249-7253.

[88] T. Suzuki, T. Takeda, E. Ohta, K. Wada, R. Katoono, H. Kawai und K. Fujiwara, *Chem. Rec.* **2015**, *15*, 280-294.

[89] M. Horner und S. Hünig, *J. Am. Chem. Soc.* **1977**, *99*, 6122-6124.

[90] T. Suzuki, J.-i. Nishida und T. Tsuji, *Chem. Commun.* **1998**, 2193-2194.

[91] S. Hünig, M. Kemmer, H. Wenner, I. F. Perepichka, P. Bäuerle, A. Emge und G. Gescheid, *Chem. - Eur. J.* **1999**, *5*, 1969-1973.

[92] H. John, C. Briehn, J. Schmidt, S. Hünig und J. Heinze, *Angew. Chem. Int. Ed.* **2007**, *46*, 449-453.

[93] M. Gomberg, *J. Am. Chem. Soc.* **1900**, *22*, 757-771.

[94] M. Gomberg, *Ber. Dtsch. Chem. Ges.* **1900**, *33*, 3150-3163.

[95] H. Lankamp, W. T. Nauta und C. MacLean, *Tetrahedron Lett.* **1968**, *9*, 249-254.

[96] B. Kahr, D. Van Engen und K. Mislow, *J. Am. Chem. Soc.* **1986**, *108*, 8305-8307.

[97] J. P. Wagner und P. R. Schreiner, *Angew. Chem. Int. Ed.* **2015**, *54*, 12274-12296.

[98] P. Maslak und J. N. Narvaez, *Angew. Chem. Int. Ed.* **1990**, *29*, 283-285.

[99] P. Maslak, W. H. Chapman (Jr.), T. M. Vallombroso (Jr.) und B. A. Watson, *J. Am. Chem. Soc.* **1995**, *117*, 12380-12389.

[100] T. Suzuki, T. Takeda, H. Kawai und K. Fujiwara, *Pure Appl. Chem.* **2008**, *80*, 547-553.

[101] T. Suzuki, J.-i. Nishida und T. Tsuji, *Angew. Chem. Int. Ed.* **1997**, *36*, 1329-1331.

[102] T. Suzuki, A. Migita, H. Higuchi, H. Kawai, K. Fujiwara und T. Tsuji, *Tetrahedron Lett.* **2003**, *44*, 6837-6840.

[103] T. Suzuki, Y. Ishigaki, T. Iwai, H. Kawai, K. Fujiwara, H. Ikeda, Y. Kano und K. Mizuno, *Chem. - Eur. J.* **2009**, *15*, 9434-9441.

[104] J. D. Hoefelmeyer und F. P. Gabbaï, *J. Am. Chem. Soc.* **2000**, *122*, 9054-9055.

[105] A. Hübner, A. M. Diehl, M. Diefenbach, B. Endeward, M. Bolte, H.-W. Lerner, M. C. Holthausen und M. Wagner, *Angew. Chem. Int. Ed.* **2014**, *53*, 4832-4835.

[106] A. Hübner, T. Kaese, M. Diefenbach, B. Endeward, M. Bolte, H.-W. Lerner, M. C. Holthausen und M. Wagner, *J. Am. Chem. Soc.* **2015**, *137*, 3705-3714.
[107] H. M. Quitián-Lara, F. Fantuzzi, M. A. C. Nascimento, W. Wolff und H. M. Boechat-Roberty, *ApJ* **2018**, *854*, 61.
[108] A. Hübner, M. Bolte, H.-W. Lerner und M. Wagner, *Angew. Chem. Int. Ed.* **2014**, *53*, 10408-10411.
[109] X.-M. Chen, N. Ma, Q.-F. Zhang, J. Wang, X. Feng, C. Wei, L.-S. Wang, J. Zhang und X. Chen, *J. Am. Chem. Soc.* **2018**, *140*, 6718-6726.
[110] A. J. Arduengo (III), R. L. Harlow und M. Kline, *J. Am. Chem. Soc.* **1991**, *113*, 361-363.
[111] D. Bourissou, O. Guerret, F. P. Gabbaï und G. Bertrand, *Chem. Rev.* **2000**, *100*, 39-91.
[112] D. Enders, O. Niemeier und A. Henseler, *Chem. Rev.* **2007**, *107*, 5606-5655.
[113] H. V. Huynh, *Chem. Rev.* **2018**, DOI: 10.1021/acs.chemrev.1028b00067.
[114] E. Krause, *Ber. dtsch. Chem. Ges. A/B* **1924**, *57*, 216-217.
[115] E. Krause und H. Polack, *Ber. dtsch. Chem. Ges. A/B* **1926**, *59*, 777-785.
[116] J. J. Eisch, T. Dluzniewski und M. Behrooz, *Heteroatom Chem.* **1993**, *4*, 235-241.
[117] J. E. Leffler, G. B. Watts, T. Tanigaki, E. Dolan und D. S. Miller, *J. Am. Chem. Soc.* **1970**, *92*, 6825-6830.
[118] R. J. Kwaan, C. J. Harlan und J. R. Norton, *Organometallics* **2001**, *20*, 3818-3820.
[119] M. M. Olmstead und P. P. Power, *J. Am. Chem. Soc.* **1986**, *108*, 4235-4236.
[120] A. Blumenthal, P. Bissinger und H. Schmidbaur, *J. Organomet. Chem.* **1993**, *462*, 107-110.
[121] T. Imamoto und T. Hikosaka, *J. Org. Chem.* **1994**, *59*, 6753-6759.
[122] J. Monot, A. Solovyev, H. Bonin-Dubarle, É. Derat, D. P. Curran, M. Robert, L. Fensterbank, M. Malacria und E. Lacôte, *Angew. Chem. Int. Ed.* **2010**, *49*, 9166-9169.
[123] M. M. Morgan, J. M. Rautiainen, W. E. Piers, H. M. Tuononen und C. Gendy, *Dalton Trans.* **2018**, *47*, 734-741.
[124] E. Bernhardt, V. Bernhardt-Pitchougina, H. Willner und N. Ignatiev, *Angew. Chem. Int. Ed.* **2011**, *50*, 12085-12088.
[125] J. Landmann, J. A. P. Sprenger, R. Bertermann, N. Ignat'ev, V. Bernhardt-Pitchougina, E. Bernhardt, H. Willner und M. Finze, *Chem. Commun.* **2015**, *51*, 4989-4992.
[126] Y. Segawa, M. Yamashita und K. Nozaki, *Science* **2006**, *314*, 113-115.
[127] T. B. Marder, *Science* **2006**, *314*, 69-70.
[128] H. Braunschweig, *Angew. Chem. Int. Ed.* **2007**, *46*, 1946-1948.
[129] Y. Segawa, Y. Suzuki, M. Yamashita und K. Nozaki, *J. Am. Chem. Soc.* **2008**, *130*, 16069-16079.
[130] M. Yamashita, Y. Suzuki, Y. Segawa und K. Nozaki, *Chem. Lett.* **2008**, *37*, 802-803.
[131] M. Yamashita und K. Nozaki, *Bull. Chem. Soc. Jpn.* **2008**, *81*, 1377-1392.
[132] M. Yamashita, Y. Suzuki, Y. Segawa und K. Nozaki, *J. Am. Chem. Soc.* **2007**, *129*, 9570-9571.
[133] N. Dettenrieder, Y. Aramaki, B. M. Wolf, C. Maichle-Mössmer, X. Zhao, M. Yamashita, K. Nozaki und R. Anwander, *Angew. Chem. Int. Ed.* **2014**, *53*, 6259-6262.
[134] T. Kajiwara, T. Terabayashi, M. Yamashita und K. Nozaki, *Angew. Chem. Int. Ed.* **2008**, *47*, 6606-6610.
[135] A. V. Protchenko, K. H. Birjkumar, D. Dange, A. D. Schwarz, D. Vidovic, C. Jones, N. Kaltsoyannis, P. Mountford und S. Aldridge, *J. Am. Chem. Soc.* **2012**, *134*, 6500-6503.
[136] N. Dettenrieder, H. M. Dietrich, C. Schädle, C. Maichle-Mössmer, K. W. Törnroos und R. Anwander, *Angew. Chem. Int. Ed.* **2012**, *51*, 4461-4465.
[137] A. V. Protchenko, D. Dange, J. R. Harmer, C. Y. Tang, A. D. Schwarz, M. J. Kelly, N. Phillips, R. Tirfoin, K. H. Birjkumar, C. Jones, N. Kaltsoyannis, P. Mountford und S. Aldridge, *Nat. Chem.* **2014**, *6*, 315-319.
[138] N. Dettenrieder, C. Schädle, C. Maichle-Mössmer und R. Anwander, *Dalton Trans.* **2014**, *43*, 15760-15770.

[139] T. Arnold, H. Braunschweig, W. C. Ewing, T. Kramer, J. Mies und J. K. Schuster, *Chem. Commun.* **2015**, *51*, 737-740.
[140] D. Dange, A. Davey, J. A. B. Abdalla, S. Aldridge und C. Jones, *Chem. Commun.* **2015**, *51*, 7128-7131.
[141] A. V. Protchenko, J. I. Bates, L. M. A. Saleh, M. P. Blake, A. D. Schwarz, E. L. Kolychev, A. L. Thompson, C. Jones, P. Mountford und S. Aldridge, *J. Am. Chem. Soc.* **2016**, *138*, 4555-4564.
[142] Y. Segawa, M. Yamashita und K. Nozaki, *Angew. Chem. Int. Ed.* **2007**, *46*, 6710-6713.
[143] T. Terabayashi, T. Kajiwara, M. Yamashita und K. Nozaki, *J. Am. Chem. Soc.* **2009**, *131*, 14162-14163.
[144] S. Li, J. Cheng, Y. Chen, M. Nishiura und Z. Hou, *Angew. Chem. Int. Ed.* **2011**, *50*, 6360-6363.
[145] R. Frank, J. Howell, J. Campos, R. Tirfoin, N. Phillips, S. Zahn, D. M. P. Mingos und S. Aldridge, *Angew. Chem. Int. Ed.* **2015**, *54*, 9586-9590.
[146] L. Weber, *Eur. J. Inorg. Chem.* **2017**, 3461-3488.
[147] J. Cid, H. Gulyás, J. J. Carbó und E. Fernández, *Chem. Soc. Rev.* **2012**, *41*, 3558-3570.
[148] S. Pietsch, E. C. Neeve, D. C. Apperley, R. Bertermann, F. Mo, D. Qiu, M. S. Cheung, L. Dang, J. Wang, U. Radius, Z. Lin, C. Kleeberg und T. B. Marder, *Chem. - Eur. J.* **2015**, *21*, 7082-7098.
[149] E. C. Neeve, S. J. Geier, I. A. I. Mkhalid, S. A. Westcott und T. B. Marder, *Chem. Rev.* **2016**, *116*, 9091-9161.
[150] C. Kleeberg, L. Dang, Z. Lin und T. B. Marder, *Angew. Chem. Int. Ed.* **2009**, *48*, 5350-5354.
[151] R. D. Dewhurst, E. C. Neeve, H. Braunschweig und T. B. Marder, *Chem. Commun.* **2015**, *51*, 9594-9607.
[152] K. Takahashi, T. Ishiyama und N. Miyaura, *Chem. Lett.* **2000**, *29*, 982-983.
[153] K. Takahashi, T. Ishiyama und N. Miyaura, *J. Organomet. Chem.* **2001**, *625*, 47-53.
[154] K.-s. Lee, A. R. Zhugralin und A. H. Hoveyda, *J. Am. Chem. Soc.* **2009**, *131*, 7253-7255.
[155] A. Bonet, H. Gulyás und E. Fernández, *Angew. Chem. Int. Ed.* **2010**, *49*, 5130-5134.
[156] A. Bonet, C. Pubill-Ulldemolins, C. Bo, H. Gulyás und E. Fernández, *Angew. Chem. Int. Ed.* **2011**, *50*, 7158-7161.
[157] S. Radomkit und A. H. Hoveyda, *Angew. Chem. Int. Ed.* **2014**, *53*, 3387-3391.
[158] A.-F. Pécharman, A. L. Colebatch, M. S. Hill, C. L. McMullin, M. F. Mahon und C. Weetman, *Nat. Commun.* **2017**, *8*, 15022.
[159] A.-F. Pécharman, M. S. Hill, C. L. McMullin und M. F. Mahon, *Angew. Chem. Int. Ed.* **2017**, *56*, 16363-16366.
[160] H. Braunschweig, C.-W. Chiu, K. Radacki und T. Kupfer, *Angew. Chem. Int. Ed.* **2010**, *49*, 2041-2044.
[161] R. Bertermann, H. Braunschweig, R. D. Dewhurst, C. Hörl, T. Kramer und I. Krummenacher, *Angew. Chem. Int. Ed.* **2014**, *53*, 5453-5457.
[162] J. Landmann, F. Keppner, D. B. Hofmann, J. A. P. Sprenger, M. Häring, S. H. Zottnick, K. Müller-Buschbaum, N. V. Ignat'ev und M. Finze, *Angew. Chem. Int. Ed.* **2017**, *56*, 2795-2799.
[163] D. A. Ruiz, G. Ung, M. Melaimi und G. Bertrand, *Angew. Chem. Int. Ed.* **2013**, *52*, 7590-7592.
[164] R. Böser, L. C. Haufe, M. Freytag, P. G. Jones, G. Hörner und R. Frank, *Chem. Sci.* **2017**, *8*, 6274-6280.
[165] M. Krasowska, M. Edelmann und H. F. Bettinger, *J. Phys. Chem. A* **2016**, *120*, 6332-6341.
[166] M. Soleilhavoup und G. Bertrand, *Angew. Chem. Int. Ed.* **2017**, *56*, 10282-10292.
[167] M. C. Holthausen, W. Koch und Y. Apeloig, *J. Am. Chem. Soc.* **1999**, *121*, 2623-2624.
[168] J. Teichmann und M. Wagner, *Chem. Commun.* **2018**, *54*, 1397-1412.
[169] M. Krasowska und H. F. Bettinger, *J. Am. Chem. Soc.* **2012**, *134*, 17094-17103.

[170] S. M. van der Kerk, J. Boersma und G. J. M. van der Kerk, *Tetrahedron Lett.* **1976**, *17*, 4765-4766.
[171] B. Pachaly und R. West, *Angew. Chem. Int. Ed.* **1984**, *23*, 454-455.
[172] A. Meller, D. Bromm, W. Maringgele, D. Böhler und G. Elter, *J. Organomet. Chem.* **1988**, *347*, 11-16.
[173] A. Meller, U. Seebold, W. Maringgele, M. Noltemeyer und G. M. Sheldrick, *J. Am. Chem. Soc.* **1989**, *111*, 8299-8300.
[174] M. Ito, N. Tokitoh, T. Kawashima und R. Okazaki, *Tetrahedron Lett.* **1999**, *40*, 5557-5560.
[175] R. Kinjo, B. Donnadieu, M. A. Celik, G. Frenking und G. Bertrand, *Science* **2011**, *333*, 610-613.
[176] H. Wang, J. Zhang, Z. Lin und Z. Xie, *Chem. Commun.* **2015**, *51*, 16817-16820.
[177] M. Arrowsmith, D. Auerhammer, R. Bertermann, H. Braunschweig, G. Bringmann, M. A. Celik, R. D. Dewhurst, M. Finze, M. Grüne, M. Hailmann, T. Hertle und I. Krummenacher, *Angew. Chem. Int. Ed.* **2016**, *55*, 14464-14468.
[178] H. Wang, J. Zhang, Z. Lin und Z. Xie, *Organometallics* **2016**, *35*, 2579-2582.
[179] D. A. Ruiz, M. Melaimi und G. Bertrand, *Chem. Commun.* **2014**, *50*, 7837-7839.
[180] L. Kong, Y. Li, R. Ganguly, D. Vidovic und R. Kinjo, *Angew. Chem. Int. Ed.* **2014**, *53*, 9280-9283.
[181] L. Kong, R. Ganguly, Y. Li und R. Kinjo, *Chem. Sci.* **2015**, *6*, 2893-2902.
[182] L. Kong, W. Lu, L. Yongxin, R. Ganguly und R. Kinjo, *Inorg. Chem.* **2017**, *56*, 5586-5593.
[183] L. Kong, W. Lu, Y. Li, R. Ganguly und R. Kinjo, *J. Am. Chem. Soc.* **2016**, *138*, 8623-8629.
[184] D. Wu, Y. Li, R. Ganguly und R. Kinjo, *Chem. Commun.* **2017**, *53*, 12734-12737.
[185] D. Wu, L. Kong, Y. Li, R. Ganguly und R. Kinjo, *Nat. Commun.* **2015**, *6*, 7340.
[186] D. Wu, R. Ganguly, Y. Li, S. N. Hoo, H. Hirao und R. Kinjo, *Chem. Sci.* **2015**, *6*, 7150-7155.
[187] D. Wu, R. Wang, Y. Li, R. Ganguly, H. Hirao und R. Kinjo, *Chem* **2017**, *3*, 134-151.
[188] H. Braunschweig, M. Burzler, R. D. Dewhurst und K. Radacki, *Angew. Chem. Int. Ed.* **2008**, *47*, 5650-5653.
[189] H. Braunschweig, P. Brenner, R. D. Dewhurst, M. Kaupp, R. Müller und S. Östreicher, *Angew. Chem. Int. Ed.* **2009**, *48*, 9735-9738.
[190] H. Braunschweig, A. Damme, R. D. Dewhurst, T. Kramer, S. Östreicher, K. Radacki und A. Vargas, *J. Am. Chem. Soc.* **2013**, *135*, 2313-2320.
[191] R. Bertermann, H. Braunschweig, W. C. Ewing, T. Kramer, A. K. Phukan, A. Vargas und C. Werner, *Chem. Commun.* **2014**, *50*, 5729-5732.
[192] H. Braunschweig, R. D. Dewhurst, F. Hupp, M. Nutz, K. Radacki, C. W. Tate, A. Vargas und Q. Ye, *Nature* **2015**, *522*, 327-330.
[193] H. Braunschweig, M. A. Celik, R. D. Dewhurst, K. Ferkinghoff, A. Hermann, J. O. C. Jimenez-Halla, T. Kramer, K. Radacki, R. Shang, E. Siedler, F. Weißenberger und C. Werner, *Chem. - Eur. J.* **2016**, *22*, 11736-11744.
[194] F. Dahcheh, D. Martin, D. W. Stephan und G. Bertrand, *Angew. Chem. Int. Ed.* **2014**, *53*, 13159-13163.
[195] G. Maier, J. Henkelmann und H. P. Reisenauer, *Angew. Chem. Int. Ed.* **1985**, *24*, 1065-1066.
[196] B. Glaser und H. Nöth, *Angew. Chem. Int. Ed.* **1985**, *24*, 416-417.
[197] R. Boese, P. Paetzold und A. Tapper, *Chem. Ber.* **1987**, *120*, 1069-1071.
[198] A. Berndt, *Angew. Chem. Int. Ed.* **1993**, *32*, 985-1009.
[199] A. D. Ledet und T. W. Hudnall, *Dalton Trans.* **2016**, *45*, 9820-9826.
[200] H. Braunschweig, R. D. Dewhurst und S. Mozo, *ChemCatChem* **2015**, *7*, 1630-1638.
[201] M. Arrowsmith, H. Braunschweig und T. E. Stennett, *Angew. Chem. Int. Ed.* **2017**, *56*, 96-115.
[202] R. J. Brotherton, A. L. McCloskey, L. L. Petterson und H. Steinberg, *J. Am. Chem. Soc.* **1960**, *82*, 6242-6245.

[203] D. Loderer, H. Nöth, H. Pommerening, W. Rattay und H. Schick, *Chem. Ber.* **1994**, *127*, 1605-1611.
[204] N. R. Anastasi, K. M. Waltz, W. L. Weerakoon und J. F. Hartwig, *Organometallics* **2003**, *22*, 365-369.
[205] A. Stock, A. Brandt und H. Fischer, *Ber. dtsch. Chem. Ges. A/B* **1925**, *58*, 643-657.
[206] X. Liu, *Synlett* **2003**, 2442-2443.
[207] K. H. Hermannsdörfer, E. Matejčikova und H. Nöth, *Chem. Ber.* **1970**, *103*, 516-527.
[208] H. Nöth und H. Pommerening, *Angew. Chem. Int. Ed.* **1980**, *19*, 482-483.
[209] T. Mennekes, P. Paetzold, R. Boese und D. Bläser, *Angew. Chem. Int. Ed.* **1991**, *30*, 173-175.
[210] A. Stock und H. Laudenklos, *Z. Anorg. Allg. Chem.* **1936**, *228*, 178-192.
[211] L. Klemm und W. Klemm, *Z. Anorg. Allg. Chem.* **1935**, *225*, 258-261.
[212] W. V. Hough, L. J. Edwards und A. D. McElroy, *J. Am. Chem. Soc.* **1956**, *78*, 689.
[213] W. V. Hough, L. J. Edwards und A. D. McElroy, *J. Am. Chem. Soc.* **1958**, *80*, 1828-1829.
[214] W. V. Hough und L. J. Edwards, *Adv. Chem. Ser.* **1961**, *32*, 184-194.
[215] D. F. Gaines, R. Schaeffer und F. Tebbe, *Inorg. Chem.* **1963**, *2*, 526-528.
[216] S. Heřmánek und J. Plešek, *Collect. Czech. Chem. Comm.* **1966**, *31*, 177-189.
[217] R. A. Godfroid, T. G. Hill, T. P. Onak und S. G. Shore, *J. Am. Chem. Soc.* **1994**, *116*, 12107-12108.
[218] Y. Shoji, T. Matsuo, D. Hashizume, M. J. Gutmann, H. Fueno, K. Tanaka und K. Tamao, *J. Am. Chem. Soc.* **2011**, *133*, 11058-11061.
[219] Y. Shoji, S. Kaneda, H. Fueno, K. Tanaka, K. Tamao, D. Hashizume und T. Matsuo, *Chem. Lett.* **2014**, *43*, 1587-1589.
[220] J. Landmann, J. A. P. Sprenger, M. Hailmann, V. Bernhardt-Pitchougina, H. Willner, N. Ignat'ev, E. Bernhardt und M. Finze, *Angew. Chem. Int. Ed.* **2015**, *54*, 11259-11264.
[221] L. L. Cao und D. W. Stephan, *Organometallics* **2017**, *36*, 3163-3170.
[222] E. W. Corcoran (Jr.) und L. G. Sneddon, *Inorg. Chem.* **1983**, *22*, 182-182.
[223] S. Shimada, A. S. Batsanov, J. A. K. Howard und T. B. Marder, *Angew. Chem. Int. Ed.* **2001**, *40*, 2168-2171.
[224] H. Braunschweig und F. Guethlein, *Angew. Chem. Int. Ed.* **2011**, *50*, 12613-12616.
[225] O. Ciobanu, P. Roquette, S. Leingang, H. Wadepohl, J. Mautz und H.-J. Himmel, *Eur. J. Inorg. Chem.* **2007**, 4530-4534.
[226] O. Ciobanu, F. Allouti, P. Roquette, S. Leingang, M. Enders, H. Wadepohl und H.-J. Himmel, *Eur. J. Inorg. Chem.* **2008**, 5482-5493.
[227] O. Ciobanu, E. Kaifer, M. Enders und H.-J. Himmel, *Angew. Chem. Int. Ed.* **2009**, *48*, 5538-5541.
[228] N. Schulenberg, O. Ciobanu, E. Kaifer, H. Wadepohl und H.-J. Himmel, *Eur. J. Inorg. Chem.* **2010**, 5201-5210.
[229] J. Horn, A. Widera, S. Litters, E. Kaifer und H.-J. Himmel, *Dalton Trans.* **2018**, *47*, 2009-2017.
[230] É. Rochette, N. Bouchard, J. L. Lavergne, C. F. Matta und F.-G. Fontaine, *Angew. Chem. Int. Ed.* **2016**, *55*, 12722-12726.
[231] K. K. Pandey, H. Braunschweig und R. D. Dewhurst, *Eur. J. Inorg. Chem.* **2011**, 2045-2056.
[232] H. Braunschweig, Q. Ye, A. Vargas, R. D. Dewhurst, K. Radacki und A. Damme, *Nat. Chem.* **2012**, *4*, 563-567.
[233] Y. Hayashi, Y. Segawa, M. Yamashita und K. Nozaki, *Chem. Commun.* **2011**, *47*, 5888-5890.
[234] H. C. Brown, *Hydroboration*, W. A. Benjamin, Inc., New York, **1962**.
[235] H. C. Brown, R. Liotta und C. G. Scouten, *J. Am. Chem. Soc.* **1976**, *98*, 5297-5301.
[236] *Organoboranes for Syntheses*, ed. P. V. Ramachandran und H. C. Brown, American Chemical Society, ACS Symposium Series 783, Washington D.C., **2001**.
[237] R. Wilczynski und L. G. Sneddon, *Inorg. Chem.* **1981**, *20*, 3955-3962.
[238] D. Männig und H. Nöth, *Angew. Chem. Int. Ed.* **1985**, *24*, 878-879.

[239] K. Burgess und M. J. Ohlmeyer, *Chem. Rev.* **1991**, *91*, 1179-1191.
[240] H. Braunschweig, R. D. Dewhurst, C. Hörl, A. K. Phukan, F. Pinzner und S. Ullrich, *Angew. Chem. Int. Ed.* **2014**, *53*, 3241-3244.
[241] H. Braunschweig und C. Hörl, *Chem. Commun.* **2014**, *50*, 10983-10985.
[242] M. L. Pinsky und A. C. Bond, *Inorg. Chem.* **1973**, *12*, 605-607.
[243] D. F. Gaines und T. V. Iorns, *J. Am. Chem. Soc.* **1967**, *89*, 3375-3376.
[244] A. Wagner, S. Litters, J. Elias, E. Kaifer und H.-J. Himmel, *Chem. - Eur. J.* **2014**, *20*, 12514-12527.
[245] H. Braunschweig und R. D. Dewhurst, *Organometallics* **2014**, *33*, 6271-6277.
[246] A. Moezzi, M. M. Olmstead und P. P. Power, *J. Am. Chem. Soc.* **1992**, *114*, 2715-2717.
[247] P. P. Power, *Inorg. Chim. Acta* **1992**, *198-200*, 443-447.
[248] A. Moezzi, R. A. Bartlett und P. P. Power, *Angew. Chem. Int. Ed.* **1992**, *31*, 1082-1083.
[249] H. Nöth, J. Knizek und W. Ponikwar, *Eur. J. Inorg. Chem.* **1999**, 1931-1937.
[250] Y. Wang, B. Quillian, P. Wei, C. S. Wannere, Y. Xie, R. B. King, H. F. Schaefer (III), P. v. R. Schleyer und G. H. Robinson, *J. Am. Chem. Soc.* **2007**, *129*, 12412-12413.
[251] Y. Wang, B. Quillian, P. Wei, Y. Xie, C. S. Wannere, R. B. King, H. F. Schaefer (III), P. v. R. Schleyer und G. H. Robinson, *J. Am. Chem. Soc.* **2008**, *130*, 3298-3299.
[252] M. Arrowsmith, J. Böhnke, H. Braunschweig, M. A. Celik, T. Dellermann und K. Hammond, *Chem. - Eur. J.* **2016**, *22*, 17169-17172.
[253] P. Bissinger, H. Braunschweig, A. Damme, T. Kupfer und A. Vargas, *Angew. Chem. Int. Ed.* **2012**, *51*, 9931-9934.
[254] P. Bissinger, H. Braunschweig, A. Damme, T. Kupfer, I. Krummenacher und A. Vargas, *Angew. Chem. Int. Ed.* **2014**, *53*, 5689-5693.
[255] P. Bissinger, H. Braunschweig, M. A. Celik, C. Claes, R. D. Dewhurst, S. Endres, H. Kelch, T. Kramer, I. Krummenacher und C. Schneider, *Chem. Commun.* **2015**, *51*, 15917-15920.
[256] P. Bissinger, A. Steffen, A. Vargas, R. D. Dewhurst, A. Damme und H. Braunschweig, *Angew. Chem. Int. Ed.* **2015**, *54*, 4362-4366.
[257] H. Braunschweig, P. Constantinidis, T. Dellermann, W. C. Ewing, I. Fischer, M. Hess, F. R. Knight, A. Rempel, C. Schneider, S. Ullrich, A. Vargas und J. D. Woollins, *Angew. Chem. Int. Ed.* **2016**, *55*, 5606-5609.
[258] M. Solà, *Front. Chem.* **2013**, *1*, 22.
[259] T. Kaese, *Reaktivität ausgewählter 9-Borafluoren-Derivate*, Masterarbeit, Goethe-Universität, Frankfurt a. M., **2014**.
[260] A. Hübner, *Die dynamische kovalente Chemie des 9-Borafluorens*, Dissertation, Goethe-Universität, Frankfurt a. M., **2015**.
[261] T. Trageser, *Untersuchung der Reaktivität reduzierter Arylborane gegenüber Halogenkohlenwasserstoffen*, Masterarbeit, Goethe-Universität, Frankfurt a. M., **2017**.
[262] H. Budy, *Synthese und Reaktivität reduzierter Derivate von 9-Borafluoren*, Bachelorarbeit, Goethe-Universität, Frankfurt a. M., **2016**.
[263] A. Hübner, A. M. Diehl, M. Bolte, H.-W. Lerner und M. Wagner, *Organometallics* **2013**, *32*, 6827-6833.
[264] S. K. Talapatra, S. Chakrabarti, A. K. Mallik und B. Talapatra, *Tetrahedron* **1990**, *46*, 6047-6052.
[265] R. G. Harvey, *Polycyclic Aromatic Hydrocarbons*, Wiley-VCH, New York, Chichester, Weinheim, Brisbane, Singapore, Toronto, **1997**.
[266] H. Braunschweig, A. Damme, R. D. Dewhurst, T. Kramer, T. Kupfer, K. Radacki, E. Siedler, A. Trumpp, K. Wagner und C. Werner, *J. Am. Chem. Soc.* **2013**, *135*, 8702-8707.
[267] R. W. Alder und J. N. Harvey, *J. Am. Chem. Soc.* **2004**, *126*, 2490-2494.
[268] A. F. Holleman, E. Wiberg und N. Wiberg, *Lehrbuch der Anorganischen Chemie*, *102*, de Gruyter, Berlin, New York, **2007**.
[269] D. E. Young und S. G. Shore, *J. Am. Chem. Soc.* **1969**, *91*, 3497-3504.
[270] K. S. Pitzer, *J. Am. Chem. Soc.* **1945**, *67*, 1126-1132.

[271] D. J. Goebbert, H. Hernandez, J. S. Francisco und P. G. Wenthold, *J. Am. Chem. Soc.* **2005**, *127*, 11684-11689.
[272] Umsetzungen von **12** mit LDA und LiHMDS wurden im Rahmen meiner Masterarbeit bereits im NMR-Maßstab durchgeführt.
[273] W.-C. Liu, Y.-H. Liu, T.-S. Lin, S.-M. Peng und C.-W. Chiu, *Inorg. Chem.* **2017**, *56*, 10543-10548.
[274] T. Doba, S. Noda und H. Yoshida, *Bull. Chem. Soc. Jpn.* **1979**, *52*, 21-24.
[275] C. D. Entwistle, T. B. Marder, P. S. Smith, J. A. K. Howard, M. A. Fox und S. A. Mason, *J. Organomet. Chem.* **2003**, *680*, 165-172.
[276] K. M. Waltz und J. F. Hartwig, *Science* **1997**, *277*, 211-213.
[277] A. E. Shilov und G. B. Shul'pin, *Chem. Rev.* **1997**, *97*, 2879-2932.
[278] K. M. Waltz und J. F. Hartwig, *J. Am. Chem. Soc.* **2000**, *122*, 11358-11369.
[279] I. A. I. Mkhalid, J. H. Barnard, T. B. Marder, J. M. Murphy und J. F. Hartwig, *Chem. Rev.* **2010**, *110*, 890-931.
[280] T. Mennekes, P. Paetzold und R. Boese, *Angew. Chem. Int. Ed.* **1990**, *29*, 899-900.
[281] W. J. Grigsby und P. Power, *Chem. - Eur. J.* **1997**, *3*, 368-375.
[282] P. Bissinger, H. Braunschweig, A. Damme, R. D. Dewhurst, T. Kupfer, K. Radacki und K. Wagner, *J. Am. Chem. Soc.* **2011**, *133*, 19044-19047.
[283] Y. Wang und G. H. Robinson, *Inorg. Chem.* **2011**, *50*, 12326-12337.
[284] D. P. Curran, A. Boussonnière, S. J. Geib und E. Lacôte, *Angew. Chem. Int. Ed.* **2012**, *51*, 1602-1605.
[285] Y.-L. Rao, L. D. Chen, N. J. Mosey und S. Wang, *J. Am. Chem. Soc.* **2012**, *134*, 11026-11034.
[286] L. Wang, Y. Fang, H. Mao, Y. Qu, J. Zuo, Z. Zhang, G. Tan und X. Wang, *Chem. - Eur. J.* **2017**, *23*, 6930-6936.
[287] G. Ménard und D. W. Stephan, *Angew. Chem. Int. Ed.* **2012**, *51*, 4409-4412.
[288] G. Ménard, J. A. Hatnean, H. J. Cowley, A. J. Lough, J. M. Rawson und D. W. Stephan, *J. Am. Chem. Soc.* **2013**, *135*, 6446-6449.
[289] É. Rochette, M.-A. Courtemanche und F.-G. Fontaine, *Chem. - Eur. J.* **2017**, *23*, 3567-3571.
[290] M. Brookhart und M. L. H. Green, *J. Organomet. Chem.* **1983**, *250*, 395-408.
[291] M. Saunders und E. L. Hagen, *J. Am. Chem. Soc.* **1968**, *90*, 6881-6882.
[292] G. A. Olah und A. M. White, *J. Am. Chem. Soc.* **1969**, *91*, 5801-5810.
[293] G. A. Olah und A. M. White, *J. Am. Chem. Soc.* **1969**, *91*, 6883-6885.
[294] L. Radom, J. A. Pople, V. Buss und P. v. R. Schleyer, *J. Am. Chem. Soc.* **1972**, *94*, 311-321.
[295] D. Griller und K. U. Ingold, *Acc. Chem. Res.* **1980**, *13*, 317-323.
[296] D. C. Nonhebel, *Chem. Soc. Rev.* **1993**, *22*, 347-359.
[297] C. Chen, L. Ouyang, Q. Lin, Y. Liu, C. Hou, Y. Yuan und Z. Weng, *Chem. - Eur. J.* **2014**, *20*, 657-661.
[298] E. von Grotthuss, M. Diefenbach, M. Bolte, H.-W. Lerner, M. C. Holthausen und M. Wagner, *Angew. Chem. Int. Ed.* **2016**, *55*, 14067-14071.
[299] A. Lorbach, M. Bolte, H.-W. Lerner und M. Wagner, *Chem. Commun.* **2010**, *46*, 3592-3594.
[300] L. Schweighauser und H. A. Wegner, *Chem. - Eur. J.* **2016**, *22*, 14094-14103.
[301] L. Striepe und T. Baumgartner, *Chem. - Eur. J.* **2017**, *23*, 16924-16940.
[302] B. L. Feringa, *Angew. Chem. Int. Ed.* **2017**, *56*, 11060-11078.
[303] J.-P. Sauvage, *Angew. Chem. Int. Ed.* **2017**, *56*, 11080-11093.
[304] J. F. Stoddart, *Angew. Chem. Int. Ed.* **2017**, *56*, 11094-11125.
[305] J. Gilmer, *Untersuchung der Reaktivität reduzierten 9-Borafluorens*, Bachelorarbeit, Goethe-Universität, Frankfurt a. M., **2017**.
[306] H. Nöth und B. Wrackmeyer, *Nuclear Magnetic Resonance Spectroscopy of Boron Compounds* in *NMR Basic Principles and Progress*, ed. P. Diehl, E. Fluck und R. Kosfeld, Springer Verlag, Berlin, Heidelberg, New York, **1978**.
[307] C. Kleeberg, A. G. Crawford, A. S. Batsanov, P. Hodgkinson, D. C. Apperley, M. S. Cheung, Z. Lin und T. B. Marder, *J. Org. Chem.* **2012**, *77*, 785-789.

[308] K. R. Seddon, *Cryst. Growth Des.* **2004**, *4*, 1087-1087.
[309] T. Kaese, H. Budy, M. Bolte, H.-W. Lerner und M. Wagner, *Angew. Chem. Int. Ed.* **2017**, *56*, 7546-7550.
[310] T. Kaese, T. Trageser, H. Budy, M. Bolte, H.-W. Lerner und M. Wagner, *Chem. Sci.* **2018**, *9*, 3881-3891.
[311] T. Trageser, Promotion (unveröffentlichte Ergebnisse), Goethe-Universität, Frankfurt a. M.
[312] G. R. Fulmer, A. J. M. Miller, N. H. Sherden, H. E. Gottlieb, A. Nudelman, B. M. Stoltz, J. E. Bercaw und K. I. Goldberg, *Organometallics* **2010**, *29*, 2176-2179.
[313] *X-AREA: Diffractometer Control Program System*, Stoe & Cie, Darmstadt, Germany, **2002.**
[314] G. M. Sheldrick, *Acta Crystallogr., Sect. A: Found. Crystallogr.* **2008**, *64*, 112-122.

6 Anhang

6.1 Publikationsliste mit Angabe des eigenen Anteils

Allgemeine Anmerkungen:

- Die folgenden Nummerierungen der Verbindungen beziehen sich auf die jeweiligen Veröffentlichungen in den Fachjournalen und unterscheiden sich daher von denen in den Kapiteln 1–5.
- Das Lösen der Röntgenstrukturen von mir gezüchteter Einkristalle erfolgte in allen Fällen von Dr. Michael Bolte.

I) *A Redox-Active Diborane Platform Performs C(sp^3)–H Activation and Nucleophilic Substitution Reactions*
von T. Kaese, T. Trageser, H. Budy, M. Bolte, H.-W. Lerner und M. Wagner
Chem. Sci. **2018**, *9*, 3881-3891.

a. Sämtliche präparative Arbeiten und Analytik. Ausnahmen: Unter meiner Betreuung wurden Li_2[**11**], **13** und **14**^{Cn} (n = 1,2) von Hendrik Budy sowie **14**^{Cn} (n = 3,4), Li[**15**^{Cn,X}] (n = 4-6), Li[**16**] und Li[**17**] von Timo Trageser dargestellt.
b. Quantenchemische Rechnungen

II) *Doping Polycyclic Aromatics with Boron for Superior Performance in Materials Science and Catalysis*
von E. von Grotthuss,[†] A. John,[†] T. Kaese[†] und M. Wagner
([†] Diese Autoren haben zu gleichen Teilen an der Arbeit beigetragen)
Asian J. Org. Chem. **2018**, *7*, 37-53.

III) *Deprotonation of a Seemingly Hydridic Diborane(6) to Build a B–B Bond*
von T. Kaese, H. Budy, M. Bolte, H.-W. Lerner und M. Wagner
Angew. Chem. Int. Ed. **2017**, *56*, 7546-7550.

a. Sämtliche präparative Arbeiten. Ausnahme: Die Protonierung von Li_2[**1**] wurde unter meiner Anleitung von Hendrik Budy durchgeführt.

IV) *Hydroboration as an Efficient Tool for the Preparation of Electronically and Structurally Diverse N→B-Heterocycles*
von M. Grandl, T. Kaese, A. Krautsieder, Y. Sun und F. Pammer
Chem. – Eur. J. **2016**, *22*, 14373-14382.

a. Synthese des THF-Addukts von 2,7-Di-*t*Bu-9*H*-9-borafluoren

V) *Forming B–B Bonds by the Controlled Reduction of a Tetraaryldiborane(6)*
von T. Kaese, A. Hübner, M. Bolte, H.-W. Lerner und M. Wagner
J. Am. Chem. Soc. **2016**, *138*, 6224-6233.

a. Sämtliche präparative Arbeiten und Analytik. Ausnahme: Die Verbindungen Li_2[**6**] und Li_2[**7**] wurden von Dr. Alexander Hübner im Rahmen seiner Promotion untersucht.[260]

VI) *A Preorganized Ditopic Borane as Highly Efficient One- or Two-Electron Trap*
von A. Hübner, T. Kaese, M. Diefenbach, B. Endeward, M. Bolte, H.-W. Lerner, M. C. Holthausen und M. Wagner
J. Am. Chem. Soc. **2015**, *137*, 3705-3714.

a. Synthese und Analytik von **1**, Li[**1**$^{\bullet}$] und Li_2[**1**]

6.2 Eigene Publikationen in Fachjournalen

6.2.1 A Redox-Active Diborane Platform Performs C(sp³)–H Activation and Nucleophilic Substitution Reactions

Chemical Science

EDGE ARTICLE

View Article Online
View Journal | View Issue

Check for updates

Cite this: *Chem. Sci.*, 2018, **9**, 3881

A redox-active diborane platform performs C(sp³)–H activation and nucleophilic substitution reactions†

Thomas Kaese, Timo Trageser, Hendrik Budy, Michael Bolte, Hans-Wolfram Lerner and Matthias Wagner *

Organoboranes are among the most versatile and widely used reagents in synthetic chemistry. A significant further expansion of their application spectrum would be achievable if boron-containing reactive intermediates capable of inserting into C–H bonds or performing nucleophilic substitution reactions were readily available. However, current progress in the field is still hampered by a lack of universal design concepts and mechanistic understanding. Herein we report that the doubly arylene-bridged diborane(6) **1**H_2 and its B=B-bonded formal deprotonation product Li_2[**1**] can activate the particularly inert C(sp³)–H bonds of added H_3CLi and H_3CCl, respectively. The first case involves the attack of $[H_3C]^-$ on a Lewis-acidic boron center, whereas the second case follows a polarity-inverted pathway with nucleophilic attack of the B=B double bond on H_3CCl. Mechanistic details were elucidated by means of deuterium-labeled reagents, a radical clock, α,ω-dihaloalkane substrates, the experimental identification of key intermediates, and quantum-chemical calculations. It turned out that both systems, H_3CLi/**1**H_2 and H_3CCl/Li_2[**1**], ultimately funnel into the same reaction pathway, which likely proceeds past a borylene-type intermediate and requires the cooperative interaction of both boron atoms.

Received 13th February 2018
Accepted 19th March 2018

DOI: 10.1039/c8sc00743h

rsc.li/chemical-science

Open Access Article. Published on 19 March 2018. Downloaded on 19/04/2018 11:29:01.
This article is licensed under a Creative Commons Attribution 3.0 Unported Licence.

Introduction

For decades, organoboranes remained limited to a passive role as reagents in organic synthesis, where boryl substituents either serve as placeholders for other functional groups (*e.g.*, halides, hydroxy, and amino groups),[1] or are involved in Pd-catalyzed C–C-coupling reactions.[2] Another useful asset, the potential of boron compounds to actively promote the cleavage of element–element bonds, lay dormant until the concepts of "Boron Lewis-acid catalysis"[3–6] and "Frustrated Lewis pairs"[7–9] were introduced about 15 years ago. Since then, it became increasingly apparent that appropriately selected main group compounds can rival transition metal complexes in mediating the transformation of organic substrates.

Certain organoboranes are catalytically active not only in their Lewis-acidic neutral forms, but also in their exhaustively reduced states. As prominent examples, 9,10-dihydro-9,10-diboraanthracenes (DBAs) catalyze inverse electron-demand Diels–Alder reactions of 1,2-diazines[3] as well as the dehydrogenation of ammonia-borane.[5] Upon reduction, the corresponding $[DBA]^{2-}$ anions readily add C(sp)–H or H–H bonds across the two boron atoms; the latter reaction can be exploited for the economic conversion of chlorosilanes into hydrosilanes.[10,11]

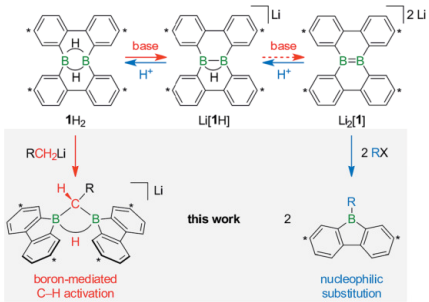

Scheme 1 The members of the triad **1**H_2/Li[**1**H]/Li_2[**1**] are linked through redox processes as well as protonation/deprotonation reactions. Treatment of **1**H_2 with RCH_2Li leads to C(sp³)–H activations and skeletal rearrangements to furnish 1,1-bis(9-borafluorenyl)methanes (together with Li[**1**H]; R = H, C_3H_7). The addition of haloalkanes RX to Li_2[**1**] results in nucleophilic substitution reactions and again skeletal rearrangements to afford 9-*R*-9-borafluorenes (in some cases accompanied by C(sp³)–H activations; X = Cl, Br, I). Carbon atoms marked with asterisks bear *t*Bu substituents.

Institut für Anorganische und Analytische Chemie, Goethe-Universität Frankfurt, Max-von-Laue-Straße 7, D-60438 Frankfurt am Main, Germany. E-mail: matthias.wagner@chemie.uni-frankfurt.de

† Electronic supplementary information (ESI) available. CCDC 1819687–1819695. For ESI and crystallographic data in CIF or other electronic format see DOI: 10.1039/c8sc00743h

Open Access Article. Published on 19 March 2018. Downloaded on 19/04/2018 11:29:01.
This article is licensed under a Creative Commons Attribution 3.0 Unported Licence.

With the triad $\mathbf{1}H_2$/Li[**1**H]/Li_2[**1**] (Scheme 1), we recently developed a system of ditopic boranes, which is comparable to the DBA/$[DBA]^{2-}$ pair, because it encompasses a Lewis-acidic ($\mathbf{1}H_2$) together with a dianionic species ($[\mathbf{1}]^{2-}$). As a decisive difference, however, the boron atoms in $[DBA]^{2-}$ are linked by two *o*-phenylene rings, whereas in $[\mathbf{1}]^{2-}$ they are directly connected by a double bond. Both systems thus possess different frontier orbitals and should exhibit different reactivities.

The anions $[\mathbf{1}H]^-$ and $[\mathbf{1}]^{2-}$ are accessible in good yields *via* alkali-metal reduction of $\mathbf{1}H_2$.[12–14] Stepwise protonation with ethereal HCl cleanly takes $[\mathbf{1}]^{2-}$ back to $[\mathbf{1}H]^-$ and finally $\mathbf{1}H_2$.[14] The reverse deprotonation reaction of $\mathbf{1}H_2$ to afford $[\mathbf{1}H]^-$ is also quantitative, provided that the sterically demanding bases $(Me_3Si)_2NLi$ and $(Me_3Si)_3CLi$ are used. In case of the smaller *n*BuLi, the deprotonation reaction (20%) is accompanied by the formation of an anionic diborylmethane featuring a boron-bridging hydrogen atom (30%; Scheme 1, R = C_3H_7).[14] These remarkable results immediately raise the following questions: (i) can $\mathbf{1}H_2$ activate C(sp^3)–H bonds of added alkyllithium reagents RCH_2Li? (ii) Will $[\mathbf{1}]^{2-}$ show nucleophilic behavior also toward electrophiles other than the proton (*i.e.*, RX)?

Derivatization reactions of the inert C(sp^3)–H bond are as topical as they are challenging – even if transition-metal catalysts are present.[15–18] The few known boron-promoted examples fall into the three categories compiled in Scheme 2: (1) Braunschweig performed the reductive dechlorination of a dichloroborane precursor to generate an intermediate borylene, which inserted into the H_3C group of a nearby mesityl substituent.[19] (2) Wang *et al.* observed hydrogen-atom abstraction from a H_3C group with concomitant formation of B–H and B–C bonds when they reduced 2,6-bis($BMes_2$)mesitylene to its diradical state.[20] (3) Fontaine exploited an intramolecular deprotonation step on an FLP platform to establish an NCH_2–B bond; subsequent H_2 liberation provided the necessary thermodynamic driving force.[21]

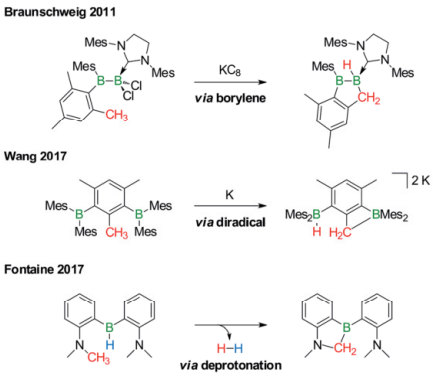

Scheme 2 Selected examples of transition metal-free intramolecular C(sp^3)–H activations through borylene (top), diradical (middle), and deprotonation reactions (bottom). Mes = 2,4,6-$(H_3C)_3C_6H_2$.

The umpolung of carbon electrophiles through their conversion in, *e.g.*, nucleophilic organolithium or Grignard reagents was one of the most important breakthroughs for the laboratory synthesis of organic compounds. A comparably high impact on the future progress of boron chemistry can be expected from the development of efficient tools to accomplish a polarity inversion of the intrinsically electrophilic boron center.[22]

In 2006, Yamashita and Nozaki pioneered the field of nucleophilic boron compounds by disclosing a lithium boryl isostere of stable *N*-heterocyclic carbenes (NHCs; Fig. 1).[23] More than 10 years later, Hill expanded the class of compounds to include an isolable magnesium pinacolatoboryl complex.[24] In the intervening period, a wealth of chemistry had already been developed based on the *in situ* generation of pinacolatoboryl nucleophiles *via* the alkoxide-induced heterolytic cleavage of bis(pinacolato)diboron (Lin, Kleeberg, Marder and others).[25] Boryl nucleophiles can also be stabilized through π delocalization of the boron lone pair, as exemplified by Braunschweig's NHC-adduct of a borolyl salt (which may in fact react *via* radical pathways),[26] the cyclic (alkyl)(amino)carbene-coordinated BH fragment of Kinjo/Bertrand,[27] as well as Willner's/Finze's alkali metal tricyanoborate (Fig. 1).[28]

Before the background provided by the literature and our own previous results, we regarded the triad $\mathbf{1}H_2$/Li[**1**H]/Li_2[**1**] as a perfect platform for further studies into boron-promoted C–H-activation processes and boron-centered nucleophiles. Herein we present evidence that the reactions of $\mathbf{1}H_2$ with RCH_2Li indeed proceed through C(sp^3)–H-cleavage steps and that the boron-bridging H atoms in the diborylmethane products stem from the organolithium reagents and are not remains of $\mathbf{1}H_2$ (*cf.* Scheme 1; R = H, C_3H_7). We also show that the B=B double bond of the dianion $[\mathbf{1}]^{2-}$ behaves as a closed-shell nucleophile toward organohalides and that specifically H_3CCl/Li_2[**1**] and $H_3CLi/\mathbf{1}H_2$ funnel into the same reaction channel. When H_3CCl is replaced by an excess of H_3C–I, C–H-activation is completely suppressed by a second nucleophilic substitution reaction to afford 2 equiv. of 9-methyl-9-borafluorene (Scheme 1; R = H_3C). Employing α,ω-dihaloalkanes $X(CH_2)_nX$ and Li_2[**1**], we gained

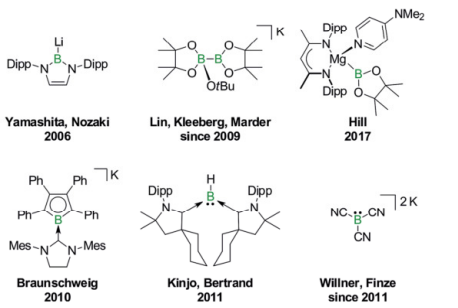

Fig. 1 Selected isolable boron compounds showing formal nucleophilic behavior. Dipp = 2,6-$(iPr)_2C_6H_3$.

This journal is © The Royal Society of Chemistry 2018

Open Access Article. Published on 19 March 2018. Downloaded on 19/04/2018 11:29:01.
This article is licensed under a Creative Commons Attribution 3.0 Unported Licence.

further insight into the competition between the nucleophilic substitution and C–H-activation scenarios as well as the cooperativity of the two adjacent boron centers (X = Cl, Br).

Results and discussion

We started our study by addressing the question: why and how does the reaction of $\mathbf{1H_2}$ with *n*BuLi furnish not only the deprotonation product Li[**1H**], but also the diborylmethane-hydride adduct shown in Scheme 1 (R = C_3H_7)?

First, we confirmed that a simplified system using H_3CLi in place of *n*BuLi maintains the same general reactivity (Scheme 3). From equimolar mixtures of $\mathbf{1H_2}$ and H_3CLi, the products Li[**1H**] and Li[**2**] are formed in slightly varying relative amounts but constant combined yields of close to 50% (the analogous finding holds for the *n*BuLi case). The ^{1}H NMR spectroscopic monitoring of the reaction in a sealed NMR tube (THF-d_8, room temperature) showed no free H_2 (δ 4.55 ppm),[29] which is an important observation considering that the starting materials $\mathbf{1H_2}$ and H_3CLi contain a sum of five BHB/H_3CLi protons, of which only three remain in the product Li[**2**].

Deuterium-labeling experiments with $D_3CLi/\mathbf{1H_2}$ or $H_3CLi/\mathbf{1D_2}$ combinations furnished isotopically pure Li[**2**-d_3] or Li[**2**], respectively (Scheme 4). Thus, not only the methylene linker (δ(^{1}H) 0.49 ppm, d), but also the boron-bridging hydrogen atom (δ(^{1}H) 1.94 ppm, br) in Li[**2**] originate from the organolithium reagent. None of the two BHB atoms of $\mathbf{1H_2}$ is still present in the product Li[**2**-d_3] (see the ESI† for more information). We also note the appearance of two sets of aryl-proton signals that neither belong to Li[**1H**] nor Li[**2**] (or their partly deuterated counterparts) and are consequently accountable for the missing 50% product yield (see below).

In the following, a plausible mechanistic model for the conversion of $\mathbf{1H_2}$ with H_3CLi will be described (black arrows in Scheme 5), which accounts for all available experimental evidence. It explains (i) the C–H activation of $[H_3C]^-$, (ii) the fate of the boron-bonded hydrogen atoms of $\mathbf{1H_2}$, and (iii) the combined yield of only 50% for Li[**1H**] and Li[**2**]: similar to the case $(Me_3Si)_3CLi/\mathbf{1H_2}$, the reaction $H_3CLi/\mathbf{1H_2}$ starts with the deprotonation of $\mathbf{1H_2}$ to afford Li[**1H**]. The byproduct CH_4 was detected by ^{1}H and $^{13}C\{^1H\}$ NMR spectroscopy; when D_3CLi was employed as the Brønsted base, we instead observed the formation of D_3CH (sealed NMR tubes; see the ESI† for more details).

Contrary to the case $(Me_3Si)_3CLi/\mathbf{1H_2}$, the reaction involving H_3CLi does not necessarily stop at the stage of Li[**1H**], because the small $[H_3C]^-$ ion also has the potential to act as a Lewis base. Nucleophilic attack of H_3CLi on a boron atom of Li[**1H**]

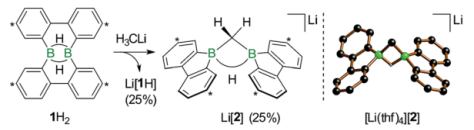

Scheme 3 The addition of H_3CLi to $\mathbf{1H_2}$ furnishes the C–H activation product Li[**2**] together with the deprotonated compound Li[**1H**] (left; carbon atoms marked with asterisks bear *t*Bu substituents). Molecular structure of [Li(thf)$_4$][**2**] in the solid state (right). The solvent-separated [Li(thf)$_4$]$^+$ cation, all *t*Bu groups, and all CH atoms are omitted for clarity. Selected atom···atom distance [Å] and bond angle [°]: B···B = 1.974(6); B–CH_2–B = 76.8(3).

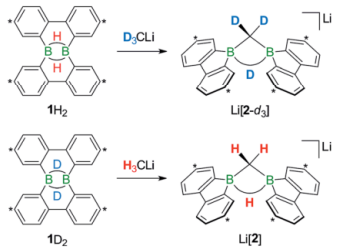

Scheme 4 The reactions $D_3CLi/\mathbf{1H_2}$ (top) or $H_3CLi/\mathbf{1D_2}$ (bottom) give the C–D- or C–H-activation products Li[**2**-d_3] or Li[**2**], respectively. Carbon atoms marked with asterisks bear *t*Bu substituents.

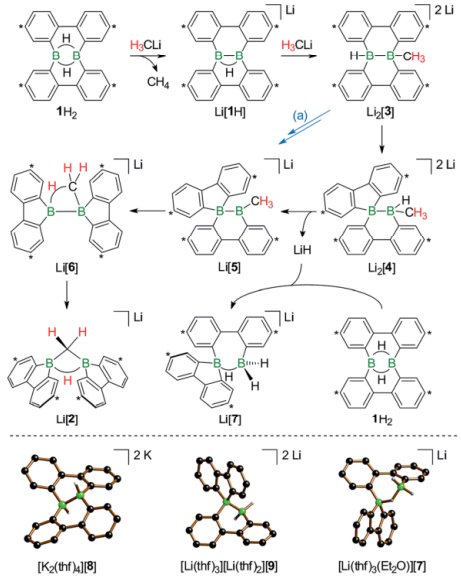

Scheme 5 Proposed reaction mechanism explaining the formation of Li[**1H**], Li[**2**], and Li[**7**] from an equimolar mixture of H_3CLi and $\mathbf{1H_2}$ (top; carbon atoms marked with asterisks bear *t*Bu substituents). The alternative pathway (a) leads from Li_2[**3**] to Li[**5**], first *via* hydride elimination and second *via* a 1,2-phenyl shift. Molecular structures of [K_2(thf)$_4$][**8**], [Li(thf)$_3$][Li(thf)$_2$][**9**], and [Li(thf)$_3$(Et_2O)][**7**] in the solid state (bottom). The solvent-separated cations, all *t*Bu groups, and all CH atoms are omitted for clarity.

Open Access Article. Published on 19 March 2018. Downloaded on 19/04/2018 11:29:01.
This article is licensed under a Creative Commons Attribution 3.0 Unported Licence.

establishes a B–CH_3 bond and shifts the boron-bridging hydrogen atom to a terminal position. The structural motif of the resulting intermediate $[\mathbf{3}]^{2-}$ has precedence in the crystallographically characterized dianion $[\mathbf{8}]^{2-}$,[13] which carries a further hydrogen atom rather than a boron-bonded methyl group (Scheme 5, top and bottom). $Li_2[\mathbf{3}]$ rearranges to $Li_2[\mathbf{4}]$ through a 1,2-phenyl shift, accompanied by a 1,2-hydride shift. Again, a comparable hydrogen-containing species $Li_2[\mathbf{9}]$ exists (Scheme 5, bottom), and its molecular structure has been confirmed by X-ray analysis.[13] $Li_2[\mathbf{9}]$ can isomerize to Li_2[FluB(H)–(H)BFlu] (BFlu = 9-borafluorenyl),[13] thereby providing an example of a 1,2-phenyl/1,2-hydride-shift cascade closely related to the isomerization of $Li_2[\mathbf{3}]$ to $Li_2[\mathbf{4}]$. The latter reaction continues with an LiH-elimination step to generate Li[**5**], which possesses a three-coordinate boron atom with a vacant p_z orbital and therefore easily undergoes a 1,2-phenyl shift to produce Li[**6**]. The anion $[\mathbf{6}]^-$ can be viewed as the $[H_3C]^-$ adduct of a diborane(4) containing two 9-borafluorene units that are linked by a B–B single bond. Only the sp^3-hybridized boron atom has acquired an electron octet, however, also the B(sp^2) center might gain some electron density from an agostic interaction with the methyl group and thereby reduce its strong Lewis acidity.[36] Finally, this interaction turns into C–H-bond activation accompanied by B–B-bond cleavage and ultimately results in the formation of Li[**2**]. It is well known that B(sp^2)–B(sp^3) diboranes readily undergo B–B-bond heterolysis and thereby act as mild sources of nucleophilic boron.[31] Moreover, the core parts of $[\mathbf{2}]^-$ and $[\mathbf{6}]^-$ are isoelectronic with protonated cyclopropane $[C_3H_7]^+$. This cation has been thoroughly investigated by experimental[32–34] and theoretical[35,36] methods and found to be a highly fluctional system,[37] which supports the idea of $[\mathbf{6}]^-$ rearranging to $[\mathbf{2}]^-$. At this stage, the dynamic behavior comes to an end, because, contrary to the case of $[C_3H_7]^+$, the three corners of $[\mathbf{2}]^-$ are not equivalent and the BHB bridge should be thermodynamically favored over alternative BHC bridges.

In addition to the qualitative comparison with the all-carbon model system $[C_3H_7]^+$, we studied the key C–H-activation step of the organoboron anion $[\mathbf{6}]^-$ by quantum-chemical calculations (Fig. 2). Apart from the Li^+ counterion, which likely is solvent-separated in THF solution (*cf.* the solid-state structure of $[Li(thf)_4][\mathbf{2}]$; Scheme 3, right), we also omitted the *t*Bu substituents. The computed parent systems will be denoted with a superscript 'c' (*e.g.*, $[\mathbf{5}^c]^-$ represents Li[**5**]). The 1,2-phenyl shift in $[\mathbf{5}^c]^-$ proceeds *via* **TS1** with an activation barrier of $\Delta G^\ddagger = 9.9$ kcal mol^{-1} and is endoergic by $\Delta G_R = 5.9$ kcal mol^{-1}. The resulting open-chain rearrangement product $[\mathbf{6}^c\text{-open}]^-$ features a large B–B–CH_3 bond angle of 121° and the vacant p_z orbital of the B(sp^2) atom is oriented almost orthogonal to the B–CH_3-bond vector, which precludes an agostic interaction in this isomer. To establish the B–H–C bridge proposed above, the tricoordinate borafluorene fragment must be rotated by approximately 70° and the B–B–CH_3 bond angle contracted – ultimately to a value of 68° in the local-minimum structure $[\mathbf{6}^c]^-$. The conversion of $[\mathbf{6}^c\text{-open}]^-$ to the cyclic isomer $[\mathbf{6}^c]^-$ *via* **TS2** ($\Delta G^\ddagger = 7.0$ kcal mol^{-1}) is associated with a moderate energy penalty of $\Delta G_R = 4.6$ kcal mol^{-1}. The actual C–H-activation process involves the transition state **TS3** in which the B–B bond and one C–H bond are concertedly cleaved and a new B–C bond is formed ($\Delta G^\ddagger = 4.4$ kcal mol^{-1}).

The primary, open-chain activation product $[\mathbf{2}^c\text{-open}]^-$ is thermodynamically favored by −14.1 kcal mol^{-1} and −3.6 kcal mol^{-1} compared to $[\mathbf{6}^c]^-$ and $[\mathbf{5}^c]^-$, respectively. A further stabilization is achievable through rotation about a B–C bond and placement of the hydrogen atom into a boron-bridging position to obtain the final product $[\mathbf{2}^c]^-$ (**TS4**: $\Delta G^\ddagger = 2.7$ kcal mol^{-1}; $\Delta G_R = -6.3$ kcal mol^{-1}). In summary, the reaction cascade from $[\mathbf{5}^c]^-$ to $[\mathbf{2}^c]^-$ possesses an overall activation barrier of $\Delta G^\ddagger = 14.9$ kcal mol^{-1}, which is easily surmountable at room temperature. An appreciable thermodynamic driving force is provided by the exergonicity of the $[\mathbf{2}^c]^-$ formation ($\Delta G_R = -9.9$ kcal mol^{-1}).

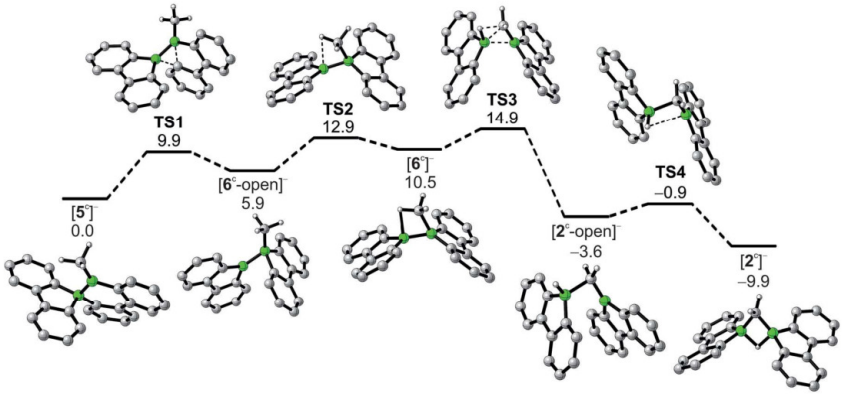

Fig. 2 Reaction pathway for the conversion of $[\mathbf{5}^c]^-$ to $[\mathbf{2}^c]^-$, calculated at the PBE0D/TZVP level of theory with the SMD polarized continuum model for solvation in THF. Gibbs free energies at 298 K (ΔG) are given in kcal mol^{-1} relative to $[\mathbf{5}^c]^-$.

 This journal is © The Royal Society of Chemistry 2018

Open Access Article. Published on 19 March 2018. Downloaded on 19/04/2018 11:29:01.
This article is licensed under a Creative Commons Attribution 3.0 Unported Licence.

To experimentally substantiate the role of Li[**1**H] as the first intermediate along the pathway from $\mathbf{1}H_2$ to Li[**2**], we treated an isolated sample of Li[**1**H] with 1 equiv. of H_3CLi in THF. Even though the reaction started as expected, it stopped at the stage of Li_2[**4**] (which enabled us to record a ^{1}H NMR spectrum of this compound). The elimination of LiH from Li_2[**4**] is thus not a spontaneous process, but apparently requires a hydride-trapping reagent. Compound $\mathbf{1}H_2$ constitutes an ideal candidate for this purpose and, indeed, after the addition of 1 equiv. of $\mathbf{1}H_2$, Li_2[**4**] quantitatively vanished and Li[**2**] formed instead. Moreover, we found two sets of proton resonances that are assignable to two isomeric hydride-trapping products of $\mathbf{1}H_2$ (*cf.* Li[**7**], Li[**10**]; Schemes 5 and 6).

As a caveat we emphasize that the reaction from $\mathbf{1}H_2$ to Li[**2**] may bypass the intermediate Li_2[**4**] if hydride transfer from Li_2[**3**] to $\mathbf{1}H_2$ is faster than the rearrangement from Li_2[**3**] to Li_2[**4**] (blue path (a) in Scheme 5). Arguments in favor of this alternative route include: (i) the 1,2-phenyl shift required to generate intermediate Li[**5**] should be more facile on a B(sp^2)–B(sp^3) rather than a B(sp^3)–B(sp^3) scaffold (*cf.* Li_2[**3**] → Li_2[**4**]; Scheme 5). (ii) Li_2[**4**] was observed only when the reaction was started from Li[**1**H], *i.e.*, when the hydride trap $\mathbf{1}H_2$ was absent, thus rendering the blue path impassable.

After the above discussion of a plausible mechanistic picture underlying the overall reaction scenario, we now present analytical data of key intermediates and products. The reaction $H_3CLi/\mathbf{1}H_2$ furnishes Li[**1**H] and Li[**2**] besides the isomeric hydride-trapping products Li[**7**] and Li[**10**]. The first species, Li[**1**H], is a known compound and therefore does not require further discussion.[14] The second species, Li[**2**], is reminiscent of the published C–H-activation product obtained from the reaction *n*BuLi/$\mathbf{1}H_2$ (*cf.* Scheme 1, R = C_3H_7).[14] The main difference between both compounds relates to the fact that Li[**2**] possesses an average C_{2v} symmetry in solution, whereas a pending C_3H_7 substituent reduces the symmetry to C_s. Consequently, the ^{1}H NMR spectrum of Li[**2**] contains only one set of signals for all four *t*Bu-C_6H_3 rings. The corresponding spectrum of its C_s-symmetric congener features two sets of resonances,[14] one of them with chemical shift values almost identical to those of Li[**2**] and thus likely assignable to those halves of the 9-borafluorene subunits, which point into the same direction as the proton residing on the methylene bridge. A similar interpretation is valid for the $^{13}C\{^1H\}$ NMR spectrum of Li[**2**]. Single crystals of [Li(thf)$_4$][**2**] suitable for X-ray analysis were grown from THF-hexane (Scheme 3). Like its C_3H_7 derivative,[14] [Li(thf)$_4$][**2**] forms solvent-separated ion pairs in the crystal lattice, and all key geometric parameters of the two anions are identical within the experimental error margins. We also note a pleasingly good agreement between the experimentally determined structure of [**2**]$^-$ and the computed structure of [$\mathbf{2}^c$]$^-$ (*cf.* the ESI† for full details).

^{1}H NMR spectra measured on $H_3CLi/\mathbf{1}H_2$ mixtures reproducibly showed resonances pointing toward a primary hydride-trapping product Li[**10**], which features a BHB bridge and two terminal hydrogen substituents in mutual *trans* arrangement (Scheme 6). For comparison, we prepared an authentic sample of Li[**10**] from $\mathbf{1}H_2$ and 1 equiv. of the 'superhydride' Li[HBEt_3]. At low temperatures, Li[**10**] forms quantitatively; since the compound is thermolabile, its NMR spectra had to be recorded at −30 °C. Li[**10**] gives rise to a double set of proton resonances in THF solution. On average, the two 2,2′-biphenylylene fragments of the anion [**10**]$^-$ should be related by a mirror plane containing the B_2H_3 core. The two phenylene rings of each individual 2,2′-biphenylylene moiety, however, are chemically inequivalent (as confirmed by 2D NMR experiments).

At room temperature, Li[**10**] readily isomerizes to the secondary hydride-trapping product Li[**7**], which we have isolated and characterized by NMR spectroscopy as well as X-ray crystallography. The anion of [Li(thf)$_3$(Et$_2$O)][**7**] consists of one 9-borafluorenyl and one BH_2 fragment that are linked by a μ-H atom and a 2,2′-biphenylylene bridge (Scheme 5, bottom). As a result, both boron atoms are tetracoordinate and placed at a distance of B···B = 2.382(8) Å. In the solid state, the central seven-membered HB_2C_4 ring is non-planar and the anion possesses C_1 symmetry (the torsion angle of the bridging 2,2′-biphenylylene amounts to 36°).

The molecular scaffolds of [**7**]$^-$ and the known anion [**9**]$^{2-}$ are essentially superimposable, apart from the fact that the latter features a covalent B–B bond (1.810(5) Å) instead of the μ-H atom (Scheme 5, bottom).[13] In line with their marked structural resemblance, both anions exhibit similar ^{1}H NMR spectra: in each case, three sets of aryl resonances are detectable. Two of those are well resolved at room temperature (H-a, H-b), whereas the third set consists of very broad signals, each of them integrating 2H (H-c; Scheme 6). This points toward a dynamic behavior of the compounds in solution, which likely arises from conformational changes of the twisted boron heterocycles. The

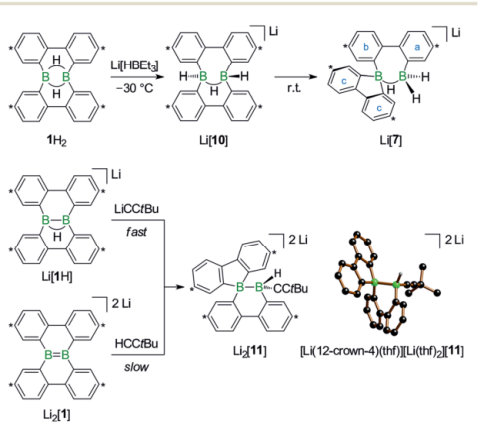

Scheme 6 Reaction of $\mathbf{1}H_2$ with Li[HBEt_3] at −30 °C to give Li[**10**], which isomerizes to Li[**7**] at room temperature (top). Compound Li_2[**11**] forms in both reactions, *t*BuCCLi/Li[**1**H] and *t*BuCCH/Li_2[**1**] (bottom; carbon atoms marked with asterisks bear *t*Bu substituents). Molecular structure of [Li(12-crown-4)(thf)][Li(thf)$_2$][**11**] in the solid state. The solvent-separated cations, phenyl-bonded *t*Bu groups, and all CH atoms are omitted for clarity.

Open Access Article. Published on 19 March 2018. Downloaded on 19/04/2018 11:29:01.
This article is licensed under a Creative Commons Attribution 3.0 Unported Licence.

^{11}B NMR spectrum of [**7**]$^-$ is characterized by two resonances with chemical shift values of δ −3.6 and −10.1 ppm, testifying to the presence of two magnetically inequivalent, tetracoordinate boron nuclei.[38]

Turning our attention from the products of the reaction $CH_3Li/\mathbf{1}H_2$ to its intermediates, we note that the ^{1}H NMR spectrum of Li_2[**4**] shows the same peculiarities as those of its structural congeners Li[**7**] and Li_2[**9**]: well resolved resonances coexist with severely broadened signals. Together with a BCH_3 resonance at δ −0.1 ppm, this can be taken as a support for our structural proposal of Li_2[**4**], but the motional broadening precludes the measurement of meaningful $^{13}C\{^1H\}$ NMR and 2D correlation spectra. Despite numerous efforts, we have not succeeded in growing crystals of Li_2[**4**] and therefore considered replacing the H_3C group with an alternative sterically undemanding organic substituent: The reaction *t*BuCCLi/Li[**1**H] provided the alkynyl analogue Li_2[**11**] of Li_2[**4**] in single-crystalline form ([Li(12-crown-4)(thf)][Li(thf)$_2$][**11**]; Scheme 6). X-ray crystallography confirmed the proposed ring-contracted, H-shifted structure of [**11**]$^{2-}$.

NMR spectroscopy reproduced the characteristic distribution of well-resolved and motionally broadened line shapes; the chemical shift values of the aryl protons of Li_2[**11**] are reasonably close to those of Li_2[**4**] (*cf.* the ESI† for an overlay of the respective ^{1}H NMR spectra). Remarkably, Li_2[**11**] is also accessible *via* a different approach, starting from the doubly boron-doped dibenzo[*g*,*p*]chrysene Li_2[**1**] and *t*BuCCH, the conjugate weak acid of [*t*BuCC]$^-$ (Scheme 6).

The facile protonation[14] of Li_2[**1**] prompted us to investigate whether an umpolung approach to synthesize compounds of the type Li[**2**] might also be successful, which would provide fundamentally interesting insights into the reactivities of B=B double-bonded species. As mentioned above, the intermediate Li[**6**] of the reaction $H_3CLi/\mathbf{1}H_2$ can be regarded as the [H_3C]$^-$ adduct of a diborane(4). Conceptually, it should be possible to arrive at the same molecule by formally transferring two electrons from the carbon nucleophile to the redox-active organoborane and thus starting from methylium-ion sources and the anion [**1**]$^{2-}$ (Fig. 3).[39]

Indeed, when a THF solution of Li_2[**1**] is stirred at room temperature under a blanket of H_3CCl gas (1 atm), a quantitative conversion to Li[**2**] occurs (Scheme 7).[40] This approach is far more atom- and time-economic than the previous access route *via* the polarity-inverted couple $H_3CLi/\mathbf{1}H_2$, because we avoid wasting 50% of $\mathbf{1}H_2$ as a hydride-trapping reagent and do no longer have to separate the resulting hydride-trapping products. Mechanistically, the electron-rich B=B fragment of Li_2[**1**] likely acts as a nucleophile toward H_3CCl to form [**12**]$^-$, which carries a boron-bonded methyl substituent and contains a central B–B single bond. The B(sp^2)–B(sp^3) species Li[**12**] then undergoes a 1,2-phenyl shift to afford Li[**5**] and thereby funnels into the reaction cascade outlined above for the formation of Li[**2**] from $H_3CLi/\mathbf{1}H_2$ (Scheme 7).

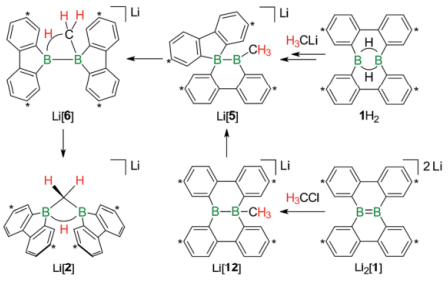

Scheme 7 The addition of H_3CCl to Li_2[**1**] quantitatively furnishes Li[**2**]. The reaction pathways to Li[**2**], starting from either $\mathbf{1}H_2$ or Li_2[**1**], merge at the stage of Li[**5**] (*cf.* also Scheme 5). Carbon atoms marked with asterisks bear *t*Bu substituents.

When H_3CCl is replaced by 1 equiv. of iodomethane (H_3C–I), the outcome is a mixture of Li[**2**], 9-methyl-9-borafluorene (**13**), and residual Li_2[**1**] (Scheme 8). After increasing the relative amount of H_3C–I to 3 equiv., we almost exclusively obtained **13**. The different behaviors of the two halomethanes can be rationalized by viewing the intermediate Li[**6**] as an adduct between the 9-borafluorenyl anion ([BFlu]$^-$) and (H_3C)BFlu (**13**; Scheme 9). [BFlu]$^-$ is isoelectronic to the carbene 9-fluorenylidene. A formal carbene-like reactivity is reflected by the intramolecular insertion of [BFlu]$^-$ into the C–H bond of the 9-methyl-9-borafluorene moiety to afford Li[**2**]. When the strong electrophile H_3C–I with its excellent iodide leaving group is present, also the nucleophilic character of [BFlu]$^-$ comes into play and opens a competing intermolecular pathway, which ultimately leads to **13**. As the relative amount of H_3C–I is increased, the substitution reaction becomes dominant (we note in passing that the reaction with H_3C–I can alternatively be viewed as a carbene-like insertion of [BFlu]$^-$ into the C–I bond with subsequent elimination of LiI).

In case of the system H_3C–I/Li_2[**1**], the methyl group initially gets attached to only one of the symmetry-related boron centers, but the other is equally important for the subsequent C–H-activation and nucleophilic substitution steps. The degree of B–B cooperativity in Li_2[**1**] as well as the insertion *vs.* nucleophilic behavior of [BFlu]$^-$ thus deserve a detailed assessment. To this end, we conducted a systematic study using 1 : 1 mixtures of Li_2[**1**] and α,ω-dihaloalkanes $X(CH_2)_nX$ with chain lengths in the range of n = 2–6 and leaving groups of different qualities (*e.g.*, X = Cl, Br). In these experiments, smaller alkylidene linkers are supposed to mimic higher local concentrations of the electrophile. As summarized in Scheme 8, clean

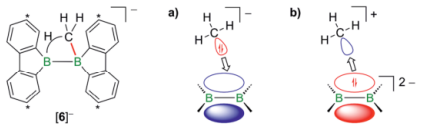

Fig. 3 Two borderline cases to describe the bonding situation in [**6**]$^-$ as (a) the [H_3C]$^-$ adduct of a diborane(4) and (b) the [H_3C]$^+$ adduct of a [**1**]$^{2-}$ anion. Carbon atoms marked with asterisks bear *t*Bu substituents.

This journal is © The Royal Society of Chemistry 2018

Open Access Article. Published on 19 March 2018. Downloaded on 19/04/2018 11:29:01.
This article is licensed under a Creative Commons Attribution 3.0 Unported Licence.

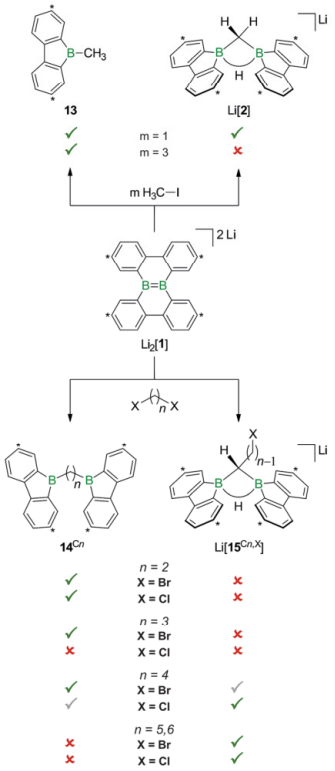

Scheme 8 The outcome of the reaction H_3C–I/Li_2[**1**] depends on the stoichiometries employed. While 1 : 1 mixtures give **13** together with Li[**2**], 3 : 1 mixtures exclusively furnish **13**. Use of α,ω-dihaloalkanes $X(CH_2)_nX$ instead of H_3C–I affords ditopic boranes $\mathbf{14}^{Cn}$ ($n = 2$–4) and/or Li[$\mathbf{15}^{Cn,X}$] ($n = 4$–6; X = Cl, Br). Carbon atoms marked with asterisks bear *t*Bu substituents.

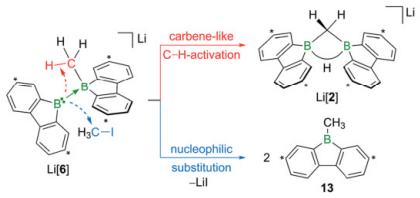

Scheme 9 The intermediate Li[**6**] can be interpreted as an adduct between the 9-borafluorenyl anion ($[BFlu]^-$) and 9-methyl-9-borafluorene (**13**). Intramolecular C–H insertion of the carbene-like $[BFlu]^-$ furnishes Li[**2**]; intermolecular nucleophilic attack on H_3C–I affords 2 equiv. of **13**. Carbon atoms marked with asterisks bear *t*Bu substituents.

twofold substitution reactions are observed with the short-chain substrates ($n = 2$ and 3, *cf.* $\mathbf{14}^{C2}$ and $\mathbf{14}^{C3}$; 1,3-dichloropropane leads to a complex mixture of products). Clean C–H-activation reactions occur with the long-chain substrates ($n = 5$ and 6) to afford the haloalkyl species Li[$\mathbf{15}^{C5,Cl}$]/Li[$\mathbf{15}^{C5,Br}$] and Li[$\mathbf{15}^{C6,Cl}$]/Li[$\mathbf{15}^{C6,Br}$]. The medium-chain substrates ($n = 4$) mark the switching point between both scenarios: with the worse chloride leaving group, C–H-activation is preferred over the twofold substitution. The reverse is true in the case of the better bromide leaving group. The solid-state structures of $\mathbf{14}^{C2}$·thf, $\mathbf{14}^{C3}$ (Fig. 4), $\mathbf{14}^{C4}$, and [Li(12-crown-4)$_2$][$\mathbf{15}^{C5,Cl}$] (Fig. 4) were characterized by X-ray crystallography (*cf.* the ESI† for full information). Also the connectivities of [Li(thf)$_4$][$\mathbf{15}^{C4,Cl}$], [Li(thf)$_4$][$\mathbf{15}^{C6,Cl}$], and [Li(thf)$_4$][$\mathbf{15}^{C6,Br}$] are supported by X-ray diffraction studies, however, due to disordered haloalkyl chains, *t*Bu groups, and THF molecules, the quality of these three structures prevents their inclusion into this publication.[41]

The observed chain-length dependence of the product distribution suggests that the carbene-type insertion and the second nucleophilic substitution both follow an intramolecular pathway involving two cooperating boron atoms.

If the remaining CH_2X center and the BCH_2 group are similarly close to the B–B bond, the nucleophilic process occurs at a higher rate than the carbene-type C–H-activation. As the alkylidene spacer grows, the second electrophilic functionality moves further apart whereas the reactive α-CH_2 unit stays in place such that the C–H-activation becomes more and more relevant until it finally takes over.

Although the reaction between Li_2[**1**] and, *e.g.*, H_3C–I can convincingly be rationalized by assuming a nucleophilic pathway, the possible operation of a radical mechanism remains to be ruled out. We first note in this context that 1,2-dihaloethane in the presence of Li_2[**1**] did not undergo reductive dehalogenation with ethene formation. Yamashita, Nozaki *et al.* have treated their boryllithium compound with methyl trifluoromethanesulfonate (H_3COTf)[42] on the one hand and benzyl bromide (BnBr) on the other (Scheme 10, top). In the first case, they observed the corresponding methyl borane in yields of 85%, whereas in the second case exclusively the bromoborane was obtained.[43] To explain the different outcomes, they proposed halogenophilic attack of the boryllithium or single electron transfer to the benzyl halide. We repeated Nozaki's

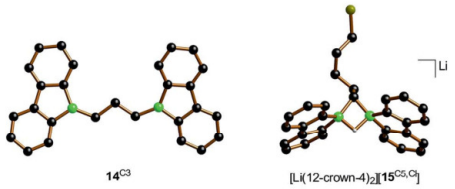

Fig. 4 Molecular structures of $\mathbf{14}^{C3}$ and of the terminally chlorine-substituted [Li(12-crown-4)$_2$][$\mathbf{15}^{C5,Cl}$] in the solid state. The solvent-separated $[Li(12\text{-crown-4})_2]^+$ cation, all *t*Bu groups, and all CH atoms are omitted for clarity.

Open Access Article. Published on 19 March 2018. Downloaded on 19/04/2018 11:29:01.
This article is licensed under a Creative Commons Attribution 3.0 Unported Licence.

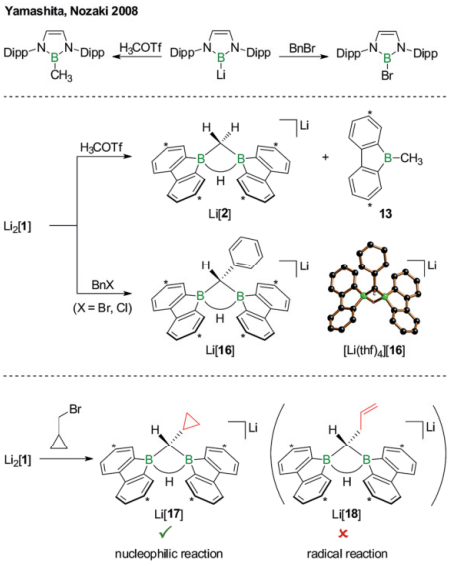

Scheme 10 The reactions of Yamashita's and Nozaki's boryllithium compound with H_3COTf or BnBr furnish the corresponding methyl borane or bromoborane, respectively (top). In the analogous reactions with Li_2[**1**], only the organyl moieties are transferred to boron (middle; *cf.* Li[**2**]/**13** and Li[**16**]). The reaction of Li_2[**1**] with the radical clock (bromomethyl)cyclopropane quantitatively furnishes Li[**17**], which is a strong indication for a closed-shell, nucleophilic pathway (bottom). Dipp = 2,6-(*i*Pr)$_2$C$_6$H$_3$, Bn = $CH_2C_6H_5$, H_3COTf = $H_3COSO_2CF_3$; carbon atoms marked with asterisks bear *t*Bu substituents. In the crystal structure plot of [Li(thf)$_4$][**16**], the solvent-separated cation, the *t*Bu groups, and all C(sp^2)–H atoms are omitted for clarity.

experiments with Li_2[**1**] (Scheme 10, middle): H_3COTf showed the same reactivity as described above for H_3C–I (*cf.* Li[**2**] and **13**); BnBr (as well as BnCl) gave the C–H-activation product Li[**16**] rather than any haloboranes, as confirmed by NMR spectroscopy and X-ray crystallography on [Li(thf)$_4$][**16**].

As the ultimate test, we added Li_2[**1**] to 1 equiv. of (bromomethyl)cyclopropane, a well-established radical clock (Scheme 10, bottom).[44–46] A quantitative conversion to the C–H-activation product Li[**17**], still carrying an intact cyclopropyl substituent, occurred (NMR-spectroscopic control). The absence of the ring-opened olefin derivative Li[**18**] in the reaction mixture strongly supports the proposal of a closed-shell scenario in contrast to an open-shell process.

The results collected thus far are not only fundamentally interesting with respect to the reactivities of electron-rich B=B double bonds, but open new access routes to ditopic boranes of high Lewis acidity. Molecules containing two or more potentially cooperating boron sites are of great current interest, *inter alia*, as organocatalysts[5,11,47] or electron-storage media.[48,49] Compounds of the class **14**^{Cn} already constitute free Lewis

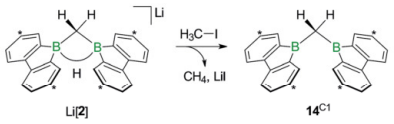

Scheme 11 The addition of H_3C–I to Li[**2**] furnishes the bis(9-borafluorenyl)methane **14**^{C1}. Carbon atoms marked with asterisks bear *t*Bu substituents.

acids, but do not contain functional groups amenable to further derivatization.

The opposite is true for the salts Li[**15**^{Cn,X}]. Here, the terminal halogen atoms provide ample opportunities, *e.g.*, for grafting the organoboron units onto polymers, dendrimers, or surfaces, but the Lewis acids need to be activated through LiH elimination prior to use.

While the bulky hydride scavenger $(H_3C)_3SiCl$ failed in this respect, the smaller electrophile H_3C–I efficiently transformed the model compound Li[**2**] to its conjugate acid **14**^{C1} (Scheme 11). As important diagnostic criteria, the BHB proton resonance vanishes in the course of the reaction, and the ^{11}B NMR signal shifts from the tetracoordinate (Li[**2**]: δ −14 ppm) to the tricoordinate spectral region (**14**^{C1}: δ 45 ppm).[49,50]

In line with the reaction H_3C–I/Li[**2**], the haloalkyl derivatives Li[**15**^{Cn,X}] are not long-term stable in THF at room temperature: ^{1}H NMR monitoring of the solutions revealed in each case a gradual decrease of the CH_2X resonance and a concomitant increase of a signal assignable to a terminal CH_3 group, which leads to the conclusion that the pending haloalkyl substituent can take a similar role as added H_3C–I. It is important to note in this context that the follow-up X/H exchange reactions are completely suppressed at −78 °C and even at room temperature slow enough not to interfere with targeted derivatizations of the CH_2X termini.

Conclusion

In summary, C(sp^3)–H activation and nucleophilic substitution reactions have been performed on the same redox-active diborane platform. We propose that the doubly 2,2′-biphenylylene-bridged diborane(6) **1**H$_2$ reacts with H_3CLi to furnish the rearranged B(sp^2)–B(sp^3) intermediate Li[FluB–BFlu(CH$_3$)] (Li[**6**]; BFlu = 9-borafluorenyl). Li[**6**] also forms *via* an umpolung approach starting from H_3CX and the B=B bonded, nucleophilic Li_2[**1**], a compound which can be regarded as the product of a double deprotonation of **1**H$_2$ (X = Cl, I). Li[**6**] readily undergoes B–B-bond heterolysis to formally give the [BFlu]$^-$ anion and (H_3C)BFlu (**13**). The final product distribution depends on the relative amount of H_3CX and the leaving-group qualities of X, because [BFlu]$^-$ can either insert into a C(sp^3)–H bond of **13** or replace the halogen atom of a second equivalent of H_3CX. The product of the carbene-type C–H insertion is Li[FluB(μ-CH$_2$)(μ-H)BFlu] (Li[**2**]) while the nucleophilic substitution on C–X generates 2 equiv. of **13**. Further insight into the competition between the two scenarios was

 This journal is © The Royal Society of Chemistry 2018

Open Access Article. Published on 19 March 2018. Downloaded on 19/04/2018 11:29:01.
This article is licensed under a Creative Commons Attribution 3.0 Unported Licence.

gained with the help of α,ω-dihaloalkanes $X(CH_2)_nX$ (X = Cl, Br). In the resulting intermediates Li[FluB–BFlu($(CH_2)_nX$)], both possible follow-up reactions should be intramolecular processes. A longer alkylidene chain corresponds to a lower local concentration of the electrophile, while the BCH_2 groups are always similarly close to the reactive B–B bond. Consequently, short chains (n = 2,3) result in double substitution products $FluB(CH_2)_nBFlu$ and long chains (n = 5,6) in C–H-activation products $Li[FluB(\mu\text{-}C(H)(CH_2)_{n-1}X)(\mu\text{-}H)BFlu]$. In the case of the intermediate chain length n = 4, a mixture of both compounds is obtained: the worse leaving group X = Cl leads to a higher proportion of the C–H-activated species, the better leaving group X = Br furnishes more $FluB(CH_2)_4BFlu$. We finally note that the B–B-bond heterolysis of Li[**6**] with concomitant transfer of a reactive $[BFlu]^-$ moiety is reminiscent of the reactivity patterns of the widely used alkoxy-diborane(4) adducts $[pinB–Bpin(OR)]^-$.[25] As a decisive difference, however, $[BFlu]^-$ appears to be considerably more reactive than *in situ*-generated $[Bpin]^-$, because C–H-insertion reactions of the latter are so far unknown.

Conflicts of interest

There are no conflicts to declare.

Acknowledgements

T. K. thanks the Fonds der Chemischen Industrie for a Ph.D. grant. The authors are grateful to Dr M. Diefenbach for helpful discussions regarding the quantum-chemical calculations. We acknowledge Prof. E. D. Jemmis and Sagar Ghorai for discussions. We thank Albemarle Lithium GmbH (Frankfurt) for the generous gift of chemicals. Credit for the TOC-background picture: European Southern Observatory, ESO/L. Calçada.

Notes and references

1 *Organoboranes for Syntheses*, ed. P. V. Ramachandran and H. C. Brown, American Chemical Society, ACS Symposium Series, Washington D.C., 2001.
2 N. Miyaura and A. Suzuki, *Chem. Rev.*, 1995, **95**, 2457–2483.
3 S. N. Kessler and H. A. Wegner, *Org. Lett.*, 2010, **12**, 4062–4065.
4 J. B. Grande, T. Urlich, T. Dickie and M. A. Brook, *Polym. Chem.*, 2014, **5**, 6728–6739.
5 L. Schweighauser and H. A. Wegner, *Chem.–Eur. J.*, 2016, **22**, 14094–14103.
6 E. von Grotthuss, A. John, T. Kaese and M. Wagner, *Asian J. Org. Chem.*, 2018, **7**, 37–53.
7 *Frustrated Lewis Pairs I & II*, ed. G. Erker and D. W. Stephan, Springer, Heidelberg, 2013.
8 D. W. Stephan and G. Erker, *Angew. Chem., Int. Ed.*, 2015, **54**, 6400–6441.
9 D. W. Stephan, *Science*, 2016, **354**, aaf7229.
10 A. Lorbach, M. Bolte, H.-W. Lerner and M. Wagner, *Organometallics*, 2010, **29**, 5762–5765.
11 E. von Grotthuss, M. Diefenbach, M. Bolte, H.-W. Lerner, M. C. Holthausen and M. Wagner, *Angew. Chem., Int. Ed.*, 2016, **55**, 14067–14071.
12 (*a*) A. Hübner, M. Bolte, H.-W. Lerner and M. Wagner, *Angew. Chem., Int. Ed.*, 2014, **53**, 10408–10411; (*b*) A. Hübner, A. M. Diehl, M. Bolte, H.-W. Lerner and M. Wagner, *Organometallics*, 2013, **32**, 6827–6833.
13 T. Kaese, A. Hübner, M. Bolte, H.-W. Lerner and M. Wagner, *J. Am. Chem. Soc.*, 2016, **138**, 6224–6233.
14 T. Kaese, H. Budy, M. Bolte, H.-W. Lerner and M. Wagner, *Angew. Chem., Int. Ed.*, 2017, **56**, 7546–7550.
15 K. M. Waltz and J. F. Hartwig, *Science*, 1997, **277**, 211–213.
16 A. E. Shilov and G. B. Shul'pin, *Chem. Rev.*, 1997, **97**, 2879–2932.
17 K. M. Waltz and J. F. Hartwig, *J. Am. Chem. Soc.*, 2000, **122**, 11358–11369.
18 I. A. Mkhalid, J. H. Barnard, T. B. Marder, J. M. Murphy and J. F. Hartwig, *Chem. Rev.*, 2010, **110**, 890–931.
19 (*a*) P. Bissinger, H. Braunschweig, A. Damme, R. D. Dewhurst, T. Kupfer, K. Radacki and K. Wagner, *J. Am. Chem. Soc.*, 2011, **133**, 19044–19047. Related examples include: (*b*) T. Mennekes, P. Paetzold and R. Boese, *Angew. Chem., Int. Ed.*, 1990, **29**, 899–900; (*c*) W. J. Grigsby and P. P. Power, *J. Am. Chem. Soc.*, 1996, **118**, 7981–7988; (*d*) W. J. Grigsby and P. P. Power, *Chem.–Eur. J.*, 1997, **3**, 368–375; (*e*) Y. Wang and G. H. Robinson, *Inorg. Chem.*, 2011, **50**, 12326–12337; (*f*) D. P. Curran, A. Boussonnière, S. J. Geib and E. Lacôte, *Angew. Chem., Int. Ed.*, 2012, **51**, 1602–1605; (*g*) Y.-L. Rao, L. D. Chen, N. J. Mosey and S. Wang, *J. Am. Chem. Soc.*, 2012, **134**, 11026–11034.
20 L. Wang, Y. Fang, H. Mao, Y. Qu, J. Zuo, Z. Zhang, G. Tan and X. Wang, *Chem.–Eur. J.*, 2017, **23**, 6930–6936.
21 (*a*) É. Rochette, M.-A. Courtemanche and F.-G. Fontaine, *Chem.–Eur. J.*, 2017, **23**, 3567–3571. Related examples include: (*b*) G. Ménard and D. W. Stephan, *Angew. Chem., Int. Ed.*, 2012, **51**, 4409–4412; (*c*) G. Ménard, J. A. Hatnean, H. J. Cowley, A. J. Lough, J. M. Rawson and D. W. Stephan, *J. Am. Chem. Soc.*, 2013, **135**, 6446–6449.
22 The following literature survey focuses entirely on free boron-centered nucleophiles and does not cover corresponding transition-metal complexes. For an overview of these and related compound classes, see: (*a*) H. Braunschweig and T. Wagner, *Angew. Chem., Int. Ed.*, 1995, **34**, 825–826; (*b*) H. Braunschweig, M. Burzler, R. D. Dewhurst and K. Radacki, *Angew. Chem., Int. Ed.*, 2008, **47**, 5650–5653; (*c*) T. Kajiwara, T. Terabayashi, M. Yamashita and K. Nozaki, *Angew. Chem., Int. Ed.*, 2008, **47**, 6606–6610; (*d*) H. Braunschweig, R. D. Dewhurst, T. Herbst and K. Radacki, *Angew. Chem., Int. Ed.*, 2008, **47**, 5978–5980; (*e*) T. Terabayashi, T. Kajiwara, M. Yamashita and K. Nozaki, *J. Am. Chem. Soc.*, 2009, **131**, 14162–14163; (*f*) H. Braunschweig, P. Brenner, R. D. Dewhurst, M. Kaupp, R. Müller and S. Östreicher, *Angew. Chem., Int. Ed.*, 2009, **48**, 9735–9738; (*g*) Y. Segawa, M. Yamashita and K. Nozaki, *Angew. Chem., Int. Ed.*, 2007, **46**, 6710–6713; (*h*) A. Steffen, R. M. Ward, W. D. Jones and T. B. Marder, *Coord. Chem. Rev.*, 2010, **254**, 1950–1976; (*i*) R. Frank,

Open Access Article. Published on 19 March 2018. Downloaded on 19/04/2018 11:29:01.
This article is licensed under a Creative Commons Attribution 3.0 Unported Licence.

J. Howell, J. Campos, R. Tirfoin, N. Phillips, S. Zahn, D. M. P. Mingos and S. Aldridge, *Angew. Chem., Int. Ed.*, 2015, **54**, 9586–9590; (*j*) H. Braunschweig, J. O. C. Jimenez-Halla, K. Radacki and R. Shang, *Chem. Commun.*, 2015, **51**, 16569–16572.

23 (*a*) Y. Segawa, M. Yamashita and K. Nozaki, *Science*, 2006, **314**, 113–115; (*b*) Y. Segawa, Y. Suzuki, M. Yamashita and K. Nozaki, *J. Am. Chem. Soc.*, 2008, **130**, 16069–16079; (*c*) M. Soleilhavoup and G. Bertrand, *Angew. Chem., Int. Ed.*, 2017, **56**, 10282–10292; (*d*) L. Weber, *Eur. J. Inorg. Chem.*, 2017, 3461–3488. Related examples include: (*e*) M. Unverzagt, G. Subramanian, M. Hofmann, P. von Ragué Schleyer, S. Berger, K. Harms, W. Massa and A. Berndt, *Angew. Chem., Int. Ed.*, 1997, **36**, 1469–1472; (*f*) S. Robinson, J. McMaster, W. Lewis, A. J. Blake and S. T. Liddle, *Chem. Commun.*, 2012, **48**, 5769–5771; (*g*) W. Lu, H. Hu, Y. Li, R. Ganguly and R. Kinjo, *J. Am. Chem. Soc.*, 2016, **138**, 6650–6661; (*h*) B. Wang, Y. Li, R. Ganguly, H. Hirao and R. Kinjo, *Nat. Commun.*, 2016, **7**, 11871; (*i*) M. M. Morgan, J. M. Rautiainen, W. E. Piers, H. M. Tuononen and C. Gendy, *Dalton Trans.*, 2018, **47**, 734–741.

24 (*a*) A.-F. Pécharman, A. L. Colebatch, M. S. Hill, C. L. McMullin, M. F. Mahon and C. Weetman, *Nat. Commun.*, 2017, **8**, 15022; (*b*) A.-F. Pécharman, M. S. Hill, C. L. McMullin and M. F. Mahon, *Angew. Chem., Int. Ed.*, 2017, **56**, 16363–16366.

25 (*a*) C. Kleeberg, L. Dang, Z. Lin and T. B. Marder, *Angew. Chem., Int. Ed.*, 2009, **48**, 5350–5354; (*b*) R. D. Dewhurst, E. C. Neeve, H. Braunschweig and T. B. Marder, *Chem. Commun.*, 2015, **51**, 9594–9607; (*c*) S. Pietsch, E. C. Neeve, D. C. Apperley, R. Bertermann, F. Mo, D. Qiu, M. S. Cheung, L. Dang, J. Wang, U. Radius, Z. Lin, C. Kleeberg and T. B. Marder, *Chem.–Eur. J.*, 2015, **21**, 7082–7098; (*d*) E. C. Neeve, S. J. Geier, I. A. Mkhalid, S. A. Westcott and T. B. Marder, *Chem. Rev.*, 2016, **116**, 9091–9161; (*e*) J. Cid, H. Gulyás, J. J. Carbó and E. Fernández, *Chem. Soc. Rev.*, 2012, **41**, 3558–3570.

26 (*a*) H. Braunschweig, C.-W. Chiu, K. Radacki and T. Kupfer, *Angew. Chem., Int. Ed.*, 2010, **49**, 2041–2044; (*b*) R. Bertermann, H. Braunschweig, R. D. Dewhurst, C. Hörl, T. Kramer and I. Krummenacher, *Angew. Chem., Int. Ed.*, 2014, **53**, 5453–5457. For an overview of *N*-heterocyclic carbene boranes, see: (*c*) D. P. Curran, A. Solovyev, M. Makhlouf Brahmi, L. Fensterbank, M. Malacria and E. Lacôte, *Angew. Chem., Int. Ed.*, 2011, **50**, 10294–10317.

27 (*a*) R. Kinjo, B. Donnadieu, M. A. Celik, G. Frenking and G. Bertrand, *Science*, 2011, **333**, 610–613. Related examples include: (*b*) T. Imamoto and T. Hikosaka, *J. Org. Chem.*, 1994, **59**, 6753–6759; (*c*) J. Monot, A. Solovyev, H. Bonin-Dubarle, É. Derat, D. P. Curran, M. Robert, L. Fensterbank, M. Malacria and E. Lacôte, *Angew. Chem., Int. Ed.*, 2010, **49**, 9166–9169; (*d*) D. A. Ruiz, G. Ung, M. Melaimi and G. Bertrand, *Angew. Chem., Int. Ed.*, 2013, **52**, 7590–7592; (*e*) D. A. Ruiz, M. Melaimi and G. Bertrand, *Chem. Commun.*, 2014, **50**, 7837–7839; (*f*) L. Kong, Y. Li, R. Ganguly, D. Vidovic and R. Kinjo, *Angew. Chem., Int. Ed.*, 2014, **53**, 9280–9283; (*g*) L. Kong, R. Ganguly, Y. Li and R. Kinjo, *Chem. Sci.*, 2015, **6**, 2893–2902.

28 (*a*) E. Bernhardt, V. Bernhardt-Pitchougina, H. Willner and N. Ignatiev, *Angew. Chem., Int. Ed.*, 2011, **50**, 12085–12088; (*b*) J. Landmann, J. A. P. Sprenger, R. Bertermann, N. Ignat'ev, V. Bernhardt-Pitchougina, E. Bernhardt, H. Willner and M. Finze, *Chem. Commun.*, 2015, **51**, 4989–4992; (*c*) J. Landmann, J. A. P. Sprenger, M. Hailmann, V. Bernhardt-Pitchougina, H. Willner, N. Ignat'ev, E. Bernhardt and M. Finze, *Angew. Chem., Int. Ed.*, 2015, **54**, 11259–11264; (*d*) H. Braunschweig, R. D. Dewhurst, L. Pentecost, K. Radacki, A. Vargas and Q. Ye, *Angew. Chem., Int. Ed.*, 2016, **55**, 436–440.

29 G. R. Fulmer, A. J. M. Miller, N. H. Sherden, H. E. Gottlieb, A. Nudelman, B. M. Stoltz, J. E. Bercaw and K. I. Goldberg, *Organometallics*, 2010, **29**, 2176–2179.

30 (*a*) L. Kaufmann, H. Vitze, M. Bolte, H.-W. Lerner and M. Wagner, *Organometallics*, 2008, **27**, 6215–6221; (*b*) A. Iida, A. Sekioka and S. Yamaguchi, *Chem. Sci.*, 2012, **3**, 1461–1466.

31 See ref. 25b.

32 M. Saunders and E. L. Hagen, *J. Am. Chem. Soc.*, 1968, **90**, 6881–6882.

33 G. A. Olah and A. M. White, *J. Am. Chem. Soc.*, 1969, **91**, 5801–5810.

34 G. A. Olah and A. M. White, *J. Am. Chem. Soc.*, 1969, **91**, 6883–6885.

35 L. Radom, J. A. Pople, V. Buss and P. v. R. Schleyer, *J. Am. Chem. Soc.*, 1972, **94**, 311–321.

36 P. C. Hariharan, L. Radom, J. A. Pople and P. v. R. Schleyer, *J. Am. Chem. Soc.*, 1974, **96**, 599–601.

37 M. Saunders, P. Vogel, E. L. Hagen and J. Rosenfeld, *Acc. Chem. Res.*, 1973, **6**, 53–59.

38 H. Nöth and B. Wrackmeyer, *Nuclear Magnetic Resonance Spectroscopy of Boron Compounds*, in *NMR Basic Principles and Progress*, ed. P. Diehl, E. Fluck and R. Kosfeld, Springer Verlag, Berlin, Heidelberg, New York, 1978.

39 Scattered precedence for comparable reactivity of electron-precise B–B single and multiple bonds exists: (*a*) A. Hübner, T. Kaese, M. Diefenbach, B. Endeward, M. Bolte, H.-W. Lerner, M. C. Holthausen and M. Wagner, *J. Am. Chem. Soc.*, 2015, **137**, 3705–3714; (*b*) H. Braunschweig, P. Constantinidis, T. Dellermann, W. C. Ewing, I. Fischer, M. Hess, F. R. Knight, A. Rempel, C. Schneider, S. Ullrich, A. Vargas and J. D. Woollins, *Angew. Chem., Int. Ed.*, 2016, **55**, 5606–5609; (*c*) M. Frick, E. Kaifer and H.-J. Himmel, *Angew. Chem., Int. Ed.*, 2017, **56**, 11645–11648; (*d*) M. Arrowsmith, H. Braunschweig and T. E. Stennett, *Angew. Chem., Int. Ed.*, 2017, **56**, 96–115; (*e*) A. Widera, E. Kaifer, H. Wadepohl and H.-J. Himmel, *Chem.–Eur. J.*, 2018, **24**, 1209–1216; (*f*) J. Horn, A. Widera, S. Litters, E. Kaifer and H.-J. Himmel, *Dalton Trans.*, 2018, **47**, 2009–2017.

40 A comparable selectivity toward C–H activation was also observed for EtBr (*cf.* Li[**19**] in the ESI†).

41 T. Kaese, T. Trageser, H. Budy, M. Bolte, H.-W. Lerner and M. Wagner, 2018, Private communication to the

 This journal is © The Royal Society of Chemistry 2018

Open Access Article. Published on 19 March 2018. Downloaded on 19/04/2018 11:29:01.
This article is licensed under a Creative Commons Attribution 3.0 Unported Licence.

Cambridge Structural Database; deposition numbers: CCDC 1819625 ([Li(thf)$_4$][**15**^{C4,Cl}]·THF), CCDC 1819626 ([Li(thf)$_4$][**15**^{C6,Cl}]·THF), and CCDC 1819627 ([Li(thf)$_4$][**15**^{C6,Br}]).†

42 S. J. Tremont and H. U. Rahman, *J. Am. Chem. Soc.*, 1984, **106**, 5759–5760.

43 See ref. 23b.

44 D. Griller and K. U. Ingold, *Acc. Chem. Res.*, 1980, **13**, 317–323.

45 D. C. Nonhebel, *Chem. Soc. Rev.*, 1993, **22**, 347–359.

46 C. Chen, L. Ouyang, Q. Lin, Y. Liu, C. Hou, Y. Yuan and Z. Weng, *Chem.–Eur. J.*, 2014, **20**, 657–661.

47 A. Lorbach, M. Bolte, H.-W. Lerner and M. Wagner, *Chem. Commun.*, 2010, **46**, 3592–3594.

48 A. Hübner, A. M. Diehl, M. Diefenbach, B. Endeward, M. Bolte, H.-W. Lerner, M. C. Holthausen and M. Wagner, *Angew. Chem., Int. Ed.*, 2014, **53**, 4832–4835.

49 See ref. 39a.

50 A. Hübner, Z.-W. Qu, U. Englert, M. Bolte, H.-W. Lerner, M. C. Holthausen and M. Wagner, *J. Am. Chem. Soc.*, 2011, **133**, 4596–4609.

Electronic Supplementary Material (ESI) for Chemical Science.
This journal is © The Royal Society of Chemistry 2018

Electronic Supplementary Information

A Redox-Active Diborane Platform Performs C(sp^3)–H Activation and Nucleophilic Substitution Reactions

Thomas Kaese, Timo Trageser, Hendrik Budy, Michael Bolte, Hans-Wolfram Lerner and Matthias Wagner*

Content:

1.	Experimental details and characterization data	ESI2-ESI22
2.	Plots of NMR spectra	ESI23-ESI46
3.	X-ray	ESI47-ESI59
4.	Computational details	ESI60-ESI69
5.	References	ESI70

1. Experimental details and characterization data

General considerations. All reactions and manipulations were carried out in an argon-filled glovebox or by applying standard Schlenk techniques under an argon atmosphere. Hexane was dried over Na, THF and Et_2O were dried over Na/benzophenone, THF-d_8 was dried over Na-K alloy. Prior to use, the solvents were distilled from the drying agent, degassed by applying three freeze-pump-thaw cycles, and stored over activated molecular sieves (3 Å). Compounds **1**H_2,[S1] Li[**1**H],[S2] and Li_2[**1**][S3] were synthesized according to literature procedures. The Et_2O solution of the $D_3CLi{\cdot}LiI$ complex (Sigma Aldrich) is commercially available with 99 atom-% deuterium and was used as received. Commercial Et_3SiD (Santa Cruz Biotechnology) contained 98 atom-% deuterium. Prior to use, the liquid haloalkanes were degassed by applying three freeze-pump-thaw cycles. NMR: Bruker DPX 250, Avance 300, Avance III 500 HD. Chemical shifts are referenced to (residual) solvent signals ($^1H/^{13}C\{^1H\}$; THF-d_8: δ = 3.58/67.21 ppm),[S4] external LiCl in D_2O (^7Li), or external $BF_3{\cdot}Et_2O$ (^{11}B; $^{11}B\{^1H\}$). Abbreviations: s = singlet, d = doublet, t = triplet, q = quartet, m = multiplet, br = broad, n.r. = multiplet expected in the NMR spectrum but not resolved, n.o. = not observed, vq = virtual quartet, vquint = virtual quintet.

Reaction of $1H_2$ with 1 equiv. of H_3CLi. An Et_2O solution of H_3CLi (0.5 M, 0.05 mL, 25 µmol) was evaporated to dryness in an NMR tube and the colorless solid residue was dissolved in THF-d_8 (0.6 mL) at room temperature. The solution was frozen at –196 °C and colorless $\mathbf{1}H_2$ (14 mg, 25 µmol) was added. The NMR tube was evacuated, flame sealed, and warmed to room temperature. The ^{1}H NMR spectroscopic investigation of the orange reaction solution revealed Li[**1**H],[S2] Li[**2**], and Li[**7**] as the major products (each ca. 20-40%; the product distribution varied to some extent between repeated experiments).

In a glovebox, a representative NMR sample was transferred to an uncapped glass vial, and the vial was placed in a larger glass vessel containing hexane (2 mL). The outer vessel was covered with a lid to allow for gas-phase diffusion of the solvents in a closed environment. After 2-3 d, three types of single crystals (1 x yellow, 2 x colorless) had grown. According to X-ray crystallography, the yellow crystals consisted of the known salt [Li(thf)$_3$][**1**H].[S2] Of the colorless specimen, the first kind were too poorly diffracting to perform a full refinement, but, according to ^{1}H NMR spectroscopy, they consisted of Li[**7**] (cf. the reaction of $\mathbf{1}H_2$ with Li[HBEt$_3$] for a targeted synthesis and the characterization of Li[**7**]). The second kind of colorless crystals turned out to be [Li(thf)$_4$][**2**] (for the X-ray crystal structure of the differently solvated analog [Li(thf)$_3$][**2**], see the reaction of Li_2[**1**] with methyl triflate).

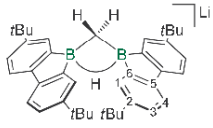

Figure S1. NMR numbering scheme for Li[**2**].

*Li[**2**]*

^{1}H NMR (500.2 MHz, THF-d_8): δ = 7.99 (d, ^4J(H,H) = 1.9 Hz, 4H; H-1), 7.41 (d, ^3J(H,H) = 7.9 Hz, 4H; H-4), 7.06 (dd, ^3J(H,H) = 7.9 Hz, ^4J(H,H) = 1.9 Hz, 4H; H-3), 1.94 (br, 1H; μ-H), 1.42 (s, 36H; CH_3), 0.49 (d, ^3J(H,H) = 4.8 Hz, 2H; CH_2).

^{7}Li NMR (194.4 MHz, THF-d_8): δ = –0.3.

^{11}B NMR (160.5 MHz, THF-d_8): δ = –14.0 (br).

^{13}C{^{1}H} NMR (125.8 MHz, THF-d_8): δ = 159.1 (C-6), 147.8 (C-5), 146.3 (C-2), 127.9 (C-1), 121.8 (C-3), 117.7 (C-4), 35.2 (CCH_3), 32.6 (CH_3), 5.1 (CH_2).

Reaction of Li[2] with H_3C–I. An NMR tube was charged at room temperature with $[Li(thf)_4]$[**2**] (5.0 mg, 5.8 µmol), THF-d_8 (0.5 mL), and H_3C–I (1.0 µl, 2.3 mg, 16 µmol). According to ^1H, ^{11}B, and ^{13}C NMR spectroscopic investigations, Li[**2**] had vanished after 3 d and **14**^{C1} formed as the major product besides trace amounts of **13**.

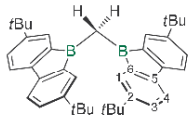

Figure S2. NMR numbering scheme for **14**^{C1}.

14^{C1}

^1H NMR (500.2 MHz, THF-d_8): δ = 7.41 (d, ^4J(H,H) = 1.9 Hz, 4H; H-1), 7.13 (d, ^3J(H,H) = 7.8 Hz, 4H; H-4), 7.07 (dd, ^3J(H,H) = 7.8 Hz, ^4J(H,H) = 1.9 Hz, 4H; H-3), 1.93 (s, 2H; CH_2), 1.18 (s, 36H; CH_3).

^{11}B NMR (160.5 MHz, THF-d_8): δ = 45 (vbr).

$^{13}C\{^1H\}$ NMR (125.8 MHz, THF-d_8): δ = 149.3 (C-5), 149.2 (C-2), 147.8 (C-6), 129.7 (C-1), 127.2 (C-3), 118.4 (C-4), 34.9 (CCH_3), 31.7 (CH_3), 14.8 (CH_2).

HRMS: Calculated for $C_{41}H_{50}B_2$: 564.40931, found: 564.41115.

Reaction of $1H_2$ with 1 equiv. Li[$HBEt_3$].

At –30°C

In an NMR tube, a THF solution of Li[$HBEt_3$] (1 M, 38 µL, 38 µmol) was evaporated to dryness at room temperature in a dynamic vacuum. During the addition of a THF-d_8 solution of $\mathbf{1}H_2$ (0.5 mL, 21 mg, 38 µmmol) and the subsequent flame-sealing of the NMR tube, the lower part of the tube was cooled to –196 °C. The sample was stored at –70 °C for 3 h prior to its NMR spectroscopic investigation at –30 °C, which showed a selective transformation to the primary hydride trapping product Li[**10**].

At room temperature

When carried out in neat THF (6 mL) at room temperature, the reaction between $\mathbf{1}H_2$ (79 mg, 143 µmol) and Li[$HBEt_3$] (0.05 M in THF, 2.7 mL, 135 µmol) furnished a clear, pale yellow solution. A ^{1}H NMR spectroscopic investigation (THF-d_8) showed the quantitative consumption of $\mathbf{1}H_2$ and the formation of two new major compounds (*i.e.*, the primary hydride trapping product Li[**10**] and its isomer Li[**7**]). After heating the sample at 50 °C for 1 h, Li[**7**] became by far the major constituent of the product mixture (>70%).

To obtain crystals, a solution of Li[$HBEt_3$] (0.2 M, 0.36 mL, 72 µmol) in THF/Et_2O (1:4) was added at room temperature to a colorless suspension of $\mathbf{1}H_2$ (40 mg, 72 µmol) in Et_2O (3 mL). After stirring for 10 min, the reaction mixture was filtered through a PTFE syringe filter (0.2 µm). Colorless thin needles of [Li(thf)$_3$(Et_2O)][**7**] grew from the filtrate at room temperature within 1 d.

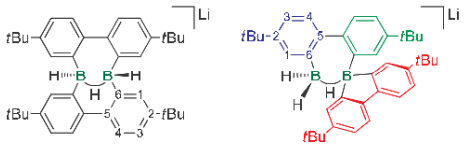

Figure S3. NMR numbering scheme for the primary hydride trapping product Li[**10**] (left) and its isomer Li[**7**] (right).

*Li[**10**]*

^{1}H NMR (500.2 MHz, THF-d_8): δ = 7.61 (d, ^4J(H,H) = 1.9 Hz, 2H; H-1), 7.27 (d, ^3J(H,H) = 8.0 Hz, 2H; H-4), 7.11 (dd, ^3J(H,H) = 8.0 Hz, ^4J(H,H) = 1.9 Hz, 2H; H-3), 6.94 (d, ^3J(H,H) = 8.0 Hz, 2H; H-4), 6.78 (d, ^4J(H,H) = 1.9 Hz, 2H; H-1), 6.59 (dd, ^3J(H,H) = 8.0 Hz, ^4J(H,H) = 1.9 Hz, 2H; H-3), 1.38 (s, 18H; CH_3), 0.94 (s, 18H; CH_3).

^{7}Li NMR (194.4 MHz, THF-d_8): δ = –0.6.

^{11}B NMR (96.3 MHz, THF-d_8): δ = 33.5 (br), 8.2 (br).

^{13}C{^{1}H} NMR (125.8 MHz, THF-d_8): δ = 149.6 (C-6), 149.2 (C-6), 145.4 (C-2), 144.8 (C-5), 144.5 (C-2), 141.5 (C-5), 134.4 (C-1), 129.6 (C-1), 125.7 (C-4), 125.4 (C-4), 122.1 (C-3), 119.9 (C-3), 34.6 (CCH_3), 34.2 (CCH_3), 32.1 (CH_3), 31.6 (CH_3).

Resonances of the same color belong to the same phenyl ring (as confirmed by 2D NMR experiments).

*Li[**7**]*

^{1}H NMR (500.2 MHz, THF-d_8): δ = 7.48 (d, ^{4}J(H,H) = 2.3 Hz, 1H; H-1), 7.39 (d, ^{4}J(H,H) = 2.3 Hz, 1H; H-1), 7.38 (d, ^{3}J(H,H) = 8.0 Hz, 1H; H-4), 7.31 (d, ^{3}J(H,H) = 7.9 Hz, 2H; H-4), 7.29 (d, ^{3}J(H,H) = 8.0 Hz, 1H; H-4), 7.23 (dd, ^{3}J(H,H) = 8.0 Hz, ^{4}J(H,H) = 2.3 Hz, 1H; H-3), 7.05 (dd, ^{3}J(H,H) = 8.0 Hz, ^{4}J(H,H) = 2.3 Hz, 1H; H-3), 6.97 (n.r., 2H; H-3), 2.6 (vbr, 1H; BH), 1.34 (s, 9H; CH_3), 1.18 (s, 9H; CH_3), 1.18 (br, 18H; CH_3), n.o. (H-1 (2H), BH (2H)).

^{7}Li NMR (194.4 MHz, THF-d_8): δ = –0.7.

^{11}B NMR (96.3 MHz, THF-d_8): δ = –3.6 (br), –10.1 (br).

^{13}C{^{1}H} NMR (125.8 MHz, THF-d_8): δ = 147.4 (br), 147.0, 146.5, 145.9, 145.6, 145.5, 133.9 (C-1), 130.2 (C-1), 129.6 (C-1), 126.4 (C-4), 125.9 (C-4), 122.9 (C-3), 122.3 (C-3), 121.8 (C-3), 117.5 (C-4), 34.9 (CCH_3), 34.8 (CCH_3), 34.6 (CCH_3), 32.2 (CH_3), 32.0 (CH_3), n.o. (3 x C^{Ar}).

Resonances of the same color belong to the same phenyl ring (as confirmed by 2D NMR experiments). Signals marked in red could be unequivocally assigned, because they possess double intensity; the blue/green resonances were tentatively assigned by comparison of their chemical shift values with those of a related compound featuring a B–B bond instead of the bridging H atom.[S5]

Reaction of 1H_2 with exc. LiH. In an NMR tube, THF-d_8 (0.6 mL) was added at room temperature to a solid mixture of **1**H_2 (7 mg, 13 µmol) and LiH (15 mg, 1.9 mmol). ^{1}H and ^{11}B NMR spectra recorded on this mixture after 10 h showed no reaction. However, upon heating (60 °C, 1 d) the lithium dihydrido-2,7-di(*t*Bu)-9-boratafluorene[S3] evolved as the major product (ca. 80%); further heating at 100 °C for 1d resulted in the quantitative conversion of **1**H_2 to the lithium dihydrido-2,7-di(*t*Bu)-9-boratafluorene.

Deuterium-labeling experiments

*(A) Synthesis of **1**D$_2$*

Compound **1**D$_2$ was obtained according to the published synthesis of **1**H$_2$,[S1] but by using Et$_3$SiD instead of Et$_3$SiH (Scheme S1).

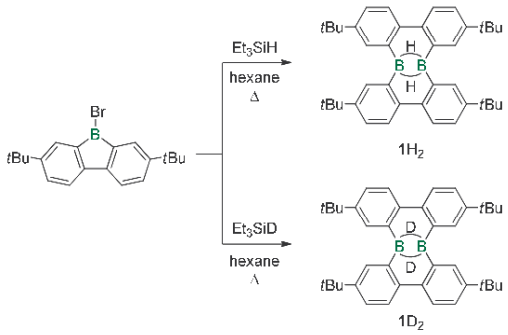

Scheme S1. Reaction of 2,7-di(*t*Bu)-9-Br-9-borafluorene with Et$_3$SiH or Et$_3$SiD to afford **1**H$_2$ or **1**D$_2$, respectively.

***1**D$_2$*

The ^{1}H, ^{11}B{^{1}H}, and ^{13}C{^{1}H} NMR spectra (C_6D_6) of **1**H$_2$[S1] and **1**D$_2$ are identical with the exception of a broad proton resonance at 3.5 ppm, which has been assigned to the bridging H-atoms in **1**H$_2$[S1] and which is missing in **1**D$_2$. Instead, **1**D$_2$ shows a signal at 3.4 ppm in the ^{2}H NMR spectrum.

*(B) Reaction of **1**H$_2$ with D$_3$CLi*

A solution of D$_3$CLi·LiI in Et$_2$O (0.5 M, 0.05 mL, 25 µmol) was evaporated to dryness in an NMR tube. The resulting colorless residue was dissolved in THF-d_8 and the solution was frozen at –196 °C. Colorless **1**H$_2$ (14 mg, 25 µmol) was added, the NMR tube was vacuum sealed, and warmed to room temperature. The orange reaction mixture was analyzed by NMR spectroscopy (see section *D*).

*(C) Reaction of **1**D$_2$ with H$_3$CLi*

A solution of H$_3$CLi in Et$_2$O (0.25 M, 0.14 mL, 35 µmol) was evaporated to dryness in an NMR tube. The resulting colorless residue was dissolved in THF-d_8 and the solution was frozen at –196 °C. Colorless **1**D$_2$ (20 mg, 36 µmol) was added, the NMR tube was vacuum sealed, and warmed to room temperature. The orange reaction mixture was analyzed by NMR spectroscopy (see section *D*).

(D) Results of the deuterium-labeling experiments

The reactions D$_3$CLi/**1**H$_2$ and H$_3$CLi/**1**D$_2$ in THF-d_8 give complex product mixtures in which Li[**1**H]/Li[**1**D] and Li[**2**]/Li[**2**-d_3] are present as major constituents (Figure S4). The additional, poorly resolved signals in the range 7.7 ppm to 6.5 ppm are due to hydride-trapping products. The product distributions critically depend on the exact stoichiometries employed.

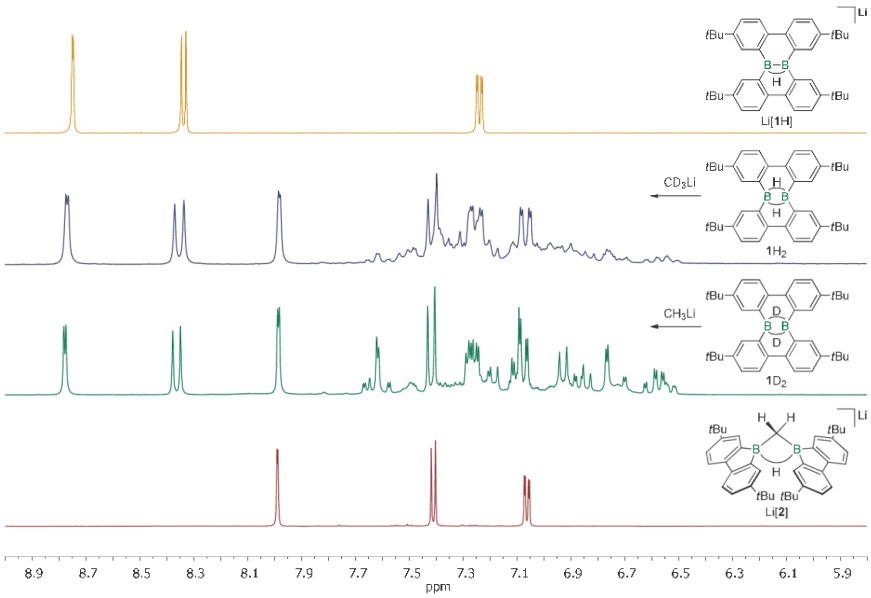

Figure S4. Aromatic regions of ^{1}H NMR spectra (THF-d_8) recorded on the reaction mixtures of D$_3$CLi/**1**H$_2$ (blue; 250.1 MHz) and H$_3$CLi/**1**D$_2$ (green; 300.0 MHz). Matching spectra of Li[**1**H] (orange; 500.2 MHz) and Li[**2**] (red; 500.2 MHz) are shown for comparison. *Note*: The spectra have been recorded at different spectrometer frequencies, which leads to slight differences in the line shapes of corresponding signals.

Li[**2**] shows two characteristic ^{1}H NMR signals, which are particularly relevant for the mechanistic considerations: a broad resonance at 1.94 ppm (μ-H) and a doublet at 0.49 ppm (CH_2). Both signals are observed in the ^{1}H NMR spectra of H_3CLi/**1**D_2, but absent in D_3CLi/**1**H_2 (Figure S5). Thus, the μ-H atom of Li[**2**] does not originate from the boron-bonded H atoms of the diborane(6) starting material (**1**H_2). Rather, all the CH_2 and μ-H atoms originate from the methyllithium reagent.

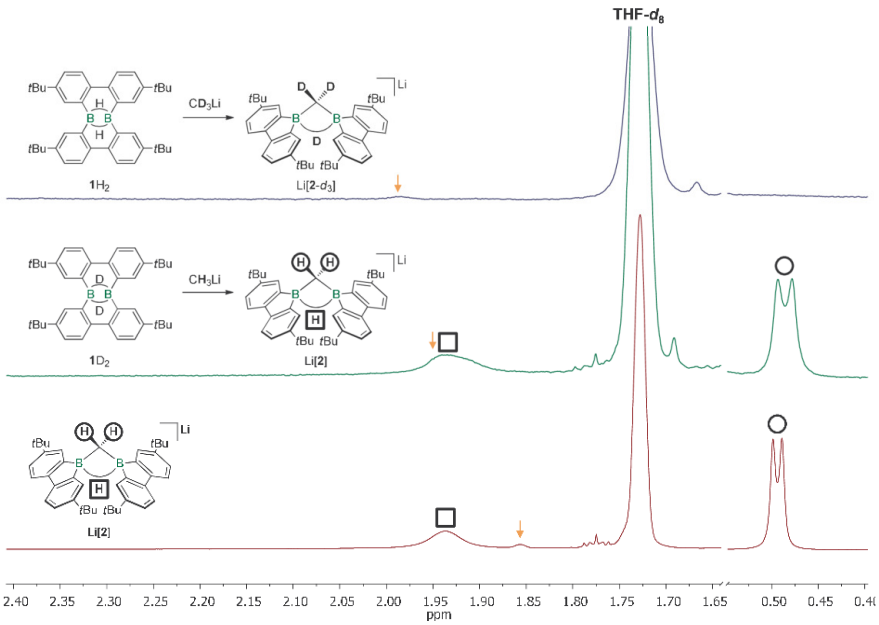

Figure S5. ^{1}H NMR spectra (THF-d_8) recorded on the reaction solutions of D_3CLi/**1**H_2 (blue; 250.1 MHz) and H_3CLi/**1**D_2 (green; 300.0 MHz). A spectrum of Li[**2**] (red; 500.2 MHz) is shown for comparison. *Note*: The orange-colored arrows mark the ^{13}C satellites of the solvent. The spectra have been recorded at different spectrometer frequencies, which leads to slight differences in the line shapes of corresponding signals and in the positions of the satellites. The integral values of the satellite signals are negligible compared to those of the other resonances. Both in the green and in the red spectrum, the integral ratio of the μ-H signal relative to the CH_2 signal is 1:2.

The reactions D_3CLi/**1**H_2 and H_3CLi/**1**D_2 afford D_3CH [$\delta(^1H)$ = 0.14, sept, ^2J(H,D) = 1.9 Hz; $\delta(^2H)$ = 0.14, d, ^2J(H,D) = 1.9 Hz] and CH_3D [$\delta(^1H)$ = 0.18, t, ^2J(H,D) = 1.9 Hz; $\delta(^2H)$ = 0.18, q, ^2J(H,D) = 1.9 Hz], respectively, as byproducts (Figure S6). The presence of small amounts of CH_4 are attributable to the fact that the Et_3SiD employed contained only 98 atom-% deuterium and to minor hydrolysis during sample preparation.

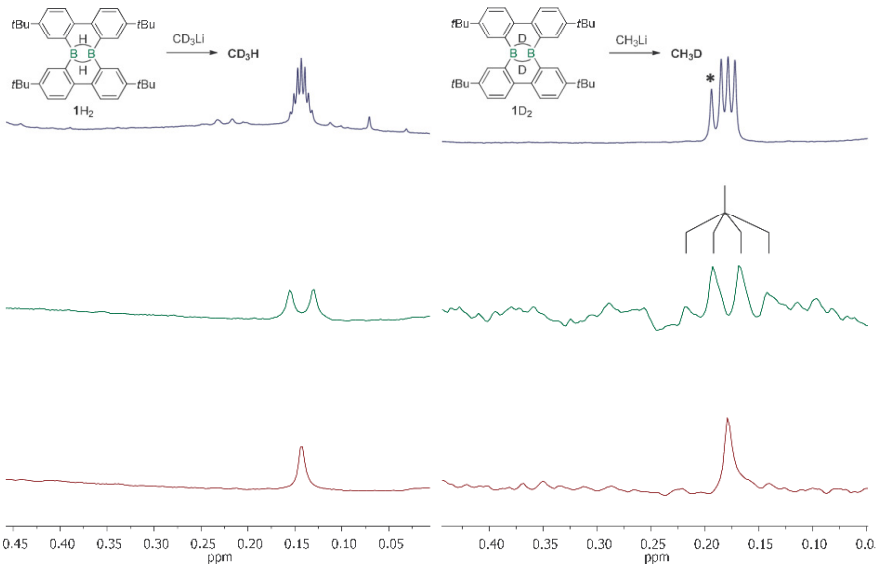

Figure S6. Stacked ^1H (blue; 500.2 MHz), ^2H (green; 76.8 MHz) and $^2H\{^1H\}$ (red) NMR spectra, recorded on the mixtures D_3CLi/**1**H_2 (left) and H_3CLi/**1**D_2 (right). The reactions were carried out in sealed NMR tubes (THF-d_8) and the spectra confirm the presence of D_3CH (left) and CH_3D (right). The signal marked with an asterisk corresponds to CH_4 (approximately 10% relative to CH_3D according to the integral values).

Reaction of Li[1H] with H_3CLi to furnish Li_2[4] and follow-up reaction with $1H_2$. A solution of H_3CLi in Et_2O (1.4 M, 15 µL, 21 µmol) was evaporated to dryness in an NMR tube. The addition of yellow $[Li(thf)_3]$[**1**H] (16 mg, 21 µmol) in THF-d_8 (0.6 mL) at room temperature furnished an orange-colored solution. The NMR tube was vacuum sealed and ^1H and ^{11}B NMR spectra were recorded. The spectra did not show the resonances of Li[**2**], but rather signal patterns assignable to Li_2[**4**] (Figures S8 and Figures S26). The sample was transferred to a new NMR tube, which had already been charged with $\mathbf{1}H_2$ (11 mg, 20 µmol). ^1H NMR spectroscopy confirmed an approximate 45% conversion to Li[**2**] and revealed the presence of a primary hydride trapping product Li[**10**], together with its rearranged isomer Li[**7**] (Figure S8).

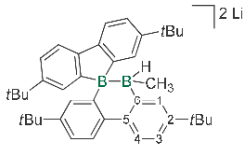

Figure S7. NMR numbering scheme for Li_2[**4**].

*Li_2[**4**]*

^1H NMR (300.0 MHz, THF-d_8): δ = 8.1 (vbr, 1H), 7.64 (d, ^3J(H,H) = 8.0 Hz, 1H; H-4), 7.53 (n.r., 1H), 7.2 (vbr, 2H), 7.19 (d, ^3J(H,H) = 7.9 Hz, 1H; H-4), 6.9 (vbr, 1H), 6.88 (dd, ^3J(H,H) = 7.9 Hz, ^4J(H,H) = 2.4 Hz, 1H; H-3), 6.76 (vbr, 2H), 1.35 (vbr, 9H; CCH_3), 1.26 (s, 9H; CCH_3), 1.20 (br, 9H; CCH_3), 1.08 (vbr, 9H; CCH_3), –0.1 (vbr, 3H; BCH_3). *Note*: An aryl resonance contributing the missing 2H is likely present at approximately 7.3 ppm, however, due to the broad line shapes and signal overlaps it cannot be unequivocally detected. Integration of the entire aryl region gives a sufficiently high integral value to match the required overall 12 aryl protons.

^{11}B NMR (96.3 MHz, THF-d_8): δ = –10.3 ($h_{1/2}$ = 80 Hz), –12.8 ($h_{1/2}$ = 200 Hz, *B*(H)CH_3). *Note*: Only the signal at –12.8 ppm becomes significantly sharper upon proton decoupling.

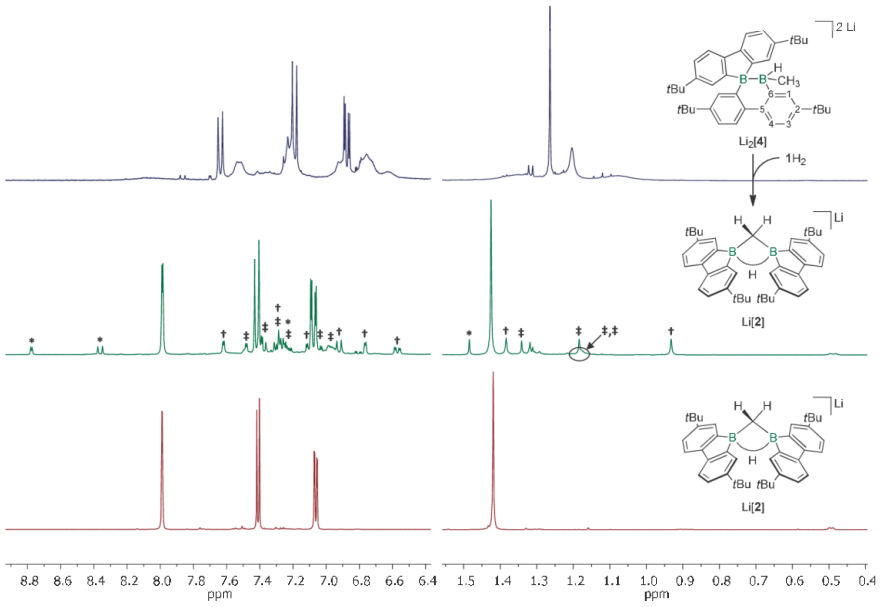

Figure S8. ^{1}H NMR spectrum of Li_2[**4**], obtained from the reaction H_3CLi/Li[**1**H] (top; 300.0 MHz). Middle: ^{1}H NMR spectrum showing the formation of Li[**2**] as major product of the reaction H_3CLi/Li[**1**H], after the addition of 1 equiv. **1**H_2 (middle; 300.0 MHz). The marked minor signals belong to Li[**1**H] (*) and the primary hydride trapping product Li[**10**] (†), which isomerizes over time to give Li[**7**] (‡). ^{1}H NMR spectrum of an authentic sample of Li[**2**] (bottom; 500.2 MHz).
All NMR spectra were recorded in THF-d_8; aromatic and alkyl regions are scaled differently.

Formation of Li_2[11]

Method A: *Reaction of Li[**1**H] with tBuCCLi.* Yellow [Li(thf)$_3$][**1**H] (20 mg, 26 µmol) in THF-d_8 (0.5 mL) was added at room temperature to an NMR tube charged with solid colorless *t*BuCCLi (2.3 mg, 26 µmol). A ^{1}H NMR spectroscopic investigation of the orange-colored solution revealed an almost quantitative consumption of the starting material and the concomitant formation of Li_2[**11**]. The reaction mixture was layered with hexane/12-crown-4 and stored at room temperature, whereupon orange single crystals of [Li(thf)(12-crown-4)][Li(thf)$_2$][**11**] formed.

Method B: *Reaction of Li_2[**1**] with HCCtBu***.*** A twofold excess of neat *t*BuCCH (4 µL, 2.7 mg, 33 µmol) was added at room temperature to a solution of [Li(thf)$_3$]$_2$[**1**] (15 mg, 15 µmol) in THF-d_8 (0.5 mL). The progress of the slow reaction was monitored by ^{1}H NMR spectroscopy (Figure S10). After 1 month, the signal pattern of Li_2[**11**] had developed to a significant extent.

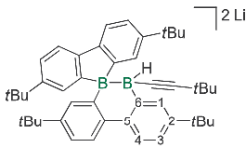

Figure S9. Schematic representation of Li_2[**11**].

*Li_2[**11**]*

^{1}H NMR (300.0 MHz, THF-d_8): δ = 8.2 (vbr, 1H), 7.61 (d, ^3J(H,H) = 8.0 Hz, 1H; H-4), 7.50 (n.r., 1H), 7.32 (n.r., 2H), 7.23 (d, ^3J(H,H) = 7.9 Hz, 1H; H-4), 7.12-6.95 (m, 2H), 6.82 (dd, ^3J(H,H) = 7.8 Hz, ^4J(H,H) = 2.1 Hz, 2H; H-3), 1.36 (vbr, 9H; C(CH$_3$)$_3$), 1.30 ppm (s, 9H; C(CH$_3$)$_3$), 1.19 (s, 9H; C(CH$_3$)$_3$), 1.09 (vbr, 9H; C(CH$_3$)$_3$), 0.97 (br, 9H; C≡CC(CH$_3$)$_3$). *Note*: An aryl resonance contributing the missing 2H cannot be unequivocally detected. Integration of the entire aryl region gives a sufficiently high integral value to match the required overall 12 aryl protons.

^{11}B NMR (96.3 MHz, THF-d_8): δ = –11.8 ($h_{1/2}$ = 60 Hz), –23.3 ($h_{1/2}$ = 190 Hz; *B*(H)CC*t*Bu). *Note*: Only the signal at –23.3 ppm becomes significantly sharper upon proton decoupling.

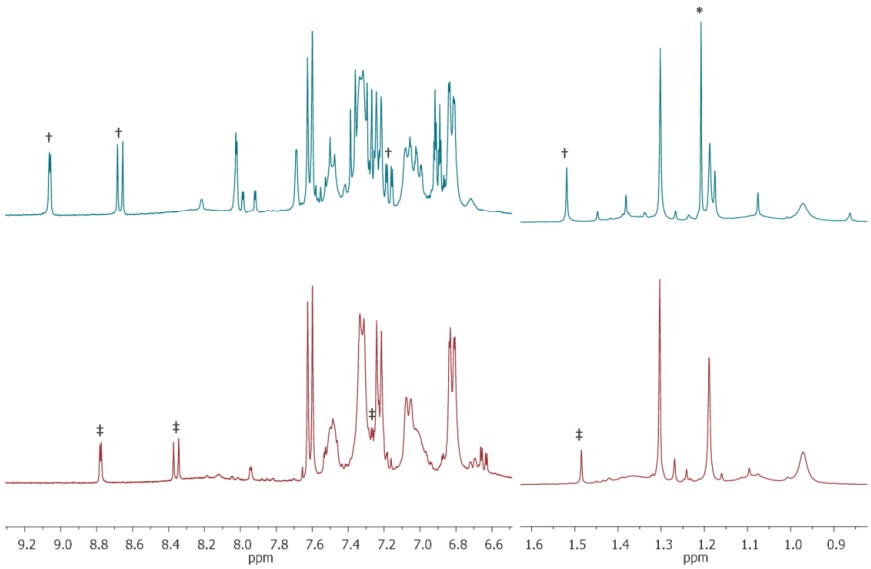

Figure S10: ^{1}H NMR spectra (300.0 MHz; THF-d_8) of the reaction mixtures 2 *t*BuCCH/Li_2[**1**] after 30 d (top) and *t*BuCCLi/Li[**1**H] after 1 d (bottom). Additional signals belong to residual Li_2[**1**] (†), Li[**1**H] (‡), and *t*BuCCH (*).

Reaction of Li_2[1] with 1 equiv. of H_3C–I. Neat H_3C–I (0.9 µL, 2.1 mg, 15 µmol) was added at room temperature with stirring to a dark red solution of $[Li(thf)_3]_2$[**1**] (15 mg, 15 µmol) in THF-d_8 (0.6 mL). A ^{1}H, ^{11}B, and ^{13}C{^{1}H} NMR spectroscopic investigation of the resulting pale yellow solution revealed the conversion of Li_2[**1**] to Li[**2**] (major product) and **13** (minor product).
For the NMR data of Li[**2**] see the reaction H_3CLi/**1**H_2.

Reaction of Li_2[1] with excess H_3CCl. Neat dark red $[Li(thf)_3]_2$[**1**] (25 mg, 25 µmol) was placed in a J. Young flask (30 mL) and dissolved in THF (2 mL). The solution was frozen at –196 °C. The flask was evacuated, closed, allowed to warm to room temperature, and filled with H_3CCl gas (1 atm), whereupon the stirred solution instantaneously changed its color from red to orange. All volatiles were removed in a dynamic vacuum and the orange solid residue was dissolved in THF-d_8. A ^{1}H and ^{11}B NMR spectroscopic investigation revealed the quantitative conversion of Li_2[**1**] to Li[**2**]. The entire sample was transferred to a small vial, which was placed in a larger vessel containing hexane (2 mL). The outer vessel was covered with a lid to allow for gas-phase diffusion of the solvents in a closed environment. Colorless crystalline material of $[Li(thf)_4]$[**2**] (17 mg, 20 µmol, 80%) was obtained. For the NMR data of Li[**2**], see the reaction H_3CLi/**1**H_2.

Reaction of Li_2[1] with 3 equiv. of H_3C–I. Neat H_3C–I (2.8 µL, 6.4 mg, 45 µmol) was added at room temperature with stirring to a dark red solution of $[Li(thf)_3]_2$[**1**] (15 mg, 15 µmol) in THF-d_8 (0.6 mL). A ^{1}H, ^{11}B, and ^{13}C{^{1}H} NMR spectroscopic investigation of the resulting pale yellow solution revealed the quantitative conversion of Li_2[**1**] to **13**.

Reaction of Li_2[1] with 2 equiv. of methyl triflate. Neat methyl triflate (2.8 µL, 4.0 mg, 25 µmol) was added at room temperature with stirring to a dark red solution of $[Li(thf)_3]_2$[**1**] (12 mg, 12 µmol) in C_6H_6 (0.5 mL). All volatiles were removed in a dynamic vacuum and the residue was dissolved in THF-d_8. A ^{1}H, ^{11}B, and ^{13}C{^{1}H} NMR spectroscopic investigation of the yellow solution confirmed the quantitative conversion of Li_2[**1**] to **13**. The addition of only 1.1 equiv. of methyl triflate to $[Li(thf)_3]_2$[**1**] in C_6H_6 furnished Li[**2**] as the major product, which crystallizes as at room temperature from the reaction solution in the form of $[Li(thf)_3]$[**2**]. For the NMR data of Li[**2**], see the reaction H_3CLi/**1**H_2.

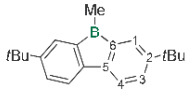

Figure S11. NMR numbering scheme for **13**.

13

^{1}H NMR (500.2 MHz, THF-d_8): δ = 7.50 (dd, ^4J(H,H) = 2.0 Hz, ^5J(H,H) = 0.6 Hz, 2H; H-1), 7.38 (dd, ^3J(H,H) = 7.9 Hz, ^5J(H,H) = 0.6 Hz, 2H; H-4), 7.16 (dd, ^3J(H,H) = 7.9 Hz, ^4J(H,H) = 2.0 Hz, 2H; H-3), 1.33 (s, 18H; CCH_3), 0.31 (s, 3H; BCH_3).
^{11}B NMR (160.5 MHz, THF-d_8): δ = 13.7.
^{13}C{^{1}H} NMR (125.8 MHz, THF-d_8): δ = 152.6 (br, C-6), 148.6 (C-2), 147.3 (C-5), 127.3 (C-1), 124.5 (C-3), 118.5 (C-4), 34.9 (CCH_3), 31.9 (CH_3), 3.2 (BCH_3).
Note: An authentic sample of **13**, prepared from 2,7-di(*t*Bu)-9-Br-9-borafluorene and H_3CMgI in Et_2O/toluene, gave identical NMR shift values.

Reaction of Li_2[1] with 1 equiv. ethyl bromide. Neat ethyl bromide (1.3 µL, 1.9 mg, 17 µmol) was added at room temperature with stirring to a dark red solution of $[Li(thf)_3]_2$[**1**] (15 mg, 15 µmol) in THF-d_8 (0.5 mL). A ^{1}H, ^{11}B, and ^{13}C{^{1}H} NMR spectroscopic investigation of the resulting yellow solution revealed the quantitative conversion of Li_2[**1**] to Li[**19**].

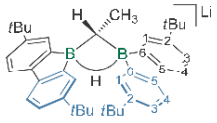

Figure S12. NMR numbering scheme for Li[**19**].

*Li[**19**]*

^{1}H NMR (500.2 MHz, THF-d_8): δ = 8.14 (d, ^4J(H,H) = 1.6 Hz, 2H; H-1), 7.99 (d, ^4J(H,H) = 1.6 Hz, 2H; H-1), 7.45 (d, ^3J(H,H) = 7.8 Hz, 2H; H-4), 7.42 (d, ^3J(H,H) = 7.8 Hz, 2H; H-4), 7.09 (dd, ^3J(H,H) = 7.8 Hz, ^4J(H,H) = 1.6 Hz, 2H; H-3), 7.06 (dd, ^3J(H,H) = 7.8 Hz, ^4J(H,H) = 1.6 Hz, 2H; H-3), 2.02 (br, 1H; μ-H), 1.47 (d, ^3J(H,H) = 7.0 Hz, 3H; CHCH_3), 1.44 (s, 18H, C(CH_3)$_3$), 1.43 (s, 18H, C(CH_3)$_3$), 0.95 (qd, ^3J(H,H) = 7.0 Hz, ^3J(H,H) = 3.0 Hz, 1H; CHCH$_3$).

^{7}Li NMR (116.6 MHz, THF-d_8): δ = –1.8.

^{11}B NMR (160.5 MHz, THF-d_8): δ = –12.6 (br).

^{13}C{^{1}H} NMR (125.8 MHz, THF-d_8): δ = 159.6 (C-6), 156.5 (C-6), 148.3 (C-5), 147.4 (C-5), 146.3 (C-2), 146.0 (C-2), 130.1 (C-1), 127.9 (C-1), 121.7 (C-3), 121.6 (C-3), 117.7 (C-4), 117.6 (C-4), 35.2 (*C*(CH$_3$)$_3$), 35.2 (*C*(CH$_3$)$_3$), 32.6 (C(*C*H$_3$)$_3$), 14.3 (CH*C*H$_3$), 11.0 (br, *C*HCH$_3$).

Note: The tentative assignment of resonances to the blue *vs* black aromatic rings is based on 2D NMR experiments and a comparison with the NMR spectra of the corresponding compound Li[**2**] featuring a symmetrical CH_2 bridge.

Reaction of Li_2[1] with benzyl chloride. A dark red solution of $[Li(thf)_3]_2$[**1**] (30 mg, 30 µmol) in THF-d_8 (0.3 mL) was added dropwise with stirring at room temperature to benzyl chloride (4.1 µL, 4.5 mg, 36 µmol) in THF-d_8 (0.2 mL). A ^{1}H, ^{11}B, and ^{13}C{^{1}H} NMR spectroscopic investigation of the resulting yellow solution revealed the selective conversion of Li_2[**1**] to Li[**16**] (> 90%). Upon addition of the reaction mixture to hexane (2 mL), a colorless precipitate formed. The mother liquor was removed, the precipitate washed with hexane (3 x 0.2 mL), and dried under vacuum to obtain pure Li[**16**] (according to NMR spectroscopy). Colorless single crystals of $[Li(thf)_4]$[**16**] were grown by gas-phase diffusion of hexane into a THF solution of Li[**16**] (3 d, room temperature). *Note*: Li[**16**] was also observed as the major product (> 90%) when 1 equiv. of benzyl bromide was used instead of benzyl chloride.

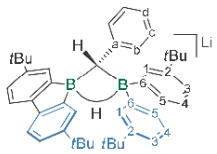

Figure S13. NMR numbering scheme for Li[**16**].

*Li[**16**]*

^{1}H NMR (500.2 MHz, THF-d_8): δ = 8.09 (n.r., 2H; H-1), 7.51 (n.r., 2H; H-1), 7.45 (d, ^3J(H,H) = 7.9 Hz, 2H; H-4), 7.43 (d, ^3J(H,H) = 7.9 Hz, 2H; H-4), 7.10 (dd, ^3J(H,H) = 7.9 Hz, ^4J(H,H) = n.r., 2H; H-3), 7.03-7.02 (m, 4H; H-3, H-b), 6.80-6.77 (m, 2H; H-c), 6.71-6.68 (m, 1H; H-d), 2.73 (s, 1H; BCH), 2.26 (br, 1H; BHB), 1.44 (s, 18H; CH_3), 1.23 (s, 18H; CH_3).

^{11}B NMR (160.5 MHz, THF-d_8): δ = −13.1 (br).

^{13}C{^{1}H} NMR (125.8 MHz, THF-d_8): δ = 158.4 (br; C-6), 155.5 (br; C-6), 150.7 (C-a), 148.1 (C-5), 147.8 (C-5), 146.4 (C-2), 145.8 (C-2), 134.6 (C-b), 131.5 (C-1), 127.8 (C-1), 126.4 (C-c), 122.1 (C-3), 121.8 (C-d), 121.7 (C-3), 117.7 (C-4), 117.5 (C-4), 35.2 (CCH_3), 35.0 (CCH_3), 32.6 (CH_3), 32.4 (CH_3), 27.3 (br; BCH).

Reaction of Li_2[1] with the radical clock (bromomethyl)cyclopropane. A dark red solution of $[Li(thf)_3]_2$[**1**] (12 mg, 12 µmol) in THF-d_8 (0.3 mL) was added dropwise with stirring at room temperature to (bromomethyl)cyclopropane (1.4 µL, 1.9 mg, 14 µmol) in THF-d_8 (0.2 mL). A ^{1}H, ^{11}B, and ^{13}C{^{1}H} NMR spectroscopic investigation of the resulting yellow solution revealed the selective conversion of Li_2[**1**] to Li[**17**] (> 90%). No signals were observed in the allylic region of the ^{1}H NMR spectrum. Note: Li[**17**] decomposes in THF-d_8 at room temperature within days.

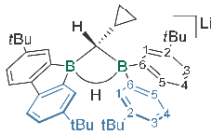

Figure S14. NMR numbering scheme for Li[**17**].

*Li[**17**]*

^{1}H NMR (300.0 MHz, THF-d_8): δ = 8.27 (d, ^4J(H,H) = 1.8 Hz, 2H; H-1), 7.92 (d, ^4J(H,H) = 1.8 Hz, 2H; H-1), 7.44 (d, ^3J(H,H) = 7.9 Hz, 2H; H-4), 7.41 (d, ^3J(H,H) = 7.9 Hz, 2H; H-4), 7.08 (dd, ^3J(H,H) = 7.9 Hz, ^4J(H,H) = 1.8 Hz, 2H; H-3), 7.05 (dd, ^3J(H,H) = 7.9 Hz, ^4J(H,H) = 1.8 Hz, 2H; H-3), 2.09 (br, 1H; BHB), 1.58-1.50 (m, 1H; CH_2CH), 1.44 (s, 18H; CH_3), 1.41 (s, 18H; CH_3), 0.86 (dd, ^3J(H,H) = 6.3 Hz, ^3J(H,H) = 2.9 Hz, 1H; BCH), 0.25-0.19 (m, 2H; CH_2), –0.14-(–0.19) (m, 2H; CH_2).

^{11}B NMR (96.3 MHz, THF-d_8): δ = –14.9 (br).

^{13}C{^{1}H} NMR (125.8 MHz, THF-d_8): δ = 159.4 (C-6), 156.8 (C-6), 148.2 (C-5), 147.5 (C-5), 146.4 (C-2), 145.9 (C-2), 130.6 (C-1), 127.7 (C-1), 121.8 (C-3), 121.6 (C-3), 117.7 (C-4), 117.6 (C-4), 35.2 (CCH_3) 32.6 (CH_3), 24.6 (br; BCH), 13.1 ($CHCH_2$), 9.5 (CH_2).

Reactions of Li_2[1] with α,ω-dihaloalkanes

All reactions were conducted by adding a dark red solution of $[Li(thf)_3]_2$[**1**] in THF-d_8 (0.3 mL) at room temperature with stirring to a small excess of an α,ω-dihaloalkane $X(CH_2)_nX$ in THF-d_8 (0.2 mL). The amounts of starting materials used in each individual experiment and the products obtained are listed in Table S1.

Table S1: Starting materials and products of the reactions of α,ω-dihaloalkanes $X(CH_2)_nX$ with $[Li(thf)_3]_2$[**1**]. The percentages of conversion of the boron compound (determined through integration of the ^{1}H NMR spectra) are listed in parentheses.

	starting materials	product(s)
	1,2-dihaloethane	
Cl	1,2-dichloroethane (1.7 µL, 2.1 mg, 21 µmol), $[Li(thf)_3]_2$[**1**] (17 mg, 17 µmol)	**14**^{C2} (100%)
Br	1,2-dibromoethane (1.8 µL, 3.9 mg, 21 µmol), $[Li(thf)_3]_2$[**1**] (17 mg, 17 µmol)	**14**^{C2} (100%)
	1,3-dihalopropane	
Cl	1,3-dichloropropane (3.2 µL, 3.8 mg, 34 µmol), $[Li(thf)_3]_2$[**1**] (30 mg, 30 µmol)	Complex mixture of yet unidentified products
Br	1,3-dibromopropane (3.6 µL, 7.2 mg, 35 µmol), $[Li(thf)_3]_2$[**1**] (30 mg, 30 µmol)	**14**^{C3} (> 90%; yield: 15 mg, 25 µmol, 83%)
	1,4-dihalobutane	
Cl	1,4-dichlorobutane (3.9 µL, 4.5 mg, 36 µmol), $[Li(thf)_3]_2$[**1**] (30 mg, 30 µmol)	Li[**15**^{C4,Cl}] (92%; yield: 17 mg, 21 µmol, 70% (calcd for $[Li(thf)_{2.5}]$[**15**^{C4,Cl}])), **14**^{C4} (8%)
Br	1,4-dibromobutane (6.0 µL, 11 mg, 50 µmol), $[Li(thf)_3]_2$[**1**] (42 mg, 42 µmol)	**14**^{C4} (92%), Li[**15**^{C4,Br}] (8%)
	1,5-dihalopentane	
Cl	1,5-dichloropentane (4.4 µL, 4.8 mg, 34 µmol), $[Li(thf)_3]_2$[**1**] (29 mg, 29 µmol)	Li[**15**^{C5,Cl}] (> 90%)
Br	1,5-dibromopentane (4.8 µL, 8.1 mg, 35 µmol), $[Li(thf)_3]_2$[**1**] (30 mg, 30 µmol)	Li[**15**^{C5,Br}] (> 90%)
	1,6-dihalohexane	
Cl	1,6-dichlorohexane (5.0 µL, 5.3 mg, 34 µmol), $[Li(thf)_3]_2$[**1**] (29 mg, 29 µmol)	Li[**15**^{C6,Cl}] (> 90%)
Br	1,6-dibromohexane (5.0 µL, 7.9 mg, 33 µmol), $[Li(thf)_3]_2$[**1**] (28 mg, 28 µmol)	Li[**15**^{C6,Br}] (> 90%)

The neutral compounds **14**^{C2}, **14**^{C3}, and **14**^{C4} were crystallized by slow evaporation of the solvent. The crystals were rinsed with small volumes of hexane (**14**^{C2}: 0 mL, **14**^{C3}: 3 x 0.2 mL, **14**^{C4}: 3 x 0.2 mL) and THF (**14**^{C2}: 0 mL, **14**^{C3} 2 x 0.1 mL, **14**^{C4}: 0 mL), and dried in a dynamic vacuum. The salts Li[**15**^{C4,Cl}], Li[**15**^{C4,Br}], Li[**15**^{C5,Cl}], Li[**15**^{C5,Br}], Li[**15**^{C6,Cl}], and Li[**15**^{C6,Br}] were precipitated from the reaction mixtures by addition of hexane (2 mL). The precipitates were washed with hexane (3 x 0.2 mL) and dried in a dynamic vacuum. Colorless single crystals of $[Li(12\text{-crown-}4)_2]$[**15**^{C5,Cl}] were obtained by layering a solution of Li[**15**^{C5,Cl}] in THF with hexane/12-crown-4 (3 d; room temperature).

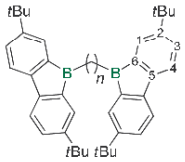

Figure S15. NMR numbering scheme for **14**^{Cn}.

14^{C2}

^{1}H NMR (500.2 MHz, THF-*d*$_8$): δ = 7.66 (d, ^{4}J(H,H) = 1.9 Hz, 4H; H-1), 7.39 (d, ^{3}J(H,H) = 7.8 Hz, 4H; H-4), 7.17 (dd, ^{3}J(H,H) = 7.8 Hz, ^{4}J(H,H) = 1.9 Hz, 4H; H-3), 1.35 (s, 36H; CH_3), 1.07 (s, 4H; C_2H_4).

^{11}B NMR (160.5 MHz, THF-*d*$_8$): δ = 15.9.

^{13}C{^{1}H} NMR (125.8 MHz, THF-*d*$_8$): δ = 153.0 (C-6), 148.2 (C-2), 147.6 (C-5), 128.0 (C-1), 124.3 (C-3), 118.5 (C-4), 34.9 (CCH_3), 32.0 (CH_3), 16.1 (C_2H_4).

14^{C3}

^{1}H NMR (500.2 MHz, THF-*d*$_8$): δ = 7.48 (d, ^{4}J(H,H) = 1.9 Hz, 4H; H-1), 7.37 (d, ^{3}J(H,H) = 7.9 Hz, 4H; H-4), 7.13 (dd, ^{3}J(H,H) = 7.9 Hz, ^{4}J(H,H) = 1.9 Hz, 4H; H-3), 1.53-1.47 (m, 2H; CCH_2), 1.30 (s, 36H; CH_3), 0.95-0.92 (m, 4H; BCH_2).

^{11}B NMR (160.5 MHz, THF-*d*$_8$): δ = 15.4 (vbr).

^{13}C{^{1}H} NMR (125.8 MHz, THF-*d*$_8$): δ = 152.7 (br; C-6), 148.3 (C-2), 147.6 (C-5), 128.1 (C-1), 124.2 (C-3), 118.4 (C-4), 34.9 (CCH_3), 32.0 (CH_3), 26.0 (br; BCH_2), 23.0 (CCH_2).

14^{C4}

^{1}H NMR (500.2 MHz, THF-*d*$_8$): δ = 7.51 (d, ^{4}J(H,H) = 1.9 Hz, 4H; H-1), 7.37 (d, ^{3}J(H,H) = 7.9 Hz, 4H; H-4), 7.14 (dd, ^{3}J(H,H) = 7.9 Hz, ^{4}J(H,H) = 1.9 Hz, 4H; H-3), 1.32 (s, 36H; CH_3), 1.32-1.29 (m, 4H; $BCCH_2$), 0.92-0.90 (m, 4H; BCH_2).

^{11}B NMR (160.5 MHz, THF-*d*$_8$): δ = 14.4 (vbr).

^{13}C{^{1}H} NMR (125.8 MHz, THF-*d*$_8$): δ = 152.4 (br; C-6), 148.3 (C-2), 147.6 (C-5), 127.9 (C-1), 124.3 (C-3), 118.4 (C-4), 34.9 (CCH_3), 32.0 (CH_3), 30.9 ($BCCH_2$), 21.5 (br; BCH_2).

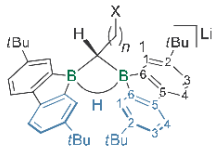

Figure S16. NMR numbering scheme for **15**^{Cn,X}.

*Li[**15**^{C4,Cl}]*

^{1}H NMR (500.2 MHz, THF-d_8): δ = 8.15 (d, ^{4}J(H,H) = 1.9 Hz, 2H; H-1), 8.01 (d, ^{4}J(H,H) = 1.9 Hz, 2H; H-1), 7.46 (d, ^{3}J(H,H) = 7.9 Hz, 2H; H-4), 7.43 (d, ^{3}J(H,H) = 7.9 Hz, 2H; H-4), 7.10 (dd, ^{3}J(H,H) = 7.9 Hz, ^{4}J(H,H) = 1.9 Hz, 2H; H-3), 7.07 (dd, ^{3}J(H,H) = 7.9 Hz, ^{4}J(H,H) = 1.9 Hz, 2H; H-3), 3.19 (t, ^{3}J(H,H) = 7.4 Hz, 2H; $ClCH_2$), 2.16 (vq, ^{3}J(H,H) = 7.4 Hz, 2H; $BCCH_2$), 2.04 (br, 1H; BHB), 1.52 (vquint, ^{3}J(H,H) = 7.4 Hz, 2H; $ClCCH_2$), 1.45 (s, 18H; CH_3), 1.43 (s, 18H; CH_3), 0.94 (dt, ^{3}J(H,H) = 7.8 Hz, ^{3}J(H,H) = 2.6 Hz, 1H; BCH).

^{11}B NMR (160.5 MHz, THF-d_8): δ = −13.0 (br).

^{13}C{^{1}H} NMR (125.8 MHz, THF-d_8): δ = 159.0 (br; C-6), 156.4 (br; C-6), 148.3 (C-5), 147.4 (C-5), 146.5 (C-2), 146.1 (C-2), 129.8 (C-1), 127.8 (C-1), 121.8 (C-3), 121.7 (C-3), 117.8 (C-4), 117.7 (C-4), 46.8 ($ClCH_2$), 38.8 ($ClCCH_2$), 35.3 (CCH_3), 35.2 (CCH_3), 32.7 (CH_3 or CH_3), 32.6 (CH_3 or CH_3), 28.2 ($BCCH_2$), 19.3 (br; BCH).

*Li[**15**^{C5,Cl}]*

^{1}H NMR (500.2 MHz, THF-d_8): δ = 8.16 (d, ^{4}J(H,H) = 1.8 Hz, 2H; H-1), 8.01 (d, ^{4}J(H,H) = 1.8 Hz, 2H; H-1), 7.46 (d, ^{3}J(H,H) = 7.9 Hz, 2H; H-4), 7.42 (d, ^{3}J(H,H) = 7.9 Hz, 2H; H-4), 7.09 (dd, ^{3}J(H,H) = 7.9 Hz, ^{4}J(H,H) = 1.8 Hz, 2H; H-3), 7.07 (dd, ^{3}J(H,H) = 7.9 Hz, ^{4}J(H,H) = 1.8 Hz, 2H; H-3), 3.14 (t, ^{3}J(H,H) = 7.3 Hz, 2H; $ClCH_2$), 2.07 (vq, ^{3}J(H,H) = 7.5 Hz, 2H; $BCCH_2$), 2.04 (br, 1H; BHB), 1.51 (vquint, ^{3}J(H,H) = 7.3 Hz, 2H; $ClCCH_2$), 1.45 (s, 18H; CH_3), 1.43 (s, 18H; CH_3), 1.14 (vquint, ^{3}J(H,H) = 7.3 Hz, 2H; $ClCCCH_2$), 0.93 (td, ^{3}J(H,H) = 7.6 Hz, ^{3}J(H,H) = 2.3 Hz, 1H; BCH).

^{11}B NMR (160.5 MHz, THF-d_8): δ = −13.7 (br).

^{13}C{^{1}H} NMR (125.8 MHz, THF-d_8): δ = 159.3 (br; C-6), 156.6 (br; C-6), 148.3 (C-5), 147.3 (C-5), 146.4 (C-2), 146.1 (C-2), 129.8 (C-1), 127.8 (C-1), 121.7 (C-3), 121.7 (C-3), 117.8 (C-4), 117.7 (C-4), 46.0 ($ClCH_2$), 35.3 (CCH_3), 35.2 (CCH_3), 34.1 ($ClCCH_2$), 32.7 (CH_3, CH_3), 32.4 ($ClCCCH_2$), 29.7 ($BCCH_2$), 20.4 (br; BCH).

*Li[**15**^{C5,Br}]*

^{1}H NMR (500.2 MHz, THF-d_8): δ = 8.15 (d, ^{4}J(H,H) = 1.8 Hz, 2H; H-1), 8.01 (d, ^{4}J(H,H) = 1.8 Hz, 2H; H-1), 7.46 (d, ^{3}J(H,H) = 7.9 Hz, 2H; H-4), 7.43 (d, ^{3}J(H,H) = 7.9 Hz, 2H; H-4), 7.10 (dd, ^{3}J(H,H) = 7.9 Hz, ^{4}J(H,H) = 1.8 Hz, 2H; H-3), 7.07 (dd, ^{3}J(H,H) = 7.9 Hz, ^{4}J(H,H) = 1.8 Hz, 2H; H-3), 3.03 (t, ^{3}J(H,H) = 7.3 Hz, 2H; $BrCH_2$), 2.07 (vq, ^{3}J(H,H) = 7.5 Hz, 2H; $BCCH_2$), 2.04 (br, 1H; BHB), 1.60 (vquint, ^{3}J(H,H) = 7.3 Hz, 2H; $BrCCH_2$), 1.45 (s, 18H; CH_3), 1.43 (s, 18H; CH_3), 1.15 (vquint, ^{3}J(H,H) = 7.3 Hz, 2H; $BrCCCH_2$), 0.93 (td, ^{3}J(H,H) = 7.6 Hz, ^{3}J(H,H) = 2.3 Hz, 1H; BCH).

^{11}B NMR (160.5 MHz, THF-d_8): δ = −12.9 (br).

^{13}C{^{1}H} NMR (125.8 MHz, THF-d_8): δ = 159.4 (br; C-6), 156.6 (br; C-6), 148.2 (C-5), 147.3 (C-5), 146.5 (C-2), 146.1 (C-2), 129.8 (C-1), 127.8 (C-1), 121.8 (C-3), 121.7 (C-3), 117.8 (C-4), 117.7 (C-4), 35.3 (CCH_3), 35.2 ($BrCH_2$, CCH_3), 34.3 ($BrCCH_2$), 33.7 ($BrCCCH_2$), 32.7 (CH_3), 29.5 ($BCCH_2$), 20.4 (br; BCH).

*Li[**15**^{C6,Cl}]*

^{1}H NMR (500.2 MHz, THF-d_8): δ = 8.17 (d, ^{4}J(H,H) = 1.8 Hz, 2H; H-1), 8.01 (d, ^{4}J(H,H) = 1.8 Hz, 2H; H-1), 7.45 (d, ^{3}J(H,H) = 7.9 Hz, 2H; H-4), 7.42 (d, ^{3}J(H,H) = 7.9 Hz, 2H; H-4), 7.09 (dd, ^{3}J(H,H) = 7.9 Hz, ^{4}J(H,H) = 1.8 Hz, 2H; H-3), 7.06 (dd, ^{3}J(H,H) = 7.9 Hz, ^{4}J(H,H) = 1.8 Hz, 2H; H-3), 3.15 (t, ^{3}J(H,H) = 7.1 Hz, 2H; $ClCH_2$), 2.05 (vq, ^{3}J(H,H) = 7.5 Hz, 2H; $BCCH_2$), 2.04 (br, 1H; BHB), 1.45 (s, 18H; CH_3), 1.44 (vquint, ^{3}J(H,H) = 7.2 Hz, 2H; $ClCCH_2$), 1.43 (s, 18H; CH_3), 1.16 (vquint, ^{3}J(H,H) = 7.5 Hz, 2H; $ClCCCH_2$), 1.07 (vquint, ^{3}J(H,H) = 7.3 Hz, 2H; $BCCCH_2$), 0.94 (td, ^{3}J(H,H) = 7.6 Hz, ^{4}J(H,H) = 2.6 Hz, 1H; BCH).

^{11}B NMR (160.5 MHz, THF-d_8): δ = −14.0 (br).

^{13}C{^{1}H} NMR (125.8 MHz, THF-d_8): δ = 159.6 (br; C-6), 156.8 (br; C-6), 148.2 (C-5), 147.4 (C-5), 146.4 (C-2), 146.0 (C-2), 129.9 (C-1), 127.8 (C-1), 121.6 (C-3), 121.6 (C-3), 117.7 (C-4), 117.6 (C-4), 45.8 ($ClCH_2$), 35.3 (CCH_3), 35.2 (CCH_3), 34.4 ($BCCCH_2$), 33.8 ($ClCCH_2$), 32.7 (CH_3), 30.2 ($BCCH_2$), 27.7 ($ClCCCH_2$), 20.6 (br; BCH).

*Li[**15**^{C6,Br}]*

^{1}H NMR (500.2 MHz, THF-d_8): δ = 8.16 (d, ^{4}J(H,H) = 1.8 Hz, 2H; H-1), 8.01 (d, ^{4}J(H,H) = 1.8 Hz, 2H; H-1), 7.46 (d, ^{3}J(H,H) = 7.9 Hz, 2H; H-4), 7.43 (d, ^{3}J(H,H) = 7.9 Hz, 2H; H-4), 7.10 (dd, ^{3}J(H,H) = 7.9 Hz, ^{4}J(H,H) = 1.8 Hz, 2H; H-3), 7.07 (dd, ^{3}J(H,H) = 7.9 Hz, ^{4}J(H,H) = 1.8 Hz, 2H; H-3), 3.05 (t, ^{3}J(H,H) = 7.2 Hz, 2H; $BrCH_2$), 2.05 (vq, ^{3}J(H,H) = 7.5 Hz, 2H; $BCCH_2$), 2.03 (br, 1H; BHB), 1.54 (vquint, ^{3}J(H,H) = 7.3 Hz, 2H; $BrCCH_2$), 1.45 (s, 18H; CH_3), 1.44 (s, 18H; CH_3), 1.17 (vquint, ^{3}J(H,H) = 7.3 Hz, 2H; $BrCCCH_2$), 1.07 (vquint, ^{3}J(H,H) = 7.3 Hz, 2H; $BCCCH_2$), 0.94 (td, ^{3}J(H,H) = 7.5 Hz, ^{3}J(H,H) = 2.2 Hz, 1H; BCH).

^{11}B NMR (160.5 MHz, THF-d_8): δ = −13.6 (br).

^{13}C{^{1}H} NMR (125.8 MHz, THF-d_8): δ = 159.5 (br; C-6), 156.8 (br; C-6), 148.2 (C-5), 147.3 (C-5), 146.5 (C-2), 146.1 (C-2), 129.9 (C-1), 127.9 (C-1), 121.7 (C-3), 121.7 (C-3), 117.8 (C-4), 117.7 (C-4), 35.3 (CCH_3), 35.2 (CCH_3), 34.8 ($BrCH_2$), 34.2 ($BCCCH_2$), 34.1 ($BrCCH_2$), 32.7 (CH_3, CH_3), 30.2 ($BCCH_2$), 29.0 ($BrCCCH_2$), 20.7 (br; BCH).

2. Plots of NMR spectra

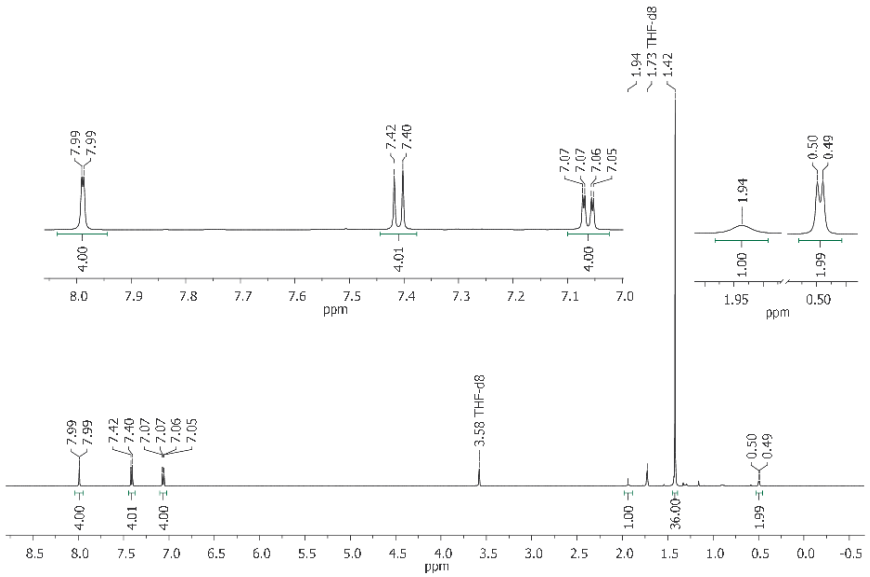

Figure S17: ^{1}H NMR spectrum of Li[**2**] (500.2 MHz, THF-d_8).

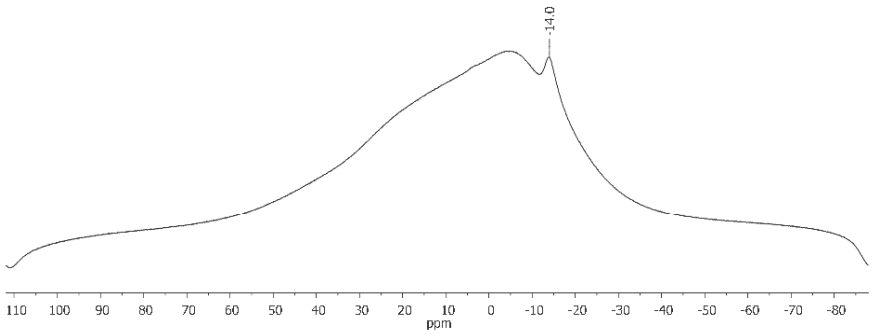

Figure S18: ^{11}B NMR spectrum of Li[**2**] (160.5 MHz, THF-d_8).

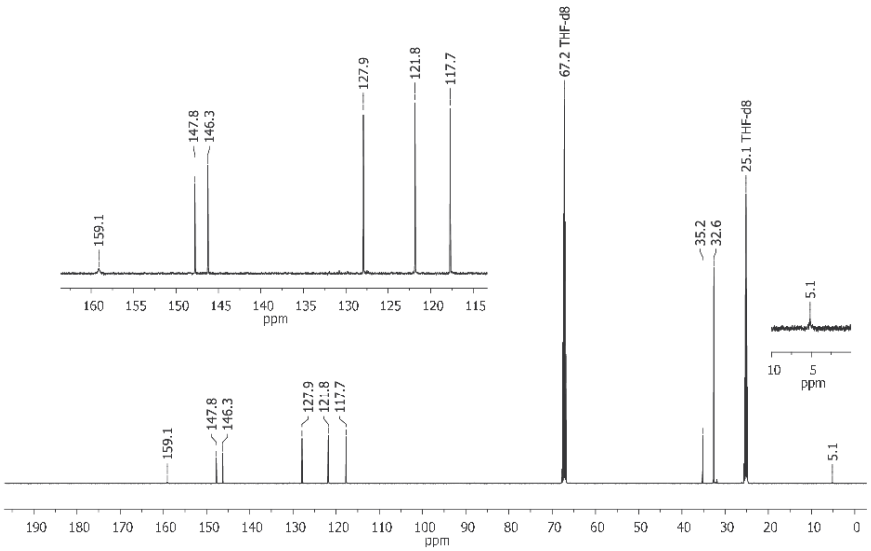

Figure S19: $^{13}C\{^{1}H\}$ NMR spectrum of Li[**2**] (125.8 MHz, THF-d_8).

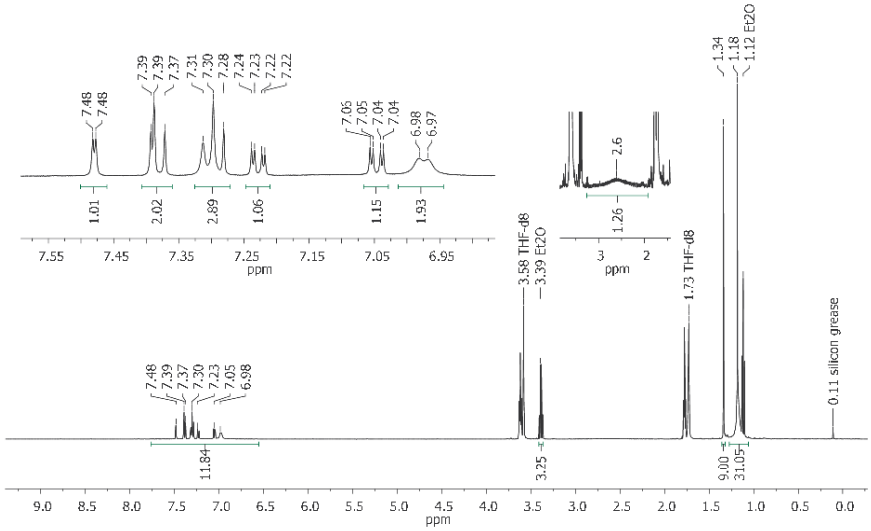

Figure S20: ^{1}H NMR spectrum of Li[**7**] (500.2 MHz, THF-d_8).

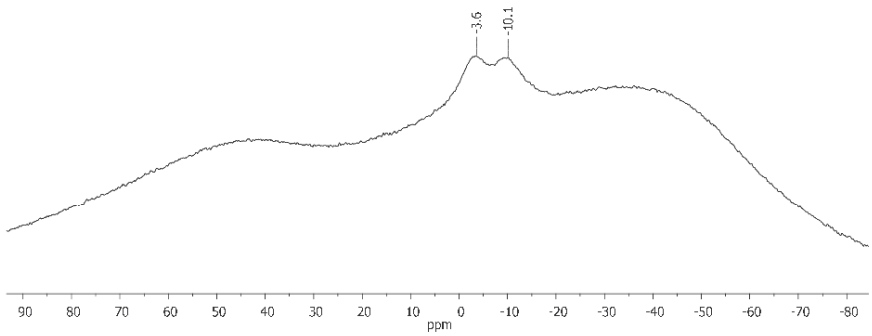

Figure S21: ^{11}B NMR spectrum of Li[**7**] (96.3 MHz, THF-d_8).

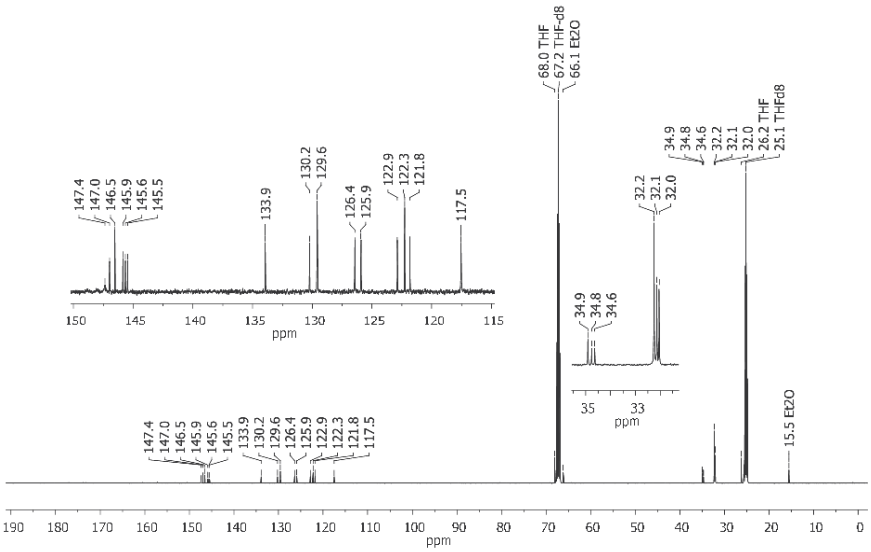

Figure S22: ^{13}C{^{1}H} NMR spectrum of Li[**7**] (125.8 MHz, THF-d_8).

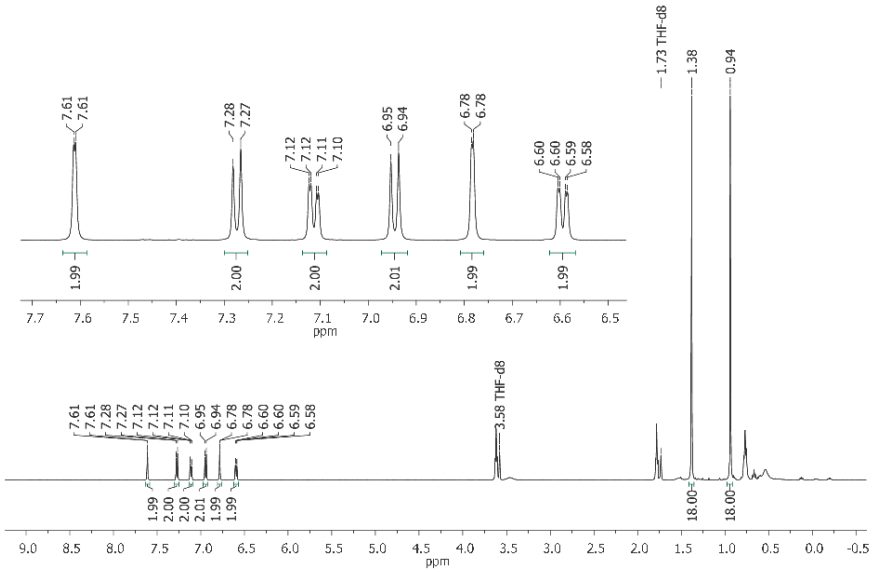

Figure S23: ^{1}H NMR spectrum of Li[**10**] (500.2 MHz, THF-d_8).

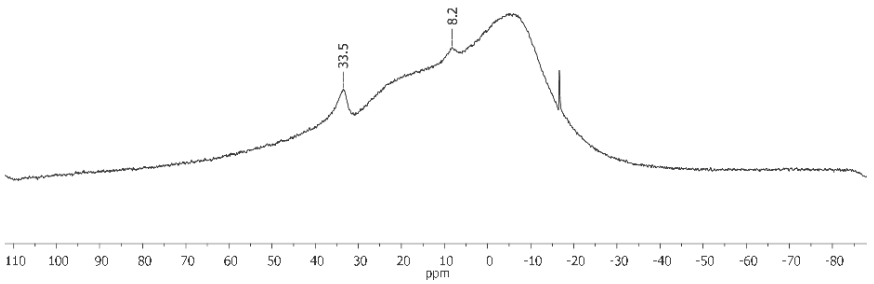

Figure S24: ^{11}B NMR spectrum of Li[**10**] (96.3 MHz, THF-d_8).

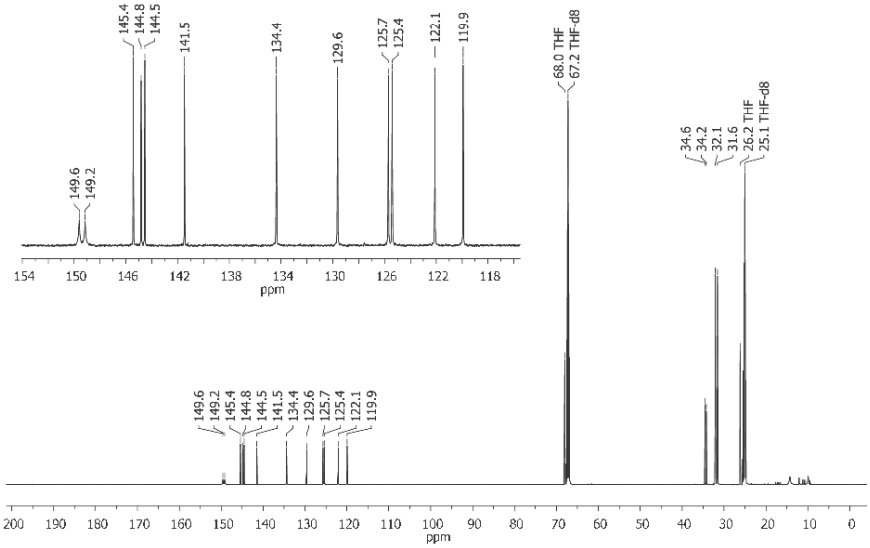

Figure S25: $^{13}C\{^{1}H\}$ NMR spectrum of Li[**10**] (125.8 MHz, THF-d_8).

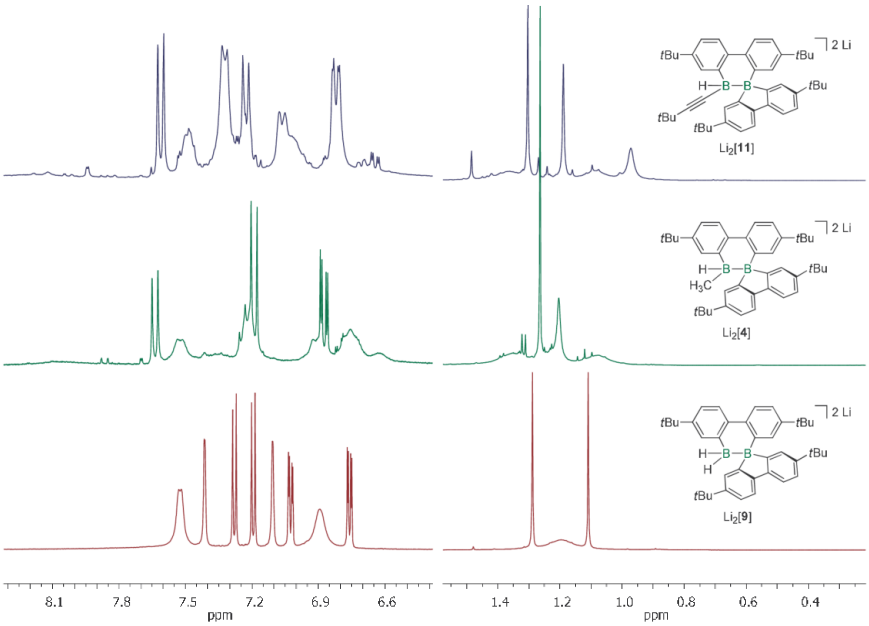

Figure S26: ^{1}H NMR spectra of Li_2[**11**] (top; 300.0 MHz), Li_2[**4**] (middle; 300.0 MHz), and Li_2[**9**] (bottom; 500.2 MHz) in THF-d_8. Aryl and alkyl regions are scaled differently. In the case of Li_2[**9**], the poor resolution of some signals in the aromatic and aliphatic spectral region originates from a dynamic behavior of the system in solution, which arises from conformational changes of the twisted B_2C_4 ring and/or from an association-dissociation equilibrium between the cations and the anions.[S5] In the cases of Li_2[**4**] and Li_2[**11**], the phenomenon is even more pronounced due to further symmetry breaking by the boron-bonded organyl substituents.

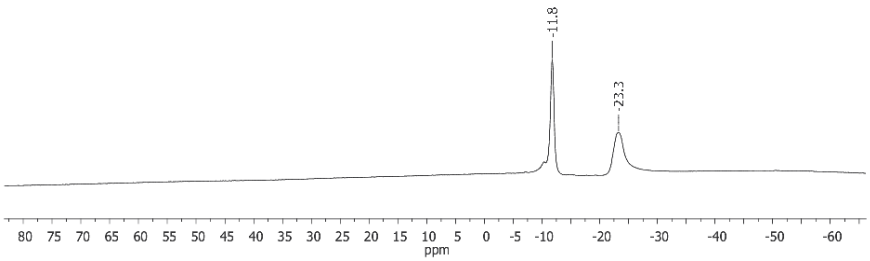

Figure S27: ^{11}B NMR spectrum of Li_2[**11**] (96.3 MHz, THF-d_8).

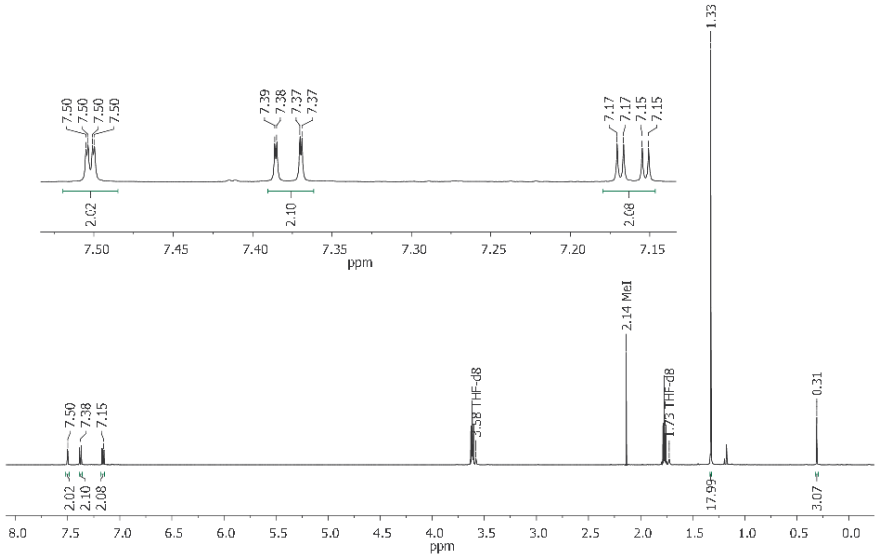

Figure S28: ^{1}H NMR spectrum of **13** (500.2 MHz, THF-d_8).

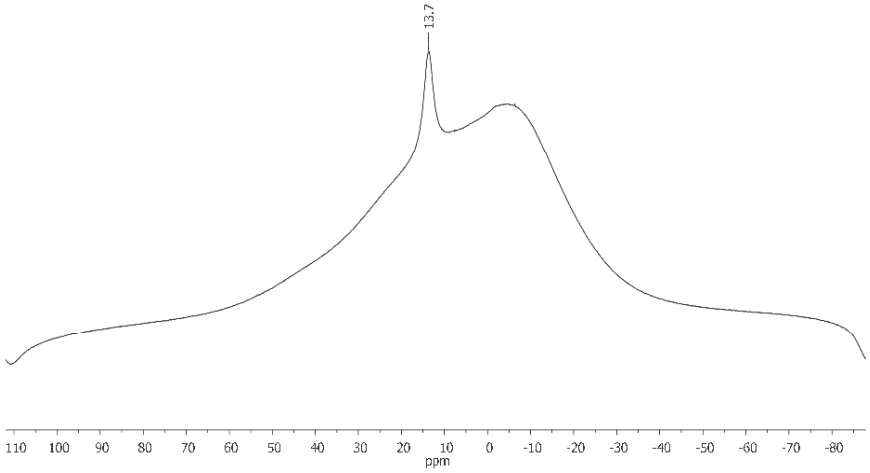

Figure S29: ^{11}B NMR spectrum of **13** (160.5 MHz, THF-d_8).

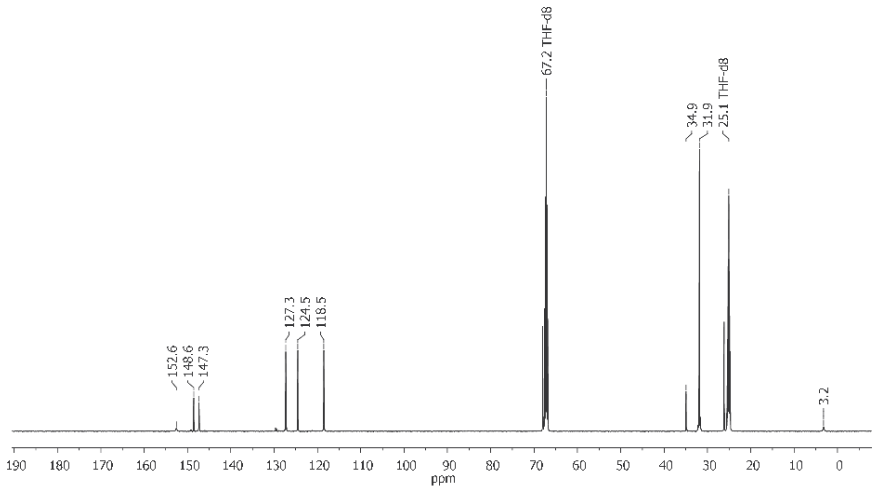

Figure S30: $^{13}C\{^{1}H\}$ NMR spectrum of **13** (125.8 MHz, THF-d_8).

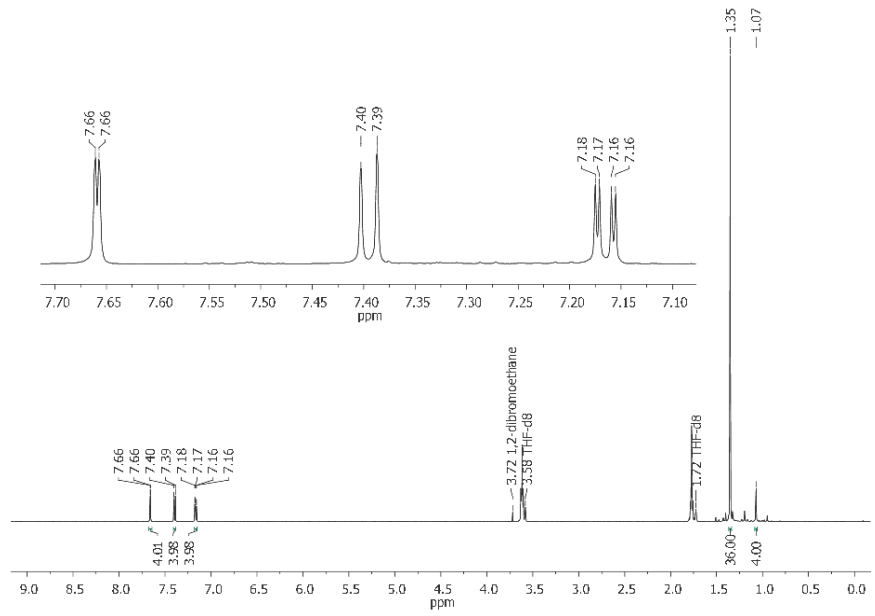

Figure S31: ^{1}H NMR spectrum of **14**^{C2} (500.2 MHz, THF-d_8).

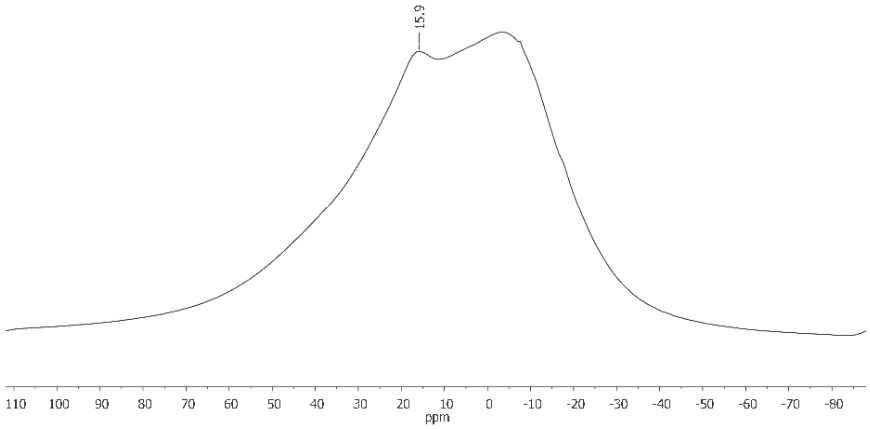

Figure S32: ^{11}B NMR spectrum of **14**^{C2} (160.5 MHz, THF-d_8).

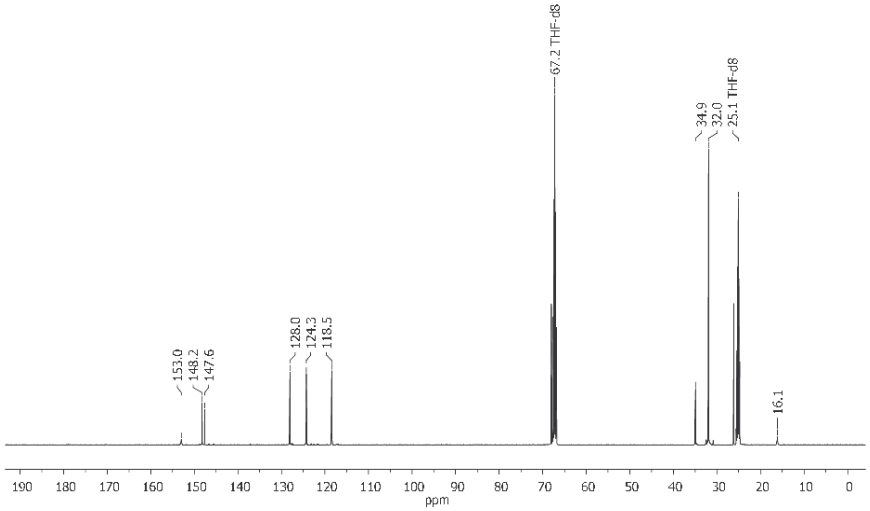

Figure S33: ^{13}C{^{1}H} NMR spectrum of **14**^{C2} (125.8 MHz, THF-d_8).

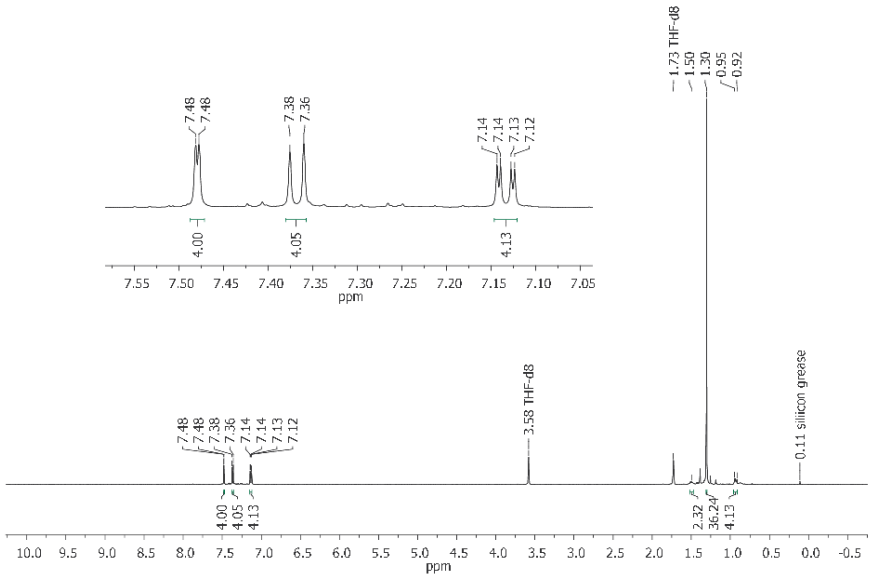

Figure S34: ^{1}H NMR spectrum of **14**^{C3} (500.2 MHz, THF-d_8).

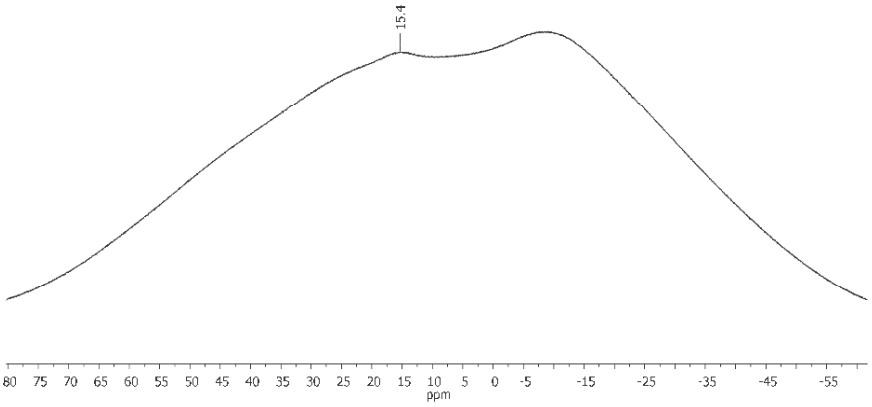

Figure S35: ^{11}B NMR spectrum of **14**^{C3} (160.5 MHz, THF-d_8).

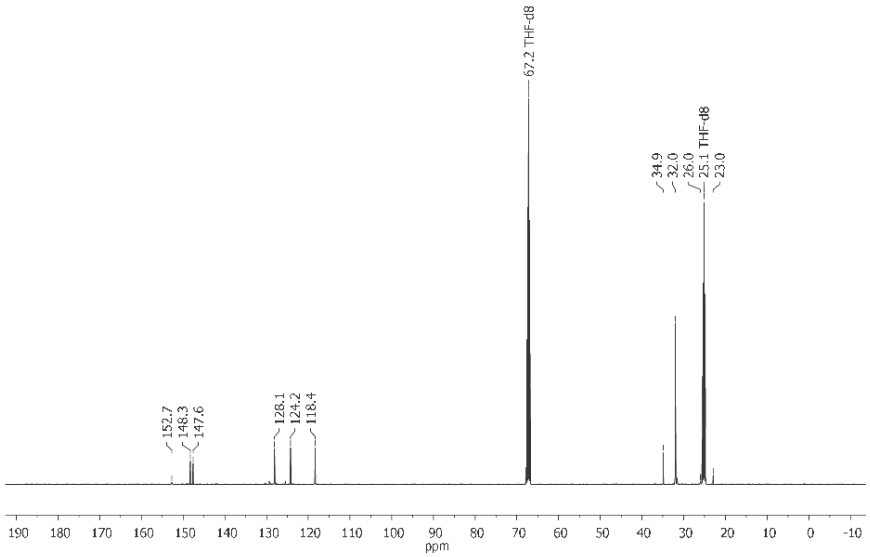

Figure S36: $^{13}C\{^1H\}$ NMR spectrum of **14**^{C3} (125.8 MHz, THF-d_8).

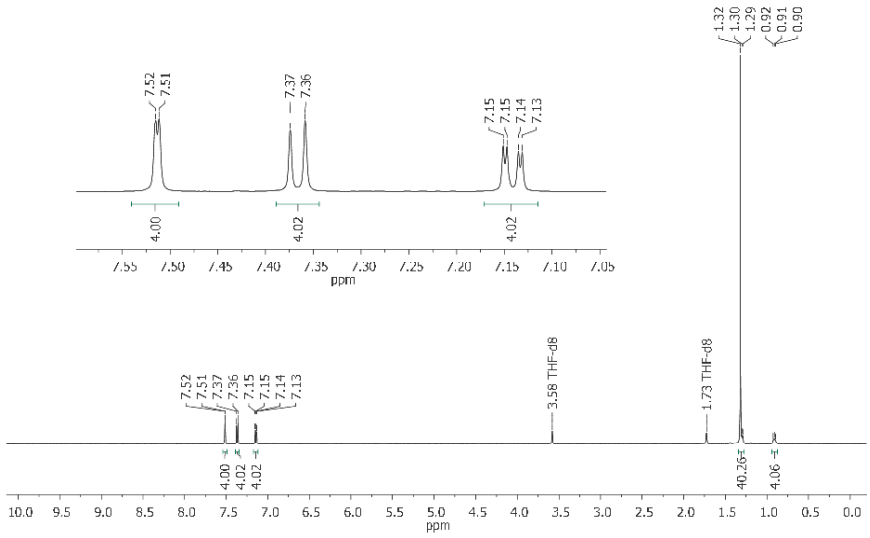

Figure S37: ^1H NMR spectrum of **14**^{C4} (500.2 MHz, THF-d_8).

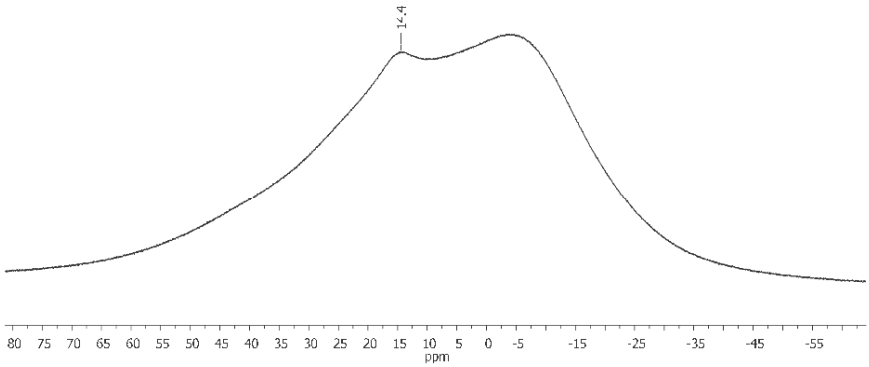

Figure S38: ^{11}B NMR spectrum of **14**^{C4} (160.5 MHz, THF-d_8).

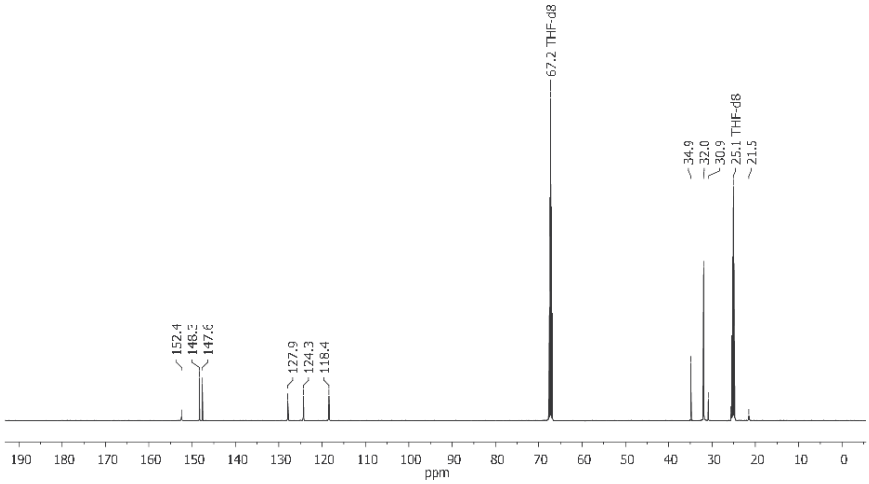

Figure S39: ^{13}C{^{1}H} NMR spectrum of **14**^{C4} (125.8 MHz, THF-d_8).

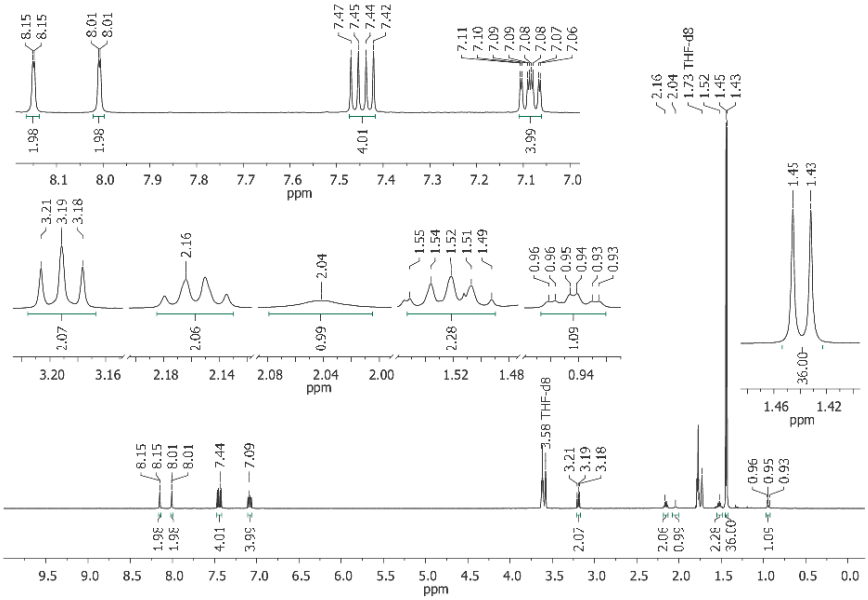

Figure S40: ^{1}H NMR spectrum of Li[**15**^{C4,Cl}] (500.2 MHz, THF-d_8).

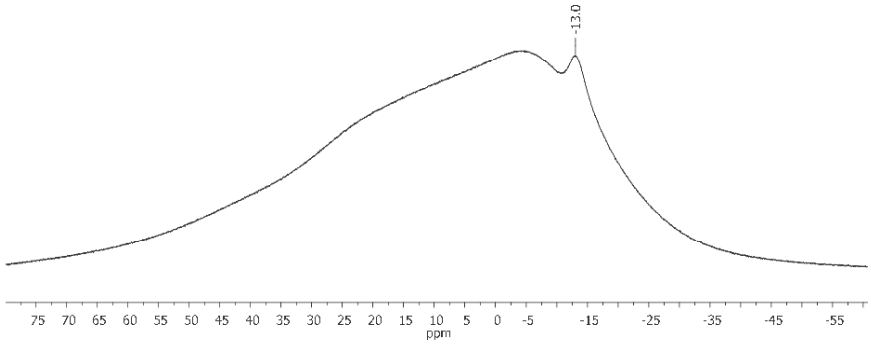

Figure S41: ^{11}B NMR spectrum of Li[**15**^{C4,Cl}] (160.5 MHz, THF-d_8).

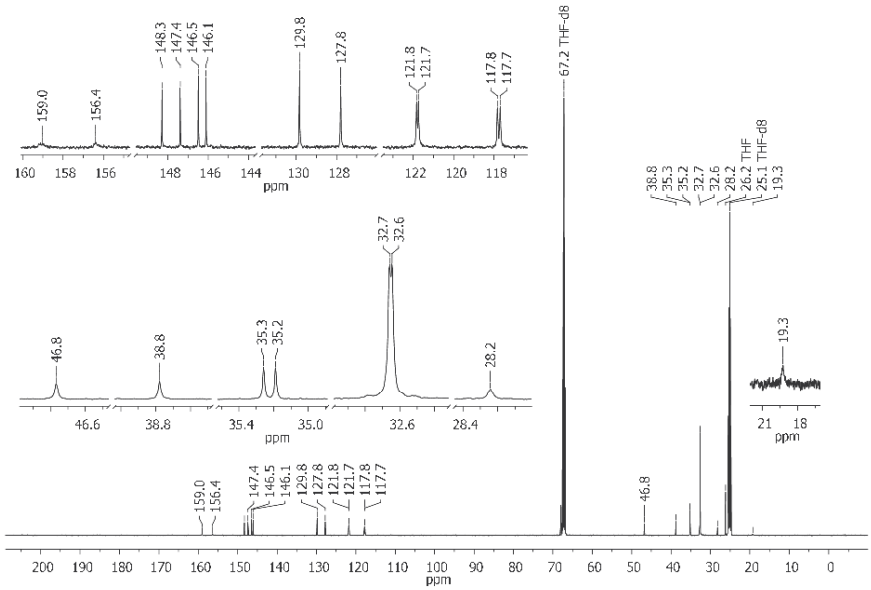

Figure S42: $^{13}C\{^{1}H\}$ NMR spectrum of Li[**15**^{C4,Cl}] (125.8 MHz, THF-d_8).

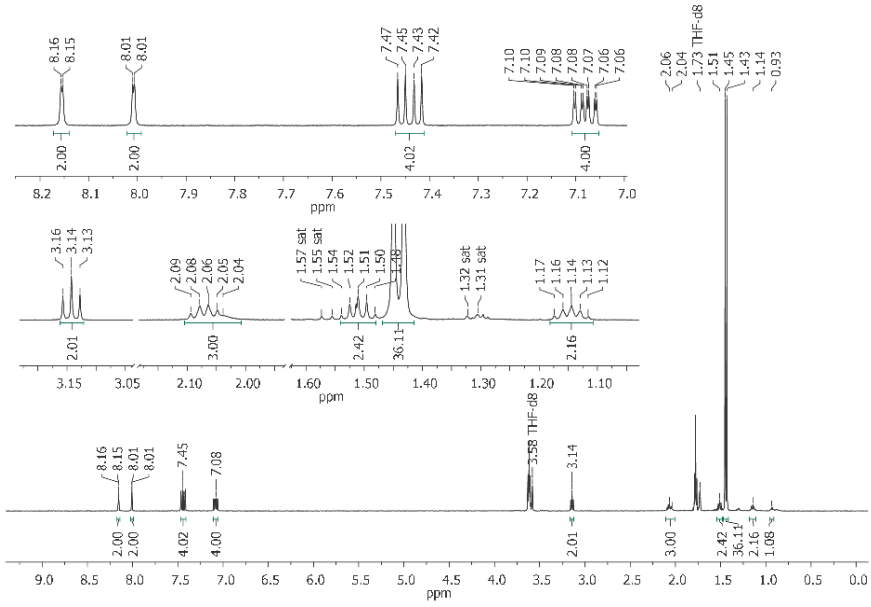

Figure S43: ^{1}H NMR spectrum of Li[**15**^{C5,Cl}] (500.2 MHz, THF-d_8; sat = ^{13}C satellite of a CH_3 signal).

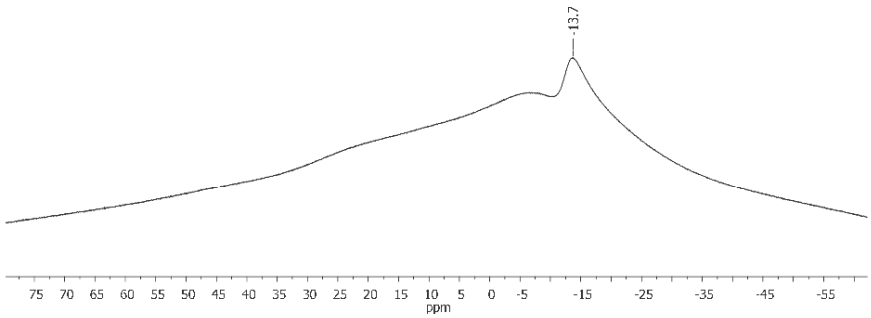

Figure S44: ^{11}B NMR spectrum of Li[**15**^{C5,Cl}] (160.5 MHz, THF-d_8).

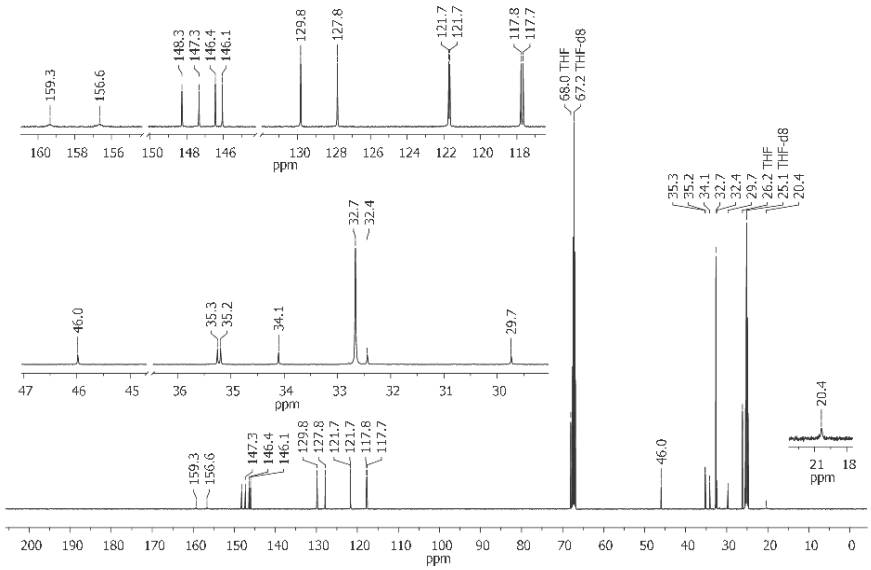

Figure S45: ^{13}C{^{1}H} NMR spectrum of Li[**15**^{C5,Cl}] (125.8 MHz, THF-d_8).

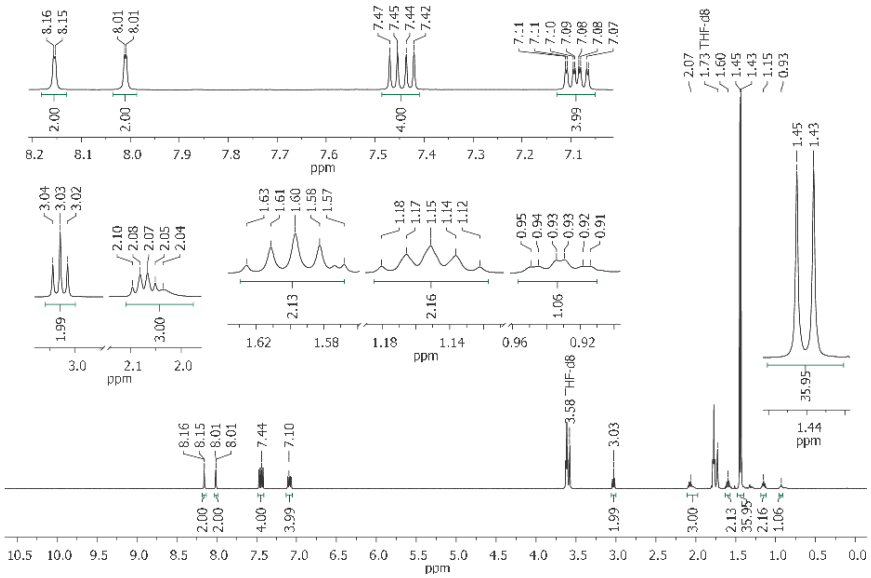

Figure S46: ^{1}H NMR spectrum of Li[**15**^{C5,Br}] (500.2 MHz, THF-d_8).

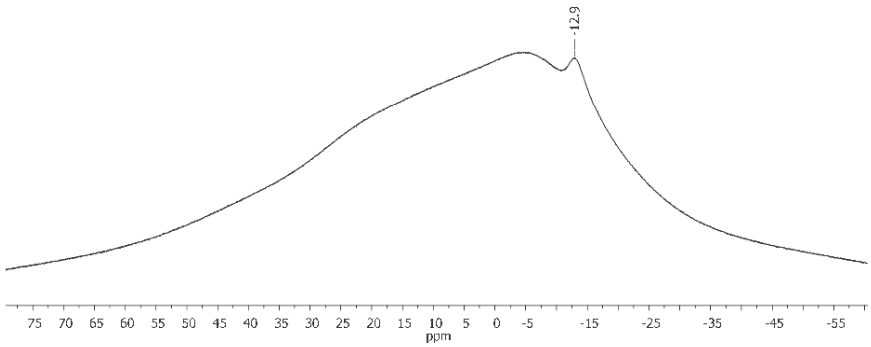

Figure S47: ^{11}B NMR spectrum of Li[**15**^{C5,Br}] (160.5 MHz, THF-d_8).

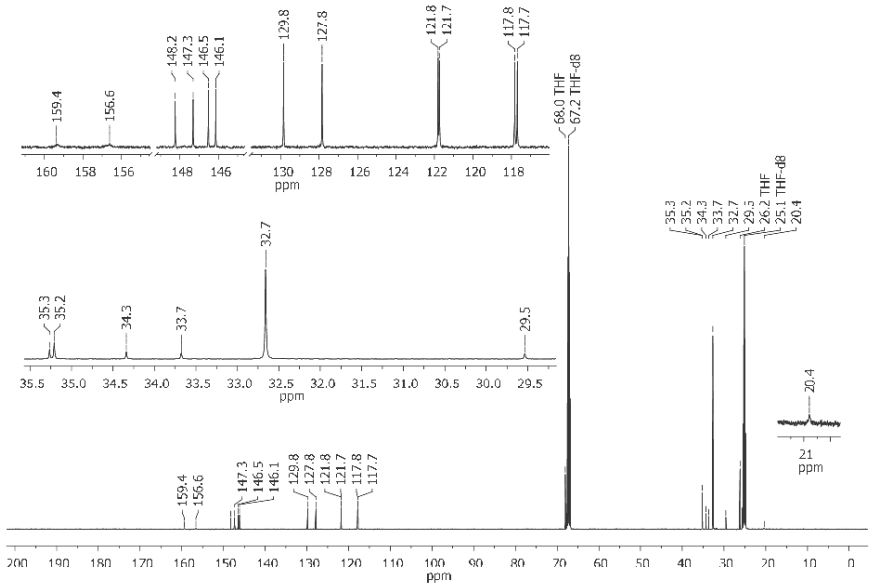

Figure S48: $^{13}C\{^{1}H\}$ NMR spectrum of Li[**15**^{C5,Br}] (125.8 MHz, THF-d_8).

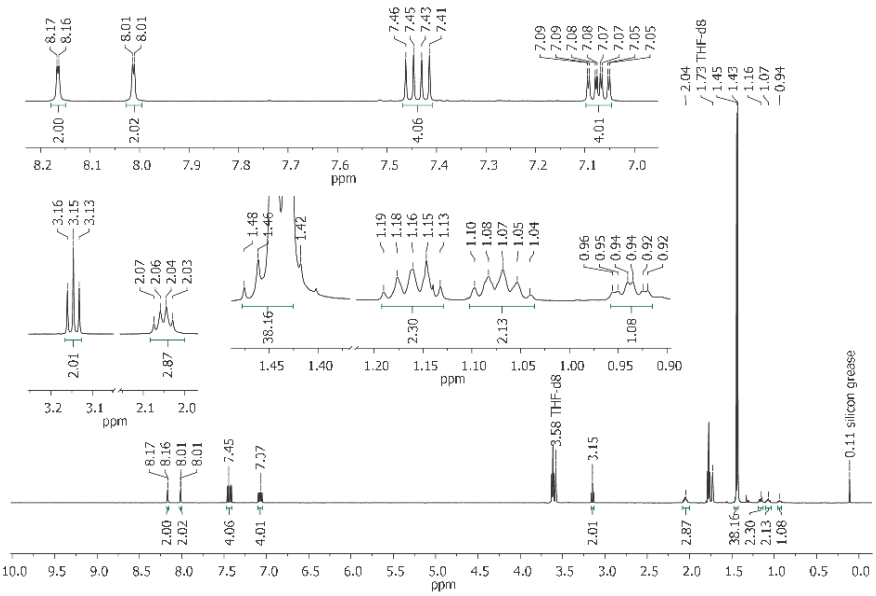

Figure S49: ^{1}H NMR spectrum of Li[**15**^{C6,Cl}] (500.2 MHz, THF-d_8).

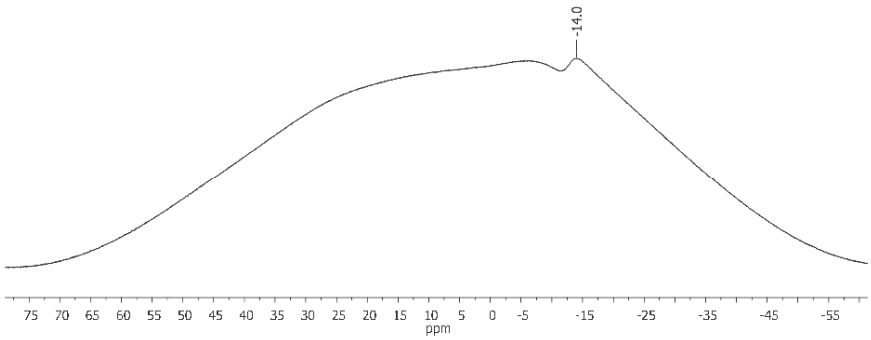

Figure S50: ^{11}B NMR spectrum of Li[**15**^{C6,Cl}] (160.5 MHz, THF-d_8,).

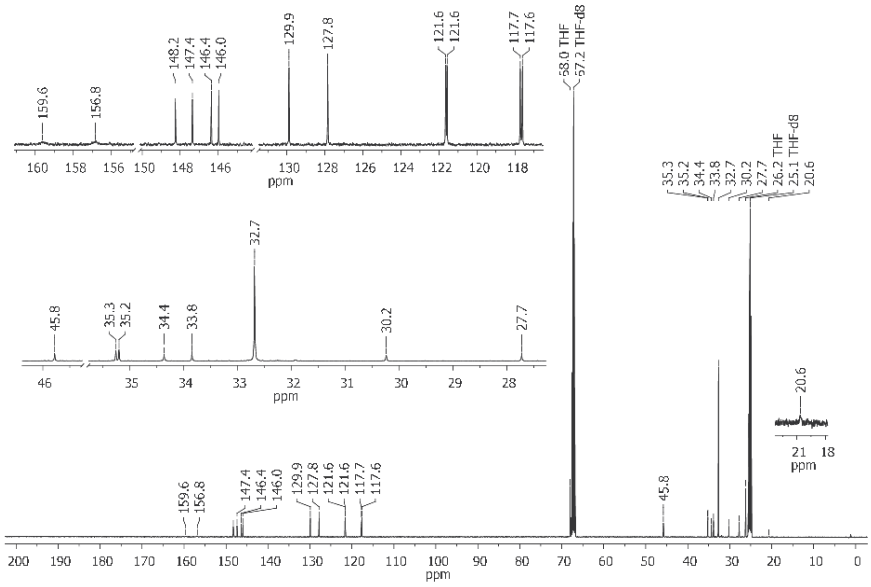

Figure S51: ^{13}C{^{1}H} NMR spectrum of Li[**15**^{C6,Cl}] (125.8 MHz, THF-d_8,).

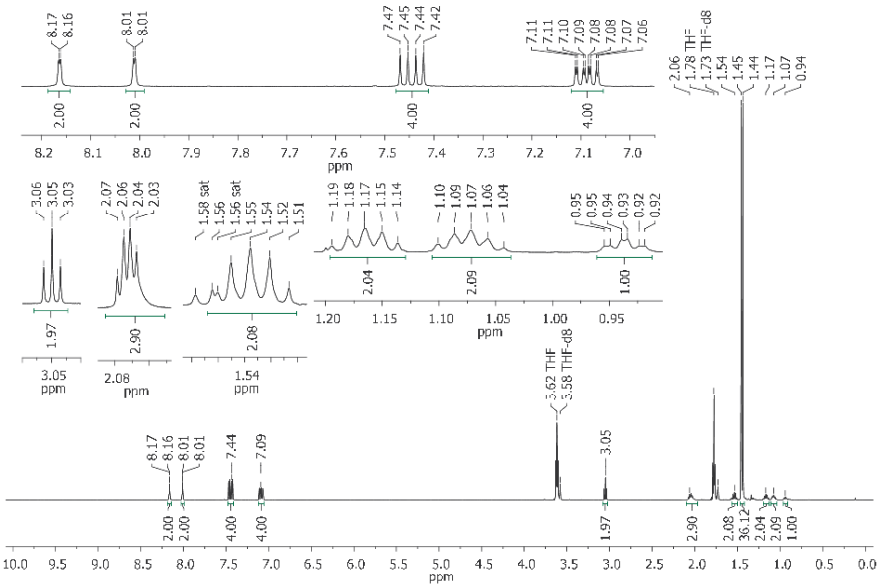

Figure S52: ^{1}H NMR spectrum of Li[**15**^{C6,Br}] (500.2 MHz, THF-d_8; sat = ^{13}C satellite of a CH_3 signal).

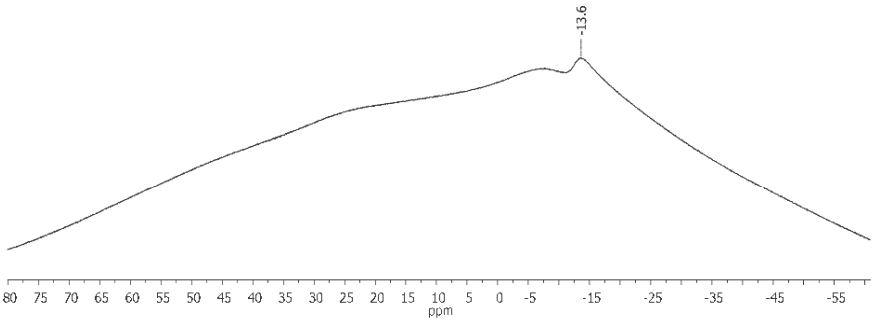

Figure S53: ^{11}B NMR spectrum of Li[**15**^{C6,Br}] (160.5 MHz, THF-d_8).

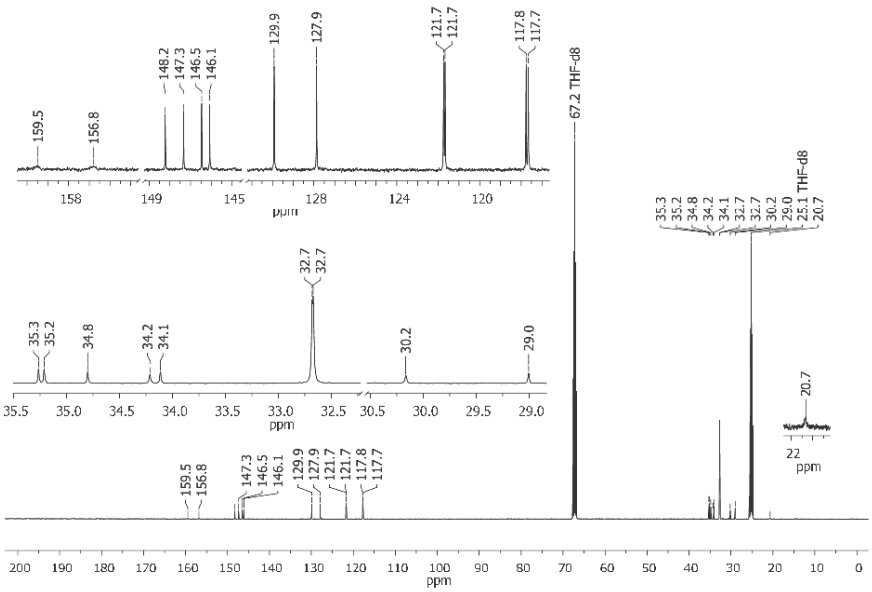

Figure S54: $^{13}C\{^{1}H\}$ NMR spectrum of Li[**15**^{C6,Br}] (125.8 MHz, THF-d_8).

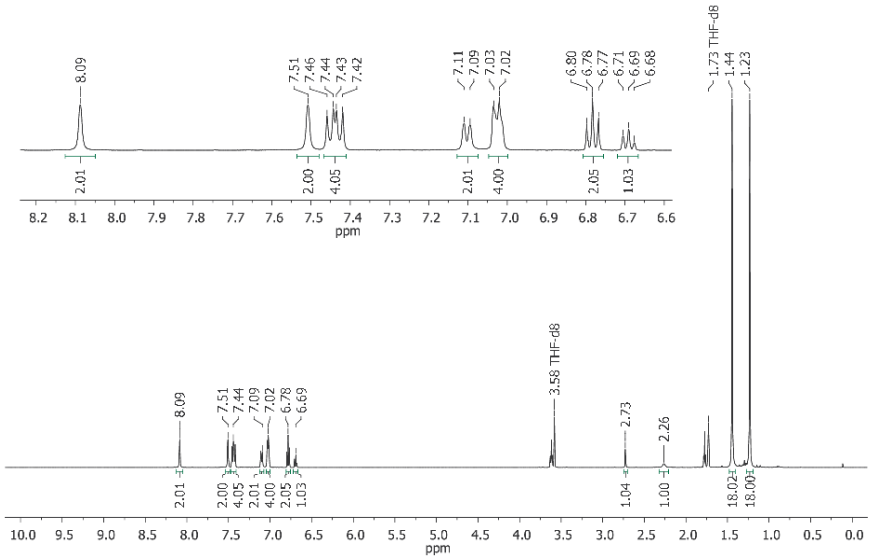

Figure S55: ^{1}H NMR spectrum of Li[**16**] (500.2 MHz, THF-d_8).

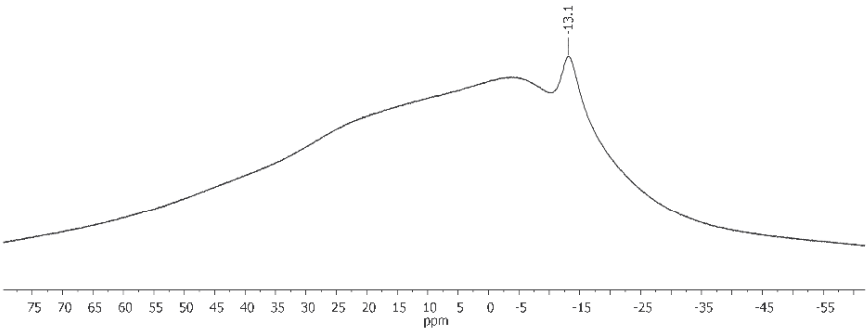

Figure S56: ^{11}B NMR spectrum of Li[**16**] (160.5 MHz, THF-d_8).

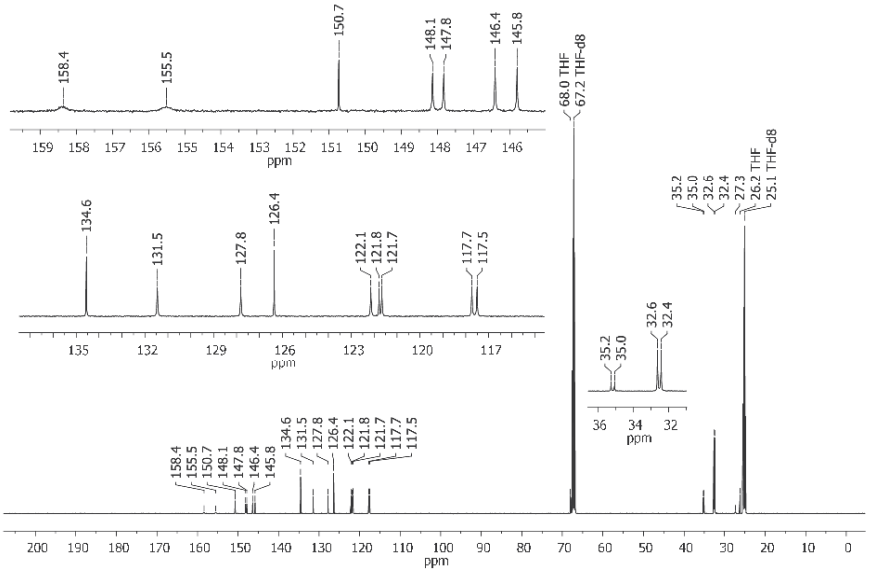

Figure S57: ^{13}C{^{1}H} NMR spectrum of Li[**16**] (125.8 MHz, THF-d_8).

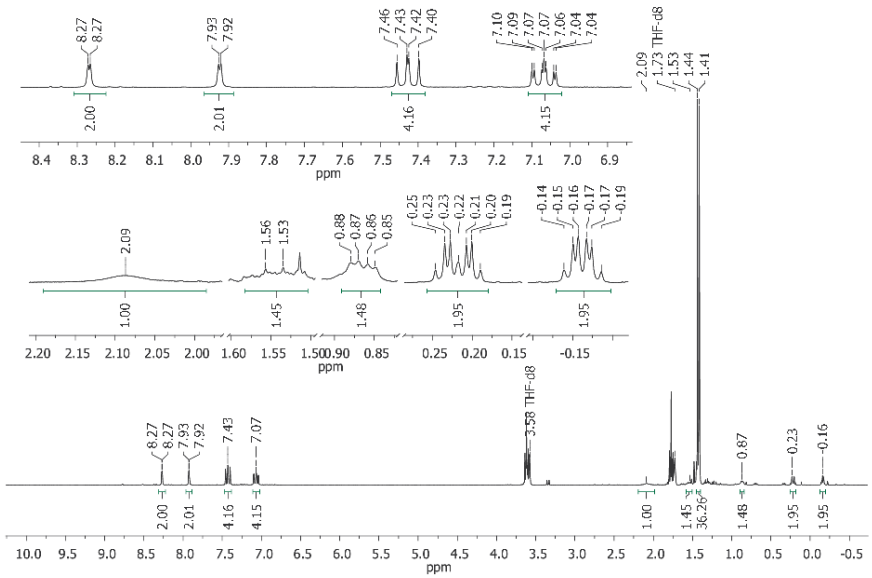

Figure S58: ^{1}H NMR spectrum of Li[**17**] (300.0 MHz, THF-d_8).

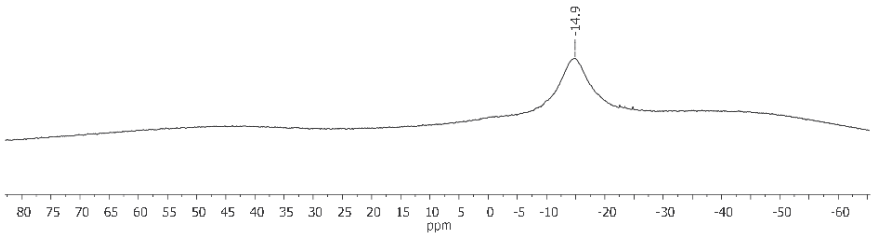

Figure S59: ^{11}B NMR spectrum of Li[**17**] (96.3 MHz, THF-d_8).

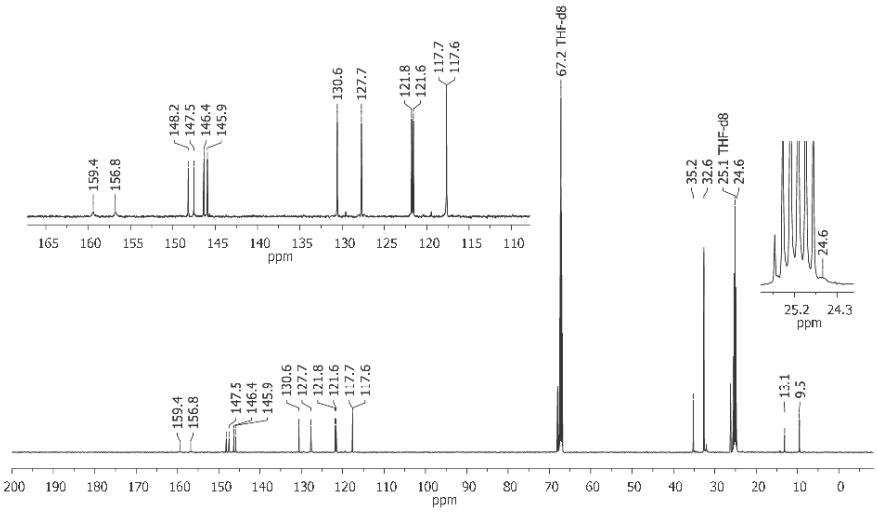

Figure S60: $^{13}C\{^{1}H\}$ NMR spectrum of Li[**17**] (125.8 MHz, THF-d_8).

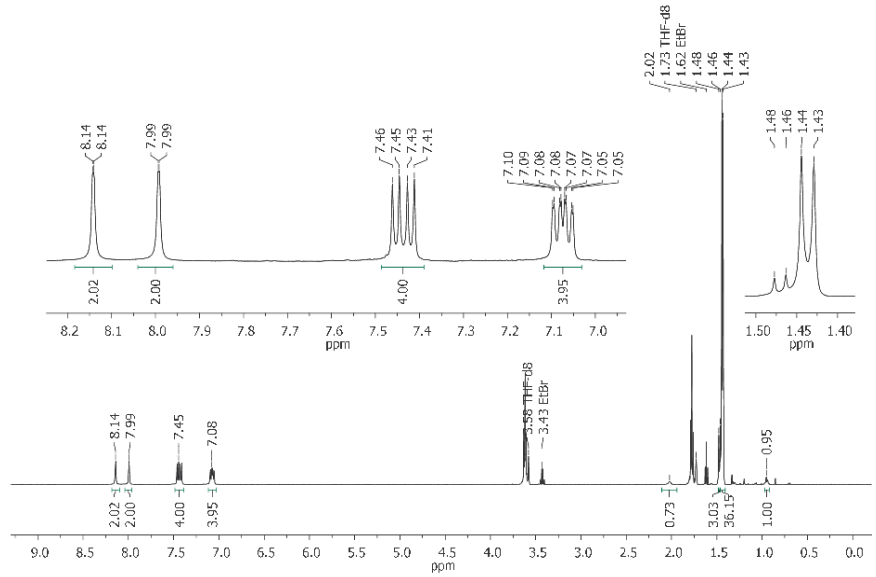

Figure S61: ^{1}H NMR spectrum of Li[**19**] (500.2 MHz, THF-d_8).

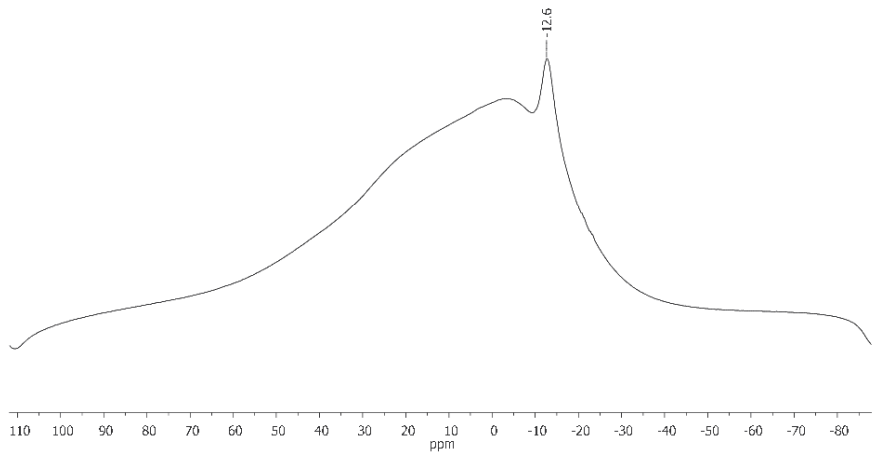

Figure S62: ^{11}B NMR spectrum of Li[**19**] (160.5 MHz, THF-d_8).

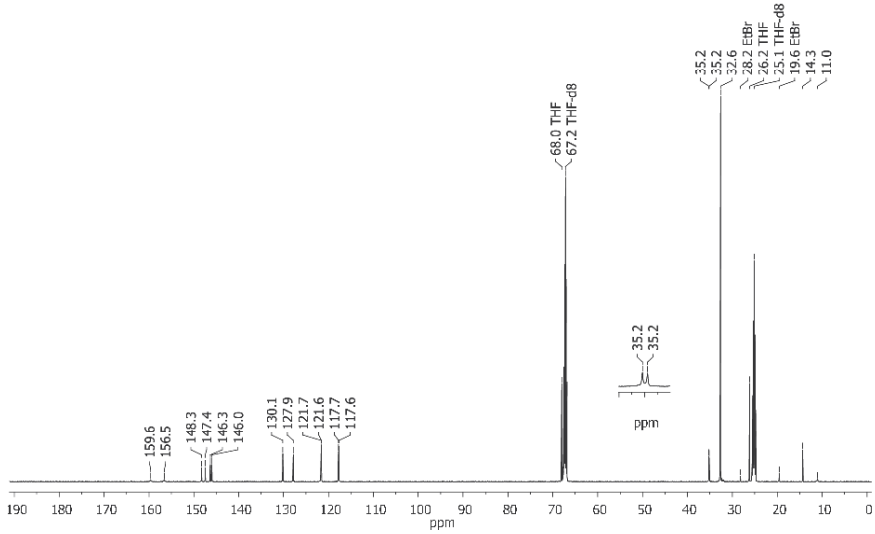

Figure S63: ^{13}C{^{1}H} NMR spectrum of Li[**19**] (125.8 MHz, THF-d_8).

3. X-ray

Data for all structures were collected on a STOE IPDS II two-circle diffractometer with a Genix Microfocus tube with mirror optics using MoK_α radiation (λ = 0.71073 Å). The data were scaled using the frame-scaling procedure in the *X-AREA* program system.[S6] The structures were solved by direct methods using the program *SHELXS*[S7] and refined against F^2 with full-matrix least-squares techniques using the program *SHELXL*.[S7]

Structure	Internal code	CCDC reference number
$[Li(thf)_4][\mathbf{2}]$	wa2120	1819687
$[Li(thf)_3][\mathbf{2}]$	wa2506	1819688
$[Li(thf)_3(Et_2O)][\mathbf{7}]$	wa2456	1819689
[Li(12-crown-4)(thf)][Li(thf)$_2$][**11**]	wa2374	1819690
$[Li(thf)_4][\mathbf{16}]$	wa2467	1819691
$(\mathbf{14}^{C2}\cdot thf)\cdot 4C_6H_6$	wa2473	1819692
$\mathbf{14}^{C3}$	wa2461	1819693
$\mathbf{14}^{C4}$	wa2477	1819694
$[Li(12\text{-crown-}4)_2][\mathbf{15}^{C5,Cl}]$	wa2518	1819695

*[Li(thf)$_4$][**2**]*

Yellow single crystals of [Li(thf)$_4$][**2**] were grown by gas-phase diffusion of hexane into a THF solution of Li[**2**] (3 d, room temperature).

The H atom bridging B1 and B2 was isotropically refined; the coordinates of the two H atoms bonded to C1 were also refined. One *t*Bu group is disordered over two positions with a site occupation factor of 0.793(9) for the major occupied site. In two thf ligands, two methylene groups are disordered over two positions with site occupation factors of 0.66(2) and 0.51(2) for the major occupied sites. In one thf ligand, three methylene groups are disordered over two positions, each with a site occupation factor of 0.63(2) for the major occupied site. The lengths of the C–C bonds involving the disordered atoms in the thf ligands were restrained to 1.50(1) Å and the 1-3 distances involving disordered C atoms in the thf ligands were restrained to 2.3(1) Å or 2.3(3) Å. The displacement ellipsoids of all disordered atoms were restrained to an isotropic behavior.

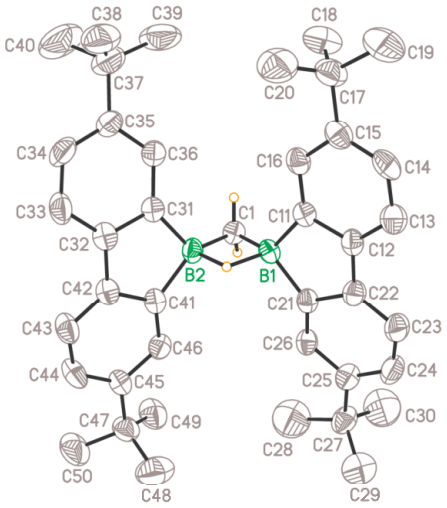

Figure S64: Molecular structure of [Li(thf)$_4$][**2**] in the solid state. The solvent-separated [Li(thf)$_4$]$^+$ cation and the C*H* atoms (except on C1) are omitted for clarity. Displacement ellipsoids are drawn at the 50% probability level. Selected atom···atom distance [Å], bond lengths [Å], and bond angles [°]: B(1)···B(2) = 1.974(6); B(1)–C(1) = 1.598(6), B(1)–C(11) = 1.624(5), B(1)–C(21) = 1.615(6), B(2)–C(1) = 1.581(6), B(2)–C(31) = 1.613(6), B(2)–C(41) = 1.629(6); B(1)–C(1)–B(2) = 76.8(3), C(11)–B(1)–C(21) = 100.7(3), C(31)–B(2)–C(41) = 100.2(3).

*[Li(thf)$_3$][**2**]*

Colorless single crystals of [Li(thf)$_3$][**2**] precipitated from a C_6H_6 solution of methyl triflate/[Li(thf)$_3$]$_2$[**1**] (1.1:1; 4 d, room temperature).

The asymmetric unit contains two crystallographically independent molecules of [Li(thf)$_3$][**2**]. The H atom bridging the boron atoms and the H atoms located on the C atoms bonded to both boron atoms were isotropically refined for both independent molecules. In the asymmetric unit, two *t*Bu groups are disordered over two positions with site occupation factors of 0.78(2) and 0.53(4) for the major occupied sites. In two thf ligands, two methylene groups are disordered over two positions with site occupation factors of 0.63(2) and 0.53(1) for the major occupied sites. In one thf ligand, three methylene groups are disordered over two positions, each with a site occupation factor of 0.62(4) for the major occupied site. The displacement ellipsoids of all atoms in the coordinating [Li(thf)$_3$]$^+$ ion were refined with a rigid bond restraint. The displacement ellipsoids of the disordered atoms were restrained to an isotropic behavior. Due to the absence of anomalous scatterers, the absolute structure could not be determined (Flack-x-parameter 1.5(10)).

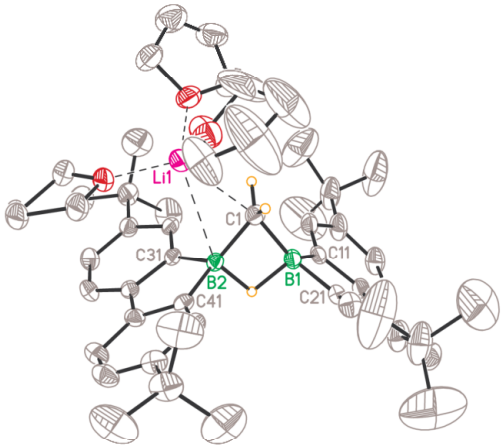

Figure S65: Molecular structure of one of the two crystallographically independent molecules of [Li(thf)$_3$][**2**] in the solid state. The *CH* atoms (except on C1) are omitted for clarity. Displacement ellipsoids are drawn at the 30% probability level. Selected atom···atom distance [Å], bond lengths [Å], and bond angles [°] of the two crystallographically independent molecules: B(1)···B(2) = 1.967(9)/1.950(9); B(1)–C(1) = 1.608(8)/1.606(8), B(1)–C(11) = 1.592(9)/1.618(8), B(1)–C(21) = 1.602(9)/1.613(9), B(2)–C(1) = 1.600(9)/1.601(8), B(2)–C(31) = 1.611(9)/1.622(9), B(2)–C(41) = 1.613(9)/1.606(9); B(1)–C(1)–B(2) = 75.7(4)/74.9(4), C(11)–B(1)–C(21) = 101.3(5)/101.1(5), C(31)–B(2)–C(41) = 100.9(5)/100.6(5).

*[Li(thf)$_3$(Et$_2$O)][**7**]*

Colorless single crystals of [Li(thf)$_3$(Et$_2$O)][**7**] precipitated from the THF/Et$_2$O filtrate of the reaction Li[HBEt$_3$]/**1**H$_2$ (1 d, room temperature).

All the H atoms bonded to B were isotropically refined. Three *t*Bu groups are disordered over two positions with site occupation factors of 0.62(1), 0.59(2), and 0.52(2) for the major occupied sites. In one thf ligand, three methylene groups are disordered over two positions, each with a site occupation factor of 0.62(2) for the major occupied site. The disordered atoms were isotropically refined. Bond lengths and bond angles of one disordered *t*Bu group were restrained to be equal to those of the non-disordered *t*Bu group. Bond lengths and bond angles of the disordered thf ligand were restrained to be equal to those of a non-disordered thf ligand.

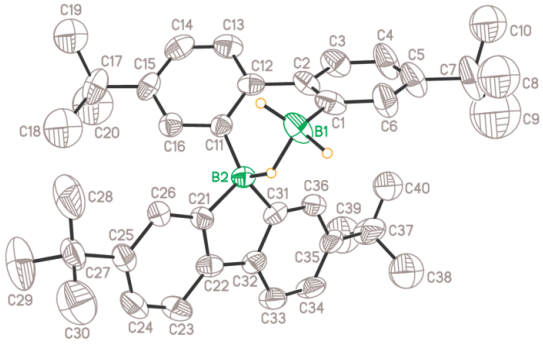

Figure S66: Molecular structure of [Li(thf)$_3$(Et$_2$O)][**7**] in the solid state. The solvent-separated [Li(thf)$_3$(Et$_2$O)]$^+$ cation and all C*H* atoms are omitted for clarity. Displacement ellipsoids are drawn at the 50% probability level. Selected atom···atom distance [Å], bond lengths [Å], bond angles [°], and torsion angle [°]: B(1)···B(2) = 2.382(8); B(1)–C(1) = 1.603(7), B(2)–C(11) = 1.623(7); B(1)–C(1)–C(2) = 122.5(5), B(2)–C(11)–C(12) = 124.6(4), C(21)–B(2)–C(31) = 100.3(3); C(1)–C(2)–C(12)–C(11) = –36.0(7).

*[Li(12-crown-4)(thf)][Li(thf)$_2$][**11**]*

The reaction mixture *t*BuCCLi/Li[**1**H] in THF was layered with hexane/12-crown-4 and stored at room temperature, whereupon orange single crystals of [Li(12-crown-4)(thf)][Li(thf)$_2$][**11**] formed.

The H atom bonded to B1 was isotropically refined. Two *t*Bu groups are disordered over two positions with site occupation factors of 0.58(2) and 0.51(2) for the major occupied sites. In one thf ligand, one methylene group is disordered over two positions with a site occupation factor of 0.79(3) for the major occupied site. The displacement ellipsoids of the disordered atoms were restrained to an isotropic behavior.

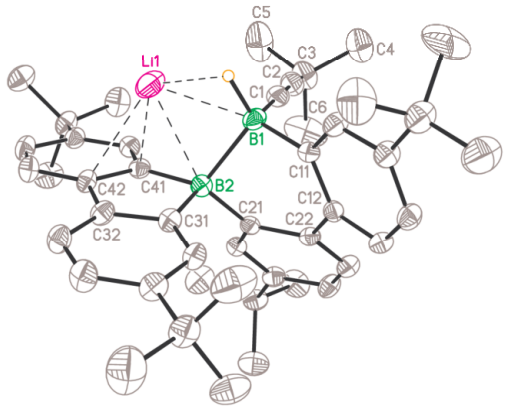

Figure S67: Molecular structure of [Li(12-crown-4)(thf)][Li(thf)$_2$][**11**] in the solid state. The solvent-separated [Li(12-crown-4)(thf)]$^+$ cation, thf ligands, and all C*H* atoms are omitted for clarity. Displacement ellipsoids are drawn at the 30% probability level. Selected bond lengths [Å], bond angles [°], and torsion angle [°]: B(1)–B(2) = 1.879(5), B(1)–C(1) = 1.612(6), B(1)–C(11) = 1.617(5), B(2)–C(21) = 1.625(5), B(2)–C(31) = 1.631(5), B(2)–C(41) = 1.630(5), C(1)–C(2) = 1.221(5); B(1)–B(2)–C(21) = 97.5(2), B(1)–C(1)–C(2) = 175.1(3), B(1)–C(11)–C(12) = 120.3(3), B(2)–B(1)–C(1) = 105.9(2), B(2)–B(1)–C(11) = 102.2(2), B(2)–C(21)–C(22) = 121.3(2), C(1)–B(1)–C(11) = 114.4(3); C(11)–C(12)–C(22)–C(21) = –31.8(4).

*[Li(thf)$_4$][**16**]*

Colorless single crystals of [Li(thf)$_4$][**16**] were grown by gas-phase diffusion of hexane into a THF solution of Li[**16**] (3 d, room temperature).

There are two crystallographically independent molecules of [Li(thf)$_4$][**16**] in the asymmetric unit. Boron-bridging H atoms were isotropically refined. In one of the independent molecules three *t*Bu groups are disordered over two positions with site occupation factors of 0.54(1), 0.75(2), and 0.83(2). In the other independent molecule, three *t*Bu groups are disordered over two positions with site occupation factors of 0.52(3), 0.55(1), and 0.57(1). In one thf ligand, the O atom and two methylene groups are disordered over two positions, each with a site occupation factor of 0.69(1) for the major occupied site. In one thf ligand, two methylene groups are disordered over two positions, each with a site occupation factor of 0.51(1) for the major occupied site. The displacement ellipsoids of all disordered atoms and all atoms in the [Li(thf)$_4$]$^+$ ions were restrained to an isotropic behavior. Bond lengths and angles in the disordered thf ligands were restrained to be equal to those in a non-disordered thf ligand.

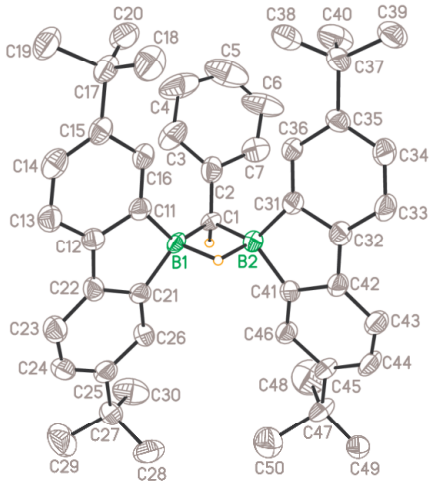

Figure S68: Molecular structure of one of the crystallographically independent molecules of [Li(thf)$_4$][**16**] in the solid state. The solvent-separated [Li(thf)$_4$]$^+$ cation and the C*H* atoms (except on C1) are omitted for clarity. Displacement ellipsoids are drawn at the 30% probability level. Selected atom···atom distance [Å], bond lengths [Å], and bond angles [°] of the two crystallographically independent molecules: B(1)···B(2) = 1.974(8)/1.990(8); B(1)–C(1) = 1.597(8)/1.625(7), B(1)–C(11) = 1.624(8)/1.615(8), B(1)–C(21) = 1.618(8)/1.601(8), B(2)–C(1) = 1.605(7)/1.613(9), B(2)–C(31) = 1.633(8)/1.609(8), B(2)–C(41) = 1.630(8)/1.602(9); B(1)–C(1)–B(2) = 76.1(4)/75.8(4), C(11)–B(1)–C(21) = 100.2(4)/102.3(4), C(31)–B(2)–C(41) = 101.0(4)/102.2(5).

*(**14**^{C2}·thf)·4C_6H_6*

Yellow single crystals of (**14**^{C2}·thf)·4C_6H_6 were grown from the reaction mixture 1,2-dichloroethane/[Li(thf)$_3$]$_2$[**1**] in C_6H_6 by slow evaporation of all volatiles at room temperature.

One of the two boron atoms is tetracoordinated by the thf ligand. Two *t*Bu groups are disordered over two positions with site occupation factors of 0.818(6) and 0.61(2) for the major occupied sites. The displacement ellipsoids of the disordered atoms were restrained to an isotropic behavior.

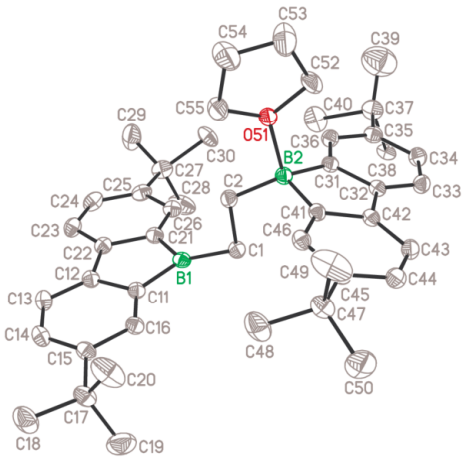

Figure S69: Molecular structure of (**14**^{C2}·thf)·4C_6H_6 in the solid state. C*H* atoms and C_6H_6 molecules are omitted for clarity. Displacement ellipsoids are drawn at the 30% probability level. Selected bond lengths [Å], bond angles [°], and torsion angle [°]: B(1)–C(1) = 1.544(2), B(1)–C(11) = 1.577(2), B(1)–C(21) = 1.577(2), B(2)–C(2) = 1.609(2), B(2)–C(31) = 1.625(2), B(2)–C(41) = 1.620(2), B(2)–O(51) = 1.644(2), C(1)–C(2) = 1.566(2); C(1)–B(1)–C(11) = 128.0(1), C(1)–B(1)–C(21) = 128.3(1), C(11)–B(1)–C(21) = 102.8(1), C(2)–B(2)–C(31) = 118.0(1), C(2)–B(2)–C(41) = 118.1(1), C(31)–B(2)–C(41) = 100.0(1); B(1)–C(1)–C(2)–B(2) = –179.1(1); ∑(C–B(1)–C) = 359°; ∑(C–B(2)–C)= 336°.

14^{C3}

Yellow plates of **14**^{C3} suitable for X-ray crystallography were grown from the reaction mixture 1,3-dibromopropane/Li_2[**1**] in THF by slow evaporation of all volatiles at room temperature.

Due to the absence of anomalous scatterers, the absolute structure could not be determined (Flack-x-parameter 1.8(10)).

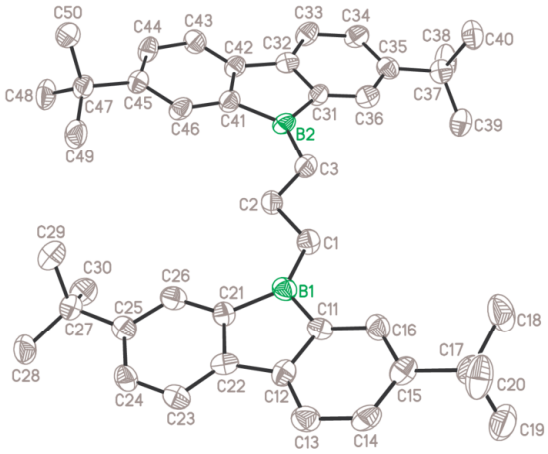

Figure S70: Molecular structure of **14**^{C3} in the solid state. C*H* atoms are omitted for clarity. Displacement ellipsoids are drawn at the 50% probability level. Selected bond lengths [Å] and bond angles [°]: B(1)–C(1) = 1.563(9), B(1)–C(11) = 1.569(9), B(1)–C(21) = 1.571(9), B(2)–C(3) = 1.577(9), B(2)–C(31) = 1.560(9), B(2)–C(41) = 1.571(10); C(1)–B(1)–C(11) = 125.1(6), C(1)–B(1)–C(21) = 131.8(6), C(11)–B(1)–C(21) = 103.0(5), C(3)–B(2)–C(31) = 121.9(6), C(3)–B(2)–C(41) = 132.6(6), C(31)–B(2)–C(41) = 105.5(5). Angle between the planes of the borol rings [°]: 22.0. ∑(C–B(1)–C) = 359.9°; ∑(C–B(2)–C) = 360.0°.

14^{C4}

Yellow single crystals of **14**^{C4} were grown from the reaction mixture 1,4-dibromobutane/Li_2[**1**] in THF by slow evaporation of all volatiles at room temperature.

The asymmetric unit contains two half crystallographically independent molecules of **14**^{C4} both located on a crystallographic center of inversion. The crystal was non-merohedrally twinned with a fractional contribution of 0.341(3) of the minor component.

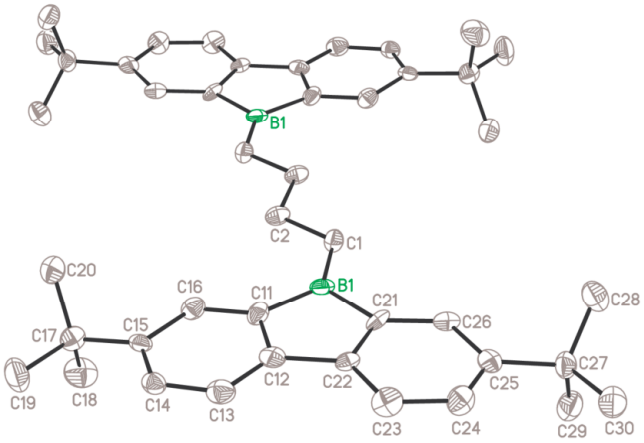

Figure S71: One of the two half crystallographically independent molecules of **14**^{C4} in the solid state. C*H* atoms are omitted for clarity. Displacement ellipsoids are drawn at the 50% probability level. Selected bond lengths [Å] and bond angles [°] of the two half crystallographically independent molecules: B(1)–C(1) = 1.566(10)/1.577(9), B(1)–C(11) = 1.558(10)/1.595(9), B(1)–C(21) = 1.579(9)/1.558(10); C(1)–B(1)–C(11) = 131.7(6)/125.4(6), C(1)–B(1)–C(21) = 125.1(6)/131.4(5), C(11)–B(1)–C(21) = 103.2(6)/103.1(5). Angle between the planes of the borol rings [°]: 0.0. ∑(C–B(1)–C) = 360.0°/359.9°. Symmetry transformations used to generate equivalent atoms: 1) –x+1, –y+1, –z–1; 2) –x, –y+1, –z–2.

*[Li(12-crown-4)$_2$][**15**^{C5,Cl}]*

The reaction mixture 1,5-dichloropentane/Li$_2$[**1**] in THF was layered with hexane/12-crown-4 and stored at room temperature, whereupon colorless single crystals of [Li(12-crown-4)$_2$][**15**^{C5,Cl}] formed.

The asymmetric unit contains one-half of a molecule of [Li(12-crown-4)$_2$][**15**^{C5,Cl}] located on a crystallographic C_2 axis. Three methylene groups and the terminal Cl atom of the pentyl chain are disordered over the C_2 axis with two equally occupied positions. One *t*Bu group is disordered over two positions with a site occupation factor of 0.83(3) for the major occupied site. The C–C bond lengths in the pentyl chain were restrained to 1.50(1) Å and 1-3 C-C distances in this chain were restrained to 2.50(1) Å. The C–Cl bond length was restrained to 1.80(1) Å. The displacement ellipsoids of the disordered C atoms were restrained to an isotropic behavior. The Flack-x-parameter refined to –0.2(2). The boron-bridging H atom was isotropically refined.

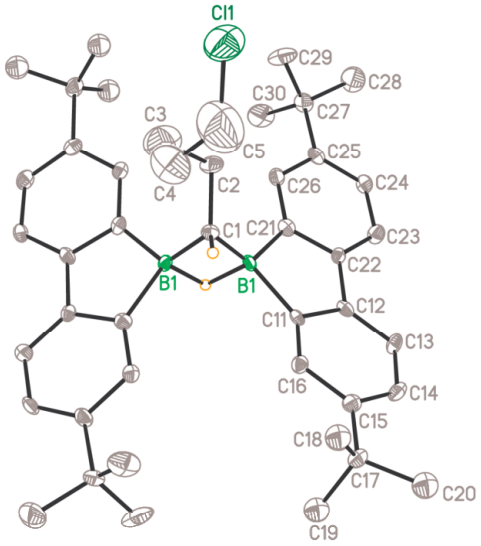

Figure S72: Molecular structure of [Li(12-crown-4)$_2$][**15**^{C5,Cl}] in the solid state. The solvent-separated [Li(12-crown-4)$_2$]$^+$ cation and C*H* atoms (except on C1) are omitted for clarity. Displacement ellipsoids are drawn at the 30% probability level. Selected atom···atom distance [Å], bond lengths [Å], and bond angles [°]: B(1)···B(1) = 1.93(1); B(1)–C(1) = 1.60(1), B(1)–C(11) = 1.656(9), B(1)–C(21) = 1.643(9); C(1)–B(1)–C(11) = 122.8(5), C(1)–B(1)–C(21) = 124.6(5), C(11)–B(1)–C(21) = 98.6(5). Symmetry transformation used to generate equivalent atoms: –x+1, –y+1, z.

Table S2. Selected crystallographic data for [Li(thf)$_4$][**2**], [Li(thf)$_3$][**2**], and [Li(thf)$_3$(Et$_2$O)][**7**].

	[Li(thf)$_4$][**2**]	[Li(thf)$_3$][**2**]	[Li(thf)$_3$(Et$_2$O)][**7**]
formula	$C_{57}H_{83}B_2LiO_4$	$C_{53}H_{75}B_2LiO_3$	$C_{56}H_{85}B_2LiO_4$
M_r	860.79	788.69	850.79
color, shape	colorless, needle	colorless, block	colorless, needle
T [K]	173(2)	173(2)	173(2)
radiation, λ [Å]	MoK_α, 0.71073	MoK_α, 0.71073	MoK_α, 0.71073
crystal system	orthorhombic	monoclinic	monoclinic
space group	*Pccn*	$P2_1$	$P2_1/n$
a [Å]	21.5605(15)	14.7750(10)	10.7242(12)
b [Å]	26.1802(19)	19.9973(10)	21.4641(16)
c [Å]	19.2608(13)	17.9098(12)	24.027(3)
α [°]	90	90	90
β [°]	90	109.105(5)	97.208(9)
γ [°]	90	90	90
V [Å^3]	10871.9(13)	5000.2(6)	5487.0(10)
Z	8	4	4
D_{calcd} [g cm^{-3}]	1.052	1.048	1.030
μ [mm^{-1}]	0.063	0.062	0.061
F(000)	3760	1720	1864
crystal size [mm]	0.28 x 0.18 x 0.12	0.24 x 0.22 x 0.17	0.21 x 0.11 x 0.02
rflns collected	42030	44665	66414
independent rflns (R_{int})	9821 (0.1664)	18711 (0.0674)	10391 (0.1431)
data/restraints/parameters	9821 / 190 / 681	18711 / 484 / 1209	10391 / 164 / 572
GOF on F^2	0.946	0.910	1.443
R_1, wR_2 [$I > 2\sigma(I)$]	0.0860, 0.1598	0.0712, 0.1404	0.1344, 0.2573
R_1, wR_2 (all data)	0.2038, 0.2033	0.1458, 0.1670	0.2251, 0.2877
largest diff peak and hole [e Å^{-3}]	0.418, –0.233	0.421, –0.211	0.933, –0.296

Table S3. Selected crystallographic data for [Li(12-crown-4)(thf)][Li(thf)$_2$][**11**], [Li(thf)$_4$][**16**], and (**14**^{C2}·thf)·4C$_6$H$_6$.

	[Li(12-crown-4)(thf)][Li(thf)$_2$][**11**]	[Li(thf)$_4$][**16**]	(**14**^{C2}·thf)·4C$_6$H$_6$
formula	$C_{66}H_{98}B_2Li_2O_7$	$C_{63}H_{87}B_2LiO_4$	$C_{70}H_{84}B_2O$
M_r	1038.94	936.88	962.99
color, shape	orange, plate	colorless, plate	yellow, block
T [K]	173(2)	173(2)	173(2)
radiation, λ [Å]	MoK_α, 0.71073	MoK_α, 0.71073	MoK_α, 0.71073
crystal system	monoclinic	monoclinic	triclinic
space group	$P2_1/c$	$P2_1/c$	P-1
a [Å]	12.9451(8)	19.4970(15)	10.4041(3)
b [Å]	18.3459(7)	24.7864(18)	11.5484(3)
c [Å]	27.0962(17)	23.972(2)	25.7360(7)
α [°]	90	90	79.323(2)
β [°]	101.393(5)	92.463(7)	85.313(2)
γ [°]	90	90	81.220(2)
V [Å^3]	6308.3(6)	11574.0(16)	2998.51(14)
Z	4	8	2
D_{calcd} [g cm^{-3}]	1.094	1.075	1.067
μ [mm^{-1}]	0.068	0.064	0.060
F(000)	2264	4080	1044
crystal size [mm]	0.24 x 0.19 x 0.04	0.17 x 0.17 x 0.03	0.24 x 0.19 x 0.14
rflns collected	59630	87491	69450
independent rflns (R_{int})	11144 (0.0915)	21394 (0.1445)	12158 (0.0402)
data/restraints/parameters	11144 / 72 / 764	21394 / 891 / 1484	12158 / 84 / 714
GOF on F^2	1.134	1.302	1.037
R_1, wR_2 [$I > 2\sigma(I)$]	0.0785, 0.1585	0.1210, 0.2070	0.0673, 0.1755
R_1, wR_2 (all data)	0.1447, 0.1797	0.2818, 0.2432	0.0782, 0.1838
largest diff peak and hole [e Å^{-3}]	0.306, –0.212	0.704, –0.334	0.539, –0.424

Table S4. Selected crystallographic data for **14**^{C3}, **14**^{C4}, and [Li(12-crown-4)$_2$][**15**^{C5,Cl}].

	14^{C3}	**14**^{C4}	[Li(12-crown-4)$_2$][**15**^{C5,Cl}]
formula	$C_{43}H_{54}B_2$	$C_{44}H_{56}B_2$	$C_{61}H_{90}B_2ClLiO_8$
M_r	592.48	606.50	1015.33
color, shape	yellow, plate	yellow, block	colorless, plate
T [K]	173(2)	173(2)	173(2)
radiation, λ [Å]	MoK_α, 0.71073	MoK_α, 0.71073	MoK_α, 0.71073
crystal system	orthorhombic	triclinic	orthorhombic
space group	$Pca2_1$	P-1	$Fdd2$
a [Å]	41.344(3)	5.9740(9)	12.2698(10)
b [Å]	14.2720(12)	14.639(2)	43.946(3)
c [Å]	6.1349(5)	21.461(3)	21.961(2)
α [°]	90	82.273(12)	90
β [°]	90	89.910(12)	90
γ [°]	90	86.790(12)	90
V [Å^3]	3620.0(5)	1856.9(5)	11841.6(17)
Z	4	2	8
D_{calcd} [g cm^{-3}]	1.087	1.085	1.139
μ [mm^{-1}]	0.060	0.060	0.116
F(000)	1288	660	4400
crystal size [mm]	0.17 x 0.13 x 0.08	0.14 x 0.09 x 0.04	0.26 x 0.24 x 0.11
rflns collected	24978	16800	29925
independent rflns (R_{int})	6651 (0.1309)	16800	5586 (0.1140)
data/restraints/parameters	6651 / 1 / 406	16800 / 0 / 416	5586 / 63 / 379
GOF on F^2	0.840	1.207	1.121
R_1, wR_2 [$I > 2\sigma(I)$]	0.0673, 0.1049	0.0880, 0.1686	0.0854, 0.1603
R_1, wR_2 (all data)	0.1448, 0.1282	0.1850, 0.1839	0.1296, 0.1780
largest diff peak and hole [e Å^{-3}]	0.177, –0.162	0.359, –0.328	0.649, –0.220

4. Computational details

DFT calculations were carried out with the Gaussian program package.[S8] The PBE0[S9-12] hybrid functional was used and combined with the D3BJ atom-pairwise dispersion correction with Becke-Johnson damping as devised by Grimme.[S13, 14] Geometry optimizations and harmonic frequency calculations were computed under gas-phase conditions with the TZVP basis set.[S15] All stationary points reported were characterized as minima or first order saddle points by eigenvalue analysis of the diagonalized Hessians. Gibbs energies reported correspond to the total energies of single point calculations with the SMD solvation model[S16] (to account for effects of the THF solvent), corrected by thermal contributions from the gas-phase frequency analyses. Graphical representations of molecular geometries were produced with the *CYLview* software.[S17]

Minima

[5^{c}]$^{-}$

Total energy = –1013.13778138 Hartree

Thermal correction to Gibbs free energy = 0.315916 Hartree

d(B···B) = 1.690623 Å

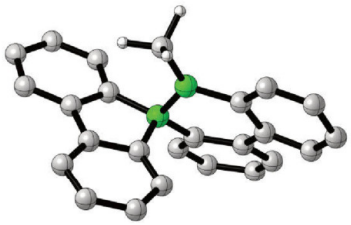

B	-0.441967198	0.464857702	0.127632617	C	2.890633354	2.347533655	-0.658552086
B	0.225700371	-0.679245183	1.178087245	C	1.061197048	3.771214531	-1.248071155
C	-0.571464517	-1.630514359	2.156272199	H	-0.881937078	2.945367287	-0.914556789
C	-1.938766773	0.851279774	0.488876060	C	3.925080647	-0.252221994	0.063459838
C	-2.827741254	-0.138378499	0.005023636	C	3.779272020	-2.202133390	1.454558172
C	-0.711703468	-0.832404114	-0.809277259	H	1.838040302	-2.610152226	2.237639834
C	0.621563346	1.537209407	-0.350327269	H	-3.671719519	-2.469913882	-1.396959802
C	1.790603414	-0.837354507	1.044791777	C	-1.754129712	-3.067852268	-2.157963939
C	-2.481883990	1.890935817	1.244952002	H	-5.765328215	1.008762496	1.245390892
C	-2.100180930	-1.136160851	-0.769401309	H	3.960676850	2.217991538	-0.544309920
C	-4.192188896	-0.093660389	0.284151242	C	2.430670628	3.557561064	-1.145398242
C	0.122999207	-1.678474373	-1.542352293	H	4.525956006	0.373420776	-0.585496480
C	2.015866005	1.321973362	-0.269736172	C	4.521762246	-1.360580706	0.636620842
C	0.188216342	2.775086435	-0.846665187	H	-2.148048827	-3.933502799	-2.681881169
C	2.574236105	0.061804526	0.278656991	H	3.136513462	4.331636258	-1.430343275
C	2.433904652	-1.930841048	1.636349844	H	5.568849148	-1.569562460	0.438157369
C	-3.845293467	1.951460778	1.505035807	H	-4.250553999	2.775549227	2.086047459
H	-1.828623917	2.667125114	1.635910729	H	0.269230697	-3.416972514	-2.794549574
C	-2.608635995	-2.247157632	-1.433386684	H	0.679336625	4.714925827	-1.627555126
H	-4.857533294	-0.870726355	-0.083265376	H	4.237309131	-3.072275506	1.914749260
C	-4.702154460	0.957599006	1.030913842	H	-0.291522991	-1.381184548	3.189353696
C	-0.393309405	-2.776983353	-2.219119525	H	-0.345561851	-2.695052685	2.022475016
H	1.188190946	-1.474342020	-1.587150586	H	-1.653252231	-1.502801358	2.071277747

[6^{c}-open]$^{-}$

Total energy = –1013.12607437 Hartree

Thermal correction to Gibbs free energy = 0.313661 Hartree

d(B···B) = 1.689778 Å

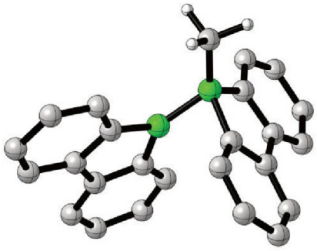

B	0.720147961	-1.135240335	1.206158149	C	-2.207807885	2.932925812	-0.745189863
B	-0.549192749	-0.161076673	0.662901704	H	-3.241465759	3.230229136	-0.898166136
C	0.475381457	-2.271006271	2.337009714	C	-1.176257495	3.810335799	-1.063658056
C	2.107279432	-0.341259185	1.227308617	H	-1.406260279	4.790900996	-1.469774313
C	2.692089520	-0.305127243	-0.060500408	C	0.146015628	3.438696737	-0.853273124
C	3.870833210	0.392946363	-0.311718541	C	0.453118986	2.186457363	-0.325406501
H	4.294454186	0.424204145	-1.312194215	H	1.488416357	1.918887820	-0.149663413
C	4.503498912	1.057829213	0.729161353	C	-2.113139427	-0.497714940	0.666975322
H	5.424616629	1.603347954	0.548017743	C	-2.824831333	0.616940320	0.174036316
C	3.954268169	1.020657011	2.010469389	C	-4.210642339	0.627837411	0.120454105
C	2.770238150	0.333077728	2.251637414	H	-4.747139950	1.493495207	-0.257575647
H	2.350404367	0.330345323	3.254561673	C	-4.915040203	-0.492077329	0.552979444
C	0.726379746	-1.594191318	-0.364092128	H	-6.000082420	-0.497656020	0.511022710
C	1.867049287	-1.042353773	-1.009848143	C	-4.234519413	-1.599715469	1.042115433
C	2.093775785	-1.243672477	-2.365712580	C	-2.841835243	-1.595786719	1.105114934
H	2.969671092	-0.817575202	-2.847409694	H	-2.323323884	-2.460950440	1.503699835
C	1.196648612	-2.002007008	-3.107556384	H	4.455712783	1.540230934	2.822632090
H	1.369674701	-2.161960115	-4.167558667	H	-0.622334772	-3.146285889	-3.081063662
C	0.075619899	-2.555134335	-2.495549713	H	-4.791349294	-2.467709764	1.382026822
C	-0.161591610	-2.340677439	-1.142639316	H	0.945655281	4.131920197	-1.095852287
H	-1.053375709	-2.759990626	-0.687620430	H	1.350242848	-2.926411213	2.437180993
C	-0.557471678	1.282145551	-0.018741001	H	-0.378713997	-2.920819903	2.119088638
C	-1.893869290	1.682435291	-0.233629283	H	0.289276503	-1.831984054	3.324866689

[6^{c}]$^{-}$

Total energy = –1013.11924082 Hartree

Thermal correction to Gibbs free energy = 0.314099 Hartree

d(B···B) = 1.672597 Å

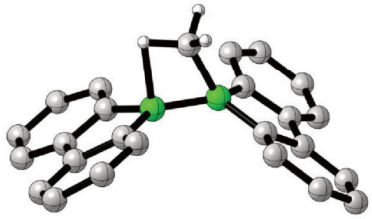

B	0.845333366	-0.123641900	0.772344246	C	-3.658202096	1.875976237	-1.047446566
B	-0.807549224	0.080432464	0.617700224	H	-4.568694722	1.532485257	-1.530240970
C	0.077242733	-0.080809613	2.284120336	C	-3.344734473	3.228556034	-1.038508614
C	1.911146323	1.023933395	0.507228162	H	-4.008159542	3.944255501	-1.514285535
C	2.965688132	0.488105971	-0.269678648	C	-2.177337343	3.663263881	-0.420131263
C	4.031699809	1.274072372	-0.692740603	C	-1.310724712	2.752423546	0.175642605
H	4.825647376	0.847374852	-1.299841548	H	-0.390213579	3.116332854	0.611855638
C	4.097155421	2.607159203	-0.307457188	C	-1.916075530	-1.042969577	0.439254445
H	4.928294139	3.227503641	-0.628810687	C	-3.000807711	-0.470859556	-0.264487730
C	3.109211753	3.135863190	0.517809126	C	-4.100799084	-1.228516824	-0.646247436
C	2.034892629	2.348293737	0.919957177	H	-4.917981915	-0.776780221	-1.201440312
H	1.294911754	2.781270253	1.587981390	C	-4.165863164	-2.568023405	-0.283349670
C	1.624675988	-1.403483736	0.233431984	H	-5.023602837	-3.168223002	-0.570794519
C	2.787725157	-0.953549612	-0.443888906	C	-3.141700557	-3.132204585	0.469551434
C	3.631371688	-1.830950653	-1.115796911	C	-2.029527872	-2.374671576	0.824178305
H	4.508748673	-1.458613278	-1.637883046	H	-1.253878713	-2.835856453	1.425006792
C	3.358714685	-3.192032747	-1.104338715	H	3.180271281	4.167277156	0.851503195
H	4.014996205	-3.885726795	-1.621060199	H	2.031964048	-4.727109934	-0.398058682
C	2.242467680	-3.661485132	-0.419435726	H	-3.209127116	-4.170871442	0.779001807
C	1.388844473	-2.777275987	0.232280537	H	-1.932252485	4.721175128	-0.414856139
H	0.520321620	-3.181839781	0.736922938	H	0.593359029	0.695994150	2.846381238
C	-1.601038313	1.391052471	0.192733423	H	0.163282023	-1.063683775	2.744886097
C	-2.805037684	0.972661461	-0.425635411	H	-1.000733532	0.183912091	2.381245301

[2^{c}-open]$^{-}$

Total energy = −1013.14164203 Hartree

Thermal correction to Gibbs free energy = 0.314067 Hartree

d(B···B) = 2.343491 Å

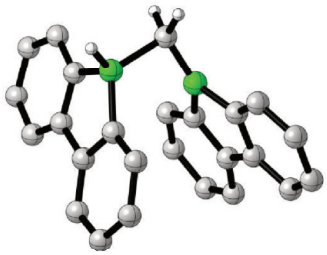

B	-0.656663047	0.008448156	-1.578232600	H	-2.917086865	-1.856388644	-2.246277428
B	0.924016051	-1.684198359	-1.219971128	C	0.299339576	-1.673813670	0.292200336
H	1.017934020	-2.843701814	-1.603452847	C	1.236892488	-1.109852867	1.186128070
C	0.142922501	-0.848116115	-2.517753641	C	0.983672394	-1.019746706	2.551161843
H	0.950937694	-0.390977444	-3.087574191	H	1.714156930	-0.572967603	3.220138618
H	-0.411756896	-1.553356816	-3.137115487	C	-0.212434246	-1.507909808	3.056828161
C	-0.233492773	1.295074225	-0.752204824	H	-0.425250549	-1.434156723	4.119193099
C	-1.340887837	1.716773899	0.012962834	C	-1.136934397	-2.097707252	2.199545892
C	-1.255233840	2.808323648	0.861954730	C	-0.875954245	-2.184478780	0.836902094
H	-2.107465819	3.122025942	1.457702449	H	-1.617641300	-2.638772552	0.188007235
C	-0.048127766	3.496015481	0.956074629	C	2.343752771	-1.002175372	-0.895709477
H	0.035877837	4.347177895	1.625189262	C	2.444713667	-0.689086681	0.475305368
C	1.048614321	3.098790044	0.202820179	C	3.564631525	-0.044741675	0.993175210
C	0.955165254	2.002415374	-0.652640691	H	3.621250258	0.205151715	2.049055912
H	1.823755548	1.688049053	-1.220978677	C	4.607714414	0.298701199	0.143753230
C	-2.177616684	-0.166891663	-1.154964839	H	5.483187427	0.807557430	0.536282149
C	-2.507870706	0.849718191	-0.237806679	C	4.528537121	-0.002973123	-1.213724359
C	-3.782458415	0.942094725	0.299247034	C	3.403305458	-0.645157135	-1.722914767
H	-4.033330375	1.722011839	1.012091689	H	3.350158686	-0.861471597	-2.787930465
C	-4.747091092	0.013802753	-0.083757519	H	1.987562058	3.636064101	0.290855320
H	-5.747503219	0.073508471	0.334205969	H	-5.203239645	-1.700729086	-1.291509528
C	-4.440339331	-0.985733486	-0.998858985	H	5.347471273	0.269255967	-1.874009700
C	-3.156485385	-1.069446907	-1.535964779	H	-2.071790717	-2.482798898	2.596590971

[2^{c}]$^{-}$

Total energy = –1013.15160474 Hartree

Thermal correction to Gibbs free energy = 0.314029 Hartree

d(B···B) = 1.916075 Å

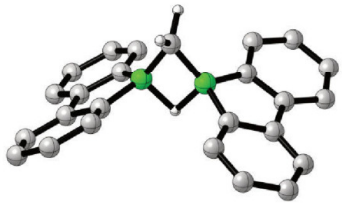

B	-0.955185592	0.073866560	0.721830180	H	-0.664912282	3.116995251	0.555495530
B	0.955186640	-0.073860255	0.721835402	C	1.810984502	-1.335790407	0.199526715
H	0.000005965	0.000004772	-0.268992240	C	3.028757590	-0.861326347	-0.335320007
C	-0.000002751	0.000006632	1.989491668	C	3.975623742	-1.724762292	-0.875046273
H	-0.106671534	-0.895803478	2.597947110	H	4.906657646	-1.339141390	-1.280893378
H	0.106663546	0.895820250	2.597942444	C	3.724136909	-3.089970727	-0.892694259
C	-1.974809555	-1.127350574	0.403057252	H	4.456065929	-3.773359331	-1.312370606
C	-3.130852473	-0.596042867	-0.204010831	C	2.532335276	-3.578367488	-0.370407143
C	-4.208915011	-1.404252671	-0.548948199	C	1.588411209	-2.707139139	0.166932989
H	-5.092030973	-0.978812030	-1.017207477	H	0.664915124	-3.116987462	0.555537018
C	-4.158561339	-2.763941782	-0.271886902	C	1.974815798	1.127353700	0.403062041
H	-4.993781339	-3.404623202	-0.537894536	C	3.130849380	0.596043324	-0.204021906
C	-3.046019733	-3.299191883	0.367804175	C	4.208911939	1.404249455	-0.548967829
C	-1.971703394	-2.482050495	0.708189535	H	5.092019595	0.978807176	-1.017241312
H	-1.132767190	-2.915041641	1.242199339	C	4.158570454	2.763936496	-0.271894307
C	-1.810986117	1.335794505	0.199518562	H	4.993791129	3.404614873	-0.537907127
C	-3.028765814	0.861326733	-0.335310789	C	3.046042646	3.299187182	0.367820076
C	-3.975639755	1.724758354	-0.875030380	C	1.971725416	2.482049634	0.708211997
H	-4.906678364	1.339133907	-1.280863305	H	1.132802738	2.915039466	1.242243826
C	-3.724153982	3.089966662	-0.892691613	H	-3.019897471	-4.357638630	0.609566433
H	-4.456088851	3.773351994	-1.312363091	H	-2.335130439	4.646270355	-0.383184734
C	-2.532344995	3.578367056	-0.370425063	H	3.019932866	4.357630902	0.609596906
C	-1.588413742	2.707143231	0.166909763	H	2.335121465	-4.646271065	-0.383154341

Transition states

TS1

Total energy = –1013.12056760 Hartree
Thermal correction to Gibbs free energy = 0.314542 Hartree
Imaginary frequency: –241.0656
d(B···B) = 1.634340 Å

B	0.532998293	-0.156226601	0.510418886	C	-2.332863407	-1.646867975	-2.024923581
B	-0.667226025	-0.804368792	1.410663562	C	-0.283071371	-2.874281753	-2.259244957
C	-0.553161829	-2.016399372	2.447619510	H	1.195730954	-2.534373237	-0.754485773
C	2.075325768	-0.549017900	0.589012778	C	-3.855763309	0.422129148	-0.291187441
C	2.839761795	0.557332944	0.147866108	C	-3.923133719	1.346497746	1.926568231
C	0.606033215	1.257543425	-0.225146057	H	-2.283496348	0.857529103	3.218509008
C	-0.555087955	-1.352153855	-0.386554408	H	3.397298331	3.126564701	-0.939987344
C	-2.060188990	-0.065650481	1.290546212	C	1.371994037	3.741356758	-1.309974935
C	2.770341313	-1.664867887	1.050788260	H	5.977400884	-0.600765990	0.690035613
C	1.966145635	1.627744077	-0.341314402	H	-3.339735824	-1.426654581	-2.366297403
C	4.228942299	0.547493095	0.192802324	C	-1.545744857	-2.543821112	-2.731270235
C	-0.349488972	2.166857431	-0.674472294	H	-4.291254811	0.317120145	-1.280895848
C	-1.853824746	-1.056819031	-0.859252152	C	-4.492950802	1.202551230	0.665359924
C	0.198044614	-2.284510732	-1.096112911	H	1.657054071	4.702382717	-1.727767491
C	-2.654246998	-0.202386610	0.023150554	H	-1.926245047	-3.000348311	-3.639972971
C	-2.719186780	0.721078624	2.232430163	H	-5.429262162	1.697915253	0.429073487
C	4.162055769	-1.687808262	1.079834916	H	4.681681833	-2.571176325	1.440108927
H	2.225893913	-2.537211076	1.399095596	H	-0.734154006	4.084823005	-1.559802771
C	2.346801163	2.857790069	-0.866882290	H	0.332935918	-3.586499585	-2.799567244
H	4.798523461	1.410671502	-0.141085003	H	-4.420515301	1.958256784	2.673827754
C	4.892159109	-0.581740612	0.657393965	H	-1.356304931	-2.755008876	2.332318289
C	0.027769940	3.392078610	-1.213751807	H	-0.652129201	-1.606437972	3.461760607
H	-1.403822179	1.927068479	-0.596142088	H	0.401573558	-2.545644205	2.416149554

TS2

Total energy = –1013.11549001 Hartree

Thermal correction to Gibbs free energy = 0.314249 Hartree

Imaginary frequency: –116.0814

d(B···B) = 1.674970 Å

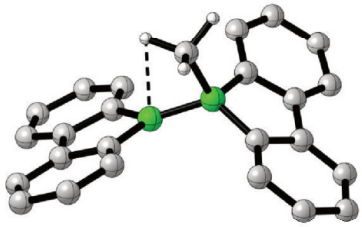

B	0.823342668	-0.244773625	0.748845532	C	-3.779222362	1.949358951	-0.897073309
B	-0.775530180	-0.002793182	0.312296136	H	-4.800587335	1.680584218	-1.151034249
C	0.245781499	-0.433839904	2.320737283	C	-3.338032719	3.256957505	-1.077488521
C	1.874189686	0.960366612	0.609823352	H	-4.020655805	4.008994398	-1.461679977
C	2.995656592	0.531612607	-0.135256788	C	-2.024979546	3.598944777	-0.781508326
C	4.055729049	1.387612102	-0.418270504	C	-1.138372247	2.637280085	-0.298905615
H	4.904705461	1.042874316	-1.003023866	H	-0.106819922	2.904551694	-0.104636474
C	4.038994652	2.685408280	0.076717677	C	-1.980782722	-1.057811375	0.324343146
H	4.863940888	3.359636418	-0.133492584	C	-3.152637991	-0.422763904	-0.139125228
C	2.973484474	3.110774366	0.865420652	C	-4.348592200	-1.109833636	-0.279895649
C	1.909017113	2.253020758	1.128641237	H	-5.239788918	-0.608804377	-0.646750542
H	1.092765711	2.603198925	1.756740905	C	-4.402588526	-2.454489610	0.074878891
C	1.689406367	-1.432904928	0.097334668	H	-5.333744045	-3.003742831	-0.025225322
C	2.877654996	-0.892209126	-0.454537476	C	-3.270766734	-3.091522179	0.565774472
C	3.786627753	-1.678485902	-1.155458175	C	-2.069571675	-2.394824505	0.686813471
H	4.686343358	-1.237177189	-1.576624653	H	-1.199905856	-2.906526757	1.081501589
C	3.546826044	-3.037545486	-1.306384032	H	2.976986258	4.116013743	1.278263332
H	4.252715968	-3.660653302	-1.847411436	H	2.212191950	-4.662077715	-0.863685225
C	2.398562045	-3.597091645	-0.754517562	H	-3.322354235	-4.137045622	0.853546030
C	1.484831065	-2.801044498	-0.070361347	H	-1.684300195	4.617519972	-0.939902567
H	0.593059152	-3.271048158	0.330681157	H	1.030426183	-0.074730649	2.995503314
C	-1.560958050	1.332784367	-0.078880860	H	0.034362507	-1.483476412	2.535623845
C	-2.896216991	1.004016523	-0.398310750	H	-0.662640982	0.127121936	2.588834136

TS3

Total energy = –1013.11106266 Hartree

Thermal correction to Gibbs free energy = 0.312907 Hartree

Imaginary frequencies: –686.9080

d(B···B) = 1.870943 Å

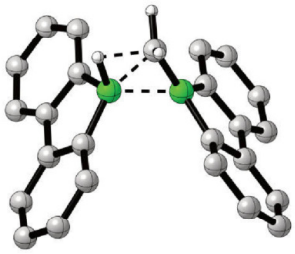

B	-0.826974644	-0.379670080	1.228647026	C	3.784888128	-0.226617992	-1.003987811
B	0.869216144	0.409290660	1.258752301	H	4.230023499	0.333176114	-1.821752333
C	-0.157148429	-0.114867485	2.582327985	C	4.328632723	-1.445853137	-0.622780608
C	-0.965290065	-1.731926439	0.417308576	H	5.188900221	-1.846492265	-1.149976942
C	-2.042357505	-1.581665417	-0.491538883	C	3.779169040	-2.146749362	0.447696255
C	-2.404303002	-2.599518136	-1.365977238	C	2.669867318	-1.646951036	1.119489784
H	-3.229868750	-2.462057888	-2.058960260	H	2.266831381	-2.207054618	1.959087211
C	-1.709414607	-3.801646399	-1.344806247	C	0.988181579	1.756957228	0.448424374
H	-1.983469228	-4.602010106	-2.025389659	C	2.029657571	1.574882938	-0.498024387
C	-0.663071697	-3.977452349	-0.444706536	C	2.362267196	2.574069487	-1.406538286
C	-0.299580413	-2.954788057	0.424598038	H	3.155354505	2.412855843	-2.131468501
H	0.526696546	-3.120090963	1.105019723	C	1.685920133	3.785148543	-1.376667328
C	-2.055296851	0.463478017	0.699342430	H	1.939119479	4.569248437	-2.083455039
C	-2.695691655	-0.281274328	-0.317942572	C	0.683037596	3.991357564	-0.433094901
C	-3.827604294	0.200651032	-0.964542422	C	0.341034825	2.990101931	0.467032040
H	-4.305769951	-0.380983037	-1.747854321	H	-0.452893211	3.178158639	1.178980811
C	-4.358244028	1.429677874	-0.592313467	H	-0.123188921	-4.919745480	-0.423527273
H	-5.240791589	1.815294005	-1.093564320	H	-4.199025727	3.106225121	0.741663578
C	-3.768061689	2.156902526	0.436830782	H	0.158448108	4.941896192	-0.403778321
C	-2.632045577	1.671539225	1.076458578	H	4.220118393	-3.089863168	0.757103700
H	-2.203706275	2.248228426	1.891928144	H	0.296781094	-0.930817938	3.140689487
C	2.083264133	-0.444663988	0.736224173	H	-0.591123166	0.647772130	3.226706021
C	2.681965907	0.277821850	-0.323149301	H	1.097698094	0.646473120	2.483573491

TS4

Total energy = –1013.13848805 Hartree

Thermal correction to Gibbs free energy = 0.315252 Hartree

Imaginary frequency: –13.9254

d(B···B) = 2.377687 Å

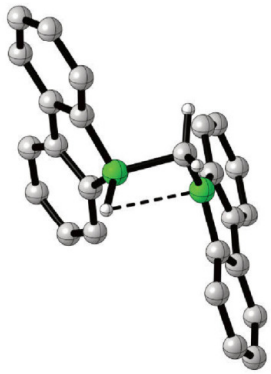

B	0.811745936	-0.902545467	0.987350017	H	1.752775470	-3.451981186	-0.289694671
B	-1.175652854	-1.486649396	-0.179897039	C	-0.894963353	-0.145091789	-1.068926462
H	-0.937211902	-2.502153968	-0.815830502	C	-2.053751109	0.662679474	-1.082973719
C	-0.410181361	-1.670897840	1.380829332	C	-2.098699005	1.867963672	-1.777571049
H	-1.055042801	-1.217090611	2.132823160	H	-2.999488833	2.476136726	-1.770903230
H	-0.331423330	-2.746245234	1.533257822	C	-0.986840807	2.283674829	-2.496277481
C	1.157455929	0.621601403	1.247840684	H	-1.008191727	3.225106830	-3.037196131
C	2.485494082	0.854878243	0.839306890	C	0.150162813	1.482753068	-2.532913327
C	3.068593330	2.105406949	0.974083752	C	0.186994053	0.280071254	-1.836200957
H	4.092336409	2.283603244	0.657703740	H	1.087305719	-0.324700729	-1.880691217
C	2.315247058	3.145887621	1.510538589	C	-2.731563697	-1.230527411	0.155223898
H	2.755962254	4.132914626	1.612344618	C	-3.143019630	0.023731439	-0.339680715
C	0.999829979	2.933394019	1.904957168	C	-4.434162160	0.499566134	-0.126427526
C	0.424581090	1.670902040	1.777855699	H	-4.737371648	1.470341330	-0.509632822
H	-0.608412237	1.511909884	2.072434416	C	-5.339895141	-0.278768574	0.582599412
C	2.127009825	-1.419594897	0.269059125	H	-6.350014946	0.082025329	0.752875120
C	3.068579816	-0.369587367	0.255784729	C	-4.952087768	-1.521712797	1.076797720
C	4.333600167	-0.550836033	-0.282208628	C	-3.655921752	-1.984513827	0.870238403
H	5.058431097	0.257929703	-0.291859563	H	-3.361865082	-2.949753323	1.276012881
C	4.665836687	-1.789282057	-0.826134479	H	0.418887732	3.757922045	2.306110419
H	5.651197604	-1.940691531	-1.256401703	H	4.014270556	-3.785812373	-1.266419789
C	3.744534959	-2.829392296	-0.829330474	H	-5.666057558	-2.127725990	1.627985865
C	2.477676547	-2.643507099	-0.277250374	H	1.016384518	1.801450589	-3.105504564

5. References

S1 A. Hübner, M. Diefenbach, M. Bolte, H.-W. Lerner, M. C. Holthausen and M. Wagner, *Angew. Chem. Int. Ed.*, 2012, **51**, 12514-12518.

S2 T. Kaese, H. Budy, M. Bolte, H.-W. Lerner and M. Wagner, *Angew. Chem. Int. Ed.*, 2017, **56**, 7546-7550.

S3 A. Hübner, M. Bolte, H.-W. Lerner and M. Wagner, *Angew. Chem. Int. Ed.*, 2014, **53**, 10408-10411.

S4 G. R. Fulmer, A. J. M. Miller, N. H. Sherden, H. E. Gottlieb, A. Nudelman, B. M. Stoltz, J. E. Bercaw and K. I. Goldberg, *Organometallics*, 2010, **29**, 2176-2179.

S5 T. Kaese, A. Hübner, M. Bolte, H.-W. Lerner and M. Wagner, *J. Am. Chem. Soc.*, 2016, **138**, 6224-6233.

S6 *X-AREA: Diffractometer Control Program System*, Stoe & Cie, Darmstadt, Germany, 2002.

S7 G. M. Sheldrick, *Acta Crystallogr., Sect. A: Found. Crystallogr.*, 2008, **64**, 112-122.

S8 M. J. Frisch, G. W. Trucks, H. B. Schlegel, G. E. Scuseria, M. A. Robb, J. R. Cheeseman, G. Scalmani, V. Barone, B. Mennucci, G. A. Petersson, H. Nakatsuji, M. Caricato, X. Li, H. P. Hratchian, A. F. Izmaylov, J. Bloino, G. Zheng, J. L. Sonnenberg, M. Hada, M. Ehara, K. Toyota, R. Fukuda, J. Hasegawa, M. Ishida, T. Nakajima, Y. Honda, O. Kitao, H. Nakai, T. Vreven, J. A. Montgomery, Jr., J. E. Peralta, F. Ogliaro, M. Bearpark, J. J. Heyd, E. Brothers, K. N. Kudin, V. N. Staroverov, R. Kobayashi, J. Normand, K. Raghavachari, A. Rendell, J. C. Burant, S. S. Iyengar, J. Tomasi, M. Cossi, N. Rega, J. M. Millam, M. Klene, J. E. Knox, J. B. Cross, V. Bakken, C. Adamo, J. Jaramillo, R. Gomperts, R. E. Stratmann, O. Yazyev, A. J. Austin, R. Cammi, C. Pomelli, J. W. Ochterski, R. L. Martin, K. Morokuma, V. G. Zakrzewski, G. A. Voth, P. Salvador, J. J. Dannenberg, S. Dapprich, A. D. Daniels, Ö. Farkas, J. B. Foresman, J. V. Ortiz, J. Cioslowski and D. J. Fox, *Gaussian 09*, Revision D.01, Gaussian, Inc., Wallingford, CT, 2013; http://www.gaussian.com.

S9 J. P. Perdew, K. Burke and M. Ernzerhof, *Phys. Rev. Lett.*, 1996, **77**, 3865-3868.

S10 J. P. Perdew, K. Burke and M. Ernzerhof, *Phys. Rev. Lett.*, 1997, **78**, 1396-1396.

S11 J. P. Perdew, M. Ernzerhof and K. Burke, *J. Chem. Phys.*, 1996, **105**, 9982-9985.

S12 C. Adamo and V. Barone, *J. Chem. Phys.*, 1999, **110**, 6158-6170.

S13 L. Goerigk and S. Grimme, *J. Chem. Theory Comput.*, 2011, **7**, 291-309.

S14 S. Grimme, S. Ehrlich and L. Goerigk, *J. Comput. Chem.*, 2011, **32**, 1456-1465.

S15 A. Schäfer, C. Huber and R. Ahlrichs, *J. Chem. Phys.*, 1994, **100**, 5829-5835.

S16 A. V. Marenich, C. J. Cramer and D. G. Truhlar, *J. Phys. Chem. B*, 2009, **113**, 6378-6396.

S17 C. Y. Legault, *CYLview*, 1.0b; Université de Sherbrooke, Canada, 2009; http://www.cylview.org.

6.2.2 Doping Polycyclic Aromatics with Boron for Superior Performance in Materials Science and Catalysis

ACES Asian Chemical Editorial Society
DOI: 10.1002/ajoc.201700495
ASIAN JOURNAL OF ORGANIC CHEMISTRY
Focus Review

Polycyclic Aromatic Hydrocarbons

Doping Polycyclic Aromatics with Boron for Superior Performance in Materials Science and Catalysis

Esther von Grotthuss[+], Alexandra John[+], Thomas Kaese[+], and Matthias Wagner*[a]

Dedicated to Professor Wolfgang A. Herrmann on the occasion of his 70th birthday

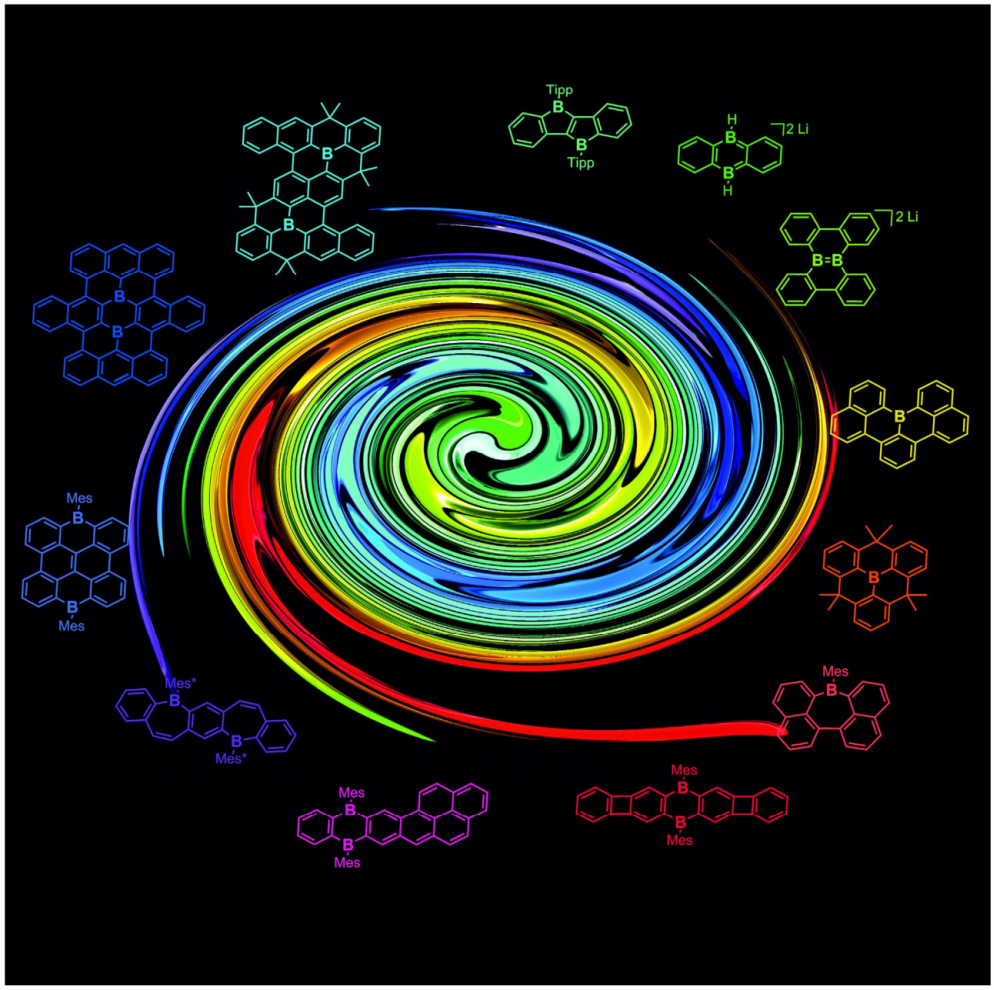

© 2018 Wiley-VCH Verlag GmbH & Co. KGaA, Weinheim

ACES Asian Chemical Editorial Society

ASIAN JOURNAL OF ORGANIC CHEMISTRY
Focus Review

Abstract: Boron has one valence electron less than a carbon atom and an available vacant p_z orbital. The incorporation of sp^2-hybridized boron atoms into the host lattice of a polycyclic aromatic hydrocarbon (PAH) is formally related to oxidative doping. A boron-containing B-PAH has an energetically low-lying LUMO and a narrow HOMO–LUMO gap, which renders it a strong Lewis acid/electron acceptor and promotes fluorescence in the visible range of the electromagnetic spectrum. Many methods have been developed to access B-PAHs that are deliberately designed for specific tasks. Herein, we highlight recent breakthroughs in the field of B-PAH synthesis and the scope of their applications, which range from Lewis acid and redox catalysis to device fabrication. We will also report on the dynamic covalent chemistry of neutral and anionic B-PAHs, as it is a potential limitation in the design of catalyst systems but can also provide a powerful synthetic tool for the preparation of otherwise inaccessible B-PAHs.

1. Introduction

Extended, conjugated organic π-electron systems are not only fundamentally interesting but also provide the basis of materials for optoelectronic devices, such as organic light-emitting diodes (OLEDs), organic field-effect transistors (OFETs), and organic photovoltaic cells (OPVs), as well as the materials for electrodes in lithium batteries.[1] Among compounds currently considered as most relevant for future development, polycyclic aromatic hydrocarbons (PAHs) are particularly promising, as they allow for the controlled design of their molecular structures and often show predictable supramolecular arrangements.[2] In the past few years, the atomically precise synthesis of nanoscale PAHs with customized edge configurations[3] has witnessed rapid development.[4] It has also become more and more obvious that the performance of parent all-carbon compounds can often be improved if selected carbon atoms are replaced by other main group elements. Nitrogen, phosphorus, or sulfur atoms have been employed as dopant atoms for decades.[4,5] Boron has only recently entered the center stage of PAH development, but since its introduction, it has turned out to be among the most effective electronically perturbative elements to be incorporated into PAH core structures. As a key feature, the three-coordinate, sp^2-hybridized boron centers have vacant p_z orbitals (rendering them formally equivalent to carbenium ions) and low Pauling electronegativities [EN(B) = 2.0, EN(C) = 2.6]. As a consequence, they act simultaneously as π-electron acceptors and σ-electron donors.

This review presents the most efficient strategies for the synthesis of boron-containing PAHs (B-PAHs), including approaches that rely on electrons as catalysts[6] and on dynamic covalent chemistry. It further highlights unusual bonding situations that have been encountered in this context and describes the impact of incorporated boron atoms on the overall electronic structures of B-PAHs. Recent advances in optoelectronic applications and B-PAH-catalyzed molecular transformations will be summarized. We will conclude with an outlook on boron-doped nanographenes and nanoribbons. To maintain a focus on species that exclusively contain boron heteroatoms, which are integral parts of rigid, π-delocalized scaffolds,[7] we omit compounds with dangling boryl substituents, borylene-bridged polymers, and B–N/O isosteres of PAHs. For an overview of these compound classes, we refer the reader to earlier review articles.[4,8–16]

[a] E. von Grotthuss,[+] A. John,[+] T. Kaese,[+] Prof. Dr. M. Wagner
Institut für Anorganische Chemie
Goethe-Universität Frankfurt
Max-von-Laue-Strasse 7, 60438
Frankfurt a. M. (Germany)
E-mail: Matthias.Wagner@chemie.uni-frankfurt.de

[+] These authors contributed equally to this work.

The ORCID identification number(s) for the author(s) of this article can be found under https://doi.org/10.1002/ajoc.201700495.

2. Electronic Structures and Classification of Boron-Doped PAHs (B-PAHs)

To illustrate the effects of the incorporation of boron atoms on the electronic structures of PAH frameworks, Figure 1 compares the calculated relative energies and nodal structures of the frontier orbitals of three prototypical compounds, that is, benzene, 9,10-dihydro-9,10-diboraanthracene (DBA), and anthracene.[17] DBA can be regarded as either a doubly borylated benzene or doubly boron-doped anthracene. Relative to the HOMO energy level of benzene, that of DBA remains unchanged, as the two boron atoms do not contribute to this molecular orbital. In stark contrast, the vacant boron p_z orbitals do participate in the LUMO of DBA, which is thus more energetically favored than that of benzene. Both the HOMO and LUMO of DBA are lower in energy relative to those of anthra-

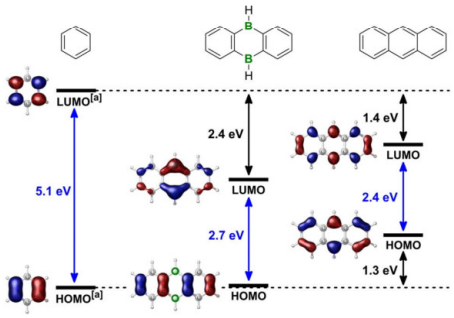

Figure 1. Comparison of the calculated energy levels and nodal structures of the frontier orbitals of benzene, 9,10-dihydro-9,10-diboraanthracene, and anthracene. [a] Only one orbital of the doubly degenerate set is shown.

© 2018 Wiley-VCH Verlag GmbH & Co. KGaA, Weinheim

ACES Asian Chemical Editorial Society

ASIAN JOURNAL OF ORGANIC CHEMISTRY
Focus Review

cene, but the orbital energy gaps are similar in both species. These specific observations can be generalized to two useful rules of thumb: (1) B-PAHs tend to be excellent electron acceptors and (2) the HOMO–LUMO transitions of B-PAHs are in an ideal range to bring about visible light emission.

Because of their vacant p_z orbitals, boron atoms are well-suited to facilitate electronic communication between adjacent aryl substituents. With the addition of a Lewis base, there is the possible formation of a Lewis acid-base adduct, which results in pyramidalization of the trigonal planar boron center, a shutdown of the conjugation pathway at this position, and a concomitant change in the absorption and emission characteristics of the molecule. With respect to chemical sensing, this can be a desirable effect, given the adduct formation is specific for a certain Lewis basic analyte.[18] The Lewis acidity of the boron atom is also a decisive asset in terms of B-PAH catalysis, as adduct formation influences the frontier orbitals of the Lewis base substrate.

Unfortunately, water is a ubiquitous Lewis base, and the readiness of boron to expand its coordination number from three to four provides a pathway for subsequent hydrolytic degradation. Benchtop-stable B-PAHs, of which a considerable number already exist, are usually designed in one of three ways (Figure 2): (1) The introduction of a π-donor substituent

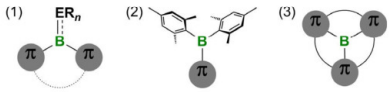

Figure 2. Three strategies to generate benchtop-stable arylboranes: (1) the introduction of a π-donor substituent ER_n, (2) steric shielding by the attachment of bulky groups, and (3) structural constraint by incorporation of the boron atom at a central site.

ER_n, such as an alkoxy group, to reduce the electron deficiency at the boron site through partial double-bond formation. As a downside, this can lead to a loss in the unique character of the boron center. (2) The attachment of bulky groups, such as mesityl (Mes) rings, onto the boron site, which leads to kinetic protection but can also hinder the dense π-stacking of the molecules in the solid state and thus be detrimental to the charge-carrier properties of the bulk material in optoelectronic devices. (3) Incorporation at the central position, rather than at the perimeter, of the PAH to provide full structural constraint of the boron atom within the rigid PAH framework. As a result, boron pyramidalization in the course of the formation of a water adduct is now associated with a considerable energy penalty and thus becomes unfavorable. B–C bond cleavage is also prevented by the chelating effect. B-PAHs with centrally located boron atoms, however, are challenging to prepare. Thus, for each specific application, the most viable and cost-efficient method must be carefully considered to alleviate the problem of hydrolysis.

For a classification of B-PAH structures, it is helpful to first consider the two simplest, uncharged, and completely conjugated cyclic hydrocarbons, namely, antiaromatic cyclobutadiene and aromatic benzene (Figure 3). The formal insertion of borylene units into the former leads to borole (**A**) and 1,4-diboracyclohexa-2,5-diene (**B**). As the number of π-electrons remains unchanged, both boron heterocycles are still antiaromatic species.[19–21] An analogous ring expansion transforms benzene into the aromatic borepin (**E**). Conjugated six-mem-

Esther von Grotthuss, born in 1991, received her B.Sc. degree from the Philipps-Universität Marburg (Germany) and her M.Sc. degree from the Goethe-Universität Frankfurt/Main (Germany). She was supported by a grant from the "Studienstiftung des deutschen Volkes". Since 2015, she has been pursuing her Ph.D. in Prof. Dr. M. Wagner's research group. Focusing on the reactivity of reduced 9,10-dihydro-9,10-diboraanthracene derivatives, she seeks to establish their use in catalysis.

Alexandra John, born in 1991, studied chemistry (B.Sc., M.Sc.) at the Goethe-Universität Frankfurt/Main (Germany). During her master's studies, she stayed for 6 months with Prof. Dr. F. Jäkle and afterwards joined Prof. Dr. M. Wagner's research group for her Ph.D. thesis. Her current research interests include the synthesis of π-conjugated arylboranes for potential applications in organic electronics.

Thomas Kaese, born in 1990, obtained his B.Sc. and M.Sc. degrees from the Goethe-Universität Frankfurt/Main (Germany). He is currently working on his Ph.D. thesis in the group of Prof. Dr. M. Wagner and focuses on the reactivity of reduced boranes to elucidate their dynamic covalent chemistry and unusual bonding situations. He was supported by grants from the "Studienstiftung des deutschen Volkes" and the "Fonds der Chemischen Industrie".

Prof. Dr. Matthias Wagner obtained his Ph.D. with Prof. Dr. H. Nöth at the Ludwig-Maximilians-Universität München (Germany). He stayed for a postdoc position with Prof. M. L. H. Green, FRS, at Oxford University (UK) and finished his Habilitation in 1997 at the Technische Universität München in the group of Prof. Dr. W. A. Herrmann. Since 1999, he holds the chair of Organometallic Chemistry at the Goethe-Universität Frankfurt/Main (Germany). His current research interests are general boron and silicon chemistry, the investigation of reactive intermediates, and organometallic catalysis directed toward materials synthesis.

© 2018 Wiley-VCH Verlag GmbH & Co. KGaA, Weinheim

ACES Asian Chemical Editorial Society
ASIAN JOURNAL OF ORGANIC CHEMISTRY
Focus Review

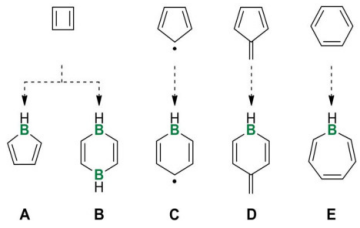

Figure 3. Formal borylene insertion into cyclobutadiene, the cyclopentadienyl radical, fulvene, and benzene to furnish neutral boron heterocycles **A**–**E**.

bered heterocycles that contain only one boron atom require either a carbon radical (i.e., **C**) or an exocyclic double bond (i.e., **D**) at the 4-position and are formally derived through borylene insertion into the cyclopentadienyl radical or fulvene, respectively.[22] Although the extreme reactivity of parent compounds **A**–**E** has precluded their isolation, a number of derivatives that have dangling substituents, especially from the borole family, have been reported.[23–29] Another mode of stabilization is provided by benzannulation, and the vast majority of B-PAHs can be regarded as derivatives of **A**–**E**, in which an increasing number of benzene rings are grouped around the heterocyclic core.

3. Syntheses of B-PAHs

3.1. General Synthetic Approaches to Arylboranes

B–C(aryl) bonds can be formed in numerous ways. A selection of particularly versatile and/or atom-economic protocols are shown in Figure 4. One of the most well-known synthetic methods involves the reaction of aryllithium (ArLi) or aryl Grignard (ArMgBr) reagents with haloboranes (XBR_2) or alkoxyboranes ($ROBR_2$).[30] Fluoroboranes are the reagent of choice if

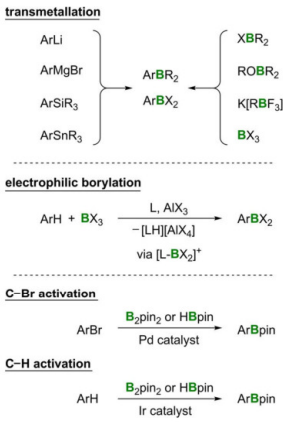

Figure 4. Common synthetic strategies for the preparation of arylboranes [B_2pin_2 = bis(pinacolato)diboron, HBpin = pinacolatoborane].

the more reactive higher haloboranes undergo unselective transformations. Nucleophilic substitution reactions that involve $ROBR_2$ often stop at the stage of the adducts $[Ar(RO)BR_2]^-$, from which the three-coordinate target products $ArBR_2$ have to be liberated by aqueous workup under acidic conditions.[30] Alkoxyboranes are thus particularly valuable starting materials to prevent the formation of unwanted ate complexes $[Ar_2BR_2]^-$. Recently, the Molander salts $K[RBF_3]$, which are conveniently accessible from arylboronates and $K[HF_2]$,[31,32] have been successfully employed in cases in which haloboranes or alkoxyboranes failed to provide the desired products.[29,33–35]

In addition to varying the leaving groups at the electrophilic boron sites, it can also be beneficial to modify the transmetalation agents. Arylsilanes ($ArSiR_3$) and arylstannanes ($ArSnR_3$) are classic starting materials for the preparation of aryldihaloboranes through electrophilic Si/B or Sn/B exchange reactions with BX_3 (X = Cl, Br).[30] By using multiply silylated arenes, multiply borylated arenes are conveniently accessible. However, the first Si/B exchange generally proceeds under milder conditions than that needed to introduce a second or third BX_2 group, especially if the electron-withdrawing boryl substituents are introduced in mutual *ortho* or *para* positions.[36]

Parent arenes can undergo electrophilic borylation reactions in a manner reminiscent of a Friedel–Crafts transformation. Highly electrophilic borenium cation intermediates $[L\text{-}BX_2]^+$ are generated from BX_3, a bulky amine ligand (L), and AlX_3 to attach BX_2 groups to the organic scaffold.[37,38] In addition to its role as a stabilizing ligand for the cationic boron intermediate, the amine ligand also acts as a Brønsted base to trap liberated HX. Electrophilic aryl borylations can also be conducted with dihalo(aryl)boranes as borylation reagents, which make them highly versatile synthetic tools.

Further synthetic strategies increasingly rely on Pd-mediated C–Br or Ir-catalyzed C–H activation/borylation reactions.[39,40] Bis(pinacolato)diboron (B_2pin_2) and pinacolatoborane (HBpin) act as the boron sources. C–H activation/borylation reactions are mainly governed by steric factors and thus usually occur *meta* and *para* to a preexisting substituent in statistical ratios of 2:1.

A less common, but potentially powerful approach, takes advantage of substituent redistribution reactions. Dihydro(aryl)boranes ($ArBH_2$) tend to engage in exchange equilibria, in which all four conceivable species Ar_nBH_{3-n} (n = 0–3) are present.[13] However, under carefully controlled conditions (i.e., the removal of the volatile B_2H_6 from the reaction mixture and proper choice of the steric demand of the aryl substituent), the equilibrium can be shifted toward either Ar_2BH or Ar_3B.[41] Even condensation polymerization protocols that lead to the formation of main-chain boron-containing macromolecules have been elaborated by comparable dismutation reactions.[42–45]

3.2. Specific Synthetic Approaches to B-PAHs

Boron-halogenated dibenzo[*b*,*d*]boroles (borafluorenes) **G**[46,47] and dibenzo[*b*,*f*]borepins (DBBs) **I**[48,49] are commonly synthe-

© 2018 Wiley-VCH Verlag GmbH & Co. KGaA, Weinheim

ACES Asian Chemical Editorial Society
ASIAN JOURNAL OF ORGANIC CHEMISTRY
Focus Review

sized by the treatment of corresponding silacycles or stannacycles, **F** or **H**, with BX_3 (X = Cl, Br; Scheme 1). 9,10-Dihydro-9,10-diboraanthracenes (DBAs) **K** are not usually prepared from 9,10-dihydro-9,10-disilaanthracenes but rather by a cyclocondensation reaction between 1,2-bis(trimethylsilyl)benzenes **J**[50–52] and BX_3.[52–56] As a general feature, substituents may be located *meta* to the boron atoms, but not at the sterically more encumbered *ortho* positions of **K**.

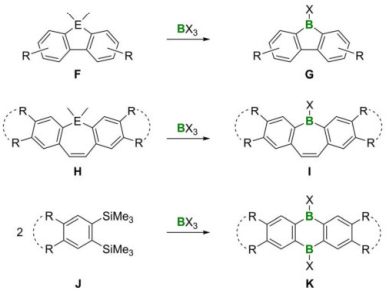

Scheme 1. Syntheses of dibenzo[*b*,*d*]boroles **G** and dibenzo[*b*,*f*]borepins **I** by E/B exchange reactions of the corresponding silacycles or stannacycles, **F** or **H**. Formation of DBAs **K** by cyclocondensation reactions between **J** and BX_3 (R = unspecified substituent; E = Si, Sn; X = halogen atom).

ortho-Substituted DBAs are accessible through Li/Br exchange of appropriately functionalized (2-bromophenyl)boronates **L**, which afford dianionic DBA derivatives **M** through twofold B–C adduct formation (Scheme 2).[57] Upon aqueous workup, the corresponding borinic acids **N** are generated, which can readily be transformed into the 9,10-dibromo-DBAs **O** for further derivatization.[55,58]

Recently, a widely applicable synthetic strategy towards unsymmetrical annulated DBAs was developed. The reaction between 4,5-dichloro-1,2-bis(trimethylsilyl)benzene (**1**), BBr_3, and various PAHs furnished the vicinally borylated compounds **2a–i**, which were easily converted into benchtop-stable derivatives **3a–i** by a mesitylation reaction (Scheme 3).[59] With one exception (i.e., **3g**), the preferred sites of electrophilic attack have

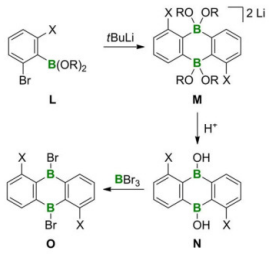

Scheme 2. Preparation of 1,5-dihalogenated DBAs **N** and **O** from **L** by Li/Br exchange and twofold B–C adduct formation (X = F, Cl, Br).

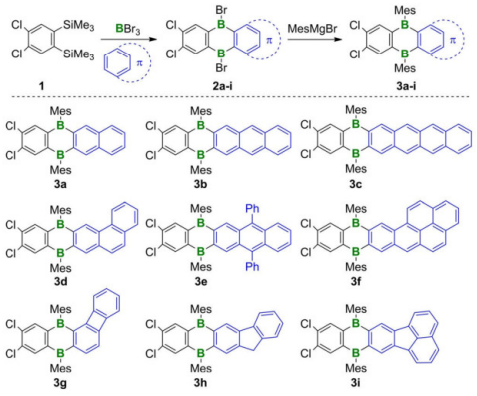

Scheme 3. Three-component reactions to furnish unsymmetrical benzannulated B-PAHs **3a–i** by electrophilic vicinal diborylation of commercial PAHs (shown in blue).

hydrogen atoms in their *ortho* positions, which minimizes unfavorable steric congestion in the transition states of the borylation reactions. To achieve decent yields, the sterically induced selectivity preferences need to be compatible with the nodal structure of the HOMO of the respective PAH, that is, the atomic orbitals of the carbon atoms at the sites of attack need to significantly contribute to this frontier molecular orbital. The two electron-withdrawing Cl atoms in **1** are needed to accomplish efficient PAH borylation. After the borylation step, these Cl substituents can either be removed through a Pd-catalyzed reduction with Et_3SiH or employed in a Stille-type derivatization reaction.[59]

In all of the B-PAH syntheses described so far, the closure of the boron-containing ring occurred through B–C bond formation in the final stages of the reaction sequence. In the past few years, however, transition-metal-mediated C–C coupling protocols that are compatible with preexisting B–C bonds in a substrate have been identified and are applicable to late-stage cyclization reactions of appropriately functionalized triarylboranes. For example, the benchtop-stable quadruply benzannulated borepin **6a** was prepared by starting from bis(8-bromonaphth-1-yl)mesitylborane (**4a**) under Yamamoto conditions (Scheme 4).[35] The reaction is also applicable to the corresponding acenaphthene and acenaphthylene precursors **4b** and **4c** to yield borepin derivatives **6b** and **6c**.

Only in the case of **4b**, which contains the most electron-rich naphthyl fragment, the Yamamoto dehalogenation reaction was accompanied by dehydrohalogenation and led to C–H activation product **9** (Scheme 5). The local concentration of the Ni^0 reagent was the determining factor that governed the relative ratio of **6b**/**9**, which could be varied from 3:1 to 1:2.5.[35] The Yamamoto approach to B-PAHs is highly modular and also applicable to the synthesis of B-doped [4]helicenes. The replacement of the chemically inert mesityl group in **4a–c** by a 2,6-dibromophenyl ring (i.e., **5**) allowed for the formation

© 2018 Wiley-VCH Verlag GmbH & Co. KGaA, Weinheim

ACES Asian Chemical Editorial Society
ASIAN JOURNAL OF ORGANIC CHEMISTRY
Focus Review

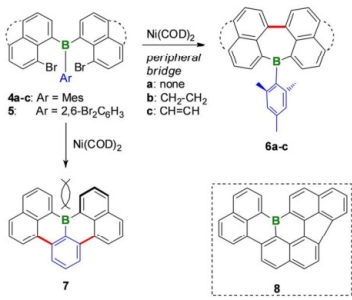

Scheme 4. Modular synthesis of the benzannulated borepins **6a–c** and the B-doped [4]helicene **7** by Yamamoto C–C coupling starting from triarylborane precursors **4a–c** and **5** [bottom right: B-PAH **8** (structurally related to **7**); COD = 1,5-cyclooctadiene].

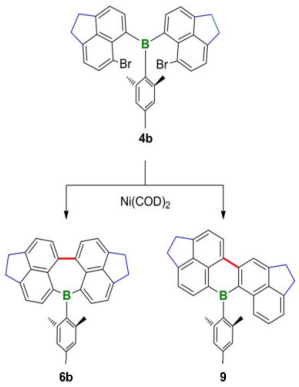

Scheme 5. Formation of isomers **6b** and **9** by competing dehalogenation and dehydrohalogention reactions upon treatment of **4b** with $Ni(COD)_2$.

of two C–C bonds to afford compound **7** (Scheme 4).[34] X-ray crystallography reveals a slight helical distortion to the molecular scaffold of **7**, which renders it soluble even in hexane despite the absence of solubilizing side groups. As it is structurally constrained, compound **7** is inert towards air and moisture, although it still forms weak adducts with pyridine bases.[34] An alternative approach to helicene **7** involves the tandem intramolecular electrophilic arene borylation reaction of 1-dibromoboryl-2,6-bis(naphth-1-yl)benzene.[60] The relevance of the helical distortion to the pronounced solubility of **7** is evident by examining the structurally related but poorly soluble B-PAH **8** (Scheme 4), which was prepared from tris(8-bromonaphth-1-yl)borane through an intramolecular radical cyclization [$(Me_3Si)_3SiH$, ABCN = 1,1′-azobis(cyclohexanecarbonitrile)].[61] Because of its peripheral bridge, the cove region[3] of **8** is widened, which leads to fewer intramolecular steric repulsions and an essentially planar molecular framework.

In addition to the dehalogenation (to give **6** or **7**) and dehydrohalogenation C–C coupling protocols (to give **9**), various dehydrogenation reactions have also been employed for the preparation of extended B-PAHs. Under Scholl reaction conditions, 6,13-bis(anthr-9-yl)-6,13-dihydro-6,13-diborapentacenes **10a–c** underwent an eightfold C–H activation and fourfold C–C coupling reaction to furnish the doubly boron-doped nanographenes **11a–c** (Scheme 6).[62,63] The bulky organyloxy sub-

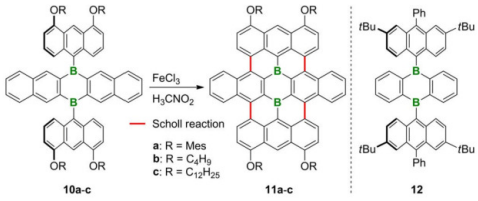

Scheme 6. Preparation of doubly B-doped nanographenes **11a–c** through the Scholl cyclization of 6,13-dihydro-6,13-diborapentacenes **10a–c**. 9,10-Dihydro-9,10-diboraanthracene **12** does not undergo an analogous planarization reaction.

stituents at the 4,5-positions of the anthryl substituents are required to accomplish the regioselective C–C bond formation at their *para* positions. By the same token, the diborapentacene core seems essential for a successful cyclization reaction, as related 9,10-bis(anthr-9-yl)-9,10-dihydro-9,10-diboraanthracenes (e.g., **12**) have failed to proceed through a comparable transformation.[64,65] The purple graphene flake **11a** represents another prototypical example of an air-stable arylborane because of the structural constraint of its rigid molecular framework.

Friedel–Crafts-type reactions are well-suited to generate further planarized triarylboranes, which are configurationally constrained by multiple methylene tethers (Scheme 7).[66,67] Compound **14** was obtained by the treatment of 2,6-di(2-propenyl)-phenyl-substituted precursor **13** with scandium(III) triflate. The doubly boron-doped species **17** was generated in a similar manner by starting from the corresponding doubly 2,6-di(2-propenyl)phenyl-substituted DBA. The use of $Sc(OTf)_3$ has been shown as crucial to the success of the cyclization reaction, as a broad selection of other Lewis (and Brønsted) acids failed in this respect. The oxidation of monoborane **14** at the CH_2 bridge by treatment with CrO_3 yields carbonyl derivative **15**, which can be readily transformed into the fully methylated, D_{3h}-symmetric congener **16**. Ketone **15** is also the key precursor to the unique radical species **18** (Scheme 7), which is a representative example of a **C**-type species (Figure 3). Radical **18** is accessible by a four-step sequence that involves the addition of 2,6-di(2-propenyl)phenyllithium to **15**, the reduction of the resulting tertiary alcohol, a Friedel–Crafts cyclization, and an H-atom abstraction. Because of the (moderate) π-conjugation of the odd electron with the boron center, **18** exhibits outstanding thermal stability and resistance toward atmospheric conditions.[68]

Only a few doubly boron-doped PAHs that do not have a DBA framework currently exist. Examples include dibenzodi-

© 2018 Wiley-VCH Verlag GmbH & Co. KGaA, Weinheim

ACES Asian Chemical Editorial Society
ASIAN JOURNAL OF ORGANIC CHEMISTRY
Focus Review

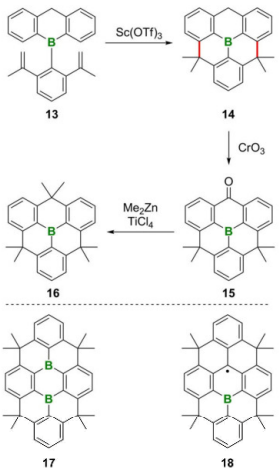

Scheme 7. Synthesis of methylene-tethered B-PAHs **14** and **16** along with structurally related planarized DBA **17** and radical **18** (OTf = trifluoromethanesulfonate).

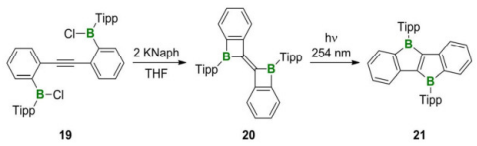

Scheme 8. Photorearrangement of **20** to afford the doubly boron-bridged stilbene **21** (Tipp = 2,4,6-triisopropylphenyl, Naph = naphthalenide).

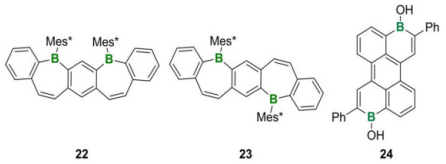

Figure 5. Conjugated *meta*- and *para*-*B*-entacenes (i.e., **22** and **23**) and the 3,9-boron-doped perylene **24** (Mes* = 2,4,6-tri-*tert*-butylphenyl).

borapentalene **21** (synthesized by reduction of **19** and photoisomerization of the resulting **20**; Scheme 8),[69,70] fused benzoborepin isomers **22** and **23** (synthesized by Sn/B exchange; Figure 5),[71,72] and 3,9-diboraperylene **24** (one-pot synthesis through alkene hydroboration, electrophilic borylation, dehydrogenation, and hydrolysis to furnish the borinic acid; Figure 5).[73] Another example is diborabisanthene **28** (Scheme 9),[74] in which the structural motif of a six-membered bora-heterocycle with exocyclic C=C bond has been realized (see also **D**; Figure 3). The synthesis of **28** starts with sila-heterocycles **25** and **26** and proceeds through a Peterson olefination, a stilbene-type photocyclization, and an Si/B exchange reaction. After mesitylation, the resulting compound **28** is stable towards air and moisture over the long term.

This general approach for the preparation of **28** is compatible with a variety of aryl ketones and aryl aldehydes.[74] If the Peterson olefination between **25** and suitable alkynyl carbonyl compounds such as **27** is carried out, then a subsequent Ru-catalyzed ene–yne benzannulation step expands the range of readily accessible B-PAHs further (e.g., **33**).[75] The proper sequences of these four synthetic modules thus provide access to a complete series of mutually related B-PAHs **28**–**33** as shown in Scheme 9.[76]

An alternative approach affords 1,6-diborapyrenes **37** and **38** (Scheme 10). The sequence of linear steps[77] involves a twofold borylative-cyclization reaction[78] followed by an intramolecular electrophilic C–H borylation, which converts diyne **34** into double boracycle compound **35**. Then, **35** is oxidized to give fully conjugated B-PAH **36**, which is stabilized either by incorporation into a planarized structurally constrained framework (i.e., **37**) or by the introduction of bulky 2,4,6-triisopropylphenyl rings at the boron sites (i.e., **38**). A detailed comparison

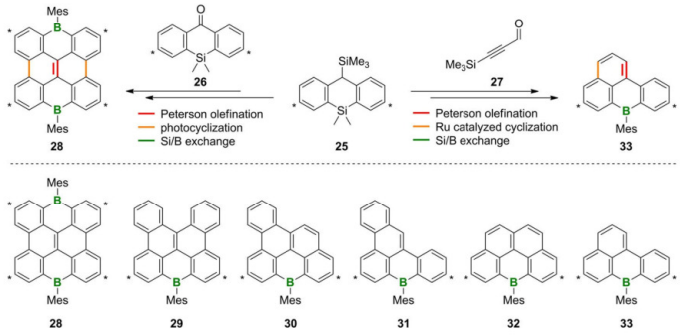

Scheme 9. Modular route to B-PAHs **28**–**33** with π-systems of different sizes and shapes by combining Peterson olefination, photocyclization, Ru-catalyzed cyclization, and Si/B exchange reactions (* = *tert*-butyl).

© 2018 Wiley-VCH Verlag GmbH & Co. KGaA, Weinheim

ACES Asian Chemical Editorial Society
ASIAN JOURNAL OF ORGANIC CHEMISTRY
Focus Review

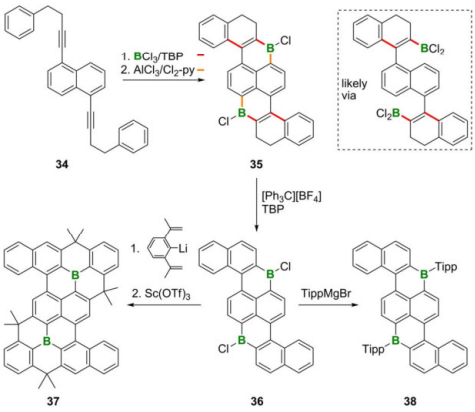

Scheme 10. Sequential borylative cyclization/electrophilic C–H borylation/oxidation reaction to form B-PAH **36** with a 1,6-diborapyrene core along with the stabilization of **36** through structural constraint (i.e., **37**) and steric shielding (i.e., **38**; TBP = 2,4,6-tri-*tert*-butylpyridine and Cl_2-py = 2,6-dichloropyridine).

of mutually related B-PAHs, such as **37** and **38**, provides essential information about the influence of the different stabilization modes on key optoelectronic and bulk structural parameters.[77,79]

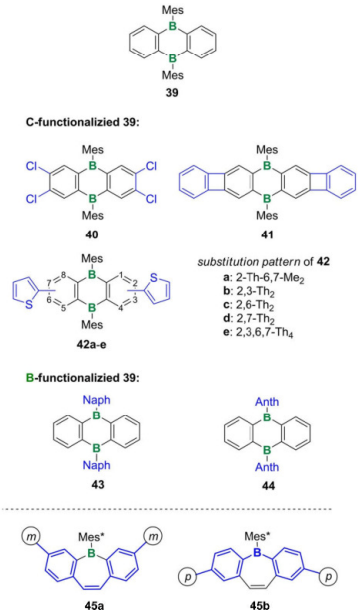

Figure 6. Derivatives of **39** substituted on either the organic scaffold or the boron atom (top); *meta*- and *para*-substituted borepins (bottom; Th = 2-thienyl, Np = naphth-1-yl derivative, Anth = anthr-9-yl derivative).

4. Specific Reactivities and Applications of B-PAHs

4.1. B-PAHs in Organic Optoelectronic Materials

Until now, the development of B-PAHs has mainly focused on their potential applications as future organic optoelectronic materials.[7,15] On the basis of available experimental data, some general trends are beginning to emerge.

B-PAHs have energetically low-lying LUMOs and thus are good electron acceptors (see Figure 1). More specifically, a majority of PAHs that contain one boron atom show one reversible reduction wave in their cyclic voltammograms (e.g., **29**–**33**; Scheme 9). A significant number of compounds that contain two incorporated boron atoms are able to accept a second electron in a reversible manner (e.g., **28** and members of the DBA family of compounds).

If boron doping is applied to extended PAH frameworks, even ambipolar species that are capable of undergoing reversible reduction as well as oxidation become available (e.g., **11a**, **28**, and **29**; Schemes 6 and 9). Especially the latter are of recent interest, as they have the potential to simultaneously act as electron- and hole-transporting materials in organic optoelectronic devices. The influence of substitution patterns on the redox potentials of B-PAHs has been thoroughly evaluated for DBA-based systems. In tetrahydrofuran (THF), 9,10-dimesityl-9,10-dihydro-9,10-diboraanthracene (**39**; Figure 6) has redox potentials of $E_{1/2} = -1.84$, -2.73 V relative to the ferrocene/ferrocenium couple.[17] Three strategies turned out to effectively improve the electron affinity of the parent system: (1) The introduction of electronegative substituents (tetrachlorinated **40**: $E_{1/2} = -1.38$ V; the compound decomposes at potential values more cathodic than approximately -2.5 V).[56] (2) The incorporation of antiaromatic moieties (biphenylene derivative **41**: $E_{1/2} = -1.52$, -2.30 V).[52] (3) The extension of the π-conjugated scaffold (nanographene **11a** in Scheme 6: $E_{1/2} = -1.45$, -1.66 V).[62]

To date, three types of systematically varied series of related B-PAH derivatives are available, which allows for the assessment of the relationship between their molecular structures and photoemission properties. The first series includes the vicinally diborylated PAHs **3a**–**f** (Scheme 3), which show bathochromically shifted emission wavelengths (λ_{em}) compared with their respective PAH moieties (drawn in blue in Scheme 3).[59] Nevertheless, the order of the λ_{em} values determined for the B-PAHs still reflects the sequence measured for the corresponding PAHs. These observations agree with the computed orbital scheme for the model pair DBA-benzene as outlined in Figure 1.

The second series begins with the singly boron-doped 7*H*-benzo[*de*]anthracene **33** and ends with the doubly boron-doped bisanthene **28** (Scheme 9).[74,75] All members emit in the

© 2018 Wiley-VCH Verlag GmbH & Co. KGaA, Weinheim

ACES Asian Chemical Editorial Society
ASIAN JOURNAL OF ORGANIC CHEMISTRY
Focus Review

blue spectral region, and the number and position of the annulated benzene rings have only a minor influence on the emission wavelengths. However, compared with 7,14-di(mesityl)bisanthene (λ_{em} = 705 nm), the fluorescence band of **28** is dramatically blueshifted (λ_{em} = 449 nm). Relative to dibenzo[*g*,*p*]chrysene (λ_{em} = 395 nm), the emission maxima of **28** and **29** undergo bathochromic shifts to λ_{em} = 449 and 439 nm, respectively. Most importantly, the boron-bridged molecules **28** and **29** exhibit fourfold higher photoluminescence quantum yields (Φ_{PL}) than dibenzo[*g*,*p*]chrysene.

In the third series of compounds, the number and positional arrangement of the peripheral substituents are varied, as the central B-PAH scaffold of DBA remains unchanged. Compounds **42a**–**e** have significant charge-transfer character because of the electron-donating effect of the 2-thienyl rings and the electron-accepting nature of the DBA core (Figure 6).[56,80] Increasing the number of attached 2-thienyl groups results in a continuous redshift of the emission wavelengths from λ_{em} = 469 (for **42a**) to 540 nm (for **42e**). The fluorescence maxima of the 2,3- (i.e., **42b**) and 2,6-disubstituted isomer (i.e., **42c**) also differ by as much as 38 nm. Changing the positions of the pendant substituents thus provides a tool to modify the emission properties of DBA fluorophores. The positional arrangement of the 2-thienyl rings also has a marked influence on the photoluminescence quantum efficiencies. The highest values were achieved by gathering all of the substituents on the same half of the molecule, thereby generating donor-acceptor dyads as opposed to donor-acceptor-donor triads.[56]

Noticeable substituent effects are also obvious for the three DBA derivatives **39**, **43**, and **44** (Figure 6), which contain phenyl, naphth-1-yl, and anthr-9-yl groups on the boron atoms. These compounds give rise to blue (**39**), green (**43**), and red (**44**) emissions that emanate from a twisted internal charge-transfer (TICT) state. In contrast, their three all-carbon congeners are characterized by the local π–π^* photoexcitation of their 9,10-anthrylene cores and corresponding blue fluorescence.[17,64]

From an inspection of the series of *meta*- and *para*-substituted dibenzo[*b*,*f*]borepins **45a** and **45b** (Figure 6),[81] it was concluded that the installation of *meta* substituents decreases the HOMO–LUMO gap relative to that of the unsubstituted system and that charge delocalization should occur mainly through the stilbene backbone without the participation of the boron atom (**45a**). The installation of *para* substituents increases the electron affinities of the compounds, as the electron-deficient boron center becomes an integral part of the conjugation pathway (**45b**).

A comparison of (pseudo)isomeric B-PAHs provides further insight into key structure-property relationships (Figure 7). Similar to the PAH biphenylene, the deep red, vicinally boron-bridged species **41** is nonfluorescent, whereas the yellow 6,13-dihydro-6,13-diborapentacene **46** shows blue luminescence (λ_{em} = 412 nm; Φ_{PL} = 47%).[52] Its isomer **47**, in which the two central boron atoms have been formally shifted to an adjacent ring, features a lower energy emission band and an almost doubled quantum yield (λ_{em} = 456 nm; Φ_{PL} = 87%).[52,59] Fundamental differences in key optical properties are also apparent

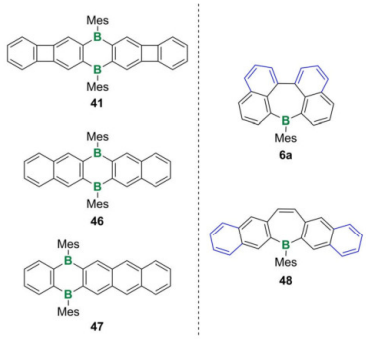

Figure 7. Comparison of (pseudo)isomers of benzannulated DBAs (left) and borepins (right).

for the borepin pair **6a**[35] and **48**.[49] The linear annulation scheme of **48** results in a bathochromically shifted fluorescence [λ_{em}(**6a** vs. **48**) = 432 vs. 477 nm] but at the expense of the Φ_{PL}, which precipitously drops from 38 to 1%, respectively.[35]

Finally, the pair of planarized B-PAHs **8** and **16** (Schemes 4 and 7) demonstrate that structural constraints can impart unique flexibility to molecules, which is immediately relevant to their optical behavior. Because of their compressed B–C bonds, these compounds readily interconvert between planar and bowl-shaped conformations. As a result, the molecular frameworks are compatible with both three- and four-coordinate boron centers. Consequently, trinaphthylborane **8** still retains a sufficiently high Lewis acidity to form isolable adducts with pyridine (i.e., **8**·Py).[61] Acid-base pairing is reversible, and the nitrogen ligand can be released quantitatively upon thermal treatment. Moreover, when **8**·Py is photoexcited, a partial dissociation of the adduct occurs in the lowest singlet excited state (S_1). As a result, dual emission is observed with the higher energy band originating from the residual adduct and the bathochromic band from the fraction of liberated borane.[61] Methylene-tethered triphenylborane **16** shows related excited state dynamics, even in the absence of Lewis bases. Two local minimum structures (i.e., planar and bowl-shaped) exist in the S_1 state, and their respective relaxations to the ground state (S_0) again give rise to dual fluorescence.[66,67]

As outlined above, B-PAHs combine exceptional redox properties with unique UV/vis emission characteristics and offer ample opportunities to customize their molecular and electronic structures. They are, therefore, widely regarded as promising building blocks for next-generation organic optoelectronic materials, and a number of proof of concept devices have already been fabricated. For example, ambipolar compounds **49a** and **49b** (Figure 8) have successfully been incorporated into the electron-transporting layer of organic light-emitting diodes (OLEDs).[82] These compounds are based on the planarized triphenylborane **14** (Scheme 7), which is readily deprotonable[83] and therefore constitutes an ideal functional group to

© 2018 Wiley-VCH Verlag GmbH & Co. KGaA, Weinheim

ACES Asian Chemical Editorial Society
ASIAN JOURNAL OF ORGANIC CHEMISTRY
Focus Review

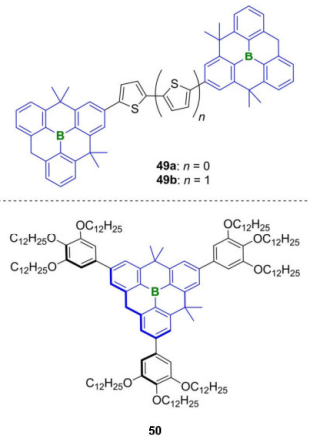

Figure 8. Ambipolar species **49a** and **49b** as building blocks for electron-transporting layers in OLEDs (top). The trigonally π-extended compound **50** forms liquid-crystalline aggregates with significant electron and hole mobilities (bottom).

host negative charges (permethylated **16** is also reducible to give a stable anionic radical[84]). The structural constraint exerted by the rigid organic scaffold gives **49a** and **49b** sufficient stability for subsequent processing by vacuum vapor deposition. Moreover, the absence of kinetically protecting side groups enables a dense packing of the molecules in the solid state and, thus, promotes charge-carrier mobility.

The use of **14** (Scheme 7) in charge-transport materials is not restricted to solid-state applications.[85] The trigonally π-extended derivative **50** (Figure 8) is a discotic liquid-crystalline mesogen that forms a hexagonal columnar phase with short vertical disc-to-disc distances of 3.6 Å, indicative of close π-stacking (see also Ref. [61]). Electron and hole mobilities of 10^{-3} and 3×10^{-5} $cm^2V^{-1}s^{-1}$ have been determined for these liquid crystals at ambient temperature.[85]

The applicability of B-PAHs goes beyond their use in charge-transporting devices. An OLED that generates green electroluminescence and shows good performance in terms of driving voltage and luminous efficiencies has been fabricated with B-doped [4]helicene **7**[34,60] (Scheme 4) as an emissive component.[60] Spin-coated thin films of **7** are also promising semiconducting materials. The transfer and output curves of a corresponding organic field-effect transistor are indicative of p-type modulation.[60] One particularly remarkable example of a p-type OFET has been found, in which the peculiar features of its boron dopant atom have not only been used to imprint the desired electronic properties on the parent PAH, but also to facilitate the fabrication of the device by cost-efficient spin-coating from precursor solutions.[86] trinaphthylborane **8** (Scheme 4)[61] is poorly soluble in common organic solvents as a result of its planar molecular structure, which promotes the formation of densely π-stacked columnar aggregates. As mentioned above, the addition of pyridine generates the four-coordinate boron-nitrogen adduct **8**·Py and induces a plane-to-bowl conversion of the B-PAH skeleton, thereby disfavoring intermolecular π-interactions. Importantly, upon moderate heating, the nitrogen ligand is released to regenerate the tricoordinate B-PAH. Thus, spin-coating solutions of **8**·Py on glass substrates first gives amorphous thin films. After briefly annealing at 180 °C, the coated adduct film is converted into a polycrystalline film of parent **8**. The solution-processed layer exhibits electronic characteristics that are identical to those of a thin film that was prepared by the laborious vacuum vapor deposition of **8**. The neutral π-monoradical **18** (Scheme 7) provides the materials basis for another OFET and an organic Mott-insulator transistor.[68] The thermally and hydrolytically stable compound shows well-balanced ambipolar charge-transport abilities that result from virtually identical spatial distributions of its singly occupied and unoccupied molecular orbitals.

The electron-acceptor capacity of B-PAHs suggests their possible use as active electrode materials in lithium-ion batteries. In this context, the utility of **11**-type nanographenes (Scheme 6) was assessed with the help of a half cell coupled to a counter electrode made of Li metal.[63] When electrodes that consist of carbon black blended with **11a** (R=Mes) or **11b** (R=C_4H_9) are compared, a higher specific capacity is observed for the nanographene compound that contains the smaller substituents, as they allow for a more densely packed supramolecular structure. The battery with **11b** shows a stable performance over 10 charge/discharge cycles. In this context, the poor solubility of **11b** in the electrolyte is essential, given that dianion $[\mathbf{11a}]^{2-}$, which has a triplet biradical ground state, degrades rapidly in solution at room temperature.

Finally, we note reports of OLEDs and organic solar cells (OSCs) that contain borafluorene or DBA moieties with four-coordinate boron atoms and chelating 2-(2-hydroxyphenyl)benzimidazole, 8-hydroxyquinoline, and aza-dipyrromethene ligands.[87–89]

4.2. Dynamic Covalent Chemistry of B-PAHs

Under inert conditions, 9,10-dihydro-9,10-diboraanthracene (DBA) derivatives retain their structural integrity regardless of which substituents are chosen for installation at the boron centers (e.g., H, alkyl, aryl, halogen, NR_2, OR). This is also true for the smallest possible substituent, namely, the hydrogen atom. Parent **52**, which is accessible from 9,10-dibromo-DBA **51** and Et_3SiH, forms coordination polymer $(\mathbf{52})_n$ in the solid state, in which individual DBA monomers are linked by B–H–B two-electron three-center bonds (Scheme 11).[90] Me_2S cleanly splits this polymer into its monomeric building blocks to furnish *syn*-Me_2S–B diadduct **52**·$(SMe_2)_2$ (Scheme 11).[91,92]

The borafluorene scaffold is also compatible with a wide variety of substituents at the boron atom.[93] Contrary to parent DBA **52**, however, parent 9*H*-9-borafluorene **54** exhibits extensive dynamic covalent behavior. Its central borole ring remains intact only if coordinating Lewis bases, such as pyridine,[94] THF,[95] or SMe_2,[96] are available.[97] In the absence of the appropriate ligands, **54** forms partly ring-opened, C_1-symmetric dimers $(\mathbf{54})_2$, in which the boron atoms are bridged by one hy-

© 2018 Wiley-VCH Verlag GmbH & Co. KGaA, Weinheim

ACES Asian Chemical Editorial Society
ASIAN JOURNAL OF ORGANIC CHEMISTRY
Focus Review

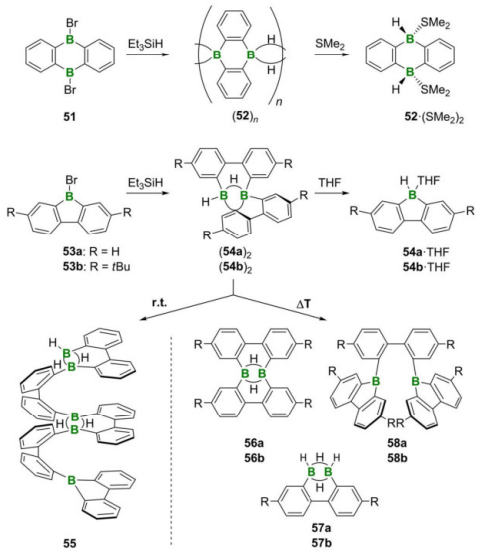

Scheme 11. The comparison between polymeric parent DBA $(\mathbf{52})_n$ to dimeric parent borafluorene $(\mathbf{54a})_2$. At ambient temperature, $(\mathbf{54a})_2$ undergoes a ring-opening oligomerization to furnish **55**. At elevated temperatures, $(\mathbf{54a})_2$ and $(\mathbf{54b})_2$ form the lower molecular weight products **56a**–**58a** and **56b**–**58b** (**a**: R=H; **b**: R=*t*Bu).

drogen atom and one of the aryl rings.[94] A crystal structure has been reported for *t*Bu-substituted derivative $(\mathbf{54b})_2$ (Scheme 11).[47] Without the kinetically stabilizing *t*Bu substituents, the ring-opening reaction proceeds further, already at ambient temperature, to afford main-chain boron-containing oligophenylenes, such as **55**. The oligomer main chain of **55** is reinforced and conformationally constrained by intrastrand B–H–B bonds (Scheme 11).[94]

At elevated temperatures of 120 °C, entropy comes into play, and $(\mathbf{54a})_2$ and $(\mathbf{54b})_2$ are converted into the lower molecular weight species **56a**–**58a** and **56b**–**58b**, respectively (Scheme 11).[98] Alternative rational and high-yielding syntheses have been developed for **57a** and **58a**,[96,98] whereas the thermolysis of $(\mathbf{54a})_2$ and $(\mathbf{54b})_2$ still provides the only route to 1,2:1,2-bis(2,2′-biphenylylen)diborane(6) derivatives, which are isomers of $(\mathbf{54a})_2$ and $(\mathbf{54b})_2$ (yields of **56a** and **56b**: 34%). With respect to the synthetic utility of $(\mathbf{54a})_2$, it is important to note that the partial ring-opening reaction is reversible in the presence of Lewis bases[95] or unsaturated hydrocarbons. For example, the reaction of freshly prepared solutions of $(\mathbf{54a})_2$ with *tert*-butylacetylene cleanly affords diborylmethane **59** through the twofold hydroboration of the C≡C bond (Scheme 12).[94]

Rearrangement reactions not only are observed for the neutral 9*H*-9-borafluorenes $(\mathbf{54a})_2$ and $(\mathbf{54b})_2$ but also can be induced by electron injection. Contrary to the readily reducible DBA polymer $(\mathbf{52})_n$ and its resultant discrete dianion

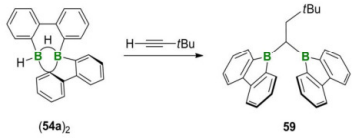

Scheme 12. Synthesis of diborylmethane **59** by twofold hydroboration of *tert*-butylacetylene with $(\mathbf{54a})_2$.

$[\mathbf{52}]^{2-}$,[99,100] the C_1-dimer $(\mathbf{54b})_2$ furnishes the doubly boron-doped dibenzo[*g*,*p*]chrysene $[\mathbf{60}]^{2-}$ in yields of 43% when treated with an excess amount of Li granules in THF (Scheme 13; the reaction likely proceeds through adduct **54b**·THF).[101] Doubly boron-doped $[\mathbf{60}]^{2-}$ is interesting not only because of its use in PAH chemistry but also because of its localized B=B bond, which likely has unique reactivity (four Clar sextets can be drawn for the dianion, which leaves an isolated B=B fragment behind).

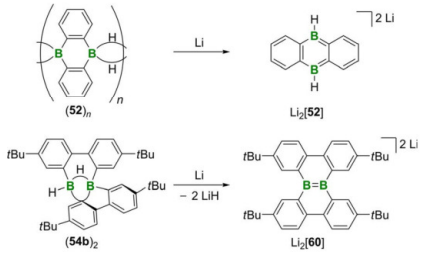

Scheme 13. Lithium reduction of $(\mathbf{52})_n$ produces discrete dianions $[\mathbf{52}]^{2-}$, whereas $(\mathbf{54b})_2$ loses hydrogen atoms and rearranges to the B=B bonded species $[\mathbf{60}]^{2-}$.

As the B_2H_2 core is ideally preorganized for reductive B–B coupling, the redox behavior of **56b** was also investigated.[95] The reaction outcome is strongly dependent on the number of redox equivalents employed and on the nature of the reducing agent, that is, lithium metal or lithium naphtalenide versus potassium graphite (KC_8). The treatment of **56b** with increasing amounts of lithium napthalenide furnishes Li_2[**61**], Li_2[**62**], and Li_2[**60**] as the major products, respectively (Scheme 14). In the case of isomers Li_2[**61**] and Li_2[**62**], B–B bond formation is accompanied by skeletal rearrangement. The use of an excess amount of KC_8 did not provide any $[\mathbf{60}]^{2-}$ but led to the formation of $[\mathbf{63}]^{2-}$, the nonrearranged isomer of Li_2[**61**] and Li_2[**62**]. From this reactivity study, it was concluded that (1) more reducing agent leads to less rearrangement and (2) hydride abstraction with concomitant overreduction (to afford $[\mathbf{60}]^{2-}$) takes place only in the presence of Li^+ counterions. These experimental findings were rationalized by assuming that the rearrangement cascade is triggered by the addition of the first electron, which acts as a catalyst, and is terminated immediate-

© 2018 Wiley-VCH Verlag GmbH & Co. KGaA, Weinheim

ACES Asian Chemical Editorial Society
ASIAN JOURNAL OF ORGANIC CHEMISTRY
Focus Review

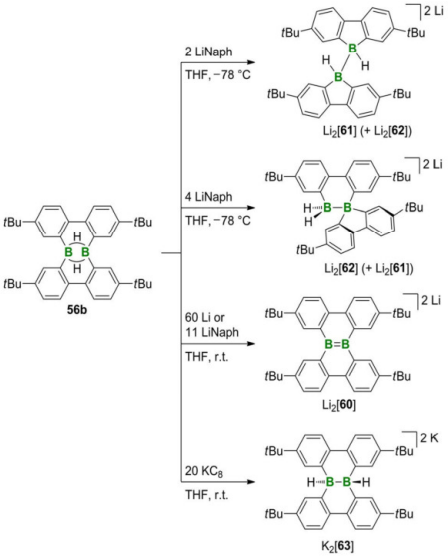

Scheme 14. Degree of skeletal rearrangement upon reduction of **56b** as a function of the amount and nature of the reducing agent. In all cases, B–B bonds are formed (minor side products are listed in brackets).

ly after the second electron has been accepted by the system.[95]

Organo(hydro)boranes are generally regarded as hydridic species. As a fundamental change of paradigm, the successful deprotonation of **56b** with concomitant formation of $[\mathbf{64}]^-$ has been reported (Scheme 15). In the presence of $[(Me_3Si)_3C]^-$ or

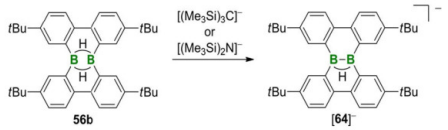

Scheme 15. Deprotonation of **56b** by using bulky bases to generate the B–B bond in $[\mathbf{64}]^-$ (note that B*H* atoms are generally regarded as hydridic).

$[(Me_3Si)_2N]^-$ as a base, one of the B–H–B bridges is transformed into a B–B bond, which is a unique strategy for the coupling of two boron atoms.[102]

The rich dynamic covalent chemistry of parent **54a** and **54b** clearly correlates with their boron-bonded hydrogen atoms. For instance, Tipp-substituted borafluorene **65** is electrochemically well-behaved, as it undergoes a reversible first reduction ($E_{1/2} = -2.11$ V in THF vs. FcH/FcH$^+$; FcH = ferrocene), and electron injection results in no significant structural modifications (Figure 9).[103] The less sterically shielded ditopic arylboranes **58a** and **59** also undergo reversible reductions, already at markedly more anodic potential values of $E_{1/2} = -1.49$, -1.75 V

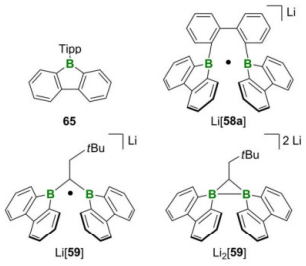

Figure 9. Borafluorene **65** undergoes reversible electrochemical reduction. Compounds containing one-electron two-center bonds (i.e., Li[**58a**], Li[**59**]) and two-electron two-center bonds (i.e., Li_2[**59**]) are accessible by reduction of the structurally preorganized ditopic boranes **58a** and **59**.

(**58a**)[104] and $E_{1/2} = -1.76$, -2.17 V (**59**).[105] In both compounds, the organyl bridges impose a face-to-face arrangement of the borafluorenyl units, thereby promoting an overlap of the vacant boron p_z orbitals. The resulting cooperativity between the two boron atoms greatly increases the electron affinities of both systems. Arylboranes **58a** and **59** have also been chemically reduced on a preparative scale by using lithium napthalenide or Li metal. In the case of **58a**, it was possible to isolate monoanion radical $[\mathbf{58a}]^{\bullet-}$, which represents the first example of a fully characterized compound featuring a B·B one-electron two-center bond (EPR spectroscopic data exists for a comparable bonding situation in the 1,8-bis(diphenylboryl)naphthalene radical anion[106]).[104] Upon reduction of the diborylmethane derivative **59**, both the B·B-bonded radical anion $[\mathbf{59}]^{\bullet-}$ and the B–B bonded dianion $[\mathbf{59}]^{2-}$ became accessible, the latter of which is isoelectronic to highly strained cyclopropanes. The B···B distance continuously decreases along the sequence **59** → $[\mathbf{59}]^{\bullet-}$ → $[\mathbf{59}]^{2-}$, which is in accordance with an increasing B···B bond order.

Borafluorenes tend to engage in B–C insertion reactions, thereby expanding their antiaromatic[103] central borole rings. For example, 9-amino-9-borafluorene **66** undergoes a rearrangement well below ambient temperature to give heteroaromatic, benzannulated 1,2-dihydro-1,2-azaborine **67** (Scheme 16).[12,107] By the same token, the thermolysis of

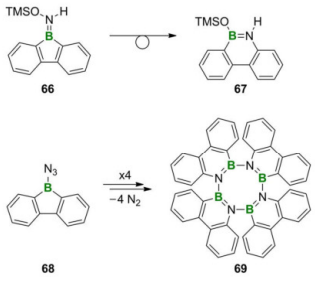

Scheme 16. Nitrogen atom insertion into the central borole rings of **66** and **68** to give azaborine motifs (TMS = trimethylsilyl).

© 2018 Wiley-VCH Verlag GmbH & Co. KGaA, Weinheim

ACES Asian Chemical Editorial Society
ASIAN JOURNAL OF ORGANIC CHEMISTRY
Focus Review

9-azido-9-borafluorene **68**[108] at reflux in heptane generates the tetramer (i.e., **69**) of a 9,10-*B*,*N* analogue of 9,10-phenanthryne (Scheme 16).[109,110] This chemistry has further been exploited for the on-surface synthesis of large B,N-doped aromatic networks.[111]

A wide variety of alkynes readily insert into 9-chloro-9-borafluorene **70** by a 1,2-carboboration reaction to furnish vicinally substituted, doubly benzannulated borepins (e.g., **71**; Scheme 17). The subsequent one-electron oxidation by using

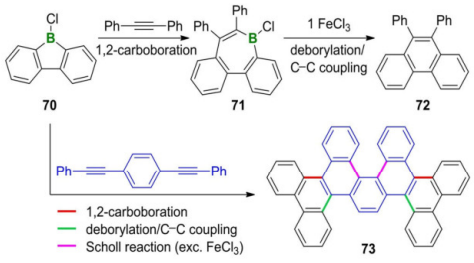

Scheme 17. Synthesis of highly substituted borepins (e.g., **71**) by the 1,2-carboboration of diarylacetylenes with 9-chloro-9-borafluorene (**70**). The oxidation by treatment with $FeCl_3$ results in the deborylation/C–C coupling reaction sequence to give **72**. An excess amount of $FeCl_3$ can be employed to perform an additional Scholl dehydrogenation reaction to give **73**.

atmospheric O_2, $FeCl_3$, or MnO_2 results in a deborylation/C–C coupling reaction sequence to afford 9,10-disubstituted phenanthrenes (e.g., **72**).[112] It should be noted that the $FeCl_3$-promoted variant is related to the dehydrogenative Scholl reaction. Thus, by using an excess amount of $FeCl_3$ and suitably designed substrates, it is possible to perform the deborylation/C–C coupling and Scholl coupling reactions as one-pot protocols to conveniently assemble sophisticated molecular structures. The reaction sequence is extremely versatile and substrates that contain multiple alkyne moieties have already been used for the preparation of high-molecular weight PAHs (e.g., **73**; Scheme 17) and helicenes.[112]

In summary, the high reactivity of the antiaromatic borole is still echoed by its benzannulated congener 9-borafluorene.[113] If the kinetically shielding boron-bonded substituents are missing, as in the cases of 9*H*- and 9-chloro-9-borafluorene, the compounds have a pronounced tendency to undergo B–C bond cleavage, which is increasingly recognized as a potentially useful reactivity pattern.

4.3. B-PAHs in Organocatalysis

In the preceding chapter, we have reviewed reactions that ultimately result in structural modifications of B-PAHs. Yet, B-PAHs also serve an essential role in the transformation of external substrates, sometimes in a catalytic manner. Lewis acid catalysis is a well-developed synthetic tool in organic chemistry, and several reports have been published about ditopic boranes, especially derivatives of 9,10-dihydro-9,10-diboraanthracene (DBA). DBA can serve as a structurally well-defined, bidentate Lewis acid that is capable of interacting simultaneously with two Lewis basic sites of the same substrate molecule. When equipped with small substituents (e.g., H and Me) at the boron centers, DBA readily coordinates with 1,2-diazines (e.g., pyrazolides and phthalazines) to generate tricyclic paddle-wheel structures, such as **74** (Figure 10).[91,114] As a consequence, the electron density of the respective 1,2-diazine is reduced, and its LUMO energy level is lowered, which facilitates inverse electron-demand Diels–Alder (IEDDA) reactions with electron-rich dienophiles.[115] The primary cycloadducts release N_2 and in turn DBA, which can subsequently coordinate to the next 1,2-diazine molecule. DBA is thus required only in catalytic amounts. As a model reaction, phthalazine **75** is converted into naphthalene derivative **78** in the presence of oxazolidine **76** (1.5 equiv) and 9,10-dimethyl-DBA **77** (5 mol%). An oxazolidine ring-opening occurs in the course of a final H-atom shift to aromatize the naphthalene moiety (Scheme 18).[116]

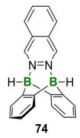

Figure 10. Paddle-wheel structure of the phthalazine adduct of **52** (i.e., **74**).

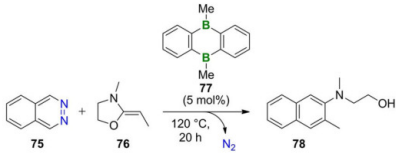

Scheme 18. Model IEDDA reaction between phthalazine **75** and dienophile **76** in the presence of **77** as the catalyst.

This general catalytic scheme has been further developed to include one-pot domino processes that merge IEDDAs and (1) cyclopropanation reactions to prepare benzonorcaradienes[117] or (2) normal electron-demand Diels–Alder reactions to produce bridged tri- and tetracyclic 1,2,3,4-tetrahydronaphthalenes.[118] In addition to varying the dienophile, it is also possible to expand the substrate scope with regard to the diene. To this end, DBA catalysis has been elegantly exploited twice: (1) for the synthesis of 2,3-diazaanthraquinones (e.g., **81**) from 1,4-naphthoquinones (e.g., **79**) and 1,2,4,5-tetrazine **80** and (2) for the IEDDA of 2,3-diazaanthraquinones with an alkene or alkyne to furnish substituted anthraquinones (e.g., **82**; Scheme 19).[119] The products of the reaction are relevant as building blocks for organic optoelectronic materials and substructures of pharmacologically active molecules.

The efficient catalytic dehydrogenation of ammonia-borane (NH_3BH_3, **83**) is a topic of continuing interest in terms of both hydrogen storage and ceramic materials production (e.g., hexagonal boron nitride). As one of only four metal-free systems capable of releasing H_2 from **83** at moderate temperatures, 9,10-dichloro-DBA **84** mediates the evolution of up to 2.5 equiv of H_2 by starting from 1 equiv of **83** (Scheme 20).[120] Borazine **85** and its cross-linked oligomers $(\mathbf{85})_n$ have been

© 2018 Wiley-VCH Verlag GmbH & Co. KGaA, Weinheim

ACES Asian Chemical Editorial Society
ASIAN JOURNAL OF ORGANIC CHEMISTRY
Focus Review

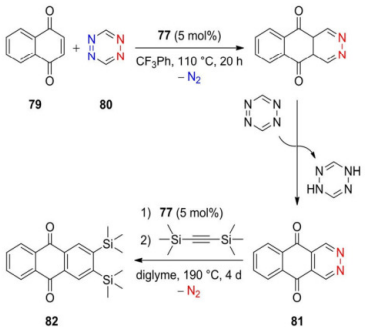

Scheme 19. Model IEDDA reaction of 1,4-naphthoquinone **79** and 1,2,4,5-tetrazine **80** as both the diene and oxidant to afford **81**. The subsequent synthesis of anthraquinone **82** through the IEDDA reaction of **81**.

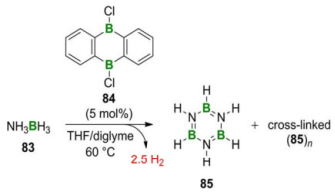

Scheme 20. Dehydrogenation of ammonia-borane **83** in the presence of catalytic amounts of 9,10-dichloro-DBA **84**.

identified as the main dehydrogenation products. Under the employed conditions (5 mol% **84**, THF/diglyme, 60 °C, 7 h), the DBA catalyst could be used 15 times without substantial loss of activity.

The activation of element-element bonds has long been regarded as the exclusive domain of transition-metal complexes. This view has changed since "frustrated Lewis pairs" (FLPs) have proven their potential in the transformation of many substrate molecules through the concerted action of main-group Lewis acids (e.g., boranes) and bases (e.g., phosphines).[121] As shown above, uncharged DBA **84** promotes B–H and N–H activation reactions without the addition of a Lewis base. Moreover, DBAs readily accept two electrons, and the resulting dianions can formally be viewed as FLPs in which the Lewis base is broken down to its absolute essence, the electron lone pair. Doubly reduced DBAs are capable of activating even C–H bonds and H_2.[99,100] For example, the treatment of Li_2[**52**] with *tert*-butylacetylene does not result in the hydroboration of the C≡C bond but rather in the splitting of the terminal C–H bond to form the mixed acetylide/hydride adduct Li_2[**86**] (Scheme 21).[99] In the presence of an excess amount of the alkyne, a subsequent acid-base reaction (hydridic B*H*, protic C≡C*H*) leads to the formation of double acetylide adduct Li_2[**87**] with the concomitant liberation of H_2. 1,4-B_2C_4 heterocycles with four-coordinate boron centers prefer to adopt boat conformations. In the case of Li_2[**87**], the small hydrogen substituents will occupy both axial positions and, thus, are ideally prearranged to liberate H_2. In a closed system at moderately elevated temperatures, a dynamic equilibrium is established between Li_2[**87**] and Li_2[**88**]/H_2 (Scheme 21).[100] At 100 °C, the equilibrium is shifted to the thermolysis products, whereas at 50 °C, Li_2[**87**] and Li_2[**88**] are equally abundant. Rapid cooling from either 100 or 50 °C to room temperature largely freezes the respective equilibria. The doubly reduced parent DBA Li_2[**52**] activates H_2 quantitatively to furnish Li_2[**89**] at a temperature of 100 °C and a pressure of 1 atm. Although the boron substituents (alkynyl vs. H) determine the position of the H_2-activation equilibrium at a given temperature, the counter cations influence the reaction rate. As a general rule, cations with a high tendency to bind to the electron-rich B_2C_4 ring of the DBA dianion (e.g., Li^+) inhibit the access of H_2 to the reactive boron sites, thereby slowing down the reaction rate. Conversely, less strongly coordinating cations (e.g., K^+) help to achieve faster H_2 activation.

In summary, DBA-based Lewis acids can bring about enhanced reactivities relative to monotopic arylboranes. After a twofold reduction, the compounds lose their Lewis acidity, but, in line with the nodal structures of their frontier orbitals, acquire metal-like behavior instead (e.g., the ability to activate C–H and H–H bonds).

5. Growing Even Bigger: Boron-Doped Graphene Flakes and Nanoribbons

Future developments will continue to go beyond B-PAHs with the goal to customize nanosized boron-doped substructures of graphene. The associated challenges are formidable if starting from soluble precursors and performing multiple C–C coupling reactions in the liquid phase to obtain monodisperse, defect-free, atomically precise graphene flakes or ribbons.[122] Fortunately, the fabrication process can be facilitated by an on-sur-

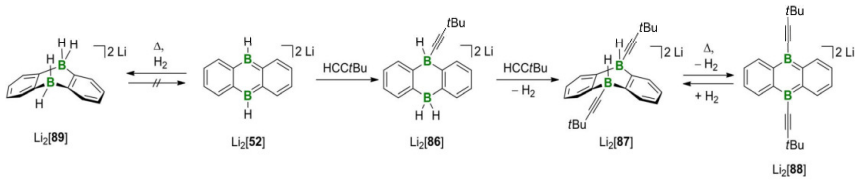

Scheme 21. C–H activation of *tert*-butylacetylene by Li_2[**52**] to form Li_2[**86**]. An excess amount of the alkyne furnishes Li_2[**87**] along with the release of H_2. Both DBA salts Li_2[**52**] and Li_2[**88**] add H_2 across their boron centers, the latter of them in a reversible fashion.

© 2018 Wiley-VCH Verlag GmbH & Co. KGaA, Weinheim

ACES Asian Chemical Editorial Society
ASIAN JOURNAL OF ORGANIC CHEMISTRY
Focus Review

face approach, thereby confining the reaction space from three to two dimensions.[123,124] The ideal surface fulfills two purposes, including: (1) the minimization of the possible number of mutual orientations of the adsorbed precursor molecules and (2) the catalysis of the required C–C coupling steps.

Encouraging results have been obtained by vacuum deposition of the bromine-functionalized 9,10-bis(anthr-9-yl)-DBA **90** onto an Au(111) surface and the thermal annealing of the resulting adsorbate (Scheme 22). At approximately 200 °C, the

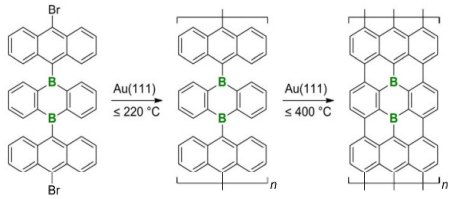

90 **91** **92**

Scheme 22. Temperature-induced dehalogenation of DBA derivative **90** on an Au(111) surface to give polymer **91**. Further heating leads to cyclodehydrogenation and the formation of boron-doped nanoribbon **92**.

precursor molecules undergo surface catalytic dehalogenation to form linear polymer **91**. Subsequent heating up to 400 °C results in a clean cyclodehydrogenation to furnish the target nanoribbon **92**. The armchair-edged structure has a uniform width of seven carbon atoms and features boron sites at its center row with a fixed doping density of 4.8 atom-%.[125,126]

6. Conclusions

Plastic electronics are a key future technology given that organic materials are mechanically flexible, lightweight, film-forming species that can be easily tailored for specific tasks using the broad and sophisticated toolbox of organic reactions. Among potential organic building blocks, polycyclic aromatic hydrocarbons (PAHs) already hold a dominant position but are still the subject of intense development. Boron doping provides a means to endow PAH materials with superior optoelectronic properties relative to their all-carbon congeners. Many of the resulting B-PAHs are excellent electron acceptors as well as visible-light emitters and have therefore been applied as materials for organic light-emitting diodes (OLEDs) and organic field-effect transistors (OFETs) as well as components of next-generation battery electrodes. However, challenging questions remain, among which include: (1) how to simplify the syntheses of B-PAHs by exploiting atom- and step-economic domino reactions, (2) how to impart chemical inertness without sacrificing the chance for the optimal π-stacking of the molecules in deposited thin films, and (3) how to transfer surface-generated, boron-containing nanoribbons to the actual device (e.g., by stamping techniques).

Recently, the range of applications has been expanded to the field of organocatalysis, which takes advantage of the Lewis acidity and pronounced electron affinity of suitably designed B-PAHs. Especially 9,10-dihydro-9,10-diboraanthracenes serve as proper catalysts to promote electrocyclic reactions and activate B–H and N–H bonds. After a twofold reduction, dianionic DBAs are capable of splitting C–H bonds and H_2 molecules. Desirable improvements in the years to come would include: (1) the development of electroreduction methods in place of a chemical B-PAH reduction with hazardous alkali metals and (2) the design of chiral B-PAH catalysts, e.g., derived from configurationally stable boron-doped helicenes.

Finally, certain B-PAHs exhibit rich dynamic covalent chemistry, which so far has little practical implications but is fundamentally important for a deeper understanding of the specificities of the B–C bond. Given vigorous advances in B-PAH chemistry and the interesting questions that arise from it, we expect that exciting results will likely continue to emerge from this fruitful area.

Acknowledgements

T.K. thanks the Fonds der Chemischen Industrie for a Ph.D. grant. This work was partially funded by the Bundesministerium für Wirtschaft und Energie through the WIPANO (Wissens- und Technologietransfer durch Patente und Normen) grant number 03THW10F04. We are grateful to Soren K. Mellerup (honored B.Sc.), Queen's University, Kingston (Canada) for helpful discussions.

Conflict of interest

The authors declare no conflict of interest.

Keywords: boron · dynamic covalent chemistry · luminescence · organocatalysis · polycycles

[1] F. So, *Organic Electronics: Materials, Processing, Devices and Applications*, CRC Press, Boca Raton, **2010**.
[2] J. Wu, W. Pisula, K. Müllen, *Chem. Rev.* **2007**, *107*, 718–747.
[3] R. Rieger, K. Müllen, *J. Phys. Org. Chem.* **2010**, *23*, 315–325.
[4] A. Narita, X.-Y. Wang, X. Feng, K. Müllen, *Chem. Soc. Rev.* **2015**, *44*, 6616 6643.
[5] M. Stępień, E. Gońka, M. Żyła, N. Sprutta, *Chem. Rev.* **2017**, *117*, 3479–3716.
[6] A. Studer, D. P. Curran, *Nature Chem.* **2014**, *6*, 765–773.
[7] A. Escande, M. J. Ingleson, *Chem. Commun.* **2015**, *51*, 6257–6274.
[8] C. D. Entwistle, T. B. Marder, *Angew. Chem. Int. Ed.* **2002**, *41*, 2927–2931; *Angew. Chem.* **2002**, *114*, 3051–3056.
[9] F. Jäkle, *Coord. Chem. Rev.* **2006**, *250*, 1107–1121.
[10] S. Yamaguchi, A. Wakamiya, *Pure Appl. Chem.* **2006**, *78*, 1413–1424.
[11] F. Jäkle, *Chem. Rev.* **2010**, *110*, 3985–4022.
[12] P. G. Campbell, A. J. V. Marwitz, S.-Y. Liu, *Angew. Chem. Int. Ed.* **2012**, *51*, 6074–6092; *Angew. Chem.* **2012**, *124*, 6178–6197.
[13] A. Lorbach, A. Hübner, M. Wagner, *Dalton Trans.* **2012**, *41*, 6048–6063.
[14] A. Wakamiya, S. Yamaguchi, *Bull. Chem. Soc. Jpn.* **2015**, *88*, 1357–1377.
[15] L. Ji, S. Griesbeck, T. B. Marder, *Chem. Sci.* **2017**, *8*, 846–863.
[16] Z. M. Hudson, S. Wang, *Acc. Chem. Res.* **2009**, *42*, 1584–1596.
[17] C. Hoffend, M. Diefenbach, E. Januszewski, M. Bolte, H.-W. Lerner, M. C. Holthausen, M. Wagner, *Dalton Trans.* **2013**, *42*, 13826–13837.
[18] C. R. Wade, A. E. J. Broomsgrove, S. Aldridge, F. P. Gabbaï, *Chem. Rev.* **2010**, *110*, 3958–3984.

© 2018 Wiley-VCH Verlag GmbH & Co. KGaA, Weinheim

ACES Asian Chemical Editorial Society

ASIAN JOURNAL OF ORGANIC CHEMISTRY
Focus Review

[19] J. J. Eisch, J. E. Galle, S. Kozima, *J. Am. Chem. Soc.* **1986**, *108*, 379–385.
[20] H. Braunschweig, I. Fernández, G. Frenking, T. Kupfer, *Angew. Chem. Int. Ed.* **2008**, *47*, 1951–1954; *Angew. Chem.* **2008**, *120*, 1977–1980.
[21] H. Braunschweig, C. Hörl, L. Mailänder, K. Radacki, J. Wahler, *Chem. Eur. J.* **2014**, *20*, 9858–9861.
[22] Further stabilization is provided with the help of N-hetereocyclic carbene (NHC) ligands. For details, see: T. K. Wood, W. E. Piers, B. A. Keay, M. Parvez, *Angew. Chem. Int. Ed.* **2009**, *48*, 4009–4012; *Angew. Chem.* **2009**, *121*, 4069–4072.
[23] C.-W. So, D. Watanabe, A. Wakamiya, S. Yamaguchi, *Organometallics* **2008**, *27*, 3496–3501.
[24] C. Fan, L. G. Mercier, W. E. Piers, H. M. Tuononen, M. Parvez, *J. Am. Chem. Soc.* **2010**, *132*, 9604–9606.
[25] H. Braunschweig, T. Kupfer, *Chem. Commun.* **2011**, *47*, 10903–10914.
[26] H. Braunschweig, V. Dyakonov, J. O. C. Jimenez-Halla, K. Kraft, I. Krummenacher, K. Radacki, A. Sperlich, J. Wahler, *Angew. Chem. Int. Ed.* **2012**, *51*, 2977–2980; *Angew. Chem.* **2012**, *124*, 3031–3034.
[27] R. Bertermann, H. Braunschweig, R. D. Dewhurst, C. Hörl, T. Kramer, I. Krummenacher, *Angew. Chem. Int. Ed.* **2014**, *53*, 5453–5457; *Angew. Chem.* **2014**, *126*, 5557–5561.
[28] J. H. Barnard, S. Yruegas, K. Huang, C. D. Martin, *Chem. Commun.* **2016**, *52*, 9985–9991.
[29] Z. Zhang, R. M. Edkins, M. Haehnel, M. Wehner, A. Eichhorn, L. Mailänder, M. Meier, J. Brand, F. Brede, K. Müller-Buschbaum, H. Braunschweig, T. B. Marder, *Chem. Sci.* **2015**, *6*, 5922–5927.
[30] T. Onak, *Organoborane Chemistry*, Academic Press, New York, **1975**.
[31] G. A. Molander, N. Ellis, *Acc. Chem. Res.* **2007**, *40*, 275–286.
[32] G. A. Molander, *J. Org. Chem.* **2015**, *80*, 7837–7848.
[33] K. Samigullin, M. Bolte, H.-W. Lerner, M. Wagner, *Organometallics* **2014**, *33*, 3564–3569.
[34] K. Schickedanz, T. Trageser, M. Bolte, H.-W. Lerner, M. Wagner, *Chem. Commun.* **2015**, *51*, 15808–15810.
[35] K. Schickedanz, J. Radtke, M. Bolte, H.-W. Lerner, M. Wagner, *J. Am. Chem. Soc.* **2017**, *139*, 2842–2851.
[36] M. C. Haberecht, J. B. Heilmann, A. Haghiri, M. Bolte, J. W. Bats, H.-W. Lerner, M. C. Holthausen, M. Wagner, *Z. Anorg. Allg. Chem.* **2004**, *630*, 904–913.
[37] T. S. De Vries, A. Prokofjevs, E. Vedejs, *Chem. Rev.* **2012**, *112*, 4246–4282.
[38] M. J. Ingleson, *Synlett* **2012**, *23*, 1411–1415.
[39] T. Ishiyama, N. Miyaura, *Chem. Rec.* **2004**, *3*, 271–280.
[40] I. A. I. Mkhalid, J. H. Barnard, T. B. Marder, J. M. Murphy, J. F. Hartwig, *Chem. Rev.* **2010**, *110*, 890–931.
[41] A. Schnurr, K. Samigullin, J. M. Breunig, M. Bolte, H.-W. Lerner, M. Wagner, *Organometallics* **2011**, *30*, 2838–2843.
[42] J. B. Heilmann, Y. Qin, F. Jäkle, H.-W. Lerner, M. Wagner, *Inorg. Chim. Acta* **2006**, *359*, 4802–4806.
[43] J. B. Heilmann, M. Scheibitz, Y. Qin, A. Sundararaman, F. Jäkle, T. Kretz, M. Bolte, H.-W. Lerner, M. C. Holthausen, M. Wagner, *Angew. Chem. Int. Ed.* **2006**, *45*, 920–925; *Angew. Chem.* **2006**, *118*, 934–939.
[44] C. Cui, J. Heilmann-Brohl, A. Sánchez Perucha, M. D. Thomson, H. G. Roskos, M. Wagner, F. Jäkle, *Macromolecules* **2010**, *43*, 5256–5261.
[45] M. Scheibitz, H. Li, J. Schnorr, A. Sánchez Perucha, M. Bolte, H.-W. Lerner, F. Jäkle, M. Wagner, *J. Am. Chem. Soc.* **2009**, *131*, 16319–16329.
[46] U. Gross, D. Kaufmann, *Chem. Ber.* **1987**, *120*, 991–994.
[47] A. Hübner, M. Diefenbach, M. Bolte, H.-W. Lerner, M. C. Holthausen, M. Wagner, *Angew. Chem. Int. Ed.* **2012**, *51*, 12514–12518; *Angew. Chem.* **2012**, *124*, 12682–12686.
[48] A. J. Ashe III, W. Klein, R. Rousseau, *Organometallics* **1993**, *12*, 3225–3231.
[49] L. G. Mercier, W. E. Piers, M. Parvez, *Angew. Chem. Int. Ed.* **2009**, *48*, 6108–6111; *Angew. Chem.* **2009**, *121*, 6224–6227.
[50] A. Lorbach, C. Reus, M. Bolte, H.-W. Lerner, M. Wagner, *Adv. Synth. Catal.* **2010**, *352*, 3443–3449.
[51] C. Reus, N.-W. Liu, M. Bolte, H.-W. Lerner, M. Wagner, *J. Org. Chem.* **2012**, *77*, 3518–3523.
[52] S. Kirschner, J.-M. Mewes, M. Bolte, H.-W. Lerner, A. Dreuw, M. Wagner, *Chem. Eur. J.* **2017**, *23*, 5104–5116.
[53] W. Schacht, D. Kaufmann, *J. Organomet. Chem.* **1987**, *331*, 139–152.
[54] J. Chen, J. W. Kampf, A. J. Ashe III, *Organometallics* **2008**, *27*, 3639–3641.
[55] E. Januszewski, A. Lorbach, R. Grewal, M. Bolte, J. W. Bats, H.-W. Lerner, M. Wagner, *Chem. Eur. J.* **2011**, *17*, 12696–12705.
[56] C. Reus, S. Weidlich, M. Bolte, H.-W. Lerner, M. Wagner, *J. Am. Chem. Soc.* **2013**, *135*, 12892–12907.
[57] S. Luliński, J. Smętek, K. Durka, J. Serwatowski, *Eur. J. Org. Chem.* **2013**, 8315–8322.
[58] K. Schickedanz, Dissertation, Goethe Universität (Frankfurt/Main), **2017**.
[59] A. John, M. Bolte, H.-W. Lerner, M. Wagner, *Angew. Chem. Int. Ed.* **2017**, *56*, 5588–5592; *Angew. Chem.* **2017**, *129*, 5680–5684.
[60] F. Miyamoto, S. Nakatsuka, K. Yamada, K. Nakayama, T. Hatakeyama, *Org. Lett.* **2015**, *17*, 6158–6161.
[61] K. Matsuo, S. Saito, S. Yamaguchi, *J. Am. Chem. Soc.* **2014**, *136*, 12580–12583.
[62] C. Dou, S. Saito, K. Matsuo, I. Hisaki, S. Yamaguchi, *Angew. Chem. Int. Ed.* **2012**, *51*, 12206–12210; *Angew. Chem.* **2012**, *124*, 12372–12376.
[63] S. Osumi, S. Saito, C. Dou, K. Matsuo, K. Kume, H. Yoshikawa, K. Awaga, S. Yamaguchi, *Chem. Sci.* **2016**, *7*, 219–227.
[64] C. Hoffend, F. Schödel, M. Bolte, H.-W. Lerner, M. Wagner, *Chem. Eur. J.* **2012**, *18*, 15394–15405.
[65] C. Dou, S. Saito, S. Yamaguchi, *J. Am. Chem. Soc.* **2013**, *135*, 9346–9349.
[66] Z. Zhou, A. Wakamiya, T. Kushida, S. Yamaguchi, *J. Am. Chem. Soc.* **2012**, *134*, 4529–4532.
[67] T. Kushida, C. Camacho, A. Shuto, S. Irle, M. Muramatsu, T. Katayama, S. Ito, Y. Nagasawa, H. Miyasaka, E. Sakuda, N. Kitamura, Z. Zhou, A. Wakamiya, S. Yamaguchi, *Chem. Sci.* **2014**, *5*, 1296–1304.
[68] T. Kushida, S. Shirai, N. Ando, T. Okamoto, H. Ishii, H. Matsui, M. Yamagishi, T. Uemura, J. Tsurumi, S. Watanabe, J. Takeya, S. Yamaguchi, *J. Am. Chem. Soc.* **2017**, *139*, 14336–14339.
[69] J. F. Araneda, B. Neue, W. E. Piers, M. Parvez, *Angew. Chem. Int. Ed.* **2012**, *51*, 8546–8550; *Angew. Chem.* **2012**, *124*, 8674–8678.
[70] J. F. Araneda, W. E. Piers, M. J. Sgro, M. Parvez, *Chem. Sci.* **2014**, *5*, 3189–3196.
[71] A. Caruso, Jr., J. D. Tovar, *Org. Lett.* **2011**, *13*, 3106–3109.
[72] D. R. Levine, A. Caruso, Jr., M. A. Siegler, J. D. Tovar, *Chem. Commun.* **2012**, *48*, 6256–6258.
[73] J. M. Farrell, D. Schmidt, V. Grande, F. Würthner, *Angew. Chem. Int. Ed.* **2017**, *56*, 11846–11850; *Angew. Chem.* **2017**, *129*, 12008–12012.
[74] V. M. Hertz, M. Bolte, H.-W. Lerner, M. Wagner, *Angew. Chem. Int. Ed.* **2015**, *54*, 8800–8804; *Angew. Chem.* **2015**, *127*, 8924–8928.
[75] V. M. Hertz, H.-W. Lerner, M. Wagner, *Org. Lett.* **2015**, *17*, 5240–5243.
[76] V. M. Hertz, J. G. Massoth, M. Bolte, H.-W. Lerner, M. Wagner, *Chem. Eur. J.* **2016**, *22*, 13181–13188.
[77] D. Crossley, R. Kahan, S. Endres, A. Warner, R. A. Smith, J. Cid, J. Dunsford, J. E. Jones, I. Vitorica-Yrzebal, M. J. Ingleson, *Chem. Sci.* **2017** https://doi.org/10.1039/C7SC02793A.
[78] A. J. Warner, J. R. Lawson, V. Fasano, M. J. Ingleson, *Angew. Chem. Int. Ed.* **2015**, *54*, 11245–11249; *Angew. Chem.* **2015**, *127*, 11397–11401.
[79] V. M. Hertz, N. Ando, M. Hirai, M. Bolte, H.-W. Lerner, S. Yamaguchi, M. Wagner, *Organometallics* **2017**, *36*, 2512–2519.
[80] C. Reus, F. Guo, A. John, M. Winhold, H.-W. Lerner, F. Jäkle, M. Wagner, *Macromolecules* **2014**, *47*, 3727–3735.
[81] A. Caruso, Jr., J. D. Tovar, *J. Org. Chem.* **2011**, *76*, 2227–2239.
[82] A. Shuto, T. Kushida, T. Fukushima, H. Kaji, S. Yamaguchi, *Org. Lett.* **2013**, *15*, 6234–6237.
[83] T. Kushida, Z. Zhou, A. Wakamiya, S. Yamaguchi, *Chem. Commun.* **2012**, *48*, 10715–10717.
[84] T. Kushida, S. Yamaguchi, *Organometallics* **2013**, *32*, 6654–6657.
[85] T. Kushida, A. Shuto, M. Yoshio, T. Kato, S. Yamaguchi, *Angew. Chem. Int. Ed.* **2015**, *54*, 6922–6925; *Angew. Chem.* **2015**, *127*, 7026–7029.
[86] K. Matsuo, S. Saito, S. Yamaguchi, *Angew. Chem. Int. Ed.* **2016**, *55*, 11984–11988; *Angew. Chem.* **2016**, *128*, 12163–12167.
[87] Z. Zhang, H. Zhang, C. Jiao, K. Ye, H. Zhang, J. Zhang, Y. Wang, *Inorg. Chem.* **2015**, *54*, 2652–2659.
[88] K. Durka, I. Głowacki, S. Luliński, B. Łuszczyńska, J. Smętek, P. Szczepanik, J. Serwatowski, U. E. Wawrzyniak, G. Wesela-Bauman, E. Witkowska, G. Wiosna-Sałyga, K. Woźniak, *J. Mater. Chem. C* **2015**, *3*, 1354–1364.
[89] M. Lorenz-Rothe, K. S. Schellhammer, T. Jägeler-Hoheisel, R. Meerheim, S. Kraner, M. P. Hein, C. Schünemann, M. L. Tietze, M. Hummert, F. Ort-

© 2018 Wiley-VCH Verlag GmbH & Co. KGaA, Weinheim

ACES Asian Chemical Editorial Society

ASIAN JOURNAL OF ORGANIC CHEMISTRY
Focus Review

mann, G. Cuniberti, C. Körner, K. Leo, *Adv. Electron. Mater.* **2016**, *2*, 1600152.
[90] A. Lorbach, M. Bolte, H. Li, H.-W. Lerner, M. C. Holthausen, F. Jäkle, M. Wagner, *Angew. Chem. Int. Ed.* **2009**, *48*, 4584 – 4588; *Angew. Chem.* **2009**, *121*, 4654 – 4658.
[91] A. Lorbach, M. Bolte, H.-W. Lerner, M. Wagner, *Chem. Commun.* **2010**, *46*, 3592 – 3594.
[92] Ö. Seven, Z.-W. Qu, H. Zhu, M. Bolte, H.-W. Lerner, M. C. Holthausen, M. Wagner, *Chem. Eur. J.* **2012**, *18*, 11284 – 11295.
[93] M. F. Smith, S. J. Cassidy, I. A. Adams, M. Vasiliu, D. L. Gerlach, D. A. Dixon, P. A. Rupar, *Organometallics* **2016**, *35*, 3182 – 3191.
[94] A. Hübner, Z.-W. Qu, U. Englert, M. Bolte, H.-W. Lerner, M. C. Holthausen, M. Wagner, *J. Am. Chem. Soc.* **2011**, *133*, 4596 – 4609.
[95] T. Kaese, A. Hübner, M. Bolte, H.-W. Lerner, M. Wagner, *J. Am. Chem. Soc.* **2016**, *138*, 6224 – 6233.
[96] A. Das, A. Hübner, M. Weber, M. Bolte, H.-W. Lerner, M. Wagner, *Chem. Commun.* **2011**, *47*, 11339 – 11341.
[97] For examples of luminescent 9-borafluorene base adducts, see: C. J. Berger, G. He, C. Merten, R. McDonald, M. J. Ferguson, E. Rivard, *Inorg. Chem.* **2014**, *53*, 1475 – 1486.
[98] A. Hübner, A. M. Diehl, M. Bolte, H.-W. Lerner, M. Wagner, *Organometallics* **2013**, *32*, 6827 – 6833.
[99] A. Lorbach, M. Bolte, H.-W. Lerner, M. Wagner, *Organometallics* **2010**, *29*, 5762 – 5765.
[100] E. von Grotthuss, M. Diefenbach, M. Bolte, H.-W. Lerner, M. C. Holthausen, M. Wagner, *Angew. Chem. Int. Ed.* **2016**, *55*, 14067 – 14071; *Angew. Chem.* **2016**, *128*, 14273 – 14277.
[101] A. Hübner, M. Bolte, H.-W. Lerner, M. Wagner, *Angew. Chem. Int. Ed.* **2014**, *53*, 10408 – 10411; *Angew. Chem.* **2014**, *126*, 10576 – 10579.
[102] T. Kaese, H. Budy, M. Bolte, H.-W. Lerner, M. Wagner, *Angew. Chem. Int. Ed.* **2017**, *56*, 7546 – 7550; *Angew. Chem.* **2017**, *129*, 7654 – 7658.
[103] A. Iida, S. Yamaguchi, *J. Am. Chem. Soc.* **2011**, *133*, 6952 – 6955.
[104] A. Hübner, A. M. Diehl, M. Diefenbach, B. Endeward, M. Bolte, H.-W. Lerner, M. C. Holthausen, M. Wagner, *Angew. Chem. Int. Ed.* **2014**, *53*, 4832 – 4835; *Angew. Chem.* **2014**, *126*, 4932 – 4935.
[105] A. Hübner, T. Kaese, M. Diefenbach, B. Endeward, M. Bolte, H.-W. Lerner, M. C. Holthausen, M. Wagner, *J. Am. Chem. Soc.* **2015**, *137*, 3705 – 3714.
[106] J. D. Hoefelmeyer, F. P. Gabbaï, *J. Am. Chem. Soc.* **2000**, *122*, 9054 – 9055.
[107] S. Biswas, C. Maichle-Mössmer, H. F. Bettinger, *Chem. Commun.* **2012**, *48*, 4564 – 4566.
[108] S. Biswas, I. M. Oppel, H. F. Bettinger, *Inorg. Chem.* **2010**, *49*, 4499 – 4506.
[109] M. Müller, C. Maichle-Mössmer, H. F. Bettinger, *Angew. Chem. Int. Ed.* **2014**, *53*, 9380 – 9383; *Angew. Chem.* **2014**, *126*, 9534 – 9537.
[110] H. F. Bettinger, M. Müller, *J. Phys. Org. Chem.* **2015**, *28*, 97 – 103.
[111] C. Sánchez-Sánchez, S. Brüller, H. Sachdev, K. Müllen, M. Krieg, H. F. Bettinger, A. Nicolaï, V. Meunier, L. Talirz, R. Fasel, P. Ruffieux, *ACS Nano* **2015**, *9*, 9228 – 9235.
[112] Y. Shoji, N. Tanaka, S. Muranaka, N. Shigeno, H. Sugiyama, K. Takenouchi, F. Hajjaj, T. Fukushima, *Nat. Commun.* **2016**, *7*, 12704.
[113] A. Iida, A. Sekioka, S. Yamaguchi, *Chem. Sci.* **2012**, *3*, 1461 – 1466.
[114] Ö. Seven, S. Popp, M. Bolte, H.-W. Lerner, M. Wagner, *Dalton Trans.* **2014**, *43*, 8241 – 8253.
[115] L. Schweighauser, H. A. Wegner, *Chem. Eur. J.* **2016**, *22*, 14094 – 14103.
[116] S. N. Kessler, H. A. Wegner, *Org. Lett.* **2010**, *12*, 4062 – 4065.
[117] S. N. Kessler, M. Neuburger, H. A. Wegner, *J. Am. Chem. Soc.* **2012**, *134*, 17885 – 17888.
[118] L. Schweighauser, I. Bodoky, S. N. Kessler, D. Häussinger, C. Donsbach, H. A. Wegner, *Org. Lett.* **2016**, *18*, 1330 – 1333.
[119] L. Hong, S. Ahles, M. A. Strauss, C. Logemann, H. A. Wegner, *Org. Chem. Front.* **2017**, *4*, 871 – 875.
[120] Z. Lu, L. Schweighauser, H. Hausmann, H. A. Wegner, *Angew. Chem. Int. Ed.* **2015**, *54*, 15556 – 15559; *Angew. Chem.* **2015**, *127*, 15777 – 15780.
[121] D. W. Stephan, *Science* **2016**, *354*, 1248 – 1255.
[122] S. Agnoli, M. Favaro, *J. Mater. Chem. A* **2016**, *4*, 5002 – 5025.
[123] J. Cai, P. Ruffieux, R. Jaafar, M. Bieri, T. Braun, S. Blankenburg, M. Muoth, A. P. Seitsonen, M. Saleh, X. Feng, K. Müllen, R. Fasel, *Nature* **2010**, *466*, 470 – 473.
[124] M. Treier, C. A. Pignedoli, T. Laino, R. Rieger, K. Müllen, D. Passerone, R. Fasel, *Nature Chem.* **2011**, *3*, 61 – 67.
[125] S. Kawai, S. Saito, S. Osumi, S. Yamaguchi, A. S. Foster, P. Spijker, E. Meyer, *Nat. Commun.* **2015**, *6*, 8098.
[126] R. R. Cloke, T. Marangoni, G. D. Nguyen, T. Joshi, D. J. Rizzo, C. Bronner, T. Cao, S. G. Louie, M. F. Crommie, F. R. Fischer, *J. Am. Chem. Soc.* **2015**, *137*, 8872 – 8875.

Manuscript received: September 4, 2017
Revised manuscript received: October 5, 2017
Version of record online: November 24, 2017

 © 2018 Wiley-VCH Verlag GmbH & Co. KGaA, Weinheim

6.2.3 Deprotonation of a Seemingly Hydridic Diborane(6) to Build a B–B Bond

GDCh Communications Angewandte International Edition Chemie

Boranes

International Edition: DOI: 10.1002/anie.201702393
German Edition: DOI: 10.1002/ange.201702393

Deprotonation of a Seemingly Hydridic Diborane(6) To Build a B–B Bond

*Thomas Kaese, Hendrik Budy, Michael Bolte, Hans-Wolfram Lerner, and Matthias Wagner**

Abstract: *Deprotonation of the doubly arylene-bridged diborane(6) derivative* ***1H***$_2$ *with* $(Me_3Si)_3CLi$ *or* $(Me_3Si)_2NK$ *gives the B–B σ-bonded species M[**1H**] in essentially quantitative yields (THF, room temperature; M = Li, K, arylene = 4,4′-di-tert-butyl-2,2′-biphenylylene). With nBuLi as the base, the yield of Li[**1H**] drops to 20% and the 1,1-bis(9-borafluorenyl)butane Li[**2H**] is formed as a side product (30%). In addition to the 1,1-butanediyl fragment, the two boron atoms of Li[**2H**] are linked by a μ-H bridge. In the closely related molecule Li[**3H**], the corresponding μ-H atom can be abstracted with* $(Me_3Si)_3CLi$ *to afford the B–B-bonded conjugated base* Li_2[**3**] *(THF, 150°C; 15%). Li[**1H**] and Li[**2H**] were characterized by NMR spectroscopy and X-ray crystallography.*

The essence of chemical transformations lies in the making and breaking of covalent bonds. Compared to the art of organic synthesis, which has already arrived at a high level of sophistication, the chemistry of molecules containing electron-precise boron–boron bonds is far less developed. The lack of generally applicable B–B coupling methods stands in sharp contrast to the practical importance of certain diboranes(4), such as bis(pinacolato)diboron (B_2pin_2), which is widely used for the diboration of alkenes and alkynes[1] as well as for arene C–H activation/borylation reactions.[2] Even though recent years have witnessed remarkable advances in B–B coupling methods (e.g., reactions between boryl anions and haloboranes, metal-catalyzed dehydrocoupling, and the hydroboration of B=B bonds),[3] the vast majority of electron-precise diboranes are still prepared through the Wurtz-type coupling of haloboranes.[4]

It has been shown that ditopic triarylboranes behave as electron traps to furnish B·B- and B–B-bonded species, provided that the two vacant boron p_z orbitals are properly aligned by carefully designed organic bridges (Scheme 1a).[5–7] A worthwhile generalization of this approach would require the use of a more abundant class of compounds, such as diborane(6) derivatives (Scheme 1b), in which the two μ-H atoms first hold the boron centers in close proximity, but can later take up terminal positions to vacate space for the added electrons.

[*] M. Sc. T. Kaese, B. Sc. H. Budy, Dr. M. Bolte, Dr. H.-W. Lerner, Prof. Dr. M. Wagner
Institut für Anorganische Chemie, Goethe-Universität Frankfurt
Max-von-Laue-Strasse 7, 60438 Frankfurt am Main (Germany)
E-mail: Matthias.Wagner@chemie.uni-frankfurt.de
Supporting information and the ORCID identification number(s) for the author(s) of this article can be found under: https://doi.org/10.1002/anie.201702393.

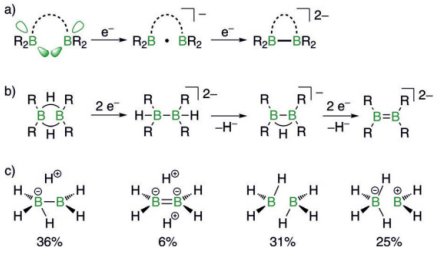

Scheme 1. B–B bond formation through reduction of preorganized ditopic triorganoboranes (a) and diborane(6) derivatives (b); and the four most relevant canonical structures of B_2H_6 (c).

Indeed, this concept has been successfully applied to prepare the entire sequence of products shown in Scheme 1b.[8–11] Specifically, our group generated the compound K[**1H**] from diborane **1H**$_2$[12,13] through a reduction/hydride elimination sequence (Scheme 2).[11] The anion [**1H**]$^-$ contains a central B–B single bond, supported by one residual μ-H atom, and may therefore be regarded as a formal deprotonation product of **1H**$_2$. Examples of clear-cut B–B coupling reactions through the deprotonation of neutral B(μ-H)B fragments are so far restricted to higher clusters B_nH_m with $n \geq 4$.[14] Scheme 2 shows the corresponding conversion of B_5H_9 to give $B_5H_8^-$.[15] Transformations involving the abstraction of terminal B–H protons are even scarcer and have only been observed for Bertrand's carbene adduct[16] and Finze's monohydridotricyanoborate anion,[17] which are equipped with strongly electron-withdrawing cyano/cAAC substituents (Scheme 2). Himmel's cation $[H_3B_2(hpp)_2]^+$ can be deprotonated with KO*t*Bu to give the diborane adduct $[HB(hpp)]_2$ (Scheme 2; hpp = 1,3,4,6,7,8-hexahydro-2*H*-pyrimido[1,2-*a*]pyrimidinate). Even though the positive charge and the guanidinate bridges should facilitate the proton abstraction, the reaction was described as "not clean".[18] A second example that comes close to the deprotonation of a diborane-(6) is the temperature-induced elimination of H_2 from Fontaine's dimeric Lewis pair (Scheme 2).[19] According to quantum-chemical calculations, the process is likely assisted by the intramolecular amine base, but thermodynamically driven by the release of H_2. Importantly, the product of the H_2 elimination reaction remains uncharged and is not the conjugate base of the starting material.

For decades, the reaction of B_2H_6 with donor molecules (Do) has been discussed exclusively with regard to the symmetrical (2 Do-BH_3) or unsymmetrical ($[Do_2BH_2]^+$-$[BH_4]^-$) cleavage of the dimeric scaffold.[20] The removal of

 © 2017 Wiley-VCH Verlag GmbH & Co. KGaA, Weinheim

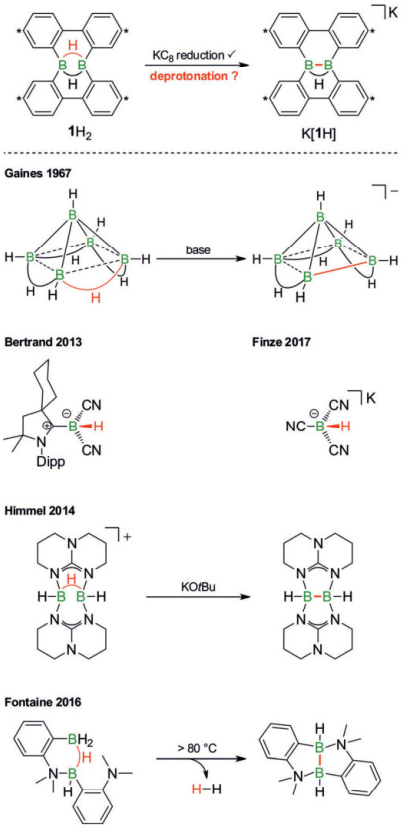

Scheme 2. Top: The formation of K[**1**H] from **1**H_2 as an example of a reductive B–B-coupling/H-elimination sequence; C atoms marked with an asterisk bear *t*Bu substituents. Bottom: Five examples are given of deprotonable B–H species.

μ-H atoms has never been an issue. As a fundamental change of paradigm, we now describe the first unequivocal deprotonation of a neutral diborane(6) derivative (**1**H_2) with concomitant B–B-bond formation.

Back in 1945, Pitzer formulated the electronic structure of B_2H_6 in analogy to the isoelectronic ethylene as a B=B double bond with two embedded protons.[21] His theory was immediately rebutted and instead, it became generally accepted that "the bridge protons [of B_2H_6] are not directly removable"[22] and that "the bridge hydrogen atoms are negatively charged"[23] (cf. the higher Allred–Rochow electronegativity of H (2.2) compared to B (2.0), as well as NMR evidence[24] and the anti-Markovnikov selectivity of typical hydroboration reactions). However, recent quantum-chemical calculations on B_2H_6 seem to revive Pitzer's formulation: The μ-H atoms in fact carry positive atomic charges of 0.10, and the μ-H–B bonds are 50% covalent and 50% ionic. The two mesomeric forms of B_2H_6 relating to the symmetrical (31%) and unsymmetrical (25%) base-cleavage products have a joint relative weight of only 56% (Scheme 1c). The main resonance structure (36%), however, consists of a proton and a boron-substituted borohydride. The predicted B–B bond order amounts to 0.5. A fourth resonance structure, featuring two protons and a B=B double bond, possesses a relative weight of 6%.[25]

Given this background, we started our investigation by titrating a [D_8]THF solution of the B=B-bonded species Li_2[**1**][9,11] with ethereal HCl (Scheme 3). According to ^{1}H NMR spectroscopy (Figure 1), the gradual addition of the acid resulted first in clean conversion of the starting material to Li[**1**H] ($\leq$1 equiv HCl) and second in the consumption of Li[**1**H] with concomitant formation of **1**H_2

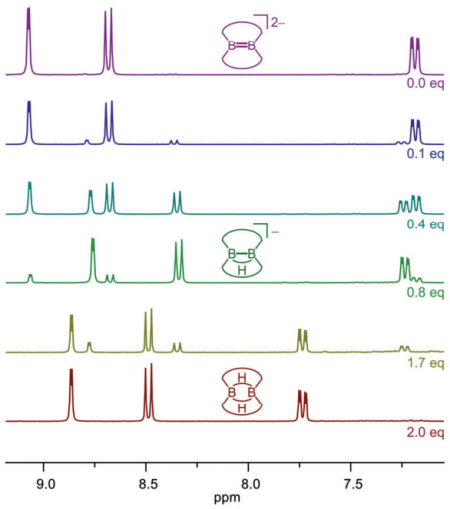

Figure 1. ^{1}H NMR monitoring of the conversion of Li_2[**1**] (top) to Li[**1**H] (middle) and **1**H_2 (bottom) upon titration with ethereal HCl.

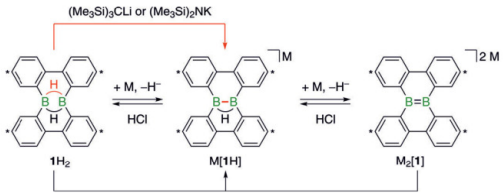

Scheme 3. Deprotonation of **1**H_2 to furnish M[**1**H]; sequential B–B-bond formation to give M[**1**H] and M_2[**1**] through reduction of **1**H_2 with M = Li or K;[11] the reverse reaction through titration of Li_2[**1**] with ethereal HCl; and the comproportionation of **1**H_2 and Li_2[**1**] to afford Li[**1**H]. All reactions were carried out in THF at room temperature. C atoms marked with an asterisk bear *t*Bu substituents.

 © 2017 Wiley-VCH Verlag GmbH & Co. KGaA, Weinheim

(1–2 equiv HCl). As the protonation reaction progressed, the color of the sample changed from deep red (Li_2[**1**]) to yellow (Li[**1**H]) to colorless ($\mathbf{1}H_2$). These experimental findings not only agree with Pitzer's view on the electronic structure of B_2H_6, but also show that Li_2[**1**] constitutes a significantly stronger Brønsted base than Li[**1**H]. In terms of the reverse reaction, the titration study indicates that only the single abstraction of a bridging proton from diboranes(6) remains a realistic goal.

Our initial attempt toward this goal was made by treating $\mathbf{1}H_2$ with an equimolar amount of Li_2[**1**], whereupon Li[**1**H] was obtained as the exclusive product (Scheme 3; see the Supporting Information for more information). Even though this transformation is a formal proton-transfer reaction, the actual mechanism might well be distinctly different: Li_2[**1**] is a very unique, highly redox-active base, which could deliver an electron to $\mathbf{1}H_2$ and, in turn, accept a hydrogen atom from the resulting radical $[\mathbf{1}H_2]^{\bullet-}$.

Suitable common Brønsted bases first and foremost must possess sufficiently high steric demand to prevent the unwanted cleavage of the diborane(6) through Lewis acid/base pairing. This requirement is fulfilled by the bulky lithium methanide $(Me_3Si)_3CLi$, which was consequently employed in the subsequent deprotonation experiment. Upon the addition of [D_8]THF to an equimolar solid mixture of $\mathbf{1}H_2$ and $(Me_3Si)_3CLi$ at room temperature, the resulting clear solution immediately adopted a yellow color. NMR spectroscopic control of the sample confirmed a quantitative conversion of the starting material to Li[**1**H]. On a preparative scale, this synthesis furnished yellow crystals of $[Li(thf)_3]$[**1**H] in 93% yield. X-ray crystallography unequivocally established the constitution of the product, however, the data quality was too poor for a reliable determination of geometric parameters (see the Supporting Information). We therefore repeated the reaction in Et_2O to obtain crystals of $[Li(Et_2O)_2]$[**1**H], which allowed a satisfactory structure analysis. The asymmetric unit contains two whole and two half independent molecules, which differ mainly in the twist of their anionic moieties (Figure 2; the torsion angles between the central C–C bonds of the respective 2,2′-biphenylylene bridges range between 4.2(2)° and 32.1(3)°). In all of the independent molecules, the $[Li(Et_2O)_2]^+$ cations are located side-on to the electron-rich B–B bonds and close to the positions previously occupied by the μ-H atoms. All key bond lengths and angles of $[\mathbf{1}H]^-$ are very similar to those of the corresponding K^+ salt; the same is true for the NMR data (see the Supporting Information for full details).[11] In principle, the $[(Me_3Si)_3C]^-$ anion could also act as a reducing agent rather than a Brønsted base toward $\mathbf{1}H_2$ and thereby trigger an electron-transfer/H-abstraction scenario. The following observations argue against such a radical mechanism: 1) A putative $[(Me_3Si)_3C]^{\bullet}$ intermediate should preferentially react with the abundant solvent molecules and would then no longer be available to abstract an H atom from $[\mathbf{1}H_2]^{\bullet-}$; moreover, we never observed the formation of $(Me_3Si)_3CD$ when the reaction was carried out in [D_8]THF. 2) We have previously shown that $[\mathbf{1}H_2]^{\bullet-}$ tends to undergo fast structural rearrangement reactions, which is not in accord with the highly selective conversion reported here.[11] 3) The presence of $n$$Bu_3SnH$, a prominent spin-trapping reagent,[26] did not change the reaction outcome; the compound rather remained untouched, according to NMR spectroscopy. 4) The use of $(Me_3Si)_2NM$ (M = Li, K) instead of $(Me_3Si)_3CLi$ also resulted in the quantitative formation of M[**1**H], even though the amide is a weaker reducing agent than the methanide.

The successful deprotonation of $\mathbf{1}H_2$ with $(Me_3Si)_2NM$ not only renders M[**1**H] readily available, but also shows that the steric demand of the base can be reduced from three to two Me_3Si substituents without appreciable yield losses resulting from N–B adduct formation. A further move to tBuLi and nBuLi, however, pushes the limits too far, because the yields of Li[**1**H] undergo a precipitous drop to approximately 45% and 20%, respectively. As a significant side product, the nBuLi reaction produced the diborylmethane derivative Li[**2**H] (about 30% according to ^{1}H NMR spectroscopy; Scheme 4a).

According to X-ray crystallography on manually selected crystals of $[Li(thf)_4]$[**2**H], the anionic component consists of two 9-borafluorenyl substituents attached to the same termi-

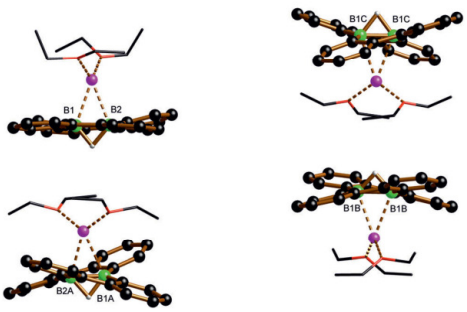

Figure 2. Solid-state structure of $[Li(Et_2O)_2]$[**1**H] (tBu groups and C*H* atoms omitted for clarity). The molecules B and C contain a two-fold rotation axis; the anions present in the asymmetric unit differ mainly in their intramolecular twist.

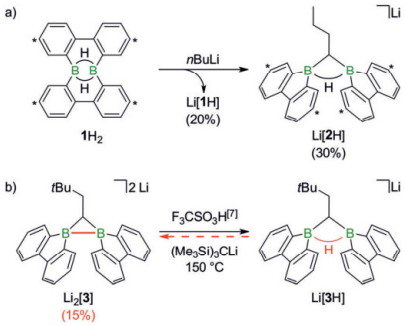

Scheme 4. a) Addition of nBuLi to $\mathbf{1}H_2$ furnishes Li[**1**H] together with the rearranged diborylmethane Li[**2**H]; C atoms marked with an asterisk bear tBu substituents. b) Deprotonation of Li[**3**H] gives Li_2[**3**] in 15% yield.

 © 2017 Wiley-VCH Verlag GmbH & Co. KGaA, Weinheim

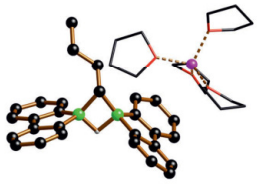

Figure 3. Solid-state structure of [Li(thf)$_4$][**2**H] (*t*Bu groups and C*H* atoms omitted for clarity).

nal C atom of an *n*-butyl chain (Figure 3). The negative charge, which is counterbalanced by a solvent-separated $[Li(thf)_4]^+$ cation, originates from a formally hydridic H atom that bridges both B atoms. The B···B distance amounts to 1.967(4) Å and the corresponding B-C-B angle possesses a value of 75.6(2)°. The sum of the C-B-C angles around each borafluorene unit, which is a measure of boron pyramidalization, is 353.0° and 343.7° (planar boron center: 360°, tetrahedral boron center: 328.4°). NMR spectroscopy reveals the magnetic equivalence of the two 9-borafluorenyl fragments, which results from an average C_s symmetry of the anion [**2**H]$^-$ in [D$_8$]THF solution. Due to the prochiral alkyl bridge, the two *t*Bu-C$_6$H$_3$ halves of each 9-borafluorenyl unit are not symmetry-related. The ^{11}B NMR spectrum of Li[**2**H] shows one broad resonance at −13 ppm. As in the cases of **1**H$_2$ and Li[**1**H], μ-H–B coupling is not resolved. The proton resonance assignable to μ-H overlaps with a CH_2 signal of the *n*-butyl chain to give a multiplet between 2.05–2.00 ppm. The ^{13}C{^{1}H} NMR resonance of the bridging C atom (δ = 20.5 ppm) is broadened almost beyond detection, because of the two neighboring quadrupolar B nuclei.

The 1,1-butanediyl moiety of Li[**2**H] obviously stems from the added *n*BuLi and has likely been introduced through nucleophilic attack by the sterically undemanding *n*BuLi on a B atom of **1**H$_2$ or Li[**1**H]. The mechanism of the α-CH-activation reaction, by which the second B–C(bridge) bond is formed, still remains to be elucidated. Lewis base induced ring-contraction reactions leading from **1**H$_2$ (and related molecules) to 9-borafluorene derivatives have previously been observed and are therefore not entirely surprising.[11,12,27,28] All in all, Li[**2**H] closely resembles compound Li[**3**H], which has been prepared through protonation of the dianionic salt Li$_2$[**3**] (Scheme 4 b).[7]

The interrelation between Li[**3**H] and Li$_2$[**3**] suggests Li[**3**H] as an alternative proof-of-principle substrate for B–B coupling through B(μ-H)B deprotonation: Upon the addition of (Me$_3$Si)$_3$CLi, Li[**3**H] can indeed be converted into Li$_2$[**3**], albeit only at elevated temperatures of 150 °C and in low yields of 15 %. We assume that the reason lies partly in the limited steric accessibility of the μ-H atom, but mainly in the negative charge of the starting material. In line with that and with initial expectations, all our attempts at the deprotonation of the [**1**H]$^-$ anion (or the double deprotonation of **1**H$_2$) provided only trace amounts of [**1**]$^{2-}$, even though the starting materials were always fully consumed.[29] In the case of K[**1**H] and (Me$_3$Si)$_2$NK ([D$_8$]THF, room temperature), we identified the major reaction products as the amide and hydride adducts of 9*H*-9-borafluorene (see the Supporting Information). The complex formation and the structural rearrangement are reminiscent of the reaction between **1**H$_2$ and *n*BuLi. Corresponding adducts were also observed in the reaction of (Mes$_2$BH)$_2$ with (Me$_3$Si)$_2$NK, which failed to give any B–B-coupling product (Mes = 2,4,6-trimethylphenyl; see the Supporting Information for NMR data and X-ray analyses).

In summary, we succeeded in the deprotonation of a diborane(6) derivative (**1**H$_2$), which belongs to a class of compounds previously regarded as entirely hydridic species. In the course of the reaction, a B–B bond is formed, which suggests that our method may find future applications for the synthesis of electron-precise diboranes. A successful B(μ-H)B deprotonation with Brønsted bases (Do) requires the suppression of the competing B–Do Lewis acid/base reaction. The following general rules regarding the selection of suitable starting materials can be deduced: 1) The Brønsted bases should be sterically demanding. 2) Increasing the steric bulk around the B(μ-H)B fragment, such as in (Mes$_2$BH)$_2$, is counterproductive because it shifts the monomer–dimer equilibrium to the side of the monomers, which are efficiently trapped even by bulky bases. 3) A monomer–dimer equilibrium is not an issue once the diborane core is supported by one (Li[**3**H]) or two intramolecular bridges (**1**H$_2$). In addition, a B(μ-H)B unit embedded into a rigid cyclic structure experiences a substantial degree of structural constraint, which disfavors nucleophilic attack on the B atoms.[30] 4) Anionic starting materials should be avoided in order to ensure that the μ-H atom is sufficiently protic and the accumulation of negative charge in the deprotonation product is prevented. A variety of diborane(6) derivatives meeting the above requirements are already known[20,31,32] and others will be developed to put the deprotonation/B–B-coupling reaction on a broader basis.

Acknowledgements

T.K. thanks the Fonds der Chemischen Industrie for a Ph.D. grant. We also thank Albemarle Lithium GmbH (Frankfurt) for the generous gift of chemicals.

Conflict of interest

The authors declare no conflict of interest.

Keywords: acidity · B–B coupling · boranes · C–H activation · hydrides

How to cite: *Angew. Chem. Int. Ed.* **2017**, *56*, 7546–7550
Angew. Chem. **2017**, *129*, 7654–7658

[1] J. Takaya, N. Iwasawa, *ACS Catal.* **2012**, *2*, 1993–2006.
[2] I. A. I. Mkhalid, J. H. Barnard, T. B. Marder, J. M. Murphy, J. F. Hartwig, *Chem. Rev.* **2010**, *110*, 890–931.
[3] M. Arrowsmith, H. Braunschweig, T. E. Stennett, *Angew. Chem. Int. Ed.* **2017**, *56*, 96–115; *Angew. Chem.* **2017**, *129*, 100–120.
[4] R. J. Brotherton, A. L. McCloskey, L. L. Petterson, H. Steinberg, *J. Am. Chem. Soc.* **1960**, *82*, 6242–6245.

 © 2017 Wiley-VCH Verlag GmbH & Co. KGaA, Weinheim

[5] J. D. Hoefelmeyer, F. P. Gabbaï, *J. Am. Chem. Soc.* **2000**, *122*, 9054 – 9055.
[6] A. Hübner, A. M. Diehl, M. Diefenbach, B. Endeward, M. Bolte, H.-W. Lerner, M. C. Holthausen, M. Wagner, *Angew. Chem. Int. Ed.* **2014**, *53*, 4832 – 4835; *Angew. Chem.* **2014**, *126*, 4932 – 4935.
[7] A. Hübner, T. Kaese, M. Diefenbach, B. Endeward, M. Bolte, H.-W. Lerner, M. C. Holthausen, M. Wagner, *J. Am. Chem. Soc.* **2015**, *137*, 3705 – 3714.
[8] Y. Shoji, T. Matsuo, D. Hashizume, M. J. Gutmann, H. Fueno, K. Tanaka, K. Tamao, *J. Am. Chem. Soc.* **2011**, *133*, 11058 – 11061.
[9] A. Hübner, M. Bolte, H.-W. Lerner, M. Wagner, *Angew. Chem. Int. Ed.* **2014**, *53*, 10408 – 10411; *Angew. Chem.* **2014**, *126*, 10576 – 10579.
[10] Y. Shoji, S. Kaneda, H. Fueno, K. Tanaka, K. Tamao, D. Hashizume, T. Matsuo, *Chem. Lett.* **2014**, *43*, 1587 – 1589.
[11] T. Kaese, A. Hübner, M. Bolte, H.-W. Lerner, M. Wagner, *J. Am. Chem. Soc.* **2016**, *138*, 6224 – 6233.
[12] A. Hübner, M. Diefenbach, M. Bolte, H.-W. Lerner, M. C. Holthausen, M. Wagner, *Angew. Chem. Int. Ed.* **2012**, *51*, 12514 – 12518; *Angew. Chem.* **2012**, *124*, 12682 – 12686.
[13] A. Hübner, A. M. Diehl, M. Bolte, H.-W. Lerner, M. Wagner, *Organometallics* **2013**, *32*, 6827 – 6833.
[14] M. L. Pinsky, A. C. Bond, *Inorg. Chem.* **1973**, *12*, 605 – 607.
[15] D. F. Gaines, T. V. Iorns, *J. Am. Chem. Soc.* **1967**, *89*, 3375 – 3376.
[16] D. A. Ruiz, G. Ung, M. Melaimi, G. Bertrand, *Angew. Chem. Int. Ed.* **2013**, *52*, 7590 – 7592; *Angew. Chem.* **2013**, *125*, 7739 – 7742.
[17] J. Landmann, F. Keppner, D. B. Hofmann, J. A. P. Sprenger, M. Häring, S. H. Zottnick, K. Müller-Buschbaum, N. V. Ignat'ev, M. Finze, *Angew. Chem. Int. Ed.* **2017**, *56*, 2795 – 2799; *Angew. Chem.* **2017**, *129*, 2839 – 2843.
[18] A. Wagner, S. Litters, J. Elias, E. Kaifer, H.-J. Himmel, *Chem. Eur. J.* **2014**, *20*, 12514 12527; it remains to be firmly established, whether the bridging or a terminal H atom is deprotonated. Transition-metal catalyzed dehydrogenative B–B coupling reactions have also been reported by Himmel et al.: a) O. Ciobanu, P. Roquette, S. Leingang, H. Wadepohl, J. Mautz, H.-J. Himmel, *Eur. J. Inorg. Chem.* **2007**, 4530 – 4534; b) O. Ciobanu, E. Kaifer, M. Enders, H.-J. Himmel, *Angew. Chem. Int. Ed.* **2009**, *48*, 5538 – 5541; *Angew. Chem.* **2009**, *121*, 5646 – 5649.
[19] É. Rochette, N. Bouchard, J. L. Lavergne, C. F. Matta, F.-G. Fontaine, *Angew. Chem. Int. Ed.* **2016**, *55*, 12722 – 12726; *Angew. Chem.* **2016**, *128*, 12914 – 12918.
[20] D. E. Young, S. G. Shore, *J. Am. Chem. Soc.* **1969**, *91*, 3497 – 3504.
[21] K. S. Pitzer, *J. Am. Chem. Soc.* **1945**, *67*, 1126 – 1132.
[22] A. B. Burg, *J. Am. Chem. Soc.* **1947**, *69*, 747 – 750.
[23] B. J. Duke, J. W. Linnett, *Trans. Faraday Soc.* **1966**, *62*, 2955 – 2968.
[24] R. A. Ogg, Jr., *J. Chem. Phys.* **1954**, *22*, 1933 – 1935.
[25] D. J. Goebbert, H. Hernandez, J. S. Francisco, P. G. Wenthold, *J. Am. Chem. Soc.* **2005**, *127*, 11684 – 11689.
[26] T. Doba, S. Noda, H. Yoshida, *Bull. Chem. Soc. Jpn.* **1979**, *52*, 21 – 24.
[27] A. Das, A. Hübner, M. Weber, M. Bolte, H.-W. Lerner, M. Wagner, *Chem. Commun.* **2011**, *47*, 11339 – 11341.
[28] A. Hübner, Z.-W. Qu, U. Englert, M. Bolte, H.-W. Lerner, M. C. Holthausen, M. Wagner, *J. Am. Chem. Soc.* **2011**, *133*, 4596 – 4609.
[29] In contrast to the acid-base reaction, treatment of Li[**1**H] with excess Li converts the starting material to Li_2[**1**] to a degree of 75% (cf. the SI).
[30] Z. Zhou, A. Wakamiya, T. Kushida, S. Yamaguchi, *J. Am. Chem. Soc.* **2012**, *134*, 4529 – 4532.
[31] S. Pospiech, S. Brough, M. Bolte, H.-W. Lerner, H. F. Bettinger, M. Wagner, *Chem. Commun.* **2012**, *48*, 5886 – 5888.
[32] S. Pospiech, M. Bolte, H.-W. Lerner, M. Wagner, *Chem. Eur. J.* **2015**, *21*, 8229 – 8236.

Manuscript received: March 6, 2017
Version of record online: May 22, 2017

 © 2017 Wiley-VCH Verlag GmbH & Co. KGaA, Weinheim

Angewandte Chemie
Eine Zeitschrift der Gesellschaft Deutscher Chemiker

Supporting Information

Deprotonation of a Seemingly Hydridic Diborane(6) to Build a B–B Bond

*Thomas Kaese, Hendrik Budy, Michael Bolte, Hans-Wolfram Lerner, and Matthias Wagner**

anie_201702393_sm_miscellaneous_information.pdf

Table of contents:

1. General experimental procedures S1
2. Nomenclature and numbering for NMR assignments S1
3. Experimental details and characterization data S2
4. Titration of Li_2[**1**] with ethereal HCl S7
5. Comproportionation of Li_2[**1**] with **1**H_2 S8
6. Influence of the cation on the ^{1}H NMR shift values of the [**1**H]$^-$ anion S9
7. Plots of NMR spectra S10
8. X-ray S20
9. References S29

1. General experimental procedures

All reactions, manipulations, and analyses were carried out in an argon-filled glovebox or by applying standard Schlenk techniques under an argon atmosphere. Hexane was dried over Na. THF and Et_2O were dried over Na/benzophenone (2-3 d); [D_8]THF was dried over Na-K alloy. Prior to use, the solvents were distilled from the drying agent and degassed by applying three freeze-pump-thaw cycles. Compound 2,7-di-*tert*-butyl-9-bromo-9-borafluorene (**BF**Br),[1] 2,7-di-*tert*-butyl-9*H*-9-borafluorene (**BF**H),[1] **1**H_2,[1] $(Me_3Si)_2NLi$,[2] and $(Me_3Si)_3CLi$[3] were synthesized according to literature procedures. $(Me_3Si)_2NK$ is commercially available and was used as received (Sigma Aldrich). NMR: Avance 300, Avance III 500 HD. Chemical shifts are referenced to (residual) solvent signals ($^1H/^{13}C\{^1H\}$; [D_8]THF: δ = 3.58/67.21 ppm)[4] or external $BF_3{\cdot}Et_2O$ (^{11}B; $^{11}B\{^1H\}$). Abbreviations: s = singlet, d = doublet, t = triplet, q = quartet, m = multiplet, br = broad, n.r. = multiplet expected in the NMR spectrum but not resolved, n.o. = not observed.

2. Nomenclature and numbering for NMR assignments

All-carbon compounds	**Boron-containing compounds**	
Dibenzo[*g*,*p*]chrysene	[**1**H]$^-$	
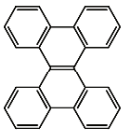	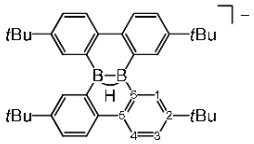	
Fluorene	**BF**R	[**BF**(H)R]$^-$
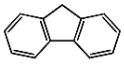	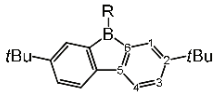	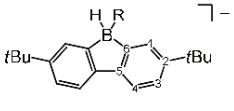

3. Experimental details and characterization data

Synthesis of K[1H] through deprotonation of $1H_2$:
In a glovebox, THF (3 mL) was added at room temperature to a glass vial charged with a solid mixture of $\mathbf{1}H_2$ (150 mg, 0.272 mmol) and $(Me_3Si)_2NK$ (55 mg, 0.28 mmol). The resulting clear, yellow solution was stirred for 3 min. The uncapped vial was placed into a larger glass vessel containing hexane (12 mL). The vessel was closed and stored for 2-3 d (to allow for gas-phase diffusion of the solvents), whereupon yellow single crystals formed. The mother liquor was removed via a syringe to isolate the crystals of $[K(thf)_2][\mathbf{1}H]$. Yield: 171 mg (0.23 mmol, 86%).
The ^{1}H, ^{11}B, and $^{13}C\{^{1}H\}$ NMR spectroscopic data ($[D_8]$THF) of $[K(thf)_2][\mathbf{1}H]$ were identical to those of a sample of the same compound obtained through reduction of $\mathbf{1}H_2$ with 1 equiv of KC_8.[5]

Synthesis of Li[1H] through deprotonation of $1H_2$:
$(Me_3Si)_2NLi$ as the base: In a glovebox, THF (3 mL) was added at room temperature to a glass vial charged with a solid mixture of $\mathbf{1}H_2$ (70 mg, 0.13 mmol) and $(Me_3Si)_2NLi$ (23 mg, 0.14 mmol). The resulting clear, yellow solution was stirred for 3 min. The uncapped vial was placed into a larger glass vessel containing hexane (5 mL). The vessel was closed and stored for 2-3 d (to allow for gas-phase diffusion of the solvents), whereupon yellow single crystals formed. The mother liquor was removed via a syringe to isolate the crystals of $[Li(thf)_3][\mathbf{1}H]$. Yield: 80 mg (0.10 mmol, 81%).

$(Me_3Si)_3CLi$ as the base: In a glovebox, THF (1.5 mL) was added at room temperature to a glass vial charged with a solid mixture of $\mathbf{1}H_2$ (50 mg, 0.09 mmol) and $(Me_3Si)_3CLi{\cdot}2THF$ (43 mg, 0.11 mmol). The resulting clear, yellow solution was stirred for 3 min. The uncapped vial was placed into a larger glass vessel containing hexane (5 mL). The vessel was closed and stored for 2-3 d (to allow for gas-phase diffusion of the solvents), whereupon yellow single crystals formed. The mother liquor was removed via a syringe to isolate the crystals of $[Li(thf)_3][\mathbf{1}H]$. Yield: 65 mg (0.08 mmol, 93%). Higher-quality crystals of $[Li(Et_2O)_2][\mathbf{1}H]$ were obtained from the analogous reaction between $\mathbf{1}H_2$ (50 mg, 0.09 mmol) and $(Me_3Si)_3CLi{\cdot}2THF$ (60 mg, 0.16 mmol) in Et_2O (7 mL). Since $\mathbf{1}H_2$ is much less soluble in Et_2O than in THF, the reaction solution should be decanted from any precipitate prior to the gas-phase diffusion step.

tBuLi as the base: A pentane solution of *t*BuLi (1.9 M, 0.07 mL, 0.13 mmol) was added at room temperature via a syringe to a stirred colorless suspension of $\mathbf{1}H_2$ (56 mg, 0.10 mmol) in Et_2O (3 mL). The resulting orange-red suspension was diluted with THF (2 mL) to give an orange-red solution. According to ^{1}H NMR spectroscopy, Li[**1**H] was the major constituent of the product mixture (ca. 45%). In a glovebox, the reaction solution was transferred to an uncapped glass vial, which was subsequently placed in a larger glass vessel containing hexane (6 mL). The outer vessel was closed to allow for gas-phase diffusion of the solvents.

After 2-3 d, two types of crystals had formed: yellow blocks and pale yellow needles. X-ray diffraction revealed the yellow blocks to consist of [Li(thf)$_3$][**1**H]. The solid-state structure of the co-precipitated needles could not be fully solved, even though it was possible to determine a unit cell: a = 26.321(5) Å, b = 10.694(2) Å, c = 21.388(4) Å; α = 90°, β = 114.94(3)°, γ= 90°; crystal system: monoclinic, space group: *Cc*.
Note: The analogous reaction of **1**H$_2$ with *t*BuLi in THF gave smaller yields of Li[**1**H] (< 20%).

*Li[**1**H]*
^{1}H NMR (500.2 MHz, [D$_8$]THF): δ = 8.75 (d, ^4J(H,H) = 2.2 Hz, 4H; H-1), 8.34 (d, ^3J(H,H) = 8.5 Hz, 4H; H-4), 7.24 (dd, ^3J(H,H) = 8.5 Hz, ^4J(H,H) = 2.2 Hz, 4H; H-3), 1.47 (s, 36H; CH$_3$), –1.19 ppm (br s, 1H; μ-H).
^{7}Li NMR (194.4 MHz, [D$_8$]THF): δ = –1.2 ppm.
^{11}B NMR (160.5 MHz, [D$_8$]THF): δ = 22.2 ppm (br).
^{13}C{^{1}H} NMR (125.8 MHz, [D$_8$]THF): δ = 146.5 (C-6), 144.8 (C-2), 138.9 (C-5), 127.8 (C-1), 125.3 (C-4), 120.0 (C-3), 35.0 (*C*(CH$_3$)$_3$), 32.4 ppm (C(*C*H$_3$)$_3$).

Reaction of 1H$_2$ with *n*BuLi:
A hexane solution of *n*BuLi (1.6 M, 0.07 mL, 0.11 mmol) was added at room temperature via a syringe to a stirred colorless solution of **1**H$_2$ (60 mg, 0.11 mmol) in THF (2 mL). According to ^{1}H NMR spectroscopy, Li[**1**H] formed in approximately 20% yield. In a glovebox, the reaction solution was transferred to an uncapped glass vial, which was subsequently placed in a larger glass vessel containing hexane (6 mL). The outer vessel was closed to allow for gas-phase diffusion of the solvents. After 2-3 d, two types of crystals had formed: yellow blocks and pale yellow needles. X-ray diffraction revealed the yellow blocks to consist of [Li(thf)$_4$][**2**H]. The compound was also characterized by NMR spectroscopy on manually selected single-crystalline material; with these data at hand, we were subsequently able to identify the resonances of Li[**2**H] also in the spectra of the crude reaction mixture (ca. 30% conversion to this compound). The crystal structure of the co-precipitated pale yellow needles could not be fully solved, even though it was possible to determine a unit cell, which was identical to the one of the reaction with *t*BuLi as the base.
Note: The analogous reaction of **1**H$_2$ with *n*BuLi in Et$_2$O with subsequent addition of THF (cf. the reaction with *t*BuLi as the base) gave comparable yields of Li[**1**H] and Li[**2**H].

*[Li(thf)$_4$][**2**H]*
^{1}H NMR (500.2 MHz, [D$_8$]THF): δ = 8.19 (d, ^4J(H,H) = 1.8 Hz, 2H; H-1), 8.02 (d, ^4J(H,H) = 1.8 Hz, 2H; H-1), 7.45 (d, ^3J(H,H) = 8.0 Hz, 2H; H-4), 7.42 (d, ^3J(H,H) = 8.0 Hz, 2H; H-4), 7.08 (dd, ^3J(H,H) = 8.0 Hz, ^4J(H,H) = 1.8 Hz, 2H; H-3), 7.06 (dd, ^3J(H,H) = 8.0 Hz, ^4J(H,H) = 1.8 Hz, 2H; H-3), 2.05-2.00 (m, 3H; CHC*H*$_2$, μ-H), 1.45 (s, 18H; C(CH$_3$)$_3$), 1.43 (s, 18H; C(CH$_3$)$_3$), 1.06-0.99 (m, 3H; CH, C*H*$_2$CH$_3$), 0.63 ppm (t, ^3J(H,H) = 7.4 Hz, 3H; CH$_2$C*H*$_3$).
^{7}Li NMR (116.6 MHz, [D$_8$]THF): δ = –2.8 ppm.
^{11}B NMR (160.5 MHz, [D$_8$]THF): δ = –12.8 ppm (br).
^{13}C{^{1}H} NMR (125.8 MHz, [D$_8$]THF): δ = 159.7* (C-6), 157.1* (C-6), 148.2 (C-5), 147.4 (C-5), 146.4 (C-2), 146.0 (C-2), 130.0 (C-1), 127.9 (C-1), 121.7 (C-3), 121.5 (C-3), 117.7 (C-4), 117.6 (C-4), 35.3

(*C*(CH)$_3$), 35.2 (*C*(CH)$_3$), 33.2 (CH*C*H$_2$), 32.7 (C(*C*H)$_3$), 32.7 (C(*C*H)$_3$), 28.2 (*C*H$_2$CH$_3$), 20.5 (CH), 14.9 ppm (CH$_2$*C*H$_3$). *) assigned via HMBC.

Attempts at the synthesis of K$_2$[1] through deprotonation of K[1H]:

In an attempt to achieve double deprotonation, we have also treated [K(thf)$_2$][**1**H] with (Me$_3$Si)$_2$NK (1.5 eq) in [D$_8$]THF at room temperature. The reaction was monitored by ^{1}H and ^{11}B NMR spectroscopy. The progress was slow, but after storage of the sample for approximately 1 month the starting material was consumed and the solution had adopted a red-purple color. The ^{1}H NMR spectrum revealed the presence of the [**1**]$^{2-}$ anion (which is a red compound),[5, 6] albeit only in trace amounts. As the two major products, we identified K[**BF**H$_2$][5] and K[**BF**(H)N(SiMe$_3$)$_2$]. Moreover, we observed the intermediate appearance of a yet unidentified species giving rise to an ^{11}B resonance at –11.8 ppm (d, ^1J(B,H) = 70 Hz). K$_3$(Et$_2$O)$_2$[**BF**H$_2$]$_3$ was crystallized in the form of light yellow needles from an analogous reaction between **1**H$_2$ (10 mg, 0.018 mmol) and (Me$_3$Si)$_2$NK (9 mg, 0.045 mmol) in Et$_2$O (1 mL). For the crystallization process, the reaction mixture was decanted and the clear solution was exposed to gas-phase diffusion with hexane (3 mL). An authentic sample of K[**BF**(H)N(SiMe$_3$)$_2$] was obtained on an NMR scale by the addition of **BF**H (13 mg, 0.047 mmol) in [D$_8$]THF to (Me$_3$Si)$_2$NK (10 mg, 0.050 mmol) in [D$_8$]THF.

*K[**BF**(H)N(SiMe$_3$)$_2$]*
^{1}H NMR (500.2 MHz, [D$_8$]THF): δ = 7.67 (d, ^4J(H,H) = 2.0 Hz, 2H; H-1), 7.40 (d, ^3J(H,H) = 7.8 Hz, 2H; H-4), 7.02 (dd, ^3J(H,H) = 7.8 Hz, ^4J(H,H) = 2.0 Hz, 2H; H-3), 3.08 (q, ^1J(B,H) = 74 Hz, 1H; BH), 1.35 (s, 18H; C(CH$_3$)$_3$), 0.25 (s, 9H; Si(CH$_3$)$_3$), –0.47 ppm (s, 9H; Si(CH$_3$)$_3$).
^{11}B NMR (160.5 MHz, [D$_8$]THF): δ = –8.2 ppm (d, ^1J(B,H) = 74 Hz).
^{13}C{^{1}H} NMR (125.8 MHz, [D$_8$]THF): δ = 168.9 (br q, C-6), 146.9 (C-2), 144.4 (C-5), 128.2 (C-1), 120.8 (C-3), 118.0 (C-4), 35.0 (*C*(CH$_3$)$_3$), 32.2 (C(*C*H$_3$)$_3$), 4.9 ppm (Si(*C*H$_3$)$_3$).
^{29}Si NMR (99.4 MHz, [D$_8$]THF): δ = –1.2, –8.4 ppm.

Synthesis of BFN(SiMe$_3$)$_2$:
In a glovebox, a colorless solution of (Me$_3$Si)$_2$NK (33 mg, 0.17 mmol) in toluene (2 mL) was added at room temperature with stirring to an orange-colored solution of **BF**Br (60 mg, 0.17 mmol) in toluene (2 mL). The resulting colorless precipitate (KBr) was removed via a glass frit and washed with toluene (2 x 1 mL). The yellow liquid phases were combined and all volatiles were removed in vacuo to give **BF**N(SiMe$_3$)$_2$ as a yellow solid. NMR samples in [D$_8$]THF and CDCl$_3$ show a blue-green fluorescence. A derivative of **BF**N(SiMe$_3$)$_2$ without *t*Bu groups has been described as a red semisolid by Rivard et al.[7]

^{1}H NMR (500.2 MHz, [D$_8$]THF): δ = 7.68 (dd, ^4J(H,H) = 1.9 Hz, ^5J(H,H) = 0.7 Hz, 2H; H-1), 7.31 (dd, ^3J(H,H) = 7.9 Hz, ^5J(H,H) = 0.7 Hz, 2H; H-4), 7.28 (dd, ^3J(H,H) = 7.9 Hz, ^4J(H,H) = 1.9 Hz, 2H; H-3), 1.33 (s, 18H; C(CH$_3$)$_3$), 0.40 ppm (s, 18H; Si(CH$_3$)$_3$).
^{11}B NMR (160.5 MHz, [D$_8$]THF): δ = 54.4 ppm.

$^{13}C\{^1H\}$ NMR (125.8 MHz, [D$_8$]THF): δ = 150.9 (C-5), 149.9 (C-2), 142.2 (br, C-6), 131.1 (C-1), 129.3 (C-3), 119.1 (C-4), 35.2 ($C(CH_3)_3$), 31.6 ($C(CH_3)_3$), 4.7 ppm ($Si(CH_3)_3$).
^{29}Si NMR (99.4 MHz, [D$_8$]THF): δ = 3.3 ppm.

^1H NMR (500.2 MHz, $CDCl_3$): δ = 7.68 (dd, ^4J(H,H) = 1.9 Hz, ^5J(H,H) = 0.7 Hz, 2H; H-1), 7.31 (dd, ^3J(H,H) = 7.9 Hz, ^5J(H,H) = 0.7 Hz, 2H; H-4), 7.27 (dd, ^3J(H,H) = 7.9 Hz, ^4J(H,H) = 1.9 Hz, 2H; H-3), 1.33 (s, 18H; $C(CH_3)_3$), 0.38 ppm (s, 18H; $Si(CH_3)_3$).
^{11}B NMR (160.5 MHz, $CDCl_3$): δ = 53.9 ppm.
$^{13}C\{^1H\}$ NMR (125.8 MHz, $CDCl_3$): δ = 150.1 (C-5), 149.5 (C-2), 141.9 (br, C-6), 130.9 (C-1), 128.5 (C-3), 118.5 (C-4), 34.9 ($C(CH_3)_3$), 31.6 ($C(CH_3)_3$), 4.9 ppm ($Si(CH_3)_3$).
^{29}Si NMR (99.4 MHz, $CDCl_3$): δ = 3.4 ppm.

Synthesis of Li_2[1] from Li[1H] and lithium granules:
In a glovebox, THF (2.5 mL) was added at room temperature to a glass vial charged with a solid mixture of $[Li(thf)_3]$[**1**H] (40 mg, 0.052 mmol) and Li granules (48 mg, 6.9 mmol). After 15 min of stirring, the initially yellow-colored solution had adopted a dark red color. The mixture was stirred overnight and unconsumed Li granules were removed by filtration via a glass frit. Compound $[Li(thf)_3]_2$[**1**][6] crystallized from the filtrate at –30 °C. Yield of crystalline product: 29 mg (0.029 mmol, 56%).
Note: The mother liquor was evaporated to dryness. According to NMR spectroscopy, the residue (26 mg) still contained about 40% of $[Li(thf)_3]_2$[**1**]. Thus, approximately 75% of $[Li(thf)_3]$[**1**H] was actually converted to $[Li(thf)_3]_2$[**1**].

Reaction of Li[3H] with $(Me_3Si)_3CLi$:
In a glovebox, $[Li(thf)_4]$[**3**H][8] (10 mg, 0.014 mmol) in [D$_8$]THF (0.6 mL) was placed at room temperature into an NMR tube already charged with solid $(Me_3Si)_3CLi{\cdot}2THF$ (10 mg, 0.026 mmol). The tube was flame sealed and the clear yellow reaction solution was heated to 150 °C for 90 min, whereupon the reaction mixture adopted an intense purple color (indicative of Li_2[**3**][8]). According to ^1H and ^{11}B NMR spectroscopy, the starting material had been consumed and Li_2[**3**] had formed in approximately 15% yield.

Reaction of $(Mes_2BH)_2$ with $(Me_3Si)_2NK$:
In a glovebox, [D$_8$]THF (1 mL) was added at room temperature to a glass vial charged with a solid mixture of $(Mes_2BH)_2$ (100 mg, 0.20 mmol) and $(Me_3Si)_2NK$ (100 mg, 0.50 mmol). The resulting purple solution was stirred for 10 min. Only two products were visible in the ^{11}B NMR spectrum of the reaction mixture: $K[Mes_2(H)B\text{-}N(SiMe_3)_2]$ (ca. 95%) and likely $K[Mes_2BH_2]$ (ca. 5%; δ = –22.5 ppm, t, ^1J(B,H) = 76 Hz). Colorless crystal plates of $[K(thf)_6][Mes_2(H)B\text{-}N(SiMe_3)_2]$ formed upon storage of the reaction solution at –40 °C.
Note: According to ^{11}B NMR spectroscopy, the use of an equimolar amount of $(Me_3Si)_2NK$ leads to the same product distribution together with some unconsumed starting material (ca. 33%).

K[Mes$_2$(H)B-N(SiMe$_3$)$_2$]

^{1}H NMR (500.2 MHz, [D$_8$]THF): δ = 6.47 (s, 1H; *m*-H), 6.34 (s, 1H; *m*-H), 6.28 (s, 1H; *m*-H), 6.22 (s, 1H; *m*-H), 3.83 (q, ^1J(B,H) = 83 Hz, 1H; BH), 2.70 (s, 3H; *o*-CH$_3$), 2.55 (s, 3H; *o*-CH$_3$), 2.07 (s, 6H; *p*-CH$_3$), 1.75 (s, 3H; *o*-CH$_3$), 1.61 (s, 3H; *o*-CH$_3$), –0.09 (s, 9H; Si(CH$_3$)$_3$), –0.26 ppm (s, 9H; Si(CH$_3$)$_3$).

^{11}B NMR (160.5 MHz, [D$_8$]THF): δ = –8.4 ppm (d, ^1J(B,H) = 83 Hz).

^{13}C{^{1}H} NMR (125.8 MHz, [D$_8$]THF): δ = 128.3 (*m*-CH), 127.4 (*m*-CH), 26.4 (*o*-CH$_3$), 26.0 (*o*-CH$_3$), 25.4 (*o*-CH$_3$)*, 23.6 (*o*-CH$_3$), 21.2 (*p*-CH$_3$), 6.2 (Si(CH$_3$)$_3$), 5.4 ppm (Si(CH$_3$)$_3$); n.o.: *o*-*C*CH$_3$, *p*-*C*CH$_3$, BC. *) detected via HSQC.

^{29}Si NMR (99.4 MHz, [D$_8$]THF): δ = –7.7, –6.0 ppm (detected via HMBC).

Reaction of (Mes$_2$BH)$_2$ with (Me$_3$Si)$_3$CLi:

In a glovebox, THF (1.5 mL) was added at room temperature to a glass vial charged with a solid mixture of (Mes$_2$BH)$_2$ (300 mg, 0.60 mmol) and (Me$_3$Si)$_3$CLi·2THF (315 mg, 0.82 mmol). The resulting magenta-colored solution was stirred for 3 min. Only two products were visible in the ^{11}B NMR spectrum ([D$_8$]THF, 96.3 MHz) of the reaction mixture: The major product (about 70%) possessed a chemical shift value of –13.3 ppm; the signal was not resolved at 298 K, but showed a doublet structure at 323 K (^1J(B,H) = 77 Hz). The minor product (about 30%) gave rise to a triplet already at 298 K with a chemical shift value of –23.6 ppm (^1J(B,H) = 73 Hz).

With the aim to grow crystals, 12-crown-4 (0.04 mL) was added to an aliquot (1 mL) of the reaction mixture, whereupon a magenta-colored precipitate formed. The mother liquor was discarded and the solid residue was dissolved in toluene at 90 °C. Colorless crystals of [Li(12-crown-4)$_2$][Mes$_2$BH$_2$] formed when the solution was slowly allowed to reach room temperature. We assume the major product to possess the structure Li[Mes$_2$(H)B-*C*(SiMe$_3$)$_3$] – similar to the amide adduct above.

[Li(12-crown-4)$_2$][Mes$_2$BH$_2$]

^{1}H NMR (500.2 MHz, [D$_8$]THF): δ = 6.44 (s, 4H; *m*-H), 3.60 (s, 32H; 12-crown-4), 2.32 (q, ^1J(B,H) = 76 Hz, 2H; BH), 2.17 (s, 12H; *o*-CH$_3$), 2.08 ppm (s, 6H; *p*-CH$_3$).

^{7}Li NMR (194.4 MHz, [D$_8$]THF): δ = –0.3 ppm (s).

^{11}B NMR (160.5 MHz, [D$_8$]THF): δ = –22.6 ppm (t, ^1J(B,H) = 76 Hz).

^{13}C{^{1}H} NMR (125.8 MHz, [D$_8$]THF): δ = 156.2 (q, ^1J(B,C) = 52 Hz; BC), 142.2 (*o*-*C*CH$_3$), 129.6 (*p*-*C*CH$_3$), 127.2 (*m*-CH), 70.4 (12-crown-4), 24.6 (*o*-CH$_3$), 21.1 ppm (*p*-CH$_3$).

4. Titration of Li_2[1] with ethereal HCl

To investigate the Brønsted basicity of Li_2[**1**], the compound was treated with varying amounts of an ethereal HCl solution:

An NMR tube was charged with $[Li(thf)_3]_2$[**1**] (20 mg, 0.02 mmol) in [D_8]THF (0.6 mL), cooled to −196 °C, flame-sealed, warmed to room temperature, and investigated by ^{1}H NMR spectroscopy (0.0 eq of HCl; Figure 1). The tube was re-opened under inert conditions, the solution was transferred to a new NMR tube, and an aliquot of an ethereal HCl solution (2.0 M) was added via a syringe. The flame-sealed sample was again measured by ^{1}H NMR spectroscopy. This procedure was repeated four times to gradually increase the amount of HCl in the reaction mixture from 0.1 eq to 2.0 eq.

As shown in Figure 1, the addition of substoichiometric amounts of an ethereal HCl solution to Li_2[**1**] leads to the consumption of the starting material with concomitant formation of Li[**1**H]. After 0.8 eq of HCl had been added, Li[**1**H] constituted the major product (ca. 80%), Li_2[**1**] was nearly spent (20%), and no **1**H_2 had been formed. A further increase in the amount of acid (1.7 eq in total) led to a color change from deep red to yellow and the proton signals of Li_2[**1**] completely vanished. **1**H_2 now appeared as the major product (ca. 70%), accompanied by Li[**1**H] as the minor product. The fact that Li_2[**1**] can cleanly be protonated twice to quantitatively furnish **1**H_2 is evident from the last titration step (2.0 equiv in total).

Importantly, compound **1**H_2 proved to be stable toward an excess (4 eq) of ethereal HCl in [D_8]THF for several days (note that slow degradation of **1**H_2 takes place in THF, even in the absence of a Brønsted acid[5]).

5. Comproportionation of Li_2[1] with $1H_2$

In order to find out whether Li_2[**1**] and **1**H_2 undergo proton exchange to furnish Li[**1**H], a solid mixture of these starting materials was placed in an NMR tube and dissolved in [D_8]THF. After a few minutes, the initially red color of the mixture (characteristic of Li_2[**1**]) had changed to yellow and subsequent ^{1}H and ^{11}B NMR spectroscopy revealed the clean and essentially quantitative formation of Li[**1**H] (Figure S1).

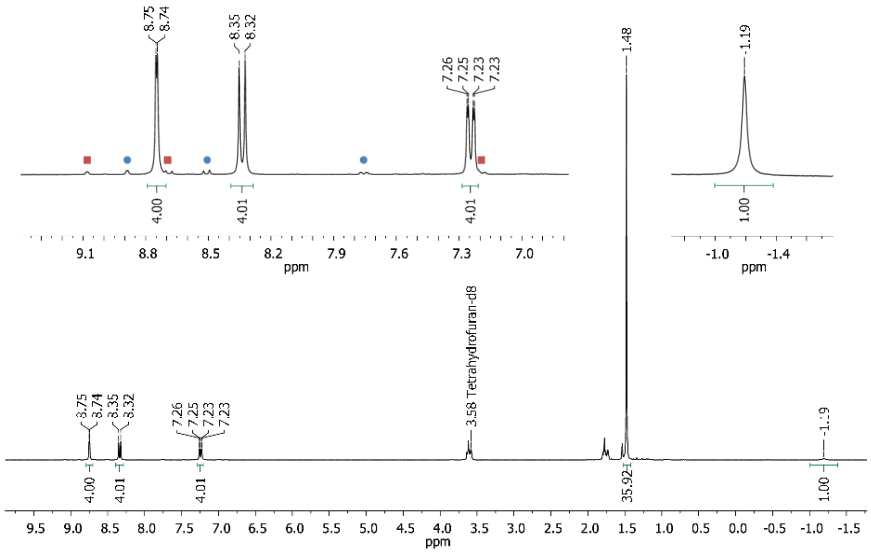

Figure S1. ^{1}H NMR spectrum ([D_8]THF, 300.0 MHz) of the reaction mixture of **1**H_2 (blue circles) and Li_2[**1**] (red squares) showing the essentially quantitative conversion to Li[**1**H]. *Note*: When the sample was measured again later, the signals of **1**H_2 and Li_2[**1**] had vanished completely.

6. Influence of the cation on the ^{1}H NMR shift values of the [1H]$^{-}$ anion

The ^{1}H NMR chemical shift values of [**1**H]$^{-}$ in [D$_8$]THF at room temperature depend on the respective counter cation Li^{+} or K^{+} (Figure S2). For the lithium salt, the ^{7}Li NMR resonance at –1.2 ppm indicates solvent-separated ion pairs.[9] K^{+} ions are known to possess a higher tendency to form contact-ion pairs with delocalized π systems than Li^{+} ions.[5, 10] The observed differences in the ^{1}H NMR chemical shifts of Li[**1**H] vs K[**1**H] are likely due to such enhanced cation-anion interactions.

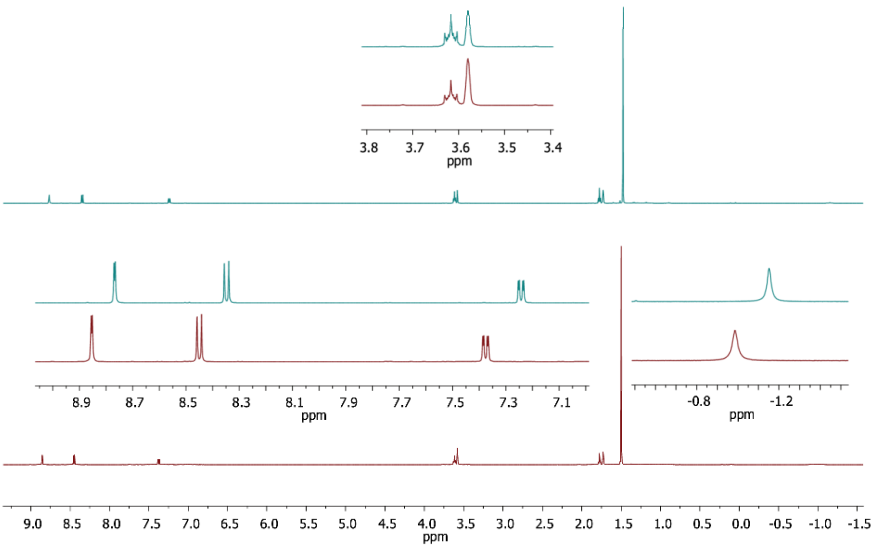

Figure S2. Comparison of the ^{1}H NMR spectra ([D$_8$]THF, 500.2 MHz) of Li[**1**H] (blue) and K[**1**H] (red).

7. Plots of NMR spectra

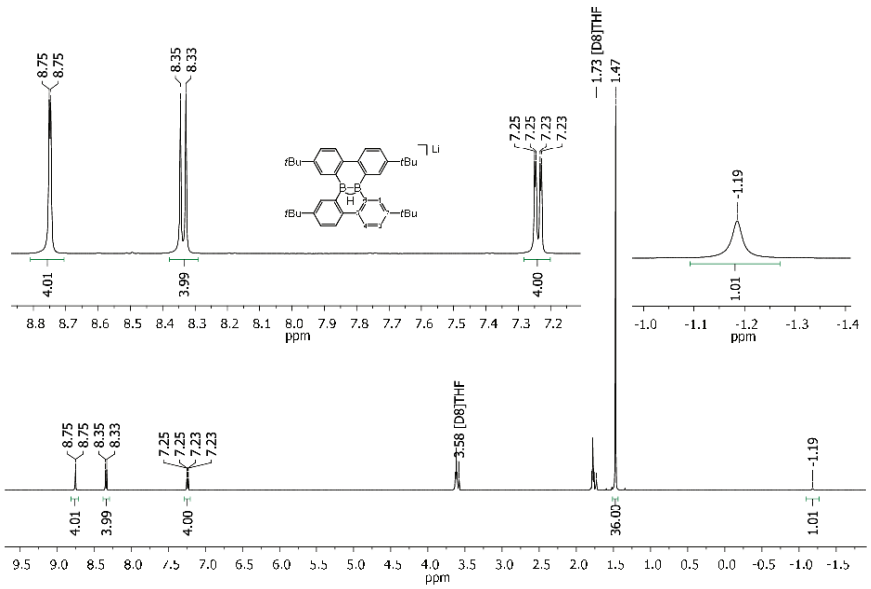

Figure S3. ^{1}H NMR spectrum of Li[**1**H] ([D_8]THF, 500.2 MHz).

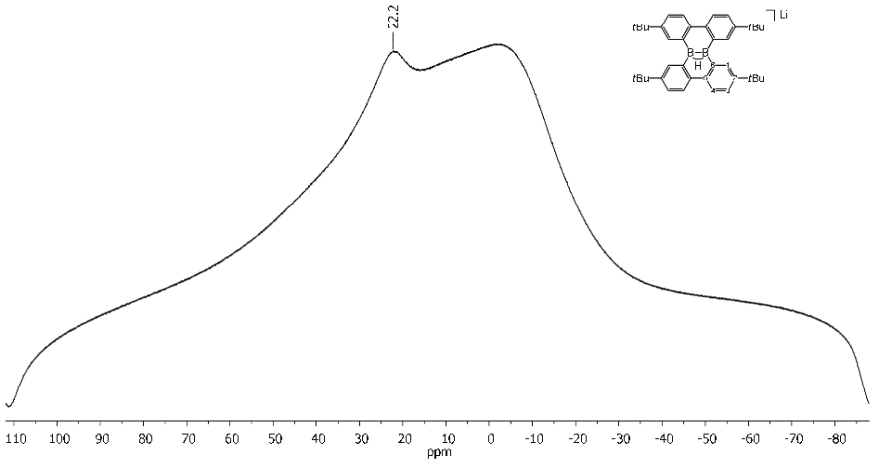

Figure S4. ^{11}B NMR spectrum of Li[**1**H] ([D_8]THF, 160.5 MHz).

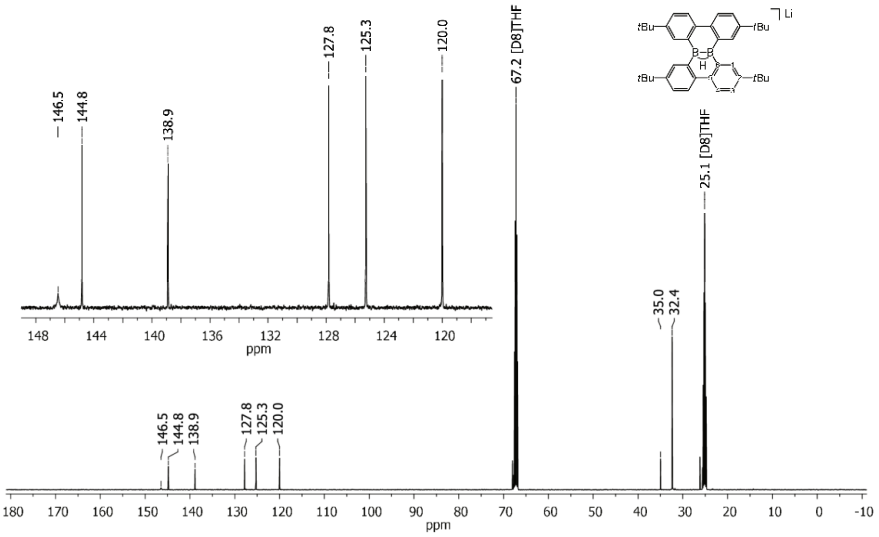

Figure S5. $^{13}C\{^{1}H\}$ NMR spectrum of Li[**1**H] ([D_8]THF, 125.8 MHz).

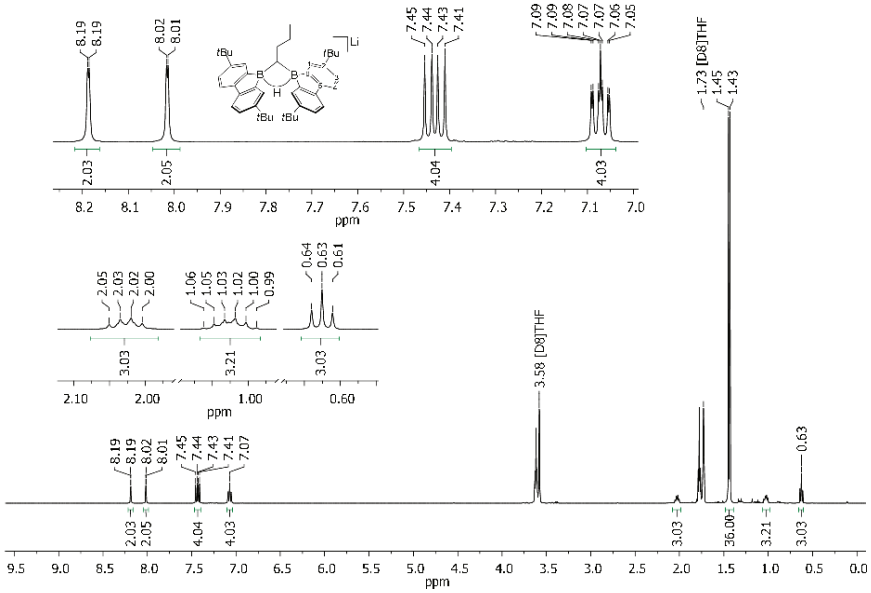

Figure S6. ^{1}H NMR spectrum of Li[**2**H] ([D_8]THF, 500.2 MHz).

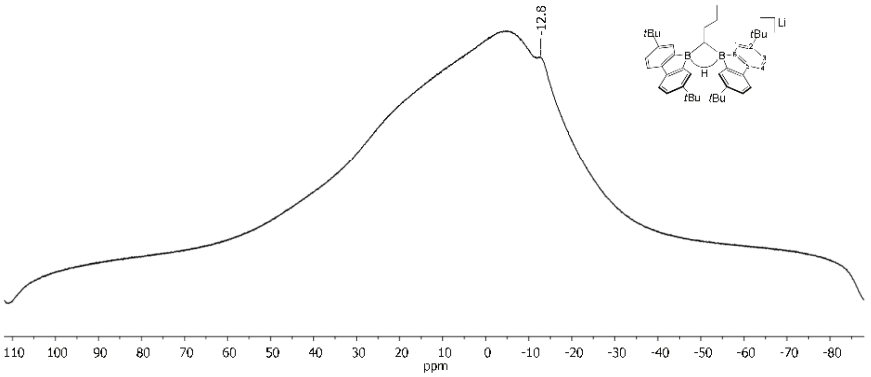

Figure S7. ^{11}B NMR spectrum of Li[**2**H] ([D_8]THF, 160.5 MHz).

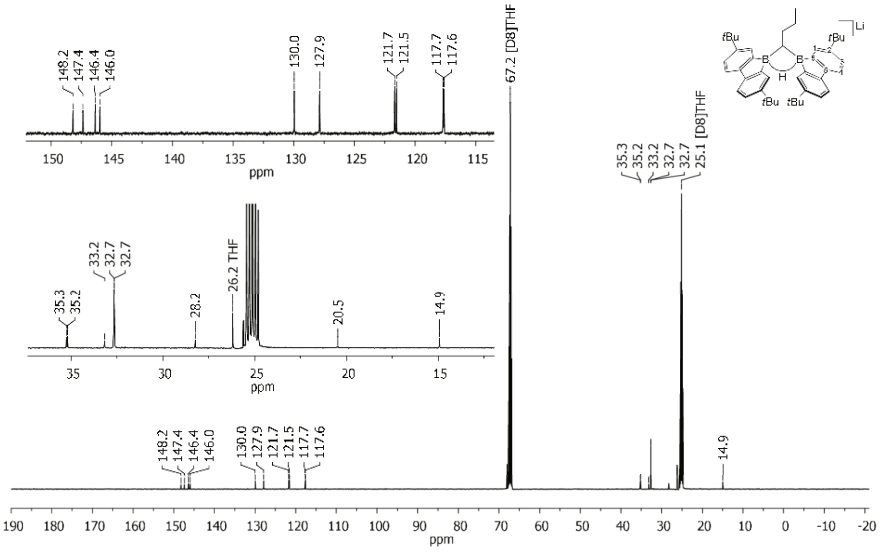

Figure S8. $^{13}C\{^{1}H\}$ NMR spectrum of Li[**2**H] ([D_8]THF, 125.8 MHz).

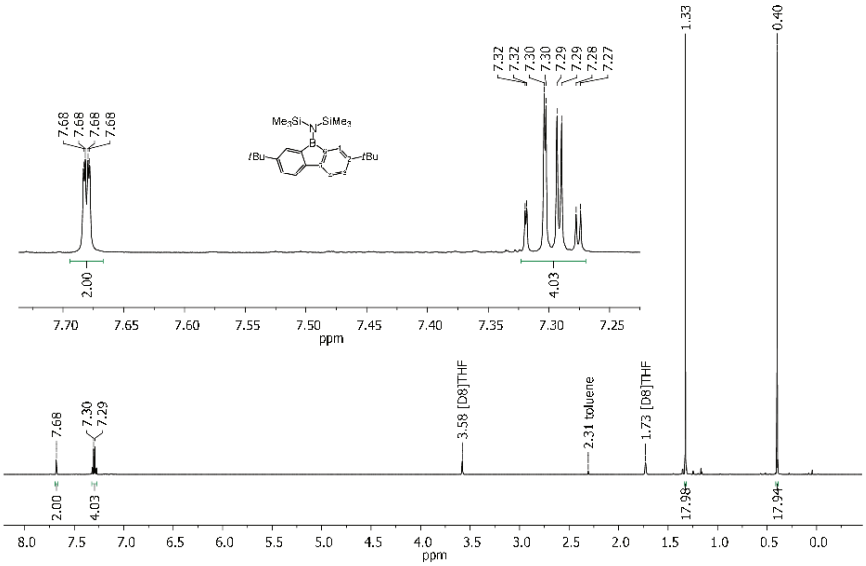

Figure S9. ^{1}H NMR spectrum of **BF**N(SiMe$_3$)$_2$ ([D$_8$]THF, 500.2 MHz).

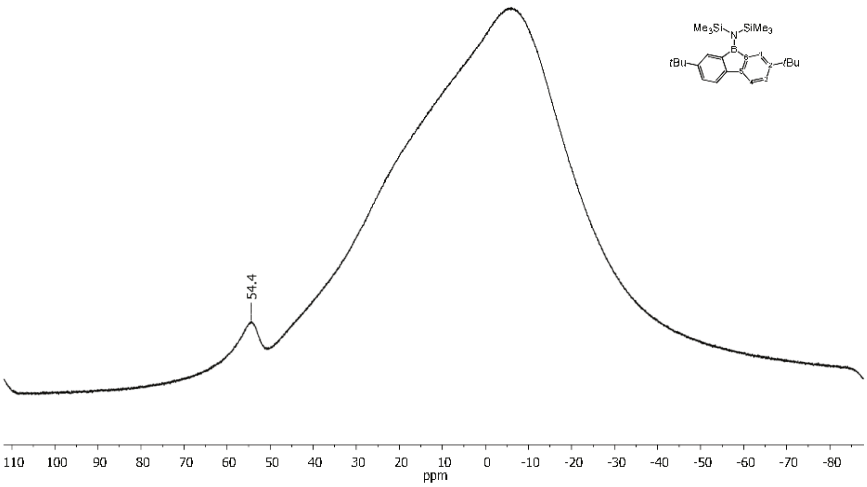

Figure S10. ^{11}B NMR spectrum of **BF**N(SiMe$_3$)$_2$ ([D$_8$]THF, 160.5 MHz).

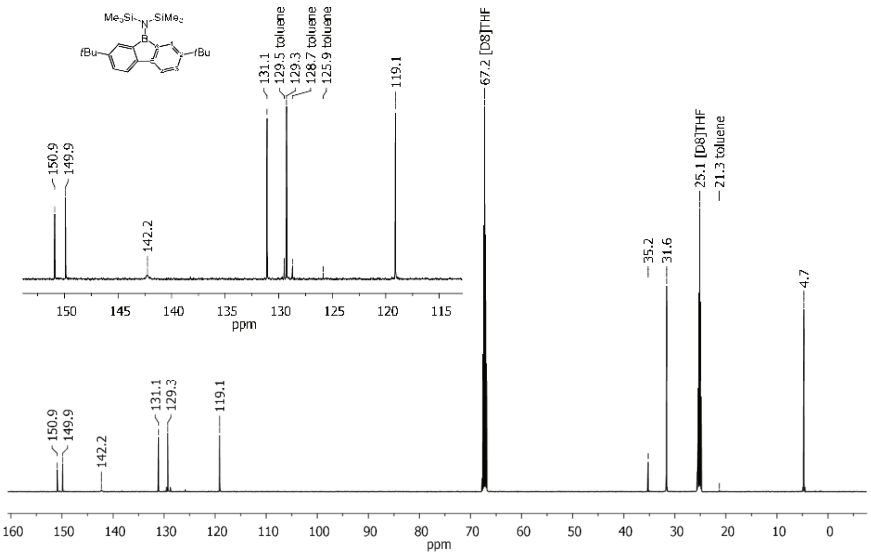

Figure S11. $^{13}C\{^{1}H\}$ NMR spectrum of **BF**N(SiMe$_3$)$_2$ ([D$_8$]THF, 125.8 MHz).

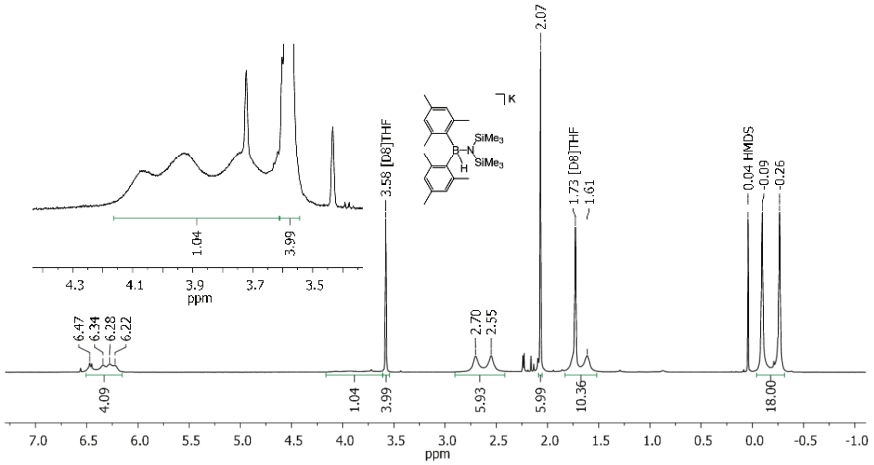

Figure S12. ^{1}H NMR spectrum of K[Mes_2(H)B-N($SiMe_3$)$_2$] ([D_8]THF, 500.2 MHz).

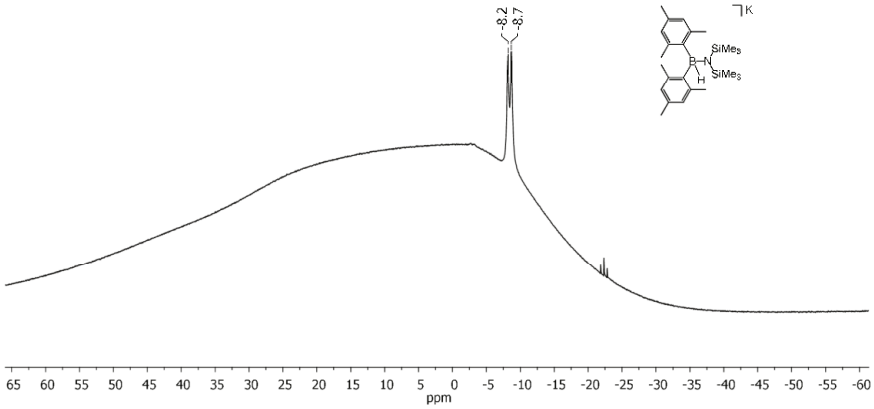

Figure S13. ^{11}B NMR spectrum of K[Mes_2(H)B-N($SiMe_3$)$_2$] ([D_8]THF, 160.5 MHz).

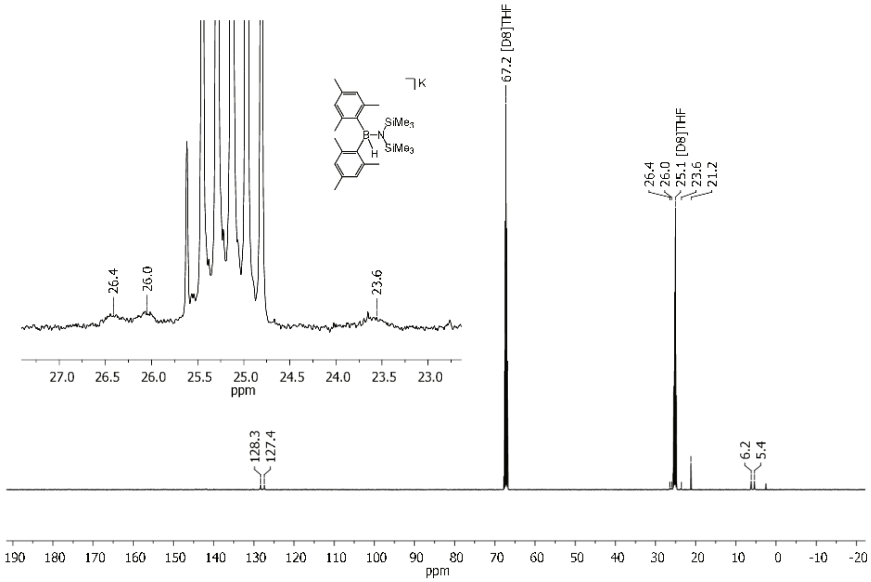

Figure S14. $^{13}C\{^{1}H\}$ NMR spectrum of $K[Mes_2(H)B\text{-}N(SiMe_3)_2]$ ($[D_8]THF$, 125.8 MHz).

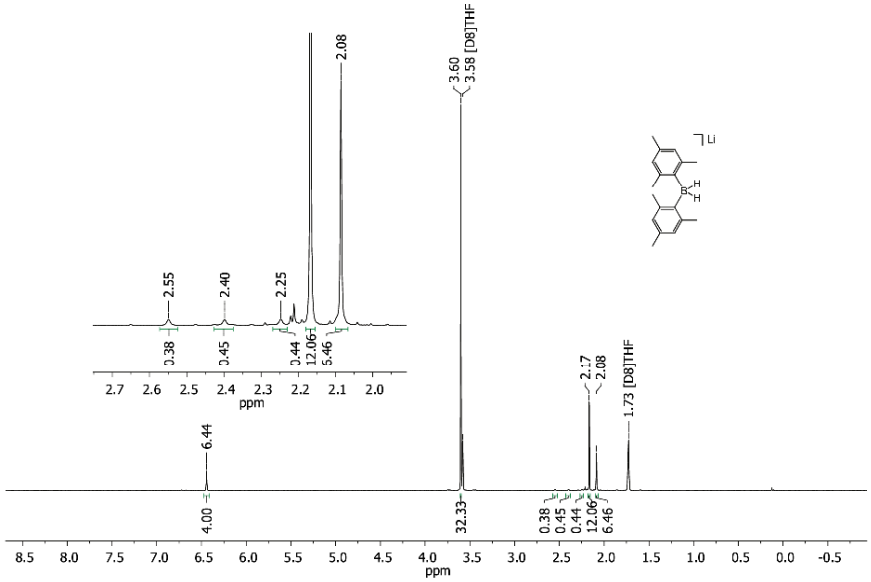

Figure S15. ^{1}H NMR spectrum of [Li(12-crown-4)$_2$][Mes$_2$BH$_2$] ([D$_8$]THF, 500.2 MHz).

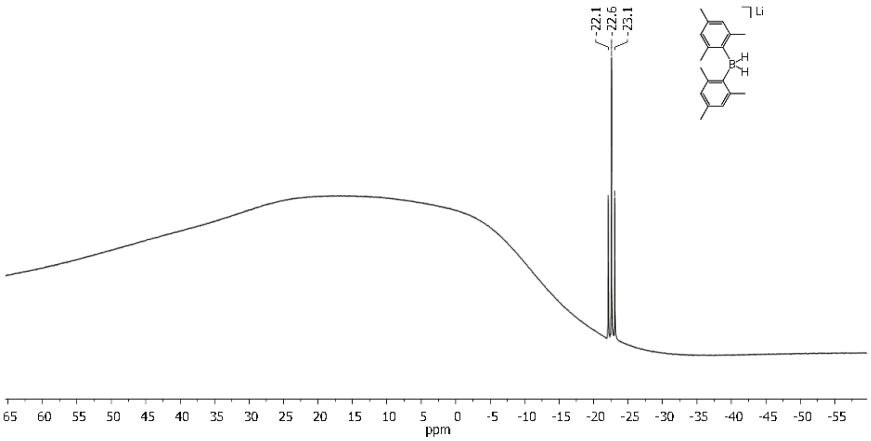

Figure S16. ^{11}B NMR spectrum of [Li(12-crown-4)$_2$][Mes$_2$BH$_2$] ([D$_8$]THF, 160.5 MHz).

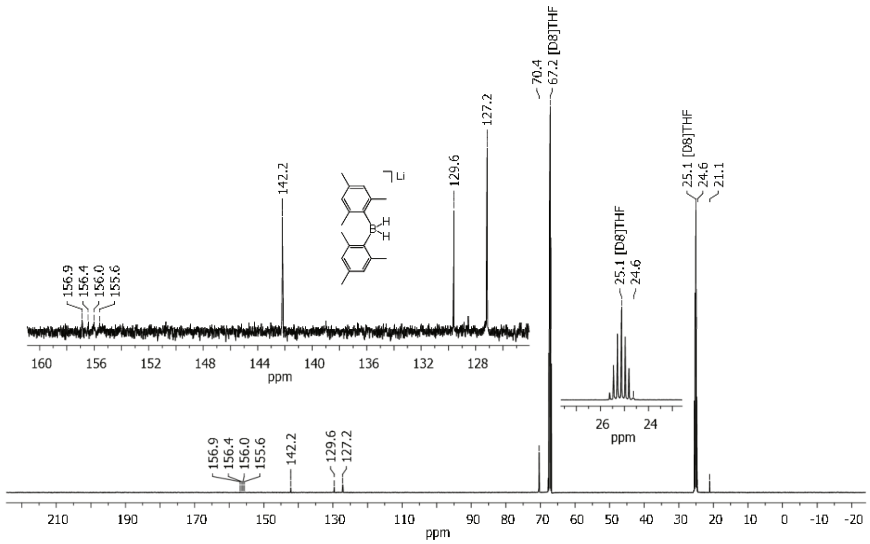

Figure S17. $^{13}C\{^{1}H\}$ NMR spectrum of $[Li(12\text{-crown-}4)_2][Mes_2BH_2]$ ($[D_8]THF$, 125.8 MHz).

8. X-ray

Data for all structures were collected on a STOE IPDS II two-circle diffractometer with a Genix Microfocus tube with mirror optics using MoK_α radiation (λ = 0.71073 Å). The data were scaled using the frame-scaling procedure in the *X-AREA* program system.[11] The structures were solved by direct methods using the program *SHELXS*[12] and refined against F^2 with full-matrix least-squares techniques using the program *SHELXL*.[12]

Structure	Internal code	CCDC reference number
$[Li(thf)_3][\mathbf{1}H]$	wa2059	1535883
$[Li(Et_2O)_2][\mathbf{1}H]$	wa2065	1535884
$[Li(thf)_4][\mathbf{2}H]$	wa2154	1535885
$[K(thf)_6][Mes_2(H)B\text{-}N(SiMe_3)_2]$	wa2250	1535886
$K[K(Et_2O)]_2[\mathbf{BF}H_2]_3$	wa2390	1535887
$[Li(12\text{-crown-}4)_2][Mes_2BH_2]$	wa2112	1535888

*[Li(thf)$_3$][**1**H]*

The structure shows pseudo-symmetry. The space group looks like $P2_1/c$, but refinement in this space group leads to $R1$ = 0.29, $wR2$ = 0.67, and two atoms are non-positive definite (NPD). The structure was finally refined in $P2_1$ with two crystallographically independent molecules in the asymmetric unit. In two thf ligands of molecule 1, one methylene group is disordered over two positions with site occupation factors of 0.62(6) and 0.65(7) for the major occupied sites. In one thf ligand of molecule 2, one methylene group is disordered over two positions with a site occupation factor of 0.56(3) for the major occupied site. One *t*Bu group is disordered over two positions with a site occupation factor of 0.65(3) for the major occupied site. The displacement parameters of all atoms in the thf ligands were restrained to an isotropic behavior. Equivalent bond lengths and angles in the *t*Bu groups and in the thf ligands, respectively, were restrained to be equal. The H atoms bonded to B were refined using a riding model. Due to the absence of anomalous scatterers, the absolute structure could not be determined reliably.

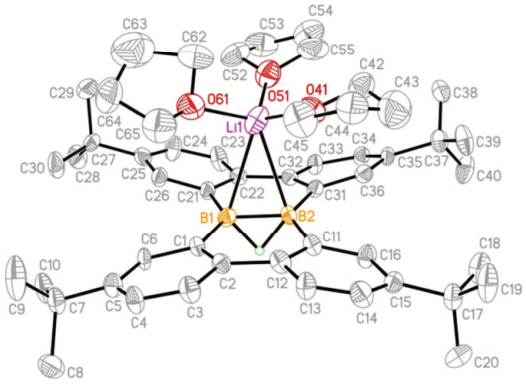

Figure S18. Molecular structure of [Li(thf)$_3$][**1**H] in the solid state. Displacement ellipsoids are shown at the 30% probability level; C*H* atoms are omitted for clarity. Although the poor quality of the crystal does not allow for a meaningful discussion of bond lengths and angles, the data were sufficient to provide proof of connectivity and confirm the presence of three thf ligands in the coordination sphere of the Li^+ ion.

*[Li(Et$_2$O)$_2$][**1**H]*

The asymmetric unit of [Li(Et$_2$O)$_2$][**1**H] contains two plus two half independent molecules. While their bond lengths differ only negligibly, the twists in their backbones vary significantly.

Five *t*Bu groups are disordered over two positions with site occupation factors of 0.584(8), 0.795(8), 0.56(2), 0.631(8), and 0.80(1) for the major occupied sites. The displacement parameters of the disordered atoms in the *t*Bu groups were restrained to an isotropic behavior. In one ether molecule, the O–C distances were restrained to 1.4(1) Å and the C–C distances to 1.500(2) Å. The displacement parameters of the atoms in this molecule were restrained to an isotropic behavior and the ellipsoids of bonded atoms were restrained to be similar. The H atoms bonded to B were isotropically refined.

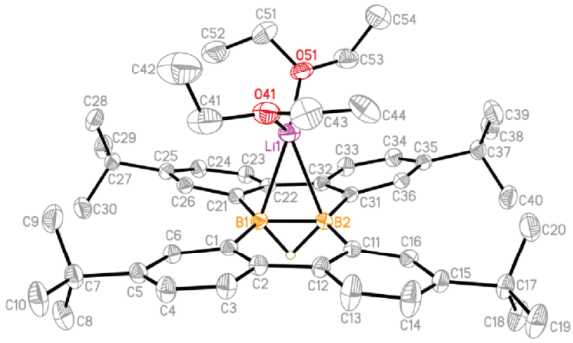

Figure S19. Molecular structure of one of the crystallographically independent molecules of [Li(Et$_2$O)$_2$][**1**H] in the solid state. Displacement ellipsoids are shown at the 30% probability level; C*H* atoms are omitted for clarity. Selected bond lengths [Å], atom···atom distances [Å], and torsion angles [°]: B1–B2 = 1.664(5), B1A–B2A = 1.662(5), B1B–B1B# = 1.678(7), B1C–B1C# = 1.656(6); Li1···B1 = 2.413(7), Li1···B2 = 2.450(7), Li1A···B1A = 2.510(7), Li1A···B2A = 2.379(7), Li1B···B1B = 2.427(8), Li1C···B1C = 2.422(8); C1–B1–B2–C11 = 1.9(4), C1A–B1A–B2A–C11A = 20.0(4), C1B–B1B–B1B#–C11B = –13.1(2), C1C–B1C–B1C#–C11C = –19.9(2), C2–C12–C32–C22 = 4.2(2), C2A–C12A–C32A–C22A = 31.6(2), C2B–C12B–C2B#–C12B# = 23.5(3), C2C–C12C–C2C#–C12C# = 32.1(3). Symmetry transformation used to generate equivalent atoms (#): –x+1, y, –z+1/2.

*[Li(thf)$_4$][**2**H]*

One *t*Bu group is disordered over two positions with a site occupation factor of 0.697(9) for the major occupied site. The displacement parameters of the disordered atoms and of C10, C19, C30, C44 (cation), and C74 (cation) were restrained to an isotropic behavior. The geometric parameters of the disordered *t*Bu group were restrained to those of the non-disordered group C7-C10. The H atoms bonded to B and C1' were isotropically refined.

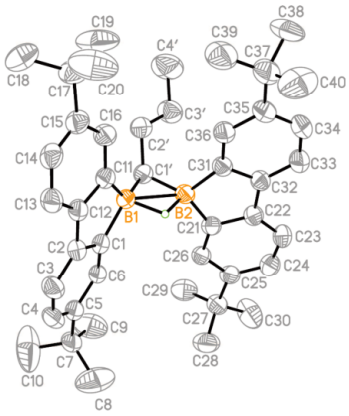

Figure S20. Molecular structure of the anion [**2**H]$^-$ of [Li(thf)$_4$][**2**H] in the solid state. Displacement ellipsoids are shown at the 50% probability level; C*H* atoms are omitted for clarity. Selected atom···atom distance [Å], bond lengths [Å], and bond angles [°]: B1···B2 = 1.967(4); B1–C1 = 1.626(4), B1–C11 = 1.629(4), B1–C1′ = 1.579(4), B2–C21 = 1.617(4), B2–C31 = 1.618(4), B2–C1′ = 1.631(4); B1–C1'–B2 = 75.6(2), C1–B1–C11 = 100.4(2), C1'–B1–C1 = 127.0(2), C1'–B1–C11 = 125.6(2), C21–B2–C31 = 101.1(2), C21–B2–C1' = 119.1(2), C31–B2–C1' = 123.5(2).

[K(thf)$_6$][Mes$_2$(H)B-N(SiMe$_3$)$_2$]

The crystal of [K(thf)$_6$][Mes$_2$(H)B-N(SiMe$_3$)$_2$] was a non-merohedral twin with a fractional contribution of 0.526(1) for the major domain. The asymmetric unit contains 2 crystallographically independent molecules.
Six thf ligands are disordered, each of them over two positions with site occupation factors of 0.59(4), 0.52(4), 0.62(2), 0.55(3), 0.72(3), and 0.78(4) for the major occupied sites. The geometric parameters of the disordered thf ligands were restrained to those of the non-disordered ligand thf(O81-C85). The displacement parameters of the K^+ cations and the thf ligands were restrained to an isotropic behavior and the ellipsoids of bonded atoms were restrained to be similar. The H atoms bonded to B were refined using a riding model.

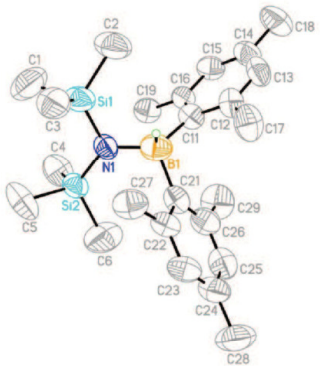

Figure S21. Molecular structure of the anion [Mes$_2$(H)B-N(SiMe$_3$)$_2$]$^-$ of [K(thf)$_6$][Mes$_2$(H)B-N(SiMe$_3$)$_2$] in the solid state. Displacement ellipsoids are shown at the 50% probability level; *CH* atoms are omitted for clarity. Selected bond lengths [Å], and bond angles [°] for the two crystallographically independent anions [Mes$_2$(H)B-N(SiMe$_3$)$_2$]$^-$: B1–N1 = 1.570(10)/1.616(9), B1–C11 = 1.664(9)/1.682(11), B1–C21 = 1.692(10)/1.630(10), N1–Si1 = 1.719(5)/1.716(6), N1–Si2 = 1.719(5)/1.702(5); N1–B1–C11 = 118.8(6)/111.8(5), N1–B1–C21 = 113.4(5)/115.8(6), C11–B1–C21 = 111.5(5)/115.7(6), B1–N1–Si1 = 109.1(4)/108.5(4), B1–N1–Si2 = 130.5(4)/129.1(5), Si1–N1–Si2 = 119.6(3)/121.2(3).

*K[K(Et$_2$O)]$_2$[**BF**H$_2$]$_3$*

One *t*Bu group is disordered over two positions with a site occupation factor of 0.77(1) for the major occupied site. One Et_2O molecule is disordered over two positions with a site occupation factor of 0.51(3) for the major occupied site. The displacement parameters of the disordered atoms were restrained to an isotropic behavior. The coordinates of the H atoms bonded to B were isotropically refined.

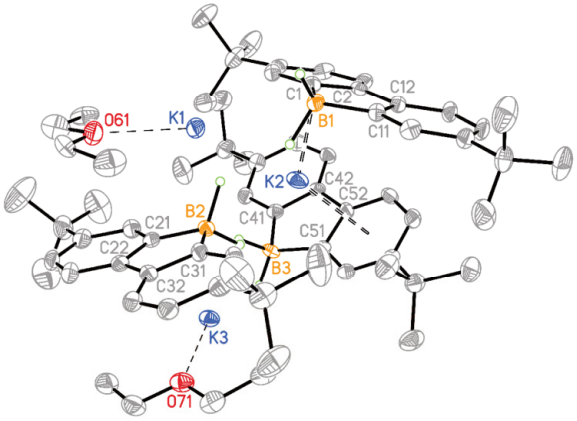

Figure S22. Molecular structure of K[K(Et$_2$O)]$_2$[**BF**H$_2$]$_3$ in the solid state. Displacement ellipsoids are shown at the 30% probability level; C*H* atoms are omitted for clarity. Selected bond lengths [Å], bond angles [°], and torsion angles [°]: B1–C1 = 1.627(9), B1–C11 = 1.603(8), B2–C21 = 1.637(9), B2–C31 = 1.628(9), B3–C41 = 1.617(9), B3–C51 = 1.626(9), K1–B1 = 3.232(7), K1–B2 = 3.318(7), K1–O61 = 2.597(6), K2–B2 = 3.148(7), K2–B3 = 3.408(7), K3–B2 = 3.407(7), K3–B3 = 3.168(7), K3–O71 = 2.608(5); C1–B1–C11 = 100.0(5), C21–B2–C31 = 99.9(5), C41–B3–C51 = 98.6(5); C1–C2–C12–C11 = 1.2(6), C21–C22–C32–C31 = 4.6(6), C41–C42–C52–C51 = 1.7(6).

[Li(12-crown-4)$_2$][Mes$_2$BH$_2$]

The H atoms bonded to B were isotropically refined. Due to the absence of anomalous scatterers, the absolute structure could not be determined reliably.

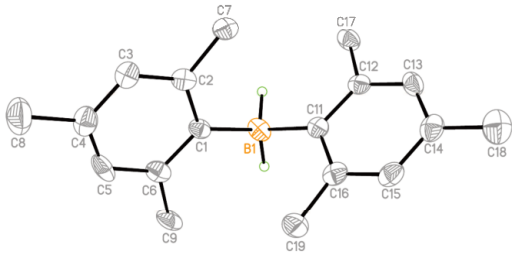

Figure S23. Molecular structure of the anion [Mes$_2$BH$_2$]$^-$ of [Li(12-crown-4)$_2$][Mes$_2$BH$_2$] in the solid state. Displacement ellipsoids are shown at the 50% probability level; C*H* atoms are omitted for clarity. Selected bond lengths [Å], bond angle [°], and torsion angles [°]: B1–C1 = 1.657(8), B1–C11 = 1.619(9); C11–B1–C1 = 117.7(4); C1–B1–C11–C16 = 62.6(7), C11–B1–C1–C2 = 61.4(8).

Table S1. Selected crystallographic data for [Li(thf)$_3$][**1**H], [Li(Et$_2$O)$_2$][**1**H], and [Li(thf)$_4$][**2**H].

	[Li(thf)$_3$][**1**H]	[Li(Et$_2$O)$_2$][**1**H]	[Li(thf)$_4$][**2**H]
formula	$C_{52}H_{73}B_2LiO_3$	$C_{48}H_{69}B_2LiO_2$	$C_{60}H_{89}B_2LiO_4$
M_r	774.66	706.59	902.87
color, shape	light yellow, block	light yellow, plate	yellow, block
T [K]	173(2)	173(2)	173(2)
radiation, λ [Å]	MoK_α, 0.71073	MoK_α, 0.71073	MoK_α, 0.71073
crystal system	monoclinic	monoclinic	monoclinic
space group	$P2_1$	$C2/c$	$P2_1/n$
a [Å]	14.6712(4)	34.7774(11)	12.1956(5)
b [Å]	21.2778(8)	15.2332(5)	24.7502(6)
c [Å]	15.5361(4)	49.4591(12)	19.0757(7)
α [°]	90	90	90
β [°]	106.415(2)	90.952(2)	93.467(3)
γ [°]	90	90	90
V [Å^3]	4652.2(3)	26198.4(14)	5747.3(3)
Z	4	24	4
D_{calcd} [g cm^{-3}]	1.106	1.075	1.043
μ [mm^{-1}]	0.065	0.062	0.062
F(000)	1688	9264	1976
crystal size [mm]	0.34 x 0.28 x 0.26	0.32 x 0.27 x 0.11	0.32 x 0.28 x 0.23
rflns collected	57805	91604	55481
independent rflns (R_{int})	17615 (0.0701)	23046 (0.1159)	10134 (0.0524)
data/restraints/parameters	17615 / 440 / 1042	23046 / 240 / 1585	10134 / 84 / 641
GOF on F^2	1.554	0.884	1.041
R_1, wR_2 [$I > 2\sigma(I)$]	0.1341, 0.3796	0.0687, 0.1594	0.0914, 0.2602
R_1, wR_2 (all data)	0.1487, 0.3896	0.1464, 0.1891	0.1175, 0.2832
largest diff peak and hole [e Å^{-3}]	0.915, –0.603	1.012, –0.707	0.850, –0.329

Table S2. Selected crystallographic data for $[K(thf)_6][Mes_2(H)B\text{-}N(SiMe_3)_2]$, $K[K(Et_2O)]_2[\mathbf{BF}H_2]_3$, and $[Li(12\text{-crown-}4)_2][Mes_2BH_2]$.

	$[K(thf)_6][Mes_2(H)B\text{-}N(SiMe_3)_2]$	$K[K(Et_2O)]_2[\mathbf{BF}H_2]_3$	$[Li(12\text{-crown-}4)_2][Mes_2BH_2]$
formula	$C_{48}H_{89}BKNO_6Si_2$	$C_{68}H_{98}B_3K_3O_2$	$C_{34}H_{56}BLiO_8$
M_r	882.29	1097.19	610.53
color, shape	colorless, block	light yellow, needle	colorless, needle
T [K]	173(2)	173(2)	173(2)
radiation, λ [Å]	MoK_α, 0.71073	MoK_α, 0.71073	MoK_α, 0.71073
crystal system	triclinic	triclinic	monoclinic
space group	*P*–1	*P*–1	*Pn*
a [Å]	15.1347(8)	13.668(2)	9.7235(9)
b [Å]	17.5190(12)	15.362(3)	8.4710(7)
c [Å]	20.7967(15)	18.499(4)	20.918(2)
α [°]	78.139(6)	91.970(16)	90
β [°]	87.398(5)	90.887(15)	98.755(8)
γ [°]	88.852(5)	114.828(13)	90
V [Å^3]	5390.5(6)	3521.2(12)	1702.9(3)
Z	4	2	2
D_{calcd} [g cm^{-3}]	1.087	1.035	1.191
μ [mm^{-1}]	0.185	0.232	0.082
F(000)	1936	1188	664
crystal size [mm]	0.29 x 0.24 x 0.23	0.27 x 0.11 x 0.09	0.29 x 0.11 x 0.08
rflns collected	81718	45984	12321
independent rflns (R_{int})	81718	12407 (0.1446)	5710 (0.0885)
data/restraints/parameters	81718 / 2320 / 1181	12407 / 84 / 768	5710 / 2 / 411
GOF on F^2	0.964	1.187	0.909
R_1, wR_2 [$I > 2\sigma(I)$]	0.1040, 0.2491	0.1099, 0.1575	0.0603, 0.1191
R_1, wR_2 (all data)	0.1821, 0.2995	0.2167, 0.1843	0.1010, 0.1329
largest diff peak and hole [e Å^{-3}]	0.539, –0.280	0.357, –0.294	0.383, –0.198

9. References

[1] A. Hübner, M. Diefenbach, M. Bolte, H.-W. Lerner, M. C. Holthausen, M. Wagner, *Angew. Chem. Int. Ed.* **2012**, *51*, 12514-12518; *Angew. Chem.* **2012**, *124*, 12682 –12686.

[2] M. W. Rathke, *Org. Synth.* **1973**, *53*, 66.

[3] M. A. Cook, C. Eaborn, A. E. Jukes, D. R. M. Walton, *J. Organomet. Chem.* **1970**, *24*, 529-535.

[4] G. R. Fulmer, A. J. M. Miller, N. H. Sherden, H. E. Gottlieb, A. Nudelman, B. M. Stoltz, J. E. Bercaw, K. I. Goldberg, *Organometallics* **2010**, *29*, 2176-2179.

[5] T. Kaese, A. Hübner, M. Bolte, H.-W. Lerner, M. Wagner, *J. Am. Chem. Soc.* **2016**, *138*, 6224-6233.

[6] A. Hübner, M. Bolte, H.-W. Lerner, M. Wagner, *Angew. Chem. Int. Ed.* **2014**, *53*, 10408-10411; *Angew. Chem.* **2014**, *126*, 10576 –10579.

[7] C. J. Berger, G. He, C. Merten, R. McDonald, M. J. Ferguson, E. Rivard, *Inorg. Chem.* **2014**, *53*, 1475-1486.

[8] A. Hübner, T. Kaese, M. Diefenbach, B. Endeward, M. Bolte, H.-W. Lerner, M. C. Holthausen, M. Wagner, *J. Am. Chem. Soc.* **2015**, *137*, 3705-3714.

[9] C. Elschenbroich, *Organometallics*, Wiley-VCH, Weinheim, **2006**.

[10] A. H. Ilkhechi, M. Bolte, H.-W. Lerner, M. Wagner, *J. Organomet. Chem.* **2005**, *690*, 1971-1977.

[11] Stoe & Cie, *X-AREA*. Diffractometer control program system, Darmstadt, Germany, **2002**.

[12] G. M. Sheldrick, *Acta Crystallogr., Sect. A: Found. Crystallogr.* **2008**, *64*, 112-122.

6.2.4 Hydroboration as an Efficient Tool for the Preparation of Electronically and Structurally Diverse N→B-Heterocycles

ChemPubSoc Europe

DOI: 10.1002/chem.201602458

CHEMISTRY A European Journal Full Paper

Structure–Property Relationships

Hydroboration as an Efficient Tool for the Preparation of Electronically and Structurally Diverse N→B-Heterocycles

Markus Grandl,[a] Thomas Kaese,[b] Anke Krautsieder,[a] Yu Sun,[c] and Frank Pammer*[a]

Abstract: Ladder-type organoboranes featuring intramolecular N→B coordination have been prepared through hydroboration of a 2-(*ortho*-styryl)pyridine (**PhPy**) with a series of hydroboranes, including 9*H*-9-borabicyclo[3.3.1]nonyl (9*H*-BBN), BH_3·THF, $HBCl_2$·SMe_2, $HB(C_6F_5)_2$, and a 9*H*-9-borafluorene derivative. The hydroboration reaction results in highly regioselective borylation under mild conditions and gives the products in good to excellent yields. The molecular structure and electronic properties of the obtained boranes have been experimentally investigated in detail, and complemented with DFT calculations to further elucidate the origin of differences in optical and electronic properties. The electron affinity of the conjugated system can be controlled through variation of the borane, while the optical properties are likewise directly linked to the type and molecular structure of the substituents on boron. The broad substrate range shows that this preparative approach is widely applicable to introduce chemically diverse boryl groups into conjugated systems.

Introduction

Organic materials featuring tri- and tetracoordinated boron centers have attracted growing attention due to their unusual optical and electronic properties.[1] Boron-containing conjugated materials are being investigated as chemical sensors[2] and as active components in organic light-emitting diodes,[3] and organic photovoltaics.[4,5]

However, one area of organoborane chemistry that has gained increasing traction in recent years is the isosteric substitution of C=C double bonds in conjugated systems by covalent B–N moieties,[6,7] particularly because individual N–B-substituted organic semiconducting materials outperform their all-carbon analogues.[8] Consequently, there is vital interest in the development of methods that give preparative access to these kinds of compounds, or to suitable precursors that may be converted into the B–N isosters. One such class of precursor are alkylboryl-functionalized conjugated heteroarenes, wherein the molecular geometry allows for intramolecular N→B Lewis adduct formation that gives rise to six-membered coordinative N→B rings (e.g., Scheme 1 a–d). Only recently has it been shown that these systems can undergo elimination to the corresponding fully conjugated N–B substituted isosters of polycyclic aromatic hydrocarbons.[9] However, a key hurdle in the study of these types of N→B ladder compounds is the limited number of chemical transformations by which they can be generated, and lack of broadly applicable methods to introduce different substituents on boron with moderate preparative effort. The latter is particularly desirable because both the electronic and chemical properties of a given conjugated N→B ladder system can be further modulated through variation of the substituents on boron and can thus be tailored towards specific applications.

Conjugated π-systems that contain five-membered coordinative N→B rings have been variously prepared by nucleophilic aromatic substitution,[10] direct electrophilic C-H borylation,[11] and, most commonly, by stepwise lithiation and electrophilic borylation of suitable precursors.[1,12–15] Conversely, methods to prepare the alkylboryl-bridged six-membered ring systems of interest herein have so far been limited to stepwise lithiation and electrophilic borylation of suitable precursors (Scheme 1 a),[9b–d] and to an unusual 1,1-hydroboration of highly reactive isoindoles (Scheme 1 b).[9a,e,f] In our group, we are interested in generating the same basic structure from more readily available functional groups through classical 1,2-hydroboration. 1,2-Hydroboration is a mild, efficient, and atom-economic method to introduce boryl groups into organic compounds[16] and is increasingly used to functionalize conjugated electronic materials,[17–20] or to prepare boron-containing polymers through polyhydroboration.[18b,21,22] Regioselectivity in hydroboration reactions is primarily controlled by steric factors.[16a] However, earlier reports and our own current results have shown that the hydroboration of 2-(1-alkenyl)-[23,24] and 2-ethy-

[a] M. Grandl, A. Krautsieder, Dr. F. Pammer
Institute of Organic Chemistry II and Advanced Materials University of Ulm, Albert-Einstein-Allee 11, 89081 Ulm (Germany)
E-mail: frank.pammer@uni-ulm.de

[b] T. Kaese
Institut für Anorganische und Analytische Chemie
Goethe-Universität Frankfurt, Max-von-Laue-Strasse 7
30438 Frankfurt am Main (Germany)

[c] Dr. Y. Sun
Fachbereich Chemie Technische Universität Kaiserslautern
Erwin-Schrödinger-Strasse 54,67663 Kaiserslautern (Germany)

Supporting information and the ORCID identification number(s) for the author(s) of this article can be found under http://dx.doi.org/10.1002/chem.201602458.

© 2016 Wiley-VCH Verlag GmbH & Co. KGaA, Weinheim

ChemPubSoc Europe

CHEMISTRY
A European Journal
Full Paper

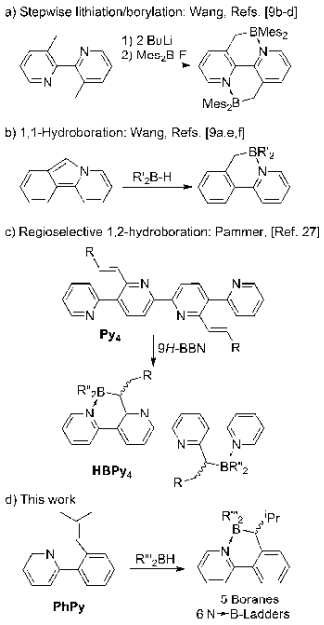

Scheme 1. Examples for the preparation of alkylboryl-bridged N→B ladder boranes. R'$_2$B-H: Mes$_2$BH, 9*H*-BBN, HB(C$_6$F$_5$)$_2$, 9*H*-BBN: 9*H*-9-borabicyclo[3.3.1]-nonyl; BR''$_2$=9-BBN, 2,4,6-trimethylphenyl; R''$_2$BH: 9*H*-9BBN, HBCl$_2$·SMe$_2$, H$_3$B·THF, HB(C$_6$F$_5$)$_2$, and 2,7-di(*tert*-butyl)-9*H*-9-borafluorene.

nylpyridines[25,26] results in highly selective borylation at the benzylic α-position. We have recently taken advantage of this selectivity in the preparation of the N→B ladder borane **HBPy$_4$** through hydroboration of a quaterpyridine substrate with 9*H*-BBN (Scheme 1c).[27]

Herein, we demonstrate that 2-(*ortho*-styryl)pyridine **PhPy** (Scheme 1d) can also be readily hydroborated with electronically and structurally diverse boranes to give the corresponding N→B ladders. The trisubstituted double bond has been introduced into **PhPy** to assure quantitative regioselectivity, and to avoid tedious separation of *E*/*Z*-mixtures that can also show different reactivity and regioselectivity.[16a] This is not mandatory, however, because α selectivities of 85–97% have also been reported for the hydroboration of 1-phenylpropene, depending on the employed borane.[24,28] The properties of the obtained boranes have been experimentally investigated in detail and complemented with quantum chemical calculations to elucidate the origin of differences in the optical and electronic properties that are directly linked to the molecular structure and type of substituent on boron.

Results and Discussion

Synthesis and structure

The 2-(*ortho*-styryl)pyridine substrate **PhPy** was synthesized in 75% yield through a Negishi coupling of 1-bromo-2-(1-isobutenyl)benzene and 2-bromopyridine (Scheme 2). Substrate **PhPy** was then hydroborated with 9*H*-BBN, H$_3$B·THF, 2,7-di-*tert*-butyl-9*H*-9-borafluorene (9*H*-BFlu),[20b,29,30] dichloroborane (HBCl$_2$·SMe$_2$),[31] and Piers' borane (HB(C$_6$F$_5$)$_2$)[32] to give the corresponding N→B heterocyclic compounds **PhPyBBN**, **PhPyBH$_2$**, **PhPyBFlu**, **PhPyBCl$_2$**, and **PhPyBPF** in good to excellent yields. The boranes were used in moderate excess to assure complete conversion of the substrate. Exclusive borylation at the benzylic α-position was observed, even for the highly reactive and sterically nonhindered boranes HBCl$_2$·SMe$_2$ and BH$_3$·THF. The reactions were usually carried out in THF,

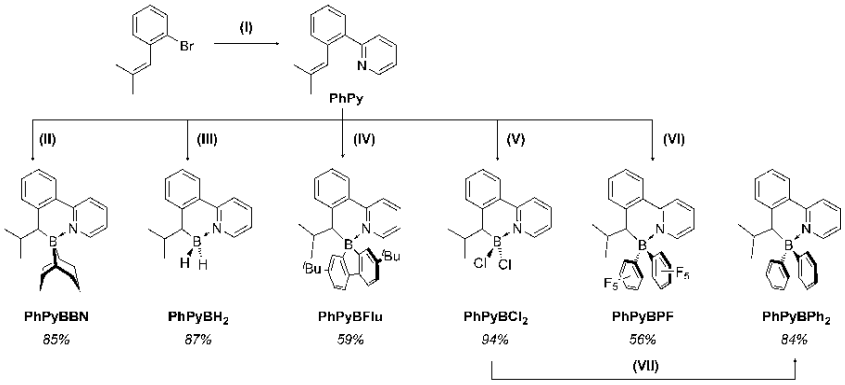

Scheme 2. Ladder-type compounds **PhPyBBN**, **PhPyBH$_2$**, **PhPyBFlu**, **PhPyBCl$_2$**, **PhPyBPF**, and **PhPyBPh$_2$**; I) 1) *n*BuLi, 2) ZnCl$_2$, 3) 2-bromopyridine, 4 mol% [Pd(PPh$_3$)$_2$Cl$_2$], THF, −78 °C to RT, 20 h; II) 9*H*-BBN, THF, 60 °C, 2 d; III) BH$_3$·THF, THF, 50 °C, 3 d; IV) 2,7-di-*tert*-butyl-9-*H*-9-borafluorene, THF, 75 °C, 4 d; V) HBCl$_2$·SMe$_2$, PhMe, RT, 20 h; VI) HB(C$_6$F$_5$)$_2$, C$_6$D$_6$, 85 °C, 3 d; VII) Ph$_2$Zn, PhMe, 60 °C, 3 h.

 © 2016 Wiley-VCH Verlag GmbH & Co. KGaA, Weinheim

ChemPubSoc Europe

CHEMISTRY A European Journal Full Paper

except for hydroborations with $HBCl_2$ and $HB(C_6F_5)_2$, which were not compatible with this solvent, and were therefore reacted in either toluene or benzene.

The reactions proceed via the initial formation of coordination complexes that can readily be observed when monitoring the reaction progress by ^1H and ^{11}B NMR spectroscopy (Figure 1 and Figure S4 in the Supporting Information). Further

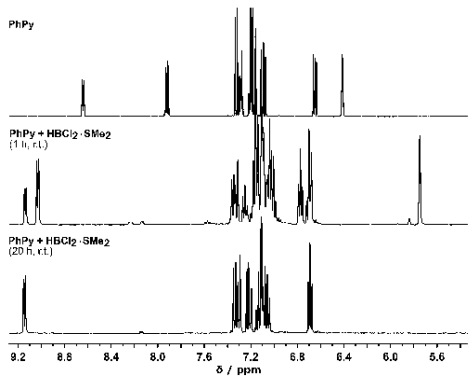

Figure 1. Hydroboration of **PhPy** with $HBCl_2$, as monitored by ^1H NMR spectroscopy in C_6D_6.

reaction progress is sluggish, however, and heating to between 50–85 °C is required to effect quantitative conversion within 2–4 days. The exception is highly reactive $HBCl_2{\cdot}SMe_2$, which readily reacts at ambient temperature and, despite its lower steric demand, also exclusively gives the α-borylated product (Figure 1). As shown by the NMR spectroscopic analysis of this reaction, two sets of signals attributed to Lewis adducts can be observed in the early stages of the reaction; these signals all but disappear as the reaction proceeds. Traces of a single side product remain. We tentatively identified this as the product of hydroboration with H_2BCl, which is also present in solutions of $HBCl_2$ in dimethylsulfide.[33]

Hydroboration with 9*H*-BFlu and $HB(C_6F_5)_2$ led to somewhat lower yields, which we attributed to a combination of the formation of strong Lewis adducts and steric hindrance that, in turn, required prolonged heating to effect full conversion. The long reaction times were likely detrimental to the overall yield, particularly in the case of the generally thermally sensitive 9*H*-BFlu.[20b,29,30] Nevertheless, to the best of our knowledge, this is one of only three examples of preparative hydroboration with a 9-borafluorene derivative that allowed the isolation of a defined product containing an intact 9-borafluorenyl moiety.[30b,34]

In an additional experiment, substrate **PhPyBCl$_2$** was reacted with diphenylzinc, which led to clean conversion and gave the corresponding diphenylboryl derivative **PhPyBPh$_2$** in 84% yield.[11a] This exemplifies that different substituents on boron can be easily introduced by the preparative approach outlined herein, even when the required hydroboranes, such as Ph_2BH, are not easily available.

Compounds **PhPyBBN**, **PhPyBPF**, and **PhPyBPh$_2$** are reasonably under ambient conditions and can, for example, be purified by column chromatography over silica. Compounds **PhPyBFlu**, **PhPyBH$_2$**, and **PhPyBCl$_2$** are more sensitive to air and moisture and were purified under inert gas conditions, but as solids can also be handled in air.

All compounds were fully characterized by ^1H, ^{13}C, and ^{11}B NMR spectroscopy, HRMS/elemental analysis, single-crystal X-ray analysis, UV/Vis spectroscopy, and cyclic voltammetry (CV) and square-wave voltammetry (SWV). All signals in the ^1H and ^{13}C NMR spectra can be individually assigned, including those of the newly formed isobutylboryl bridge: Starting from the signals of the diastereotopic terminal methyl groups, the centrosymmetric multiplet of the neighboring isopropylic methine group (m_c, $\delta = 1.70$–2.85 ppm, ^{13}C: $\delta = 32.7$–29.6 ppm), and the newly formed benzylic methine group (d, $\delta = 3.05$–2.11 ppm, ^{13}C: br, $\delta = 43.1$–39.5 ppm) were unambiguously identified, even in **PhPyBBN**.

The ^{11}B NMR spectra of all compounds show sharp signals within the typical range for tetracoordinated boron between $\delta = +9.4$ ppm (s, **PhPyBCl$_2$**) and -7.2 ppm (t, $^1J(H,B) = 100$ Hz, **PhPyBH$_2$**). This observation indicates that the N→B coordinated species are predominant in solution, even in the presence of the sterically demanding 9-BBN moiety.[35]

The molecular geometries of the above boranes were also unambiguously established by single-crystal XRD analyses, which proved that all boranes assumed an N→B coordinated ladder structure in the solid state (Figure 2 and Table 1). Compound **PyPyBPh$_2$** crystallized in the orthorhombic space group *Pccn*, whereas all others crystallized in the monoclinic space groups $P2_1/n$ or $P2_1/c$. The N→B bond lengths correlate with the Lewis acidity at the boron center, but also with the steric demand of the substituents on boron: **PhPyBBN** exhibits the longest N→B bonds (1.646(2) Å), whereas **PhPyBCl$_2$** (1.596(4) Å) and **PhPyBH$_2$** (1.609(2) Å) show the tightest coordination. Despite the higher Lewis acidity at the boron center, N→B coordination in **PhPyBPF** (1.627(2) Å) is comparable to that in **PhPyBPh$_2$** (1.632(2) Å) and **PhPyBFlu** (1.619(3) to 1.629(3) Å). For the latter, four crystallographically independent molecules are present in the unit cell. The N→B bond lengths of **PhPyBBN** and **PhPyBPF** are comparable to corresponding bonds in known examples,[3,4] although, to the best of our knowledge, structurally similar boranes featuring other substituents on boron have not yet been reported. The six-membered N→B rings adopt a half-chair conformation, with the isopropyl group placed in an axial position to reduce steric strain (Scheme 3, see below). The resulting torsion of the phenyl–pyridine backbone (angle **N1-C5-C6-C11**) ranges from 29.5(2) (**PhPyBPF**) to 19.6(3)° (**PhPyBCl$_2$**). Tight N→B coordination in **PhPyBCl$_2$** leads to a more coplanar conformation. However, the torsion angles are similarly affected by packing effects, as evidenced by the range of different torsion angles observed for **PhPyBFlu** (−27.8(3) to 22.4(3)°).

© 2016 Wiley-VCH Verlag GmbH & Co. KGaA, Weinheim

ChemPubSoc Europe

CHEMISTRY A European Journal Full Paper

Table 1. Space groups, characteristic bond lengths [Å] and angles [°] of the synthesized ladder compounds derived from their crystal structures, and structural parameters calculated by DFT. Numbering according to Figure 2. C_{iPr}: methine-*C* of the axial *i*Pr group. X_{ax}: axial substituent on boron.

PhPy	Space group	N1→B1	N1-C5-C6-C11	C5–C6	C12–B1	C_{iPr}-C12-B1-X_{ax}	C5-N1-B1-X_{ax}	DFT[b] N→B	DFT[b] N1-C5-C6-C11
BBN	*P*21/*n*	1.646(2)	23.3(2)	1.482(2)	1.642(2)	171.9(1)	75.5(2)	1.650	26.4
BPF	*P*21/*c*	1.627(2)	29.5(2)	1.471(2)	1.635(4)	179.9(1)	68.3(2)	1.641	27.7
BCl_2	*P*21/*c*	1.596(4)	19.6(3)	1.483(4)	1.592(4)	166.2(1)	84.4(2)	1.623	22.5
BPh_2	*Pccn*	1.632(2)	23.9(2)	1.476(2)	1.639(2)	168.3(1)	87.0(1)	1.642	27.4
BH_2	*P*21/*c*	1.609(2)	25.0(2)	1.474(2)	1.614(2)	179.3(8)	102.6(8)	1.621	23.3
BFlu[a]	*P*21/*n*	1.623(3)	−22.4(3)	1.477(3)	1.627(3)	−165.0(2)	−84.5(2)	1.647	28.4
		1.626(3)	−27.8(3)	1.478(3)	1.638(4)	−163.8(2)	−84.7(2)		
		1.629(3)	23.7(3)	1.480(3)	1.637(4)	157.7(2)	87.7(2)		
		1.619(3)	24.4(3)	1.477(3)	1.624(4)	166.2(2)	81.4(2)		

[a] The structure of **PhPyBFlu** contains four crystallographically independent molecules. [b] From ***i*Pr$_{ax}$** structures optimized by DFT at the M06-2X/6-31G(d,p) level. Additional information on the calculated structures is included in Section 3 of the Supporting Information.

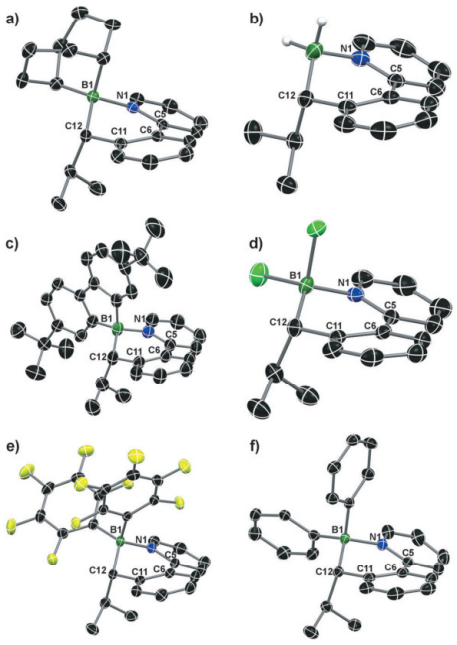

Figure 2. Crystal structures of compounds a) **PhPyBBN**, b) **$PhPyBH_2$**, c) **PhPyBFlu**, d) **$PhPyBCl_2$**, e) **PhPyBPF**, and f) **$PhPyBPh_2$**. Ellipsoids are shown at the 50% probability level. All hydrogen atoms, except those of structural relevance in **$PhPyBH_2$**, have been omitted for clarity.

Optical and electronic properties

Having made available a series of boranes with electronically diverse substituents on boron, we studied their electronic properties in more detail by UV/Vis spectroscopy and electrochemical methods. All boranes exhibit absorption maxima in the range of $\lambda = 303–313$ nm (see Figures 3a and 6 (see below), Table 2, and Table S3 in the Supporting Information), with the exception of **PhPyBFlu**, for which a shoulder is observed that corresponds to a maximum at $\lambda \approx 319$ nm.[36] However, the shape of the absorption bands indicates the presence of additional optical transitions at longer wavelength, as evi-

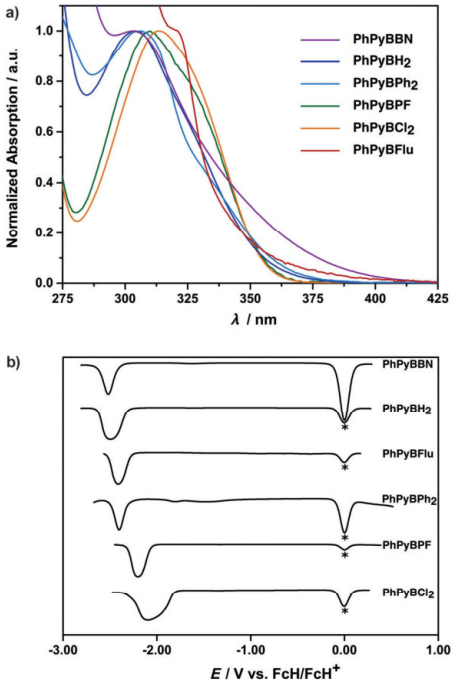

Figure 3. a) UV/Vis absorption spectra of N→B boranes recorded in THF. b) Square wave voltammograms of synthesized ladder compounds. Recorded in THF with 0.1 M $[nBu_4N][PF_6]$ as supporting electrolyte at a scan rate of 100 mVs^{-1}. * internal reference ferrocene.

© 2016 Wiley-VCH Verlag GmbH & Co. KGaA, Weinheim

ChemPubSoc Europe

CHEMISTRY A European Journal Full Paper

Table 2. Optical and electronic properties of N→B boranes.

PhPy	E^{red}_{peak} [a]	E^{red}_{onset} [b]	E^{ox}_{onset} [b]	E^{opt}_{g} [c]		λ_{max}	$HOMO^{CV}$ [g]	$LUMO^{SWV}$ [g]
	[V]	[V]	[V]	[nm]	[eV]	[nm]	[eV]	[eV]
BBN	−2.52	−2.44	0.58[d]	391	3.17	303	−5.68	−2.58
BH_2	−2.50	−2.39	0.99[d]	358	3.46	304	−6.09	−2.60
BFlu	−2.41	−2.32[c]	0.62[d]	375	3.31	319[f]	−5.72	−2.69
BPh_2	−2.40	−2.27	0.98[d]	363	3.42	306	−6.08	−2.70
BPF	−2.20	−2.13[c]	1.87[d]	354	3.50	310	−6.97	−2.90
BCl_2	−2.15	−1.88[d]	1.37[d]	354	3.50	313	−6.47	−2.95

[a] Peak potentials determined by square-wave voltammetry (SWV). [b] Determined by cyclic voltammetry (CV). [c] Quasi-reversible. [d] Irreversible. [e] Onset of the optical absorption in THF. [f] Derived by Gaussian fitting. [g] Based on the onset of electrochemical oxidation by CV (HOMO) and the peak potential of electrochemical reduction by SWV (LUMO), relative to the HOMO of ferrocene (5.1 eV[37]).

denced particularly by the distinct shoulder in the spectrum of **$PhPyBPh_2$** and the very gradual decrease of the absorption of **PhPyBBN**. For the latter, this results in a significantly lowered optical gap of about 3.17 eV (onset: $\lambda = 391$ nm), relative to 3.50–3.31 eV ($\lambda = 354$–375 nm) for the other boranes, based on the onset of optical absorption in solution. This observation is consistent with time-dependent DFT calculations discussed below. Also, in agreement with previous reports,[9,27] all ladder compounds are nonfluorescent. The exception is **$PhPyBCl_2$**, which shows blue fluorescence with an emission maximum at $\lambda = 423$ nm and vibronic structuring (see Figure S3 in the Supporting Information), upon excitation at $\lambda = 340$ nm. Fluorescence is very weak, however, with an estimated quantum yield of less than 0.1 %. The fact that the fluorescence of **$PhPyBCl_2$** is observable at all is likely linked to tighter N→B coordination and the resulting increased rigidity of this molecule, which prevents rapid vibrational relaxation and secondary reactions. There were no changes to the absorption and emission spectra of all boranes during the measurements, even after prolonged irradiation. This indicates that the ladder compounds investigated herein show lower tendencies to undergo photoreactions than related ladder-type boranes without additional substituents on the alkylboryl bridge.[9]

Although the absorption properties of all systems under investigation are fairly similar, variation of the substituents on boron still allows the electrochemical properties of the ladder compounds to be systematically varied (see Figure 3b, Table 2, and Table S3 and Figures S1 and S2 in the Supporting Information). Analyses by CV and SWV in THF with 0.1 M [nBu$_4$N][PF$_6$] as the supporting electrolyte showed the direct correlation of the electrochemical reduction potentials of the ladder boranes with the Lewis acidity of the boron center. The comparatively electron-rich boranes **PhPyBBN** and **$PhPyBH_2$** undergo reversible electrochemical reduction with peak potentials at −2.52 and −2.50 V (SWV), respectively, relative to the ferrocene/ferrocenium (FcH/FcH$^+$) redox couple (−5.1 eV).[37] The potentials for the quasi-reversible reduction of **PhPyBFlu** and the reversible reduction of **$PhPyBPh_2$** appear to be shifted to −2.41 and −2.40 V versus FcH/FcH$^+$ (SWV), whereas strongly acceptor-substituted **PhPyBPF** also undergoes quasi-reversible reduction with a peak potential at −2.20 V (SWV). The peak potential of **$PhPyBCl_2$** was observed at −2.15 V versus FcH/FcH$^+$, which was in agreement with the general perception that chloro and pentafluorophenyl substituents on boron have comparable electron-withdrawing effects.[38]

However, the electrochemical reduction of **$PhPyBCl_2$** is irreversible (see Figure S1a in the Supporting Information), and therefore not directly comparable to that of **PhPyBPF**. Overall, the reduction potentials, and thereby the energy level of the LUMO of the phenyl–pyridine moiety, can be varied over a range of 0.37 V by the substituents screened herein. The electrochemical oxidation was irreversible in all cases, but showed a similar correlation (see Figure S2a/b in the Supporting Information). For **PhPyBBN** and **PhPyBFlu**, the onset of irreversible oxidation was observed at +0.58 and +0.62 V (CV) versus FcH/FcH$^+$, and at +0.99 and +0.98 V (CV) for **$PhPyBH_2$** and **$PhPyBPh_2$**, respectively. Oxidation of **$PhPyBCl_2$** could be observed at +1.37 V, whereas oxidation of **PhPyBPF** occurred at +1.87 V, at the edge of the electrochemical window of the solvent dichloromethane. The oxidation potentials correlate less well with the acceptor strength of the boranes than the reduction potentials. This may be linked to the irreversibility of electrochemical oxidation, which precludes a direct comparison.

This assumption was corroborated by quantum chemical simulations of the investigated boranes that were carried out to further elucidate their electronic and structural properties. Geometry optimizations were performed for three conformers of each borane: two N→B coordinated ones with the isopropyl group placed either in an equatorial (***i*Pr$_{eq}$**) or an axial (***i*Pr$_{ax}$**) position, as observed in the crystals structures, as well as an open (**open**) conformer without the N→B bond (Scheme 3).

Compared with the corresponding **open** conformers, the formation of ladder structures is generally strongly energetically favored by between 69 and 132 kJ mol^{-1}.[39] This confirms the NMR spectroscopy data, which indicated that N→B coordinated species are predominant in solution. The greatest stabilizations were calculated for **$PhPyBCl_2$** (132 kJ mol^{-1}), **PhPyBPF** (132 kJ mol^{-1}), and **$PhPyBH_2$** (120 kJ mol^{-1}), in line with both the high Lewis acidity at the boron centers of **$PhPyBCl_2$** and **PhPyBPF** and the lack of steric hindrance in the case of **$PhPyBH_2$**. Compound **PhPyBBN** shows the least stabilization (69 kJ mol^{-1}), possibly due to the overall bulk of the 9-BBN-moiety, which also renders an equatorial orientation of the iso-

© 2016 Wiley-VCH Verlag GmbH & Co. KGaA, Weinheim

ChemPubSoc Europe

CHEMISTRY A European Journal Full Paper

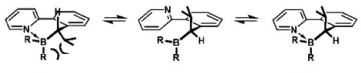

	*i*Pr$_{eq}$	open	*i*Pr$_{ax}$
PhPyBPF	+14	+132	0
PhPyBFlu	+8	+93	0
PhPyBPh$_2$	−4	+88	0
PhPyBCl$_2$	+10	+120	0
PhPyBH$_2$	+17	+132	0
PhPyBBN	+57	+69	0

Scheme 3. Schematic representation of possible borane conformers and calculated relative energies in kJ mol^{-1}.

propyl group almost as unfavorable as complete decoordination. Indeed, the ***i*Pr$_{ax}$** conformers are more stable by 10 to 57 kJ mol^{-1} than the ***i*Pr$_{eq}$** conformers, or else the energetic difference between the two is negligible (**PhPyBPh$_2$**: ΔG(*i*Pr$_{ax/eq}$) = −4 kJ mol^{-1}). The calculations therefore confirm that exclusive observation of ***i*Pr$_{ax}$** conformers in the crystal structures is attributed to their inherent greater stability, rather than packing effects. Nevertheless, with the possible exception of **PhPyBBN**, the energetic differences remain small enough for both conformers to be present in solution under ambient conditions. However, particularly for the more rigid and sterically encumbered **BPF**, **BFlu**, and **BPh$_2$** compounds, substantial barriers to inversion may exist that effectively lock the systems in the energetically most stable conformation. This is of interest because the computed optical and electronic properties of **axial** and **equatorial** conformers differ slightly (see Figure 6 below and Section 3.2 in the Supporting Information).

The reason for preferred axial orientation of the isopropyl group becomes intuitively clear from the depiction of ***i*Pr$_{ax}$** and ***i*Pr$_{eq}$** in Scheme 3. A *trans*-axial orientation relative to one substituent on boron reduces steric repulsion with the second, then equatorial, substituent. Also, substituents that would render an axial conformation of the isopropyl group unfavorable are not present on the phenyl–pyridyl backbone. The reduced steric strain in the ***i*Pr$_{ax}$** conformers, relative to ***i*Pr$_{eq}$**, generally leads to a shortening of the N→B bond lengths and smaller torsion angles. Calculated N→B bond lengths correlate well with those derived from crystal structures, but are generally somewhat longer (Table 1, see also Figure S29 in the Supporting Information). We tentatively attribute these differences to packing effects. This is almost certainly true for the torsion angles of the phenyl–pyridyl backbone derived from the crystal structures, which barely correlate with the calculated ones, and differ strongly, even for the individual structures of **PhPyBFlu**.

Aside from structural effects, the nature of the substituents on boron also strongly affects the electronic structure of the N→B ladder species.[39] This becomes especially apparent upon comparing the spatial distributions of the HOMOs and LUMOs (Figure 4, see also Table S2 and Figure S30 in Section 3 in the Supporting Information). In all cases, the LUMOs represent π^*-orbitals that are delocalized exclusively throughout the phenyl-pyridyl moiety; thus reflecting both electron deficiency of the

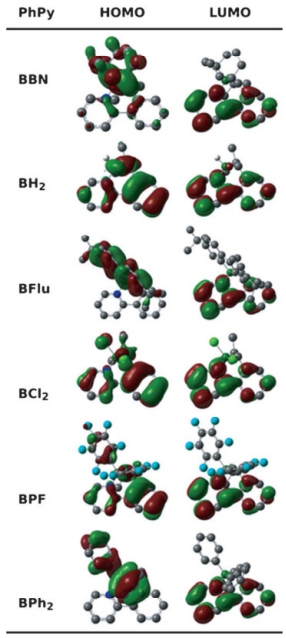

Figure 4. Frontier orbital plots of **PhPyBBN**, **PhPyBPF**, **PhPyBFlu**, **PhPyBCl$_2$**, **PhPyBH$_2$**, and **PhPyBPh$_2$**. Orbital plots were generated by using GaussView 5.0; isovalue: 0.02.

pyridyl ring and the electron-withdrawing effect of N→B coordination. Furthermore, the energy levels of both LUMO and LUMO+1 experience increasing stabilization, for example, from −1.24 eV for the LUMO in **PhPyBH$_2$** to −1.80 eV for the one in **PhPyBPF** (Figure 5). This shift is in agreement with the acceptor strength of the boryl group, and also effectively covers the same range as the electrochemical data.

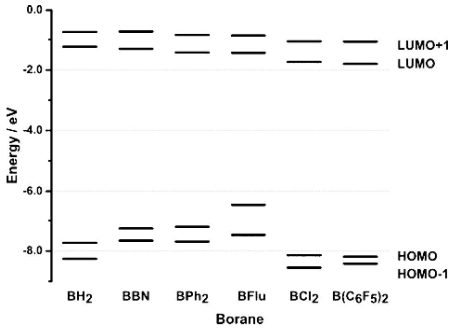

Figure 5. Calculated frontier orbital levels of ladder-type compounds in the *i*Pr$_{ax}$ conformation (M06-2X/6-311+G(d,p)).

© 2016 Wiley-VCH Verlag GmbH & Co. KGaA, Weinheim

ChemPubSoc Europe

CHEMISTRY A European Journal Full Paper

Contrarily, the structure of the HOMOs is directly linked to the nature the individual boryl moieties. For **PhPyBCl$_2$** and **PhPyBH$_2$**, the HOMOs resemble π-orbitals on the phenyl–pyridyl backbone, with only minor contributions from the boryl bridge. In **PhPyBFlu** and **PhPyBPh$_2$**, the HOMOs are delocalized throughout the fluorenyl and phenyl substituents, respectively, on boron. The highest HOMO level, and thus, the lowest HOMO–LUMO gap, was found for the fully conjugated planar borafluorene moiety (Figure 5).

Interestingly, both the HOMO and HOMO-1 of **PhPyBPF** show significant contributions from C_6F_5 π-orbitals. This may be explained by inductive electron donation from electropositive, tetracoordinate boron, which carries a negative formal charge. In connection with the significant stabilization of occupied orbitals localized on the phenyl–pyridyl moiety, due to N→B coordination, this effect seems strong enough to partially offset the electron-withdrawing effect of perfluorination. The electronic situation is again markedly different for **PhPyBBN**, wherein the HOMO is a σ-type orbital, made up from contributions from the B–C bonds in the trialkylboryl moiety.

These differences in shape and type of the frontier orbitals also help to explain differences in the experimentally recorded UV/Vis spectra. The UV/Vis spectra of ***i*Pr$_{ax}$**, ***i*Pr$_{eq}$**, and **open** conformers were simulated by time-dependent DFT calculations at the M06-2X/6-311+G(d,p)-level (Figure 6, see also Table S3 and associated content in Section 3.2 in the Supporting Information). The simulations predict strong absorption maxima for all ***i*Pr$_{eq}$** and ***i*Pr$_{ax}$** conformers in the UV region at $\lambda = 240–250$ nm that are sums of complex transitions involving multiple orbitals (typically from HOMO-4 to LUMO+1, see Table S3 and Section 3.2.2 in the Supporting Information). However, in good agreement with the experimental data, the calculations also predict less intense, near-exclusive HOMO–LUMO-transitions at $\lambda = 290–320$ nm. The energy of the transitions and oscillator strengths differ slightly for axial and equatorial conformers (e.g., **PhPyBH$_2$**: ***i*Pr$_{ax}$**: 4.20 eV; $f = 0.10$, ***i*Pr$_{eq}$**: 3.90 eV; $f = 0.06$); the equatorial conformers consistently exhibit lower transitional energies.

As pointed out above, the energetic differences between axial and equatorial structures are sufficiently small for both conformers to be present in solution. The observation of shoulder bands in the experimental spectra may therefore be attributed to the superimposed absorptions of both conformers. This tentative conclusion is supported by the near-quantitative agreement of the simulated and experimental absorption spectra of **PhPyBH$_2$** and **PhPyBPh$_2$**.

The simulated spectra also explain the differences and similarities of the spectra of **PhPyBFlu** and **PhPyBBN** with those of other boranes under investigation. The absorption spectrum of **PhPyBFlu** is very similar to those of the other boranes, despite **PhPyBFlu** exhibiting the lowest HOMO–LUMO gap of all systems under investigation. We attribute this to the fact that the HOMO–LUMO transition in **PhPyBFlu**, albeit π–π* in nature, is effectively forbidden due to the spiro structure[40] of the molecule. Electronic coupling between the π-type HOMO on the borafluorene and the π*-type LUMO on the phenyl–pyridyl group is hampered, since the frontier orbitals share no spatial overlap, and stand at an angle of >80°, according to DFT calculations and crystal data (angle C5-N1-B1-X$_{ax}$ in Table 1). Consequently, the calculations indicate these transitions are very weakly populated in both conformers (**PhPyFlu**: HOMO–LUMO: ***i*Pr$_{ax}$**: 3.51 eV; $f = 0.004$, ***i*Pr$_{eq}$**: 3.58 eV; $f = 0.005$). The HOMO–LUMO transition may contribute, however, to the slight tailing of the experimental spectrum towards longer wavelength. The experimentally observed shoulder band ($\lambda =$ 319 nm,[36] 3.89 eV) corresponds to the significantly more populated second excited states in both the equatorial and axial conformers that involve primarily the orbitals HOMO-1 and LUMO+1 (**PhPyFlu**: 2nd excited state: HOMO-1–LUMO+1: ***i*Pr$_{ax}$**: 3.91 eV; $f = 0.04$, ***i*Pr$_{eq}$**: 3.91 eV; $f = 0.04$). The experimental UV absorption spectrum of **PhPyBBN** also shows a distinct tailing toward longer wavelength that results in a pronounced redshift of the absorption onset (exp. $\lambda_{onset} = 391$ nm, 3.17 eV) compared with the other boranes. This tailing is attributed to the HOMO–LUMO transition (calcd ***i*Pr$_{ax}$**: 3.83 eV, $f =$ 0.04, ***i*Pr$_{eq}$**: 3.72 eV, $f = 0.04$), which is effectively σ–π* in nature, whereas the experimentally observed maximum ($\lambda_{max} =$ 3.11 nm, 3.98 eV) is dominated by the second excited state, which is mainly a HOMO-1–LUMO transition (**PhPyBBN**: 2nd excited state: HOMO-1–LUMO: ***i*Pr$_{ax}$**: 4.13 eV; $f = 0.04$, ***i*Pr$_{eq}$**: 4.09 eV; $f = 0.03$.).

Overall, the impact of the variation of the substituents on boron is surprisingly limited, since the molecular and orbital geometry hinder electronic coupling between the phenyl–pyridyl moiety and substituents on boron, particularly in **PhPyBBN** and **PhPyFlu**.

Conclusion

We demonstrated that hydroboration of **PhPy** resulted in highly regioselective borylation under mild conditions and allowed us to readily access the corresponding N→B coordinated ladder boranes. Five electronically and structurally diverse boranes were employed to this end, including $HB(C_6F_5)_2$, which was a highly reactive $HBCl_2$ that gave a versatile dichloroboryl intermediate for further syntheses, and a 9-borafluorene-derivative that resulted in the formation of an effectively spiro-conjugated π-system.

The structure and properties of the obtained boranes were experimentally investigated in detail and complemented with quantum chemical calculations to elucidate the origin of differences in the optical and electronic properties. The electron affinity of the π-system could be directly controlled through variation of the hydroborane, while the optical properties were also linked to the molecular structure and type of substituent on boron.

Furthermore, although the steric bulk of the isobutenyl group served to assure highly selective borylation, it did not hamper conversion of the substrate. The ease and broad scope of the reactivity demonstrated herein may allow multiple, chemically diverse boryl groups to be simultaneously introduced into more complex substrates, particularly because the employed functional group (i.e., *ortho*-β,β-dimethylstyryl) is both chemically robust and readily accessible. Further explora-

© 2016 Wiley-VCH Verlag GmbH & Co. KGaA, Weinheim

ChemPubSoc Europe

CHEMISTRY A European Journal Full Paper

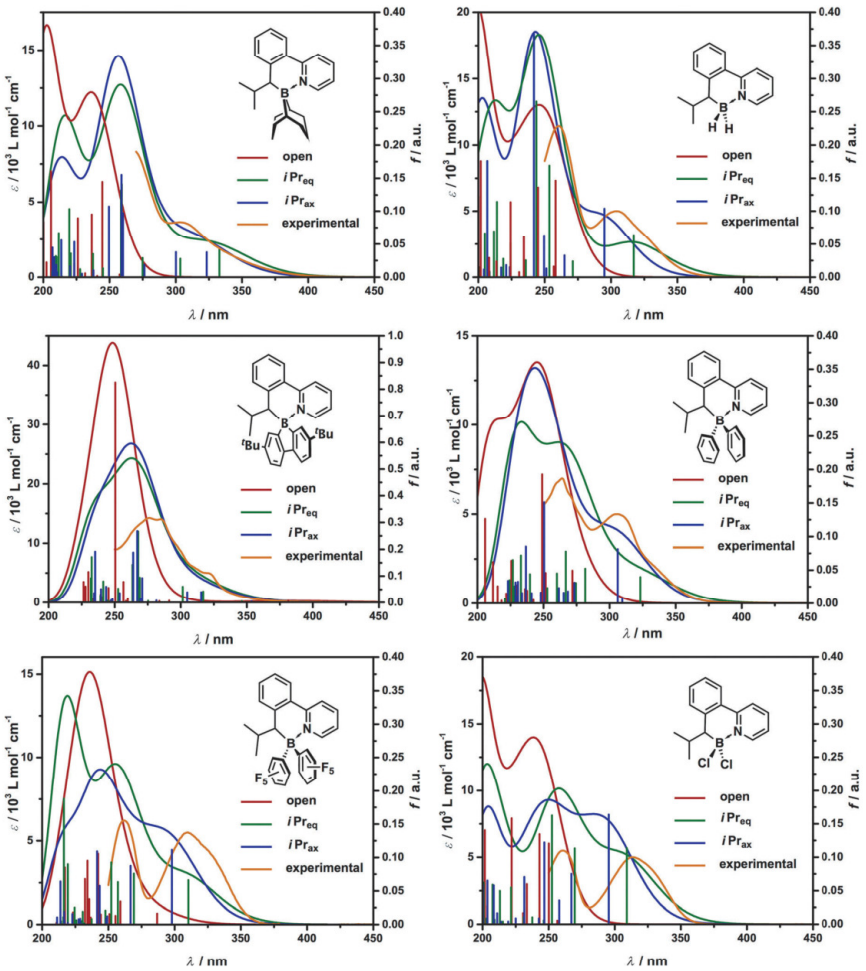

Figure 6. Comparison of experimental UV/Vis spectra with spectra of ***i*Pr$_{ax}$**, ***i*Pr$_{eq}$**, and **open** conformers simulated by time-dependent DFT calculations. Simulated spectra based on the first 15 excited states superimposed with a half-width at half-height of 0.333 eV. Geometry: M06-2X/6-31G(d,p); TD-DFT: M06-2X/6-311+G(d,p). Experimental spectra are scaled arbitrarily to fit on the graph.

tion of the substrate scope and possible conversion of the prepared N→B ladders into fully conjugated B–N-substituted arenes are currently in progress in our laboratory.

Computational Details

Quantum chemical calculations were performed on the Campus Ulm Shared Science Cluster (CUSS) compute server of the University of Ulm by using release D.01 of the Gaussian 09 program package. Geometry optimization of the synthesized boranes were performed at the M06-2X/6-31G(d,p) level of theory in the gas phase. Frequency calculations confirmed the optimized structures to be local minimum structures (no imaginary frequencies). Frontier orbital levels and the first 15 excited states were simulated by single-point calculation on the optimized structures by time-dependent DFT at the M06-2X/6-311+G(d,p) level in the gas phase. The M06-2X[41] functional was chosen because it accounts well for dispersion interactions and has been shown to accurately represent coordination complexes of organoboranes.[42]

© 2016 Wiley-VCH Verlag GmbH & Co. KGaA, Weinheim

ChemPubSoc Europe

CHEMISTRY
A European Journal
Full Paper

Acknowledgements

We thank the German Chemical Industry Fund (FCI) (doctoral scholarships for M. G. and T. K., and Liebig scholarship for F. P.), and the German Science Foundation (DFG) for financial support. We also thank Prof. Matthias Wagner (Goethe-Universität Frankfurt, Germany) and Prof. Martin Korth (University of Ulm) for support and helpful discussions, and Bernhard Müller for support with X-ray data collection.

Keywords: boranes · density functional calculations · hydroboration · Lewis pairs · n-Type Materials

[1] a) F. Jäkle, *Top. Organomet. Chem.* **2015**, *49*, 297–325; b) A. Doshi, F. Jäkle, *Boron-Containing Polymers - Comprehensive Inorganic Chemistry*, Elsevier, Amsterdam, **2013**; c) F. Jäkle, *Chem. Rev.* **2010**, *110*, 3985–4022; d) F. Jäkle, *Coord. Chem. Rev.* **2006**, *250*, 1107–1121; e) F. Jäkle in *Encyclopedia of Inorganic Chemistry*, (Ed. B. King), Wiley-VCH, Weinheim, **2005**, p. 560; f) C. D. Entwistle, T. B. Marder, *Chem. Mater.* **2004**, *16*, 4574–4585; g) C. D. Entwistle, T. B. Marder, *Angew. Chem. Int. Ed.* **2002**, *41*, 2927–2931; *Angew. Chem.* **2002**, *114*, 3051–3056; h) T. Noda, Y. Shirota, *J. Am. Chem. Soc.* **1998**, *120*, 9714–9715.

[2] a) C. R. Wade, A. E. J. Broomsgrove, S. Aldridge, F. P. Gabbai, *Chem. Rev.* **2010**, *110*, 3958–3984; b) G. R. Kumar, S. K. Sarkar, P. Thilagar, *Phys. Chem. Chem. Phys.* **2015**, *17*, 30424–30403; c) G. R. Kumar, P. Thilagar, *Dalton Trans.* **2014**, *43*, 3871–3879; d) C. Wang, J. Jia, W. Zhang, H.-Y. Zhang, C. Zhao, *Chem. Eur. J.* **2014**, *20*, 16590–16601.

[3] a) K. Tanaka, Y. Chujo, *Macromol. Rapid Commun.* **2012**, *33*, 1235–1286; b) C. Sun, Z. M. Hudson, M. G. Helander, Z.-H. Lu, S. Wang, *Organometallics* **2011**, *30*, 5552–5555; c) Y. Shirota, *J. Mater. Chem.* **2005**, *15*, 75–93.

[4] a) S. Cataldo, S. Fabiano, F. Ferrante, F. Previti, S. Patan, B. Pignataro, *Macromol. Rapid Commun.* **2010**, *31*, 1281–1286; b) J. Chai, C. Wang, L. Jia, Y. Pang, M. Graham, S. Z. D. Cheng, *Synth. Met.* **2009**, *159*, 1443–1449.

[5] a) C. Dou, Z. Ding, Z. Zhang, Z. Xie, J. Liu, L. Wang, *Angew. Chem. Int. Ed.* **2015**, *54*, 3648–3652; *Angew. Chem.* **2015**, *127*, 3719–3723; b) Z. Zhang, Z. Ding, C. Dou, J. Liu, L. Wang, *Polym. Chem.* **2015**, *6*, 8029–8035; c) C. Dou, X. Long, Z. Ding, Z. Xie, J. Liu, L. Wang, *Angew. Chem. Int. Ed.* **2016**, *55*, 1436–1440; *Angew. Chem.* **2016**, *128*, 1458–1462.

[6] Reviews: a) M. M. Morgan, W. Piers, *Dalton Trans.* **2016**, *45*, 5920–5924; b) M. J. D. Bosdet, W. E. Piers, *Can. J. Chem.* **2009**, *87*, 8–29; c) J. S. A. Ishibashi, J. L. Marshall, A. Mazie, G. J. Lovinger, B. Li, L. N. Zakharov, A. Dargelos, A. Graciaa, A. Chrostowska, S. Liu, *J. Am. Chem. Soc.* **2014**, *136*, 15414–15421; d) P. G. Campbell, A. J. Marwitz, S.-Y. Liu, *Angew. Chem. Int. Ed.* **2012**, *51*, 6074–6092; *Angew. Chem.* **2012**, *124*, 6178–6197; e) Z. Liu, T. B. Marder, *Angew. Chem. Int. Ed.* **2008**, *47*, 242–244; *Angew. Chem.* **2008**, *120*, 248–250; f) X. Wang, J. Wang, J. Pei, *Chem. Eur. J.* **2015**, *21*, 3528 3539.

[7] For recent publications, see: a) A. J. V. Marwitz, M. H. Matus, L. N. Zakharov, D. A. Dixon, S.-Y. Liu, *Angew. Chem. Int. Ed.* **2009**, *48*, 973–977; *Angew. Chem.* **2009**, *121*, 991–995; b) A. N. Lamm, S.-Y. Liu, *Mol. Biosyst.* **2009**, *5*, 1303–1305; c) M. Müller, C. Maichle-Mössmer, H. F. Bettinger, *Angew. Chem. Int. Ed.* **2014**, *53*, 9380–9383; *Angew. Chem.* **2014**, *126*, 9534–9537; d) X.-Y. Wang, A. Narita, X. Feng, K. Müllen, *J. Am. Chem. Soc.* **2015**, *137*, 7668–7671; e) A. W. Baggett, F. Guo, B. Li, S.-Y. Liu, F. Jäkle, *Angew. Chem. Int. Ed.* **2015**, *54*, 11191–11195; *Angew. Chem.* **2015**, *127*, 11343–11347; f) K. Edel, S. A. Brough, A. N. Lamm, S.-Y. Liu, H. F. Bettinger, *Angew. Chem. Int. Ed.* **2015**, *54*, 7819–7822; *Angew. Chem.* **2015**, *127*, 7930–7933.

[8] T. Hatakeyama, S. Hashimoto, S. Seki, M. Nakamura, *J. Am. Chem. Soc.* **2011**, *133*, 18614–18617.

[9] a) D.-T. Yang, S. K. Mellerup, X. Wang, J.-S. Lu, S. Wang, *Angew. Chem. Int. Ed.* **2015**, *54*, 5498–5501; *Angew. Chem.* **2015**, *127*, 5588–5592; b) S. Wang, D.-T. Yang, J. Lu, H. Shimogawa, S. Gong, X. Wang, S. K. Mellerup, A. Wakamiya, Y.-L. Chang, C. Yang, Z.-H. Lu, *Angew. Chem. Int. Ed.* **2015**, *54*, 15074–15078; *Angew. Chem.* **2015**, *127*, 15289–15293; c) J. S. Lu, S. B. Ko, N. R. Walters, Y. Kang, F. Sauriol, S. Wang, *Angew. Chem. Int. Ed.* **2013**, *52*, 4544–4548; *Angew. Chem.* **2013**, *125*, 4642–4646; d) S. B. Ko, J. S. Lu, S. Wang, *Org. Lett.* **2014**, *16*, 616–619; e) S. M. McDonald, S. K. Mellerup, J. Peng, D. Yang, Q.-S. Li, S. Wang, *Chem. Eur. J.* **2015**, *21*, 13961–13970; f) Y. Shi, D. Yang, S. K. Mellerup, N. Wang, T. Peng, S. Wang, *Org. Lett.* **2016**, *18*, 1626–1626.

[10] a) A. Job, A. Wakamiya, G. Kehr, G. Erker, S. Yamaguchi, *Org. Lett.* **2010**, *12*, 5470–5473; b) D. Vagedes, G. Erker, G. Kehr, K. Bergander, O. Kataeva, R. Fröhlich, S. Grimme, C. Mück-Lichtenfeld, *Dalton Trans.* **2003**, 1337–1344; c) D. Vagedes, G. Kehr, D. König, K. Wedeking, R. Fröhlich, G. Erker, C. Mück-Lichtenfeld, S. Grimme, *Eur. J. Inorg. Chem.* **2002**, 2015–2021.

[11] For five-membered rings, see: a) M. Yusuf, K. Liu, F. Guo, R. A. Lalancette, F. Jäkle, *Dalton Trans.* **2016**, *45*, 4580–4587; b) A. C. Shaikh, D. S. Ranade, S. Thorat, A. Maity, P. P. Kulkarni, R. G. Gonnade, P. Munshi, N. T. Patil, *Chem. Commun.* **2015**, *51*, 16115–16118; c) Z. J. Zhao, Z. F. Chang, B. R. He, B. Chen, C. M. Deng, P. Lu, H. Y. Qiu, B. Z. Tang, *Chem. Eur. J.* **2013**, *19*, 11512–11517; d) H.-L. Wong, W.-T. Wong, V. W.-W. Yam, *Org. Lett.* **2012**, *14*, 1862–1865; e) N. Ishida, T. Moriya, T. Goya, M. Murakami, *J. Org. Chem.* **2010**, *75*, 8709–8712; f) C. Zhu, Z.-H. Guo, A. U. Mu, Y. Liu, S. E. Wheeler, L. Fang, *J. Org. Chem.* **2016**, *81*, 4347–4352; six-membered rings are also accessible through this method, see: g) D. L. Crossley, I. A. Cade, E. R. Clark, A. Escande, M. J. Humphries, S. M. King, I. Vitorica-Yrezabal, M. J. Ingleson, M. L. Turner, *Chem. Sci.* **2015**, *6*, 5144–5151; h) D. L. Crossley, J. Cid, L. D. Curless, M. L. Turner, M. J. Ingleson, *Organometallics* **2015**, *34*, 5767–5774; i) L. Niu, H. Yang, R. Wang, H. Fu, *Org. Lett.* **2012**, *14*, 2618–2621; see also ref. [8].

[12] a) A. Wakamiya, T. Taniguchi, S. Yamaguchi, *Angew. Chem. Int. Ed.* **2006**, *45*, 3170–3173; *Angew. Chem.* **2006**, *118*, 3242–3245; b) S. Yamaguchi, A. Wakamiya, *Pure Appl. Chem.* **2006**, *78*, 1413–1424; c) Y.-L. Rao, H. Amarne, L. D. Chen, M. L. Brown, N. J. Mosey, S. Wang, *J. Am. Chem. Soc.* **2013**, *135*, 3407–3410; d) X. Y. Wang, F. D. Zhuang, R. B. Wang, X. C. Wang, X. Y. Cao, J. Y. Wang, J. Pei, *J. Am. Chem. Soc.* **2014**, *136*, 3764–3767.

[13] J. Yoshino, N. Kano, T. Kawashima, *Chem. Commun.* **2007**, 559–561.

[14] Y.-L. Rao, L. D. Chen, N. J. Mosey, S. Wang, *J. Am. Chem. Soc.* **2012**, *134*, 11026–11034.

[15] a) Y.-L. Rao, H. Amarne, J.-S. Lu, S. Wang, *Dalton Trans.* **2013**, *42*, 638–644; b) Y.-L. Rao, S. Wang, *Organometallics* **2011**, *30*, 4453–4458; c) S. K. Murphy, C. Baik, J.-S. Lu, S. Wang, *Org. Lett.* **2010**, *12*, 5266–5269; d) H. Amarne, C. Baik, S. K. Murphy, S. Wang, *Chem. Eur. J.* **2010**, *16*, 4750–4761; e) Y.-L. Rao, H. Amarne, S.-B. Zhao, T. M. McCormick, S. Martic, Y. Sun, R.-Y. Wang, S. Wang, *J. Am. Chem. Soc.* **2008**, *130*, 12898–12900.

[16] a) R. S. Dhillon, *Hydroboration, Organic Synthesis*, Springer, Heidelberg, **2007**; b) K. Smith, A. Pelter, *Hydroboration of C=C and C≡C in Comprehensive Organic Synthesis Vol. 8*, (Eds.: B. M. Trost, I. Fleming), Elsevier, Oxford, **1991**, p. 703; c) H. C. Brown, C. F. Lane, *J. Am. Chem. Soc.* **1970**, *92*, 6660–6661; d) H. C. Brown, *Hydroboration*, W. A. Benjamin, New York, **1962**.

[17] $TipBH_2$: a) D. M. Hinkens, Q. Chen, M. K. Siddiki, D. Gosztola, M. A. Tapsak, Q. Qiao, M. Jeffries-El, S. B. Darling, *Polymer* **2013**, *54*, 3510–3520. Mes_2BH: b) J. Lu, S. Ko, N. R. Walters, S. Wang, *Org. Lett.* **2012**, *14*, 5660–5663; c) F. Pammer, F. Guo, R. A. Lalancette, F. Jäkle, *Macromolecules* **2012**, *45*, 6333–6343; d) F. Pammer, F. Jäkle, *Chem. Sci.* **2012**, *3*, 2598–2606; e) Z. Yuan, C. D. Entwistle, J. C. Collings, D. Albesa-Jové, A. S. Batsanov, J. A. K. Howard, N. J. Taylor, H. M. Kaiser, D. E. Kaufmann, S.-Y. Poon, W.-Y. Wong, C. Jardin, S. Fathallah, A. Boucekkine, J.-F. Halet, T. B. Marder, *Chem. Eur. J.* **2006**, *12*, 2758–2771.

[18] For 9,10-dihydro-9,10-diboraanthracene, see: a) A. Lorbach, M. Bolte, H. Li, H.-W. Lerner, M. C. Holthausen, F. Jäkle, M. Wagner, *Angew. Chem. Int. Ed.* **2009**, *48*, 4584–4588; *Angew. Chem.* **2009**, *121*, 4654–4658; b) A. Lorbach, M. Bolte, H.-W. Lerner, M. Wagner, *Chem. Commun.* **2010**, *46*, 3592–3594; c) A. Lorbach, M. Bolte, H.-W. Lerner, M. Wagner, *Organometallics* **2010**, *29*, 5762–5765; d) E. Januszewski, A. Lorbach, R. Grewal, M. Bolte, J. W. Bats, H.-W. Lerner, M. Wagner, *Chem. Eur. J.* **2011**, *17*, 12696–12705.

[19] A. Lorbach, A. Hübner, M. Wagner, *Dalton Trans.* **2012**, *41*, 6048–6833.

[20] a) A. Hübner, A. M. Diehl, M. Bolte, H.-W. Lerner, M. Wagner, *Organometallics* **2013**, *32*, 6827–6833; b) A. Hübner, Z. Qu, U. Englert, M. Bolte, H.-W. Lerner, M. C. Holthausen, M. Wagner, *J. Am. Chem. Soc.* **2011**, *133*, 4596–4609.

© 2016 Wiley-VCH Verlag GmbH & Co. KGaA, Weinheim

ChemPubSoc Europe

CHEMISTRY
A European Journal
Full Paper

[21] a) N. Matsumi, Y. Chujo, *Polym. J.* **2008**, *40*, 77–89; b) N. Matsumi, M. Miyata, Y. Chujo, *Macromolecules* **1999**, *32*, 4467–4469.
[22] For the polyhydroboration of dinitriles, see: A. Nagai, J. Miyake, K. Kokado, Y. Nagata, Y. Chujo, *Macromolecules* **2009**, *42*, 1560–1564, and references cited therein.
[23] H. C. Brown, J. V. N. V. Prasad, S.-H. Zee, *J. Org. Chem.* **1986**, *51*, 439–445.
[24] M. Grandl, F. Pammer, *Macromol. Chem. Phys.* **2015**, *216*, 2249–2262.
[25] C. D. Entwistle, A. S. Batsanov, J. A. K. Howard, M. A. Fox, T. B. Marder, *Chem. Commun.* **2004**, 702–703.
[26] A recent report indicated that the scope of this reaction might be limited because the opposite regioselectivity was observed in the hydroboration of 2-alkynylpyridines featuring internal alkynes, see: K. Yuan, N. Suzuki, S. K. Mellerup, X. Wang, S. Yamaguchi, S. Wang, *Org. Lett.* **2016**, *18*, 720–723.
[27] M. Grandl, Y. Sun, F. Pammer, *Chem. Eur. J.* **2016**, *22*, 3976–3980.
[28] J. M. Clay, E. Vedejs, *J. Am. Chem. Soc.* **2005**, *127*, 5766–5767.
[29] a) A. Hübner, M. Diefenbach, M. Bolte, H. W. Lerner, M. C. Holthausen, M. Wagner, *Angew. Chem. Int. Ed.* **2012**, *51*, 12514–12518; *Angew. Chem.* **2012**, *124*, 12682–12686; b) A. Hübner, M. Bolte, H. W. Lerner, M. Wagner, *Angew. Chem. Int. Ed.* **2014**, *53*, 10408–10411; *Angew. Chem.* **2014**, *126*, 10576–10579.
[30] For the chemistry of unsubstituted 9-borafluorene, see: a) A. Das, A. Hübner, M. Weber, M. Bolte, H.-W. Lerner, M. Wagner, *Chem. Commun.* **2011**, *47*, 11339–11341; b) R. Köster, G. Benedikt, W. Fenzl, K. Reinert, *Justus Liebigs Ann. Chem.* **1967**, *702*, 197–223; c) R. Köster, G. Benedikt, *Angew. Chem. Int. Ed. Engl.* **1963**, *2*, 323–324; *Angew. Chem.* **1963**, *75*, 419–419; d) G. Benedikt, R. Köster, W. Larbig, K. Reinert, G. Rotermund, *Angew. Chem. Int. Ed. Engl.* **1964**, *3*, 174–185; *Angew. Chem.* **1963**, *75*, 1079–1090.
[31] J. V. B. Kanth, H. C. Brown, *J. Org. Chem.* **2001**, *66*, 5359–5365.
[32] a) D. J. Parks, W. E. Piers, G. P. A. Yap, *Organometallics* **1998**, *17*, 5492–5503; b) W. E. Piers, D. J. Parks, R. E. von H. Spence, *Angew. Chem. Int. Ed. Engl.* **1995**, *34*, 809–811; *Angew. Chem.* **1995**, *107*, 895–897.
[33] ^{1}H and ^{11}B NMR spectra of a commercially obtained $HBCl_2$·SMe_2 in C_6D_6 showed $HBCl_2$ (≈86%) to be in equilibrium with H_2BCl (≈7%) and BCl_3 (≈7%).
[34] Q. Zhao, H. Zhang, A. Wakamiya, S. Yamaguchi, *Synthesis* **2009**, 127–132.
[35] Tricoordinated boron centers usually yield broader signals in the ^{11}B NMR spectrum than tetracoordinate ones. Small amounts of **open** conformer may therefore be present, but may not be detectable by this analytical method.
[36] Determined by Gaussian fitting of the experimental absorption spectrum.
[37] a) B. C. Thompson, Y.-G. Kim, T. D. McCarley, J. R. Reynolds, *J. Am. Chem. Soc.* **2006**, *128*, 12714–12725; b) W. N. Hansen, G. J. Hansen, *Phys. Rev. A: At. Mol. Opt. Phys.* **1987**, *36*, 1396–1402; c) V. V. Pavlishchuk, A. W. Addison, *Inorg. Chim. Acta* **2000**, *298*, 97–102.
[38] G. C. Welch, G. C. Bazan, *J. Am. Chem. Soc.* **2011**, *133*, 4632.
[39] Both the molecular structures and electronic properties of the **open** conformers are markedly different, particularly for **PhPyBPF** and **PhPyB-Flu**. However, because the **open** conformers are energetically unfavorable, their properties are not be explicitly discussed herein. The corresponding orbital plots and electronic and structural data have been included in Section 3 in the Supporting Information.
[40] a) T. P. I. Saragi, T. Spehr, A. Siebert, T. Fuhrmann-Lieker, J. Salbeck, *Chem. Rev.* **2007**, *107*, 1011–1065; b) C. Poriel, N. Cocherel, J. Rault-Berthelot, L. Vignau, O. Jeannin, *Chem. Eur. J.* **2011**, *17*, 12631–12645; c) D. Thirion, J. Rault-Berthelot, L. Vignau, C. Poriel, *Org. Lett.* **2011**, *13*, 4418–4421; d) J. Wang, W. Wan, H. Jiang, Y. Gao, X. Jiang, H. Lin, W. Zhao, J. Hao, *Org. Lett.* **2010**, *12*, 3874–3877; e) C. Poriel, J. Rault-Berthelot, D. Thirion, F. Barriere, L. Vignau, *Chem. Eur. J.* **2011**, *17*, 14031–14046.
[41] Y. Zhao, D. G. Truhlar, *J. Chem. Theory Comput.* **2008**, *4*, 1849–1868.
[42] a) Z. M. Heiden, A. P. Lathem, *Organometallics* **2015**, *34*, 1818–1827; b) E. R. Clark, A. Del Grosso, M. J. Ingleson, *Chem. Eur. J.* **2013**, *19*, 2462–2466; c) T. S. De Vries, A. Prokofjevs, E. Vedejs, *Chem. Rev.* **2012**, *112*, 4246–4282.

Received: May 23, 2016
Published online on August 18, 2016

 © 2016 Wiley-VCH Verlag GmbH & Co. KGaA, Weinheim

CHEMISTRY
A European Journal

Supporting Information

Hydroboration as an Efficient Tool for the Preparation of Electronically and Structurally Diverse N→B-Heterocycles

Markus Grandl,[a] Thomas Kaese,[b] Anke Krautsieder,[a] Yu Sun,[c] and Frank Pammer*[a]

chem_201602458_sm_miscellaneous_information.pdf

Supporting Information

[Title]

[Authors]

Contents

1. Experimental Section 3
1.1. Materials and Instrumentation 3
1.2. Chemical Synthesis 4
2. Supplementary Analytical Data 10
2.1. Electrochemical Data 10
Figure S 1 a) Cyclic voltammogramms of PhPyBBN, $PhPyBH_2$, PhPyFlu, $PhPyBPh_2$, PhPyBPF, and $PhPyBCl_2$.. 10
Figure S 2. Cyclic voltammogramms of PhPyBBN, $PhPyBH_2$, PhPyFlu, and $PhPyBCl_2$.. 10
Figure S 3 UV-vis absorption (solid) and emission (dashed) spectra of $PhPyBCl_2$ in THF solution. 11
2.2. NMR- and MS-Data 11
Figure S 4 ^{1}H NMR-spectra of compound PhPy and reaction monitoring of hydroboration with $HB(C_6F_5)_2$ by ^{1}H NMR in C_6D_6. 11
Figure S 5 ^{1}H NMR-spectrum of PhPy in $CDCl_3$. 12
Figure S 6 ^{13}C NMR-spectrum of PhPy in $CDCl_3$. 12
Figure S 7 HR-FTMS-spectrum of PhPy 13
Figure S 8 ^{1}H NMR-spectrum of $PhPyBH_2$ in C_6D_6. 14
Figure S 9 ^{13}C NMR-spectrum of $PhPyBH_2$ in C_6D_6. 14
Figure S 10 ^{11}B NMR-spectrum of $PhPyBH_2$ in C_6D_6. 15
Figure S 11 ^{1}H NMR-spectrum of PhPyBBN in C_6D_6. 15
Figure S 12 ^{13}C NMR-spectrum of PhPyBBN in C_6D_6. 16
Figure S 13 ^{11}B NMR-spectrum of PhPyBBN in C_6D_6. 16
Figure S 14 ^{1}H NMR-spectrum of $PhPyBCl_2$ in C_6D_6. 17
Figure S 15 ^{13}C NMR-spectrum of $PhPyBCl_2$ in C_6D_6. 17
Figure S 16 ^{11}B NMR-spectrum of $PhPyBCl_2$ in C_6D_6. 18
Figure S 17 ^{1}H NMR-spectrum of PhPyBFlu in C_6D_6. 18
Figure S 18 ^{13}C NMR-spectrum of PhPyBFlu in C_6D_6. 19
Figure S 19 ^{11}B NMR-spectrum of PhPyBFlu in C_6D_6. 19
Figure S 20 HR-FTMS-spectrum of PhPyBFlu 20
Figure S 21 ^{1}H NMR-spectrum of PhPyBPF in C_6D_6 20

Figure S 22 ^{13}C NMR-spectrum of PhPyBPF in C_6D_6. 21
Figure S 23 ^{11}B NMR-spectrum of PhPyBPF in C_6D_6. 21
Figure S 24 ^{19}F NMR spectrum of PhPyBPF in C_6D_6. 22
Figure S 25 ^{1}H NMR-spectrum of PhPyBPh$_2$ in CD_2Cl_2. 23
Figure S 26 ^{13}C NMR-spectrum of PhPyBPh$_2$ in CD_2Cl_2. 23
Figure S 27 ^{11}B NMR-spectrum of PhPyBPh$_2$ in CD_2Cl_2. 24
Figure S 28 ^{11}B NMR-spectrum of PhPyBPh$_2$ in C_6D_6. 24

3. DFT-calculations 25
3.1. Structure and Properties of N→B-Ladder Boranes 25
Table S 1. Characteristic bond lengths [Å] and angles [°] of the simulated ladder compounds. 25
Figure S 29. Calculated and Experimental N→B bond lengths (left) 26
Table S 2 Frontier orbital plots of borylated compounds depending on their conformation. 27
Figure S 30 Calculated frontier orbital levels of borylated compounds depending on their conformation 29
3.2. TD-DFT calculations 30
3.2.1. Simulated UV/Vis spectra 30
Table S3. Calculated[a] and experimental electronic properties of the investigated ladder-boranes. 30
3.2.2. Electronic Transitions 31

4. Crystal Data 71
4.1. PhPyBBN 71
4.1. PhPyBH$_2$ 77
4.2. PhPyBCl$_2$ 81
4.3. PhPyBPF 85
4.4. PhPyBFlu 91
4.5. PhPyBPh$_2$ 110

1. Experimental Section

1.1. Materials and Instrumentation

All reactions and manipulations of sensitive compounds were carried out under an atmosphere of pre-purified argon using either Schlenk techniques or an inert-atmosphere glovebox (MBraun Labmaster). Toluene, Et_2O, THF, DMF and dichloromethane were purified using a solvent purification system (MBraun; alumina / copper columns for hydrocarbon solvents). Hexane, and benzene were dried by distillation from CaH_2 under argon atmosphere prior to use. 1-Bromo-2-(2-methylprop-1-en-1-yl)benzene[i], bis(pentafluorophenyl)borane[ii], and 9-bromo-(2,7-di-*tert*-butyl)-9-borafluorene[iii] were prepared according to literature procedures. Other reagents were commercially available (Aldrich, Acros, Alfa Aesar) and were either used as obtained or purified by standard procedures.[iv] ^1H, ^{13}C, and ^{11}B NMR spectra were recorded at 293 K on a Bruker Avance DRX 400 (400 MHz) spectrometer or a Bruker Avance 500 AMX (500 MHz). Solution ^1H and ^{13}C NMR spectra were referenced internally to the solvent residual signals.[v] Solution ^{11}B NMR spectra were referenced externally to $BF_3 \bullet Et_2O$ (10% in $CHCl_3$). Individual signals are referred to as singlet (s), doublet (d), pseudo-doublet (psd), triplet (t), multiplet (m), centro-symmetric multiplet (m_c), and broadened (br). Following abbreviation are used for signal assignment: Ph (phenyl), Py (pyridyl), BFlu (2,7-di-tert-butyl-9-borafluoren-9-yl), BBN (9-borabicyclo[3.3.1]non-9-yl), PF (2,3,4,5,6-pentafluorophenyl). High resolution mass spectrometry measurements were performed on a Bruker SolariX FTMS using MALDI (Matrix Assisted Laser Desorption Ionization). *Trans*-2-[3-(4-*tert*-butylphenyl)-2-methyl-2-propenylidene]malononitrile (DCTB) was used as matrix in MALDI measurements. UV-visible absorption spectra and photoluminescence spectra were acquired on a Perkin Elmer Lambda 19 UV-vis/NIR spectrometer and a Perkin Elmer LS 55 fluorescence spectrometer, respectively. Fluorescein was used as standard to determine fluorescence quantum yields (φ) (φ(fluorescein) = 79%).[vi] Elemental analyses were performed on an Elemental Vario EL analyzer. Melting points were measured on a Büchi M-565 melting point apparatus with a heating rate of 2 K/min. Electrochemical analyses were performed both in cyclic voltammetry- and square-wave voltammetry-mode with an Autolab Potentiostat Galvanostat with a three electrode system, consisting of a Pt working electrode (0.785 mm^2), a Pt-counter electrode, and an Ag/AgCl-reference electrode. The measurements were carried out in THF or CH_2Cl_2 with $[N(n\text{-}Bu)_4][PF_6]$ (0.1 M) as supporting electrolyte, and were internally referenced against the ferrocene/ferrocenium redox-couple.

Quantum chemical calculations were performed on the **C**ampus **U**lm **S**hared **S**cience Cluster (CUSS) compute server at Ulm University, using release D.01 of the Gaussian09 program package. All geometry optimization of synthesized boranes, and intermediates and transitional states of the hydroboration mechanism were performed at the M06-2X/6-31G(d,p) level of theory. Frequency calculation confirmed the optimized structures (zero imaginary frequencies). Frontier

orbital levels and the first 15 excited states were simulated by time-dependent DFT (td-dft) at the M06-2X/6-311+G(d,p) level. The M06-2X[vii] functional was chosen, as it accounts well dispersion interactions, and has been shown to perform well in the modeling of organoboranes.[viii]

X-ray diffraction intensities were collected on an Agilent Technologies SuperNova single-crystal X-ray diffractometer at 150 K with Mo-Kα radiation. Crystal data and refinement parameters are collected in the Supporting Information. The structures were solved using direct methods (SIR92[ix] or Shlexs-2014[x]), completed by subsequent difference Fourier syntheses, and refined by full-matrix least-squares procedures. Semi-empirical absorption corrections from equivalents (Multiscan) were carried out, except an analytical numeric absorption correction was applied on compound **PhPyBBN**[xi]. In the structure of **PhPyBH$_2$**, the hydrogen atoms H1A and H1B, which are bound to B1, were observed clearly in the following difference Fourier synthesis, and then were allowed to be refined freely. All the other hydrogen atoms were placed in calculated positions and refined by using a riding model. In the structure of **PhPyBFlu**, because of the existence of partially occupied/severely disordered n-hexane/H_2O, SQUEEZE process integrated in PLATON was used. And the detailed information has been posted in the final CIF file. CCDC 1476602-1476607 contain the supplementary crystallographic data for this paper. These data can be obtained free of charge from The Cambridge Crystallographic Data Centre via www.ccdc.cam.ac.uk/data_request/cif.

1.2. Chemical Synthesis

1.2.1. Preparation of PhPy

A solution of 1-bromo-2-(2-methylprop-1-en-1-yl)benzene[i] (1.77 g, 8.38 mmol) in THF (10 mL) is cooled to –78 °C and a solution of *n*-BuLi (1.6 M in n-hexane, 5.35 mL, 8.55 mmol) is added within 15 minutes. The pale yellow solution is stirred for 2 hours at –78 °C before a solution of zinc chloride (1.17 g, 8.55 mmol) in THF (3 mL) is added slowly. The colorless solution is stirred for 45 minutes before it is allowed to reach room temperature. Addition of $PdCl_2(PPh_3)_2$ (235 mg, 340 µmol), and 2-bromopyridine (1.66 g, 10.5 mml) is followed by stirring of the solution at room temperature for 18 hours. The solvent is removed and the crude product is purified by column chromatography over silica using petroleum ether / ethyl acetate (12/1 → 10/1) as eluent to yield 1.31 g (6.26 mmol, 75%) of compound **PhPy** as pale yellow oil.

^{1}H NMR (400 MHz, $CDCl_3$): δ = 8.70 (psd, *J* = 4.9 Hz, 1H), 7.66 (m_c, 1H), 7.63–7.60 (m, 1H), 7.44 (psd, *J* = 7.9 Hz, 1H), 7.38–7.28 (m, 3H), 7.20 (m_c, 1H), 6.19 [m_c, 1H, C*H*=C(CH_3)$_2$], 1.80 (d, ^4J = 1.5 Hz, 3H, CH_3), 1.69 (d, ^4J = 1.3 Hz, 3H, CH_3) ppm.

^{13}C NMR (101 MHz, $CDCl_3$): δ = 159.2, 149.4, 139.6, 136.8, 135.7, 135.6, 130.4, 129.9, 128.1, 126.7,

125.2, 124.7, 121.6, 26.2, 19.5 ppm.

HR-FTMS (ESI, positive mode): m/z calcd for $C_{15}H_{15}N$ $[M+H]^+$: 210.12773 Da; found: 210.12826 Da.

Elemental analysis calcd (%) for $C_{15}H_{15}N$: C 86.08, H 7.22, N 6.69; found: C 86.19, H 7.33, N 6.80.

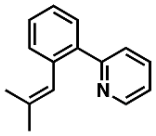

1.2.2. Preparation of PhPyBH2

A solution of **PhPy** (150 mg, 717 µmol) in borane tetrahydrofurane complex (0.5 M in THF, 2.15 mL, 1080 µmol) is heated to 50 °C over 3 days. The solvent is removed and the remaining oil is treated with *n*-hexane. The resulting precipitate is collected by centrifugation and recrystallized from diethyl ether / *n*-hexane to furnish the product (139 mg, 623 µmol, 87%) as pale yellow crystals.

m.p. = 71 °C.

^{1}H NMR (400 MHz, C_6D_6): δ = 8.27 (psd, *J* = 5.7 Hz, 1H, Py-6), 7.36 (psd, *J* = 7.9 Hz, 1H, Ph-3), 7.23–7.18 (m, 2H, Ph-4, Ph-6), 7.03 (m_c, 1H, Ph-5), 6.97 (psd, *J* = 8.2 Hz, 1H, Py-3), 6.70 (m_c, 1H, Py-4), 6.13 (m_c, 1H, Py-5), 4.01–3.12 (br m, 2H, BH_2), 2.12 (m_c, 1H, Py*CH*BH_2), 1.69 [m_c, 1H, *CH*$(CH_3)_2$], 1.22 (d, *J* = 6.6 Hz, 3H, CH_3), 1.04 (d, *J* = 6.7 Hz, 3H, CH_3) ppm.

^{13}C NMR (126 MHz, C_6D_6): δ = 154.3 (s, Py-2), 151.7 (s, Ph-2), 147.7 (s, Py-6), 139.5 (s, Py-4), 132.2 (s, Ph-3), 131.5 (s, Ph-4), 130.9 (s, Ph-1), 127.3 (Ph-6), 125.4 (s, Ph-5), 122.4 (s, Py-5), 122.0 (s, Py-3), 40.2 (br s, *C*H-BH_2), 32.7 [s, *C*H$(CH_3)_2$], 23.8 (s, CH_3), 23.0 (s, CH_3) ppm.

^{11}B NMR (128 MHz, C_6D_6, 41 °C): δ = -7.2 (psd, $^1J_{BH}$ = 100 Hz) ppm.

Elemental analysis calcd (%) for $C_{15}H_{18}BN$: C 80.75, H 8.13, N 6.28; found: C 80.67, H 7.98, N 6.25.

λ_{max}(THF) = 304 nm.

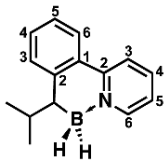

5

1.2.3. Preparation of PhPyBBN

A thick walled pressure tube is charged with **PhPy** (200 mg, 956 µmol), and 9*H*-BBN-dimer (163 mg, 669 µmol) and dry THF (4 mL). The solution is stirred for 2 days at 60 °C. The solvent is removed under reduced pressure and the remaining solid is purified by column chromatography over silica using petroleum ether / ethyl acetate (15/1) as eluent. Recrystallization of the resulting solid from diethyl ether / *n*-hexane furnishes the product as yellow crystals (270 mg, 860 µmol, 85%).
m.p. = 165 °C.

^{1}H NMR (400 MHz, C_6D_6): δ = 8.57 (psd, *J* = 5.9 Hz, 1H, Py-6), 7.26–7.21 (m, 2H, Ph-3, Ph-6), 7.18 (m_c, 1H, Ph-4), 7.02 (m_c, 1H, Ph-5), 6.96 (psd, *J* = 8.1 Hz, 1H, Py-3), 6.78 (m_c, 1H, Py-4), 6.32 (m_c, 1H, Py-5), 2.70–2.60 (m, 1H, BBN-H), 2.43–2.32 (m, 2H, BBN-H, Py-C*H*-BBN), 2.32–2.10 (m, 5H, BBN-H), 2.07–1.99 (m, 1H, BBN-H), 1.94–1.85 [m, 1H, C*H*(CH_3)$_2$], 1.85–1.69 (m, 3H, BBN-H) 1.52 (br m_c, 1H, BBN-bridgehead), 1.25–1.15 (m, 4H, CH_3, BBN-H), 0.62 (br m_c, 1H, BBN-bridgehead), 0.33 (d, *J* = 7.0 Hz, 3H, CH_3) ppm.

^{13}C NMR (126 MHz, C_6D_6): δ = 155.1 (s, Py-2), 147.9 (s, Ph-2), 146.3 (s, Py-6), 138.7 (s, Py-4), 133.1 (s, Ph-6), 132.7 (s, Ph-1), 130.8 (s, Ph-4), 125.9 (Ph-3), 125.2 (s, Ph-5), 123.1 (s, Py-3), 121.8 (s, Py-5), 40.4 (br s, *C*H-BBN), 36.1 (s, BBN), 32.3 (s, BBN), 31.4 (s, BBN), 31.3 (s, BBN), 29.6 (s, *C*H(CH_3)$_2$), 25.3 (s, CH_3), 25.2 (s, BBN), 25.2 (br s, BBN-bridgehead), 24.9 (s, BBN), 23.5 (br s, BBN-bridgehead), 20.9 (s, CH_3) ppm.
^{11}B NMR (128 MHz, C_6D_6): δ = -0.9 (br s) ppm.
Elemental analysis calcd (%) for $C_{23}H_{30}BN$: C 83.38, H 9.13, N 4.23; found: C 83.50, H 9.07, N 4.22.
λ_{max}(THF) = 303 nm.

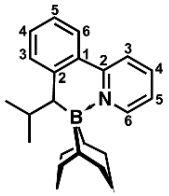

1.2.4. Preparation of PhPyBCl2

Inside the glovebox compound **PhPy** (68 mg, 325 µmol), and neat dichloroborane dimethylsulfide complex (100 µL, ρ = 1.26 mg/mL, ca. 125 mg / 870 µmol) were dissolved in PhMe (1 mL). The solution was stirred for 20 h at ambient temperature. After removal of the solvent and excess borane the residue was dried at 70 °C under reduced pressure. The remaining solid is redissolved with benzene and precipitated by the addition of *n*-hexane. Removing of the supernatant and drying under reduced pressure furnishes 89 mg (305 µmol, 94%) of compound **PhPyBCl$_2$** as a colorless crystalline solid.
m.p. = 154 °C.

^{1}H NMR (400 MHz, C_6D_6): δ = 9.24 (psd, *J* = 6.1 Hz, 1H, Py-6), 7.19–7.16 (m, 2H, Ph-3, Ph-6), 7.12 (m_c, 1H, Ph-4), 7.02–6.98 (m, 1H, Ph-5), 6.93 (psd, *J* = 8.2 Hz, 1H, Py-3), 6.70–6.66 (m_c, 1H, Py-4), 6.23 (m_c, 1H, Py-5), 2.90–2.78 [m, 2H, C*H*(CH_3)$_2$, Py-C*H*BCl_2], 0.94 (d, ^{3}J = 6.9 Hz, 3H, CH_3), 0.17 (d, ^{3}J = 6.8 Hz, 3H, CH_3) ppm.

^{13}C NMR (126 MHz, C_6D_6): δ = 153.2 (s, Py-2), 143.6 (s, Py-6), 142.9 (s, Ph-2), 142.2 (s, Py-4), 134.1 (s, Ph-3), 131.5 (s, Ph-4), 130.4 (s, Ph-1), 127.2 (s, Ph-6), 126.4 (s, Ph-5), 123.3 (s, Py-5), 122.5 (s, Py-3), 43.1 (br s, Py-C$HBCl_2$), 31.0 [s, *C*$H(CH_3)_2$], 23.7 (s, CH_3), 17.7 (s, CH_3) ppm.

^{11}B NMR (128 MHz, C_6D_6): δ = 9.4 (br s) ppm.

Elemental analysis calcd (%) for $C_{15}H_{16}BCl_2N$: C 61.70, H 5.52, N 4.80; found: C 61.59, H 5.35, N 4.72.

UV-vis absorption: λ_{max}(THF) = 314 nm. Fluorescence: λ_{max}(THF) = 423 nm

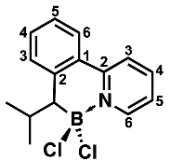

1.2.5. Preparation of PhPyBFlu

a) Preparation of 2,7-Di-*tert*-butyl-9-*H*-9-borafluorene (**9*H*-BFlu**)[iii]

Inside the glovebox a PTFE-sealed NMR tube is charged with 2,7-di-*tert*-butyl-9-bromo-9-borafluorene (100 mg, 282 µmol), 1 mL benzene, and triethylsilane (81.9 mg, 704 µmol). After four hours at ambient temperature all volatiles are removed *in vacuo*.

b) Hydroboration of 1-(2-pyridyl)-2-(isobutenyl)-benzene (**PyPh**)

Inside the glovebox crude **9*H*-BFlu** is dissolved in THF-d_8 (0.5 mL), and **PhPy** (64.8 mg, 310 µmol) is added. The solution is heated to 75 °C until ^{1}H-NMR indicated full conversion (4 days). Removing of the solvent *in vacuo* is followed by recrystallization of the remaining solid from *n*-hexane which yields the product as pale yellow solid (80.0 mg, 165 µmol, 59%).

m.p. = 94 °C.

^{1}H NMR (400 MHz, C_6D_6): δ = 8.16 (psd, *J* = 5.9 Hz, 1H, Py-6), 7.99 (d, ^{3}J = 8.0 Hz, 1H, BFlu-d'), 7.87–7.83 (m, 2H, BFlu-d, BFlu-a'), 7.54 (dd, ^{3}J = 8.0 Hz, ^{4}J = 2.0 Hz, 1H, BFlu-c'), 7.45–7.42 (m, 1H, Ph-6), 7.32 (dd, ^{3}J = 8.0 Hz, ^{4}J = 2.0 Hz, 1H, BFlu-c), 7.23–7.19 (m, 2H, Ph-4, Py-5), 7.15–7.10 (overlapped w. solvent, m, 2H, Py-3, Ph-3), 6.65 (m_c, 1H, Py-4), 6.51 (d, ^{4}J = 2.0 Hz, 1H, BFlu-a), 5.88 (m_c, 1H, Py-5), 2.79 [m_c, 1H, C*H*(CH_3)$_2$], 2.11 (d, ^{3}J = 3.5 Hz, 1H, Py-C*H*-BFlu), 1.50 [s, 9H, C(C*H*)$_3$], 1.16 [s, 9H, C(CH_3)$_3$], 0.95 [d, ^{3}J= 6.8 Hz, 3H, CH(CH_3)$_3$], 0.62 [d, ^{3}J = 6.9 Hz, 3H, CH(CH_3)$_2$] ppm.

^{13}C NMR (126 MHz, C_6D_6): δ = 158.2 (br s, BFlu-f), 154.8 (s, Py-2), 154.0 (br s, BFlu-f'), 148.9 (s, BFlu-e'),

148.1 (s, BFlu-b'), 147.8 (s, BFlu-b), 145.0 (s, BFlu-e), 144.1 (s, Py-6), 139.9 (s, Py-4), 134.6 (s, Ph-3), 133.0 (s, Ph-1), 130.4 (s, Ph-4), 129.0 (s, BFlu-a'), 126.7 (s, Ph-6), 126.4 (s, BFlu-a), 125.7 (s, Ph-5), 124.4 (s, BFlu-c'), 123.7 (s, BFlu-c), 122.5 (s, Py-5), 121.9 (s, Py-3), 119.3 (s, BFlu-d'), 118.6 (s, BFlu-d), 39.9 (br s, Py-*C*HBFlu), 34.7 [s, *C*'(CH_3)$_2$], 34.4 [s, *C*(CH_3)$_3$], 31.9 [s, C'(*C*H_3)$_3$], 31.5 [s, C(*C*H_3)$_3$], 31.4 [s, *C*H(CH_3)$_2$], 23.9 (s, CH_3), 19.0 (s, CH_3) ppm.

^{11}B NMR (128 MHz, C_6D_6): δ = 0.4 (br s) ppm.

HR-FTMS (MALDI, positive mode): m/z calcd for $C_{35}H_{40}BN$ $[M]^+$: 484.32846 Da; found: 484.32864 Da.

λ_{max}(THF) = 319 nm. (Derived by Gaussian fit)

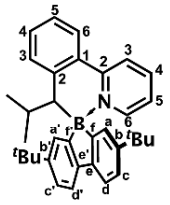

1.2.6. Preparation of PhPyBPF

Inside the glovebox compound a PTFE-sealed NMR-tube is charged with a solution of **PhPy** (25.0 mg, 119 µmol), and $HB(C_6F_5)_2$ (66.0 mg, 191 µmol) in C_6D_6 (0.5 mL). The solution was heated to 85 °C until ^{1}H-NMR indicated full conversion (ca. 3 d). The solvent is removed in vacuo and the residue is purified by column chromatography over silica using petroleum ether / ethyl acetate (6/1) as eluent. The solvent was removed to give compound **PhPyBPF** as colorless solid (37.0 mg, 66.6 µmol, 56%).

m.p. = 166 °C.

^{1}H NMR (400 MHz, C_6D_6): δ = 8.07 (br psd, *J* = 8.0 Hz, 1H , Py-6), 7.11 (overlapped with solvent, psd, *J* = 7.9 Hz, 1H, Ph-3), 7.07 (psd, *J* = 8.3 Hz, 1H, Ph-6), 6.97–6.93 (m, 2H, Py-3, Ph-4), 6.87 (m_c, 1H, Py-4), 6.82 (m_c, 1H, Ph-5), 6.37 (m_c, 1H, Py-5), 3.05 [br psd, ^3J = 3.7 Hz, 1H, Py-CH-B(PF)$_2$], 1.89 [m_c, 1H, C*H*(CH_3)$_2$], 1.06 (d, ^3J = 6.8 Hz, 3H, CH_3), 0.13 (d, ^3J = 6.7 Hz, 3H, CH_3) ppm.

^{13}C NMR (126 MHz, C_6D_6): δ = 155.7 (s, Py-2), 148.7 (br d, ^1J(^{13}C,^{19}F) = 238 Hz, C-F), 148.1 (br d, ^1J(^{13}C,^{19}F) = 235 Hz, C-F), 146.3 (s, Ph-2), 145.9 (s, Py-6), 141.6 (s, Py-4), 140.6 (overlapped, br d, ^1J(^{13}C,^{19}F) = 239 Hz, C-F), 139.7 (overlapped, br d, ^1J(^{13}C,^{19}F) = 249 Hz, C-F), 138.1 (br d, ^1J(^{13}C,^{19}F) = 246 Hz, C-F), 137.3 (overlapped, br d, ^1J(^{13}C,^{19}F) = 239 Hz, C-F), 131.8 (s, Ph-3), 131.7 (s, Ph-4), 131.2 (s, Ph-1), 126.3 (overlapped, s, Ph-6), 126.3 (overlapped, s, Ph-5), 123.4 (s, Py-3), 122.2 (br s, C_q-PF), 121.9 (s, Py-5), 118.2 (br s, C_q-PF), 39.5 [br s, *C*HB(PF)$_2$], 31.2 [s, *C*H(CH_3)$_2$], 25.0 (s, CH_3), 20.1 (s, CH_3) ppm.

^{11}B NMR (128 MHz, C_6D_6): δ = –1.0 (br s) ppm.

^{19}F NMR (377 MHz, C_6D_6): δ = –125.9 (br s, 1F), –131.4 (br s, 1F), –135.6 (br s, 1F), –155.6 (m_c, 1F), –

158.3 (m_c, 1F), –162.0 (m_c, 2F), –164.2 (br s, 2F) ppm.

Elemental analysis calcd (%) for $C_{27}H_{16}BF_{10}N$: C 58.41, H 2.90, N 2.52; found: C 58.34, H 2.84, N 2.48.

λ_{max}(THF) = 310 nm.

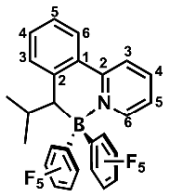

1.2.7. Preparation of PhPyBPh2

A suspension of **PhPyBCl$_2$** (120 mg, 411 µmol), diphenylzinc (203 mg, 925 µmol), in toluene (3 mL) is heated for 3 hours to 60 °C. The solvent is removed and the residue is purified by column chromatography over silica using petroleum ether / ethyl acetate (6/1 → 3/1) as eluent to give 130 mg (345 µmol, 84%) of compound **PhPyBPh$_2$** as colorless solid.

m.p. = 262 °C (decomp.)

^{1}H NMR (400 MHz, CD_2Cl_2): δ = 8.85 (psd, *J* = 6.2 Hz, 1H, Py-6), 8.15–8.07 (m, 2H, Py-4, Py-3), 7.62 (psd, *J* = 7.9, 1H, Ph-6), 7.51 (m_c, 1H, Py-5), 7.35–7.29 (m, 2H, Ph-3, Ph-4), 7.22–7.17 (m, 3H, Ph-5, 2×BPh_2), 7.15–7.11 (m, 3H, 3×BPh_2), 7.01–6.89 (m, 5H, 5×BPh_2), 2.35 (d, ^2J = 2.7 Hz, 1H, Py-C*H*-BPh_2), 2.05–1.98 [m, 1H, C*H*(CH_3)$_2$], 0.83 (d, ^3J = 7.0 Hz, 3H, CH_3), 0.27 (d, ^3J = 6.9 Hz, 3H, CH_3) ppm.

^{13}C NMR (126 MHz, CD_2Cl_2): δ = 155.6 (s, Py-2), 153.7 (br s, BPh_2), 151.8 (br s, BPh_2), 146.9 (s, Py-6), 146.2 (s, Ph-2), 141.5 (s, Py-4), 135.3 (s, BPh_2), 133.8 (s, Ph-3), 132.8 (s, BPh_2), 132.0 (s, Ph-1), 130.7 (s, Ph-4), 127.2 (overlapped, s, BPh_2), 127.1 (overlapped, s, Ph-6), 127.1 (overlapped, s, BPh_2), 125.7 (s, Ph-5), 125.4 (s, BPh_2), 124.7 (s, BPh_2), 123.5 (s, Ph-3), 123.0 (s, Py-5), 41.6 (br s, Py-CH-BPh_2), 29.9 [s, *C*H(CH_3)$_2$], 24.8 (s, CH_3), 19.2 (s, CH_3) ppm.

^{11}B NMR (128 MHz, CD_2Cl_2): δ = 0.3 (br s) ppm.

^{11}B NMR (128 MHz, C_6D_6): δ = 0.9 (br s) ppm.

Elemental analysis calcd (%) for $C_{27}H_{26}BN$: C 86.40, H 6.98, N 3.73; found: C 86.19, H 6.81, N 3.73.

λ_{max}(THF) = 306 nm.

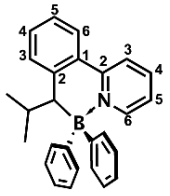

2. Supplementary Analytical Data

2.1. Electrochemical Data

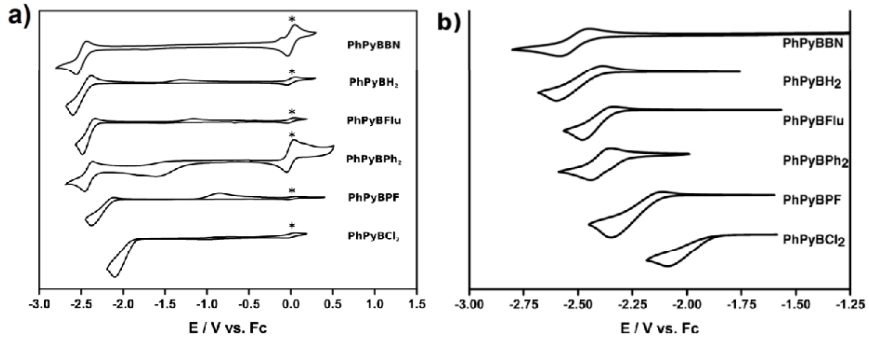

Figure S 1 a) Cyclic voltammogramms of PhPyBBN, PhPyBH$_2$, PhPyFlu, PhPyBPh$_2$, PhPyBPF, and PhPyBCl$_2$. Recorded in THF with [N*n*-Bu$_4$][PF$_6$] (0.1 M) as electrolyte at 100 mV/s. * = internal standard ferrocene. b) enlarged reduction waves without ferrocene added.

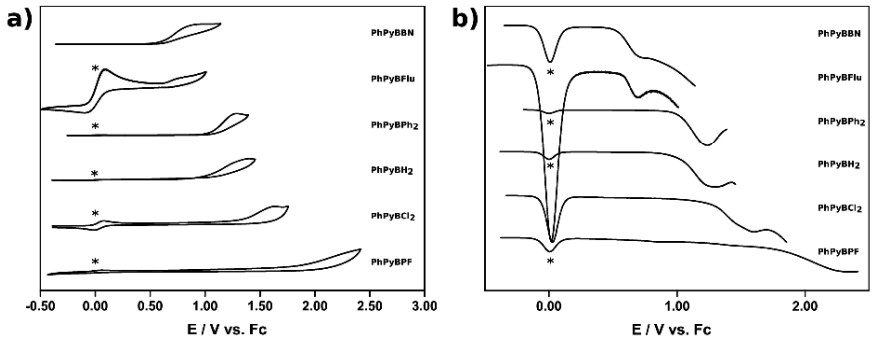

Figure S 2. a) Cyclic voltammograms and b) square-wave voltammograms of PhPyBBN, PhPyFlu, PhPyBPh$_2$, PhPyBH$_2$, PhPyBCl$_2$, and PhPyBPF. Recorded in CH$_2$Cl$_2$ with [N*n*-Bu$_4$][PF$_6$] (0.1 M) as electrolyte at 100 mV/s. * = internal standard ferrocene.

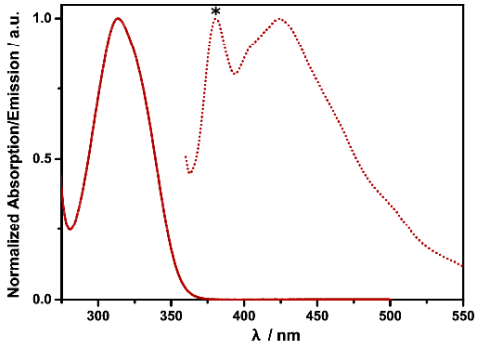

Figure S 3 UV-vis absorption (solid) and emission (dashed) spectra of $PhPyBCl_2$ in THF solution. * Raman scattering of solvent THF. Excitation wavelength 340 nm.

2.2. NMR- and MS-Data

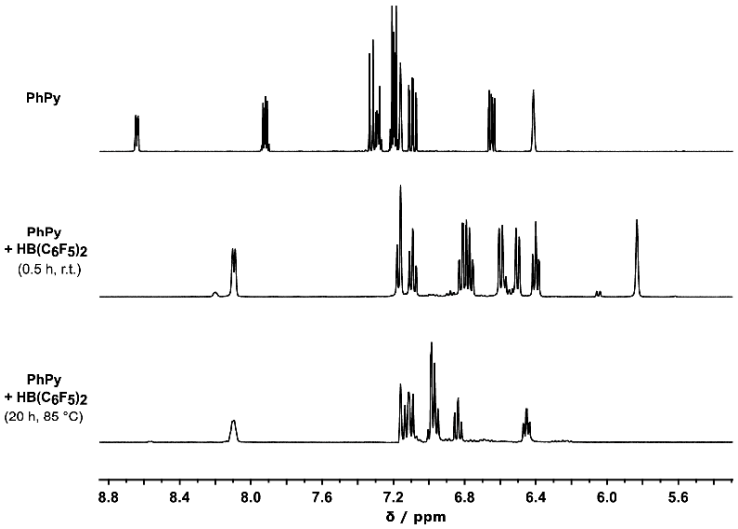

Figure S 4 ^1H NMR-spectra of compound PhPy and reaction monitoring of hydroboration with $HB(C_6F_5)_2$ by ^1H NMR in C_6D_6.

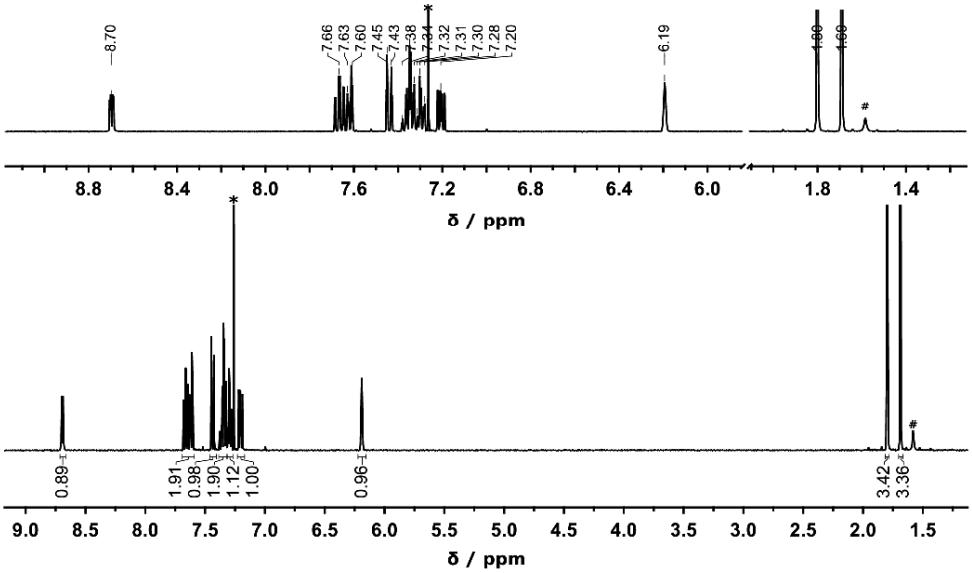

Figure S 5 ^{1}H NMR-spectrum of PhPy in $CDCl_3$. Residual H_2O at 2.56 ppm.

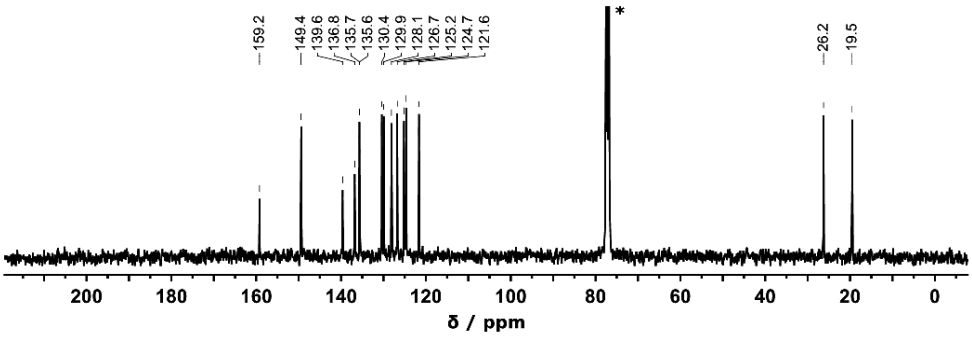

Figure S 6 ^{13}C NMR-spectrum of PhPy in $CDCl_3$.

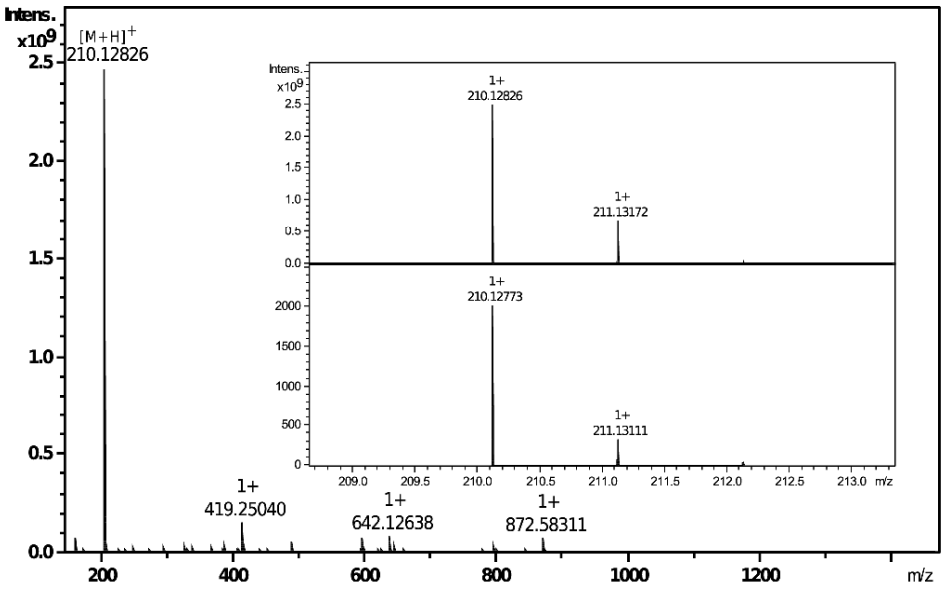

Figure S 7 HR-FTMS-spectrum of PhPy. The insert shows enlarged the experimental (top) and calculated (bottom) isotope-pattern of the molecular ion.

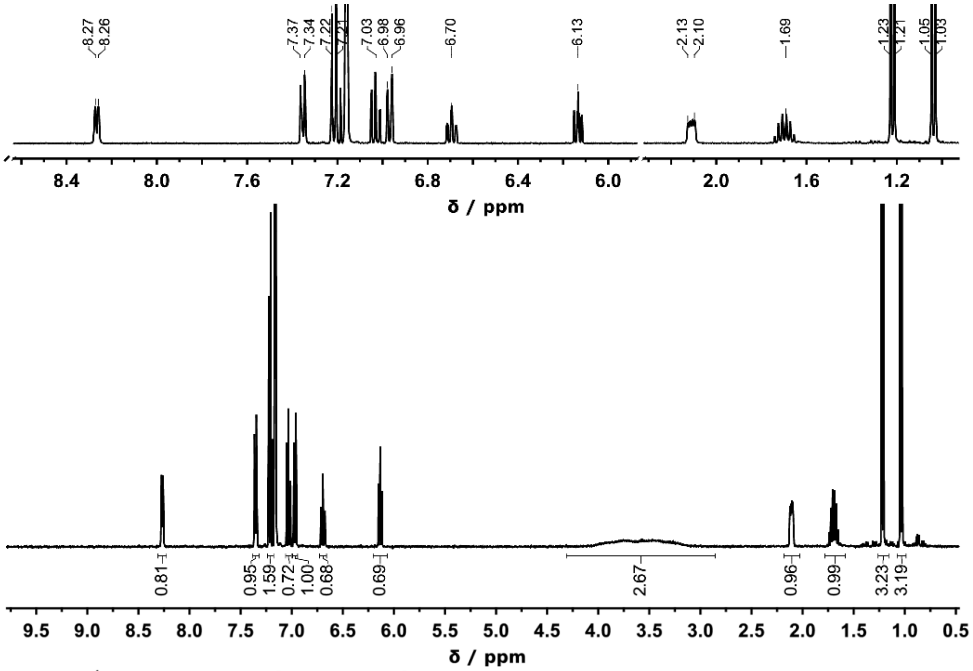

Figure S 8 ^{1}H NMR-spectrum of PhPyBH$_2$ in C_6D_6.

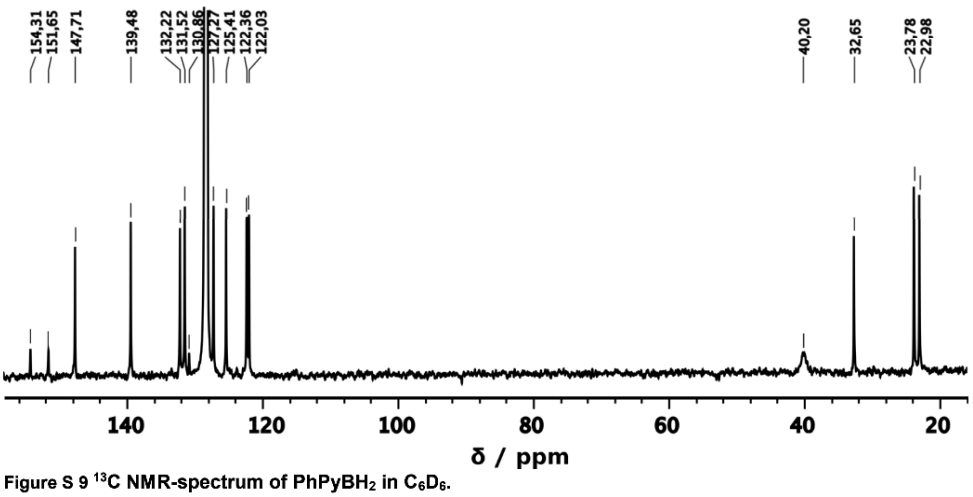

Figure S 9 ^{13}C NMR-spectrum of PhPyBH$_2$ in C_6D_6.

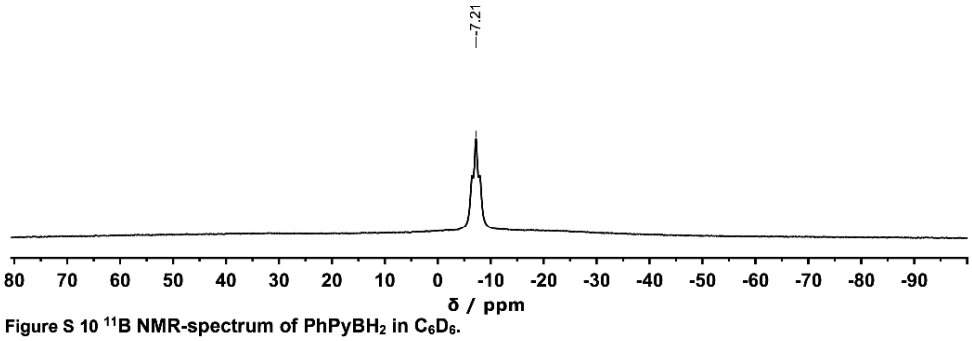

Figure S 10 ^{11}B NMR-spectrum of $PhPyBH_2$ in C_6D_6.

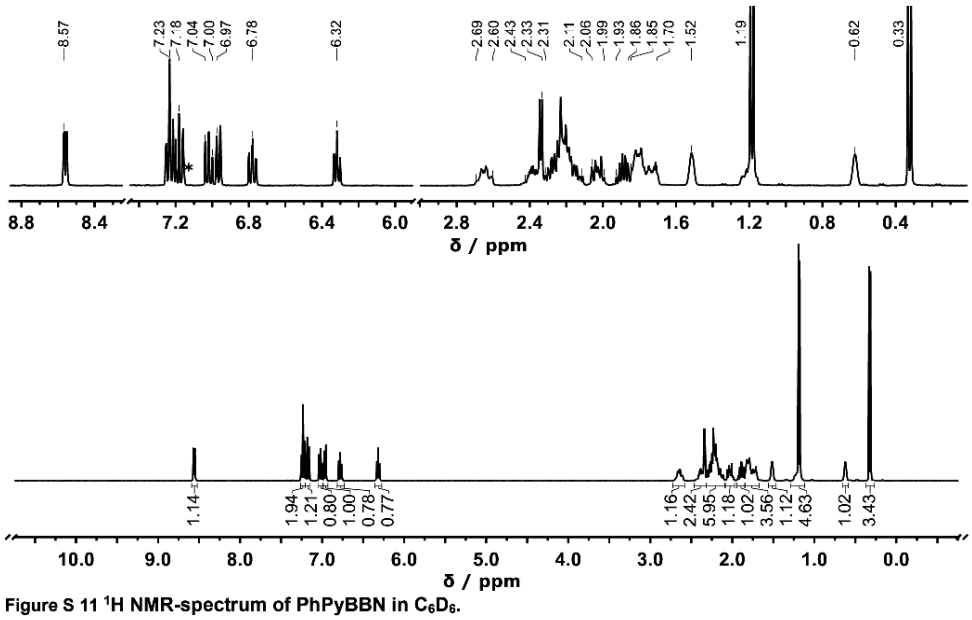

Figure S 11 ^{1}H NMR-spectrum of PhPyBBN in C_6D_6.

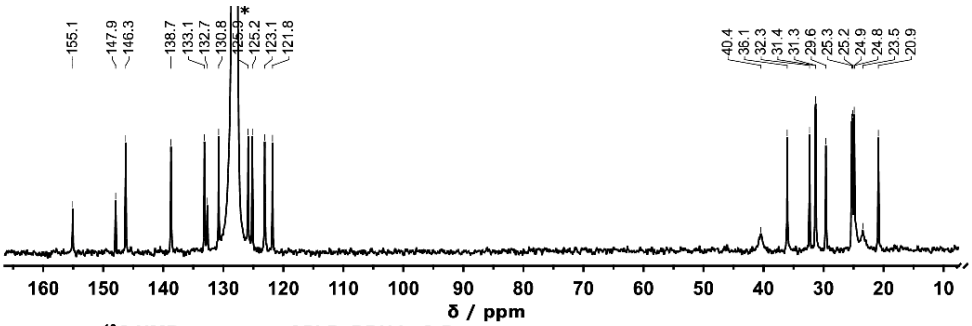

Figure S 12 ^{13}C NMR-spectrum of PhPyBBN in C_6D_6.

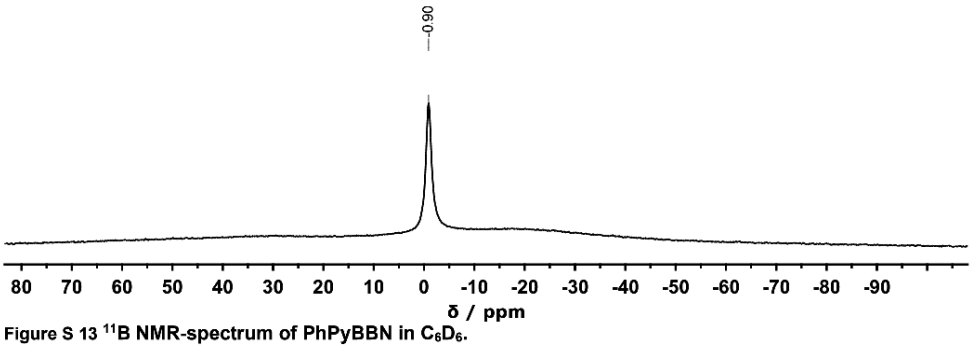

Figure S 13 ^{11}B NMR-spectrum of PhPyBBN in C_6D_6.

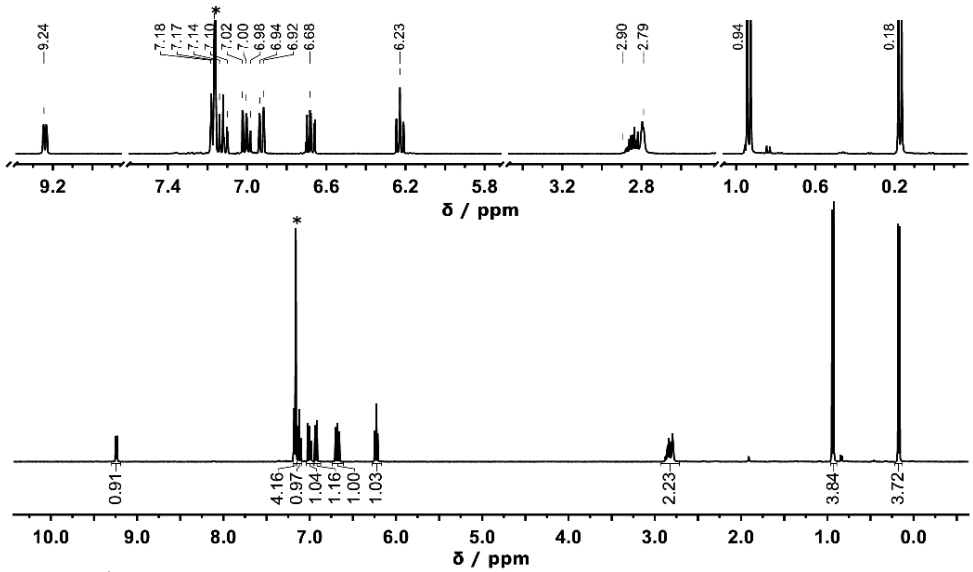

Figure S 14 ^{1}H NMR-spectrum of $PhPyBCl_2$ in C_6D_6.

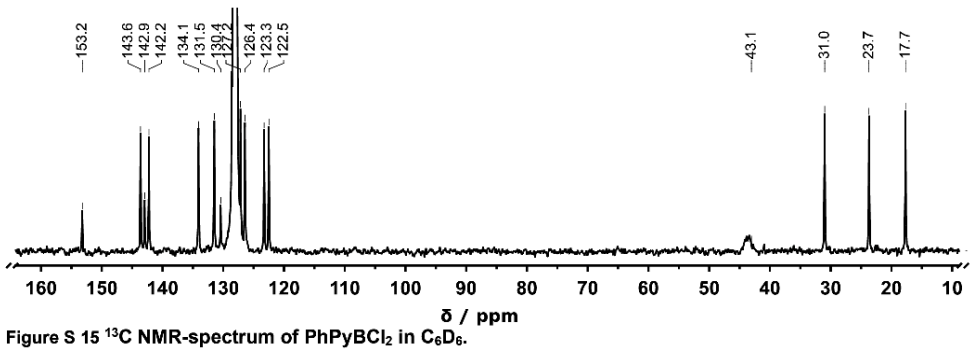

Figure S 15 ^{13}C NMR-spectrum of $PhPyBCl_2$ in C_6D_6.

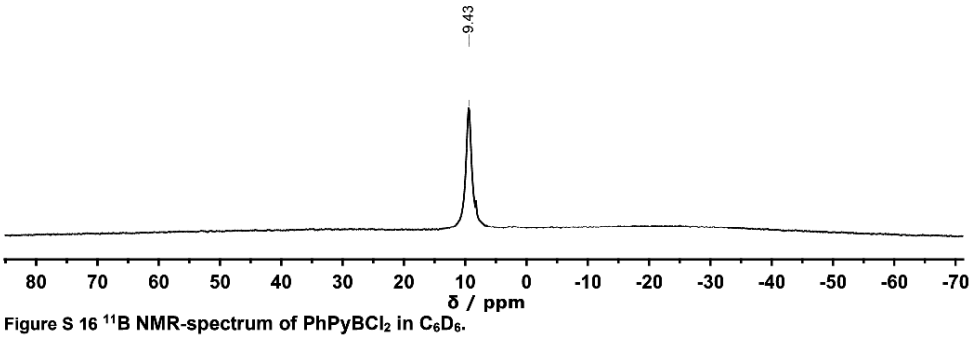

Figure S 16 ^{11}B NMR-spectrum of PhPyBCl$_2$ in C_6D_6.

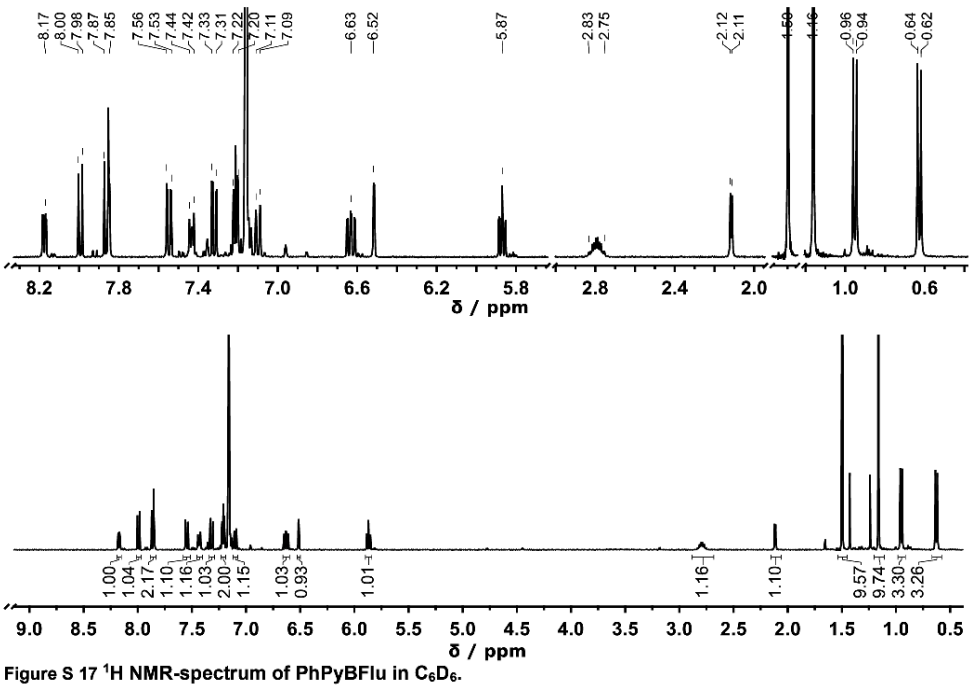

Figure S 17 ^{1}H NMR-spectrum of PhPyBFlu in C_6D_6.

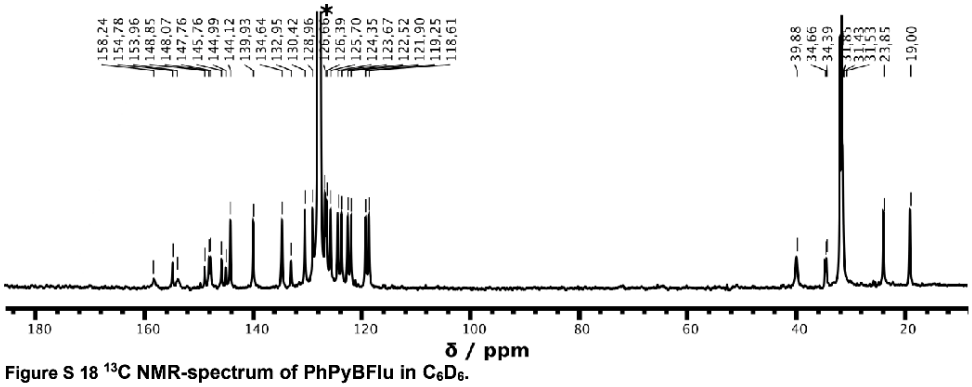

Figure S 18 ^{13}C NMR-spectrum of PhPyBFlu in C_6D_6.

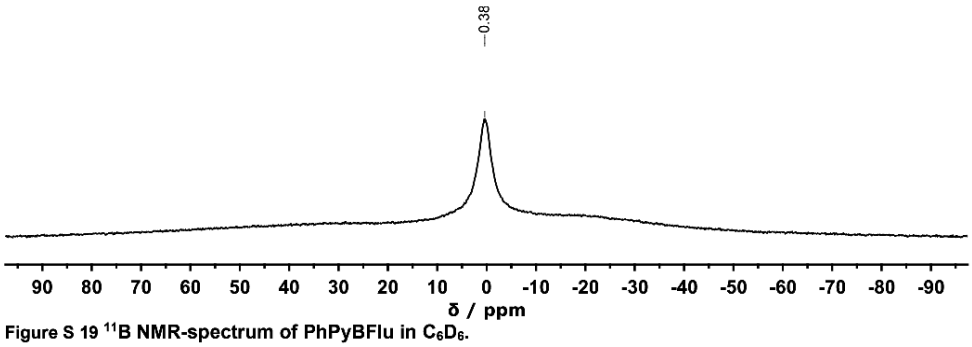

Figure S 19 ^{11}B NMR-spectrum of PhPyBFlu in C_6D_6.

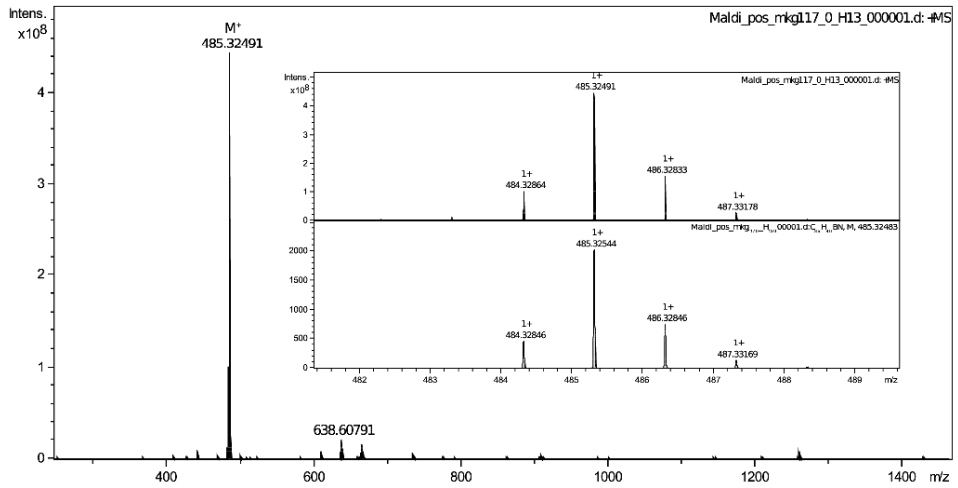

Figure S 20 HR-FTMS-spectrum of PhPyBFlu. The insert shows enlarged the experimental (top) and calculated (bottom) isotope-pattern of the molecular ion.

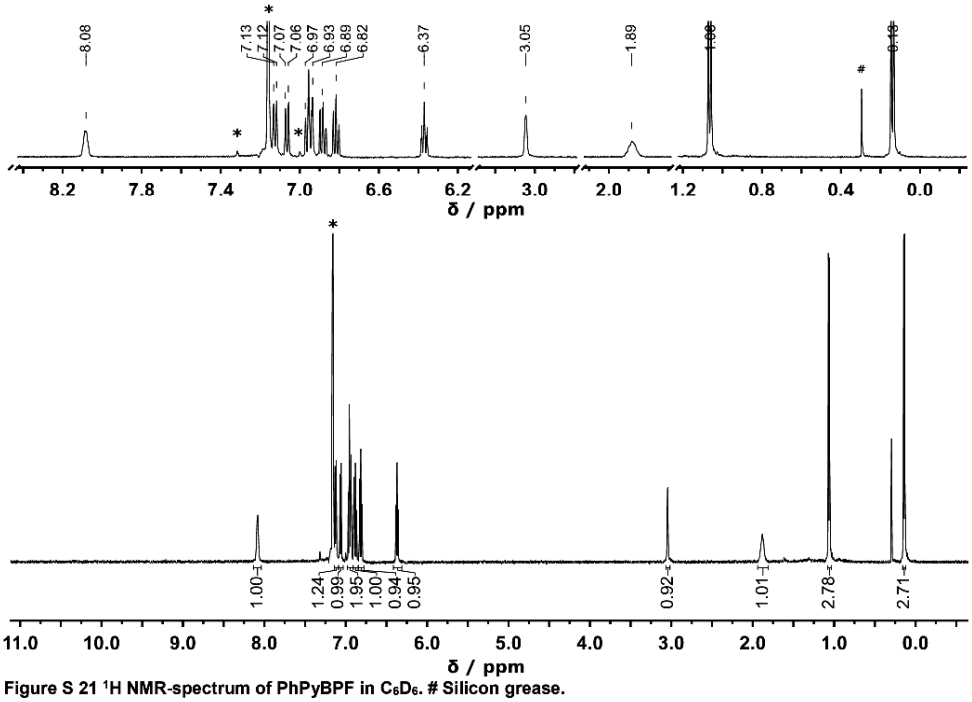

Figure S 21 ^{1}H NMR-spectrum of PhPyBPF in C_6D_6. # Silicon grease.

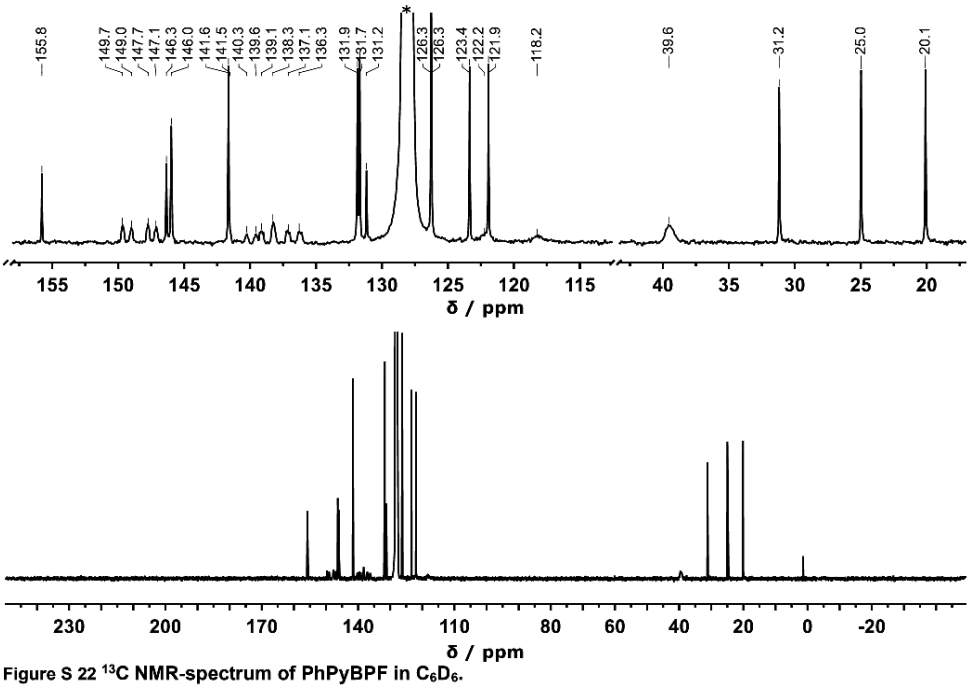

Figure S 22 ^{13}C NMR-spectrum of PhPyBPF in C_6D_6.

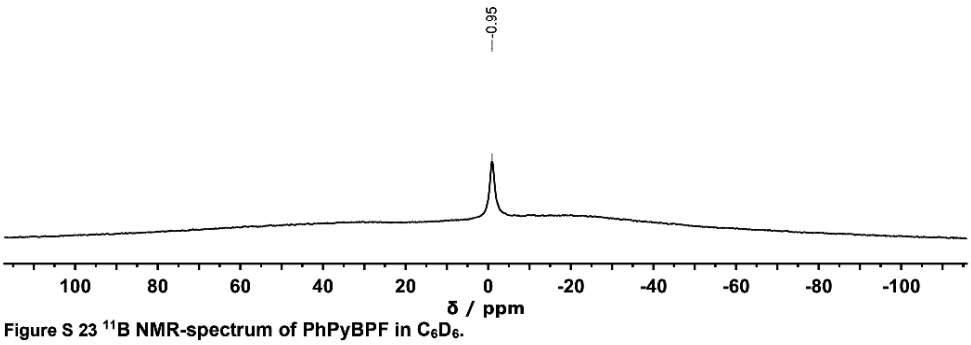

Figure S 23 ^{11}B NMR-spectrum of PhPyBPF in C_6D_6.

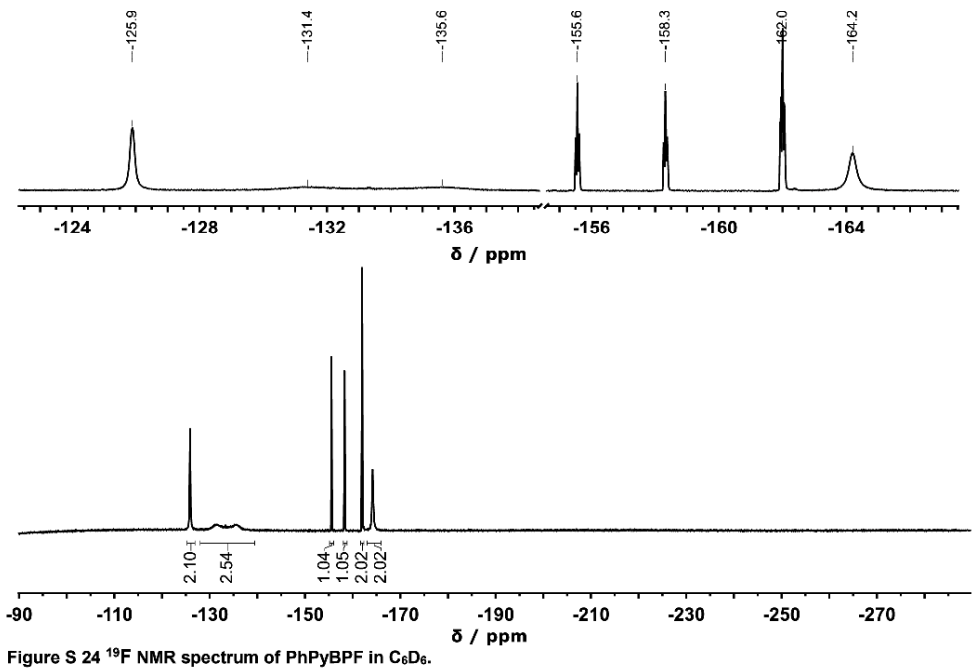

Figure S 24 ^{19}F NMR spectrum of PhPyBPF in C_6D_6.

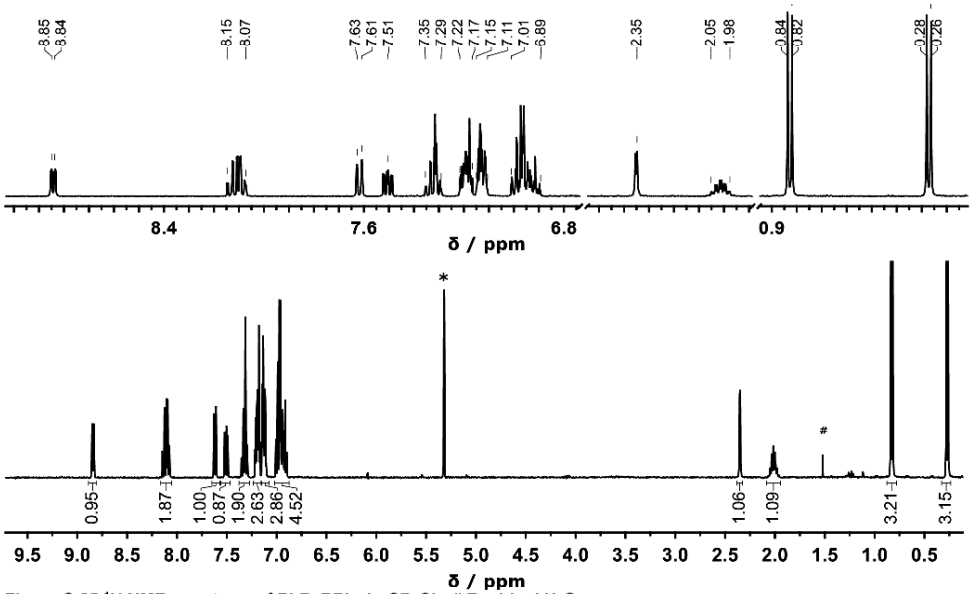

Figure S 25 ^{1}H NMR-spectrum of PhPyBPh$_2$ in CD_2Cl_2. # Residual H_2O.

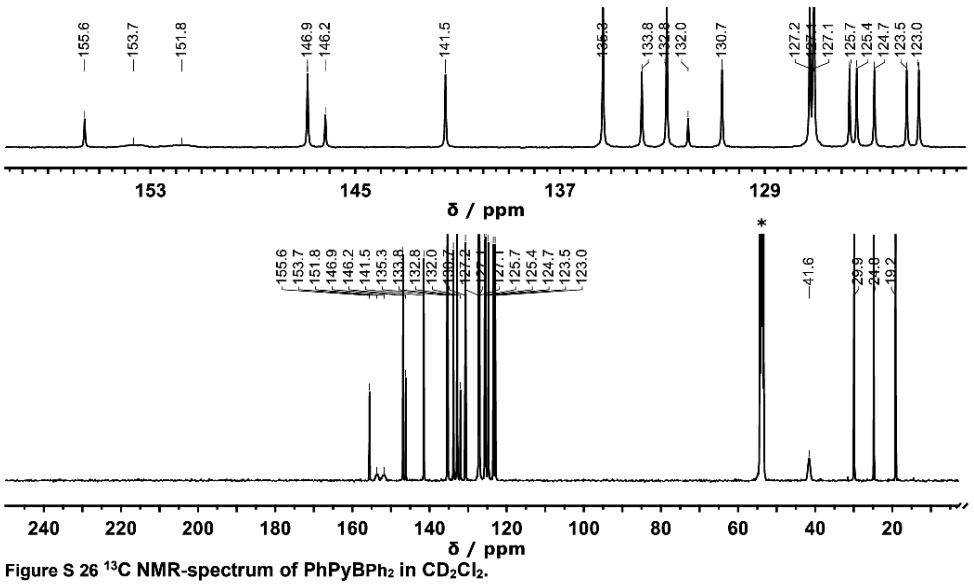

Figure S 26 ^{13}C NMR-spectrum of PhPyBPh$_2$ in CD_2Cl_2.

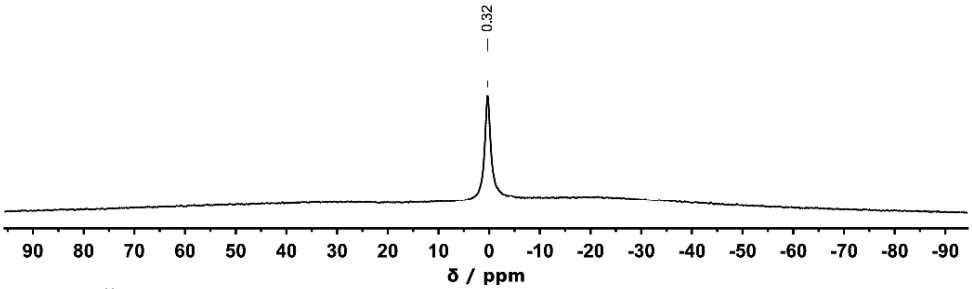

Figure S 27 ^{11}B NMR-spectrum of $PhPyBPh_2$ in CD_2Cl_2.

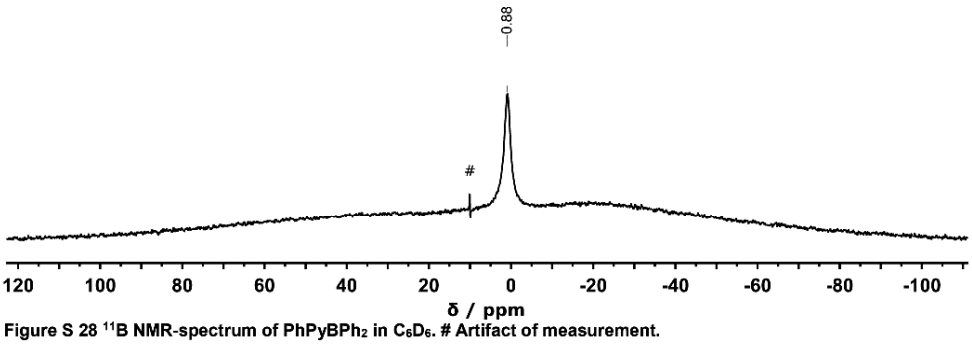

Figure S 28 ^{11}B NMR-spectrum of $PhPyBPh_2$ in C_6D_6. # Artifact of measurement.

3. DFT-calculations

3.1. Structure and Properties of N→B-Ladder Boranes

Table S 1. Characteristic bond lengths [Å] and angles [°] of the simulated ladder compounds. Numbering in accordance with Figure 2. Level of theory: M06-2X/6-31G(d,p).

PhPy	Conformer	N1→B1 [Å]	C5–C6 [Å]	C12–B1 [Å]	N1-C5-C6-C11 [°]	N1-B1-C12 [°]	ΔG^0 [kJ mol^{-1}]
BBN	*i*Pr$_{ax}$	1.650	1.478	1.644	26.4	102.8	0
	*i*Pr$_{eq}$	1.684	1.476	1.688	28.7	95.6	+57
	open	–	1.491	1.581	50.7	–	+69
BPF	*i*Pr$_{ax}$	1.641	1.478	1.634	27.7	105.3	0
	*i*Pr$_{eq}$	1.650	1.473	1.665	31.8	101.5	+14
	open	–	1.492	1.562	54.7	–	+132
BCl$_2$	*i*Pr$_{ax}$	1.623	1.477	1.609	22.5	108.7	0
	*i*Pr$_{eq}$	1.629	1.476	1.616	26.9	105.1	+10
	open	–	1.492	1.577	45.7	–	+120
BPh$_2$	*i*Pr$_{ax}$	1.642	1.479	1.637	27.4	102.5	0
	*i*Pr$_{eq}$	1.667	1.473	1.659	28.8	102.3	–4
	open	–	1.500	1.596	70.1	–	+88
BH$_2$	*i*Pr$_{ax}$	1.621	1.478	1.621	23.3	107.6	0
	*i*Pr$_{eq}$	1.615	1.478	1.629	28.3	104.5	+17
	open	–	1.492	1.577	42.4	–	+132
BFlu	*i*Pr$_{ax}$	1.647	1.476	1.634	28.4	104.0	0
	*i*Pr$_{eq}$	1.658	1.474	1.643	30.5	103.5	+8
	open	–	1.496	1.587	68.8	–	+93

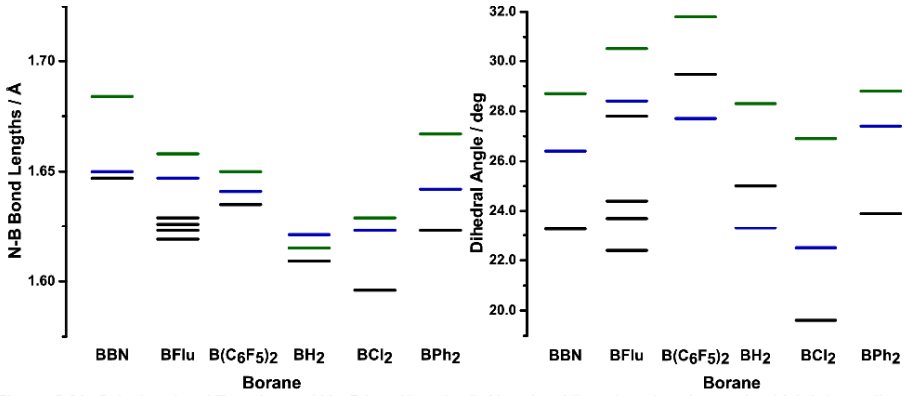

Figure S 29. Calculated and Experimental N→B bond lengths (left) and pyridine-phenyl torsion angles (right) depending on the borane. Green: ***i*Pr$_{eq}$**; blue: ***i*Pr$_{ax}$**, black: crystal data. Level of theory: M06-2X/6-31g(d,p)

Table S 2 Frontier orbital plots of borylated compounds depending on their conformation. (M06-2X/6-311+G(d,p); Isovalue: 0.02)

Borane, conformation	Geometry	HOMO-1	HOMO	LUMO	LUMO+1
PhPyBBN, open	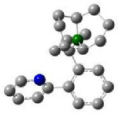	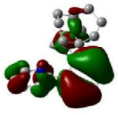	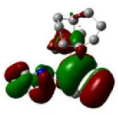	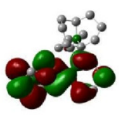	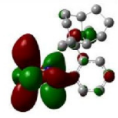
PhPyBBN, *i*Pr$_{ax}$	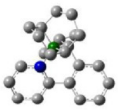		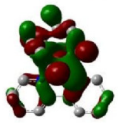	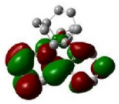	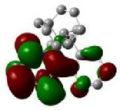
PhPyBBN, *i*Pr$_{eq}$					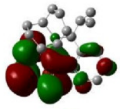
PhPyBH$_2$, open	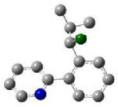		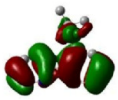		
PhPyBH$_2$, *i*Pr$_{ax}$	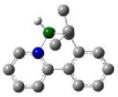	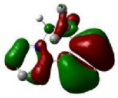	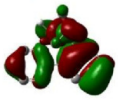	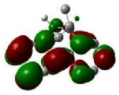	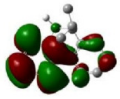
PhPyBH$_2$, *i*Pr$_{eq}$		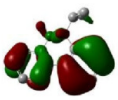	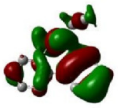	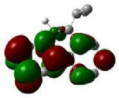	
PhPyBFlu, open	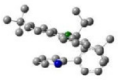	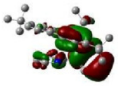	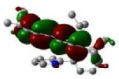	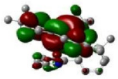	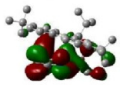
PhPyBFlu, *i*Pr$_{ax}$		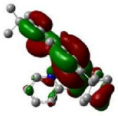	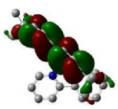	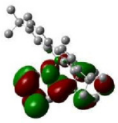	
PhPyBFlu, *i*Pr$_{eq}$		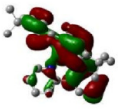	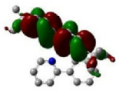		

Borane, conformation	Geometry	HOMO-1	HOMO	LUMO	LUMO+1
$PhPyBPh_2$, open		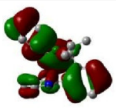	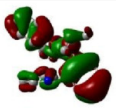	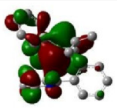	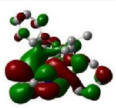
$PhPyBPh_2$, $i\mathrm{Pr}_{ax}$		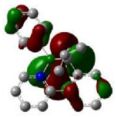	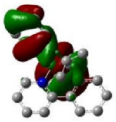	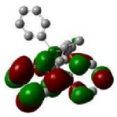	
$PhPyBPh_2$, $i\mathrm{Pr}_{eq}$		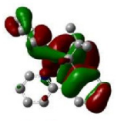	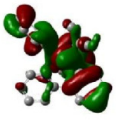	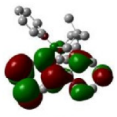	
PhPyBPF, open	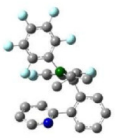	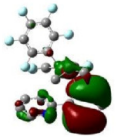	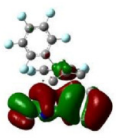	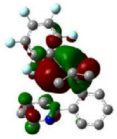	
PhPyBPF, $i\mathrm{Pr}_{ax}$	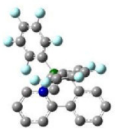	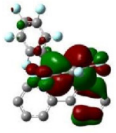	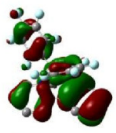	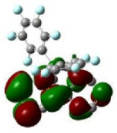	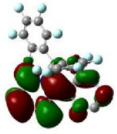
PhPyBPF, $i\mathrm{Pr}_{eq}$		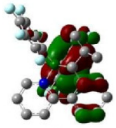	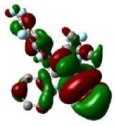	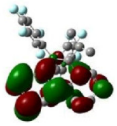	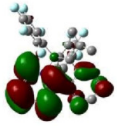
$PhPyBCl_2$, open		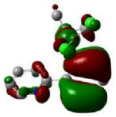		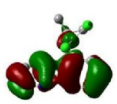	
$PhPyBCl_2$, $i\mathrm{Pr}_{ax}$		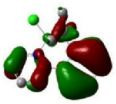	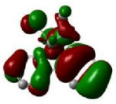		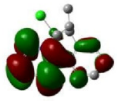
$PhPyBCl_2$, $i\mathrm{Pr}_{eq}$	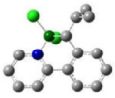	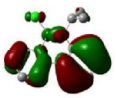	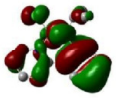	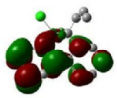	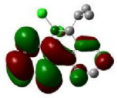

28

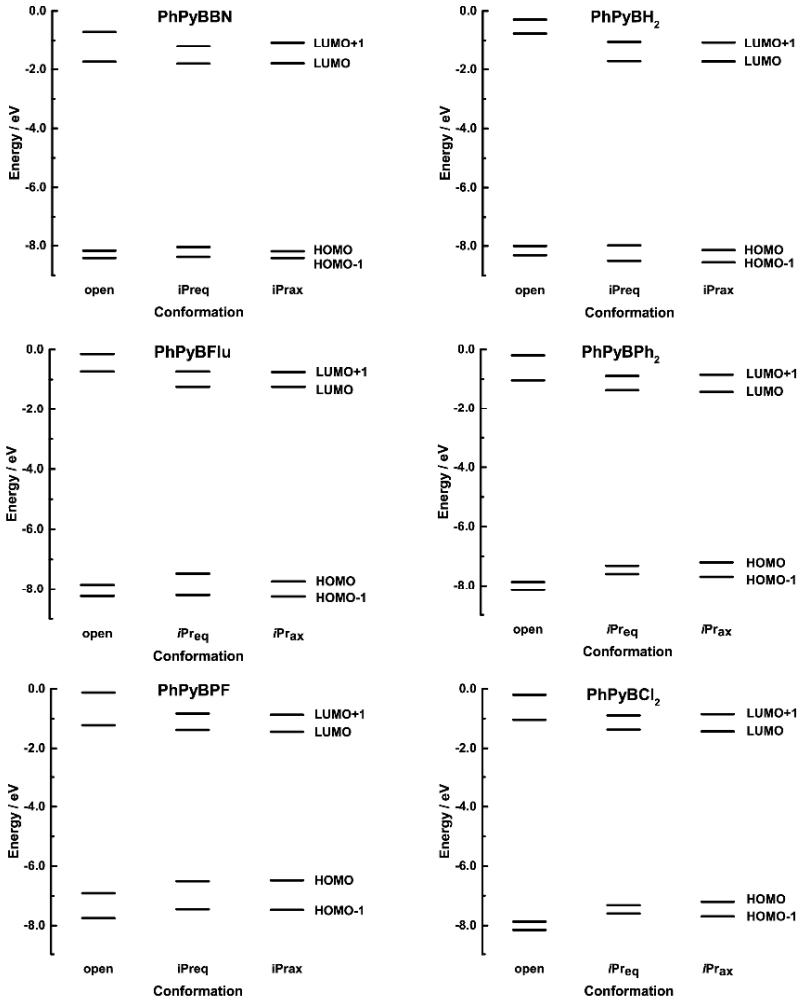

Figure S 30 Calculated frontier orbital levels of borylated compounds depending on their conformation (M06-2X/6-311+g(d,p)).

3.2. TD-DFT calculations

3.2.1. Simulated UV/Vis spectra

Table S3. Calculated[a] and experimental electronic properties of the investigated ladder-boranes. Calculated: E_{max}^{opt}: most intensive single electronic transition. E_g^{opt}: lowest energy transition (mostly HOMO-to-LUMO in character), λ_{max}: longest-wavelength absorption maximum of simulated UV-vis-spectra (see also Figure 6 in the main article). Experimental: λ_{max} and onset of optical absorption derived from experimental UV-vis absorption spectra in THF solution. Additional transitions (λ_2) derived via Gaussian fit of the experimental spectra. sh.: shoulder band.

		Calculated[a]							Experimental		
PhPy	Conf.	HOMO–1	HOMO	LUMO	LUMO+1	E_{max}^{opt} [eV] (*f*)	λ_{max} [eV] [nm]	E_g^{opt} [eV] (*f*)	λ_{max} [eV] [nm]	λ_2 [eV] [nm]	λ_{onset} [eV] [nm]
BBN	^{i}Pr$_{ax}$	-7.66	-7.26	-1.31	-0.74	4.79 (0.155)	4.84 (sh 3.84) 256 (sh 323)	3.83 (0.038)	3.98 311	3.59 345	3.17 391
	^{i}Pr$_{eq}$	-7.46	-7.31	-1.30	-0.69	4.78 (0.141)	3.81 (sh 3.79) 258 (sh 327)	3.72 (0.041)			
	open	-8.11	-7.77	-0.38	-0.08	6.02 (0.161)	5.25 236	4.81 (0.004)			
BH_2	^{i}Pr$_{ax}$	-8.26	-7.73	-1.24	-0.75	5.13 (0.370)	5.10 (sh 4.22) 243 (sh 294)	4.20 (0.104)	4.04 307	3.76 330	4.46 358
	^{i}Pr$_{eq}$	-8.21	-7.47	-1.24	-0.73	5.09 (0.266)	5.06 (sh 3.92) 245 (sh 316)	3.91 (0.064)			
	open	-8.24	-7.85	-0.73	-0.15	6.14 (0.176)	5.06 245	4.80 (0.146)			
BFlu	^{i}Pr$_{ax}$	-7.47	-6.48	-1.44	-0.87	4.64 (0.268)	4.73 262	3.51 (0.004)	3.89[b] 319		3.42 363
	^{i}Pr$_{eq}$	-7.45	-6.51	-1.38	-0.83	4.63 (0.266)	4.73 262	3.58 (0.005)			
	open	-7.75	-6.91	-1.22	-0.12	4.95 (0.826)	5.00 248	3.25 (0.007)			
BPh_2	*i*Pr$_{ax}$	-7.69	-7.20	-1.43	-0.85	4.95 (0.151)	5.08 (sh 4.08) 244 (sh 304)	4.00 (0.007)	4.01 309	3.70 335	3.42 363
	*i*Pr$_{eq}$	-7.60	-7.32	-1.37	-0.89	4.65 (0.078)	5.32 (sh 3.84) 233 (sh 323)	3.84 (0.040)			
	open	-8.15	-7.87	-1.04	-0.20	4.98 (0.193)	5.06 245	4.56 (0.049)			
BPF	*i*Pr$_{ax}$	-8.42	-8.19	-1.80	-1.07	4.16 (0.112)	5.08 (sh 4.31) 244 (sh 288)	4.16 (0.112)	4.03 308	3.77 329	3.50 354
	*i*Pr$_{eq}$	-8.38	-8.05	-1.81	-1.20	5.73 (0.188)	4.86 (sh 3.99) 255 (sh 311)	4.00 (0.066)			
	open	-8.42	-8.17	-1.74	-0.71	5.12 (0.106)	5.25 236	4.32 (0.016)			
BCl_2	*i*Pr$_{ax}$	-8.55	-8.14	-1.73	-1.06	4.20 (0.164)	4.96 (sh 4.23) 250 (sh 293)	4.20 (0.164)	3.95 314	3.71 334	3.50 354
	*i*Pr$_{eq}$	-8.50	-7.98	-1.72	-1.04	4.01 (0.163)	4.81 (sh 4.03) 258 (sh 308)	4.01 (0.114)			
	open	-8.31	-8.00	-0.76	-0.29	5.58 (0.158)	5.21 238	4.83 (0.005)			

[a] Geometry optimizations performed at the M06-2X / 6-31G(d,p) level of theory; electronic transition calculated by time-dependent DFT at the M06-2X / 6-311+G(d,p) level. [b] Shoulder band; maximum derived via Gaussian fit.

3.2.2. Electronic Transitions

PhPyBBN - open

Excitation energies and oscillator strengths:

Excited State 1: Singlet-A 4.8130 eV 257.60 nm f=0.0040 <S**2>=0.000
86 -> 91 0.49292
86 -> 92 0.30324
87 -> 91 0.23861
87 -> 92 0.14072
This state for optimization and/or second-order correction.
Total Energy, E(TD-HF/TD-KS) = -973.775513297
Copying the excited state density for this state as the 1-particle RhoCI density.

Excited State 2: Singlet-A 5.0712 eV 244.49 nm f=0.1446 <S**2>=0.000
89 -> 91 0.11306
89 -> 92 -0.12583
90 -> 91 0.58430
90 -> 97 -0.16287

Excited State 3: Singlet-A 5.1507 eV 240.71 nm f=0.0017 <S**2>=0.000
88 -> 92 -0.18109
88 -> 93 0.16402
88 -> 94 0.15858
88 -> 95 -0.17114
88 -> 96 0.20364
88 -> 97 -0.20561
88 -> 98 -0.25719
88 -> 99 0.10916
88 ->100 0.30578
88 ->102 -0.17150
88 ->106 0.15125

Excited State 4: Singlet-A 5.2418 eV 236.53 nm f=0.0949 <S**2>=0.000
85 -> 91 0.11870
86 -> 92 -0.10530
89 -> 91 0.44974
90 -> 91 -0.21125
90 -> 92 -0.19881
90 -> 93 0.10263
90 -> 97 -0.26370

Excited State 5: Singlet-A 5.3533 eV 231.60 nm f=0.0059 <S**2>=0.000
86 -> 91 -0.28533
86 -> 92 0.40995
86 -> 93 -0.15958
87 -> 91 -0.16860
87 -> 92 0.22136
89 -> 92 0.12446
90 -> 92 -0.13920

Excited State 6: Singlet-A 5.4837 eV 226.10 nm f=0.0894 <S**2>=0.000
83 -> 91 0.10855
85 -> 91 -0.18022
86 -> 92 0.10445
89 -> 91 0.18154
89 -> 92 -0.16457
90 -> 91 -0.18285
90 -> 92 0.44514
90 -> 93 -0.13982
90 -> 97 -0.11506

```
Excited State   7:      Singlet-A      5.5506 eV  223.37 nm  f=0.0211  <S**2>=0.000
     86 -> 92        -0.12823
     87 -> 94        -0.10075
     87 -> 95         0.10807
     87 -> 96        -0.13078
     87 -> 97         0.13310
     87 -> 98         0.16548
     87 ->100        -0.19678
     87 ->102         0.10217
     89 -> 92         0.13171
     89 -> 93        -0.10640
     89 -> 97         0.14901
     90 -> 94        -0.12094
     90 -> 95         0.13468
     90 -> 96        -0.10585
     90 -> 97         0.11600
     90 -> 98         0.12522
     90 ->100        -0.15287

Excited State   8:      Singlet-A      6.0229 eV  205.85 nm  f=0.1605  <S**2>=0.000
     85 -> 91         0.15641
     88 -> 91        -0.11020
     89 -> 91         0.38194
     90 -> 91         0.13930
     90 -> 92         0.13052
     90 -> 93        -0.21083
     90 -> 97         0.35055
     90 -> 98        -0.12325

Excited State   9:      Singlet-A      6.1252 eV  202.42 nm  f=0.0223  <S**2>=0.000
     85 -> 91         0.19768
     89 -> 92         0.19681
     89 -> 94         0.10806
     89 -> 97        -0.11843
     90 -> 92         0.31711
     90 -> 93         0.34209
     90 -> 95        -0.25124
     90 -> 98         0.14238

Excited State  10:      Singlet-A      6.1962 eV  200.10 nm  f=0.0838  <S**2>=0.000
     85 -> 92        -0.11035
     89 -> 92        -0.24209
     89 -> 97         0.35144
     90 -> 91        -0.10068
     90 -> 93         0.29081
     90 -> 95        -0.20029
     90 -> 97         0.15959
     90 ->100         0.15890
     90 ->104         0.11304
     90 ->105         0.10281

Excited State  11:      Singlet-A      6.2003 eV  199.97 nm  f=0.1353  <S**2>=0.000
     85 -> 91         0.19568
     87 -> 97        -0.10658
     88 -> 91        -0.18224
     89 -> 91        -0.22837
     89 -> 92         0.12251
     89 -> 93        -0.18143
     89 -> 97         0.26877
     89 -> 98        -0.10223
     90 -> 92         0.21602
     90 -> 93        -0.16293
     90 -> 95         0.10326                90 -> 97        -0.16291
```

Excited State 12: Singlet-A 6.2338 eV 198.89 nm f=0.0021 <S**2>=0.000
88 -> 91 0.58666
89 -> 92 0.16271
89 -> 93 -0.12274
90 -> 92 0.12305

Excited State 13: Singlet-A 6.3284 eV 195.92 nm f=0.0033 <S**2>=0.000
85 -> 91 0.16770
87 -> 92 0.10444
89 -> 93 0.28639
89 -> 95 -0.21892
90 -> 93 -0.14233
90 -> 94 0.37033
90 -> 98 -0.11250
90 ->100 0.11364

Excited State 14: Singlet-A 6.3630 eV 194.85 nm f=0.0020 <S**2>=0.000
85 -> 91 -0.34475
87 -> 92 -0.10323
88 -> 91 -0.12167
89 -> 92 0.42290
89 -> 97 0.11496
90 -> 94 0.22652

Excited State 15: Singlet-A 6.4349 eV 192.68 nm f=0.0188 <S**2>=0.000
86 -> 91 -0.21612
87 -> 91 0.54052
87 -> 97 0.10943
90 -> 98 0.10100
SavETr: write IOETrn= 770 NScale= 10 NData= 16 NLR=1 NState= 15 LETran= 280.

PhPyBBN - *i*Pr$_{ax}$

Excitation energies and oscillator strengths:

Excited State 1: Singlet-A 3.8344 eV 323.35 nm f=0.0375 <S**2>=0.000
89 -> 91 -0.23501
90 -> 91 0.65516
This state for optimization and/or second-order correction.
Total Energy, E(TD-HF/TD-KS) = -973.841879004
Copying the excited state density for this state as the 1-particle RhoCI density.

Excited State 2: Singlet-A 4.1317 eV 300.08 nm f=0.0377 <S**2>=0.000
89 -> 91 0.64864
90 -> 91 0.24003

Excited State 3: Singlet-A 4.4872 eV 276.31 nm f=0.0187 <S**2>=0.000
87 -> 91 0.14721
88 -> 91 -0.24643
89 -> 92 -0.11990
90 -> 92 0.60605

Excited State 4: Singlet-A 4.7670 eV 260.09 nm f=0.0971 <S**2>=0.000
87 -> 91 -0.32811
88 -> 91 0.30582
89 -> 92 0.39769
90 -> 92 0.31219

```
Excited State   5:      Singlet-A      4.7862 eV  259.04 nm  f=0.1551  <S**2>=0.000
     85 -> 91        0.12069
     87 -> 91        0.29107
     88 -> 91        0.53995
     89 -> 92       -0.20289
     90 -> 92        0.11702

Excited State   6:      Singlet-A      4.9687 eV  249.53 nm  f=0.1070  <S**2>=0.000
     87 -> 91        0.39860
     87 -> 92       -0.17896
     88 -> 91       -0.10726
     89 -> 92        0.49427

Excited State   7:      Singlet-A      5.2140 eV  237.79 nm  f=0.0105  <S**2>=0.000
     82 -> 91        0.11245
     85 -> 91       -0.18036
     86 -> 91        0.59673
     87 -> 91        0.11786

Excited State   8:      Singlet-A      5.4092 eV  229.21 nm  f=0.0052  <S**2>=0.000
     87 -> 92       -0.15707
     88 -> 92        0.65273

Excited State   9:      Singlet-A      5.5520 eV  223.32 nm  f=0.0532  <S**2>=0.000
     86 -> 91       -0.10479
     87 -> 91        0.22147
     87 -> 92        0.20731
     89 -> 95       -0.10178
     89 -> 97       -0.15000
     90 -> 93        0.34923
     90 -> 94       -0.13132
     90 -> 95        0.30644
     90 -> 96       -0.16280
     90 -> 97        0.18818

Excited State  10:      Singlet-A      5.6327 eV  220.12 nm  f=0.0164  <S**2>=0.000
     87 -> 91       -0.16361
     87 -> 92       -0.34826
     88 -> 92       -0.10542
     89 -> 95        0.10108
     89 -> 97        0.11205
     90 -> 93        0.42431
     90 -> 94       -0.13875
     90 -> 95        0.13267

Excited State  11:      Singlet-A      5.8051 eV  213.58 nm  f=0.0558  <S**2>=0.000
     86 -> 92        0.10332
     87 -> 92        0.40276
     88 -> 92        0.13321
     89 -> 95        0.14662
     89 -> 97        0.15057
     90 -> 93        0.23553
     90 -> 95       -0.20810
     90 -> 96        0.13101
     90 -> 97       -0.28364

Excited State  12:      Singlet-A      5.8926 eV  210.41 nm  f=0.0074  <S**2>=0.000
     86 -> 92       -0.15920
     89 -> 93        0.37719
     89 -> 95        0.23937
     89 -> 97        0.11343
     90 -> 93       -0.21908
     90 -> 94       -0.32297
```

```
    90 -> 95        0.15555
    90 -> 97        0.14094

Excited State  13:      Singlet-A      5.9088 eV  209.83 nm  f=0.0186  <S**2>=0.000
    85 -> 92       -0.14147
    86 -> 92        0.54270
    89 -> 97        0.11219
    90 -> 95        0.19929
    90 -> 96       -0.10450
    90 -> 97        0.13235

Excited State  14:      Singlet-A      5.9510 eV  208.34 nm  f=0.0300  <S**2>=0.000
    85 -> 91        0.34774
    86 -> 91        0.15496
    86 -> 92       -0.17677
    87 -> 92        0.19382
    89 -> 93       -0.12017
    89 -> 96       -0.11246
    89 -> 97        0.20559
    90 -> 94        0.28924
    90 -> 95        0.17718
    90 -> 96       -0.11365

Excited State  15:      Singlet-A      5.9919 eV  206.92 nm  f=0.0446  <S**2>=0.000
    85 -> 91        0.45725
    86 -> 91        0.12548
    86 -> 92        0.15012
    89 -> 95       -0.14106
    89 -> 96        0.11686
    89 -> 97       -0.19797
    90 -> 94       -0.25221
    90 -> 95       -0.12266
    90 -> 96        0.11652
SavETr:  write IOETrn=   770 NScale= 10 NData=  16 NLR=1 NState=   15 LETran=    280.
```

PhPyBBN - *i*Pr$_{eq}$

Excitation energies and oscillator strengths:

```
Excited State   1:      Singlet-A      3.7241 eV  332.92 nm  f=0.0414  <S**2>=0.000
    89 -> 91       -0.15174
    90 -> 91        0.67515
This state for optimization and/or second-order correction.
Total Energy, E(TD-HF/TD-KS) =  -973.825183265
Copying the excited state density for this state as the 1-particle RhoCI density.

Excited State   2:      Singlet-A      4.0862 eV  303.42 nm  f=0.0279  <S**2>=0.000
    89 -> 91        0.67865
    90 -> 91        0.15801

Excited State   3:      Singlet-A      4.5091 eV  274.96 nm  f=0.0289  <S**2>=0.000
    87 -> 91       -0.11958
    88 -> 91        0.31486
    90 -> 92        0.58164

Excited State   4:      Singlet-A      4.7820 eV  259.27 nm  f=0.1412  <S**2>=0.000
    88 -> 91        0.44219
    89 -> 92        0.49061
    90 -> 92       -0.18383
```

```
Excited State   5:      Singlet-A      4.7933 eV  258.66 nm  f=0.1325  <S**2>=0.000
     87 -> 91        0.10433
     88 -> 91       -0.37571
     89 -> 92        0.46856
     90 -> 92        0.30595

Excited State   6:      Singlet-A      5.0618 eV  244.94 nm  f=0.0133  <S**2>=0.000
     85 -> 91       -0.12489
     87 -> 91        0.55613
     87 -> 92        0.10101
     88 -> 91        0.15852
     88 -> 92       -0.15276
     89 -> 92       -0.12025
     90 -> 97       -0.16786

Excited State   7:      Singlet-A      5.2213 eV  237.46 nm  f=0.0350  <S**2>=0.000
     85 -> 91       -0.32927
     86 -> 91        0.46792
     87 -> 91       -0.21933
     87 -> 92        0.11655
     88 -> 92       -0.10919

Excited State   8:      Singlet-A      5.4420 eV  227.83 nm  f=0.0120  <S**2>=0.000
     82 -> 91        0.10862
     86 -> 91        0.16122
     87 -> 91        0.14703
     88 -> 92        0.61547
     90 -> 92        0.11262

Excited State   9:      Singlet-A      5.6172 eV  220.72 nm  f=0.0358  <S**2>=0.000
     86 -> 91       -0.12825
     87 -> 91       -0.16234
     88 -> 92        0.10459
     90 -> 93        0.47031
     90 -> 94        0.12869
     90 -> 95        0.23441
     90 -> 97       -0.28892

Excited State  10:      Singlet-A      5.6454 eV  219.62 nm  f=0.1032  <S**2>=0.000
     82 -> 91        0.11682
     86 -> 91        0.18098
     87 -> 91        0.19264
     87 -> 92       -0.13281
     88 -> 92       -0.14444
     90 -> 93        0.36963
     90 -> 96       -0.25754
     90 -> 97        0.23541
     90 -> 98       -0.10273
     90 ->100        0.13418

Excited State  11:      Singlet-A      5.7818 eV  214.44 nm  f=0.0005  <S**2>=0.000
     89 -> 93        0.57323
     89 -> 94       -0.16879
     89 -> 95        0.24309
     90 -> 94       -0.13948
     90 -> 96        0.10350

Excited State  12:      Singlet-A      5.8593 eV  211.60 nm  f=0.0667  <S**2>=0.000
     81 -> 91       -0.10783
     82 -> 91       -0.10390
     85 -> 91       -0.14334
     86 -> 91       -0.19197
     86 -> 92       -0.10392
```

```
    87 -> 92        0.45895
    90 -> 94       -0.20003
    90 -> 96       -0.18281
    90 -> 97        0.13015
    90 ->100        0.12013
    90 ->102       -0.12175

Excited State  13:      Singlet-A      5.9048 eV  209.97 nm  f=0.0306  <S**2>=0.000
    82 -> 91       -0.12048
    83 -> 91        0.10351
    85 -> 91        0.38066
    86 -> 91        0.31201
    90 -> 94       -0.26908
    90 -> 97       -0.11490
    90 ->100        0.10437
    90 ->102       -0.18799

Excited State  14:      Singlet-A      5.9207 eV  209.41 nm  f=0.0317  <S**2>=0.000
    84 -> 91       -0.12038
    85 -> 91        0.28195
    86 -> 91        0.18152
    86 -> 92       -0.22860
    87 -> 92        0.30737
    88 -> 97       -0.11360
    90 -> 94        0.26105
    90 -> 96        0.11525
    90 ->102        0.14137

Excited State  15:      Singlet-A      6.0012 eV  206.60 nm  f=0.0087  <S**2>=0.000
    81 -> 91       -0.10116
    82 -> 91       -0.15725
    85 -> 92       -0.21119
    86 -> 92        0.33896
    89 -> 94       -0.24947
    89 -> 96       -0.19694
    89 -> 97        0.13298
    90 -> 94        0.11739
    90 -> 96       -0.12747
    90 -> 97        0.22246
SavETr:  write IOETrn=   770 NScale= 10 NData=  16 NLR=1 NState=   15 LETran=    280.
```

PhPyBH₂ – open

```
Excitation energies and oscillator strengths:

Excited State   1:      Singlet-A      4.8025 eV  258.17 nm  f=0.1462  <S**2>=0.000
    58 -> 62        0.12233
    59 -> 61       -0.34282
    60 -> 61        0.53268
This state for optimization and/or second-order correction.
Total Energy, E(TD-HF/TD-KS) =  -661.713257929
Copying the excited state density for this state as the 1-particle RhoCI density.

Excited State   2:      Singlet-A      4.8265 eV  256.88 nm  f=0.0160  <S**2>=0.000
    58 -> 61        0.37198
    58 -> 62        0.48008
    58 -> 63       -0.13508
    58 -> 64        0.13511
    59 -> 62       -0.12163
    60 -> 61       -0.17561
```

Excited State 3: Singlet-A 5.0599 eV 245.03 nm f=0.1359 <S**2>=0.000
58 -> 62 0.11703
59 -> 61 0.47099
60 -> 61 0.32997
60 -> 62 0.10161
60 -> 65 0.17191
60 -> 66 -0.20739

Excited State 4: Singlet-A 5.2916 eV 234.30 nm f=0.0606 <S**2>=0.000
55 -> 61 0.15168
56 -> 63 0.14391
57 -> 61 -0.11054
57 -> 62 -0.15041
58 -> 61 0.14667
58 -> 63 0.15000
59 -> 63 -0.14140
60 -> 62 0.50191
60 -> 63 -0.10909
60 -> 64 0.14557
60 -> 66 0.10455

Excited State 5: Singlet-A 5.3723 eV 230.79 nm f=0.0077 <S**2>=0.000
58 -> 61 0.32158
58 -> 63 0.47474
58 -> 64 -0.17621
60 -> 62 -0.18093

Excited State 6: Singlet-A 5.5296 eV 224.22 nm f=0.1142 <S**2>=0.000
55 -> 61 0.11643
55 -> 62 -0.12007
55 -> 63 -0.10471
56 -> 61 -0.23117
57 -> 61 0.15227
59 -> 62 -0.16177
60 -> 61 0.18093
60 -> 63 0.46553

Excited State 7: Singlet-A 5.8018 eV 213.70 nm f=0.0237 <S**2>=0.000
50 -> 61 -0.10756
51 -> 61 0.11797
54 -> 61 0.37213
54 -> 62 -0.20571
54 -> 63 -0.14264
55 -> 61 -0.21314
56 -> 61 0.17427
57 -> 61 -0.16258
59 -> 62 -0.10243
60 -> 63 0.14199

Excited State 8: Singlet-A 5.9569 eV 208.14 nm f=0.0292 <S**2>=0.000
54 -> 61 -0.12822
55 -> 61 -0.15725
56 -> 61 0.10754
59 -> 61 -0.12947
59 -> 62 0.21542
59 -> 63 0.15911
60 -> 61 -0.13399
60 -> 62 0.26661
60 -> 63 0.34297
60 -> 65 0.15895
60 -> 66 -0.20944

Excited State 9: Singlet-A 6.1440 eV 201.80 nm f=0.1756 <S**2>=0.000
57 -> 61 0.27159
59 -> 61 -0.22894
59 -> 62 -0.25260
59 -> 65 -0.15981
59 -> 66 0.15829
60 -> 62 0.20000
60 -> 63 -0.19185
60 -> 64 -0.14083
60 -> 65 0.19200
60 -> 66 -0.21350

Excited State 10: Singlet-A 6.1941 eV 200.16 nm f=0.1228 <S**2>=0.000
51 -> 61 -0.10930
54 -> 61 -0.18807
54 -> 62 0.11050
55 -> 61 -0.22682
56 -> 61 0.22753
57 -> 61 0.22715
59 -> 61 0.20868
59 -> 65 -0.10540
59 -> 66 0.18732
60 -> 62 0.10605
60 -> 65 -0.21275
60 -> 66 0.19497

Excited State 11: Singlet-A 6.2478 eV 198.44 nm f=0.0191 <S**2>=0.000
54 -> 61 0.11461
56 -> 61 -0.10857
57 -> 61 0.18791
57 -> 62 0.11557
59 -> 62 0.34178
59 -> 63 0.22543
60 -> 62 0.12435
60 -> 63 -0.14279
60 -> 64 -0.32632
60 -> 65 -0.12267
60 -> 66 0.17743

Excited State 12: Singlet-A 6.2835 eV 197.32 nm f=0.0500 <S**2>=0.000
54 -> 61 0.11974
57 -> 61 0.16532
59 -> 62 0.21316
59 -> 63 0.20933
59 -> 64 0.10661
59 -> 65 -0.19822
59 -> 66 0.17337
60 -> 64 0.42103

Excited State 13: Singlet-A 6.4098 eV 193.43 nm f=0.0871 <S**2>=0.000
56 -> 63 -0.11151
57 -> 61 0.12934
57 -> 62 0.19917
59 -> 62 -0.20143
59 -> 63 0.18410
59 -> 65 0.25160
59 -> 66 -0.27904
60 -> 62 0.11203
60 -> 63 -0.13860
60 -> 64 0.27887
60 -> 66 0.10751

```
Excited State  14:      Singlet-A      6.4712 eV  191.59 nm  f=0.0566  <S**2>=0.000
    57 -> 61       -0.26960
    59 -> 62       -0.26238
    59 -> 63        0.47226
    59 -> 65       -0.20600

Excited State  15:      Singlet-A      6.5566 eV  189.10 nm  f=0.0073  <S**2>=0.000
    59 -> 64        0.10361
    60 -> 65        0.42090
    60 -> 66        0.40554
    60 -> 67        0.17446
    60 -> 68        0.16560
SavETr:  write IOETrn=   770 NScale= 10 NData=  16 NLR=1 NState=   15 LETran=    280.
```

PhPyBH$_2$ - *i*Pr$_{ax}$

Excitation energies and oscillator strengths:

```
Excited State   1:      Singlet-A      4.2035 eV  294.96 nm  f=0.1039  <S**2>=0.000
    60 -> 61        0.68773
This state for optimization and/or second-order correction.
Total Energy, E(TD-HF/TD-KS) =  -661.789469829
Copying the excited state density for this state as the 1-particle RhoCI density.

Excited State   2:      Singlet-A      4.6795 eV  264.95 nm  f=0.0327  <S**2>=0.000
    55 -> 61       -0.10200
    58 -> 61       -0.14152
    59 -> 61        0.43793
    60 -> 62        0.47708

Excited State   3:      Singlet-A      4.9347 eV  251.25 nm  f=0.0131  <S**2>=0.000
    57 -> 61        0.34024
    58 -> 61        0.35848
    59 -> 61        0.31454
    59 -> 62        0.19364
    60 -> 62       -0.18379
    60 -> 65        0.16764

Excited State   4:      Singlet-A      4.9684 eV  249.54 nm  f=0.0629  <S**2>=0.000
    57 -> 61        0.58154
    58 -> 61       -0.28427
    59 -> 61       -0.16459
    59 -> 62       -0.10666
    60 -> 62        0.12385

Excited State   5:      Singlet-A      5.1254 eV  241.90 nm  f=0.3695  <S**2>=0.000
    58 -> 61        0.45570
    59 -> 61       -0.31504
    60 -> 62        0.40937

Excited State   6:      Singlet-A      5.5434 eV  223.66 nm  f=0.0151  <S**2>=0.000
    55 -> 61       -0.13269
    57 -> 61        0.10761
    57 -> 62        0.40987
    58 -> 61        0.10105
    58 -> 62       -0.40586
    59 -> 62       -0.24944
    60 -> 62       -0.11092
    60 -> 65       -0.10227
```

```
Excited State   7:      Singlet-A      5.6115 eV  220.95 nm  f=0.0183  <S**2>=0.000
     58 -> 61       -0.10489
     58 -> 62       -0.36723
     59 -> 61       -0.13562
     59 -> 62        0.54766
     60 -> 62        0.10731

Excited State   8:      Singlet-A      5.7085 eV  217.19 nm  f=0.0144  <S**2>=0.000
     57 -> 62        0.52958
     58 -> 61       -0.10641
     58 -> 62        0.30756
     59 -> 61       -0.12919
     60 -> 65        0.19230
     60 -> 66       -0.10356

Excited State   9:      Singlet-A      5.9556 eV  208.18 nm  f=0.0094  <S**2>=0.000
     52 -> 61       -0.16030
     53 -> 61        0.27312
     55 -> 61        0.18250
     56 -> 61        0.54280

Excited State  10:      Singlet-A      5.9993 eV  206.67 nm  f=0.1760  <S**2>=0.000
     57 -> 62       -0.14308
     58 -> 62       -0.22285
     59 -> 61       -0.12509
     59 -> 62       -0.18927
     60 -> 62       -0.10576
     60 -> 63       -0.14538
     60 -> 65        0.47879
     60 -> 66       -0.19975

Excited State  11:      Singlet-A      6.0703 eV  204.25 nm  f=0.0116  <S**2>=0.000
     60 -> 63        0.58232
     60 -> 64        0.25515
     60 -> 66       -0.16698

Excited State  12:      Singlet-A      6.2736 eV  197.63 nm  f=0.1387  <S**2>=0.000
     55 -> 61        0.19096
     59 -> 65        0.42120
     59 -> 66       -0.24560
     60 -> 66       -0.12563
     60 -> 70       -0.27738
     60 -> 71       -0.17341

Excited State  13:      Singlet-A      6.3056 eV  196.63 nm  f=0.0117  <S**2>=0.000
     51 -> 62       -0.13369
     55 -> 61        0.53154
     55 -> 62       -0.12665
     56 -> 61       -0.12460
     58 -> 62       -0.11708
     59 -> 62       -0.12135
     60 -> 66        0.11171
     60 -> 70        0.16918
     60 -> 71        0.10215

Excited State  14:      Singlet-A      6.3704 eV  194.62 nm  f=0.0095  <S**2>=0.000
     59 -> 63        0.34746
     59 -> 64        0.20211
     60 -> 63       -0.19039
     60 -> 64        0.40662
     60 -> 65       -0.10361
     60 -> 66       -0.25281
```

Excited State 15: Singlet-A 6.5127 eV 190.37 nm f=0.0193 <S**2>=0.000
57 -> 65 0.51410
57 -> 66 -0.30556
58 -> 65 0.12159
59 -> 65 0.13737
SavETr: write IOETrm= 770 NScale= 10 NData= 16 NLR=1 NState= 15 LETran= 280.

PhPyBH$_2$ - *i*Pr$_{eq}$

Excitation energies and oscillator strengths:

Excited State 1: Singlet-A 3.9095 eV 317.14 nm f=0.0636 <S**2>=0.000
60 -> 61 0.69090
This state for optimization and/or second-order correction.
Total Energy, E(TD-HF/TD-KS) = -661.793294344
Copying the excited state density for this state as the 1-particle RhoCI density.

Excited State 2: Singlet-A 4.5728 eV 271.13 nm f=0.0240 <S**2>=0.000
58 -> 61 0.11366
59 -> 61 -0.34429
60 -> 62 0.56579

Excited State 3: Singlet-A 4.8904 eV 253.52 nm f=0.1689 <S**2>=0.000
58 -> 61 0.22884
59 -> 61 0.52739
59 -> 62 0.17913
60 -> 62 0.29404
60 -> 66 0.12590

Excited State 4: Singlet-A 5.0876 eV 243.70 nm f=0.2655 <S**2>=0.000
58 -> 61 0.58305
59 -> 61 -0.19827
59 -> 62 0.10449
60 -> 62 -0.24554

Excited State 5: Singlet-A 5.2590 eV 235.76 nm f=0.0255 <S**2>=0.000
57 -> 61 0.54290
58 -> 61 0.15934
58 -> 62 -0.20094
59 -> 62 -0.21404
60 -> 66 -0.14915

Excited State 6: Singlet-A 5.5293 eV 224.23 nm f=0.0511 <S**2>=0.000
57 -> 61 0.29765
57 -> 62 0.13960
58 -> 61 -0.16950
59 -> 62 0.55244
60 -> 62 -0.10735

Excited State 7: Singlet-A 5.6677 eV 218.75 nm f=0.0279 <S**2>=0.000
57 -> 61 0.17550
57 -> 62 0.14258
58 -> 62 0.59898
59 -> 62 -0.22600

Excited State 8: Singlet-A 5.7947 eV 213.96 nm f=0.1146 <S**2>=0.000
57 -> 61 -0.14629
57 -> 62 0.12950
59 -> 61 0.12774
60 -> 63 0.44040
60 -> 65 0.31980
60 -> 66 -0.25526

```
Excited State  9:      Singlet-A      5.8544 eV  211.78 nm  f=0.0693  <S**2>=0.000
    57 -> 61        0.15235
    57 -> 62       -0.13767
    59 -> 61       -0.11759
    60 -> 63        0.39620
    60 -> 64       -0.20081
    60 -> 66        0.34257
    60 -> 67       -0.23114

Excited State  10:      Singlet-A      5.9472 eV  208.47 nm  f=0.0081  <S**2>=0.000
    51 -> 61        0.17802
    53 -> 61       -0.23234
    54 -> 61       -0.19369
    56 -> 61        0.54155

Excited State  11:      Singlet-A      6.0517 eV  204.88 nm  f=0.0662  <S**2>=0.000
    57 -> 62        0.20969
    59 -> 65        0.12630
    59 -> 66       -0.21530
    60 -> 64       -0.26709
    60 -> 65       -0.25521
    60 -> 66        0.11250
    60 -> 67        0.14495
    60 -> 70        0.29094
    60 -> 71        0.20814

Excited State  12:      Singlet-A      6.1727 eV  200.86 nm  f=0.0149  <S**2>=0.000
    57 -> 62        0.55923
    58 -> 62       -0.16556
    60 -> 64        0.16875
    60 -> 66        0.10237
    60 -> 67       -0.21247

Excited State  13:      Singlet-A      6.2178 eV  199.40 nm  f=0.0110  <S**2>=0.000
    57 -> 62       -0.11262
    59 -> 63        0.19492
    60 -> 63        0.24537
    60 -> 64        0.43855
    60 -> 65       -0.31519
    60 -> 66       -0.12978
    60 -> 67       -0.11886

Excited State  14:      Singlet-A      6.2838 eV  197.31 nm  f=0.0295  <S**2>=0.000
    52 -> 62       -0.13764
    54 -> 61        0.32973
    55 -> 61        0.45899
    55 -> 62       -0.11498
    58 -> 62        0.14800
    59 -> 61       -0.11207
    59 -> 62        0.14444
    59 -> 66        0.13270

Excited State  15:      Singlet-A      6.3746 eV  194.50 nm  f=0.0401  <S**2>=0.000
    59 -> 63       -0.16706
    59 -> 64        0.14519
    59 -> 66       -0.19490
    59 -> 67        0.10055
    60 -> 64        0.22811
    60 -> 65        0.31394
    60 -> 66        0.17188
    60 -> 67       -0.22375
    60 -> 68       -0.10620
    60 -> 70        0.18952
```

60 -> 71 0.22264
SavETr: write IOETrn= 770 NScale= 10 NData= 16 NLR=1 NState= 15 LETran= 280.

PhPyBFlu – open

Excitation energies and oscillator strengths:

Excited State 1: Singlet-A 3.2507 eV 381.41 nm f=0.0067 <S**2>=0.000
131 -> 132 0.69334
This state for optimization and/or second-order correction.
Total Energy, E(TD-HF/TD-KS) = -1437.08551379
Copying the excited state density for this state as the 1-particle RhoCI density.

Excited State 2: Singlet-A 4.2578 eV 291.19 nm f=0.0068 <S**2>=0.000
121 -> 132 0.10931
129 -> 132 0.30096
130 -> 132 0.50413
131 -> 134 -0.32571

Excited State 3: Singlet-A 4.3692 eV 283.77 nm f=0.0053 <S**2>=0.000
121 -> 132 -0.18743
129 -> 132 0.44044
130 -> 132 -0.39632
131 -> 134 -0.26878

Excited State 4: Singlet-A 4.7703 eV 259.91 nm f=0.0145 <S**2>=0.000
123 -> 132 0.41521
124 -> 132 -0.15875
124 -> 133 -0.22344
125 -> 133 -0.13195
127 -> 132 -0.31902
131 -> 133 -0.11937

Excited State 5: Singlet-A 4.7947 eV 258.59 nm f=0.0058 <S**2>=0.000
123 -> 132 0.40921
124 -> 133 0.34030
124 -> 135 -0.12835
125 -> 133 0.20608
126 -> 133 -0.12278
127 -> 133 0.12254
131 -> 133 0.12759

Excited State 6: Singlet-A 4.8308 eV 256.65 nm f=0.0782 <S**2>=0.000
123 -> 132 0.22947
124 -> 133 -0.16532
125 -> 133 -0.10332
126 -> 132 0.18418
127 -> 132 0.43634
129 -> 132 -0.14202
131 -> 134 -0.15712
131 -> 150 0.12768

Excited State 7: Singlet-A 4.9515 eV 250.40 nm f=0.8256 <S**2>=0.000
127 -> 132 0.21608
128 -> 132 0.10980
129 -> 132 0.36046
130 -> 132 0.12395
131 -> 134 0.49913

Excited State 8: Singlet-A 5.0527 eV 245.38 nm f=0.0553 <S**2>=0.000
121 -> 132 -0.11255
124 -> 132 0.12350

126 -> 132 -0.19111
128 -> 132 0.56890
129 -> 132 -0.10199
131 -> 133 -0.11295

Excited State 9: Singlet-A 5.1575 eV 240.40 nm f=0.0205 <S**2>=0.000
124 -> 136 0.10355
125 -> 132 -0.16237
127 -> 132 -0.15482
128 -> 132 0.15082
131 -> 133 0.51681
131 -> 135 -0.18716
131 -> 136 0.10219

Excited State 10: Singlet-A 5.1805 eV 239.33 nm f=0.0308 <S**2>=0.000
124 -> 132 0.19650
124 -> 136 -0.25194
125 -> 132 0.22510
125 -> 136 -0.14763
126 -> 132 -0.12729
130 -> 136 0.13073
131 -> 133 0.36453
131 -> 136 -0.18313

Excited State 11: Singlet-A 5.3182 eV 233.13 nm f=0.0136 <S**2>=0.000
125 -> 132 0.26906
126 -> 132 -0.10303
128 -> 132 -0.13064
128 -> 133 -0.17208
130 -> 136 -0.12958
130 -> 143 0.10966
131 -> 135 -0.24562
131 -> 136 0.41375
131 -> 137 -0.10395

Excited State 12: Singlet-A 5.3340 eV 232.44 nm f=0.0032 <S**2>=0.000
126 -> 132 -0.20794
128 -> 132 0.14185
128 -> 133 0.20032
128 -> 141 0.10231
128 -> 145 -0.16150
129 -> 136 -0.10592
130 -> 136 0.24084
130 -> 143 -0.22508
131 -> 135 -0.17851
131 -> 136 0.25408

Excited State 13: Singlet-A 5.3887 eV 230.08 nm f=0.1153 <S**2>=0.000
122 -> 136 -0.12985
125 -> 132 0.12084
125 -> 133 -0.20314
128 -> 133 0.25829
129 -> 133 -0.13261
130 -> 133 0.45638

Excited State 14: Singlet-A 5.4409 eV 227.87 nm f=0.0608 <S**2>=0.000
124 -> 132 0.22984
124 -> 136 -0.10170
125 -> 132 -0.15158
126 -> 132 0.25503
127 -> 132 -0.13772
127 -> 134 0.10531
131 -> 133 -0.13161

131 -> 135 -0.29419
131 -> 137 -0.12796
131 -> 138 0.29430
131 -> 140 0.12352

Excited State 15: Singlet-A 5.4768 eV 226.38 nm f=0.0782 <S**2>=0.000
124 -> 132 0.23326
126 -> 132 0.22825
127 -> 132 -0.16045
127 -> 134 0.11731
131 -> 135 0.18152
131 -> 136 0.32652
131 -> 138 -0.28257
131 -> 139 -0.10328
131 -> 140 -0.11166
SavETr: write IOETrm= 770 NScale= 10 NData= 16 NLR=1 NState= 15 LETran= 280.

PhPyBFlu – *i*Pr$_{ax}$

Excitation energies and oscillator strengths:

Excited State 1: Singlet-A 3.5059 eV 353.64 nm f=0.0042 <S**2>=0.000
131 -> 132 0.69574
This state for optimization and/or second-order correction.
Total Energy, E(TD-HF/TD-KS) = -1437.11357108
Copying the excited state density for this state as the 1-particle RhoCI density.

Excited State 2: Singlet-A 3.9294 eV 315.53 nm f=0.0394 <S**2>=0.000
128 -> 132 0.27675
129 -> 132 -0.19507
130 -> 132 0.59986

Excited State 3: Singlet-A 4.0668 eV 304.87 nm f=0.0391 <S**2>=0.000
131 -> 133 0.67832

Excited State 4: Singlet-A 4.4044 eV 281.50 nm f=0.0073 <S**2>=0.000
128 -> 132 -0.22799
129 -> 132 0.57156
130 -> 132 0.29771

Excited State 5: Singlet-A 4.5771 eV 270.88 nm f=0.0919 <S**2>=0.000
125 -> 132 0.10972
126 -> 132 -0.11694
127 -> 132 0.15092
128 -> 132 0.21340
128 -> 133 0.11438
129 -> 137 0.12498
130 -> 133 0.15262
131 -> 133 0.11120
131 -> 135 -0.13922
131 -> 136 0.29322
131 -> 137 -0.24606
131 -> 138 0.17348
131 -> 141 0.10859
131 -> 143 -0.22703

Excited State 6: Singlet-A 4.6034 eV 269.33 nm f=0.0143 <S**2>=0.000
125 -> 132 0.13207
126 -> 132 -0.15942
127 -> 132 0.17063
128 -> 132 0.13810

128 -> 133 0.13896
129 -> 133 -0.15898
130 -> 133 0.27608
131 -> 133 -0.10053
131 -> 135 0.14058
131 -> 136 -0.17457
131 -> 137 -0.14716
131 -> 141 -0.16819
131 -> 143 0.29525

Excited State 7: Singlet-A 4.6427 eV 267.05 nm f=0.2678 <S**2>=0.000
126 -> 132 -0.11164
127 -> 132 0.10957
128 -> 133 0.14440
129 -> 133 -0.10980
130 -> 133 0.29841
131 -> 137 0.42077
131 -> 138 -0.26966
131 -> 141 0.11518
131 -> 143 -0.16471

Excited State 8: Singlet-A 4.6957 eV 264.04 nm f=0.1882 <S**2>=0.000
128 -> 132 0.46005
129 -> 132 0.31660
129 -> 133 0.12453
130 -> 132 -0.12234
130 -> 133 -0.28343
131 -> 137 0.15168

Excited State 9: Singlet-A 4.8868 eV 253.71 nm f=0.0355 <S**2>=0.000
125 -> 132 -0.14466
126 -> 132 -0.33058
127 -> 132 0.37886
128 -> 132 -0.15841
130 -> 133 -0.31358
130 -> 136 0.10801

Excited State 10: Singlet-A 4.9943 eV 248.25 nm f=0.0123 <S**2>=0.000
125 -> 132 0.32237
127 -> 132 -0.11677
128 -> 133 0.12815
129 -> 133 -0.16806
130 -> 133 -0.16940
130 -> 137 -0.10750
131 -> 134 0.36060
131 -> 135 -0.16527
131 -> 137 0.12241
131 -> 139 -0.14356
131 -> 155 0.12609

Excited State 11: Singlet-A 5.0132 eV 247.32 nm f=0.0085 <S**2>=0.000
125 -> 132 -0.38652
128 -> 133 -0.10475
129 -> 133 0.10634
130 -> 133 0.20992
131 -> 134 0.38958
131 -> 135 -0.12911
131 -> 139 -0.15493

Excited State 12: Singlet-A 5.0912 eV 243.53 nm f=0.0598 <S**2>=0.000
125 -> 132 0.28120
126 -> 132 -0.14170
129 -> 133 0.55914

```
Excited State  13:      Singlet-A      5.1731 eV  239.67 nm  f=0.0511  <S**2>=0.000
   125 -> 132        0.17865
   128 -> 133       -0.13355
   128 -> 137       -0.12447
   129 -> 133       -0.18050
   130 -> 133       -0.10704
   130 -> 136       -0.12774
   130 -> 137        0.29188
   130 -> 138       -0.18563
   131 -> 134        0.12684
   131 -> 153       -0.16227
   131 -> 155       -0.27906

Excited State  14:      Singlet-A      5.2729 eV  235.14 nm  f=0.1916  <S**2>=0.000
   124 -> 132        0.31381
   125 -> 132       -0.18086
   127 -> 132       -0.22987
   128 -> 133        0.40679
   130 -> 137        0.14319
   130 -> 138       -0.11313

Excited State  15:      Singlet-A      5.2905 eV  234.35 nm  f=0.0356  <S**2>=0.000
   124 -> 132       -0.25930
   125 -> 132       -0.11029
   126 -> 133       -0.17911
   127 -> 132        0.15738
   127 -> 133        0.23647
   128 -> 132       -0.15267
   128 -> 133        0.34110
   129 -> 133        0.16115
   130 -> 133       -0.10228
   131 -> 136       -0.18401
SavETr:  write IOETrm=   770 NScale= 10 NData=  16 NLR=1 NState=   15 LETran=    280.
```

PhPyBFlu – *i*Pr$_{eq}$

Excitation energies and oscillator strengths:

```
Excited State   1:      Singlet-A      3.5812 eV  346.20 nm  f=0.0048  <S**2>=0.000
   131 -> 132        0.69402
This state for optimization and/or second-order correction.
Total Energy, E(TD-HF/TD-KS) =  -1437.10795641
Copying the excited state density for this state as the 1-particle RhoCI density.

Excited State   2:      Singlet-A      3.9114 eV  316.98 nm  f=0.0418  <S**2>=0.000
   128 -> 132        0.24690
   130 -> 132        0.63904

Excited State   3:      Singlet-A      4.1131 eV  301.44 nm  f=0.0602  <S**2>=0.000
   131 -> 133        0.66911
   131 -> 136        0.12320

Excited State   4:      Singlet-A      4.5041 eV  275.27 nm  f=0.0058  <S**2>=0.000
   128 -> 132        0.18215
   129 -> 132        0.57046
   130 -> 132       -0.15306
   130 -> 133       -0.18819
   131 -> 137       -0.11210
```

Excited State 5: Singlet-A 4.5706 eV 271.26 nm f=0.0019 <S**2>=0.000
129 -> 137 -0.14886
131 -> 133 -0.14182
131 -> 135 0.10839
131 -> 136 0.33723
131 -> 137 -0.20136
131 -> 138 -0.12124
131 -> 139 -0.14432
131 -> 141 -0.21660
131 -> 142 0.10070
131 -> 143 0.34887

Excited State 6: Singlet-A 4.6079 eV 269.07 nm f=0.0937 <S**2>=0.000
126 -> 132 0.12593
127 -> 132 0.25379
128 -> 132 0.27536
128 -> 133 0.13014
129 -> 132 0.18414
130 -> 132 -0.12409
130 -> 133 0.30556
131 -> 136 0.13047
131 -> 137 0.31067
131 -> 138 -0.12539

Excited State 7: Singlet-A 4.6301 eV 267.78 nm f=0.2663 <S**2>=0.000
127 -> 132 -0.14147
128 -> 133 -0.13011
130 -> 133 -0.35677
131 -> 133 -0.11069
131 -> 136 0.19653
131 -> 137 0.43571
131 -> 138 -0.18307

Excited State 8: Singlet-A 4.7068 eV 263.41 nm f=0.1426 <S**2>=0.000
127 -> 132 0.12607
128 -> 132 0.46784
129 -> 132 -0.31666
130 -> 132 -0.16713
130 -> 133 -0.28788

Excited State 9: Singlet-A 4.9084 eV 252.59 nm f=0.0528 <S**2>=0.000
125 -> 132 -0.11433
126 -> 132 0.20976
127 -> 132 0.44879
127 -> 133 -0.12471
128 -> 132 -0.20774
129 -> 133 0.11074
130 -> 133 -0.27592
130 -> 136 -0.12999

Excited State 10: Singlet-A 5.0289 eV 246.54 nm f=0.0042 <S**2>=0.000
131 -> 134 0.52998
131 -> 135 -0.19991
131 -> 137 0.12277
131 -> 139 -0.25147
131 -> 142 0.10578

Excited State 11: Singlet-A 5.0644 eV 244.81 nm f=0.0061 <S**2>=0.000
125 -> 132 0.43817
128 -> 133 0.21126
129 -> 133 0.15618
130 -> 133 -0.15816
130 -> 137 -0.16372

131 -> 134 0.13638
131 -> 153 -0.14560
131 -> 154 0.10562
131 -> 155 -0.12080

Excited State 12: Singlet-A 5.1385 eV 241.29 nm f=0.0796 <S**2>=0.000
125 -> 132 -0.36589
126 -> 132 -0.11087
129 -> 133 0.45827
130 -> 137 -0.16298

Excited State 13: Singlet-A 5.1830 eV 239.21 nm f=0.0263 <S**2>=0.000
125 -> 132 0.22087
128 -> 133 -0.11107
128 -> 137 -0.14544
129 -> 133 0.43889
130 -> 133 -0.10748
130 -> 136 0.14041
130 -> 137 0.19490
130 -> 138 -0.10253
131 -> 153 0.16928
131 -> 154 -0.11317
131 -> 155 0.14067

Excited State 14: Singlet-A 5.3306 eV 232.59 nm f=0.1711 <S**2>=0.000
124 -> 132 -0.10111
125 -> 132 -0.17540
127 -> 132 -0.12763
128 -> 133 0.53788
130 -> 133 -0.13860
130 -> 137 0.20921

Excited State 15: Singlet-A 5.3434 eV 232.03 nm f=0.0924 <S**2>=0.000
124 -> 132 -0.20079
126 -> 133 -0.10629
127 -> 132 -0.18498
127 -> 133 -0.24794
128 -> 132 0.12355
130 -> 136 -0.16193
130 -> 137 0.14727
131 -> 134 0.12688
131 -> 136 0.28050
131 -> 139 0.15086
131 -> 141 0.16522
SavETr: write IOETrn= 770 NScale= 10 NData= 16 NLR=1 NState= 15 LETran= 280.

PhPyBPh$_2$ – open

Excitation energies and oscillator strengths:

Excited State 1: Singlet-A 4.5603 eV 271.88 nm f=0.0492 <S**2>=0.000
90 ->101 0.14158
98 ->101 0.13001
99 ->101 -0.23247
100 ->101 0.59332
This state for optimization and/or second-order correction.
Total Energy, E(TD-HF/TD-KS) = -1123.78297276
Copying the excited state density for this state as the 1-particle RhoCI density.

Excited State 2: Singlet-A 4.7550 eV 260.75 nm f=0.0094 <S**2>=0.000
93 ->101 -0.26780
93 ->102 -0.29241

```
     93 ->104       -0.23213
     94 ->101        0.24836
     94 ->102        0.25984
     94 ->104        0.19505
     99 ->101       -0.10557
    100 ->101       -0.10604

Excited State  3:      Singlet-A      4.9286 eV  251.56 nm  f=0.0456  <S**2>=0.000
     95 ->101       -0.29462
     96 ->101       -0.24191
     97 ->101        0.29974
     98 ->101       -0.26903
     99 ->101        0.24213
    100 ->101        0.16236

Excited State  4:      Singlet-A      4.9794 eV  249.00 nm  f=0.1927  <S**2>=0.000
     96 ->101        0.27825
     97 ->101       -0.20254
     99 ->101        0.50185
    100 ->101        0.19359

Excited State  5:      Singlet-A      5.1162 eV  242.34 nm  f=0.0049  <S**2>=0.000
     95 ->101        0.19143
     96 ->101        0.30485
     97 ->101        0.44795
     97 ->109        0.17651

Excited State  6:      Singlet-A      5.2198 eV  237.53 nm  f=0.0192  <S**2>=0.000
     92 ->101        0.31600
     95 ->101        0.41188
     96 ->101       -0.21097
     98 ->101       -0.32636

Excited State  7:      Singlet-A      5.2531 eV  236.02 nm  f=0.0217  <S**2>=0.000
     90 ->101       -0.13425
     92 ->101        0.11871
     93 ->101        0.11472
     96 ->101       -0.20936
     98 ->101        0.37561
     98 ->102        0.17003
     98 ->111        0.10401
     99 ->101        0.10877
     99 ->102        0.14312
    100 ->103       -0.10783
    100 ->104        0.15769
    100 ->111       -0.11329

Excited State  8:      Singlet-A      5.3243 eV  232.87 nm  f=0.0225  <S**2>=0.000
     93 ->102        0.27971
     93 ->104       -0.14716
     94 ->101        0.20647
     94 ->102       -0.15366
     94 ->103       -0.10259
     94 ->104        0.22137
     96 ->102        0.10241
    100 ->102        0.19931
    100 ->105       -0.10593

Excited State  9:      Singlet-A      5.3866 eV  230.17 nm  f=0.0276  <S**2>=0.000
     90 ->101       -0.13679
     92 ->101        0.19145
     93 ->101        0.19098
     93 ->102       -0.14732
```

93 ->104 0.19875
94 ->102 0.24815
94 ->104 -0.11101
98 ->101 0.13105
98 ->111 -0.12984
100 ->102 0.17204
100 ->105 -0.10267
100 ->111 0.10540

Excited State 10: Singlet-A 5.4942 eV 225.66 nm f=0.0640 <S**2>=0.000
90 ->101 0.15671
91 ->101 0.13128
92 ->101 -0.30910
94 ->102 0.10504
95 ->101 0.23708
96 ->101 -0.10914
98 ->101 -0.10997
98 ->102 0.15487
99 ->102 0.17309
100 ->102 0.35649

Excited State 11: Singlet-A 5.5900 eV 221.80 nm f=0.0146 <S**2>=0.000
90 ->101 -0.15198
92 ->101 0.18411
95 ->101 -0.19627
96 ->101 0.23773
97 ->101 -0.10206
98 ->101 -0.22731
98 ->102 0.15593
99 ->101 -0.22361
99 ->102 0.16627
100 ->102 0.26660
100 ->110 0.12859

Excited State 12: Singlet-A 5.6811 eV 218.24 nm f=0.0040 <S**2>=0.000
90 ->101 0.11820
91 ->102 -0.11464
93 ->101 0.20931
94 ->101 0.28419
94 ->102 0.11556
95 ->102 -0.10245
96 ->102 0.10231
97 ->101 -0.17659
98 ->101 -0.16530
100 ->102 -0.27208
100 ->104 0.11783

Excited State 13: Singlet-A 5.7590 eV 215.29 nm f=0.0257 <S**2>=0.000
94 ->101 0.11546
96 ->101 0.16327
97 ->101 0.30051
97 ->109 -0.22739
98 ->110 -0.11338
99 ->102 -0.18746
99 ->106 -0.10156
99 ->110 0.13685
100 ->110 -0.15900

Excited State 14: Singlet-A 5.8545 eV 211.78 nm f=0.0620 <S**2>=0.000
90 ->101 0.40642
91 ->101 0.17899
92 ->101 0.25078
98 ->101 0.12775

```
    99 ->101        0.10861
   100 ->101       -0.19196
   100 ->104       -0.21242

 Excited State  15:      Singlet-A     6.0229 eV  205.85 nm  f=0.1265  <S**2>=0.000
    90 ->101       -0.14902
    98 ->102        0.27818
    99 ->102        0.20657
   100 ->102       -0.19075
   100 ->103        0.31477
   100 ->104       -0.17002
   100 ->105       -0.16706
   100 ->109       -0.10652
   100 ->110       -0.10419
   100 ->111       -0.11822
 SavETr:  write IOETrm=   770 NScale= 10 NData=  16 NLR=1 NState=   15 LETran=    280.
```

PhPyBPh$_2$ - *i*Pr$_{ax}$

Excitation energies and oscillator strengths:

```
 Excited State   1:      Singlet-A     4.0049 eV  309.58 nm  f=0.0069  <S**2>=0.000
    98 ->101        0.36607
   100 ->101        0.58495
 This state for optimization and/or second-order correction.
 Total Energy, E(TD-HF/TD-KS) =  -1123.83944590
 Copying the excited state density for this state as the 1-particle RhoCI density.

 Excited State   2:      Singlet-A     4.0504 eV  306.11 nm  f=0.0813  <S**2>=0.000
    96 ->101       -0.12722
    98 ->101        0.56634
    99 ->101        0.10644
   100 ->101       -0.36267

 Excited State   3:      Singlet-A     4.5350 eV  273.39 nm  f=0.0311  <S**2>=0.000
    95 ->101       -0.21596
    96 ->101       -0.10253
    97 ->101       -0.15395
    98 ->102        0.16042
    99 ->101        0.58034
   100 ->101        0.10394
   100 ->102        0.11058

 Excited State   4:      Singlet-A     4.6181 eV  268.48 nm  f=0.0182  <S**2>=0.000
    95 ->101        0.24823
    97 ->101       -0.36523
    98 ->102       -0.17246
   100 ->102        0.46996

 Excited State   5:      Singlet-A     4.6743 eV  265.25 nm  f=0.0160  <S**2>=0.000
    95 ->101       -0.36199
    98 ->102        0.36315
    99 ->101       -0.34287
   100 ->102        0.25557

 Excited State   6:      Singlet-A     4.7398 eV  261.58 nm  f=0.0231  <S**2>=0.000
    94 ->101       -0.14451
    96 ->101        0.12762
    97 ->101        0.48588
    99 ->101        0.11515
   100 ->102        0.41854
```

```
Excited State   7:      Singlet-A      4.9495 eV  250.50 nm  f=0.1510  <S**2>=0.000
     95 ->101         0.41094
     95 ->102        -0.19655
     97 ->101         0.13679
     98 ->102         0.45195
     99 ->102         0.10841

Excited State   8:      Singlet-A      5.0001 eV  247.96 nm  f=0.0162  <S**2>=0.000
     93 ->101        -0.16514
     96 ->101         0.59655
     97 ->101        -0.22028
     98 ->101         0.11262

Excited State   9:      Singlet-A      5.1450 eV  240.98 nm  f=0.0153  <S**2>=0.000
     94 ->101        -0.19269
     96 ->101        -0.13507
     96 ->102        -0.14355
     97 ->102        -0.27134
     99 ->102         0.51505

Excited State  10:      Singlet-A      5.2383 eV  236.69 nm  f=0.0851  <S**2>=0.000
     92 ->101        -0.10958
     93 ->101         0.29384
     94 ->101         0.30358
     95 ->101        -0.15886
     96 ->101         0.19742
     97 ->102         0.14912
     98 ->102        -0.17240
     99 ->102         0.25744

Excited State  11:      Singlet-A      5.3057 eV  233.68 nm  f=0.0156  <S**2>=0.000
     93 ->101        -0.15658
     96 ->102        -0.13213
     96 ->108         0.15116
     96 ->110         0.16154
     96 ->112        -0.10373
     97 ->102         0.33323
     97 ->110        -0.12980
     97 ->112        -0.12927
     97 ->115         0.11834
    100 ->106         0.13991
    100 ->108        -0.10156
    100 ->112         0.21218
    100 ->114         0.10877
    100 ->115        -0.11795

Excited State  12:      Singlet-A      5.3755 eV  230.65 nm  f=0.0325  <S**2>=0.000
     93 ->101         0.47202
     94 ->101        -0.44386
     97 ->101        -0.11872

Excited State  13:      Singlet-A      5.3807 eV  230.42 nm  f=0.0113  <S**2>=0.000
     93 ->101        -0.13250
     94 ->101        -0.17353
     95 ->102         0.11169
     96 ->101        -0.12037
     96 ->102         0.31039
     96 ->110        -0.12106
     97 ->102         0.41088
     99 ->102         0.13103
```

Excited State 14: Singlet-A 5.4195 eV 228.78 nm f=0.0317 <S**2>=0.000
95 ->102 -0.13995
97 ->102 0.13910
99 ->102 0.29323
99 ->106 -0.12725
99 ->112 -0.11655
99 ->117 -0.11816
99 ->122 -0.10419
99 ->123 -0.10969
100 ->106 -0.15885
100 ->107 0.10733
100 ->110 0.23151
100 ->117 0.27383

Excited State 15: Singlet-A 5.5561 eV 223.15 nm f=0.0340 <S**2>=0.000
93 ->101 0.12543
94 ->101 0.19816
95 ->102 0.46354
96 ->102 0.24600
97 ->102 -0.11129
98 ->102 0.12391
99 ->102 0.14630
SavETr: write IOETrn= 770 NScale= 10 NData= 16 NLR=1 NState= 15 LETran= 280.

PhPyBPh$_2$ – *i*Pr$_{eq}$

Excitation energies and oscillator strengths:

Excited State 1: Singlet-A 3.8362 eV 323.19 nm f=0.0395 <S**2>=0.000
96 ->101 0.10371
97 ->101 0.17236
99 ->101 -0.19037
100 ->101 0.62957
This state for optimization and/or second-order correction.
Total Energy, E(TD-HF/TD-KS) = -1123.84695284
Copying the excited state density for this state as the 1-particle RhoCI density.

Excited State 2: Singlet-A 4.4036 eV 281.55 nm f=0.0522 <S**2>=0.000
96 ->101 -0.10915
97 ->101 -0.16987
99 ->101 0.61332
100 ->101 0.25210

Excited State 3: Singlet-A 4.5167 eV 274.50 nm f=0.0307 <S**2>=0.000
95 ->101 0.31085
97 ->101 -0.12144
97 ->102 0.11835
99 ->102 -0.17415
100 ->102 0.53473

Excited State 4: Singlet-A 4.6467 eV 266.82 nm f=0.0777 <S**2>=0.000
95 ->101 -0.14812
96 ->101 0.16163
97 ->101 0.51911
98 ->101 -0.11764
99 ->101 0.25099
100 ->101 -0.12622
100 ->102 0.22412

```
Excited State   5:      Singlet-A      4.7668 eV  260.10 nm  f=0.0449  <S**2>=0.000
     95 ->101        -0.32887
     95 ->102        -0.10526
     98 ->101         0.50082
    100 ->102         0.27592

Excited State   6:      Singlet-A      4.9031 eV  252.87 nm  f=0.0231  <S**2>=0.000
     95 ->101         0.39984
     97 ->101         0.21554
     98 ->101         0.46172
    100 ->102        -0.15184

Excited State   7:      Singlet-A      4.9995 eV  247.99 nm  f=0.0144  <S**2>=0.000
     95 ->101         0.12532
     95 ->102         0.13007
     97 ->102        -0.12610
     99 ->102         0.59240
    100 ->102         0.16546

Excited State   8:      Singlet-A      5.1109 eV  242.59 nm  f=0.0006  <S**2>=0.000
     96 ->101         0.64096
     96 ->102        -0.14185
     97 ->101        -0.21195

Excited State   9:      Singlet-A      5.1708 eV  239.78 nm  f=0.0438  <S**2>=0.000
     94 ->101         0.14748
     95 ->102        -0.12833
     96 ->102         0.20635
     97 ->101         0.10220
     97 ->102         0.47369
     99 ->102         0.15250
    100 ->111         0.11984

Excited State  10:      Singlet-A      5.3225 eV  232.94 nm  f=0.0718  <S**2>=0.000
     91 ->101         0.12242
     94 ->101         0.39460
     95 ->101         0.18112
     95 ->102        -0.33334
     97 ->101         0.12878
     98 ->102         0.15179
    100 ->107         0.12619

Excited State  11:      Singlet-A      5.4040 eV  229.43 nm  f=0.0016  <S**2>=0.000
     94 ->101        -0.15634
     98 ->102         0.59967
     99 ->102         0.11903
    100 ->102         0.10721

Excited State  12:      Singlet-A      5.4347 eV  228.13 nm  f=0.0258  <S**2>=0.000
     94 ->101        -0.11582
     96 ->106         0.10812
     96 ->107        -0.17627
     96 ->111         0.16958
     97 ->102         0.37071
     97 ->110         0.11303
     97 ->112         0.14846
     97 ->118        -0.10513
     98 ->102         0.13116
    100 ->110        -0.12142
    100 ->111        -0.21556
```

Excited State 13: Singlet-A 5.4679 eV 226.75 nm f=0.0652 <S**2>=0.000
93 ->101 0.11053
94 ->101 0.45302
95 ->102 0.29600
96 ->102 -0.11844
98 ->119 0.10784
99 ->111 0.10847
100 ->106 0.10056
100 ->107 -0.12883

Excited State 14: Singlet-A 5.5254 eV 224.39 nm f=0.0350 <S**2>=0.000
94 ->101 0.16136
95 ->102 0.13491
98 ->102 0.22686
98 ->111 0.12182
98 ->115 0.13366
98 ->117 -0.15579
98 ->119 -0.16823
99 ->102 -0.17498
99 ->111 -0.16901
99 ->113 -0.11253
99 ->116 -0.13902
99 ->117 -0.14420
99 ->118 -0.10131
100 ->113 -0.12544
100 ->116 -0.13325
100 ->117 -0.15090

Excited State 15: Singlet-A 5.6143 eV 220.84 nm f=0.0068 <S**2>=0.000
95 ->102 0.11915
96 ->102 0.56114
97 ->102 -0.12220
100 ->107 0.14149
100 ->111 -0.12413
SavETr: write IOETrn= 770 NScale= 10 NData= 16 NLR=1 NState= 15 LETran= 280.

PhPyBPF - open

Excitation energies and oscillator strengths:

Excited State 1: Singlet-A 4.3231 eV 286.79 nm f=0.0162 <S**2>=0.000
133 ->141 -0.11004
139 ->141 0.29418
140 ->141 0.58049
This state for optimization and/or second-order correction.
Total Energy, E(TD-HF/TD-KS) = -2116.14313913
Copying the excited state density for this state as the 1-particle RhoCI density.

Excited State 2: Singlet-A 4.7867 eV 259.02 nm f=0.0344 <S**2>=0.000
133 ->141 -0.14622
136 ->141 0.10993
139 ->141 0.54275
140 ->141 -0.32970

Excited State 3: Singlet-A 4.8562 eV 255.31 nm f=0.0129 <S**2>=0.000
137 ->141 0.29541
137 ->143 0.21374
137 ->144 -0.27592
137 ->145 0.23645
137 ->146 -0.23683
137 ->147 -0.18749
140 ->141 0.12056

Excited State 4: Singlet-A 4.9432 eV 250.82 nm f=0.0155 <S**2>=0.000
133 ->147 0.12338
134 ->141 0.32855
136 ->141 0.47315
137 ->141 0.15836
138 ->141 0.21228

Excited State 5: Singlet-A 5.0743 eV 244.34 nm f=0.0150 <S**2>=0.000
133 ->141 0.22153
134 ->141 0.35807
135 ->141 -0.10918
136 ->141 -0.30417
137 ->141 0.21402
137 ->144 0.15501
139 ->141 0.23417
139 ->144 0.12238

Excited State 6: Singlet-A 5.1180 eV 242.25 nm f=0.1055 <S**2>=0.000
133 ->141 -0.34156
134 ->141 0.42321
136 ->141 -0.11736
137 ->141 -0.23539
137 ->144 -0.19256
138 ->141 -0.10408

Excited State 7: Singlet-A 5.2378 eV 236.71 nm f=0.0105 <S**2>=0.000
133 ->141 0.14637
136 ->141 -0.17077
137 ->141 -0.15566
137 ->144 -0.15876
138 ->141 0.55194
138 ->143 0.11409

Excited State 8: Singlet-A 5.2627 eV 235.59 nm f=0.0378 <S**2>=0.000
133 ->141 0.37525
136 ->141 0.11956
137 ->141 -0.10880
137 ->143 0.11497
137 ->144 -0.25465
137 ->146 0.14889
138 ->141 -0.28047
139 ->141 0.12704
140 ->144 -0.10508

Excited State 9: Singlet-A 5.2940 eV 234.20 nm f=0.0951 <S**2>=0.000
132 ->141 0.10522
139 ->143 0.15960
139 ->144 -0.28428
140 ->143 -0.24878
140 ->144 0.29659
140 ->145 -0.11970
140 ->147 0.13023
140 ->150 0.10481
140 ->151 -0.21433

Excited State 10: Singlet-A 5.3371 eV 232.30 nm f=0.0681 <S**2>=0.000
133 ->141 0.10119
135 ->141 0.10811
135 ->144 -0.10329
137 ->144 -0.11126
139 ->143 -0.14073
139 ->144 0.20378

```
   139 ->158       0.11303
   140 ->143      -0.18421
   140 ->144       0.32022
   140 ->145      -0.15475
   140 ->151       0.23349

Excited State  11:      Singlet-A      5.5084 eV  225.08 nm  f=0.0057  <S**2>=0.000
   134 ->147       0.11721
   134 ->148      -0.25598
   136 ->147      -0.12758
   136 ->148       0.18245
   138 ->141      -0.17249
   138 ->142      -0.16539
   138 ->143       0.41360
   138 ->144       0.18315
   138 ->147       0.15226

Excited State  12:      Singlet-A      5.5548 eV  223.20 nm  f=0.0181  <S**2>=0.000
   135 ->141       0.47682
   136 ->141      -0.12527
   140 ->142       0.12876
   140 ->143       0.11403
   140 ->144      -0.25307
   140 ->146       0.21517
   140 ->147       0.12340

Excited State  13:      Singlet-A      5.7093 eV  217.16 nm  f=0.0850  <S**2>=0.000
   131 ->141       0.10897
   132 ->141      -0.20442
   135 ->141       0.40255
   135 ->144       0.11857
   136 ->141      -0.11658
   140 ->142      -0.17197
   140 ->143      -0.10220
   140 ->144       0.18994
   140 ->145       0.13382
   140 ->146      -0.24820
   140 ->147      -0.12840

Excited State  14:      Singlet-A      5.8539 eV  211.80 nm  f=0.0002  <S**2>=0.000
   136 ->145      -0.12508
   138 ->142       0.46855
   138 ->143       0.13400
   138 ->144       0.19242
   138 ->145       0.25508
   138 ->146       0.15206
   138 ->169      -0.10107

Excited State  15:      Singlet-A      5.8813 eV  210.81 nm  f=0.0030  <S**2>=0.000
   134 ->142       0.28248
   134 ->145      -0.11949
   136 ->142       0.41087
   136 ->145      -0.15577
   136 ->146      -0.12692
   137 ->142       0.12710
   138 ->145      -0.17620
   138 ->146      -0.12366
SavETr:  write IOETrn=   770 NScale= 10 NData=  16 NLR=1 NState=   15 LETran=    280.
```

PhPyBPF - *i*Pr$_{ax}$

Excitation energies and oscillator strengths:

Excited State	1:	Singlet-A	4.1612 eV	297.95 nm	f=0.1115	<S**2>=0.000
140 ->141	0.67292					

This state for optimization and/or second-order correction.
Total Energy, E(TD-HF/TD-KS) = -2116.20697289
Copying the excited state density for this state as the 1-particle RhoCI density.

Excited State	2:	Singlet-A	4.6478 eV	266.76 nm	f=0.0875	<S**2>=0.000
136 ->141	0.46690					
137 ->141	-0.16533					
138 ->141	0.16561					
139 ->141	0.30098					
140 ->142	-0.24768					

Excited State	3:	Singlet-A	4.9772 eV	249.10 nm	f=0.0121	<S**2>=0.000
137 ->141	0.12862					
138 ->141	0.62399					
139 ->141	-0.23432					

Excited State	4:	Singlet-A	4.9941 eV	248.26 nm	f=0.0091	<S**2>=0.000
135 ->141	0.11768					
136 ->141	-0.25877					
137 ->141	0.15126					
138 ->141	0.15355					
139 ->141	0.56573					
140 ->141	-0.10037					

Excited State	5:	Singlet-A	5.0942 eV	243.38 nm	f=0.0577	<S**2>=0.000
133 ->141	-0.10319					
134 ->141	-0.15179					
135 ->141	-0.24713					
136 ->141	0.16111					
136 ->142	-0.22155					
137 ->142	0.11382					
138 ->141	0.13312					
140 ->142	0.50258					

Excited State	6:	Singlet-A	5.1345 eV	241.47 nm	f=0.1092	<S**2>=0.000
134 ->141	0.22643					
135 ->141	0.46976					
136 ->141	0.20500					
137 ->141	-0.19881					
140 ->141	0.11255					
140 ->142	0.29450					

Excited State	7:	Singlet-A	5.3867 eV	230.17 nm	f=0.0010	<S**2>=0.000
135 ->141	0.14791					
136 ->141	0.27494					
137 ->141	0.58722					
138 ->141	-0.13194					

Excited State	8:	Singlet-A	5.4215 eV	228.69 nm	f=0.0086	<S**2>=0.000
138 ->142	-0.12211					
138 ->149	0.11044					
138 ->154	0.22539					
138 ->155	-0.14575					
139 ->141	-0.11620					
139 ->142	0.32659					
139 ->145	-0.15007					
139 ->147	-0.20872					

```
   139 ->149       -0.23409
   139 ->150       -0.21663
   139 ->151        0.10396

Excited State  9:      Singlet-A      5.4524 eV  227.40 nm  f=0.0079  <S**2>=0.000
   135 ->149       -0.22561
   135 ->150        0.21085
   136 ->144        0.11608
   137 ->141       -0.10943
   137 ->142       -0.10485
   137 ->144        0.27074
   137 ->145       -0.17892
   137 ->146        0.24149
   137 ->147        0.23100
   140 ->149       -0.12460
   140 ->150        0.11635

Excited State  10:      Singlet-A      5.5657 eV  222.77 nm  f=0.0155  <S**2>=0.000
   133 ->141        0.18311
   135 ->141       -0.23885
   136 ->141        0.15800
   136 ->142        0.38741
   137 ->142       -0.12188
   138 ->142        0.10404
   139 ->142        0.24652
   140 ->142        0.15943
   140 ->145       -0.13427
   140 ->147       -0.13832

Excited State  11:      Singlet-A      5.6521 eV  219.36 nm  f=0.0026  <S**2>=0.000
   138 ->142       -0.10019
   139 ->142       -0.17487
   139 ->143        0.31802
   139 ->145        0.12251
   139 ->146        0.26845
   139 ->147       -0.16398
   139 ->148       -0.19813
   139 ->151        0.10195
   139 ->152       -0.10472
   139 ->172       -0.10172
   140 ->143       -0.12634

Excited State  12:      Singlet-A      5.7146 eV  216.96 nm  f=0.0064  <S**2>=0.000
   134 ->141        0.12133
   135 ->141       -0.11197
   136 ->143        0.12729
   137 ->143        0.33038
   137 ->144       -0.17283
   137 ->145       -0.23417
   138 ->142       -0.27783
   138 ->145        0.12612

Excited State  13:      Singlet-A      5.7229 eV  216.65 nm  f=0.0189  <S**2>=0.000
   134 ->141       -0.13113
   135 ->141        0.12025
   135 ->142        0.11893
   137 ->142        0.12285
   137 ->143        0.19866
   137 ->144       -0.13960
   137 ->145       -0.16457
   138 ->142        0.38465
   138 ->143       -0.16879
   138 ->146       -0.11031
```

139 ->142 0.10270

Excited State 14: Singlet-A 5.7984 eV 213.82 nm f=0.0642 <S**2>=0.000
134 ->141 -0.22115
135 ->141 0.12462
135 ->142 0.24374
135 ->143 0.10972
135 ->144 -0.11077
136 ->142 0.18230
137 ->142 -0.14123
138 ->142 -0.22056
138 ->143 0.17898
138 ->146 0.13656
140 ->144 -0.16359

Excited State 15: Singlet-A 5.8695 eV 211.24 nm f=0.0107 <S**2>=0.000
132 ->141 -0.12077
134 ->141 0.32649
135 ->141 -0.17083
135 ->143 0.25981
135 ->144 -0.20123
135 ->145 -0.13407
140 ->143 0.25494
140 ->144 -0.14377
SavETr: write IOETrm= 770 NScale= 10 NData= 16 NLR=1 NState= 15 LETran= 280.

PhPyBPF - *i*Pr$_{eq}$

Excitation energies and oscillator strengths:

Excited State 1: Singlet-A 3.9955 eV 310.31 nm f=0.0662 <S**2>=0.000
140 ->141 0.67972
This state for optimization and/or second-order correction.
Total Energy, E(TD-HF/TD-KS) = -2116.20925954
Copying the excited state density for this state as the 1-particle RhoCI density.

Excited State 2: Singlet-A 4.6048 eV 269.25 nm f=0.0760 <S**2>=0.000
136 ->141 0.37890
137 ->141 0.26203
138 ->141 0.26072
139 ->141 0.15045
140 ->142 -0.36129

Excited State 3: Singlet-A 4.8204 eV 257.21 nm f=0.0634 <S**2>=0.000
138 ->141 0.59873
139 ->141 -0.20892
140 ->142 0.23203

Excited State 4: Singlet-A 4.9175 eV 252.13 nm f=0.0928 <S**2>=0.000
136 ->141 0.21358
136 ->142 -0.14094
137 ->141 0.16957
139 ->141 0.33962
140 ->142 0.49816

Excited State 5: Singlet-A 5.0043 eV 247.75 nm f=0.0209 <S**2>=0.000
136 ->141 -0.28874
137 ->141 -0.20668
138 ->141 0.20150
139 ->141 0.54532
140 ->142 -0.11536

Excited State 6: Singlet-A 5.2245 eV 237.31 nm f=0.0081 <S**2>=0.000
134 ->141 0.14162
135 ->141 0.41340
136 ->142 0.20132
137 ->141 0.29597
137 ->142 0.19463
138 ->142 0.16723

Excited State 7: Singlet-A 5.3463 eV 231.91 nm f=0.0020 <S**2>=0.000
136 ->141 -0.37383
136 ->142 -0.16067
137 ->141 0.43680
137 ->144 -0.14463
138 ->142 -0.14716
139 ->142 -0.12608

Excited State 8: Singlet-A 5.3751 eV 230.66 nm f=0.0189 <S**2>=0.000
135 ->141 -0.18834
136 ->141 -0.17758
137 ->141 0.14190
137 ->144 0.14144
138 ->142 0.34911
138 ->147 -0.12300
138 ->154 0.10553
138 ->156 0.11613
139 ->147 -0.15254
139 ->149 0.12869
139 ->150 -0.13055
139 ->151 0.11306

Excited State 9: Singlet-A 5.3891 eV 230.06 nm f=0.0053 <S**2>=0.000
135 ->142 0.11427
135 ->148 -0.12266
135 ->149 0.14592
135 ->150 0.16842
136 ->144 -0.21324
137 ->144 0.35994
138 ->142 -0.14368
140 ->148 -0.11332
140 ->149 0.10720

Excited State 10: Singlet-A 5.4918 eV 225.76 nm f=0.0063 <S**2>=0.000
135 ->141 0.44541
136 ->142 -0.30471
137 ->142 -0.22203
138 ->142 -0.17333
140 ->142 -0.12148

Excited State 11: Singlet-A 5.5219 eV 224.53 nm f=0.0251 <S**2>=0.000
135 ->141 -0.15572
138 ->142 -0.36666
139 ->142 0.44241
139 ->146 0.15939
140 ->144 0.13853

Excited State 12: Singlet-A 5.6519 eV 219.37 nm f=0.0900 <S**2>=0.000
135 ->142 -0.11949
138 ->142 -0.13070
139 ->142 -0.25418
139 ->143 -0.14822
139 ->144 -0.10316
139 ->146 -0.24945
139 ->149 0.17660

```
   139 ->150       -0.12771
   140 ->144        0.28299
   140 ->148        0.10570

Excited State  13:      Singlet-A      5.7299 eV  216.38 nm  f=0.1881  <S**2>=0.000
   136 ->142       -0.17269
   137 ->142       -0.17359
   137 ->143       -0.14543
   137 ->145        0.10419
   138 ->142        0.19489
   138 ->144        0.10124
   139 ->143        0.12043
   139 ->146        0.17199
   139 ->149       -0.10205
   140 ->143       -0.19767
   140 ->144        0.32631

Excited State  14:      Singlet-A      5.7411 eV  215.96 nm  f=0.0109  <S**2>=0.000
   136 ->143       -0.20026
   136 ->145        0.14757
   137 ->141        0.13449
   137 ->142       -0.22814
   137 ->143        0.33743
   137 ->145       -0.26589
   138 ->142        0.12035
   140 ->144        0.10403

Excited State  15:      Singlet-A      5.7861 eV  214.28 nm  f=0.0049  <S**2>=0.000
   138 ->142        0.16154
   139 ->142        0.40157
   139 ->143       -0.11902
   139 ->144       -0.13580
   139 ->146       -0.31214
   139 ->153       -0.11672
   139 ->154        0.10882
SavETr:  write IOETrn=   770 NScale= 10 NData=  16 NLR=1 NState=   15 LETran=    280.
```

PhPyBCl₂ - open

Excitation energies and oscillator strengths:

```
Excited State   1:      Singlet-A      4.8328 eV  256.54 nm  f=0.0054  <S**2>=0.000
    74 -> 77       -0.30012
    74 -> 78        0.54133
    74 -> 79       -0.14916
    74 -> 80        0.14255
    75 -> 77       -0.12057
    75 -> 78        0.11632
This state for optimization and/or second-order correction.
Total Energy, E(TD-HF/TD-KS) =  -1581.03014999
Copying the excited state density for this state as the 1-particle RhoCI density.

Excited State   2:      Singlet-A      4.9564 eV  250.15 nm  f=0.1206  <S**2>=0.000
    75 -> 77        0.43528
    76 -> 77        0.47030
    76 -> 82        0.13709

Excited State   3:      Singlet-A      5.1015 eV  243.04 nm  f=0.1345  <S**2>=0.000
    74 -> 78       -0.10478
    75 -> 77       -0.37054
    75 -> 78        0.10698
    75 -> 89        0.11111
```

76 -> 77 0.43654
76 -> 79 0.13446
76 -> 82 -0.20808

Excited State 4: Singlet-A 5.3089 eV 233.54 nm f=0.0600 <S**2>=0.000
72 -> 79 0.13373
73 -> 78 -0.16068
74 -> 77 -0.20468
74 -> 79 0.20818
75 -> 79 0.12466
76 -> 78 0.48159
76 -> 79 -0.12360
76 -> 80 0.11276

Excited State 5: Singlet-A 5.3746 eV 230.69 nm f=0.0167 <S**2>=0.000
73 -> 77 -0.10350
74 -> 77 -0.29566
74 -> 79 0.41889
74 -> 80 -0.20983
74 -> 82 0.11213
76 -> 78 -0.28400
76 -> 82 0.10105

Excited State 6: Singlet-A 5.5848 eV 222.00 nm f=0.1582 <S**2>=0.000
71 -> 77 0.16466
71 -> 78 0.11723
72 -> 77 0.13119
73 -> 78 0.11495
75 -> 77 0.15745
75 -> 78 0.22973
76 -> 77 -0.18110
76 -> 78 0.13497
76 -> 79 0.43890
76 -> 80 -0.15767

Excited State 7: Singlet-A 5.9618 eV 207.96 nm f=0.0159 <S**2>=0.000
71 -> 77 0.16909
73 -> 78 -0.14408
75 -> 78 0.30394
75 -> 79 0.17648
76 -> 77 -0.17445
76 -> 78 -0.27421
76 -> 79 -0.28748
76 -> 82 -0.24989

Excited State 8: Singlet-A 6.0927 eV 203.50 nm f=0.0278 <S**2>=0.000
70 -> 77 0.44506
70 -> 78 0.25285
70 -> 79 0.15249
71 -> 77 -0.25986
71 -> 78 -0.13331
72 -> 77 -0.12173
73 -> 77 0.13258
76 -> 79 0.10281

Excited State 9: Singlet-A 6.1475 eV 201.68 nm f=0.1404 <S**2>=0.000
70 -> 77 -0.27475
70 -> 78 -0.16038
71 -> 77 -0.14565
73 -> 77 0.28498
75 -> 77 0.22620
75 -> 79 0.13256
75 -> 82 -0.22829

```
    76 -> 79       0.18901
    76 -> 82      -0.15850

Excited State  10:      Singlet-A     6.2159 eV  199.46 nm  f=0.0212  <S**2>=0.000
    70 -> 77      -0.14400
    71 -> 77      -0.29855
    71 -> 78      -0.13621
    73 -> 78       0.10896
    75 -> 78       0.46185
    75 -> 82       0.10303
    76 -> 78       0.14980
    76 -> 79      -0.13088
    76 -> 82       0.12436

Excited State  11:      Singlet-A     6.2453 eV  198.52 nm  f=0.1300  <S**2>=0.000
    71 -> 77       0.15567
    73 -> 77       0.20530
    75 -> 77      -0.21092
    75 -> 78       0.16783
    75 -> 79       0.20735
    75 -> 82      -0.24328
    76 -> 81      -0.11094
    76 -> 82       0.36518
    76 -> 83      -0.13797

Excited State  12:      Singlet-A     6.2936 eV  197.00 nm  f=0.0376  <S**2>=0.000
    73 -> 80      -0.10844
    75 -> 82       0.19041
    75 -> 83      -0.10414
    76 -> 78      -0.10831
    76 -> 79       0.24153
    76 -> 80       0.50140
    76 -> 84       0.10441

Excited State  13:      Singlet-A     6.4299 eV  192.82 nm  f=0.1021  <S**2>=0.000
    72 -> 79       0.12083
    73 -> 77       0.37354
    73 -> 78      -0.17881
    75 -> 79      -0.23441
    75 -> 80       0.10585
    75 -> 82       0.26597
    76 -> 80      -0.27370
    76 -> 83      -0.10205
    76 -> 89       0.12334

Excited State  14:      Singlet-A     6.4850 eV  191.19 nm  f=0.0041  <S**2>=0.000
    72 -> 77      -0.13967
    73 -> 78      -0.12332
    73 -> 79       0.11660
    75 -> 78      -0.18053
    75 -> 79       0.44658
    75 -> 81      -0.20379
    75 -> 82       0.22128
    76 -> 80      -0.13827
    76 -> 81      -0.15125

Excited State  15:      Singlet-A     6.5895 eV  188.15 nm  f=0.0159  <S**2>=0.000
    72 -> 77       0.10941
    73 -> 77       0.15538
    73 -> 78       0.17118
    73 -> 79      -0.13892
    75 -> 79       0.18622
    75 -> 81      -0.14592
```

```
    76 -> 80       0.10877
    76 -> 81       0.44646
    76 -> 83      -0.16259
    76 -> 84      -0.15462
SavETr:  write IOETrn=   770 NScale= 10 NData=  16 NLR=1 NState=   15 LETran=    280
```

PhPyBCl$_2$ - *i*Pr$_{ax}$

Excitation energies and oscillator strengths:

```
Excited State   1:      Singlet-A      4.1970 eV  295.41 nm  f=0.1637  <S**2>=0.000
    76 -> 77        0.68620
This state for optimization and/or second-order correction.
Total Energy, E(TD-HF/TD-KS) =  -1581.10341952
Copying the excited state density for this state as the 1-particle RhoCI density.

Excited State   2:      Singlet-A      4.6398 eV  267.22 nm  f=0.0752  <S**2>=0.000
    75 -> 77        0.59796
    76 -> 78        0.26634
    76 -> 80       -0.14135

Excited State   3:      Singlet-A      4.8060 eV  257.98 nm  f=0.0356  <S**2>=0.000
    74 -> 77        0.68094

Excited State   4:      Singlet-A      5.0254 eV  246.72 nm  f=0.1222  <S**2>=0.000
    72 -> 77        0.17062
    73 -> 77        0.27638
    75 -> 77       -0.22989
    75 -> 78       -0.20023
    76 -> 78        0.52670

Excited State   5:      Singlet-A      5.1106 eV  242.60 nm  f=0.0089  <S**2>=0.000
    73 -> 77        0.62365
    75 -> 78        0.14988
    76 -> 78       -0.20683

Excited State   6:      Singlet-A      5.3550 eV  231.53 nm  f=0.0706  <S**2>=0.000
    72 -> 77        0.64500
    76 -> 78       -0.20035

Excited State   7:      Singlet-A      5.5084 eV  225.08 nm  f=0.0088  <S**2>=0.000
    70 -> 77        0.17666
    72 -> 77        0.13860
    73 -> 77       -0.11990
    75 -> 77       -0.18175
    75 -> 78        0.52345
    76 -> 78        0.17337
    76 -> 80       -0.17674

Excited State   8:      Singlet-A      5.6527 eV  219.34 nm  f=0.0041  <S**2>=0.000
    74 -> 78        0.66334
    76 -> 80       -0.10052

Excited State   9:      Singlet-A      5.7971 eV  213.87 nm  f=0.0040  <S**2>=0.000
    68 -> 77        0.13173
    71 -> 77        0.60064
    73 -> 78        0.19334
    75 -> 78       -0.11846

Excited State  10:      Singlet-A      5.8731 eV  211.10 nm  f=0.0166  <S**2>=0.000
    70 -> 77       -0.18968
    72 -> 78        0.19359
```

```
    73 -> 78       0.57184
    74 -> 78      -0.10397
    75 -> 77      -0.10414
    75 -> 78       0.13876

Excited State  11:      Singlet-A      5.9493 eV  208.40 nm  f=0.0581  <S**2>=0.000
    70 -> 77      -0.30760
    71 -> 77       0.17940
    72 -> 78       0.21029
    73 -> 78      -0.14921
    74 -> 78       0.10039
    75 -> 78       0.30268
    75 -> 80      -0.11889
    76 -> 80       0.33676
    76 -> 81       0.12599

Excited State  12:      Singlet-A      6.0873 eV  203.68 nm  f=0.0651  <S**2>=0.000
    69 -> 77      -0.19159
    70 -> 77      -0.10315
    72 -> 78       0.45185
    73 -> 78      -0.26754
    75 -> 77      -0.10020
    76 -> 80      -0.26504
    76 -> 81      -0.11327

Excited State  13:      Singlet-A      6.1898 eV  200.30 nm  f=0.0591  <S**2>=0.000
    68 -> 77       0.19480
    69 -> 77      -0.17823
    70 -> 77       0.39174
    72 -> 78       0.30822
    73 -> 78       0.12111
    76 -> 79       0.15565
    76 -> 80       0.19834
    76 -> 81       0.13678

Excited State  14:      Singlet-A      6.2573 eV  198.14 nm  f=0.0033  <S**2>=0.000
    65 -> 77      -0.24180
    68 -> 77       0.51960
    70 -> 77      -0.19206
    71 -> 77      -0.14170
    72 -> 78      -0.15577
    75 -> 80       0.11191

Excited State  15:      Singlet-A      6.2824 eV  197.35 nm  f=0.0287  <S**2>=0.000
    70 -> 77      -0.11190
    75 -> 80       0.14645
    76 -> 79       0.56099
    76 -> 80      -0.10671
    76 -> 81       0.23898
SavETr:  write IOETm=   770 NScale= 10 NData=  16 NLR=1 NState=   15 LETran=    280.
```

PhPyBCl$_2$ – *i*Pr$_{eq}$

Excitation energies and oscillator strengths:

```
Excited State   1:      Singlet-A      4.0104 eV  309.15 nm  f=0.1137  <S**2>=0.000
    76 -> 77       0.68929
This state for optimization and/or second-order correction.
Total Energy, E(TD-HF/TD-KS) =  -1581.10551275
Copying the excited state density for this state as the 1-particle RhoCI density.
```

Excited State 2: Singlet-A 4.5976 eV 269.67 nm f=0.1133 <S**2>=0.000
75 -> 77 0.60181
76 -> 78 0.28404
76 -> 81 0.11854

Excited State 3: Singlet-A 4.9112 eV 252.45 nm f=0.1626 <S**2>=0.000
73 -> 77 -0.22072
74 -> 77 -0.20608
75 -> 77 -0.27918
75 -> 78 0.12576
76 -> 78 0.54106

Excited State 4: Singlet-A 5.0348 eV 246.25 nm f=0.0058 <S**2>=0.000
73 -> 77 0.18654
74 -> 77 0.56600
75 -> 78 0.19106
76 -> 78 0.22680
76 -> 81 -0.10884

Excited State 5: Singlet-A 5.2191 eV 237.56 nm f=0.0105 <S**2>=0.000
71 -> 77 0.11287
73 -> 77 0.58157
74 -> 77 -0.31528
75 -> 78 0.10437

Excited State 6: Singlet-A 5.3677 eV 230.98 nm f=0.0108 <S**2>=0.000
68 -> 77 -0.17538
70 -> 77 0.10207
72 -> 77 -0.29507
73 -> 77 -0.18091
74 -> 77 -0.14031
75 -> 77 0.10197
75 -> 78 0.45368
76 -> 78 -0.18617
76 -> 81 -0.14197

Excited State 7: Singlet-A 5.5961 eV 221.56 nm f=0.0549 <S**2>=0.000
71 -> 77 0.19797
72 -> 77 0.52875
74 -> 78 0.15095
75 -> 78 0.34303

Excited State 8: Singlet-A 5.7571 eV 215.36 nm f=0.0040 <S**2>=0.000
69 -> 77 0.12292
70 -> 77 0.14868
71 -> 77 0.55609
72 -> 77 -0.17364
73 -> 77 -0.11639
74 -> 78 0.14823
75 -> 78 -0.16047

Excited State 9: Singlet-A 5.8180 eV 213.10 nm f=0.0498 <S**2>=0.000
68 -> 77 0.12847
71 -> 77 -0.16374
72 -> 77 -0.19853
72 -> 78 -0.12876
73 -> 77 0.10275
73 -> 78 0.23430
74 -> 78 0.36412
75 -> 78 0.12819
75 -> 81 0.10422
75 -> 85 -0.10041
76 -> 81 0.32261

```
Excited State  10:      Singlet-A      5.9333 eV  208.96 nm  f=0.0071  <S**2>=0.000
     68 -> 77       -0.25334
     71 -> 78        0.10424
     72 -> 78        0.13690
     73 -> 78        0.49784
     74 -> 78       -0.23494
     75 -> 77       -0.10153
     75 -> 78       -0.14917

Excited State  11:      Singlet-A      5.9733 eV  207.57 nm  f=0.0590  <S**2>=0.000
     68 -> 77       -0.12392
     70 -> 77        0.12982
     71 -> 77       -0.14569
     72 -> 78        0.10577
     74 -> 78        0.48676
     75 -> 78       -0.16878
     76 -> 81       -0.30594

Excited State  12:      Singlet-A      6.0865 eV  203.70 nm  f=0.0089  <S**2>=0.000
     70 -> 77        0.57474
     71 -> 78        0.16397
     72 -> 77        0.10935
     73 -> 78       -0.17346
     76 -> 81        0.13368

Excited State  13:      Singlet-A      6.1120 eV  202.85 nm  f=0.0085  <S**2>=0.000
     75 -> 79        0.11175
     76 -> 79        0.58618
     76 -> 80        0.25196
     76 -> 82       -0.16906

Excited State  14:      Singlet-A      6.1757 eV  200.76 nm  f=0.0622  <S**2>=0.000
     68 -> 77        0.41532
     72 -> 78       -0.15047
     73 -> 78        0.31066
     76 -> 79       -0.11216
     76 -> 81       -0.30462

Excited State  15:      Singlet-A      6.2503 eV  198.37 nm  f=0.1334  <S**2>=0.000
     69 -> 77        0.15781
     73 -> 78       -0.13290
     75 -> 81        0.41055
     76 -> 81       -0.21372
     76 -> 82        0.12949
     76 -> 85        0.32918
     76 -> 86       -0.10770
SavETr:  write IOETrn=   770 NScale= 10 NData=  16 NLR=1 NState=   15 LETran=    280.
```

4. Crystal Data

4.1. PhPyBBN

Table S 3. Crystal data and structure refinement for PhPyBBN.

Identification code	**PhPyBBN**	
Empirical formula	$C_{23}H_{30}BN$	
Formula weight	331.29	
Temperature	150(2) K	
Wavelength	0.71073 Å	
Crystal system	Monoclinic	
Space group	$P2_1/n$	
Unit cell dimensions	a = 8.7712(4) Å	α= 90°.
	b = 16.1585(5) Å	β= 107.257(4)°.
	c = 13.7772(5) Å	γ= 90°.
Volume	1864.73(13) $Å^3$	
Z	4	
Density (calculated)	1.180 Mg/m^3	
Absorption coefficient	0.066 mm^{-1}	
F(000)	720	
Crystal colour and habit	Colorless prism	
Crystal size	0.195 x 0.112 x 0.086 mm^3	
Theta range for data collection	2.959 to 29.391°.	
Index ranges	-12<=h<=9, -21<=k<=22, -18<=l<=17	
Reflections collected	11259	
Independent reflections	4461 [R(int) = 0.0290]	
Completeness to theta = 25.242°	99.8 %	
Absorption correction	Gaussian	
Max. and min. transmission	1.054 and 0.892	
Refinement method	Full-matrix least-squares on F^2	
Data / restraints / parameters	4461 / 0 / 228	
Goodness-of-fit on F^2	1.073	
Final R indices [I>2sigma(I)]	R1 = 0.0506, wR2 = 0.1087	
R indices (all data)	R1 = 0.0731, wR2 = 0.1196	
Extinction coefficient	n/a	
Largest diff. peak and hole	0.280 and -0.220 $e.Å^{-3}$	

Definitions:

$$R_1 = \frac{\sum \| F_o | - | F_c \|}{\sum | F_o |} \qquad wR_2 = \sqrt{\frac{\sum \left[w\left(F_o^2 - F_c^2 \right)^2 \right]}{\sum \left[w\left(F_o^2 \right)^2 \right]}}$$

$$GooF = \sqrt{\frac{\sum \left[w\left(F_o^2 - F_c^2 \right) \right]}{(n-p)}}$$

n = number of reflections; p = number of parameters

Notes on the refinement of PhPyBBN.

All hydrogen atoms were placed in calculated positions and refined by using a riding model.

Table S 4. Atomic coordinates (x 10^4) and equivalent isotropic displacement parameters ($Å^2$x 10^3) for PhPyBBN. U(eq) is defined as one third of the trace of the orthogonalized U^{ij} tensor.

	x	y	z	U(eq)
C(1)	3304(2)	1293(1)	379(1)	24(1)
C(2)	2158(2)	1722(1)	-344(1)	29(1)
C(3)	1051(2)	2180(1)	-46(1)	28(1)
C(4)	1137(2)	2188(1)	970(1)	23(1)
C(5)	2316(2)	1749(1)	1682(1)	19(1)
C(6)	2341(2)	1718(1)	2762(1)	20(1)
C(7)	1616(2)	2349(1)	3161(1)	24(1)
C(8)	1551(2)	2316(1)	4150(1)	29(1)
C(9)	2226(2)	1651(1)	4761(1)	29(1)
C(10)	2967(2)	1030(1)	4375(1)	26(1)
C(11)	3043(2)	1043(1)	3375(1)	20(1)
C(12)	3907(2)	384(1)	2965(1)	20(1)
C(13)	2853(2)	-382(1)	2520(1)	26(1)
C(14)	2236(2)	-817(1)	3316(2)	38(1)
C(15)	1462(2)	-226(1)	1570(1)	38(1)
C(16)	6123(2)	1531(1)	2803(1)	22(1)
C(17)	6874(2)	1951(1)	2053(1)	27(1)
C(18)	7800(2)	1363(1)	1562(1)	30(1)
C(19)	6937(2)	549(1)	1158(1)	28(1)
C(20)	5913(2)	170(1)	1788(1)	23(1)
C(21)	7033(2)	-265(1)	2735(1)	29(1)
C(22)	8140(2)	328(1)	3504(1)	31(1)
C(23)	7359(2)	1136(1)	3723(1)	28(1)
N(1)	3419(1)	1306(1)	1381(1)	19(1)
B(1)	4855(2)	817(1)	2233(1)	19(1)

Table S 5. Bond lengths [Å] and angles [°] for PhPyBBN.

C(1)-N(1)	1.3539(18)	C(22)-C(23)	1.545(2)
C(1)-C(2)	1.373(2)	C(22)-H(22A)	0.9900
C(1)-H(1)	0.9500	C(22)-H(22B)	0.9900
C(2)-C(3)	1.377(2)	C(23)-H(23A)	0.9900
C(2)-H(2)	0.9500	C(23)-H(23B)	0.9900
C(3)-C(4)	1.379(2)	N(1)-B(1)	1.646(2)
C(3)-H(3)	0.9500	N(1)-C(1)-C(2)	123.25(14)
C(4)-C(5)	1.390(2)	N(1)-C(1)-H(1)	118.4
C(4)-H(4)	0.9500	C(2)-C(1)-H(1)	118.4
C(5)-N(1)	1.3634(18)	C(1)-C(2)-C(3)	118.98(14)
C(5)-C(6)	1.482(2)	C(1)-C(2)-H(2)	120.5
C(6)-C(7)	1.399(2)	C(3)-C(2)-H(2)	120.5
C(6)-C(11)	1.405(2)	C(2)-C(3)-C(4)	118.42(15)
C(7)-C(8)	1.381(2)	C(2)-C(3)-H(3)	120.8
C(7)-H(7)	0.9500	C(4)-C(3)-H(3)	120.8
C(8)-C(9)	1.384(2)	C(3)-C(4)-C(5)	121.13(14)
C(8)-H(8)	0.9500	C(3)-C(4)-H(4)	119.4
C(9)-C(10)	1.385(2)	C(5)-C(4)-H(4)	119.4
C(9)-H(9)	0.9500	N(1)-C(5)-C(4)	119.95(13)
C(10)-C(11)	1.400(2)	N(1)-C(5)-C(6)	119.18(13)
C(10)-H(10)	0.9500	C(4)-C(5)-C(6)	120.79(13)
C(11)-C(12)	1.510(2)	C(7)-C(6)-C(11)	119.98(13)
C(12)-C(13)	1.558(2)	C(7)-C(6)-C(5)	119.81(13)
C(12)-B(1)	1.642(2)	C(11)-C(6)-C(5)	120.17(13)
C(12)-H(12)	1.0000	C(8)-C(7)-C(6)	121.05(15)
C(13)-C(15)	1.523(2)	C(8)-C(7)-H(7)	119.5
C(13)-C(14)	1.529(2)	C(6)-C(7)-H(7)	119.5
C(13)-H(13)	1.0000	C(7)-C(8)-C(9)	119.64(15)
C(14)-H(14A)	0.9800	C(7)-C(8)-H(8)	120.2
C(14)-H(14B)	0.9800	C(9)-C(8)-H(8)	120.2
C(14)-H(14C)	0.9800	C(8)-C(9)-C(10)	119.63(14)
C(15)-H(15A)	0.9800	C(8)-C(9)-H(9)	120.2
C(15)-H(15B)	0.9800	C(10)-C(9)-H(9)	120.2
C(15)-H(15C)	0.9800	C(9)-C(10)-C(11)	122.10(15)
C(16)-C(17)	1.539(2)	C(9)-C(10)-H(10)	119.0
C(16)-C(23)	1.540(2)	C(11)-C(10)-H(10)	119.0
C(16)-B(1)	1.633(2)	C(10)-C(11)-C(6)	117.59(13)
C(16)-H(16)	1.0000	C(10)-C(11)-C(12)	122.24(13)
C(17)-C(18)	1.532(2)	C(6)-C(11)-C(12)	120.11(12)
C(17)-H(17A)	0.9900	C(11)-C(12)-C(13)	113.72(12)
C(17)-H(17B)	0.9900	C(11)-C(12)-B(1)	109.33(11)
C(18)-C(19)	1.537(2)	C(13)-C(12)-B(1)	116.55(12)
C(18)-H(18A)	0.9900	C(11)-C(12)-H(12)	105.4
C(18)-H(18B)	0.9900	C(13)-C(12)-H(12)	105.4
C(19)-C(20)	1.548(2)	B(1)-C(12)-H(12)	105.4
C(19)-H(19A)	0.9900	C(15)-C(13)-C(14)	109.18(14)
C(19)-H(19B)	0.9900	C(15)-C(13)-C(12)	115.91(13)
C(20)-C(21)	1.550(2)	C(14)-C(13)-C(12)	112.22(13)
C(20)-B(1)	1.634(2)	C(15)-C(13)-H(13)	106.3
C(20)-H(20)	1.0000	C(14)-C(13)-H(13)	106.3
C(21)-C(22)	1.540(2)	C(12)-C(13)-H(13)	106.3
C(21)-H(21A)	0.9900	C(13)-C(14)-H(14A)	109.5
C(21)-H(21B)	0.9900	C(13)-C(14)-H(14B)	109.5

H(14A)-C(14)-H(14B)	109.5
C(13)-C(14)-H(14C)	109.5
H(14A)-C(14)-H(14C)	109.5
H(14B)-C(14)-H(14C)	109.5
C(13)-C(15)-H(15A)	109.5
C(13)-C(15)-H(15B)	109.5
H(15A)-C(15)-H(15B)	109.5
C(13)-C(15)-H(15C)	109.5
H(15A)-C(15)-H(15C)	109.5
H(15B)-C(15)-H(15C)	109.5
C(17)-C(16)-C(23)	113.46(13)
C(17)-C(16)-B(1)	110.77(12)
C(23)-C(16)-B(1)	108.43(12)
C(17)-C(16)-H(16)	108.0
C(23)-C(16)-H(16)	108.0
B(1)-C(16)-H(16)	108.0
C(18)-C(17)-C(16)	114.26(13)
C(18)-C(17)-H(17A)	108.7
C(16)-C(17)-H(17A)	108.7
C(18)-C(17)-H(17B)	108.7
C(16)-C(17)-H(17B)	108.7
H(17A)-C(17)-H(17B)	107.6
C(17)-C(18)-C(19)	115.04(13)
C(17)-C(18)-H(18A)	108.5
C(19)-C(18)-H(18A)	108.5
C(17)-C(18)-H(18B)	108.5
C(19)-C(18)-H(18B)	108.5
H(18A)-C(18)-H(18B)	107.5
C(18)-C(19)-C(20)	116.08(12)
C(18)-C(19)-H(19A)	108.3
C(20)-C(19)-H(19A)	108.3
C(18)-C(19)-H(19B)	108.3
C(20)-C(19)-H(19B)	108.3
H(19A)-C(19)-H(19B)	107.4
C(19)-C(20)-C(21)	108.87(12)
C(19)-C(20)-B(1)	116.53(13)
C(21)-C(20)-B(1)	105.23(11)
C(19)-C(20)-H(20)	108.7
C(21)-C(20)-H(20)	108.7
B(1)-C(20)-H(20)	108.7
C(22)-C(21)-C(20)	114.16(13)
C(22)-C(21)-H(21A)	108.7
C(20)-C(21)-H(21A)	108.7
C(22)-C(21)-H(21B)	108.7
C(20)-C(21)-H(21B)	108.7
H(21A)-C(21)-H(21B)	107.6
C(21)-C(22)-C(23)	115.74(13)
C(21)-C(22)-H(22A)	108.3
C(23)-C(22)-H(22A)	108.3
C(21)-C(22)-H(22B)	108.3
C(23)-C(22)-H(22B)	108.3
H(22A)-C(22)-H(22B)	107.4
C(16)-C(23)-C(22)	115.74(12)
C(16)-C(23)-H(23A)	108.3
C(22)-C(23)-H(23A)	108.3
C(16)-C(23)-H(23B)	108.3
C(22)-C(23)-H(23B)	108.3
H(23A)-C(23)-H(23B)	107.4
C(1)-N(1)-C(5)	118.25(13)
C(1)-N(1)-B(1)	122.00(12)
C(5)-N(1)-B(1)	119.75(11)
C(16)-B(1)-C(20)	104.51(12)
C(16)-B(1)-C(12)	113.71(12)
C(20)-B(1)-C(12)	113.93(12)
C(16)-B(1)-N(1)	105.79(11)
C(20)-B(1)-N(1)	116.03(11)
C(12)-B(1)-N(1)	102.90(11)

Table S 6. Anisotropic displacement parameters ($Å^2 x\ 10^3$)for PhPyBBN. The anisotropic displacement factor exponent takes the form: $-2\pi^2[\ h^2 a^{*2} U^{11} + ... + 2\ h\ k\ a^*\ b^*\ U^{12}\ ]$

	U^{11}	U^{22}	U^{33}	U^{23}	U^{13}	U^{12}
C(1)	27(1)	25(1)	21(1)	-2(1)	8(1)	-2(1)
C(2)	34(1)	33(1)	19(1)	4(1)	6(1)	-2(1)
C(3)	28(1)	29(1)	26(1)	9(1)	4(1)	0(1)
C(4)	22(1)	20(1)	28(1)	4(1)	7(1)	0(1)
C(5)	21(1)	15(1)	22(1)	0(1)	6(1)	-4(1)
C(6)	19(1)	19(1)	21(1)	-2(1)	6(1)	-3(1)
C(7)	26(1)	19(1)	28(1)	-1(1)	8(1)	0(1)
C(8)	29(1)	28(1)	32(1)	-9(1)	13(1)	0(1)
C(9)	34(1)	35(1)	22(1)	-2(1)	13(1)	-1(1)
C(10)	28(1)	27(1)	23(1)	3(1)	8(1)	0(1)
C(11)	19(1)	20(1)	22(1)	0(1)	6(1)	-2(1)
C(12)	21(1)	19(1)	21(1)	2(1)	6(1)	3(1)
C(13)	30(1)	17(1)	36(1)	1(1)	14(1)	2(1)
C(14)	45(1)	23(1)	53(1)	5(1)	26(1)	0(1)
C(15)	36(1)	28(1)	44(1)	-3(1)	5(1)	-12(1)
C(16)	20(1)	25(1)	21(1)	-4(1)	6(1)	-1(1)
C(17)	26(1)	28(1)	28(1)	-3(1)	8(1)	-8(1)
C(18)	26(1)	39(1)	27(1)	0(1)	11(1)	-5(1)
C(19)	25(1)	37(1)	24(1)	-5(1)	9(1)	2(1)
C(20)	21(1)	25(1)	23(1)	-5(1)	6(1)	-1(1)
C(21)	26(1)	29(1)	31(1)	0(1)	9(1)	9(1)
C(22)	24(1)	41(1)	26(1)	3(1)	4(1)	6(1)
C(23)	24(1)	36(1)	21(1)	-4(1)	3(1)	-2(1)
N(1)	20(1)	18(1)	18(1)	-1(1)	4(1)	-3(1)
B(1)	20(1)	21(1)	16(1)	0(1)	4(1)	1(1)

Table S 7. Hydrogen coordinates (x 10^4) and isotropic displacement parameters ($Å^2$x 10^3) for PhPyBBN.

	x	y	z	U(eq)
H(1)	4052	972	165	29
H(2)	2131	1703	-1038	35
H(3)	246	2483	-529	34
H(4)	379	2499	1187	28
H(7)	1159	2809	2745	29
H(8)	1048	2747	4410	34
H(9)	2180	1622	5440	35
H(10)	3439	580	4804	31
H(12)	4761	172	3568	24
H(13)	3568	-787	2321	32
H(14A)	1683	-1328	3027	57
H(14B)	1492	-451	3518	57
H(14C)	3136	-950	3912	57
H(15A)	1872	-48	1015	57
H(15B)	772	207	1709	57
H(15C)	845	-737	1374	57
H(16)	5525	1961	3064	26
H(17A)	6017	2219	1509	33
H(17B)	7607	2392	2417	33
H(18A)	8832	1228	2070	36
H(18B)	8037	1655	992	36
H(19A)	7749	136	1115	34
H(19B)	6237	646	458	34
H(20)	5181	-253	1362	28
H(21A)	6372	-574	3083	34
H(21B)	7698	-672	2508	34
H(22A)	9046	477	3248	37
H(22B)	8582	28	4153	37
H(23A)	6831	1020	4251	33
H(23B)	8214	1546	4008	33

4.1. $PhPyBH_2$

Table S 8. Crystal data and structure refinement for $PhPyBH_2$.

Identification code	**$PhPyBH_2$**	
Empirical formula	$C_{15}H_{18}BN$	
Formula weight	223.11	
Temperature	150(2) K	
Wavelength	0.71073 Å	
Crystal system	Monoclinic	
Space group	$P2_1/c$	
Unit cell dimensions	a = 10.1144(4) Å	α= 90°.
	b = 7.8288(3) Å	β= 96.949(4)°.
	c = 16.3506(7) Å	γ= 90°.
Volume	1285.19(9) $Å^3$	
Z	4	
Density (calculated)	1.153 Mg/m^3	
Absorption coefficient	0.065 mm^{-1}	
F(000)	480	
Crystal colour and habit	Colorless prism	
Crystal size	0.245 x 0.220 x 0.132 mm^3	
Theta range for data collection	2.889 to 29.299°.	
Index ranges	-10<=h<=13, -10<=k<=10, -22<=l<=21	
Reflections collected	7368	
Independent reflections	3091 [R(int) = 0.0235]	
Completeness to theta = 25.242°	99.9 %	
Absorption correction	Semi-empirical from equivalents	
Max. and min. transmission	1.00000 and 0.82897	
Refinement method	Full-matrix least-squares on F^2	
Data / restraints / parameters	3091 / 0 / 164	
Goodness-of-fit on F^2	1.087	
Final R indices [I>2sigma(I)]	R1 = 0.0485, wR2 = 0.1095	
R indices (all data)	R1 = 0.0629, wR2 = 0.1187	
Extinction coefficient	n/a	
Largest diff. peak and hole	0.218 and -0.202 e.$Å^{-3}$	

Definitions:

$$R_1 = \frac{\sum \| F_o | - | F_c \|}{\sum | F_o |} \qquad wR_2 = \sqrt{\frac{\sum \left[w\left(F_o^2 - F_c^2 \right)^2 \right]}{\sum \left[w\left(F_o^2 \right)^2 \right]}}$$

$$GooF = \sqrt{\frac{\sum \left[w\left(F_o^2 - F_c^2 \right) \right]}{(n-p)}}$$

n = number of reflections; p = number of parameters

Notes on the refinement of $PhPyBH_2$.

The hydrogen atoms H1A and H1B, which are bound to B1, were observed clearly in the following difference Fourier synthesis, and then were allowed to be refined freely. All the other hydrogen atoms were placed in calculated positions and refined by using a riding model.

Table S 9. Atomic coordinates (x 10^4) and equivalent isotropic displacement parameters ($Å^2$x 10^3) for $PhPyBH_2$. U(eq) is defined as one third of the trace of the orthogonalized U^{ij} tensor.

	x	y	z	U(eq)
C(1)	8501(2)	6960(2)	5418(1)	38(1)
C(2)	8078(2)	8621(2)	5317(1)	43(1)
C(3)	6844(2)	9058(2)	5523(1)	42(1)
C(4)	6067(2)	7814(2)	5820(1)	34(1)
C(5)	6512(1)	6133(2)	5899(1)	26(1)
C(6)	5711(1)	4755(2)	6206(1)	25(1)
C(7)	4321(1)	4907(2)	6121(1)	32(1)
C(8)	3548(2)	3665(2)	6425(1)	39(1)
C(9)	4152(2)	2250(2)	6813(1)	41(1)
C(10)	5520(2)	2069(2)	6888(1)	35(1)
C(11)	6331(1)	3301(2)	6589(1)	26(1)
C(12)	7828(1)	3120(2)	6656(1)	28(1)
C(13)	8522(1)	4012(2)	7440(1)	28(1)
C(14)	8067(2)	3324(2)	8232(1)	36(1)
C(15)	10034(2)	3866(2)	7499(1)	41(1)
N(1)	7740(1)	5733(2)	5699(1)	29(1)
B(1)	8266(2)	3796(2)	5796(1)	36(1)

Table S 10. Bond lengths [Å] and angles [°] for $PhPyBH_2$.

C(1)-N(1)	1.3461(18)
C(1)-C(2)	1.372(2)
C(1)-H(1)	0.9500
C(2)-C(3)	1.375(2)
C(2)-H(2)	0.9500
C(3)-C(4)	1.375(2)
C(3)-H(3)	0.9500
C(4)-C(5)	1.3920(19)
C(4)-H(4)	0.9500
C(5)-N(1)	1.3580(17)
C(5)-C(6)	1.4738(18)
C(6)-C(7)	1.4005(19)
C(6)-C(11)	1.4094(19)
C(7)-C(8)	1.377(2)
C(7)-H(7)	0.9500
C(8)-C(9)	1.383(2)
C(8)-H(8)	0.9500
C(9)-C(10)	1.381(2)
C(9)-H(9)	0.9500
C(10)-C(11)	1.3933(19)
C(10)-H(10)	0.9500
C(11)-C(12)	1.5108(18)
C(12)-C(13)	1.5512(19)
C(12)-B(1)	1.614(2)
C(12)-H(12)	1.0000
C(13)-C(14)	1.5249(19)
C(13)-C(15)	1.525(2)
C(13)-H(13)	1.0000
C(14)-H(14A)	0.9800
C(14)-H(14B)	0.9800
C(14)-H(14C)	0.9800
C(15)-H(15A)	0.9800
C(15)-H(15B)	0.9800
C(15)-H(15C)	0.9800
N(1)-B(1)	1.609(2)
B(1)-H(1A)	1.160(16)
B(1)-H(1B)	1.151(16)
N(1)-C(1)-C(2)	122.31(15)
N(1)-C(1)-H(1)	118.8
C(2)-C(1)-H(1)	118.8
C(1)-C(2)-C(3)	119.02(14)
C(1)-C(2)-H(2)	120.5
C(3)-C(2)-H(2)	120.5
C(2)-C(3)-C(4)	118.96(15)
C(2)-C(3)-H(3)	120.5
C(4)-C(3)-H(3)	120.5
C(3)-C(4)-C(5)	120.68(14)
C(3)-C(4)-H(4)	119.7
C(5)-C(4)-H(4)	119.7
N(1)-C(5)-C(4)	119.36(13)
N(1)-C(5)-C(6)	118.03(12)
C(4)-C(5)-C(6)	122.60(12)
C(7)-C(6)-C(11)	120.03(12)
C(7)-C(6)-C(5)	119.41(12)
C(11)-C(6)-C(5)	120.56(12)
C(8)-C(7)-C(6)	120.72(14)
C(8)-C(7)-H(7)	119.6
C(6)-C(7)-H(7)	119.6
C(7)-C(8)-C(9)	119.55(14)
C(7)-C(8)-H(8)	120.2
C(9)-C(8)-H(8)	120.2
C(10)-C(9)-C(8)	120.32(14)
C(10)-C(9)-H(9)	119.8
C(8)-C(9)-H(9)	119.8
C(9)-C(10)-C(11)	121.64(15)
C(9)-C(10)-H(10)	119.2
C(11)-C(10)-H(10)	119.2
C(10)-C(11)-C(6)	117.72(13)
C(10)-C(11)-C(12)	122.49(13)
C(6)-C(11)-C(12)	119.79(12)
C(11)-C(12)-C(13)	111.54(11)
C(11)-C(12)-B(1)	106.48(11)
C(13)-C(12)-B(1)	115.35(12)
C(11)-C(12)-H(12)	107.7
C(13)-C(12)-H(12)	107.7
B(1)-C(12)-H(12)	107.7
C(14)-C(13)-C(15)	108.88(12)
C(14)-C(13)-C(12)	112.95(11)
C(15)-C(13)-C(12)	111.63(12)
C(14)-C(13)-H(13)	107.7
C(15)-C(13)-H(13)	107.7
C(12)-C(13)-H(13)	107.7
C(13)-C(14)-H(14A)	109.5
C(13)-C(14)-H(14B)	109.5
H(14A)-C(14)-H(14B)	109.5
C(13)-C(14)-H(14C)	109.5
H(14A)-C(14)-H(14C)	109.5
H(14B)-C(14)-H(14C)	109.5
C(13)-C(15)-H(15A)	109.5
C(13)-C(15)-H(15B)	109.5
H(15A)-C(15)-H(15B)	109.5
C(13)-C(15)-H(15C)	109.5
H(15A)-C(15)-H(15C)	109.5
H(15B)-C(15)-H(15C)	109.5
C(1)-N(1)-C(5)	119.65(13)
C(1)-N(1)-B(1)	120.70(12)
C(5)-N(1)-B(1)	119.64(11)
N(1)-B(1)-C(12)	105.83(11)
N(1)-B(1)-H(1A)	105.5(8)
C(12)-B(1)-H(1A)	111.9(8)
N(1)-B(1)-H(1B)	105.8(8)
C(12)-B(1)-H(1B)	116.0(8)
H(1A)-B(1)-H(1B)	110.9(11)

Table S 11. Anisotropic displacement parameters ($Å^2 x\ 10^3$)for $PhPyBH_2$. The anisotropic displacement factor exponent takes the form: $-2\pi^2[\ h^2 a^{*2} U^{11} + ... + 2\ h\ k\ a^*\ b^*\ U^{12}\ ]$

	U^{11}	U^{22}	U^{33}	U^{23}	U^{13}	U^{12}
C(1)	39(1)	47(1)	28(1)	5(1)	7(1)	-9(1)
C(2)	59(1)	40(1)	29(1)	6(1)	3(1)	-20(1)
C(3)	64(1)	27(1)	32(1)	2(1)	-1(1)	-4(1)
C(4)	44(1)	28(1)	29(1)	-1(1)	3(1)	3(1)
C(5)	31(1)	27(1)	19(1)	-2(1)	2(1)	0(1)
C(6)	29(1)	26(1)	20(1)	-4(1)	4(1)	-1(1)
C(7)	30(1)	38(1)	27(1)	-8(1)	2(1)	2(1)
C(8)	28(1)	55(1)	34(1)	-14(1)	6(1)	-9(1)
C(9)	43(1)	47(1)	35(1)	-5(1)	10(1)	-21(1)
C(10)	46(1)	30(1)	28(1)	1(1)	5(1)	-9(1)
C(11)	33(1)	25(1)	21(1)	-4(1)	4(1)	-2(1)
C(12)	33(1)	23(1)	28(1)	0(1)	5(1)	5(1)
C(13)	30(1)	23(1)	32(1)	2(1)	4(1)	1(1)
C(14)	43(1)	36(1)	29(1)	0(1)	1(1)	-2(1)
C(15)	31(1)	36(1)	54(1)	3(1)	1(1)	0(1)
N(1)	32(1)	33(1)	22(1)	2(1)	7(1)	-2(1)
B(1)	38(1)	38(1)	34(1)	3(1)	13(1)	11(1)

Table S 12. Hydrogen coordinates (x 10^4) and isotropic displacement parameters ($Å^2 x\ 10^3$) for $PhPyBH_2$.

	x	y	z	U(eq)
H(1)	9362	6667	5286	45
H(2)	8629	9456	5107	52
H(3)	6532	10201	5462	50
H(4)	5219	8105	5972	41
H(7)	3907	5878	5851	38
H(8)	2607	3781	6368	47
H(9)	3624	1397	7030	50
H(10)	5917	1081	7151	42
H(12)	8043	1874	6702	33
H(13)	8288	5253	7401	34
H(14A)	7099	3446	8208	54
H(14B)	8502	3968	8704	54
H(14C)	8307	2114	8295	54
H(15A)	10289	2658	7498	61
H(15B)	10438	4404	8010	61
H(15C)	10348	4443	7026	61
H(1A)	7723(15)	3070(20)	5235(10)	39(4)
H(1B)	9394(16)	3860(20)	5759(10)	44(5)

4.2. $PhPyBCl_2$

Table S 13. Crystal data and structure refinement for $PhPyBCl_2$.

Identification code	**$PhPyBCl_2$**	
Empirical formula	$C_{15}H_{16}BCl_2N$	
Formula weight	292.00	
Temperature	150(2) K	
Wavelength	0.71073 Å	
Crystal system	Monoclinic	
Space group	$P2_1/c$	
Unit cell dimensions	a = 13.1705(6) Å	α= 90°.
	b = 10.7108(5) Å	β= 94.122(4)°.
	c = 10.3692(5) Å	γ= 90°.
Volume	1458.96(12) $Å^3$	
Z	4	
Density (calculated)	1.329 Mg/m^3	
Absorption coefficient	0.429 mm^{-1}	
F(000)	608	
Crystal colour and habit	Colorless prism	
Crystal size	0.196 x 0.160 x 0.076 mm^3	
Theta range for data collection	3.076 to 29.280°.	
Index ranges	-16<=h<=18, -13<=k<=10, -14<=l<=12	
Reflections collected	8360	
Independent reflections	3420 [R(int) = 0.0456]	
Completeness to theta = 25.242°	99.9 %	
Absorption correction	Semi-empirical from equivalents	
Max. and min. transmission	1.00000 and 0.66243	
Refinement method	Full-matrix least-squares on F^2	
Data / restraints / parameters	3420 / 0 / 174	
Goodness-of-fit on F^2	1.070	
Final R indices [I>2sigma(I)]	R1 = 0.0580, wR2 = 0.1409	
R indices (all data)	R1 = 0.0837, wR2 = 0.1557	
Extinction coefficient	n/a	
Largest diff. peak and hole	0.826 and -0.324 e.$Å^{-3}$	

Definitions:

$$R_1 = \frac{\sum \left| |F_o| - |F_c| \right|}{\sum |F_o|} \qquad wR_2 = \sqrt{\frac{\sum \left[w\left(F_o^2 - F_c^2\right)^2 \right]}{\sum \left[w\left(F_o^2\right)^2 \right]}}$$

$$GooF = \sqrt{\frac{\sum \left[w\left(F_o^2 - F_c^2\right) \right]}{(n-p)}}$$

n = number of reflections; p = number of parameters

Notes on the refinement of $PhPyBCl_2$.

All hydrogen atoms were placed in calculated positions and refined by using a riding model.

Table S 14. Atomic coordinates (x 10^4) and equivalent isotropic displacement parameters ($Å^2$x 10^3) for $PhPyBCl_2$. U(eq) is defined as one third of the trace of the orthogonalized U^{ij} tensor.

	x	y	z	U(eq)
C(1)	3126(2)	4344(3)	-1412(3)	33(1)
C(2)	2953(3)	5110(3)	-2460(3)	43(1)
C(3)	2275(3)	6081(3)	-2388(3)	45(1)
C(4)	1787(3)	6250(3)	-1267(3)	36(1)
C(5)	1965(2)	5447(2)	-220(2)	24(1)
C(6)	1420(2)	5581(2)	976(2)	23(1)
C(7)	502(2)	6240(3)	928(3)	32(1)
C(8)	-37(2)	6361(3)	2015(3)	35(1)
C(9)	322(2)	5800(3)	3157(3)	35(1)
C(10)	1227(2)	5142(3)	3221(3)	29(1)
C(11)	1804(2)	5028(2)	2141(2)	22(1)
C(12)	2782(2)	4300(2)	2212(2)	24(1)
C(13)	3732(2)	5090(3)	2672(3)	30(1)
C(14)	3629(3)	5624(3)	4030(3)	41(1)
C(15)	3984(2)	6141(3)	1743(3)	36(1)
N(1)	2652(2)	4507(2)	-308(2)	23(1)
B(1)	2859(2)	3575(3)	882(3)	24(1)
Cl(1)	1819(1)	2367(1)	642(1)	30(1)
Cl(2)	4098(1)	2774(1)	768(1)	37(1)

Table S 15. Bond lengths [Å] and angles [°] for PhPyBCl$_2$.

C(1)-N(1)	1.354(3)
C(1)-C(2)	1.368(4)
C(1)-H(1)	0.9500
C(2)-C(3)	1.376(5)
C(2)-H(2)	0.9500
C(3)-C(4)	1.380(4)
C(3)-H(3)	0.9500
C(4)-C(5)	1.392(4)
C(4)-H(4)	0.9500
C(5)-N(1)	1.361(3)
C(5)-C(6)	1.483(4)
C(6)-C(7)	1.399(4)
C(6)-C(11)	1.406(4)
C(7)-C(8)	1.380(4)
C(7)-H(7)	0.9500
C(8)-C(9)	1.381(4)
C(8)-H(8)	0.9500
C(9)-C(10)	1.382(4)
C(9)-H(9)	0.9500
C(10)-C(11)	1.404(4)
C(10)-H(10)	0.9500
C(11)-C(12)	1.503(4)
C(12)-C(13)	1.556(4)
C(12)-B(1)	1.592(4)
C(12)-H(12)	1.0000
C(13)-C(15)	1.534(4)
C(13)-C(14)	1.536(4)
C(13)-H(13)	1.0000
C(14)-H(14A)	0.9800
C(14)-H(14B)	0.9800
C(14)-H(14C)	0.9800
C(15)-H(15A)	0.9800
C(15)-H(15B)	0.9800
C(15)-H(15C)	0.9800
N(1)-B(1)	1.596(4)
B(1)-Cl(2)	1.855(3)
B(1)-Cl(1)	1.888(3)
N(1)-C(1)-C(2)	122.2(3)
N(1)-C(1)-H(1)	118.9
C(2)-C(1)-H(1)	118.9
C(1)-C(2)-C(3)	118.8(3)
C(1)-C(2)-H(2)	120.6
C(3)-C(2)-H(2)	120.6
C(2)-C(3)-C(4)	119.2(3)
C(2)-C(3)-H(3)	120.4
C(4)-C(3)-H(3)	120.4
C(3)-C(4)-C(5)	120.9(3)
C(3)-C(4)-H(4)	119.6
C(5)-C(4)-H(4)	119.6
N(1)-C(5)-C(4)	118.7(2)
N(1)-C(5)-C(6)	119.5(2)
C(4)-C(5)-C(6)	121.9(3)
C(7)-C(6)-C(11)	120.0(2)
C(7)-C(6)-C(5)	119.2(2)
C(11)-C(6)-C(5)	120.8(2)
C(8)-C(7)-C(6)	120.8(3)
C(8)-C(7)-H(7)	119.6
C(6)-C(7)-H(7)	119.6
C(7)-C(8)-C(9)	119.7(3)
C(7)-C(8)-H(8)	120.2
C(9)-C(8)-H(8)	120.2
C(8)-C(9)-C(10)	120.2(3)
C(8)-C(9)-H(9)	119.9
C(10)-C(9)-H(9)	119.9
C(9)-C(10)-C(11)	121.4(3)
C(9)-C(10)-H(10)	119.3
C(11)-C(10)-H(10)	119.3
C(10)-C(11)-C(6)	117.8(2)
C(10)-C(11)-C(12)	121.2(2)
C(6)-C(11)-C(12)	121.0(2)
C(11)-C(12)-C(13)	113.6(2)
C(11)-C(12)-B(1)	108.5(2)
C(13)-C(12)-B(1)	115.5(2)
C(11)-C(12)-H(12)	106.2
C(13)-C(12)-H(12)	106.2
B(1)-C(12)-H(12)	106.2
C(15)-C(13)-C(14)	109.9(2)
C(15)-C(13)-C(12)	114.4(2)
C(14)-C(13)-C(12)	111.2(2)
C(15)-C(13)-H(13)	107.0
C(14)-C(13)-H(13)	107.0
C(12)-C(13)-H(13)	107.0
C(13)-C(14)-H(14A)	109.5
C(13)-C(14)-H(14B)	109.5
H(14A)-C(14)-H(14B)	109.5
C(13)-C(14)-H(14C)	109.5
H(14A)-C(14)-H(14C)	109.5
H(14B)-C(14)-H(14C)	109.5
C(13)-C(15)-H(15A)	109.5
C(13)-C(15)-H(15B)	109.5
H(15A)-C(15)-H(15B)	109.5
C(13)-C(15)-H(15C)	109.5
H(15A)-C(15)-H(15C)	109.5
H(15B)-C(15)-H(15C)	109.5
C(1)-N(1)-C(5)	120.1(2)
C(1)-N(1)-B(1)	120.6(2)
C(5)-N(1)-B(1)	119.2(2)
C(12)-B(1)-N(1)	110.3(2)
C(12)-B(1)-Cl(2)	113.0(2)
N(1)-B(1)-Cl(2)	110.04(17)
C(12)-B(1)-Cl(1)	110.98(18)
N(1)-B(1)-Cl(1)	104.19(18)
Cl(2)-B(1)-Cl(1)	107.96(15)

Table S 16. Anisotropic displacement parameters ($Å^2 x\ 10^3$)for $PhPyBCl_2$. The anisotropic displacement factor exponent takes the form: $-2\pi^2[\ h^2 a^{*2} U^{11} + ... + 2\ h\ k\ a^*\ b^*\ U^{12}\ ]$

	U^{11}	U^{22}	U^{33}	U^{23}	U^{13}	U^{12}
C(1)	42(2)	32(2)	25(1)	-4(1)	9(1)	-5(1)
C(2)	63(2)	44(2)	23(1)	1(1)	10(1)	-10(2)
C(3)	71(3)	36(2)	27(2)	12(1)	-1(2)	-13(2)
C(4)	51(2)	25(1)	31(2)	7(1)	-5(1)	-1(1)
C(5)	29(2)	21(1)	23(1)	1(1)	-3(1)	-3(1)
C(6)	24(1)	16(1)	29(1)	-1(1)	1(1)	-1(1)
C(7)	30(2)	27(2)	37(2)	-3(1)	-6(1)	4(1)
C(8)	23(2)	31(2)	52(2)	-9(1)	1(1)	5(1)
C(9)	32(2)	33(2)	41(2)	-9(1)	11(1)	-1(1)
C(10)	35(2)	28(1)	27(1)	-2(1)	10(1)	0(1)
C(11)	23(1)	18(1)	25(1)	-2(1)	2(1)	-2(1)
C(12)	24(1)	25(1)	22(1)	5(1)	2(1)	2(1)
C(13)	27(2)	37(2)	26(1)	0(1)	0(1)	-1(1)
C(14)	45(2)	50(2)	27(2)	-3(1)	0(1)	-12(2)
C(15)	37(2)	43(2)	30(2)	-1(1)	4(1)	-14(1)
N(1)	28(1)	22(1)	20(1)	0(1)	2(1)	-3(1)
B(1)	23(2)	23(1)	26(2)	4(1)	5(1)	5(1)
Cl(1)	34(1)	21(1)	33(1)	2(1)	4(1)	-2(1)
Cl(2)	30(1)	41(1)	40(1)	2(1)	9(1)	13(1)

Table S 17. Hydrogen coordinates ($x\ 10^4$) and isotropic displacement parameters ($Å^2 x\ 10^3$) for $PhPyBCl_2$.

	x	y	z	U(eq)
H(1)	3594	3674	-1460	39
H(2)	3294	4975	-3224	52
H(3)	2144	6628	-3101	54
H(4)	1323	6924	-1209	43
H(7)	245	6609	138	38
H(8)	-652	6827	1977	42
H(9)	-54	5867	3902	42
H(10)	1463	4758	4012	35
H(12)	2714	3644	2887	28
H(13)	4328	4510	2735	36
H(14A)	4278	5996	4354	61
H(14B)	3446	4953	4613	61
H(14C)	3096	6265	3991	61
H(15A)	4552	6637	2131	55
H(15B)	3387	6677	1576	55
H(15C)	4176	5779	927	55

4.3. PhPyBPF

Table S 18. Crystal data and structure refinement for PhPyBPF.

Identification code	**PhPyBPF**	
Empirical formula	$C_{27}H_{16}BF_{10}N$	
Formula weight	555.22	
Temperature	150(2) K	
Wavelength	0.71073 Å	
Crystal system	Monoclinic	
Space group	$P2_1/c$	
Unit cell dimensions	a = 10.9500(2) Å	α= 90°.
	b = 11.9877(3) Å	β= 91.325(2)°.
	c = 17.6453(4) Å	γ= 90°.
Volume	2315.60(9) $Å^3$	
Z	4	
Density (calculated)	1.593 Mg/m^3	
Absorption coefficient	0.149 mm^{-1}	
F(000)	1120	
Crystal colour and habit	Colorless prism	
Crystal size	0.194 x 0.179 x 0.089 mm^3	
Theta range for data collection	2.867 to 29.463°.	
Index ranges	-11<=h<=14, -11<=k<=16, -22<=l<=24	
Reflections collected	15037	
Independent reflections	5549 [R(int) = 0.0237]	
Completeness to theta = 25.242°	99.9 %	
Absorption correction	Semi-empirical from equivalents	
Max. and min. transmission	1.00000 and 0.93963	
Refinement method	Full-matrix least-squares on F^2	
Data / restraints / parameters	5549 / 0 / 354	
Goodness-of-fit on F^2	1.033	
Final R indices [I>2sigma(I)]	R1 = 0.0408, wR2 = 0.0880	
R indices (all data)	R1 = 0.0554, wR2 = 0.0966	
Extinction coefficient	n/a	
Largest diff. peak and hole	0.279 and -0.235 $e.Å^{-3}$	

Definitions:

$$R_1 = \frac{\sum \left| |F_o| - |F_c| \right|}{\sum |F_o|} \qquad wR_2 = \sqrt{\frac{\sum \left[w\left(F_o^2 - F_c^2\right)^2 \right]}{\sum \left[w\left(F_o^2\right)^2 \right]}}$$

$$GooF = \sqrt{\frac{\sum \left[w\left(F_o^2 - F_c^2\right) \right]}{(n-p)}}$$

n = number of reflections; p = number of parameters

Notes on the refinement of PhPyBPF.

All hydrogen atoms were placed in calculated positions and refined by using a riding model.

Table S 19. Atomic coordinates (x 10^4) and equivalent isotropic displacement parameters ($Å^2$x 10^3) for PhPyBPF. U(eq) is defined as one third of the trace of the orthogonalized U^{ij} tensor.

	x	y	z	U(eq)
C(1)	3306(1)	-577(1)	8402(1)	26(1)
C(2)	3736(2)	-1144(2)	9035(1)	33(1)
C(3)	3455(2)	-735(2)	9740(1)	38(1)
C(4)	2796(2)	238(2)	9789(1)	33(1)
C(5)	2394(1)	799(1)	9139(1)	25(1)
C(6)	1783(1)	1889(1)	9179(1)	24(1)
C(7)	1069(2)	2161(2)	9799(1)	31(1)
C(8)	531(2)	3198(2)	9847(1)	34(1)
C(9)	707(2)	3977(2)	9282(1)	32(1)
C(10)	1409(2)	3712(1)	8662(1)	27(1)
C(11)	1957(1)	2670(1)	8597(1)	22(1)
C(12)	2663(1)	2331(1)	7904(1)	22(1)
C(13)	4066(1)	2575(1)	8002(1)	27(1)
C(14)	4276(2)	3839(2)	8008(1)	37(1)
C(15)	4727(2)	2069(2)	8694(1)	32(1)
C(16)	675(1)	1088(1)	7636(1)	20(1)
C(17)	144(1)	1729(1)	7059(1)	21(1)
C(18)	-1094(1)	1844(1)	6927(1)	25(1)
C(19)	-1890(1)	1332(1)	7405(1)	28(1)
C(20)	-1428(1)	677(1)	7982(1)	28(1)
C(21)	-178(1)	553(1)	8079(1)	24(1)
C(22)	2611(1)	479(1)	6907(1)	22(1)
C(23)	3204(1)	996(1)	6313(1)	24(1)
C(24)	3414(2)	488(2)	5624(1)	30(1)
C(25)	3028(2)	-587(2)	5493(1)	32(1)
C(26)	2417(1)	-1139(1)	6053(1)	28(1)
C(27)	2206(1)	-590(1)	6726(1)	24(1)
N(1)	2631(1)	358(1)	8443(1)	22(1)
B(1)	2186(2)	1071(2)	7703(1)	21(1)
F(17)	865(1)	2297(1)	6579(1)	28(1)
F(18)	-1522(1)	2470(1)	6349(1)	36(1)
F(19)	-3103(1)	1474(1)	7310(1)	44(1)
F(20)	-2199(1)	154(1)	8449(1)	43(1)
F(21)	183(1)	-139(1)	8646(1)	34(1)
F(23)	3582(1)	2067(1)	6367(1)	32(1)
F(24)	3992(1)	1047(1)	5078(1)	43(1)
F(25)	3230(1)	-1088(1)	4829(1)	47(1)
F(26)	2042(1)	-2192(1)	5943(1)	38(1)
F(27)	1554(1)	-1164(1)	7240(1)	30(1)

Table S 20. Bond lengths [Å] and angles [°] for PhPyBPF.

C(1)-N(1)	1.345(2)	C(25)-F(25)	1.3392(18)
C(1)-C(2)	1.381(2)	C(25)-C(26)	1.375(2)
C(1)-H(1)	0.9500	C(26)-F(26)	1.3405(19)
C(2)-C(3)	1.378(3)	C(26)-C(27)	1.381(2)
C(2)-H(2)	0.9500	C(27)-F(27)	1.3548(17)
C(3)-C(4)	1.376(3)	N(1)-B(1)	1.627(2)
C(3)-H(3)	0.9500	N(1)-C(1)-C(2)	122.93(15)
C(4)-C(5)	1.392(2)	N(1)-C(1)-H(1)	118.5
C(4)-H(4)	0.9500	C(2)-C(1)-H(1)	118.5
C(5)-N(1)	1.3663(19)	C(3)-C(2)-C(1)	118.40(17)
C(5)-C(6)	1.471(2)	C(3)-C(2)-H(2)	120.8
C(6)-C(7)	1.399(2)	C(1)-C(2)-H(2)	120.8
C(6)-C(11)	1.406(2)	C(4)-C(3)-C(2)	119.16(15)
C(7)-C(8)	1.379(3)	C(4)-C(3)-H(3)	120.4
C(7)-H(7)	0.9500	C(2)-C(3)-H(3)	120.4
C(8)-C(9)	1.383(2)	C(3)-C(4)-C(5)	120.87(16)
C(8)-H(8)	0.9500	C(3)-C(4)-H(4)	119.6
C(9)-C(10)	1.388(2)	C(5)-C(4)-H(4)	119.6
C(9)-H(9)	0.9500	N(1)-C(5)-C(4)	119.39(15)
C(10)-C(11)	1.392(2)	N(1)-C(5)-C(6)	118.86(13)
C(10)-H(10)	0.9500	C(4)-C(5)-C(6)	121.65(14)
C(11)-C(12)	1.516(2)	C(7)-C(6)-C(11)	120.27(15)
C(12)-C(13)	1.569(2)	C(7)-C(6)-C(5)	120.51(14)
C(12)-B(1)	1.635(2)	C(11)-C(6)-C(5)	119.19(13)
C(12)-H(12)	1.0000	C(8)-C(7)-C(6)	120.32(15)
C(13)-C(15)	1.530(2)	C(8)-C(7)-H(7)	119.8
C(13)-C(14)	1.532(2)	C(6)-C(7)-H(7)	119.8
C(13)-H(13)	1.0000	C(7)-C(8)-C(9)	119.91(15)
C(14)-H(14A)	0.9800	C(7)-C(8)-H(8)	120.0
C(14)-H(14B)	0.9800	C(9)-C(8)-H(8)	120.0
C(14)-H(14C)	0.9800	C(8)-C(9)-C(10)	120.12(16)
C(15)-H(15A)	0.9800	C(8)-C(9)-H(9)	119.9
C(15)-H(15B)	0.9800	C(10)-C(9)-H(9)	119.9
C(15)-H(15C)	0.9800	C(9)-C(10)-C(11)	121.26(15)
C(16)-C(21)	1.388(2)	C(9)-C(10)-H(10)	119.4
C(16)-C(17)	1.393(2)	C(11)-C(10)-H(10)	119.4
C(16)-B(1)	1.656(2)	C(10)-C(11)-C(6)	118.11(14)
C(17)-F(17)	1.3555(17)	C(10)-C(11)-C(12)	122.44(13)
C(17)-C(18)	1.377(2)	C(6)-C(11)-C(12)	119.35(14)
C(18)-F(18)	1.3422(17)	C(11)-C(12)-C(13)	112.17(12)
C(18)-C(19)	1.372(2)	C(11)-C(12)-B(1)	104.88(12)
C(19)-F(19)	1.3454(18)	C(13)-C(12)-B(1)	120.19(13)
C(19)-C(20)	1.373(2)	C(11)-C(12)-H(12)	106.2
C(20)-F(20)	1.3474(18)	C(13)-C(12)-H(12)	106.2
C(20)-C(21)	1.384(2)	B(1)-C(12)-H(12)	106.2
C(21)-F(21)	1.3526(18)	C(15)-C(13)-C(14)	108.59(14)
C(22)-C(27)	1.392(2)	C(15)-C(13)-C(12)	117.25(13)
C(22)-C(23)	1.392(2)	C(14)-C(13)-C(12)	109.35(13)
C(22)-B(1)	1.649(2)	C(15)-C(13)-H(13)	107.1
C(23)-F(23)	1.3519(19)	C(14)-C(13)-H(13)	107.1
C(23)-C(24)	1.384(2)	C(12)-C(13)-H(13)	107.1
C(24)-F(24)	1.3439(19)	C(13)-C(14)-H(14A)	109.5
C(24)-C(25)	1.374(3)	C(13)-C(14)-H(14B)	109.5

H(14A)-C(14)-H(14B)	109.5
C(13)-C(14)-H(14C)	109.5
H(14A)-C(14)-H(14C)	109.5
H(14B)-C(14)-H(14C)	109.5
C(13)-C(15)-H(15A)	109.5
C(13)-C(15)-H(15B)	109.5
H(15A)-C(15)-H(15B)	109.5
C(13)-C(15)-H(15C)	109.5
H(15A)-C(15)-H(15C)	109.5
H(15B)-C(15)-H(15C)	109.5
C(21)-C(16)-C(17)	113.04(13)
C(21)-C(16)-B(1)	129.64(13)
C(17)-C(16)-B(1)	117.32(12)
F(17)-C(17)-C(18)	115.52(13)
F(17)-C(17)-C(16)	119.64(13)
C(18)-C(17)-C(16)	124.84(14)
F(18)-C(18)-C(19)	120.14(14)
F(18)-C(18)-C(17)	120.57(14)
C(19)-C(18)-C(17)	119.28(14)
F(19)-C(19)-C(18)	120.33(15)
F(19)-C(19)-C(20)	120.78(15)
C(18)-C(19)-C(20)	118.88(14)
F(20)-C(20)-C(19)	119.57(14)
F(20)-C(20)-C(21)	120.45(15)
C(19)-C(20)-C(21)	119.97(14)
F(21)-C(21)-C(20)	115.37(13)
F(21)-C(21)-C(16)	120.75(13)
C(20)-C(21)-C(16)	123.89(15)
C(27)-C(22)-C(23)	112.83(13)
C(27)-C(22)-B(1)	119.87(13)
C(23)-C(22)-B(1)	126.57(14)
F(23)-C(23)-C(24)	115.03(14)
F(23)-C(23)-C(22)	121.12(13)
C(24)-C(23)-C(22)	123.81(16)
F(24)-C(24)-C(25)	119.74(14)
F(24)-C(24)-C(23)	120.04(16)
C(25)-C(24)-C(23)	120.22(15)
F(25)-C(25)-C(24)	120.70(16)
F(25)-C(25)-C(26)	120.40(16)
C(24)-C(25)-C(26)	118.90(14)
F(26)-C(26)-C(25)	120.09(14)
F(26)-C(26)-C(27)	121.08(15)
C(25)-C(26)-C(27)	118.84(16)
F(27)-C(27)-C(26)	115.77(14)
F(27)-C(27)-C(22)	118.92(13)
C(26)-C(27)-C(22)	125.31(14)
C(1)-N(1)-C(5)	119.14(13)
C(1)-N(1)-B(1)	123.27(12)
C(5)-N(1)-B(1)	117.31(12)
N(1)-B(1)-C(12)	102.87(11)
N(1)-B(1)-C(22)	111.90(12)
C(12)-B(1)-C(22)	119.21(12)
N(1)-B(1)-C(16)	110.10(11)
C(12)-B(1)-C(16)	108.50(12)
C(22)-B(1)-C(16)	104.20(11)

Table S 21. Anisotropic displacement parameters ($Å^2 x\ 10^3$)for PhPyBPF. The anisotropic displacement factor exponent takes the form: $-2\pi^2[\ h^2 a^{*2} U^{11} + ... + 2\ h\ k\ a^*\ b^*\ U^{12}\ ]$

	U^{11}	U^{22}	U^{33}	U^{23}	U^{13}	U^{12}
C(1)	25(1)	26(1)	28(1)	2(1)	-5(1)	0(1)
C(2)	31(1)	29(1)	40(1)	8(1)	-11(1)	1(1)
C(3)	44(1)	37(1)	31(1)	14(1)	-14(1)	-2(1)
C(4)	41(1)	38(1)	21(1)	7(1)	-6(1)	-1(1)
C(5)	28(1)	29(1)	19(1)	4(1)	-2(1)	-3(1)
C(6)	26(1)	30(1)	17(1)	0(1)	-3(1)	-4(1)
C(7)	36(1)	38(1)	18(1)	2(1)	2(1)	-4(1)
C(8)	36(1)	45(1)	21(1)	-6(1)	5(1)	1(1)
C(9)	34(1)	32(1)	29(1)	-5(1)	2(1)	5(1)
C(10)	31(1)	27(1)	23(1)	1(1)	0(1)	-2(1)
C(11)	22(1)	26(1)	18(1)	-1(1)	-3(1)	-3(1)
C(12)	23(1)	25(1)	17(1)	2(1)	0(1)	-1(1)
C(13)	23(1)	36(1)	22(1)	-1(1)	1(1)	-2(1)
C(14)	30(1)	40(1)	41(1)	9(1)	-3(1)	-13(1)
C(15)	26(1)	35(1)	35(1)	2(1)	-8(1)	-4(1)
C(16)	23(1)	20(1)	16(1)	-3(1)	0(1)	0(1)
C(17)	24(1)	22(1)	18(1)	-2(1)	2(1)	1(1)
C(18)	28(1)	24(1)	24(1)	-3(1)	-5(1)	6(1)
C(19)	19(1)	32(1)	34(1)	-9(1)	0(1)	3(1)
C(20)	26(1)	32(1)	26(1)	-5(1)	8(1)	-6(1)
C(21)	30(1)	26(1)	18(1)	0(1)	0(1)	-2(1)
C(22)	20(1)	26(1)	19(1)	1(1)	-1(1)	3(1)
C(23)	23(1)	27(1)	24(1)	1(1)	-1(1)	0(1)
C(24)	28(1)	42(1)	21(1)	2(1)	4(1)	3(1)
C(25)	30(1)	42(1)	23(1)	-10(1)	-1(1)	8(1)
C(26)	26(1)	26(1)	32(1)	-6(1)	-7(1)	5(1)
C(27)	21(1)	25(1)	24(1)	3(1)	-2(1)	2(1)
N(1)	24(1)	23(1)	20(1)	4(1)	-2(1)	-2(1)
B(1)	23(1)	24(1)	16(1)	3(1)	0(1)	2(1)
F(17)	28(1)	34(1)	22(1)	9(1)	-1(1)	0(1)
F(18)	33(1)	38(1)	35(1)	5(1)	-9(1)	12(1)
F(19)	20(1)	54(1)	58(1)	-2(1)	1(1)	7(1)
F(20)	31(1)	60(1)	39(1)	5(1)	11(1)	-12(1)
F(21)	35(1)	40(1)	27(1)	13(1)	-1(1)	-7(1)
F(23)	39(1)	31(1)	26(1)	3(1)	5(1)	-8(1)
F(24)	49(1)	58(1)	24(1)	3(1)	13(1)	-3(1)
F(25)	51(1)	60(1)	31(1)	-20(1)	4(1)	6(1)
F(26)	39(1)	30(1)	46(1)	-12(1)	-7(1)	2(1)
F(27)	32(1)	26(1)	31(1)	4(1)	0(1)	-4(1)

Table S 22. Hydrogen coordinates (x 10^4) and isotropic displacement parameters ($Å^2$x 10^3) for PhPyBPF.

	x	y	z	U(eq)
H(1)	3495	-859	7916	31
H(2)	4214	-1800	8986	40
H(3)	3712	-1121	10186	45
H(4)	2613	532	10274	40
H(7)	953	1628	10190	37
H(8)	40	3377	10267	41
H(9)	347	4696	9318	38
H(10)	1519	4252	8276	32
H(12)	2361	2819	7481	26
H(13)	4469	2273	7543	32
H(14A)	5153	3992	8058	56
H(14B)	3853	4171	8437	56
H(14C)	3955	4161	7533	56
H(15A)	4699	1253	8660	48
H(15B)	4325	2312	9157	48
H(15C)	5580	2317	8709	48

4.4. PhPyBFlu

Table S 23. Crystal data and structure refinement for PhPyBFlu.

Identification code	**PhPyBFlu**	
Empirical formula	$C_{35}H_{40}BN$	
Formula weight	485.49	
Temperature	150(2) K	
Wavelength	1.54184 Å	
Crystal system	Monoclinic	
Space group	$P2_1/n$	
Unit cell dimensions	a = 18.4422(2) Å	α= 90°.
	b = 25.8144(3) Å	β= 102.2410(10)°.
	c = 26.6621(4) Å	γ= 90°.
Volume	12404.6(3) $Å^3$	
Z	16	
Density (calculated)	1.040 Mg/m^3	
Absorption coefficient	0.437 mm^{-1}	
F(000)	4192	
Crystal colour and habit	Colorless prism	
Crystal size	0.195 x 0.149 x 0.133 mm^3	
Theta range for data collection	2.990 to 74.204°.	
Index ranges	-22<=h<=22, -31<=k<=22, -29<=l<=33	
Reflections collected	48199	
Independent reflections	24260 [R(int) = 0.0250]	
Completeness to theta = 67.684°	99.5 %	
Absorption correction	Semi-empirical from equivalents	
Max. and min. transmission	1.00000 and 0.92483	
Refinement method	Full-matrix least-squares on F^2	
Data / restraints / parameters	24260 / 76 / 1394	
Goodness-of-fit on F^2	1.053	
Final R indices [I>2sigma(I)]	R1 = 0.0703, wR2 = 0.2007	
R indices (all data)	R1 = 0.0951, wR2 = 0.2198	
Extinction coefficient	n/a	
Largest diff. peak and hole	0.858 and -0.377 $e.Å^{-3}$	

Definitions:

$$R_1 = \frac{\sum \| F_o | - | F_c \|}{\sum | F_o |} \qquad wR_2 = \sqrt{\frac{\sum \left[w \left(F_o^2 - F_c^2 \right)^2 \right]}{\sum \left[w \left(F_o^2 \right)^2 \right]}}$$

$$GooF = \sqrt{\frac{\sum \left[w \left(F_o^2 - F_c^2 \right) \right]}{(n-p)}}$$

n = number of reflections; p = number of parameters

Notes on the refinement of PhPyBFlu.

Because of the existence of partially occupied/severely disordered n-hexane/H_2O, SQUEEZE process integrated in PLATON was used. And the detailed information has been posted in the final CIF file. All hydrogen atoms were placed in calculated positions and refined by using a riding model.

Table S 24. Atomic coordinates (x 10^4) and equivalent isotropic displacement parameters ($Å^2$x 10^3) for PhPyBFlu. U(eq) is defined as one third of the trace of the orthogonalized U^{ij} tensor.

	x	y	z	U(eq)
C(1O)	3050(1)	1930(1)	3501(1)	37(1)
C(1M)	1910(1)	1883(1)	2866(1)	34(1)
C(1P)	2664(1)	2059(1)	3882(1)	36(1)
C(1Q)	1893(1)	2121(1)	3733(1)	38(1)
C(16)	-973(1)	2192(1)	2794(1)	39(1)
C(1K)	1606(1)	1602(1)	1918(1)	43(1)
C(1L)	1415(1)	1784(1)	2362(1)	37(1)
C(1A)	-1170(1)	1274(1)	2815(1)	47(1)
C(1B)	-693(1)	1697(1)	2942(1)	41(1)
C(1N)	2680(1)	1845(1)	2995(1)	36(1)
C(17)	-1707(1)	2251(1)	2523(1)	44(1)
C(15)	-500(1)	2658(1)	2909(1)	39(1)
C(11)	684(1)	3026(1)	3065(1)	46(1)
C(1G)	669(1)	1884(1)	2379(1)	39(1)
C(18)	-2162(1)	1821(1)	2403(1)	48(1)
C(1C)	109(1)	1620(1)	3206(1)	42(1)
C(1R)	1501(1)	2032(1)	3235(1)	36(1)
C(1W)	3051(1)	2125(1)	4447(1)	42(1)
C(1H)	132(1)	1805(1)	1928(1)	46(1)
C(1J)	1057(1)	1521(1)	1479(1)	48(1)
C(14)	-801(1)	3149(1)	2940(1)	45(1)
C(19)	-1895(1)	1336(1)	2550(1)	49(1)
C(13)	-352(1)	3583(1)	3024(1)	49(1)
C(12)	407(1)	3519(1)	3083(1)	50(1)
C(1I)	315(1)	1624(1)	1474(1)	49(1)
C(1D)	238(1)	1581(1)	3796(1)	52(1)
C(1F)	27(2)	2066(1)	4053(1)	60(1)
C(1E)	-149(2)	1110(1)	3973(1)	67(1)
C(1Z)	2935(2)	2675(1)	4625(1)	68(1)
C(1S)	-270(2)	1535(1)	973(1)	67(1)
C(1Y)	3884(2)	2021(1)	4548(1)	63(1)
C(1X)	2712(2)	1741(1)	4771(1)	73(1)
C(1V)	-1054(2)	1617(2)	1038(2)	89(1)
C(1T)	-203(2)	976(2)	780(2)	95(1)
C(1U)	-106(2)	1907(2)	562(2)	105(2)
B(11)	619(1)	2031(1)	2966(1)	39(1)
N(11)	248(1)	2601(1)	2984(1)	39(1)
C(2H)	8573(1)	7709(1)	2975(1)	44(1)
C(25)	8662(1)	6893(1)	1887(1)	42(1)
C(2L)	7923(1)	8413(1)	2495(1)	41(1)
C(2R)	8119(1)	8369(1)	1643(1)	41(1)
C(2C)	9463(1)	7878(1)	1962(1)	39(1)
C(2M)	7776(1)	8651(1)	1981(1)	41(1)
C(21)	7581(1)	7286(1)	1432(1)	45(1)
C(24)	8373(2)	6409(1)	1701(1)	54(1)
C(2B)	9797(1)	7412(1)	2262(1)	43(1)
C(2G)	8378(1)	7976(1)	2513(1)	38(1)
C(2K)	7681(1)	8575(1)	2934(1)	49(1)
C(26)	9402(1)	6940(1)	2229(1)	45(1)
C(2I)	8322(1)	7855(1)	3412(1)	52(1)
C(2N)	7377(1)	9097(1)	1822(1)	51(1)

C(27)	9710(2)	6516(1)	2528(1)	59(1)
C(22)	7283(1)	6819(1)	1245(1)	55(1)
C(2D)	9696(1)	7936(1)	1438(1)	47(1)
C(2J)	7875(1)	8293(1)	3381(1)	53(1)
C(2A)	10496(1)	7433(1)	2594(1)	55(1)
C(23)	7690(2)	6373(1)	1381(1)	57(1)
C(2E)	10522(2)	8016(1)	1500(1)	59(1)
C(2F)	9437(2)	7505(1)	1059(1)	62(1)
C(2Q)	8065(1)	8566(1)	1153(1)	51(1)
C(2O)	7347(2)	9285(1)	1334(1)	58(1)
C(2P)	7703(2)	9037(1)	994(1)	59(1)
C(29)	10791(2)	7008(2)	2881(1)	72(1)
C(2S)	8519(2)	7540(2)	3913(1)	72(1)
C(28)	10396(2)	6548(1)	2843(1)	71(1)
C(2W)	7752(2)	9282(2)	478(1)	80(1)
C(2U)	7767(3)	7343(2)	4032(2)	111(2)
C(2Z)	7200(4)	9709(3)	317(2)	168(3)
C(2V)	8824(3)	7885(2)	4367(2)	133(2)
C(2T)	8988(4)	7091(2)	3885(2)	146(3)
C(2X)	7540(7)	8892(3)	55(2)	262(6)
C(2Y)	8507(3)	9507(4)	515(3)	252(6)
B(21)	8579(1)	7888(1)	1953(1)	37(1)
N(21)	8258(1)	7325(1)	1743(1)	37(1)
C(3B)	4404(1)	206(1)	3093(1)	35(1)
C(3G)	5729(1)	7(1)	2550(1)	36(1)
C(35)	4614(1)	-755(1)	3107(1)	39(1)
C(3A)	3939(1)	622(1)	2920(1)	39(1)
C(3M)	6981(1)	37(1)	3011(1)	37(1)
C(36)	4141(1)	-296(1)	2949(1)	37(1)
C(3P)	7775(1)	-99(1)	4024(1)	46(1)
C(37)	3435(1)	-363(1)	2634(1)	42(1)
C(3O)	8138(1)	20(1)	3629(1)	45(1)
C(3Q)	6999(1)	-167(1)	3891(1)	44(1)
C(39)	3243(1)	552(1)	2605(1)	43(1)
C(3K)	6626(1)	274(1)	2051(1)	46(1)
C(31)	5807(1)	-1112(1)	3307(1)	48(1)
C(38)	2993(1)	59(1)	2460(1)	44(1)
C(3H)	5176(1)	52(1)	2105(1)	41(1)
C(3D)	5288(1)	309(1)	3975(1)	46(1)
C(3C)	5193(1)	287(1)	3384(1)	37(1)
C(3J)	6066(2)	319(1)	1622(1)	50(1)
C(34)	4317(1)	-1241(1)	3166(1)	49(1)
C(3I)	5329(1)	206(1)	1635(1)	46(1)
C(32)	5532(2)	-1600(1)	3355(1)	56(1)
C(3E)	4889(2)	777(1)	4142(1)	60(1)
C(3W)	8191(2)	-153(1)	4582(1)	61(1)
C(33)	4774(2)	-1667(1)	3287(1)	58(1)
C(3F)	5061(2)	-182(1)	4219(1)	59(1)
C(3S)	4726(2)	239(1)	1141(1)	62(1)
C(3N)	7750(1)	86(1)	3130(1)	42(1)
C(3T)	4931(3)	-109(3)	749(2)	136(2)
C(3Y)	8171(5)	-722(3)	4722(3)	233(5)
C(3Z)	8987(2)	-18(2)	4670(2)	119(2)
C(3V)	3975(2)	137(2)	1227(1)	104(2)
C(3L)	6467(1)	112(1)	2514(1)	37(1)
C(3X)	7809(3)	110(4)	4928(2)	238(6)
C(3R)	6595(1)	-100(1)	3397(1)	39(1)

C(3U)	4744(3)	786(2)	907(2)	115(2)
B(31)	5711(1)	-121(1)	3145(1)	37(1)
N(31)	5364(1)	-694(1)	3189(1)	38(1)
C(4VA)	2665(7)	7919(3)	4570(3)	92(3)
C(4WA)	1922(7)	7876(6)	4725(4)	171(5)
C(4VB)	3229(8)	8033(4)	4559(3)	91(3)
C(4WB)	4049(6)	8170(4)	4644(3)	117(3)
C(4Y)	3124(4)	7438(2)	4684(2)	126(2)
C(4X)	2984(4)	8359(2)	4900(2)	143(2)
C(45)	1349(1)	10088(1)	3058(1)	36(1)
C(4G)	1466(1)	9284(1)	1967(1)	37(1)
C(4K)	2115(1)	8568(1)	2432(1)	34(1)
C(4F)	1674(1)	9018(1)	2426(1)	34(1)
C(44)	1589(1)	10576(1)	3243(1)	43(1)
C(4L)	2312(1)	8345(1)	2949(1)	38(1)
C(4B)	258(1)	9524(1)	2699(1)	45(1)
C(41)	2446(1)	9737(1)	3535(1)	38(1)
C(43)	2258(1)	10642(1)	3582(1)	45(1)
C(4H)	1702(1)	9136(1)	1520(1)	42(1)
C(46)	618(1)	10006(1)	2713(1)	42(1)
C(4M)	2755(2)	7913(1)	3113(1)	51(1)
C(42)	2696(1)	10216(1)	3732(1)	44(1)
C(4I)	2134(1)	8692(1)	1542(1)	44(1)
C(4Q)	2028(1)	8646(1)	3301(1)	45(1)
C(47)	287(2)	10410(1)	2396(1)	55(1)
C(4R)	1450(2)	9454(1)	1027(1)	53(1)
C(4A)	-447(1)	9476(1)	2372(1)	62(1)
C(48)	-407(2)	10348(1)	2081(1)	70(1)
C(49)	-771(2)	9881(2)	2073(1)	76(1)
C(4P)	2227(2)	8511(1)	3815(1)	77(1)
C(4T)	1683(2)	10019(1)	1125(1)	67(1)
C(4U)	1787(2)	9256(1)	586(1)	80(1)
C(4N)	2934(2)	7792(1)	3622(1)	83(1)
C(4S)	605(2)	9429(2)	861(1)	82(1)
C(4O)	2683(3)	8089(1)	3987(1)	107(2)
C(4J)	2332(1)	8404(1)	1989(1)	40(1)
B(41)	1508(1)	9102(1)	2998(1)	36(1)
N(41)	1788(1)	9671(1)	3211(1)	34(1)
C(4C)	632(1)	9077(1)	3008(1)	43(1)
C(4D)	430(2)	9024(1)	3542(1)	61(1)
C(4EA)	-434(3)	8931(2)	3464(2)	96(2)
C(4EB)	505(9)	8501(6)	3769(6)	64(5)
C(4EC)	600(2)	9476(2)	3885(2)	82(1)

Table S 25. Bond lengths [Å] and angles [°] for PhPyBFlu.

C(1O)-C(1N)	1.394(3)	C(1F)-H(1F1)	0.9800
C(1O)-C(1P)	1.398(3)	C(1F)-H(1F2)	0.9800
C(1O)-H(1O)	0.9500	C(1F)-H(1F3)	0.9800
C(1M)-C(1N)	1.392(3)	C(1E)-H(1E1)	0.9800
C(1M)-C(1R)	1.414(3)	C(1E)-H(1E2)	0.9800
C(1M)-C(1L)	1.478(3)	C(1E)-H(1E3)	0.9800
C(1P)-C(1Q)	1.402(3)	C(1Z)-H(1Z1)	0.9800
C(1P)-C(1W)	1.534(3)	C(1Z)-H(1Z2)	0.9800
C(1Q)-C(1R)	1.389(3)	C(1Z)-H(1Z3)	0.9800
C(1Q)-H(1Q)	0.9500	C(1S)-C(1V)	1.509(5)
C(16)-C(17)	1.401(3)	C(1S)-C(1U)	1.532(5)
C(16)-C(1B)	1.403(3)	C(1S)-C(1T)	1.546(5)
C(16)-C(15)	1.480(3)	C(1Y)-H(1Y1)	0.9800
C(1K)-C(1L)	1.385(3)	C(1Y)-H(1Y2)	0.9800
C(1K)-C(1J)	1.392(3)	C(1Y)-H(1Y3)	0.9800
C(1K)-H(1K)	0.9500	C(1X)-H(1X1)	0.9800
C(1L)-C(1G)	1.410(3)	C(1X)-H(1X2)	0.9800
C(1A)-C(19)	1.382(3)	C(1X)-H(1X3)	0.9800
C(1A)-C(1B)	1.397(3)	C(1V)-H(1V1)	0.9800
C(1A)-H(1A)	0.9500	C(1V)-H(1V2)	0.9800
C(1B)-C(1C)	1.511(3)	C(1V)-H(1V3)	0.9800
C(1N)-H(1N)	0.9500	C(1T)-H(1T1)	0.9800
C(17)-C(18)	1.386(3)	C(1T)-H(1T2)	0.9800
C(17)-H(17)	0.9500	C(1T)-H(1T3)	0.9800
C(15)-N(11)	1.360(3)	C(1U)-H(1U1)	0.9800
C(15)-C(14)	1.395(3)	C(1U)-H(1U2)	0.9800
C(11)-N(11)	1.349(3)	C(1U)-H(1U3)	0.9800
C(11)-C(12)	1.376(3)	B(11)-N(11)	1.629(3)
C(11)-H(11)	0.9500	C(2H)-C(2G)	1.389(3)
C(1G)-C(1H)	1.401(3)	C(2H)-C(2I)	1.395(3)
C(1G)-B(11)	1.630(4)	C(2H)-H(2H)	0.9500
C(18)-C(19)	1.374(4)	C(25)-N(21)	1.351(3)
C(18)-H(18)	0.9500	C(25)-C(24)	1.405(3)
C(1C)-C(1D)	1.543(4)	C(25)-C(26)	1.477(3)
C(1C)-B(11)	1.637(3)	C(2L)-C(2G)	1.401(3)
C(1C)-H(1C)	1.0000	C(2L)-C(2K)	1.401(3)
C(1R)-B(11)	1.631(3)	C(2L)-C(2M)	1.474(4)
C(1W)-C(1Z)	1.525(4)	C(2R)-C(2Q)	1.387(4)
C(1W)-C(1Y)	1.526(3)	C(2R)-C(2M)	1.408(3)
C(1W)-C(1X)	1.532(4)	C(2R)-B(21)	1.626(3)
C(1H)-C(1I)	1.404(4)	C(2C)-C(2B)	1.503(3)
C(1H)-H(1H)	0.9500	C(2C)-C(2D)	1.553(3)
C(1J)-C(1I)	1.391(4)	C(2C)-B(21)	1.627(3)
C(1J)-H(1J)	0.9500	C(2C)-H(2C)	1.0000
C(14)-C(13)	1.381(3)	C(2M)-C(2N)	1.383(3)
C(14)-H(14)	0.9500	C(21)-N(21)	1.349(3)
C(19)-H(19)	0.9500	C(21)-C(22)	1.375(3)
C(13)-C(12)	1.384(4)	C(21)-H(21)	0.9500
C(13)-H(13)	0.9500	C(24)-C(23)	1.367(4)
C(12)-H(12)	0.9500	C(24)-H(24)	0.9500
C(1I)-C(1S)	1.546(4)	C(2B)-C(2A)	1.401(3)
C(1D)-C(1F)	1.519(4)	C(2B)-C(26)	1.413(3)
C(1D)-C(1E)	1.534(4)	C(2G)-B(21)	1.629(3)
C(1D)-H(1D)	1.0000	C(2K)-C(2J)	1.378(4)
		C(2K)-H(2K)	0.9500

C(26)-C(27)	1.401(4)	C(3B)-C(3C)	1.512(3)
C(2I)-C(2J)	1.390(4)	C(3G)-C(3H)	1.396(3)
C(2I)-C(2S)	1.540(4)	C(3G)-C(3L)	1.410(3)
C(2N)-C(2O)	1.378(4)	C(3G)-B(31)	1.629(3)
C(2N)-H(2N)	0.9500	C(35)-N(31)	1.362(3)
C(27)-C(28)	1.366(4)	C(35)-C(34)	1.392(3)
C(27)-H(27)	0.9500	C(35)-C(36)	1.478(3)
C(22)-C(23)	1.380(4)	C(3A)-C(39)	1.388(3)
C(22)-H(22)	0.9500	C(3A)-H(3A)	0.9500
C(2D)-C(2F)	1.511(4)	C(3M)-C(3N)	1.393(3)
C(2D)-C(2E)	1.512(3)	C(3M)-C(3R)	1.414(3)
C(2D)-H(2D)	1.0000	C(3M)-C(3L)	1.470(3)
C(2J)-H(2J)	0.9500	C(36)-C(37)	1.404(3)
C(2A)-C(29)	1.381(4)	C(3P)-C(3O)	1.396(3)
C(2A)-H(2A)	0.9500	C(3P)-C(3Q)	1.410(3)
C(23)-H(23)	0.9500	C(3P)-C(3W)	1.528(4)
C(2E)-H(2E1)	0.9800	C(37)-C(38)	1.380(3)
C(2E)-H(2E2)	0.9800	C(37)-H(37)	0.9500
C(2E)-H(2E3)	0.9800	C(3O)-C(3N)	1.382(4)
C(2F)-H(2F1)	0.9800	C(3O)-H(3O)	0.9500
C(2F)-H(2F2)	0.9800	C(3Q)-C(3R)	1.379(3)
C(2F)-H(2F3)	0.9800	C(3Q)-H(3Q)	0.9500
C(2Q)-C(2P)	1.410(4)	C(39)-C(38)	1.381(3)
C(2Q)-H(2Q)	0.9500	C(39)-H(39)	0.9500
C(2O)-C(2P)	1.382(4)	C(3K)-C(3J)	1.374(4)
C(2O)-H(2O)	0.9500	C(3K)-C(3L)	1.393(3)
C(2P)-C(2W)	1.536(5)	C(3K)-H(3K)	0.9500
C(29)-C(28)	1.385(5)	C(31)-N(31)	1.349(3)
C(29)-H(29)	0.9500	C(31)-C(32)	1.373(4)
C(2S)-C(2T)	1.459(6)	C(31)-H(31)	0.9500
C(2S)-C(2V)	1.511(6)	C(38)-H(38)	0.9500
C(2S)-C(2U)	1.572(5)	C(3H)-C(3I)	1.398(3)
C(28)-H(28)	0.9500	C(3H)-H(3H)	0.9500
C(2W)-C(2Y)	1.491(6)	C(3D)-C(3F)	1.523(4)
C(2W)-C(2X)	1.499(8)	C(3D)-C(3E)	1.530(4)
C(2W)-C(2Z)	1.500(6)	C(3D)-C(3C)	1.549(3)
C(2U)-H(2U1)	0.9800	C(3D)-H(3D)	1.0000
C(2U)-H(2U2)	0.9800	C(3C)-B(31)	1.638(3)
C(2U)-H(2U3)	0.9800	C(3C)-H(3C)	1.0000
C(2Z)-H(2Z1)	0.9800	C(3J)-C(3I)	1.399(4)
C(2Z)-H(2Z2)	0.9800	C(3J)-H(3J)	0.9500
C(2Z)-H(2Z3)	0.9800	C(34)-C(33)	1.380(4)
C(2V)-H(2V1)	0.9800	C(34)-H(34)	0.9500
C(2V)-H(2V2)	0.9800	C(3I)-C(3S)	1.534(4)
C(2V)-H(2V3)	0.9800	C(32)-C(33)	1.383(4)
C(2T)-H(2T1)	0.9800	C(32)-H(32)	0.9500
C(2T)-H(2T2)	0.9800	C(3E)-H(3E1)	0.9800
C(2T)-H(2T3)	0.9800	C(3E)-H(3E2)	0.9800
C(2X)-H(2X1)	0.9800	C(3E)-H(3E3)	0.9800
C(2X)-H(2X2)	0.9800	C(3W)-C(3X)	1.444(6)
C(2X)-H(2X3)	0.9800	C(3W)-C(3Z)	1.478(4)
C(2Y)-H(2Y1)	0.9800	C(3W)-C(3Y)	1.519(7)
C(2Y)-H(2Y2)	0.9800	C(33)-H(33)	0.9500
C(2Y)-H(2Y3)	0.9800	C(3F)-H(3F1)	0.9800
B(21)-N(21)	1.623(3)	C(3F)-H(3F2)	0.9800
C(3B)-C(3A)	1.391(3)	C(3F)-H(3F3)	0.9800
C(3B)-C(36)	1.407(3)	C(3S)-C(3V)	1.475(5)

C(3S)-C(3T)	1.489(5)	C(4K)-C(4L)	1.468(3)
C(3S)-C(3U)	1.547(5)	C(4F)-B(41)	1.632(3)
C(3N)-H(3N)	0.9500	C(44)-C(43)	1.377(3)
C(3T)-H(3T1)	0.9800	C(44)-H(44)	0.9500
C(3T)-H(3T2)	0.9800	C(4L)-C(4M)	1.397(3)
C(3T)-H(3T3)	0.9800	C(4L)-C(4Q)	1.403(3)
C(3Y)-H(3Y1)	0.9800	C(4B)-C(46)	1.408(3)
C(3Y)-H(3Y2)	0.9800	C(4B)-C(4A)	1.408(3)
C(3Y)-H(3Y3)	0.9800	C(4B)-C(4C)	1.498(4)
C(3Z)-H(3Z1)	0.9800	C(41)-N(41)	1.344(3)
C(3Z)-H(3Z2)	0.9800	C(41)-C(42)	1.383(3)
C(3Z)-H(3Z3)	0.9800	C(41)-H(41)	0.9500
C(3V)-H(3V1)	0.9800	C(43)-C(42)	1.373(3)
C(3V)-H(3V2)	0.9800	C(43)-H(43)	0.9500
C(3V)-H(3V3)	0.9800	C(4H)-C(4I)	1.390(3)
C(3X)-H(3X1)	0.9800	C(4H)-C(4R)	1.535(3)
C(3X)-H(3X2)	0.9800	C(46)-C(47)	1.398(4)
C(3X)-H(3X3)	0.9800	C(4M)-C(4N)	1.365(4)
C(3R)-B(31)	1.626(3)	C(4M)-H(4M)	0.9500
C(3U)-H(3U1)	0.9800	C(42)-H(42)	0.9500
C(3U)-H(3U2)	0.9800	C(4I)-C(4J)	1.385(3)
C(3U)-H(3U3)	0.9800	C(4I)-H(4I)	0.9500
B(31)-N(31)	1.626(3)	C(4Q)-C(4P)	1.385(4)
C(4VA)-C(4X)	1.480(11)	C(4Q)-B(41)	1.621(3)
C(4VA)-C(4Y)	1.497(9)	C(47)-C(48)	1.384(4)
C(4VA)-C(4WA)	1.518(16)	C(47)-H(47)	0.9500
C(4VA)-C(4O)	1.620(9)	C(4R)-C(4S)	1.528(4)
C(4WA)-H(4W1)	0.9800	C(4R)-C(4T)	1.528(4)
C(4WA)-H(4W2)	0.9800	C(4R)-C(4U)	1.531(4)
C(4WA)-H(4W3)	0.9800	C(4A)-C(49)	1.373(5)
C(4VB)-C(4X)	1.383(10)	C(4A)-H(4A)	0.9500
C(4VB)-C(4WB)	1.524(16)	C(48)-C(49)	1.378(5)
C(4VB)-C(4Y)	1.592(11)	C(48)-H(48)	0.9500
C(4VB)-C(4O)	1.645(11)	C(49)-H(49)	0.9500
C(4WB)-H(4W4)	0.9800	C(4P)-C(4O)	1.395(5)
C(4WB)-H(4W5)	0.9800	C(4P)-H(4P)	0.9500
C(4WB)-H(4W6)	0.9800	C(4T)-H(4T1)	0.9800
C(4Y)-H(4Y1)	0.9800	C(4T)-H(4T2)	0.9800
C(4Y)-H(4Y2)	0.9800	C(4T)-H(4T3)	0.9800
C(4Y)-H(4Y3)	0.9800	C(4U)-H(4U1)	0.9800
C(4Y)-H(4Y4)	0.9800	C(4U)-H(4U2)	0.9800
C(4Y)-H(4Y5)	0.9800	C(4U)-H(4U3)	0.9800
C(4Y)-H(4Y6)	0.9800	C(4N)-C(4O)	1.392(5)
C(4X)-H(4X1)	0.9800	C(4N)-H(4N)	0.9500
C(4X)-H(4X2)	0.9800	C(4S)-H(4S1)	0.9800
C(4X)-H(4X3)	0.9800	C(4S)-H(4S2)	0.9800
C(4X)-H(4X4)	0.9800	C(4S)-H(4S3)	0.9800
C(4X)-H(4X5)	0.9800	C(4J)-H(4J)	0.9500
C(4X)-H(4X6)	0.9800	B(41)-N(41)	1.619(3)
C(45)-N(41)	1.356(3)	B(41)-C(4C)	1.624(3)
C(45)-C(44)	1.392(3)	C(4C)-C(4D)	1.551(4)
C(45)-C(46)	1.477(3)	C(4C)-H(4C)	1.0000
C(4G)-C(4F)	1.385(3)	C(4D)-C(4EC)	1.474(4)
C(4G)-C(4H)	1.407(3)	C(4D)-C(4EB)	1.475(15)
C(4G)-H(4G)	0.9500	C(4D)-C(4EA)	1.581(5)
C(4K)-C(4J)	1.390(3)	C(4D)-H(4D1)	1.0000
C(4K)-C(4F)	1.417(3)	C(4D)-H(4D2)	1.0000

C(4EA)-H(4E1)	0.9800	C(1D)-C(1C)-B(11)	117.64(19)
C(4EA)-H(4E2)	0.9800	C(1B)-C(1C)-H(1C)	105.1
C(4EA)-H(4E3)	0.9800	C(1D)-C(1C)-H(1C)	105.1
C(4EB)-H(4E4)	0.9800	B(11)-C(1C)-H(1C)	105.1
C(4EB)-H(4E5)	0.9800	C(1Q)-C(1R)-C(1M)	117.58(19)
C(4EB)-H(4E6)	0.9800	C(1Q)-C(1R)-B(11)	133.5(2)
C(4EC)-H(4E7)	0.9800	C(1M)-C(1R)-B(11)	108.79(19)
C(4EC)-H(4E8)	0.9800	C(1Z)-C(1W)-C(1Y)	108.1(2)
C(4EC)-H(4E9)	0.9800	C(1Z)-C(1W)-C(1X)	109.1(3)
		C(1Y)-C(1W)-C(1X)	107.6(2)
C(1N)-C(1O)-C(1P)	121.33(19)	C(1Z)-C(1W)-C(1P)	110.0(2)
C(1N)-C(1O)-H(1O)	119.3	C(1Y)-C(1W)-C(1P)	113.2(2)
C(1P)-C(1O)-H(1O)	119.3	C(1X)-C(1W)-C(1P)	108.8(2)
C(1N)-C(1M)-C(1R)	120.9(2)	C(1G)-C(1H)-C(1I)	122.2(2)
C(1N)-C(1M)-C(1L)	127.9(2)	C(1G)-C(1H)-H(1H)	118.9
C(1R)-C(1M)-C(1L)	111.25(18)	C(1I)-C(1H)-H(1H)	118.9
C(1O)-C(1P)-C(1Q)	117.5(2)	C(1I)-C(1J)-C(1K)	121.3(2)
C(1O)-C(1P)-C(1W)	122.49(19)	C(1I)-C(1J)-H(1J)	119.4
C(1Q)-C(1P)-C(1W)	119.97(19)	C(1K)-C(1J)-H(1J)	119.4
C(1R)-C(1Q)-C(1P)	123.0(2)	C(13)-C(14)-C(15)	120.9(2)
C(1R)-C(1Q)-H(1Q)	118.5	C(13)-C(14)-H(14)	119.6
C(1P)-C(1Q)-H(1Q)	118.5	C(15)-C(14)-H(14)	119.6
C(17)-C(16)-C(1B)	120.2(2)	C(18)-C(19)-C(1A)	120.0(2)
C(17)-C(16)-C(15)	118.7(2)	C(18)-C(19)-H(19)	120.0
C(1B)-C(16)-C(15)	121.07(19)	C(1A)-C(19)-H(19)	120.0
C(1L)-C(1K)-C(1J)	119.8(2)	C(14)-C(13)-C(12)	118.7(2)
C(1L)-C(1K)-H(1K)	120.1	C(14)-C(13)-H(13)	120.7
C(1J)-C(1K)-H(1K)	120.1	C(12)-C(13)-H(13)	120.7
C(1K)-C(1L)-C(1G)	121.1(2)	C(11)-C(12)-C(13)	118.6(2)
C(1K)-C(1L)-C(1M)	128.0(2)	C(11)-C(12)-H(12)	120.7
C(1G)-C(1L)-C(1M)	110.9(2)	C(13)-C(12)-H(12)	120.7
C(19)-C(1A)-C(1B)	121.7(2)	C(1J)-C(1I)-C(1H)	118.1(2)
C(19)-C(1A)-H(1A)	119.1	C(1J)-C(1I)-C(1S)	119.0(3)
C(1B)-C(1A)-H(1A)	119.1	C(1H)-C(1I)-C(1S)	123.0(2)
C(1A)-C(1B)-C(16)	117.8(2)	C(1F)-C(1D)-C(1E)	109.5(2)
C(1A)-C(1B)-C(1C)	120.9(2)	C(1F)-C(1D)-C(1C)	114.0(2)
C(16)-C(1B)-C(1C)	121.15(19)	C(1E)-C(1D)-C(1C)	112.6(2)
C(1M)-C(1N)-C(1O)	119.56(19)	C(1F)-C(1D)-H(1D)	106.8
C(1M)-C(1N)-H(1N)	120.2	C(1E)-C(1D)-H(1D)	106.8
C(1O)-C(1N)-H(1N)	120.2	C(1C)-C(1D)-H(1D)	106.8
C(18)-C(17)-C(16)	120.2(2)	C(1D)-C(1F)-H(1F1)	109.5
C(18)-C(17)-H(17)	119.9	C(1D)-C(1F)-H(1F2)	109.5
C(16)-C(17)-H(17)	119.9	H(1F1)-C(1F)-H(1F2)	109.5
N(11)-C(15)-C(14)	119.6(2)	C(1D)-C(1F)-H(1F3)	109.5
N(11)-C(15)-C(16)	118.65(19)	H(1F1)-C(1F)-H(1F3)	109.5
C(14)-C(15)-C(16)	121.79(19)	H(1F2)-C(1F)-H(1F3)	109.5
N(11)-C(11)-C(12)	123.0(2)	C(1D)-C(1E)-H(1E1)	109.5
N(11)-C(11)-H(11)	118.5	C(1D)-C(1E)-H(1E2)	109.5
C(12)-C(11)-H(11)	118.5	H(1E1)-C(1E)-H(1E2)	109.5
C(1H)-C(1G)-C(1L)	117.6(2)	C(1D)-C(1E)-H(1E3)	109.5
C(1H)-C(1G)-B(11)	133.1(2)	H(1E1)-C(1E)-H(1E3)	109.5
C(1L)-C(1G)-B(11)	109.14(19)	H(1E2)-C(1E)-H(1E3)	109.5
C(19)-C(18)-C(17)	120.1(2)	C(1W)-C(1Z)-H(1Z1)	109.5
C(19)-C(18)-H(18)	120.0	C(1W)-C(1Z)-H(1Z2)	109.5
C(17)-C(18)-H(18)	120.0	H(1Z1)-C(1Z)-H(1Z2)	109.5
C(1B)-C(1C)-C(1D)	114.13(19)	C(1W)-C(1Z)-H(1Z3)	109.5
C(1B)-C(1C)-B(11)	108.59(18)	H(1Z1)-C(1Z)-H(1Z3)	109.5

H(1Z2)-C(1Z)-H(1Z3)	109.5	C(2M)-C(2R)-B(21)	109.1(2)
C(1V)-C(1S)-C(1U)	109.6(3)	C(2B)-C(2C)-C(2D)	113.26(19)
C(1V)-C(1S)-C(1I)	112.9(3)	C(2B)-C(2C)-B(21)	108.48(18)
C(1U)-C(1S)-C(1I)	108.5(3)	C(2D)-C(2C)-B(21)	116.94(19)
C(1V)-C(1S)-C(1T)	108.4(3)	C(2B)-C(2C)-H(2C)	105.8
C(1U)-C(1S)-C(1T)	107.8(3)	C(2D)-C(2C)-H(2C)	105.8
C(1I)-C(1S)-C(1T)	109.6(2)	B(21)-C(2C)-H(2C)	105.8
C(1W)-C(1Y)-H(1Y1)	109.5	C(2N)-C(2M)-C(2R)	121.1(2)
C(1W)-C(1Y)-H(1Y2)	109.5	C(2N)-C(2M)-C(2L)	127.8(2)
H(1Y1)-C(1Y)-H(1Y2)	109.5	C(2R)-C(2M)-C(2L)	111.1(2)
C(1W)-C(1Y)-H(1Y3)	109.5	N(21)-C(21)-C(22)	122.5(2)
H(1Y1)-C(1Y)-H(1Y3)	109.5	N(21)-C(21)-H(21)	118.8
H(1Y2)-C(1Y)-H(1Y3)	109.5	C(22)-C(21)-H(21)	118.8
C(1W)-C(1X)-H(1X1)	109.5	C(23)-C(24)-C(25)	120.7(3)
C(1W)-C(1X)-H(1X2)	109.5	C(23)-C(24)-H(24)	119.6
H(1X1)-C(1X)-H(1X2)	109.5	C(25)-C(24)-H(24)	119.6
C(1W)-C(1X)-H(1X3)	109.5	C(2A)-C(2B)-C(26)	117.7(2)
H(1X1)-C(1X)-H(1X3)	109.5	C(2A)-C(2B)-C(2C)	121.6(2)
H(1X2)-C(1X)-H(1X3)	109.5	C(26)-C(2B)-C(2C)	120.6(2)
C(1S)-C(1V)-H(1V1)	109.5	C(2H)-C(2G)-C(2L)	118.1(2)
C(1S)-C(1V)-H(1V2)	109.5	C(2H)-C(2G)-B(21)	132.6(2)
H(1V1)-C(1V)-H(1V2)	109.5	C(2L)-C(2G)-B(21)	109.4(2)
C(1S)-C(1V)-H(1V3)	109.5	C(2J)-C(2K)-C(2L)	119.6(2)
H(1V1)-C(1V)-H(1V3)	109.5	C(2J)-C(2K)-H(2K)	120.2
H(1V2)-C(1V)-H(1V3)	109.5	C(2L)-C(2K)-H(2K)	120.2
C(1S)-C(1T)-H(1T1)	109.5	C(27)-C(26)-C(2B)	119.8(2)
C(1S)-C(1T)-H(1T2)	109.5	C(27)-C(26)-C(25)	119.7(2)
H(1T1)-C(1T)-H(1T2)	109.5	C(2B)-C(26)-C(25)	120.5(2)
C(1S)-C(1T)-H(1T3)	109.5	C(2J)-C(2I)-C(2H)	117.8(3)
H(1T1)-C(1T)-H(1T3)	109.5	C(2J)-C(2I)-C(2S)	120.6(2)
H(1T2)-C(1T)-H(1T3)	109.5	C(2H)-C(2I)-C(2S)	121.6(3)
C(1S)-C(1U)-H(1U1)	109.5	C(2O)-C(2N)-C(2M)	119.7(2)
C(1S)-C(1U)-H(1U2)	109.5	C(2O)-C(2N)-H(2N)	120.2
H(1U1)-C(1U)-H(1U2)	109.5	C(2M)-C(2N)-H(2N)	120.2
C(1S)-C(1U)-H(1U3)	109.5	C(28)-C(27)-C(26)	120.9(3)
H(1U1)-C(1U)-H(1U3)	109.5	C(28)-C(27)-H(27)	119.5
H(1U2)-C(1U)-H(1U3)	109.5	C(26)-C(27)-H(27)	119.5
N(11)-B(11)-C(1G)	110.43(19)	C(21)-C(22)-C(23)	118.8(2)
N(11)-B(11)-C(1R)	111.73(17)	C(21)-C(22)-H(22)	120.6
C(1G)-B(11)-C(1R)	99.73(17)	C(23)-C(22)-H(22)	120.6
N(11)-B(11)-C(1C)	107.14(17)	C(2F)-C(2D)-C(2E)	110.0(2)
C(1G)-B(11)-C(1C)	112.22(19)	C(2F)-C(2D)-C(2C)	115.0(2)
C(1R)-B(11)-C(1C)	115.53(19)	C(2E)-C(2D)-C(2C)	112.3(2)
C(11)-N(11)-C(15)	119.21(19)	C(2F)-C(2D)-H(2D)	106.3
C(11)-N(11)-B(11)	119.99(18)	C(2E)-C(2D)-H(2D)	106.3
C(15)-N(11)-B(11)	120.79(17)	C(2C)-C(2D)-H(2D)	106.3
C(2G)-C(2H)-C(2I)	122.5(2)	C(2K)-C(2J)-C(2I)	121.5(2)
C(2G)-C(2H)-H(2H)	118.8	C(2K)-C(2J)-H(2J)	119.2
C(2I)-C(2H)-H(2H)	118.8	C(2I)-C(2J)-H(2J)	119.2
N(21)-C(25)-C(24)	119.3(2)	C(29)-C(2A)-C(2B)	121.5(3)
N(21)-C(25)-C(26)	119.1(2)	C(29)-C(2A)-H(2A)	119.3
C(24)-C(25)-C(26)	121.5(2)	C(2B)-C(2A)-H(2A)	119.3
C(2G)-C(2L)-C(2K)	120.4(2)	C(24)-C(23)-C(22)	119.0(2)
C(2G)-C(2L)-C(2M)	111.0(2)	C(24)-C(23)-H(23)	120.5
C(2K)-C(2L)-C(2M)	128.6(2)	C(22)-C(23)-H(23)	120.5
C(2Q)-C(2R)-C(2M)	117.4(2)	C(2D)-C(2E)-H(2E1)	109.5
C(2Q)-C(2R)-B(21)	133.1(2)	C(2D)-C(2E)-H(2E2)	109.5

H(2E1)-C(2E)-H(2E2)	109.5	H(2T1)-C(2T)-H(2T2)	109.5
C(2D)-C(2E)-H(2E3)	109.5	C(2S)-C(2T)-H(2T3)	109.5
H(2E1)-C(2E)-H(2E3)	109.5	H(2T1)-C(2T)-H(2T3)	109.5
H(2E2)-C(2E)-H(2E3)	109.5	H(2T2)-C(2T)-H(2T3)	109.5
C(2D)-C(2F)-H(2F1)	109.5	C(2W)-C(2X)-H(2X1)	109.5
C(2D)-C(2F)-H(2F2)	109.5	C(2W)-C(2X)-H(2X2)	109.5
H(2F1)-C(2F)-H(2F2)	109.5	H(2X1)-C(2X)-H(2X2)	109.5
C(2D)-C(2F)-H(2F3)	109.5	C(2W)-C(2X)-H(2X3)	109.5
H(2F1)-C(2F)-H(2F3)	109.5	H(2X1)-C(2X)-H(2X3)	109.5
H(2F2)-C(2F)-H(2F3)	109.5	H(2X2)-C(2X)-H(2X3)	109.5
C(2R)-C(2Q)-C(2P)	122.3(3)	C(2W)-C(2Y)-H(2Y1)	109.5
C(2R)-C(2Q)-H(2Q)	118.9	C(2W)-C(2Y)-H(2Y2)	109.5
C(2P)-C(2Q)-H(2Q)	118.9	H(2Y1)-C(2Y)-H(2Y2)	109.5
C(2N)-C(2O)-C(2P)	121.7(3)	C(2W)-C(2Y)-H(2Y3)	109.5
C(2N)-C(2O)-H(2O)	119.1	H(2Y1)-C(2Y)-H(2Y3)	109.5
C(2P)-C(2O)-H(2O)	119.1	H(2Y2)-C(2Y)-H(2Y3)	109.5
C(2O)-C(2P)-C(2Q)	117.6(3)	N(21)-B(21)-C(2R)	113.35(18)
C(2O)-C(2P)-C(2W)	121.6(3)	N(21)-B(21)-C(2C)	106.35(17)
C(2Q)-C(2P)-C(2W)	120.7(3)	C(2R)-B(21)-C(2C)	115.65(19)
C(2A)-C(29)-C(28)	120.0(3)	N(21)-B(21)-C(2G)	107.69(17)
C(2A)-C(29)-H(29)	120.0	C(2R)-B(21)-C(2G)	99.43(17)
C(28)-C(29)-H(29)	120.0	C(2C)-B(21)-C(2G)	114.22(18)
C(2T)-C(2S)-C(2V)	112.7(4)	C(21)-N(21)-C(25)	119.6(2)
C(2T)-C(2S)-C(2I)	114.1(3)	C(21)-N(21)-B(21)	120.08(19)
C(2V)-C(2S)-C(2I)	111.3(3)	C(25)-N(21)-B(21)	120.31(18)
C(2T)-C(2S)-C(2U)	108.2(4)	C(3A)-C(3B)-C(36)	117.97(19)
C(2V)-C(2S)-C(2U)	102.9(4)	C(3A)-C(3B)-C(3C)	121.47(19)
C(2I)-C(2S)-C(2U)	106.8(3)	C(36)-C(3B)-C(3C)	120.32(19)
C(27)-C(28)-C(29)	120.1(3)	C(3H)-C(3G)-C(3L)	117.9(2)
C(27)-C(28)-H(28)	120.0	C(3H)-C(3G)-B(31)	133.10(19)
C(29)-C(28)-H(28)	120.0	C(3L)-C(3G)-B(31)	108.96(19)
C(2Y)-C(2W)-C(2X)	113.8(7)	N(31)-C(35)-C(34)	119.6(2)
C(2Y)-C(2W)-C(2Z)	107.5(5)	N(31)-C(35)-C(36)	118.11(18)
C(2X)-C(2W)-C(2Z)	103.1(5)	C(34)-C(35)-C(36)	122.2(2)
C(2Y)-C(2W)-C(2P)	109.4(3)	C(39)-C(3A)-C(3B)	121.7(2)
C(2X)-C(2W)-C(2P)	109.9(4)	C(39)-C(3A)-H(3A)	119.1
C(2Z)-C(2W)-C(2P)	113.1(4)	C(3B)-C(3A)-H(3A)	119.1
C(2S)-C(2U)-H(2U1)	109.5	C(3N)-C(3M)-C(3R)	120.2(2)
C(2S)-C(2U)-H(2U2)	109.5	C(3N)-C(3M)-C(3L)	128.6(2)
H(2U1)-C(2U)-H(2U2)	109.5	C(3R)-C(3M)-C(3L)	111.16(18)
C(2S)-C(2U)-H(2U3)	109.5	C(37)-C(36)-C(3B)	119.9(2)
H(2U1)-C(2U)-H(2U3)	109.5	C(37)-C(36)-C(35)	119.2(2)
H(2U2)-C(2U)-H(2U3)	109.5	C(3B)-C(36)-C(35)	120.85(19)
C(2W)-C(2Z)-H(2Z1)	109.5	C(3O)-C(3P)-C(3Q)	117.5(2)
C(2W)-C(2Z)-H(2Z2)	109.5	C(3O)-C(3P)-C(3W)	122.1(2)
H(2Z1)-C(2Z)-H(2Z2)	109.5	C(3Q)-C(3P)-C(3W)	120.5(2)
C(2W)-C(2Z)-H(2Z3)	109.5	C(38)-C(37)-C(36)	120.6(2)
H(2Z1)-C(2Z)-H(2Z3)	109.5	C(38)-C(37)-H(37)	119.7
H(2Z2)-C(2Z)-H(2Z3)	109.5	C(36)-C(37)-H(37)	119.7
C(2S)-C(2V)-H(2V1)	109.5	C(3N)-C(3O)-C(3P)	121.3(2)
C(2S)-C(2V)-H(2V2)	109.5	C(3N)-C(3O)-H(3O)	119.3
H(2V1)-C(2V)-H(2V2)	109.5	C(3P)-C(3O)-H(3O)	119.3
C(2S)-C(2V)-H(2V3)	109.5	C(3R)-C(3Q)-C(3P)	122.6(2)
H(2V1)-C(2V)-H(2V3)	109.5	C(3R)-C(3Q)-H(3Q)	118.7
H(2V2)-C(2V)-H(2V3)	109.5	C(3P)-C(3Q)-H(3Q)	118.7
C(2S)-C(2T)-H(2T1)	109.5	C(38)-C(39)-C(3A)	120.0(2)
C(2S)-C(2T)-H(2T2)	109.5	C(38)-C(39)-H(39)	120.0

C(3A)-C(39)-H(39)	120.0	H(3F2)-C(3F)-H(3F3)	109.5
C(3J)-C(3K)-C(3L)	120.0(2)	C(3V)-C(3S)-C(3T)	112.7(4)
C(3J)-C(3K)-H(3K)	120.0	C(3V)-C(3S)-C(3I)	113.0(2)
C(3L)-C(3K)-H(3K)	120.0	C(3T)-C(3S)-C(3I)	108.8(3)
N(31)-C(31)-C(32)	122.6(2)	C(3V)-C(3S)-C(3U)	109.1(3)
N(31)-C(31)-H(31)	118.7	C(3T)-C(3S)-C(3U)	103.7(4)
C(32)-C(31)-H(31)	118.7	C(3I)-C(3S)-C(3U)	109.0(3)
C(37)-C(38)-C(39)	119.7(2)	C(3O)-C(3N)-C(3M)	120.2(2)
C(37)-C(38)-H(38)	120.1	C(3O)-C(3N)-H(3N)	119.9
C(39)-C(38)-H(38)	120.1	C(3M)-C(3N)-H(3N)	119.9
C(3G)-C(3H)-C(3I)	122.4(2)	C(3S)-C(3T)-H(3T1)	109.5
C(3G)-C(3H)-H(3H)	118.8	C(3S)-C(3T)-H(3T2)	109.5
C(3I)-C(3H)-H(3H)	118.8	H(3T1)-C(3T)-H(3T2)	109.5
C(3F)-C(3D)-C(3E)	109.9(2)	C(3S)-C(3T)-H(3T3)	109.5
C(3F)-C(3D)-C(3C)	115.0(2)	H(3T1)-C(3T)-H(3T3)	109.5
C(3E)-C(3D)-C(3C)	111.6(2)	H(3T2)-C(3T)-H(3T3)	109.5
C(3F)-C(3D)-H(3D)	106.6	C(3W)-C(3Y)-H(3Y1)	109.5
C(3E)-C(3D)-H(3D)	106.6	C(3W)-C(3Y)-H(3Y2)	109.5
C(3C)-C(3D)-H(3D)	106.6	H(3Y1)-C(3Y)-H(3Y2)	109.5
C(3B)-C(3C)-C(3D)	114.56(17)	C(3W)-C(3Y)-H(3Y3)	109.5
C(3B)-C(3C)-B(31)	106.79(17)	H(3Y1)-C(3Y)-H(3Y3)	109.5
C(3D)-C(3C)-B(31)	118.00(19)	H(3Y2)-C(3Y)-H(3Y3)	109.5
C(3B)-C(3C)-H(3C)	105.5	C(3W)-C(3Z)-H(3Z1)	109.5
C(3D)-C(3C)-H(3C)	105.5	C(3W)-C(3Z)-H(3Z2)	109.5
B(31)-C(3C)-H(3C)	105.5	H(3Z1)-C(3Z)-H(3Z2)	109.5
C(3K)-C(3J)-C(3I)	121.6(2)	C(3W)-C(3Z)-H(3Z3)	109.5
C(3K)-C(3J)-H(3J)	119.2	H(3Z1)-C(3Z)-H(3Z3)	109.5
C(3I)-C(3J)-H(3J)	119.2	H(3Z2)-C(3Z)-H(3Z3)	109.5
C(33)-C(34)-C(35)	120.7(2)	C(3S)-C(3V)-H(3V1)	109.5
C(33)-C(34)-H(34)	119.7	C(3S)-C(3V)-H(3V2)	109.5
C(35)-C(34)-H(34)	119.7	H(3V1)-C(3V)-H(3V2)	109.5
C(3H)-C(3I)-C(3J)	117.6(2)	C(3S)-C(3V)-H(3V3)	109.5
C(3H)-C(3I)-C(3S)	122.6(2)	H(3V1)-C(3V)-H(3V3)	109.5
C(3J)-C(3I)-C(3S)	119.8(2)	H(3V2)-C(3V)-H(3V3)	109.5
C(31)-C(32)-C(33)	119.0(2)	C(3K)-C(3L)-C(3G)	120.4(2)
C(31)-C(32)-H(32)	120.5	C(3K)-C(3L)-C(3M)	128.4(2)
C(33)-C(32)-H(32)	120.5	C(3G)-C(3L)-C(3M)	111.10(19)
C(3D)-C(3E)-H(3E1)	109.5	C(3W)-C(3X)-H(3X1)	109.5
C(3D)-C(3E)-H(3E2)	109.5	C(3W)-C(3X)-H(3X2)	109.5
H(3E1)-C(3E)-H(3E2)	109.5	H(3X1)-C(3X)-H(3X2)	109.5
C(3D)-C(3E)-H(3E3)	109.5	C(3W)-C(3X)-H(3X3)	109.5
H(3E1)-C(3E)-H(3E3)	109.5	H(3X1)-C(3X)-H(3X3)	109.5
H(3E2)-C(3E)-H(3E3)	109.5	H(3X2)-C(3X)-H(3X3)	109.5
C(3X)-C(3W)-C(3Z)	112.9(4)	C(3Q)-C(3R)-C(3M)	118.1(2)
C(3X)-C(3W)-C(3Y)	104.9(6)	C(3Q)-C(3R)-B(31)	132.9(2)
C(3Z)-C(3W)-C(3Y)	105.3(4)	C(3M)-C(3R)-B(31)	108.88(19)
C(3X)-C(3W)-C(3P)	111.5(3)	C(3S)-C(3U)-H(3U1)	109.5
C(3Z)-C(3W)-C(3P)	114.2(3)	C(3S)-C(3U)-H(3U2)	109.5
C(3Y)-C(3W)-C(3P)	107.2(3)	H(3U1)-C(3U)-H(3U2)	109.5
C(34)-C(33)-C(32)	118.7(2)	C(3S)-C(3U)-H(3U3)	109.5
C(34)-C(33)-H(33)	120.6	H(3U1)-C(3U)-H(3U3)	109.5
C(32)-C(33)-H(33)	120.6	H(3U2)-C(3U)-H(3U3)	109.5
C(3D)-C(3F)-H(3F1)	109.5	N(31)-B(31)-C(3R)	112.11(18)
C(3D)-C(3F)-H(3F2)	109.5	N(31)-B(31)-C(3G)	110.16(18)
H(3F1)-C(3F)-H(3F2)	109.5	C(3R)-B(31)-C(3G)	99.74(16)
C(3D)-C(3F)-H(3F3)	109.5	N(31)-B(31)-C(3C)	106.61(16)
H(3F1)-C(3F)-H(3F3)	109.5	C(3R)-B(31)-C(3C)	115.72(19)

C(3G)-B(31)-C(3C)	112.47(18)	C(4H)-C(4G)-H(4G)	118.7
C(31)-N(31)-C(35)	119.3(2)	C(4J)-C(4K)-C(4F)	120.6(2)
C(31)-N(31)-B(31)	121.04(18)	C(4J)-C(4K)-C(4L)	128.3(2)
C(35)-N(31)-B(31)	119.64(18)	C(4F)-C(4K)-C(4L)	110.99(18)
C(4X)-C(4VA)-C(4Y)	112.3(7)	C(4G)-C(4F)-C(4K)	117.79(19)
C(4X)-C(4VA)-C(4WA)	99.3(9)	C(4G)-C(4F)-B(41)	133.57(19)
C(4Y)-C(4VA)-C(4WA)	112.8(9)	C(4K)-C(4F)-B(41)	108.64(18)
C(4X)-C(4VA)-C(4O)	106.0(7)	C(43)-C(44)-C(45)	121.2(2)
C(4Y)-C(4VA)-C(4O)	107.1(6)	C(43)-C(44)-H(44)	119.4
C(4WA)-C(4VA)-C(4O)	119.0(7)	C(45)-C(44)-H(44)	119.4
C(4VA)-C(4WA)-H(4W1)	109.5	C(4M)-C(4L)-C(4Q)	120.7(2)
C(4VA)-C(4WA)-H(4W2)	109.5	C(4M)-C(4L)-C(4K)	128.2(2)
H(4W1)-C(4WA)-H(4W2)	109.5	C(4Q)-C(4L)-C(4K)	111.04(19)
C(4VA)-C(4WA)-H(4W3)	109.5	C(46)-C(4B)-C(4A)	117.6(2)
H(4W1)-C(4WA)-H(4W3)	109.5	C(46)-C(4B)-C(4C)	120.5(2)
H(4W2)-C(4WA)-H(4W3)	109.5	C(4A)-C(4B)-C(4C)	121.9(2)
C(4X)-C(4VB)-C(4WB)	102.4(10)	N(41)-C(41)-C(42)	122.6(2)
C(4X)-C(4VB)-C(4Y)	112.2(7)	N(41)-C(41)-H(41)	118.7
C(4WB)-C(4VB)-C(4Y)	110.7(7)	C(42)-C(41)-H(41)	118.7
C(4X)-C(4VB)-C(4O)	109.6(7)	C(42)-C(43)-C(44)	118.8(2)
C(4WB)-C(4VB)-C(4O)	120.7(7)	C(42)-C(43)-H(43)	120.6
C(4Y)-C(4VB)-C(4O)	101.6(8)	C(44)-C(43)-H(43)	120.6
C(4VB)-C(4WB)-H(4W4)	109.5	C(4I)-C(4H)-C(4G)	117.7(2)
C(4VB)-C(4WB)-H(4W5)	109.5	C(4I)-C(4H)-C(4R)	123.0(2)
H(4W4)-C(4WB)-H(4W5)	109.5	C(4G)-C(4H)-C(4R)	119.2(2)
C(4VB)-C(4WB)-H(4W6)	109.5	C(47)-C(46)-C(4B)	120.0(2)
H(4W4)-C(4WB)-H(4W6)	109.5	C(47)-C(46)-C(45)	119.6(2)
H(4W5)-C(4WB)-H(4W6)	109.5	C(4B)-C(46)-C(45)	120.3(2)
C(4VA)-C(4Y)-H(4Y1)	109.5	C(4N)-C(4M)-C(4L)	119.6(2)
C(4VA)-C(4Y)-H(4Y2)	109.5	C(4N)-C(4M)-H(4M)	120.2
H(4Y1)-C(4Y)-H(4Y2)	109.5	C(4L)-C(4M)-H(4M)	120.2
C(4VA)-C(4Y)-H(4Y3)	109.5	C(43)-C(42)-C(41)	118.6(2)
H(4Y1)-C(4Y)-H(4Y3)	109.5	C(43)-C(42)-H(42)	120.7
H(4Y2)-C(4Y)-H(4Y3)	109.5	C(41)-C(42)-H(42)	120.7
C(4VB)-C(4Y)-H(4Y4)	109.5	C(4J)-C(4I)-C(4H)	121.6(2)
C(4VB)-C(4Y)-H(4Y5)	109.5	C(4J)-C(4I)-H(4I)	119.2
H(4Y4)-C(4Y)-H(4Y5)	109.5	C(4H)-C(4I)-H(4I)	119.2
C(4VB)-C(4Y)-H(4Y6)	109.5	C(4P)-C(4Q)-C(4L)	117.7(2)
H(4Y4)-C(4Y)-H(4Y6)	109.5	C(4P)-C(4Q)-B(41)	132.8(2)
H(4Y5)-C(4Y)-H(4Y6)	109.5	C(4L)-C(4Q)-B(41)	109.5(2)
C(4VA)-C(4X)-H(4X1)	109.5	C(48)-C(47)-C(46)	120.6(3)
C(4VA)-C(4X)-H(4X2)	109.5	C(48)-C(47)-H(47)	119.7
H(4X1)-C(4X)-H(4X2)	109.5	C(46)-C(47)-H(47)	119.7
C(4VA)-C(4X)-H(4X3)	109.5	C(4S)-C(4R)-C(4T)	108.9(3)
H(4X1)-C(4X)-H(4X3)	109.5	C(4S)-C(4R)-C(4U)	108.6(3)
H(4X2)-C(4X)-H(4X3)	109.5	C(4T)-C(4R)-C(4U)	107.8(2)
C(4VB)-C(4X)-H(4X4)	109.5	C(4S)-C(4R)-C(4H)	109.2(2)
C(4VB)-C(4X)-H(4X5)	109.5	C(4T)-C(4R)-C(4H)	109.9(2)
H(4X4)-C(4X)-H(4X5)	109.5	C(4U)-C(4R)-C(4H)	112.4(3)
C(4VB)-C(4X)-H(4X6)	109.5	C(49)-C(4A)-C(4B)	121.5(3)
H(4X4)-C(4X)-H(4X6)	109.5	C(49)-C(4A)-H(4A)	119.2
H(4X5)-C(4X)-H(4X6)	109.5	C(4B)-C(4A)-H(4A)	119.2
N(41)-C(45)-C(44)	119.2(2)	C(49)-C(48)-C(47)	119.8(3)
N(41)-C(45)-C(46)	118.82(18)	C(49)-C(48)-H(48)	120.1
C(44)-C(45)-C(46)	122.0(2)	C(47)-C(48)-H(48)	120.1
C(4F)-C(4G)-C(4H)	122.5(2)	C(4A)-C(49)-C(48)	120.4(3)
C(4F)-C(4G)-H(4G)	118.7	C(4A)-C(49)-H(49)	119.8

C(48)-C(49)-H(49)	119.8
C(4Q)-C(4P)-C(4O)	122.4(3)
C(4Q)-C(4P)-H(4P)	118.8
C(4O)-C(4P)-H(4P)	118.8
C(4R)-C(4T)-H(4T1)	109.5
C(4R)-C(4T)-H(4T2)	109.5
H(4T1)-C(4T)-H(4T2)	109.5
C(4R)-C(4T)-H(4T3)	109.5
H(4T1)-C(4T)-H(4T3)	109.5
H(4T2)-C(4T)-H(4T3)	109.5
C(4R)-C(4U)-H(4U1)	109.5
C(4R)-C(4U)-H(4U2)	109.5
H(4U1)-C(4U)-H(4U2)	109.5
C(4R)-C(4U)-H(4U3)	109.5
H(4U1)-C(4U)-H(4U3)	109.5
H(4U2)-C(4U)-H(4U3)	109.5
C(4M)-C(4N)-C(4O)	121.7(3)
C(4M)-C(4N)-H(4N)	119.2
C(4O)-C(4N)-H(4N)	119.2
C(4R)-C(4S)-H(4S1)	109.5
C(4R)-C(4S)-H(4S2)	109.5
H(4S1)-C(4S)-H(4S2)	109.5
C(4R)-C(4S)-H(4S3)	109.5
H(4S1)-C(4S)-H(4S3)	109.5
H(4S2)-C(4S)-H(4S3)	109.5
C(4N)-C(4O)-C(4P)	117.8(3)
C(4N)-C(4O)-C(4VA)	126.8(4)
C(4P)-C(4O)-C(4VA)	113.1(5)
C(4N)-C(4O)-C(4VB)	111.8(5)
C(4P)-C(4O)-C(4VB)	125.5(4)
C(4I)-C(4J)-C(4K)	119.7(2)
C(4I)-C(4J)-H(4J)	120.1
C(4K)-C(4J)-H(4J)	120.1
N(41)-B(41)-C(4Q)	112.00(18)
N(41)-B(41)-C(4C)	105.92(17)
C(4Q)-B(41)-C(4C)	116.65(19)
N(41)-B(41)-C(4F)	109.77(17)
C(4Q)-B(41)-C(4F)	99.32(17)
C(4C)-B(41)-C(4F)	113.17(19)
C(41)-N(41)-C(45)	119.60(18)
C(41)-N(41)-B(41)	121.08(18)
C(45)-N(41)-B(41)	119.32(17)
C(4B)-C(4C)-C(4D)	113.6(2)
C(4B)-C(4C)-B(41)	107.73(18)
C(4D)-C(4C)-B(41)	116.8(2)
C(4B)-C(4C)-H(4C)	106.0
C(4D)-C(4C)-H(4C)	106.0
B(41)-C(4C)-H(4C)	106.0
C(4EC)-C(4D)-C(4EB)	118.7(7)
C(4EC)-C(4D)-C(4C)	116.0(2)
C(4EB)-C(4D)-C(4C)	116.0(6)
C(4EC)-C(4D)-C(4EA)	106.1(3)
C(4C)-C(4D)-C(4EA)	108.9(3)
C(4EC)-C(4D)-H(4D1)	108.5
C(4C)-C(4D)-H(4D1)	108.5
C(4EA)-C(4D)-H(4D1)	108.5
C(4EC)-C(4D)-H(4D2)	100.2
C(4EB)-C(4D)-H(4D2)	100.2
C(4C)-C(4D)-H(4D2)	100.2
C(4D)-C(4EA)-H(4E1)	109.5
C(4D)-C(4EA)-H(4E2)	109.5
H(4E1)-C(4EA)-H(4E2)	109.5
C(4D)-C(4EA)-H(4E3)	109.5
H(4E1)-C(4EA)-H(4E3)	109.5
H(4E2)-C(4EA)-H(4E3)	109.5
C(4D)-C(4EB)-H(4E4)	109.5
C(4D)-C(4EB)-H(4E5)	109.5
H(4E4)-C(4EB)-H(4E5)	109.5
C(4D)-C(4EB)-H(4E6)	109.5
H(4E4)-C(4EB)-H(4E6)	109.5
H(4E5)-C(4EB)-H(4E6)	109.5
C(4D)-C(4EC)-H(4E7)	109.5
C(4D)-C(4EC)-H(4E8)	109.5
H(4E7)-C(4EC)-H(4E8)	109.5
C(4D)-C(4EC)-H(4E9)	109.5
H(4E7)-C(4EC)-H(4E9)	109.5
H(4E8)-C(4EC)-H(4E9)	109.5

Table S 26. Anisotropic displacement parameters ($Å^2 x\ 10^3$)for PhPyBFlu. The anisotropic displacement factor exponent takes the form: $-2\pi^2[\ h^2 a^{*2} U^{11} + ... + 2\ h\ k\ a^*\ b^*\ U^{12}\ ]$

	U^{11}	U^{22}	U^{33}	U^{23}	U^{13}	U^{12}
C(1O)	28(1)	32(1)	50(1)	-1(1)	8(1)	-3(1)
C(1M)	30(1)	25(1)	46(1)	1(1)	9(1)	-3(1)
C(1P)	33(1)	29(1)	46(1)	-1(1)	10(1)	-5(1)
C(1Q)	33(1)	34(1)	49(1)	-4(1)	14(1)	-2(1)
C(16)	29(1)	35(1)	54(1)	3(1)	13(1)	1(1)
C(1K)	42(1)	36(1)	49(1)	1(1)	6(1)	4(1)
C(1L)	35(1)	26(1)	48(1)	3(1)	6(1)	0(1)
C(1A)	35(1)	35(1)	72(2)	6(1)	10(1)	-2(1)
C(1B)	29(1)	35(1)	60(1)	6(1)	13(1)	-1(1)
C(1N)	32(1)	30(1)	46(1)	-1(1)	12(1)	-1(1)
C(17)	33(1)	41(1)	58(1)	5(1)	11(1)	4(1)
C(15)	32(1)	35(1)	49(1)	6(1)	10(1)	2(1)
C(11)	38(1)	37(1)	65(2)	4(1)	14(1)	-4(1)
C(1G)	33(1)	28(1)	55(1)	5(1)	4(1)	-2(1)
C(18)	29(1)	52(1)	62(2)	3(1)	5(1)	-1(1)
C(1C)	30(1)	31(1)	65(2)	6(1)	9(1)	1(1)
C(1R)	30(1)	28(1)	53(1)	1(1)	12(1)	-2(1)
C(1W)	40(1)	39(1)	45(1)	-3(1)	9(1)	-4(1)
C(1H)	37(1)	37(1)	59(2)	7(1)	-1(1)	2(1)
C(1J)	53(1)	44(1)	43(1)	1(1)	1(1)	5(1)
C(14)	39(1)	37(1)	60(2)	5(1)	9(1)	6(1)
C(19)	34(1)	41(1)	71(2)	0(1)	8(1)	-7(1)
C(13)	52(1)	33(1)	61(2)	3(1)	10(1)	5(1)
C(12)	49(1)	35(1)	66(2)	1(1)	12(1)	-9(1)
C(1I)	48(1)	42(1)	50(1)	7(1)	-4(1)	1(1)
C(1D)	36(1)	52(1)	67(2)	15(1)	8(1)	-4(1)
C(1F)	54(2)	65(2)	61(2)	8(1)	16(1)	-4(1)
C(1E)	49(2)	64(2)	87(2)	29(2)	13(1)	-6(1)
C(1Z)	70(2)	59(2)	67(2)	-22(1)	-7(1)	7(1)
C(1S)	60(2)	74(2)	55(2)	11(1)	-13(1)	2(1)
C(1Y)	49(2)	83(2)	52(2)	-6(1)	2(1)	6(1)
C(1X)	82(2)	84(2)	52(2)	6(2)	12(2)	-24(2)
C(1V)	58(2)	115(3)	78(2)	8(2)	-18(2)	0(2)
C(1T)	94(3)	101(3)	72(2)	-24(2)	-23(2)	3(2)
C(1U)	87(3)	146(4)	70(2)	38(3)	-15(2)	7(3)
B(11)	29(1)	32(1)	57(2)	0(1)	8(1)	-2(1)
N(11)	32(1)	33(1)	52(1)	3(1)	12(1)	-3(1)
C(2H)	35(1)	49(1)	47(1)	-8(1)	9(1)	-1(1)
C(25)	41(1)	37(1)	53(1)	-8(1)	20(1)	-3(1)
C(2L)	30(1)	36(1)	57(1)	-11(1)	12(1)	-7(1)
C(2R)	32(1)	38(1)	51(1)	-4(1)	7(1)	-4(1)
C(2C)	31(1)	39(1)	48(1)	-13(1)	10(1)	-5(1)
C(2M)	29(1)	33(1)	60(1)	-7(1)	10(1)	-6(1)
C(21)	35(1)	49(1)	49(1)	-7(1)	10(1)	-9(1)
C(24)	52(1)	40(1)	74(2)	-14(1)	26(1)	-6(1)
C(2B)	32(1)	49(1)	50(1)	-10(1)	11(1)	3(1)
C(2G)	29(1)	38(1)	48(1)	-9(1)	10(1)	-4(1)
C(2K)	37(1)	44(1)	70(2)	-17(1)	22(1)	-3(1)
C(26)	41(1)	42(1)	56(1)	-7(1)	16(1)	6(1)
C(2I)	43(1)	68(2)	46(1)	-11(1)	12(1)	-7(1)
C(2N)	41(1)	38(1)	74(2)	-2(1)	12(1)	1(1)

C(27)	63(2)	49(2)	69(2)	-2(1)	21(1)	14(1)
C(22)	44(1)	64(2)	57(2)	-15(1)	14(1)	-19(1)
C(2D)	35(1)	52(1)	55(1)	-8(1)	14(1)	-6(1)
C(2J)	48(1)	62(2)	54(2)	-17(1)	22(1)	-5(1)
C(2A)	38(1)	67(2)	59(2)	-13(1)	5(1)	6(1)
C(23)	55(2)	48(1)	72(2)	-21(1)	26(1)	-20(1)
C(2E)	48(1)	57(2)	76(2)	-15(1)	24(1)	-14(1)
C(2F)	54(2)	83(2)	57(2)	-26(2)	27(1)	-28(1)
C(2Q)	44(1)	55(2)	51(1)	-1(1)	8(1)	-1(1)
C(2O)	47(1)	46(1)	78(2)	5(1)	4(1)	4(1)
C(2P)	52(2)	57(2)	62(2)	7(1)	-1(1)	-5(1)
C(29)	50(2)	94(2)	65(2)	-8(2)	0(1)	23(2)
C(2S)	80(2)	92(2)	45(2)	1(2)	12(1)	2(2)
C(28)	66(2)	71(2)	73(2)	3(2)	10(2)	27(2)
C(2W)	82(2)	84(2)	66(2)	18(2)	1(2)	2(2)
C(2U)	105(3)	151(5)	85(3)	25(3)	40(2)	2(3)
C(2Z)	165(6)	228(8)	111(4)	95(5)	29(4)	89(5)
C(2V)	162(5)	173(6)	53(2)	-10(3)	-2(3)	18(4)
C(2T)	201(6)	179(6)	66(3)	48(3)	46(3)	107(5)
C(2X)	600(20)	120(5)	86(4)	35(4)	123(8)	89(8)
C(2Y)	116(4)	453(15)	165(6)	208(9)	-22(4)	-96(7)
B(21)	33(1)	33(1)	44(1)	-7(1)	9(1)	-3(1)
N(21)	31(1)	39(1)	44(1)	-7(1)	13(1)	-4(1)
C(3B)	32(1)	36(1)	39(1)	-4(1)	13(1)	-3(1)
C(3G)	36(1)	29(1)	47(1)	1(1)	16(1)	2(1)
C(35)	40(1)	35(1)	45(1)	-1(1)	16(1)	-4(1)
C(3A)	36(1)	34(1)	50(1)	-5(1)	13(1)	-3(1)
C(3M)	36(1)	26(1)	51(1)	4(1)	17(1)	3(1)
C(36)	32(1)	37(1)	45(1)	-2(1)	16(1)	-6(1)
C(3P)	36(1)	42(1)	59(1)	10(1)	9(1)	4(1)
C(37)	39(1)	41(1)	47(1)	-7(1)	15(1)	-12(1)
C(3O)	31(1)	39(1)	68(2)	10(1)	15(1)	3(1)
C(3Q)	35(1)	48(1)	52(1)	12(1)	14(1)	0(1)
C(39)	36(1)	43(1)	50(1)	1(1)	9(1)	2(1)
C(3K)	46(1)	44(1)	54(1)	4(1)	24(1)	-1(1)
C(31)	50(1)	41(1)	56(1)	9(1)	19(1)	9(1)
C(38)	34(1)	49(1)	47(1)	-3(1)	9(1)	-6(1)
C(3H)	42(1)	37(1)	47(1)	1(1)	14(1)	0(1)
C(3D)	37(1)	54(1)	47(1)	-10(1)	9(1)	-1(1)
C(3C)	30(1)	34(1)	47(1)	-2(1)	11(1)	-4(1)
C(3J)	57(2)	53(1)	45(1)	7(1)	20(1)	-1(1)
C(34)	50(1)	39(1)	62(2)	-1(1)	20(1)	-8(1)
C(3I)	50(1)	45(1)	45(1)	2(1)	14(1)	2(1)
C(32)	64(2)	37(1)	72(2)	11(1)	22(1)	9(1)
C(3E)	53(2)	65(2)	62(2)	-21(1)	14(1)	-3(1)
C(3W)	40(1)	80(2)	61(2)	21(2)	4(1)	-1(1)
C(33)	70(2)	36(1)	74(2)	8(1)	27(1)	-4(1)
C(3F)	67(2)	68(2)	46(1)	1(1)	21(1)	3(1)
C(3S)	66(2)	73(2)	46(1)	9(1)	9(1)	4(1)
C(3N)	36(1)	35(1)	62(1)	9(1)	21(1)	3(1)
C(3T)	102(3)	237(7)	62(2)	-56(3)	0(2)	17(4)
C(3Y)	287(9)	166(6)	166(6)	120(5)	-134(6)	-105(6)
C(3Z)	60(2)	211(6)	76(2)	23(3)	-7(2)	-36(3)
C(3V)	63(2)	181(5)	61(2)	24(3)	-6(2)	-28(3)
C(3L)	39(1)	27(1)	48(1)	1(1)	17(1)	1(1)
C(3X)	99(4)	530(17)	67(3)	-91(6)	-24(3)	121(6)
C(3R)	34(1)	36(1)	52(1)	7(1)	15(1)	1(1)

C(3U)	104(3)	132(4)	99(3)	53(3)	-2(2)	0(3)
B(31)	31(1)	36(1)	45(1)	4(1)	11(1)	-1(1)
N(31)	40(1)	34(1)	45(1)	3(1)	17(1)	1(1)
C(4VA)	154(8)	68(4)	52(4)	18(3)	14(4)	34(5)
C(4WA)	198(9)	250(15)	75(6)	81(7)	55(6)	36(7)
C(4VB)	132(7)	81(5)	67(5)	40(4)	37(5)	49(5)
C(4WB)	143(7)	118(7)	68(5)	13(5)	-31(5)	15(5)
C(4Y)	217(6)	83(3)	73(3)	36(2)	20(3)	39(3)
C(4X)	241(6)	118(4)	56(2)	9(2)	-4(3)	50(4)
C(45)	32(1)	30(1)	49(1)	-3(1)	13(1)	-2(1)
C(4G)	36(1)	30(1)	44(1)	-2(1)	6(1)	-5(1)
C(4K)	29(1)	29(1)	45(1)	-5(1)	9(1)	-7(1)
C(4F)	31(1)	29(1)	42(1)	-5(1)	9(1)	-6(1)
C(44)	37(1)	32(1)	60(1)	-5(1)	12(1)	-2(1)
C(4L)	39(1)	29(1)	48(1)	-4(1)	9(1)	-2(1)
C(4B)	33(1)	44(1)	60(1)	-18(1)	14(1)	-5(1)
C(41)	33(1)	42(1)	40(1)	-1(1)	9(1)	1(1)
C(43)	42(1)	37(1)	59(1)	-10(1)	16(1)	-12(1)
C(4H)	41(1)	44(1)	39(1)	-4(1)	7(1)	-16(1)
C(46)	33(1)	37(1)	56(1)	-9(1)	9(1)	2(1)
C(4M)	61(2)	32(1)	58(2)	-4(1)	7(1)	9(1)
C(42)	37(1)	51(1)	43(1)	-7(1)	9(1)	-10(1)
C(4I)	40(1)	48(1)	45(1)	-12(1)	14(1)	-11(1)
C(4Q)	60(1)	30(1)	45(1)	1(1)	14(1)	2(1)
C(47)	50(1)	45(1)	66(2)	-6(1)	2(1)	8(1)
C(4R)	62(2)	56(2)	40(1)	2(1)	6(1)	-14(1)
C(4A)	35(1)	66(2)	83(2)	-29(2)	8(1)	-10(1)
C(48)	57(2)	66(2)	76(2)	-11(2)	-9(1)	19(1)
C(49)	41(1)	89(2)	86(2)	-26(2)	-11(1)	10(2)
C(4P)	144(3)	43(2)	45(2)	5(1)	24(2)	26(2)
C(4T)	92(2)	56(2)	50(2)	12(1)	8(1)	-11(2)
C(4U)	118(3)	79(2)	45(2)	3(2)	23(2)	-9(2)
C(4N)	134(3)	42(2)	63(2)	3(1)	-1(2)	36(2)
C(4S)	68(2)	103(3)	61(2)	18(2)	-14(2)	-17(2)
C(4O)	210(5)	57(2)	48(2)	9(2)	10(2)	53(3)
C(4J)	33(1)	38(1)	51(1)	-10(1)	15(1)	-4(1)
B(41)	41(1)	25(1)	43(1)	-4(1)	12(1)	-3(1)
N(41)	31(1)	31(1)	41(1)	-2(1)	11(1)	-2(1)
C(4C)	44(1)	34(1)	57(1)	-13(1)	21(1)	-11(1)
C(4D)	75(2)	51(2)	68(2)	-14(1)	41(2)	-18(1)
C(4EA)	88(3)	121(4)	99(3)	-49(3)	63(3)	-65(3)
C(4EB)	75(10)	53(6)	75(10)	9(6)	43(8)	-26(7)
C(4EC)	89(2)	86(2)	83(2)	-26(2)	41(2)	-30(2)

Table S 27. Hydrogen coordinates (x 10^4) and isotropic displacement parameters ($Å^2$x 10^3) for PhPyBFlu.

	x	y	z	U(eq)
H(1O)	3575	1899	3589	44
H(1Q)	1626	2227	3983	45
H(1K)	2111	1532	1914	51
H(1A)	-991	936	2913	57
H(1N)	2951	1762	2740	43
H(17)	-1894	2586	2421	52
H(11)	1206	2983	3113	56
H(18)	-2659	1863	2218	58
H(1C)	245	1271	3091	50
H(1H)	-373	1876	1930	55
H(1J)	1191	1393	1177	58
H(14)	-1322	3187	2903	55
H(19)	-2209	1042	2470	59
H(13)	-560	3917	3041	59
H(12)	730	3810	3134	60
H(1D)	783	1529	3925	62
H(1F1)	-497	2147	3915	89
H(1F2)	336	2357	3985	89
H(1F3)	106	2009	4424	89
H(1E1)	-26	1091	4348	101
H(1E2)	18	793	3829	101
H(1E3)	-687	1145	3854	101
H(1Z1)	2402	2749	4564	103
H(1Z2)	3174	2921	4433	103
H(1Z3)	3153	2706	4992	103
H(1Y1)	4120	2273	4358	94
H(1Y2)	3971	1670	4433	94
H(1Y3)	4096	2054	4916	94
H(1X1)	2948	1784	5134	109
H(1X2)	2794	1386	4663	109
H(1X3)	2178	1805	4722	109
H(1V1)	-1122	1980	1125	133
H(1V2)	-1149	1394	1315	133
H(1V3)	-1402	1529	718	133
H(1T1)	-308	730	1035	142
H(1T2)	302	919	728	142
H(1T3)	-559	925	454	142
H(1U1)	-432	1825	231	158
H(1U2)	413	1869	535	158
H(1U3)	-195	2264	659	158
H(2H)	8888	7416	2993	53
H(2C)	9677	8186	2170	47
H(21)	7300	7592	1339	53
H(24)	8656	6104	1800	64
H(2K)	7384	8877	2923	59
H(2N)	7125	9272	2047	61
H(27)	9437	6202	2510	71
H(22)	6805	6803	1025	65
H(2D)	9454	8259	1278	56
H(2J)	7701	8400	3675	63
H(2A)	10772	7746	2623	66
H(23)	7498	6045	1254	68
H(2E1)	10785	7701	1643	88
H(2E2)	10681	8307	1733	88
H(2E3)	10636	8091	1165	88

H(2F1)	9606	7573	741	93
H(2F2)	8894	7487	985	93
H(2F3)	9644	7174	1205	93
H(2Q)	8280	8377	916	61
H(2O)	7076	9593	1228	70
H(29)	11265	7031	3105	86
H(28)	10603	6254	3037	85
H(2U1)	7530	7102	3764	166
H(2U2)	7437	7639	4043	166
H(2U3)	7864	7167	4365	166
H(2Z1)	7317	10000	558	252
H(2Z2)	6700	9581	318	252
H(2Z3)	7222	9826	-29	252
H(2V1)	8787	7706	4685	199
H(2V2)	8537	8207	4338	199
H(2V3)	9345	7965	4372	199
H(2T1)	9464	7206	3815	219
H(2T2)	8741	6861	3608	219
H(2T3)	9075	6903	4211	219
H(2X1)	7434	9070	-277	393
H(2X2)	7097	8703	101	393
H(2X3)	7950	8648	66	393
H(2Y1)	8547	9649	181	378
H(2Y2)	8881	9236	616	378
H(2Y3)	8588	9784	773	378
H(3A)	4102	963	3020	47
H(37)	3258	-703	2539	50
H(3O)	8663	56	3705	54
H(3Q)	6745	-263	4151	53
H(39)	2939	844	2489	52
H(3K)	7123	354	2032	55
H(31)	6328	-1067	3360	57
H(38)	2519	11	2242	52
H(3H)	4678	-24	2122	49
H(3D)	5829	360	4120	55
H(3C)	5337	638	3281	44
H(3J)	6182	430	1308	60
H(34)	3796	-1281	3122	59
H(32)	5859	-1887	3433	68
H(3E1)	4353	743	4011	89
H(3E2)	5066	1095	4005	89
H(3E3)	4993	795	4518	89
H(33)	4570	-2000	3324	70
H(3F1)	5155	-138	4593	89
H(3F2)	5350	-475	4135	89
H(3F3)	4532	-247	4087	89
H(3N)	8009	165	2867	51
H(3T1)	4890	-471	851	204
H(3T2)	5443	-38	720	204
H(3T3)	4596	-49	416	204
H(3Y1)	8218	-756	5094	350
H(3Y2)	8582	-904	4619	350
H(3Y3)	7699	-874	4544	350
H(3Z1)	9040	355	4621	178
H(3Z2)	9218	-208	4427	178
H(3Z3)	9231	-112	5022	178
H(3V1)	3606	229	918	156
H(3V2)	3891	344	1517	156
H(3V3)	3928	-232	1302	156
H(3X1)	7993	-17	5278	357

H(3X2)	7276	43	4824	357
H(3X3)	7900	484	4917	357
H(3U1)	4441	789	557	173
H(3U2)	5257	878	897	173
H(3U3)	4546	1039	1117	173
H(4W1)	1991	7711	5063	256
H(4W2)	1583	7666	4472	256
H(4W3)	1712	8223	4741	256
H(4W4)	4102	8533	4552	176
H(4W5)	4288	7948	4428	176
H(4W6)	4285	8116	5005	176
H(4Y1)	2893	7158	4457	189
H(4Y2)	3623	7504	4627	189
H(4Y3)	3156	7337	5042	189
H(4Y4)	3304	7222	4434	189
H(4Y5)	3406	7359	5030	189
H(4Y6)	2597	7367	4665	189
H(4X1)	2666	8664	4812	215
H(4X2)	3014	8269	5261	215
H(4X3)	3482	8436	4845	215
H(4X4)	2452	8304	4878	215
H(4X5)	3256	8285	5250	215
H(4X6)	3069	8720	4814	215
H(4G)	1152	9578	1954	45
H(44)	1285	10870	3134	51
H(41)	2752	9442	3634	46
H(43)	2414	10976	3711	54
H(4M)	2931	7704	2870	61
H(42)	3160	10249	3965	52
H(4I)	2298	8584	1245	52
H(47)	541	10731	2398	66
H(4A)	-704	9155	2359	74
H(48)	-631	10625	1870	84
H(49)	-1250	9839	1859	91
H(4P)	2046	8715	4060	92
H(4T1)	1469	10157	1404	101
H(4T2)	1505	10222	813	101
H(4T3)	2225	10041	1221	101
H(4U1)	2330	9274	685	120
H(4U2)	1614	9471	281	120
H(4U3)	1635	8896	508	120
H(4N)	3237	7499	3731	100
H(4S1)	451	9069	784	123
H(4S2)	440	9642	554	123
H(4S3)	382	9558	1139	123
H(4J)	2615	8096	1993	48
H(4C)	436	8758	2813	52
H(4D1)	695	8716	3720	73
H(4D2)	-122	9052	3442	73
H(4E1)	-558	8861	3797	145
H(4E2)	-578	8634	3236	145
H(4E3)	-700	9240	3311	145
H(4E4)	611	8529	4144	95
H(4E5)	912	8318	3662	95
H(4E6)	42	8309	3653	95
H(4E7)	432	9409	4203	124
H(4E8)	346	9782	3715	124
H(4E9)	1137	9537	3964	124

4.5. $PhPyBPh_2$

Table S 28. Crystal data and structure refinement for $PhPyBPh_2$.

Identification code	**$PhPyBPh_2$**	
Empirical formula	$C_{27}H_{26}BN$	
Formula weight	375.30	
Temperature	150(2) K	
Wavelength	0.71073 Å	
Crystal system	Orthorhombic	
Space group	Pccn	
Unit cell dimensions	a = 13.4057(3) Å	α= 90°.
	b = 15.1283(3) Å	β= 90°.
	c = 20.2250(5) Å	γ= 90°.
Volume	4101.74(16) $Å^3$	
Z	8	
Density (calculated)	1.215 Mg/m^3	
Absorption coefficient	0.069 mm^{-1}	
F(000)	1600	
Crystal colour and habit	Colorless prism	
Crystal size	0.244 x 0.181 x 0.142 mm^3	
Theta range for data collection	2.860 to 29.470°.	
Index ranges	-17<=h<=18, -15<=k<=20, -26<=l<=27	
Reflections collected	20641	
Independent reflections	5084 [R(int) = 0.0342]	
Completeness to theta = 25.242°	99.8 %	
Absorption correction	Semi-empirical from equivalents	
Max. and min. transmission	1.00000 and 0.86784	
Refinement method	Full-matrix least-squares on F^2	
Data / restraints / parameters	5084 / 0 / 264	
Goodness-of-fit on F^2	1.077	
Final R indices [I>2sigma(I)]	R1 = 0.0478, wR2 = 0.1078	
R indices (all data)	R1 = 0.0669, wR2 = 0.1174	
Extinction coefficient	n/a	
Largest diff. peak and hole	0.257 and -0.239 e.$Å^{-3}$	

Definitions:

$$R_1 = \frac{\sum \| F_o | - | F_c \|}{\sum | F_o |} \qquad wR_2 = \sqrt{\frac{\sum \left[w\left(F_o^2 - F_c^2 \right)^2 \right]}{\sum \left[w\left(F_o^2 \right)^2 \right]}}$$

$$GooF = \sqrt{\frac{\sum \left[w\left(F_o^2 - F_c^2 \right) \right]}{(n-p)}}$$

n = number of reflections; p = number of parameters

Notes on the refinement of $PhPyBPh_2$.

All hydrogen atoms were placed in calculated positions and refined by using a riding model.

Table S 29. Atomic coordinates (x 10^4) and equivalent isotropic displacement parameters ($Å^2$x 10^3) for $PhPyBPh_2$. U(eq) is defined as one third of the trace of the orthogonalized U^{ij} tensor.

	x	y	z	U(eq)
C(1)	5497(1)	5394(1)	2769(1)	27(1)
C(2)	5810(1)	5365(1)	3418(1)	34(1)
C(3)	6724(1)	4987(1)	3551(1)	36(1)
C(4)	7261(1)	4613(1)	3045(1)	30(1)
C(5)	6904(1)	4632(1)	2398(1)	22(1)
C(6)	7448(1)	4197(1)	1853(1)	22(1)
C(7)	8094(1)	3494(1)	1999(1)	29(1)
C(8)	8619(1)	3072(1)	1503(1)	34(1)
C(9)	8499(1)	3336(1)	856(1)	33(1)
C(10)	7856(1)	4025(1)	707(1)	28(1)
C(11)	7325(1)	4470(1)	1195(1)	21(1)
C(12)	6643(1)	5234(1)	1042(1)	19(1)
C(13)	7225(1)	6127(1)	1025(1)	24(1)
C(14)	7923(1)	6187(1)	430(1)	35(1)
C(15)	7809(1)	6328(1)	1652(1)	32(1)
C(16)	5002(1)	4271(1)	1355(1)	19(1)
C(17)	4391(1)	3869(1)	1826(1)	26(1)
C(18)	3811(1)	3132(1)	1683(1)	30(1)
C(19)	3819(1)	2769(1)	1056(1)	28(1)
C(20)	4408(1)	3153(1)	576(1)	28(1)
C(21)	4985(1)	3885(1)	727(1)	25(1)
C(22)	4968(1)	6053(1)	1427(1)	19(1)
C(23)	4223(1)	6073(1)	943(1)	20(1)
C(24)	3701(1)	6836(1)	783(1)	25(1)
C(25)	3889(1)	7612(1)	1121(1)	30(1)
C(26)	4608(1)	7619(1)	1611(1)	30(1)
C(27)	5139(1)	6856(1)	1754(1)	26(1)
B(1)	5645(1)	5165(1)	1507(1)	19(1)
N(1)	6035(1)	5063(1)	2267(1)	20(1)

Table S 30. Bond lengths [Å] and angles [°] for $PhPyBPh_2$.

C(1)-N(1)	1.3430(18)	C(25)-H(25)	0.9500
C(1)-C(2)	1.377(2)	C(26)-C(27)	1.387(2)
C(1)-H(1)	0.9500	C(26)-H(26)	0.9500
C(2)-C(3)	1.379(3)	C(27)-H(27)	0.9500
C(2)-H(2)	0.9500	B(1)-N(1)	1.6322(18)
C(3)-C(4)	1.372(2)		
C(3)-H(3)	0.9500	N(1)-C(1)-C(2)	122.94(15)
C(4)-C(5)	1.393(2)	N(1)-C(1)-H(1)	118.5
C(4)-H(4)	0.9500	C(2)-C(1)-H(1)	118.5
C(5)-N(1)	1.3607(18)	C(1)-C(2)-C(3)	118.02(15)
C(5)-C(6)	1.476(2)	C(1)-C(2)-H(2)	121.0
C(6)-C(7)	1.403(2)	C(3)-C(2)-H(2)	121.0
C(6)-C(11)	1.4043(19)	C(4)-C(3)-C(2)	119.45(15)
C(7)-C(8)	1.383(2)	C(4)-C(3)-H(3)	120.3
C(7)-H(7)	0.9500	C(2)-C(3)-H(3)	120.3
C(8)-C(9)	1.377(2)	C(3)-C(4)-C(5)	120.76(15)
C(8)-H(8)	0.9500	C(3)-C(4)-H(4)	119.6
C(9)-C(10)	1.386(2)	C(5)-C(4)-H(4)	119.6
C(9)-H(9)	0.9500	N(1)-C(5)-C(4)	119.11(13)
C(10)-C(11)	1.390(2)	N(1)-C(5)-C(6)	119.37(12)
C(10)-H(10)	0.9500	C(4)-C(5)-C(6)	121.52(13)
C(11)-C(12)	1.5061(19)	C(7)-C(6)-C(11)	119.68(14)
C(12)-C(13)	1.5601(19)	C(7)-C(6)-C(5)	119.02(13)
C(12)-B(1)	1.639(2)	C(11)-C(6)-C(5)	121.30(12)
C(12)-H(12)	1.0000	C(8)-C(7)-C(6)	120.75(15)
C(13)-C(15)	1.522(2)	C(8)-C(7)-H(7)	119.6
C(13)-C(14)	1.527(2)	C(6)-C(7)-H(7)	119.6
C(13)-H(13)	1.0000	C(9)-C(8)-C(7)	119.76(14)
C(14)-H(14A)	0.9800	C(9)-C(8)-H(8)	120.1
C(14)-H(14B)	0.9800	C(7)-C(8)-H(8)	120.1
C(14)-H(14C)	0.9800	C(8)-C(9)-C(10)	119.86(15)
C(15)-H(15A)	0.9800	C(8)-C(9)-H(9)	120.1
C(15)-H(15B)	0.9800	C(10)-C(9)-H(9)	120.1
C(15)-H(15C)	0.9800	C(9)-C(10)-C(11)	121.88(15)
C(16)-C(17)	1.3961(19)	C(9)-C(10)-H(10)	119.1
C(16)-C(21)	1.3972(19)	C(11)-C(10)-H(10)	119.1
C(16)-B(1)	1.634(2)	C(10)-C(11)-C(6)	118.06(13)
C(17)-C(18)	1.390(2)	C(10)-C(11)-C(12)	122.46(13)
C(17)-H(17)	0.9500	C(6)-C(11)-C(12)	119.47(12)
C(18)-C(19)	1.383(2)	C(11)-C(12)-C(13)	111.39(11)
C(18)-H(18)	0.9500	C(11)-C(12)-B(1)	109.20(11)
C(19)-C(20)	1.379(2)	C(13)-C(12)-B(1)	118.44(11)
C(19)-H(19)	0.9500	C(11)-C(12)-H(12)	105.6
C(20)-C(21)	1.385(2)	C(13)-C(12)-H(12)	105.6
C(20)-H(20)	0.9500	B(1)-C(12)-H(12)	105.6
C(21)-H(21)	0.9500	C(15)-C(13)-C(14)	109.27(12)
C(22)-C(23)	1.3989(19)	C(15)-C(13)-C(12)	114.32(12)
C(22)-C(27)	1.4023(19)	C(14)-C(13)-C(12)	112.07(12)
C(22)-B(1)	1.629(2)	C(15)-C(13)-H(13)	106.9
C(23)-C(24)	1.3873(19)	C(14)-C(13)-H(13)	106.9
C(23)-H(23)	0.9500	C(12)-C(13)-H(13)	106.9
C(24)-C(25)	1.383(2)	C(13)-C(14)-H(14A)	109.5
C(24)-H(24)	0.9500	C(13)-C(14)-H(14B)	109.5
C(25)-C(26)	1.382(2)	H(14A)-C(14)-H(14B)	109.5

C(13)-C(14)-H(14C)	109.5
H(14A)-C(14)-H(14C)	109.5
H(14B)-C(14)-H(14C)	109.5
C(13)-C(15)-H(15A)	109.5
C(13)-C(15)-H(15B)	109.5
H(15A)-C(15)-H(15B)	109.5
C(13)-C(15)-H(15C)	109.5
H(15A)-C(15)-H(15C)	109.5
H(15B)-C(15)-H(15C)	109.5
C(17)-C(16)-C(21)	115.35(13)
C(17)-C(16)-B(1)	122.80(12)
C(21)-C(16)-B(1)	121.75(12)
C(18)-C(17)-C(16)	122.45(14)
C(18)-C(17)-H(17)	118.8
C(16)-C(17)-H(17)	118.8
C(19)-C(18)-C(17)	120.26(14)
C(19)-C(18)-H(18)	119.9
C(17)-C(18)-H(18)	119.9
C(20)-C(19)-C(18)	118.95(14)
C(20)-C(19)-H(19)	120.5
C(18)-C(19)-H(19)	120.5
C(19)-C(20)-C(21)	120.01(14)
C(19)-C(20)-H(20)	120.0
C(21)-C(20)-H(20)	120.0
C(20)-C(21)-C(16)	122.98(14)
C(20)-C(21)-H(21)	118.5
C(16)-C(21)-H(21)	118.5
C(23)-C(22)-C(27)	115.33(12)
C(23)-C(22)-B(1)	119.05(12)
C(27)-C(22)-B(1)	125.19(12)
C(24)-C(23)-C(22)	122.79(13)
C(24)-C(23)-H(23)	118.6
C(22)-C(23)-H(23)	118.6
C(25)-C(24)-C(23)	119.96(14)
C(25)-C(24)-H(24)	120.0
C(23)-C(24)-H(24)	120.0
C(26)-C(25)-C(24)	119.22(14)
C(26)-C(25)-H(25)	120.4
C(24)-C(25)-H(25)	120.4
C(25)-C(26)-C(27)	120.08(14)
C(25)-C(26)-H(26)	120.0
C(27)-C(26)-H(26)	120.0
C(26)-C(27)-C(22)	122.60(14)
C(26)-C(27)-H(27)	118.7
C(22)-C(27)-H(27)	118.7
C(22)-B(1)-N(1)	110.54(11)
C(22)-B(1)-C(16)	111.71(11)
N(1)-B(1)-C(16)	105.55(10)
C(22)-B(1)-C(12)	110.18(11)
N(1)-B(1)-C(12)	106.60(10)
C(16)-B(1)-C(12)	112.05(11)
C(1)-N(1)-C(5)	119.46(12)
C(1)-N(1)-B(1)	120.31(11)
C(5)-N(1)-B(1)	120.23(11)

Table S 31. Anisotropic displacement parameters ($Å^2 x\ 10^3$)for $PhPyBPh_2$. The anisotropic displacement factor exponent takes the form: $-2\pi^2[\ h^2a^{*2}U^{11} + ... + 2\ h\ k\ a^*\ b^*\ U^{12}\ ]$

	U^{11}	U^{22}	U^{33}	U^{23}	U^{13}	U^{12}
C(1)	33(1)	24(1)	25(1)	-1(1)	1(1)	3(1)
C(2)	51(1)	30(1)	22(1)	-3(1)	1(1)	2(1)
C(3)	52(1)	34(1)	23(1)	2(1)	-11(1)	-3(1)
C(4)	33(1)	27(1)	30(1)	6(1)	-10(1)	-3(1)
C(5)	23(1)	16(1)	27(1)	4(1)	-5(1)	-3(1)
C(6)	19(1)	17(1)	31(1)	1(1)	-3(1)	-2(1)
C(7)	21(1)	21(1)	44(1)	6(1)	-7(1)	-1(1)
C(8)	21(1)	21(1)	60(1)	1(1)	-2(1)	4(1)
C(9)	24(1)	26(1)	50(1)	-10(1)	4(1)	2(1)
C(10)	23(1)	27(1)	35(1)	-6(1)	1(1)	-2(1)
C(11)	17(1)	17(1)	29(1)	-2(1)	-1(1)	-3(1)
C(12)	19(1)	19(1)	20(1)	-1(1)	-2(1)	0(1)
C(13)	23(1)	20(1)	28(1)	3(1)	0(1)	0(1)
C(14)	33(1)	31(1)	41(1)	7(1)	9(1)	-3(1)
C(15)	33(1)	23(1)	38(1)	3(1)	-9(1)	-9(1)
C(16)	16(1)	18(1)	23(1)	1(1)	-2(1)	4(1)
C(17)	26(1)	26(1)	24(1)	-1(1)	2(1)	-1(1)
C(18)	26(1)	29(1)	35(1)	5(1)	4(1)	-6(1)
C(19)	22(1)	21(1)	42(1)	-2(1)	-4(1)	-2(1)
C(20)	27(1)	26(1)	30(1)	-6(1)	-4(1)	-1(1)
C(21)	26(1)	25(1)	24(1)	-1(1)	1(1)	-3(1)
C(22)	18(1)	19(1)	21(1)	2(1)	4(1)	0(1)
C(23)	20(1)	21(1)	20(1)	1(1)	2(1)	-1(1)
C(24)	22(1)	27(1)	26(1)	3(1)	-3(1)	4(1)
C(25)	28(1)	22(1)	38(1)	2(1)	0(1)	7(1)
C(26)	31(1)	19(1)	39(1)	-5(1)	-2(1)	2(1)
C(27)	23(1)	23(1)	32(1)	-3(1)	-5(1)	1(1)
B(1)	19(1)	18(1)	19(1)	1(1)	-3(1)	1(1)
N(1)	23(1)	18(1)	20(1)	0(1)	-2(1)	-1(1)

Table S 32. Hydrogen coordinates (x 10^4) and isotropic displacement parameters ($Å^2$x 10^3) for $PhPyBPh_2$.

	x	y	z	U(eq)
H(1)	4872	5661	2673	33
H(2)	5408	5599	3763	41
H(3)	6980	4985	3989	43
H(4)	7882	4338	3137	36
H(7)	8172	3306	2444	35
H(8)	9062	2602	1607	41
H(9)	8855	3046	513	40
H(10)	7777	4199	259	34
H(12)	6406	5134	579	23
H(13)	6718	6607	973	28
H(14A)	8216	6780	409	52
H(14B)	7546	6072	24	52
H(14C)	8456	5748	474	52
H(15A)	7350	6352	2029	47
H(15B)	8147	6899	1605	47
H(15C)	8305	5863	1726	47
H(17)	4370	4109	2260	31
H(18)	3408	2875	2019	36
H(19)	3424	2264	957	34
H(20)	4418	2914	141	33
H(21)	5387	4136	389	30
H(23)	4069	5543	713	24
H(24)	3213	6824	442	30
H(25)	3530	8135	1017	35
H(26)	4738	8147	1850	36
H(27)	5639	6878	2087	31

[i] M. Y. Lin, A. Das, R. S. Liu, *J. Am. Chem. Soc.* **2006**, *128*, 9340–9341.
[ii] D. J. Parks, W. E. Piers, G. P. A. Yap, *Organometallics* **1998**, *17*, 5492–5503.
[iii] A. Hübner, M. Diefenbach, M. Bolte, H. W. Lerner, M. C. Holthausen, M. Wagner, *Angew. Chem. - Int. Ed.* **2012**, *51*, 12514–12518.
[iv] W. L. F. Armarego, D. D. Perrin, *Purification of Laboratory Chemicals*, 4th Ed. Butterworth-Heinemann, Oxford, **1997**.
[v] G. R. Fulmer, A. J. M. Miller, N. H. Sherden, H. E. Gottlieb, A. Nudelman, B. M. Stoltz, J. E. Bercaw, K. I. Goldberg, *Organometallics* **2010**, *29*, 2176-2179.
[vi] J. Q. Umberger, V. K. LaMer, *J. Am. Chem. Soc.* **1945**, *67*, 1099.
[vii] Y.Zhao, D. G. Truhlar, *J.* Chem. *Theory Comput.* **2008**, *4*, 1849.
[viii] a) Z. M. Heiden, A. P. Lathem, *Organometallics* **2015**, *34*, 1818; b) E. R. Clark, A. Del Grosso, M. J. Ingleson, *Chem. Eur. J.* **2013**, *19*, 2462; c) T. S. De Vries, A. Prokofjevs, E. Vedejs, *Chem. Rev.* **2012**, *112*, 4246.
[ix] A. Altomare, G. Cascarano, C. Giacovazzo, A. Guagliardi, M. C. Burla, G. Polidori, M. Camalli, *J. Appl. Cryst.* **1994**, *27*, 435.
[x] G. M. Sheldrick, *Acta Cryst.* **2008**, *A64*, 112.
[xi] CrysAlisPro 1.171.38.41, Rigaku Oxford Diffraction, **2015**.

6.2.5 Forming B–B Bonds by the Controlled Reduction of a Tetraaryldiborane(6)

This is an open access article published under an ACS AuthorChoice License, which permits copying and redistribution of the article or any adaptations for non-commercial purposes.

JACS
JOURNAL OF THE AMERICAN CHEMICAL SOCIETY
Article
pubs.acs.org/JACS

Forming B–B Bonds by the Controlled Reduction of a Tetraaryldiborane(6)

Thomas Kaese, Alexander Hübner, Michael Bolte, Hans-Wolfram Lerner, and Matthias Wagner*

Institut für Anorganische und Analytische Chemie, Goethe-Universität Frankfurt, Max-von-Laue-Straße 7, D-60438 Frankfurt am Main, Germany

Supporting Information

ABSTRACT: Dimeric aryl(hydro)boranes can provide suitable platforms for the synthesis of boron-containing graphene flakes through reductive B–B coupling. Two-electron reduction of 1,2:1,2-bis(4,4′-di-*tert*-butyl-2,2′-biphenylylene)diborane(6) (**4**) with LiNaph/THF establishes a B–B σ bond but can be accompanied by substituent redistribution. In the singly rearranged product, Li_2[**6**], only one 1,2-phenyl shift has occurred. The doubly ring-contracted product, Li_2[**7**], consists of two 9*H*-9-borafluorenyl moieties that are linked via their boron atoms. When the amount of LiNaph/THF is increased to 4 equiv, Li_2[**6**] is subsequently observed as the dominant species. Addition of 11 equiv of LiNaph/THF results in over-reduction with hydride elimination to afford the doubly boron-doped dibenzo[*g*,*p*]chrysene Li_2[**1**]. In contrast, excess KC_8 reduces **4** to the corresponding dihydrodibenzo[*g*,*p*]chrysene, K_2[**5**], with a *trans*-HB–BH core. Hydride abstraction from K_2[**5**] with 1 equiv of **4** leads to K[**8**], in which the central B–B bond is bridged by a single hydrogen atom. K[**8**] is also obtained upon treatment of **4** with 1 equiv of KC_8. All products have been characterized by multinuclear NMR spectroscopy and X-ray crystallography.

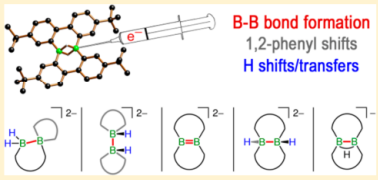

INTRODUCTION

Boron is among the most powerful electronically perturbative elements that can be incorporated into the core structures of fused polycyclic aromatic hydrocarbons (PAHs) in order to modify their optoelectronic properties.[1−13] Formally, a tricoordinate boron atom is isoelectronic to a carbenium ion. When the vacant p orbital efficiently interacts with the extended π-electron cloud of the surrounding all-carbon system, the absorption and emission maxima of the corresponding PAH shift to the red and charge mobilities are enhanced.[14] Applications of the resulting materials are very diverse and range from electron-transporting materials,[15] field-effect transistors,[13,16] supercapacitors,[17] and Li-ion batteries[18] to organic light-emitting devices[13] and solar cells.[19]

In the past, our group has prepared a number of 9,10-dihydro-9,10-diboraanthracene (DBA)[20−22] derivatives **A** (Figure 1), which turned out to be air and water tolerant, strongly fluorescent, and capable of accepting two electrons in a reversible manner.[7,8,23,24] Recently, the focus has been expanded toward the development of more extended core structures, such as **B** (Figure 1), which can be viewed not only as a stretched DBA but also as a doubly boron-bridged dibenzo[*g*,*p*]chrysene.[10,11] For a systematic assessment of key structure–property relationships, we next decided to move the two boron atoms from the outer rim of **B** to its central part. Even though the neutral molecule **C** (Figure 1) has so far remained elusive, we have already succeeded in the synthesis of its corresponding dianion, $[\mathbf{1}]^{2-}$ (Scheme 1).[25] While the dianion may find future applications in coordination chemistry,[26−28] neutral **C** would constitute a unique planar, ditopic Lewis acid with directly adjacent boron centers.

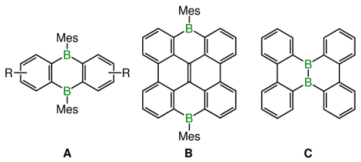

Figure 1. 9,10-Dihydro-9,10-diboraanthracenes (**A**), a doubly boron-bridged dibenzo[*g*,*p*]chrysene (**B**), and a related polycyclic aromatic hydrocarbon with central B–B core (**C**).

Li_2[**1**] is available via reduction of the C_1-symmetric 9*H*-9-borafluorene dimer **2**[29,30] with excess Li granules in THF (Scheme 1).[25] NMR spectroscopy shows that the dimeric framework of **2** gets quantitatively cleaved to the adduct **3** by THF at room temperature.[31] Electron injection apparently induces dimerization and skeletal rearrangements that annihilate the structural differences between the starting material **3** and the reaction product. Unfortunately, this process lacks the desired selectivity and therefore furnishes Li_2[**1**] in only moderate yields.

As a consequence, we will herein switch from **2**/**3** to compound **4**[29,30,32] (Scheme 1), which seems ideally preorganized for reductive B–B coupling.[33]

Received: March 2, 2016
Published: April 25, 2016

ACS Publications © 2016 American Chemical Society

DOI: 10.1021/jacs.6b02303
J. Am. Chem. Soc. 2016, 138, 6224−6233

Scheme 1. Synthesis of $Li_2[1]$, Starting from 2 or 4

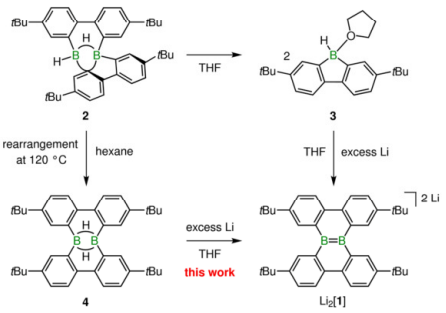

Apart from the role of **4** as a potential precursor of $Li_2[1]$, the reduction chemistry of its diboron core is fundamentally important in its own right. Interest dates back to the early days of A. Stock, who attempted to prepare $[H_3B{-}BH_3]^{2-}$ through reduction of B_2H_6.[34] The reaction was revisited several times[35] until 1994, when Shore et al. reported ^{11}B NMR evidence for the intermediate generation of $[H_3B{-}BH_3]^{2-}$, which reacts further to provide $[BH_4]^-$ and $[B_3H_8]^-$ as final products.[36] The first isolable molecules that came close to $[H_3B{-}BH_3]^{2-}$ were published in 2011/2014 by Matsuo and Tamao et al., who introduced exceptionally bulky phenyl groups (Ph*) to create isolable dianions $[(Ph^*)H_2B{-}BH_2(Ph^*)]^{2-}$ from diborane(6) precursors $H(Ph^*)B(\mu\text{-}H)_2B(Ph^*)H$.[37,38] Inspired by these results, our group recently managed to establish a B−B two-electron two-center (2e2c) bond within a BBC three-membered ring through reduction of a diborylmethane. The crystallographically characterized product represents the first example of a $[R_3B{-}BR_3]^{2-}$ anion.[39,40] By carefully adjusting the number of redox equivalents, even radicals containing B•B one-electron two-center (1e2c) bonds are accessible from ditopic triarylboranes and have been fully characterized.[39,41] Compared to the plethora of protocols developed for C−C bond formation, methods for selectively connecting two boron atoms are still scarce.[42] The simple addition of electrons to organoboranes may usefully expand the existing toolbox of reactions and therefore merits a detailed investigation.

In contrast to the vast majority of other B_2H_6 derivatives the two boron atoms of **4** are not just linked by hydrogen atoms, but also by two 2,2′-biphenylylene bridges. Given that partial rotation about the C−C single bonds is still possible, the molecular scaffold should retain sufficient conformational flexibility to support sp^2- as well as sp^3-hybridized boron atoms after reduction. The available structural options raise the following questions: *Is it possible to establish a B−B σ bond by trapping added electrons in the space amid the two boron atoms? Does over-reduction of diboranes(6) (such as 4) with formal elimination of hydride substituents lead to B=B double-bonded species (such as $[1]^{2-}$)? What are the key factors governing the extent of substituent scrambling during reduction of diboranes(6)?* Answers are provided in this paper.

■ RESULTS AND DISCUSSION

Prior to the reduction of **4** by chemical means and on a preparative scale, its electrochemical properties were investigated by cyclic voltammetry and potentiostatic coulometry. In the cyclic voltammogram (Figure 2; room temperature; THF/$[n\text{Bu}_4\text{N}][PF_6]$; vs FcH/$FcH^+$, FcH = ferrocene), **4** shows a single, irreversible reduction wave at $E_{pc} = -2.74$ V. Two irreversible oxidation events with peak potentials of $E_{pa} = -2.17$ and -1.97 V were recorded in the back scan. The irreversibility of the reduction process strongly indicates that a significant structural change is associated with the electron-transfer step.[43] Both boron atoms of **4** are tetracoordinate and therefore do not provide an energetically low-lying unoccupied orbital for the incoming electron (cf. the highly cathodic reduction potential of **4**).[44] Thus, electron injection should be accompanied at least by a hydrogen shift from the bridging to a terminal position.[37]

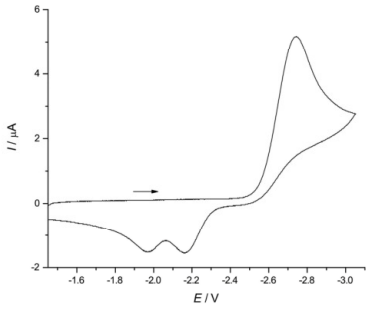

Figure 2. Cyclic voltammogram of **4** in THF at room temperature (vs FcH/FcH^+; supporting electrolyte, $[n\text{Bu}_4\text{N}][PF_6]$ (0.1 mol L^{-1}); scan rate, 200 mV s^{-1}).

A coulometric measurement carried out at an applied potential of $E_w = -3.0$ V (THF; $[n\text{Bu}_4\text{N}][PF_6]$) gave an electron count of approximately 1.5 e^- per molecule **4**. Coulometry on main-group compounds is notoriously problematic and tends to give a low electron count due to the inherent instability of radical species, reactions between the electrode products and still untransformed analyte molecules, or adsorption of the electrogenerated species to the electrode surface.[41,45] In the present case, the problem is aggravated by THF polymerization at the anode.[46] Given this background, our bulk electrolysis indicates that, in fact, two electrons could be delivered at the same potential value. For a two-electron reduction, the occurrence of only one irreversible reduction wave in the cyclic voltammogram again points toward a structural reorganization associated with one or both electron-transfer steps that leads to similar or inverted energetic potentials.[43] When dealing with the preparative reduction of **4**, one must therefore be aware of the possibility that doubly reduced **4** could already be generated while unconsumed starting material is still present.

In the following, the reduction of **4** by chemical means will be described. Since the outcome depends heavily on the reaction conditions applied, we will, for reasons of clarity, first restrict ourselves to an overview of the complex product distributions and discuss analytical details of the isolated products in a subsequent section. A third section is devoted to mechanistic considerations.

Product Distributions of the Reduction of 4 as a Function of the Reaction Conditions. Staying close to the published protocol,[25] we initially performed the alternative synthesis of $Li_2[1]$ from **4** at room temperature using excess Li in THF (Scheme 1). After workup, we isolated $Li_2[1]$, as its thf solvate $[Li(thf)_3]_2[1]$, in a 41% yield. $Li_2[1]$ also forms in

DOI: 10.1021/jacs.6b02303
J. Am. Chem. Soc. 2016, 138, 6224−6233

toluene, provided that a small volume of THF is added for Li^+ solvation (otherwise the reaction is negligibly slow). After filtration to remove unreacted Li, red single crystals of $[Li_2(thf)_3][\mathbf{1}]$, which contained 0.5 equiv of toluene molecules, precipitated from the cooled filtrate in a yield of 30% (see Figure 3, below).

Contrary to *a priori* expectations, even the highest yields of $Li_2[\mathbf{1}]$ gained from the reduction of **4** (41%) did not exceed the yields obtained from the reduction of **3** (43%). In order to identify relevant reaction intermediates and thereby to develop a deeper understanding of key mechanistic details, we investigated next the reduction of **4** under more controlled conditions. For this purpose, Li metal was replaced by LiNaph/THF (LiNaph = lithium naphthalenide). Use of the homogeneous reducing agent should accelerate electron-transfer rates, circumvent surface effects, and facilitate the precise adjustment of the number of added redox equivalents.

First, we targeted the lithium hydridoborate $Li_2[\mathbf{5}]$ (Scheme 2), which features an electron-precise B−B single bond and is a

Scheme 2. Major Products Formed upon Reduction of Compound 4 with 2 or 4 equiv of LiNaph/THF in Toluene at −78 °C[a]

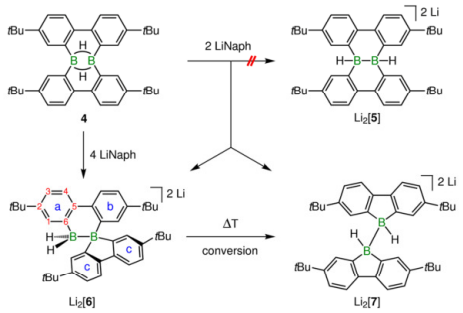

[a]At moderately elevated temperatures, $Li_2[\mathbf{6}]$ rearranges to $Li_2[\mathbf{7}]$.

conceivable intermediate on the way from **4** to $Li_2[\mathbf{1}]$. The requisite two-electron reduction of **4** was performed by adding 2 equiv of LiNaph/THF at −78 °C in toluene. The reaction did not furnish $Li_2[\mathbf{5}]$, but rather its rearranged isomers $Li_2[\mathbf{6}]$ and $Li_2[\mathbf{7}]$ (Scheme 2). The experiment was repeated several times. $Li_2[\mathbf{6}]$ and $Li_2[\mathbf{7}]$ always remained major products, but their relative ratios varied to a certain extent (^{1}H NMR spectroscopic control of the crude product). Notably, $Li_2[\mathbf{6}]$ tends to transform to $Li_2[\mathbf{7}]$, promoted by apolar solvents and elevated temperatures (Scheme 2; NMR spectroscopic monitoring during workup). From a representative experiment, $Li_2[\mathbf{7}]$ could be isolated in a yield of 51%. Single crystals of $[Li(thf)]_3[Li][\mathbf{7}]_2$ grew from pentane at room temperature (see Figure 5, below). Like $Li_2[\mathbf{5}]$, the compounds $Li_2[\mathbf{6}]$ and $Li_2[\mathbf{7}]$ are diborane(6) dianions. As planned, B−B 2e2c bonds have been established through reduction of the diborane(6) precursor. However, under the conditions applied, the desired transformation was accompanied by substituent scrambling, leading to ring-contraction reactions.

$Li_2[\mathbf{6}]$ formed preferentially over $Li_2[\mathbf{7}]$ when the amount of reducing agent was increased from 2 equiv to 4 equiv of LiNaph/THF (toluene, −78 °C). After workup, $Li_2[\mathbf{6}]$ was isolated in 23% yield by precipitation from THF at −30 °C. Single crystals of $[Li(thf)_3][Li(thf)_2][\mathbf{6}]$ were grown from more dilute THF solutions (see Figure 4, below). As a side product, we observed small quantities of $Li_2[\mathbf{1}]$, even though its putative precursor, $Li_2[\mathbf{5}]$, was still not detectable in the reaction mixture.

In the presence of 11 equiv of LiNaph/THF, **4** furnished only small amounts of $Li_2[\mathbf{6}]$, whereas $Li_2[\mathbf{1}]$ became the dominant product (THF-d_8; NMR spectroscopic control of the crude reaction mixture). The separation of $Li_2[\mathbf{1}]$ from unreacted LiNaph was successfully accomplished by fractional crystallization. As a drawback, however, quantitative removal of co-precipitated naphthalene through hexane extraction results in yield losses, because the solubility of $Li_2[\mathbf{1}]$ in hexane is significant.

Since it should be easier to separate organoboron products from insoluble graphite rather than from naphthalene, we next attempted the synthesis of $K_2[\mathbf{1}]$ from **4** using excess KC_8 (20 equiv, THF, room temperature). Yet, it turned out that the nature of the alkali metal (cation) has a decisive influence on the reaction outcome: instead of $K_2[\mathbf{1}]$, the initial target anion $[\mathbf{5}]^{2-}$ (Scheme 3) formed reproducibly in a highly selective transformation (83% isolated yield). $[K_2(thf)_4][\mathbf{5}]$ crystallized from THF in the form of deep orange blocks (see Figure 6, below).

Scheme 3. Reduction of 4 with 20 equiv or 1 equiv of KC_8 Proceeds without Rearrangement of the Original Backbone and Leads to $K_2[\mathbf{5}]$ or $K[\mathbf{8}]$, Respectively

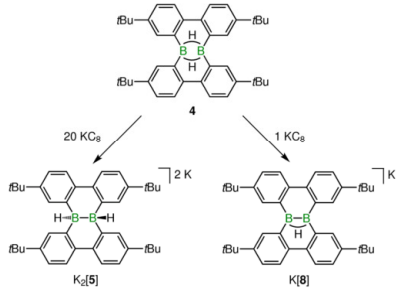

Interestingly, the reactivity differences between KC_8 and LiNaph become less pronounced when fewer reduction equivalents are employed (Table 1). For comparability reasons, these experiments were performed in toluene containing a small volume of added THF. According to ^{1}H and ^{11}B NMR spectroscopy, reaction of **4** with 4 equiv of KC_8 mainly yielded $K_2[\mathbf{6}]$ together with $K_2[\mathbf{5}]$; as a reminder, LiNaph gave $Li_2[\mathbf{6}]$ and small amounts of $Li_2[\mathbf{1}]$ under these conditions. Addition of 2 equiv of KC_8 to **4** afforded $K_2[\mathbf{6}]$, $K_2[\mathbf{7}]$, and approximately 10% of the singly hydrogen-bridged species $K[\mathbf{8}]$. The anions $[\mathbf{6}]^{2-}$ and $[\mathbf{7}]^{2-}$ are known from the corresponding LiNaph reduction, whereas $[\mathbf{8}]^-$ is a newly observed compound.

With the aim to access $K[\mathbf{8}]$ on a preparative scale, the stoichiometric ratio between **4** and KC_8 was systematically varied. It finally turned out that use of 1 equiv of KC_8 in THF provided $K[\mathbf{8}]$ in yields of 58% (Scheme 3). Yellow crystals of

DOI: 10.1021/jacs.6b02303
J. Am. Chem. Soc. 2016, 138, 6224−6233

Table 1. Major Products (≥30%, shown in bold) and Minor Products (≥10%) of the Reduction of 4 in Toluene or *THF* (shown in italics) According to NMR Spectroscopy (THF-d_8)

red. agent	equiv	products	red. agent	equiv	products
LiNaph	2	**Li_2[6]**, **Li_2[7]**	KC_8	2	**K_2[6]**, **K_2[7]**, **K[8]**
LiNaph	4	Li_2[1], **Li_2[6]**	KC_8	4	K_2[5], **K_2[6]**
LiNaph	11	*Li_2[1]*, *Li_2[6]*	KC_8	20	***K_2[5]***
Li	60	*Li_2[1]*, *Li_2[6]*			
Li	125	Li_2[1], **Li_2[6]**			

[K(thf)$_2$][**8**] were grown from THF/hexane (see Figure 7, below).

Finally, coming back again to the initial transformation of **4** with excess Li metal in THF, we were now able to identify the NMR signature of Li_2[**6**] in spectra recorded on the crude reaction mixtures. Both compounds, Li_2[**1**] and Li_2[**6**], reproducibly appeared in almost equimolar ratio, which answers our initial question regarding the 41% yield of Li_2[**1**]. Subsequent attempts to promote Li_2[**1**] formation by accelerating the hydride abstraction through added Me_3SiCl led to only marginally improved yields. The presence of the chlorosilane nevertheless had a beneficial effect, because it facilitated the workup process.[25] Instead of Li_2[**6**] (and some other side products), mainly lithium 9-trimethylsilyl-9-hydridoboratafluorene[25] formed (together with Li_2[**1**]) and remained in solution under the conditions applied to crystallize the boron-doped PAH.

Characterization of the Reduction Products. *Solid-State Structure of [Li_2(thf)$_3$][**1**].* Compound [Li_2(thf)$_3$][**1**] exists as a coordination polymer in the solid state. Within each polymer chain, dianions [**1**]$^{2-}$ are linked by [Li_2(thf)$_3$]$^{2+}$ aggregates, in which two Li^+ cations share three thf ligands (Figure 3). The asymmetric unit of the crystal contains two

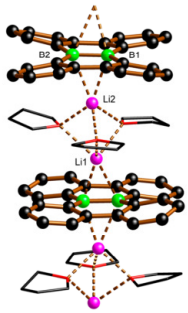

Figure 3. One strand of the coordination polymer [Li_2(thf)$_3$][**1**] in the solid state. *t*Bu groups and C*H* atoms are omitted for clarity.

crystallographically independent polymer subunits (I and II) with similar geometric parameters, leading to {I}$_\infty$ and {II}$_\infty$ strands. The B═B bond lengths amount to 1.641(6) Å (subunit I)/1.627(6) Å (subunit II), and all Li···B distances within the contact ion pairs fall in the narrow range between 2.413(9) Å and 2.525(9) Å. Compared to the solid-state structure of [Li(thf)$_3$]$_2$[**1**], which crystallizes as discrete inverse sandwich complexes,[25] the B═B bonds in polymeric [Li_2(thf)$_3$][**1**] are slightly elongated (Δ_{av} = 0.026 Å), while the Li···B contacts are contracted (Δ_{av} = −0.089 Å). Similar to the all-carbon relative dibenzo[*g*,*p*]chrysene,[47] steric repulsion between *ortho*-H atoms of adjacent phenylene rings forces the [**1**]$^{2-}$ scaffolds out of planarity. The two 2,2′-biphenylylene bridges within the same [**1**]$^{2-}$ anion possess opposite curvatures.

*Solid-State Structure and NMR Data of Li_2[**6**].* The all-carbon congener of the dianion [**6**]$^{2-}$ is already known and possesses a spirocyclic framework, composed of a 9,10-dihydrophenanthrene molecule that is fused with a fluorene moiety.[48] From this compound, [**6**]$^{2-}$ can formally be generated through an exchange of the two aliphatic carbon atoms for tetracoordinate borate anions. In the solid state, the central B_2C_4 ring adopts the characteristic twisted 1,3-cyclohexadiene conformation with torsion angles C(21)−C(22)−C(32)−C(31) = −31.0(4)° and B(1)−B(2)−C(22)−C(32) = 44.6(2)°. The B(1)−B(2) bond length of [**6**]$^{2-}$ amounts to 1.810(5) Å, and is therefore larger by 0.021 Å than the B−B bond length of [**7**]$^{2-}$ (see below). For comparison, in the typical isoelectronic C(sp^3)−C(sp^3) single bond, the two carbon atoms are only 1.54 Å apart.[49] The ligand sphere of B(1) in [Li(thf)$_3$][Li(thf)$_2$][**6**] deviates significantly from an ideal tetrahedral geometry, because the C(1)C(11)-C(31) basal plane is distorted due to the small angle C(1)−B(1)−C(11) = 98.2(3)° within the five-membered ring. Moreover, the B(2)−B(1) vector does not run perpendicular to the C_3 plane: the endocyclic angle C(31)−B(1)−B(2) = 99.6(3)° is significantly compressed, while the exocyclic angle C(11)−B(1)−B(2) = 119.8(3)° is expanded to a value normally observed for sp^2-hybridized boron centers. Contrary to B(1), B(2) features an essentially unstrained environment (B(1)−B(2)−C(21) = 104.3(3)°). [Li(thf)$_3$][Li(thf)$_2$][**6**] forms contact-ion pairs in the crystal lattice. The [**6**]$^{2-}$ ion binds each of its Li^+ counterions in a chelating manner through one B*H* hydride substituent and one boron-bonded carbon atom. Li(1)$^+$, which carries only two thf ligands, establishes the shorter Li−C contact (2.327(7) Å), while Li(2)$^+$ (three thf ligands) binds at a longer Li−C distance (2.639(7) Å). The above-mentioned widening of the C(11)−B(1)−B(2) angle may be associated with Li(1)$^+$ chelation (Figure 4).

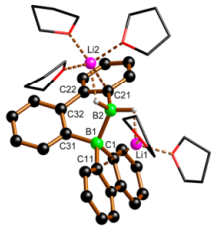

Figure 4. Molecular structure of [Li(thf)$_3$][Li(thf)$_2$][**6**] in the solid state. *t*Bu groups and C*H* atoms are omitted for clarity.

DOI: 10.1021/jacs.6b02303
J. Am. Chem. Soc. 2016, 138, 6224−6233

NMR spectra of $Li_2[6]$ were recorded in THF-d_8. In the $^{11}B\{^1H\}$ NMR spectrum, the compound gives rise to two resonances at −11.0 ppm and −19.9 ppm (cf. $Li_2[7]$: −13.4 ppm). Upon proton coupling, the width at half height of the signal at −19.9 ppm doubles (R_2BH_2), whereas that of the other resonance remains unchanged (R_4B). Three sets of ^1H aryl resonances are detectable for $Li_2[6]$. Two of those are well-resolved at room temperature (H-a, H-b), while the third set consists of very broad signals, each of them integrating 2H (H-c; Scheme 2). At a measurement temperature of 50 °C and a spectrometer field strength of 250 MHz (instead of 500 MHz), the ill-defined proton signals become considerably sharpened. This indicates a dynamic behavior of the system in solution, which likely arises from conformational changes of the twisted B_2C_4 ring and/or from an association−dissociation equilibrium between the $[Li(thf)_n]^+$ and $[6]^{2-}$ ions. According to a 2D $^1H,^{13}C$ HMBC experiment (500 MHz, room temperature), all six well-resolved proton resonances belong to the same biphenyl unit. Correspondingly, the poorly resolved signals arise from the second biphenyl fragment of $[6]^{2-}$. The benzene rings marked "a" and "b" in Scheme 2, are necessarily different from each other. In contrast, both benzene rings "c" can become magnetically equivalent as soon as fast intramolecular motion leads to an average C_s symmetry of the molecular scaffold. We therefore assign the set of broad resonances to the 9-borafluorene fragment. The two remaining signal sets were assigned to the rings "a" and "b" by means of an $^1H,^{11}B$ correlation experiment, which showed a cross peak between one *ortho*-H signal and the BH_2 boron signal (a), while the second *ortho*-H atom was correlated with the other boron atom (b).

Solid-State Structure and NMR Data of Li_2[7]. According to X-ray diffraction on a crystal of $[Li(thf)]_3[Li][7]_2$, the dianion $[7]^{2-}$ consists of two 9*H*-9-borafluorene molecules that are linked through an electron pair to form a B−B single bond (Figure 5).

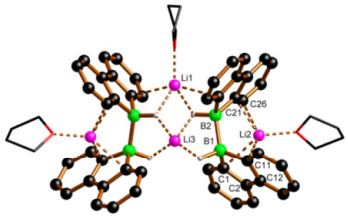

Figure 5. Molecular structure of $[Li(thf)]_3[Li][7]_2$ in the solid state. *t*Bu groups and C*H* atoms are omitted for clarity.

The corresponding B(1)−B(2) bond length of 1.789(7) Å is slightly shorter than that of a related electron-precise diborate (1.83(2) Å), which Power et al. obtained through the reduction of 2,6-$Trip_2C_6H_3BBr_2$ with KC_8 (Trip = 2,4,6-triisopropylphenyl).[50] We also emphasize that the all-carbon analogue of $[7]^{2-}$, i.e., 9,9′-bifluorenyl, has been synthesized through reductive coupling of 9-bromofluorene with a variety of reducing agents.[51] In the crystal lattice of $[Li(thf)]_3[Li][7]_2$, two dianions are linked by $Li(1)^+$ and $Li(3)^+$ to give a C_2-symmetric dimer. The $Li(3)^+$ ion is surrounded by four B*H* hydride substituents in a strongly distorted tetrahedral fashion; both $[7]^{2-}$ ions act as chelating ligands. $Li(1)^+$ possesses a coordination number of five with close contacts to two B*H* hydride substituents and two boron-bonded carbon atoms. The coordination sphere is completed by one thf molecule. Reminiscent of an *ansa*-metallocene structure, the $[Li(2)(thf)]^+$ ion occupies the pocket built by the two 9-borafluorenyl units of $[7]^{2-}$.[52]

The ^{11}B NMR resonance of $Li_2[7]$ in THF-d_8 appears as a doublet at −13.4 ppm with a $^1J(B,H)$ coupling constant of 71 Hz. Both values are in good agreement with those reported for Power's compound.[50] The signal of the B*H* hydrogen atom is broadened almost beyond detection in the ^1H NMR spectrum. Its chemical shift value of 2.1 ppm was finally determined with the help of a ^1H, ^{11}B-HSQC experiment. NMR spectroscopy further shows the four aryl rings of $Li_2[7]$ to be magnetically equivalent at room temperature, thereby indicating free librational motion about the B−B axis on the NMR time scale.

Solid-State Structure and NMR Data of K_2[5]. Similar to $[Li_2(thf)_3][1]$, $[K_2(thf)_4][5]$ forms coordination polymers in the crystal lattice, which consist of twisted $[5]^{2-}$ dianions linked by $[K_2(thf)_4]^{2+}$ aggregates (Figure 6).

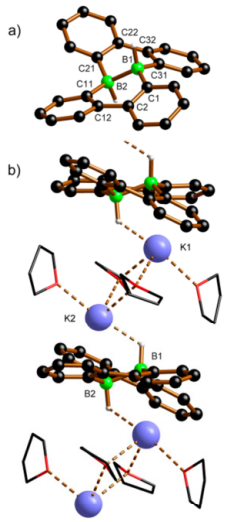

Figure 6. Molecular structures of the anion $[5]^{2-}$ (a) and its coordination polymer $[K_2(thf)_4][5]$ (b) in the solid state. *t*Bu groups and C*H* atoms are omitted for clarity.

The central B(1)−B(2) bond (1.755(4) Å) is longer by Δ_{av} = 0.12 Å than the B═B double bonds in $[Li_2(thf)_3][1]$ (two crystallographically independent polymer strands) and therefore falls in the range of B−B single bonds. We have previously published the calculated molecular structure of the hypothetical neutral compound 5′,[29] that corresponds to a molecule of **4** in which the bridging hydrogen atoms have been shifted into terminal positions to create electron deficient, three-coordinate boron centers. The B···B distance in 5′ amounts to 2.591 Å. Thus, the injection of two electrons into the molecule pulls the two boron atoms closer together by 0.836 Å (cf. ref 39 for a closely related experimentally assessed redox pair). Also for $[5]^{2-}$, an all-carbon equivalent exists, i.e., 8b,16b-dihydro-

DOI: 10.1021/jacs.6b02303
J. Am. Chem. Soc. 2016, 138, 6224−6233

dibenzo[*g*,*p*]chrysene.[48,53] Thus, both the H−B−B−H and the H−C−C−H cores are compatible with the geometric constraints imposed by two 2,2′-biphenylylene bridges. While *cis* and *trans* configurations are known for 8b,16b-dihydrodibenzo[*g*,*p*]chrysene,[53] the crystal structure analysis of $[K_2(thf)_4][\mathbf{5}]$ revealed exclusively the *trans* isomer with a corresponding torsion angle H(1)−B(1)−B(2)−H(2) of −159(2)°. In fact, the entire transformation of **4** to $K_2[\mathbf{5}]$ appears to be *trans* selective, because the crude product $K_2[\mathbf{5}]$ also gave rise to only one set of signals in the ^{1}H and ^{13}C NMR spectra.

In the ^{11}B NMR spectrum of $K_2[\mathbf{5}]$, ^1J(B,H) coupling is not resolved, but the ^{11}B chemical shift value (−17.9 ppm) is highly diagnostic: it nicely agrees with the shift value of isomer $Li_2[\mathbf{7}]$ (−13.4 ppm), but differs greatly from that of the dehydrogenated congener $Li_2[\mathbf{1}]$ (32 ppm[25]). The boron-bonded hydrogen atoms give rise to one broad ^{1}H NMR signal at 1.7 ppm. All four benzene rings are magnetically equivalent at room temperature in solution.

*Solid-State Structure and NMR Data of K[**8**].* The asymmetric unit of $[K(thf)_2][\mathbf{8}]$ contains a twisted monoanionic molecular flake featuring a single μ-H atom that bridges a short B(1)−B(2) bond of 1.651(6) Å (Figure 7a).

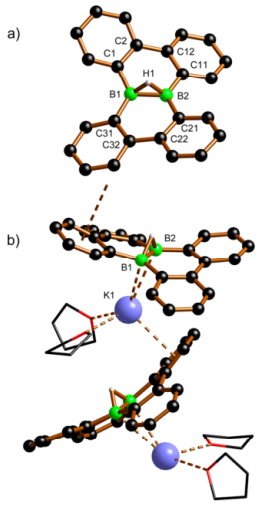

Figure 7. Molecular structures of the anion $[\mathbf{8}]^-$ (a) and its coordination polymer $[K(thf)_2][\mathbf{8}]$ (b) in the solid state. *t*Bu groups and C*H* atoms are omitted for clarity.

This value is close to the average B═B bond length in $[Li_2(thf)_3][\mathbf{1}]$ (1.634 Å), but smaller by 0.10 Å than the B−B bond length in $[K_2(thf)_4][\mathbf{5}]$ (1.755(4) Å). The C−B−C/B bond angles about B(1) as well as B(2) in $[\mathbf{8}]^-$ sum up to 360°, again similar to the structure of $[\mathbf{1}]^{2-}$ but in stark contrast to that of $[\mathbf{5}]^{2-}$ ($\sum$(C−B−C/B) = 335°, 338°). These results are in line with theoretical works on $[(\mu\text{-H})H_2BBH_2]^-$. For this anion, Lammertsma et al. calculated a distance between both boron atoms of 1.624 Å and concluded that the central part of the molecule can be thought to result from protonation of a B═B bond.[54] Moreover, for the related system [(μ-H)(Eind)-HBBH(Eind)]$^-$, Tamao et al. observed a B···B distance of 1.655(2) Å and claimed that this indicated double-bond character of the diboron core (Eind = 1,1,3,3,5,5,7,7-octaethyl-*s*-hydrindacen-4-yl).[37] The K$^+$ counterion coordinates both B atoms from the side opposite to the μ-H atom. The coordination sphere is completed by two thf ligands and the aryl ring of an adjacent $[\mathbf{8}]^-$ anion to form a coordination polymer (Figure 7b).

The ^{11}B NMR spectrum of K[**8**] further confirms a certain degree of B═B double-bond character within the diboron core. The broad ^{11}B signal (20.4 ppm) lies relatively near to that of $Li_2[\mathbf{1}]$ (32 ppm),[25] but is downfield-shifted by 38.3 ppm compared to the resonance of $K_2[\mathbf{5}]$ (−17.9 ppm). According to the ^{1}H and ^{13}C NMR spectra, all aryl rings contained in K[**8**] are magnetically equivalent at room temperature in solution. A broadened proton signal was detectable at −0.99 ppm, which sharpened upon ^{11}B decoupling; its integral value equals a quarter of the integral value of each aryl proton resonance. The signal is therefore assignable to the boron-bonded hydrogen atom.

Mechanistic Considerations. Up to this point, we have unveiled the behavior of **4** under reducing conditions in dependence of the number of redox equivalents employed and the reducing agents chosen. Some of the transformations are highly selective (cf. the synthesis of $K_2[\mathbf{5}]$), others lead to product mixtures containing two or three dominant species (Table 1). In all cases, the major products have been isolated and characterized by NMR spectroscopy and X-ray crystallography. On the basis of the data obtained, we can now identify common motifs between the individual reactions and finally propose a mechanistic model to explain the complex scenario.

*Hydride Transfer and Hydride Elimination Processes in the Course of the Reduction of **4**.* First, we consider the reduction of **4** with a large excess of reducing agent. Use of LiNaph/THF leads to $Li_2[\mathbf{1}]$, whereas KC_8 gives $K_2[\mathbf{5}]$. The $[\mathbf{1}]^{2-}$ anion can conceivably be generated from $[\mathbf{5}]^{2-}$ if (i) a hydride scavenger is present to create three-coordinate boron intermediates and (ii) the number of redox equivalents supplied suffices to alleviate the resulting electron deficiency at boron by establishing a B═B double bond. The small, hard Li$^+$ ion constitutes a stronger Lewis acid than the larger K$^+$ ion, and the heat of formation of LiH (−91 kJ mol^{-1}) exceeds that of KH (−56 kJ mol^{-1}) by 35 kJ mol^{-1}.[55] Consequently, Li$^+$ could well take the role of a hydride scavenger while K$^+$ is much less likely to do so. Hydride elimination is not an issue when **4** is treated with only 2 equiv of LiNaph/THF or KC_8, because the number of electrons available is too small to compensate for the loss of a hydride substituent. Therefore, the same anions are generated ($[\mathbf{6}]^{2-}$, $[\mathbf{7}]^{2-}$), irrespective of the selected reducing agent. Upon addition of 4 reduction equivalents to **4**, we are facing an intermediate situation where mostly $[\mathbf{6}]^{2-}$ is accompanied by $Li_2[\mathbf{1}]$ (LiNaph/THF) or $K_2[\mathbf{5}]$ (KC_8).

The argumentation outlined above does not account for the synthesis of K[**8**] (about 50%) from **4** and 1 equiv of KC_8. The anion $[\mathbf{8}]^-$ contains one hydrogen substituent less than **4** or $[\mathbf{5}]^{2-}$, even though the potential hydride scavenger Li$^+$ is missing. As an alternative pathway, $[\mathbf{8}]^-$ formation might be triggered by an interaction between already reduced product molecules, $K_2[\mathbf{5}]$, and not yet consumed **4** (note the electrochemical investigations outlined above, which support such a scenario). Compound **4** still is a potential Lewis acid and could therefore engage in hydride exchange reactions. This possibility is particularly relevant when electrons are in short

DOI: 10.1021/jacs.6b02303
J. Am. Chem. Soc. 2016, 138, 6224−6233

supply (as in the present case), because otherwise the concentration of neutral **4** will rapidly decrease such that it becomes less available for hydride abstraction.

To scrutinize this hypothesis, we prepared a 1:1 mixture of K_2[**5**] and **4** in THF-d_8 and monitored it by NMR spectroscopy after the orange color of K_2[**5**] had faded (Scheme 4). The

Scheme 4. Three Major Compounds Are Generated from 4 and K_2[5]; K[9] and K_2[10] Are Also the Products of the Reaction Between 4 and KH[a]

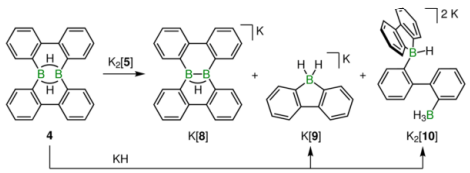

[a]Room temperature, THF; *t*Bu groups are omitted for clarity).

NMR signals of **4** and K_2[**5**] had completely vanished and the resonances of K[**8**] had appeared instead. However, the NMR spectra gave no indication for a hydride adduct [**4**·H]$^-$, which should adopt the highly symmetric bridged structure [Ar_2(H)-B(μ-H)B(H)Ar_2]$^-$.[56]

A plausible explanation would be that [**4**·H]$^-$ possesses only a short lifetime and rapidly rearranges to other products. As a test, we charged an NMR tube with a mixture of **4** and excess KH in THF-d_8 (Scheme 4). The reaction was rather slow, likely due to the limited solubility of KH in THF. Nevertheless, **4** was consumed after 2 weeks and the resonances assignable to K[**9**] (cf. ref 25) were prominent in the ^{1}H and ^{11}B NMR spectra. Moreover, crystals of [K(thf)$_3$][K(thf)][**10**] precipitated in the NMR tube (Figure 8; cf. the SI for a structure discussion). Despite its poor solubility, the ^{1}H and ^{11}B NMR signals of K_2[**10**] could be determined in THF-d_8. Afterward, we

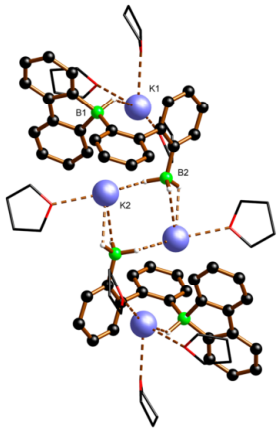

Figure 8. Molecular structure of [K(thf)$_3$][K(thf)][**10**] in the solid state. *t*Bu groups and C*H* atoms are omitted for clarity.

identified the resonance patterns of K[**9**] and K_2[**10**] also in the NMR spectra of the **4**/K_2[**5**] mixture (Scheme 4).

In conclusion, the products obtained from the reaction of **4** and K_2[**5**] support the assumption that K[**8**] can be generated through hydride transfer from K_2[**5**] to **4**. The resulting hydride adduct [**4**·H]$^-$ would subsequently turn into K[**9**] and K_2[**10**]. Remarkably, the ^{1}H NMR spectrum recorded on the **4**/K_2[**5**] sample was almost identical to the spectrum of the crude product mixture gained from **4** and 1 equiv of KC_8 (cf. the SI for plots of the spectra). In line with our initial suggestion, this points toward a similar hydride transfer process also in this case, after the KC_8 has converted half of **4** into K_2[**5**].

Skeletal Rearrangement Processes in the Course of the Reduction of **4**. The reduction of **4** can be carried out in a way to preserve the original molecular backbone (cf. Li_2[**1**], K_2[**5**], K[**8**]). Yet, under certain conditions 1,2-phenyl shifts occur, resulting in ring contraction and furnishing Li_2[**6**]/Li_2[**7**]. Related phenyl shifts are known for comparable PAHs: A classical synthesis of dibenzo[*g*,*p*]chrysene (≙ Li_2[**1**]) takes advantage of the Clemmensen reduction of 9*H*-fluoren-9-one and proceeds via 9,9′-bifluorenyl derivatives (≙ Li_2[**7**]) such as 9-hydroxy-9,9′-bifluorenyl. The generally accepted mechanism rests on Wagner−Meerwein-type rearrangement of tetraphenylethylium ions such as [**D**]$^+$ (Scheme 5).[57] Given the

Scheme 5. Tetraphenylethylium Ion [D]$^+$ Is Thought To Link Dibenzo[*g*,*p*]chrysene and 9-Hydroxy-9,9′-bifluorenyl Under Clemmensen Conditions[a]

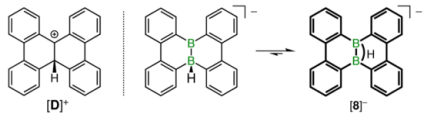

[a]The putative borane-borate carrying a terminal hydrogen substituent is the isoelectronic analogue of [D]$^+$. The anion was isolated in the form of its hydrogen-bridged isomer [**8**]$^-$; *t*Bu groups omitted.

isoelectronic relationship between carbenium ions and three-coordinate boranes, the tetraphenylethylium mechanism provides a plausible model to explain also the processes leading to Li_2[**6**]/Li_2[**7**] (see the SI for the detailed mechanistic proposal). In this scenario, borane-borates would act as analogues of tetraphenylethylium intermediates (e.g., [**8**]$^-$ is equivalent to [**D**]$^+$; Scheme 5). The required borane-borates might conceivably be generated through hydride exchange processes such as the ones taking place between K_2[**5**] and **4** (Scheme 4). However, if the borane-borate mechanism was indeed valid, K[**8**] would have to show a pronounced tendency to rearrange, but we always found it long-term stable in solution under inert conditions. We currently assume that the decisive difference between, e.g., [**D**]$^+$ and [**8**]$^-$ lies in the bridging hydrogen atom, which possibly shuts down 1,2-phenyl shifts in the boron species.

As an alternative to the borane-borate mechanism, the rearrangement cascade of **4** might be triggered by one-electron injection to create open-shell intermediates. Such a route would parallel the facile radical-promoted rearrangement of bifluorenylidene to dibenzo[*g*,*p*]chrysene. Harvey et al. have performed a detailed quantum-chemical study of the latter transformation[58] and the computed steps along the reaction coordinate are shown in Scheme 6 (left). An analogous

DOI: 10.1021/jacs.6b02303
J. Am. Chem. Soc. 2016, 138, 6224−6233

sequence can be written down also for the reduction of **4** (Scheme 6, right).

Scheme 6. Quantum-Chemically Calculated Mechanism of the Rearrangement Reaction Linking Dibenzo[*g*,*p*]chrysene and Bifluorenylidene (Left), and Analogous Reduction-Induced Sequence Explaining the Formation of $[5]^{2-}$, $[6]^{2-}$, and $[7]^{2-}$ from 4 (Right; Bold Indicates Isolated Species)[a]

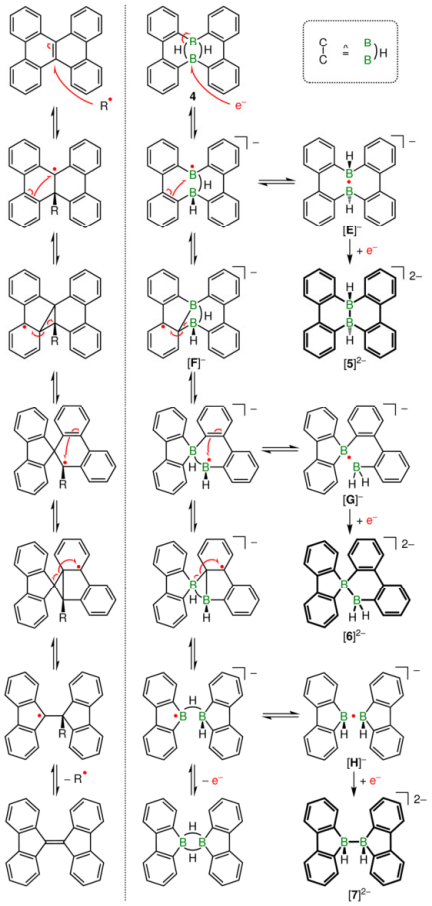

[a]In all boron compounds, *t*Bu groups were omitted for clarity.

Three general classes of reactions are involved: (i) electron injection, (ii) homolytic cleavage of a C=C π bond with concomitant formation of a B–C bond (and vice versa), (iii) hydrogen shift from a B–B bridging position to a terminal position accompanied by a shift of the odd electron into the space between the two B atoms.

The seemingly most exotic among the suggested boron intermediates are the B•B half-bonded (1e2c) species $[\mathbf{E}]^-$, $[\mathbf{G}]^-$, and $[\mathbf{H}]^-$. It is therefore important to recall the isolable and fully characterized B•B compounds Li[**I**] and Li[**J**],[39,41] which are structurally very similar to $[\mathbf{G}]^-$ and $[\mathbf{H}]^-$ (Figure 9a). Furthermore, $[\mathbf{H}]^-$ is a most plausible primary product of

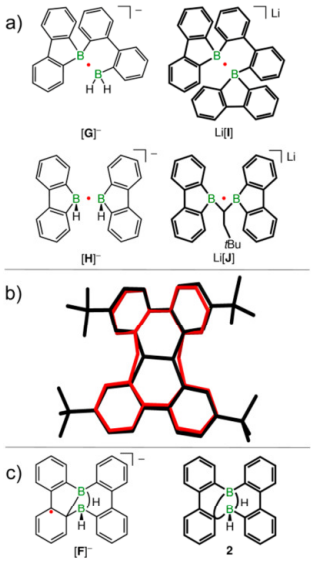

Figure 9. (a) Proposed B•B half-bonded reduction intermediates $[\mathbf{G}]^-$ and $[\mathbf{H}]^-$, and their synthetically accessible analogues Li[**I**] and Li[**J**]. (b) Overlay of the crystallographically determined molecular structure of $[\mathbf{5}]^{2-}$ (black) onto the calculated structure of its doubly oxidized congener **5′** (red; no B–B bond, no *t*Bu groups). (c) Proposed B–C–B-bridged radical intermediate $[\mathbf{F}]^-$ and the structurally related, isolable diborane(6) **2** (*t*Bu groups omitted).

the reduction of **3** and therefore provides an entry path for the experimentally observed reaction sequence ultimately leading to $[\mathbf{1}]^{2-}$ (cf. Scheme 1). With respect to $[\mathbf{E}]^-$, we note that the molecular backbones of its reduced form $[\mathbf{5}]^{2-}$ and its oxidized form **5′** (no B–B bond; calculated structure)[29] are virtually identical, apart from the larger B···B distance in **5′** (2.591 Å) as compared to $[\mathbf{5}]^{2-}$ (1.755(4) Å; cf. overlay of **5′** and $[\mathbf{5}]^{2-}$ in Figure 9b). Thus, a B•B 1e2c bond should likewise be compatible with the steric constraints imposed by the two 2,2′-biphenylene bridges. Finally, the molecular scaffold of $[\mathbf{F}]^-$ is reminiscent of the 9*H*-9-borafluorene dimer **2**, which we have used as starting material for the synthesis of **4** and $Li_2[\mathbf{1}]$ (cf. Scheme 1 and Figure 9c).

The most important conclusion that can be drawn from the radical mechanism outlined in Scheme 6 relates to our initial question: *Why does the extent of skeletal rearrangement correlate with the amount of added reducing agent?*

The monoreduced radical anions are dynamic, but these processes come to an end as soon as the second reduction has taken place to give closed-shell products. If the reducing agent is in large supply (11 equiv of LiNaph/THF, 20 equiv of KC_8), a second electron becomes available immediately after the first electron has been accepted. The primary radical has not enough time to rearrange such that $Li_2[\mathbf{1}]$ and $K_2[\mathbf{5}]$ are obtained.

DOI: 10.1021/jacs.6b02303
J. Am. Chem. Soc. 2016, 138, 6224–6233

Lowering the amount of LiNaph or KC_8 to 4 equiv gives the radical time to rearrange at least once and to finally furnish $[\mathbf{6}]^{2}$. In the presence of only 2 reduction equivalents, the radical can complete the full cascade and thereby form also $[\mathbf{7}]^{2-}$ after the second reduction step. Of course, up to a specific point in time an equilibrating mixture will not have generated one single species, but a distribution of several products in different stoichiometric ratios. Consequently, the reactions observed are not perfectly selective and this explains why we are usually facing more than one product.

■ CONCLUSION

Molecular chemistry is based upon the directed manipulation of covalent bonds. Underlying redistributions of the valence-electron shell can be investigated in their purest form by adding individual electrons without their accompanying atomic nuclei. In the systematic study presented herein, we have examined the reduction of 1,2:1,2-bis(4,4′-di-*tert*-butyl-2,2′-biphenylylene)-diborane(6) ($R_2B(\mu\text{-}H)_2BR_2$, **4**). Irrespective of the conditions applied, the formation of a B−B 2e2c bond could be achieved. In some cases, this process was accompanied by 1,2-phenyl shifts leading to the structurally characterized ring-contracted derivatives $Li_2[\mathbf{6}]$ and $Li_2[\mathbf{7}]$. The degree of rearrangement critically depends on the number of redox equivalents used and the way they are supplied. Excess reducing agent is helpful to suppress the rearrangement reactions. Under these conditions, KC_8 furnishes $K_2[R_2(H)B{-}B(H)R_2]$ ($K_2[\mathbf{5}]$) and Li granules or LiNaph/THF produce $Li_2[R_2B{=}BR_2]$ ($Li_2[\mathbf{1}]$), but no $Li_2[\mathbf{5}]$. A reason why $K_2[\mathbf{5}]$ is isolable whereas $Li_2[\mathbf{5}]$ remains elusive may be the higher heat of formation/lattice energy of LiH vs KH: Hydride abstraction from $[\mathbf{5}]^{2-}$ with concomitant double-electron injection would provide a straightforward route to $[\mathbf{1}]^{2-}$. Hydride transfer also plays a role in the reaction of **4** with 1 equiv of KC_8, which provides access to $K[(\mu\text{-}H)R_2B{-}BR_2]$ ($K[\mathbf{8}]$). In an independent experiment, a mixture of **4** and $K_2[\mathbf{5}]$ also gave $K[\mathbf{8}]$.

We finally outlined a closed-shell borane-borate as well as an open-shell mechanism, which could both account for the complex rearrangement scenario. Considering the currently available experimental data, we are inclined to prefer the radical mechanism. It not only explains how all experimentally observed products are generated, but also rationalizes the correlation between the product distribution and the amount of reducing agent employed.

■ ASSOCIATED CONTENT

Supporting Information

The Supporting Information is available free of charge on the ACS Publications website at DOI: 10.1021/jacs.6b02303.

Experimental details and characterization data (PDF)
X-ray crystallographic data (CIF)

■ AUTHOR INFORMATION

Corresponding Author

*matthias.wagner@chemie.uni-frankfurt.de

Notes

The authors declare no competing financial interest.

■ ACKNOWLEDGMENTS

T.K. and A.H. thank the Fonds der Chemischen Industrie for Ph.D. grants. Donations of lithium organyls by Rockwood Lithium GmbH are gratefully acknowledged.

■ REFERENCES

(1) Zhou, Z.; Wakamiya, A.; Kushida, T.; Yamaguchi, S. *J. Am. Chem. Soc.* **2012**, *134*, 4529−4532.
(2) Dou, C.; Saito, S.; Matsuo, K.; Hisaki, I.; Yamaguchi, S. *Angew. Chem., Int. Ed.* **2012**, *51*, 12206−12210.
(3) Saito, S.; Matsuo, K.; Yamaguchi, S. *J. Am. Chem. Soc.* **2012**, *134*, 9130−9133.
(4) Caruso, A., Jr.; Tovar, J. D. *Org. Lett.* **2011**, *13*, 3106−3109.
(5) Caruso, A., Jr.; Tovar, J. D. *J. Org. Chem.* **2011**, *76*, 2227−2239.
(6) Levine, D. R.; Caruso, A., Jr.; Siegler, M. A.; Tovar, J. D. *Chem. Commun.* **2012**, *48*, 6256−6258.
(7) Hoffend, C.; Schödel, F.; Bolte, M.; Lerner, H.-W.; Wagner, M. *Chem. - Eur. J.* **2012**, *18*, 15394−15405.
(8) Reus, C.; Weidlich, S.; Bolte, M.; Lerner, H.-W.; Wagner, M. *J. Am. Chem. Soc.* **2013**, *135*, 12892−12907.
(9) Berger, C. J.; He, G.; Merten, C.; McDonald, R.; Ferguson, M. J.; Rivard, E. *Inorg. Chem.* **2014**, *53*, 1475−1486.
(10) Hertz, V. M.; Bolte, M.; Lerner, H.-W.; Wagner, M. *Angew. Chem., Int. Ed.* **2015**, *54*, 8800−8804.
(11) Hertz, V. M.; Lerner, H.-W.; Wagner, M. *Org. Lett.* **2015**, *17*, 5240−5243.
(12) Schickedanz, K.; Trageser, T.; Bolte, M.; Lerner, H.-W.; Wagner, M. *Chem. Commun.* **2015**, *51*, 15808−15810.
(13) Miyamoto, F.; Nakatsuka, S.; Yamada, K.; Nakayama, K.; Hatakeyama, T. *Org. Lett.* **2015**, *17*, 6158−6161.
(14) For selected review articles on organoboron materials, see: (a) Entwistle, C. D.; Marder, T. B. *Angew. Chem., Int. Ed.* **2002**, *41*, 2927−2931. (b) Yamaguchi, S.; Wakamiya, A. *Pure Appl. Chem.* **2006**, *78*, 1413−1424. (c) Jäkle, F. *Chem. Rev.* **2010**, *110*, 3985−4022. (d) Hudson, Z. M.; Wang, S. *Dalton Trans.* **2011**, *40*, 7805−7816. (e) Rao, Y.-L.; Amarne, H.; Wang, S. *Coord. Chem. Rev.* **2012**, *256*, 759−770. (f) Lorbach, A.; Hübner, A.; Wagner, M. *Dalton Trans.* **2012**, *41*, 6048−6063. (g) Escande, A.; Ingleson, M. J. *Chem. Commun.* **2015**, *51*, 6257−6274.
(15) Doi, H.; Kinoshita, M.; Okumoto, K.; Shirota, Y. *Chem. Mater.* **2003**, *15*, 1080−1089.
(16) Wu, T.; Shen, H.; Sun, L.; Cheng, B.; Liu, B.; Shen, J. *New J. Chem.* **2012**, *36*, 1385−1391.
(17) Han, J.; Zhang, L. L.; Lee, S.; Oh, J.; Lee, K.-S.; Potts, J. R.; Ji, J.; Zhao, X.; Ruoff, R. S.; Park, S. *ACS Nano* **2013**, *7*, 19−26.
(18) Wu, Z.-S.; Ren, W.; Xu, L.; Li, F.; Cheng, H.-M. *ACS Nano* **2011**, *5*, 5463−5471.
(19) Fang, H.; Yu, C.; Ma, T.; Qiu, J. *Chem. Commun.* **2014**, *50*, 3328−3330.
(20) Lorbach, A.; Bolte, M.; Li, H.; Lerner, H.-W.; Holthausen, M. C.; Jäkle, F.; Wagner, M. *Angew. Chem., Int. Ed.* **2009**, *48*, 4584−4588.
(21) Januszewski, E.; Lorbach, A.; Grewal, R.; Bolte, M.; Bats, J. W.; Lerner, H.-W.; Wagner, M. *Chem. - Eur. J.* **2011**, *17*, 12696−12705.
(22) Seven, Ö.; Qu, Z.-W.; Zhu, H.; Bolte, M.; Lerner, H.-W.; Holthausen, M. C.; Wagner, M. *Chem. - Eur. J.* **2012**, *18*, 11284−11295.
(23) Hoffend, C.; Diefenbach, M.; Januszewski, E.; Bolte, M.; Lerner, H.-W.; Holthausen, M. C.; Wagner, M. *Dalton Trans.* **2013**, *42*, 13826−13837.
(24) Reus, C.; Guo, F.; John, A.; Winhold, M.; Lerner, H.-W.; Jäkle, F.; Wagner, M. *Macromolecules* **2014**, *47*, 3727−3735.
(25) Hübner, A.; Bolte, M.; Lerner, H.-W.; Wagner, M. *Angew. Chem., Int. Ed.* **2014**, *53*, 10408−10411.
(26) Bissinger, P.; Braunschweig, H.; Damme, A.; Kupfer, T.; Vargas, A. *Angew. Chem., Int. Ed.* **2012**, *51*, 9931−9934.
(27) Braunschweig, H.; Damme, A.; Dewhurst, R. D.; Vargas, A. *Nat. Chem.* **2013**, *5*, 115−121.
(28) Bissinger, P.; Steffen, A.; Vargas, A.; Dewhurst, R. D.; Damme, A.; Braunschweig, H. *Angew. Chem., Int. Ed.* **2015**, *54*, 4362−4366.
(29) Hübner, A.; Qu, Z.-W.; Englert, U.; Bolte, M.; Lerner, H.-W.; Holthausen, M. C.; Wagner, M. *J. Am. Chem. Soc.* **2011**, *133*, 4596−4609.

DOI: 10.1021/jacs.6b02303
J. Am. Chem. Soc. 2016, 138, 6224−6233

(30) Hübner, A.; Diefenbach, M.; Bolte, M.; Lerner, H.-W.; Holthausen, M. C.; Wagner, M. *Angew. Chem., Int. Ed.* **2012**, *51*, 12514−12518.
(31) For the corresponding Me_2S adduct, see: Das, A.; Hübner, A.; Weber, M.; Bolte, M.; Lerner, H.-W.; Wagner, M. *Chem. Commun.* **2011**, *47*, 11339−11341. For the NMR data of **3**, see the SI.
(32) Hübner, A.; Diehl, A. M.; Bolte, M.; Lerner, H.-W.; Wagner, M. *Organometallics* **2013**, *32*, 6827−6833.
(33) THF has only a negligible influence on the structural integrity of **4** under the conditions applied. According to ^{1}H NMR spectroscopy, a solution of the compound in THF-d_8 contains no **3** after 2 h at room temperature, about 1% after 1 d, and 5−10% after 30 d.
(34) Stock, A.; Laudenklos, H. *Z. Anorg. Allg. Chem.* **1936**, *228*, 178−192.
(35) (a) Klemm, L.; Klemm, W. *Z. Anorg. Allg. Chem.* **1935**, *225*, 258−261. (b) Hough, W. V.; Edwards, L. J.; McElroy, A. D. *J. Am. Chem. Soc.* **1956**, *78*, 689−689. (c) Hough, W. V.; Edwards, L. J.; McElroy, A. D. *J. Am. Chem. Soc.* **1958**, *80*, 1828−1829. (d) Hough, W. V.; Edwards, L. J. *Adv. Chem. Ser.* **1961**, *32*, 184−194. (e) Heřmánek, S.; Plešek, J. *Collect. Czech. Chem. Commun.* **1966**, *31*, 177−189. (f) Gaines, D. F.; Schaeffer, R.; Tebbe, F. *Inorg. Chem.* **1963**, *2*, 526−528.
(36) Godfroid, R. A.; Hill, T. G.; Onak, T. P.; Shore, S. G. *J. Am. Chem. Soc.* **1994**, *116*, 12107−12108.
(37) Shoji, Y.; Matsuo, T.; Hashizume, D.; Gutmann, M. J.; Fueno, H.; Tanaka, K.; Tamao, K. *J. Am. Chem. Soc.* **2011**, *133*, 11058−11061.
(38) Shoji, Y.; Kaneda, S.; Fueno, H.; Tanaka, K.; Tamao, K.; Hashizume, D.; Matsuo, T. *Chem. Lett.* **2014**, *43*, 1587−1589.
(39) Hübner, A.; Kaese, T.; Diefenbach, M.; Endeward, B.; Bolte, M.; Lerner, H.-W.; Holthausen, M. C.; Wagner, M. *J. Am. Chem. Soc.* **2015**, *137*, 3705−3714.
(40) In the meantime, also the dianion $[(NC)_3B{-}B(CN)_3]^{2-}$ has been synthesized: Landmann, J.; Sprenger, J. A. P.; Hailmann, M.; Bernhardt-Pitchougina, V.; Willner, H.; Ignat'ev, N.; Bernhardt, E.; Finze, M. *Angew. Chem., Int. Ed.* **2015**, *54*, 11259−11264.
(41) Hübner, A.; Diehl, A. M.; Diefenbach, M.; Endeward, B.; Bolte, M.; Lerner, H.-W.; Holthausen, M. C.; Wagner, M. *Angew. Chem., Int. Ed.* **2014**, *53*, 4832−4835.
(42) Braunschweig, H.; Dewhurst, R. D.; Mozo, S. *ChemCatChem* **2015**, *7*, 1630−1638.
(43) Evans, D. H.; Hu, K. *J. Chem. Soc., Faraday Trans.* **1996**, *92*, 3983−3990.
(44) The reduction potential of **4** is significantly more cathodic than the potentials of other arylboranes containing two tricoordinate boron atoms, cf. refs 7, 8, 10, 23.
(45) DuPont, T. J.; Mills, J. L. *J. Am. Chem. Soc.* **1975**, *97*, 6375−6382.
(46) Nakahama, S.; Hashimoto, K.; Yamazaki, N. *Polym. J.* **1973**, *4*, 437−445.
(47) Hatakeyama, T.; Hashimoto, S.; Seki, S.; Nakamura, M. *J. Am. Chem. Soc.* **2011**, *133*, 18614−18617.
(48) Eisch, J. J.; Kovacs, C. A.; Chobe, P. *J. Org. Chem.* **1989**, *54*, 1275−1284.
(49) Fox, M. A.; Whitesell, J. K. *Organic Chemistry*, 3rd ed.; Jones and Bartlett Publishers: Boston, Toronto, London, and Singapore, 2004.
(50) Grigsby, W. J.; Power, P. P. *J. Am. Chem. Soc.* **1996**, *118*, 7981−7988.
(51) Sridevi, V. S.; Leong, W. K.; Zhu, Y. *Organometallics* **2006**, *25*, 283−288.
(52) Littger, R.; Metzler, N.; Nöth, H.; Wagner, M. *Chem. Ber.* **1994**, *127*, 1901−1908.
(53) Wittig, G.; Barendt, E.; Schoch, W. *Justus Liebigs Ann. Chem.* **1971**, *749*, 24−37.
(54) Lammertsma, K.; Ohwada, T. *J. Am. Chem. Soc.* **1996**, *118*, 7247−7254.
(55) Holleman, A. F.; Wiberg, E.; Wiberg, N. *Lehrbuch der Anorganischen Chemie*, 101st ed.; de Gruyter: Berlin and New York, 1995.
(56) (a) Hertz, R. K.; Johnson, H. D., II; Shore, S. G. *Inorg. Chem.* **1973**, *12*, 1875−1877. (b) Khan, S. I.; Chiang, M. Y.; Bau, R.; Koetzle, T. F.; Shore, S. G.; Lawrence, S. H. *J. Chem. Soc., Dalton Trans.* **1986**, 1753−1757. (c) Wrackmeyer, B. *Z. Naturforsch., B: J. Chem. Sci.* **2004**, *59*, 1192−1199. (d) Pospiech, S.; Bolte, M.; Lerner, H.-W.; Wagner, M. *Chem. - Eur. J.* **2015**, *21*, 8229−8236.
(57) (a) Braunschweig, H.; Damme, A.; Dewhurst, R. D.; Kramer, T.; Kupfer, T.; Radacki, K.; Siedler, E.; Trumpp, A.; Wagner, K.; Werner, C. *J. Am. Chem. Soc.* **2013**, *135*, 8702−8707. (b) Harvey, R. G. *Polycyclic Aromatic Hydrocarbons*; Wiley-VCH: Weinheim and New York, 1997. (c) Talapatra, S. K.; Chakrabarti, S.; Mallik, A. K.; Talapatra, B. *Tetrahedron* **1990**, *46*, 6047−6052. (d) Suzuki, K. *Bull. Chem. Soc. Jpn.* **1962**, *35*, 735−740.
(58) Alder, R. W.; Harvey, J. N. *J. Am. Chem. Soc.* **2004**, *126*, 2490−2494.

DOI: 10.1021/jacs.6b02303
J. Am. Chem. Soc. 2016, 138, 6224−6233

Supporting Information

Forming B–B Bonds by the Controlled Reduction of a Tetraaryl-diborane(6)

*Thomas Kaese, Alexander Hübner, Michael Bolte, Hans-Wolfram Lerner, and Matthias Wagner**

Content:

1. Experimental details and characterization data
2. NMR spectroscopic characterization of the 9*H*-9-borafluorene THF-d_8 adduct **3**.
3. Plots of the ^{1}H, ^{11}B, and ^{13}C{^{1}H} NMR spectra of Li_2[**6**], Li_2[**7**], K_2[**5**], and K[**8**].
4. Plot of the ^{1}H NMR spectrum of the reaction mixture between **4** and K_2[**5**].
5. NMR spectra of the reaction mixture of **4** with KH in THF-d_8 to give K[**9**] and K_2[**10**].
6. Comparison of the tetraphenylethylium reaction mechanism and the borane-borate mechanism.
7. X-ray crystal structure analyses of **4**, $[Li_2(thf)_3][\mathbf{1}]\cdot 0.5C_7H_8$, $[Li(thf)_3][Li(thf)_2][\mathbf{6}]$, $[Li(thf)]_3[Li][\mathbf{7}]_2$, $[K_2(thf)_4][\mathbf{5}]$, $[K(thf)_2][\mathbf{8}]$, and $[K(thf)_3][K(thf)][\mathbf{10}]$.
8. References

1. Experimental details and characterization data

General Considerations. All reactions, manipulations and analyses were carried out in an argon-filled glovebox or by applying standard Schlenk techniques under an argon atmosphere. Toluene and THF were dried over Na/benzophenone (2-3 d); THF-d_8 was dried over Na-K alloy without benzophenone. Prior to use, the solvents were distilled from the drying agent and degassed by applying three freeze-pump-thaw cycles. Compound **4** was synthesized according to a literature procedure.[1] NMR: Avance III 500 HD. Chemical shifts are referenced to (residual) solvent signals (^{1}H/^{13}C{^{1}H}; THF-d_8: δ = 3.58/67.21 ppm) or external $BF_3{\cdot}Et_2O$ (^{11}B; ^{11}B{^{1}H}). Abbreviations: s = singlet, d = doublet, t = triplet, q = quartet, m = multiplet, br = broad, n.r. = multiplet expected in the NMR spectrum but not resolved, n.o. = not observed. The cyclic voltammogram was recorded at room temperature in a one-chamber, three electrode cell using an EG&G Princeton Applied Research 263A potentiostat with a platinum disk working electrode (diameter 2.00 mm). The reference electrode was a silver wire on which AgCl had been deposited by immersing the wire into HCl/HNO_3 (3:1). [nBu$_4$N][PF_6] (0.1 M) was employed as the supporting electrolyte. All potential values are referenced against the FcH/FcH^+ couple ($E_{1/2}$ = 0 V). The coulometric measurement was performed at room temperature using a Pt-net electrode. Combustion analyses were performed by the Microanalytical Laboratory Pascher (Remagen, Germany).

Synthesis of [Li(thf)$_3$]$_2$[1]. THF (5 mL) was added at room temperature with vigorous stirring to a mixture of **4** (80 mg, 0.14 mmol), and lithium granules (60 mg, 8.6 mmol). The initially colorless reaction mixture instantaneously adopted a dark red color. After 16 h, insoluble material was removed by filtration (G4 frit). NMR spectroscopic control (^{1}H, ^{11}B; THF-d_8) of the deep red filtrate revealed the presence of Li_2[**6**] and Li_2[**1**] as the major products in approximately equal amounts. The filtrate was concentrated to about 40% of its original volume under vacuum. Upon storage at –30 °C for several days, a red solid precipitated. The supernatant was removed and the red microcrystalline residue was dried under vacuum. Molecular formula according to ^{1}H NMR spectroscopy: Li_2[**1**] × THF (636.35 g mol^{-1}). Yield: 37 mg (0.058 mmol, 41%). Red single crystals of [Li(thf)$_3$]$_2$[**1**] were grown from a concentrated THF solution at 5 °C. For NMR data and the X-ray crystal structure analysis, see ref[2].

Synthesis of [Li$_2$(thf)$_3$][1]: A mixture of **4** (83 mg, 0.15 mmol) and lithium granules (125 mg, 18.0 mmol) was suspended in toluene (8 mL). THF (80 µL) was added at room temperature with vigorous stirring. Within 20 min, the color of the liquid phase changed from colorless to dark red. Stirring was continued at room temperature overnight. NMR spectroscopic control (^{1}H, ^{11}B; THF-d_8) of the reaction solution revealed the presence of Li_2[**6**] and Li_2[**1**] as the major products in an approximate stoichiometric ratio of 3:2. Excess lithium metal was removed by filtration (G4 frit), and the filtrate

was concentrated to 20% of its original volume under vacuum. The dark red solution was stored at −30 °C for 2 d and subsequently at 5 °C for 30 d, whereupon red single crystals of $[Li_2(thf)_3][\mathbf{1}]$ formed in 30% yield.

Synthesis of Li_2[6]. A colorless solution of **4** (36 mg, 0.065 mmol) in toluene (10 mL) was added dropwise with stirring at −78 °C to a dark green solution of LiNaph in THF (0.90 M, 0.29 mL, 0.26 mmol). After 2 h, the reaction mixture was allowed to warm to room temperature, and stirring was continued for 16 h. The dark red solution was evaporated to dryness under vacuum. The solid residue was suspended in hexane (4 mL), insoluble material was collected on a frit (G4), washed with hexane (3 × 3 mL), and dried under vacuum. The yellow crude product (16 mg) was dissolved in THF (0.5 mL) and stored at −30 °C for 4 d, whereupon a yellow precipitate formed. The mother liquor was discarded and the solid was dried under vacuum. Molecular formula according to ^{1}H NMR spectroscopy: Li_2[**6**] × 2 THF (710.48 g mol^{-1}). Yield: 11 mg (0.015 mmol, 23%). Yellow crystals of $[Li(thf)_3][Li(thf)_2]$[**6**] suitable for X-ray crystallography were obtained by storing a solution of the product in THF (4 mL) at −30 °C.

^{1}H NMR (500.2 MHz, THF-d_8, 298 K): δ = 7.59-7.47 (n.r., 2H; H-c), 7.41 (n.r., 1H; H-1a), 7.28 (d, ^3J(H,H) = 7.8 Hz, 1H; H-4a), 7.19 (d, ^3J(H,H) = 7.9 Hz, 1H; H-4b), 7.11 (n.r., 1H; H-1b), 7.03 (dd, ^3J(H,H) = 7.8 Hz, ^4J(H,H) = 2.3 Hz, 1H; H-3a), 6.98-6.80 (n.r., 2H; H-c), 6.76 (dd, ^3J(H,H) = 7.9 Hz, ^4J(H,H) = 2.3 Hz, 1H; H-3b), 1.29 (s, 9H; $C(CH_3)_3$-a), 1.20 (br, 18H; $C(CH_3)_3$-c), 1.11 (s, 9H; $C(CH_3)_3$-b), n.o. (2 × 2H; H-c, BH_2).

^{11}B{^{1}H} NMR (160.5 MHz, THF-d_8, 298 K): δ = −11.0 (s, $h_{½}$ = 80 Hz), −19.9 (s, $h_{½}$ = 90 Hz; BH_2).

^{11}B NMR (160.5 MHz, THF-d_8, 298 K): δ = −11.0 (s, $h_{½}$ = 90 Hz), −19.9 (br, $h_{½}$ = 180 Hz; BH_2).

^{13}C{^{1}H} NMR (125.8 MHz, THF-d_8, 298 K): δ = 164.8 (C-6b; determined by ^{1}H-^{13}C-HMBC), 158.8 (C-6a; determined by ^{1}H-^{13}C-HMBC), 147.2 (C-5a), 145.8 (C-2b), 145.1 (C-2a), 144.3 (br, C-c), 142.8 (C-5b), 133.0 (C-1a), 129.5 (br, *C*H-c), 129.0 (C-1b), 123.8 (C-4a), 123.7 (C-4b), 121.0 (C-3a), 119.2 (br, *C*H-c), 118.9 (C-3b), 118.2 (br, *C*H-c), 35.0 (br, 2 × $C(CH_3)_3$-c), 34.8 ($C(CH_3)_3$-b), 34.6 ($C(CH_3)_3$-a), 32.5 (2 × $C(CH_3)_3$-c), 32.2 ($C(CH_3)_3$-a or b), 32.2 ($C(CH_3)_3$-a or b), n.o. (2 × C-c).

Synthesis of Li_2[7]. A dark green solution of LiNaph in THF (0.90 M, 0.16 mL, 0.14 mmol) was added in one portion with vigorous stirring at –78 °C to a colorless suspension of **4** (40 mg, 0.072 mmol) in toluene (15 mL). Stirring of the resulting orange solution was continued for 2.5 h at –78 °C and for 16 h at room temperature. The reaction mixture was evaporated to dryness under vacuum, the solid residue was suspended in pentane (5 mL), insoluble material was collected on a frit (G4), washed with pentane (2 × 2 mL), and dried under vacuum. Molecular formula according to ^{1}H NMR spectroscopy: Li_2[**7**] × 1.5 THF (674.45 g mol^{-1}). Yield: 25 mg (0.037 mmol, 51%). Colorless crystals of $[Li(thf)]_3[Li][\mathbf{7}]_2$ suitable for X-ray analysis crystallized from the pentane filtrate at room temperature within a few hours.

^{1}H NMR (500.2 MHz, THF-d_8, 298 K): δ = 7.23 (d, ^{3}J(H,H) = 7.9 Hz, 4H; H-4), 6.96 (br, 4H; H-1), 6.70 (dd, ^{3}J(H,H) = 7.9 Hz, ^{4}J(H,H) = 2.0 Hz, 4H; H-3), 2.1 (br q, 2H; BH; further confirmed by ^{1}H-^{11}B-HSQC), 1.23 (s, 36H; C(CH$_3$)$_3$).

^{11}B NMR (160.5 MHz, THF-d_8, 298 K): δ = –13.4 (d, ^{1}J(B,H) = 71 Hz).

^{13}C{^{1}H} NMR (125.8 MHz, THF-d_8, 298 K): δ = 167.3 (C-6; confirmed by ^{1}H-^{13}C-HMBC), 144.3 (C-5), 142.7 (C-2), 126.9 (C-1), 117.5 (C-3), 117.4 (C-4), 34.8 (*C*(CH$_3$)$_3$), 32.5 (C(*C*H$_3$)$_3$).

Synthesis of K$_2$[5]: THF (12 mL) was added with stirring at room temperature to a solid mixture of **4** (100 mg, 0.181 mmol) and KC$_8$ (490 mg, 3.62 mmol). The mixture instantaneously adopted a dark red color. After 1 h, insoluble material was separated by filtration (G4 frit) from the dark red liquid phase. The filtrate was evaporated to dryness under vacuum and the brown solid residue was redissolved in THF (2 mL). Et$_2$O (6 mL) was added, whereupon an orange powder precipitated. The supernatant was discarded and the solid was dried under vacuum. Molecular formula according to ^{1}H NMR spectroscopy: K$_2$[**5**] × 0.5 THF (666.65 g mol^{-1}). Yield: 101 mg (0.151 mmol, 83%). Orange crystal blocks of [K$_2$(thf)$_4$][**5**] suitable for X-ray analysis were grown from a THF solution at 5 °C.

^{1}H NMR (500.2 MHz, THF-d_8, 298 K): δ = 8.03 (d, ^{4}J(H,H) = 2.0 Hz, 4H; H-1), 7.31 (d, ^{3}J(H,H) = 8.0 Hz, 4H; H-4), 6.80 (dd, ^{3}J(H,H) = 8.0 Hz, ^{4}J(H,H) = 2.0 Hz, 4H; H-3), 1.7 (br, 2H; BH; confirmed by ^{1}H-^{11}B-HSQC), 1.37 (s, 36H; C(CH$_3$)$_3$).

^{11}B NMR (160.5 MHz, THF-d_8, 298 K): δ = –17.9 (br, $h_{1/2}$ = 180 Hz).

^{13}C{^{1}H} NMR (125.8 MHz, THF-d_8, 298 K): δ = 167.7 (br, C-6), 145.5 (C-2), 144.7 (C-5), 127.4 (C-1), 124.6 (C-4), 118.0 (C-3), 34.8 (*C*(CH$_3$)$_3$), 32.3 (C(*C*H$_3$)$_3$).

Anal. Calcd for C$_{56}$H$_{82}$B$_2$K$_2$O$_4$ [919.03]: C, 73.18; H, 8.99; Found: C, 72.75; H, 7.99.

Synthesis of K[8]:

Method A: THF (2 mL) was added at room temperature with stirring to a solid mixture of **4** (70 mg, 0.13 mmol) and KC$_8$ (18 mg, 0.13 mmol). The initially orange-red suspension turned yellow within 30 min. After 3 h, the suspension was filtered over a frit (G4). Yellow crystals of [K(thf)$_2$][**8**] were grown by gas phase diffusion of hexane into the filtrate. The mother liquor was discarded and the crystals were dried under vacuum. Yield: 55 mg (0.075 mmol, 58%).

Method B: An NMR tube equipped with a J. Young valve was charged with K$_2$[**5**] × 0.5 THF (8.0 mg, 12 µmol) and THF-d_8 (0.5 mL). Neat solid **4** (6.6 mg, 12 µmol) was added at room temperature, the valve was closed, and the sample investigated by NMR spectroscopy.

^{1}H NMR (500.2 MHz, THF-d_8, 298 K): δ = 8.85 (d, ^{4}J(H,H) = 2.3 Hz, 4H; H-1), 8.45 (d, ^{3}J(H,H) = 8.5 Hz, 4H; H-4), 7.38 (dd, ^{3}J(H,H) = 8.5 Hz, ^{4}J(H,H) = 2.3 Hz, 4H; H-3), 1.50 (s, 36H; C(CH$_3$)$_3$), –0.99 (br, 1H; BH).

^{11}B NMR (160.5 MHz, THF-d_8, 298 K): δ = 20.4 (br).

^{13}C{^{1}H} NMR (125.8 MHz, THF-d_8, 298 K): δ = 146.0 (C-2), 145.2 (br, C-6), 138.7 (C-5), 127.8 (C-1), 125.9 (C-4), 121.4 (C-3), 35.1 (*C*(CH$_3$)$_3$), 32.3 (C(*C*H$_3$)$_3$).

Anal. Calcd for C$_{48}$H$_{65}$B$_2$KO$_2$ [734.72]: C, 78.46; H, 8.92; Found: C, 78.66; H, 8.86.

Generation of K[9] and K_2[10]: An NMR tube equipped with a J. Young valve was charged with **4** (20 mg, 36 µmol) and KH (5 mg, 0.1 mmol). THF-d_8 (0.5 mL) was added at room temperature and the valve was closed. NMR spectra recorded after 12 h revealed the presence of K[**9**] together with substantial amounts of unreacted **4**. Two weeks later, **4** was essentially consumed and K[**9**] constituted the major product in the liquid phase. A second, poorly soluble, major product could be identified, after colorless crystals of [K(thf)$_3$][K(thf)][**10**] had grown to a size that enabled their manual separation from unreacted, fine-grained KH.

K[**9**]:

^{1}H NMR (500.2 MHz, THF-d_8, 298 K): δ = 7.62 (br, 2H; H-1), 7.46 (d, ^3J(H,H) = 7.9 Hz, 2H; H-4), 7.01 (br d, ^3J(H,H) = 7.9 Hz, 2H; H-3), 2.19 (q, ^1J(B,H) = 82 Hz, 2H; BH), 1.33 (s, 18H; C(CH$_3$)$_3$).

^{11}B NMR (160.5 MHz, THF-d_8, 298 K): δ = –20.2 (t, ^1J(B,H) = 82 Hz).

^{13}C{^{1}H} NMR (125.8 MHz, THF-d_8, 298 K): δ = 165.9 (q, ^1J(C,B) = 48 Hz; C-6), 147.0 (C-5), 145.8 (C-2), 128.7 (C-1), 120.2 (C-3), 118.0 (C-4), 34.9 (*C*(CH$_3$)$_3$), 32.3 (C(*C*H$_3$)$_3$).

K_2[**10**]:

^{1}H NMR (500.2 MHz, THF-d_8, 298 K): δ = 7.73 (n.r., 1H), 7.65 (n.r., 1H), 7.48 (n.r., 1H), 7.45 (d, ^3J(H,H) = 7.8 Hz, 1H), 7.40 (d, ^3J(H,H) = 8.1 Hz, 1H), 7.20 (d, ^3J(H,H) = 7.9 Hz, 1H), 7.09 (d, ^3J(H,H) = 8.0 Hz, 1H), 7.02 (n.r., 1H), 6.99-6.96 (m, 3H), 6.92 (dd, ^3J(H,H) = 8.0 Hz, ^4J(H,H) = 2.4 Hz, 1H), 2.60 (q, ^1J(B,H) = 77 Hz, 1H), 1.38 (q, ^1J(B,H) = 80 Hz, 3H), 1.33 (s, 9H), 1.29 (br s, 9H), 1.27 (br s, 9H), 1.08 (s, 9H).

^{11}B NMR (160.5 MHz, THF-d_8, 298 K): δ = –13.2 (d, ^1J(B,H) = 77 Hz), –24.6 (q, ^1J(B,H) = 80 Hz).

Crystal Structure Determinations. Data for all structures were collected on a STOE IPDS II two-circle diffractometer with a Genix Microfocus tube with mirror optics using MoK$_\alpha$ radiation (λ = 0.71073 Å). The data were scaled using the frame-scaling procedure in the *X-AREA* program system.[3] The structures were solved by direct methods using the program *SHELXS*[4] and refined against F^2 with full-matrix least-squares techniques using the program *SHELXL-97*.[4] **4**: The H atom bonded to B was isotropically refined. One *t*Bu group is disordered over two positions with a site occupation factor of 0.639(5) for the major occupied site. [Li$_2$(thf)$_3$][**1**]·0.5C$_7$H$_8$: Only 37% of the measured reflections were observed. In subunit I, two *t*Bu groups are disordered over two positions with site occupation factors of 0.61(1) and 0.609(9) for the major occupied sites. In two thf ligands of subunit I, two methylene groups are disordered over two positions with site occupation factors of 0.70(2) and 0.64(2) for the major occupied sites. In one thf ligand of subunit I, one methylene group is disordered over two positions with equal occupancies (0.50(3)). In subunit II, one *t*Bu group is disordered over two positions with a site occupation factor of 0.539(9) for the major occupied site. In two thf ligands of subunit II, two methylene groups are disordered over two positions with site occupation factors of 0.59(2) and 0.54(2) for the major occupied sites. The disordered atoms were isotropically refined. [Li(thf)$_3$][Li(thf)$_2$][**6**]: The H atoms bonded to B were isotropically refined. In two thf ligands, one methylene group is disordered over two positions with site occupation factors of 0.67(3) and 0.62(2) for the major occupied sites. One *t*Bu group is disordered over two positions with a site occupation

factor of 0.63(1) for the major occupied site. The disordered atoms were isotropically refined. Due to the absence of anomalous scatterers, the absolute structure could not be determined reliably. $[Li(thf)]_3[Li][\mathbf{7}]_2$: The H atoms bonded to B were isotropically refined. $[K_2(thf)_4][\mathbf{5}]$: The H atoms bonded to B were isotropically refined. $[K(thf)_2][\mathbf{8}]$: The H atom bonded to B was isotropically refined. In one thf ligand, one methylene group is disordered over two positions with a site occupation factor of 0.53(4) for the major occupied site. One *t*Bu group is disordered over two positions with a site occupation factor of 0.85(2) for the major occupied site. The lower occupied sites of the disordered atoms were isotropically refined. The higher occupied sites of the disordered atoms were anisotropically refined with their displacement ellipsoids restrained to an isotropic behavior. The absolute structure could be determined (Flack-x-parameter 0.05(3)). $[K(thf)_3][K(thf)][\mathbf{10}]$: The H atoms bonded to B were isotropically refined. In three thf ligands, one methylene group is disordered over two positions with site occupation factors of 0.61(2), 0.78(2), and 0.52(4), respectively, for the major occupied sites. In one thf ligand, two methylene groups are disordered over two positions with site occupation factors of 0.53(2) for the major occupied sites. One *t*Bu group is disordered over two positions with a site occupation factor of 0.56(1) for the major occupied sites. The displacement ellipsoids of the disordered atoms were restrained to an isotropic behavior.

CCDC reference numbers: 1456609 (**4**), 1456610 ($[Li_2(thf)_3][\mathbf{1}]\cdot 0.5C_7H_8$), 1456611 ($[Li(thf)_3][Li(thf)_2][\mathbf{6}]$), 1456612 ($[Li(thf)]_3[Li][\mathbf{7}]_2$), 1456613 ($[K_2(thf)_4][\mathbf{5}]$), 1456614 ($[K(thf)_2][\mathbf{8}]$), 1456615 ($[K(thf)_3][K(thf)][\mathbf{10}]$).

2. NMR spectroscopic characterization of the 9*H*-9-borafluorene THF-d_8 adduct 3

Crystalline **2** was dissolved in THF-d_8 to quantitatively give the 9*H*-9-borafluorene THF-d_8 adduct **3** after 1h.

^{1}H NMR (500.2 MHz, THF-d_8, 298 K): δ = 7.55 (d, ^4J(H,H) = 2.0 Hz, 2H; H-1), 7.39 (d, ^3J(H,H) = 8.0 Hz, 2H; H-4), 7.16 (dd, ^3J(H,H) = 8.0, ^4J(H,H) = 2.0 Hz, 2H; H-3), 3.8 (n.r., 1H), 1.33 (s, 18H).
^{11}B NMR (160.5 MHz, THF-d_8, 298 K): δ = 7.5 (n.r., $h_{1/2}$ = 350 Hz).
^{13}C{^{1}H} NMR (125.8 MHz, THF-d_8, 298 K): δ = 150.7 (C-6), 148.3 (C-2), 148.0 (C-5), 128.9 (C-1), 124.4 (C-3), 118.6 (C-4), 34.9 (C(CH$_3$)$_3$), 31.9 (C(CH$_3$)$_3$).

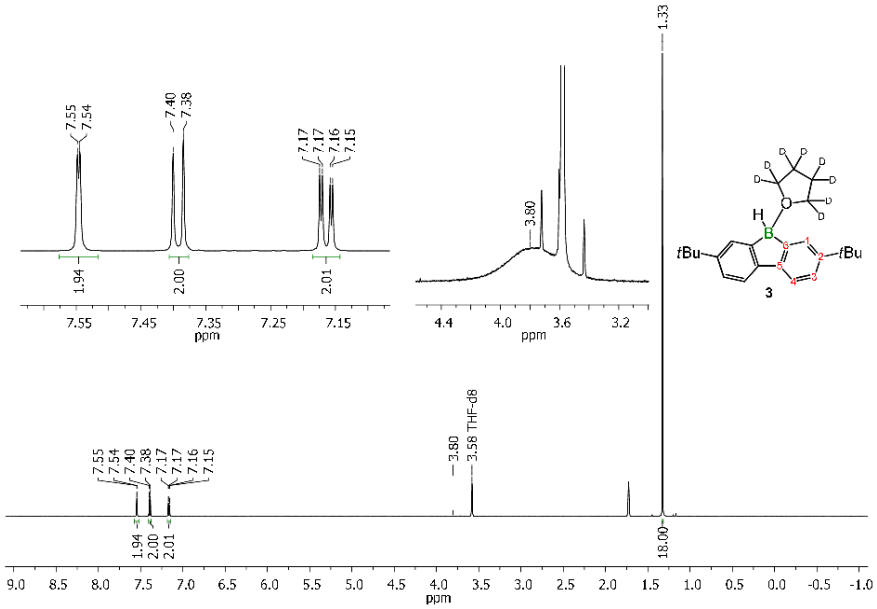

Figure S1. ^{1}H NMR spectrum of **3** (THF-d_8, 500.2 MHz).

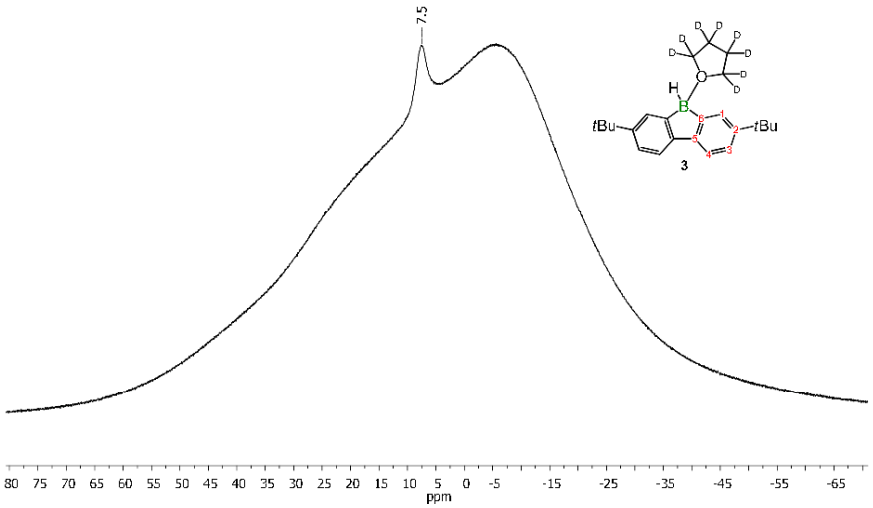

Figure S2. ^{11}B NMR spectrum of **3** (THF-d_8, 160.5 MHz).

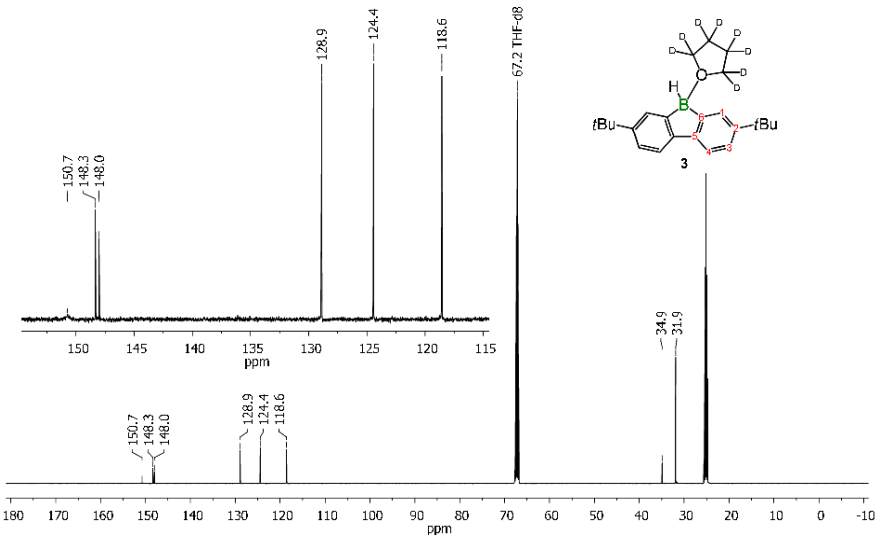

Figure S3. ^{13}C{^{1}H} NMR spectrum of **3** (THF-d_8, 125.8 MHz).

3. Plots of the ^{1}H, ^{11}B, and ^{13}C{1H} NMR spectra of Li_2[6], Li_2[7], K_2[5], and K[8].

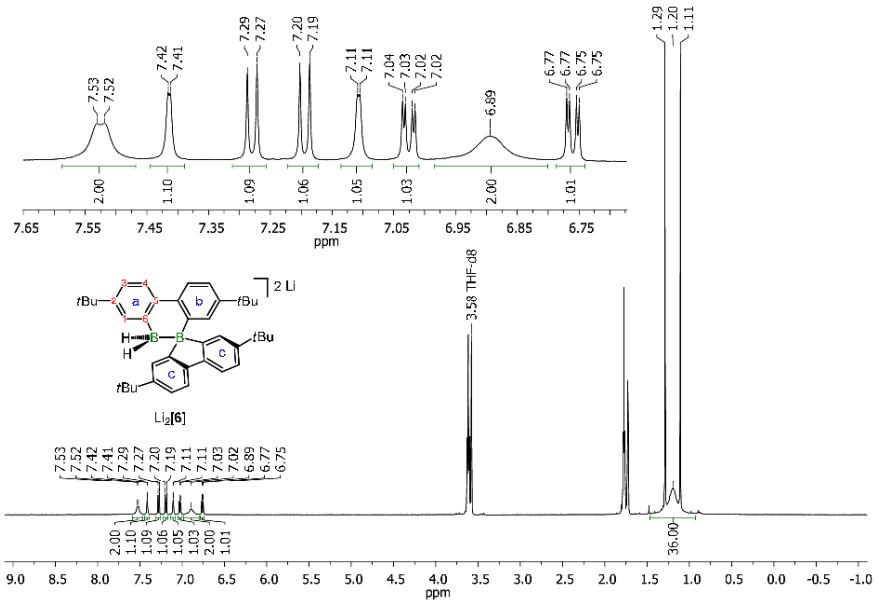

Figure S4. ^{1}H NMR spectrum of Li_2[**6**] (THF-d_8, 500.2 MHz).

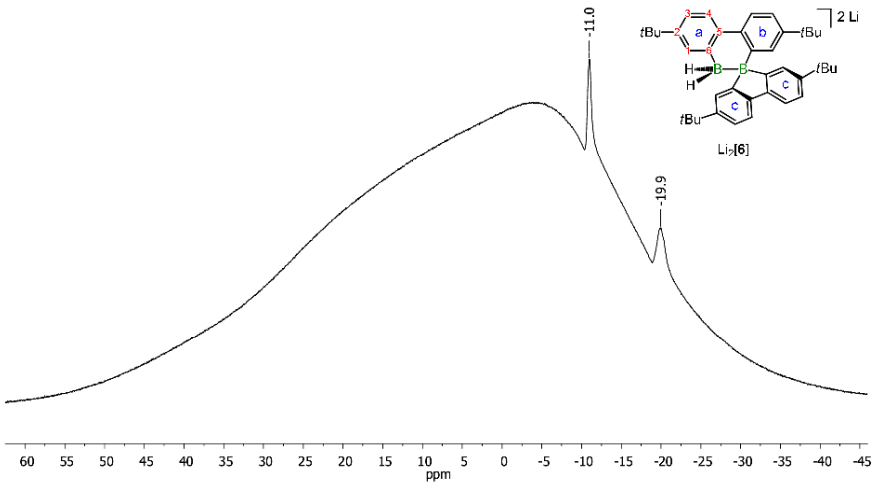

Figure S5. ^{11}B NMR spectrum of Li_2[**6**] (THF-d_8, 160.5 MHz).

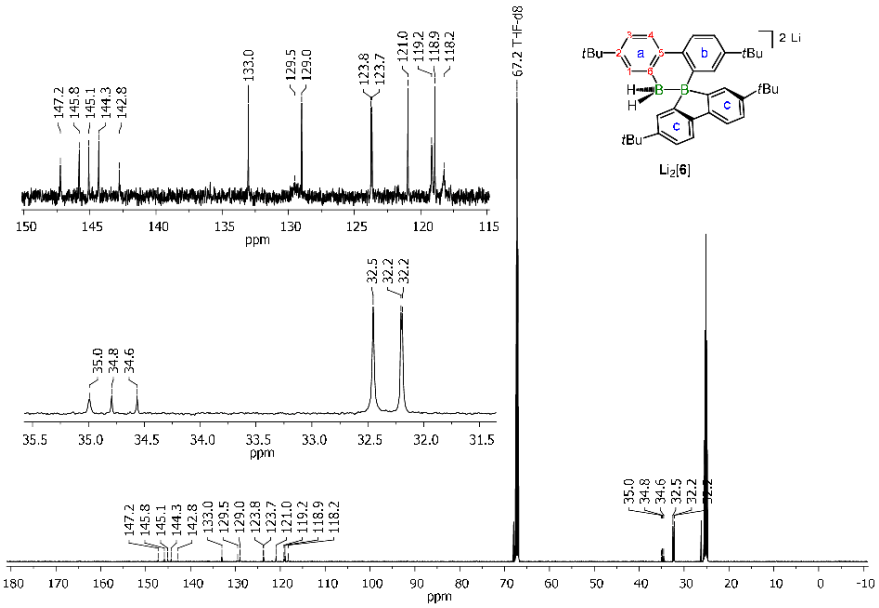

Figure S6. $^{13}C\{^{1}H\}$ NMR spectrum of Li_2[**6**] (THF-d_8, 125.8 MHz).

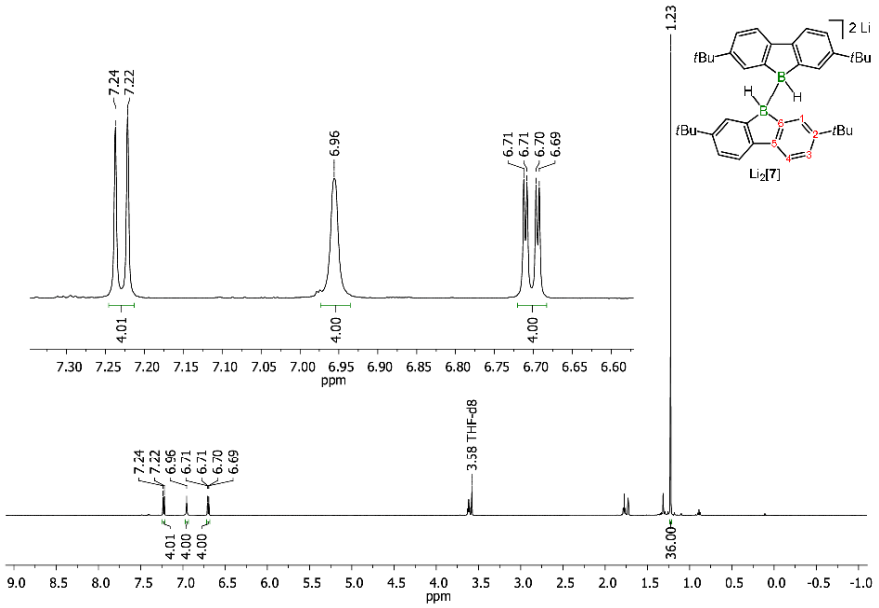

Figure S7. ^{1}H NMR spectrum of Li_2[**7**] (THF-d_8, 500.2 MHz).

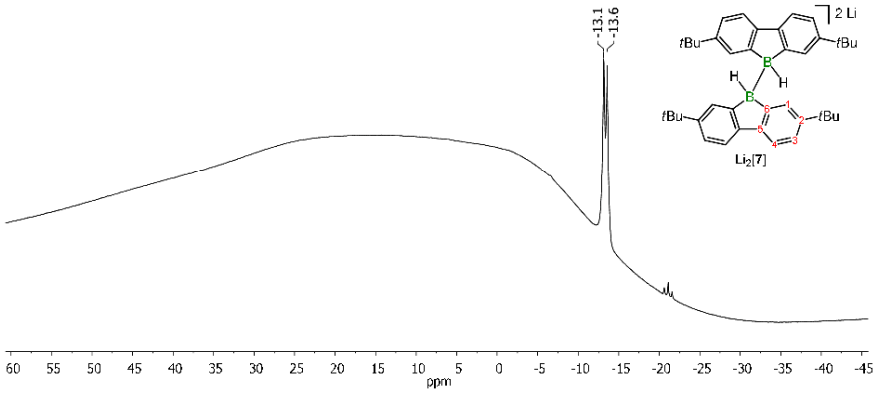

Figure S8. ^{11}B NMR spectrum of Li_2[**7**] (THF-d_8, 160.5 MHz).

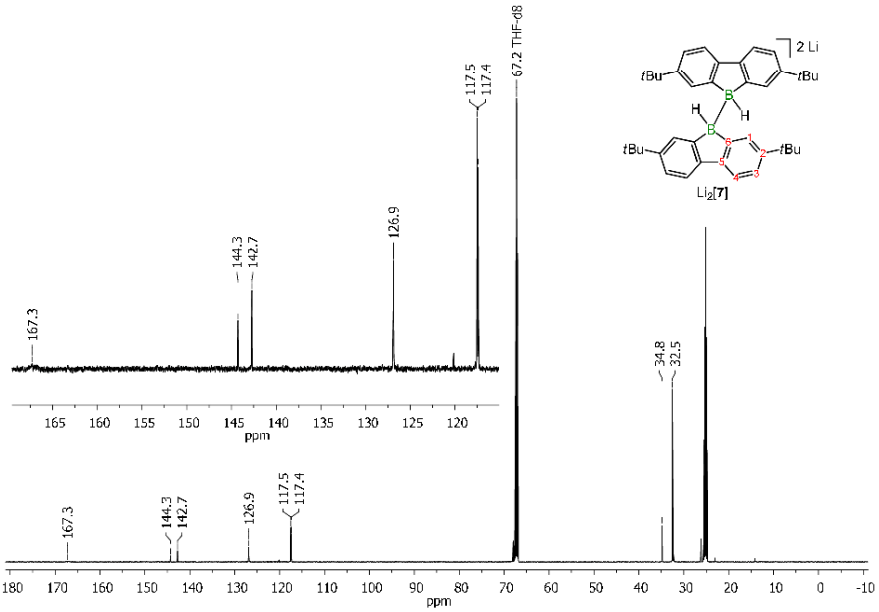

Figure S9. ^{13}C{^{1}H} NMR spectrum of Li_2[**7**] (THF-d_8, 125.8 MHz).

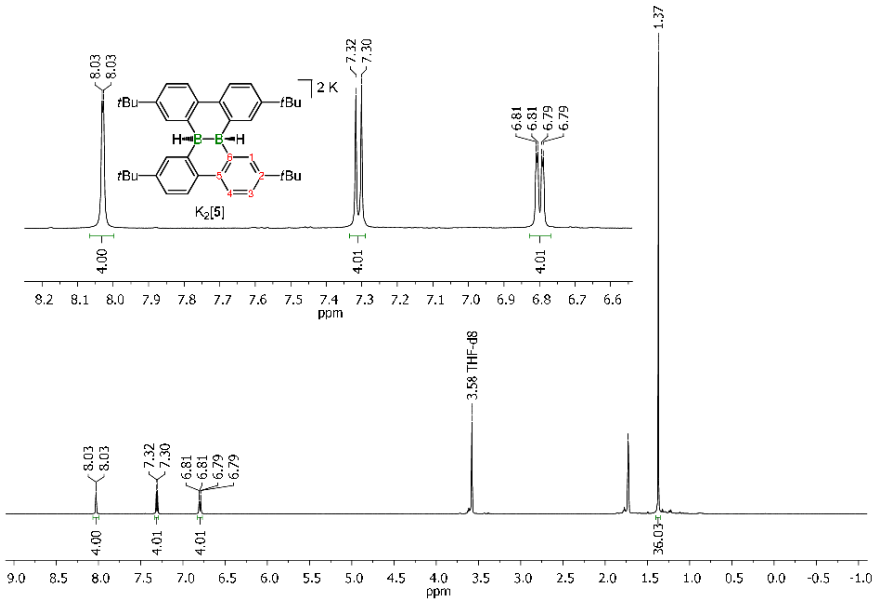

Figure S10. ^{1}H NMR spectrum of K_2[**5**] (THF-d_8, 500.2 MHz).

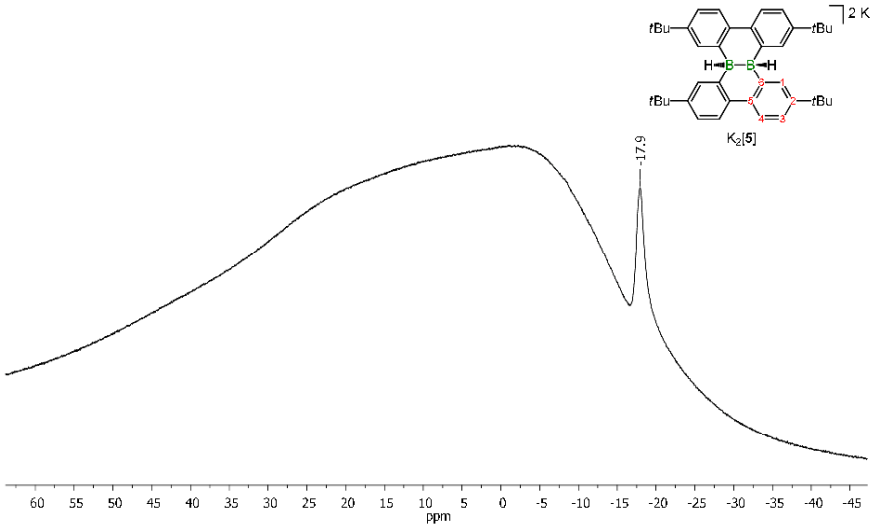

Figure S11. ^{11}B NMR spectrum of K_2[**5**] (THF-d_8, 160.5 MHz).

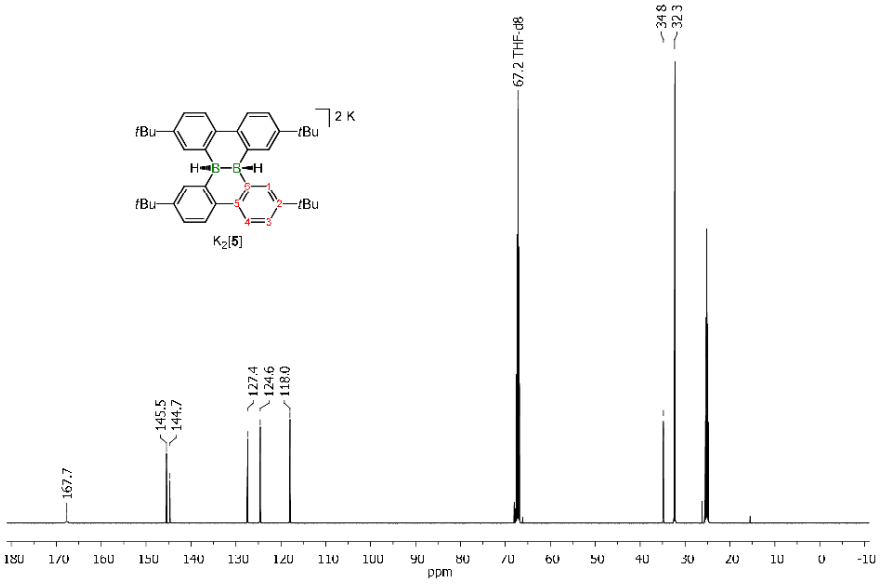

Figure S12. $^{13}C\{^{1}H\}$ NMR spectrum of K_2[**5**] (THF-d_8, 125.8 MHz).

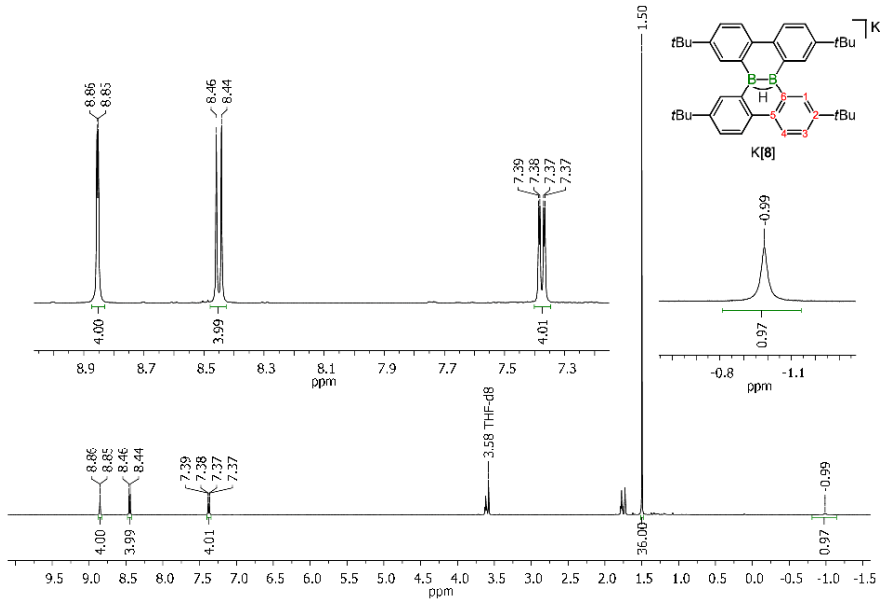

Figure S13. ^{1}H NMR spectrum of K[**8**] (THF-d_8, 500.2 MHz).

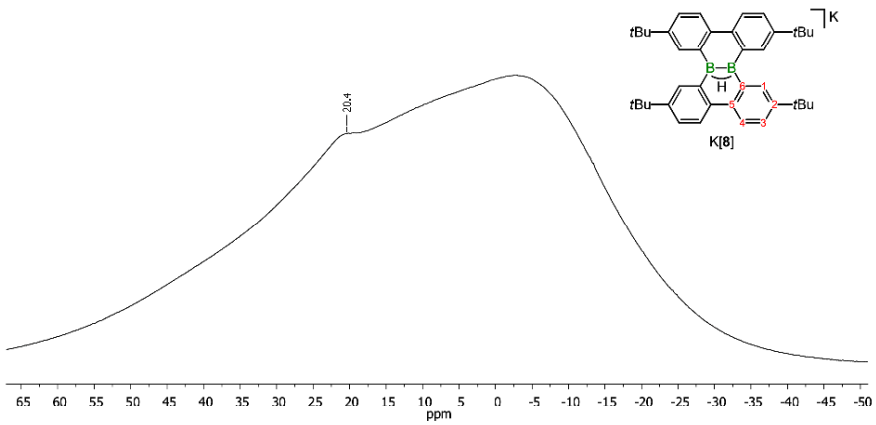

Figure S14. ^{11}B NMR spectrum of K[**8**] (THF-d_8, 160.5 MHz).

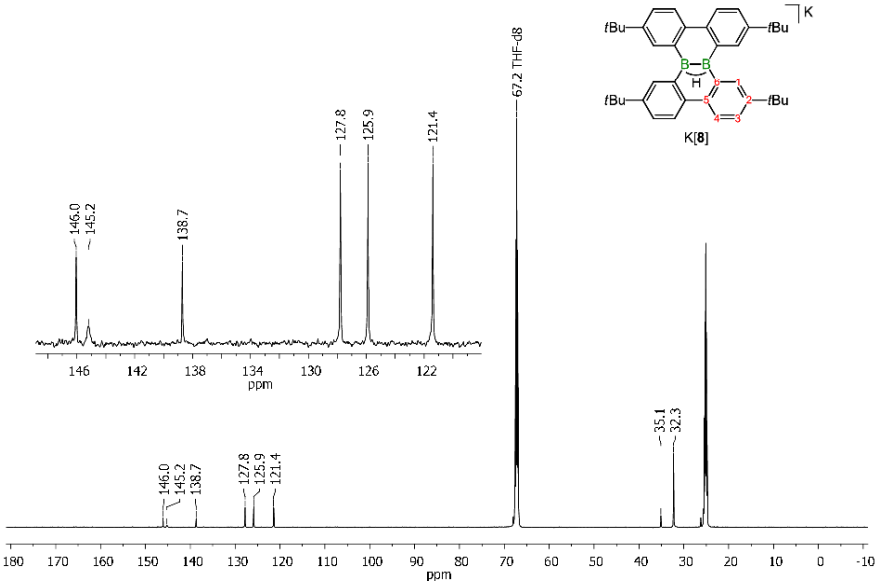

Figure S15. ^{13}C{^{1}H} NMR spectrum of K[**8**] (THF-d_8, 125.8 MHz).

4. Plot of the ^{1}H NMR spectrum of the reaction mixture between 4 and K_2[5]

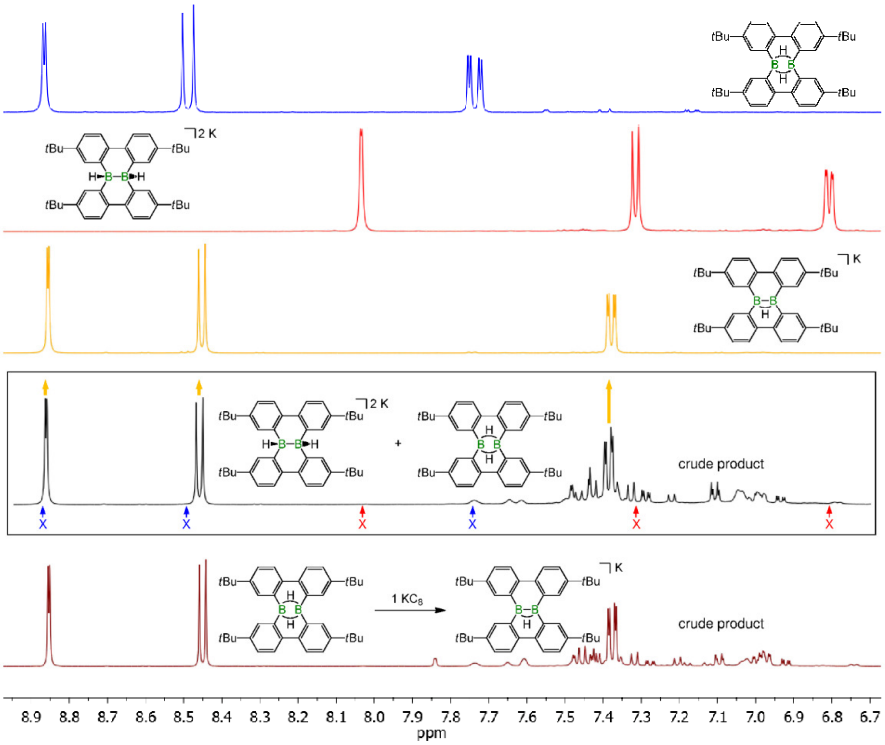

Figure S16. Comparison of the ^{1}H NMR spectra (THF-d_8) of **4** (blue), K_2[**5**] (red), K[**8**] (yellow), a stoichiometric mixture of **4** and K_2[**5**] (after 2 h, black), and the crude reaction product of **4** with 1 equiv KC_8 (dark red, bottom). After 2 h, there are no signals of the starting materials left in the ^{1}H NMR spectrum of the stoichiometric mixture of **4** and K_2[**5**] (cf. blue and red crosses). Instead, one observes the same main product as generated in the reaction of **4** with 1 equiv KC_8.

5. NMR spectra of the reaction mixture of 4 with KH in THF-d_8 to give K[9] and K_2[10]

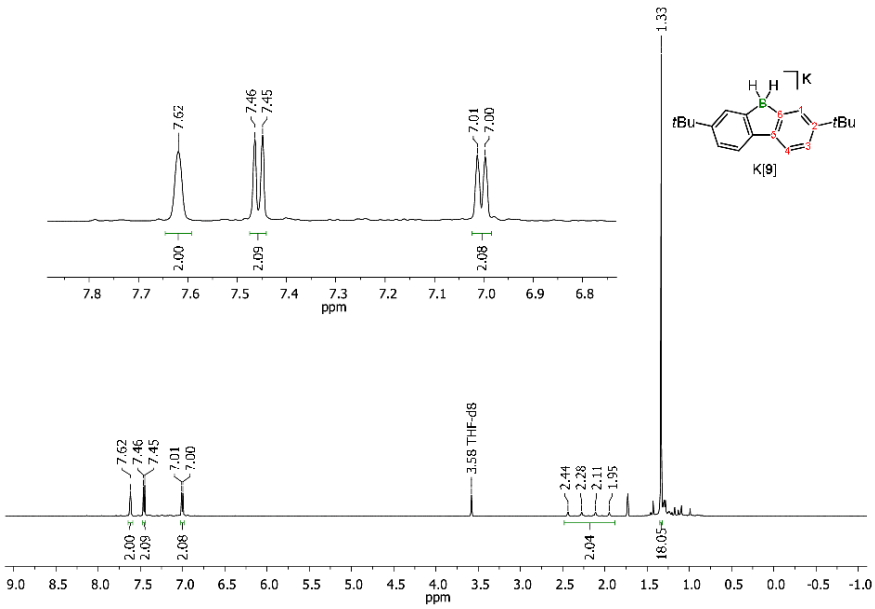

Figure S17. ^{1}H NMR spectrum of the crude reaction mixture of **4** and KH, which shows K[**9**] as the major product in solution (THF-d_8, 500.2 MHz).

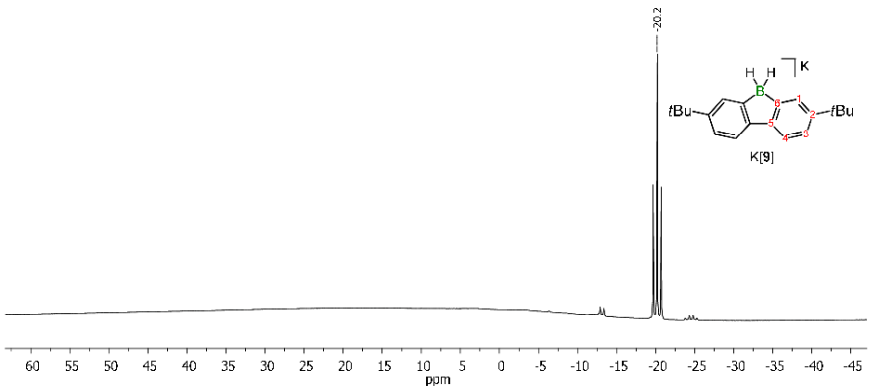

Figure S18. ^{11}B NMR spectrum of the crude reaction mixture of **4** and KH, which shows K[**9**] as the major product in solution (THF-d_8, 160.5 MHz).

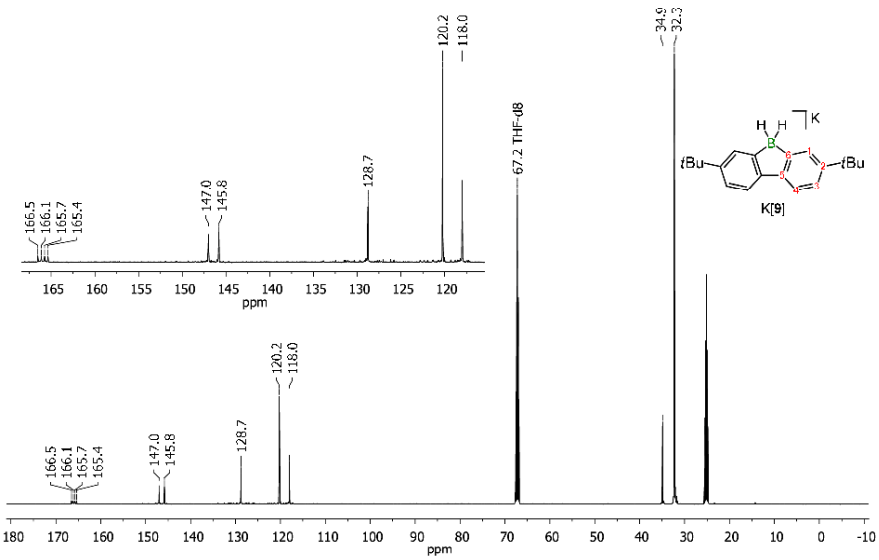

Figure S19. $^{13}C\{^{1}H\}$ NMR spectrum of the crude reaction mixture of **4** and KH, which shows K[**9**] as the major product in solution (THF-d_8, 125.8 MHz).

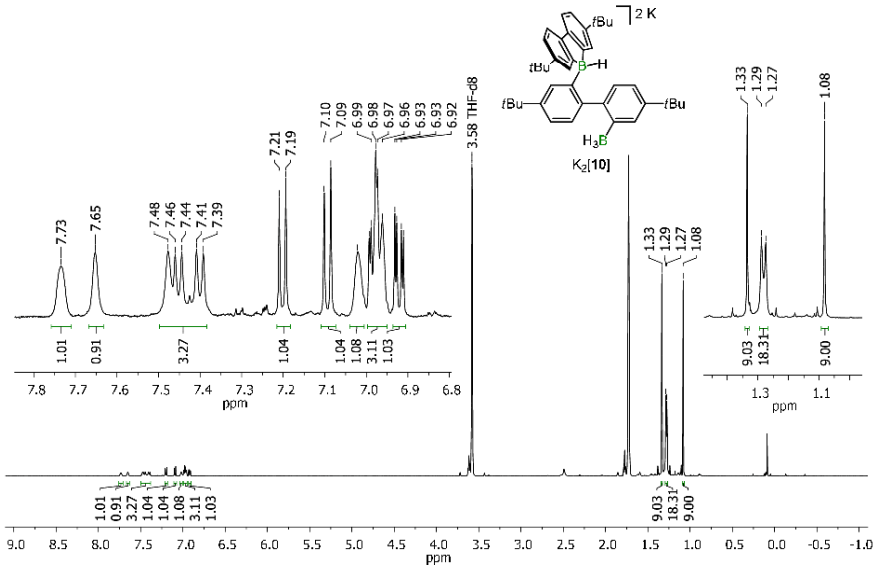

Figure S20. ^{1}H NMR spectrum of K_2[**10**], which crystallizes from the reaction mixture of **4** and KH (THF-d_8, 500.2 MHz).

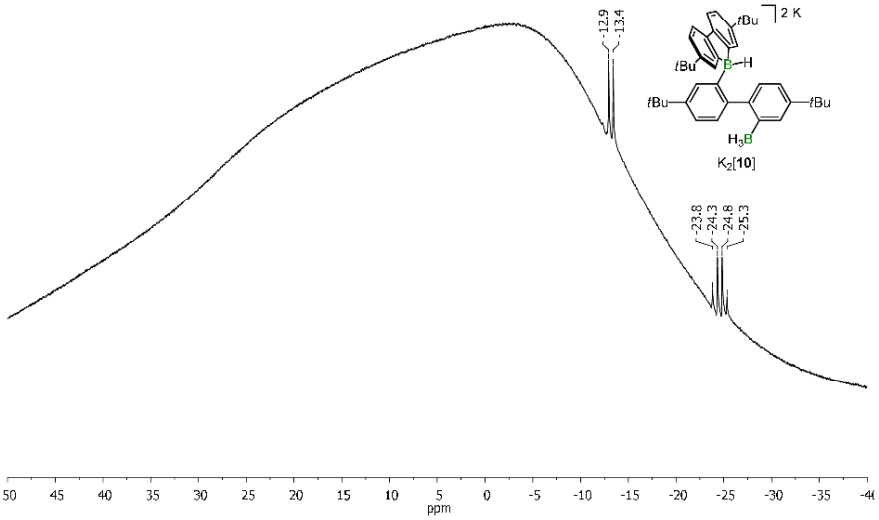

Figure S21. ^{11}B NMR spectrum of K_2[**10**], which crystallizes from the reaction mixture of **4** and KH (THF-d_8, 160.5 MHz).

6. Comparison of the tetraphenylethylium reaction mechanism and the borane-borate mechanism

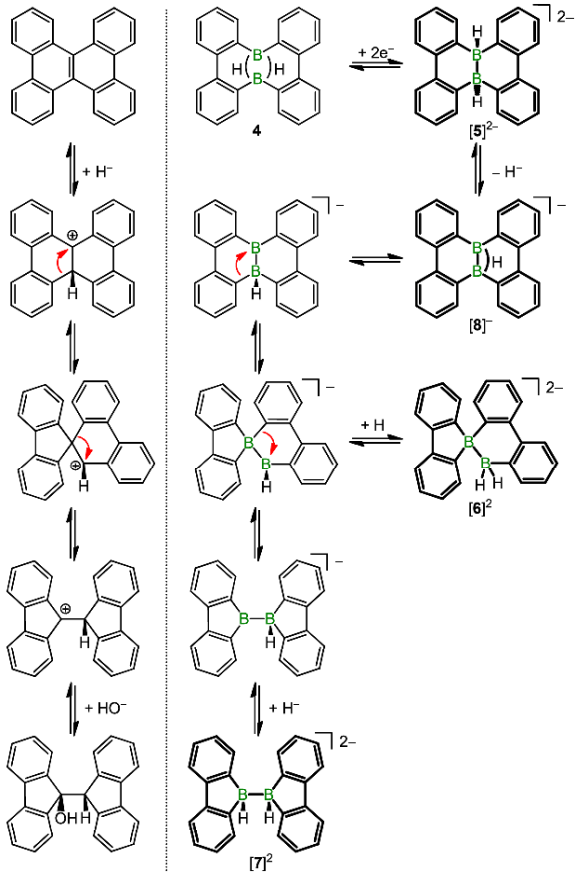

Scheme S1. Tetraphenylethylium ions are thought to connect dibenzo[*g*,*p*]chrysene and 9-hydroxy-9,9'-bifluorenyl under Clemmensen conditions (left). The formal exchange of C–C 2e2c bonds by BHB 2e3c bonds allows to write down an analogous borane-borate mechanism for the rearrangement reactions of **4** upon reduction (right; *t*Bu groups omitted for clarity; bold: isolated compounds).

7. X-ray crystal structure analyses

X-ray crystal structure analysis of 4

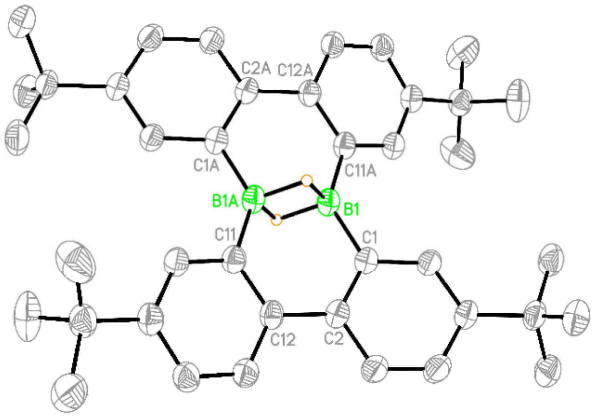

Figure S22. Molecular structure of **4** in the solid state. Displacement ellipsoids are shown at the 50% probability level; C*H* atoms are omitted for clarity. Selected atom···atom distance [Å], bond lengths [Å], bond angle [°], and torsion angle [°]: B(1)···B(1A) = 1.781(3); B(1)–C(1) = 1.571(2), B(1)–C(11) = 1.578(2), C(1)–C(2) = 1.425(2), C(2)–C(12) = 1.500(2), C(11)–C(12) = 1.429(2); C(1)–B(1)–C(11A) = 131.24(14); C(1)–C(2)–C(12)–C(11) = −4.5(2). Symmetry transformation used to generate equivalent atoms: A: −x+2, −y+1, −z+1.

X-ray crystal structure analysis of $[Li_2(thf)_3][\mathbf{1}]$

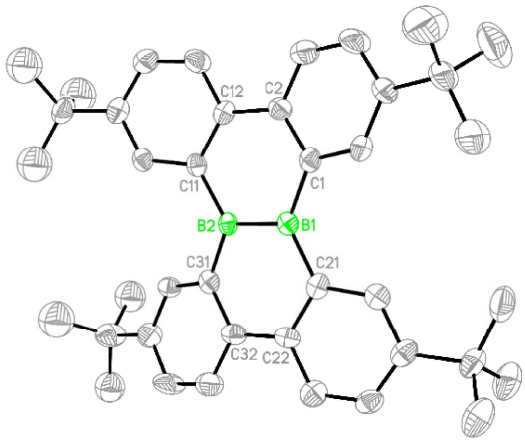

Figure S23. Molecular structure of one of the two crystallographically independent anions $[\mathbf{1}]^{2-}$ in $[Li_2(thf)_3][\mathbf{1}]$ in the solid state. Displacement ellipsoids are shown at the 50% probability level; C*H* atoms are omitted for clarity. Selected bond lengths [Å], atom···atom distances [Å], bond angles [°], and torsion angles [°] for the two crystallographically independent anions $[\mathbf{1}]^{2-}$: B(1)–B(2) = 1.641(6)/1.627(6), B(1)–C(1) = 1.585(7)/1.569(6), B(1)−C(21) = 1.572(5)/1.592(6), B(2)−C(11) = 1.570(5)/1.574(5), B(2)−C(31) = 1.562(6)/1.562(7); Li(1)···B(1) = 2.413(9)/2.508(9), Li(1)···B(2) = 2.525(9)/2.475(9), Li(2)···B(1) = 2.429(9)/2.461(9), Li(2)···B(2) = 2.524(9)/2.481(9); C(21)–B(1)–C(1) = 128.4(3)/128.0(3), C(21)–B(1)–B(2) = 115.3(4)/115.4(4), C(1)–B(1)–B(2) = 116.3(3)/116.6(3), C(31)–B(2)–C(11) = 125.2(3)/125.1(3), C(31)–B(2)–B(1) = 117.3(3)/118.2(3), C(11)–B(2)–B(1) = 117.5(4)/116.6(4); C(1)−C(2)−C(12)−C(11) = −2.1(7)/3.1(7), C(21)–C(22)−C(32)−C(31) = 1.0(7)/−0.8(7), C(21)–B(1)–B(2)–C(31) = –2.5(6)/ –2.4(6).

X-ray crystal structure analysis of $[Li(thf)_3][Li(thf)_2][\mathbf{6}]$:

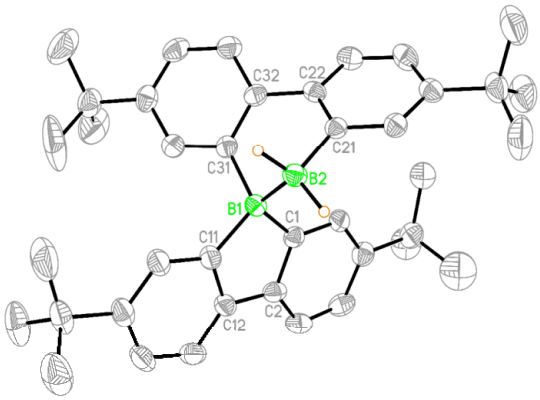

Figure S24. Molecular structure of the anion $[\mathbf{6}]^{2-}$ in $[Li(thf)_3][Li(thf)_2][\mathbf{6}]$ in the solid state. Displacement ellipsoids are shown at the 50% probability level; C*H* atoms are omitted for clarity. Selected bond lengths [Å], atom···atom distances [Å], bond angles [°] and torsion angles [°]: B(1)–B(2) = 1.810(5), B(1)–C(1) = 1.624(5), B(1)–C(11) = 1.620(5), B(1)–C(31) = 1.640(5), B(2)–C(21) = 1.605(5), C(2)–C(12) = 1.474(5), C(22)–C(32) = 1.485(5); Li(1)···C(11) = 2.327(7), Li(2)···C(21) = 2.639(7); C(1)–B(1)–C(11) = 98.2(3), C(31)–B(1)–B(2) = 99.6(3), B(1)–B(2)–C(21) = 104.3(3), C(11)–B(1)–B(2) = 119.8(3); C(21)–C(22)–C(32)–C(31) = –31.0(4), B(1)–B(2)–C(22)–C(32) = 44.6(2).

X-ray crystal structure analysis of $[Li(thf)]_3[Li][7]_2$:

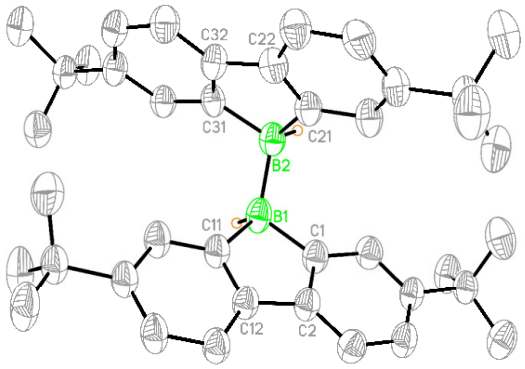

Figure S25. Molecular structure of the anion $[7]^{2-}$ in $[Li(thf)]_3[Li][7]_2$ in the solid state. Displacement ellipsoids are shown at the 30% probability level; C*H* atoms are omitted for clarity. Selected bond lengths [Å], atom···atom distances [Å], and torsion angle [°]: B(1)–B(2) = 1.789(7), B(1)–C(1) = 1.624(6), B(1)–C(11) = 1.640(5), B(2)–C(21) = 1.616(6), B(2)–C(31) = 1.640(6); Li(1)···B(2) = 2.529(9), Li(1)···C(31) = 2.449(4), Li(2)···B(1) = 2.326(9), Li(2)···B(2) = 2.506(8), Li(2)···C(1) = 2.438(8), Li(2)···C(11) = 2.331(8), Li(2)···C(21) = 2.207(9), Li(2)···C(26) = 2.445(8), Li(3)···B(1) = 2.309(5), Li(3)···B(2) = 2.399(7); H(1)–B(1)–B(2)–H(2) = −53(2).

X-ray crystal structure analysis of $[K_2(thf)_4][\mathbf{5}]$:

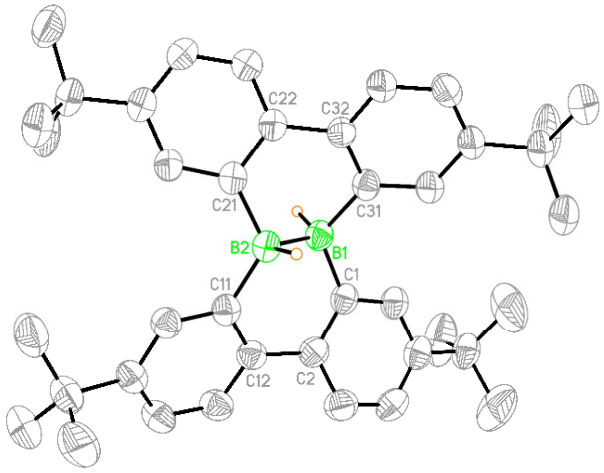

Figure S26. Molecular structure of the anion $[\mathbf{5}]^{2-}$ in $[K_2(thf)_4][\mathbf{5}]$ in the solid state. Displacement ellipsoids are shown at the 50% probability level; C*H* atoms are omitted for clarity. Selected bond lengths [Å], bond angles [°], and torsion angles [°]: B(1)−B(2) = 1.755(4), B(1)–C(1) = 1.629(3), B(1)−C(31) = 1.615(3), B(2)−C(11) = 1.633(3), B(2)−C(21) = 1.623(3), C(1)−C(2) = 1.415(3), C(2)−C(12) = 1.507(3), C(11)−C(12) = 1.420(3); C(31)−B(1)−C(1) = 119.11(19), C(21)−B(2)−C(11) = 120.99(19); C(1)−C(2)−C(12)−C(11) = −25.6(4), C(21)−C(22)−C(32)−C(31) = 30.9(3), B(1)–B(2)–C(12)–C(2) = 26.4(2), B(1)–B(2)–C(22)–C(32) = –44.0(2), H(1)–B(1)–B(2)–H(2) = –159(2).

X-ray crystal structure analysis of [K(thf)$_2$][8]

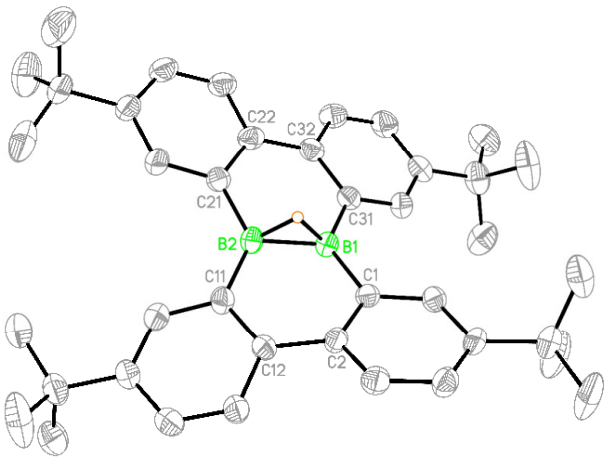

Figure S27. Molecular structure of the anion [**8**]$^-$ in [K(thf)$_2$][**8**] in the solid state. Displacement ellipsoids are shown at the 50% probability level; C*H* atoms are omitted for clarity. Selected bond lengths [Å], bond angles [°], and torsion angles [°]: B(1)−B(2) = 1.651(6), B(1)–C(1) = 1.588(6), B(1)−C(31) = 1.576(6), B(2)−C(11) = 1.563(6), B(2)−C(21) = 1.574(6), C(1)−C(2) = 1.431(5), C(2)−C(12) = 1.480(6), C(11)−C(12) = 1.431(6); C(31)−B(1)−C(1) = 128.2(4), C(1)−B(1)−B(2) = 116.5(3), C(31)−B(1)−B(2) = 115.3(4); C(1)−C(2)−C(12)−C(11) = −20.3(7), C(21)−C(22)−C(32)−C(31) = −11.0(7).

X-ray crystal structure analysis of [K(thf)$_3$][K(thf)][10]

The anion [**10**]$^{2-}$ is the dihydride adduct of a 2-biphenylborane bearing a 9-borafluorenyl substituent. The underlying arylborane scaffold can formally be generated from **4** by Ar/H substituent scrambling. A double pyridine complex related to the dihydride adduct [**10**]$^{2-}$ has previously been isolated.[5] [K(thf)$_3$][K(thf)][**10**] forms inversion-symmetric dimers in the solid state: Two [K(thf)]$^+$ cations are bridging two [ArBH$_3$]$^-$ moieties through η^1 and η^2 B–H···K$^+$ interactions. Each of the two [K(thf)$_3$]$^+$ cations establishes a close contact to the hydride substituent of one [Ar$_3$BH]$^-$ fragment. Finally, the π electrons of four benzene rings contribute to K$^+$ coordination.

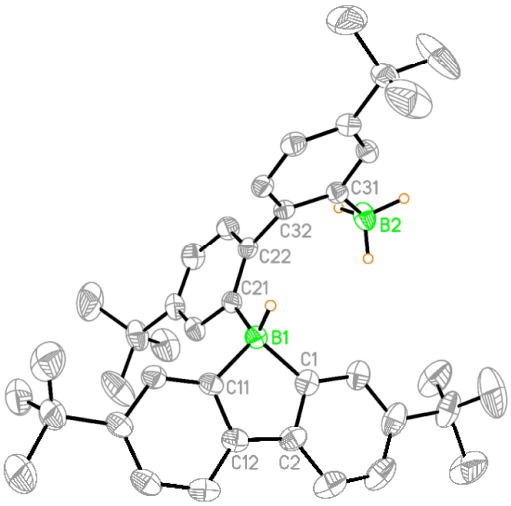

Figure S28. Molecular structure of the anion [**10**]$^{2-}$ in [K(thf)$_3$][K(thf)][**10**] in the solid state. Displacement ellipsoids are shown at the 50% probability level; C*H* atoms are omitted for clarity. Selected bond lengths [Å], and torsion angles [°]: B(1)–C(1) = 1.645(3), B(1)–C(11) = 1.620(3), B(1)–C(21) = 1.626(3), B(2)–C(31) = 1.612(3), C(2)–C(12) = 1.475(3), C(22)–C(32) = 1.500(3); C(1)–C(2)–C(12)–C(11) = 1.3(3), C(21)–C(22)–C(32)–C(31) = 115.8(2).

Table S1. Selected crystallographic data for **4**, $[Li_2(thf)_3][\mathbf{1}]\cdot 0.5C_7H_8$, and $[Li(thf)_3][Li(thf)_2][\mathbf{6}]$.

	4	$[Li_2(thf)_3][\mathbf{1}]\cdot 0.5C_7H_8$	$[Li(thf)_3][Li(thf)_2][\mathbf{6}]$
formula	$C_{40}H_{50}B_2$	$C_{52}H_{72}B_2Li_2O_3\cdot 0.5C_7H_8$	$C_{60}H_{90}B_2Li_2O_5$
M_r	552.42	826.66	926.81
color, shape	colorless, block	red, plate	light yellow, block
T [K]	173(2)	173(2)	173(2)
radiation, λ [Å]	MoK_α, 0.71073	MoK_α, 0.71073	MoK_α, 0.71073
crystal system	triclinic	monoclinic	orthorhombic
space group	P-1	$P2_1/n$	$Pna2_1$
a [Å]	6.1037(10)	23.6888(17)	26.7566(10)
b [Å]	10.0273(14)	14.3688(7)	10.1400(3)
c [Å]	14.3207(19)	29.305(2)	20.7717(8)
α [°]	109.973(11)	90	90
β [°]	91.761(12)	100.858(6)	90
γ [°]	90.472(12)	90	90
V [Å^3]	823.2(2)	9796.2(11)	5635.6(3)
Z	1	8	4
D_{calcd} [g cm^{-3}]	1.114	1.121	1.092
F(000)	300	3592	2024
μ [mm^{-1}]	0.061	0.065	0.066
crystal size [mm]	0.24 x 0.24 x 0.16	0.37 x 0.14 x 0.07	0.17 x 0.16 x 0.16
rflns collected	8255	60578	59903
independent rflns (R_{int})	3341 (0.0393)	18015 (0.1614)	10792 (0.0981)
data/restraints/parameters	3341 / 0 / 222	18015 / 0 / 1117	10792 / 1 / 628
GOF on F^2	1.041	0.876	1.021
R_1, wR_2 [$I > 2\sigma(I)$]	0.0656, 0.1775	0.0816, 0.1486	0.0580, 0.1413
R_1, wR_2 (all data)	0.0766, 0.1872	0.2150, 0.1912	0.0733, 0.1494
largest diff peak and hole [e Å^{-3}]	0.301, –0.206	0.312, –0.240	0.329, –0.231

Table S2. Selected crystallographic data for $[Li(thf)]_3[Li][\mathbf{7}]_2$, $[K_2(thf)_4][\mathbf{5}]$, and $[K(thf)_2][\mathbf{8}]$.

	$[Li(thf)]_3[Li][\mathbf{7}]_2$	$[K_2(thf)_4][\mathbf{5}]$	$[K(thf)_2][\mathbf{8}]$
formula	$C_{92}H_{124}B_4Li_4O_3$	$C_{56}H_{82}B_2K_2O_4$	$C_{48}H_{65}B_2KO_2$
M_r	1348.90	919.03	734.72
color, shape	colorless, rod	orange, block	yellow, block
T [K]	173(2)	173(2)	173(2)
radiation, λ [Å]	MoK_α, 0.71073	MoK_α, 0.71073	MoK_α, 0.71073
crystal system	monoclinic	monoclinic	orthorhombic
space group	$C2/c$	$P2_1/c$	$P2_12_12_1$
a [Å]	28.292(3)	15.5756(7)	13.6225(10)
b [Å]	10.6612(8)	21.2523(10)	16.3106(8)
c [Å]	30.648(3)	17.6877(8)	19.6114(11)
α [°]	90	90	90
β [°]	113.952(7)	112.775(4)	90
γ [°]	90	90	90
V [Å^3]	8448.2(14)	5398.4(5)	4357.5(5)
Z	4	4	4
D_{calcd} [g cm^{-3}]	1.061	1.131	1.120
F(000)	2928	1992	1592
μ [mm^{-1}]	0.060	0.218	0.158
crystal size [mm]	0.26 x 0.14 x 0.12	0.28 x 0.13 x 0.13	0.36 x 0.31 x 0.27
rflns collected	29211	56993	19597
independent rflns (R_{int})	7463 (0.1041)	9533 (0.0924)	7695 (0.0444)
data/restraints/parameters	7463 / 0 / 474	9533 / 0 / 585	7695 / 24 / 500
GOF on F^2	1.152	0.966	1.038
R_1, wR_2 [$I > 2\sigma(I)$]	0.0799, 0.1555	0.0505, 0.1262	0.0668, 0.1820
R_1, wR_2 (all data)	0.1899, 0.1830	0.0812, 0.1398	0.0780, 0.1907
largest diff peak and hole [e Å^{-3}]	0.229, –0.179	0.290, –0.259	1.140, –0.790

Table S3. Selected crystallographic data for $[K(thf)_3][K(thf)][\mathbf{10}]$.

	$[K(thf)_3][K(thf)][\mathbf{10}]$
formula	$C_{56}H_{84}B_2K_2O_4$
M_r	921.05
color, shape	colorless, block
T [K]	173(2)
radiation, λ [Å]	MoK_α, 0.71073
crystal system	monoclinic
space group	$P2_1/c$
a [Å]	13.8340(11)
b [Å]	19.2446(12)
c [Å]	21.4964(17)
α [°]	90
β [°]	103.878(6)
γ [°]	90
V [Å^3]	5555.9(7)
Z	4
D_{calcd} [g cm^{-3}]	1.101
F(000)	2000
μ [mm^{-1}]	0.212
crystal size [mm]	0.33 x 0.23 x 0.21
rflns collected	23423
independent rflns (R_{int})	9759 (0.0388)
data/restraints/parameters	9759 / 96 / 670
GOF on F^2	1.009
R_1, wR_2 [$I > 2\sigma(I)$]	0.0543, 0.1369
R_1, wR_2 (all data)	0.0805, 0.1483
largest diff peak and hole [e Å^{-3}]	0.387, –0.330

8. References

(1) Hübner, A.; Diefenbach, M.; Bolte, M.; Lerner, H.-W.; Holthausen, M. C.; Wagner, M. *Angew. Chem. Int. Ed.* **2012**, *51*, 12514-12518.

(2) Hübner, A.; Bolte, M.; Lerner, H.-W.; Wagner, M. *Angew. Chem. Int. Ed.* **2014**, *53*, 10408-10411.

(3) *X-AREA: Diffractometer Control Program System;* Stoe & Cie: Darmstadt, Germany, 2002

(4) Sheldrick, G. M. *Acta Crystallogr., Sect. A: Found. Crystallogr.* **2008**, *64*, 112-122.

(5) Hübner, A.; Qu, Z.-W.; Englert, U.; Bolte, M.; Lerner, H.-W.; Holthausen, M. C.; Wagner, M. *J. Am. Chem. Soc.* **2011**, *133*, 4596-4609.

6.2.6 A Preorganized Ditopic Borane as Highly Efficient One- or Two-Electron Trap

JACS
JOURNAL OF THE AMERICAN CHEMICAL SOCIETY
Article
pubs.acs.org/JACS

A Preorganized Ditopic Borane as Highly Efficient One- or Two-Electron Trap

Alexander Hübner,[†] Thomas Kaese,[†] Martin Diefenbach,[†] Burkhard Endeward,[‡] Michael Bolte,[†] Hans-Wolfram Lerner,[†] Max C. Holthausen,*[,†] and Matthias Wagner*[,†]

[†]Institut für Anorganische Chemie, Goethe-Universität Frankfurt, Max-von-Laue-Str. 7, D-60438 Frankfurt am Main, Germany
[‡]Institut für Physikalische und Theoretische Chemie, Goethe-Universität Frankfurt, Max-von-Laue-Str. 7, D-60438 Frankfurt am Main, Germany

Supporting Information

ABSTRACT: Reduction of the bis(9-borafluorenyl)methane **1** with excess lithium furnishes the red dianion salt $Li_2[\mathbf{1}]$. The corresponding dark green monoanion radical $Li[\mathbf{1}]$ is accessible through the comproportionation reaction between **1** and $Li_2[\mathbf{1}]$. EPR spectroscopy on $Li[\mathbf{1}]$ reveals hyperfine coupling of the unpaired electron to two magnetically equivalent boron nuclei ($a(^{11}B)$ = 5.1 ± 0.1 G, $a(^{10}B)$ = 1.7 ± 0.2 G). Further coupling is observed to the unique B−C*H*−B bridgehead proton ($a(^1H)$ = 7.2 ± 0.2 G) and to eight aromatic protons ($a(^1H)$ = 1.4 ± 0.1 G). According to X-ray crystallography, the B···B distances continuously decrease along the sequence **1** → $[\mathbf{1}]^{\bullet-}$ → $[\mathbf{1}]^{2-}$ with values of 2.534(2), 2.166(4), and 1.906(3) Å, respectively. Protonation of $Li_2[\mathbf{1}]$ leads to the cyclic borohydride species $Li[\mathbf{1H}]$ featuring a B−H−B two-electron-three-center bond. This result strongly indicates a nucleophilic character of the boron atoms; the reaction can also be viewed as rare example of the protonation of an element−element σ bond. According to NMR spectroscopy, EPR spectroscopy, and quantum-chemical calculations, $[\mathbf{1}]^{2-}$ represents a closed-shell singlet without any spin contamination. Detailed wave function analyses of $[\mathbf{1}]^{\bullet-}$ and $[\mathbf{1}]^{2-}$ reveal strongly localized interactions of the two boron p_z-type orbitals, with small delocalized contributions of the 9-borafluorenyl π systems. Overall, our results provide evidence for a direct B−B one-electron and two-electron bonding interaction in $[\mathbf{1}]^{\bullet-}$ and $[\mathbf{1}]^{2-}$, respectively.

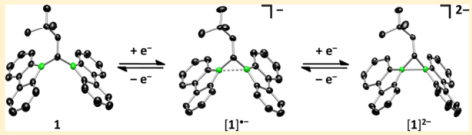

INTRODUCTION

Our groups have recently reported the first structurally characterized compound containing a B·B one-electron-two-center (*1e2c*) σ bond ($[\mathbf{I}]^{\bullet-}$; Figure 1).[1] Key to success was the design of a preorganized ditopic borane **I**,[2] in which an optimal σ overlap of the two empty boron p orbitals offered suitable conditions for the incorporation of the odd electron. The obvious question arising next is to ask: Can we also create a B−B *two*-electron σ bond simply by placing *two* electrons in between a pair of tricoordinate boron atoms?[2] On the one hand, the resulting species $[R_3B{-}BR_3]^{2-}$ would be isoelectronic to common alkanes, on the other hand, the electrostatic repulsion between the two anionic boron centers is expected to destabilize the molecular scaffold. The adverse effect of Coulomb repulsion must indeed be taken seriously, as underscored by the facts that we were so far unable to prepare $[\mathbf{I}]^{2-}$ through further injection of electrons into $[\mathbf{I}]^{\bullet-}$ and that only two examples of $[R_3B{-}BR_3]^{2-}$ anions have been described in the literature so far: (1) Matsuo, Tamao et al. synthesized the dilithium diborane(6) dianion $Li_2[\mathbf{II}]$ through the reduction of the corresponding sterically shielded diborane(6) with lithium naphthalenide (Figure 1).[3] (2) Power et al. isolated small quantities of the dimeric 9*H*-9-borafluorene dianion $[\mathbf{III}]^{2-}$ after they had treated the bulky arylboron dibromide 2,6-$Trip_2C_6H_3BBr_2$ with KC_8 (Trip = 2,4,6-*i*$Pr_3C_6H_2$; Figure 1).[4]

Especially the latter serendipitous finding can be taken as good indication that 9-borafluorene-9-yl may in fact serve as a proper organoboron moiety for the targeted synthesis of $[R_3B{-}BR_3]^{2-}$ species. Our failure to prepare $[\mathbf{I}]^{2-}$ from $[\mathbf{I}]^{\bullet-}$ is thus likely attributable to the choice of the 2,2′-biphenyldiyl backbone, which leads to the conclusion that B−B two-electron and B·B one-electron σ bonds are not necessarily best supported by the same bridging unit. After careful screening of a number of different linkers, we now found that two-electron reduction of the diborylmethane **1**[5] with elemental lithium cleanly furnishes the closed-shell dianion $Li_2[\mathbf{1}]$ (Scheme 1), and herein we report its full characterization. Concerning its reactivity, we will show that treatment of $Li_2[\mathbf{1}]$ with the neutral borane **1** leads to the isolable radical anion $[\mathbf{1}]^{\bullet-}$, whereas the addition of a strong Brønsted acid yields $Li[\mathbf{1H}]$ through protonation of the formal B−B σ bond (Scheme 1). We further report the results of a detailed quantum chemical bonding analysis of **1**, $[\mathbf{1}]^{\bullet-}$, $[\mathbf{1}]^{2-}$, and of the Li-complexed species of the latter two compounds, and comparison is made to the bonding properties of $[\mathbf{I}]^{\bullet-}$ and $[\mathbf{I}]^{2-}$.

Received: February 6, 2015
Published: February 27, 2015

ACS Publications © 2015 American Chemical Society

DOI: 10.1021/jacs.5b01192
J. Am. Chem. Soc. 2015, 137, 3705−3714

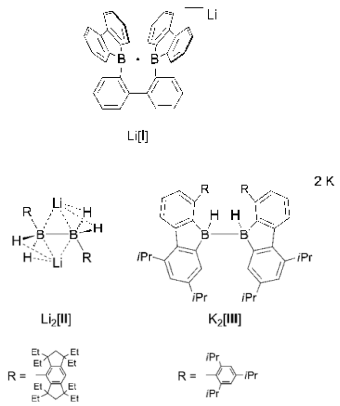

Figure 1. Compound Li[**I**] features a one-electron-two-center bond between two borane moieties, whereas compounds Li_2[**II**] and K_2[**III**] contain two-electron-two-center bonds.

Scheme 1. Two-Electron Reduction of the Diborylmethane 1 to Give Li_2[1]; Comproportionation of 1 and Li_2[1] to Give Li[1]; Synthesis of the B–H–B-Bridged Species Li[1H] through Protonation of Li_2[1] or Hydride Addition to 1[a]

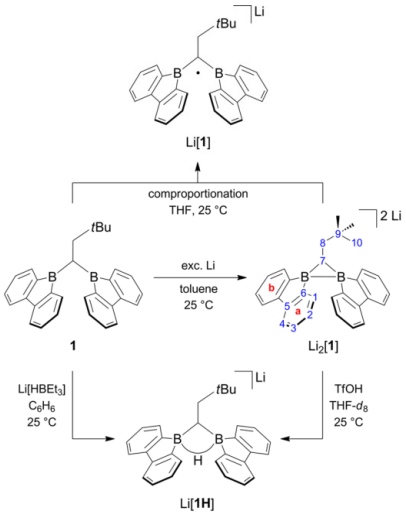

[a]The numbering scheme for the assignment of NMR data is shown using Li_2[1] as the example.

■ RESULTS AND DISCUSSION

In the cyclic voltammogram (CV) the diborylmethane **1** (Scheme 1)[5] undergoes two reversible redox transitions at half-wave potentials of $E_{1/2}$ = −1.76 and −2.17 V (THF, vs FcH/FcH^+; FcH = ferrocene, cf. the Supporting Information (SI) for the CV plot). With $E_{1/2}$ values of −1.49 and −1.75 V the 2,2′-biphenyldiyl-bridged species **I** is easier to reduce under comparable conditions.[1] We suppose that these differences are due to a more efficient σ overlap between the boron p-orbitals in **I** compared to **1**: While **I** possesses a somewhat longer B···B distance (2.920(6) Å)[2] than **1** (2.534(2) Å),[5] the angle between the normals to the two BC_3 planes is only 12.4(2)°[2] in **I** but as large as 74.3(1)°[5] in **1**. Controlled exhaustive reduction of **1** at an electrode potential of E_w = −1.9 V leads to the simultaneous evolution of several new UV–vis absorption bands in a one-electron process (λ_{max} = 357, 432, and 775 nm; Figure 2 top, green curves). If the reduction is

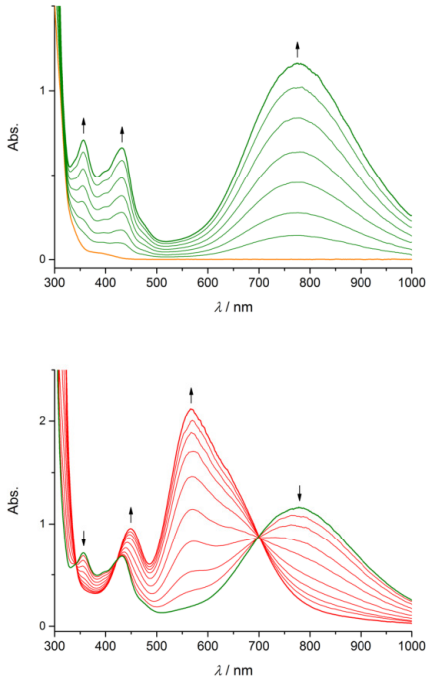

Figure 2. UV–vis absorption spectra were recorded in THF at room temperature during controlled potential electrolysis of **1** at a Pt-net electrode (supporting electrolyte: $[nBu_4N][PF_6]$ (0.1 M)). Top: reduction of **1** (orange) to $[\mathbf{1}]^{\bullet-}$ (green) at E_w = −1.9 V. Bottom: subsequent reduction of the electrogenerated $[\mathbf{1}]^{\bullet-}$ (green) to $[\mathbf{1}]^{2-}$ (red) at E_w = −2.4 V.

continued further at a more cathodic potential of E_w = −2.4 V, the absorption bands of the primary reduction product gradually decrease with the concomitant appearance of new absorption bands at λ_{max} = 450 and 568 nm (one-electron process; Figure 2 bottom, red curves). Isosbestic points at λ_{iso} = 342, 423, and 700 nm point toward a clean conversion of $[\mathbf{1}]^{\bullet-}$ to $[\mathbf{1}]^{2-}$ without the formation of intermediates or byproducts. Moreover, at applied potentials of E_w = −1.8 V and E_w = −1.3 V the sample is sequentially taken back to the oxidation state of the neutral diborylmethane **1** (UV–vis spectroscopical control). The observation that **1** and its reduction products are well-behaved under the conditions of spectroelectrochemistry is a strong indication for the accessibility of $[\mathbf{1}]^{\bullet-}$ and

DOI: 10.1021/jacs.5b01192
J. Am. Chem. Soc. 2015, 137, 3705–3714

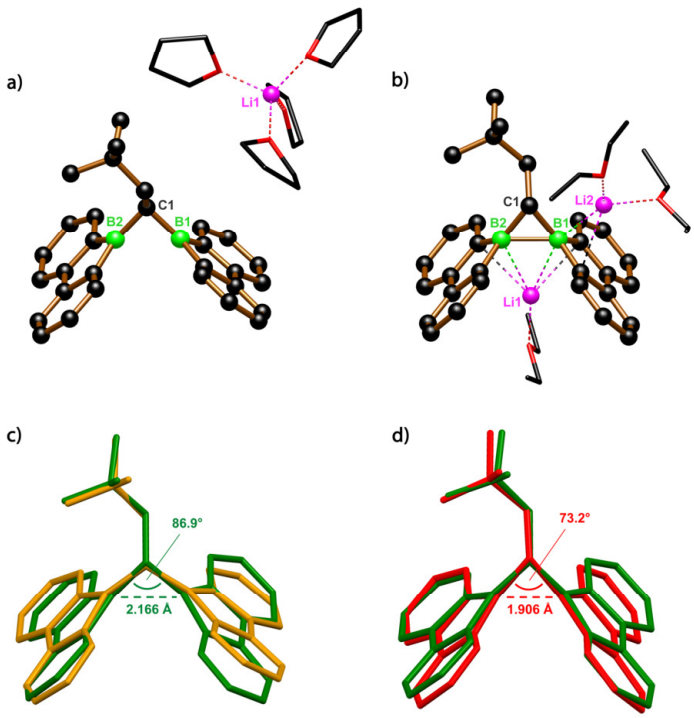

Figure 3. Solid-state structures of (a) $[Li(thf)_4][\mathbf{1}] \times THF$ (cocrystallized THF omitted for clarity) and (b) $[Li(Et_2O)_2][Li(Et_2O)][\mathbf{1}]$. Overlay of the molecular scaffolds of (c) **1** (orange) with $[\mathbf{1}]^{\bullet-}$ (green) and (d) $[\mathbf{1}]^{\bullet-}$ (green) with $[\mathbf{1}]^{2-}$ (red).

$[\mathbf{1}]^{2-}$ on a preparative scale. There is pleasing qualitative agreement between the experimental and the computed UV–vis absorption spectra of the three species **1**, $[\mathbf{1}]^{\bullet-}$, and $[\mathbf{1}]^{2-}$ (see Figure S22 in the SI). Natural transition orbital (NTO) analyses reveal that the dominant features in the computed spectra of the intensely colored anions $[\mathbf{1}]^{\bullet-}$ and $[\mathbf{1}]^{2-}$ originate from charge-transfer transitions (see Table S4 in the SI). The excitations promote a shift of electron density from orbitals strongly localized in the region between the two boron atoms to orbitals located on the borafluorene moieties.

Addition of excess lithium metal to a yellow toluene solution of **1** leads to the precipitation of the red compound $Li_2[\mathbf{1}]$ in yields up to 80% within 14 d (Scheme 1; *note*: the yield is only slightly lower if the product is harvested already after 7 d).[6] Crystals of $[Li(Et_2O)_2][Li(Et_2O)][\mathbf{1}]$ suitable for X-ray diffraction were obtained from Et_2O at room temperature. A comproportionation reaction between equimolar amounts of $Li_2[\mathbf{1}]$ and **1** in THF at room temperature provides clean access to the persistent dark green radical $Li[\mathbf{1}]$. X-ray-quality crystal blocks of $[Li(thf)_4][\mathbf{1}] \times THF$ were grown from a saturated THF/Et_2O solution at −30 °C.

Figure 3a and 3b display the solid-state structures of $[Li(thf)_4][\mathbf{1}] \times THF$ and $[Li(Et_2O)_2][Li(Et_2O)][\mathbf{1}]$, respectively. While the Li^+ ion of $[Li(thf)_4][\mathbf{1}] \times THF$ is fully solvent separated (Figure 3a), both Li^+ ions of $[Li(Et_2O)_2][Li(Et_2O)][\mathbf{1}]$ form close contacts with the $[\mathbf{1}]^{2-}$ anion (Figure 3b): Li(1) binds to only one Et_2O ligand and resides between the two 9-borafluorene-9-yl planes with Li(1)···B(1) and Li(1)···B(2) distances of 2.326(5) and 2.383(5) Å, respectively. The shortest Li(1)···C contacts are shown as dashed lines and amount to 2.464(6) and 2.496(6) Å. Li(2) carries two Et_2O ligands; its coordination sphere is completed by B(1) (2.328(4) Å) and one carbon atom (2.462(4) Å). Figure 3c and 3d show overlays of the molecular scaffolds of **1** (orange) with $[\mathbf{1}]^{\bullet-}$ (green) and $[\mathbf{1}]^{\bullet-}$ (green) with $[\mathbf{1}]^{2-}$ (red). We observe a gradual contraction of the B(1)···B(2) distance along the sequence **1** (2.534(2) Å) → $[\mathbf{1}]^{\bullet-}$ (2.166(4) Å) → $[\mathbf{1}]^{2-}$ (1.906(3) Å) with differences of 0.37 and 0.26 Å, respectively (Table 1). This contraction is accompanied by a continuous compression of the B(1)–C(1)–B(2) angle from 105.5(2)° (**1**) to 86.9(2)° ($[\mathbf{1}]^{\bullet-}$), and finally to 73.2(1)° ($[\mathbf{1}]^{2-}$; Table 1).

The B(1)···B(2) distance in $[\mathbf{1}]^{\bullet-}$ is shorter by 0.099 Å than the corresponding B·B *1e2c* bond in $[\mathbf{I}]^{\bullet-}$ (2.265(4) Å; Table 1). In $[\mathbf{1}]^{2-}$, the B(1)···B(2) distance is comparable to that in $[\mathbf{II}]^{2-}$ (1.924(3) Å), and longer than the B···B distance in $[\mathbf{III}]^{2-}$ (1.83(2) Å). Another parameter of interest is the degree of boron pyramidalization. As a quantitative measure, we take the angle θ at which the exocyclic B–C bond vector intersects the endocyclic BCC plane. In a trigonal-planar boron environment θ equals 180°, whereas θ = 125.3° signifies a tetrahedral situation. Both in $[\mathbf{1}]^{\bullet-}$ and in $[\mathbf{1}]^{2-}$, the boron

DOI: 10.1021/jacs.5b01192
J. Am. Chem. Soc. 2015, 137, 3705–3714

Table 1. Comparison of Key Structural Parameters of 1,[5] $[1]^{\bullet-}$, $[1]^{2-}$, $[1H]^{-}$, I,[2] $[I]^{\bullet-}$,[1] and $[I]^{2-}$ According to X-ray Crystallography and DFT Calculations[a]

	B(1)···B(2)/Å		B(1)–C(1)–B(2)/°		θ_{av}/°	
compound	X-ray	calcd	X-ray	calcd	X-ray	calcd
1	2.534(2)	2.376	105.5(2)	98.7	178.5	176.4
$[1]^{\bullet-}$	2.166(4)	2.129	86.9(2)	85.2	174.0	177.6
		2.126		*85.2*		*174.8*
$[1]^{2-}$	1.906(3)	1.878	73.2(1)	72.4	168.4	167.4
		1.948		*75.9*		*167.0*
$[1H]^{-}$	1.954(5)	1.901	75.4(2)	72.8	150.8	148.4
		1.908		*73.3*		*143.4*
I	2.920(6)	2.894	–	174.9	177.0	174.9
$[I]^{\bullet-}$	2.265(4)	*2.251*	–	*157.3*	156.1	*157.3*
$[I]^{2-}$	–	*1.889*	–	*141.0*	–	*141.0*

[a]Experimental and DFT metrics given refer to the Li-complexes; computed data for the bare, Li^+-free species are shown in italics.

atoms remain essentially planar with mean values θ_{av} of 174.0° and 168.4°, respectively (Table 1). All experimentally determined key structural parameters are coherent with the computed molecular structures of $[Li(thf)_4][1]$ and $[Li(Et_2O)_2][Li(Et_2O)][1]$ (cf. the SI for full details).

An EPR spectrum confirming the open-shell electronic structure of $[1]^{\bullet-}$ was recorded in THF at room temperature (Figure 4a). Using the hyperfine coupling constants predicted for this species at the PBE0D/EPR-III/COSMO(THF) level as initial guesses (mean DFT-derived values for the two boron nuclei: $a(^{11}B)$ = 5.8 G, $a(^{10}B)$ = 1.9 G), the observed spectrum was finally simulated by assuming hyperfine coupling of the unpaired electron (g_{iso} = 1.998 ± 0.001) to two magnetically equivalent boron nuclei with isotropic coupling constants of $a(^{11}B)$ = 5.1 ± 0.1 G and $a(^{10}B)$ = 1.7 ± 0.2 G. We further assumed coupling to one proton with $a(^1H)$ = 7.2 ± 0.2 G and eight magnetically equivalent protons with $a(^1H)$ = 1.4 ± 0.1 G.

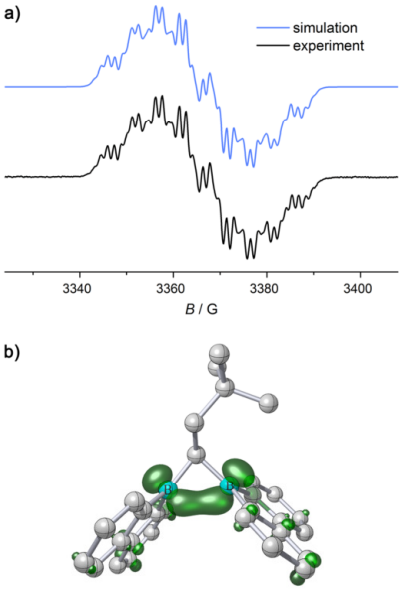

Figure 4. (a) EPR spectrum of the radical anion $[1]^{\bullet-}$ in THF (experimental spectrum at room temperature (black), simulation fit (blue)). (b) Computed spin density distribution of $[1]^{\bullet-}$ at an isovalue of 0.0075 a_0^{-3} (green; PBE0D/EPR-III level).

The larger $a(^1H)$ coupling constant can reasonably be assigned to the unique B–C*H*–B bridgehead hydrogen atom (DFT-derived value $a(^1H)$ = 8.0 G). In line with basic mesomeric structure considerations, the spin-density plot of $[1]^{\bullet-}$ (Figure 4b) indicates that the smaller $a(^1H)$ coupling constant is likely due to the four *ortho* and the four *para* 9-borafluorenyl protons. Both $a(^{11}B)$ and $a(^{10}B)$ values of $[1]^{\bullet-}$ are close to those reported for $[I]^{\bullet-}$ (seven-line spectrum; $a(^{11}B)$ = 4.8 ± 0.1 G, $a(^{10}B)$ = 1.6 ± 0.1 G).[1] Moreover, the small value of $a(^{11}B)$ in $[1]^{\bullet-}$ and the low degree of boron pyramidalization in its solid-state structure provides strong evidence that each boron atom essentially contributes a p_z orbital to the molecule's SOMO (cf. Figure 7a) akin to the situation found for $[I]^{\bullet-}$. In stark contrast to $[I]^{\bullet-}$, however, the observed coupling to 9-borafluorenyl protons in $[1]^{\bullet-}$ indicates that the unpaired electron is no longer exclusively trapped between the two boron atoms, but that spin-density is delocalized to a certain extent within the π-electron systems. We will return to the electronic structure of $[1]^{\bullet-}$ in considerable detail further below.

In line with a singlet electron configuration, $Li_2[1]$ is EPR silent in THF solution and gives perfectly well resolved NMR spectra with chemical shift values in ranges typical of diamagnetic species (THF-d_8). This spin-state characterization is further corroborated by the fact that NMR shifts computed for the closed-shell singlet ground state of the bare (i.e., Li^+-free) dianion $[1]^{2-}$ are in reasonable qualitative agreement with the experimental data (cf. the SI for more details). The ^7Li NMR spectrum contains one single resonance at −1.2 ppm, assignable to the $[Li(thf)_4]^+$ solvate complex,[7] which indicates that Li(1) no longer occupies a B–B-bridging position. The ^{11}B resonance of $Li_2[1]$ appears at −6.7 ppm, thereby testifying to the presence of tetracoordinate boron nuclei;[8] for comparison, K_2[**III**] gives rise to an ^{11}B NMR signal at −7.0 ppm (C_6D_6).[4] In contrast to the neutral starting material **1**, which exhibits only one set of ^1H or $^{13}C\{^1H\}$ resonances, two sets of signals with equal ratios are observed for the aromatic rings of $Li_2[1]$, both in the ^1H and in the $^{13}C\{^1H\}$ NMR spectrum (cf. the SI for plots of the spectra). The conformational flexibility of $Li_2[1]$ thus appears to be more restricted than in the neutral starting material.

All key structural and spectroscopic parameters of $[1]^{\bullet-}$ and $[1]^{2-}$ are consistent with a predominant accumulation of negative charge density in the space amid B(1) and B(2): (i) If the excess electrons were mainly delocalized over the 9-borafluorenyl π systems, one would expect a more symmetric coordination of the Li^+ ions to the two BC_4 rings of $[Li(Et_2O)_2][Li(Et_2O)][1]$. (ii) X-ray crystallography reveals a pronounced contraction of the B(1)···B(2) distances along the sequence **1** → $Li[1]$ → $Li_2[1]$. Since this trend is quantitatively reproduced by quantum-chemical calculations on the bare anions $[1]^{\bullet-}$ (2.126 Å) and $[1]^{2-}$ (1.948 Å), the short B(1)···B(2) distance in $Li_2[1]$ is clearly not the result of attractive electrostatic interactions within the B···Li···B moiety (cf. the SI for full details). (iii) The lack of conformational flexibility of

DOI: 10.1021/jacs.5b01192
J. Am. Chem. Soc. 2015, 137, 3705–3714

$Li_2[\mathbf{1}]$ in solution together with the absence of B–B bridging Li^+ ions, as revealed by NMR spectroscopy, can straightforwardly be explained assuming the presence of a covalent B(1)–B(2) two-electron-two-center (*2e2c*) bond.

In order to experimentally validate the postulate of a B(1)–B(2) bond by protonation of the accumulated negative charge density, we treated a solution of $Li_2[\mathbf{1}]$ in THF-d_8 with trifluoromethanesulfonic acid (TfOH) and indeed proved the formation of the B–H–B-bridged species Li[**1H**] by NMR spectroscopy (Scheme 1; cf. the SI for more details). To obtain an authentic sample, Li[**1H**] was also synthesized on a preparative scale from **1** and $Li[HBEt_3]$ in C_6H_6 (Scheme 1); single crystals of $[Li(thf)_4][\mathbf{1H}]$ formed from C_6H_6 in the presence of small amounts of THF (Figure 5). The newly

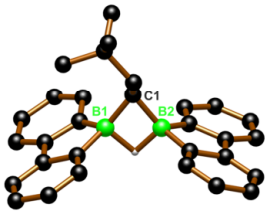

Figure 5. Solid-state structure of $[Li(thf)_4][\mathbf{1H}]$ (solvent separated $[Li(thf)_4]^+$ omitted for clarity).

introduced hydrogen atom gives rise to an extremely broad resonance at 1.83 ppm in the ^1H NMR spectrum (THF-d_8). Similar to $Li_2[\mathbf{1}]$, both the ^1H and the $^{13}C\{^1H\}$ NMR spectrum of Li[**1H**] reveal two sets of aryl resonances. This recurring feature supports our previous assumption that a linking of B(1) and B(2) reduces the average symmetry of the bis(9-borafluorenyl)methane skeleton in solution. With respect to the molecular structures of $[Li(Et_2O)_2][Li(Et_2O)][\mathbf{1}]$ and $[Li(thf)_4][\mathbf{1H}]$ we note a moderate expansion of the B(1)···B(2) distance from 1.906(3) to 1.954(5) Å. The average degree of boron pyramidalization, however, is substantially more pronounced in the latter molecule (θ_{av} = 150.8°) than in the former (θ_{av} = 168.4°; Table 1).

The successful transformation of $Li_2[\mathbf{1}]$ into Li[**1H**] is remarkable for several aspects: (i) We obtain the same result when we add a hydride ion to **1** as when we first inject two electrons and supply the accompanying atomic nucleus at a later stage. (ii) Judging from the experimental evidence gathered so far, $[\mathbf{1}]^{2-}$ belongs to the class of $[R_3B{-}BR_3]^{2-}$ dianions. Its reaction with TfOH represents a very rare example of the successful protonation of an element–element σ bond to furnish an E–H–E two-electron-three-center (*2e3c*) bond.[9] (iii) Taking together the apparent Brønsted basicity of the boron atoms in $[\mathbf{1}]^{2-}$ and the well-known α-acidity of alkylboranes,[10] an (intramolecular) proton shift could conceivably lead to the corresponding borata-alkene/hydridoborate isomer (Figure 6; BR_2 = 9-borafluorenyl, R′ = $CH_2C(CH_3)_3$). Yet, pursuant to the fact that we never observed any indications of the rearranged product in the experiments, the quantum-chemical assessment of such a process in $[\mathbf{1}]^{2-}$ reveals that the rearrangement is endergonic by ΔG^{298} = 12.6 kcal mol^{-1} and kinetically hindered by a significant barrier of 33.1 kcal mol^{-1}. Remarkably, a reversed isomer stability is computed for the parent diboracyclopropane dianion (R = R′ = H), but an even

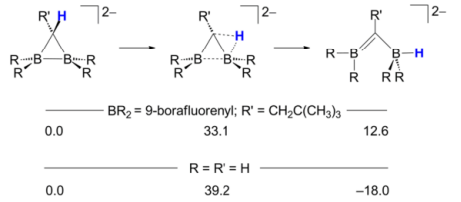

Figure 6. Relative Gibbs energies in kcal mol^{-1} (PBE0D/TZVP) of diboracyclopropane dianions compared to their borata-alkene/hydridoborate isomers for the real system (BR_2 = 9-borafluorenyl, R′ = $CH_2C(CH_3)_3$) and the parent model system (R = R′ = H) together with interconnecting transition states.

higher kinetic barrier is predicted for this model system. (iv) The Li^+ ion is the heavier homologue of the proton. Thus, at first glance the B–H–B bridge in $[Li(thf)_4][\mathbf{1H}]$ and the B···Li···B bridge in $[Li(Et_2O)_2][Li(Et_2O)][\mathbf{1}]$ appear closely related. However, while a QTAIM topological electron density analysis clearly reveals the expected characteristics for covalent B–H–B bond paths in $[\mathbf{1H}]^-$ (see below), the corresponding analyses for any of the Li-coordinated species studied indicate a fundamentally different bonding situation (cf. the SI).

We performed a detailed quantum chemical investigation to gain further insight into the electronic structures of the species under study. To this end, we first verified the suitability of the PBE0D functional to properly assess a potential singlet biradical character of the dianion's wave function by careful comparison of broken-symmetry DFT and MRCI results obtained for the diboracyclopropane model systems $[cyc\text{-}CH_2B_2H_4]^{\bullet-/2-}$ (cf. Figure 6) and the all-carbon analog cyclopropane, $cyc\text{-}C_3H_6$. While the details of this study are provided as Supporting Information, suffice it here to state that the results inspire full confidence in the PBE0D approach and that the ground-state wave functions of all dianionic species discussed in the following represent closed-shell singlet situations without any spin contamination.

We first note that the key frontier molecular orbitals, i.e., the LUMO in **1**, the SOMO in $[\mathbf{1}]^{\bullet-}$, and the HOMO in $[\mathbf{1}]^{2-}$, are dominated by the strongly localized interaction of the two boron p_z-type orbitals, with small delocalized contributions of the borafluorene π systems visible (Figure 7a). As a result of the methylene-bridge enforced orientation of the 9-borafluorenyl moieties the boron p_z orbitals are obviously only poorly aligned. Because of the increasingly closer B–B contact arising upon successive injection of electrons, the orbital interaction is gradually improved in the SOMO of $[\mathbf{1}]^{\bullet-}$ and in the HOMO of $[\mathbf{1}]^{2-}$, but still overlap appears not ideally suited for the formation of a σ bond in both cases.

Evidence for a direct B–B bonding interaction in $[\mathbf{1}]^{\bullet-}$ and $[\mathbf{1}]^{2-}$ was also found among the natural localized molecular orbitals (NLMOs) resulting from a natural bond orbital (NBO) analysis (Figure 7b). For both molecules the corresponding B–B bonding NLMOs involve contributions arising from interaction of the boron atomic orbitals, augmented by a significant participation of orbitals at an adjacent carbon atom of one of the borafluorene rings. In the realm of NBO theory such a semilocalized nature of NLMOs reflects the presence of a physically relevant delocalization of an electron pair (or a single electron in the radical case[11,12]) in the sense of deviations from the representability of the wave function as a set of

DOI: 10.1021/jacs.5b01192
J. Am. Chem. Soc. 2015, 137, 3705–3714

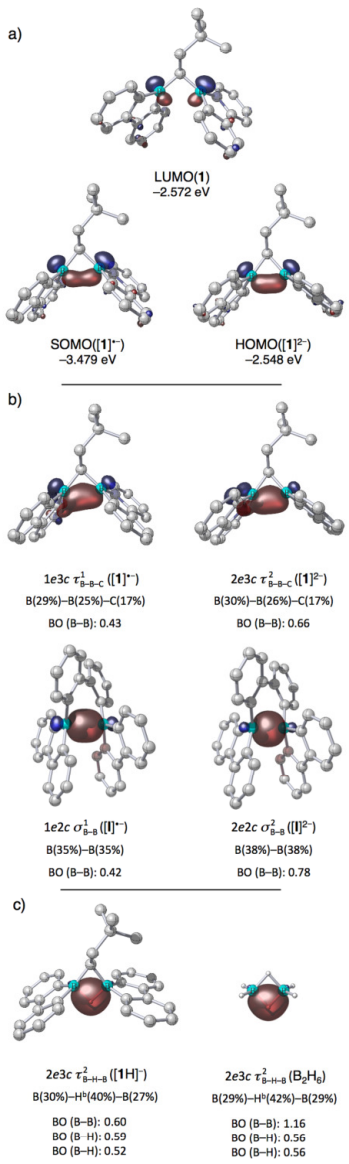

Figure 7. (a) Selected molecular orbitals for the Li^+-free species **1**, $[\mathbf{1}]^{\bullet-}$, and $[\mathbf{1}]^{2-}$. (b) Selected NLMOs for the Li^+-free species $[\mathbf{1}]^{\bullet-}$, $[\mathbf{1}]^{2-}$, $[\mathbf{I}]^{\bullet-}$, and $[\mathbf{I}]^{2-}$. (c) Selected NLMOs for $[\mathbf{1H}]^-$ and B_2H_6. NLMO occupancies, dominantly contributing NAOs, and NLMO/NPA bond orders (BO) are given. Results are based on PBE0D/TZVP wave functions and isosurfaces are plotted at an isovalue of 0.075 $a_0^{-3/2}$; carbon-bonded H atoms omitted for clarity.

localized one-center and two-center NBOs, which serve as a conveniently interpretable basis of a *natural Lewis structure*.[13] Correspondingly, the nature of both NLMOs is characterized by the NBO analysis as a one-electron- and two-electron-three-center B–B bonding situation, respectively. In other words, a Lewis-like description of the boron–boron bonding interaction would involve further resonance structures in addition to the representation as a one-electron bond between the boron atoms in $[\mathbf{1}]^{\bullet-}$ or a two-electron bond between the boron atoms in $[\mathbf{1}]^{2-}$. This contrasts the B–B bonding situation in $[\mathbf{I}]^{\bullet-}$ and $[\mathbf{I}]^{2-}$ displayed for comparison in Figure 7b: for both species the NBO analysis reveals substantially more localized NLMOs, clearly characterized as *1e2c* and *2e2c* B–B bonding situations, respectively. Notwithstanding these qualitative differences, the computed NLMO/NPA bond orders[14] are almost identical for $[\mathbf{1}]^{\bullet-}$ and $[\mathbf{I}]^{\bullet-}$, whereas those for $[\mathbf{1}]^{2-}$ and $[\mathbf{I}]^{2-}$ indicate a slightly stronger B–B bonding interaction in the latter (NPA: natural population analysis; Figure 7). Overall, the NBO picture of a more delocalized B–B single-electron bond in $[\mathbf{1}]^{\bullet-}$ as compared to $[\mathbf{I}]^{\bullet-}$ is reflected as well in the computed spin-density distributions for both species (cf. Figure 4 and ref 1) and is in line with the EPR results discussed above. With bond orders of 0.66 and 0.78 the B–B bonding interactions in $[\mathbf{1}]^{2-}$ and $[\mathbf{I}]^{2-}$ are characterized as moderately weak, comparable to the direct B–B bond order of 0.60 present in the B–H–B bridged species $[\mathbf{1H}]^-$ (Figure 7c). The B–H–B hydride bridge in the latter species represents, according to the NBO analysis, a genuine *2e3c* bonding situation. The corresponding NLMO is shown in Figure 7c and comparison with one of the two corresponding NLMOs in diborane reveals almost identical characteristics in terms of natural atomic orbital (NAO) composition of the three contributing atomic centers as well as B–H–B NLMO/NPA bond orders.

A B–B bonding interaction in compounds $[\mathbf{1}]^{\bullet-}$ and $[\mathbf{1}]^{2-}$ is indicated by both, the structural B–B distance metrics as well as the orbital analyses. Yet, topological analyses of the computed electron densities according to Bader's quantum theory of atoms in molecules (QTAIM) revealed no B–B bond path in either molecule. This result is surprising in view of the marked similarities between the orbital-analysis results for both species and those obtained for $[\mathbf{I}]^{\bullet-}$ and $[\mathbf{I}]^{2-}$ and the fact that the NBO bonding picture for the latter two species is consistently complemented by the finding of B–B bond paths[1] with bond-critical-point (bcp) characteristics revealing covalent bonding interactions between the QTAIM boron atomic basins.

Bader has clearly stressed that a bond path must not be understood as representing a bond.[15] Rather, the concept of a *chemical bond* linking atoms is replaced within QTAIM by the concept of *chemical bonding*, which is indicated by a shared interatomic surface between atomic basins, the presence of an associated bond path ("a line of maximum electron density that denotes that the atoms it links are bonded to one another"[16]), and a bond-critical point located at the minimum of electron density along the bond path where the density gradient vanishes. For a system at equilibrium geometry[17] the network of bond paths, the molecular graph, represents the molecular structure in terms of pairwise chemical bonding interactions among atoms as a consequence of electronic charge density accumulated between them. A vast body of investigations on molecular graphs illustrates that in most of the cases a bond path exists where, intuitively, a chemical bond is expected, although the (common) finding of chemically unexpected bond

DOI: 10.1021/jacs.5b01192
J. Am. Chem. Soc. 2015, 137, 3705–3714

paths has led to controversial discussions regarding the validity of the conceptual connection between a bond path and interatomic bonding.[16,18−24] Precedence for the opposite situation, that is, the absence of a bond path where a chemical bond is expected, also exists, and a number of experimental and theoretical charge-density studies have investigated difficulties in assessing the nature of bonding interactions by means of QTAIM.[25−33] Further analysis of the QTAIM results for $[\mathbf{1}]^{\bullet-}$ and $[\mathbf{1}]^{2-}$ reveals that the respective atomic basins of the bridging carbon atoms extend between those of the boron atoms in both cases. Correspondingly, the gradient vector field plots in Figure 8 illustrate the lack of shared boron−boron

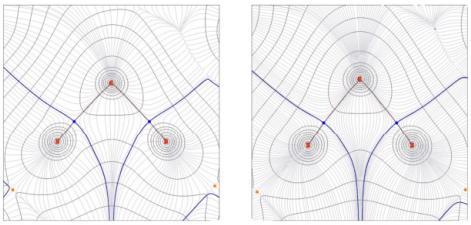

Figure 8. Plot of the gradient vector field of ρ for $[\mathbf{1}]^{\bullet-}$ (left) and $[\mathbf{1}]^{2-}$ (right) in the central B−C−B plane; bond paths are shown in red, zero-flux surfaces and B−C bond critical points (circles) in blue.

interatomic surfaces. This topological feature in the density distribution ρ clearly excludes the presence of B−B bond paths. We note, however, that the charge densities in the regions between the boron atoms are rather low (e.g., ρ = 0.075 and 0.09 au at the midpoint between the boron atoms in $[\mathbf{1}]^{\bullet-}$ and $[\mathbf{1}]^{2-}$, respectively) and exhibit a rather flat topology.

In the light of earlier studies emphasizing the dependence of the charge density topology on the theoretical level[33,34] we investigated the dianion $[\mathbf{1}]^{2-}$ together with the diboracyclopropane dianion model system (cf. Figure 6; R = R′ = H) in some more detail. The QTAIM analysis at the gas phase equilibrium structure of the diboracyclopropane dianion model disclosed a B−B bond path and, with negative values of the Laplacian and the total energy density, the bcp properties indicate a covalent bonding interaction (cf. the SI for details). However, the associated ring-critical point (rcp) is located merely 0.08 Å apart and both reside in a very flat density region (ρ_{bcp} = 0.15 au, ρ_{rcp} = 0.14 au).[35] This situation indicates a topologically unstable molecular structure close to a catastrophe point.[36] As a characteristic of such topologies, subtle changes in the density (caused, e.g., by small changes of the nuclear coordinates) often lead to a collapse of the rcp into the bcp; both critical points will thereby vanish, which causes an abrupt change in the molecular graph. Accordingly, we found no B−B bond path in the partially optimized model system with fixed coordinates of the BCB ring atoms taken from the optimized structure of $[\mathbf{1}]^{2-}$. For the full system $[\mathbf{1}]^{2-}$, artificial compression of the B−B distance during a relaxed scan actually evokes a B−B bond path and a bcp, but only at a B−B distance below 1.6 Å. Because this compression is associated with an increase in total energy by 18 kcal mol^{-1}, this point is clearly not accessible assuming a thermally feasible displacement along the low B−C−B bending vibrational mode in $[\mathbf{1}]^{2-}$ ($\tilde{\nu}$ = 185 cm^{-1}). This excludes the relevant supposition of a dynamic occurrence of a B−B bond path in $[\mathbf{1}]^{2-}$ in the sense of judicious discussions on the influence of nuclear vibrational motions on the charge density topology.[27,37]

Hence at this point we are left to conclude that there is no chemical bonding between the boron atoms in $[\mathbf{1}]^{\bullet-}$ or in $[\mathbf{1}]^{2-}$ within Bader's definition.[17] We have gathered information indicating that the nuclear configurations of the central B−C−B moieties in $[\mathbf{1}]^{\bullet-}$ and $[\mathbf{1}]^{2-}$ give rise to topologically unstable charge density characteristics. Apart from potential problems related to the pronouncedly diffuse and flat character of the excess electron density in the anions $[\mathbf{1}]^{\bullet-}$ and $[\mathbf{1}]^{2-}$, there is growing evidence in the available pertinent literature that triangular nuclear arrangements generally tend to provoke topological instabilities,[29] which might in fact explain reported QTAIM failings to identify expected bond paths.[25−33] Correspondingly, the QTAIM analysis of $[\mathbf{1H}]^{-}$ with its *four-membered* central ring smoothly unveils bonding interactions typical for a B−H−B *2e3c* bridge, with curved bond paths and bcp characteristics closely resembling those of the bcps in parent B_2H_6 (Figure 9).

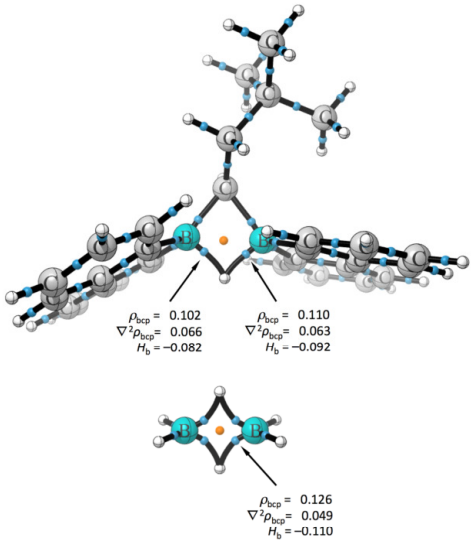

Figure 9. Molecular graphs for $[\mathbf{1H}]^{-}$ and B_2H_6 together with bcp properties for the B−H−B bridges (electron density ρ in $e\ a_0^{-3}$, Laplacian $\nabla^2\rho$ in $e\ a_0^{-5}$, total energy density H_b in $E_h\ a_0^{-3}$); bond paths are shown as black lines, bcps as blue spheres, and rcps as orange spheres.

■ CONCLUSION

In the present contribution we have shown that one and also two electrons can be trapped amid two three-coordinate boron atoms, provided they are properly preorganized within suitable organoborane scaffolds. The injected electron density has pronounced consequences for key structural features. First and foremost, the B−C−B bond angle becomes more acute, and the B−B distance decreases, along the sequence from the neutral diborylmethane **1** via the anion radical $[\mathbf{1}]^{\bullet-}$ to the closed-shell dianion $[\mathbf{1}]^{2-}$. At first glance this indicates the presence of

DOI: 10.1021/jacs.5b01192
J. Am. Chem. Soc. 2015, 137, 3705−3714

covalent bonding interactions, insinuating the formation of *1e2c* and *2e2c* bonds, respectively, among the formerly electron-deficient boron atoms. Such an interpretation inherently rests upon the assumption that the added charge density is largely localized in the void space between the boron atoms, and indeed, we were able to map it by subsequent introduction of a proton, yielding the hydride-bridged B−H−B species $[\mathbf{1H}]^-$. Before this clear-cut experimental background, the lack of a bond path between the boron atoms in either species, $[\mathbf{1}]^{\bullet-}$ and $[\mathbf{1}]^{2-}$, is intriguing, as this is one of the most relied-upon criteria that theory can provide to identify interatomic bonding interactions. Analyses within the NBO framework, in turn, provide a well-defined basis for the interpretation of our experimental findings and fully support the view of covalent B−B bonding. Striking discrepancies resulting from the application of NBO theory and QTAIM, both widely used quantum-chemical tools, to interpret one and the same molecular charge density have been observed earlier. These problems appear to be particularly notorious for topologically unstable three-membered ring systems, in which the collapse of ring-critical and bond-critical points can lead to unexpected disappearance of a bond path.[28]

■ EXPERIMENTAL SECTION

General Considerations. All reactions and manipulations were carried out in an argon-filled glovebox or by applying standard Schlenk techniques under an argon atmosphere. C_6H_6/C_6D_6, toluene, and THF/THF-d_8 were dried over Na/K alloy *without* benzophenone (2−3 d). Prior to use, the solvents were distilled from the drying agent and degassed by applying four freeze−pump−thaw cycles. Compound **1** was synthesized according to a literature procedure.[5]

NMR: Avance 300, Avance 400, Avance III 500 HD. Chemical shifts are referenced to (residual) solvent signals (^{1}H/^{13}C{^{1}H}; C_6D_6: δ = 7.16/128.06 ppm; THF-d_8: δ = 3.58/67.21 ppm) or external aqueous LiCl (^{7}Li), $BF_3{\cdot}Et_2O$ (^{11}B; ^{11}B{^{1}H}), and $Si(CH_3)_4$ (^{29}Si INEPT). Abbreviations: s = singlet, d = doublet, t = triplet, vt = virtual triplet, m = multiplet, n. r. = multiplet expected in the NMR spectrum but not resolved, n. o. = not observed. Cyclic voltammograms were recorded at room temperature using an EG&G Princeton Applied Research 263A potentiostat with a platinum disk working electrode (diameter 2.00 mm). The reference electrode was a silver wire on which AgCl had been deposited by immersing the wire into HCl/HNO_3 (3:1). [nBu$_4$N][PF_6] (0.1 M) was employed as the supporting electrolyte. All potential values are referenced against the FcH/FcH$^+$ couple ($E_{1/2}$ = 0 V). Coulometric measurements were performed at room temperature using a Pt-net electrode. EPR spectra were recorded with a Bruker Elexsys E500 CW EPR spectrometer at X-band frequencies in a TE 102 cavity and at room temperature. EPR simulations were done using the SimFonia software of Bruker. Combustion analyses were performed by the Microanalytical Laboratory of the Goethe-University Frankfurt or by the Microanalytical Laboratory Pascher (Remagen, Germany).

Synthesis of Li_2[1]. Lithium granules (120 mg, 17.3 mmol) were manually divided into small pieces and added at room temperature to a yellow solution of **1** (100 mg, 0.244 mmol) in toluene (20 mL). The reaction mixture was stirred for 14 d, whereupon its color changed to red and a deep red precipitate formed. The suspension was separated from unreacted lithium granules via syringe, the red precipitate of $Li_2[\mathbf{1}]$ was collected on a frit and dried under vacuum. Yield: 78 mg (0.19 mmol, 78%). Red crystals of $[Li(Et_2O)_2][Li(Et_2O)][\mathbf{1}]$ suitable for X-ray crystallography were obtained from an Et_2O solution by slow evaporation of the solvent at room temperature. ^{1}H NMR (400.1 MHz, THF-d_8, 298 K) δ = 8.20 (d, ^3J(H,H) = 7.6 Hz, 2H; H-1a), 7.98 (d, ^3J(H,H) = 7.5 Hz, 2H; H-1b), 7.59 (d, ^3J(H,H) = 7.6 Hz, 2H; H-4a), 7.57 (d, ^3J(H,H) = 7.5 Hz, 2H; H-4b), 6.92−6.86 (m, 4H; H-2a,2b), 6.65 (dvt, ^4J(H,H) = 1.0 Hz, 2H; H-3a), 6.64 (dvt, ^4J(H,H) = 1.1 Hz, 2H; H-3b), 2.41 (d, ^3J(H,H) = 7.4 Hz, 2H; H-8), 2.05 (t, ^3J(H,H) = 7.4 Hz, 1H; H-7), 0.78 (s, 9H; H-10); ^{7}Li NMR (116.6 MHz, THF-d_8, 298 K) δ = −1.2 ($h_{1/2}$ = 80 Hz); ^{11}B NMR (128.4 MHz, THF-d_8, 298 K) δ = −6.7 ($h_{1/2}$ = 270 Hz); ^{13}C{^{1}H} NMR (100.6 MHz, THF-d_8, 298 K) δ = 162.2* (C-6b), 161.0* (C-6a), 143.6 (C-5a), 143.1 (C-5b), 131.1 (C-1a), 129.0 (C-1b), 121.5, 121.4 (C-2a,2b), 118.3, 118.2 (C-4a,4b), 117.6 (C-3b), 117.4 (C-3a), 45.6 (C-8), 33.2 (C-9), 30.5 (C-10), 27.6* (br, C-7). (*) This signal was detected through HSQC/HMBC experiments.

Protonation of Li_2[1] with TfOH (NMR experiment). In an NMR tube, $Li_2[1]$ (13 mg, 0.03 mmol) was dissolved in THF-d_8 (0.6 mL) to obtain a deep violet solution. One drop of neat TfOH was added via syringe at room temperature, whereupon the upper layer of the reaction solution immediately turned colorless. The initial deep violet color of the entire mixture was restored by slight agitation of the NMR tube.

An NMR spectroscopic (^{1}H, ^{11}B) investigation of the reaction mixture revealed Li[**1H**] as the major reaction product (see the SI for a plot of the ^{1}H NMR spectrum). We aimed at the addition of substoichiometric amounts of TfOH, and indeed, the ratio between the formed Li[**1H**] and the unreacted $Li_2[\mathbf{1}]$ is approximately 1:3. *Note*: We have also synthesized Li[**1H**] from **1** and $Li[HBEt_3]$ on a preparative scale and isolated Li[**1H**] in pure form to obtain an authentic sample for comparison (see below).

Synthesis of Li[1]. THF (5 mL) was added with stirring at room temperature to a solid mixture of red, microcrystalline $Li_2[\mathbf{1}] \times 0.7$ C_7H_8 (46 mg, 0.094 mmol; the amount of C_7H_8 contained in the sample was estimated by ^{1}H NMR spectroscopy) and crystalline **1** (42 mg, 0.10 mmol). Within 1 min, both solids were completely dissolved to give a dark green solution. Stirring was continued for 1 h and all volatiles were removed in vacuo to obtain a dark green solid. Yield: 108 mg. Very dark green crystal blocks of $[Li(thf)_4][\mathbf{1}] \times$ THF suitable for X-ray crystallography were grown by addition of Et_2O to a solution of Li[**1**] in THF until a precipitate formed. The precipitate was allowed to settle, the clear, saturated supernatant was decanted, and stored at −30 °C. Anal. Calcd for $C_{50}H_{68}B_2LiO_5$ (777.60): C, 77.23; H, 8.81; Found: C, 76.55; H, 8.67.

Synthesis of Li[1H]. A solution of $Li[HBEt_3]$ in THF (1.0 M; 0.24 mL, 0.24 mmol) was added dropwise with stirring at room temperature via syringe to a yellow solution of **1** (100 mg, 0.24 mmol) in C_6H_6 (8 mL). The reaction mixture turned colorless and a colorless precipitate formed within 1 h. After the suspension had been stored at room temperature for 16 h without stirring, the supernatant was discarded and the colorless microcrystalline solid was briefly dried under vacuum. Yield: 142 mg (0.20 mmol, 83%). Colorless crystals of $[Li(thf)_4][\mathbf{1H}]$ suitable for X-ray crystallography were grown by recrystallization of this material from C_6H_6. *Note*: The molecular composition $[Li(thf)_4][\mathbf{1H}]$ was used to calculate the obtained yield. However, upon prolonged storage of the sample under a vacuum, the Li^+ ions gradually lose some of their thf ligands. According to ^{1}H NMR spectroscopy, exhaustively dried microcrystalline samples finally had a composition of approximately $[Li(thf)_2][\mathbf{1H}]$. ^{1}H NMR (500.2 MHz, THF-d_8, 298 K) δ = 8.09−8.05 (m, 2H; H-1a), 8.00−7.96 (m, 2H; H-1b), 7.57−7.49 (m, 4H; H-4a,4b), 7.03−6.96 (m, 8H; H-2a,2b,3a,3b), 2.00 (d, ^3J(H,H) = 7.0 Hz, 2H; H-8), 1.83* (n. r., 1H; BHB), 1.03 (dt, ^3J(H,H) = 7.0 Hz, 2.4 Hz, 1H; H-7), 0.58 (s, 9H; H-10); ^{1}H NMR (500.2 MHz, C_6D_6, 298 K) δ = 8.50 (m, 2H; H-1a), 8.38 (m, 2H; H-1b), 7.79 (m, 2H; H-4a), 7.76 (m, 2H; H-4b), 7.33−7.25 (m, 8H; H-2a,2b,3a,3b), 2.44 (d, ^3J(H,H) = 7.1 Hz, 2H; H-8), 2.03 (t, ^3J(H,H) = 7.1 Hz, 1H; H-7), 1.01 (s, 9H; H-10), n. o. (BHB); ^{11}B NMR (96.3 MHz, THF-d_8, 298 K) δ = −11.6 (n. r.; $h_{1/2}$ = 360 Hz); ^{11}B{^{1}H} NMR (96.3 MHz, THF-d_8, 298 K) δ = −11.6 ($h_{1/2}$ = 340 Hz); ^{13}C{^{1}H} NMR (125.8 MHz, THF-d_8, 298 K) δ = 159.6** (br, C-6b), 157.3** (br, C-6a), 150.6 (C-5a), 149.8 (C-5b), 133.4 (C-1a), 131.3 (C-1b), 125.0, 124.6, 124.4, 124.4 (C-2a,2b,3a,3b), 118.5, 118.3 (C-4a,4b), 44.2 (C-8), 32.8 (C-9), 30.0 (C-10), 14.2 (br, C-7). (*) This signal was clearly visible only upon ^{11}B decoupling; its chemical shift value was further confirmed by a cross peak in the ^{1}H,^{1}H−COSY (to CH_2CH) and in the ^{1}H,^{11}B-HSQC spectrum. (**) This signal was detected through HSQC/HMBC experiments.

DOI: 10.1021/jacs.5b01192
J. Am. Chem. Soc. 2015, 137, 3705−3714

Anal. Calcd for $C_{46}H_{61}B_2LiO_4$ (706.51): C, 78.20; H, 8.70; Found: C, 77.55; H, 8.60; MS (ESI): *m/z* (%): 411.6 (100) ([**1H**]$^-$).

Crystal Structure Determinations. Data were collected on a STOE IPDS II two-circle diffractometer with a Genix Microfocus tube with mirror optics using Mo Kα radiation (λ = 0.71073 Å). The data were scaled using the frame scaling procedure in the *X-AREA* program system.[38] The structures were solved by direct methods using the program *SHELXS*[39] and refined against F^2 with full-matrix least-squares techniques using the program *SHELXL-97*.[39] [Li(Et$_2$O)$_2$][Li(Et$_2$O)][**1**]: In one Et$_2$O molecule, two C atoms are disordered over two positions with a site occupation factor of 0.55(1) for each of the major occupied sites. In a second Et$_2$O molecule, all four C atoms are disordered over two positions with a site occupation factor of 0.516(6) for each of the major occupied sites. The disordered atoms were isotropically refined. The H atom bonded to C(1) was freely refined. [Li(thf)$_4$][**1**] × THF: In one thf molecule, one methylene group is disordered over two positions with a site occupation factor of 0.55(2) for the major occupied site. In two thf molecules, two methylene groups are disordered over two positions with a site occupation factor of 0.528(9) and 0.51(1), respectively, for the major occupied site. The disordered atoms were isotropically refined. [Li(thf)$_4$][**1H**]: In one thf molecule, one C atom is disordered over two positions with a site occupation factor of 0.57(3) for the major occupied site. In another thf molecule, one C atom is disordered over two positions with a site occupation factor of 0.61(4) for the major occupied site. In a third thf molecule, two C atoms are disordered over two positions with a site occupation factor of 0.57(1) for each of the major occupied sites. The disordered atoms were isotropically refined. Bond lengths and angles in the disordered thf molecules were restrained to the same values as those in the nondisordered thf molecule. Due to the absence of anomalous scatterers, the absolute structure could not be determined and Friedel pairs were merged. The H atom bridging B(1) and B(2) was found in the difference Fourier map and freely refined.

CCDC reference numbers: 1037135 ([Li(Et$_2$O)$_2$][Li(Et$_2$O)][**1**]), 1037136 ([Li(thf)$_4$][**1**] × THF), 1037134 ([Li(thf)$_4$][**1H**]).

Computational Details. DFT calculations were carried out with the Gaussian program package.[40] The PBE0[41−44] hybrid functional was used and combined with the D3BJ atom-pairwise dispersion correction with Becke-Johnson damping as devised by Grimme.[45,46] Geometry optimizations, harmonic frequency calculations and wave function analyses were computed under gas-phase conditions with the TZVP basis set.[47] All stationary points reported were characterized as minima by eigenvalue analysis of the diagonalized Hessians. Natural localized molecular orbitals (NLMOs) were generated with the natural bond orbital (NBO) program.[48] Topological analyses of the electron density according to Bader's quantum theory of atoms in molecules (QTAIM)[15,49] were carried out with the Multiwfn code.[50,51] In all QTAIM-related cases the Poincaré−Hopf relationship for a consistent set of critical points, $n_{ncp} - n_{bcp} + n_{rcp} - n_{ccp} = 1$, was fulfilled. To account for effects of solvents (tetrahydrofuran), a polarizable continuum model[52] within the COSMO[53] approach was employed for the evaluation of orbital energies, NMR shieldings, absorption spectra, and isotropic hyperfine coupling constants. UV−vis absorption spectra along with the corresponding natural transition orbitals (NTO)[54] were computed using the TD-DFT approach.[55] For the calculation of EPR properties,[56] the GIAO formalism[57−59] together with the EPR-III basis set[60] was used. Multireference configuration interaction (MRCI)[61] calculations for the small cyclopropane and diboracyclopropane model systems were performed with the Molpro program suite[62] in conjunction with the cc-pVTZ basis sets.[63] The preceding multiconfigurational self-consistent field (MCSCF)[64] wave functions were constructed from a set of six active orbitals comprising the three bonding and three antibonding σ-type molecular orbitals of the three-membered ring, i.e., CAS(6,6) type wave functions. Graphical representations of molecular geometries, isosurfaces, and AIM bond paths were produced with the POV-Ray[65] software.

■ ASSOCIATED CONTENT

Supporting Information

Plots of the ^{1}H and ^{13}C{^{1}H} NMR spectra of Li$_2$[**1**] and Li[**1H**]; plot of the ^{1}H NMR spectrum of protonated Li$_2$[**1**] (NMR experiment). Details of the X-ray crystal structure analyses of [Li(Et$_2$O)$_2$][Li(Et$_2$O)][**1**], [Li(thf)$_4$][**1**] × THF, and [Li(thf)$_4$][**1H**]. Cyclic voltammetric and spectroelectrochemical investigation of **1**. Details of the EPR spectroscopic measurement of in situ-generated Li[**1**] in THF solution. Details of quantum-chemical calculations. This material is available free of charge via the Internet at http://pubs.acs.org.

■ AUTHOR INFORMATION

Corresponding Authors

max.holthausen@chemie.uni-frankfurt.de

matthias.wagner@chemie.uni-frankfurt.de

Notes

The authors declare no competing financial interest.

■ ACKNOWLEDGMENTS

A.H. wishes to thank the Fonds der Chemischen Industrie for a Ph.D. grant. The authors are grateful to Professor Dietmar Stalke for helpful literature hints regarding problematic charge-density topology situations. Quantum-chemical calculations have been performed at the Center for Scientific Computing (CSC) Frankfurt on the FUCHS and LOEWE-CSC high-performance computer clusters. This work was supported by the Beilstein-Institut, Frankfurt (Main), Germany, within the research collaboration NanoBiC.

■ REFERENCES

(1) Hübner, A.; Diehl, A. M.; Diefenbach, M.; Endeward, B.; Bolte, M.; Lerner, H.-W.; Holthausen, M. C.; Wagner, M. *Angew. Chem., Int. Ed.* **2014**, *53*, 4832−4835. For an earlier example of an EPR-spectroscopically characterized B·B *1e2c* bond, see: Hoefelmeyer, J. D.; Gabbaï, F. P. *J. Am. Chem. Soc.* **2000**, *122*, 9054−9055.

(2) Hübner, A.; Diehl, A. M.; Bolte, M.; Lerner, H.-W.; Wagner, M. *Organometallics* **2013**, *32*, 6827−6833. The formation of B−B σ bonds has been suggested as result of the two-electron reduction of 1,8-diborylated naphthalenes during cyclic voltammetry: Melaïmi, M.; Solé, S.; Chiu, C.-W.; Wang, H.; Gabbaï, F. P. *Inorg. Chem.* **2006**, *45*, 8136−8143.

(3) Shoji, Y.; Matsuo, T.; Hashizume, D.; Gutmann, M. J.; Fueno, H.; Tanaka, K.; Tamao, K. *J. Am. Chem. Soc.* **2011**, *133*, 11058−11061.

(4) Grigsby, W. J.; Power, P. P. *J. Am. Chem. Soc.* **1996**, *118*, 7981−7988.

(5) Hübner, A.; Qu, Z.-W.; Englert, U.; Bolte, M.; Lerner, H.-W.; Holthausen, M. C.; Wagner, M. *J. Am. Chem. Soc.* **2011**, *133*, 4596−4609.

(6) In THF solution, the two-electron reduction of **1** proceeds much more rapidly and is complete within hours. We have confirmed the formation of Li$_2$[**1**] by NMR spectroscopy and by X-ray crystallography ([Li(thf)$_2$]$_2$[**1**] and [Li(thf)$_4$][Li(thf)$_2$][**1**]; in both cases, the poor crystal quality precludes publication of the data). However, the reaction in THF is less selective than in toluene, and in the case of the latter solvent, precipitation of Li$_2$[**1**] facilitates its isolation in pure form.

(7) Elschenbroich, C. *Organometallics*; Wiley-VCH: Weinheim, 2006.

(8) Nöth, H.; Wrackmeyer, B. Nuclear Magnetic Resonance Spectroscopy of Boron Compounds. In *NMR Basic Principles and Progress*; Diehl, P., Fluck, E., Kosfeld, R., Eds.; Springer: Berlin, 1978.

(9) (a) East, A. L. L.; Liu, Z. F.; McCague, C.; Cheng, K.; Tse, J. S. *J. Phys. Chem. A* **1998**, *102*, 10903−10911. (b) Takeuchi, T.; Shirai, Y.; Matsumura, Y.; Iwai, K.; Matsutani, T.; Oshita, J.; Naka, A. *Surf. Interface Anal.* **2006**, *38*, 1650−1653. (c) Watanabe, Y.; Maeda, S.;

DOI: 10.1021/jacs.5b01192
J. Am. Chem. Soc. 2015, 137, 3705−3714

Ohno, K. *Chem. Phys. Lett.* **2007**, *447*, 21−26. (d) Savoca, M.; Langer, J.; Dopfer, O. *Angew. Chem., Int. Ed.* **2013**, *52*, 1568−1571.
(10) (a) Rathke, M. W.; Kow, R. *J. Am. Chem. Soc.* **1972**, *94*, 6854−6856. (b) Matteson, D. S. *Synthesis* **1975**, 147−158. (c) Wilson, J. W. *J. Organomet. Chem.* **1980**, *186*, 297−300. (d) Matteson, D. S.; Moody, R. J. *Organometallics* **1982**, *1*, 20−28. (e) Power, P. P. *Chem. Rev.* **1999**, *99*, 3463−3503. (f) Yu, J.; Kehr, G.; Daniliuc, C. G.; Erker, G. *Eur. J. Inorg. Chem.* **2013**, 3312−3315.
(11) Carpenter, J. E.; Weinhold, F. *J. Mol. Struct.: THEOCHEM* **1988**, *46*, 41−62.
(12) Weinhold, F.; Landis, C. R. *Discovering Chemistry with Natural Bond Orbitals*; John Wiley & Sons: Hoboken, NJ, 2012.
(13) Landis, C. R.; Weinhold, F. The NBO View of Chemical Bonding. In *The Chemical Bond: Fundamental Aspects of Chemical Bonding*; Frenking, G., Shaik, S., Eds.; Wiley-VCH: Weinheim, 2014.
(14) Reed, A. E.; Schleyer, P. v. R. *J. Am. Chem. Soc.* **1990**, *112*, 1434−1445.
(15) Bader, R. F. W. *Atoms in Molecules: A Quantum Theory*; Oxford University Press: Oxford, 1994.
(16) Bader, R. F. W. *J. Phys. Chem. A* **2009**, *113*, 10391−10396.
(17) Bader, R. F. W. *J. Phys. Chem. A* **1998**, *102*, 7314−7323.
(18) Matta, C. F.; Hernández-Trujillo, J.; Tang, T.-H.; Bader, R. F. W. *Chem.—Eur. J.* **2003**, *9*, 1940−1951.
(19) Bader, R. F. W.; Fang, D.-C. *J. Chem. Theory Comput.* **2005**, *1*, 403−414.
(20) Bader, R. F. W. *Chem.—Eur. J.* **2006**, *12*, 7769−7772.
(21) Bader, R. F. W. *Chem.—Eur. J.* **2006**, *12*, 2896−2901.
(22) Poater, J.; Solà, M.; Bickelhaupt, F. M. *Chem.—Eur. J.* **2006**, *12*, 2889−2895.
(23) Poater, J.; Solà, M.; Bickelhaupt, F. M. *Chem.—Eur. J.* **2006**, *12*, 2902−2905.
(24) Weinhold, F.; Schleyer, P. v. R.; McKee, W. C. *J. Comput. Chem.* **2014**, *35*, 1499−1508.
(25) Macchi, P.; Garlaschelli, L.; Sironi, A. *J. Am. Chem. Soc.* **2002**, *124*, 14173−14184.
(26) Macchi, P.; Sironi, A. *Coord. Chem. Rev.* **2003**, *238*, 383−412.
(27) Farrugia, L. J.; Evans, C.; Tegel, M. *J. Phys. Chem. A* **2006**, *110*, 7952−7961.
(28) Henn, J.; Leusser, D.; Stalke, D. *J. Comput. Chem.* **2007**, *28*, 2317−2324.
(29) Flierler, U.; Burzler, M.; Leusser, D.; Henn, J.; Ott, H.; Braunschweig, H.; Stalke, D. *Angew. Chem., Int. Ed.* **2008**, *47*, 4321−4325.
(30) Farrugia, L. J.; Evans, C.; Lentz, D.; Roemer, M. *J. Am. Chem. Soc.* **2009**, *131*, 1251−1268.
(31) Mousavi, M.; Frenking, G. *Organometallics* **2013**, *32*, 1743−1751.
(32) Mousavi, M.; Frenking, G. *J. Organomet. Chem.* **2013**, *748*, 2−7.
(33) Jacobsen, H. *J. Comput. Chem.* **2009**, *30*, 1093−1102.
(34) Götz, K.; Kaupp, M.; Braunschweig, H.; Stalke, D. *Chem.—Eur. J.* **2009**, *15*, 623−632.
(35) We note in passing that a QTAIM analysis performed on a charge density obtained from a MRCISD/cc-pVTZ single point calculation on the PBE0D/TZVP minimum structure resulted in essentially identical results, which validates again the suitability of the chosen DFT approach.
(36) See chapter 4 in ref 15.
(37) Foroutan-Nejad, C.; Shahbazian, S.; Marek, R. *Chem.—Eur. J.* **2014**, *20*, 10140−10152.
(38) *X-AREA: Diffractometer Control Program System*; Stoe & Cie: Darmstadt, Germany, 2002.
(39) Sheldrick, G. M. *Acta Crystallogr., Sect. A: Found. Crystallogr.* **2008**, *64*, 112−122.
(40) Frisch, M. J.; Trucks, G. W.; Schlegel, H. B.; Scuseria, G. E.; Robb, M. A.; Cheeseman, J. R.; Scalmani, G.; Barone, V.; Mennucci, B.; Petersson, G. A.; Nakatsuji, H.; Caricato, M.; Li, X.; Hratchian, H. P.; Izmaylov, A. F.; Bloino, J.; Zheng, G.; Sonnenberg, J. L.; Hada, M.; Ehara, M.; Toyota, K.; Fukuda, R.; Hasegawa, J.; Ishida, M.; Nakajima, T.; Honda, Y.; Kitao, O.; Nakai, H.; Vreven, T.; Montgomery, J. A., Jr.; Peralta, J. E.; Ogliaro, F.; Bearpark, M.; Heyd, J. J.; Brothers, E.; Kudin, K. N.; Staroverov, V. N.; Kobayashi, R.; Normand, J.; Raghavachari, K.; Rendell, A.; Burant, J. C.; Iyengar, S. S.; Tomasi, J.; Cossi, M.; Rega, N.; Millam, J. M.; Klene, M.; Knox, J. E.; Cross, J. B.; Bakken, V.; Adamo, C.; Jaramillo, J.; Gomperts, R.; Stratmann, R. E.; Yazyev, O.; Austin, A. J.; Cammi, R.; Pomelli, C.; Ochterski, J. W.; Martin, R. L.; Morokuma, K.; Zakrzewski, V. G.; Voth, G. A.; Salvador, P.; Dannenberg, J. J.; Dapprich, S.; Daniels, A. D.; Farkas, Ö.; Foresman, J. B.; Ortiz, J. V.; Cioslowski, J.; Fox, D. J. *Gaussian 09*, Revision D.01; Gaussian, Inc.: Wallingford, CT, 2013; http://www.gaussian.com.
(41) Perdew, J. P.; Burke, K.; Ernzerhof, M. *Phys. Rev. Lett.* **1996**, *77*, 3865−3868.
(42) Perdew, J. P.; Burke, K.; Ernzerhof, M. *Phys. Rev. Lett.* **1997**, *78*, 1396−1396.
(43) Perdew, J. P.; Ernzerhof, M.; Burke, K. *J. Chem. Phys.* **1996**, *105*, 9982−9985.
(44) Adamo, C.; Barone, V. *J. Chem. Phys.* **1999**, *110*, 6158−6170.
(45) Goerigk, L.; Grimme, S. *J. Chem. Theory Comput.* **2011**, *7*, 291−309.
(46) Grimme, S.; Ehrlich, S.; Goerigk, L. *J. Comput. Chem.* **2011**, *32*, 1456−1465.
(47) Schäfer, A.; Huber, C.; Ahlrichs, R. *J. Chem. Phys.* **1994**, *100*, 5829−5835.
(48) Glendening, E. D.; Landis, C. R.; Weinhold, F. *Wiley Interdiscip. Rev.: Comput. Mol. Sci.* **2012**, *2*, 1−42.
(49) Matta, C. F., Boyd, R. J., Eds.; *The Quantum Theory of Atoms in Molecules*; Wiley-VCH: Weinheim, 2007.
(50) Lu, T. *Multiwfn 3.2.1—A Multifunctional Wavefunction Analyzer*; School of Chemical and Biological Engineering, University of Science and Technology: Beijing, China, 2013; http://multiwfn.codeplex.com.
(51) Lu, T.; Chen, F. *J. Comput. Chem.* **2012**, *33*, 580−592.
(52) Tomasi, J.; Mennucci, B.; Cammi, R. *Chem. Rev.* **2005**, *105*, 2999−3094.
(53) Klamt, A. *Wiley Interdiscip. Rev.: Comput. Mol. Sci.* **2011**, *1*, 699−709.
(54) Martin, R. L. *J. Chem. Phys.* **2003**, *118*, 4775−4777.
(55) Scalmani, G.; Frisch, M. J.; Mennucci, B.; Tomasi, J.; Cammi, R.; Barone, V. *J. Chem. Phys.* **2006**, *124* (094107), 1−15.
(56) Ciofini, I.; Adamo, C.; Barone, V. *J. Chem. Phys.* **2004**, *121*, 6710−6718.
(57) Ditchfield, R. *Mol. Phys.* **1974**, *27*, 789−807.
(58) Wolinski, K.; Hinton, J. F.; Pulay, P. *J. Am. Chem. Soc.* **1990**, *112*, 8251−8260.
(59) Cheeseman, J. R.; Trucks, G. W.; Keith, T. A.; Frisch, M. J. *J. Chem. Phys.* **1996**, *104*, 5497−5509.
(60) Barone, V. Structure, Magnetic Properties and Reactivities of Open-Shell Species from Density Functional and Self-Consistent Hybrid Methods. In *Recent Advances in Density Functional Methods*; World Scientific: Singapore, 1995; Vol. *1*, pp 287−334.
(61) Werner, H.-J.; Knowles, P. J. *J. Chem. Phys.* **1988**, *89*, 5803−5814.
(62) Werner, H.-J.; Knowles, P. J.; Knizia, G.; Manby, F. R.; Schütz, M.; Celani, P.; Korona, T.; Lindh, R.; Mitrushenkov, A.; Rauhut, G.; Shamasundar, K. R.; Adler, T. B.; Amos, R. D.; Bernhardsson, A.; Berning, A.; Cooper, D. L.; Deegan, M. J. O.; Dobbyn, A. J.; Eckert, F.; Goll, E.; Hampel, C.; Hesselmann, A.; Hetzer, G.; Hrenar, T.; Jansen, G.; Köppl, C.; Liu, Y.; Lloyd, A. W.; Mata, R. A.; May, A. J.; McNicholas, S. J.; Meyer, W.; Mura, M. E.; Nicklaß, A.; O'Neill, D. P.; Palmieri, P.; Peng, D.; Pflüger, K.; Pitzer, R.; Reiher, M.; Shiozaki, T.; Stoll, H.; Stone, A. J.; Tarroni, R.; Thorsteinsson, T.; Wang, M. *MOLPRO*, Version 2012.1; University College Cardiff Consultants Ltd.: Cardiff, U.K., 2012; http://www.molpro.net.
(63) Dunning, T. H. *J. Chem. Phys.* **1989**, *90*, 1007−1023.
(64) Werner, H.-J.; Knowles, P. J. *J. Chem. Phys.* **1985**, *82*, 5053−5063.
(65) *Persistence of Vision Raytracer*, Version 3.6; Persistence of Vision Pty. Ltd.: Williamstown, Victoria, Australia, 2004; http://www.povray.org.

DOI: 10.1021/jacs.5b01192
J. Am. Chem. Soc. 2015, 137, 3705−3714

Supporting Information

A Preorganized Ditopic Borane as Highly Efficient One- or Two-Electron Trap

Alexander Hübner, Thomas Kaese, Martin Diefenbach, Burkhard Endeward, Michael Bolte, Hans-Wolfram Lerner, Max C. Holthausen, and Matthias Wagner**

Content:

1. Plots of the ^{1}H and $^{13}C\{^{1}H\}$ NMR spectra of Li_2[**1**] and Li[**1H**]
2. Plot of the ^{1}H NMR spectrum of the protonation of Li_2[**1**] with TfOH (NMR experiment)
3. X-ray crystal structure analyses of $[Li(Et_2O)_2][Li(Et_2O)]$[**1**], $[Li(thf)_4]$[**1**] × THF, and $[Li(thf)_4]$[**1H**]
4. Cyclic voltammogram of **1** in THF
5. Spectroelectrochemical investigation of **1**
6. EPR spectroscopy
7. Quantum-chemical results

1. Plots of the ^{1}H and $^{13}C\{^{1}H\}$ NMR spectra of Li_2[1] and Li[1H]

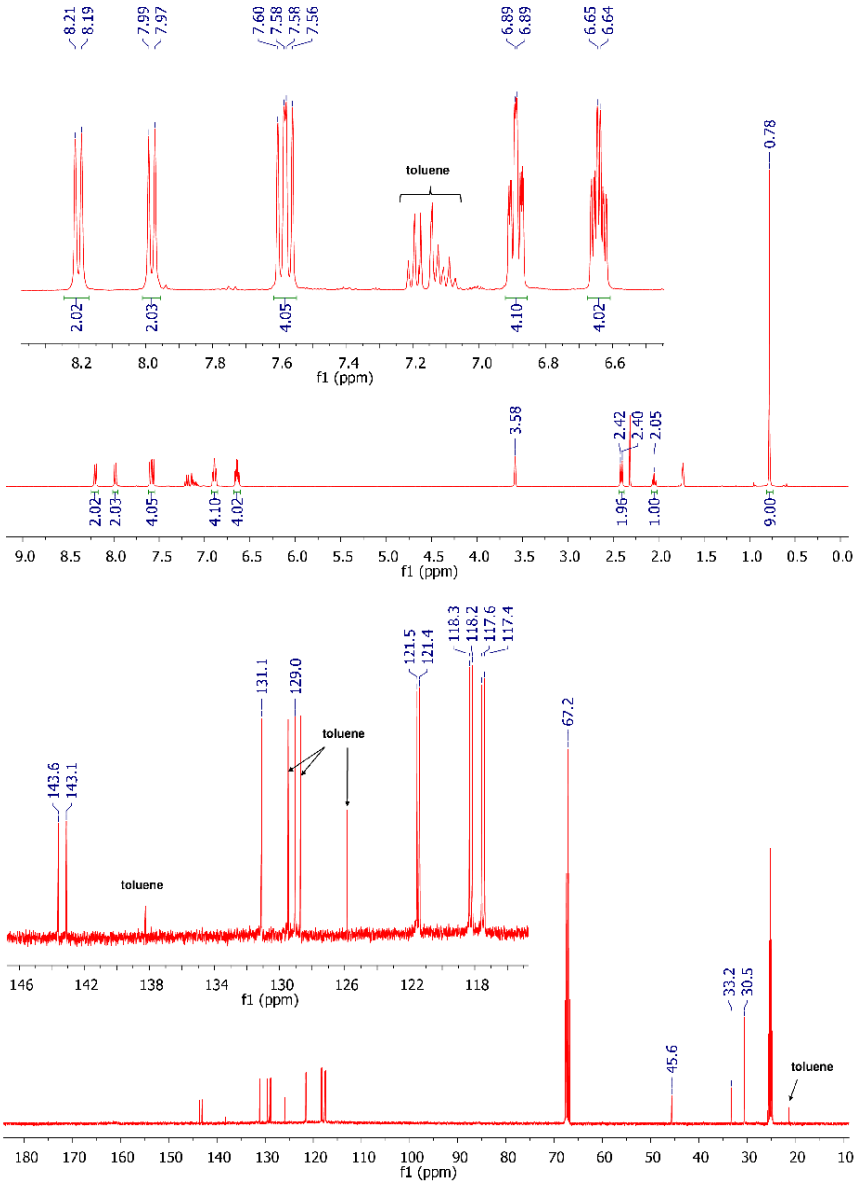

Figure S1. ^{1}H (top) and $^{13}C\{^{1}H\}$ (bottom) NMR spectrum of Li_2[**1**] (THF-d_8).

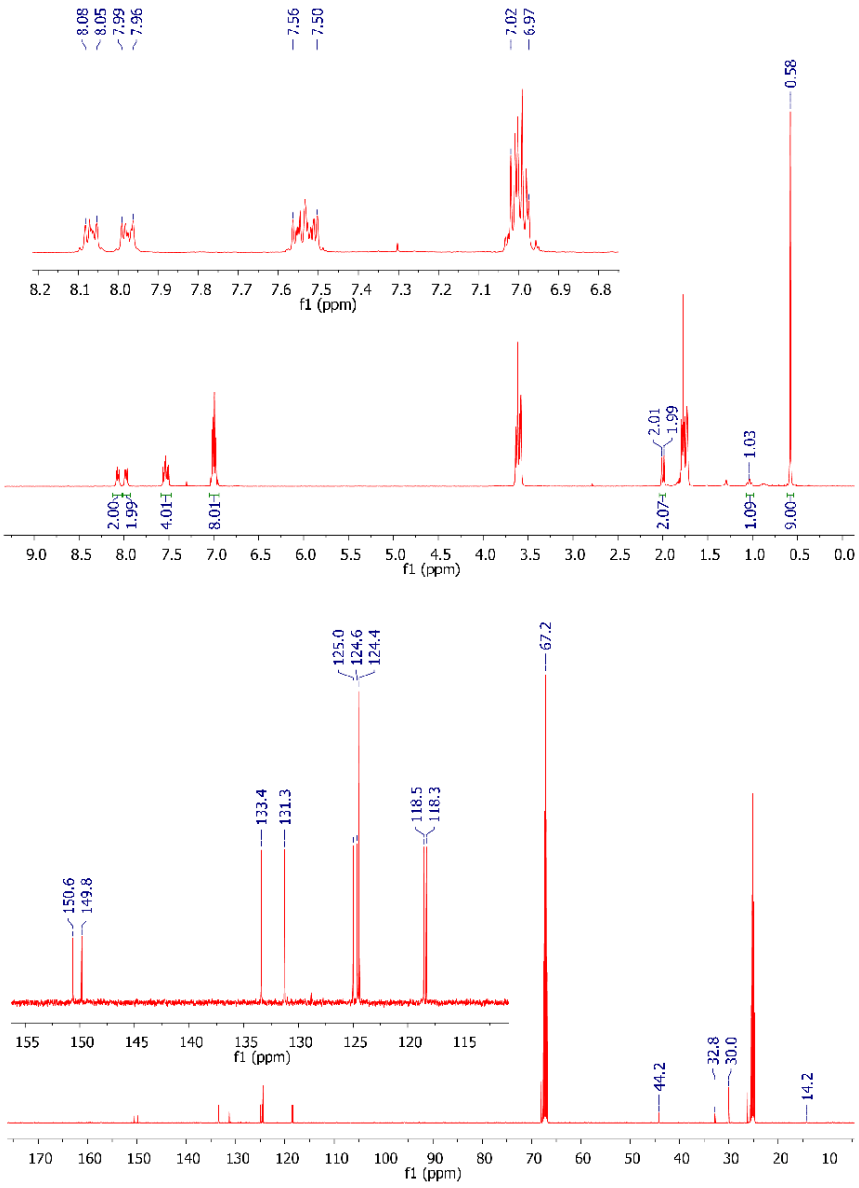

Figure S2. ^{1}H (top) and ^{13}C{^{1}H} (bottom) NMR spectrum of Li[**1H**] (THF-d_8).

2. Plot of the ^{1}H NMR spectrum of the protonation of Li_2[1] with TfOH (NMR experiment)

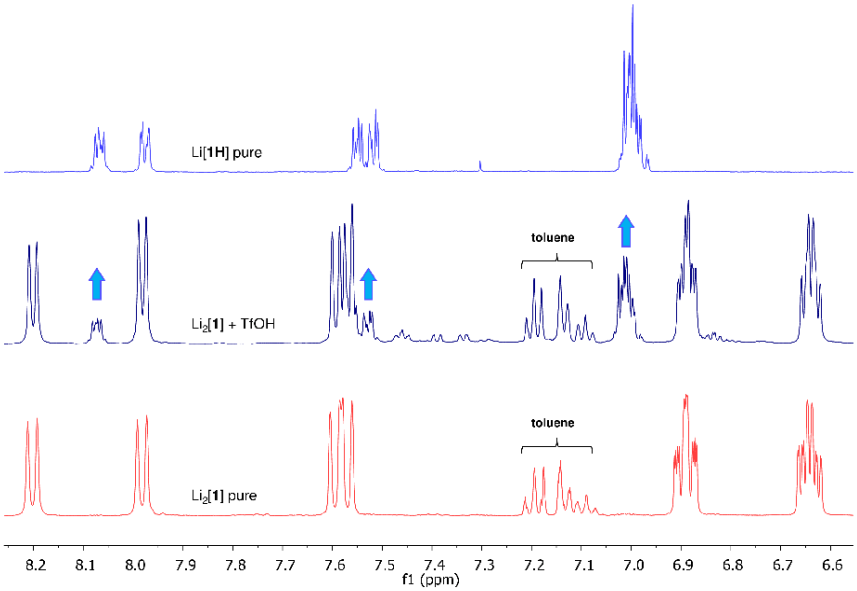

Figure S3. Comparison of the ^{1}H NMR spectra (THF-d_8) of Li_2[**1**] (bottom, red), of the mixture of Li_2[**1**] with substoichiometric amounts of TfOH (middle, dark blue; the development of the signal pattern of Li[**1H**] is indicated by arrows), and of Li[**1H**] (top, light blue).

3. X-ray crystal structure analyses of $[Li(Et_2O)_2][Li(Et_2O)][1]$, $[Li(thf)_4][1] \times THF$, and $[Li(thf)_4][1H]$

X-ray crystal structure analysis of $[Li(Et_2O)_2][Li(Et_2O)][1]$: Compound $[Li(Et_2O)_2][Li(Et_2O)][\mathbf{1}]$ exists as ion triplet in the crystal lattice. Li(1), which is located between the two 9-borafluorene-9-yl planes, carries only one Et_2O ligand and forms short contacts to both boron atoms and to the carbon atoms C(11) and C(31). The fragment $[Li(2)(Et_2O)_2]^+$ coordinates to $[\mathbf{1}]^{2-}$ in an *exo* fashion with short contacts to B(1) and C(21).

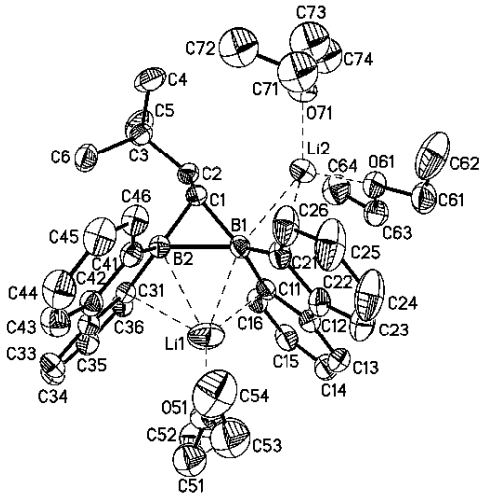

Figure S4. Molecular structure of $[Li(Et_2O)_2][Li(Et_2O)][\mathbf{1}]$. Displacement ellipsoids are shown at the 50% probability level; H atoms are omitted for clarity. Selected bond lengths [Å], atom···atom distances [Å], and bond angles [°]: B(1)–B(2) = 1.906(3), B(1)–C(1) = 1.618(3), B(1)–C(11) = 1.575(3), B(1)–C(21) = 1.576(3), B(2)–C(1) = 1.578(3), B(2)–C(31) = 1.591(3), B(2)–C(41) = 1.582(3); Li(1)···B(1) = 2.326(5), Li(1)···B(2) = 2.383(5), Li(1)···C(11) = 2.464(6), Li(1)···C(31) = 2.496(6), Li(2)···B(1) = 2.328(4), Li(2)···C(21) = 2.462(4); B(1)–C(1)–B(2) = 73.2(1), B(1)···Li(1)···B(2) = 47.7(1).

X-ray crystal structure analysis of [Li(thf)$_4$][1] × THF: The B···B distance in [Li(thf)$_4$][**1**] is 2.166(4) Å. The dihedral angle between the borafluorene systems amounts to 79.7(1)°. [Li(thf)$_4$][**1**] forms fully solvent-separated ion pairs in the crystal lattice and cocrystallizes with another molecule of THF.

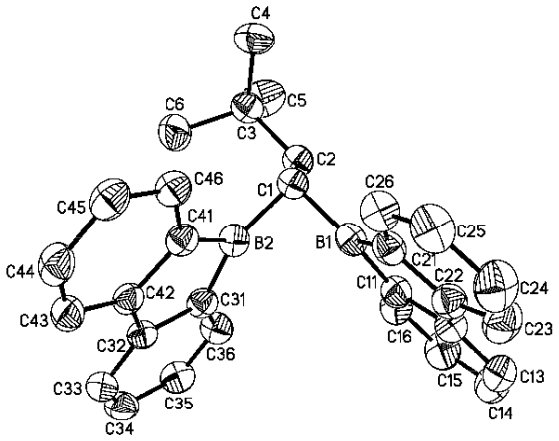

Figure S5. Molecular structure of the anionic moiety in [Li(thf)$_4$][**1**] × THF. Displacement ellipsoids are shown at the 50% probability level; H atoms, cocrystallized THF, and the [Li(thf)$_4$]$^+$ cation are omitted for clarity. Selected bond lengths [Å], atom···atom distance [Å], and bond angle [°]: B(1)–C(1) = 1.577(4), B(1)–C(11) = 1.585(4), B(1)–C(21) = 1.572(4), B(2)–C(1) = 1.573(3), B(2)–C(31) = 1.577(4), B(2)–C(41) = 1.576(3); B(1)···B(2) = 2.166(4); B(1)–C(1)–B(2) = 86.9(2).

X-ray crystal structure analysis of [Li(thf)$_4$][1H]: Compound [Li(thf)$_4$][**1H**] forms fully solvent-separated ion pairs in the crystal lattice.

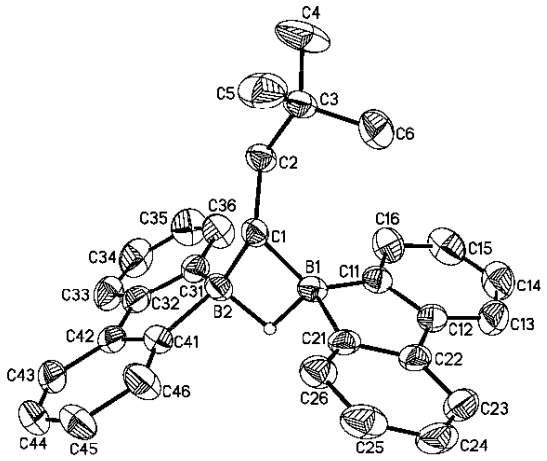

Figure S6. Molecular structure of [Li(thf)$_4$][**1H**]. Displacement ellipsoids are shown at the 50% probability level; the [Li(thf)$_4$]$^+$ ion and all hydrogen atoms, except the hydrogen atom bridging B(1) and B(2), are omitted for clarity. Selected bond lengths [Å], atom···atom distance [Å], and bond angle [°]: B(1)–C(1) = 1.593(5), B(1)–C(11) = 1.616(5), B(1)–C(21) = 1.612(5), B(2)–C(1) = 1.604(5), B(2)–C(31) = 1.614(5), B(2)–C(41) = 1.619(5); B(1)···B(2) = 1.954(5); B(1)–C(1)–B(2) = 75.4(2).

Table S1. Selected crystallographic data for $[Li(Et_2O)_2][Li(Et_2O)][\mathbf{1}]$, $[Li(thf)_4][\mathbf{1}] \times THF$, and $[Li(thf)_4][\mathbf{1H}]$.

	$[Li(Et_2O)_2][Li(Et_2O)][\mathbf{1}]$	$[Li(thf)_4][\mathbf{1}] \times THF$	$[Li(thf)_4][\mathbf{1H}]$
formula	$C_{42}H_{58}B_2Li_2O_3$	$C_{50}H_{68}B_2LiO_5$	$C_{46}H_{61}B_2LiO_4$
M_r	646.38	777.60	706.51
color, shape	dark red, plate	green-black, block	colorless, plate
T [K]	173(2)	173(2)	173(2)
radiation, λ [Å]	MoKα, 0.71073	MoKα, 0.71073	MoKα, 0.71073
crystal system	triclinic	monoclinic	monoclinic
space group	P-1	$P2_1/n$	$P2_1$
a [Å]	10.6874(7)	10.8223(6)	10.2957(7)
b [Å]	11.5577(8)	24.5017(11)	18.7762(10)
c [Å]	17.3663(12)	17.7344(9)	11.7473(8)
α [°]	101.338(5)	90	90
β [°]	99.271(5)	104.485(4)	113.372(5)
γ [°]	106.041(5)	90	90
V [Å^3]	1967.8(2)	4553.1(4)	2084.6(2)
Z	2	4	2
D_{calcd} [g cm^{-3}]	1.091	1.134	1.126
F(000)	700	1684	764
μ [mm^{-1}]	0.064	0.070	0.068
crystal size [mm]	0.34 × 0.27 × 0.11	0.33 × 0.24 × 0.15	0.18 × 0.16 × 0.03
rflns collected	31165	53086	29731
independent rflns (R_{int})	6910 (0.0720)	8216 (0.0829)	4750 (0.0951)
data/restraints/parameters	6910/0/442	8216/0/521	4750/249/481
GOF on F^2	1.032	1.048	1.077
R_1, wR_2 [$I > 2\sigma(I)$]	0.0701, 0.1740	0.0779, 0.1992	0.0610, 0.1416
R_1, wR_2 (all data)	0.0845, 0.1840	0.0988, 0.2138	0.0759, 0.1499
largest diff peak and hole [e Å^{-3}]	0.539, –0.400	0.414, –0.441	0.271, –0.206

4. Cyclic voltammogram of 1 in THF

The cyclic voltammogram of **1** in THF shows two reversible reduction processes at potential values of $E_{1/2}$ = –1.76 V and –2.17 V.

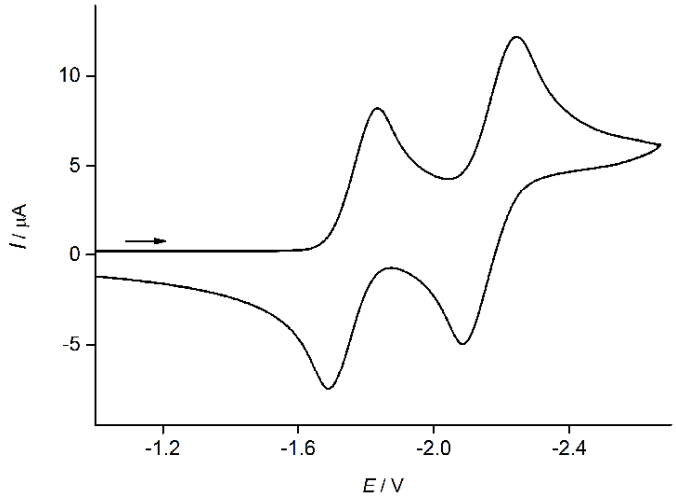

Figure S7. Cyclic voltammogram of **1** in THF at room temperature; vs FcH/FcH^+, supporting electrolyte: [nBu$_4$N][PF$_6$] (0.1 M), scan rate: 100 mV s^{-1}.

5. Spectroelectrochemical investigation of 1

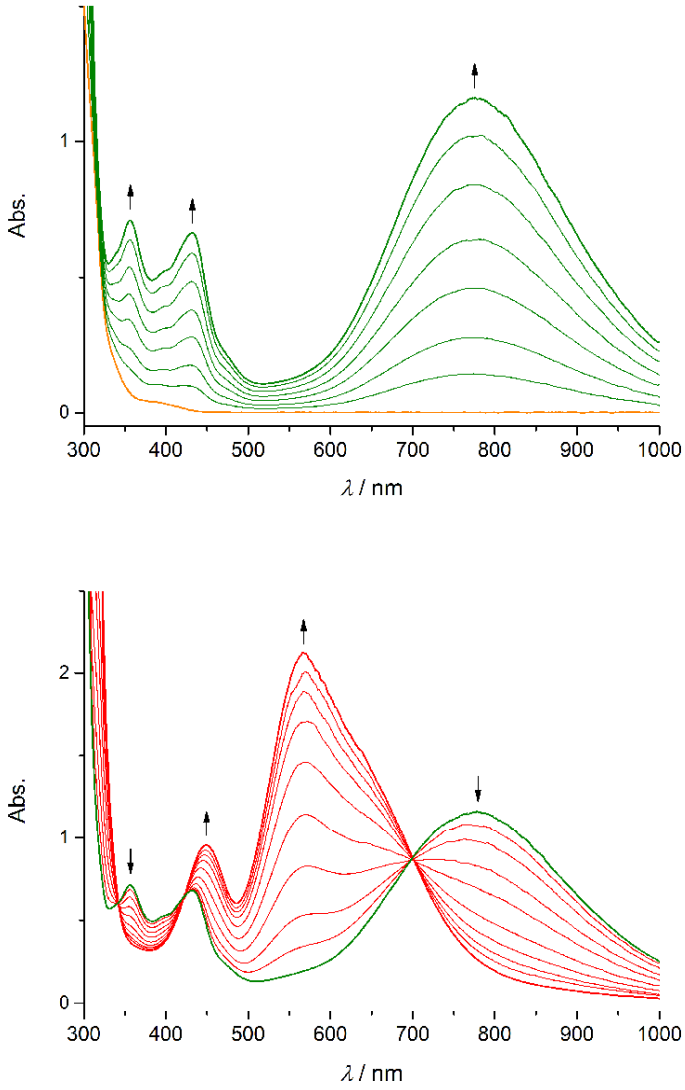

Figure S8. UV/vis absorption spectra were recorded in THF at room temperature during controlled potential electrolysis of **1** at a Pt-net electrode (supporting electrolyte: [nBu$_4$N][PF$_6$] (0.1 M)); *Top*: Reduction of **1** (orange) to $[\mathbf{1}]^{\bullet-}$ (green) at E_w = –1.9 V; *Bottom*: Subsequent reduction of the electrogenerated $[\mathbf{1}]^{\bullet-}$ (green) to $[\mathbf{1}]^{2-}$ (red) at E_w = –2.4 V.

S10

The controlled potentiometric reduction of **1** to $[\mathbf{1}]^{\bullet-}$ and further to $[\mathbf{1}]^{2-}$ at applied potentials of E_w = −1.9 V and −2.4 V (vs. FcH/FcH^+), respectively, was monitored by *in situ* UV/vis spectroscopy (THF, room temperature).

The electrochemical conversion of **1** (cf. orange curve in Figure S8, top) at a potential value of E_w = −1.9 V leads to the simultaneous evolution of several new absorption bands (λ_{max} = 357 nm, 432 nm, and 775 nm; green curves). After an overall reduction time of 15 min, no further increase of the absorption bands was observable. The broad absorption at 775 nm corresponds nicely to the green color of a THF solution of Li[**1**]. In line with that, the coulometric determination of the equivalents of the transferred electrons yielded an *n* value of 0.7 at this point.

If the electrochemical reduction is continued at a more cathodic potential value of E_w = −2.4 V, the absorption bands of the primary reduction product (cf. green curve in Figure S8, bottom) gradually decrease with the concomitant appearance of new absorption bands at λ_{max} = 450 nm and 568 nm (cf. red curves in Figure S8, bottom). Now, the longest wavelength absorption corresponds to the purple color of a THF solution of Li_2[**1**]. After a reduction time of 25 min (at E_w = −2.4 V), no further development of the absorption pattern was detectable. The coulometric determination of the equivalents of electrons transferred in the second step yielded an *n* value of 0.9. The presence of isosbestic points at λ_{iso} = 342 nm, 423 nm, and 700 nm indicates a clean conversion of $[\mathbf{1}]^{\bullet-}$ to $[\mathbf{1}]^{2-}$ without the formation of intermediates or byproducts.

The reversibility of the reduction cascade was confirmed by a stepwise electrochemical oxidation of the sample after the reduction to $[\mathbf{1}]^{2-}$ had been completed (UV/vis-spectroscopic control): The application of a potential value of E_w = −1.8 V leads quantitatively back to the radical $[\mathbf{1}]^{\bullet-}$ (first oxidation), which could then be oxidized cleanly at E_w = −1.3 V to regenerate the neutral starting material **1** (second oxidation).

6. EPR spectroscopy

The radical anion $[\mathbf{1}]^{\bullet-}$ was generated through comproportionation of **1** (2.3 mg, 5.6×10^{-3} mmol) and $[Li(Et_2O)_2][Li(Et_2O)][\mathbf{1}]$ (3.4 mg, 5.3×10^{-3} mmol) in THF (0.8 mL) at room temperature. A small volume (50 µL) of the resulting deep green solution was transferred via syringe into a 2 mm ID quartz EPR tube and diluted with THF (0.6 mL). The EPR spectrum of the light green, clear solution was recorded using a microwave power of 2 mW at 9.4520 GHz, 0.25 G modulation amplitude, and a modulation frequency of 100 kHz on a Bruker Elexsys E500 spectrometer equipped with a TE 102 cavity. The measurement was performed at room temperature and a total recording time of about 28 min was used.

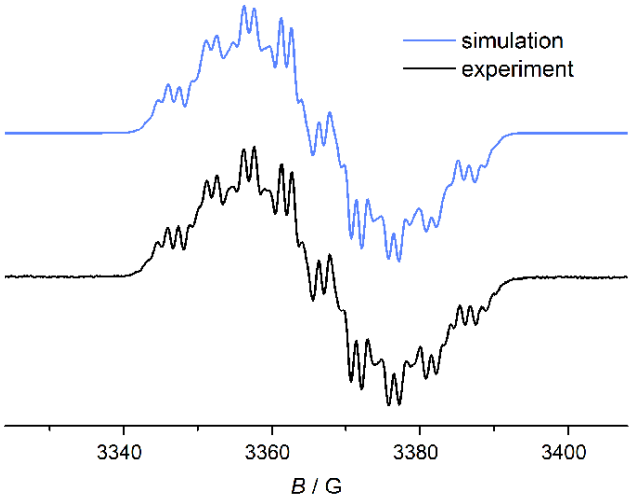

Figure S9. EPR spectrum of the radical anion $[\mathbf{1}]^{\bullet-}$ in THF (experimental at room temperature (black), simulation fit (blue)).

The EPR spectrum was simulated with the program SimFonia supplied by Bruker. The simulation was done by assuming a (visible) ^{11}B hyperfine coupling constant (hfc) of 5.1±0.1 G (2 magnetically equivalent boron nuclei) and an accompanying ^{10}B hfc of 1.7±0.2 G (this corresponds to the expected hfc of ^{10}B assuming a gyromagnetic ratio of 1/3 of the one of ^{11}B; we also assumed natural abundance). Notably, the ^{10}B hfc leads only to a spectral intensity increase and not to a 'visible' line in the spectrum (a simulation without the ^{10}B hfc results in a significant deviation from the experimental spectrum). The (visible) ^{1}H

hyperfine coupling constants were set to 7.2±0.2 G (1 proton) and 1.4±0.1 G (8 magnetically equivalent protons). A Gaussian-shaped curve with a line width of 1.4 G was used to accomplish the simulation. The estimated g_{iso} value is 1.998±0.001. The g_{iso} value was estimated by calibrating the magnetic field on the $^{55}Mn^{2+}$ ion in an MnO/MgO polycrystalline powder[S1] ($g_{iso}(^{55}Mn^{2+}) = 2.00101 \pm 0.00005$; $hfc(^{55}Mn^{2+}) = -(87.10 \pm 0.03)$ G.

[S1] O. Burghaus, M. Rohrer, T. Götzinger, M. Plato, K. Möbius, *Meas. Sci. Technol.* **1992**, *3*, 765-774.

7 Quantum-chemical results

7.1 Validation of DFT approach

To validate the PBE0D/TZVP approach we performed reference calculations at the MRCI/cc-pVTZ level of theory on the closely related diboracyclopropane model systems c-$CH_2B_2H_4^{-/2-}$, and the all-carbon analog cyclopropane, c-C_3H_6. Two-dimensional scans along the bond angles α(BCB)/α(CCC) and along the torsional angles τ(HBBH)/τ(HCCH) reveal identical profiles with respect to relative energies and wavefunction properties. Figure S10 shows a relaxed 2D-scan along the bond angle α(BCB) and along the torsional angle τ(HBBH) of the diboracyclopropane dianion computed at the unrestricted UPBE0D/TZVP level of theory. At the lowest-energy geometry, which corresponds to α(BCB) = 65 ° and τ(HBBH) = 0 °, the unrestricted wavefunction is stable and without spin contamination, and therefore resembles a closed-shell singlet structure with close B–B contacts. Torsion of τ(HBBH) merely leads to an increase in relative energy, but does not alter the properties of the wavefunction. Only upon widening the BCB angle beyond 90 ° the wavefunction begins to show signs of biradicaloid character through an increase of the $\langle\widehat{\mathbf{S}}^2\rangle$ expectation value up to the limiting value of 1.0 for a genuine biradical, in which the two unpaired electrons are located at the boron centers.

The isoelectronic all-carbon analog cyclopropane shows the same qualitative features (see top left of Figure S11). Moreover, the direct comparison of the PBE0D energy profiles with the corresponding profile computed at the MRCI level inspires full confidence in the DFT-based approach. Both, the relative energies as well as the wavefunction properties are in perfect agreement for cyclopropane (Figure S11, top), the diboracyclopropane dianion (Figure S11, middle), and the diboracyclopropane radical anion (Figure S11, bottom), respectively. An increase of the $\langle\widehat{\mathbf{S}}^2\rangle$ expectation value in the PBE0D results corresponds to a decrease of the leading CI coefficient in the MRCI calculations (see also the reference configurations and CI coefficients in Table S2). The occupations and nature of the active orbitals shown in Table S3 and Figures S12–S15 substantiate the above notion.

7.2 Molecular geometries

The B–B distance in the Li^+-free neutral, singly and doubly reduced structures **1**, $[\mathbf{1}]^{\bullet-}$, $[\mathbf{1}]^{2-}$, decreases according to the degree of reduction, which implies successive B–B bond formation. In $[\mathbf{1}H]^-$ the B–B distance is further reduced by the hydride bridge, which also induces some degree of pyramidalization at the boron centers. The bridging Li^+ ion in the

anionic equivalents of the naked doubly reduced species, $[Li(thf)_2][\mathbf{1}]^-$ and $[Li(Et_2O)][\mathbf{1}]^-$, has only a very minor influence on the B–B distance (see Figure S16). This is also true for the fully lithiated species $[Li(thf)_4][Li(thf)_2][\mathbf{1}]$ (and similarly in $[Li(thf)_4][\mathbf{1}H]$), where the B–B distance is more or less unaffected by the second (exterior) non-coordinating counterion $[Li(thf)_4]^+$. In the structures $[Li(thf)_2]_2[\mathbf{1}]$ and $[Li(Et_2O)_2][Li(Et_2O)][\mathbf{1}]$ with the less crowded counterions $[Li(thf)_2]^+$ and $[Li(Et_2O)_2]^+$ the influence of the exterior Li^+ is somewhat more pronounced, and induces some degree of pyramidalization on the proximal boron center, which in turn leads to a further contraction of the B–B distance (Figure S17).

Note that for the model system the cyclic diboracyclopropane dianion is not the lowest-energy structure, and the isomer without B–B contact is favored by 18 kcal mol^{-1} (Figure S18). In the full system, however, the analogous structure without B–B contact is 13 kcal mol^{-1} less stable than $[\mathbf{1}]^{2-}$.

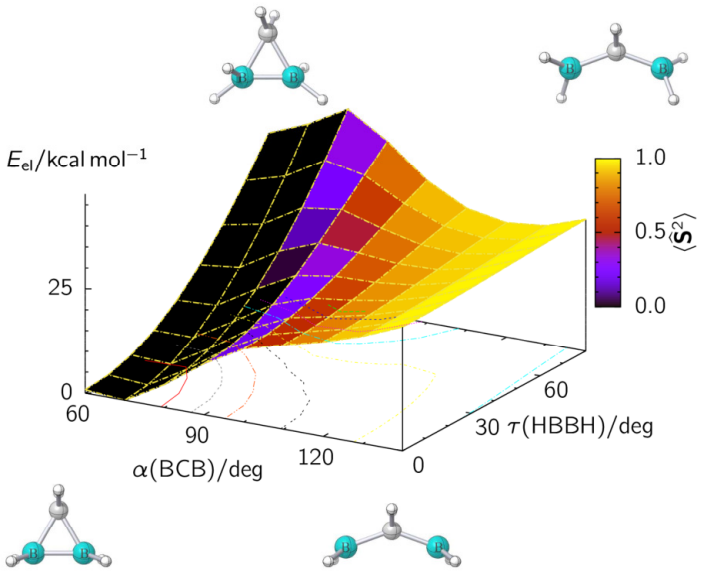

Figure S10: Relaxed two-dimensional scan along α(BCB)/τ(HBBH) in $[CH_2B_2H_4]^{2-}$ computed at the unrestricted PBE0D/TZVP level of theory.

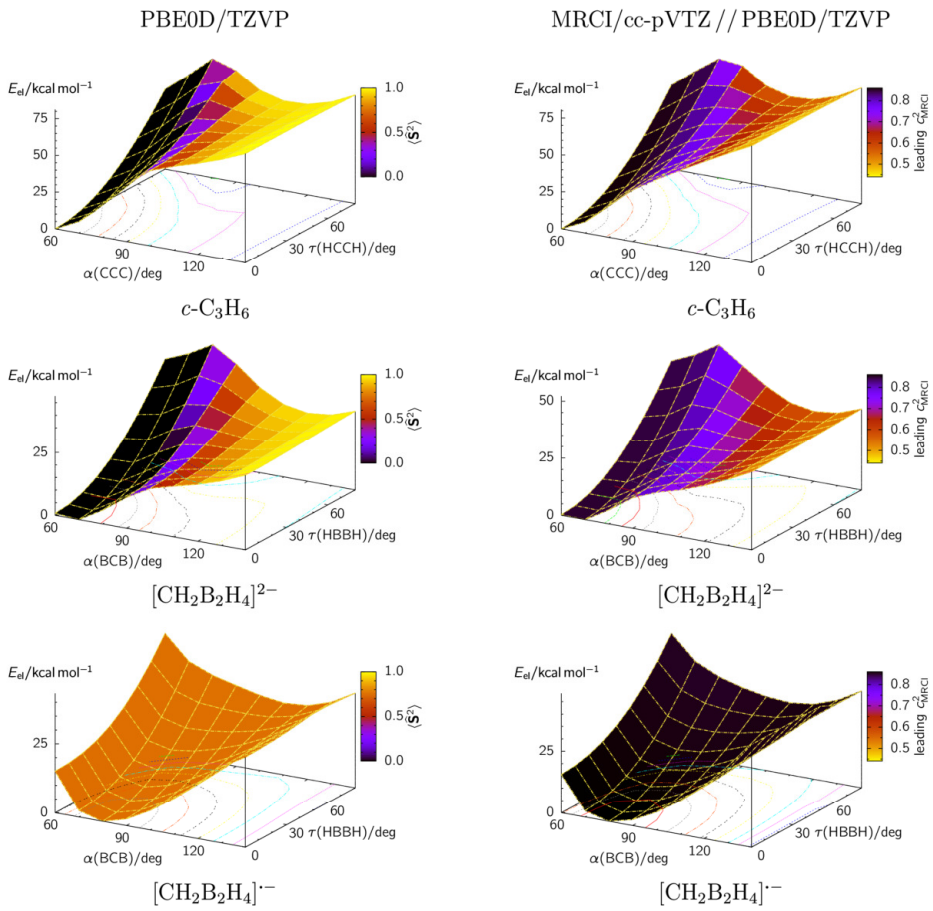

Figure S11: Relaxed two-dimensional scans along α(CCC)/τ(HCCH) in c-C_3H_6 and along α(BCB)/τ(HBBH) in $[CH_2B_2H_4]^{n-}$ ($n = 1, 2$) computed at the UPBE0D/TZVP and MRCI/CAS(6,6)/cc-pVTZ//PBE0D/TZVP levels of theory.

Table S2: MRCI reference configurations and coefficients greater than 0.05 for *c*-C_3H_6 and $[CH_2B_2H_4]^{2-}$.

config[a]						coeff			
						$\alpha(E_{\min})$ $\tau = 0°$	$\alpha = 60°$ $\tau = 80°$	$\alpha = 140°$ $\tau = 0°$	$\alpha = 140°$ $\tau = 80°$
$6a$	$5b$	$7a$	$6b$	$8a$	$7b$	***c*-C_3H_6**			
2	2	2	0	0	0	0.927	0.924	−0.636	0.715
2	2	0	2	0	0	−0.058	−0.052	0.682	−0.598
2	0	2	2	0	0	−0.058	−0.063		
2	β	α	β	α	0	−0.051	−0.060		
$6a$	$5b$	$7a$	$6b$	$8a$	$7b$	**$[CH_2B_2H_4]^{2-}$**			
2	2	2	0	0	0	0.921	0.917	0.697	0.721
2	2	0	2	0	0	−0.068		−0.611	−0.583
2	0	2	2	0	0		−0.075		
2	α	α	β	β	0		0.060		

[a] Irreducible representations within C_2 symmetry.

Table S3: MRCI occupations of active MOs for *c*-C_3H_6, $[CH_2B_2H_4]^{2-}$, and $[CH_2B_2H_4]^{\cdot-}$.

MO[a]	*c*-C_3H_6	$[CH_2B_2H_4]^{2-}$	$[CH_2B_2H_4]^{\cdot-}$
		E_{min}	
$7b$	0.024	0.021	0.017
$8a$	0.024	0.024	0.022
$6b$	0.041	0.038	0.028
$7a$	1.950	1.944	0.988
$5b$	1.950	1.950	1.948
$6a$	1.963	1.960	1.958
		$\alpha = 60°,\ \tau = 80°$	
$7b$	0.027	0.024	0.018
$8a$	0.031	0.030	0.028
$6b$	0.043	0.041	0.045
$7a$	1.947	1.946	0.991
$5b$	1.946	1.942	1.934
$6a$	1.961	1.959	1.953
		$\alpha = 140°,\ \tau = 0°$	
$7b$	0.020	0.021	0.019
$8a$	0.028	0.026	0.028
$6b$	1.059	0.864	0.035
$7a$	0.926	1.117	0.981
$5b$	1.959	1.956	1.949
$6a$	1.961	1.958	1.951
		$\alpha = 140°,\ \tau = 80°$	
$7b$	0.020	0.021	0.019
$8a$	0.028	0.027	0.028
$6b$	0.822	0.787	0.032
$7a$	1.163	1.194	0.980
$5b$	1.959	1.956	1.950
$6a$	1.961	1.957	1.955

[a] Irreducible representations within C_2 symmetry.

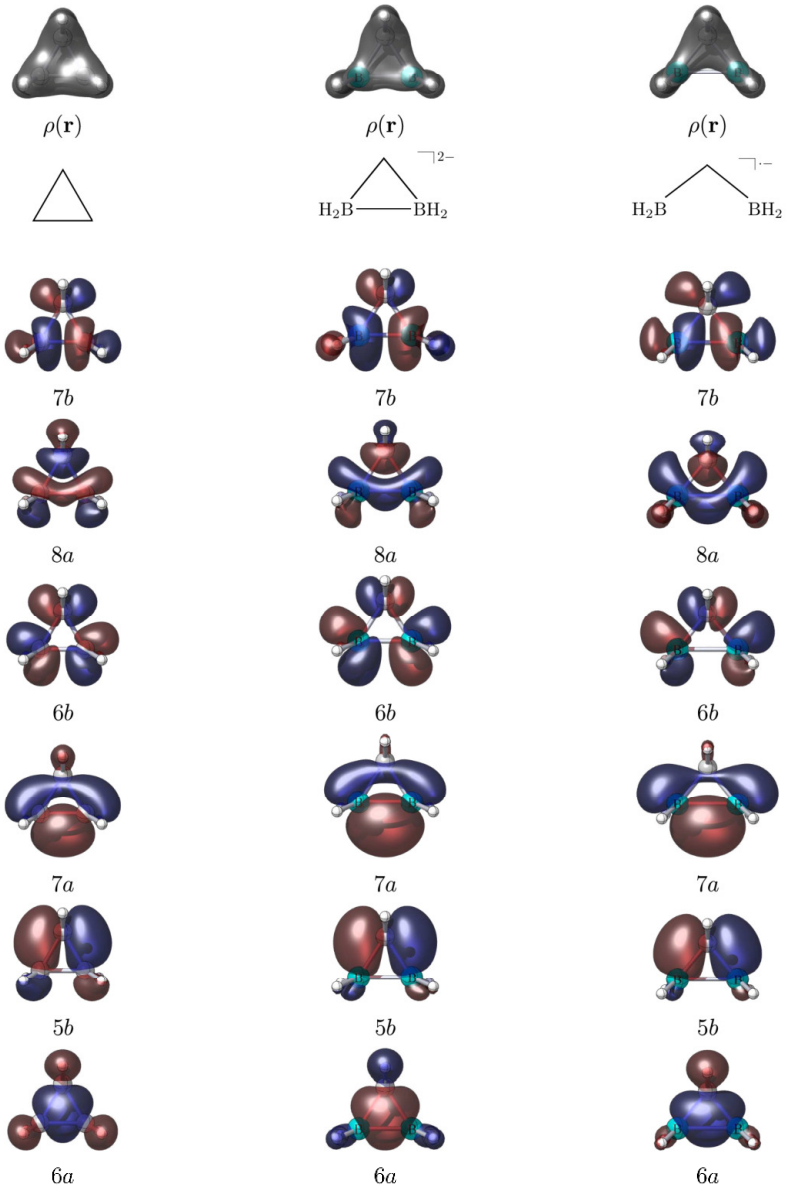

Figure S12: MRCI electron densities and frontier MOs of the CAS(6,6) reference space at the lowest-energy geometries (*c*-C_3H_6: $\alpha = 60\,°$, $[CH_2B_2H_4]^{2-}$: $\alpha = 65\,°$, $[CH_2B_2H_4]^{\bullet-}$: $\alpha = 79\,°$), $\tau = 0\,°$.

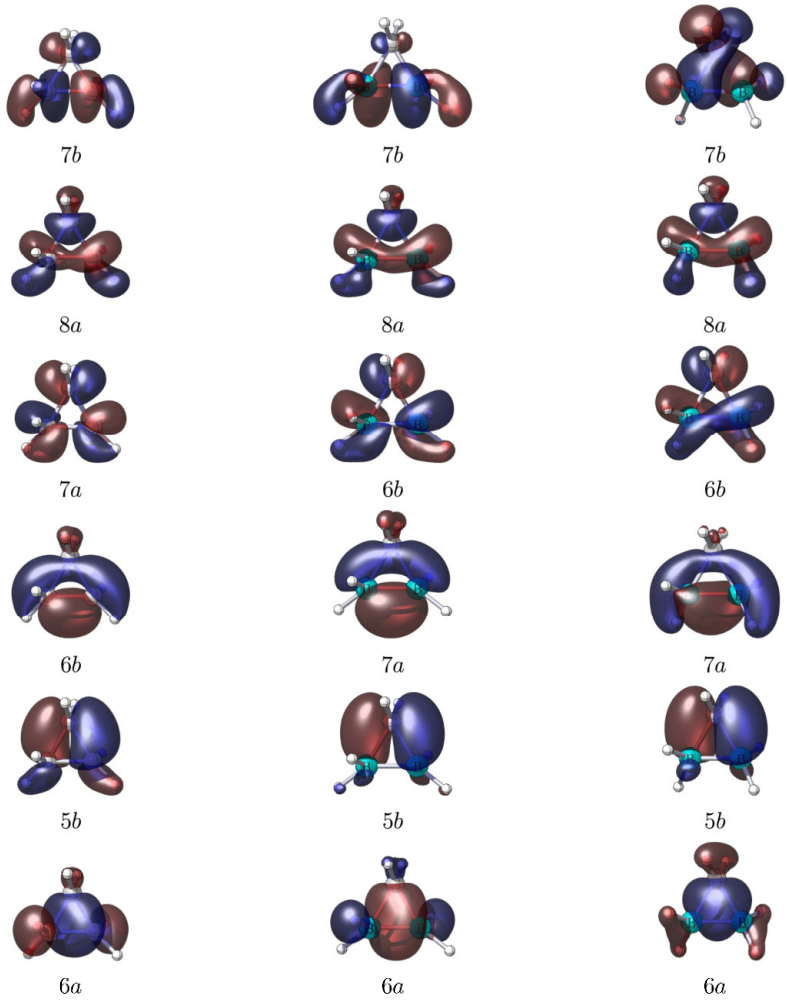

Figure S13: Frontier MOs of the CAS(6,6) reference space at $\alpha = 60\,^{\circ}$ and $\tau = 80\,^{\circ}$.

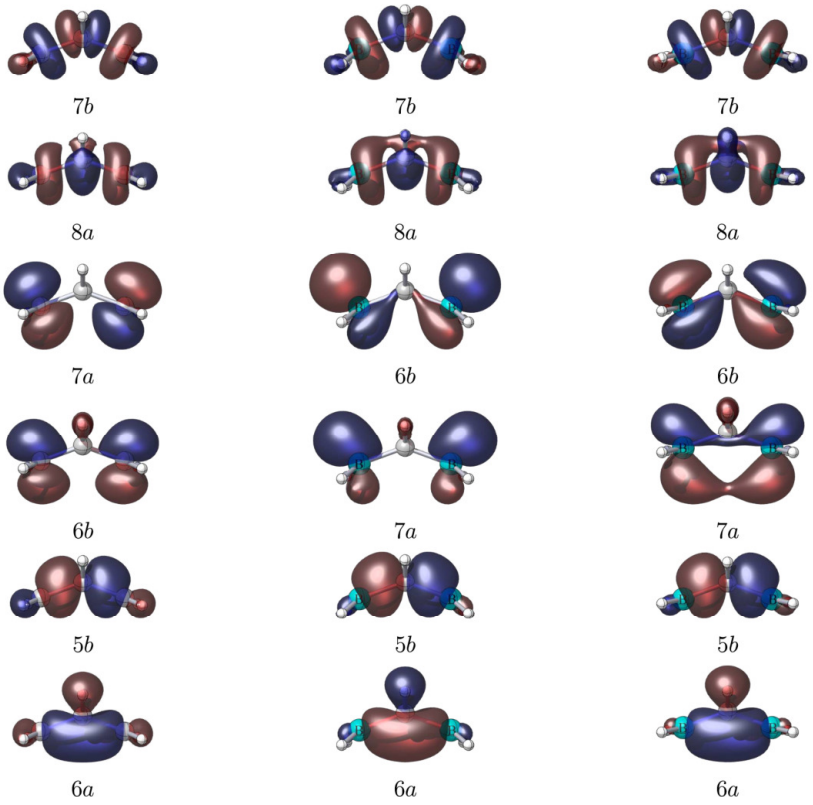

Figure S14: Frontier MOs of the CAS(6,6) reference space at $\alpha = 140\,^{\circ}$ and $\tau = 0\,^{\circ}$.

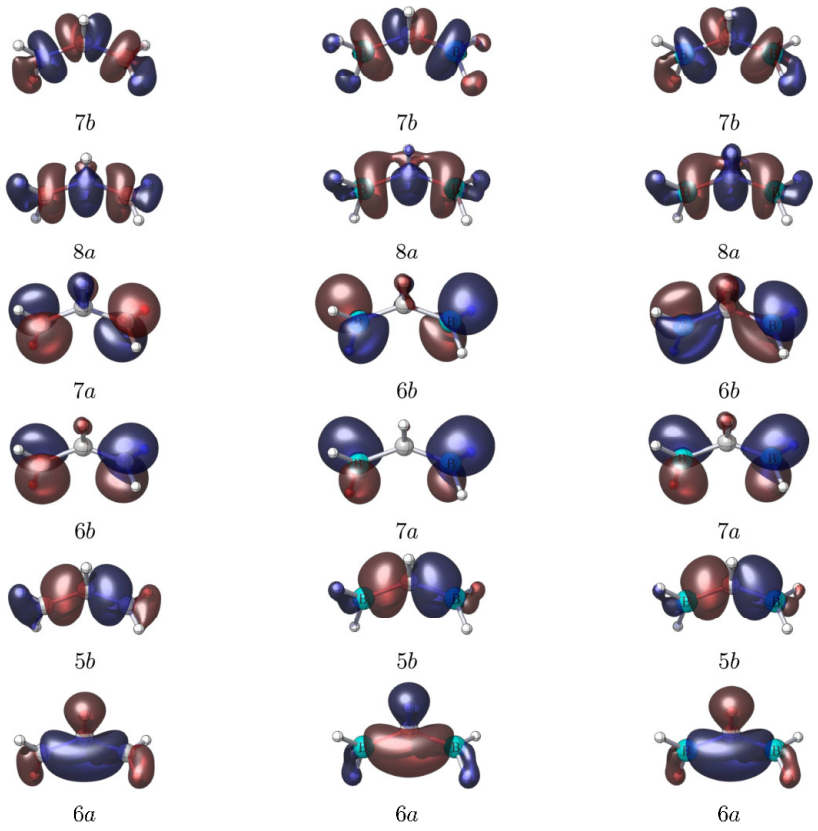

Figure S15: Frontier MOs of the CAS(6,6) reference space at $\alpha = 60\,^{\circ}$ and $\tau = 80\,^{\circ}$.

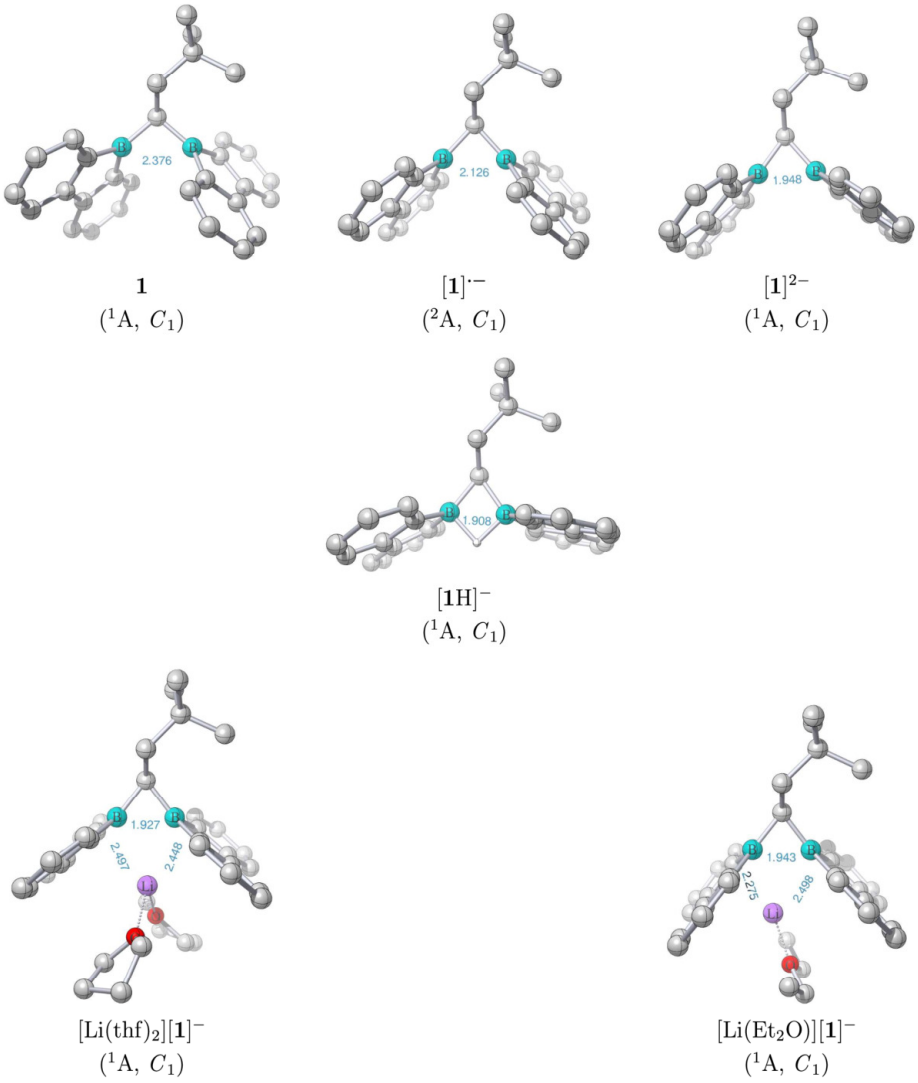

1
(^{1}A, C_1)

$[\mathbf{1}]^{\bullet-}$
(^{2}A, C_1)

$[\mathbf{1}]^{2-}$
(^{1}A, C_1)

$[\mathbf{1}\mathrm{H}]^-$
(^{1}A, C_1)

$[\mathrm{Li(thf)_2}][\mathbf{1}]^-$
(^{1}A, C_1)

$[\mathrm{Li(Et_2O)}][\mathbf{1}]^-$
(^{1}A, C_1)

Figure S16: Computed molecular structures (PBE0D/TZVP) with selected interatomic distances (Å) for the Li^+-free neutral, singly and doubly reduced structures **1**, $[\mathbf{1}]^{\bullet-}$, $[\mathbf{1}]^{2-}$, and for the Li^+-free hydride-bridged species $[\mathbf{1}\mathrm{H}]^-$, as well as for the Li^+-bridged anions $[\mathrm{Li(thf)_2}][\mathbf{1}]^-$ and $[\mathrm{Li(Et_2O)}][\mathbf{1}]^-$. The electronic states and point group symbols are given in parentheses.

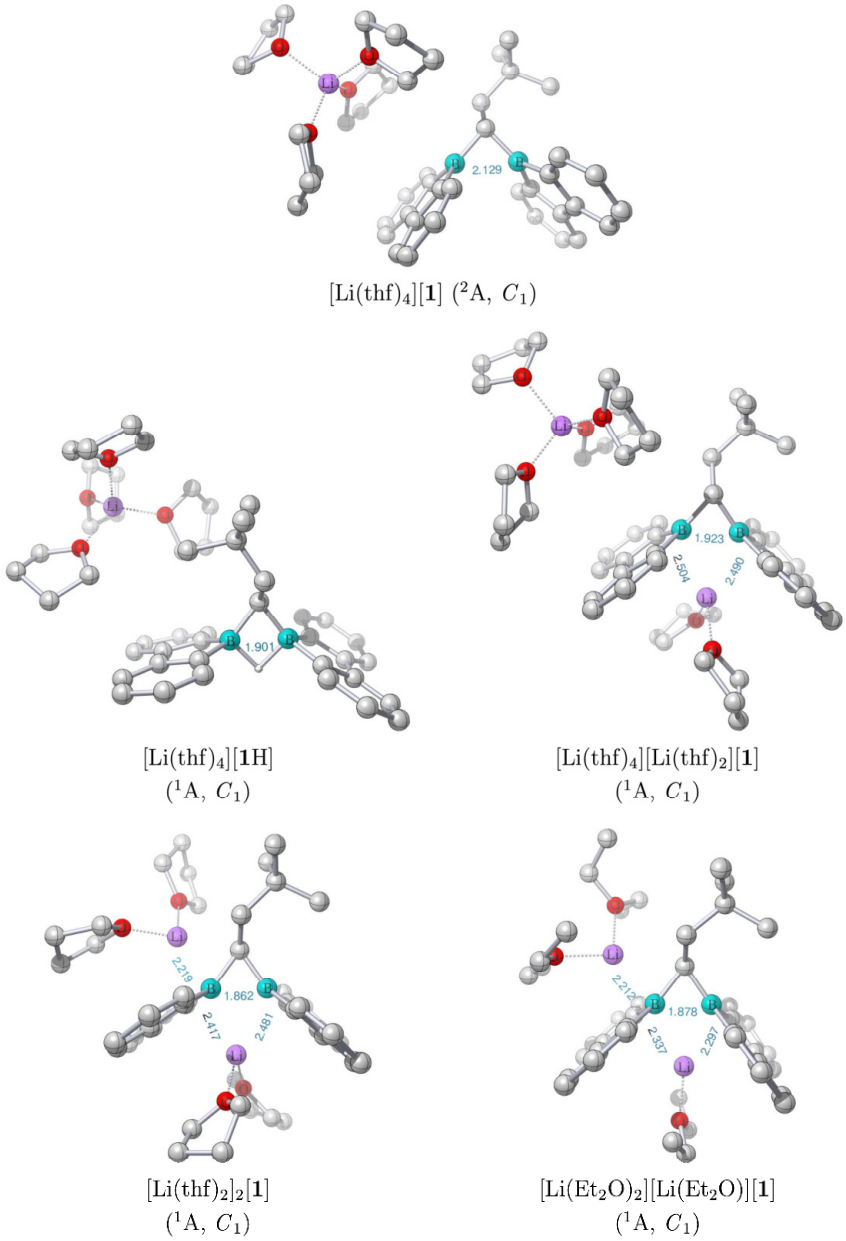

$[Li(thf)_4][\mathbf{1}]$ (^2A, C_1)

$[Li(thf)_4][\mathbf{1}H]$ (^1A, C_1)

$[Li(thf)_4][Li(thf)_2][\mathbf{1}]$ (^1A, C_1)

$[Li(thf)_2]_2[\mathbf{1}]$ (^1A, C_1)

$[Li(Et_2O)_2][Li(Et_2O)][\mathbf{1}]$ (^1A, C_1)

Figure S17: Computed molecular structures (PBE0D/TZVP) with selected interatomic distances (Å) for the reduced, fully lithiated complexes $[Li(thf)_4][\mathbf{1}]$, $[Li(thf)_4][\mathbf{1}H]$, $[Li(thf)_4][Li(thf)_2][\mathbf{1}]$, $[Li(thf)_2]_2[\mathbf{1}]$, and $[Li(Et_2O)_2][Li(Et_2O)][\mathbf{1}]$. The electronic states and point group symbols are given in parentheses.

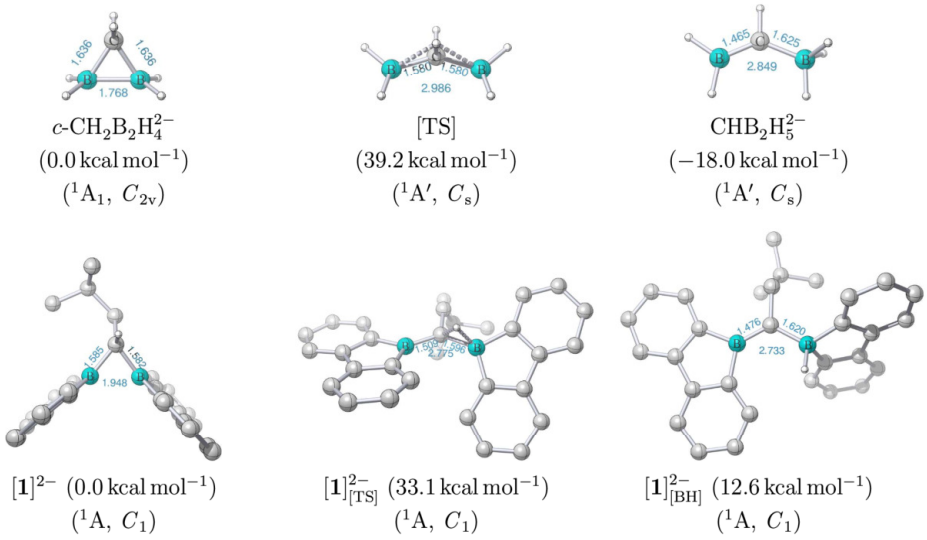

c-$CH_2B_2H_4^{2-}$
$(0.0\,\mathrm{kcal\,mol^{-1}})$
$(^1A_1,\ C_{2v})$

[TS]
$(39.2\,\mathrm{kcal\,mol^{-1}})$
$(^1A',\ C_s)$

$CHB_2H_5^{2-}$
$(-18.0\,\mathrm{kcal\,mol^{-1}})$
$(^1A',\ C_s)$

$[\mathbf{1}]^{2-}$ $(0.0\,\mathrm{kcal\,mol^{-1}})$
$(^1A,\ C_1)$

$[\mathbf{1}]^{2-}_{[TS]}$ $(33.1\,\mathrm{kcal\,mol^{-1}})$
$(^1A,\ C_1)$

$[\mathbf{1}]^{2-}_{[BH]}$ $(12.6\,\mathrm{kcal\,mol^{-1}})$
$(^1A,\ C_1)$

Figure S18: Computed molecular geometries (PBE0D/TZVP) for two isomers and the corresponding transition structure in the model system (top) and the full system (bottom). Relative Gibbs energies, electronic states and point group symbols are given in parentheses.

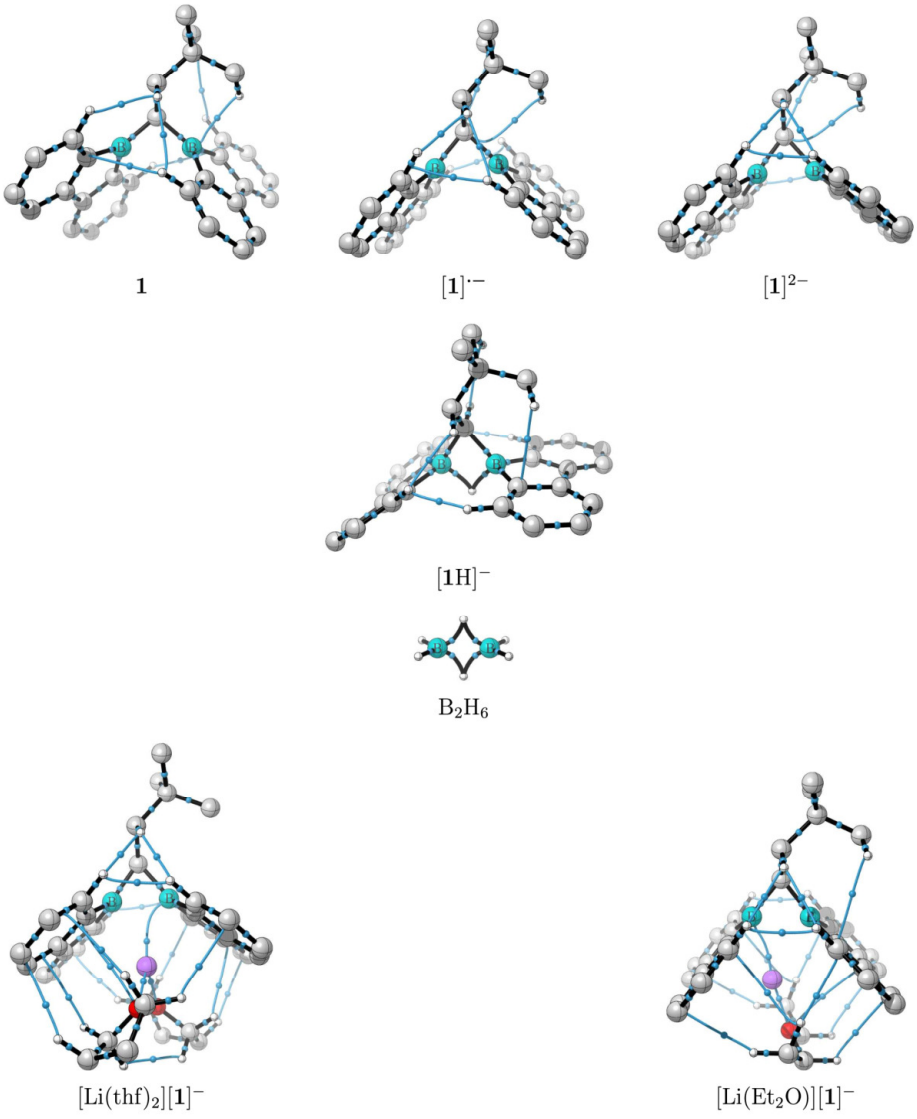

Figure S19: Bond critical points (bcp, blue) with corresponding bond paths computed from PBE0D/TZVP wavefunctions for the Li^+-free neutral, singly and doubly reduced structures **1**, $[\mathbf{1}]^{\cdot-}$, $[\mathbf{1}]^{2-}$, and for the Li^+-free hydride-bridged $[\mathbf{1H}]^-$ with the plain diborane molecule B_2H_6 for comparison, as well as for the Li^+-bridged anions $[Li(thf)_2][\mathbf{1}]^-$ and $[Li(Et_2O)][\mathbf{1}]^-$. Covalent bond paths with a total energy density value of $H_b < 0$ at the corresponding bcp are plotted in black, Coulomb- and van der Waals-type interactions with $H_b \geq 0$ are plotted in blue.

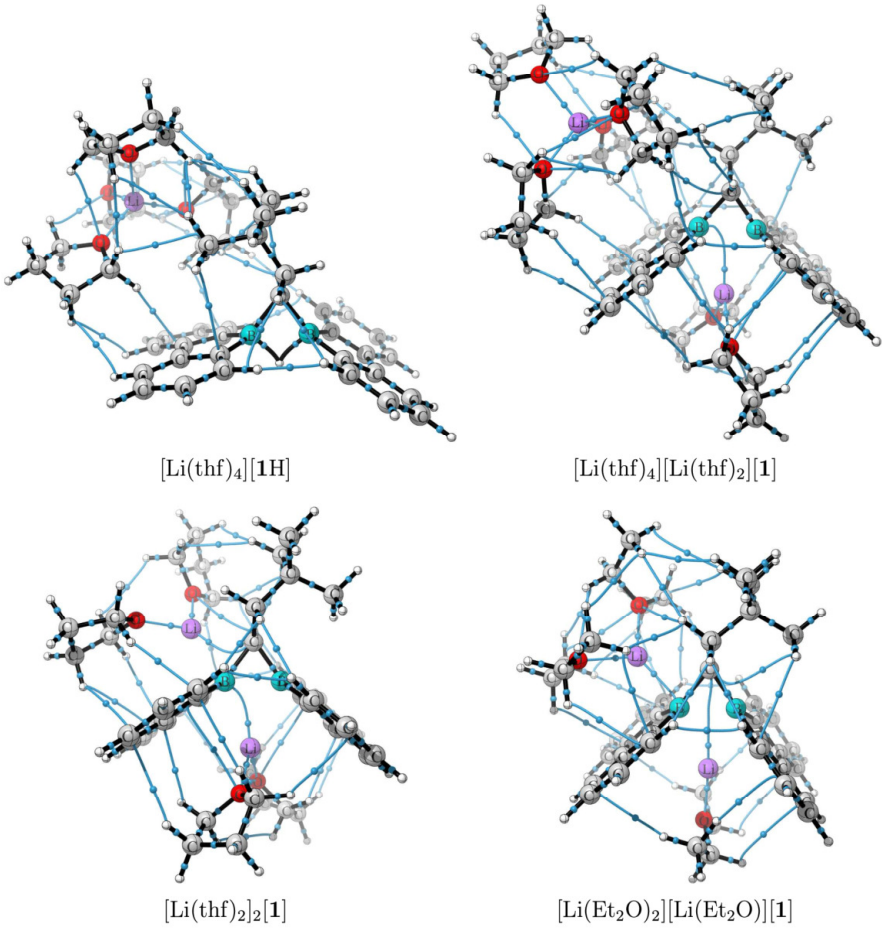

Figure S20: Bond critical points (bcp, blue) with corresponding bond paths computed from PBE0D/TZVP wavefunctions for the reduced, Li-coordinated complexes [Li(thf)$_4$][**1**H], [Li(thf)$_4$][Li(thf)$_2$][**1**] (top), [Li(thf)$_2$]$_2$[**1**], and [Li(Et$_2$O)$_2$][Li(Et$_2$O)][**1**] (bottom). Covalent bond paths with a total energy density value of $H_b < 0$ at the corresponding bcp are plotted in black, Coulomb- and van der Waals-type interactions with $H_b \geq 0$ are plotted in blue.

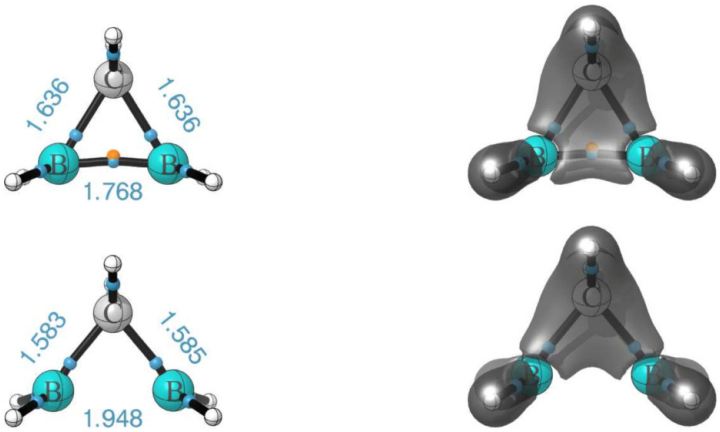

Figure S21: Bond critical points (bcp, blue) and ring critical points (rcp, orange) with corresponding bond paths computed from PBE0D/TZVP wavefunctions for the diboracyclopropane dianion model system at the equilibrium geometry (top) and at the geometry of the full system $[\mathbf{1}]^{2-}$ (bottom); in the latter, only the positions of the atoms which remain identical to those in $[\mathbf{1}]^{2-}$, i.e., B^1, B^2, C^7, H^7, are kept at fixed coordinates, while the positions of the hydrogen atoms which replace carbon atoms of $[\mathbf{1}]^{2-}$ are fully relaxed. Isodensity plots at $0.1\,a_0^{-3}$ of the valence electron density are also given.

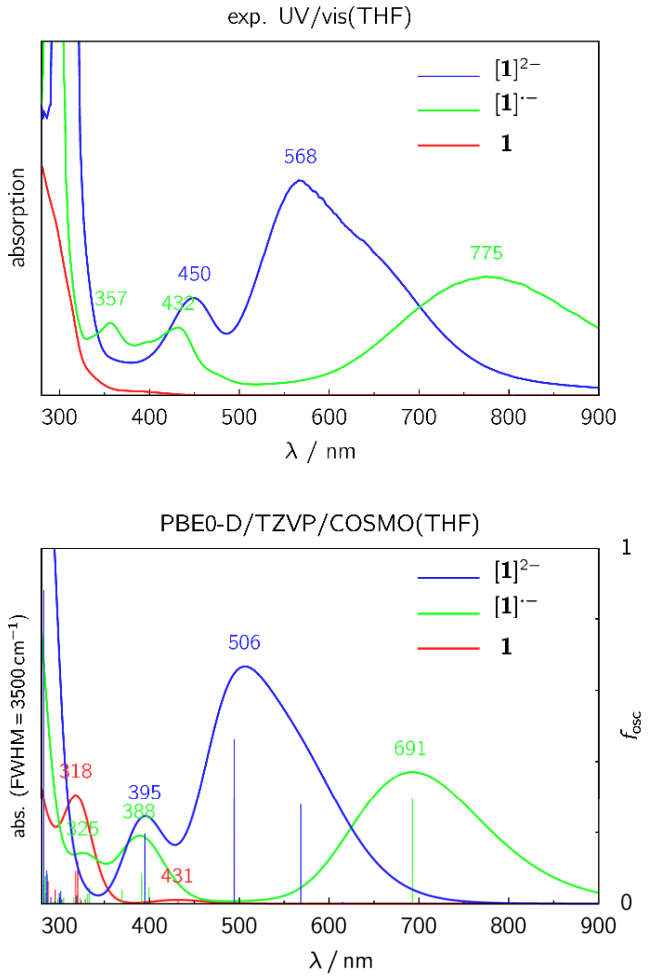

Figure S22: Experimental and computed UV/vis spectra (PBE0D/TZVP/COSMO(THF)) for structures **1**, $[\mathbf{1}]^{\cdot-}$, and $[\mathbf{1}]^{2-}$. Peak labels are assigned to maxima of the absorption curves.

Table S4: Natural transition orbitals (NTO) for selected excited states of structures **1**, $[\mathbf{1}]^{\bullet-}$, and $[\mathbf{1}]^{2-}$, computed at the PBE0D/TZVP/COSMO(THF) level.

state	"hole"		"particle"	state	"hole"		"particle"
	1				**1**		
1	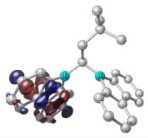	432 nm	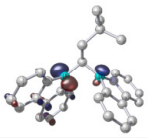	6	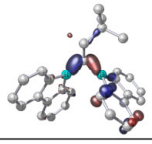	320 nm	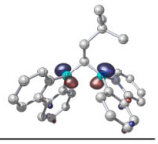
	$[\mathbf{1}]^{\bullet-}$				$[\mathbf{1}]^{\bullet-}$		
1	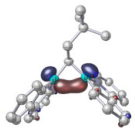	693 nm	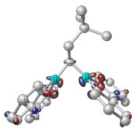	7	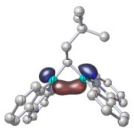	391 nm	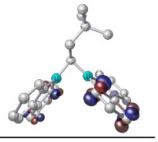
	$[\mathbf{1}]^{2-}$				$[\mathbf{1}]^{2-}$		
2	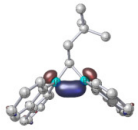	569 nm	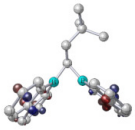	3	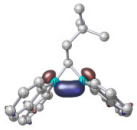	494 nm	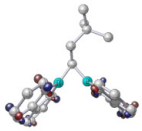

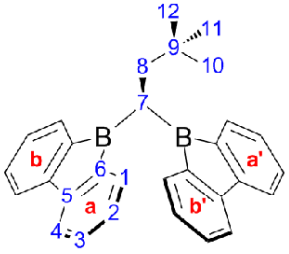

Figure S23: Numbering scheme for the assignment of NMR and EPR data.

Table S5: NMR shieldings σ, and shifts δ, computed from PBE0D/TZVP wavefunctions without (gas) and with (THF) implicit solvent model, in comparison with experiment (THF-d_8). Note that in the computed values an explicit coordination of the THF solvent is not included. Signed deviations Δ are given as $\delta(\text{exp}) - \delta(\text{calc})$. Chemical shifts for carbon and hydrogen are relative to TMS, for boron diborane was chosen as internal standard and corrected for the experimentally used standard $BF_3{\cdot}OMe_2$ ($\delta(B_2H_6) = 18.0$ ppm relative to $BF_3{\cdot}OMe_2$).

nucleus	σ(calc)	δ(calc)	δ(exp)	Δ	σ(calc)	δ(calc)	δ(exp)	Δ
				1 (^{1}**A**, C_1)				
	gas				THF			
B^1	36.5	68.3	44.2	−24.1	35.9	70.0	44.2	−25.8
B^2	37.8	67.0	44.2	−22.8	37.2	68.7	44.2	−24.5
C^7	147.4	41.9	28.3	−13.6	146.1	44.3	28.3	−16.0
C^8	139.2	50.1	47.4	−2.7	139.5	50.9	47.4	−3.5
C^9	157.1	32.2	32.7	0.5	157.1	33.3	32.7	−0.6
C^{10}	162.5	26.8	30.1	3.3	163.3	27.1	30.1	3.0
C^{11}	156.2	33.1	30.1	−3.0	157.3	33.1	30.1	−3.0
C^{12}	158.8	30.5	30.1	−0.4	159.3	31.1	30.1	−1.0
C^{1a}	47.9	141.4	133.5	−7.9	46.9	143.5	133.5	−10.0
C^{2a}	56.9	132.4	126.7	−5.7	55.9	134.5	126.7	−7.8
C^{3a}	50.4	138.9	130.1	−8.8	49.3	141.1	130.1	−11.0
C^{4a}	65.7	123.6	119.1	−4.5	65.0	125.4	119.1	−6.3
C^{5a}	27.8	161.5	151.5	−10.0	28.6	161.8	151.5	−10.3
C^{6a}	41.8	147.5	147.3	−0.2	42.3	148.1	147.3	−0.8
C^{1b}	48.5	140.8	133.5	−7.3	48.5	141.9	133.5	−8.4
C^{2b}	57.4	131.9	126.7	−5.2	57.0	133.4	126.7	−6.7
C^{3b}	50.1	139.2	130.1	−9.1	49.0	141.4	130.1	−11.3
C^{4b}	67.0	122.3	119.1	−3.2	66.0	124.4	119.1	−5.3
C^{5b}	29.1	160.2	151.5	−8.7	29.4	161.0	151.5	−9.5
C^{6b}	41.1	148.2	147.3	−0.9	41.5	148.9	147.3	−1.6
$C^{1a'}$	51.1	138.2	133.5	−4.7	49.6	140.8	133.5	−7.3
$C^{2a'}$	56.9	132.4	126.7	−5.7	55.8	134.6	126.7	−7.9
$C^{3a'}$	50.4	138.9	130.1	−8.8	49.5	140.9	130.1	−10.8
$C^{4a'}$	66.2	123.1	119.1	−4.0	65.6	124.8	119.1	−5.7
$C^{5a'}$	29.1	160.2	151.5	−8.7	30.0	160.4	151.5	−8.9
$C^{6a'}$	41.6	147.7	147.3	−0.4	41.9	148.5	147.3	−1.2
$C^{1b'}$	48.4	140.9	133.5	−7.4	48.4	142.0	133.5	−8.5
$C^{2b'}$	57.2	132.1	126.7	−5.4	56.8	133.6	126.7	−6.9
$C^{3b'}$	50.6	138.7	130.1	−8.6	49.5	140.9	130.1	−10.8
$C^{4b'}$	66.2	123.1	119.1	−4.0	65.3	125.1	119.1	−6.0
$C^{5b'}$	29.3	160.0	151.5	−8.5	29.5	160.9	151.5	−9.4
$C^{6b'}$	41.5	147.8	147.3	−0.5	41.8	148.6	147.3	−1.3

nucleus	σ(calc)	δ(calc)	δ(exp)	Δ	σ(calc)	δ(calc)	δ(exp)	Δ
				$[\mathbf{1}]^{2-}$ ($^1\mathbf{A}$, C_1)				
		gas				THF		
B^1	111.3	−6.6	−6.7	−0.1	112.9	−7.0	−6.7	0.3
B^2	110.8	−6.0	−6.7	−0.7	111.5	−5.7	−6.7	−1.0
C^7	159.2	30.1	27.6	−2.5	160.0	30.4	27.6	−2.8
C^8	142.0	47.3	45.6	−1.7	142.9	47.5	45.6	−1.9
C^9	155.8	33.5	33.2	−0.3	156.2	34.2	33.2	−1.0
C^{10}	161.6	27.7	30.5	2.8	162.3	28.1	30.5	2.4
C^{11}	159.5	29.8	30.5	0.7	161.0	29.4	30.5	1.1
C^{12}	154.1	35.2	30.5	−4.7	155.7	34.7	30.5	−4.2
C^{1a}	53.6	135.7	131.1	−4.6	54.6	135.8	131.1	−4.7
C^{2a}	69.7	119.6	121.5	1.9	66.4	124.0	121.5	−2.5
C^{3a}	76.1	113.2	117.4	4.2	71.6	118.8	117.4	−1.4
C^{4a}	71.5	117.8	118.3	0.5	68.9	121.5	118.3	−3.2
C^{5a}	38.5	150.8	143.6	−7.2	40.3	150.1	143.6	−6.5
C^{6a}	16.1	173.2	161.0	−12.2	20.2	170.2	161.0	−9.2
C^{1b}	58.3	131.0	129.0	−2.0	60.1	130.3	129.0	−1.3
C^{2b}	69.8	119.5	121.4	1.9	66.5	123.9	121.4	−2.5
C^{3b}	76.5	112.8	117.6	4.8	72.2	118.2	117.6	−0.6
C^{4b}	71.3	118.0	118.2	0.2	68.6	121.8	118.2	−3.6
C^{5b}	42.5	146.8	143.1	−3.7	44.1	146.3	143.1	−3.2
C^{6b}	17.0	172.3	162.2	−10.1	20.7	169.7	162.2	−7.5
$C^{1a'}$	56.2	133.1	131.1	−2.0	57.0	133.4	131.1	−2.3
$C^{2a'}$	69.3	120.0	121.5	1.5	65.8	124.6	121.5	−3.1
$C^{3a'}$	76.1	113.2	117.4	4.2	71.2	119.2	117.4	−1.8
$C^{4a'}$	71.4	117.9	118.3	0.4	69.0	121.4	118.3	−3.1
$C^{5a'}$	40.1	149.2	143.6	−5.6	41.4	149.0	143.6	−5.4
$C^{6a'}$	16.3	173.0	161.0	−12.0	19.8	170.6	161.0	−9.6
$C^{1b'}$	56.0	133.3	129.0	−4.3	56.9	133.5	129.0	−4.5
$C^{2b'}$	69.7	119.6	121.4	1.8	66.5	123.9	121.4	−2.5
$C^{3b'}$	76.5	112.8	117.6	4.8	71.9	118.5	117.6	−0.9
$C^{4b'}$	71.6	117.7	118.2	0.5	69.2	121.2	118.2	−3.0
$C^{5b'}$	42.0	147.3	143.1	−4.2	43.3	147.1	143.1	−4.0
$C^{6b'}$	17.6	171.7	162.2	−9.5	20.5	169.9	162.2	−7.7

nucleus	σ(calc)	δ(calc)	δ(exp)	Δ	σ(calc)	δ(calc)	δ(exp)	Δ
				$[\mathbf{1H}]^-$ ($^1\mathbf{A}$, C_1)				
		gas				THF		
B^1	121.6	−16.8	−11.6	5.2	121.5	−15.7	−11.6	4.1
B^2	124.7	−20.0	−11.6	8.4	125.0	−19.1	−11.6	7.5
H^{bridge}	29.4	2.4	1.8	−0.6	29.5	2.2	1.8	−0.4
C^7	169.3	20.0	14.2	−5.8	169.6	20.8	14.2	−6.6
C^8	144.8	44.5	44.2	−0.3	145.1	45.3	44.2	−1.1
C^9	156.9	32.4	32.8	0.4	157.1	33.3	32.8	−0.5
C^{10}	162.9	26.4	30.0	3.6	163.6	26.8	30.0	3.2
C^{11}	160.3	29.0	30.0	1.0	161.5	28.9	30.0	1.1
C^{12}	155.0	34.3	30.0	−4.3	156.2	34.2	30.0	−4.2
C^{1a}	50.5	138.8	133.4	−5.4	50.9	139.5	133.4	−6.1
C^{2a}	62.6	126.7	124.6	−2.1	60.6	129.8	124.6	−5.2
C^{3a}	62.3	127.0	124.4	−2.6	59.5	130.9	124.4	−6.5
C^{4a}	68.3	121.0	118.3	−2.7	66.5	123.9	118.3	−5.6
C^{5a}	31.4	157.9	150.6	−7.3	32.1	158.3	150.6	−7.7
C^{6a}	24.0	165.3	157.3	−8.0	26.9	163.5	157.3	−6.2
C^{1b}	52.8	136.5	131.3	−5.2	53.2	137.2	131.3	−5.9
C^{2b}	62.1	127.2	125.0	−2.2	60.1	130.3	125.0	−5.3
C^{3b}	62.4	126.9	124.4	−2.5	59.5	130.9	124.4	−6.5
C^{4b}	67.9	121.4	118.5	−2.9	66.1	124.3	118.5	−5.8
C^{5b}	32.4	156.9	149.8	−7.1	33.0	157.4	149.8	−7.6
C^{6b}	22.3	167.0	159.6	−7.4	25.2	165.2	159.6	−5.6
$C^{1a'}$	53.5	135.8	133.4	−2.4	54.3	136.2	133.4	−2.8
$C^{2a'}$	62.0	127.3	124.6	−2.7	60.2	130.2	124.6	−5.6
$C^{3a'}$	63.6	125.7	124.4	−1.3	61.1	129.3	124.4	−4.9
$C^{4a'}$	68.6	120.7	118.3	−2.4	66.9	123.5	118.3	−5.2
$C^{5a'}$	34.7	154.6	150.6	−4.0	35.2	155.2	150.6	−4.6
$C^{6a'}$	18.1	171.2	157.3	−13.9	20.3	170.1	157.3	−12.8
$C^{1b'}$	51.6	137.7	131.3	−6.4	52.0	138.4	131.3	−7.1
$C^{2b'}$	62.7	126.6	125.0	−1.6	60.9	129.5	125.0	−4.5
$C^{3b'}$	63.5	125.8	124.6	−1.2	61.1	129.3	124.6	−4.7
$C^{4b'}$	68.5	120.8	118.5	−2.3	66.9	123.5	118.5	−5.0
$C^{5b'}$	33.8	155.5	149.8	−5.7	34.5	155.9	149.8	−6.1
$C^{6b'}$	20.6	168.7	159.6	−9.1	22.4	168.0	159.6	−8.4

Table S6: Isotropic g-values and hyperfine couplings for Li^+-free $[\mathbf{1}]^{\bullet-}$ computed at the PBE0D/EPR-III/COSMO(THF) level of theory.

$[1]^{\bullet-}$ (^{2}A, C_1): $g_{iso} = 2.002669$					
nucleus	a/MHz	a/G	nucleus	a/MHz	a/G
$^{11}B^1$	15.76	5.62	$^{10}B^1$	5.28	1.88
$^{11}B^2$	16.74	5.97	$^{10}B^2$	5.60	2.00
$^{13}C^7$	−7.82	−2.79	$^{1}H^7$	22.37	7.98
$^{13}C^8$	16.09	5.74	$^{1}H^{8a}$	0.40	0.14
			$^{1}H^{8b}$	−0.35	−0.13
$^{13}C^9$	−0.50	−0.18			
$^{13}C^{10}$	1.60	0.57	$^{1}H^{10a}$	−0.08	−0.03
			$^{1}H^{10b}$	−0.06	−0.02
			$^{1}H^{10c}$	0.42	0.15
$^{13}C^{11}$	0.80	0.29	$^{1}H^{11a}$	0.03	0.01
			$^{1}H^{11b}$	−0.01	−0.00
			$^{1}H^{11c}$	−0.06	−0.02
$^{13}C^{12}$	3.57	1.27	$^{1}H^{12a}$	0.05	0.02
			$^{1}H^{12b}$	3.20	1.14
			$^{1}H^{12c}$	1.65	0.59
$^{13}C^{1a}$	3.42	1.22	$^{1}H^{1a}$	−3.61	−1.29
$^{13}C^{2a}$	−4.15	−1.48	$^{1}H^{2a}$	0.79	0.28
$^{13}C^{3a}$	4.82	1.72	$^{1}H^{3a}$	−4.56	−1.63
$^{13}C^{4a}$	−4.83	−1.72	$^{1}H^{4a}$	1.28	0.46
$^{13}C^{5a}$	2.08	0.74			
$^{13}C^{6a}$	−13.17	−4.70			
$^{13}C^{1b}$	5.91	2.11	$^{1}H^{1b}$	−5.38	−1.92
$^{13}C^{2b}$	−6.58	−2.35	$^{1}H^{2b}$	1.81	0.65
$^{13}C^{3b}$	7.53	2.69	$^{1}H^{3b}$	−6.70	−2.39
$^{13}C^{4b}$	−7.26	−2.59	$^{1}H^{4b}$	2.38	0.85
$^{13}C^{5b}$	5.51	1.97			
$^{13}C^{6b}$	−13.10	−4.68			
$^{13}C^{1a'}$	3.22	1.15	$^{1}H^{1a'}$	−3.59	−1.28
$^{13}C^{2a'}$	−4.11	−1.47	$^{1}H^{2a'}$	0.83	0.30
$^{13}C^{3a'}$	4.72	1.68	$^{1}H^{3a'}$	−4.41	−1.57
$^{13}C^{4a'}$	−4.77	−1.70	$^{1}H^{4a'}$	1.24	0.44
$^{13}C^{5a'}$	1.88	0.67			
$^{13}C^{6a'}$	−13.53	−4.83			
$^{13}C^{1b'}$	5.59	1.99	$^{1}H^{1b'}$	−5.23	−1.87
$^{13}C^{2b'}$	−6.37	−2.27	$^{1}H^{2b'}$	1.72	0.61
$^{13}C^{3b'}$	7.24	2.58	$^{1}H^{3b'}$	−6.44	−2.30
$^{13}C^{4b'}$	−6.96	−2.48	$^{1}H^{4b'}$	2.27	0.81
$^{13}C^{5b'}$	5.27	1.88			
$^{13}C^{6b'}$	−13.20	−4.71			

7.3 Cartesian coordinates of optimized geometries

The cartesian coordinates are given in Å, together with the term symbols, point groups, and total electronic energies at the PBE0D/TZVP level of theory.

9
c-C_3H_6 ($^1A_1'$, D_{3h}): E_{tot} = -117.790031010

C	0.000000000000	0.865017719189	0.000000000000
H	0.000000000000	1.452190825644	0.910260473671
H	0.000000000000	1.452190825644	-0.910260473671
C	0.749127319541	-0.432508859594	0.000000000000
H	1.257634146151	-0.726095412822	-0.910260473671
H	1.257634146151	-0.726095412822	0.910260473671
C	-0.749127319541	-0.432508859594	0.000000000000
H	-1.257634146151	-0.726095412822	0.910260473671
H	-1.257634146151	-0.726095412822	-0.910260473671

9
$[CH_2B_2H_4]^{\cdot-}$ ($^2A_1$, C_{2v}): E_{tot} = -91.3008004722

C	0.000000000000	0.000000000000	0.799392882549
B	0.000000000000	1.000474823527	-0.422135428188
B	0.000000000000	-1.000474823527	-0.422135428188
H	-0.906140757234	0.000000000000	1.408946830400
H	0.906140757234	0.000000000000	1.408946830400
H	1.037176411078	1.463635509805	-0.848224168553
H	-1.037176411078	1.463635509805	-0.848224168553
H	-1.037176411078	-1.463635509805	-0.848224168553
H	1.037176411078	-1.463635509805	-0.848224168553

9
$[CH_2B_2H_4]^{2-}$ ($^1A_1$, C_{2v}): E_{tot} = -91.1187321139

C	0.000000000000	0.000000000000	0.864878035424
H	0.900080523840	0.000000000000	1.497831668617
H	-0.900080523840	0.000000000000	1.497831668617
B	0.000000000000	0.883956956098	-0.511538628268
H	-1.033739980010	1.538637392174	-0.767386316774
H	1.033739980010	1.538637392174	-0.767386316774
B	0.000000000000	-0.883956956098	-0.511538628268
H	1.033739980010	-1.538637392174	-0.767386316774
H	-1.033739980010	-1.538637392174	-0.767386316774

9
$[CH_2B_2H_4]^{2-}$ @ $[\mathbf{1}]^{2-}$ (^1A, C_1): E_{tot} = -91.1113158823

C	0.003561414500	0.792135343172	-0.033737897870
H	0.017264181033	1.316701548955	0.912025107471
H	0.005591217860	1.513677483822	-0.868038869532
B	0.971048012160	-0.459367619008	0.011279455046
H	1.528953303336	-0.849460526402	-1.027876881536
H	1.627895312492	-0.674774033649	1.045015642127
B	-0.976671362111	-0.452903322343	0.013057138867
H	-1.538431757306	-0.833463980764	-1.027187435077
H	-1.634523994665	-0.664137844238	1.046806854202

9
$TS[CH_2B_2H_4]^{2-}$ ($^1A'$, C_s): E_{tot} = -91.0508182535

C	0.078077425580	-0.321199064933	0.000000000000
H	0.178574028104	-1.418385670741	0.000000000000
H	-1.051893649620	-0.122945833674	0.000000000000
B	0.078077425580	0.197702188627	1.492867915604
H	0.013901111335	-0.618172850377	2.416011173218
B	0.078077425580	0.197702188627	-1.492867915604
H	0.013901111335	-0.618172850377	-2.416011173218
H	-0.201860705220	1.363924854247	-1.770249677813
H	-0.201860705220	1.363924854247	1.770249677813

9
$[CHB_2H_5]^{2-}$ ($^1A'$, C_s): E_{tot} = -91.1439985935

C	0.000000000000	0.423423981538	0.000000000000
H	-0.331965579985	1.483664271784	0.000000000000
H	-2.025340966290	-0.452657407651	1.000679316142
B	-1.253614653440	-0.610038602069	0.000000000000
H	-2.025340966290	-0.452657407651	-1.000679316142
B	1.456657770252	0.267586695300	0.000000000000
H	2.244122100054	1.242778415355	0.000000000000
H	2.040558000311	-0.829831899037	0.000000000000
H	-0.917248171860	-1.819580328186	0.000000000000

8
B_2H_6 (^1A_g, D_{2h}): E_{tot} = -53.2112289534

B	0.873903580935	0.000000000000	0.000000000000
B	-0.873903580935	0.000000000000	0.000000000000
H	1.453538870683	1.040606928808	0.000000000000
H	1.453538870683	-1.040606928808	0.000000000000
H	-1.453538870683	1.040606928808	0.000000000000
H	-1.453538870683	-1.040606928808	0.000000000000
H	0.000000000000	0.000000000000	0.982655039393
H	0.000000000000	0.000000000000	-0.982655039393

60
1 (^{1}A, C_1): E_{tot} = −1208.80179325

B	−1.186043012615	0.246852368360	−0.913542084199
B	1.043307001813	0.238260011429	−0.092661327131
C	0.153848346548	1.022678304634	−1.121184995839
H	0.524614075888	0.782553716800	−2.126216982776
C	0.088539512615	2.539660387897	−0.910867989275
H	−0.244327596807	2.749533814302	0.110632897950
H	−0.672959999523	2.963529204295	−1.576561258560
C	1.394424093831	3.319296749128	−1.133170920246
C	1.935399357919	3.089723913228	−2.542185316826
H	2.253247177303	2.054608531132	−2.687763075149
H	2.804202190721	3.727571974151	−2.727539186739
H	1.179305928367	3.324009105837	−3.297777102688
C	1.079868888716	4.804373255616	−0.956362322710
H	0.685728918813	5.004593666257	0.044529365691
H	0.334913011527	5.137230207880	−1.685120427098
H	1.977841434662	5.413856299097	−1.091099016540
C	2.448021546223	2.911486224864	−0.109081162637
H	2.086781396834	3.054002534954	0.912779961340
H	3.358714090094	3.504693037256	−0.234139058811
H	2.739822215411	1.861762291349	−0.220845571708
C	−2.543016067163	0.699492585665	−0.253168715085
C	−3.375977919973	−0.438552006087	−0.167844016155
C	−4.637285454186	−0.363994637638	0.391871085615
H	−5.271388600970	−1.241497721718	0.462278767264
C	−5.093416289937	0.864034481980	0.868849217382
H	−6.082482718094	0.934290800060	1.308684683401
C	−4.297416742025	1.995539259267	0.781265594642
H	−4.667790650203	2.946081150011	1.148745814306
C	−3.023400358328	1.912817044512	0.220270757245
H	−2.416317520346	2.807983986972	0.155814251519
C	−1.421358284948	−1.274919723699	−1.218053571353
C	−2.703772971112	−1.621754862068	−0.743605032976
C	−3.178722864799	−2.914749858680	−0.848063740126
H	−4.163038335396	−3.184277787507	−0.479968965422
C	−2.367004685043	−3.883276983208	−1.439115872968
H	−2.728256819282	−4.902385909069	−1.526492931012
C	−1.105067870589	−3.559419260203	−1.914282006027
H	−0.486376538939	−4.325153922691	−2.368564466309
C	−0.630736337198	−2.253319962906	−1.802333698798
H	0.362322175090	−2.012736801371	−2.165139769829
C	0.881321832683	0.133294986541	1.464434650600
C	1.854485185417	−0.773677427501	1.939228990438
C	1.939624230642	−1.089673676553	3.281627289305
H	2.685001064745	−1.787575341143	3.648369956320
C	1.040177333041	−0.500846077546	4.170444504228
H	1.096736018293	−0.742548179145	5.226416838953
C	0.070737582510	0.382568514234	3.719550438032
H	−0.627231586926	0.822969560559	4.422696422879

C	-0.010254453685	0.698303040696	2.364325076185
H	-0.782958144018	1.376665954313	2.019333508767
C	2.241918237108	-0.728561783688	-0.399096336655
C	2.677882192744	-1.283100577377	0.821208933099
C	3.739568071984	-2.168015024105	0.859060167918
H	4.078962847897	-2.599756483402	1.794761913509
C	4.379256138612	-2.503271710236	-0.334096099554
H	5.213399579887	-3.196459220647	-0.316335948426
C	3.967143593373	-1.957861887180	-1.541826606241
H	4.481269032746	-2.225930183537	-2.458045693497
C	2.897280892808	-1.064767991116	-1.571796506028
H	2.581546979495	-0.634207974771	-2.518428641816

60

[1]$^{\bullet-}$ (^{2}A, C_1): E_{tot} = -1208.86371791

B	1.044463512607	-0.254697684458	-0.881994524857
B	-0.923044128072	0.021421756325	-0.125098929541
C	-0.360465861181	-0.729411315794	-1.389633145504
H	-0.644532432479	-0.178006812646	-2.291670222694
C	-0.622175330887	-2.219424171252	-1.533804223117
H	-0.453470271933	-2.711500308677	-0.570877160046
H	0.098252746156	-2.666955704435	-2.233679456906
C	-2.033173425175	-2.622967421417	-2.001910838624
C	-2.319884494681	-2.060117330509	-3.392119539587
H	-2.335862178653	-0.968188469789	-3.379003667380
H	-3.293716512869	-2.404144802388	-3.756935396404
H	-1.556377055068	-2.379178163586	-4.109252481705
C	-2.087072948549	-4.148802362665	-2.067174264739
H	-1.891288225071	-4.584948453376	-1.082565104034
H	-1.335798961685	-4.538277350257	-2.761970190142
H	-3.070569857228	-4.496508139548	-2.401039911147
C	-3.097188146984	-2.128103623070	-1.026552734962
H	-2.903942821477	-2.494238012794	-0.014561083615
H	-4.091174053487	-2.472253136314	-1.333978292141
H	-3.112667717724	-1.037119375936	-0.978778779197
C	2.147061049111	-1.048396432469	-0.078514607527
C	3.243246482645	-0.175707594646	0.144739442020
C	4.380924934410	-0.595524402846	0.817867518867
H	5.207669215260	0.088878190094	0.985769625629
C	4.462458577334	-1.906851207249	1.273723214240
H	5.348038350247	-2.243463784582	1.803884355184
C	3.413229057361	-2.789450798111	1.040034644346
H	3.486531006873	-3.817246009679	1.382665795559
C	2.272997793852	-2.363205145306	0.365990501720
H	1.479138469994	-3.079150388675	0.182192679852
C	1.720613520871	1.148667495617	-1.093184255475
C	2.987367347752	1.136661066702	-0.456324062778
C	3.819996594793	2.245580137602	-0.476936990314
H	4.786055799687	2.223431772072	0.019833008535
C	3.411206717985	3.393948589146	-1.146949244325
H	4.054015799433	4.268611256117	-1.166643106204
C	2.178278791808	3.420867778904	-1.794031812324
H	1.864774520675	4.318921821996	-2.317763142679
C	1.344733906933	2.309188367700	-1.767134359304
H	0.384192559573	2.358709258977	-2.266068429696
C	-1.017707762737	-0.404322500066	1.386435090344
C	-1.725234610485	0.610663379284	2.085187901748
C	-1.980158019245	0.514518514376	3.444977502453
H	-2.520491824202	1.302173400872	3.962763458630
C	-1.540594748392	-0.602725505739	4.146663150574
H	-1.733806631740	-0.686378147514	5.211649976495
C	-0.849495720816	-1.612012472277	3.481778196096
H	-0.502997589115	-2.480879218999	4.033179948803

C	-0.591344725387	-1.511715090305	2.119840162529
H	-0.030300690548	-2.301633151964	1.635792439394
C	-1.686186900210	1.394220735307	-0.144151453250
C	-2.132647517679	1.680422756049	1.168318566901
C	-2.886314183997	2.812386583365	1.442124164277
H	-3.223059633265	3.024676341524	2.452975807139
C	-3.221160895311	3.676297911873	0.403898515721
H	-3.808598055065	4.566133066375	0.608407243395
C	-2.820373512981	3.393889529226	-0.898941114494
H	-3.102546487032	4.063283604511	-1.706055654331
C	-2.065198945875	2.256848799429	-1.167509638504
H	-1.778986537651	2.039084734138	-2.193042710357

60
$[\mathbf{1}]^{2-}$ (^{1}A, C_1): E_{tot} = -1208.80063671

B	0.994545615834	-0.324482097518	-0.703145938596
B	-0.785940134025	0.234098191349	-0.144738657689
C	-0.368460329682	-0.495176340884	-1.488795572665
H	-0.408447547335	0.190083264972	-2.342071577082
C	-0.892379648518	-1.865951790350	-1.847223779276
H	-0.896058254151	-2.500830669363	-0.954675864775
H	-0.215682021316	-2.365239352704	-2.561550296598
C	-2.311351388143	-1.931162056311	-2.453070664537
C	-2.360738919016	-1.154546266990	-3.767044680853
H	-2.156657821440	-0.096024324435	-3.593648408060
H	-3.348560201195	-1.240976561184	-4.236927922242
H	-1.611069626508	-1.532216005209	-4.471739695248
C	-2.648023018443	-3.395004987123	-2.735047608642
H	-2.626223309172	-3.977912395566	-1.808464453573
H	-1.921340061600	-3.836808103776	-3.426362620418
H	-3.646967135656	-3.497186258378	-3.177700372341
C	-3.345757649359	-1.355801825470	-1.490900673460
H	-3.335232050294	-1.892147874941	-0.538216532107
H	-4.354434199078	-1.423676922624	-1.920396337837
H	-3.119445698695	-0.312642688372	-1.263239620712
C	1.796484249650	-1.369480261646	0.154949905768
C	3.085941304179	-0.823007203124	0.453188228382
C	4.025289531984	-1.522245139725	1.202948278877
H	4.992580566180	-1.073283558920	1.421482184977
C	3.739792677285	-2.803276760730	1.660011781624
H	4.469849336646	-3.353725954383	2.248273417359
C	2.505814342834	-3.379198980646	1.346065931987
H	2.282004551805	-4.389768934339	1.681666665354
C	1.563666663356	-2.676978368895	0.606678942765
H	0.628671722107	-3.172024415325	0.367452917269
C	2.055054255558	0.812435046991	-0.901922264633
C	3.238706132046	0.479596930751	-0.174442731264
C	4.350111711549	1.315615233117	-0.159863609575
H	5.235054783537	1.040752746123	0.411742955225
C	4.340390848097	2.496692578964	-0.892518559102
H	5.204874606483	3.156018718480	-0.885051710024
C	3.206469008825	2.827013732321	-1.642521749784
H	3.198277829034	3.744212876863	-2.228068933274
C	2.093515897266	1.998640054900	-1.647234669636
H	1.231616061526	2.287123975158	-2.238659062247
C	-1.322376582526	-0.335983409339	1.216589386051
C	-1.850787730443	0.747751199990	1.990057734116
C	-2.394663033172	0.553727618902	3.255027142023
H	-2.779575455566	1.401965849789	3.818500250025
C	-2.464213820019	-0.724368638543	3.795735335661
H	-2.887949266693	-0.882717263013	4.784284850972
C	-1.980353260850	-1.804619265450	3.051621400143
H	-2.036343423766	-2.809999351486	3.463877949095

C	-1.426321233496	-1.610684857899	1.794432597822
H	-1.054395899260	-2.476639920038	1.260593733868
C	-1.167315224682	1.748996907559	-0.033829687316
C	-1.764034817038	1.991039691234	1.240690977483
C	-2.224302446977	3.252095127526	1.604238339163
H	-2.668190632662	3.412349512087	2.585274563402
C	-2.138878006820	4.308410643116	0.704343008927
H	-2.495176162545	5.297181817747	0.982650784260
C	-1.605582939476	4.084048897357	-0.568922811752
H	-1.559550193789	4.902659292449	-1.284358259342
C	-1.137661711663	2.827144792333	-0.927097486868
H	-0.752867079496	2.679058219624	-1.932100273084

60

$[\mathbf{1}]^{2-}_{[TS]}$ (^{1}A, C_1): E_{tot} = −1208.74548453

B	1.295773048282	0.041850971448	−0.344837538666
B	−1.474701999840	−0.114060737399	−0.289413365316
C	−0.100015132623	−0.732629730321	−0.366637133820
C	0.008601780722	−2.236844484082	−0.520436557664
H	0.740643435996	−2.503283380236	−1.291813031895
H	−0.948161552592	−2.646586678903	−0.861070220708
C	0.425262386503	−3.004629989487	0.770768554177
C	−0.273292021858	−2.435900321940	2.003517279893
H	0.020468494187	−1.394688472922	2.150408075563
H	0.005940110483	−3.013244372695	2.894489872042
H	−1.359910185116	−2.451866334053	1.902461713531
C	0.029509942357	−4.470044582134	0.587290482371
H	0.502723717927	−4.888945830065	−0.308237248601
H	−1.054182160496	−4.576468581952	0.475681643956
H	0.343683759371	−5.072105147418	1.448961716115
C	1.932175108941	−2.942704742332	1.007449489681
H	2.488679544124	−3.334285160759	0.150993309129
H	2.198875587954	−3.534250131779	1.893404859947
H	2.261231939062	−1.914870506592	1.160745674785
C	2.701262052663	−0.401174949969	−0.910467756561
C	3.702755096296	0.451337244404	−0.345279898414
C	5.044776473951	0.334775326466	−0.691225197380
H	5.781094714776	1.001799907478	−0.246650569796
C	5.448666738232	−0.624308302840	−1.612249367570
H	6.496669560114	−0.720991549699	−1.883504800616
C	4.487169398493	−1.458212382408	−2.194376746121
H	4.793820814227	−2.203914716446	−2.925081763203
C	3.146805663800	−1.337803412334	−1.857192449730
H	2.430072247714	−1.990989855688	−2.348774437204
C	1.677951854808	1.239365522417	0.584886225941
C	3.093634627033	1.405443491530	0.569030957981
C	3.720528194869	2.355991278112	1.369255274959
H	4.802779707967	2.470135753741	1.343728103351
C	2.960729238714	3.150470236761	2.219439724808
H	3.442645899160	3.897208650174	2.845798081573
C	1.573171888577	2.977085792005	2.273987064924
H	0.982158135838	3.589138143008	2.951386012775
C	0.943637978400	2.034736528874	1.473420011130
H	−0.133789856286	1.910117876129	1.522881327405
C	−1.876881956784	1.378276619804	−0.548754070283
C	−3.300368382063	1.495313483259	−0.508959352585
C	−3.944207126275	2.701837352437	−0.761996140548
H	−5.030290469129	2.764542233168	−0.718272996025
C	−3.199031381872	3.829659141931	−1.085805527400
H	−3.694677165077	4.777761050072	−1.280178437188
C	−1.805206353992	3.731997169760	−1.166549526997
H	−1.219141097848	4.609523020499	−1.430400990418
C	−1.158889082665	2.533536966008	−0.899823214108

H	-0.075960977988	2.492536451841	-0.951183385550
C	-2.882758781086	-0.804130343528	-0.112244555310
C	-3.900009710181	0.203585970995	-0.222330707973
C	-5.251150577841	-0.091200682853	-0.080439465019
H	-5.991478978728	0.702398801530	-0.164821074005
C	-5.663099897923	-1.395595004143	0.166085981215
H	-6.718839804051	-1.629812684616	0.276522577480
C	-4.697840577895	-2.403245454025	0.267335757484
H	-5.006985737347	-3.429321675038	0.456484732659
C	-3.347833539300	-2.108195842700	0.135562878139
H	-2.642038474473	-2.926706240017	0.230046710025
H	0.502290136024	0.117466862981	-1.382323026541

60

$[\mathbf{1}]^{2-}_{[BH]}$ (^{1}A, C_1): E_{tot} = −1208.77984996

B	1.155624751807	0.406787964425	−0.721082401121
B	−1.506678619387	−0.111504673725	−0.387202937999
C	−0.105643892049	−0.572594341987	−0.446820820111
C	0.198024846265	−2.044912787563	−0.281469758899
H	1.002076392707	−2.349956980143	−0.968878539226
H	−0.675440181639	−2.644188180614	−0.562584021513
C	0.650376514732	−2.556927367575	1.118447791557
C	−0.287362812565	−2.066750748606	2.215879129384
H	−0.311166171224	−0.975241969628	2.222387627417
H	0.047746789611	−2.427429583325	3.197391524028
H	−1.312326188799	−2.407648902291	2.049811113135
C	0.633900444124	−4.085199660837	1.082231085546
H	1.283975958318	−4.457893652317	0.282340080928
H	−0.378044108303	−4.461629287414	0.896803609992
H	0.985726358199	−4.509478749628	2.031441171110
C	2.068869600159	−2.096512615232	1.438645078228
H	2.769630377792	−2.404808324107	0.657121285058
H	2.404777807073	−2.521260873733	2.394201403024
H	2.118857442865	−1.010263333337	1.514181282044
C	2.551758645105	−0.171074386376	−1.316511556395
C	3.655515774044	0.386009833630	−0.626316352467
C	4.968642357150	0.110922790165	−0.998996956030
H	5.801929596824	0.554307579916	−0.457210044163
C	5.215219487015	−0.745825683098	−2.065992099556
H	6.237091712069	−0.975515028698	−2.358031489794
C	4.145290202219	−1.309173280977	−2.758463886305
H	4.338987002641	−1.982420810457	−3.591182211145
C	2.834837529283	−1.014936997347	−2.389688273697
H	2.011564226469	−1.454185580043	−2.948922694706
C	1.778055748133	1.244043904009	0.522177879349
C	3.191500645256	1.229015713523	0.478414885033
C	3.958707513993	1.914303729522	1.417564264845
H	5.045985041257	1.890693204622	1.370851426334
C	3.324513459600	2.617791213825	2.434920954480
H	3.912530238727	3.151553235867	3.177715125137
C	1.931893945762	2.625527631951	2.507717387985
H	1.439977837222	3.164325468598	3.314693512477
C	1.170702143427	1.943027806752	1.563097294311
H	0.085742013705	1.940445184791	1.632739037401
C	−2.071803739682	1.362858603536	−0.556511943999
C	−3.492199208127	1.338733172129	−0.487789495431
C	−4.259667706248	2.494443687825	−0.606324391905
H	−5.345480916692	2.443917681877	−0.547046154233
C	−3.633660904643	3.719219072087	−0.796602684962
H	−4.222792356871	4.628690183210	−0.888811236381
C	−2.239164741533	3.771048943649	−0.869944972343
H	−1.744483542543	4.728861721605	−1.017085883608
C	−1.475556183162	2.617186948223	−0.746838199897

H	-0.395089437576	2.681117455732	-0.804653203825
C	-2.867214476658	-0.931629557648	-0.196081496086
C	-3.966876733727	-0.024279562546	-0.279667237764
C	-5.288403735802	-0.443774407966	-0.163838538164
H	-6.098793400959	0.279791562263	-0.229576842531
C	-5.577742800642	-1.787489871693	0.038506342879
H	-6.608193518303	-2.121893882705	0.130682769781
C	-4.526882130937	-2.701333146558	0.123543453850
H	-4.740510819279	-3.755744282332	0.286929479282
C	-3.207285247245	-2.276578241505	0.014916877014
H	-2.426815478853	-3.024798520983	0.103458733961
H	0.857739403990	1.273395849898	-1.556562727107

62

[I]$^{\cdot-}$ (^{2}A, C_2): E_{tot} = −1434.93126615

B	−0.827717860632	0.762657780219	0.315742218808
B	0.827717860632	−0.762657780219	0.315742218808
C	−1.470949267141	0.539311276763	−1.104932637721
C	−1.021717831812	1.565985516062	−1.966290945662
C	−1.375565696574	1.586386457956	−3.306221398915
H	−1.011927043973	2.368950100825	−3.965703136363
C	−2.195535939157	0.579995674154	−3.806993377925
H	−2.471957504791	0.581187487310	−4.856947748481
C	−2.650624401622	−0.434886723284	−2.971803956105
H	−3.277638988079	−1.224216120340	−3.375058769205
C	−2.288895726931	−0.455922862716	−1.628373786358
H	−2.620057298701	−1.273076314350	−0.994736520062
C	−0.005064641694	2.098514067369	0.110229930942
C	−0.159282012700	2.503904886557	−1.237063023145
C	0.468572692237	3.641287527475	−1.723074374185
H	0.350237323561	3.937358644046	−2.761352705152
C	1.260956046595	4.400635439236	−0.868796594567
H	1.761780000048	5.289132264974	−1.241181180939
C	1.416077041978	4.021648990587	0.460881933691
H	2.038758474983	4.616866100299	1.121914874579
C	0.784376050748	2.880647465492	0.946968195674
H	0.931436766190	2.589780487910	1.981743320267
C	−1.470949267141	0.240134188949	1.653147989606
C	−0.734323895550	−0.063124837993	2.816609480321
C	−1.389537653810	−0.525518108668	3.959124018758
H	−0.803330751040	−0.794514045142	4.832079680566
C	−2.765174528207	−0.694817799279	3.980261296067
H	−3.253514968597	−1.069272389274	4.874353037598
C	−3.504035159837	−0.400656526505	2.842661917198
H	−4.581647152354	−0.532878173313	2.840545511408
C	−2.857396056280	0.051538902621	1.702247761005
H	−3.438583860608	0.275624606884	0.814137969667
C	1.470949267141	−0.240134188949	1.653147989606
C	0.734323895550	0.063124837993	2.816609480321
C	1.389537653810	0.525518108668	3.959124018758
H	0.803330751040	0.794514045142	4.832079680566
C	2.765174528207	0.694817799279	3.980261296067
H	3.253514968597	1.069272389274	4.874353037598
C	3.504035159837	0.400656526505	2.842661917198
H	4.581647152354	0.532878173313	2.840545511408
C	2.857396056280	−0.051538902621	1.702247761005
H	3.438583860608	−0.275624606884	0.814137969667
C	0.005064641694	−2.098514067369	0.110229930942
C	0.159282012700	−2.503904886557	−1.237063023145
C	−0.468572692237	−3.641287527475	−1.723074374185
H	−0.350237323561	−3.937358644046	−2.761352705152
C	−1.260956046595	−4.400635439236	−0.868796594567
H	−1.761780000048	−5.289132264974	−1.241181180939

C	-1.416077041978	-4.021648990587	0.460881933691
H	-2.038758474983	-4.616866100299	1.121914874579
C	-0.784376050748	-2.880647465492	0.946968195674
H	-0.931436766190	-2.589780487910	1.981743320267
C	1.470949267141	-0.539311276763	-1.104932637721
C	1.021717831812	-1.565985516062	-1.966290945662
C	1.375565696574	-1.586386457956	-3.306221398915
H	1.011927043973	-2.368950100825	-3.965703136363
C	2.195535939157	-0.579995674154	-3.806993377925
H	2.471957504791	-0.581187487310	-4.856947748481
C	2.650624401622	0.434886723284	-2.971803956105
H	3.277638988079	1.224216120340	-3.375058769205
C	2.288895726931	0.455922862716	-1.628373786358
H	2.620057298701	1.273076314350	-0.994736520062

62

$[\mathbf{I}]^{2-}$ (^{1}A, C_2): E_{tot} = -1434.89368132

B	-0.702783756693	0.631370298948	0.271627077563
B	0.702783756693	-0.631370298948	0.271627077563
C	-1.472631304314	0.508988197384	-1.114417585534
C	-1.100474861000	1.584191093821	-1.960993794232
C	-1.519953481611	1.649798770451	-3.285458897522
H	-1.199543644360	2.468918622018	-3.925862055774
C	-2.346653528896	0.655470263714	-3.793400212505
H	-2.674596281141	0.693724979578	-4.829332284765
C	-2.734235858649	-0.405061626519	-2.974576007995
H	-3.366893243745	-1.192705515395	-3.377840569013
C	-2.299164647964	-0.477586580755	-1.656115206175
H	-2.578785403516	-1.333586316321	-1.047974643997
C	-0.018272893125	2.063629324738	0.086884942862
C	-0.242124920453	2.519719941812	-1.239052800444
C	0.318205121682	3.704395116183	-1.707876997887
H	0.146501261421	4.024760023553	-2.733412741545
C	1.100474861000	4.479629822691	-0.861305417755
H	1.543799674897	5.405495104950	-1.219912170403
C	1.319393798894	4.058450069863	0.450860457303
H	1.933929791973	4.662936519579	1.114677230888
C	0.766526383311	2.869820965293	0.915302589763
H	0.969551076681	2.553816513394	1.934251844533
C	-1.450947343365	0.281526471389	1.639340730072
C	-0.739758493216	-0.024707441456	2.823342574981
C	-1.423272980069	-0.406947382414	3.978776829993
H	-0.854692895304	-0.689221201496	4.860752813330
C	-2.810066795233	-0.485125456214	4.010406298302
H	-3.320238344556	-0.800682601321	4.916843432889
C	-3.524799534616	-0.177037159449	2.861465656557
H	-4.610845279899	-0.239957710865	2.858614755263
C	-2.846372180174	0.196447224542	1.707381195668
H	-3.411304078992	0.422553761422	0.807672868073
C	1.450947343365	-0.281526471389	1.639340730072
C	0.739758493216	0.024707441456	2.823342574981
C	1.423272980069	0.406947382414	3.978776829993
H	0.854692895304	0.689221201496	4.860752813330
C	2.810066795233	0.485125456214	4.010406298302
H	3.320238344556	0.800682601321	4.916843432889
C	3.524799534616	0.177037159449	2.861465656557
H	4.610845279899	0.239957710865	2.858614755263
C	2.846372180174	-0.196447224542	1.707381195668
H	3.411304078992	-0.422553761422	0.807672868073
C	0.018272893125	-2.063629324738	0.086884942862
C	0.242124920453	-2.519719941812	-1.239052800444
C	-0.318205121682	-3.704395116183	-1.707876997887
H	-0.146501261421	-4.024760023553	-2.733412741545
C	-1.100474861000	-4.479629822691	-0.861305417755
H	-1.543799674897	-5.405495104950	-1.219912170403

C	-1.319393798894	-4.058450069863	0.450860457303
H	-1.933929791973	-4.662936519579	1.114677230888
C	-0.766526383311	-2.869820965293	0.915302589763
H	-0.969551076681	-2.553816513394	1.934251844533
C	1.472631304314	-0.508988197384	-1.114417585534
C	1.100474861000	-1.584191093821	-1.960993794232
C	1.519953481611	-1.649798770451	-3.285458897522
H	1.199543644360	-2.468918622018	-3.925862055774
C	2.346653528896	-0.655470263714	-3.793400212505
H	2.674596281141	-0.693724979578	-4.829332284765
C	2.734235858649	0.405061626519	-2.974576007995
H	3.366893243745	1.192705515395	-3.377840569013
C	2.299164647964	0.477586580755	-1.656115206175
H	2.578785403516	1.333586316321	-1.047974643997

113
[Li(thf)$_4$][**1**] (^{2}A, C_1): E_{tot} = -2145.50282430

B	1.244297553865	0.118568541600	0.304105341448
B	3.144012652602	-0.442849431462	-0.474972326367
C	1.681929590507	-0.819413201983	-0.887826995510
H	1.460848123681	-0.349660007845	-1.851537798743
C	1.241457703806	-2.271311725693	-0.857038945019
H	0.142587542772	-2.339998482878	-0.815734506870
H	1.601989456620	-2.741529140560	0.062629670066
C	1.700739686675	-3.156602613464	-2.028492418148
C	1.167757575314	-4.567482835347	-1.784577833115
H	1.564569647311	-4.976931449167	-0.850704764990
H	1.452824957664	-5.244511845897	-2.595441445206
H	0.074254710985	-4.568591901183	-1.714661780915
C	1.134803282802	-2.636651409885	-3.347832196944
H	1.518640775855	-1.639684505831	-3.575376656780
H	0.040172720789	-2.585725240093	-3.312301874016
H	1.411379061049	-3.295816121090	-4.176053297066
C	3.223331741513	-3.200727221851	-2.110260059096
H	3.657387617859	-3.540929890824	-1.166451395193
H	3.638380012631	-2.212858984883	-2.322119866316
H	3.547415126384	-3.882833325684	-2.902782637082
C	1.148607669618	1.682777850481	0.316029068713
C	0.815394386899	2.103202668261	1.632483344666
C	0.753451622088	3.447482221514	1.971873537471
H	0.551212899905	3.750941307349	2.995439509232
C	0.977102069443	4.411865759016	0.995139796305
H	0.942042250853	5.465155691863	1.252471133018
C	1.256975998705	4.022412649834	-0.314515253279
H	1.435902960202	4.778287991494	-1.072489215845
C	1.344768849405	2.676868576371	-0.646144548904
H	1.617462061908	2.404806865730	-1.658833217808
C	0.830344846832	-0.263080038235	1.772753712152
C	0.590358626500	0.941074683233	2.492261636832
C	0.177172534341	0.928711986280	3.817207012293
H	-0.000094757291	1.859144180937	4.349236099679
C	0.005954627422	-0.285872346850	4.472686105832
H	-0.302039284243	-0.303982189343	5.512691207954
C	0.252259354908	-1.478014812022	3.796380716265
H	0.140843970623	-2.424084503481	4.317335730401
C	0.651543306951	-1.462940613968	2.464762030517
H	0.831027986429	-2.410068987164	1.968417670099
C	4.055526293541	0.589384066746	-1.231951708271
C	5.297049279197	0.662162375878	-0.562882704253
C	6.315638053435	1.478269973424	-1.029001051210
H	7.267303757360	1.535027556007	-0.509684600864
C	6.113088608595	2.222939184845	-2.187733330960
H	6.904177410908	2.865324970293	-2.560346096454
C	4.911644489689	2.133724552437	-2.881118647896
H	4.774989967073	2.700386631895	-3.796517789261

C	3.892830793137	1.313011953349	-2.405529925255
H	2.966907694803	1.233290397069	-2.970322698363
C	4.082913368021	-0.961639317488	0.677750772981
C	5.310460142415	-0.257872100404	0.584442433297
C	6.346538080504	-0.488183338253	1.474850642233
H	7.279398491814	0.061354391142	1.394297542399
C	6.184854567855	-1.438575192349	2.477912387322
H	6.989888012707	-1.625957943322	3.180742547640
C	4.995087145681	-2.149731903773	2.579560513323
H	4.876087359301	-2.891090171852	3.363042640140
C	3.955197386345	-1.911037281406	1.687292120049
H	3.034166451100	-2.469371797437	1.799907281668
Li	-3.665669397954	0.123554635346	-0.479057322953
O	-2.725471795930	0.146747674404	-2.135002505695
C	-3.154837381021	0.575826907414	-3.430266714434
H	-4.121224809686	1.072345813061	-3.320539308596
H	-3.281524948198	-0.301778250772	-4.075541548886
C	-2.043416181152	1.471751190177	-3.941571913602
H	-2.029042919590	1.539174059008	-5.029973693507
H	-2.150364691293	2.482522958266	-3.537519355925
C	-0.807388132636	0.793649060821	-3.359896246269
H	0.050077842883	1.460028294966	-3.274930337754
H	-0.515026242051	-0.063168378300	-3.971669186627
C	-1.295036028249	0.336729049332	-1.997706418393
H	-0.847347401541	-0.598474005715	-1.667245211843
H	-1.114143106527	1.090162753723	-1.226765795726
O	-5.575499759722	0.069923840184	-0.947727237819
C	-6.493390746420	0.497827661050	0.056621873597
H	-7.392466110702	0.900973639429	-0.426204304327
H	-6.008384768449	1.287381480870	0.629442450591
C	-6.804892995438	-0.761649659644	0.852440326022
H	-6.068635585205	-0.892467085967	1.647032254891
H	-7.792571193964	-0.722955495344	1.312627447908
C	-6.671982177144	-1.885758368007	-0.192573908660
H	-7.633721172643	-2.339995731731	-0.433594182200
H	-6.013266421322	-2.675233153556	0.169352321732
C	-6.076911610791	-1.181172542918	-1.417585312891
H	-5.248497372808	-1.716571608821	-1.882667946739
H	-6.841841667669	-0.993049366908	-2.179761570255
O	-3.210864368871	-1.466921121923	0.491883955816
C	-2.887310133769	-1.526768703970	1.896716255699
H	-3.705926727538	-1.060332618667	2.448763237037
H	-1.961606665217	-0.974265653523	2.076396803624
C	-2.706644049757	-2.998377365031	2.200506214213
H	-2.059238814938	-3.150303241244	3.063561648808
H	-3.670363346735	-3.479551511181	2.392626820486
C	-2.093793295325	-3.505324019917	0.900094516722
H	-2.208341636845	-4.579791424065	0.753490624654
H	-1.030356578950	-3.263726809357	0.867770807349
C	-2.843130852324	-2.701115305924	-0.146293699038

H	-2.244111785351	-2.472029170163	-1.030027376215
H	-3.759837441658	-3.210680462444	-0.465429493020
O	-3.470280440963	1.773054633975	0.465448965841
C	-3.478034227651	2.987396597137	-0.305260560795
H	-4.503824308610	3.373092352184	-0.336259655998
H	-3.163065102753	2.748675796120	-1.322975469185
C	-2.538887701287	3.933122020713	0.414921135273
H	-1.503776050889	3.762086517898	0.110153045680
H	-2.783868214191	4.980066085932	0.232498238089
C	-2.723514162821	3.510738481768	1.866823240859
H	-3.647094547650	3.925539030948	2.281931703575
H	-1.886123302359	3.807948751159	2.496445580198
C	-2.817246468506	2.005674956329	1.734813002259
H	-1.825593776149	1.548107477332	1.713452248121
H	-3.416423260153	1.530660743603	2.513817264118

61
[**1**H]$^-$ (^{1}A, C_1): E_{tot} = -1209.48302919

B	0.638215800184	0.291534670216	-0.277694188140
B	-1.203088428360	0.043698167448	0.158725154836
C	0.016832393447	-0.074214687088	1.162887142868
C	1.451804948365	1.665482138789	-0.460261636719
C	2.688226086889	1.367968760662	-1.072291071786
C	3.659585446497	2.343320299404	-1.270574135348
H	4.608720678760	2.090702173820	-1.734661443653
C	3.407123222922	3.649618650128	-0.875659970173
H	4.156265572192	4.420121079884	-1.029937719930
C	2.189320508792	3.967597433818	-0.285181740848
H	1.986625812003	4.991233378625	0.015777164977
C	1.227619858882	2.983059847976	-0.077317447341
H	0.287714993624	3.263658593497	0.379945742511
C	1.580389199778	-0.730002272482	-1.085250347460
C	2.762323185656	-0.046608592115	-1.445417039184
C	3.816646969089	-0.693089346672	-2.080031219032
H	4.721563913405	-0.150164362440	-2.337428268735
C	3.704487099149	-2.040976390685	-2.392835574642
H	4.521320261790	-2.555116088836	-2.889931953558
C	2.535787448807	-2.724576722478	-2.080466473270
H	2.437247808492	-3.773884392071	-2.342275379145
C	1.487438565247	-2.072201531635	-1.436746741293
H	0.584079162972	-2.629222468989	-1.226790185363
C	-2.284855361798	1.233135762579	0.227538019405
C	-3.503232203063	0.773565350522	-0.311916204551
C	-4.624325834313	1.593101105858	-0.379415354714
H	-5.555466994450	1.224575037676	-0.800317575822
C	-4.553900589711	2.887264681975	0.119702604444
H	-5.423278785949	3.535842973246	0.073651343681
C	-3.376358264235	3.341282837358	0.702508373194
H	-3.332889928106	4.341780719962	1.122382884153
C	-2.256915436888	2.515313209020	0.758194211728
H	-1.361569432851	2.878553834676	1.250653250902
C	-2.131039937576	-1.164290205370	-0.370458977820
C	-3.411197206212	-0.646769861461	-0.669037013597
C	-4.430156505027	-1.455706513001	-1.158393398558
H	-5.405422397555	-1.036436235522	-1.388427266008
C	-4.201211018956	-2.814169113152	-1.332547388600
H	-4.990859400536	-3.455136304519	-1.712268796829
C	-2.966303193166	-3.353698669632	-0.995497009039
H	-2.796095702516	-4.421000095855	-1.100018924871
C	-1.947337447545	-2.533940024744	-0.516785187120
H	-1.006654351893	-2.990057345874	-0.233293230001
H	-0.504227847557	0.393692522363	-0.995837868320
H	0.050203499498	0.777590422317	1.844052423541
C	0.348165476932	-1.374204803581	1.856468626702
H	-0.518383001447	-1.741669888492	2.426995023922
H	0.563228154461	-2.145402502830	1.108912174952

C	1.546074546094	-1.337497253687	2.825185259634
C	1.248572868273	-0.416393086732	4.006445254287
C	2.807447842753	-0.856674273886	2.114336713967
H	3.056434662529	-1.506376184925	1.271489811728
H	2.673319031148	0.151731873385	1.717777193659
H	3.658678125614	-0.846463785953	2.804560268822
H	1.114911039921	0.616885254094	3.679133352156
H	2.072834882327	-0.434134958243	4.727800905368
H	0.335404229913	-0.727395451491	4.524527290190
C	1.774643816875	-2.752743696319	3.352888856689
H	2.009297222130	-3.437071013929	2.531746193109
H	2.606515283731	-2.780532255011	4.065200036547
H	0.880907733491	-3.130186917083	3.861001927597

114
[Li(thf)$_4$][**1**H] (^{1}A, C_1): E_{tot} = −2146.10785845

B	−2.215747765834	−0.403077380160	0.793511554887
B	−3.704427135437	0.283088425516	−0.168555519070
C	−2.287296753838	−0.082785136975	−0.787137405233
H	−1.759065180664	0.825193969331	−1.084921310090
C	−2.217653512041	−1.170986275779	−1.835710955154
H	−2.921231087900	−0.950745993787	−2.651179839121
H	−2.558095843195	−2.116391871079	−1.405192926948
C	−0.850335370920	−1.438279664042	−2.489152410182
C	−0.994920523534	−2.620790189420	−3.444049889545
H	−1.298986104306	−3.520484702849	−2.901685184221
H	−0.050525813659	−2.838849282172	−3.956071576965
H	−1.751204650465	−2.417601142689	−4.207824805893
C	−0.407604355218	−0.216081780811	−3.289026926347
H	−1.159357993802	0.049442634583	−4.037559668384
H	0.533742188038	−0.408039855424	−3.816431654745
H	−0.267970572466	0.652693501306	−2.641489350487
C	0.194903034218	−1.778521490154	−1.433757595010
H	−0.095066334219	−2.667733487368	−0.868151093019
H	0.302750906537	−0.964928824723	−0.714866084433
H	1.169367002601	−1.968379536421	−1.899643122637
C	−1.947885482555	−1.903373136993	1.303971386818
C	−0.908152575892	−1.869083224228	2.258859471389
C	−0.409502714411	−3.029008292531	2.841656054882
H	0.362825254044	−2.977304014275	3.602943917843
C	−0.932807249612	−4.260497250499	2.474221746823
H	−0.558054326565	−5.171302872240	2.929786344743
C	−1.963446761182	−4.317570077328	1.543869762869
H	−2.393220247953	−5.276848135571	1.273994897238
C	−2.467337859148	−3.151534740793	0.975598084454
H	−3.295262907441	−3.234305457117	0.284106426785
C	−1.290431139189	0.427298903473	1.816885251343
C	−0.512500129613	−0.490284732439	2.557921421219
C	0.440398445053	−0.063375965945	3.478212655152
H	1.026844027886	−0.783054223877	4.042992408089
C	0.598929132559	1.296358043367	3.720309137531
H	1.321477547268	1.638380053297	4.454596306257
C	−0.214074838224	2.210531634928	3.060321533982
H	−0.131445724940	3.268671307828	3.289059041092
C	−1.147193347684	1.776960647970	2.120981420239
H	−1.785250191471	2.508395537538	1.642545071848
C	−5.106902018697	−0.469147508956	−0.409716227609
C	−6.140094938282	0.489106166702	−0.316830731768
C	−7.476656496212	0.134385304973	−0.451185686377
H	−8.257835327855	0.884273242319	−0.372588812578
C	−7.810341117090	−1.189904910012	−0.700511218043
H	−8.851092965996	−1.477183641367	−0.807960822644
C	−6.808283728136	−2.143007034831	−0.827510891394
H	−7.068394456742	−3.174324892116	−1.043615011962

C	-5.471641227567	-1.781262551014	-0.682210849507
H	-4.715103172867	-2.546623843312	-0.806484445753
C	-4.188876727381	1.811150804317	-0.086633751920
C	-5.596049359237	1.841477889882	-0.142228628298
C	-6.295030350647	3.042842750113	-0.125126840606
H	-7.379928150500	3.053404683812	-0.164549644466
C	-5.593000227770	4.240558869891	-0.085754041992
H	-6.129698562223	5.183485071369	-0.073979758206
C	-4.203290876514	4.231991495955	-0.095407442911
H	-3.658267332542	5.170869477684	-0.104965879986
C	-3.513628686628	3.022686369492	-0.104590870362
H	-2.428678948011	3.036345890095	-0.153044507750
H	-3.474601912675	-0.069247345182	1.150824595451
Li	3.828064162257	0.300946824875	-0.379811938822
O	2.419837978814	1.523190692998	-0.803137740239
C	2.294767404719	2.395437401803	-1.922104400708
H	1.622229209869	1.944590184820	-2.660630150734
H	3.282351869146	2.510447452969	-2.372677624915
C	1.706658867614	3.685521506485	-1.363081640020
H	1.048643414718	4.166938566217	-2.087049730747
H	2.497517381438	4.396157215298	-1.114864420021
C	0.957745874946	3.230453526298	-0.096347454338
H	1.317148256288	3.755756289348	0.789117892158
H	-0.114081813408	3.409681943004	-0.162265735092
C	1.245165156787	1.735114670629	0.001979487311
H	1.458804860111	1.385668682396	1.011013177292
H	0.419849707944	1.144021732482	-0.400473957093
O	5.297524363378	1.376142457278	0.337047564181
C	6.148031306532	2.198315142203	-0.456341521496
H	6.119032725156	1.815920047929	-1.476977310071
H	7.175287836878	2.116762810435	-0.080262614797
C	5.610771230089	3.620193915656	-0.294780233642
H	6.420400896003	4.350280667485	-0.276800902133
H	4.950668469240	3.882423543240	-1.122381007068
C	4.826937927385	3.571400613721	1.032405255306
H	3.771757886411	3.785062432138	0.865041360122
H	5.199919775589	4.286011578814	1.766402959982
C	5.006434063211	2.133943032492	1.511952582857
H	5.848243968594	2.045165238843	2.209575150050
H	4.117340665976	1.705905420788	1.976058417583
O	4.398823893692	-0.592073484251	-2.012957768283
C	5.093955946704	-1.839305359978	-1.933232254308
H	5.287579974991	-2.043807994660	-0.879975378545
H	6.050750003872	-1.761053632544	-2.463988765232
C	4.169938673692	-2.834253069779	-2.602258832204
H	4.685008025139	-3.738696380293	-2.927299370149
H	3.368023947607	-3.120370916194	-1.917330904764
C	3.618494125163	-2.008866992996	-3.762320518403
H	2.636153022401	-2.348021737748	-4.092396799806
H	4.296563393148	-2.055125314196	-4.617334150616

C	3.564309848666	-0.594261712400	-3.189212436280
H	3.938587467278	0.156326685481	-3.890149622121
H	2.558913302755	-0.314920913507	-2.874225706942
O	3.668237605146	-0.995450923656	1.030408110564
C	4.736491832743	-1.357839854352	1.912424862275
H	4.658297462161	-0.772168831205	2.836359008753
H	5.679584057473	-1.108957129215	1.423302763829
C	4.531844227979	-2.831987418937	2.189104483335
H	5.023054045615	-3.157619061488	3.106734226743
H	4.917574665581	-3.433671443427	1.360494763457
C	3.011489928370	-2.910748832303	2.254667332608
H	2.661239682145	-2.564626774346	3.229609065171
H	2.610627166575	-3.910220655170	2.091227733160
C	2.579525219081	-1.941934303229	1.167759852162
H	2.446403551304	-2.441047435007	0.205389097164
H	1.668024025679	-1.398207262431	1.410608560555

76
[Li(Et$_2$O)][**1**]$^-$ (^{1}A, C_1): E_{tot} = −1449.93468119

B	-0.369912799874	-1.194843203344	-1.072734101042
B	-1.102930349648	0.445334912779	-0.332663375435
C	-1.795757955737	-0.564882523245	-1.328476095602
H	-1.843968795094	-0.157639731578	-2.342203477225
C	-3.055543771040	-1.320866856094	-0.970589734399
H	-2.991218949420	-1.683030299712	0.061144642950
H	-3.141979797587	-2.224091857142	-1.593573716667
C	-4.385347710897	-0.550265917318	-1.103224857874
C	-4.591556304552	-0.092159203026	-2.545193559706
H	-4.543267757637	-0.939417380457	-3.237463388861
H	-3.825002488303	0.628171186563	-2.838553997540
H	-5.568828501355	0.389010727050	-2.662993575018
C	-5.522350112426	-1.495806933309	-0.718839640194
H	-5.405628697896	-1.841230802952	0.313431628457
H	-5.535937767546	-2.377741114319	-1.367957914148
H	-6.495797093111	-0.999513349397	-0.800029263072
C	-4.414800399903	0.665689001436	-0.182796811368
H	-4.280980862914	0.372137098381	0.861669978648
H	-5.371746226799	1.192747414105	-0.272838694166
H	-3.607964933267	1.358444771102	-0.427721314714
C	0.124821922871	-2.263788608267	-0.029463096506
C	1.509802904958	-2.542882343965	-0.269241695752
C	2.232493633914	-3.431692653908	0.527799544131
H	3.284388831429	-3.615293091450	0.325471152942
C	1.599559117131	-4.095826759810	1.562681701333
H	2.150678769122	-4.795224942906	2.183338756702
C	0.236768311136	-3.871751531924	1.796037774619
H	-0.264972817845	-4.413020097430	2.592949886652
C	-0.478682385656	-2.978561280849	1.020363200646
H	-1.536739087657	-2.855051850673	1.214638122394
C	0.906698128312	-1.023620010939	-1.970270479342
C	1.975932367273	-1.803423197244	-1.430391854612
C	3.242484076089	-1.818909888567	-2.017165431043
H	4.041054914198	-2.415267963647	-1.583817073737
C	3.470736805557	-1.090053750028	-3.170579725318
H	4.449198083082	-1.102190125471	-3.640292681028
C	2.427567177725	-0.347876952836	-3.741409739758
H	2.605440736736	0.203666184373	-4.660098689556
C	1.177708796376	-0.314880381298	-3.152157414474
H	0.385009532860	0.248414674385	-3.630908213486
C	-1.207610312874	0.579891118368	1.240818969338
C	-0.627318013315	1.825082791914	1.631932390704
C	-0.557651179779	2.217725703254	2.964597014911
H	-0.107236011297	3.170361856616	3.232581614675
C	-1.091933870962	1.403075912506	3.953275284338
H	-1.047334798398	1.704551119791	4.995074871183
C	-1.707142293071	0.203005905198	3.595077283652
H	-2.146989071884	-0.425598253383	4.363891987914

C	-1.762812468179	-0.196942106925	2.267318401177
H	-2.257753105635	-1.130354565257	2.032642750841
C	-0.468331261203	1.834984155387	-0.725039448674
C	-0.189606517252	2.574123258032	0.460051135677
C	0.381799810998	3.841815732686	0.412938845825
H	0.588845895620	4.388480946464	1.329790223931
C	0.660730779519	4.424199179598	-0.816442850729
H	1.102662400029	5.414556501657	-0.863838434982
C	0.344254166168	3.741653942541	-1.992705710368
H	0.535240531337	4.211861363689	-2.953066033842
C	-0.215395699794	2.472583499249	-1.944961038293
H	-0.469342623284	1.975512363521	-2.874386502672
Li	1.246602273208	-0.217764146871	0.194398553895
O	2.614511078359	0.638289245466	1.235604824404
C	2.641175348804	0.542427068624	2.652586315132
H	3.690618020706	0.473014326452	2.974253394148
H	2.208999122042	1.457281288845	3.077130600360
C	1.855144421068	-0.664569082295	3.088518098914
H	2.254345257475	-1.582332357201	2.651394598217
H	0.803913566145	-0.570881335859	2.809195675003
H	1.893023969219	-0.753159160589	4.176626691924
C	3.348729989779	1.750670935175	0.743330623842
H	4.387496171665	1.660063916286	1.093092451395
H	2.922281877897	2.670742625995	1.162932853977
C	3.278749358936	1.772454862591	-0.759485615504
H	3.671273861869	0.849456568877	-1.191591140588
H	3.864585468467	2.611578431646	-1.141471327903
H	2.252051518286	1.911766335056	-1.102844025972

87
[Li(thf)$_2$][**1**]$^-$ (^{1}A, C_1): E_{tot} = -1681.01562143

B	0.768106930666	-0.788839568110	1.372834712403
B	1.534063002455	0.384105851804	0.050101622512
C	2.285741886983	-0.388714405694	1.206458961347
H	2.587825939519	0.295436589504	2.003649543789
C	3.348246375270	-1.422514822869	0.918371401042
H	3.053641021642	-2.028772617897	0.055041181563
H	3.432605686450	-2.128515053452	1.759040303440
C	4.765686592464	-0.886482853109	0.631470053011
C	5.307650376086	-0.141522711257	1.849583174019
H	4.713130187477	0.750110405820	2.059840162860
H	6.342842307817	0.176321060084	1.682305883378
H	5.286623649366	-0.779435183960	2.739544703253
C	5.675337957141	-2.078819847488	0.340556410496
H	5.319448412865	-2.631180349102	-0.535043894858
H	5.695968979149	-2.771437972473	1.188609333606
H	6.702983102512	-1.755255040512	0.140811476810
C	4.766595252100	0.050640411447	-0.572604585146
H	4.384997020337	-0.454572778858	-1.464025535214
H	5.782532284449	0.404107143889	-0.784548964798
H	4.122909313906	0.913449342167	-0.393596661371
C	0.042181966762	-2.135017212380	0.973006919006
C	-1.215560886635	-2.197468459601	1.651738931596
C	-2.063926571537	-3.293774814547	1.528418841365
H	-3.009621399534	-3.318212640142	2.064861143269
C	-1.687446190183	-4.375795666284	0.744665816316
H	-2.336876341541	-5.241637799706	0.657361733428
C	-0.450977836416	-4.356409382073	0.096659211658
H	-0.139409378909	-5.215127661908	-0.491598986838
C	0.391291534613	-3.259063202441	0.209309033496
H	1.355401929394	-3.298854790811	-0.283212831679
C	-0.243464296491	-0.186105606317	2.420225918134
C	-1.396633083267	-1.022352347180	2.494366832158
C	-2.470700830292	-0.717777529889	3.327360352263
H	-3.345798811693	-1.362616902312	3.356607489227
C	-2.405480345380	0.394695964708	4.154931556911
H	-3.232144668196	0.633858962318	4.816550356230
C	-1.255429810177	1.190082204508	4.150685969059
H	-1.191466160507	2.041953194129	4.821996287410
C	-0.200510269095	0.905544300813	3.297229175731
H	0.678065011081	1.539545859085	3.322979843295
C	1.359226316806	0.021553248148	-1.476317621497
C	0.979959987825	1.203378248321	-2.190466750784
C	0.739580486536	1.187042606626	-3.562138841959
H	0.443628691193	2.097916655917	-4.076982234507
C	0.923004346232	0.015811614557	-4.282529019747
H	0.756340353500	0.000505479525	-5.355039978963
C	1.344407143615	-1.139426511693	-3.618708035974
H	1.510414721685	-2.052544785240	-4.183724145963

C	1.543956799658	-1.137307786789	-2.247283833304
H	1.860957408375	-2.055652800639	-1.770656730749
C	1.269640270092	1.935240720439	0.035938996979
C	0.946200382765	2.347321775910	-1.289643197786
C	0.698503446503	3.681585284651	-1.600997532600
H	0.456892648110	3.974379611592	-2.620132692065
C	0.791031361623	4.648490041130	-0.609022636148
H	0.610214357940	5.692755783419	-0.845069047877
C	1.154111604778	4.275143308110	0.687587183044
H	1.261149300651	5.037025179335	1.454676308375
C	1.394135010506	2.944320439512	0.998653361914
H	1.705725465115	2.689882564687	2.006079623853
O	-2.117738251614	1.538063830587	-0.182022782736
C	-2.209262361694	2.386833017895	0.970905359386
H	-1.226267255413	2.821565634872	1.170258678964
H	-2.499729305145	1.765750849999	1.817224292299
C	-3.219798940645	3.445854061472	0.583137977298
H	-3.116855101052	4.353314952025	1.180380615115
H	-4.239244517041	3.064575489237	0.701478161021
C	-2.884981791526	3.656223919840	-0.889948048133
H	-3.704048917289	4.088836309723	-1.468324277700
H	-2.008882196175	4.301900188404	-0.980520160222
C	-2.533984433332	2.247800129398	-1.351931651505
H	-3.400804847628	1.726549155975	-1.774105493423
H	-1.725020502834	2.230686825251	-2.084969339133
Li	-0.861415810809	0.046925206503	-0.325026432559
O	-2.164157230096	-0.942660032838	-1.408024372247
C	-3.199470636442	-2.499013800257	-2.813357394098
H	-3.113609251751	-3.502752801904	-3.233287235224
H	-3.674474310289	-1.850847462850	-3.556782820000
C	-3.965549414578	-2.461967894647	-1.495308932268
H	-5.050369608286	-2.474563571567	-1.618674403040
H	-3.669939801837	-3.306500611686	-0.869033983668
C	-1.855862010340	-1.934020224632	-2.395705960400
H	-1.223603590299	-2.700928331766	-1.939240203877
H	-1.298488411309	-1.443928149712	-3.193552020554
C	-3.471526679408	-1.166638137568	-0.870451619928
H	-4.104328406072	-0.314382191667	-1.142670837025
H	-3.400289654752	-1.217253643396	0.217195570807

107
[Li(Et$_2$O)$_2$][Li(Et$_2$O)][**1**] (^{1}A, C_1): E_{tot} = -1924.43063072

B	-0.184526671964	-0.048918421998	0.155172291432
B	0.928324860682	1.394989343333	-0.295797322905
C	-0.634860290522	1.461490687930	-0.185670921450
H	-1.075148433634	1.529664457953	-1.184564942633
C	-1.345861853316	2.367275948686	0.795984159439
H	-0.876210599804	2.288991143258	1.782059008858
H	-2.390605186704	2.046134495757	0.941545238076
C	-1.419019418002	3.861896171019	0.423409441070
C	-2.113208127049	4.035273185383	-0.925543613844
H	-3.095641153416	3.552882785596	-0.925894096301
H	-1.517153456134	3.603948685770	-1.733106951206
H	-2.257621501622	5.096053094042	-1.150602238537
C	-2.240118178479	4.570353760606	1.499100936698
H	-1.779213419676	4.448656893226	2.484135000001
H	-3.256715261907	4.166383323393	1.551763137710
H	-2.315507741431	5.642454742651	1.294840852673
C	-0.031198548038	4.489745918523	0.357169546802
H	0.491098568277	4.398337978549	1.312761894889
H	-0.106809182571	5.553889960794	0.112042401079
H	0.585585170684	4.003023690793	-0.399807749363
C	-0.036023914908	-0.794493659619	1.538479838480
C	0.017769737942	-2.203234251460	1.300722057780
C	0.174574974370	-3.119603532815	2.338507867549
H	0.219198982473	-4.184350007769	2.128374188035
C	0.267255783096	-2.668419193273	3.645045826982
H	0.388226623083	-3.373551183627	4.459979613101
C	0.199109233888	-1.297763319442	3.907604755399
H	0.262062798959	-0.945797590279	4.932322333257
C	0.051081070285	-0.383415426878	2.877732114701
H	-0.009935052529	0.667215191329	3.128176530317
C	-0.318881251371	-1.268176647011	-0.841493881294
C	-0.145620556178	-2.487004934736	-0.115377256969
C	-0.167115362138	-3.724531335403	-0.752781886983
H	-0.014795764974	-4.637899926439	-0.185152963319
C	-0.395172871306	-3.791013553776	-2.118834054489
H	-0.417110811176	-4.751534674872	-2.621693176282
C	-0.607198241574	-2.616995860819	-2.845659067462
H	-0.796833832550	-2.674925096873	-3.912739907997
C	-0.569870687310	-1.381094296813	-2.219435297668
H	-0.730226358220	-0.490685528667	-2.814895859755
C	2.070545675345	1.717150949159	0.752799516068
C	3.328866186741	1.624171820862	0.092710262773
C	4.530916745926	1.814131357025	0.770121721916
H	5.477606085865	1.735234829177	0.243770538023
C	4.511865910788	2.139758616247	2.115949733585
H	5.440988471557	2.301521759681	2.651480936819
C	3.291054186032	2.284398519407	2.775513049285
H	3.278508163151	2.569699607435	3.822430563482

C	2.095939813811	2.072939519355	2.106272679604
H	1.169458619893	2.220171241644	2.646126785968
C	1.756336334039	1.275438150385	-1.634890303653
C	3.141447926644	1.366324589974	-1.333201694822
C	4.113375461123	1.269759553497	-2.325918679713
H	5.167835108119	1.340758783683	-2.076248431691
C	3.724012288024	1.118830965460	-3.647108366292
H	4.471175730252	1.051882772160	-4.430401290390
C	2.367538891579	1.084496377162	-3.973815307818
H	2.069732177537	1.003799906321	-5.014257851989
C	1.401871805021	1.162111919372	-2.982145905344
H	0.355781367149	1.169130711550	-3.269196295140
Li	2.077178708309	-0.583185447988	-0.089558938497
O	3.512971817110	-1.834023797996	-0.032497857261
C	4.395464585427	-1.868149369844	1.083737166770
H	4.791682816707	-2.887512707797	1.178864616557
H	5.236776687523	-1.189430949745	0.892752744887
C	3.645759066959	-1.458652562994	2.322739822731
H	2.792067441155	-2.114459909634	2.502579817568
H	3.291961403254	-0.428049090085	2.252034961290
H	4.309851061310	-1.512706150922	3.187897921653
C	4.118356698766	-2.280112523085	-1.240176765764
H	4.526027608864	-3.285316845247	-1.071467917289
H	4.951583205369	-1.610047835837	-1.489385662531
C	3.089210824040	-2.290543478894	-2.338556016496
H	2.243935287926	-2.930797866066	-2.079705171646
H	3.538717489344	-2.670080298773	-3.258595131569
H	2.720514446339	-1.284881565639	-2.551892366669
Li	-2.377247163992	-0.284348749455	-0.022438417384
O	-3.373718128918	-1.558109641142	1.161113932106
C	-3.473427517769	-2.921417199523	0.753238347269
H	-4.315120825092	-3.377759609089	1.290632922961
H	-2.556681468621	-3.445417058085	1.044563252021
C	-3.686148644286	-3.000558386809	-0.734419782331
H	-3.783876975749	-4.046792760145	-1.030483026226
H	-2.835361658743	-2.591211300149	-1.282115805940
H	-4.594388718019	-2.473056914863	-1.032670948675
C	-3.284063310300	-1.445568238594	2.582324413860
H	-2.330425329914	-1.865543689582	2.917545110065
H	-4.097530311365	-2.036567046163	3.022602973581
C	-3.405454802365	-0.000583982642	2.982964125448
H	-3.346283528125	0.082820256383	4.069927684539
H	-4.358690229879	0.424225368524	2.658641336599
H	-2.588102491155	0.590824397644	2.568928334115
O	-3.807437862958	0.448494436495	-1.114043237960
C	-3.650139514635	0.890190099707	-2.462074360281
H	-2.617147462772	1.230454492333	-2.545938513512
H	-4.289221043534	1.762438653544	-2.633900479531
C	-3.935165432973	-0.208456946980	-3.460178206626
H	-3.783492538168	0.166924764051	-4.475311763840

H	-4.964900494534	-0.566088832650	-3.388258367481
H	-3.262320177909	-1.052660964367	-3.301114742457
C	-5.148397068907	0.500297343106	-0.629665971481
H	-5.832993705992	0.181378238701	-1.423539162750
H	-5.198432545586	-0.241768009024	0.167957591022
C	-5.518879598981	1.870848119690	-0.109797887374
H	-6.536012720553	1.853093383567	0.289781289250
H	-5.481968319728	2.630917301397	-0.892988127497
H	-4.840377248033	2.174771281428	0.689650957435

114
[Li(thf)$_2$]$_2$[**1**] (^{1}A, C_1): E_{tot} = −2153.11161515

B	−0.441576343429	0.151146460772	−0.296852158728
B	0.517563190444	−1.376079717635	−0.760313648594
C	−1.046920004736	−1.247346352496	−0.832343531141
H	−1.494869219667	−1.862474036704	−0.042680320044
C	−1.819379072558	−1.333070428374	−2.131517357451
H	−1.254603075508	−0.828928161724	−2.919761238591
H	−2.780609774225	−0.784798251784	−2.083721817068
C	−2.152338462154	−2.750677515898	−2.634480183562
C	−3.063719388851	−3.468054287737	−1.641832243234
H	−2.564912721371	−3.612824907908	−0.680817971800
H	−3.347180331137	−4.454729854924	−2.019941110453
H	−3.982125335829	−2.896540832611	−1.471251141249
C	−2.885562922654	−2.617606393582	−3.967351359109
H	−2.257748885835	−2.111734837960	−4.706808930141
H	−3.807088519811	−2.036472290979	−3.855071071093
H	−3.153100337826	−3.599188482308	−4.369876494271
C	−0.881610960924	−3.570030021663	−2.836132519179
H	−0.208289272224	−3.083842066472	−3.546331408853
H	−1.127165631275	−4.564113873338	−3.223289490606
H	−0.334070031377	−3.687056162800	−1.899521170419
C	−0.376633207541	1.519562725253	−1.082409267861
C	−0.339757243259	2.591350065740	−0.140685192557
C	−0.282073334873	3.924451169517	−0.541122629784
H	−0.245733947786	4.720271762129	0.198351039583
C	−0.289098003494	4.238877935916	−1.891109722854
H	−0.251839728983	5.273994610917	−2.213164274194
C	−0.358683587157	3.211820494670	−2.834246407551
H	−0.385550580791	3.456235381298	−3.891445040198
C	−0.401221123352	1.883454438864	−2.436594915834
H	−0.476461260126	1.123556744040	−3.203056737061
C	−0.545899381773	0.656292734198	1.199027810327
C	−0.434646677507	2.082621824088	1.217094125062
C	−0.482502561492	2.801906249723	2.407888547254
H	−0.379613050429	3.883564233885	2.401641206583
C	−0.698390089418	2.138482567894	3.607475475737
H	−0.754358949609	2.695604788667	4.536248135108
C	−0.851675265175	0.750500302913	3.612809850207
H	−1.024680013344	0.234504650144	4.552352714590
C	−0.761416402309	0.023729898612	2.434847757264
H	−0.843378494377	−1.055211794058	2.478362725832
C	1.627919216313	−1.274529963942	−1.887681826424
C	2.814367789632	−1.893612846946	−1.402076579209
C	3.985498181452	−1.926114098944	−2.153525203496
H	4.881428648308	−2.395718087902	−1.757534559164
C	3.995155367106	−1.388108452357	−3.432410643278
H	4.898646390271	−1.421652743009	−4.031721920008
C	2.829705360002	−0.829087561465	−3.952990231370
H	2.828627568460	−0.435793747883	−4.964685859935

C	1.671880147048	-0.768009130073	-3.189317420332
H	0.789331193070	-0.325178833014	-3.632501307303
C	1.246167748916	-2.264786145916	0.328933554436
C	2.577697234587	-2.512343411527	-0.097403710336
C	3.438902386629	-3.318129508891	0.640079612128
H	4.450958529357	-3.508248378248	0.294024210687
C	2.985154512361	-3.918292455155	1.807272806821
H	3.644790342631	-4.562379644316	2.379474312406
C	1.667817724217	-3.727680716329	2.219866756493
H	1.305787212775	-4.232490901949	3.110240903948
C	0.813982944178	-2.912866327048	1.487131001851
H	-0.219362121775	-2.818925606084	1.807494816382
O	2.968206604007	0.155426782635	2.042872155591
C	2.590122257140	-0.235645159235	3.370399429558
H	2.054421129870	-1.187507237445	3.313301222716
H	1.918957648475	0.527567075389	3.764833826841
C	3.894049235702	-0.374057136994	4.131757774966
H	3.807625356162	-1.058629909530	4.976687387342
H	4.225344999258	0.598275526591	4.508259995787
C	4.833972666118	-0.878512508293	3.042478732285
H	5.888692438225	-0.708138129375	3.263370079153
H	4.675878828866	-1.946047740952	2.875940584418
C	4.364940456203	-0.094191840690	1.830164031819
H	4.878891193408	0.869456240907	1.745720942731
H	4.481797738407	-0.638055508470	0.891361759380
Li	1.845321078531	0.323003202634	0.466999803257
Li	-2.607674496584	0.002091834770	0.159301072389
O	2.923172209794	1.738246209435	-0.289712555120
C	4.063556439883	3.150158238925	-1.762239881096
H	4.029407098462	3.615081692974	-2.748300543722
H	5.106248172391	2.919897518030	-1.523718588281
C	3.435519968861	4.009064164612	-0.670052249964
H	4.093880239158	4.796251146976	-0.299247415633
H	2.515203539466	4.466748308820	-1.039891686434
C	3.212260818242	1.900161000645	-1.687612929940
H	2.270981717348	2.021970036570	-2.229943885220
H	3.704753902526	0.992291989622	-2.034389807583
C	3.107897827154	2.980080002561	0.400777132985
H	3.930194577194	2.855887973054	1.113878806739
H	2.197032419330	3.213111032031	0.955424213149
O	-3.900794889799	-1.133690380945	1.045047608989
C	-5.263320127098	-1.183932377286	0.602272106846
H	-5.802277424968	-0.328974382802	1.024480717072
H	-5.275070940983	-1.097605481088	-0.485794621999
C	-5.807245645989	-2.502986458578	1.117857256164
H	-5.561306807850	-3.311273326903	0.424752210184
H	-6.888997423862	-2.481447321259	1.254354845467
C	-5.034144452435	-2.668430216713	2.421221931167
H	-4.995058584314	-3.699549644376	2.773530120969
H	-5.477183836780	-2.052874967766	3.208786229793

C	-3.663334652754	-2.137933240462	2.041494802750
H	-3.126277752853	-1.674002410187	2.869688248531
H	-3.034566243816	-2.920599004375	1.603585457781
O	-3.697879954521	1.571641067275	-0.015422857708
C	-3.770734736817	2.485426860842	-1.127048440077
H	-4.425034487838	2.046093077757	-1.883365158986
H	-2.768669333881	2.603228450752	-1.543107967797
C	-4.299521577407	3.788220415452	-0.553604347566
H	-5.393212270403	3.804497717478	-0.563377806442
H	-3.936347923938	4.650732844764	-1.113068903270
C	-3.777430144191	3.742819645229	0.877812471457
H	-4.334841157048	4.381923391938	1.563871975725
H	-2.725144508450	4.030056226022	0.905860216286
C	-3.915279452504	2.272759002912	1.219399326568
H	-3.178594169831	1.928785138905	1.948422578097
H	-4.922241290007	2.035581653919	1.584097354567

140
[Li(thf)$_4$][Li(thf)$_2$][**1**] (^{1}A, C_1): E_{tot} = -2617.66118181

B	-0.691693108570	0.212975718387	-0.248266069505
B	-2.095176632469	1.409576116089	-0.792716675013
C	-0.566595122741	1.548714216468	-1.113006719111
H	-0.355212355234	1.307767917647	-2.158638056091
C	0.270379183663	2.699025629257	-0.611619319372
H	1.327057906916	2.394894545563	-0.532786961273
H	-0.035268192863	2.955789546983	0.407761855742
C	0.247756643158	3.997741496417	-1.439924829131
C	1.110443601876	5.033370255087	-0.721226546348
H	0.712214550553	5.244782857626	0.276028533430
H	1.145441484365	5.976554653373	-1.275545211884
H	2.139573467857	4.675161428291	-0.603740274814
C	0.834704306996	3.747465587886	-2.826947763285
H	0.224653835122	3.034403515913	-3.386437782795
H	1.853075304681	3.347716714319	-2.753947693163
H	0.879503092606	4.675088659130	-3.406021174860
C	-1.172502010944	4.534077915294	-1.584260546461
H	-1.617046806411	4.739013535202	-0.607360962810
H	-1.814085577725	3.805854485387	-2.083198805523
H	-1.176505014732	5.462968182321	-2.164484150806
C	-0.585777245707	-1.246413903645	-0.822762288998
C	-0.342608911927	-2.158790152477	0.251063702809
C	-0.247676089575	-3.532747784161	0.036475242065
H	-0.124100256414	-4.212834322167	0.875922903890
C	-0.297057638290	-4.035446669915	-1.255541122565
H	-0.218803827000	-5.103342938559	-1.431599934170
C	-0.443126906888	-3.153385822650	-2.332101775238
H	-0.461063265365	-3.544111271707	-3.345401242040
C	-0.597232234769	-1.793125211781	-2.115398263237
H	-0.728863122718	-1.141131303487	-2.971531616035
C	-0.377907642898	-0.023165072101	1.278098215451
C	-0.194509487933	-1.428268709029	1.499038860544
C	0.106659005570	-1.945090222389	2.757979205466
H	0.244084340744	-3.015662914187	2.892697935860
C	0.234648599295	-1.093851176530	3.845508738920
H	0.466671578997	-1.488912459808	4.829017455807
C	0.051119780481	0.280158038090	3.661474541980
H	0.136430069136	0.949504029144	4.513142183257
C	-0.241918068419	0.798687048716	2.409384970129
H	-0.378724140075	1.868019491547	2.318709782866
C	-3.193005997644	0.938847363764	-1.828532527169
C	-4.477715605532	1.301726601250	-1.340049274179
C	-5.636392889824	1.044397651798	-2.066892054545
H	-6.607953588607	1.341966899526	-1.681833558386
C	-5.543576149763	0.439486309822	-3.312269742974
H	-6.439851058136	0.247392138125	-3.893044081087
C	-4.290307693180	0.113483043242	-3.831970849462
H	-4.218825832842	-0.325743584440	-4.822570673007

C	-3.136591621586	0.361874194829	-3.100728349338
H	-2.175531760398	0.130693406538	-3.547014700447
C	-2.979952064269	2.155937854167	0.292404797751
C	-4.352353798191	2.016569421986	-0.071944219219
C	-5.375967317260	2.581520727057	0.683331491176
H	-6.412596521692	2.454972560651	0.384375257467
C	-5.067887942756	3.343010286577	1.800968590535
H	-5.858560577521	3.798671033615	2.387430360934
C	-3.732539124847	3.538952407143	2.151756371121
H	-3.487502197750	4.160511213870	3.007530613070
C	-2.713547151639	2.950303979403	1.414433680494
H	-1.691540605179	3.148380603788	1.711056101923
Li	-2.973980544131	-0.600752010733	0.384397145102
O	-3.621947216208	-0.879628670350	2.197077925669
C	-4.173343460869	0.066561333608	3.108327405870
H	-5.260551013530	-0.080752652782	3.176461211094
H	-3.974754515794	1.061804105910	2.717485439021
C	-3.484923361509	-0.249635447843	4.418324484690
H	-2.482731526849	0.181471230976	4.407043968343
H	-4.027163767345	0.132634393438	5.284570153102
C	-3.405486044823	-1.778232739485	4.386251278444
H	-4.267512551218	-2.223911876050	4.888293827059
H	-2.501285692284	-2.149146842945	4.869925808869
C	-3.420172592480	-2.113520636415	2.888575374860
H	-2.476300061457	-2.528940576316	2.536954889475
H	-4.229125393338	-2.808018793174	2.633489056265
O	-4.125067624144	-1.992448031020	-0.342977408026
C	-3.861539959899	-2.778885111695	-1.516987367413
H	-3.267074256381	-3.644894938481	-1.212593689154
H	-3.274752674608	-2.176471746186	-2.208494252013
C	-5.221771453163	-3.168307505005	-2.071980086220
H	-5.560244324278	-2.413115289621	-2.785144093711
H	-5.201881559793	-4.137625822267	-2.572487139274
C	-6.102615993198	-3.146977580091	-0.826881122263
H	-5.974727644704	-4.066362796862	-0.247600509853
H	-7.163636996780	-3.023324417489	-1.049386999889
C	-5.529523269482	-1.962451078641	-0.074669026212
H	-5.943270361074	-1.018747423770	-0.445382391657
H	-5.666592712642	-2.009275287462	1.006516044417
Li	4.502031867752	-0.251649766122	-0.214317020657
O	3.684303243054	0.319952259134	-1.832058072611
C	4.278076050669	0.818163994738	-3.030659769200
H	5.343498050836	0.579730858762	-3.004794069324
H	4.156719835923	1.907963760472	-3.070983493044
C	3.517133157635	0.146449216692	-4.155345738754
H	3.586043955285	0.697011474460	-5.094399494907
H	3.901828554703	-0.864607607293	-4.319754164468
C	2.103947474799	0.101192964852	-3.583178357259
H	1.480998175539	-0.671896599265	-4.031090293112
H	1.604316661611	1.061774454485	-3.721223642191

C	2.341480762532	-0.163123793050	-2.106398534901
H	1.629868828702	0.343831290508	-1.454484515135
H	2.314592006959	-1.230443431841	-1.876238611723
O	6.462631088134	-0.129862458099	-0.466006741712
C	7.282570054409	-1.032800388851	0.289078293479
H	7.959103886119	-1.554095654146	-0.395375844808
H	6.614156214804	-1.763570898645	0.744903528189
C	8.054379514297	-0.181310178216	1.309702104438
H	7.886512689291	-0.517355748077	2.333051723543
H	9.127435263682	-0.232025723505	1.116532851236
C	7.525373256032	1.237524930030	1.075560106034
H	8.280303335642	2.007489151713	1.237366666791
H	6.670499899911	1.439472914254	1.723725708582
C	7.052219209076	1.163897486845	-0.361746543906
H	6.293807648768	1.900498039308	-0.629343491858
H	7.889189377949	1.248025642305	-1.067301774445
O	4.048225212607	0.888729972976	1.254860378782
C	3.437105430201	0.475808464347	2.494789450516
H	4.108545296463	-0.239432353002	2.974212814804
H	2.476712543406	-0.003784494542	2.285173937954
C	3.240181423636	1.755463632209	3.277326983784
H	2.448244618652	1.653038795790	4.017892052547
H	4.165426989414	2.049683713217	3.782495547524
C	2.890139902255	2.734310703837	2.162965553962
H	3.038371266831	3.780177308605	2.433397376634
H	1.851200841296	2.596254236205	1.859559172514
C	3.817927269087	2.294167928785	1.046517661693
H	3.391748873159	2.431554529093	0.051123301787
H	4.784047545146	2.810228511007	1.098847152307
O	4.195698534756	-2.131931130717	0.026889156929
C	4.427043152036	-2.994880972639	-1.098832355321
H	5.439223532450	-3.408037992562	-1.018197225860
H	4.367335340336	-2.394675304940	-2.009555875600
C	3.369657168404	-4.077758097281	-1.007882458953
H	2.434535410724	-3.753083862897	-1.471900719946
H	3.687659945034	-5.007635022001	-1.481063505634
C	3.174514667747	-4.197765556684	0.498258715793
H	3.979346942515	-4.784221372082	0.951509015445
H	2.218342755741	-4.647143141515	0.762126182520
C	3.250763587961	-2.748439095573	0.930778101487
H	2.283252223295	-2.250197229780	0.827819033971
H	3.618924341458	-2.609374180722	1.948376430829

6.3 Lebenslauf

Die persönlichen Daten wurden aus der digitalen Version entfernt.

Fachartikel

03/2018 **A Redox-Active Diborane Platform Performs C(sp^3)–H Activation and Nucleophilic Substitution Reactions**
von T. Kaese, T. Trageser, H. Budy, M. Bolte, H.-W. Lerner und M. Wagner
Chem. Sci. **2018**, *9*, 3881-3891.

01/2018 **Doping Polycyclic Aromatics with Boron for Superior Performance in Materials Science and Catalysis**
von E. von Grotthuss,[a] A. John,[a] T. Kaese[a] und M. Wagner
([a] Diese Autoren haben zu gleichen Teilen an der Arbeit beigetragen)
Asian J. Org. Chem. **2018**, *7*, 37-53.

05/2017 **Deprotonation of a Seemingly Hydridic Diborane(6) to Build a B–B Bond**
von T. Kaese, H. Budy, M. Bolte, H.-W. Lerner und M. Wagner
Angew. Chem. Int. Ed. **2017**, *56*, 7546-7550.

08/2016 **Hydroboration as an Efficient Tool for the Preparation of Electronically and Structurally Diverse N→B-Heterocycles**
von M. Grandl, T. Kaese, A. Krautsieder, Y. Sun und F. Pammer
Chem. – Eur. J. **2016**, *22*, 14373-14382.

04/2016 **Forming B–B Bonds by the Controlled Reduction of a Tetraaryldiborane(6)**
von T. Kaese, A. Hübner, M. Bolte, H.-W. Lerner und M. Wagner
J. Am. Chem. Soc. **2016**, *138*, 6224-6233.

02/2015 **A Preorganized Ditopic Borane as Highly Efficient One- or Two-Electron Trap**
von A. Hübner, T. Kaese, M. Diefenbach, B. Endeward, M. Bolte, H.-W. Lerner, M. C. Holthausen und M. Wagner
J. Am. Chem. Soc. **2015**, *137*, 3705-3714.

Tagungen

03/2018 **255th ACS National Meeting and Exposition, New Orleans, Louisiana**
Vortrag: “Reduction of aryl(hydro)boranes: Versatile bond-formation reactions”

06/2017 **67th Lindau Nobel Laureate Meeting (Chemistry), Lindau, Deutschland**
28 Nobelpreisträger trafen auf 420 Nachwuchswissenschaftler aus aller Welt

03/2016 **251st ACS National Meeting and Exposition, San Diego, Kalifornien**
Vortrag: “Forming new bonds: Ditopic organoboranes in reduction reactions”

6.4 Erklärung über frühere Promotionsverfahren und Versicherung

Erklärung

Ich erkläre hiermit, dass ich mich bisher keiner Doktorprüfung im mathematisch-naturwissenschaftlichen Bereich unterzogen habe.

Frankfurt a. M., den 04.12.2018

_____

Thomas Kaese

Versicherung

Ich erkläre hiermit, dass ich die vorliegende Dissertation mit dem Titel

9-Borafluoren:
Strukturelle Vielfalt durch Reduktion

selbstständig angefertigt und mich anderer Hilfsmittel als der in ihr angegebenen nicht bedient habe, insbesondere, dass alle Entlehnungen aus anderen Schriften mit Angabe der betreffenden Schrift gekennzeichnet sind.

Ich versichere, die Grundsätze der guten wissenschaftlichen Praxis beachtet und keine Hilfe einer kommerziellen Promotionsvermittlung in Anspruch genommen zu haben.

Frankfurt a. M., den 04.12.2018

_____

Thomas Kaese